INTERNATIONAL CONFERENCE ON

ACCELERATORS FOR RESEARCH AND SUSTAINABLE DEVELOPMENT

From good practices towards socioeconomic impact

Conference Material

Volume 3

Full Papers

23–27 May 2022

IAEA Headquarters, Vienna, Austria

IAEA
International Atomic Energy Agency
Atoms for Peace and Development

CN-301
#Accelerators2022
www.iaea.org/events/international-conference-on-accelerators-for-research-and-sustainable-development-2022

DISCLAIMER

The material reproduced here has been supplied by the authors and has not been edited by the IAEA. The views expressed therein remain the responsibility of the named authors and do not necessarily reflect those of the IAEA or its Member States. In particular, neither the IAEA nor any other organization or body sponsoring this event can be held responsible for this material.

Conference material collected and organized by Sotirios Charisopoulos, Physics Section/NAPC, IAEA – Dec. 2022

International Conference on Accelerators for Research and Sustainable Development

From Good Practices Towards Socioeconomic Impact

23-27 May 2022
IAEA Headquarters Vienna, Austria

Conference Material

VOLUME 3

– Full Papers –

Organized by the
International Atomic Energy Agency (IAEA)

DISCLAIMER

The material reproduced here has been supplied by the authors and has not been edited by the IAEA. The views expressed therein remain the responsibility of the named authors and do not necessarily reflect those of the IAEA or its Member States. In particular, neither the IAEA nor any other organization or body sponsoring this event can be held responsible for this material.

Contents

Accelerating a better world[1]

Tens of thousands of accelerators around the world help create radiopharmaceuticals, treat cancer, preserve food, monitor the environment, strengthen materials, understand fundamental physics, study the past, and even disclose crimes.

A first of its kind international conference, Accelerators for Research and Sustainable Development: From Good Practices Towards Socioeconomic Impact was organised by the International Atomic Energy Agency (IAEA) at its headquarters in Vienna from 23 to 27 May. It was held as a hybrid event attended by around 500 scientists from 72 IAEA member states. While focusing mainly on applications of accelerator science and technology, the conference was geared towards accelerator technologists, operators, users, entrepreneurs, and other stakeholders involved in applications of accelerator technologies as well as policy makers and regulators.

"The far-reaching capabilities of accelerator technology help countries progress towards sustainable development," said IAEA director general Rafael Mariano Grossi in his opening address. "IAEA's work with accelerators helps to fulfil a core part of its 'Atoms for Peace and Development' mandate." He also highlighted how accelerator technology plays a critical role in two IAEA initiatives launched over the past year: Rays of Hope, aimed at improving access to radiotherapy and cancer care in low- and middle-income countries, and NUTEC plastics, supporting countries in addressing plastic waste issues in the ocean and on land. Finally, he described IAEA plans to establish an accelerator of its own: a state-of-the-art ion-beam facility in Seibersdorf, Austria that will support research and help educate and train scientists.

The conference included sessions dedicated to case studies demonstrating socioeconomic impact as well as best practices in effective management, safe operation, and the sustainability of present and future accelerator facilities. It showcased the rich diversity in types of accelerators – from

[1] *Meeting report published in CERN Courier, on 25 August 2022, by Sotirios Charisopoulos, Danas Ridikas, Celina Horak and Valeriia Starovoitova, IAEA*

large-scale synchrotrons and spallation neutron sources, or medical cyclotrons and e-beam irradiators used for industrial applications, to small-scale electrostatic accelerators and compact-accelerator based neutron sources – and included updates in emerging accelerator technologies, such as laser-driven neutron and X-ray sources and their future applications. Six plenary sessions featuring 16 keynote talks captured the state of the art in various application domains, accompanied by 16 parallel and two poster sessions by young researchers.

During the summary and highlights session, important developments and future trends were presented:

- Large-scale accelerator facilities under development across the world – notably FAIR in Germany, SPIRAL-2 in France, FRIB in the US, RIBF in Japan, HIAF in China, RAON in Korea, DERICA in Russia and MYRRHA in Belgium – boost the development of advanced accelerator technologies, which are expected to deliver high-impact socioeconomical applications. Substantial interdisciplinary research programmes are foreseen from their beginning, and the IAEA could play an important role by strengthening the links and cooperation between all parties.
- Recent technology developments in Compact-Accelerator Neutron Sources (CANS) or High-Power CANS (HiCANS) are very promising. Among many projects, ERANS at RIKEN in Japan aims to realise a low-cost CANS capable of providing 1012 n/s for applications in materials research and ERANS-III a transportable CANS for testing the structure of bridges. On the HiCANS front, the French SONATE project aims to reach neutron flux levels comparable to the ageing fleet of low and medium power research reactors at least for some applications.
- CANS technology is promising for tools to fight cancer, for example via the Boron Neutron Capture Therapy (BNCT) method. Japan leads the way by operating or constructing 10 such in-hospital based facilities, with only a few other countries, e.g., Finland, considering similar technologies. Recent developments suggest that accelerator based BNCT treatments become soon more acceptable. IAEA could play an important coordinating role and as a technology bridge to developing countries to enable more widespread adoption.
- The role of accelerators in preserving cultural heritage objects and in detecting forgeries is becoming more vital, especially in countries that do not have the required capabilities. Ion-beam analysis and accelerator mass spectrometry techniques are of particular relevance, and, again, the IAEA can assist by coordinating actions to disseminate knowledge, educating the relevant communities, and possibly centralising the demands for expertise.
- The IAEA could simplify the supply of accelerator technologies between the different member states, enabling the installation and operation of facilities in low- and middle-income countries, for example by structuring the scientific and technical accelerators communities, and educating young researchers and technicians via dedicated training schools.
- One of IAEA's projects is to establish a state-of-the-art ion beam facility in Austria. This will enable applied research and provision of analytical services, as well as help educate and train scientists on the diverse applications of ion beams (including the production of secondary particles such as neutrons) and will enhance collaborations with both developed and developing countries.

- Ion-beam analysis (IBA) together with accelerator-mass spectroscopy (AMS) techniques are unique, reliable and cost-effective for Environmental Monitoring and Climate Change Related Studies, for example in characterising environmental samples and investigating isotope ratio studies for chronology and environmental remediation AMS facilities with smaller footprints have increased their distribution worldwide, resulting in accessible and affordable measurements for interdisciplinary research, while other IBA techniques offer efficient analytical methods to characterise the chemical composition of particles from air pollution.
- Materials science and accelerators are now moving ahead hand in hand, from characterisation to modification of technologically important materials including semiconductors, nano-materials, materials for emerging quantum technologies and materials relevant to energy production. Testing materials with accelerator-based light and heavy-ion beams remains a unique possibility in the case of fusion materials and offers much faster radiation-damage studies than irradiation facilities at research reactors. Equally important is the accelerator-assisted creation of gaseous products such as hydrogen and helium that allows testing the radiation resilience in unmoderated neutron systems such as fast fission and fusion reactors.
- New developments in electron-beam accelerators for industrial applications were also mentioned, in particular their application to pollution control. E-beam system technologies are also widely employed in food safety. Reducing spoilage by extending the shelf-life of foods and reducing the potential for pathogens in and on foods will become major drivers for the adoption of these technologies, for which a deeper understanding of the related effects and resistance against radiation is mandatory.

Accelerator technologies evolve very fast, presenting a challenge for regulatory bodies to authorise and inspect accelerator facilities and activities. This conference demonstrated that thanks to recent technological breakthroughs in accelerator technology and associated instrumentation, accelerators are becoming an equally attractive alternative to other sources of ionising radiation such as gamma irradiators or research reactors, among other conventional techniques. Based on the success of this conference, it is expected that the IAEA will start a new series of accelerator community gatherings periodically from now on every two to three years.

Useful links

Conference website:	(main)	https://www.iaea.org/events/accconf22
	(indico)	https://conferences.iaea.org/event/264/
Conference App pages:		https://iaea.event.do/#/e/5542/f/35897
Photos of the conference (all days):		https://photos.app.goo.gl/azkGRUnvmB6QtpgK7
Applications of Accelerators and Other Sources of Ionizing Radiation: IAEA Bulletin (Vol. 63/2, May 2022)		https://www.iaea.org/bulletin/63-2

Note on how to use this document

- To access the paper of interest, simply click the corresponding Abstract No. given in the List of Submitted Full Papers (pages 39 – 44). The reader is then guided to the corresponding paper. By clicking the left arrow on the upper-left corner of the first page of the linked full paper, the reader returns to the List of Submitted Full Papers, where the Abstract No, together with the authors and the title are given.

Conference Profile

Programme Committee:

- Nicolas Alamanos, CEA, France
- Giuliana Aquilanti, Elettra Sincrotrone Trieste, Italy
- Ceri Brenner, ANSTO, Australia
- Thomas Gutberlet, Forschungszentrum Julich, Germany
- Cornelia Hoehr, TRIUMF & University of Victoria, Canada
- Andrew Hutton, JLab, USA
- Milko Jaksic, Ruder Boskovic Institute (RBI), Croatia
- Joseph Mittendorfer, High Tech Consulting, Austria

IAEA Secretariat:

Scientific Secretaries, NAPC:	Sotirios Charisopoulos
	Valeriia Starovoitova
	Danas Ridikas
	Celina Horak
Event Organizer, MTCD:	Julie Zellinger
Administrative Support, NAPC:	Ekaterina Nazarova
	Tatiana Kornelyuk
	Olha Bilous

Location of the Event:

International Atomic Energy Agency, Vienna International Centre (VIC)

Building M, Board Rooms A, B/M1

Wagramer Strasse 5, A-1400 Vienna, Austria. Tel.: (+43 1) 2600 21330

Working Language: English

Conference website: https://www.iaea.org/events/accconf22 (main)
https://conferences.iaea.org/event/264/ (indico)

A. Background

The International Atomic Energy Agency (IAEA) organized the First International Conference on Accelerators for Research and Development: from good practices towards socioeconomics impact. Such a Conference was long awaited by the Member States to address important needs in our high-tech oriented society, where particle accelerators have become indispensable.

Nowadays, more than 20,000 particle accelerators operating world-wide are used for commercial applications, either in the medical (radiotherapy treatments) or industrial sectors (materials modification). Although only a few hundred accelerators are used for scientific research, the knowledge and technological spin-offs gained from these facilities drive the development of commercial applications and support the research and development needs of a diverse range of fields, including fundamental and applied science. The current trend is to utilize accelerators in a dedicated way to support specific high technology application areas. The main demand from researchers is for high quality X ray, neutron, and ion beams to engage in cutting-edge research in energy, food and agriculture, environment, biology, medicine, forensics, cultural heritage, materials science, and many other areas. Accelerators also play a key role in capacity building, provide education and training both in academia and industry, contributing to the solution of problems of modern society and to increased competitiveness of local economies.

Numerous innovations and accomplishments in the field of accelerator-based research and development as well as diverse applications have been already acknowledged, however it is now time to take a comprehensive look at their socioeconomic impact, assess their sustainability and ability to meet future challenges. The IAEA has been implementing programmatic activities that provide interested Member States with platforms to exchange information on new trends and applications in accelerator-based nuclear science and technology. Indeed, the IAEA successfully implements a few programmes with direct relevance to use of particle accelerators such as Nuclear Science, Radioisotope Production and Radiation Technology, Human Health, and Environment. In addition, direct support, and assistance to the Member States in the area of accelerator-based research and applications is also provided through the IAEA Technical Cooperation Programme.

B. Purpose and Objectives

The Conference aimed primarily to present an international stage for discussing accelerator applications in research and industry, foster exchange of information on best practices in accelerator facility utilization and management, and to provide a showcase how achievements and experience attained with accelerator technologies contribute to a sustainable development. All types of accelerators will be considered: from low-energy ion-beam electrostatic accelerators to cyclotrons, from compact accelerator-based neutron sources to large-scale spallation facilities, from electron-based irradiation facilities to synchrotron light sources, and many others.

Special emphasis was also be given in accelerator applications of large societal impact such as human health, environmental monitoring, cultural heritage, food quality, energy sector, forensics, nuclear security, and others promoting economic development. The Conference provided a unique opportunity to achieve the following specific objectives:

- **To disseminate**:
  - New knowledge and technologies developed through accelerator-based research and applications in a wide spectrum of scientific areas.
  - Best practices in establishing new accelerator facilities, and ensuring their effective management and sustainability

- **To review**:
  - Key developments in particle accelerator technologies, established and emerging ones, and their role in enhancing innovations
  - National, regional, and global initiatives for implementing proven accelerator applications that lead to socio-economic benefits and strengthen capacity building in Member States; and

- **To serve**:
  - As a composite platform through which academia and industry can foster new initiatives for ensuring the success of accelerator applications in addressing the emerging challenges in multiple disciplines.
  - As a bridge to enhance existing and establish new collaborations among scientists and institutions from Member States aiming at benefiting from accelerator technologies to face challenges in a series of problems of modern society.

C. Themes and Topics

The IAEA welcomed high-quality, well structured, abstracts and papers in all fields of accelerator-based research and applications which were grouped under three main themes/tracks:

1. Cutting-edge scientific results and innovation in applications
2. Success stories and case studies demonstrating socioeconomic impact
3. Best practices in effective management, safe operation, and sustainability of accelerator facilities, including establishment of new facilities

The scope of the conference was meant to cover, but not limited to, the following topical areas:

- Biology and biophysics
- Cultural heritage
- Engineering applications (including energy sector)
- Environmental applications (including geosciences and climate change)
- Food and agriculture
- Forensics and security applications
- Information and quantum technologies
- Materials research (including materials damage studies)
- Nuclear data and modelling benchmarks
- Radioactive beam applications

- Medical applications (including radioisotope production and Boron Neutron Capture Therapy)
- R&D on new accelerator and alternative technologies (including Compact Accelerator based Neutron Sources)
- Best practices in and lessons learned from:
  - Education and training with accelerators
  - Establishment of new facilities
  - Facility management and user programmes
  - Facility operations and maintenance
  - Outreach, knowledge preservation and management
  - User access programmes and regional/interregional networking
  - Strategic considerations for sustainability and self-reliance

D. Structure

The topical areas were discussed under the three main themes outlined in section C. A series of plenary sessions addressed the most interesting and crucial topics and the meeting programme included invited keynote speakers from academia and industry, giving oral presentations and participating in panel discussions and round table sessions. Poster sessions were organized to allow ample time for discussion and interaction. In addition, the participants had the opportunity to interact with conference exhibitors and participate in technical tour(s). Finally, a closing panel session reviewed the main conclusions drawn in the plenary sessions and summarized recommendations for the future development of radiation sciences and technologies using particle accelerators.

E. Outcomes

The conference achieved strengthening contacts and fostering cooperation among accelerator-based science and application researchers, accelerator manufacturers, facility operators and the coordinators of academic programmes in the accelerator sciences, leading to a comprehensive review of the status of accelerator- based research and applications. The conference also contributed to generate ideas that will form the basis of future IAEA programmes in the area of research and applications using accelerator technologies.

F. Target Audience

This conference focused on applications of accelerator science and technology, which is a multidisciplinary area covering many different branches from accelerator and nuclear physics, materials science, biology, environment, medicine, cultural heritage to engineering and industrial applications. Accordingly, the target audience for this conference comprised, but not limited to:

- research scientists engaged in accelerator-based research and applications
- accelerator operators and users
- entrepreneurs or stakeholders involved in applications of accelerator technologies
- policy makers and regulators.

TIMETABLE – Sessions Overview

Monday, 23 May 2022

Time	Session No.	Session Title / Break	Venue
10:00 – 10:30		Opening Session	M Plenary
10:30 – 11:15	Session 1 Plenary Session	Accelerators for the Environment	M Plenary
11:15 – 12:45	Session 2 Plenary Session	Accelerators for Medical Radioisotopes, Energy Production and Nuclear Research	M Plenary
12:45 – 14:00		Lunch Break	
14:00 – 15:30	Session 3.A Parallel Session	Advances in Accelerator Technologies	Board Room A
14:00 – 15:30	Session 3.B Parallel Session	Accelerators for Medical Applications - 1	M Plenary
15:30 – 16:00		Coffee / Tea Break	
16:00 – 17:30	Session 4.A Parallel Session	Accelerators for Environmental Monitoring	Board Room A
16:00 – 17:30	Session 4.B Parallel Session	Accelerators for Medical Applications - 2	M Plenary
18:00 – 20:00		Welcome Reception	M-Building

Tuesday, 24 May 2022

Time	Session No.	Session Title / Break	Venue
09:00 – 10:30	Session 5 Plenary Session	Accelerators for Neutron Therapy, Cultural Heritage, Innovation and Education	M Plenary
10:30 – 11:00		Coffee / Tea Break	
11:00 – 12:30	Session 6.A Parallel Session	Accelerators for BNCT and Cultural Heritage	Board Room A
11:00 – 12:30	Session 6.B Parallel Session	Best Practices in Using Accelerators for R&D, Education, Environmental and Industrial Applications	M Plenary
12:30 – 14:00		Lunch Break	
14:00 – 15:30	Side Event 1	Accelerator-Based Sources of Radiation: Recent Developments	Board Room A
14:00 – 15:30	Poster Session 1	**All posters** (see separate page)	M-Building 2nd Floor
15:30 – 16:00		Coffee / Tea Break	
16:00 – 17:30	Session 7.A Parallel Session	IBA Facilities and their R&D Program	Board Room A
16:00 – 17:30	Session 7.B Parallel Session	Regulatory Aspects of Accelerator Facilities	M Plenary

Wednesday, 25 May 2022

Time	Session No.	Session Title / Break	Venue
09:00 – 10:30	Session 8 Plenary Session	Accelerators for Nuclear Data and Materials Research	M Plenary
10:30 – 11:00		Coffee / Tea Break	
11:00 – 12:30	Session 9.A Parallel Session	Accelerators for Nuclear Data	Board Room A
11:00 – 12:30	Session 9.B Parallel Session	Radiation Technologies and their Applications	M Plenary
12:30 – 14:00		Lunch Break	
14:00 – 15:30	Side Event 2	Collaborating Centres of IAEA	Board Room A
14:00 – 15:30	Side Event 3	Women in Accelerator-based Science	M-Building 2nd Floor
15:30 – 16:00		Coffee / Tea Break	
16:00 – 17:30	Session 10.A Parallel Session	Applications of Heavy Ion Beams	Board Room A
16:00 – 17:30	Session 10.B Parallel Session	Societal Applications of Accelerators and Sustainable Development	M Plenary

Thursday, 26 May 2022

Time	Session No.	Session Title / Break	Venue
09:00 – 10:30	Session 11 Plenary Session	Emerging Accelerator Technologies – Accelerator Technologies for Food Safety	M Plenary
10:30 – 11:00		Coffee / Tea Break	
11:00 – 12:30	Session 12.A Parallel Session	Future Accelerator-based Neutron Sources	Board Room A
11:00 – 12:30	Session 12.B Parallel Session	Electron Beams and Applications	M Plenary
12:30 – 14:00		Lunch Break	
14:00 – 15:30	Side Event 4	Promoting Self-Reliance and Sustainability of National Nuclear Institutions Operating Accelerator Facilities	Board Room A
14:00 – 15:30	Poster Session 2	**All posters** (see separate page)	M-Building 2nd Floor
15:30 – 16:00		Coffee / Tea Break	
16:00 – 17:30	Session 13.A Parallel Session	Selected Applications of Accelerator-based Analytical Techniques	Board Room A
16:00 – 17:30	Session 13.B Parallel Session	Accelerators for Energy and other Applications	M Plenary

Friday, 27 May 2022

Time	Session No.	Session Title / Break	Venue
09:00 – 10:30	Session 14 Plenary Session	Accelerators and Multidisciplinary Research and Applications	M Plenary
10:30 – 11:00		Coffee / Tea Break	
11:00 – 11:30	Session 15 Plenary Session	Conference Summary and Highlights	M Plenary
11:30 – 12:00	Session 16 Plenary Session	Conference Closing and Award Ceremony	M Plenary

MONDAY, 23 May 2022

10:00 – 10:30 **OPENING SESSION** **M Plenary**

Time	Name	Affiliation & Designating Member State	
10:00–10:05	M. Denecke	Director NAPC, IAEA	Welcome Address
10:05-10:15	R. M. Grossi	Director General, IAEA	Opening Statement
10:15-10:25	N. Mokhtar M. Chudakov H. Liu	DDG-NA, IAEA DDG-NE, IAEA DDG-TC, IAEA	Opening Remarks

10:30 – 11:15 **Plenary Session 1: Accelerators for the Environment** **M Plenary**

Chairpersons: D. Ridikas (IAEA) and C. Horak (IAEA)

Time	Abstract No.	Name	Affiliation & Designating Member State	Title
11:15–11:45	224	D. Cohen	ANSTO, Australia	Accelerators for Environmental Monitoring and Climate Change Related Studies
	207	A. Chmielewsi	INCT, Poland	Electron Accelerator-Based Systems for Air, Water and Soil Pollution Control Studies

10:00 – 10:30 **Plenary Session 2: Accelerators for Medical Radioisotopes, Energy Production and Nuclear Research** **M Plenary**

Chairpersons: D. Ridikas (IAEA) and C. Horak (IAEA)

Time	Abstract No.	Name	Affiliation & Designating Member State	Title
11:15–11:45	209	C. S. Cutler	BNL, USA	50 Years of Isotope Production via High Energy Accelerators at Brookhaven National Laboratory
11:45–12:15	223	H. Ait Abderrahim	SCK CEN, Belgium	Realization of a new Research Infrastructure in Belgium: MYRRHA - Present Status and Focus on Latest Developments of MYRRHA ADS Accelerator
12:15–12:45	208	B. Sharkov	JINR, Russian Federation	Large Scale Accelerator Facilities for Nuclear Research and Practical Applications
12:45–14:00		Lunch Break		

14:00 – 15:30 **Parallel Session 3.A: Advances in Accelerator Technologies** Board

Chairpersons: N. Alamanos (CEA, France) and S. Charisopoulos (IAEA) Room A

Time	Abstract No.	Name	Affiliation & Designating Member State	Title
14:00–14:15	204	J. G. Weisend II	ESS, Sweden	The European Spallation Source Accelerator: Overview and Status
14:15–14:30	49	B. Hornberger	Lyncean Technologies USA	Recent Developments in Compact X-ray and Gamma-ray Sources Based on Inverse Compton Scattering
14:30–14:45	101	S. Lauber	GSI, Germany	Alternating Phase Focusing Beam Dynamics for Drift Tube Linacs
14:45–15:00	190	M. Fedurin	BNL, USA	Novel Accelerator Concept Utilizing Cyclotron Resonance (eCRA)
15:00-15:15	177	I. Strydom	iThemba LABS, South Africa	An Overview of the South African Isotope Facility (SAIF)
15:15-15:30		Questions and Answers		
12:45–14:00		Coffee / Tea Break		

14:00 – 15:30 **Parallel Session 3.B: Accelerators for Medical Applications -1** M Plenary

Chairpersons: C. S. Cutler (BNL, USA) and V. Starovoitova (IAEA)

Time	Abstract No.	Name	Affiliation & Designating Member State	Title
14:00–14:15	44	N. van der Meulen	PSI, Switzerland	The Use of PSI's High Intensity Proton Accelerator (HIPA) Complex Towards Medical-Radionuclide Development
14:15–14:30	183	A. Gerbershagen	University of Groningen, Netherlands	The New Particle Therapy Research Center (PARTREC) at Univ. Medical Center Groningen
14:30–14:45	73	G. Pupillo	INFN-LNL, Italy	Activities on the Cyclotron-based Production of Innovative Radionuclides: Experience at the Legnaro National Laboratories of INFN
14:45–15:00	124	P. Fernandes Costa Jobim	Federal Univ. Rio Grande do Sul, Brazil	IBA Techniques & Neuroscience: What's Next?
15:00-15:15	136	C. N. Coleman	Int. Cancer Expert Corps, USA	Treatment, not Terror: A Unique Cancer Treatment for Developing Novel Linear Accelerators for Resource-limited Settings
15:15-15:30		Questions and Answers		
12:45–14:00		Coffee / Tea Break		

16:00 – 17:30 **Parallel Session 4.A: Accelerators for Environmental Monitoring** Board

Chairpersons: S. Merchel (VERA, Austria) and R. Padilla Alvarez (IAEA) Room A

Time	Abstract No.	Name	Affiliation & Designating Member State	Title
16:00–16:15	186	W. E. Kieser	University of Ottawa, Canada	Accelerator Mass Spectrometry: An Analytical Tool with Applications for Sustainable Society
16:15–16:30	70	M. Santoso	BATAN, Indonesia	Characteristics of Fine Particulates of Two Largest Cities in Indonesia Using IBA
16:30–16:45	147	L. Popa-Simil	LAAS, USA	Ion beam Usage in Environmental Characterization
16:45–17:00	45	M. Roumie	LAEC/CNRS, Lebanon	Elemental Characterization of PM2.5 Aerosol Samples in Four Mideastern Cities and Source Apportionment Investigation
17:00-17:15	86	S. Pollastri	Elettra Sincrotrone, Italy	A Combined XRF and XANES Study on Bottom Ashes from Municipal Solid Waste Incinerator
17:15-17:30		Questions and Answers		

16:00 – 17:30 **Parallel Session 4.B: Accelerators for Medical Applications -2** M Plenary

Chairpersons: C. Hoehr (TRIUMF, Canada) and A. Jalilian (IAEA)

Time	Abstract No.	Name	Affiliation & Designating Member State	Title
16:00–16:15	125	E. Punzón-Quijorna	JSI, Slovenia	PIXE Reveals Crucial Information in Hip Endoprostheses Failures. MeV Ion Beams for Improving Medical Diagnostics
16:15–16:30	158	T. Pinheiro	IST/Univ. de Lisboa, Portugal	Metallacarboranes for Proton Therapy Using Research Accelerators
16:30–16:45	95	R. Khatun	BAEC, Bangladesh	Dosimetric Verification of Radiotherapy Treatment Planning System Using Thorax Phantom
16:45–17:00	52	D. Kottuparamban	Molecular Cyclotrons, India	Socioeconomic Impact of a Medical Cyclotron in Kerala, India
17:00-17:15	29	S. M. de Carvalho	NCNE, Brazil	Current Status and Perspectives of Cyclotron Facilities in Brazil and the Socioeconomic Impact.
17:15-17:30		Questions and Answers		

18:00-20:00 **WELCOME RECEPTION** M-building Ground Floor

TUESDAY, 24 May 2022

9:00 – 10:30 Plenary Session 5: Accelerators for Neutron Therapy, Cultural Heritage, Innovation and Education — M Plenary

Chairpersons: G. Aquilanti (Elettra, Italy) and I. Swainson (IAEA)

Time	Abstract No.	Name	Affiliation & Designating Member State	Title
9:00–9:30	210	H. Kumada	University of Tsukuba, Japan	Current Status of Compact Accelerator-based Neutron Sources for Boron Neutron Capture Therapy in the World
9:30–10:00	212	L. Beck	CEA, France	Use of Accelerators to Preserve Cultural Heritage Objects and Detect Forgeries
10:00–10:30	205	A. Strasser	Aerial-CRT, France	Best Practices in Establishing and Running Accelerator Facilities to Support Research, Education, and Commercial Uses
10:30–11:00		Coffee / Tea Break		

11:00 – 12:30 Parallel Session 6.A: Accelerators for Boron Neutron-Capture Therapy (BNCT) and Cultural Heritage — Board Room A

Chairpersons: G. Aquilanti (Elettra, Italy) and I. Swainson (IAEA)

Time	Abstract No.	Name	Affiliation & Designating Member State	Title
11:00–11:15	131	A. Kreiner	CNEA, Argentina	Review of the Different Accelerator-based BNCT Facilities Worldwide and an Assessment According to the Alara Criterion
11:15–11:30	140	S. Taskaev	Budker Inst., Russian Federation	Accelerator-based Neutron Source for Boron Neutron Capture Therapy & other Applications
11:30–11:45	94	I. Carlomagno	Elettra Sincrotrone, Italy	X-ray Investigations on Ancient Gold Coins: Synchrotron Radiation Contribution to History and Numismatics
11:45–12:00	10	D. M. Atwa Khalil	NILES, Egypt	Synchrotron ... based Investigations of Colored Layers, Binding Materials and Resins of the God Ptah-Sokar-Osiris Wooden Statuette ... Dating Back to 26th Pharaonic Dynasty
12:00-12:15	121	V. Corregidor	Univ. de Lisboa, Portugal	Characterization of Cultural Heritage Using a Micro-beam
12:15-12:30		Questions and Answers		
12:30–14:00		Lunch Break		

11:00 – 12:30 **Parallel Session 6.B: Best Practices in using Accelerators for R&D, Education, Environmental & Industrial Applications** M Plenary

Chairpersons: D. Cohen (ANSTO, Australia) and N. Skukan (IAEA)

Time	Abstract No.	Name	Affiliation & Designating Member State	Title
11:00–11:15	24	O. Riabukhin	Ural Fed. Univ, Russian Federation	The Practice of Electron and Proton Accelerators Utilizing for Industry, Education and Science
11:15–11:30	181	S. H. Park	Korea Univ. Sejong, Rep. of Korea	Use of Accelerators for Research and Training in the University Environment
11:30–11:45	60	P. Foka	GSI, Greece	Heady Ion Therapy MasterClass School and Capacity Building for Future Ion Research and Therapy Facilities
11:45–12:00	230	M. Pivi	MedAustron, Austria	The MedAustron Particle Therapy Center
12:00-12:15	116	F. Zanini	Elettra Sincrotrone, Italy	Life Cycle Assessment
12:15-12:30		Questions and Answers		
12:30–14:00		Lunch Break		

14:00 – 15:30 **Side Event 1: Accelerator-based Sources of Radiation: Recent Developments** M Plenary

Chairpersons: S. Pillai (Texas A&M Univ., USA) & V. Starovoitova (IAEA)

Time	Abstract No.	Name	Affiliation & Designating Member State	Title
14:00-14:10		S. Norris	DOE/NNSA, USA	Opening Remarks
14:10–14:30	236	J. Schwindling	CEA, France	Compact Accelerator-based Neutron Sources: recent developments
14:30–14:50	237	A.-L. Lamure	RadiaBeam Technologies USA	Electron Beams for research and industrial applications
14:50–15:10	238	A. Pierard	IBA, Belgium	The new generation of sustainable X-ray irradiators
15:10–15:30		Round Table Discussion - Questions and Answers		
15:30–16:00		Coffee / Tea Break		

14:00 – 15:30	Poster Session 1	All posters (see separate page)	M-Building (2nd Floor)

16:00 – 17:30 **Parallel Session 7.A: IBA Facilities and their R&D Programmes** Board Room A

Chairpersons: E. Da Costa Alves (U. de Lisboa, Portugal) & N. Skukan (IAEA)

Time	Abstract No.	Name	Affiliation & Designating Member State	Title
16:00–16:15	108	V. Rigato	LNL/INFN, Italy	Multidisciplinary Physics with MeV Ion Beams at the Laboratori Nazionali di Legnaro ...
16:15–16:30	229	S. Charisopoulos	IAEA	The IAEA Ion Beam Facility (IBF) project
16:30–16:45	118	I. Bogdanovic Radovic	RBI, Croatia	Development and Applications of the Secondary Ion Mass Spectrometry with MeV Ions (MeV SIMS) Technique at RBI Accelerator
16:45–17:00	151	A. Karydas	NCSR Demokritos, Greece	Applications of Proton-induced X-rays at the Tandem Accelerator Lab. of NCSR "Demokritos"
17:00-17:15	19	R. O. Barrachina	CNEA, Argentina	Six Decades of R&D with Accelerators in the Dept. of Interaction of Radiation with Matter of the Bariloche Atomic Center
17:15-17:30		Questions and Answers		

16:00 – 17:30 **Parallel Session 7.B: Regulatory Aspects of accelerator facilities** M Plenary

Chairpersons: R. P. Jimenez (IAEA) & N. Ramamoorthy (Indep. Consultant, India)

Time	Abstract No.	Name	Affiliation & Designating Member State	Title
16:00–16:15	47	M. Heimann	CNSC-CCSN, Canada	Agile Regulatory Oversight: Adapting Regulations to Accommodate Rapidly Changing Accelerator Technology
16:15–16:30	98	F. Schmitz	Bel V, Belgium	Licensing Unconventional Accelerator Projects: A Quest for the Safest Compromise
16:30–16:45	56	G. Rabi	Autoridad Regulatoria Nuclear, Argentina	Regulatory Control at the Construction Stage of a Radiopharmaceuticals Production Facility with Cyclotron in the Context of Covid-19 Pandemic
16:45–17:00	78	G. Garcia-Fernandez	Universidad Politecnica de Madrid, Spain	Commissioning of Operational Radiation Protection in Compact Proton Therapy Centers (CPTC) with Small Accelerators
17:00-17:30		Questions and Answers		

WEDNESDAY, 25 May 2022

9:00 – 10:30 Plenary Session 8: Accelerators for Nuclear Data and Materials Research — M Plenary

Chairpersons: F. Ott (CEA, France) and A. Koning (IAEA)

Time	Abstract No.	Name	Affiliation & Designating Member State	Title
9:00–9:30	213	M. Rubel	Royal Inst. of Technology, Sweden	Accelerator Techniques and Nuclear Data needs for IBA of wall Materials for Fusion reactors
9:30–10:00	218	Y. Wang	Los Alamos National Lab, USA	Application of Accelerators in Nanomaterials Research
10:00–10:30	220	Z. Siketic	Ruđer Bošković Institute, Croatia	Sustainability of the Tandem Accelerator Facility at the Ruđer Bošković Institute
10:30–11:00		Coffee / Tea Break		

11:00 – 12:30 Parallel Session 9.A: Accelerators for Nuclear Data — Board Room A

Chairpersons: M. Rubel (Royal Inst. of Technology, Sweden) & A. Koning (IAEA)

Time	Abstract No.	Name	Affiliation & Designating Member State	Title
11:00–11:15	232	J.C. Sublet	IAEA	Radiation Damages Bohr' s Metrics: Accelerator & Elemental Landscapes
11:15–11:30	154	N. Patronis	Univ. of Ioannina, Greece	Status Report of the n_TOF Facility after the 2nd CERN long Shutdown Period
11:30–11:45	157	R. Vlastou-Zanni	National Technical Univ. Athens, Greece	The Neutron Facility at NCSR "Demokritos" and Neutron Activation Research Activities of NTUA
11:45–12:00	109	P. Ström	Uppsala University, Sweden	Ion Accelerators for Modification and Analysis of Materials: Present Status and an Outlook Towards the Future
12:00-12:15	132	A. Widdowson	UKAEA, United Kingdom	Determination of Fuel Retention in Tokamaks by Accelerator-based Methods
12:15-12:30		Questions and Answers		
12:30–14:00		Lunch Break		

11:00 – 12:30 **Parallel Session 9.B: Radiation Technologies and their applications.** M Plenary

Chairpersons: A. Chmielewski (INCT, Poland) and V. Starovoitova (IAEA)

Time	Abstract No.	Name	Affiliation & Designating Member State	Title
11:00–11:15	92	K. Howie	Texas A&M University, USA	Electron Beam Technology for Preserving Quality Attributes of Mandarins for Enhancing Export Potential
11:15–11:30	159	D. Kaoumi	North Carolina State Univ., USA	The Use of In-situ Transmission Electron Microscopy to Investigate Microstructure Evolution under Ion Irradiation
11:30–11:45	198	R. Schwarz	Pacific Northwest Nat. Lab., USA	Penelope-based User-Friendly Fast Interface for Calculating Distribution in Irradiated Products
11:45–12:00	32	D. Chmielewska-Śmietanko	Inst. of Nucl. Chemistry & Technology, Poland	Application of Electron Beam Accelerator for Preservation Biodeteriorated Cultural Heritage Paper-Based Objects: Multiparametric Analysis
12:00-12:15	163	S. Ramarad	Heriot-Watt University, Malaysia	Rubber Recycling: Compatibilization of Waste Tire Rubber/Poly(ethylene-co-vinyl acetate) Blends Using Liquid Rubber and Electron Beam Irradiation
12:15-12:30		Questions and Answers		
12:30–14:00		Lunch Break		

14:00 – 15:30 **Side Event 2: Collaborating Centres of IAEA** Board Room A

Chairpersons: A. Simon (IAEA) and B. S. Han (IAEA)

Time	Abstract No.	Name	Affiliation & Designating Member State	Title
14:00-14:15	240	S. Hollins	ANSTO, Australia	New and Advanced Techniques and Applications of Nuclear Science & Technology towards a Sustainable Environment
14:15–14:30	241	M. Kiskinova	Elettra Sincrotrone, Italy	The IAEA-Elettra Collaborating Center
14:30–14:45	243	L. Bertrand	ENS Paris-Saclay, France	Implementation of the IAEA Collaborating Center "Atoms for Heritage" at the Université Paris-Saclay
14:45–15:00	242	R. Nchodu	iThemba LABS, South Africa	iThemba LABS: The IAEA Collaborating Centre for Accelerator Based Scientific Research and Applications
15:00–15:15	244	S. Pillai	Texas A&M University, USA	The National Center for Electron Beam Research at Texas A&M University - Two Decades of Advancing Electron Beam and X-ray Technologies Around the World
15:15–15:30		Round Table Discussion - Questions and Answers		
15:30–16:00		Coffee / Tea Break		

14:00 – 15:30 **Side Event 3: Women in Accelerator-based Science** M Plenary

Chairpersons: C. S. Cutler (BNL, USA) and A. Peeva (IAEA)

Time	Abstract No.	Name	Affiliation & Designating Member State	Title
14:00-14:10		C.S. Cutler	BNL, USA	New and Advanced Techniques and Applications of Nuclear Science & Technology towards a Sustainable Environment
14:10–14:20		J. Donner	SGIM, IAEA	The IAEA-Elettra Collaborating Center
14:20–15:20		Panel Discussion	Moderator: **A. Peeva** (IAEA) Participants: **D. Cohen** (ANSTO, Australia), **N. Alamanos** (CEA, France), **S. Carvalho** (NCNE, Brazil), **C. Gutierrez** (Elettra, Italy; recipient of the Marie Curie Fellowship Programme)	
15:20–15:30		Round Table Discussion - Questions and Answers		
15:30–16:00		Coffee / Tea Break		

16:00 – 17:30 **Parallel Session 10.A: Applications of heavy ion beams** Board Room A

Chairpersons: B. Sharkov (JINR, Russian Federation) and R. Padilla Alvarez (IAEA)

Time	Abstract No.	Name	Affiliation & Designating Member State	Title
16:00–16:15	179	P. Kluth	ANU, Australia	Swift Heavy Ion Modified Materials: Applications and Characterisation Using Synchrotron Small Angle X-ray Scattering
16:15–16:30	69	M. Wagner	GSI, Germany	3D Nanochannel Networks Fabricated with Ion Track-Etch Technology and Their Applications
16:30–16:45	233	N. Pessoa Barradas	IAEA	Specific Considerations and Guidance for the Establishment of Ionizing Radiation Facilities
16:45–17:00	195	M. Lang	Univ. of Tennessee, USA	Investigating Radiation Effects in Materials Using State-of-the-Art Particle Accelerators
17:00-17:15	165	C. Vyas	MSU (USA)/India	Isotope Harvesting Project: from White Paper to Implementation
17:15-17:30		Questions and Answers		

16:00 – 17:30 **Parallel Session 10.B: Societal Applications of Accelerators and Sustainable Development** M Plenary

Chairpersons: F. Zanini (Elettra Sincrotrone, Italy) and K. Kanaki (IAEA)

Time	Abstract No.	Name	Affiliation & Designating Member State	Title
16:00–16:15	189	S. Norris	DOE/NNSA, USA	How Support for Machine-Based Sources of Radiation Contributes to Sustainable Development
16:15–16:30	58	B. Nsouli	LAEC, Lebanon	On the Use of Ion and Cluster Beams Analysis at LAEC for Forensic Sciences: Infrastructure and Applications
16:30–16:45	106	A. Magazinik	CERN, Switzerland	Societal Impact of the Compact Linear Collider Study
16:45–17:00	74	T. Edgecock	University of Huddersfield, U.K.	IFAST Accelerators for Societal Application
17:00-17:15	54	B. List	DESY, Germany	Sustainability Studies for Linear Colliders
17:00-17:30		Questions and Answers		

THURSDAY, 26 May 2022

9:00 – 10:30 Plenary Session 11: Emerging Accelerator Technologies – Accelerators for Food Safety and Security. — M Plenary

Chairpersons: T. Gutberlet (FZ Jülich, Germany) and S. Charisopoulos (IAEA)

Time	Abstract No.	Name	Affiliation & Designating Member State	Title
9:00–9:30	219	Y. Otake	RIKEN, Japan	RIKEN Accelerator-driven Compact Neutron Systems and RANS Project
9:30–10:00	214	M. Roth	IKP, TU Darmstadt, Germany	Laser-driven Ion Accelerators: Unique Beams and Compact Neutron Sources
10:00–10:30	217	S. Pillai	Texas A&M University, USA	Accelerator Technologies for Food Safety and Food quality: Response of Microbial Populations to Ionizing Technologies
10:30–11:00		Coffee / Tea Break		

11:00 – 12:30 Parallel Session 12.A: Future Accelerator-based Neutron Sources — Board Room A

Chairpersons: A. Kreiner (CNEA, Argentina) & H. Ben Abdelouahed (IAEA)

Time	Abstract No.	Name	Affiliation & Designating Member State	Title
11:00–11:15	129	N. Mayordomo	HZ Dresden-Rossendorf, Germany	CANS Production of Technetium-99m and Technetium-101
11:15–11:30	27	R. Frost	Lund University, Sweden	A Compact Accelerator Driven Neutron Source at the Nuclear-Applications Laboratory, Lund University
11:30–11:45	221	F. Ott	CEA, France	The SONATE Project, a New Neutron Scattering Platform for Materials Science Research
11:45–12:00	77	A. Maffini	Politecnico di Milano, Italy	Towards Compact Laser-Driven Accelerators: Exploring the Potential of Advanced Double-Layer Targets
12:00-12:15	227	I. Swainson	IAEA	IAEA activities in support of Compact Accelerator based Neutron Sources
12:15-12:30		Questions and Answers		
12:30–14:00		Lunch Break		

11:00 – 12:30 **Parallel Session 12.B: Electron beams and Applications** M Plenary

Chairpersons: S. Pillai (Texas A&M Univ., USA) and B. S. Han (IAEA)

Time	Abstract No.	Name	Affiliation & Designating Member State	Title
11:00–11:15	139	A. Bryazgin	Budker Inst., Russian Federation	ILU RF Electron Accelerators for E-beam and X-ray Applications
11:15–11:30	174	W.A.P. Calvo	IPEN / CNEN / SP, Brazil	Electron Beam Processing to Improve Biodegradable Polymers and for Industrial Wastewater Treatment and Recycling
11:30–11:45	15	S. Jebri	NCNST, Tunisia	Effect of E-beam Irradiation on the Microbial Quality of Minimally Processed Products: a Case of a Commercialized Ready to Eat Salad
11:45–12:00	8	P.A.S. Vasquez	IPEN / CNEN / SP, Brazil	Preservation of Photographic and Cinemato-graphic Films by Electron-Beam Irradiation
12:00-12:15	235	A. Jalilian	IAEA	IAEA support for accelerator-based radio-isotopes and radiopharmaceuticals production
12:15-12:30		Questions and Answers		
12:30–14:00		Lunch Break		

14:00 – 15:30 **Side Event 4: Promoting Self-Reliance and Sustainability of National Nuclear Institutions** Board Room A

Chairpersons: N. Ramamoorthy (Indep. Consultant, India), N. Pessoa Barradas (IAEA)

Time	Abstract No.	Name	Affiliation & Designating Member State	Title
14:00-14:10		N. Pessoa Barradas	IAEA	Opening remarks
14:10–14:25	248	F. A. Deluchi	CNEA, Argentina	Research and Industrial Applications Electron Beam Accelerator Project
14:25–14:40	249	C. Arcilla	PNRI, Philippines	The new Nuclear Medicine Research and Innovation Center
14:40–14:55	250	S. A. Hashim	WiN, Malaysia	Promoting Application of Electron Accelerator and Radiation Processing in Malaysia
15:00–15:15	251	S. Rugmai	SLRI, Thailand	The synchrotron projects of Thailand
15:15–15:30		Round Table Discussion - Questions and Answers		
15:30–16:00		Coffee / Tea Break		

14:00 – 15:30	Poster Session 2	All posters (see separate page)	M-Building (2nd Floor)

16:00 – 17:30 **Parallel Session 13.A: Selected Applications of of Accelerator-based Analytical Techniques** Board Room A

Chairpersons: M. Jaksic (RBI, Croatia) and A. Migliori (IAEA)

Time	Abstract No.	Name	Affiliation & Designating Member State	Title
16:00–16:15	191	M. Chiari	INFN, Italy	PIGE Analysis of Fluorine in Materials for the Circular Economy
16:15–16:30	115	C. E. Iochims dos Santos	Federal Univ. Rio Grande, Brazil	Study of Silver Nanoparticles Uptake by Helianthus annuus Crop in Salinity Conditions
16:30–16:45	111	P. Pongrac	JSI, Slovenia	Using Micro-PIXE to Evaluate Nutritional Value of Edible Parts of Plants
16:45–17:00	104	S. Möller	FZ Jülich, Germany	Lithium Depth Profiling in Battery Anodes by Nuclear Reaction Analysis
17:00-17:15	119	G. Provatas	RBI, Croatia	Study of charge Transport in Semiconductors by Ion Beam Induced Charge (IBIC) Microscopy
17:15-17:30		Questions and Answers		

16:00 – 17:30 **Parallel Session 13.B: Accelerators & Interdisciplinary Applications** M Plenary

Chairpersons: L. Beck (CEA, France) and N. Pessoa Barradas (IAEA)

Time	Abstract No.	Name	Affiliation & Designating Member State	Title
16:00–16:15	231	K. Hain	VERA, Austria	Ultra-trace analysis of anthropogenic long-lived radionuclides in the environment with AMS
16:15–16:30	110	J. M. Lopez-Gutierrez	Univ. de Sevilla, Spain	Characterization of Nuclear Waste by Accelerator Mass Spectrometry
16:30–16:45	215	N. Skukan	IAEA	IAEA Activities in Support of Sustainable Operation of Electrostatic Accelerator Facilities
16:45–17:00	40	N. Arbor	Univ. of Strasbourg France	A Monte Carlo and Experimental Tool for Activation Calculations in High Energy X-rays Irradiation Process
16:45–17:00	20	S. Masic	Vinca Inst. of Nuclear Sciences, Serbia	Surface Treatment of Special High-Protein Products Using Low Energy Beams from Machine Sources
17:00-17:30		Questions and Answers		

FRIDAY, 27 May 2022

9:00 – 10:30 Plenary Session 14: Accelerator and emerging applications — M Plenary

Chairpersons: T. Oshima (NIQRST, Japan) and A. Simon (IAEA)

Time	Abstract No.	Name	Affiliation & Designating Member State	Title
9:00–9:30	216	O. Girshevitz	BINA, Israel	Implementation of Ion Beam Analysis for Forensic applications: The way to Global Forensic Database through the unification of different analytical techniques
9:30–10:00	206	A. A. Bettiol	Nat. Univ. Singapore, Singapore	Accelerators and Ion Beams for Quantum Technologies
10:00–10:30	222	T. Stora	CERN, Switzerland	Radioactive Ion Beams: from Large Scale Facilities to Nuclear Medicine Applications
10:30–11:00		Coffee / Tea Break		

11:00 – 12:00 Plenary Session 15: Conference Summary and Highlights — M Plenary

Chairpersons: D. Ridikas (IAEA) and C. Horak (IAEA)

Time	Name - Affiliation	Title
9:00–9:30	N. Alamanos (CEA, France)	Conference Summary and Highlights
9:30–10:00	N. Ramamoorthy (Independent Consultant, India)	Conference Summary and Highlights: Focus on Applications and the IAEA support

12:00 – 12:30 Plenary Session 16: Conference Closing and Award Ceremony — M Plenary

Time	Name - Affiliation	
12:00–12:15	C. Horak, V. Starovoitova D. Ridikas, S. Charisopoulos (Scientific Secretaries, IAEA)	Award Ceremony
12:15–12:30	N. Mokhtar (DDG-NA, IAEA)	Closing Remarks

12:30–17:00 Technical tour to VERA and MEDAUSTRON accelerator facilities

TUESDAY, 24 May 2022 and THURSDAY, 26 May 2022

Poster Sessions **Time: 14:00 – 15:30** **Venue: M-Building, 2nd Floor**

Abstract No.	Authors	Designating Member State / Organization	Poster Title
5	A. Zaouak Ep Ammar	Tunisia	Removal of Hydroxychloroquine and Acid Red 51 Aqueous Solutions by the Electron Beam Process
7	L. Yu	Thailand	Ion Beams & Ion-accelerators for Biology-oriented Applications and Research – CMU Practices
11	I. Vujcic, S. Masic	Serbia	Possibility of Using Sludge from Drinking Water Treatment Plant as Fertilizer in Agriculture after E-beam Treatment: Effects of aging
12	S. Ghosh	India	Low and High Energy Ion Irradiation on Structural and other Properties of Cubic Zirconia and Ceria: from the Perspective of Nuclear Energy Material
13	A. Coulibaly	Mali	Shielding Considerations of a Bunker to be taken into Account by the Regulatory Body for Authorization Purposes: Case Study of Radiotherapy Center in MALI
14	G. Stankunas	Lithuania	Concrete and stainless-steel activation/decay heat data for the IFMIF-DONES Test Cell components
16	S. Petrović, N. Starčević, M. Ćosić	Serbia	The Rainbow Ion-Solid Interaction Potential
17	A. Mejri, H. Trabelsi, J. Chatti, Z. Trabelsi, M. Kraiem	Tunisia	Developing Radiation Treatment Methodologies for Decontamination for First Use of Personal Protective Equipment (PPE) using Tunisian Electron Beam Accelerator
21	S. Mejri, I. Hemissi, C. Brinsi, A. Asmi, M. Saidi, Y. Mabrouk	Tunisia	Radiosensitivity of Two Lens Culinaris Medikus Subsp. Culinaris Varieties to Electron Beam Irradiation
22	A. Akhavan Agh Ghaleh	Iran	Electron Beam Crosslinking of PE/NG Nanocomposite for Solar Collector Applications

Abstract No.	Authors	Designating Member State / Organization	Poster Title
26	S. Rimjaem	Thailand	Establishment of the First Accelerator- based Infrared Free-electron Laser Facility in SE Asia
28	I. Aljammaz	Saudi Arabia	Socioeconomic Impact of Cyclotrons in King Faisal Specialist Hospitals & Research Centre in Saudi Arabia
30	U. Gryczka	Poland	Determination of the Effectiveness and Control of Food Irradiation Process with a Low-energy Electron Beam
34	J. Červenák, O. Lebeda	Czech Republic	Measurement of Excitation Functions of Proton-Induced Nuclear Reactions on Dy- nat.
36	M. A. Khan	Pakistan	Low Energy S–band Electron Linear Accelerator(s) Development for Research and Applications Having Socio–economic Impact
39	H. Kumada	Japan	Current Development Status of the Linac-based BNCT Device of the iBNCT Tsukuba Project
41	E. Mora-Ramirez, E. Corrales-Corrales	Costa Rica	Ventilation Air System Issue at the University of Costa Rica's Cyclotron Facility
46	L. F. Salas Tapia	Colombia	Preliminary Design for a Cyclotron Extraction Beam Line and External Target for Producing Gallium-68 & Technetium- 99m Isotopes: a Developing Countries Scenario
48	F. Kuntz, A. Nasreddine, N. Ludwig, A. Strasser	France	Feerix, a novel Irradiation Platform for R&D, Education and Training
51	I. Churkin, V. Bukhtiyarov N. Krasnikov, P. Logachev, E. Levichev	Russian Federation	Siberian circular source of photons
53	D. Kottuparamban, A. Muhammed	India	An Optimized Periodic Maintenance Planner for a Commercial Medical Cyclotron Facility

Abstract No.	Authors	Designating Member State / Organization	Poster Title
55	A. Maggiolo, G. Rabi, M. Espósito	Argentina	Development and Application of Indicators for the Assessment of Radiation Safety Systems in Radiopharmaceuticals Production Facilities with Cyclotron
57	G. Rabi, L. Martiri	Argentina	Regulatory Framework Adopted by the Nuclear Regulatory Authority of Argentina for the Licensing of the Argentine Center of Proton Therapy and Progress Achieved
61	Hassan Abd El Rehim	Egypt	The Potential Use of Electron Beam Irradiation to Preserve Micro-biologically Infected Egyptian Papyrus
62	A. Mamaras, P. Foka, A. Ioannidou,	Greece	Concepts and Methodology of the Particle Therapy Masterclass (PTMC) for Capacity Building – PTMC in Greece as a Case Study
63	A. Sagatova, M. Fulop, M. Pavlovic, S. Kotorova	Slovakia	Multipurpose Electron Beam Facility in Slovakia for Research and Industrial Applications
64	A. Lausi, M. Attal, A. A. Elkadime	SESAME, Jordan	SESAME, a Synchrotron Radiation Facility in the Cradle of History
66	M. Fulop, J. Ruzicka, P. Ragan, A. Sagatova	Slovakia	Method for detection of illegal cigarette boxes in iron ore cargo
68	E. Stancu	Romania	Radiation ISODOSE Measurements Inside Interaction Chamber During the Commissioning Experiments of CETAL Facility. Gas Target Case
71	N. Bergans	Belgium	How Induced Activated Accelerator Parts Have an Impact on the Radiation Safety of a Proton Therapy Facility
75	P. Thongjerm	Thailand	The Development of an External Beam Irradiation System for Material Analysis at the Cyclotron Facility in Thailand
79	C. da Costa, E. F. da Silveira	Brazil	Degradation of Amino Acids by MeV Ions

Abstract No.	Authors	Designating Member State / Organization	Poster Title
81	G. García	Spain	Impact Pathways for Research Infrastructures: The Case of CMAM-UAM
83	Md. N. Hossain	Bangladesh	Establishment of the Cyclotron Facilities in Bangladesh – Present Status and Experiences
87	A. Gopalakrishna, A. Kumar, P. Maletha, K. Kamaldeep, S.V. Suryanarayana, H. Naik, B.K. Nayak, S.P. Kulkarni, P. Mukherjee	India	Developmental Work on Economic Production of High and Low Specific Activity 64Cu – Suitable for Preclinical Studies Using Accelerator Neutrons
89	L. Dittrich, P. Petersson, S. Moon, M. Rubel, A. Widdowson	Sweden	Accelerator-based Quantification and Depth Profiling of Hydrogen Isotopes and Impurity Atoms in Wall Materials from Controlled Fusion Devices
90	P. R. Oliveira	Brazil	Cluster Ion Emission from C 2 H 2 and C 2 H 6 Ices induced by 252 CF Fission Fragments
91	R. Martinez	Brazil	Glycine Bombardment by Alpha Particle – destruction Cross Section Dependence with KeV Energy and Temperature
97	M. Dias	Portugal	Synthesis and Irradiation Effects on CrNbTaVWx High Entropy Alloys
99	N. Catarino, E. Alves, R. Mateus, J. Cruz	Portugal	Measurement of 9Be(3He,p_i)11B Nuclear Reaction Cross Sections at Energy Range 0.5–2.35 MeV
100	J. J. Mboukam	Cameroon	Effect of Swift Heavy Ion Irradiation on the Optical Properties of Ion Implanted Polyethylene Terephthalate
103	E. Alves, J. Borges, N. Catarino, M. Dias, M. Peres, A. Ribeiro, F. Vaz	Portugal	Formation of Au Nanoparticles in TIO2 by Ion Implantation
112	S. Chattopadhyay, P. Mukherjee	India	Utilization of 30MeV DAE Medical Cyclotron for Production of Medically Useful Radioisotopes and Corresponding Radiopharmaceuticals

Abstract No.	Authors	Designating Member State / Organization	Poster Title
113	R. Mateus	Portugal	Ion Beam Studies of Deuterium Retention in High Entropy Alloys and W Targets in the PF-1000U Facility
120	T. Dunatov	Croatia	Development and Applications of the Dual-beam Ion Irradiation Faciility for Fusion Materials (DiFU) at RBI, Zagreb
122	V. Corregidor, L. Alves, T. Pinheiro, R. C. da Silva, M. Furtado	Portugal	Artificial Neural Networks and Ion Beams for 3D Imaging
128	J. M. Lopez-Gutierrez	Spain	CNA: User-oriented Accelerator Facility Dedicated to Interdisciplinary Research in Spain
137	I. Ahmad	Pakistan	Effects of Ions Irradiation on TiO2 Nanoparticles: A Review
143	L. Popa-Simil	United States	Review of 20 Years of Industrial Applications of Ion Beam and Radiation Techniques
144	M. Nasef	Malaysia	Progress in Electron Beam Induced Grafting for Development of Ion Conducting Membranes for Polymer Electrolyte Fuel Cells in Malaysia
146	L. Popa-Simil	United States	Accelerators Use to Engineer Nano- Materials for Energy
152	T. S. Lee, K. H. Loo, S. T. Bee, C. T. Ratnam	Malaysia	Photodegradation Effect of the Electron Beam Irradiated Devulcanized Natural Rubber/ polypropylene Compound under Natural Weathering Condition
153	D. Oliveira de Souza	Italy	Organic Carbon Cycling and Stabilization in Paddy Soils Probed by Fe K-edge X- ray Absorption Spectroscopy
156	V. Gostilo	Latvia	Mobile Facility for Gamma-activation Analysis of Gold Ores
161	V. Michalopoulou	Greece	Neutron Induced Fission Studies at NCSR “Demokritos” by the NTUA

Abstract No.	Authors	Designating Member State / Organization	Poster Title
164	Z. Eleme	Greece	Neutron induced fission cross section measurement of 241-Americium at the n_TOF facility
167	V. Sharapova	Russian Federation	The Effects of Sterilization Irradiation on Properties of Commercially Available Pet Materials Used in the Production of Vacuum Tubes for Blood Sampling
168	M. Diakaki	Greece	Neutron Induced Fission Studies at the CERN n_TOF Facility
170	H. Sa'adeh	Jordan	Towards Detection and Identification of Lead in Aerosol Samples Collected in an Urban Area in Amman, Jordan
172	B. Gonsalves	Finland	Performance Comparison of Methods for the Detection of 10be at the Helsinki AMS Facility
173	S. N. Mohd Janib	Malaysia	Accelerator Application in Malaysia to Close the Gap in Realizing SDG3
175	J. Mira, H. Barnard, L. R. Strydom, H. Anderson, J. Abrahams, J. Broodryk	South Africa	Design of the Sweeper Magnets for the High-Power Bombardment Station for Radioisotope Production at iThemba LABS
178	A. H. Barnard, L. R. Strydom, J. Broodryk, G. Steyn, P. Beukes	South Africa	Modelling of the Radiation and Shielding at the South African Isotope Facility Using FLUKA
188	E. Stamati, N. Colonna, A. Mengoni, N. Patronis, R. Vlastou	Greece	NEAR at n_TOF/CERN: The First Multi-foil Activation Measurement
192	R. Hasan, H. Sa'adeh	Jordan	A Comprehensive Overview of the University of Jordan Van de Graaff Accelerator (JUVAC)
200	T. Torims, A. G. Chmielewski, Y. Sun, A. Pawelec, G. Mattausch, M. Vretenar, Z. Zimek, G. Pikurs	Latvia	The Proof-of-concept Results: Development of Hybrid Electron Accelerator System for the Treatment of Marine Diesel Exhaust Gases

Abstract No.	Authors	Designating Member State / Organization	Poster Title
201	M. Etoom, O. Natsheh	Jordan	Switching Irradiation Facility in Jordan from Co-60 to E-beam X-ray
202	S. Utermann, A. Jungstand, A. Thielmann, M. Gastrow	Germany	Comparative Analysis of Socio-economic Impact in Two Particle Accelerator Case Studies
225	I. Steblevska	Canada	Supervisor Watchdog Circuit for Monitoring Accelerator Beam Properties and Controlling the Safety Interlock System
228	Marcia Almeida Rizzutto	Brazil	Amazon Ceramics and their Color Palette - the Use of Ion Beam Analysis to Determine the Pigments
234	H. Ahiamadjie	Ghana	Environmental applications of PIXE at the accelerator facility of Ghana Atomic Energy Commission

LIST OF SUBMITTED FULL PAPERS

Oral Presentations

Poster Presentations

FULL PAPERS

from oral presentations

ACCELERATOR TECHNIQUES AND NUCLEAR ATA NEEDS FOR ION BEAM ANALYSIS OF WALL MATERIALS IN CONTROLLED FUSION DEVICES

M. RUBEL[1,2], D. PRIMETZHOFER[2], P. PETERSSON[1]
[1] KTH Royal Institute of Technology, Department of Plasma Physics Stockholm, Sweden
[2] Uppsala University, Department of Physics and Astronomy Uppsala, Sweden
Email: rubel@kth.se

S. CHARISOPOULOS [3]
[3] NAPC/Physics Section, International Atomic Energy Agency Vienna, Austria

Abstract

A brief overview of ion beam analysis methods and procedures in studies of materials exposed to fusion plasmas in controlled fusion devices with magnetic confinement is presented. The role of accelerator techniques in the examination and testing of materials for fusion applications is emphasised. Quantitative results are based on robust nuclear data sets, i.e. stopping powers and reaction cross-sections. Therefore, the work has three major strands: (i) assessment of fuel inventory and modification of wall materials by erosion and deposition processes; (ii) equipment development to perform cutting-edge research; (iii) determination of nuclear data for selected ion- target combinations. Underlying physics, advantages and limitations of methods are addressed. A note is also given on research facilities with capabilities of handling radioactive and beryllium-contaminated materials.

1. INTRODUCTION

Energy research driven by the quest for effective sources and means of electricity production is crucial for sustainable development. Despite distinct progress in energy-saving technologies and increasing number of installations based on fossil-free sources, the demand for electricity generation is ever growing to ensure functioning of transport, lighting, tele-communication and all branches of industry which require stable high-power supply. Simultaneously strong emphasis is on the safe and environmentally sound means of energy generation, while the production volume may be limited by the access to natural resources, currently available technologies, climate and, also by political situation.

Development of future technologies like Generation IV nuclear reactors and controlled thermonuclear fusion has a long history. In both cases, integrated efforts in science and technology are directed towards the construction and operation of reactor-class facilities. Controlled fusion is a multidisciplinary field encompassing plasma and ion physics, remote handling (RH) and radiofrequency (RF) technologies, nuclear physics and chemistry, demanding civil engineering, radiation protection and countless aspects of materials science and engineering: from the composition and structure of concrete for a base of a reactor containment to the detailed characterisation of the plasma-facing wall: plasma-facing materials (PFM) and components (PFC); both abbreviated jointly in the following as PFMC. The surface state of the latter class of materials is studied mainly by accelerator-based methods commonly called ion beam analysis (IBA).

In the interdisciplinary field of fusion research, the role of particle accelerators is at least five-fold: (i) ion beam analysis (IBA) of materials retrieved from vacuum vessels of controlled fusion devices; (iii) ion-induced simulation of neutron radiation effects in surfaces of solids; (iii) provision of nuclear data for ion-material interactions; (iv) ion-induced neutron generation for the material irradiation facility; (v) high current units in the neutral beam injection system for plasma (deuterium and tritium: D and T) heating. The first three aspects will be presented in the following sections with a focus on the role of accelerator techniques in the examination and testing of materials for fusion applications. Quantitative results can only be obtained using highly advanced laboratory equipment and combined with robust sets of nuclear data, i.e., stopping powers and reaction cross-sections. Therefore, the work has three essential strands: (a) assessment of fuel inventory and modification of PFMC composition by erosion and deposition processes; (b) equipment development to perform cutting-edge research; (c) determination of nuclear data for selected ion-target combinations.

2. CONTROLLED FUSION AND PLASMA-WALL INTERACTIONS: IMPACT ON MATERIALS

The goal of controlled thermonuclear fusion is to harness energy that powers stars: reactions of light nuclei characterised by Q values of several MeV and high reaction rates:

$$D + D \rightarrow T\ (1.01\ MeV) + H\ (3.03\ MeV) \quad (1a)$$

$$D + D \rightarrow {}^{3}He\ (0.82\ MeV) + n\ (2.45\ MeV) \quad (1b)$$

$$D + T \rightarrow {}^{4}He\ (3.52\ MeV) + n\ (14.06\ MeV) \quad (2)$$

$$D + {}^{3}He \rightarrow {}^{4}He\ (3.67\ MeV) + H\ (14.69\ MeV) \quad (3)$$

the branching ratio of Reactions 1a and 1b is around one. Deuterium fuel is used in most present-day devices, but the Q value (17.58 MeV) and the cross-section of the D-T process [1,2], favors that mix of hydrogen isotopes as a fuel for a reactor in a future power station. Reaction 3 has a significantly lower cross-section than Reaction 2 and, currently cannot be considered because of a very limited availability of ^{3}He.

Two major schemes of fusing nuclei have been developed. Inertial confinement fusion (ICF) uses high power photon (laser) [3] or ion beams [4] focused on a small (~1 mm in diameter) D-T containing pellet placed in a vacuum chamber of a few meters in diameter. Magnetic confinement fusion (MCF) based on plasmas generated and maintained by magnetic fields of a few T in toroidal systems [1,5]. The latter scheme exploits two reactor concepts: tokamaks [1,6] and stellarators [7]. In either case, both ICF and MCF, under terrestrial conditions the fusion plasma must be surrounded by walls of a vacuum vessel and, the energy released must then be absorbed by wall structures: 20% related to ^{4}He (α particles) by PFMC [8], while the neutron energy (80% of the total) is to be transferred to a ^{6}Li-enriched blanket where the conversion to heat and tritium production will occur [9,10]. The energy confinement time (τ_E) of particles of (up to 1.0-1.5 s) is shorter than the plasma discharge time.

Consequently, particles escape the plasma and impinge on the wall. These are electrons, ions at different ionisation states and charge exchange neutrals (CXN). In addition, there are neutrons generated in fusion reactions as well as electromagnetic radiation with a broad spectrum from RF down to hard gamma and X-rays. They are decisive for what is called plasma-wall interactions (PWI) which involve a huge range of processes: physical sputtering, chemical erosion, reflection, implantation, gas retention, desorption, melting, boiling, splashing, arcing, cracking, ionisation, recombination, compound formation, activation and consequential transmutation [8,11-13]. All of them are dynamic arising from atomic, molecular and nuclear physics and chemistry.

A scheme of interactions is shown in Figure 1. Eroded species are immediately ionised and travel along the magnetic field lines. Eventually, if not pumped out, the migrating species are re-deposited in a close or distant location with respect to the place of origin. Re-deposition involves atoms of different elements originally eroded from the wall. It is a simultaneous co-deposition in which also fuel atoms are included. As a result, mixed material layers are formed. The composition and other properties of such deposition zones significantly differ from those of the original substrates. Thermo-mechanical incompatibility between the substrate and co-deposit may lead to flaking and spalling-off of the layer thus forming dust which constitute a major operational issue if large amounts of dust are formed and, if such particles contain considerable fraction (a few atomic %) of fuel atoms, especially radioactive tritium or neutron- activation products.

In short, PWI comprises all processes of energy and mass exchange between the plasma and the surrounding surfaces. As a result, the plasma and the wall are modified with serious consequences for reactor operation. The plasma gets contaminated and loses energy, while properties of PFMC and some crucial tools for plasma diagnosis (mirrors and windows) are changed. This has an impact on the material lifetime and fuel inventory thus for the reactor safety. However, plasma-wall interactions are unavoidable but also necessary. The wall provides vacuum conditions indispensable for operation, removes heat and – only under D-T reactor conditions - ensures final thermalization of helium ash to enable its pump out and, absorption of energetic neutrons in the blanket for tritium productions and power generation.

In-vessel materials must be, in the first place, compatible with vacuum and strong magnetic fields, while the list of requirements for PFC candidates comprises in addition: high thermal conductivity (λ), i.e. over 150 m^{-1} K^{-1}, resilience to thermal shocks, low erosion yield by plasma species, low sorption of hydrogen isotopes to limit fuel inventory, high melting (T_m) and boiling (T_b) points, low-Z to minimise plasma energy losses by impurities, low erosion rate, low affinity to fuel and to oxygen impurities towards the formation of volatile products, affinity to oxygen impurities towards their gettering to form solid oxides, low neutron-induced

activation. None of the known substances has properties fulfilling such requirements especially that some of them are contradictory. Therefore, the material selection is based on the approach that properties should change as little as possible under plasma impact.

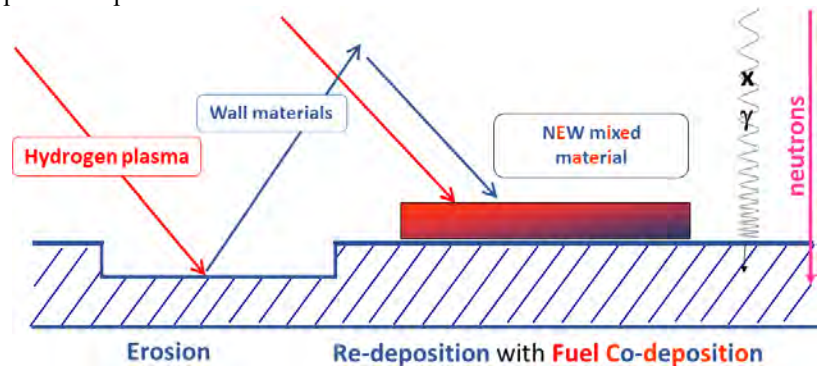

FIG. 1. Plasma-wall interactions: schematic illustration of erosion-deposition processes.

The major materials of interest for PFC are beryllium (Be), carbon (C) in the form graphite or carbon fibre composites (CFC), and tungsten (W). In addition, molybdenum (Mo) is important as material for so-called first mirrors, i.e., plasma-facing materials for optical diagnostics. Crucial advantages and drawbacks of respective wall materials are compiled in Table 1, while very detailed characteristic can be found in [8]. Graphite and several types of CFC have been used in toroidal devices since seventies of the 20th century because of their excellent power handling capabilities. Issues related to the erosion rates and the formation of fuel-rich co-deposits were known, but their dramatic seriousness was recognised after full D-T campaigns in TFTR [14,15] and JET [16-21] operated with carbon walls: nearly 30% of the injected tritium was retained in the vessel, especially in the remote areas of the divertor, i.e., places shadowed from the direct plasma line-of-sight. Such locations are very difficult to reach by any cleaning method [18,20,22]. No efficient means of fuel removal have been developed and the use of carbon in a D-T fusion reactor had to be reconsidered [22-27]. A large scale-test with all-metal walls was decided at the largest tokamak in the world: the Joint European Torus (JET) [28-30]. Carbon PFC were removed and replaced by solid Be limiters and Be coatings on the main chamber wall [31,32], while W components (bulk metal and coatings on CFC tiles) were installed in the divertor [32-34]. The operation of JET with the ITER-like wall (JET-ILW) started in 2011 and, it was clearly shown that the elimination of carbon sources resulted in a significant decrease of fuel retention [35-42] and dust generation [43-48]. In a consequence, the ITER Organisation decided to abandon carbon components in the divertor and prepare for operation with Be panels in the main chamber and tungsten in the divertor [49].

TABLE 1. Key properties of C and metals as wall materials and diagnostic components.

Element	Advantages	Drawbacks/Limitations	Remarks
C	Low-Z. Resilience to thermal shocks and no melting λ of some CFC > 300 W $m^{-1}K^{-1}$.	Chemical erosion by fuel atoms, C_xH_y formation, high erosion rate and fuel inventory in co-deposits.	PFMC in most tokamaks [8,14- 21,27,50-55] and stellarators [56-58] because of excellent power handling capabilities.
Be	Low-Z, no chemical erosion	Low T_m and high sputter yield.	Used in JET-ILW in the main chamber wall [29,31,59]; the same decided for ITER wall [49].
W	High T_m and low sputter yield by fuel	High-Z, risk for plasma contamination and disruptions. Activation and transmutation.	ASDEX Upgrade wall and divertor [60-61]. JET-ILW divertor [29,32-34,62]; the same decided for ITER divertor [49].
Mo	High T_m and low sputter yield by CXN	High activation.	Tested candidate for first mirrors in ITER diagnostic systems [63-67]

The major research objectives are to determine: (i) the lifetime of PFMC, (ii) in-vessel fuel accumulation, i.e., to obtain quantitative mapping of the distribution of D and T, (iii) quantity and properties of dust with particular emphasis on the identification of sources, generation pathways and fuel content, (iv) plasma impact on diagnostic components which are crucial for plasma characterisation and machine protection. All of them are decisive for reactor economy and safety. As such, these are key points in the licensing process. Conditio sine qua non for conclusive studies is the access to materials (specimens from diverse locations: wall tiles, probes, dust) retrieved from the vacuum vessel after experimental campaigns. Research requires a huge variety of material characterisation methods which directly implies the access to laboratories with relevant apparatus, competent research teams and – in many cases – capabilities and certificates for handling radioactive materials: T-contaminated and activated.

3. ANALYSIS METHODS AND INSTRUMENTATION

3.1 Challenges and Solutions **Analysis: Needs and Methods**

Over the years, more than fifty different material characterisation techniques have been used in the PFMC research: ion, electron, neutron and optical spectroscopies, methods based on probing solids with magnetic field, sound waves, mechanical force or thermal means applying either a steady temperature rise or shocks by flash heating. The variety of probing ('signal in') and detection means ('signal out'), their broad energy spectrum and a range of physical processes involved in the interactions create a huge number of "signal in – signal out" combinations, and – by this – research opportunities. Nearly every combination may actually be applied in a certain area of material characterization. However, only most efficient, methods for analyses of PFMC are mentioned in the following, i.e., techniques capable of sensitive and selective quantitative determination of the content and distribution (in-depth and lateral) of a wide range of elements and, in many cases, their particular isotopes present in the examined materials. Capabilities for mapping surface species on large areas on the tiles (e.g., 10x20 cm) are also required in many cases. Compositional analyses must cover a broad range of species which constitute wall and diagnostic components, fusion fuel and gases injected for auxiliary plasma heating, plasma edge cooling, disruption mitigation, wall conditioning or as markers (tracers) in material migration studies. As a result, the list extends from H, D, T, ^{3}He, ^{4}He and other noble gases (Ne – Xe), isotopes of Li, Be, B, C, N, O, F to heavier species such as Al, Si to Cr, Fe, Ni and then to W, Re, even Au is to be taken into account. The role and origin of respective species in the reactor is addressed in Table 2 in which also the information on relevant analysis methods is conveyed.

The requirement for lateral mapping and depth profiling of such diverse compositions are met by IBA methods. Their detailed description with physics basis can be found in [68,69], while the role in PFMC analysis has been addressed in overview articles [70-72]. IBA is based on the irradiation of a solid target with an ion beam and then detection and analysis of energy and/or mass spectra of signals emitted from the surface: reflected primary ions, products of nuclear reactions, recoiled atoms, photons (from visible to X and gamma rays), sputtered species such as secondary ions (monoatomic and molecular) and neutrals. Dependent on the ion (type, energy) – signal combination there is a number of methods governed by different underlying physical processes.

- Rutherford Backscattering Spectrometry (RBS) mainly with $^{4}He^{+}$ in the 1.5 – 3 MeV energy range.
- Non-Rutherford Enhanced Proton Scattering (EPS) with H^{+} in the 0.5 – 2.5 MeV range.
- Nuclear Reaction Analysis (NRA) – a huge variety of analytical capabilities using low-Z ion beams: mainly $^{3}He^{+}$ (0.6 – 6 MeV) and H^{+}, but also D^{+}, ^{12}C, ^{15}N and ^{16}O ions. Respective nuclear reactions are in Table 2.
- Particle Induced X-ray Emission (PIXE) and/or Gamma Emission (PIGE) using a primary 1.5 – 4 MeV beams of H^{+}, $^{3}He^{+}$, $^{4}He^{+}$.
- Time-of-Flight Elastic Recoil Detection Analysis (ToF-ERDA) with ^{4}He+ or the high ion version (ToF-HIERDA) using for instance multiply charged ion beams of C^{n+}, Si^{n+}, Br^{n+} or I^{n+} beams. Depth profiling down to 700 nm.
- Accelerator Mass Spectrometry (AMS) in trace analysis of T, ^{10}B, 14C.
- Medium Energy Ion Scattering (MEIS) using a 100 – 400 keV $^{4}He^{+}$ beam.
- Secondary Ion Mass Spectrometry (SIMS) with primary beams of Ar^{+}, Cs^{+} or O^{-} of a few keV. The method is sensitive but the quantification in complex mixed-material co-deposits is difficult.

TABLE 2. Species to be analysed/determined and their role in a reactor.

Species	Origin and role in a reactor	IBA Method	Reaction (of practical use)*	Remarks and references
H	Wall cleaning - conditioning gas	NRA, ERDA	$^{1}H(^{15}N,^{4}He)^{12}C$	H is always present in vacuum systems; information depth below 1 μm; strong detrapping by the ^{15}N beam.
D	Fuel	NRA, ERDA, EPS	$^{2}D(^{3}He,^{1}H)^{4}He$	NRA is the main technique in D analysis [70-80]. Depth profiling in C-H layers to over 30 μm at 6 MeV [73]
T	Fuel	NRA, ERDA, AMS	$^{3}T(^{12}C,^{4}He)^{11}B$ $^{3}T\ (^{12}C,\ ^{1}H)^{14}C$ $^{3}T\ (D,^{4}He)n$	Use of IBA is limited. Low sensitivity of ^{12}C-^{3}T reactions ^{12}C-^{3}T reactions tried on JET materials [81], while the ^{2}D -^{3}T was used on TFTR tiles [82]. AMS in trace analysis [83].
^{3}He	Minority gas for ICRF heating	ERDA		[84]
^{4}He	Ash of D-T reaction; Wall cleaning - conditioning gas	ERDA		[84]
^{6}Li, ^{7}Li	Li-beam diagnostic, wall coatings	NRA, ERDA, PIGE	$^{7}Li(^{1}H,n\gamma)^{8}Be$	
^{9}Be	Wall material	NRA, ERDA	$^{9}Be(^{3}He,^{1}H)^{11}B$ $^{9}Be(^{2}D,^{1}H)^{10}Be$ $^{9}Be(^{2}D,^{4}He)^{7}Li$	[20,71,72,75,77,85]
^{10}Be	Be migration marker	AMS		Marker n-activated ^{9}Be tile [86]
^{10}B and ^{11}B	Wall conditioning by low plasma in B_2H_6, $B(CH_3)_3$ or evaporation from $B_{10}H_{14}$	NRA, ERDA	$^{11}B(^{1}H,^{4}He)^{8}Be$ $^{11}B(^{3}He,^{1}H)^{13}C$	Analysis of PFMC from boronised machines [87-91]
^{12}C	Wall material	NRA, EPS, ERDA	$^{12}C(^{3}He,^{1}H)^{14}N$ $^{12}C(^{2}D,^{1}H)^{13}C$ $^{12}C(^{1}H,^{1}H)^{12}C$	[18,70-72,77,78,92] $^{12}C(^{2}D,^{1}H)^{13}C$ for C analysis on Be targets [85]
^{13}C	Tracer in C migration studies	NRA, EPS, ERDA	$^{13}C(^{3}He,^{1}H)^{15}N$ $^{13}C(^{1}H,^{1}H)^{13}C$	[93-96]
^{14}N	Edge cooling	NRA, ERDA	$^{14}N(^{2}D,^{1}H)^{15}N$ $^{14}N(^{2}D,^{4}He)^{12}C$	[85,93,97,98]
^{15}N	Tracer	NRA, ERDA	$^{15}N(^{1}H,^{4}He\ \gamma)^{12}C$	[96,98-100]
^{16}O	Major impurity	RBS, EPS, NRA, ERDA	$16O(^{2}D,^{1}H)^{17}O$ $^{16}O(^{1}H,^{1}H)^{16}O$	[93]
^{18}O	Tracer for in-vessel oxidation studies	NRA, ERDA	$^{18}O(^{1}H,^{4}He)^{15}N$	[65,78]

*Only reactions of practical use are listed, i.e. reactions with the detection limit of minimum $5x10^{14}$ cm^{-2}.

TABLE 2. (cont'd).

Species	Origin and role in a reactor	IBA Method	Reaction (of practical use)*	Remarks and references
^{20}Ne	Edge cooling agent	ERDA, RBS		[84,97]
^{21}Ne, ^{22}Ne	Considered as tracers	ERDA, RBS		RBS only on light substrates
Al	Impurity from structural material of RH systems	RBS, PIXE, ERDA		
Si	Component of in-vessel diagnostics	RBS, PIXE, ERDA		SiH_4 (SiD_4) used for wall conditioning (siliconisation) [101]
Ar	Edge cooling agent	RBS, PIXE, ERDA		[94]
Fe, Cr, Ni	Vacuum vessel and antennae materials: Steel, Inconel	RBS, PIXE, ERDA		Separation with RBS is difficult. ERDA and MEIS allow for separation of Cr and Ni
Cu	Impurity from NBI system	RBS, PIXE, ERDA		PIXE in presence of Fe, Cr, Ni
Kr	Edge cooling agent	RBS, PIXE, ERDA		[94]
Mo	Vacuum vessel and antennae materials: Steel, Inconel; First mirrors	RBS, PIXE, ERDA		
W	Wall material	RBS, PIXE, ERDA		
Re	Proposed addition to W	RBS, PIXE, ERDA		Only PIXE in the presence of W
Au	In-vessel diagnostics: bolometers, coated mirrors	RBS, PIXE, ERDA		

*Only reactions of practical use are listed, i.e. reactions with the detection limit of minimum $5x10^{14}$ cm^{-2}.

For most techniques, besides ERDA, the standard lateral resolution determined by beam diameter is in the range 0.6-1.2 mm. Detailed mapping of species with a resolution of 1-30 μm is carried out (if needed) with μ-RBS, μ-NRA, μ-EPS and μ-PIXE, i.e., using micro-beams formed in a quadrupole-equipped beamline. In ERDA or HIERDA which are based on the target irradiation at a shallow angle (usually 22.5o) the beam spot is elongated: 1x4 mm.

Taking into account a range of ion beams, beam spot size, broad energy spectrum, tens of nuclear reactions and data processing software, the "toolbox" offers a huge number of analytical options. It is also clear that there is no single technique to address all needs taking into account the differences in the information depth and sensitivity for detecting respective species because these parameters are decided by energy-dependent stopping powers in ion-target systems, and by cross-sections of individual processes.

The IBA methods are complementary to each other and, they are complementary to other techniques for characterisation of PFMC and fuel inventory. In the case of light isotopes, particularly in fuel retention studies, ^{3}He-based NRA plays a prominent role. It is the only method to determine quantitatively the areal distribution and depth profiles of deuterium down to tens of micrometres in light substrates [73]. Micro-NRA facilities deuterium

mapping in regions of highly not uniform content of that isotope [102,103] and even in single grains of dust [104,105]. NRA complements results of the gas balance assessment in fusion devices [50,79,106,107] and thermal desorption spectroscopy (TDS) data [108] to obtain an overview of the global fuel retention. Determination of the fuel content in PFMC is crucial to obtain reference targets in the development of in-situ techniques: laser-induced desorption (LIDS), breakdown (LIBS) or ablation (LIAS) spectroscopy techniques [109-114].

In the third column of Table 2 ERDA is listed in every set of useful/recommended techniques. ToF- HIERDA is an extremely powerful tool in the determination of low-Z isotopes on surfaces, especially when using a gas ionization chamber (GIC) detector [115], as it has been shown in studies of PFMC and wall probes from the TEXTOR [89,90], JET [77], COMPASS [91] tokamaks, and from laboratory experiments on mirror testing [116]. A great advantage is a simultaneous analysis of H, D, ^{3}He and ^{4}He [84]. High mass resolution facilitates conclusive results in material migration studies which involve the injection of tracer gases labelled with rare isotopes such as $^{13}CH_4$ [90], $^{15}N_2$ [90], $^{18}O_2$ [65,84] when it is essential to discriminate between the main and minor isotopes, e.g., ^{12}C eroded from PFMC and the injected ^{13}C tracer. The GIC detector opens possibilities for applying other tracers: $^{10}B_2H_6$, ^{21}Ne, ^{22}Ne. Figure 2 shows a spectrum of species detected with a 42 MeV $^{127}I^{8+}$ beam on the PFC surface retrieved from the TEXTOR tokamak after experiments with $^{13}CH_4$ and $^{15}N_2$ tracers.

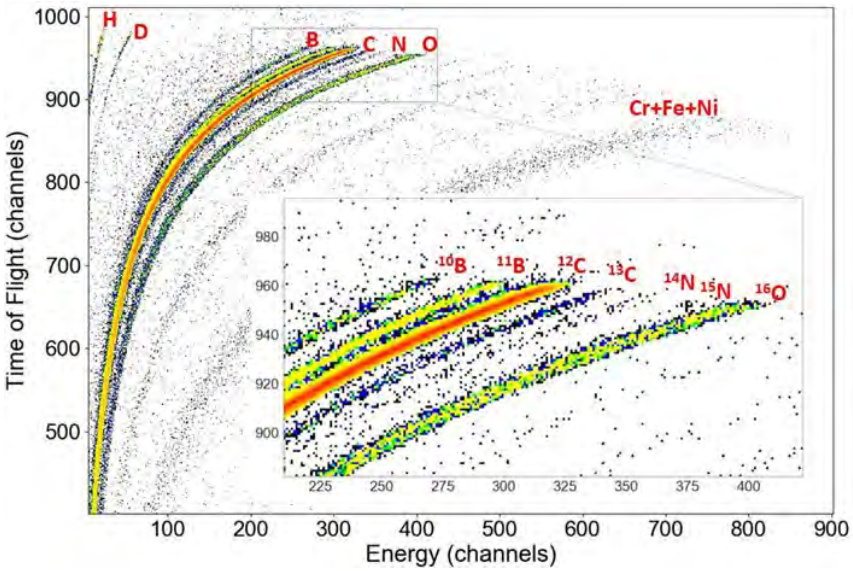

FIG. 2. ToF HIERDA spectrum recorded after tracer experiments for the limiter tile of TEXTOR.

3.2 Ion-induced damage in materials

The other role of accelerators in fusion research is in the ion-induced simulation of neutron damage in materials [10,116-118]. The damaged surface structure has a major impact on fuel retention in PFC and, also on optical performance of crucial diagnostic components like so-called first mirrors, i.e., metal mirrors acting as plasma-facing components in all optical plasma diagnosis systems (spectroscopy and imaging) in ITER, i.e., the reactor-class machine under construction. The impact of irradiation with H, ^{4}He (transmutation simulation) and Mo, Zr, Nb (simulation of n-induced damage) on the optically active layer of Mo mirrors has been presented [116-117]. There are three key points in such study: (i) the selection of irradiation conditions to by H, ^{4}He and high-Z species to influence changes in the optically active layer (OAL) of the mirror, i.e., maximum 30 nm of the outermost surface; (ii) the irradiation and determination of reflectivity changes; (iii) ToF HIERDA measurements of H and ^{4}He depth profiles, their changes in time and the dependence on the irradiation sequence. Plots in Figure 3(a) and (b) show, respectively, the depth profiles of H and He following the irradiation of polycrystalline Mo mirrors only with a 2 keV H^+ beam $14x10^{16}$ cm^{-2} and, first with $5x10^{16}$ cm^{-2} of 2 keV $^{4}He^+$ and then with $14x10^{16}$ cm^{-2} of 2 keV H^+. The results indicate that the damage produced by helium has a strong impact on the amount and depth distribution of hydrogen: the H profile is deeper when combined with He implantation. Secondly, the H retention is doubled after the He^+ irradiation in comparison to the irradiation with H^+ only: from 2% to 4% atomic.

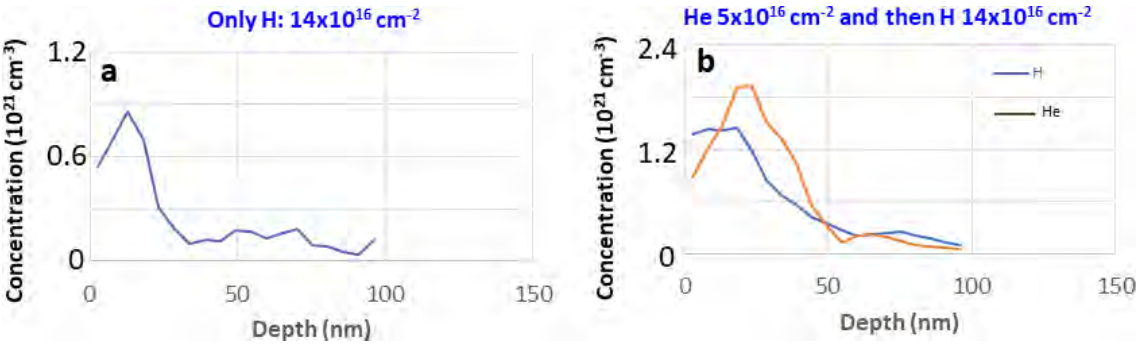

FIG. 3. ToF HIERDA depth profiles of H and He following two types of irradiation: (a) irradiation only with H; (b) irradiation with He followed by H.

3.3 Instrumentation

A pre-requisite for the advanced accelerator-based material research, either analysis or modification, is a laboratory (or a network of laboratories) with equipment providing a broad range of capabilities regarding the beam composition, energy, current, particle detection and, the control of experimental parameters: gas feed, temperature etc. A review of twelve accelerator laboratories with a detailed account on the facilities relevant to studies of fusion-related materials has been given in [72]. Among them, there are six laboratories capable of handling and analysing Be- and T- contaminated materials from JET: from full not sectioned Be tiles (12cm x 20cm) to smaller sectioned samples and dust. Work procedures with such materials (handling, transport etc.) have been addressed in [71,72], while very details are in [119].

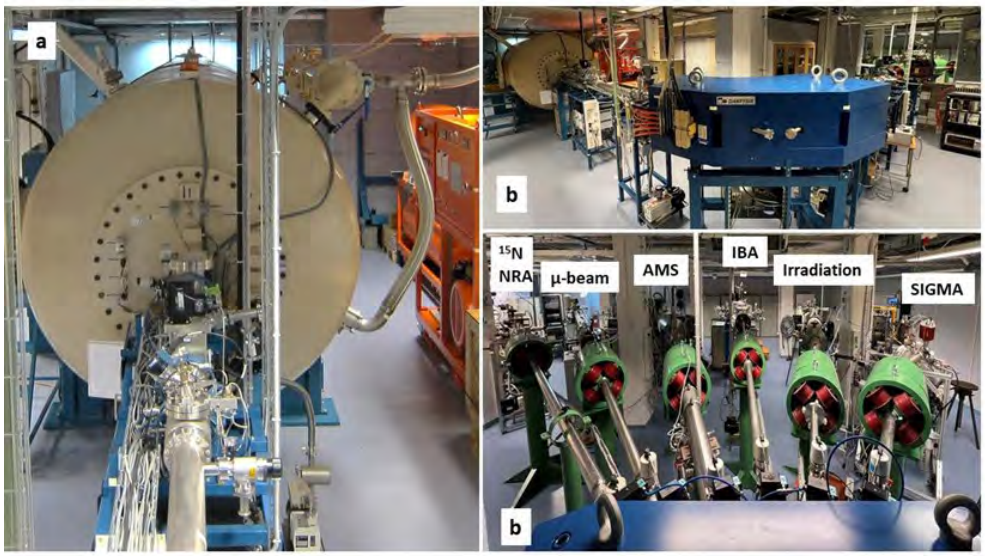

FIG. 4. Tandem Laboratory at the Uppsala University: (a) the accelerator; (b) analysing magnet; (c) six beamlines with the description of their main purpose.

New developments of the instrumentation are crucial to enhance and to broaden research capabilities. Images in Figure 4 show the 5 MV Pelletron Tandem (National Electrostatic Corporation, NEC) and the beamline arrangement at the Tandem Laboratory, Uppsala University, Sweden. Two gas and two sputter ion sources allow for the formation of beams in all mass ranges, from low-Z (H - Li), medium-Z (Be – Si) and, with some exceptions, high-Z up to Au. There are six beamlines for standard IBA (PIXE, RBS, NRA and ToF ERDA with GIC detector [115]) and very specific tasks like ^{15}N NRA with a gamma detector, AMS used mainly in the ^{10}Be [86] and ^{14}C analyses, μ-beam with PIXE, RBS, NRA. A separate line is dedicated to material modification by ion irradiation while the newly developed system on the sixth beamline is for in-situ and in-operando research: Set-up for *In- situ* Growth, Material modification and Analysis (SIGMA) [120,121].

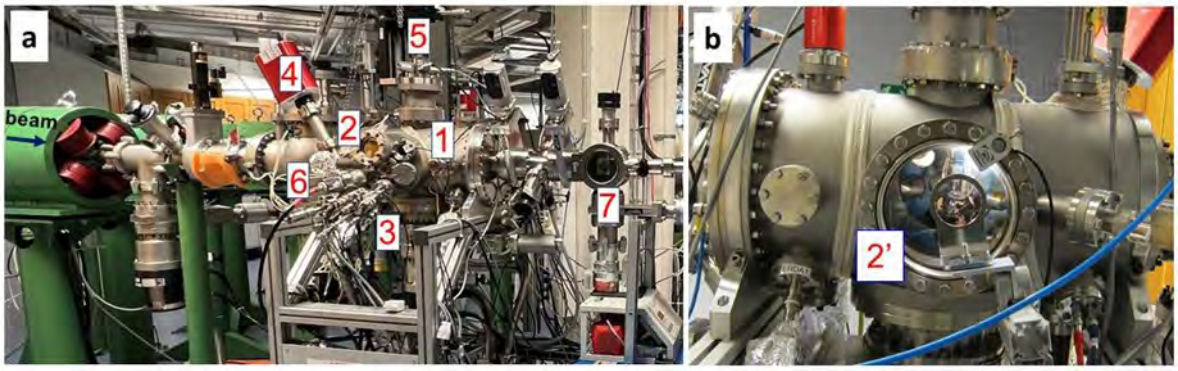

FIG. 5. SIGMA chamber – 1; viewing ports on both sides of the chamber – 2 and 2'; triple evaporator – 3; residual gas analyzer – 4; sample manipulator – 5; ion gun – 6; load-lock chamber – 7.

As already mentioned, all processes involved in PWI are dynamic. Direct in-situ material studies inside fusion devices are technically either very challenging or not possible at all. Some fundamental processes can therefore be investigated under controlled laboratory conditions. The SIGMA system, presented in Figure 5(a) and (b), has been designed to facilitate material modification with in-situ IBA employing both light and heavy beams for RBS, NRA, PIXE, PIGE, ToF-ERDA at the 2- 50 MeV energy range. Due to large viewing ports optical characterization is also carried out. Several gas feeds, three evaporation cells, a sputter gun (1-5 MeV) enable diverse material modification scenarios. Sample annealing to 1100 ºC combined with gas phase analysis offers a wide range of experimental possibilities in studies of fuel retention in fusion-relevant targets.

Two other accelerating systems at Uppsala University extend research on material modification [121]. With a 350 kV implanter (Danfysik) equipped with three changeable ion sources (gas, oven-based, sputter) the simulation of neutron-induced damage by means of light and heavy ion irradiation is carried on mirrors tested for diagnostic and heating systems in future fusion devices [116-118]. Two other beamlines are for: (i) ToF-MEIS and (ii) low energy RBS and NRA. The application of MEIS [77] ensured sensitive high-resolution determination of surface composition and has led to new topics in material migration.

A low energy ion gun (up to 10 kV) in another system equipped with two chambers is the base for ToF Low Energy Ion Scattering (ToF LEIS), Auger Electron Spectroscopy (AES) and Low Energy Electron Diffraction (LEED) [122]. Material modification capabilities annealing, sputtering and in-situ growth of thin layers. In all materials analyses, the quantification of composition is essential. In the case of IBA, it relies on the energy dependent cross-sections in the interactions of fast particles with matter.

4. STOPPING AND REACTION CROSS-SECTIONS

The energy deposition by energetic charged particles in matter is conveniently described by the energy deposition per unit path length, commonly referred to as stopping power (S). Dependent on the nature of the interaction, i.e. whether energy is deposited by elastic interaction between ion and target nuclei or by excitation of the electronic system of the target, one refers respectively to electronic (S_e) or nuclear (S_n) stopping power [123]. By a convenient transformation one obtains the stopping cross section by normalization by the atomic density N, which yields a quantity independent of the mass density of the target material. In any representation, accurate knowledge on the specific energy deposition of charged particles forms a key ingredient for quantification in ion beam analytical methods, by providing depth scales, in ion implantation by allowing for a prediction of particle range and in modelling of, e.g., sputtering processes and defect formation [69,124]. At high energies, the interaction with the target electronic system has been already early modelled successfully by Bethe [125] with subsequent further improvements [126-128]. Towards lower energies, interaction becomes more complex even for the lightest ions, as details of the electronic structure of the material were predicted to affect the energy deposition [129]. These effects of the density of states of the irradiated material were later been confirmed in several experiments for metals with excitation thresholds for specific electronic states [130-131] as well as for insulators featuring a band gap [132,133]. For light ions different from protons, also projectile excitation becomes increasingly relevant [134,135] still challenging predictions up to date [136-137]. In a similar fashion as

calculations feature an increasing complexity towards low ion energies, the same applies to experiments: stopping powers are experimentally most straightforwardly obtained in transmission experiments [138], for which, at lower energies, however the deteriorating influence of surface contaminations increases. In backscattering geometry, effects of surface contamination are drastically reduced, however, at lower energies, effects of plural and multiple scattering affect the spectra, complicating the analysis, requiring accurate simulations [139,140]. An additional option, available when sufficiently thin films of the target material cannot reliably be obtained is evaluation from the height of a spectrum recorded for a thicker film or bulk of the material of interest [141. In all cases, however, material purity is of utmost importance, which is challenging to guarantee for thin layers near a surface [142]. For all the reasons above, the database of electronic stopping powers hosted by IAEA [143,144] features only a limited number of datasets at low ion energies. Also, the materials, for which stopping powers have been measured or calculated is found limited [145]. The most commonly employed source for tabulated stopping powers, the semi empirical SRIM-code [146], is thus challenged in its predictive capacity. For many aspects of research on plasma-wall interaction is it, however, these low energies, which are most relevant. Low ion energies are not only relevant to model sputtering, fuel retention or defect formation, but are similarly necessary for quantification in analytical approaches such as Low- and Medium Energy Ion Scattering (LEIS & MEIS) [122,147]. Table 3, summarizes the status quo for a number of elemental target materials highly relevant for next generation fusion devices, indicating the almost complete absence of data at low energies, as well as the presence of an ambiguity of available data.

TABLE 3. Account on availability of the stopping powers data for selected elements.

Element	H ions	He ions
Be	No data below 10 keV – no reliable data below 1 MeV.	No data below 200 keV.
C	High number of datasets	High number of datasets; limitations at low energies.
Mo	No data below 50 keV – data spread in the stopping maximum.	Only one low-energy dataset – spread in the stopping maximum.
W	Only one dataset below 100 keV.	Only one dataset below 300 keV; two datasets differing by 10% at classical IBA energies.

Plots in Figures 6 and 7, show respectively detailed data for H in Be and He in W, thus illustrating the limited availability and reliability of reference data at intermediate energies or their complete absence at low energies respectively. Recently, the development of new computational approaches such as time-dependent density functional theory [148,149] or abandoning the modelling of a homogeneous electron gas [150] provides successively better predictions for specific systems, but commonly with high computational expenses. Dedicated experiments providing a better insight into the dependence of stopping powers on Z_2 [151] or specifically targeting materials for PFMC [152] enhance simultaneously the predictive power of semi-empirical approaches. Nevertheless, due to the large number of relevant ion-target combinations, energies and experimental approaches, a concerted action - as proposed by a number of research groups in the CRP-F11023 coordinated by IAEA - will be necessary to build up comprehensive knowledge for the relevant materials in the relevant energy range on the stopping of H and He in Be, Fe, Mo and W. A very similar lack of data and thus necessity for acquisition of high-quality reference data is found for reaction cross-sections of especially ^{3}He with isotopes of Li, Be, B, C, also N and O in the 1-6 MeV energy range.

5. CONCLUDING REMARKS

The accelerator-based analysis and modification of materials is not an isolated or a passive strand of fusion research. The results directly contribute to decisions regarding the wall composition and diagnostic planning in the current and future devices, e.g., ITER and DEMO. It is a driving force for improvements and development of analytical capabilities (nuclear data sets, detectors, chambers) to ensure cutting edge research. To keep this status, continual development of the methods in accordance with what was outlined above is required. Especially the role of in-situ and in-operando systems for the material modification and analyses will be crucial for a deep insight into the dynamics of fuel retention and segregation of metals in PFMC relevant materials such as EUROFER.

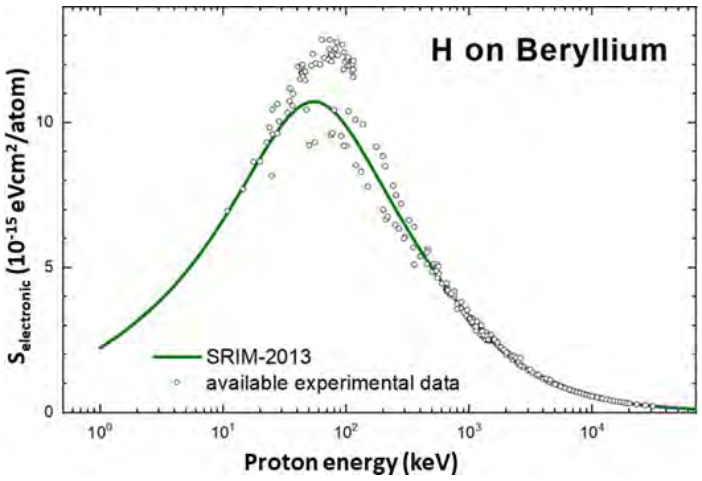

FIG. 6. Data availability of experimental reference electronic stopping cross-sections for hydrogen on beryllium.

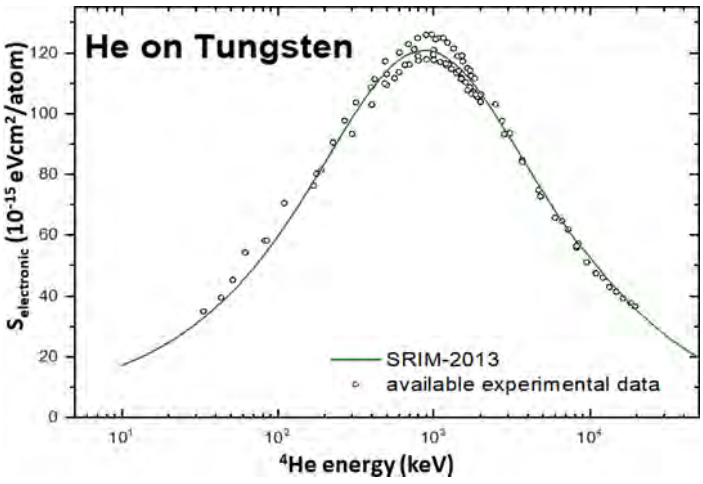

FIG. 7. Data availability on experimental reference electronic stopping cross-sections for helium-4 on tungsten.

ACKNOWLEDGEMENTS

The work has been supported by the Swedish Research Council (VR), Grant 2016–05380. Financial support of the Tandem Accelerator Infrastructure by VR-RFI (contract #2017–00646_9) as well as the Swedish Foundation for Strategic Research (SSF) under contract RIF14–0053 is gratefully acknowledged

REFERENCES

[1] WESSON J., Tokamaks, Oxford University Press, 3rd edition (2008).
[2] BOSCH H-S., HALLE G.M., Improved formulas for fusion cross-sections and thermal reactivities, Nucl. Fusion **32** (1992) 611-632.
[3] MOSES E., Advances in inertial confinement fusion at the National Ignition Facility (NIF), Fusion Eng. Des. **85** (2010) 983.
[4] HOFFMAN I., Review of accelerator driven heavy ion nuclear fusion, Matter Radiat. Extreme **3** (2018) 1.
[5] MIYAMOTO K., Plasma Physics for Controlled Fusion, Springer Series on Atomic, Optical, and Plasma Physics, vol. 92, Springer (2016).
[6] ARTSIMOVITSCH L.A., Tokamak devices, Nucl. Fusion **12** (1972) 215-251.

[7] SPITZER L., The stellarator concept, Phys. Fluids **1** (1958) 253-264.
[8] FEDERICI G. et al., Plasma-material interactions in current tokamaks and their implications for next step fusion reactors, Nucl. Fusion **41** (2001) 1967-2137.
[9] TANABE T. (Ed.), Tritium: Fuel of Fusion Reactors, Springer Verlag (2016).
[10] RUBEL M., Fusion Neutrons: Tritium breeding and impact on wall materials and components of diagnostic systems, J. Fusion Energy **38** (2019) 315-329.
[11] HOFER W.O., ROTH J. (Eds), Physical Processes of the Interaction of Fusion Plasmas with Solids, Academic Press, New York (1996).
[12] NAUJOKS D., Plasma-Material Interactions in Controlled Fusion, Springer Verlag (2006).
[13] PHILIPPS V., WIENHOLD P., KIRSCHNER A., RUBEL M., Erosion and redeposition of wall material in controlled fusion devices, Vacuum **67** (2002) 399-408.
[14] SKINNER C.H. et al., Plasma wall interaction and tritium retention in TFTR, J. Nucl. Mater. **241-243** (1977) 214-226.
[15] SKINNER C.H. et al., Tritium experience in large tokamaks: Application to ITER, Nucl. Fusion **39** (1999) 271-292.
[16] KEILHACKER M., WATKINS M.L., JET TEAM, D-T experiments in the JET tokamak, J. Nucl. Mater. **266-269** (1999) 1-13.
[17] ANDREW P. et al., Tritium retention and clean-up in JET, Fusion Eng. Design **47** (1999) 233-245.
[18] COAD J.P. et al., Erosion/deposition issues at JET, J. Nucl. Mater. **290-293** (2001) 224-230.
[19] PENZHORN R-D. et al., Tritium depth profiles in graphite and carbon fibre composite material exposed to tokamak plasmas, J. Nucl. Mater. **288** (2001) 170-178.
[20] RUBEL M. et al., Beryllium and carbon films in JET following D-T operation, J. Nucl. Mater. **313-316** (2003) 321-326.
[21] COAD J.P. et al., Material migration and fuel retention studies during the JET carbon divertor campaigns, Fusion Eng. Des. **138** (2018) 78-108.
[22] COUNSELL G.C., Tritium retention in next step devices and the requirements for mitigation and removal techniques, Plasma Phys. Control. Fusion **48** (2006) B189-B199.
[23] RUBEL M. et al., Fuel removal from plasma-facing components by oxidation-assisted technique. An overview of surface morphology after oxidation, J. Nucl. Mater. **363-365** (2007) 877-881.
[24] RUBEL M. at al., Fuel removal from plasma-facing components by oxidation techniques. An overview of surface
[25] HOPF C. et al., Oxygen glow discharge cleaning in ASDEX Upgrade, J. Nucl. Mater. **363-365** (2007) 882-887.
[26] ROTH J. et al., Tritium inventory in ITER plasma-facing materials and tritium removal procedures, Plasma Phys. Control. Fusion **50** (2008) 103001.
[27] RUBEL M. et al., Efficiency of Fuel Removal Techniques Tested on Plasma-Facing Components from the TEXTOR Tokamak, Fusion Eng. Des. **87** (2012) 935-940.
[28] MATTHEWS G.F. et al., ITER-Like Wall project overview, Phys. Scr. **T128** (2007) 137-143.
[29] MATTHEWS G.F. et al., Current status of the JET ITER-like Wall Project, Phys. Scr. **T138** (2010) 014030.
[30] MATTHEWS G.F. et al., Overview of the ITER-like wall project, Phys. Scr. **T145** (2011) 014001.
[31] RUBEL M. et al., Beryllium plasma-facing components for the ITER-Like Wall Project at JET, J. Phys. Conf. Series **100** (2008) 062028.
[32] MAIER H. et al., Tungsten and beryllium armour development for the JET ITER-like wall Project, Nucl. Fusion **47** (2007) 222-227.
[33] MERTENS Ph. et al., Clamping of solid tungsten components for the bulk W divertor row in JET—precautionary design for a brittle material, Phys. Scr. **T138** (2009) 014032.
[34] MERTENS Ph. et al., Detailed design of a solid tungsten divertor row for JET in relation to the physics goals, Phys. Scr. **T145** (2011) 014002.
[35] MATTHEWS G.F., Plasma operation with an all metal first-wall: Comparison of an ITER-like wall with a carbon wall in JET, J. Nucl. Mater. **438** (2013) S2-S10.
[36] LOARER T. et al., Comparison of fuel retention in JET between carbon and the ITER-Like Wall, J. Nucl. Mater. **438** (2013) S108-S113.

[37] WIDDOWSON A. et al., Overview of fuel inventory in JET with the ITER-like wall, Nucl. Fusion **57** (2017) 086045.
[38] WIDDOWSON A. et al., Overview of the JET ITER-like wall divertor, Nucl. Mater. Energy **12** (2017) 499-505.
[39] WIDDOWSON A. et al., Fuel inventory and material migration of JET main chamber plasma facing components compared over three operational periods, Phys. Scr. **T171** (2020) 014051. https://doi.org/10.1088/1402-4896/ab5350
[40] MAYER M. et al., Erosion and deposition in the JET divertor during the first ILW campaign, Phys. Scr. **T167** (2016) 014051.
[41] KRAT S. et al., Comparison of erosion and deposition in JET divertor during the first three ITER-like wall campaigns, Phys. Scr. **2020**, T171, 014059.
[42] BARON-WIECHEC A. et al., Global erosion and deposition patterns in JET with the ITER-like wall, J. Nucl. Mater. **463** (2015) 157-161.
[43] WIDDOWSON A. et al., Material migration patterns and overview of first surface analysis of the JET ITER-Like Wall, Phys. Scr. **T159** (2014)014010.
[44] BARON-WIECHEC A. et al., First dust study in JET with the ITER-Like Wall: Sampling, analysis and classification, Nucl. Fusion **55** (2015) 113033.
[45] FORTUNA-ZALESNA E. et al., Dust survey following the final shutdown of TEXTOR: Metal particles and fuel retention, Phys. Scr. **T167** (2016) 014059.
[46] FORTUNA-ZALESNA E. et al., Studies of dust from JET with the ITER-Like Wall: Composition and internal structure, Nucl. Mater. Energy **12** (2017) 582-587.
[47] LITAUDON X. et al**.,** Overview of the JET in support of ITER**,** Nucl. Fusion **57** (2017) 102001.
[48] RUBEL M. et al., Dust generation in tokamaks: Overview of beryllium and tungsten dust characterisation in JET with the ITER-like wall, Fusion Eng. Des. **136** (2018) 579-586.
[49] MEROLA M., et al., Overview and status of ITER internal components, Fusion Eng. Des. **89** (2014) 890-895.
[50] TSITRONE E. et al., Multi machine scaling of fuel retention in 4 carbon dominated tokamaks, J. Nucl. Mater. **415** (2011) S735-S739.
[51] WAMPLER W.R. et al., Erosion and deposition of metals and carbon in the DIII-D divertor, J. Nucl. Mater. **266-269** (1999) 791-797.
[52] ALLEN S.L. et al., ^{13}C transport studies in L-mode divertor plasmas on DIII-D, J. Nucl. Mater. **337-339** (2005) 30-34.
[53] LOARER T. et al., Gas balance and fuel retention in fusion devices, Nucl. Fusion **47** (2007) 1112-1120.
[54] MASAKI K. et al., Tritium distribution in the JT-60 W-shaped divertor, J. Nucl. Mater. **313-316** (2003) 514-518.
[55] KAMADA Y. et al., Completion of JT-60SA construction and contribution to ITER, Nucl. Fusion **62** (2022) 042002.
[56] TOKITANI M. et al., Microstructural characterization of mixed-material deposition layer on the LHD divertor tiles by using nano-geological diagnosis, J. Nucl. Mater. **438** (2013) S818-821.
[57] MAYER M. et al., Material erosion and deposition on the divertor of W7-X, Phys. Scr. **T171** (2020) 014035.
[58] BREZINSEK S. et al., Plasma-Surface Interaction in the Stellarator W7-X: Conclusion Drawn from Operation with Graphite Plasma-Facing Components, Nucl. Fusion **62** (2022) 016006.
[59] BREZINSEK S. et al., Beryllium migration in JET ITER-like wall Plasmas, Nucl. Fusion **55** (2015) 063021.
[60] NEU R. et al., Overview on plasma operation with a full tungsten wall in ASDEX Upgrade, J. Nucl. Mater. **438** (2013) S34-S41.
[61] NEU R. et al., Impurity behaviour in the ASDEX Upgrade divertor tokamak with large area tungsten walls, Plasma Phys. Control. Fusion 41 (2002) 811-826.
[62] BREZINSEK S. et al, Erosion, screening and migration of tungsten in the JET divertor, Nucl. Fusion **59** (2019) 096035.

[63] RUBEL M., Mirror Test for ITER at the JET tokamak: An overview of the programme, Rev. Sci. Instrum. **77** (2006) 063501-1 – 063501-6.
[64] IVANOVA D. et al., An overview of the Comprehensive First Mirrors Test in JET with ITER-Like Wall, Phys. Scr. **T159** (2014) 014011.
[65] MOON SUNWOO et al., First mirror test in JET for ITER: Complete overview after three ILW campaigns, Nucl. Mater. Energy **19** (2019) 59-66.
[66] LITNOVSKY A. et al., Diagnostic mirrors for ITER: research in a frame of International Tokamak Physics Activity, Nucl. Fusion **59** (2019) 066029.
[67] RUBEL M. et al., First mirror erosion-deposition studies in JET using an ITER-like mirror test assembly, Nucl. Fusion **61** (2021) 046022.
[68] CHU W.K., MAYER M., NICOLET M.A., Backscattering Spectroscopy, Academic Press, New York (1978).
[69] TESMER J.R., NASTASI M. (Eds), Handbook of Modern Ion Beam Analysis, Material Research Society, Pittsburg, PA (1995).
[70] RUBEL M, Analysis of plasma facing materials: material migration and fuel retention, Phys. Scr. **T123** (2006) 54-65.
[71] RUBEL M. et al., The role and application of ion beam analysis for studies of plasma-facing components in controlled fusion devices, Nucl. Instr. Meth. **B371** (2016) 4-11.
[72] MAYER M. et al., Ion beam analysis of fusion plasma-facing materials and components: facilities and research challenges, Nucl. Fusion **60** (2020) 025001.
[73] MAYER M. et al., Quantitative depth profiling of deuterium up to very large depths, Nucl. Instr. Meth. **B267** (2009) 506- 512.
[74] RUBEL M. et al., Fuel inventory and deposition in castellated structures in JET-ILW, Nucl. Fusion **57** (2017) 066027.
[75] DITTRICH L. et al., Fuel retention and erosion-deposition on inner wall cladding tiles in JET-ILW, Phys. Scr. **96** (2021) 124071.
[76] WIDDOWSON A. et al., Evaluation of tritium retention in plasma facing components during JET tritium operations, Phys. Scr. **96** (2021) 124075.
[77] STRÖM P. et al., Analysis of co-deposited layers with deuterium and impurity elements on samples from the divertor of JET with ITER-like wall, J. Nucl. Mater. **516** (2019) 202-213.
[78] GARCIA-CARRASCO A. et al., Impact of ion cyclotron wall conditioning on plasma-facing components, Phys. Scr. **T159** (2014) 014017.
[79] PÉGOURIÉ B. et al., Deuterium inventory in Tore Supra: coupled carbon – deuterium balance, J. Nucl. Mater. **438** (2013) S120-S126.
[80] RUBEL M., BREZINSEK S., WIDDOWSON A., "Surface modification by fusion plasmas", Plasma Applications for Material Modification: From Microelectronics to Biological Materials, Jenny Stanford Publishing, Singapore (2020).
[81] BYKOV I. et al., Investigation of tritium analysis methods for ion microbeam application, Nucl. Instrum. Meth. **B 273** (2012) 250-253.
[82] KUBOTA N. et al., "Surface Analysis for TFTR armour tile exposed to D-T plasmas using nuclear technique", 21st IAEA Conf. on Fusion Energy, EX/P4-12 (2006).
[83] FRIEDRICH M. et al., Tritium depth profiling by AMS in carbon samples from fusion experiments, Phys. Scr. **T94** (2001) 98-101.
[84] DITTRICH L. et al., "Retention of seeded gases in first wall components from the JET tokamak with the ITER-like wall", 32nd Symposium on Fusion Technology (Dubrovnik, Croatia, 2022).
[85] LAGOYANNIS A. et al., Surface Analysis of the ITER-like wall divertor Tiles at JET tokamak, Nucl. Fusion **57** (2017) 076027.
[86] BYKOV I. et al., Studies of Be migration in the JET tokamak using AMS with ^{10}Be marker, Nucl. Mater. **371** (2016) 370-375.
[87] GUDOWSKA I. et al., Fluxes of boron in the scrape-off plasma of TEXTOR following boronization, J. Nucl. Mater. **176- 177** (1990) 363-369.
[88] HAKOLA A. et al., Global transport of light elements boron and carbon in the full-W ASDEX Upgrade, J. Nucl. Mater. **415** (2011) S227-S230.

[89] STRÖM P. et al., Characterisation of layers formed on plasma-facing components in controlled fusion devices: role of heavy ion elastic recoil detection, Vacuum **122** (2015) 260-267.
[90] WECKMANN A. et al., Review of global migration, fuel retention and modelling after TEXTOR decommission, Nucl. Mater. Energy **17** (2018) 83-112.
[91] WECKMANN A. et al., Deuterium deposition patterns for fuel retention in the divertor of the COMPASS tokamak, Fusion Eng. Des. **179** (2022) 113118.
[92] COAD J.P., RUBEL M., WU C.H., The amount and distribution of deuterium retained in the JET divertor after the C and Be phases in 1994-5, J. Nucl. Mater. **241-243** (1997) 408-413.
[93] RUBEL M. et al., Accelerator-based ion beam analysis of fusion reactor materials, Vacuum **78** (2005) 255-261.
[94] RUBEL M. et al., Overview of tracer techniques in studies of material erosion, re-deposition and fuel inventory in tokamaks, J. Nucl. Mater. **329-333** (2004) 795-799.
[95] COAD J.P. et al., Overview of material re-deposition and Fuel retention studies at JET with the Gas Box divertor, Nucl. Fusion **46** (2006) 350-366.
[96] PETERSSON P. et al., Nuclear reaction and heavy ion ERD analysis of wall materials from controlled fusion devices: deuterium and nitrogen 15 studies, Nucl. Instr. Meth. **B 273** (2012) 212.
[97] RUBEL M., Nitrogen and Neon Retention in Plasma-Facing Materials, J. Nucl. Mater. **415** (2011) S223-S226.
[98] PETERSSON P. et al., Transport and retention studies in tokamaks using ^{15}N tracer gas, Phys. Scr. **T159** (2014) 014042.
[99] PETERSSON P. et al., Nuclear reaction and heavy ion ERD analysis of wall materials from controlled fusion devices: deuterium and nitrogen 15 studies, Nucl. Instr. Meth. **B 273** (2012) 212.
[100] PETERSSON P. et al., Injection of nitrogen-15 tracer into ASDEX Upgrade: New technique in material migration studies, J. Nucl. Mater. **438** (2013) S616-S619.
[101] RUBEL M. et al., Silicon fluxes in the scrape-off layer plasma during silicon-assisted operation of TEXTOR, J. Nucl. Mater. 220 - 222 (1995) 536 – 540.
[102] PETERSSON P. et al., Micro distribution of fuel and metal in carbon based plasma-facing components, Phys. Scr. **T145** (2011) 014014.
[103] RUBEL M. et al., Fuel inventory and deposition in castellated structures in JET-ILW, Nucl. Fusion **57** (2017) 066027.
[104] FAZINIĆ S. et al., Ion micro-beam analysis of dust particles and co-deposits from JET with ITER-like wallAnal. Chem. **90** (2018) 5744-5744.
[105] FAZINIĆ S. et al., Micro-analyses of dust particles generated in the JET tokamak with the ITER-Like Wall, Nucl. Fusion **60** (2020) 12606.
[106] MAYER M. et al., Hydrogen inventories in nuclear fusion devices, J. Nucl. Mater. **290-293** (2001) 381-388.
[107] LOARER T. et al., Gas balance and fuel retention in fusion devices, Nucl. Fusion **47** (2007) 1112.
[108] HEINOLA K. et al., Long-term fuel retention in JET ITER-like wall, Phys. Scr. **T167** (2016) 014075.
[109] SUMMERS D.D.D. et al., In-situ measurement of hydrogen retention in JET carbon tiles, J. Nucl. Mater **290-293** (2001) 496-500.
[110] HUBER A. et al., In-situ measurement of trapped hydrogen by laser desorption in TEXTOR-94, Phys. Scr. **T94** (2001) 102-105.
[111] SCHWEER B. et al., In-situ diagnostic for monitoring of deuterium and tritium in re-deposited carbon layers by laser induced desorption, J. Nucl. Mater **363-365** (2007) 1375-1379.
[112] PHILIPPS V. et al., Development of laser-based techniques for in-situ characterization of the first wall in ITER and future fusion devices, Nucl. Fusion **53** (2013) 093002.
[113] MALAQUIAS M. et al., Development of ITER relevant laser techniques for deposited layer characterization and tritium inventory, J. Nucl. Mater. **438** (2013) S936-S939.
[114] ZLOBINSKI M et al., Efficiency of layer-induced desorption of D from Be/D layers and surface modification due to LID, Phys. Scr. **T171** (2020) 014075.
[115] STRÖM P. et al., A combined segmented anode gas ionization chamber and time-of-flight detector for heavy ion elastic recoil detection analysis, Rev. Sci. Instrum. **87** (2016) 103303.

[116] GARCIA-CARRASCO A. et al., of helium implantation and ion-induced damage on reflectivity of molybdenum mirrors, Nucl. Instr. Meth. **B 382** (2016) 91-95.
[117] RUBEL M. et al., Metallic mirrors for plasma diagnosis in current and future reactors: Tests for ITER and DEMO, Phys. Scr. **T170** (2017) 014061.
[118] SCHWARZ-SELINGER T., Deuterium retention in MeV self-implanted tungsten: Influence of damaging dose rate, Nucl. Mater. Energy **12** (2017) 683-688.
[119] WIDDOWSON A. et al., Experience of handling beryllium, tritium and activated components from JET ITER like wall, Phys. Scr. **T167** (2016) 014057.
[120] KANTRE K. et al., Combination of in-situ ion beam analysis and thermal desorption spectroscopy for studying deuterium implanted in tungsten, Phys. Scr. **96** (2021) 124004.
[121] STRÖM P., PRIMETZHOFER D., Ion beam tools for nondestructive in-situ and in-operando composition analysis and modification of materials at the Tandem Laboratory in Uppsala, J. Intrum. (JINST) **17** (2022) P04011.
[122] J. SHAMS-LATIFI J. et al., An *in-situ* ToF-LEIS and AES study of near-surface modifications of the composition of EUROFER97 induced by thermal annealing, Nucl. Mater. Energy **30** (2022) 101139.
[123] SIGMUND P., *Particle Penetration and Radiation Effects*, Vol. 2, Springer, Switzerland (2014).
[124] SAND A.E., NORDLUND K., J. Nucl. Mater. 456 (2015) 99-105.
[125] H. BETHE H., Zur Theorie des Durchgangs schneller Korpuskularstrahlen durch Materie, Ann. Physik 5 (1930) 325- 400.
[126] BETHE H., Bremsformel für Elektronen relativistischer Geschwindigkeit., Z. Physik 76 (1932) 293–299.
[127] MÖLLER C, Zur Theorie des Durchgangs schneller Elektronen durch Materie, Ann. Physik 406 (1932) 531-585.
[128] BLOCH F., Zur Bremsung rasch bewegter Teilchen beim Durchgang durch Materie, Ann. Physik 408 (1933) 285-320 and; Bremsvermögen von Atomen mit mehreren Elektronen, Z. Physik 81 (1933) 363-376.
[129] FERMI E., TELLER E., The Capture of Negative Mesotrons in Matter, Phys. Rev. 72 (1947) 399-408.
[130] VALDES J.E. et al, Energy loss of slow protons in solids: Deviation from the proportionality with projectile velocity, Phys. Rev. A 49 (1994) 1083-1088-2695.
[131] MARKIN S.N. et al., Electronic stopping of low-energy H and He in Cu and Au investigated by time-of-flight low- energy ion scattering, Phys. Rev. B 80 (2009) 205105.
[132] AUTH C. et al, Threshold in the Stopping of Slow Protons Scattered from the Surface of a Wide-Band-Gap Insulator, Phys. Rev. Lett. **81** (1999) 4831-4834.
[133] MARKIN S.N., PRIMETZHOFER D, BAUER P., Vanishing Electronic Energy Loss of Very Slow Light Ions in Insulators with Large Band Gaps, Phys. Rev. Lett. **103** (2009) 113201.
[134] PRIMETZHOFER D. et al., Electronic Excitations of Slow Ions in a Free Electron Gas Metal: Evidence for Charge Exchange Effects, Phys. Rev. Lett. **107** (2011) 163201.
[135] LOHMANN S., PRIMETZHOFER D., Disparate Energy Scaling of Trajectory-Dependent Electronic Excitations for Slow Protons and He Ions, Phys. Rev. Letters **124** (2020) 096601.
[136] LI, C-K, et al, *Ab initio* electronic stopping power and threshold effect of channelled slow light ions in HfO_2, Phys. Rev. **B 96** (2017) 094301.
[137] QUASHIE E.E, A.A. CORREA A.A., Electronic stopping power of protons and alpha particles in nickel, Phys. Rev. **B 98** (2018) 235122.
[138] MERTENS P., How to measure absolute stopping cross sections by backscattering and transmission methods: Part II. Transmission, Nucl. Instr. Meth. **B 27** (1987) 315-322.
[139] BAUER P., SEMRAD D., MERTENS P., Reference proton stopping cross sections for five elements around the maximum, Nucl. Instr. Methods Phys. Res., Sect. **B12** (1985) 56–61.
[140] BIERSACK J.P., STEINBAUER E., BAUER P., A particularly fast TRIM version for ion backscattering and high energy ion implantation, Nucl. Instr. Meth. **B 61** (1991) 77–82.
[141] ROTH D. et al., A procedure to determine electronic energy loss from relative measurements with TOF-LEIS, Nucl. Instr. Meth. **B 317** (2013) 61-65.

[142] ROTH D. et al., Systematic analysis of different experimental approaches to measure electronic stopping of very slow hydrogen ions, Nucl. Instr. Meth. **B 437** (2018) 1–7.
[143] Stopping Power Database. Available at: https://www-nds.iaea.org/stopping/
[144] MONTANARI C.C., DIMITRIOU P., The IAEA stopping power database, following the trends in stopping power of ions in matter, Nucl. Instr. Meth. **B 408** (2017) 50-55.
[145] WITTMAACK K., Misconceptions impairing the validity of the stopping power tables in the SRIM library and suggestions for doing better in the future, Nucl. Instr. Meth. **B 380** (2016) 57-70.
[146] ZIEGLER J.F, ZIEGLER M.D., BIERSACK J.P., SRIM – The stopping and range of ions in matter (2010), Nucl. Instr. Meth. **B 268** (2010) 1818-1823.
[147] KOSLOWSKI H.R. et al., Temperature-dependent in-situ LEIS measurement of W surface enrichment by 250 eV D sputtering of EUROFER, Nucl. Mater. Energy **16** (2018) 181-190. 1
[148] SCHLEIFE A., KANAI Y., CORREA A.A., Accurate atomistic first-principles calculations of electronic stopping, Phys. Rev. **B 91** (2015) 014306.
[149] OJANPERÄ A. KRASHENINNIKOV A.V., PUSKA M., Electronic stopping power from first-principles calculations with account for core electron excitations and projectile ionization, Phys. Rev. **B 89** (2014) 035120.
[150] MATIAS F. et al., Nonlinear stopping effects of slow ions in a no-free-electron system: Titanium nitride, Phys. Rev. **A 100** (2019) 030701.
[151] MORO M.V., BAUER P., PRIMETZHOFER D., Experimental electronic stopping cross section of transition metals for light ions: Systematics around the stopping maximum, Phys. Rev. **A 102** (2022) 022808.
[152] MORO M.V. et al., Experimental electronic stopping cross section of tungsten for light ions in a large energy interval, Nucl. Instr. Meth. B 498 (2021) 1-8.

List of Acronyms

Acronym	Meaning
AMS	Accelerator Mass Spectroscopy
ERDA	Elastic Recoil Detection Analysis
GDOES	Glow Discharge Optical Emission Spectroscopy
GIC	Gas Ionization Chamber (detector)
HIERDA	Heavy Ion ERDA
IBA	Ion Beam Analysis
ILW	ITER-Like Wall
JET	Joint European Torus
JET-C	JET with Carbon wall
JET-ILW	JET with ITER-Like Wall
LEIS	Low Energy Ion Source
LIAS	Laser-Induced Ablation Spectroscopy
LIBS	Laser-Induced Breakdown Spectroscopy
LID	Laser-Induced Desorption
NRA	Nuclear Reaction Analysis
PFC	Plasma-Facing Components
PFM	Plasma-Facing Materials
RBS	Rutherford Backscattering Spectrometry
RF	Radio Frequency
RGA	Residual Gas Analyser
RH	Remote Handling
SIGMA	Set-up for In-situ Growth, Material modification and Analysis
SIMS	Secondary Ion Mass Spectroscopy
TDS	Thermal Desorption Spectroscopy
ToF-ERDA	Time-of-Flight ERDA/HIERDA

MEGAVOLT ACCELERATOR SYSTEMS FOR ENVIRONMENTAL MONITORING

David D. COHEN

Centre for Accelerator Science,
Australian Nuclear Science and technology Organisation,
Menai, NSW, Australia
Email: David.Cohen@ansto.gov.au

Abstract

The accelerator based ion beam techniques of ion beam analysis (IBA) and accelerator mass spectrometry (AMS) have been applied to environmental studies for many decades. IBA is particularly suited to fine particle air pollution studies where multi-elemental analysis of microgram samples is required. AMS, using ^{14}C isotope, is a key tool for climate change studies and other isotopes like ^{36}Cl and ^{10}Be can be applied to ground water and soil erosion studies depending on the isotopic half-life and timescale being used.

Megavolt accelerator systems together with modern detector systems are capable of individual atom and photon counting and consequently are very sensitive detection systems. They are capable of precise and accurate measurements on very small sample sizes. The multi-element IBA technique of PIXE is capable of measuring some elements with (µg/g) sensitivity on picogram (pg) samples. The AMS techniques used in ^{14}C analysis have achieved dates out to 50,000 years on 10 µg samples.

1. INTRODUCTION

Accelerator based ion beam analysis (IBA) and mass spectrometry (AMS) techniques have been applied successfully to environmental studies for many decades [1-4]. Megavolt accelerators are ideally suited for these studies They are very sensitive, capable of individual atom or photon counting and they can analysis very small samples, picograms to microgram in just a few minutes of beam time [5-7].

In particular, IBA and AMS have been used to study climate change both current and past. It is accepted by the majority of scientists that climate change is here now [8]. 2021 was the sixth warmest year since 1880, eight of the top ten warmest years on our planet occurred in the last decade. Global temperatures have risen 0.85^{o}C above the 1951-1980 average with a 1.1^{o}C increase since the Industrial Revolution around 250 years ago. Greenhouse gases like carbon dioxide account for approximately +2.5W/m^2 of global warming [8]. ^{14}C AMS studies can date carbon dioxide levels in ice cores going back 50,000 years [2,4]. It can distinguish between modern and ancient carbon to better understand the past and present levels of this greenhouse gas.

Fine particle pollution in the atmosphere from fossil fuel combustion like ammonium sulfate, secondary organics and black carbon have a total negative climate forcing of around -1.1W/m^2 reducing the impact of the greenhouse gases. Without fine particle pollution the current global temperature rise would be even higher than it currently is [8].

Fig. 1 shows fine particle pollution in Manila, Philippines on a clear and a polluted day. It demonstrates that fine particle pollution also affects visibility. Indeed, the eyes are a good detector of fine particle pollution.

Fine particle pollution is driven by the current trend globally to urbanisation [9-14]. The movement of large numbers of people from rural areas to the cities. Everyday more than 100,000 people globally move into cities. Since 2008, more than 50% of the world's population lives in cities. These cities become megacities with populations in excess of 10M people. Currently there are more than 37 megacities globally with eight out of the top ten megacities occurring in the Asia region. As cities get bigger more and more resources are needed to generate the power needed and the food required to feed and sustain them.

The IAEA has run a very successful fine particle pollution characterisation research program for decades across more than 15 countries in Asia from Pakistan in the west to the Philippines in east and Mongolia in the north to New Zealand and Australia in the south. This program has helped national programs understand their air pollution issues in megacities and also identified long range pollution transport across international borders.

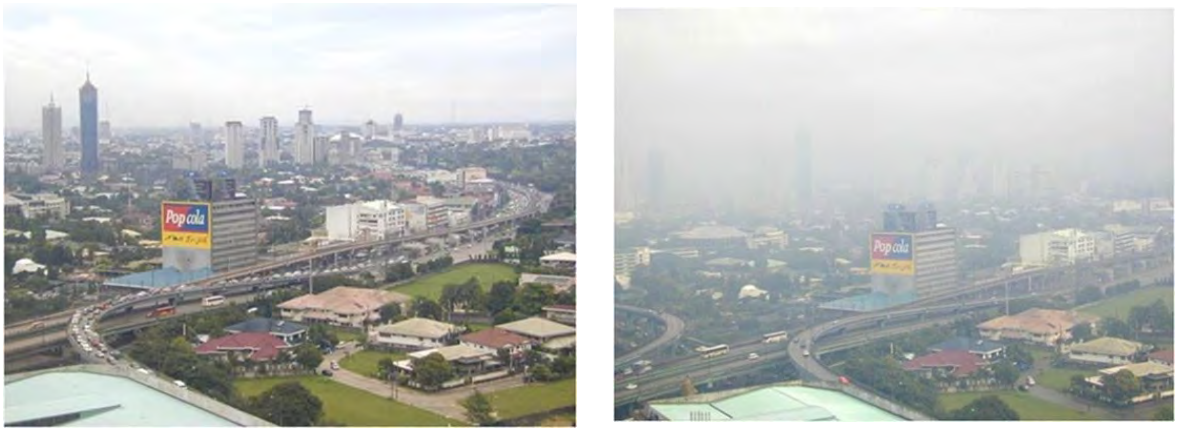

(a) (b)

FIG. 1 Aerial view of Manila, Philippines on (a) a clear day and (b) a fine particle polluted day.

Fine particle pollution has recognised health effects [15]. Even annual fine particle pollution levels as low as 10µg/m^3 have health impacts, some megacities have annual average pollution levels over 50µg/m^3. There appears to be no threshold limit for these health impacts. Fine particle pollution shortens life expectancy. It has been estimated that the average life expectancy of a person living in a major Asian megacity is reduced by between 5 to 6 years. In the State of NSW in Australia, with a population of only 6M and which has relatively clean air most days of the year, it is estimated that 420 a year die prematurely from fine particle air pollution. This is more than are killed on the roads by motor vehicles in NSW each year.

2. ION BEAM ANALYSIS

The IBA techniques of Particle Induced X-ray Emission (PIXE), Particle Induced Gamma Ray Emission (PIGE), Rutherford Backscattering (RBS), Particle Elastic Scattering Analysis (PESA) most commonly used on these machines, all have several key properties in common. They can measure micrograms of sample with parts per million sensitivity non-destructively in just a few minutes of accelerator running time. Fine particles, collected on filters are such samples. For average fine particle air pollution levels of 10µg/m^3, 30 m^3 of air passed through a filter in 24 hours will contain only 300µg of sample.

PIXE has been used since the mid 1970's to analysis filters obtained to characterise fine particle air pollution. Tens of thousands of such filters have been analysed to date across the globe in Europe, Africa, South America, Middle East and Asia by dozens of laboratories with megavolt accelerators. To date, these methods have been greatly refined.

All four IBA techniques of PIXE, PIGE, RBS and PESA can be run simultaneously to determine over 30 different elements from hydrogen to lead at concentrations from a ng/m^3 to hundreds of µg/m^3 of air sampled. Typically, a few nanoamps of 3 MeV protons with beam diameters of several millimetres are used to irradiate each filter.

Fig.2 shows the 2MV STAR accelerator at ANSTO. The high energy beamline and end station in the central foreground, is the environment beam line used for IBA analysis of Teflon filters used to collect fine particle pollution.

A typical 25mm stretched Teflon filter is shown in Fig.3. This filter was loaded with fine particles collected by a PM2.5 fine particle cyclone system using a flow rate of 22l/min and collected over a 24 hour period from midnight to midnight.

The four IBA techniques described above produce four unique spectra, these spectra are shown in Fig. 4 for a typical stretched Teflon filter. Each spectrum was run for 3 µC of 2.5 MeV protons.

These x-ray PIXE spectra provides data on elements from Al to Pb. The x-ray energy is characteristic of the element present and the area under each characteristic peak is related to the concentration of that element. In the PIXE spectra we see evidence of possible pollution sources associated with key elements. For example, Al, Si and Ti from wind blown soils, Cl from sea spray, K from biomass burning, Ca from cement production, metals from industry and Br and Pb from the use of leaded petrol in automobiles. In the PIGE gamma ray spectrum the

photon energy is higher than for x-rays with peaks identifying elements such as F at 197 keV, Na at 440 keV. Again, the area under these gamma peaks is related to the elemental concentrations. The RBS spectrum is used to determine the low Z elements C, N and O [3,6]. The blue vertical lines show the front edge back scattered energies for these elements. The area from these front edge energies back to lower energies is used to estimate the total C, N and O concentrations. The PESA spectrum is used to measure the total H concentration. Hydrogen is the lightest element in the periodic table so its peak is to the left of all other element peaks in this spectrum. All these four spectra were analysed using the iBAT codes to obtain peak areas and elemental concentrations [16].

FIG.2. ANSTO 2MV STAR accelerator used in IBA studies

FIG. 3. Exposed stretched Teflon filter, optimised for IBA analysis.

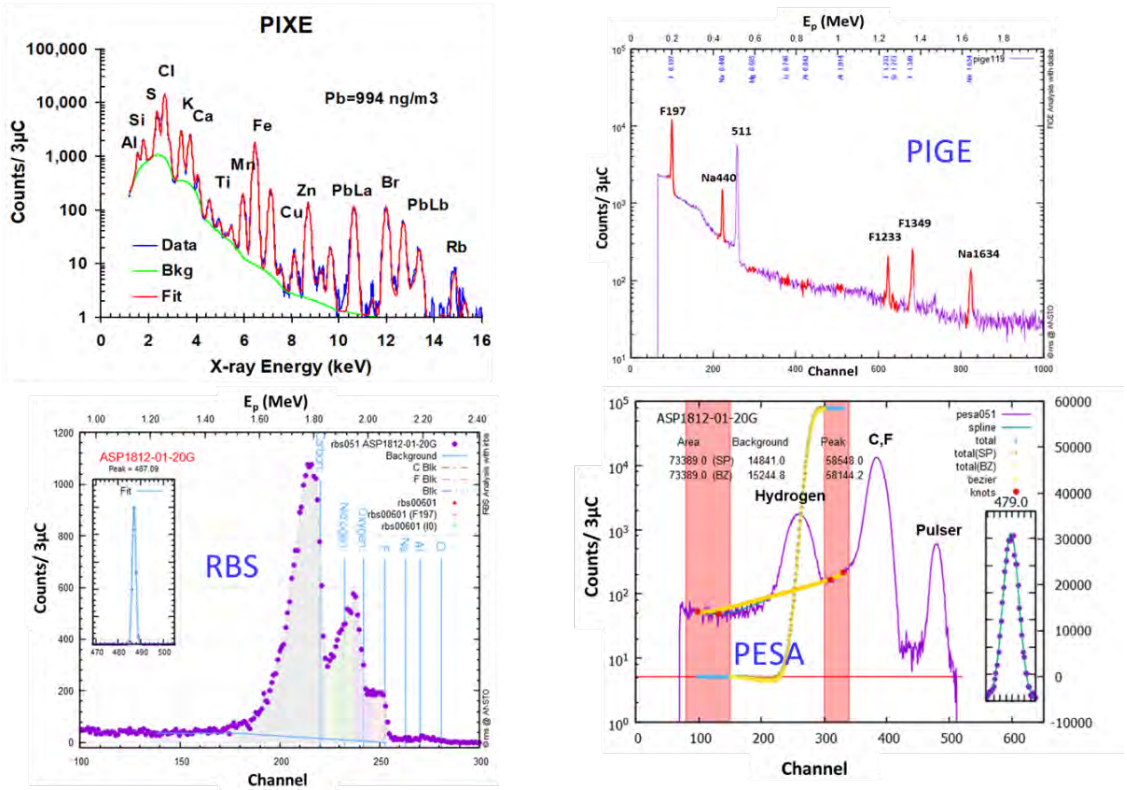

FIG. 4. PIXE, PIGE, RBS and PESA spectra for a typical exposed stretched Teflon filter.

For these spectra minimum detectable limits (MDL) for most elements range from 1 ng/m^3 to 10 ng/m^3 of air sampled through the filter. MDLs for the low atomic number elements using PIGE tend to be a bit higher at 50 ng/m^3 to 100ng/m^3.

3. SOURCE APPORTIONMENT

The elemental outputs from these methods can be used as input for statistical source apportionment methods such as Positive Matrix Factorisation (PMF) to generate elemental source fingerprints and to then determine the contribution of these fingerprints to the total measured mass of fine particles in the air [17]. PMF is a one step process that that takes the daily mass matrix M_{ij} and determines a fingerprint matrix F_{kj} with a fingerprint contribution matrix G_{ik} by minimizing the error term E_{ij} in the equation,

$$M_{ij} = \sum_{k=1}^{p} F_{kj} * G_{ik} + E_{ij}$$

Depending on the number of daily measurements and the number of chemical species measured for each day the number of source fingerprints can range from 5 to 10 [18-20].

For example, Fig. 5 shows the PMF fingerprints obtained for 2,303 PM2.5 daily filters at an urban site in Sydney, Australia for the period from January 1998 to February 2022. Eight fingerprints, *Soil, Aged Sea Spray*, fresh *Sea Spray*, *Secondary Sulfate*, *Smoke* from biomass burning, two *Automobile* fingerprints and an *Industrial Nitrate* fingerprint were obtained. Each fingerprint is composed of 24 elements and chemical species from H to Pb with black carbon (BC) and ammonium nitrate (NO3) included. The average PM2.5 mass over this 24 year period was (8.1±5.2 μg/m^3). That is the total mass of 8.1 μg/m^3 was divided into eight different and statistically significant source fingerprints. The 24 year average percentage contribution to this mass for the eight sources were 2.56%, 14.7%, 9.17%, 24.5%, 29.5%, 14.0%, 1.94% and 3.75% respectively and are shown on each of the eight plots in Fig. 5.

For each of these eight fingerprints the contributions of each element have been normalised to the element with the maximum impact for that fingerprint. This helps identify and put a name to each of these fingerprints. Note the y-axis *Source Fraction* is a four-decade log plot. The *Soil* fingerprint was driven by the elements Al, Si, Ca, Ti and Fe with the (Al/Si) ratio typical for clay aluminosilicates. The *Sea* fingerprint was driven by Na and Cl in the correct ratio for NaCl and with traces of Si, Ca and Br. The Secondary Sulfate (*2ndryS*) fingerprint was driven by H and S in the correct ratio for ammonium sulfate. The *Smoke* fingerprint was driven by H reflecting the organic component, K indicative of biomass burning, black carbon (BC) for the soot content and other trace elements such as Cl, Zn and Br typical of biomass burning.

Of the two automobile fingerprints *Auto2* represents vehicles using leaded petrol which was banned in January 2001 and so its 24 year average was quite low being essential zero for 20 years of this study period. Nevertheless, the PMF technique was able to extract this out as a separate fingerprint. The technique was also able to provide information on chemistry that takes place in airborne aerosols as they age. The sampling site was 30 km from the coast and received significant sea breezes in the summer periods. During the transport of sea salts across major urban and semi-industrial regions to the sampling site chemical reactions between the NaCl based salts reacting with the secondary sulfates produced an Aged Sea Salt (*Seaaged*) fingerprint stripped of Cl and high in S. Demonstrating the production of a sodium sulfate aerosol. This demonstrates the power of the PMF statistical method in identifying sources and their contributions.

The PMF technique also provides the daily contribution of each fingerprint to the total PM2.5 mass. This is obtained from the G_{ik} matrix. Fig. 6 is a plot of the daily *Soil* fingerprint concentration shown in Fig. 5 from January 2001 to February 2022

At this Liverpool site in Sydney, Australia there were several possible soil sources, these included desert dust storms, soil from agricultural activities such as ploughing and retrained road dust produced by vehicular movements. Dust storms and agricultural soil can be transported over large distances whereas retrained road dust tends to be a more constant source and to be localised. Fig. 6 shows that there were 166 days with the *Soil* fingerprint concentrations above 0.5 μg/cm^3. This upper-level soil concentration of 0.5 μg/m^3 was arbitrarily fixed but hopefully concentrations below this would include most retrained soil events. Some individual high *Soil* dates at the Liverpool site are labelled in Fig.6. There were clearly many more major *Soil* events between

2018 and 2021 with levels above 2 µg/m^3 than in previous years. The 166 daily soil events above 0.5 µg/cm^3 probably include most desert dust and agricultural soil events which are discussed further in the next section.

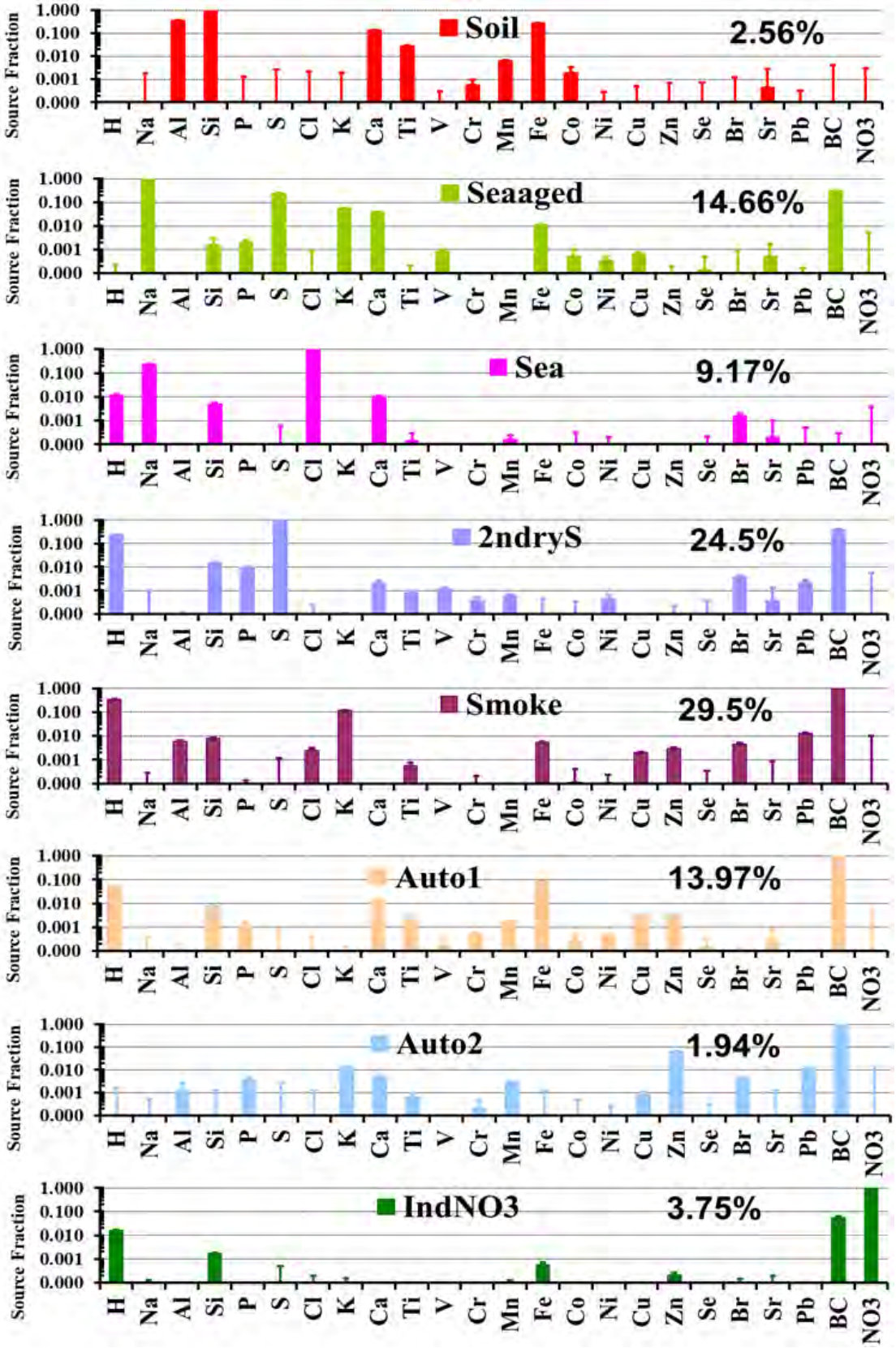

FIG. 5. PMF eight fingerprint fit to 24 years of PM2.5 mass data at the Liverpool site in Sydney Australia.

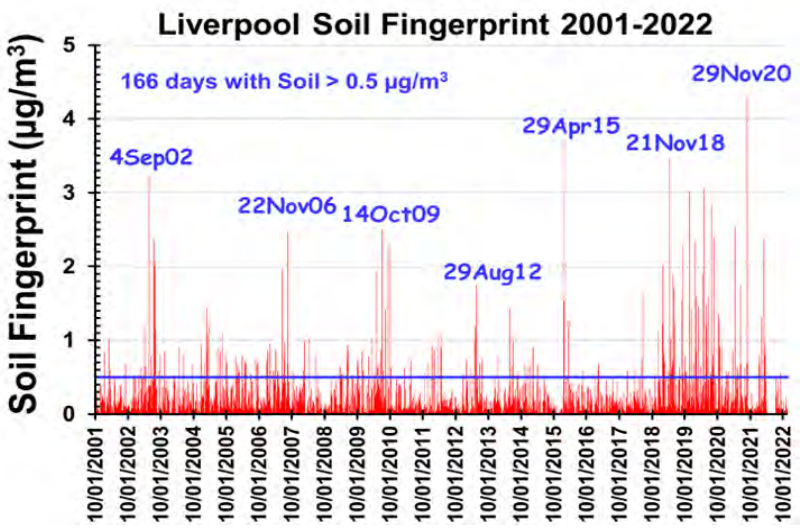

FIG. 6. A time series plot from January 2001 to February 2022 of the Soil fingerprint shown in Fig. 6.

4. HYSPLIT BACK TRAJECTORIES

The PMF source fingerprinting methods can be taken a step further with the application of hourly wind speed and direction data to pinpoint the location and long-range transport of these pollution sources often many hundreds of kilometres. The HYSPLIT codes contain hourly wind speed and direction data, based on 1°x1° grids for anywhere on the globe and are freely available on the WEB [21-22]. In our current region of interest (Australia), a 1°x1° grid corresponds to approximately 100kmx100km area.

Australia is one of the driest continents on earth and has at least fourteen major deserts mainly across its central regions. Major desert dust storms, like the one shown in Fig. 7 are readily identified as impacting at sampling sites in the Sydney basin by not only the unusually high winds needed to transport them there but also the red dust associated with the transport of soils rich in iron oxides. A basic question is - what is the major *Soil* source transporting significant soils into the Sydney basin when you consider every hour of every day for several decades?

FIG. 7. Desert dust storm in Birdsville, Queensland, Australia. 27 January 2006

Using HYSPLIT data, the Liverpool site in Sydney and a height of 300m as a starting point for hourly seven day back trajectories for each of the 166 days with the *Soil* fingerprint concentrations above 0.5 µg/m^3 we can backtrack the source of the *Soil* on each of these days. Fig. 8 is plot of the desert regions across Australia. It contains 14 boxes representing the 14 desert regions and a fifteenth box representing the agricultural region of the Riverina in state of NSW. Twenty four one hourly back trajectories for 4 September 2002 and 8 May 2019 are shown as typical examples of daily back trajectories. The 8 May 2019 back trajectory shows several of the hourly seven day back trajectories on that day passing through several of the desert boxes including box 8 (The Great Victoria Desert West) over 2,800 km west of the Liverpool site. The 4 September 2002 back trajectory was further south of the 8 May 2002 back trajectory. It spent much of its seven days over the ocean, mainly passing through box 15, the Riverina, an agricultural region in NSW in the first few days of its 7 day back trajectory.

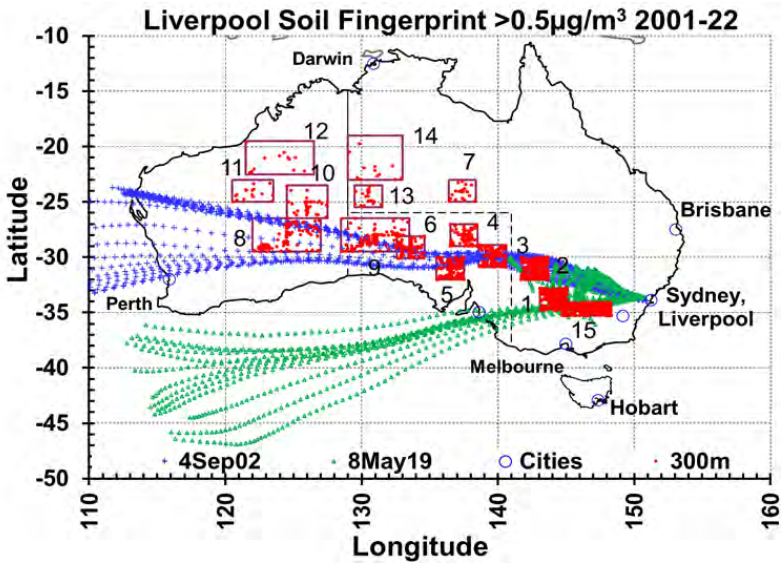

FIG. 8. Map of desert regions represented by boxes 1-14 and one major agricultural region box 15

We have continued this process for every hour of every day for all of the 166 days with a high *Soil* fingerprint during the study period from January 2001 to February 2022. Every time a 7 day hourly back trajectory crossed any one of the 15 boxes a dot was placed in that box. The number of dots in each box then presented the number of times that desert region could have contributed to the *Soil* measured at the Liverpool site in the Sydney basin during the twenty two years from January 2001 to February 2022. Table 1 summarises the percent of back trajectories crossing each of these box regions.

TABLE 1. A SUMMARY OF THE PERCENT OF BACK TRAJECTORIES CROSSING EACH OF THE FIFTEEN BOX REGIONS IN FIG. 8.

300m Desert	Trajectories (%)	Desert	Trajectories (%)
15 Riverina	41.2	6 Lake Eyre North	2.1
1 Lake Mungo	25.6	10 Gibson	0.7
2 Lake Windaunka	11.8	7 Simpson Desert	0.5
4 Olympic Dam	5.2	13 Great Sandy East	0.5
3 East Flinders	4.6	11 Little Sandy	0.4
9 Great Vic E	2.4	12 Great Sandy West	0.3
8 Great Vic West	2.2	14 Tanami	0.3
5 Emu Fields Salt	2.2		

The maximum percent of back trajectories (41.2%) crossed box 15, the Riverina agricultural region followed by the Lake Mungo desert region with 25.6% of all trajectories. *Soil* from these two regions was responsible for more than two thirds of the *Soil* entering the Sydney basin during the twenty two years from January 2001 to February 2022. The remaining thirteen desert regions only contributed about one third of the time to *Soil* levels in Sydney above 0.5 µg/m^3. The Riverina and Lake Mungo regions are between 500 and 600 km WSW from the Liverpool site in the Sydney basin so soil from these regions represented long range transport of PM2.5 particles.

5. ACCELERATOR MASS SPECTROMETRY

Accelerator mass spectrometry (AMS) is a dating technique base on the half-life of isotopes. Megavolt accelerators can accelerate almost any isotope in the periodic table. They have the potential to determine isotopic

ratios down to 1 part in 10^{15} in microgram samples with a precision approaching 0.5%. It is a dating technique capable of measuring dates out to around ten half-lives of the isotope being considered [2].

The method is based on the selected isotopes rigidity when passing through the entire accelerator system from the ion source to the end station's detector system [2,4]. The rigidity of an ion of mass M(amu) with charge q and energy E(MeV) is defined as (ME/q^2). Machine energies and ion charge states, magnetic fields and electrostatic fields along the ions path to the detection system are specifically selected to only pass the desired isotope of interest. For example, chlorine has many isotopes including ^{35}Cl, ^{36}Cl and ^{37}Cl. ^{35}Cl (76%) and ^{37}Cl (24%) are naturally occurring and stable whereas ^{36}Cl is radioactive and the isotopic ratio ($^{36}Cl/Cl$) in the environment is typically only 1 part in $7*10^{13}$. In order to separate isotopes whose masses are close together, like ^{35}Cl and ^{36}Cl, traditionally large tandem accelerators with voltages in the 5-10 MV range together with their associated large magnet systems have been used [4]. Fig. 9 shows the 10 MV ANATARES FN Tandem accelerator at ANSTO in Sydney, Australia used for AMS studies. This accelerator is capable of detecting heavy actinide isotopes like $^{235,236}U$ and ^{242,244} Pu. The low energy injection magnet and the high energy analysing magnet have (ME/q^2) of 20 and 72 respectively. Most of its magnet systems are capable of producing magnetic fields in excess of 1 Tesla and with ion charge states in excess of q= +10 for heavy ions, energies above 100 MeV are possible.

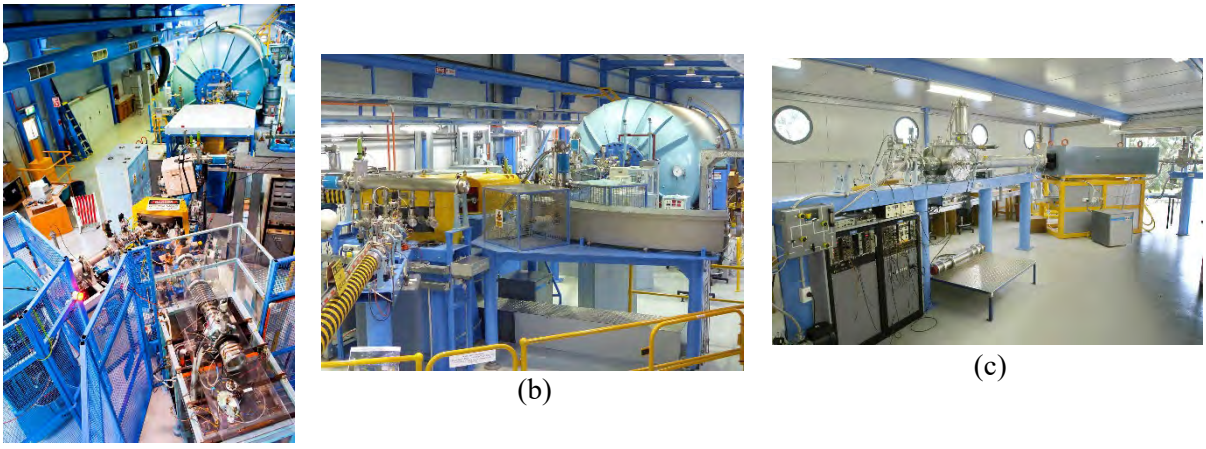

(a) (b) (c)

FIG. 9. The 10MV ANTARES accelerator at ANSTO in Sydney, Australia (a)AMS ion source, (b)10 MV tank and terminal and (c) the actinide AMS beamline and end station.

Modern ion sources have the ability to mount multiple cathodes on a wheel. For AMS each of these cathodes contains the isotopes of the atoms to be measured. Samples sizes as small as 10µg of carbon have been used for ^{14}C dating analyses [2]. Fig. 10 shows typical cathodes used in cathode wheels which are mounted in the accelerator ion source. For sputter ion sources on Tandem accelerators these cathodes are typically bombarded with a cesium beam in the ion source to produce negative ions of the isotopes required. These negative isotopes are then accelerator by the positive terminal voltage in the tank before being stripped by gas or foil stripper to produce positive ions which are then accelerator to the end station and detection system.

FIG. 10. Typical cathode systems used in the accelerator ion source for AMS studies, left is a cathode and right are cathodes in an ion source cathode wheel.

Common isotopes used for environmental studies include ^{14}C (5,730 years), ^{36}Cl (301k years) and ^{10}Be (1.386M years). Fig. 11 shows these three isotopes together span possible dates from the present to 14M years and have applications for carbon dating in climate change studies, ^{10}Be for soil erosion and formation and ^{36}Cl for ground water studies. ^{14}C is produced in the earth's atmosphere by thermal neutrons interacting with nitrogen. ^{36}Cl by spallation of ^{39}K and ^{40}Ca and neutron reactions with the stable ^{35}Cl isotope. ^{10}Be is a long lived isotope produced by cosmic ray interactions with ^{14}N and ^{16}O and the spallation of ^{16}O, ^{27}Al, ^{28}Si and ^{56}Fe in rocks in the earth's surface.

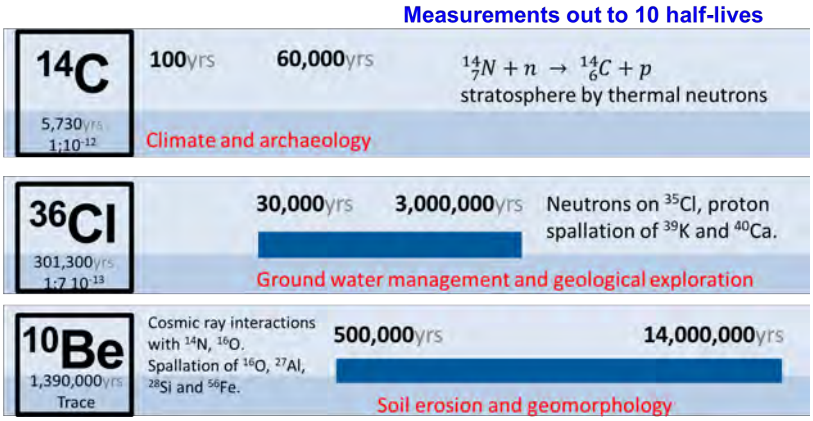

FIG. 11. Half-lives of three common AMS isotopes used in environment studies. They span a time frame from the present to 14M years ago.

Fig. 12(a) shows an ice core being extracted from the Antarctic ice shelf and Fig. 12(b) shows a typical section of ice (firn) containing historical gas bubbles. Firn is an intermediate stage in an ice core between the upper level snow and the fully compacted ice deeper down, Firn typically occurs between 40m and 120m deep, lower firn permanently traps the atmospheric gases and is therefore useful as a historical record of past atmospheric condition. This technique of extracting gases particularly, carbon dioxide and methane, can provide valuable information on atmospheric composition going back over 800,000 years [23-26].

(a) (b)

FIG. 12. (a) Extracting ice cores in Antarctica and (b) gases trapped in firn ice.

6. SUMMARY

IBA methods associated with megavolt accelerator systems are ideally suited to study fine particle pollution. The ability to analysis hundreds of samples very quickly with sensitivities of the order of 1-10 ng/m^3 means that powerful statistical source apportionment techniques like positive matrix factorisation can be applied

to determine source fingerprints and their contributions to the total measured fine mass. Furthermore, by applying wind speed back trajectory methods, such as embedded in the HYSPLIT codes available generally on the WEB, the origins of these source fingerprints can be located. These combined methods demonstrate the ability of fine particulate pollution to be transported long distances across state and country borders and even across the globe.

Accelerator -based AMS dating techniques allow environmental samples to be dated with dates ranging from the present to millions of years old. If the isotope, of any given atom of interest, is appropriately selected megavolt accelerator systems can be used to determine isotopic ratios to better than 1 part in 10^{15} with precision in some cases exceeding 0.5%.

Megavolt accelerator systems together with modern detector systems are capable of individual atom and photon counting and consequently are very sensitive detection systems. They are capable of precise and accurate measurements on very small sample sizes. The multi-element IBA technique of PIXE is capable of measuring some elements with (µg/g) sensitivity on picogram (pg) samples. The AMS techniques used in ^{14}C analysis have achieved dates out to 50,000 years on 10 µg samples.

ACKNOWLEDGEMENTS

I would like to acknowledge the support of the staff of Centre for Accelerator Science at ANSTO and the National Collaborative Research Infrastructure Scheme (NCRIS) whose technical and financial support helped provide some of the data used in this document.

REFERENCES

[1] R. BIRD AND J. WILLIAMS, Ion Beams for Materials Analysis, November 1989, ISBN 9780080916897.

[2] TUNIZ, C., et al., Accelerator mass spectrometry: ultrasensitive analysis of global science. 1998, United States: CRC Press.

[3] COHEN D.D., 1998: Characterisation of Atmospheric Fine Particle Using IBA Techniques. Nuclear Instruments and Methods in Physics Research B, 136B, 14-22.

[4] PASTUOVIC, ZELJKO BUTTON, DAVID COHEN, DAVID FINK, DAVID GARTON, DAVID HOTCHKIS, MICHAEL IONESCU, MIHAIL LONG, SHANE LEVCHENKO. VLAD MANN, MICHAEL SIEGELE, RAINER SMITH, ANDREW WILCKEN. KLAUS SIRIUS – A new 6MV accelerator system for IBA and AMS at ANSTO. Nucl. Instr. and Methods in Phys. Res., B371 (2016)142-147.

[5] COHEN D.D., STELCER E., GARTON D., 2002: Ion beam methods to determine trace heavy metals concentrations and sources in urban airsheds. Nuclear Instruments and Methods in Physics Research B190, 466-470.

[6] COHEN D.D, GARTON D., STELCER E., HAWES O., 2004: Accelerator based studies of atmospheric pollution processes. Radiation Physics and Chemistry 71, 758-567.

[7] COHEN D.D., STELCER E., GARTON D., CRAWFORD J., 2011: Fine Particle Characterisation, Source Apportionment and Long Range Dust Transport into the Sydney Basin: A long term study between 1998 and 2009. Atmospheric Pollution Research 2, 182-189.

[8] INTERGOVERNMENTAL PANEL FOR CLIMATE CHANGE (IPCC) report, *Summary for Policymakers*, April 2022, https://www.ipcc.ch/site/assets/uploads/sites/2/2022/06/SPM_version_report_LR.pdf

[9] BAYER, P., KEOHANE, N., TIMMINS, C., 2009. Migration and hedonic valuation: The case of air quality. Journal of Environmental Economics and Management 58, 1-14.

[10] GUANGSHIAXILU, HONGXIAZHANG, HAOTIANZHENG, ZHONGHUA ZHANG, SHICHENAJIAXING, SHUXIAOWANG. Air pollutant emissions induced by rural-to-urban migration during China's urbanization (2005–2015) Environmental Science and Ecotechnology 10, (2022), 100166.

[11] ZHAO, Y., 1999. Leaving the countryside: rural-to-urban migration decisions in China. The American Economic Review 89, 281-286.

[12] THIEDE, B., GRAY, C., MUELLER, V., 2016. Climate variability and inter-provincial migration in South America, 1970–2011. Global Environmental Change 41, 228-240.

[13] QIN, Y., ZHU, H., 2018. Run away? Air pollution and emigration interests in China. Journal of Population Economics 31, 235-266.

[14] RAFIQ, S., NIELSEN, I., SMYTH, R., 2017. Effect of internal migration on the environment in China. Energy Economics 64, 31-44.

[15] POPE, C.A., DOCKERY, D.W., 2006. Health effects of fine particulate air pollution: Lines that connect. Journal of the Air & Waste Management Association 56, 709-742.

[16] SIEGELE, RAINER, COHEN, DAVID D., iBAT: A new ion beam batch analysis tool for thin samples. Nucl. Instrum. and Methods B493 (2021) 35-43.

[17] PAATERO, P., TAPPER, U., 1994: Positive matrix factorisation: a non-negative factor model with optimal utilization of error estimates of data values. Environmetrics 5, 111-126.

[18] COHEN D.D., CRAWFORD J., STELCER E., ATANACIO A., 2012: Application of positive matrix factorisation, multi-linear engine and back trajectory techniques to the quantification of coal fired power station pollution in metropolitan Sydney. Atmospheric Environment, 61, 204-211.

[19] COHEN, DAVID D. ATANACIO, ARMAND CRAWFORD, JAGODA SIEGELE RAINER. Ion beam techniques for source fingerprinting fine particle air pollution in major Asian-Pacific cities. Nucl. Instrum. and Methods B477 (2020) 122-132.

[20] COHEN D.D., STELCER E., ATANACIO A., CRAWFORD J., 2014: The application of IBA techniques to air pollution source fingerprinting and source apportionment. Nucl. Instrum. and Methods, B318,113-118, doi: http//dx.doi.org/10.1016/j.nimb.2013.05.093

[21] DRAXLER R.R., 1991. The accuracy of trajectories during ANATEX calculated using dynamic model analysis versus rawinsonde observations. Journal of Applied Meteorology 30, 1466-1467.

[22] DRAXLER R. R., ROLPH G.D, 2003. HYSPLIT (HYbrid Single-Particle Lagrangian Integrated Trajectory) Model access via NOAA ARL READY Website (http://www.arl.noaa.gov/ready/hysplit4.html). NOAA Air Resources Laboratory, Silver Spring, MD.

[23] DYONISIUS, M.N., et al., Old carbon reservoirs were not important in the deglacial methane budget. Science, 2020. 367(6480): p. 907-910.

[24] HMIEL, B., et al., Preindustrial 14CH4 indicates greater anthropogenic fossil CH_4 emissions. Nature, 2020. 578(7795): p. 409-412.

[25] BUIZERT, C. Ice Core Methods | studies of firn air. Encyclopedia of Quaternary Science (Second Edition) 2013, Pages 361-372.

[26] BROOK, E.J. Ice Core Methods | Overview. . Encyclopedia of Quaternary Science (Second Edition) 2013, Pages 277-287.

ELETTRA IAEA COLLABORATING CENTER: RESEARCH OPPORTUNITIES USING LIGHT GENERATED BY ELECTRON ACCELERATORS

G. AQUILANTI
Elettra – Sincrotrone Trieste SCpA
Trieste, Italy
Email: giuliana.aquilanti@elettra.eu

L. GREGORATTI
Elettra – Sincrotrone Trieste SCpA
Trieste, Italy
Email: luca.gregoratti@elettra.eu

M. KISKINOVA
Elettra – Sincrotrone Trieste SCpA
Trieste, Italy
Email: maya.kiskinova@elettra.eu

Abstract

Large scale synchrotron and free electron laser facilities where the operated versatile experimental stations based on the photon interactions provide access to the state-of-the art techniques are the cradle of multidisciplinary research, spanning over physics, chemistry, material science and engineering to environment, biology, medicine, archeology and cultural heritage. The paper will describe the exciting opportunities offered at Elettra - Sincrotrone Trieste and how as IAEA Collaborating Centre it provides access of Member States to synchrotron-based research and coordinated research activities, fostering also know-how transfer through training, schools and workshops. The selected exemplary systems will address the most recent achievements in basic and applied research in various fields of material and life sciences. Recent activities and achievements in the frame of IAEA-Elettra partnership are outlined.

1. INTRODUCTION: HISTORIC MILESTONES AND PRESENT STATUS OF ELETTRA-SINCROTRONE TRIESTE

The photon emission generated by relativistic electrons in circular or linear accelerators, first observed in 1947 in General Electric Lab in New York and considered 'undesired' loss of electron energy, has been recognized about two decades later as light with exceptional properties. Following the first steps with USA Tantalus Synchrotron opened in 1968 a great number of 2nd generation synchrotron facilities, using only bending magnets, started operation in 1980s, paving the road to scientific discoveries, thanks to the fast developing synchrotron-based techniques. Pressed by the increasing requests for higher brightness in order to make further advances in the performance of the synchrotron-based methods the synchrotron storage rings were ongoing continuous developments and among the first 3rd generation synchrotrons starting operation in 1990s is Elettra - Sincrotrone Trieste in Europe[1].

At present the Italian non-profit company Elettra - Sincrotrone Trieste is classified as a multidisciplinary research center of excellence specialized in generating synchrotron and free-electron laser light and applying the related state-of-the art experimental techniques for fundamental and applied research in all domains of materials and life sciences. Its mission is serving international user communities to promote social and economic growth through basic and applied research, know-how transfer, education and participation in fruitful collaborations and international networks. The scientific and technical performance and developments of the facilities, managed by Elettra - Sincrotrone Trieste, are monitored by international experts, appointed as Members of the Machine Advisory Committee (MAC) and Scientific Advisory Council (SAC). Elettra is located on the Trieste-Basovizza upland zone of AREA science park[2], which hosts many other research and technology institutions, among many also is International Center of Genetic Engineering and Biotechnology, ICGEB, established as a special project of UNIDO.[3]

The name Elettra derives from ancient Greek Elektra, meaning 'shining like amber' and 'electron' has the same origin. The construction of the Elettra synchrotron facility, including accelerator, storage ring, experimental hall, the first beamlines and all infrastructure started beginning 1991. The storage ring Elettra is a double bend achromat with space in the lattice, the so-called long straight sections, to install insertion devices. undulators or wigglers, the distinctive feature of the 3rd generation synchrotrons for providing high photon brightness. In less than 3 years the light shined on October 20th 1993, consenting the first beamlines to start experiments with users in 1994. Elettra synchrotron facility underwent two upgrades – in 2007 the 1 GeV linear accelerator (LINAC) was replaced by a small LINAC and a full energy booster that accelerates and injects electrons with the final energy of 2.0 or 2.4 GeV in the storage ring. Since 2010 Elettra synchrotron operates at both energies in a top-up mode and also has implemented hybrid mode operation for allowing time resolved experiments down to the sub nsec range.[4]

The old injector was upgraded and was used to build the Free Electron Laser (FEL) facility – FERMI, the first and still the only seeded FEL worldwide. The FEL process at FERMI is triggered by an external seed laser adding full longitudinal coherence of the FERMI-FEL pulses, which are also tunable in wavelength, power, time duration and multiple polarization.[5] The two high gain harmonic generation (HGHG) lines, namely single-stage (FEL-1) and double-stage (FEL-2), cover the wavelength range 100-20 nm and 20-4 nm, respectively. The first FEL light was obtained at the end of 2010 with FEL-1 that started user operation end of 2011, whereas FEL-2 was opened for users in 2016. For pump-probe experiments to explore ultrafast femto-picosecond dynamics along with the possibility to synchronize the FEL pulses with those of an external optical laser, two FEL pulse schemes were implemented in 2015 allowing generation of two FEL pulses with desired wavelengths and temporal separation for multicolor experiments.

The high level of know-how and the accumulated experience in production of synchrotron light during the construction and operation of Elettra storage ring has also been spinned-off; Elettra founded in 2007 the company Kyma S.r.l, which is now designing and fabricating insertion devices for many facilities worldwide.[6]

Elettra storage ring feeds 29 beamlines (FIG. 1) working simultaneously, whereas FERMI-FEL has 6 beamlines, fed alternatively with the beam. Each beamline is designed to transport the photon beam, using proper optical and beam control systems for optimizing the flux density, beam dimensions and wavelength range in order to match best the requirements of the experimental techniques used at the end stations.

Elettra and CERIC-ERIC allocated users by country:

ARGENTINA	3	JORDAN	6
AUSTRALIA	6	MEXICO	6
AUSTRIA	60	MOLDOVA, REPUBLIC OF	3
BELARUS	2	NETHERLANDS	5
BELGIUM	16	NEW ZEALAND	1
BOSNIA AND HERZEGOVINA	1	NORWAY	10
BRAZIL	11	POLAND	15
BULGARIA	5	PORTUGAL	5
CANADA	7	ROMANIA	9
CHINA	10	RUSSIAN FEDERATION	33
CROATIA	34	SAUDI ARABIA	1
CZECH REPUBLIC	18	SERBIA	4
DENMARK	9	SINGAPORE	1
EGYPT	4	SLOVAKIA	1
FRANCE	53	SLOVENIA	28
GEORGIA	4	SOUTH AFRICA	1
GERMANY	116	SPAIN	38
GREECE	15	SWEDEN	18
HUNGARY	7	SWITZERLAND	28
INDIA	68	TURKEY	1
IRAN, ISLAMIC REPUBLIC OF	4	UKRAINE	22
ISRAEL	3	UNITED KINGDOM	29
ITALY	487	UNITED STATES OF AMERICA	12
JAPAN	9	VIET NAM	2
		Grand Total	**1231**

FIG. 1. (Left) Beamlines hosted by the Elettra synchrotron Storage Ring. The stars indicate the hard X-ray beamlines. The beamlines belonging or in partnership with other national, foreign or international institutions are indicated by logos and flags. (Right) Table reporting the number of users from different countries who performed experiments at Elettra beamlines in 2019. It represents the typical number - with small variations for different years. During COVID some experiments were organized with users in remote mode.

The numerous experimental stations host state-of-the art instruments where cutting-edge scattering, imaging and spectroscopic techniques are implemented, using dedicated experimental set-ups for monitoring the relevant signals of the scattered and transmitted photons or emitted photons and electrons. Ten (indicated by red stars in FIG. 1) out of all 28 beamlines use hard X-rays. They are provided by two wigglers, a permanent multipole wiggler shared by the SAXS and XRD1 beamlines and a Super Conducting multipole Wiggler (SCW), reaching 35 keV photon energy, shared by the XRD2 and XPRESS beamlines, and six bending magnets - one of them feeds the XRF (IAEA-Elettra) beamline. Seventeen beamlines work in the UV and soft X-ray range. They get light provided by ten undulators, one elliptical wiggler and two bending magnets. There are also two beamlines using bending magnet (SISSI), which work in the IR-THz range. Eight of the Elettra beamlines are built and operated by the Consiglio Nazionale delle Ricerche (CNR) and another three are operated in partnership with CNR. Two beamlines are funded and operated by foreign institutions, namely the SAXS beamline belongs to the Austrian Institute of Inorganic Chemistry of the Graz University of Technology and the Material Science beamline to the Institute of Physics of the Check Academy of Sciences and the Charles University in Prague. Another four beamlines have partnership with foreign institutions, namely the XPRESS and XRD2 beamlines are operated together with Indian Institute of Science (IISc), Bengaluru, an XPEEM at the NanoESCA beamline is operated by the Peter Grünberg Institute in Forschungszentrum Jülich, Germany, the CoSmoS station at the SuperESCA beamline is operated by the National Institute of Materials Physics in Magurele, Romania. The monochromator of the XAFS beamline was funded by the International Center of Theoretical Physics (ICTP) of UNESCO and the XRF beamline is operated in partnership with the Physics Section of IAEA. Since Elettra is also one of the eight partner facilities of Central European Research Infrastructure Consortium (CERIC)[7] some beamlines offer dedicated beamtime for international users for synchrotron-based methods complemented with NMR, SEM, TXM and Ion beam analysis available in other partner facilities.

About 80% of the total, both synchrotron and FEL beamtime, on average ~ 270 days/annum for Elettra synchrotron and ~150 days/annum of FERMI-FEL, is dedicated to the users who have to submit their project proposals the semester before the requested beamtime. The beamtime is granted on the basis of the scientific merit and/or technological impact of their projects, graded by independent international panels consisting of specialists in all research fields. On average about 50% of the projects are granted synchrotron beamtime and ~30% are granted FERMI-FEL beamtime. Materials, solid state physics and life science studies are still the most requested but the last years also energy, environmental and cultural heritage requests are continuously growing. On average annually over 1200 scientists conduct investigations using Elettra synchrotron and, as illustrated in FIG. 1b, more than 50% of the Elettra synchrotron users come from abroad with increasing number from Central-Eastern European countries, Asia, South America and Africa. In the last decade in the frame of the collaboration with IAEA and ICTP the request for using synchrotron techniques from ‘so-called’ developing countries is rising. For the case of FERMI the international participation is much higher with ~80% of users from Europe, North America and Asia. This difference between the origin of the synchrotron and FEL users is understandable considering the smaller number FEL facilities and the demand of a very advanced knowledge level requested for the FEL-type research. In the last five years (2017-2021) the results obtained at Elettra beamlines are reported in 3140 papers and those of Fermi, where a single beamline can use the beam, in 220 papers with a significant increase of the HI publications.

Elettra - Sincrotrone Trieste also offers access to several laboratories with conventional analytical techniques for production or characterization of samples to add information complementary to that obtained at the beamlines. Among them are Structural Biology[8] and NanoLab[9], both in the biomedical field with instruments used for preparation (production and crystallization), screening and complementary characterization of biomolecules and other types of bio-matter which is an added value to the most frequently used for bio-research XRD, SAXS, IR and IUVX beamlines.

Since decades Elettra is fostering know-how transfer through schools and workshops and on-site experimental training, that have led to continuous increase of the number of researchers using its facilities. Among many we should mention the following annual schools: (i) the “School on Synchrotron Radiation “Gilberto Vlaic”: Fundamentals, Methods and Applications” organized in collaboration with Italian Society of Synchrotron Radiation (SILS)[10] and (ii) the “HERCULES European School”, coordinated by ESRF[11]. Since the beginning of the century Elettra is tightly engaged in organization of the bi-annual ICTP School on Advanced Light Sources and Multidisciplinary Applications[12], where IAEA is also involved. This school is in the frame of cooperation agreement with UNESCO’s International Center of Theoretical physics (ICTP) and targets young

scientists with rather advanced basic knowledge to be introduced to the exceptional research opportunities offered by synchrotron and free-electron-laser (FEL) facilities worldwide by lecturers with international recognitions, including visits and demonstrations at Elettra and FERMI beamlines. This school that has been very popular and attracted the best young scientists from Asia, Africa and South America, unfortunately was cancelled in 2020 due to COVID but is expected to be re-started soon.

Elettra - Sincrotrone Trieste is involved in numerous international projects[13] and coordinated research activities, e.g. founder of the LEAPS Consortium[14], partner of FELs of Europe[15] and has played an active role in several European strategic programs, listed in ESFRI Roadmap, and many others[16]. The long collaboration and partnership activities with IAEA, which stated with the first nomination of Elettra as an IAEA Collaborating Center in 2005 will be described in more details in the last section.

Elettra was an IAEA Collaborating Centre in the period 2005-2014 and became partner at the XRF beamline in 2014 installing and operating in partnership the experimental end station. Along with the ongoing XRF partnership Elettra was again nominated IAEA Collaborating Centre in 2020. More details of the ongoing research education and training activities in the frame of Elettra-IAEA partnership are reported in the last section.

2. RESEARCH OPPORTUNITIES USING ELETTRA-SINCROTRONE TRIESTE FACILITIES

The synchrotron light generated by Elettra storage ring and FERMI-FEL has the appealing characteristics as high brightness (ph/mm^2/s/mrad^2, 0.1% bandwidth), broad wavelength range - from THZ to hard X-rays, tunability, multiple polarization options and coherence. The photons interact with the electrons of the atoms in the matter and have higher penetration power compared to charged particles that is controlled by the photon energy. The photon-matter interactions are very sensitive to the local structural organization and environment of the matter under investigation and compass redirection (scattering) and absorption, which result in scattered and transmitted photons, and electron and photon emission, as schematically illustrated in FIG. 2. Monitoring selectively, the photon and electron signals can be used for characterization of the spatial and electronic structure, chemical composition and function of matter down to atomic length scales and fs time scales.

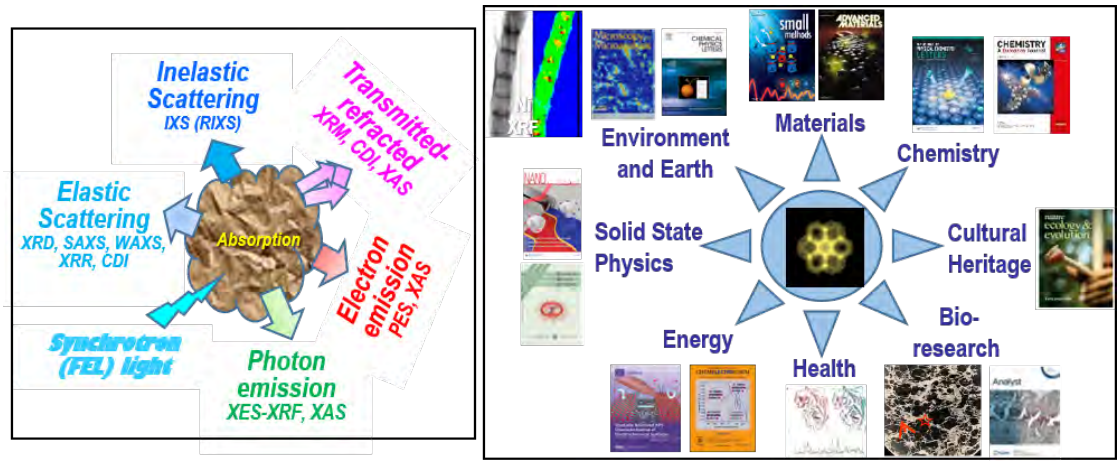

FIG. 2. (left) Photon-matter interactions; (right) Applications fields with examples using studies carried out at Elettra synchrotron and FERMI beamlines.

The type of information is first determined by the fundamental issue whether the photons loss energy when interacting with matter or not. If the photon is elastically scattered or refracted at an interface of materials with dissimilar refraction index, it is redirected preserving its energy and wavelength. The monitored scattered intensity as a function of the incident and scattered angle provides structural information, from short range, with atomic resolution for ordered lattices, called X-ray diffraction (XRD) to longer range, 1-100 nm probing the structural variations in disordered systems - Small Angle X-ray Scattering (SAXS), Wide Angle X-ray Scattering (WAXS) and X-ray Reflectivity (XRR). Grazing Angle SAXS (GISAXS) and XRR are adding enhanced surface sensitivity for exploring multilayer systems. The collected photon signal after passing through the specimen depends on the absorption of the X-rays, determined by the local density and composition, where the refraction

at interfaces adds also the phase contrast, which improves the resolution and is further enhanced using more coherent X-rays. Here it should be noted that lateral resolution when doing X-ray imaging is also determined by the beam size, de-magnified using focusing optics. The optics limitations can be overcome by Coherent Diffraction Imaging (CDI), using highly coherent light, already achievable at the 3rd generation synchrotrons and provided by the fully coherent FELs. In CDI the real image is reconstructed from the obtained speckle diffraction patterns via algorithm, retrieving the lost phase information. CDI approaches are already widely used at FERMI-FEL and also at TwinMic beamline at Elettra synchrotron. Inelastic scattering is occurring when the scattered and transmitted photons loss energy due to the generated electron excitation in specific atom and is accompanied by electron and/or photon emission. The detected and filtered photon and electron signals are the base of the Inelastic X-ray Spectroscopy (IXS), X-ray Absorption Spectroscopy (XAS), PhotoElectron Spectroscopy (PES) and X-ray Emission Spectroscopy (XES) or better known as X-ray Fluorescence Spectroscopy (XRF). Here should be outlined that XAS, also called X-Ray Absorption Fine Structure (XAFS), is the spectroscopy that requires tunability for scanning the photon energy is also the only one that can use both the emitted or transmitted photon signal and also the emitted total electron signal for obtaining the spectra. Reference 17 can be used as one of the exemplary recent books describing in details all photon-matter interactions and synchrotron-based techniques that have opened unique opportunity to reveal the geometric and electronic structure, chemical composition and other many other phenomena controlling the properties and functionality of the studied matter.

Twelve of the Elettra beamlines and one of the FERMI-FEL beamlines host experimental stations equipped with instruments and techniques based on detection of the electron emission, which provides the possibility for examination of the electronic structure, elemental and chemical composition of molecules in gas phase and of solid specimen with surface sensibility. Dedicated beamlines are capable to execute high resolution PES and XAS, angular-resolved PES (ARPES), time-resolved PES and XAS, PES and XAS microscopy with few tens nm spatial resolution. Thanks to the brightness, tunability and polarization of the synchrotron light these techniques have become state-of-the art and have provided new information about properties of strongly correlated electron and 2D materials and for surface and interface phenomena at gas/solid liquid/solid and solid/solid interfaces, which is highly requested for selecting the best materials used in electronic devices, sensor devices with broad applications fields, including biomedical appliances as well and in catalysis, the core of chemical industry, fuel and energy production, conversion and storage. Among the main targets for understanding the functionality of such systems is the response to operating conditions and external stimuli – temperature, radiation, electric and magnetic. Using total electron yield for XAS and versatility of X-ray Magnetic Circular Dichroism (XMCD) and X-Ray Magnetic Lineal Dichroism experiments using both Elettra and FERMI-FEL beamlines have allowed to observe the evolution of magnetic nanostructures, as domains, domain walls and skyrmions, the key for advances in development of new magnetic devices. Six Elettra synchrotron and three FERMI-FEL beamlines use photon-in/photon-out spectroscopies, namely XES-XRF, XAS, IUVS-Raman and InfraRed (IR), including XRF, XAS and IR microscopy and imaging. Among them is the IAEA-Elettra XRF beamline, using XRF and XAS, where the present focusing optics allows for a few micrometer spatial resolution. Five hard X-ray beamlines use scattering techniques – XRD, SAXS-GISAXS, WAXS and XRR. Another two hard X-ray beamlines (LILIT and DXRL) are lithography beamlines with strong technological impact for nano-structuring, requested for fabrication nanoparts of devices. The sixth hard X-ray beamline is SYRMEP dedicated to X-ray tomography. Elettra is the first synchrotron facility that started two decades ago a clinical program based on X-ray tomography phase contrast imaging. Now SYRMEP is a cradle of multiscale biomedical imaging bridging the gap between preclinical research and patient application.[18]

All synchrotron-based techniques have found multidisciplinary applications very schematically illustrated in FIG. 2-left, where the research examples are from studies carried out at Elettra beamlines. Health and bio-research issues are interconnected and have largely been based on the paradigm from structure to function. The recent advances in photon production and transport have enabled protein micro-crystallography, sub-micrometer X-ray imaging of tissues and cells with speciation information and even in-vivo studies using non-ionizing IR microscopy. The discovered SARS-CoV-2 main protease structure at XRD2 beamline, was recognized as a promising target for the development of effective drugs. The computed X-ray tomography image reveals alveolar dilatation and thickening in lung tissue due to COVID, thanks to the use of synchrotron light allowing to see features in anatomical fine structure and its changes due a decease, invisible with hospital instruments. Megapixel scanning transmission soft X-ray microscopy imaging coupled with compressive sensing X-ray fluorescence have opened new horizons for faster screening of large biological tissues that was advertised at the cover page

of Analyst Journal[19]. Energy is another grand challenge of our society and all devices for energy production, conversion and storage are complex functional systems involving multiple energy, time and length-scales. Synchrotron-based spectroscopy, imaging and scattering offer necessary characterization potentials to explore physical and chemical phenomena governing the performance of different energy devices. Micro-PES characterization allowing insights in chemistry of electrochemical surfaces in energy devices is advertises at the Surfaces cover page[20] and XAS Investigation of reversible redox activity cathode material with high capacity deserved ChemElectroChem cover page[21]. In solid state physics understanding spin-orbit coupling effects in quantum materials for electronics has made tremendous steps ahead thanks to the tunability and multiple polarization of the synchrotron light and the observed ferroelectric control of GeTe spin texture by ARPES deserved a NanoLetter cover page[22]. Triggering and switching magnetic moments in thin films is of key importance from spintronics to quantum information and in this respect circular and linear polarization of the beams, used for XAS and resonant imaging made major contributions - the recently reported free electron laser-based scheme for generating atomic-scale charge current loops within femtoseconds, using FERMI-FEL, got a Physical Review Letters cover page[23]. The challenges in environmental studies due to the limits of the available techniques in terms of trace element sensitivity and spatial resolution have been largely overcome using synchrotron light for shedding light on the involved bio-chemical and atmospheric processes. Thanks to the results obtained by X-ray and XRF imaging of cable bacteria at TwinMic beamline it was revealed its electrical conductivity occurs through proteins with Ni-dependent cofactors, which is remarkable and surprising, since biological electron transport typically involves Fe and Cu metalloproteins[24]. X-Ray microscopy and XRF-XAS microscopy analyses revealing the fate of lungs and pleura in the presence of inhaled asbestos in polluted areas got a Microscopy and Microanalysis cover page[25]. The monitored escape of O+ ions from the atmosphere relevant to explanation of the ion density profiles in space monitored with coincidence ARPES at Gas phase beamline got a Chemical Physics Letters cover page[26]. Material research is also linked to manufacturing. An example for advances in the field are the operando XAS studies, showing that Na-Rich Manganese Hexacyanoferrate is a promising candidate for Li and Na Ion storage, advertised at the Small cover page[27]. Recently accomplished by direct X-ray lithography at DXRL beamline nano-patterning of Metal Organic Frameworks (MOF), verified by GISAXS for being used in micro-devices to allow dynamic positioning in magnetic fields, is advertised at Nature Materials cover page[28]. In chemistry the applications are multiple spanning over synthesis of new substances, their characterization and evolution under operation or exposure to various environments. Examples are smart decomposition of cyclic alanine-alanine dipeptide by VUV Radiation marked as seed for the synthesis of biologically relevant species advertised in Journal Physical Chemistry Letters at the cover page[29]. The first stereospecific synthesis of a new class of molecular propeller - polycyclic aromatic hydrocarbons, verified by XRD at MCX beamline got cover page of Chemistry European Journal[30]. Cultural heritage studies, relevant to archaeology, palaeontology and art history are fast expanding using the powerful non-destructive synchrotron-based imaging and spectroscopy methods. As an example is the Nature-Ecology and Evolution Cover page publicizing how micro-spectroscopy analysis of lithic pieces from 40-45,000 years ago revealed their use as weapons by anatomically modern humans. Many other environment-relevant and cultural-relevant studies were performed at XRF beamline in partnership with IAEA and will be notified in the next section.

3. RECENT ACTIVITIES AND ACHIEVEMENTS IN THE FRAME OF IAEA-ELETTRA COOPERATION

After a break of six years Elettra was again nominated as Cooperation Center in 2020, which is based on the worldwide recognized experience of Elettra in production and application of both synchrotron and free electron laser light for serving international user community. As Cooperation Center Elettra has become a reference hub, enriching the Member State capabilities in construction of Synchrotron and FEL machines and beamlines and implementation of the very powerful synchrotron-based methods in all domains of material and life sciences. This renewed cooperation agreement follows the ongoing XRF beamline Elettra-IAEA Partnership agreement since 2014 for hosting the end-station of the IAEA Division of Physical and Chemical Sciences[31], which allows the execution of different experiments using all type XES-XRF approaches, complemented by XAS. The IAEA-Elettra XRF beamline was officially inaugurated by

DDG Yukiya Amano in 2014 and was later visited by the Mexican Ambassador in Italy Carlos Gracia de Alba Zepeda in 2020 and the present IAEA DDG Najat Mokhtar in 2021.

Along with the on-site user support, instructing how to execute synchrotron-based experiments and process the obtained data using the instruments at the Elettra beamline end stations, dedicated educational and training events are/will be organized for teaching how to design and build synchrotrons including accelerators, storage rings, beamlines and dedicated measurement stations. An asset for such activities as Cooperation Center is the ongoing operation and continuous upgrades of the IAEA end-station and XRF beamline, where 40% of the beamtime - ~100 days/annum is reserved for the IAEA-supported users from the Member States, most without synchrotron facilities. Although the proposals of these Member State users also pass through the International proposal review panel having such reserved beamtime fraction gives higher chance of these researchers to get access for performing experiments. In order to expand the number of the users from the Member States to be granted beamtime at other Elettra beamlines as general users, where they are competing with highly experiences in synchrotron research scientists, focused training sessions how to write good project proposals are considered as well.

In the frame of the Elettra and IAEA partnership annual training workshops are organized – the next will be July 25-29, 2022[32]. Two professional videos describing the XRF beamline, measurement station and the techniques and data handling have been accomplished by the Elettra and IAEA staff. Participation of the researchers from all Member States is also open for all other schools and workshops organized in partnership with Elettra, some already noted in Section 1.

In the last three years (2019-2021) 52 experiments, supported by IAEA were performed at the XRF beamline, one of them also complemented with operando XAS measurements at XAFS beamline. As illustrated by the chart in FIG. 3a the research projects relevant to life sciences dominate, covering the environment, biology, biomedicine and food. In the same period 35 papers are published in refereed journals and some of the results were presented at seven conferences. The three examples in FIG. 3 are selected from published results obtained at XRF beamline for representing the majority studies carried out by the IAEA-supported users, which are relevant to health, environment and earth sciences. Recognizing the great concern for health hazard due to air, water and food pollution characterization of the pollutant content using synchrotron light is of significant importance. Scientists from Egypt, Jordan and Saudi Arabia used XRF and XAFS spectroscopy to exploit the presence and chemical state of arsenic in ambient air particulates collected in different industrial zones of greater Cairo (FIG. 3b). Thanks to the beam tunability and brightness they were able to achieve high detection levels allowing to distinguish also between the different chemical states of the As in the particulate material[33]. Several publications from a Mexican team were dedicated to exploiting giant gypsum crystals of Naica cave and their evolution, focusing on the potential environmental impact including human activity as well. In their most recent papers[34] the extraction of water from the caves was pointed as a reason for the most significant anthropogenic damage, revealed by complementary grazing incidence diffraction, micro-XRF and XAS results for the structure and surface impurities, summarized in FIG. 3 (c). Scientists from Turkey and Slovenia are collaborating in controlling the presence in food of important for health elements, as Fe in seeds in particular. As illustrated in FIG. 3(d) the elemental XRF mapping of seeds, shows Fe accumulation in endosperm and seed coat and also the relevant spatial distribution of other metals[35].

The advantage of having fully tunable X-ray light has also been extensively used for measuring X-ray emission cross section of different elements varying the incident energy starting from the corresponding absorption edge, which is exclusively important experimental validation of the theoretically predicted using different model. These types of studies have been initiated from the IAEA staff and continues with financial support from IAEA, as clearly stated in Ref. 36.

4. CONCLUSION

The ongoing upgrades of the storage rings and the growing number of FELs worldwide are opening exciting opportunities for “watching” how matter behaves at ultra-short fs time scales down to the level of nano-units, atoms and molecules. They will enable high-throughput and operando structural, physical and chemical characterization fully integrated with operando syntheses, operation and data processing methods for deepening our knowledge in functionality of the complex matter for addressing key societal health, environment, energy and technology challenges. The continuous advances in accelerator technology added further narrowing of the electron

beam increasing the brightness and coherence of the emitted photons and these are the 4th Generation synchrotrons starting since 2016 with Max4 and recently with the upgraded ESRF. Upgrade of Elettra storage ring to become a 4th Generation facility is also funded and expected to start operation in 2026.[37]

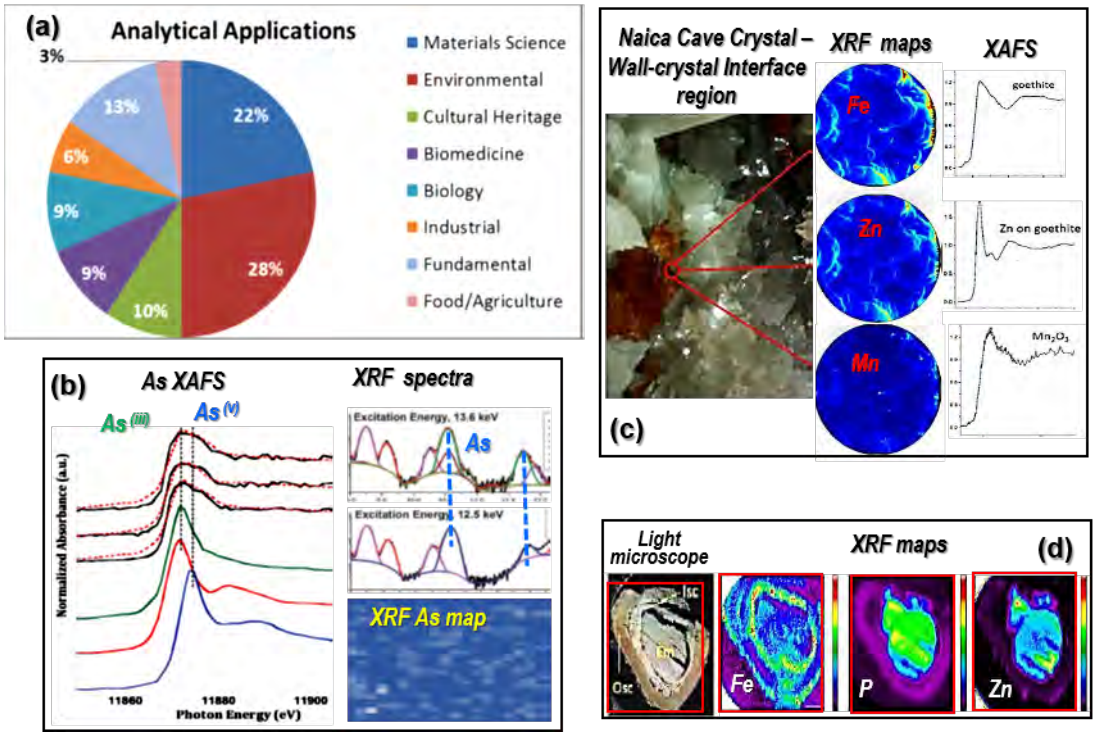

FIG. 3. (a) Chart representing the percentage of XRF beamtime used for different research areas. (b) As content (XRF spectra and maps) and variable chemical state (As XAFS spectra) in different particulate samples collected in industrial zones in Cairo region. The XRF spectra taken at two different X-ray beam energies show the advantage of tunability - by using energy lower than the one required for Br excitation the overlap with Br XRF peak to eliminated; (c) Micro-XRF map showing the distribution of Fe, Zn in Mn in the indicated on the lect zone on a gypsum sample. The corresponding XAFS spectra are fingerprints for the Fe, Zn and Mn chemical state, (d) Micro-XRF maps of a seed shown in the light microscope image on the left showing spatial distribution of Fe, P and Zn.

ACKNOWLEDGMENTS

We acknowledge our present and previous partners from the Physics Section of IAEA Division of Physical and Chemical sciences, Danas Ridikas, Ian Swainson, Alessandro Migliori, Andreas Karydas and Ralf Kaiser for their significant contributions since 2014 to the continuous developments at the XRF beamline, attracting numerous scientists from Member States to use Elettra-Sincrotrone Trieste as a research and training hub.

REFERENCES

[1] https://www.elettra.trieste.it
[2] https://www.sisfvg.it/area-science-park
[3] https://www.icgeb.org
[4] KARANTZOULIS, E., Elettra Update, Synchrotron Radiation News, **29** (2016) 29-33.
[5] ALLARIA, E., et al, Nat. Photonics, **6** (2012) 699-704.
[6] https://kyma-undulators.com
[7] https://www.ceric-eric.eu/
[8] https://www.elettra.trieste.it/labs/structural-biology
[9] https://www.elettra.eu/labs/nanostructure

[10] https://indico.elettra.eu/event/22/
[11] https://hercules-school.eu/
[12] https://indico.ictp.it/event/8308/
[13] https://www.elettra.eu/about/projects/international-projects.html; https://www.ceric-eric.eu; https://www.fels-of-europe.eu/
[14] https://leaps-initiative.eu/
[15] https://www.fels-of-europe.eu/partners/
[16] https://www.elettra.eu/about/alliances-and-partnerships.html
[17] WILLMOTT, P., An Introduction to Synchrotron Radiation: Techniques and Applications, Second Edition, 2019, John Wiley & Sons
[18] DULLIN, C., et al, Multiscale biomedical imaging at the SYRMEP beamline of Elettra – Closing the gap between preclinical research and patient applications, Physics Open **6** (2021) 100050.
[19] KOUROUSIAS, G., et al, Megapixel scanning transmission soft X-ray microscopy imaging coupled with compressive sensing X-ray fluorescence for fast investigation of large biological tissues, Analyst, **146** (2021) 5836-5842.
[20] BOZZINI, B., et al, Spatially resolved XPS characterization of electrochemical surfaces, Surfaces, **2** 2 (2019) 295-314.
[21] BUCHHOLZ, S., et al, Inside back cover: X-ray absorption spectroscopy investigation of Lithium-rich Cobalt-poor layered-oxide cathode material with high capacity, ChemElectroChm **2** (2015) 85.
[22] RINALDI, C., Ferroelectric control of the spin texture in GeTe, Nano Letters, **18** 5 (2018) 2751-2758.
[23] WATZEL, J., et al, Light-induced magnetization at the nanoscale, Phys. Rev. Lett. **128** (2022) 157205.
[24] BOSCHKER HENRICUS, S., et al, Efficient long-range conduction in cable bacteria through nickel protein wires, Nat. Comm., **12** (2021) 3996.
[25] PASCOLO, L., et al, Focused X-ray histological analyses to reveal asbestos fibers and bodies in lungs and pleura of asbestos-exposed subjects, Microsc. Microanal. **22** (2016) 1062-1071.
[26] FALCINELLI, S., et al., Double photoionization of propylene oxide: a coincidence study of the ejection of a pair of valence-shell electrons, Chem. Phys. Lett. **666** (2016) 1.
[27] BUCHHOLZ, D., et al., Inside Back Cover: X-ray Absorption Spectroscopy Investigation of Lithium-Rich, Cobalt-Poor Layered-Oxide Cathode Material with High Capacity, ChemElectroChem **2** 1 (2015) 85.
[28] TU, M., et al, Direct X-ray and electron-beam lithography of halogenated zeolitic imidazolate frameworks, Nat. Mater., **20** (2021) 93-99.
[29] BARREIRO-LAGE, D., et al., "Smart Decomposition" of Cyclic Alanine-Alanine Dipeptide by VUV Radiation: A Seed for the Synthesis of Biologically Relevant Species, J. Phys. Chem. Lett. **12** (2021) 7379.
[30] MOSCA, D., et al, Stereospecific Winding of Polycyclic Aromatic Hydrocarbons into Trinacria Propellers, Chem.Eur.J. **23** (2017) 15348.
[31] KARYDAS, J., et al, An IAEA multi-technique X-ray spectrometry endstation at Elettra Sincrotrone Trieste: benchmarking results and interdisciplinary applications, J. Synchr. Rad. **25** (2018) 189; MARGUI, E. et al, A first evaluation of the analytical capabilities of the new X-ray fluorescence facility at International Atomic Energy Agency-Elettra Sincrotrone Trieste for multipurpose total reflection X-ray fluorescence analysis, Spectrochimica Acta - Part B, **145** (2018) 8; FOULON, F., et al, IAEA Nuclear Science and Instrumentation Laboratory: Support to IAEA Member States and Recent Developments, EPJ Web of Conferences **225** (2020) 10005.
[32] https://www.iaea.org/events/evt2104017.
[33] SHALTOUT, A., et al, J. Anal. Spectr. **36** (2021) 981.
[34] PEREZ-CAZARES, B., et al, Naica's Giant Crystals: Characterization and Evolution of the Wall–Crystal Interface, Crystal Growth and Design, **21** (2021) 5712 and references therein.
[35] EROGLU, S., et al, The conservation of VIT1-dependent iron distribution in seeds, Frontiers in Plant Science, **10** (2019) 907.
[36] KAUR, S., et al, Experimental production cross sections for synchrotron radiation induced L-series X-rays of Sn and Sb at energies across their Li (i = 1–3) absorption edges, X-Ray Spectrometry **51** (2022) 15; Measurements of L-shell X-ray production cross sections for Sn and Sb using 6–14 keV synchrotron radiation, Nucl. Instr. Meth. Section B: Beam Interactions with Materials and Atoms, **521** (2022) 33.
[37] https://www.elettra.eu/lightsources/elettra/elettra-2-0.html?showall=

EFFECT OF E-BEAM IRRADIATION ON THE MICROBIAL QUALITY OF MINIMALLY PROCESSED PRODUCTS: A CASE OF A COMMERCIALIZED READY TO EAT SALAD.

Faten RAHMANI
National Center of Nuclear Sciences and Technologies
SidiThabet/Ariana, Tunisia
Email: faten.rahmani@gmail.com

Widad ZERNADJI
National Center of Nuclear Sciences and Technologies
SidiThabet/Ariana, Tunisia
Email:widadzernadji@gmail.com

Sihem JEBRI
National Center of Nuclear Sciences and Technologies
SidiThabet/Ariana, Tunisia
Email: Sihem.Jebri@cnstn.rnrt.tn

Mohamed Hedi TRABELSI
National Center of Nuclear Sciences and Technologies
SidiThabet/Ariana, Tunisia

Mariem YAHYA
National Center of Nuclear Sciences and Technologies
SidiThabet/Ariana, Tunisia
Email:mariemyahya87@gmail.com

Fatma HMAIED
National Center of Nuclear Sciences and Technologies
SidiThabet/Ariana, Tunisia
Email:hmaiedfatma@yahoo.com

Abstract

Fresh vegetables and commercialized ready to eat salad could be contaminated by pathogenic foodborne microorganisms and may constitute a potential health-risk product. Hence, the use of safe disinfecting treatment like E-beam irradiation could be a useful tool to ensure pathogens inactivation and shelf-life extension. In this study, freshly packaged ready-to-eat salads were collected from supermarket and analyzed for naturally occurring microorganisms, including aerobic plate count, *Staphylococcus* spp., yeasts, molds and *Clostridium perfringens*. Then, in a second step, ready to eat salads were processed at an E-Beam accelerator. Doses were ranging from 2kGy to 4kGy. Irradiated salads were analyzed for total aerobic plate count, *Staphylococcus* spp., yeasts and molds and *Clostridium perfringens* during 15 days of storage period at 4°C. The validity of processing treatment at 2kGy to 4kGy was challenged by artificial contamination of sterilized salad using *Staphylococcus aureus* strain (ATCC 25823). Results showed that E-beam irradiation at a dose of 4 kGy reduced concentrations of total aerobic plate count and yeast by 5 and 3 Log 10 CFU/g respectively, and inactivated *Staphylococcus* spp and molds. Hence, irradiation at 4 kGy dose contribute to maintain a satisfactory limit for naturally occurring microorganisms and extended the shelf life of commercialized ready to eat salads during more than 10 days of storage period at refrigeration temperature. Concerning resistant sporulating bacteria, E-beam irradiation at 4 kGy dose reduced the concentration of *Clostridium perfringens* by 1,5 Log10 CFU/g, initial mean concentration was estimated at (2,6 Log10 CFU/g). Results corroborate the use of E-Beam irradiation for food preservation as an efficient physical treatment for packaged ready to eat salads.

1. INTRODUCTION

Socio-economic development during last decades in Tunisia has led to tremendous changes in eating habits such as the consumption of ready to eat products, mainly fresh vegetables and commercialized ready to eat salad

[1]. Consumption of ready to eat salad provides many benefits for human health related to its nutritional properties and it is considered as a time-saving product for consumers. Fresh vegetables do not undergo bacterial heat treatment before consumption. Therefore, spoilage microorganisms could contaminate fresh salads and cause several food-borne diseases as well as industrial economic losses [2]. Microorganisms, including aerobic plate count, yeasts, molds and pathogenic foodborne microorganisms such as *Staphylococcus aureus*, *Clostridium perfringens*, *Salmonella* spp and *Listeria monocytogenes* are detected in ready to eat salad [3,4,5, 6]. Commercialized ready to eat salads could be contaminated during processing steps (trimming, washing, peeling, cutting, slicing, and shredding) and mainly after packaging step [7]. To meet consumers demand in providing nutritious, safe, and sustainable supply of food, industrials are investing in non-thermal processing for pathogens elimination and shelf-life extension. Hence, the use of safe disinfecting treatment like food irradiation seems to be a good alternative to ensure good quality and safe salads [8,9]. Food irradiation is considered as commercials use for sanitary applications based on control spoilage and food borne pathogenic microorganisms as well as prevent the spread of invasive insects pests [10]. Among irradiation tools, E beam and gamma irradiation is widely used for food irradiation, mainly for fresh produce irradiation. They can maintain food quality and address food safety without significantly affecting a food's sensory or nutritional attributes [11, 12].

This study, aimed at evaluating the effect of E-beam irradiation combined with cold temperature storage technology on naturally occurring and artificially contaminating selected microorganisms in order to extend the shelf life of commercialized ready to eat salad.

2. MATERIAL AND METHODS

2.1. Samples Collection

A Total of 15 ready to eat salads were collected from end-point commercialized products (supermarket) located in north of Tunisia. Commercialized ready to eat salads were composed of lettuce, cherry tomato, red cabbage, rocket leaves and corn, are packaged in plastic boxes, the shelf life indicated in salads is 4 to 6 days. Samples were immediately kept at 4 ± 1 °C and analysed within 24h.

2.2. Samples irradiation

Irradiation was carried out using electron-beam accelerator (CIRCE 3, SGN, France) with an energy of 10 MeV located at the ionizing radiation facility in the National Center for Nuclear Sciences and technologies (CNSTN). Fresh ready to eat salads were irradiated in their package (250g; one box per dose) at room temperature at doses ranging from 2 to 4 kGy with an average dose rate of 40kGy/min. Non irradiated samples (0 kGy) were used as control.

2.3. Microbial analysis

Samples were analysed for naturally occurring microorganisms including total aerobic plate count, *Staphylococcus* spp., yeasts, molds and *Clostridium perfringens* during 15 days of storage period at 4°C. 25g of each sample was diluted with 225 ml of Peptone Water (Biokar diagnostics, France) and homogenized by stomacher (AES, 400ml) for 2 min. Then, serial dilution was performed for inoculation in triplicate on appropriate media following the analysis method shown in table 1. Artificially contamination of sterilized ready to eat salad (exposed to 4kGy dose) was performed using 10^7 CFU/ml of *Staphylococcus aureus* (ATCC 25823).

TABLE 1. METHOD OF MICROBIAL ANALYSIS

Microorganism	Method
Total aerobic plate count	ISO 4833-2:2013
Staphylococcus aureus	ISO 6888-1:2004
Clostridium perfringens	ISO 15213:2003
Yeast and molds	ISO 08-059:2001

3. RESULTS AND DISCUSSION

3.1. Effect of E. beam irradiation on total aerobic plate count

After irradiation at 2, 3 and 4kGy, concentrations of aerobic plate count were determined during 15 days storage period (Fig 1).

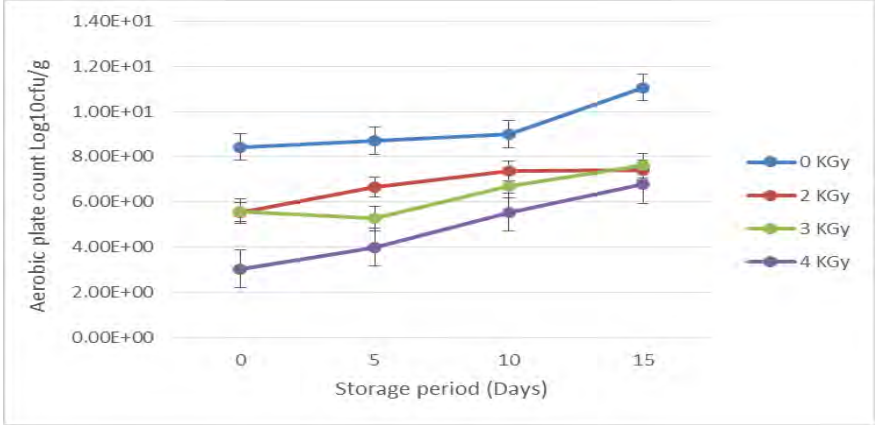

FIG.1. Concentration of aerobic plate count in commercialized ready to eat salads irradiated at 2, 3 and 4kGy and stored at 4°C for 15 days.

Initial mean concentration of aerobic plate count in commercialized ready to eat salads was 8,43 Log10 CFU/g. The E beam reduction Log scale at 2, 3, and 4kGy doses was 2.88, 2.85 and 5.41 Log10 CFU/g respectively. The E-beam treatment allowed to comply with recommended criteria for fresh fruits and vegetables regarding aerobic plate counts and reached satisfactory limit (3 log CFU/g) < 5 log CFU/g. [6]. During 15 days storage period, aerobic plate count increased in both irradiated and non-irradiated samples, which is similar to gamma irradiation effect [7]. For irradiated samples at 4kGy, the mean concentration of aerobic plate counts at 15 days was lower by 1,66 Log10 CFU/g than initial counts of non-irradiated samples at (T0).

3.2. Effect of E. beam irradiation on *Staphylococcus* spp.

After irradiation at 2, 3 and 4kGy, concentrations of *Staphylococcus* spp. were determined during 15 days storage period (Fig. 2.).

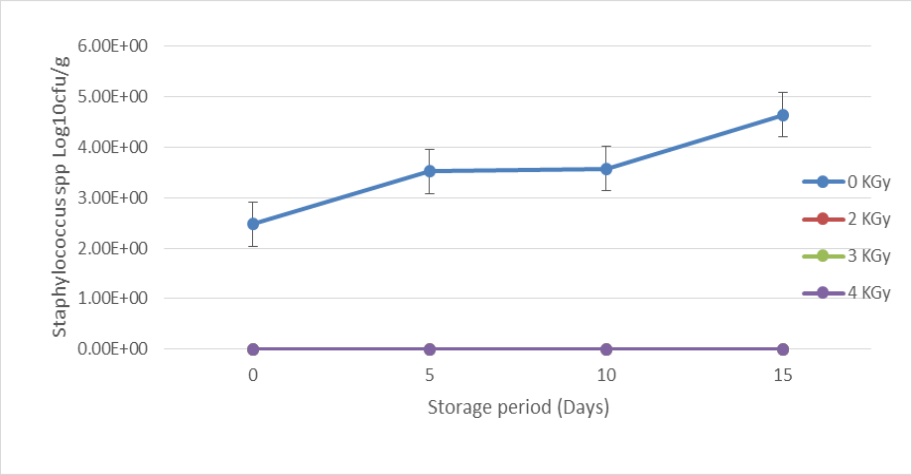

FIG.2. Concentration of Staphylococcus spp in commercialized ready to eat salads irradiated at 2, 3 and 4kGy and stored at 4°C for 15 days.

Initial mean concentration of *Staphylococcus* spp. in commercialized ready to eat salads was 2,5 Log10 CFU/g. The E beam reduction Log scale at 2, 3, and 4kGy doses was 2.5, 2.5 and 2,5 Log10 CFU/g respectively, leading to a total inactivation of Staphylococcus spp. In this case, E beam ensure pathogens control of ready to eat salad by maintaining satisfactory limit < 20 of *Staphylococcus* spp. [6]. During 15 days storage period, *Staphylococcus* spp was not detected in irradiated salads and still increasing for non-irradiated. These results were similar to those observed for the effect of gamma irradiation on *Staphylococcus* spp [7].

Regarding artificial contamination by 7 Log CFU/g of *Staphylococcus aureus* strain (ATCC 25823), E beam reduction Log scale at 2, 3, and 4kGy doses was 1.3, 1.5 and 3 Log10 CFU/g respectively (Fig. 3.)

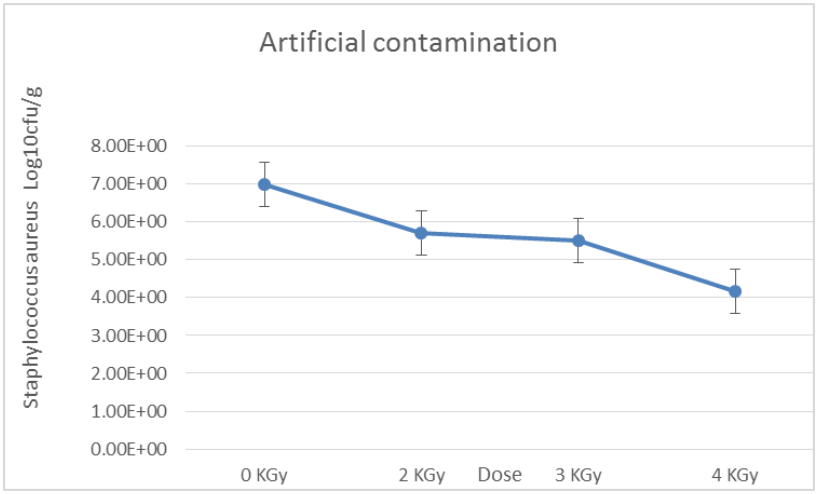

FIG. 3. Concentration of Staphylococcus aureus (ATCC 25823) in inoculated ready to eat salad irradiated at 2, 3 and 4kGy

D_{10} values were determined, as the irradiating dose needed to reduce microorganisms by 90% for irradiated samples. D_{10} value of *Staphylococcus aureus* (ATCC 25823) in inoculated ready to eat salad and irradiated by E beam was 1.6 kGy and it was higher than D_{10} value of *Staphylococcus aureus* irradiated by gamma irradiation [7].

3.3. Effect of E. beam irradiation on yeast load

After irradiation at 2, 3 and 4kGy, the concentrations of yeast were determined during 15 days storage period (Fig. 4).

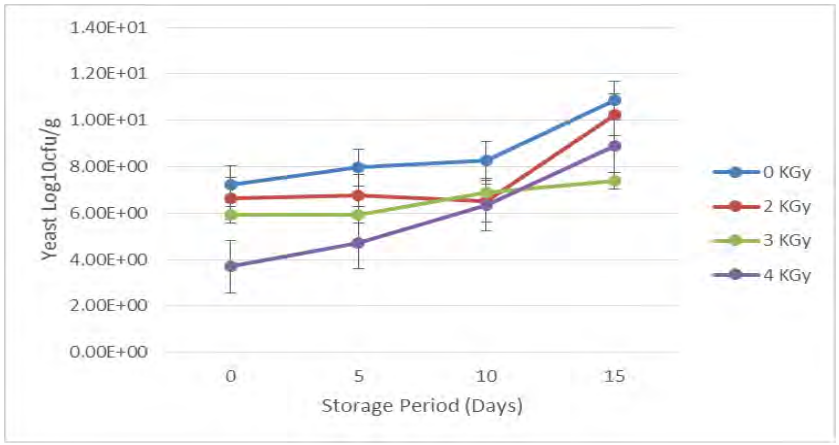

FIG.4. Concentration of yeasts in salad irradiated at 2, 3, and 4kGy and stored at 4°C for 15 days.

Initial mean concentration of yeasts in commercialized ready to eat salads was 7,25 Log10 CFU/g. The E beam reduction Log scale at 2, 3, and 4kGy doses was 0,6, 1,4 and 3,6 Log10 CFU/g respectively, leading to maintain satisfactory limit < 4 Log CFU/g [6]. During 15 days storage period, mean concentration of yeast increased for irradiated and non-irradiated salads. The concentration of yeast for irradiated during this period was always lower than control (0kGy). Previous study reported the same results of yeast load after gamma irradiation treatment [7].

3.4. Effect of E beam irradiation on molds load

After irradiation at 2, 3 and 4kGy, concentrations of molds were determined during 15 days storage period as presented in Fig. 5.

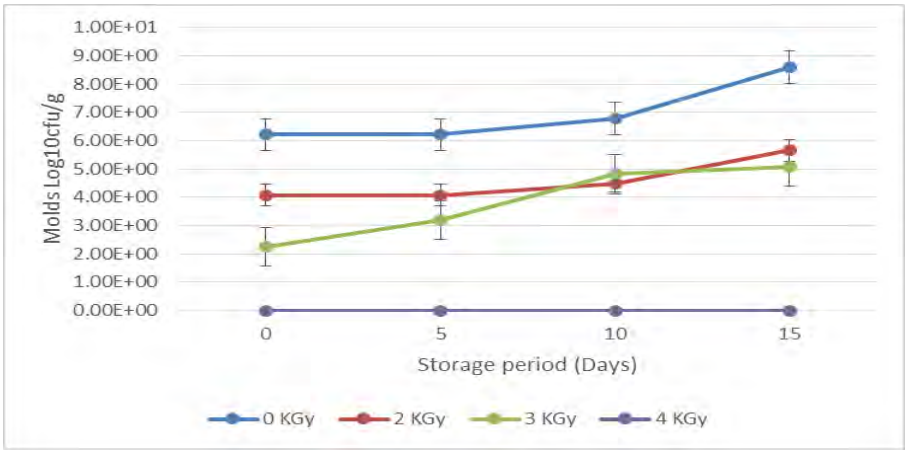

FIG.5. Concentration of molds in salad irradiated at 2, 3 and 4kGy and stored at 4°C for 15 days.

Initial mean concentration of molds in ready to eat salads was 6,22 Log10 CFU/g. Irradiation at 4 kGy ensured total inactivation of molds, contributing to maintain satisfactory limit < 4 Log CFU/g [6]. During 15 days storage period, total inactivation of molds still persist for irradiated salads at 4kGy comparatively to control (0kGy). This finding highlighted the use of E-beam treatment at 4kGy for food preservation after packaging process, as it extends its shelf-life with a reduced processing time comparatively to Gamma irradiation.

3.5. Effect of E beam on *Clostridium perfringens* load

The effect of E beam irradiation on *Clostridium perfringens* load is shown in Fig. 6.

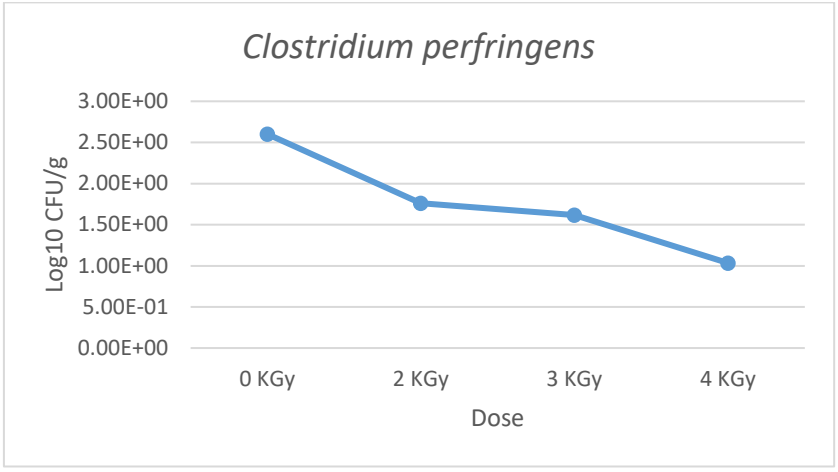

FIG.6. Concentration of Clostridium perfringens in salad irradiated at 2, 3 and 4kGy

Initial mean concentration of *Clostridium perfringens* in ready to eat salads was 2,6 Log_{10} CFU/g. The E beam reduction Log scale at 2, 3, and 4kGy doses was 0,84; 0,98 and 1,57 Log_{10} CFU/g respectively. The dose of 4 kGy is efficient against *Clostridium perfringens* espacially that D_{10} value of *Clostridium perfringens* is estimated at 3kGy. Spores are more resistant to ionizing irradiation treatment than bacteria and viruses that highlighted usefulness of *Clostridium perfringens* as indicators of irradiation treatment efficiency for food preservation.

Appearance of salads before and after E beam treatment (at 4kGy dose) during 15 days of storage period showed that irradiated samples preserved a sensory properties comparatively to control (Fig.7).

FIG.7. Appearance of salads before and after E beam treatment (at 4kGy dose); a: Control; b: Irradiated salad after 10 days; c: Irradiated salad after 15 days.

4. CONCLUSION

In conclusion, results corroborate the use of E-Beam irradiation as a treatment for ready to eat salads at a dose of 4kGy after packaging process and prior to commercialization. Its effectiveness depends on initial mean concentration of naturally occurring microorganisms. E-Beam irradiation seems to be more adequate for ready to eat food treatment to avoid contamination occurring during packaging process and to extend its shelf-life as an environmentally friendly process with a reduced processing time.

ACKNOWLEDGEMENTS

This work was supported by the National Center for Nuclear Sciences and Technologies (CNSTN). We greatly appreciate, Mr Arbi MEJRI and Mr Moktar KRAIEM for their help and collaboration.

REFERENCES

[1] MAKHLOUF, S., BEN KAHLA, K., SOUISSI, A., SEHILI, M., MESGHOUNI, N., CHAABANE, M., AGUSTIN., SEILERN, G., MARCUSSEN, E., Revue Stratégique de la Sécurité Alimentaire et Nutritionnelle en Tunisie, Institut Tunisien des études stratégiques, Tunisie (2017).

[2] LI, M., BAKER, C.A., DANYLUK, M.D., BELANGER, P., BOELAERT, F., CRESSEY, P., GHEORGHE, M., POLKINGHORNE, B., TOYOFUKU, H., HAVELAAR, A.H., Identification of biological hazards in produce consumed in industrialized countries: A review. J. Food. Prot. 81 (2018) 1171-1186.

[3] KUBHEKA, L. C., MOSUPYE, F. M., VON HOLY, A. Microbiological survey of street-vended salad and gravy in Johannesburg city, South Africa. Food control, 12(2) (2001) 127-131.

[4] NGUZ, K., SHINDANO, J., SAMAPUNDO, S., HUYGHEBAERT, A. Microbiological evaluation of fresh-cut organic vegetables produced in Zambia. Food Control. 16(7) (2005) 623-628.

[5] ABADIAS, M., USALL, J., ANGUERA, M., SOLSONA, C., VIÑAS, I. Microbiological quality of fresh, minimally-processed fruit and vegetables, and sprouts from retail establishments. Int J Food Microbiol.123 (2008)121–129.

[6] CALONICO, C., DELFINO, V., PESAVENTO, G., MUNDO, M., NOSTRO, A. L. Microbiological quality of ready-to-eat salads from processing plant to the consumers. J. Food Nutr. Res. 7 (2019) 427-434.

[7] RAHMANI, F., YAHYA, M., JEBRI, S., AMRI, I., MEJRI, A., HAMDI, M., HMAIED, F. Effect of gamma irradiation on microbial quality of minimally processed product in tunisia: a case of ready to eat salad. J. Bacteriol Mycol. 8(2): 1167 (2021).

[8] Manzoor, A.S., Shabir, A.M., Showket, A.P., Enhancing food safety and stability through irradiation: A review. J. Microbiol. Biotech Food. Sci 3 (5) (2014) 371-378.

[9] Pillai, S.D., Shayanfar, S., Electron Beam Pasteurization and Complementary Food Processing Technologies, Elsevier, UK (2015).

[10] Manual of good practice in food irradiation, sanitary, phytosanitary and other applications, Technical reports series 481 IAEA 2013

[11] MOHACSI-FARKAS, C.S., NYIRO-FEKETE, B., DAOOD, H., DALMADI, I., KISKO, G. Improving microbiological safety and maintaining sensory and nutritional quality of pre-cut tomato and carrot by gamma irradiation. Radiat. Phys. Chem. (2014) 99: 79-85.

[12] ELIAS, M. I., MADUREIRA, J., SANTOS, P. M. P., CAROLINO, M. M., MARGAÇA, F. M. A., VERDE, S. C. Preservation treatment of fresh raspberries by e-beam irradiation. Innov Food Sci Emerg Technol 66(2020) 102487.

SIX DECADES OF RESEARCH AND DEVELOPMENT WITH ACCELERATORS IN THE DEPARTMENT OF INTERACTION OF RADIATION WITH MATTER OF THE BARILOCHE ATOMIC CENTRE

R. O. BARRACHINA
Bariloche Atomic Centre, National Atomic Energy Commission Bariloche, Argentina
Email: barra@cab.cnea.gov.ar

Abstract

In 1960, Prof. Wolfgang Meckbach (1919 – 1998), together with an enthusiastic group of young researchers, technicians, and advanced students, created the first "Ion Beam Laboratory" of Argentina at the Bariloche Atomic Center, dependent on the National Atomic Energy Commission. The rich history of scientific research, applications and education and training of human resources, that occurred during the last sixty years of existence of the "Department of Interaction of Radiation with Matter" (such is its current name) is described. New facilities both for basic research in Atomic, Molecular, and Surface Physics, and for the compositional and structural characterization of samples, were continuously incorporated, with applications in branches such as archaeology, biology, environment, forensic science, analysis of materials for nuclear and non-nuclear use, medicine, nanotechnology, and others. Currently, the laboratory counts with two electrostatic accelerators of 100 and 300 keV, and a 1.7 MeV tandem accelerator with PIXE, RBS, ERDA, NRA and channeling capabilities, and a chamber for COLTRIMS reaction microscopy. One of its beam lines is dedicated to the analysis of materials and the implantation of ions, with micro beam capacity, with prospects of incorporating a WDS installation. There is also a time-of-flight system for ISS spectroscopy, surface analysis facilities with AES, UPS, XPS, EELS, ISS, DRS, LEED and GIFAD capabilities, and STM and AFM microscopes.

1. PROF. WOLFGANG MECHBACH

The Department of Interaction of Radiation with Matter (DIRM) of the National Atomic Energy Commission (CNEA) of Argentina is in an area of lakes and mountain forests in the Patagonian Andes. In fact, it is at just 10 kilometres from the tourist city of Bariloche, and at the same distance from Cerro Catedral, one of the most recognized ski resorts in South America.

This first laboratory in Argentina dedicated to Atomic, Molecular and Optical Physics was created in 1960 by Prof. Wolfgang Meckbach [1].

FIG. 1: Prof. Wolfgang Meckbach (1919 – 1998)

He was born in Frankfurt, Germany in 1919. During the war he enlisted in the Navy, where he received the title of naval engineer and was later part of a submarine corps based in La Spezia, Italy. As luck would have it, in the submarine's first incursion it was hit by a depth bomb from an English destroyer. Thus, the war for engineer Meckbach and his submarine companions ended when it had barely begun. As a prisoner of war in the United States, he was authorized to study at the University of Chicago. In May 1946, he returned to his hometown, where he married Gabriela Mack, his first and only girlfriend, and concluded his studies at Goethe University where he received his doctorate in 1951. Since his mother-in-law was Argentinean, the young couple decided to settle in Argentina. He first worked at the Universities of Bahía Blanca and La Plata. Then, in 1955 he accepted an offer from CNEA to create an Institute of Physics in Bariloche.

In 1960 an old acquaintance of Meckbach's from Chicago, Professor Samuel King Allison, director of the Enrico Fermi Institute, visited Bariloche.

FIG. 2: Prof. Samuel King Allison (1900 – 1965)

At that time, Meckbach and a young group of colleagues were building an accelerator of up to 300 kV. Being aware of the spectacular resurrection of Atomic Physics happening in those years. Meckbach asked Allison if it would not be better to dedicate the accelerator to the study of atomic collisions instead of neutron physics. Allison's answer was enthusiastic, he said:

"You are right, why don't you come to Chicago
to introduce yourself in that field working in my lab?".

After two years at the Enrico Fermi institute, Meckbach returned to Bariloche with a great knowledge of accelerators and a grant of $ 66,000 from the National Science Foundation, destined for the new Laboratory. During a second visit of Prof. Allison to the Ion beam laboratory, as it was called at that time, the first experiments were initiated.

Unfortunately, in 1965, Allison died. His 400 kV Cockcroft-Walton accelerator, nicknamed by him "Kevatron", meaning "a big machine for a low voltage", was closed in 1967, but not forgotten. In fact, the modest home-made accelerator, located 10,000 km away, inherited the name "Kevatron". Up to the present the Kevatron has served to conduct more than one hundred research projects, and master's and doctoral theses. But now, after 60 years of service, it is about to be retired.

FIG. 3: KEVATRON

It is perhaps not useless to say, that this short history shows that the value of an activity in research should not be judged by how much money it costs, but by the enthusiasm, stubbornness, and resilience of people like Meckbach and his young colleagues who built the accelerator in the 1960s.

2. TANDEM

The successor of the Kevatron, is the “Tandem”, which was installed in 2010. This is a 5 SDH Tandem accelerator from the National Electrostatics Corporation with maximum terminal voltage of 1.7 MV, reaching a maximum energy of 3.4 MeV for protons and 5.1 for alpha particles.

FIG. 4: TANDEM

The Tandem has two sources. One is a Source of Negative Ions by Cesium Sputtering, which can deliver negative ions of a wide variety of elements from solid cathodes. The other one is an Alphatross, which provides ions extracted from a gas plasma, excited with radiofrequency, which pass through a Rubidium environment. This source is used solely to produce Helium ions.

During the last ten years this equipment has been growing and incorporating different facilities and end stations. The analysis chamber used for material characterization is a RC43, made also by NEC. It works in high vacuum (10^{-8} mbar) and has surface barrier detectors to perform RBS and ERDA, one fixed and the other one mounted on a rotatable holder, a Sirius silicon drift X-ray detector for PIXE, and flanges to mount a Sodium Iodide Scintillation Detector for gamma ray spectroscopies. The chamber has a lock stage which allows to introduce samples up to 30 mm wide easily and quickly. The sample holder has a micro-positioning ability in all directions and with angular orientation.

A second line was completely designed and made in DIRM 30 years ago. The chamber is intended to analyze energy, charge state and angular distribution of charged particles (electrons and ions) after collision events between an ion beam and a gas jet, using a Channeltron detector with 180º of positioning freedom.

There is also a reaction microscope to perform Cold Target Recoil-Ion Momentum Spectroscopy (COLTRIMS), which is still installed in the Kevatron. But soon it will be moved to the Tandem.

Finally, soon, a new chamber for Surface Science will be added to the Tandem. It will allow to perform Auger Electron Spectroscopy (AES) and Wavelength Dispersive X-Ray Spectroscopy (WDS).

3. KEVATRITO

Going back in time, in the early 1970s, as the Kevatron was bearing its first fruits, a new accelerator of up to 100 kV started to be build. It was called "Kevatrito", which in Spanish is a diminutive that means "little kevatrón". The ion accelerator is an electrostatic one with voltages in the range of 2 to 100 kV. It has two types of ion sources: a radiofrequency one for ionization of gases and a solid-state alumina-silicate one for production of alkali ions. There are three collision chambers mounted in tandem (see Fig. 5). The first one is a high-vacuum chamber for material irradiation. The second one is an ultra-high-vacuum (UHV) chamber with a Time-of-flight scattering and recoiling spectrometer. The third chamber is like the second one but with a more complete surface analysis system including Ultra-violet Photoelectron Spectroscopy, Auger Electron Spectroscopy, Low Energy Electron Diffraction, and Electron Energy Loss Spectroscopy.

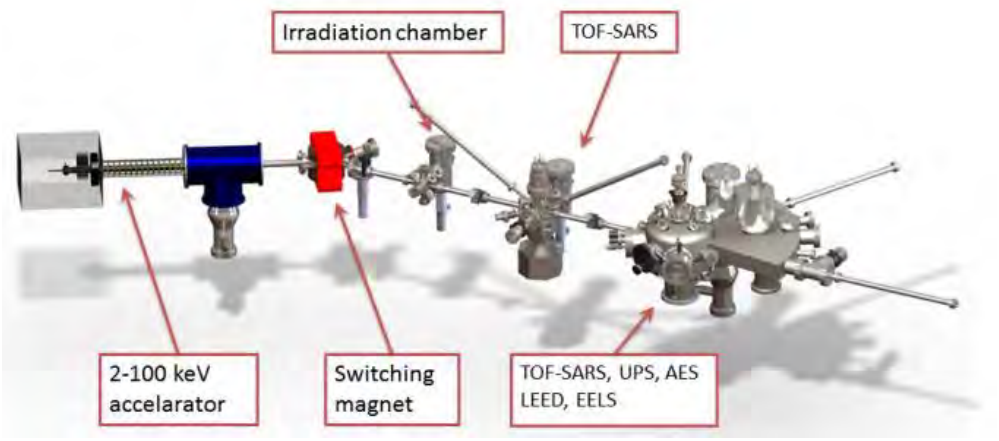

FIG. 5: Collision chambers mounted in tandem at the Kevatrito accelerator

The irradiation chamber has a linear driver for carrying multiple samples with a Faraday cup with an aperture of 1 mm for fluence determination (see Fig. 6). In front of the sample holder there are deflection plates for beam sweeping, and a carrousel with slits of different forms and sizes to control the beam shape.

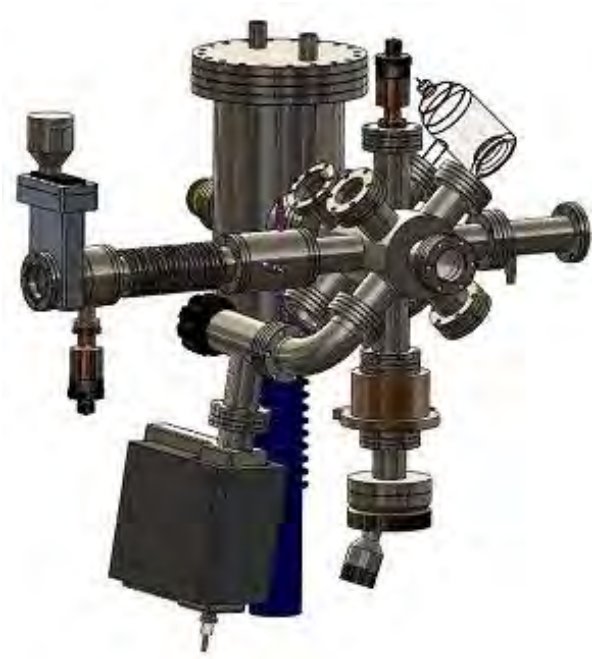

FIG. 6: Irradiation chamber of the Kevatrito.

4. STM / AFM MICROSCOPES

For the analysis of these radiation damages, the laboratory counts with two microscopes, one operating in air and the other in ultra-high vacuum (UHV). The Atomic Force microscope operates in ultra-high vacuum. Images with atomic resolution can be taken at different temperatures of the sample, in a range between 20 and 1500 Kelvin. The chamber is equipped with standard surface analysis techniques (as LEED and AES), with facilities for in-situ sample preparation by means of annealing and a sputtering for surface cleaning; and it has a sample and tip introduction tramp.

On the other hand, the Autoprobe CP microscope from Park Scientific Instruments, operates in air and allows to take images with nanometric resolution. The AFM operates in contact mode with 0.6 micrometer ultra-lever tips. It is mainly used in the topographic mode to provide services to third parties.

5. LOW-ENERGY-ACCELERATOR (LEA)

After the “Kevatron”, and the “Kevatrito”, a Low-Energy-Accelerator facility was built, to perform stopping power measurements with light ionic projectiles (H+, He+), with energies in the range of 1 to 10 keV. It has an electrostatic energy analyser that can measure scattering angles up to 45º (with respect to the forward direction). By using self-supported ultra-thin film samples (thickness < 20 nm) and the geometry of beam foil transmission (~ 0º scattering angle), the electronic stopping power can be measured with a minimum effect of the nuclear contribution.

6. XPS

The more recent acquisition of DIRM is a SPECS system for surface analysis by means of photoelectron spectroscopies. The ultra-high vacuum chamber is equipped with two photon sources, namely, a monochromatic X-ray gun (1486.6eV, Al K alpha line) and a He lamp (21.2 eV and 40.8 eV lines), a high-resolution hemispherical electron energy analyser, a sputtering gun for surface cleaning, and a rotatable sample manipulator with the possibility of cooling with liquid nitrogen. The system has a pre-chamber for fast introduction and remotion of samples.

FIG. 7: Surface Analysis Equipment (SPECS)

7. TUCUTRÓN

Another very nice and dear facility is a Low Energy 30-keV Ion Accelerator, with a Penning ion source. It was manufactured locally, as a personal project of a young researcher from our laboratory. As he was born in a city called Tucumán, he decided to call it “Tucutrón”.

8. APPLICATIONS

And this has been a summary of the six-decade history of the DIRM laboratory, of its people and of its facilities. Let us now show some few examples of how this equipment is employed.

8.1. Basic Research

In its early years, the laboratory was mainly dedicated to basic research, and even today this is very important endeavor. Possibly the most surprising and unexpected result was the first measurement done in the 1980s of the double differential cross section for the so-called capture to the continuum cusp in the single ionization of atoms by fast ions, by means of a cylindrical electron detector, as shown in Fig. 8 [2].

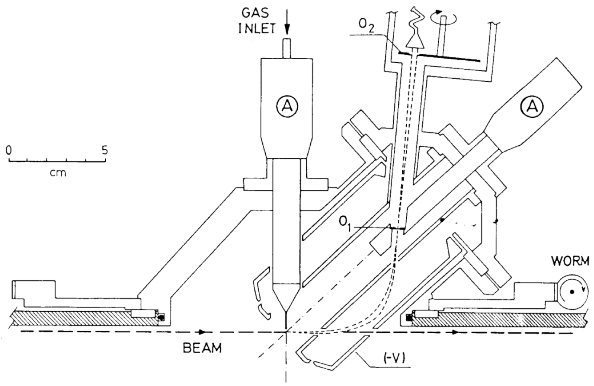

FIG. 8: Cylindrical electron spectroscopic analyzer (1980s)

8.2. CNEA

The DIRM laboratory belongs to CNEA, so it is no wonder that it is its main customer. For instance, in Fig. 9, a RBS measurement of a multilayer ZrO2/SiO2 sample is shown.

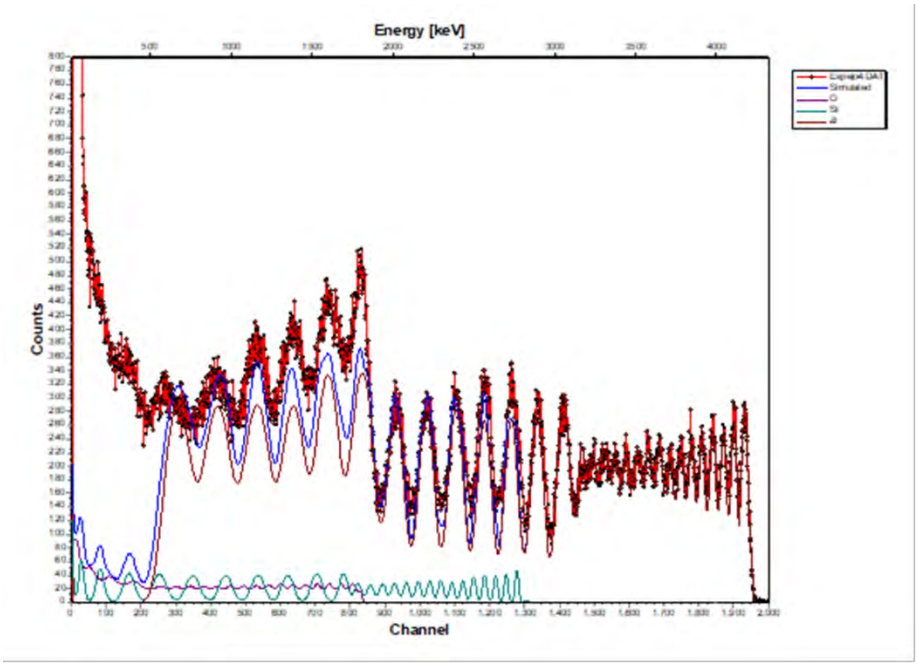

FIG. 9: RBS spectrum for a multilayer ZrO2/SiO2 sample and the fit obtained with the SIMNRA software.

At the RA-6 Nuclear Research Reactor, located in the close vicinity of DIRM, research and development are carried out on Boron Neutron Capture Therapy (BNCT). Fig. 10 shows a study done at the TANDEM accelerator in relation with the Stopping power of alpha particles in compact bone.

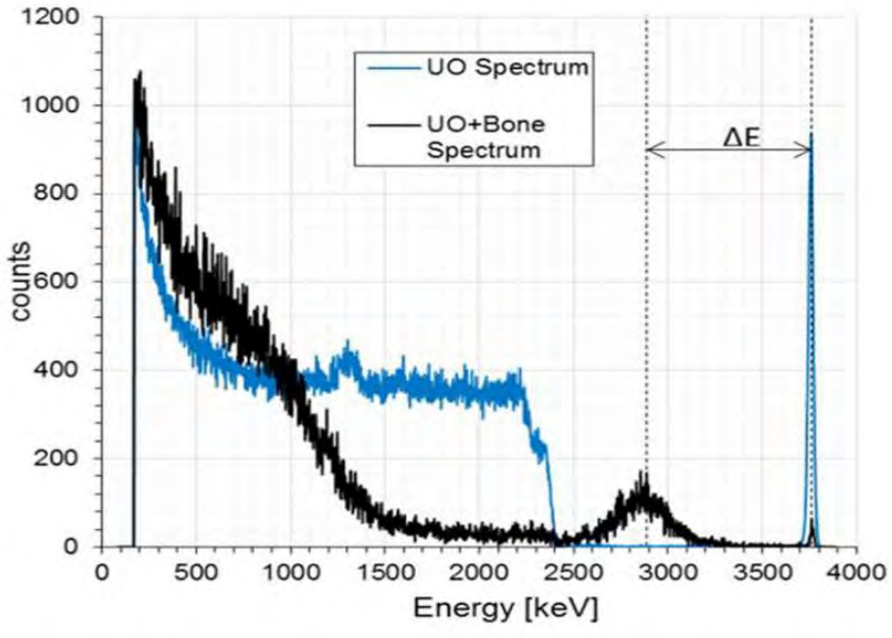

FIG. 10: Stopping power of α particles in compact bone for research in BNCT [3]

8.3. Archeology and Paleontology

Patagonia is a region known for its research in paleontology, especially in relation to dinosaur fossils, but also about prehistoric human settlements Fig. 11 shows a measurement made in DIRM of such an archeological sample.

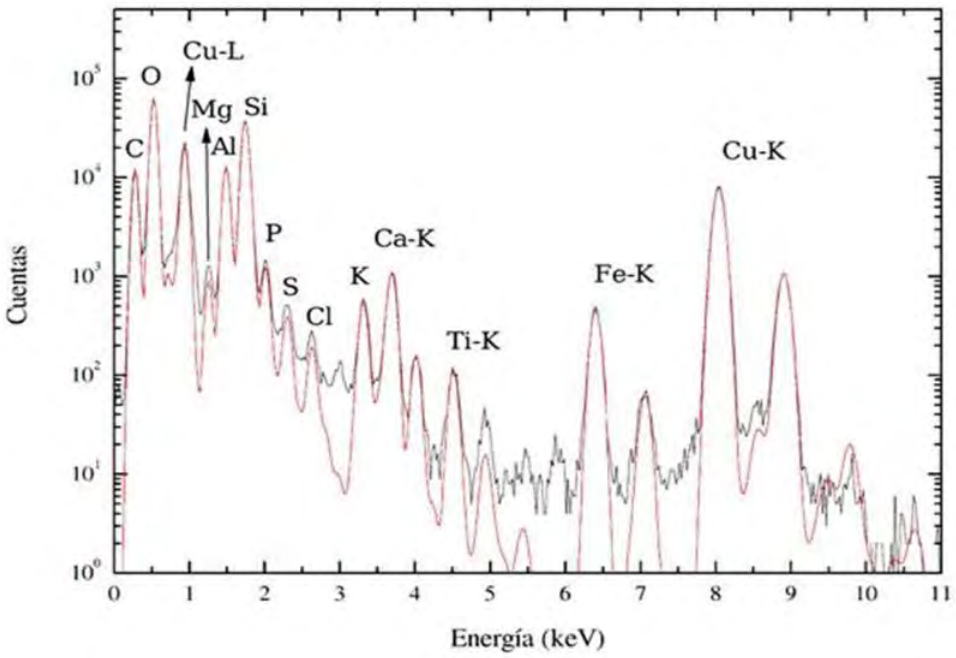

FIG. 11: X-ray spectrum of a Patagonian archeological sample and fit obtained with the GUPIX software.

8.4. Earth Sciences

Our region is surrounded by volcanoes, especially in Chile. In general, they do not represent a great danger, but every so often they become active. This happened, for instance in 2011, with the eruption of Puyehue, located 80 kilometers from Bariloche, and which literally covered the city with ash. One important environmental concern associated with volcanic eruptions is linked to the huge volumes of ashfall that may deliver hazardous elements over large distances from the source. Thus, the group of the XPS SPECS collaborated with colleagues of the Earth Sciences Center of Córdoba in the analysis of the ashes of the most recent volcanic eruptions in our region [4].

9. COORDINATED RESEARCH PROJECT

Finally, it should be mentioned that DIRM [5] is a member of the Global Network for the Atomic and Molecular Physics of Plasmas (GNAMPP) [6] and the Coordinated Research Project G42008 for "Facilitating Experiments with Ion Beam Accelerators" of the International Atomic Energy Agency. During the present year, the first visits will be received within the framework of this CRP.

ACKNOWLEDGEMENTS

Everything described here is the tangible result of 60 years of continuous and passionate work by all the scientists, technicians, and students who are and were the heart and soul of the DIRM laboratory of Bariloche. We should also thank the CNEA and other national (e.g., CONICET) and international (e.g., IAEA) organizations that provided and continue to provide the means to carry out these developments.

REFERENCES

[1] SUÁREZ, S. G., Wolfgang Meckbach y el inicio de las colisiones atómicas en Bariloche, Ciencia Hoy **15** 88 (2005) 56-59.

[2] MECKBACH W, NEMIROVSKY I. B. and GARIBOTTI C. R, Resolution dependence and asymmetry of electron capture to the continuum spectra, Phys. Rev. A **24** 4 (1981) 1793-1802.

[3] PROVENZANO L. et al., Measuring the stopping power of α particles in compact bone for BNCT, J. Phys. Conf. Series **583** (2015) 012047.

[4] BIA G., BORGNINO L., ZAMPIERI G., GARCIA M.G., Fluorine surface speciation in South Andean volcanic ashes, Chemical Geology **532** (2020) 119402.

[5] https://fisica.cab.cnea.gov.ar/dirm/

[6] https://amdis.iaea.org/GNAMPP/groups/4

SURFACE TREATMENT OF SPECIAL HIGH-PROTEIN PRODUCTS USING LOW ENERGY BEAMS FROM MACHINE SOURCES

Slobodan B. MASIC
Department for Radiation Chemistry and Physics
Vinca Institute of Nuclear Sciences
Belgrade, Serbia
Email: slobodan.masic@gmail.com

Nikola R. MIRKOVIC
MDMG Invest-Chem
Belgrade, Serbia

Ivica T. VUJCIC
Department for Radiation Chemistry and Physics
Vinca Institute of Nuclear Sciences
Belgrade, Serbia

Abstract

Special high-protein foods suitable for diabetics must be treated in such a way as to ensure the complete absence of microorganisms and bacteria. It is also important that this treatment does not change the nutritional value of the product. Among new decontamination technologies, low-energy e-beam (LEEB) treatment has proven to be an effective inactivation of bacteria with minimal impact on food quality. The aim of the paper is to analyse the influence of LEEB on microbiological properties and nutritional values of high-protein foods.

1. INTRODUCTION

According to the Serbian Diabetes Registry, over 710,000 people in Serbia suffer from this disease. They need a special diet, with the lowest possible carbohydrate content. It is well known that proper and healthy food is a prerequisite for good health.

In cooperation with a local food company, we have developed high-energy products that would be ideal for diabetics, athletes, individuals on a particular diet and anyone who cares about health. Some examples of developed high-protein products are original protein evening bread, protein burgers, protein crackers, protein chips, protein biscuits, cocoa cream with no added sugars, protein bagels and scones, protein tortillas and pancakes, protein drinks. These products are innovative because they do not use traditional raw materials, but specially designed high-protein, whey. All the products are sugar-free.

Firstly, the products were treated with gamma radiation, which guarantees the absolute absence of all microorganisms and harmful substances in said products, and significantly extends the shelf-life span. Nevertheless, it has been determined that treatment with ionizing radiation can affect the change in the nutritional values of the product. To avoid changes in nutritional value after irradiation, low energy electron beam (LEEB) was used for preservation of high-protein products. Recent developments in LEEB technology have revolutionized aseptic packaging. Advancements in electron beam technology are shrinking the footprint of the devices used to generate ionizing radiation. With the relatively recent development of reliable, compact, cost-effective, LEEBs, a new class of in-line applications is now possible. The benefits of high-speed, high efficacy treatments, with no chemicals and at room temperature, are now realized across a variety of packaging applications. Such developments are also attractive to the food industry.

The aim of the paper is to analyse the influence of LEEB on the physical and chemical parameters of the preservation of high-protein foods suitable for diabetics.

2. MATERIALS AND METHODS

2.1. Gamma irradiation

Irradiation was performed with gamma rays in a Radiation facility for industrial sterilization and conservation at the Vinca Institute of Nuclear Sciences in Belgrade. Radiation doses of 1 kGy, 3 kGy, 5 kGy, 7 kGy, and 10 kGy were used. The average irradiation dose rate was about 10 kGy·h^{-1}. The delivered radiation dose's accuracy is controlled using the ECB/oscilloscope dosimetric system. The measurement of the absorbed radiation dose was performed at 20°C.

2.2. LEEB irradiation

For irradiation of protein product samples with low energy e-beam, Laatu machine from producer Buhler Croup, was used. Laatu offers a chemical-free solution with reduced running costs thanks to its low energy consumption and minimal or no product waste. In Table 1 is shown specification of the Laatu e-beam. Irradiation dose was 10 kGy.

TABLE 1. TECHNICAL SPECIFICATIONS OF LAATU

Voltage	Voltage With supply frequency 50 Hz: 400Y/230 VAC With supply frequency 60 Hz: 400Y/230 VAC + 460 VAC
Power ≤30	≤30 kW
Product throughput (product dependent)	up to 1,000 kg/h
Air exhaust (depending on installation)	up to 8,100 m3
Ambient temperature	+5 ... +40 °C
Relative humidity, non-condensing (during operation)	10 ... 70 %

2.3. Microbiological analysis

In the accredited microbiology laboratory, the initial contamination and the number of microorganisms, total molds, and bacteria in the samples were examined. The method used to determine these parameters was Ph. Eur. 7.0 (2.6.12. – microbiological examination of nonsterile products (total viable aerobic count), and 2.6.13. – Microbiological examination of non-sterile products (total viable aerobic count)) [1]. Microbiological analyses were performed before irradiation and after gamma irradiation with different radiation doses. The used diluent (buffered peptone water) and nutrient media for the development of microorganisms (tryptone soy agar, Rose Bengal agar, iron sulfide agar) are following international standard ISO 11737-1: 2018 [2].

2.4. Nutritional properties

The samples of high protein products were analyzed to determine their content of total fat, protein, carbohydrates, sugars, and dietary fiber after gamma irradiation. These analyses were performed before irradiation and after gamma irradiation with the highest used radiation dose of 10 kGy.

2.4.1. Determination of total fat content

Determination of total fat content in the high protein products samples is performed by Weibull-Stoldt - Standard application [3]. The sample is hydrolyzed using the Hydrolysis Unit E-416. The Soxhlet extraction is performed with the Extraction Unit E-816. The calculation of the samples' total fat is realized by the gravimetric method after the extract has dried to reach permanent weight. This application is in accordance with official methods (EN 98/64/EG, AOAC 963.15, §64 /§35 06.00-6).

2.4.2. Determination of carbohydrates and sugars content

Determination of total carbohydrate and sugars present in high protein products were performed using phenol sulphuric acid method [4]. This method is often used to determine the carbohydrate content of food [5]. The method is based on dehydration of glucose to hydroxymethyl furfural in a hot acidic medium. A yellow product with phenol is formed, which has a maximum absorption at 490 nm [6, 7].

2.4.3. Determination of dietary fiber

An enzymatic-gravimetric method was used to determine the content of dietary fiber in high protein products samples. The samples were first degreased and then treated with enzymes that mimic the process of digestion in the human small intestine. Digestible carbohydrates are then broken down into simple sugars, which are removed by precipitation and filtration. After that, only dietary fiber remains in the sample.

2.4.4. Determination of protein in h high protein products

Protein content before and after irradiation was determined using a standard ISO procedure, ISO 1871:2009 [8]. This standard provides general guidelines for the determination of nitrogen by the Kjeldahl method. The standard applies to food and feed products containing nitrogen compounds that can be directly determined by the Kjeldahl method [9].

3. RESULTS AND DISCUSSION

3.1. Effects of gamma irradiation on microbiological properties

To eliminate microorganisms, total molds, and bacteria from special high-protein products, samples were treated with the different doses of gamma irradiation, from 1 kGy to 10 kGy. Table 2 shows the microbiological results after treatment with different radiation doses.

TABLE 2. TOTAL NUMBER OF MICROORGANISMS, THE TOTAL NUMBER OF MOLDS AND DIFFERENT BACTERIA BEFORE AND AFTER THE INFLUENCE OF DIFFERENT DOSES OF GAMMA IRRADIATION.

Parameter	Dose (kGy)						Permissible value
	0	1	3	5	7	10	
Total number of microorganisms (cfu·g^{-1})	$5.6\cdot10^{7}$	$2.5\cdot10^{7}$	$4\cdot10^{4}$	$2\cdot10^{3}$	<1000	<1000	<1000
Total number of mold (cfu·g^{-1})	$5.4\cdot10^{4}$	$3.5\cdot10^{4}$	$5.6\cdot10^{3}$	130	<100	<100	<100
Salmonella sp. (cfu·g^{-1})	not present	not present	not present	not present	not present	not present	must not contain
E.coli (cfu·g^{-1})	350	300	20	not present	not present	not present	must not contain
Staphylococcus aureus (cfu·g^{-1})	150	90	15	not present	not present	not present	must not contain
Pseudomonas aeruginosa (cfu·g^{-1})	not present	not present	not present	not present	not present	not present	must not contain
Bacillus cereus (cfu·g^{-1})	5500	2100	300	<100	<100	<100	<100
Sulfitoreducing clostridia(cfu·g^{-1})	10	not present	not present	not present	not present	not present	must not contain

From Table 2, one can see that the radiation dose of 7 kGy is enough to eliminate the total number of microorganisms and molds below the permitted limit. On the other hand, a treatment of 3 kGy is enough to remove all bacteria from the sample.

3.2. Effect of gamma irradiation on nutritional values of samples

To determine if gamma irradiation treatment affects the samples' nutritional properties, analysis of the nutritional values in the non-irradiated sample and the sample irradiated with the highest used dose of 10 kGy were performed. The data are shown in Table 3.

TABLE 3. NUTRITIONAL VALUES OF SAMPLES BEFORE IRRADIATION AND AFTER 10 KGY IRRADIATION

Parameter	Non-irradiated	Irradiated with a dose of 10 kGy	Measurement error
Total fat, %	14.5	9.2	3.0 %
Carbohydrate, %	31.3	32.0	5.8 %
Sugars, %	3.9	4.0	5.8 %
Dietary Fiber, %	17.9	18.0	2.5%
Protein, %	40.0	41.3	4.0 %

From Table 3, It has been determined that treatment with ionizing radiation can affect the change in the nutritional values of the product. Decrease in fat content could be due the action of high energy radiation on lipid molecules causing lipid peroxidation The biggest problem is that the proportion of carbohydrates increases, and the proportion of protein decreases after exposure to gamma radiation at a dose rate of 10 kGy/h. Increase in carbohydrate content was due to breakdown of oligosaccharides when samples were irradiated.
Decrease in protein content with gradually higher irradiation dose is because of high rate of metabolic activities. Fig 1. shows the changes in the nutritional value of the product "Protein evening bread" depending on the radiation dose to which the samples were exposed.

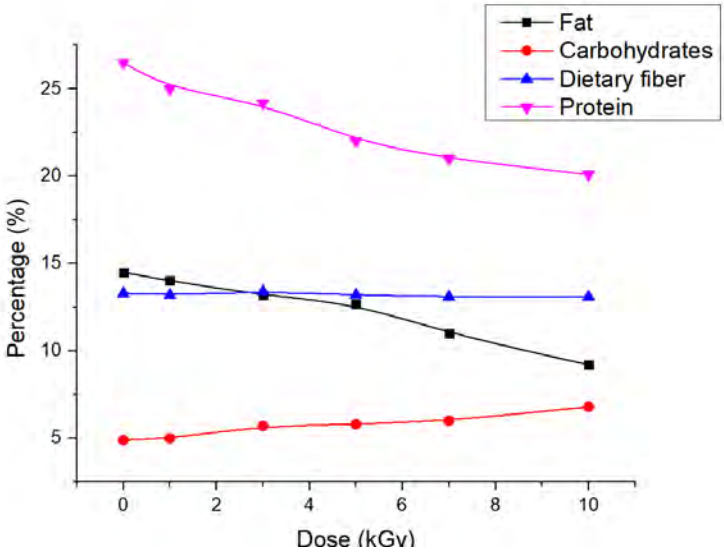

FIG 1. Changes in the nutritional value of the product "Protein evening bread" depending on the radiation dose of gamma irradiation

3.3. Effect of LEEB irradiation on microbiological properties and nutritional values of samples

To avoid changes in nutritional value after irradiation, LEEB was used for preservation of high-protein products. The use of low energy electrons has advantages over the use of gamma-rays or higher energy electrons for the direct irradiation of food. These advantages arise from details of the interaction processes which are responsible for the production of physical, chemical, and biological effects. Factors involved include:

- Depth of penetration,
- Dose distribution,
- Irradiation geometry,
- Costs.

Table 4. shows the microbiology and nutritional values of high-protein bread before irradiation and after LEEB treatment with dose of 10 kGy.

TABLE 4.

	Non-irradiated	Irradiated with LEEB (10 kGy)
Microbiological properties		
Total number of microorganisms	52000 cfu·g^{-1}	0
Molds	420 cfu·g^{-1}	0
Nutritional values		
Fat	14.5%	14.3%
Carbohydrates	4.9%	5.0%
of which sugars	1.6%	1.6%
Dietary fiber	13.3%	13.3%
Protein	26.5%	26.4%

Irradiation of the product surface with a Low Energy E-beam (LEEB) appeared as a possible ideal solution. Such a treatment would neutralize the microorganisms. Microorganisms are located on the surface of the product and are formed mainly during the handling of the product. On the other hand, the change of the nutritional values of the product under the influence of high-energy ionizing radiation would be avoided.

4. CONCLUSIONS

Advancements in electron beam technology are shrinking the footprint of the devices used to generate ionizing radiation. With the relatively recent development of reliable, compact, cost-effective, LEEBs, a new class of in-line applications is now possible. The benefits of high-speed, high-efficacy treatments, with no chemicals and at room temperature, are now realized across a variety of packaging applications. Such developments are also attractive to the food industry. The use of LEEB in the treatment of special high-protein products for diabetics has shown great potential for further development and application.

ACKNOWLEDGEMENTS

The research was funded by the Ministry of Education, Science and Technological Development of the Republic of Serbia and the IAEA.

REFERENCES

[1] European Directorate for the Quality of Medicines & HealthCare (2011). European Pharmacopoeia 7.0

[2] International Organization for Standardization (2018) ISO 11737-1:2018 Sterilization of health care products — Microbiological methods — Part 1: Determination of a population of microorganisms on products

[3] Hydrolysis Unit E-416, Extraction Unit E-816 Soxhlet (2007). Fat determination according to Weibull-Stoldt - Standard application

[4] MASUKO T., MINAMI A., IWASAKI N., MAJIMA T., NISHIMURA S., LEEY C. (2005) Carbohydrate analysis by a phenol lsulpuric acid method in microplate format. *Anal. Biochem.* 339(1):Pp.69-72.

[5] ROBERTS, R., ELIAS R. (2011) Determination of carbohydrate using phenol sulphuric acid method. Food Analysis (4thEd). S.Nielson (ed.): Springer.

[6] SADASIVAM, S., MANICKAM, A.(2005): Phenol sulphuric acid method for total carbohydrate. Biochemical methods. New Age International (P) Ltd .New Delhi.Pp.10

[7] AGRAWAL, N., HIDAME, P., GURLA, S. (2014) Estimation of Total Carbohydrate in Flour of Different Types of Grain, *International Journal of Researches In Biosciences*, Agriculture and Technology, II(3): 36-40

[8] International Organization for Standardization (2009). ISO 1871:2009 Food and feed products — General guidelines for the determination of nitrogen by the Kjeldahl method

[9] KJELDAHL, J. (1883) Neue Methode zur Bestimmung des Stickstoffs in organischen Körpern (New method for the determination of nitrogen in organic substances), *Zeitschrift für analytische Chemie*, 22 (1): 366-383.

THE PRACTICE OF ELECTRON AND PROTON ACCELERATORS UTILIZING FOR INDUSTRY, EDUCATION AND SCIENCE

O. V. RIABUKHIN
Ural Federal University
Ekaterinburg, Russia
Email: o.v.ryabuhin@urfu.ru

V. Yu. IVANOV
Ural Federal University
Ekaterinburg, Russia
Email: v.ivanov@urfu.ru

S. S. ZYRIANOV
Ural Federal University
Ekaterinburg, Russia
Email: sszyrianov@urfu.ru

T. A. MAKSIMOVA
Ural Federal University
Ekaterinburg, Russia
Email: t.a.maksimova@urfu.ru

Abstract

Seven years' experience of Radiation Sterilization Center of Ural Federal University is presented. The main aspects of accelerators utilizing for industry, education and scientific research are described.

1. E-BEAM FACILITY AND DOSIMETRY SYSTEMS

Since 2015 in Ural Federal University the linear electron beam accelerator is functioning for the purposes of radiation sterilization and modification materials, scientific research and education. The organizing of Radiation Sterilization Center (RSC) started from 2013 after design qualification procedure was finished. Firstly, the reconstruction of the building (fig1, a) was performed, and equipment installed (fig1, b, c). Then the steps of validation procedure were realized that led for certification of accelerator facility and medical products irradiation conditions according to ISO 11137. The main parameters of accelerator are energy 8-10 MeV, nominal beam current – 1mA, beam scanning width – 40 cm. Conveyor system consists of 36 pallets with moving velocity 0,6 – 4 m/min. The disadvantage of this kind conveyor system is ineffective beam utilizing due to free areas between pallets that lead to absence of continuous products irradiation. From the other hand free areas allow to perform simultaneous irradiation of material samples for scientific research activity.

FIG 1. Stages of RSC organization

For absorbed dose measurements the optical and calorimetric dosimetry systems are used. For routine dose measurements during radiation sterilization polymer films (fig. 2, a) with phenazine coating (manufactured in RF by Russian metrological institute of technical physics and radio engineering (VNIIFTRI)) are used with dose ranges 1-10 and 5-50 kGy and 30-200 kGy depending on processed product. Dosimeters are traceable to national

standard of absorbed dose. To make dose measurements traceable to international standard of absorbed dose calorimetric polystyrene dosimeters (fig2, b) and polystyrene phantom were bought in RIS0 laboratory. Calorimeters allow to measure absorbed doses in 3-40 kGy dose range and perform irradiation of different dosimeters in the same conditions with using of phantom. Calorimeters were verified on conditions of irradiation in RSC. So, these dosimeters are used from time to time for routine measurements, to test optical dosimetry system and for IAEA intercomparision program realized from 2017. RSC took part twice in this program and by the results of the last step difference between established and delivered doses were not more 5%, that is the good result for e-beam facility. Next step of intercomparision program is realized during 2022 and RSC plan to take part. Also, calorimeters used for calibration curve preparation during training courses.

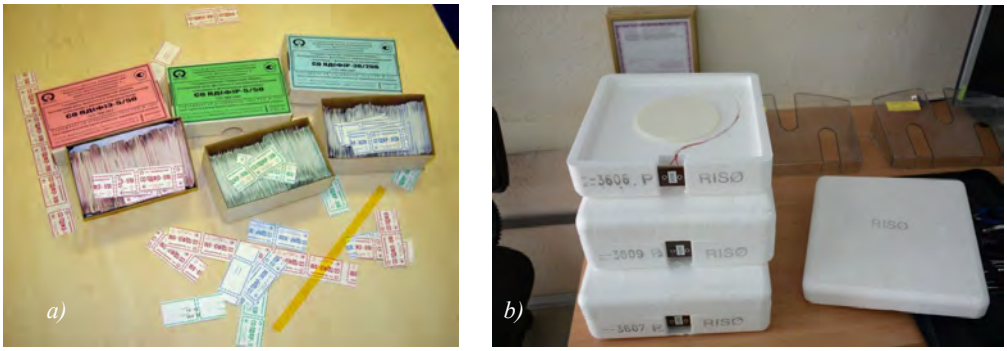

FIG. 2. Dosimetry systems used at RSC

2. INDUSTRY UTILIZING OF E-BEAM ACCELERATOR

Practically 90% of accelerator working time is used for industry purposes. RSC sterilizes different kinds of single used medical products (fig. 3, a, b, c) with sterility doses in region of 11 - 17 kGy for different products (blood test tubes, surgery sets and clothes, catgut suture material and other), processes polymer packages for juice and wine (fig.4 a) by dose 15 kGy with the goal of decontamination and shelf time extension, processes polyethylene tubes of different diameter with doses 100-120 kGy (fig.4 b) for thermoshrinkable isolation materials preparation.

FIG. 3. Medical single used production

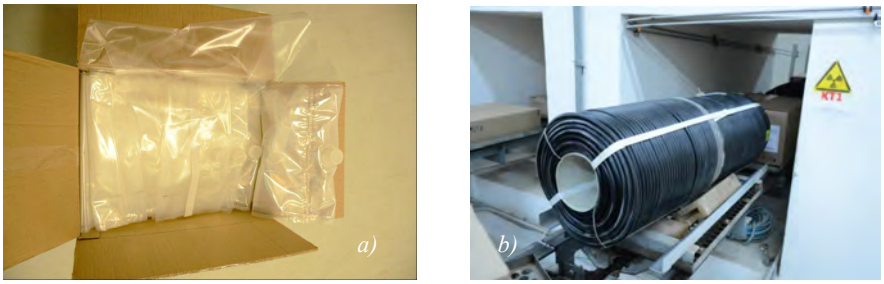

FIG. 4. Polymer production processed at RSC

The specific of medical goods irradiation validation (operation and performance qualifications) establishing of irradiation and packaging conditions in RF is attracting of licensed organization for realizing these procedures. This organization is VNIIFTRI that is carry out products dose mapping, determine minimum and maximum absorbed doses, establish the range of doses in control point and conveyor velocities. All received data with the information about type of product included in validation certificate. After PQ procedure all one type products sterilization is going according to validation certificate.

Polymer tube layout method (see fig.4 a) was suggested to customer by RCS and after dose mapping carried out by us it was showed that dose distribution is laying in the range 100-120 kGy that was is enough for cross-linking.

After six years of activity in this field we can define some critical points for successful operation of facility for radiation technology. The first one is technical condition of facility. Our efforts were applied in regular maintenance and modernization of all installation's modules needed to be done for reliability providing. During exploitation the decisions on modernization of vacuum, high voltage equipment, ventilation, remote-control and conveyor systems were taken and realized. This upgrading allowed us to increase reliability of equipment and provide RSC functioning without issues that were typical at beginning of accelerator complex exploitation.

The second critical point is strong necessity to perform radiation sterilization procedure according to standards of technology. According to national standard radiation sterilization performs on the base main document - technological regulation that is elaborated by RSC and signed by customer and Center. This regulation describes all the stages starting from initial control of delivered product (presence of packaging damages, dose indicators) continued by steps of auxiliary equipment and accelerator starting control, then radiation sterilization performing and dosimetry control, irradiated product storage and dose indicator changing color control. All this steps a detailly described in regulation with focusing on documentation provided sterility dose delivering that should be prepared for customer. Dose measurements are traceable for primary national standard through the calibration curve prepared by manufacturer of dosimeters - VNIIFTRI.

The third important moment is regular work with customers for the explaining how radiation sterilization procedure validation should be carried out. On the present day five main customers of radiation sterilization have a contract with RSC on processing medical and polymer production. Only one of them had knowledges about all the steps should be done before starting routine sterilization. This company firstly established sterility dose for their products and after performed OQ and PQ procedures at our facility with attracting of licensed organization for dosimetry measurement. All the other customers of sterilization needed to be trained by the stuff of RSC for right approach to start sterilization or processing of their product.

In principle that is well known steps but in the specific of countries and used facilities can be realized in different ways.

3. E-BEAM ACCELERATOR UTILIZING FOR EDUCATION AND TRAINING

3.1. Students' education

As usual more than one hundred students of bachelor, master and specialist education programs have more-less practice on the base of E-beam accelerator. Education starts traditionally from lectures on the basics of acceleration technologies and nuclear physics and continued by special courses on nuclear installations, metrology of dose measurements, applied nuclear physics, dosimetry, radiation action on microelectronic components and detectors. In each course the laboratory work on the base of accelerator is presented. For instance, measurement of electron beam energy is a standard laboratory work of metrology course where students get the experience of absorbed dose measurement with using of optical dosimeters, plotting absorbed dose curve, and determining of electrons range and calculating the energy. Irradiation action on detector course provides laboratory work on electrical properties of e-beam irradiated detectors measurements. Even student from biotechnological program have laboratories on studying of e-beam irradiated bio samples.

Another type of education work in our department is personal scientific research work where students take part in real R&D activity under scientific advising of teacher in the fields of physical, chemical and biological materials properties changing under the action of e-beam irradiation. Multiplicity of effects born under the action of irradiation gives a wide field of scientific challenges for scientists including students. The results of student's participation in research activity are real experience on working with complex equipment, studying investigations

methods, acquisition of scientific contacts and of course – publications. From the other hand taking part in R&D activity can be directed on studying and developing of radiation technologies that are realized at accelerator facility or can be launched. Students can apply themselves in modernization of equipment, improvement or starting radiation technology, new dosimetry system implementing etc. So, participation of student in R&D activity give the possibility of scientific or technological qualification formation.

As usual R&D activity realized by students during graduate work. In this case student have more complicated task in compare with personal scientific work. Not only make one or two measurements under advising, but independently formulate the goals and objectives of the work, master the techniques and take measurements, analyze the data and give explanations and conclusion. It can be scientific task, for instance, studying of luminescent properties changing in any compound under e-beam action or technological task – studying the dose distribution in any kind of production that planned to be processed at E-beam facility. The outcome of the work is assignment of bachelor's, master's degree or specialist qualification.

The last one type of education activity that is realized in RSC is industrial practice. It carried out in free of education time and allow students to take part in all steps of radiation technology of sterilization. They attracted for initial and post irradiation control of products, working with accelerator facility to start or close radiation process, dose measurements of routine dosimeters, controlling of beam parameters and dose distributions under stuff advising. As a result – enhancement of technological qualification in the field of applied using irradiation.

3.2. Training

Training courses at RSC were born because of close cooperation with IAEA. Starting this activity in 2011 with participation in training courses on dosimetry at gamma irradiation facility in 2015 it was continued in more closely. With increasing of our experience, it was suggested to Agency to make RSC as a place for training courses on E-beam dosimetry and after IAEA expert's visit the decision to start IAEA training program on this topic was taken. The interest of IAEA lays in possibility of attracting for participation colleagues for Former Soviet Union countries, that's why the first regional training course on dosimetry at electron beam facilities carried out at 4-8 of September 2017 (fig. 5) had official languages English and Russian. It was convenient for participants from Belarus, Uzbekistan and RF with poor knowledge of English. Also, participants from European countries – member states of IAEA took part in training. Training group was 16 people of that allowed to organize 4 groups for practical exercises. The program of the course was divided to theoretical part with lections and practical with exercises at E-beam facility. Theory includes presentations of IAEA expert on dosimetry systems and dosimetry measurements in procedures of validation (IQ, OQ and PQ) and performing (QC) radiation sterilization and presentations of RSC stuff on specific of dosimetry measurements at E-beam facility in RF. Practical exercises were measuring of E-beam energy, calibration curve of optical dosimeters, dose distributions on the surface of irradiated box, dose-conveyor velocity dependence, interruption procedure simulating, dose distribution in real medical product, routine control of products sterilization.

FIG. 5. IAEA Training Course on E-beam Dosimetry at RSC, 2017

Next one IAEA training with the same topic was carried out in August 26-30, 2019 (fig.6). Again, participants from Former Soviet Union countries have been presented also with European countries. At this training the presentation of main customer of sterilization at RSC facility - “Zdramedtech” company and excursion to plant of medical production were included in a program. It was successful addition that gave possibility to see all the chain from production of single used medical goods to sterilization and distribution of irradiated product to customers.

FIG. 6. IAEA Training Course on E-beam Dosimetry at RSC, 2019 with visiting of “Zdravmedtech” company

Took in account an experience of IAEA training courses organizing, increased skill in radiation processing of materials and huge education work experience RSC suggested to Rosatom corporation to organize the similar training with extended program including basics of dosimetry, radioactive sources and equipment for personnel dosimetry measurements additionally to lections and practical exercises on radiation processing and E-beam practical exercises. In November 2019 such first training program named “Multipurpose irradiation centre as a component in Centre of nuclear science and technologies”, supported by Rosatom Corporation have been successfully realized with participants from Europe, Africa, South America and Asia countries. Selection of participants conducted by Rosatom were directed on the countries – partners of Rosatom which have interest in implementing of radiation technologies. Finally, 16 candidates were chosen and took part in training (fig 7). The second one training course under Rosatom support was performed in October 2021 with the same geography of participants. Both events had good feedback from participants and positive outcome of IAEA and Rosatom as a customers of training programs.

FIG. 7. Rosatom supported Training Course at RSC, 2019

So, both programs under IAEA and Rosatom supporting gave us unique learnings and skill increasing in international training organizing, gave productive discussions with participants concerned of radiation technologies developing and implementing. We shared with our experience in radiation processing and got an assessment of our facility and radiation processing operation. Both training courses planned to be continued. IAEA supported training course planned to 2023 in frame or RER 1021 and Rosatom program planned to be carried out twice per year.

4. E-BEAM ACCELERATOR UTILIZING FOR SCIENCE

The construction of RSC allows to irradiate different materials by electrons directly under the beam and with step-by-step accumulation of absorbed dose with using of a conveyor. Moreover, irradiation could be done in parallel with the main process of radiation sterilization (fig.8, a). So, main implementation of accelerator is irradiation of different materials for investigation of physical chemical and biological properties changing. Through the water-cooling system, it is possible irradiate samples without essential increasing of its temperature under the direct electron beam. E-beam accelerator gives the possibility to irradiate materials by electrons with dose rates up to 1 kGy/s, by bremsstrahlung (using lead or tungsten converters) with dose rates up to Gy/s. The materials irradiated at RSC facility are solid states (polymers, dielectrics and semiconductors, microelectronic components, detectors, solar cells, powders for various purposes) and biological objects (food products, microorganisms, fungus). For example, in [1] investigation of irradiated GaAs detectors electrical properties have been conducted (fig.8, b).

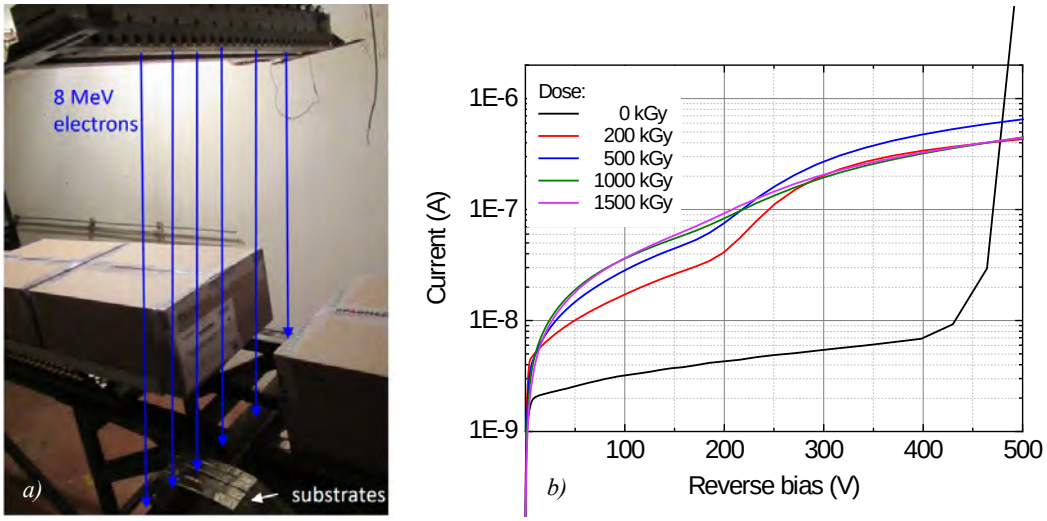

FIG. 8. Irradiation of GaAs detector under direct E-beam and electrical properties changing [1].

The same kind of work [2] were performed at RSC facility where photoluminescence spectra of glass solar cells on the base of ZnO/CdS/Cu2ZnSnSe4/Mo/ irradiated by 10 MeV were studied.

As an example of biological object investigation, the work [3] can be presented, where probiotic cultures were processed by E-beam with the goal of comparative chemical analysis to determine characteristics of amino acids, containing in whole cell and lysed by irradiation of the respective microbial cultures.

So, irradiation facility of RSC has a strong demand on irradiation performing with dose range from units of Gy up to MGy for scientific research. Some of this works lays in fundamental physics, others are directed for radiation technology developing.

5. CYCLOTRON FACILITY

The second project realized at experimental physics department is commissioning of TR-24 proton cyclotron with objective to organize radiopharmaceutical production. After rconstruction of the building cyclotron with equipment for radiopharmaceutical production was installed (fig.9). Nominal characteristics of accelerator are E_p - 18-24 MeV, beam current – up to 300 μA, dual beam configuration, external multi-CUSP ion source.

Radiopharmaceuticals production on the base of ^{18}F and ^{123}I are planned to start in 2022 using the first beam extraction channel and ^{68}Ge, ^{111}In, ^{99m}Tc two years later engaging second extraction channel. Also, experimental channel for samples irradiation is provided.

FIG. 9. Cyclotron and radiopharmaceutical production facility with analytical equipment

Finally at the present time stages of national licensing are carried out and GMP documentation started to form. Experimental channel is ready for using. Besides of industrial radiopharmaceutical production this facility is planned for using for R&D activity and education.

6. CONCLUSION

The experience of industrial irradiation facility integrated in university structure can be estimated as successful. E-beam facility installation and RSC organizing required less efforts in compare with cyclotron and Nuclear Medicine Center (NMC). Started both projects practically at the same time in 2012-2013 RSC has 7 years exploitation period whereas NMC on the stage of QMS documentation forming. The delay in Center commissioning deals with the long reconstruction of old building according to modern requirements of radiopharmaceuticals productions. Nevertheless, request on radiopharmaceuticals in our region is still high and MNC production should be in demand.

Benefits of industry accelerators university location lays in supporting of educational programs in nuclear physics, radiation technologies, radiochemistry, dosimetry etc., possibility of fundamental and applied research in radiation technologies. Accelerators as industrial facility provided by modern cooling and ventilation systems, electron and ion sources, automatic control systems, dosimetry and particle fluenses measurement equipment that gives extensive experience in servicing and maintaining of facility, developing of new electronics for improvement of irradiation process characteristics, dosimetry methodic preparation and measurements, research equipment production and etc. Acquired skills allows to organize educational and scientific tool platform for

students and distribute experience through training courses for the stuff of the same kind facilities in RF and countries – member states of IAEA and partners of Rosatom corporation.

ACKNOWLEDGEMENTS

International Atomic Energy Agency for supporting of E-beam facility of Ural Federal University in frame of Technical Cooperation projects. The last one is RER 1021 “Enhancing the Use of Radiation Technologies in Industry and Environment”. Rosatom corporation for supporting of E-beam dosimetry training course organizing. Stuff of RSC and NMC who intensively busied in providing of industrial production, educational and R&D activity.

REFERENCES

[1] SAGATOVA, A., KRSJAK, V., SOJAK, S., RIABUKHIN, O., KOVACOVA, E., ZATKO, B., Semi-insulating GaAs detectors degraded by 8 MeV electrons up to 1500 kGy, Journal of Instrumentation. Vol.16 (2021) C12032.

[2] SULIMOV, M.A., SARYCHEV, M.N., YAKUSHEV, M.V., MÁRQUEZ-PRIETO, J., IVANOV, V.YU., EDWARDS, P.R., MUDRYI, A.V., KRUSTOK, J., MARTIN, R.W., Effects of irradiation of ZnO/CdS/Cu2ZnSnSe4/Mo/glass solar cells by 10 MeV electrons on photoluminescence spectra, Materials Science in Semiconductor Processing. Vol. 121 (2021) 105301.

[3] ZHURAVLEVA, D.A., KAZAKOV, A.V., SELEZNEVA, I.S., BARANOVA, A.A., Relevance of application of irradiated starter cultures to production of fermented milk products, Chimica Techno Acta. 2020. Vol. 7, no. 4. P. 242-249.

A COMPACT ACCELERATOR DRIVEN NEUTRON SOURCE AT THE APPLIED NUCLEAR PHYSICS LABORATORY, LUND UNIVERSITY

R. J. W. FROST[*,1],
M. ELFMAN[1], K. FISSUM[1], P. KRISTIANSSON[1], N. MAURITZSON[1], J. PALLON[1],
G. PÉDEHONTAA-HIAA[1,2], H. PERREY[1], K. E. STENSTRÖM[1], A. SJÖLAND[1,3]

[1]Division of Nuclear Physics, Lund University, Lund, Sweden
[2]Medical Radiation Physics Malmö, Lund University, Malmö, Sweden
[3]Swedish Nuclear Fuel and Waste Management Company (SKB), Solna, Sweden
[*]Email: robert.frost@nuclear.lu.se

Abstract

The Applied Nuclear Physics Group at Lund University has constructed a CANS (Compact Accelerator-driven Neutron Source). The CANS is based around a 3 MV, single-ended, Pelletron accelerator, which is used to impinge a 2.8 MeV deuterium beam into a beryllium target. The anticipated neutron production will be on the order of 10^{10} n/s in 4π sr, with future upgrades expected to increase neutron production to 10^{11} n/s. Neutron energy will be up to 9 MeV with peak emission at ~5 MeV. Shielding and moderation will be provided by a large water tank surrounding the target, with exit ports to allow moderated neutrons to be directed to experiments. The thermal-neutron flux at the exit of the extraction ports is anticipated to be up to 10^{6} n/cm2/s. The CANS will be used to forward the activities of the group in the area of neutron-activation analysis, in addition to a broader range of neutron related applications.

1. INTRODUCTION

Since 2014, the Applied Nuclear Physics Group at Lund University has provided access to neutrons [1], with a well-established and user-focused infrastructure, emphasising expertise in nuclear physics and neutron-detection techniques. The use of these neutron has contributed to materials research [2] and detector development [3] related to the European Spallation Source [4]. The Applied Nuclear Physics group also has a long history of accelerator-based research; from the development of PIXE [5] in the 1970's to advanced modern detector systems [6–8] more recently. In 2017, it was decided to combine these areas of expertise and construct a dedicated beamline for neutron production [9]. The new CANS (Compact Accelerator-driven Neutron Source) offers a significant increase in flux over the neutron sources currently used at the laboratory, with an initial neutron-production rate anticipated to be on the order of 10^{10} n/s in 4pi sr and a further increase to 10^{11} n/s in 4pi sr predicted. The CANS is now entering the commissioning phase and, once fully realised, will be comparable to the Kyoto University Accelerator-driven Neutron Source [10]. A schematic overview of how the CANS fits into the pre-existing laboratory environment is presented in Fig. 1. The CANS will use a 3 MV, single-ended Pelletron accelerator to impinge a 2.8 MeV deuterium beam, with currents from 10 to 100 A, into a beryllium target. Resulting neutron energies will be up to 9 MeV with peak emission at ~5 MeV. Pulsing of the neutron source will be made possible by periodic deflection of the beam into a tantalum beam-dump. Shielding and moderation is provided by a large water tank surrounding the target.

2. INRASTRUCTURE AT THE NUCLEAR APPLICATIONS LABORATORY

The primary workhorse of the laboratory over the past 30 years, has been a single-ended NEC-3UH Pelletron accelerator, commission in 1990 [11]. This machine has been used primarily for ion-bean analysis, with the application of PIXE, RBS, STIM, NRA, ERCS to a wide variety of fields. Examples of the work conducted are: geology [12–15], medicine [16, 17], biology and ecology [18–21], meteorology [22], detector development [7, 23, 24], characterisation of nano-structures [25] and astro-geological materials [26, 27]. It is this Pelletron that has been re-purposed as the CANS system.

As well as a comprehensive inventory of alpha-particle, beta-particle and gamma-ray sources, the laboratory also possesses a number of radioactive neutron sources: ^{252}Cf, AmBe, PuBe: with a neutron-production rates on the order of 10^{6} n/s in 4pi sr. A dedicated irradiation area, incorporating 2.75 m^3 water filled shielding-tank, is installed to utilise these sources. The shielding tank, or "aquarium", has four ports to allow fast neutrons to escape. This set-up has been used extensively in work on -ray and neutron tagging [28–30], and neutron detector

development [31, 32]. In 2019, a GENI-16 neutron generator from SODERN [33] was installed to provide access to fast neutrons with a significant increase in neutron flux. The GENI-16, owned by SKB (Swedish Nuclear Fuel and Waste Management Company), has a neutron production rate of 10^8 n/s in 4pi sr. It has been used in work related to nuclear safeguards [34], and also in the prototyping of a cyclic-NAA (Neutron-Activation Analysis) system [35] which will ultimately be moved to the CANS.

The laboratory has and a triple -ray Ir spectrometer, which has been used in astro-geological research [36], [37], and can measure concentration of iridium in sample down to parts-per-trillion. In addition to the detector systems associated with the various experimental set-ups, a wide variety of infrastructure is available. This includes a range of scintillation materials and photomultipliers, HPGe detectors, ^{3}He tubes, a number of multi-channel full digitisers and a 200 channel VME data-acquisition system.

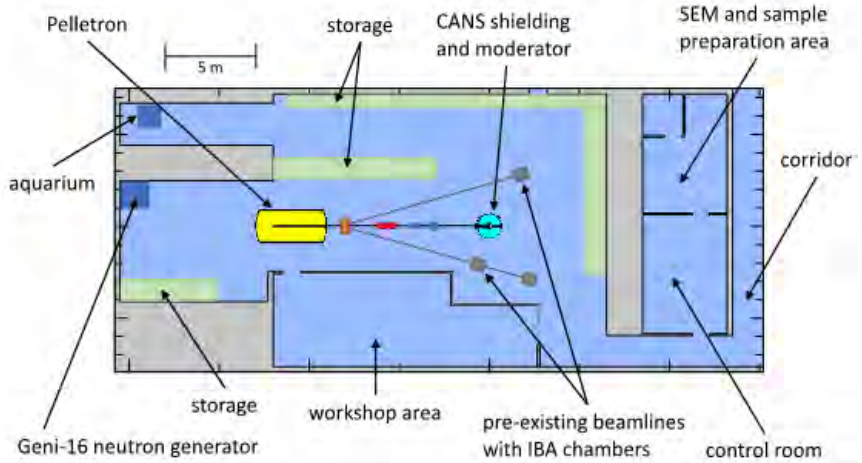

FIG. 1. Floor plan for the Nuclear Applications Laboratory, Lund University, with key features of the layout, and major infrastructure components, labelled. The new CANS, which must compete for space in already busy laboratory environment, is place between the pre-existing IBA beamlines.

2. MOTIVATIONS FOR A CANS

Broadly, the motivation for the development of a CANS at Lund University is to expand the existing efforts in neutron related research, but the immediate application will be in the field of NAA. The Nuclear Applications Laboratory has a history in NAA, that has previously relied on reactor-based irradiation of samples but a new, in-lab, cyclic-NAA system is now being developed. A prototype of the new NAA system is currently in operation [38], with the Genie-16 neutron generator used in place of the CANS which will drive the final configuration. High resolution gamma-ray spectroscopy and gamma-ray coincidence spectroscopy will be performed by an array of high-purity Ge detectors, positioned adjacent to the accelerator control room. Sample loading and unloading will be performed at the location of the measurement station to remove the necessity of having to enter the accelerator hall. The cyclic-NAA system will be used to monitor for the presence of specific radionuclides in environmental samples, taken from around the European Spallation Source [39, 40].

In addition to NAA, the CANS is intended to be used: in the develop novel state-of-the-art instruments and methods for the characterisation of spent nuclear fuel, with the purposes of nuclear safeguards; to test and categorise detectors for neutron scattering instrumentation; for work on thermal-neutron tagging; and as an educational platform. Further to these specific motivations, the commissioning of this CANS is part of a larger move towards a CANS network for Europe. At present, several CANS are either being designed or constructed with Europe, including HBS Jülich [41], ESS-Bilbao [42] and SONART [43]. For comparison, Japan boasts a wide a highly integrated network of neutron sources, with large spallation sources such as the Japan Spallation Neutron Source [44], reactor-based sources such as JRR-3 [45] and a backbone of CANS [46]. The move towards this network of CANS in Europe is becoming increasingly desirable as the available beam-time at conventional reactor facilities declines [47].

3. COMPACT ACCELERATOR DRIVEN NEUTRON SOURCE DEVELOPMENT

The CANS will generate neutrons by the Be(d,n) reaction [48], using a 3 MV, single-ended Pelletron accelerator to impinge a deuterium beam into a thick beryllium target. Deuteron-beam energy will be up to 2.8 MeV with a current of 10 micro-A, although and upgrade to the ion source of the accelerator is planned which is anticipated to raise the current to 100 micro-A. At the presently available beam current, the anticipated neutron production will be on the order of 10^{10} n/s in 4pi sr with peak neutron emission at an energy of ~5 MeV. The experimental hall in which the Pelletron accelerator is stationed, was formerly used for an electron synchrotron accelerator. The control room for the experimental hall is therefore already well shielded, with a 2 m thick wall. Due to the existing neutron related research activities that take place in the experimental hall, the majority of the other licensing requirement with regards to radiation protection are already fulfilled.

The 9 m long, high-vacuum line that will carry the deuteron beam to the target position is constructed at 0 degrees to the exit of the accelerator. A total of five dipole magnets, four inside the accelerator pressure vessel and one at 2 m from the accelerator exit are used to position the beam. A pair of quadrupole magnets are positioned at 5 m from the accelerator exit and are used to focus the beam to a diameter of 1 cm on the target. Following the quadrupole magnets, a fast electrostatic deflector is positioned to allow the beam to be periodically deflected into a Tantalum beam dump. In this way the neutron source can be run in pulse mode with an adjustable duty cycle, and pulse widths down to 25 ns. A number of viewing ports with optical cameras are positioned along the beamline, each with an electrically isolated florescent screen that can be moved into the path of the beam to measure its current and view its profile. A movable Faraday cup is also positioned at 1.5 m from the target. The target itself is a 2 mm thick piece of beryllium, mounted to an electrically isolated flange, externally cooled with deionised water. Current measurement is also made from the target flange.

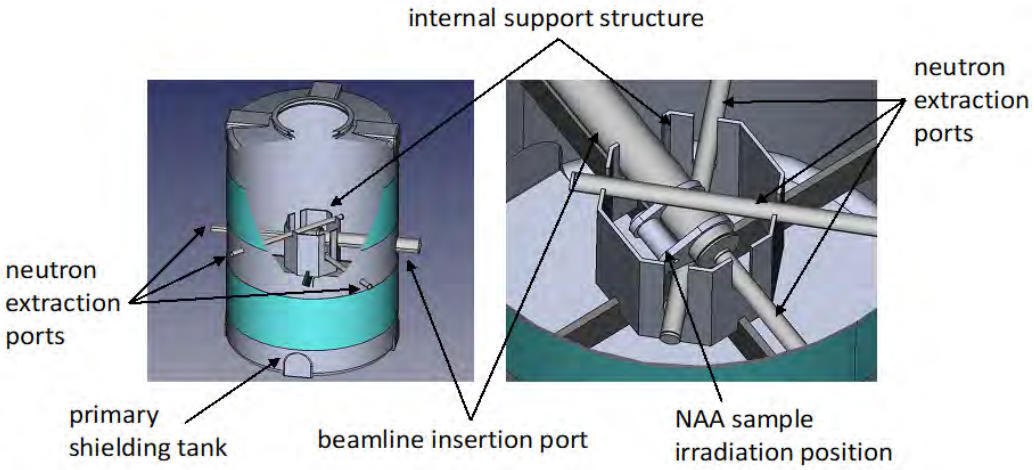

FIG. 2. Concept for the primary-shielding and moderator construction, based on a 3000 l tank of de-ionised water. The internal structure supports the ports for beamline insertion and neutron extraction, as well as providing a fixing point for sample irradiation for NAA

Shielding and moderation will be provided by a 3000 l water tank surrounding the target, with additional shielding provided by layer of layer of Mirrobor™ [49] and high-density polyethylene. Illustrations of this construction can be seen in Fig. 2, the design being developed in collaboration with Cipax AB [50]. A total of four ports penetrate the tank, one to facilitate the insertion of the beamline and three for the extraction of neutrons. The three neutron-extraction ports are presently planned to be aligned at 0 degrees 30 degrees and 150 degrees to the incoming deuteron beam. The lower angel ports will extract a higher proportion of fast neutrons, while the higher angel ports will extract a greater proportion of thermal neutrons. Fig. 3 shows simulation results, generated in PHITS [51–53], which illustrate the higher neutron flux and neutron energy produced from the target in the forward direction. Neutron flux at the NAA irradiation position is expected to on the order of 10^8 n/cm^2/s, this rising to 10^9 n/cm^2/s with the planned upgrade.

4. SUMMARY AND OUTLOOK

The Nuclear Applications Laboratory at Lund University already boasts a well-developed infrastructure, incorporating a variety of sources of ionising radiation, with a long history of applied nuclear physics research. A

CANS is soon to be added to the existing infrastructure, based on a deuterium beam and a beryllium target. The CANS is predicted to produce thermal neutron fluxes of around 10^4 n/cm^2/s, and fast neutron fluxes of around 10^6 n/cm^2/s, at the exit ports to the shielding assembly. The initial use of the CANS will be the implementation of a cyclic-NAA system, for which samples to be measured are expected to be irradiated with fluxes of around 10^8 n/cm^2/s. A future upgrade of the accelerators ion source is anticipated to increase all neutron fluxes by an order of magnitude over the aforementioned values. The new CANS is aimed at providing proof of principle for a dedicated CANS within Scandinavia, adding to the planned network of CANS for Europe.

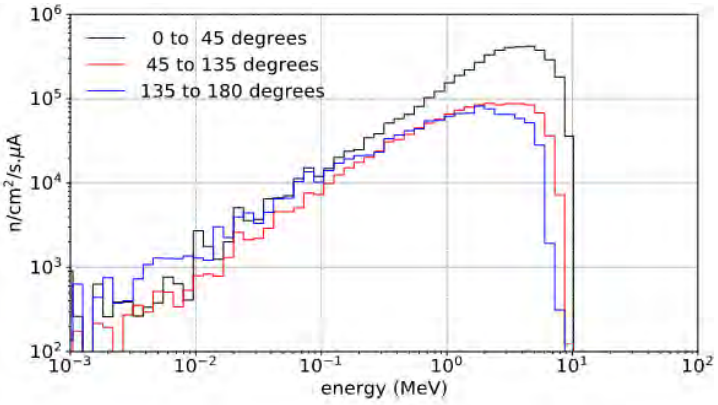

FIG. 3. Neutron energy spectra from the source without shielding and moderation in place, for a 2.8 MeV deuterium beam. The influence of the forward momentum of the beam can clearly be seen in the increased neutron flux and neutron energy in the forward direction.

ACKNOWLEDGEMENTS

The authors would like to acknowledge both The Swedish Radiation Safety Authority and The Walter Gyllenberg Foundation for funding provided towards the CANS project.

REFERENCES

[1] H. Perrey *et al.*, "From micro- to macro- neutron sources: The Lund Broad-band Neutron Facility," *EPJ Web Conf.*, vol. 231, p. 01005, 2020, doi: 10.1051/epjconf/202023101005.

[2] D. D. DiJulio *et al.*, "A polyethylene-b4c based concrete for enhanced neutron shielding at neutron research facilities," *Nucl. Instr. Meth. Phys. Res. A*, vol. 859, pp. 41–46, 2017, doi: 10.1016/j.nima.2017.03.064.

[3] F. Messi, G. Mauri, and F. Piscitelli, "The multi-blade: The 10B-based neutron detector for reflectometry at ess," *Nucl. Instr. Meth. Phys. Res. A*, vol. 936, pp. 499–500, 2019, doi: 10.1016/j.nima.2018.10.058.

[4] European Spallation Source ERIC, "Box 176, SE-221 00, Lund, Sweden." Available: https://europeanspallationsource.se.

[5] S. A. E. Johansson and T. B. Johansson, "Analytical application of particle induced X-ray emission," *Nuclear Instruments and Methods*, vol. 137, no. 3, pp. 473–516, 1976, doi: 10.1016/0029-554X(76)90470-5.

[6] J. Pallon, N. De La Rosa, M. Elfman, P. Kristiansson, E. J. C. Nilsson, and L. Ros, "A new quantitative X-ray system for micro-PIXE analysis," *X-Ray Spectrometry*, vol. 46, no. 5, pp. 319–324, 2017, doi: https://doi.org/10.1002/xrs.2779.

[7] E. Rofors *et al.*, "Response of a Li-glass/multi-anode photomultiplier detector to focused proton and deuteron beams," *Nucl. Instr. Meth. Phys. Res. A*, vol. 984, p. 164604, 2020, doi: 10.1016/j.nima.2020.164604

[8] R. J. W. Frost *et al.*, "One detector, all the light elements – Low-background NRA, RBS and ERDA for the quantification of elements from hydrogen to fluorine," *Nucl. Instr. Meth. Phys. Res. B*, vols. 494 – 495, pp. 34–45, 2021, doi: 10.1016/j.nimb.2021.02.009.

[9] M. Kristensson, "Characterisation of a neutron experimental station at the Lund Ion Beam Analysis Facility," Master's thesis, Lund University, 2018.

[10] S. Tasaki *et al.*, "Properties and possible applications of kyoto university accelerator based neutron source (kuans)," *Physics Procedia*, vol. 60, pp. 181–185, 2014, doi: 10.1016/j.phpro.2014.11.026.

[11] K. G. Malmqvist *et al.*, “Dedicated accelerator and microprobe line,” *Nucl. Instr. Meth. Phys. Res. B*, vol. 77, no. 1, pp. 3–7, 1993, doi: https://doi.org/10.1016/0168-583X(93)95514-6.

[12] [12] H.-C. Hansson, E. Swietlicki, N. P.-O. Larsson, and S. J. Johnsen, “PIXE analysis as a tool for dating of ice cores from the Greenland ice sheet,” *Nucl. Instr. Meth. Phys. Res. B*, vol. 75, no. 1, pp. 428–434, 1993, doi: 10.1016/0168-583X(93)95690-7.

[13] [13] F. Bosi *et al.*, “Late magmatic controls on the origin of schorlitic and foititic tourmalines from late-Variscan peraluminous granites of the Arbus pluton (SW Sardinia, Italy): Crystal-chemical study and petrological constraints,” *Lithos*, vols. 308-309, pp. 395–411, 2018, doi: 10.1016/j.lithos.2018.02.013.

[14] [14] E. J. C. Nilsson *et al.*, “A nuclear geochemical analysis system for boron quantification using a focused ion beam,” *J. Radioanal. Nucl. Chem.*, vol. 311, no. 1, pp. 355–364, Jan. 2017, doi: 10.1007/s10967-016-5030-z.

[15] [15] N. De La Rosa, P. Kristiansson, E. J. C. Nilsson, L. Ros, J. Pallon, and H. Skogby, “Quantification of lithium at ppm level in geological samples using nuclear reaction analysis,” *J. Radioanal. Nucl. Chem.*, vol. 317, no. 1, pp. 253–259, Jul. 2018, doi: 10.1007/s10967-018-5907-0.

[16] [16] J. Pallon, J. Knox, B. Forslind, Y. Werner-Linde, and P. Teresa, “Applications in medicine using the new lund microprobe,” *Nucl. Instr. Meth. Phys. Res. B*, vol. 77, no. 1, pp. 287–293, 1993, doi: 10.1016/0168-583X(93)95557-L.

[17] [17] K. A. Sjöland, P. Kristiansson, and P. Tallone, “Nuclear reaction analysis of boron for microbeam analysis of medical samples,” *Nucl. Instr. Meth. Phys. Res. B*, vol. 104, no. 1, pp. 255–260, 1995, doi: 10.1016/0168-583X(95)80094-8.

[18] [18] H. Wallander, S. Mahmood, D. Hagerberg, L. Johansson, and J. Pallon, “Elemental composition of ectomycorrhizal mycelia identified by pcr-rflp analysis and grown in contact with apatite or wood ash in forest soil,” *FEMS Microbiol. Ecol.*, vol. 44, no. 1, pp. 57–65, 2003, doi: 10.1016/S0168-6496(02)00456-7.

[19] [19] V. Barbin, K. Ramseyer, and M. Elfman, “Biological record of added manganese in seawater: a new efficient tool to mark in vivo growth lines in the oyster species Crassostrea gigas,” *Int. J. Earth Sci.*, vol. 97, no. 1, pp. 193–199, 2008, doi: 10.1007/s00531-006-0160-0.

[20] [20] C. Nilsson, K. Jönsson, and J. Pallon, “Tolerance to proton irradiation in the eutardigrade Richtersius coronifer–a nuclear microprobe study,” *Int. J. Radiat. Biol.*, vol. 86, no. 5, pp. 420–427, 2010, doi: 10.3109/09553000903568001.

[21] [21] L. K. E. and E. M., “Insights from two-dimensional mapping of otolith chemistry,” *J. Fish Biol.*, vol. 90, no. 2, pp. 480–491, 2017, doi: 10.1111/jfb.13048.

[22] E. Swietlicki, B. G. Martinsson, and P. Kristiansson, “The use of PIXE and complementary ion beam analytical techniques for studies of atmospheric aerosols,” *Nucl. Instr. Meth. Phys. Res. B*, vols. 109-110, pp. 385–394, 1996, doi: 10.1016/0168-583X(95)01218-4.

[23] N. S. Abdel, J. Pallon, M. Elfman, P. Kristiansson, E. J. C. Nilsson, and L. Ros, “Radiation tolerance of ultra-thin PIN silicon detectors evaluated with a MeV proton microbeam,” *Nucl. Instr. Meth. Phys. Res. B*, vols. 356-357, pp. 17–21, 2015, doi: 10.1016/j.nimb.2015.04.016.

[24] J. Pallon *et al.*, “Ion beam evaluation of silicon carbide membrane structures intended for particle detectors,” *Nucl. Instr. Meth. Phys. Res. B*, vol. 371, pp. 132–136, 2016, doi: 10.1016/j.nimb.2015.10.045.

[25] T. Winzell *et al.*, “Scanning probe microscopy characterisation of masked low energy implanted nanometer structures,” *Nucl. Instr. Meth. Phys. Res. B*, vol. 173, no. 4, pp. 447–454, 2001, doi: 10.1016/S0168-583X(00)00416-X.

[26] B. Schmitz *et al.*, “A fossil winonaite-like meteorite in Ordovician limestone: A piece of the impactor that broke up the L-chondrite parent body?” *Earth Planet. Sci. Lett.*, vol. 400, pp. 145–152, 2014, doi: 10.1016/j.epsl.2014.05.034.

[27] L. Ros *et al.*, “Deuterium/hydrogen microscopy in astrogeological material using an elastic recoil approach,” *Nucl. Instr. Meth. Phys. Res. B*, vol. 348, pp. 273–277, 2015, doi: 10.1016/j.nimb.2014.12.038.

[28] J. Scherzinger *et al.*, “A comparison of untagged gamma-ray and tagged-neutron yields from 241AmBe and 238PuBe sources,” *Applied Radiation and Isotopes*, vol. 127, pp. 98–102, 2017, doi: 10.1016/j.apradiso.2017.05.014.

[29] J. Scherzinger *et al.*, “Tagging fast neutrons from a 252Cf fission-fragment source,” *Applied Radiation and Isotopes*, vol. 128, pp. 270–274, 2017, doi: 10.1016/j.apradiso.2017.05.022.

[30] J. Scherzinger *et al.*, “Tagging fast neutrons from an 241Am/9Be source,” *Applied Radiation and Isotopes*, vol. 98, pp. 74–79, 2015, doi: 10.1016/j.apradiso.2015.01.003.

[31] J. Scherzinger *et al.*, "The light-yield response of a ne-213 liquid-scintillator detector measured using 2–6MeV tagged neutrons," *Nuclear Instruments and Methods in Physics Research Section A: Accelerators, Spectrometers, Detectors and Associated Equipment*, vol. 840, pp. 121–127, 2016, doi: 10.1016/j.nima.2016.10.011.

[32] N. Mauritzson *et al.*, "GEANT4-based calibration of an organic liquid scintillator," *Nucl. Instr. Meth. Phys. Res. A*, vol. 1023, p. 165962, 2022, doi: 10.1016/j.nima.2021.165962.

[33] P. A. Tulle, "Recent works with sealed tube neutron generators," IAEA, May 2000.

[34] H. Perrey, L. Ros, M. Elfman, U. Bäckström, P. Kristiansson, and A. Sjöland, "Evaluation of the in-situ performance of neutron detectors based on ej-426 scintillator screens for spent fuel characterization," *Nucl. Instr. Meth. Phys. Res. A*, vol. 1020, p. 165886, 2021, doi: 10.1016/j.nima.2021.165886.

[35] R. J. W. Frost *et al.*, "The prototyping of a high-resolution neutron activation analysis system – based on a Pelletron accelerator and fast pneumatic sample-transport," *Under review*, 2022.

[36] S. Boschi *et al.*, "Popigai impact ejecta layer and extraterrestrial spinels recovered in a new Italian location - The Monte Vaccaro section (Marche Apennines, Italy)," in *250 Million Years of Earth History in Central Italy: Celebrating 25 Years of the Geological Observatory of Coldigioco*, Geological Society of America, 2019. doi: 10.1130/2019.2542(19).

[37] S. Goderis *et al.*, "Globally distributed iridium layer preserved within the chicxulub impact structure," *Science Advances*, vol. 7, no. 9, 2021, doi: 10.1126/sciadv.abe3647.

[38] J. Lindsey-Clark, "Development of a neutron Activation analysis station at the Lund Ion Beam Analysis Facility." Lund University, 2021.

[39] K. E. Stenström *et al.*, "Identifying radiologically important ESS-specific radionuclides and relevant detection methods," SSM, 2020.

[40] G. Pedehontaa-Hiaa, C. Bernhardsson, V. Barkauskas, K. E. Stenström, C. Rääf, and S. Mattsson, "Region-specific radioecological evaluation of accidental releases of radionuclides from ESS," SSM, 2021.

[41] T. Gutberlet *et al.*, "The jülich high brilliance neutron source project – improving access to neutrons," *Physica B: Condensed Matter*, vol. 570, pp. 345–348, 2019, doi: 10.1016/j.physb.2018.01.019.

[42] F. Sordo *et al.*, "Baseline design of a low energy neutron source at ess-bilbao," *Physics Procedia*, vol. 60, pp. 125–137, 2014, doi: 10.1016/j.phpro.2014.11.019.

[43] Ott, Frédéric, Menelle, Alain, and Alba-Simionesco, Christiane, "The sonate project, a french cans for materials sciences research," *EPJ Web Conf.*, vol. 231, p. 01004, 2020, doi: 10.1051/epjconf/202023101004.

[44] M. Arai and F. Maekawa, "Japan spallation neutron source (jsns) of j-parc," *Nuclear Physics News*, vol. 19, no. 4, pp. 34–39, 2009, doi: 10.1080/10506890903405316.

[45] Y. Morii, "Status of the new jrr-3 at jaeri," *Neutron News*, vol. 1, no. 2, pp. 14–19, 1990, doi: 10.1080/10448639008020285.

[46] Y. Kiyanagi, "JCANS network of compact neutron facilities in japan," *The European Physical Journal Plus*, vol. 131, no. 5, p. 132, May 2016, doi: 10.1140/epjp/i2016-16132-5.

[47] ESFRI Physical Sciences and Engineering Strategy Working Group - Neutron Landscape Group, "Neutron scattering facilities in Europe - Present status and future perspectives," ESFRI, 2016.

[48] Y. Zuo *et al.*, "Neutron yields of thick be target bombarded with low energy deuterons," *Physics Procedia*, vol. 60, pp. 220–227, 2014, doi: 10.1016/j.phpro.2014.11.031.

[49] Mirrotron, "Konkoly-Thege Miklós út 29-33; H-1121 Budapest, Hungary." Available: https://mirrotron.com

[50] M. Brinkheden and C. Emander, "Cipax ab, stinsvägen 11, se-763 93 skebobruk, sweden. Https://cipax.com/." Jun. 2022.

[51] T. Sato *et al.*, "Features of particle and heavy ion transport code system (phits) version 3.02," *Journal of Nuclear Science and Technology*, vol. 55, no. 6, pp. 684–690, 2018, doi: 10.1080/00223131.2017.1419890.

[52] A. Boudard, J. Cugnon, J.-C. David, S. Leray, and D. Mancusi, "New potentialities of the liège intranuclear cascade model for reactions induced by nucleons and light charged particles," *Phys. Rev. C*, vol. 87, no. 1, p. 014606, Jan. 2013, doi: 10.1103/PhysRevC.87.014606.

[53] K. Iida, A. Kohama, and K. Oyamatsu, "Formula for proton–nucleus reaction cross section at intermediate energies and its application," *Journal of the Physical Society of Japan*, vol. 76, no. 4, p. 044201, 2007, doi: 10.1143/JPSJ.76.044201.

SOCIOECONOMIC IMPACT OF A MEDICAL CYCLOTRON IN KERALA, INDIA

Dilshad KOTTUPARAMBAN
Molecular Cyclotrons Pvt. Ltd.
Kochi, India
Email: dilshadkottuparamban@gmail.com

Anees MUHAMMED
Molecular Cyclotrons Pvt. Ltd.
Kochi, India

Raviteja NANABALA
Molecular Cyclotrons Pvt. Ltd.
Kochi, India

Maroor RAGHAVAN AMBIKALMAJAN PILLAI
Molecular Cyclotrons Pvt. Ltd.
Kochi, India

K. N. SUDHAKARAN NAIR
Molecular Cyclotrons Pvt. Ltd.
Kochi, India

Ajith JOY
Molecular Cyclotrons Pvt. Ltd.
Kochi, India

Abstract

Implementation of high-end technology in the positron emission tomography (PET) made it as a superior diagnostic tool in clinical practice. Even the major application of PET is in oncology, its wide applications spread over to other clinical specialities including cardiology, neurology, endocrinology, epidemiology etc. According to the IAEA Medical Imaging and Nuclear Medicine (iMAGiNE) global resources database, inequities in access to diagnostic nuclear medicine, especially PET, in India is in alarming stage. The number of PET scanners available per million people is less than one in India and more than three in higher income countries. In this scenario, the paper analyses inequities in access to the PET scanners for one of the states in India, that is Kerala with regards to the installation of a PET cyclotron in the state.

INTRODUCTION

Nuclear medicine is one of the branches of modern medicine which uses radiopharmaceuticals for medical imaging as well as therapy. The major application of nuclear medicine is detection of cancer and its proliferation. In addition, it is possible to identify or monitor several disease states related to the heart, brain, excretory organs, and endocrine glands.

Several radionuclides are using in nuclear medicine to prepare radiopharmaceuticals. If the radionuclides are single photon emitting type, such radionuclides can be image by Single Photon Emission Computed Tomography (SPECT) scanner. Similarly, positron emitting radionuclides can be image by positron emitting tomography (PET) scanner. With its advances in technology and availability of various new PET radiopharmaceuticals, PET scanner became the key factor in nuclear medicine imaging. All these PET radiopharmaceuticals are produced and supplied by the medical cyclotron centres.

METHODOLOGY

As per the data from International Atomic Energy Agency (IAEA) Accelerator Knowledge Portal, more than 1200 medical cyclotron centres are operational in worldwide [1]. More than 5600 PET scanning centres are depending on these cyclotron centres for the radiopharmaceuticals [2]. However, according to the IAEA

iMAGiNE data, only 50% of the countries have PET scanners (Fig. 1). The number of PET scanners per million population of the higher-income countries is more than three, upper-middle-income countries is between two and three, lower-middle-income countries is between one and two, and lower-income countries is less than one. The world average is just 0.739. The figure of India is also less than one.

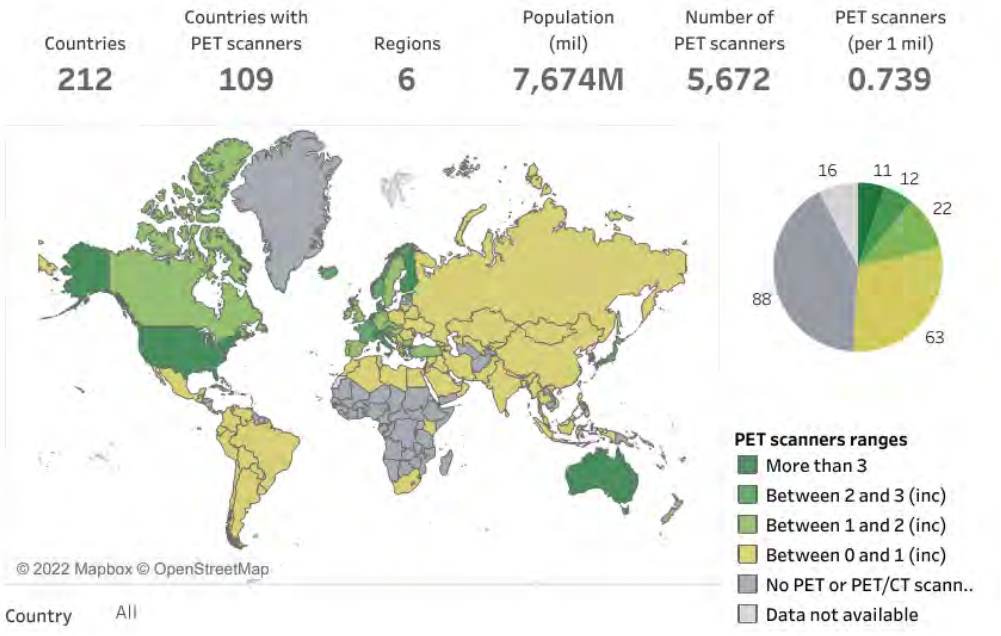

FIG. 1. PET scanners per million population of different countries (Data from IAEA iMAGiNE)

In India, there are 21 cyclotrons, and 333 PET scanners are functional now. The states which have the cyclotron centres are coloured green in the Fig. 2. Since the projected population of India is 1.4 billion [3], the number of PET scanners per million population is 0.24 or in other words, 4.2 million are served by 1 PET scanner.

FIG. 2. States in India where cyclotron centres are available coloured in green

Kerala is one of the southern states of India. The land area of the state is 38863 square kilometres, and which is comparable to that of Netherlands and Switzerland. At present, more than 35 million people are living in this state [3] which is about twice the population of Netherlands and four times that of Switzerland. According to the latest report published by the National Institute for Transforming India (NITI AAYOG), Government of India, the Kerala state performed first rank in the state-wise analysis of health index [4]. Most of the people in the state are highly educated and the healthcare system is well-diversified. The increased health awareness is appreciable. The recent approach of Kerala towards the Covid-19 pandemic that impressive recovery rate of more than 50% was noted and appreciated by the World Health Organization (WHO) [5].

Before 10 years in Kerala, there was only one PET scanner which was installed in 2008. Since there was no cyclotron facility in the state at that time, the PET centre functioned using radiopharmaceuticals procured from the neighbouring state through flights. The cost of radiopharmaceuticals and PET scan were high during that time and patients had to wait for couple of days for getting appointments for a PET scan. In this scenario, we, the Molecular Group started the first cyclotron project in the state in 2013 and successfully commissioned in 2016 at Kochi, Kerala – Molecular Cyclotrons Pvt. Ltd. The cyclotron centre built as part of a multispeciality hospital.

Our medical cyclotron centre is equipped with a Siemens Eclipse HP (Self-Shielded) cyclotron with 11 MeV dual proton beam of maximum current 120 microamperes. The radiopharmaceutical production lab of the company is certified for Good Manufacturing Practices (GMP) with lab design of European standards and sterile environment. According to the GMP guidelines, the company assures optimum quality of radiopharmaceuticals produced. Company's quality control lab is equipped with several sophisticated measures including thin layer chromatography, gas chromatography, bacterial endotoxin test, sterility test etc.

FIG. 3. Photographs of the medical cyclotron centre, Molecular Cyclotrons Pvt. Ltd.

We are producing various F-18 radiopharmaceuticals for PET scanning in addition to fluorodeoxyglucose (FDG). Those radiopharmaceuticals have unique applications diagnostic nuclear medicine. Fluoro-L-DOPA for neurology, FPSMA for prostate cancer, FCholine for prostate cancer as well as parathyroid adenoma, sodium fluoride for bone metastasis FMISO for hypoxia, FET and FLT for brain tumours.

RESULTS

Up to 2013, only one PET scanner was available in the state of Kerala. However, when we planned to install the first medical cyclotron in the state in 2013, five new PET centres installed near to our cyclotron centre within three years. When we commissioned and started our cyclotron in 2016, there were six PET centres in Kerala and gradually it increased to 16 at present.

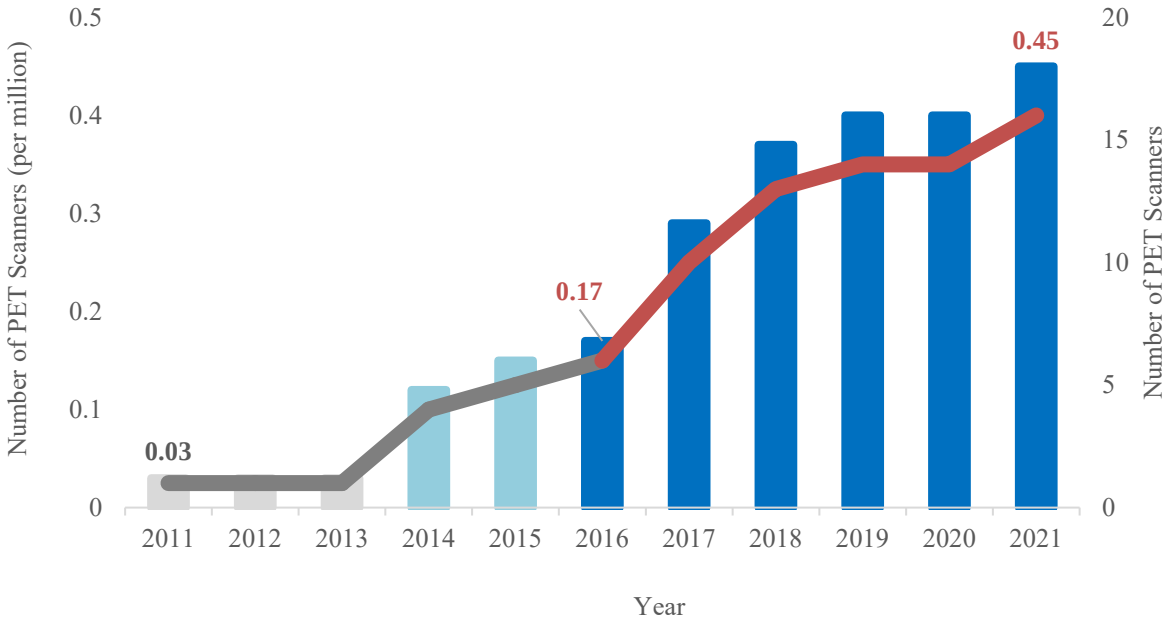

FIG. 4. Graph showing the growth of number of PET scanners in the state of Kerala from 2011 to 2021

DISCUSSION

As dedicated healthcare professionals, we could make some significant socioeconomic impact to the state of Kerala and thereby to our country. Because of the proximity of cyclotron, 15 new PET centres became available to the people of the state. The number of PET scanners per million population of Kerala was increased from 0.03 to 0.45, which is far above than the national average. It is clear evidence of reduction of inequities in access to diagnostic nuclear medicine. Around 50,000 patients per year using our radiopharmaceuticals for their PET scan.

New PET centres are evenly distributed throughout the state such that patients can reach those centres within few hours (Fig. 5). Various radiopharmaceuticals including FDG became more reliable and cost effective to the PET centres. It reduced the cost of PET scans to less than half and now it became affordable to the patients who have low income. Since 20 PET scan centres are depending on our cyclotron facility, we are supporting around 150 nuclear medicine professionals in the state and neighbouring state.

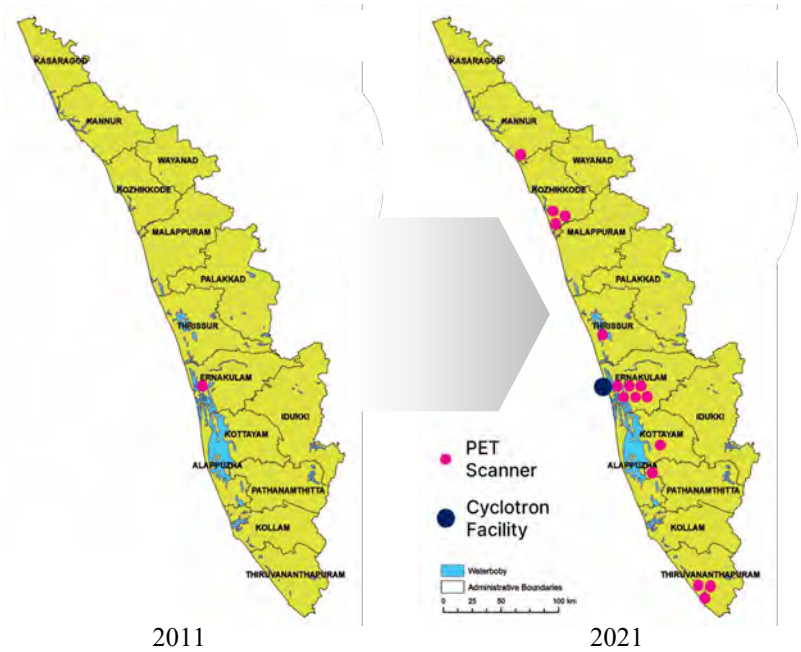

FIG. 5. Distribution of PET scanning centres in Kerala in 2011 and 2021.

CONCLUSION

In the latest World Cancer Report of WHO, it is stated that the number of cancer cases in Kerala is reducing [6]. Such reduction in cancer patients only happened because of proper diagnosis and treatment with the advanced modalities. Estimated population of Kerala in 2027 is more than 36 million [3]. So, this state requires at least 36 PET scanners to reduce inequities in access to diagnostic nuclear medicine. With our present low energy cyclotron, we can support up to 20 PET centres and one more cyclotron with higher energy and current is required for the upcoming PET centres in the state. Hence, we are planning to install our second cyclotron in another location in the state before 2023.

ACKNOWLEDGEMENTS

The authors thank all the directors of Molecular Cyclotrons Pvt. Ltd. for the support and providing the facilities. Sincere thanks to our team members Junais, Arun, Shinooj, and Vishnunath for their technical support.

REFERENCES

[1] IAEA Accelerator Knowledge Portal, Cyclotrons used for Radionuclide Production, www.nucleus.iaea.org/sites/accelerators/Pages/Cyclotron.aspx
[2] IAEA Medical Imaging and Nuclear Medicine Global Resources Database (IMAGINE), www.humanhealth.iaea.org/HHW/DBStatistics/IMAGINEMaps4.html
[3] Population Projections for India and States 2011 – 2036, National Commission on Population, Ministry of Health and Family Welfare, New Delhi (2019).
[4] Annual Report 2021-22, NITI Aayog, Government of India.
[5] Responding to COVID-19 – Learnings from Kerala, World Health Organization (02 July 2020), www.who.int/india/news/feature-stories/detail/responding-to-covid-19---learnings-from-kerala
[6] CHRISTOPHER P. WILD et al., World Cancer Report – Cancer Research for Cancer Prevention (2020)

SUSTAINABILITY STUDIES FOR LINEAR COLLIDERS

S. STAPNES
CERN
Geneva, Switzerland
Email: steinar.stapnes@cern.ch

B. LIST
Deutsches Elektronen-Synchrotron DESY
Germany

S. MICHIZONO
KEK
Tsukuba, Japan

Abstract

Sustainability has become a prioritized goal in planning and implementation of future large accelerators. ILC and CLIC, two linear collider projects proposed as a future Higgs factory and collaborating in many areas, have extensively studied novel design and technology solutions to address power efficiency and reduce the environmental impact of the facilities. The sustainability considerations, in addition to the more traditional cost concern and need for developing core technologies, are today primary R&D drivers for the projects. Approaches to improved sustainability range from overall system design, optimization of subsystems and key components, to operational concepts.

1. INTRODUCTION

Ten years after its discovery by the ATLAS and CMS collaborations at the LHC collider at CERN, the Higgs boson that gives mass to the all the elementary particles remains the most mysterious particle in the Standard Model of high energy physics. A dedicated "Higgs factory" accelerator producing Higgs bosons in electron positron collisions is therefore considered the highest priority project for a new energy frontier accelerator [1]. Such a Higgs factory produces Higgs and Z^0 bosons in conjunction in the process $e^+e^- \rightarrow h\,Z^0$, which requires a centre-of-mass energy of 250GeV. The physics programme of such a facility would be completed by studying the properties of the Top quark, requiring 350 to 380GeV, and measuring the coupling of the Higgs boson to the Top quark (in the reaction $e^+e^- \rightarrow h\,t\bar{t}$) and to itself (in $e^+e^- \rightarrow hh\,Z^0$), at 500GeV or more of energy.

Accelerators for high energy physics have been built and operated for over six decades and have always been pushing the limits of what was feasible technologically (and financially). Thus, conserving the resources necessary for the construction and operation has always been a driver in the accelerator design. Today, resource conservation is considered not only a financial necessity but a societal obligation, and sustainability is an important goal in the development of new accelerators [1].

Two large electron-positron linear colliders are currently being studied as potential future Higgs-factories, the International Linear Collider (ILC) in Japan [2-5], and the Compact Linear Collider (CLIC) at CERN, Switzerland [6-9].

In this study we present activities in the design and R&D efforts of both accelerator projects that contribute to the goal of sustainable construction and operation of these facilities. These activities entail the optimisation of

- the overall system design with the goal of resource conservation in construction and operation,
- the design of subsystems and components,
- the concept for operation and interaction with the surrounding site and society.

These aspects are discussed in turn in the following.

2. OPTIMISATION OF THE OVERALL SYSTEM DESIGN

The two most important key performance indicators of electron positron colliders for high energy physics are the centre-of-mass energy, which determines which production channels are kinematically accessible, and the

luminosity, which determines the number of reactions taking place and thus the sensitivity to rare events and the statistical accuracy of the experimental results.

For a symmetric collider the centre-of-mass energy is twice the beam energy. In a circular electron/positron storage ring, the beam energy is ultimately limited by the synchrotron radiation power that needs to be constantly replenished to keep the beam circulating, which grows proportional to E_{beam}^4/R, with R being the effective bending radius of the machine. Balancing the growth of construction costs (proportional to the ring size, given by R) and operation costs (proportional to the power consumption) leads to a quadratic increase of both, radius and power, with beam energy for circular colliders. For the Main Linac of a linear collider, on the other hand, power consumption and overall length rise linearly with beam energy, so that eventually linear accelerators become the most economical solution.

For linear colliders, the Main Linacs are the dominant systems in terms cost and power consumption, and therefore the target of intense R&D to optimise their performance.

A reduction of construction costs requires high acceleration gradients g to achieve the desired beam energy. The power losses in the cavity walls per unit length, however, grow quadratically with gradient, leading to a linear increase of power losses with gradient g for fixed beam energy $E_{beam} = g\ L$. To counter this effect, ILC and CLIC have vastly different approaches: ILC utilises superconducting cavities to reduce the primary energy loss in the cavity walls to almost zero, at the prize of a limited gradient and a large cryogenic infrastructure; CLIC operates at room temperature with high rf frequency and extremely short pulses, made possible by a unique two-beam acceleration technology. After an optimisation of costs and power consumption, both concepts arrive at almost identical values for the overall power consumption (110-111 MW) for their respective baseline designs, as shown in Fig. 1.

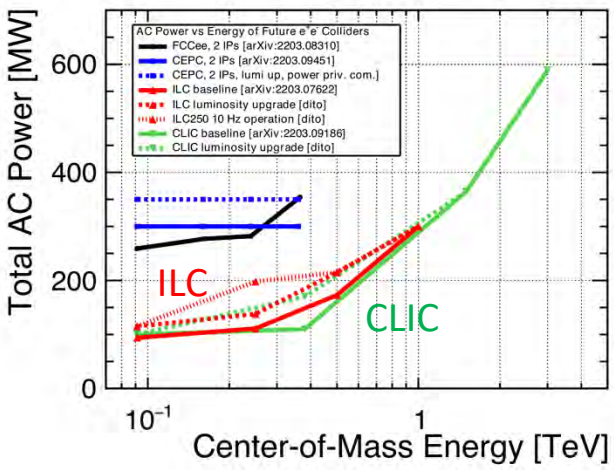

FIG. 1: Total site power versus centre-of-mass energy for linear (ILC, CLIC) and circular (CEPC, FCCee) e+e- colliders under investigation [5].

In order to maximise the delivered luminosity for a given beam power, both concepts utilize and collaborate on the nanobeam technology, where damping rings provide extremely low emittance beams and a highly optimised final focus system squeezes the beams down to nanometre beam sizes.

In the following, the two concepts, whose key parameters are listed in Tab. 1, are presented in turn.

TABLE 1. KEY PARAMETERS OF ILC [5] AND CLIC [9]

Quantity	Unit	ILC	CLIC
Centre-of-mass energy (baseline - max)	GeV	250 - 1000	380 - 3000
Luminosity (at baseline energy)	10^{34}cm^{-2}s^{-1}	1.35	2.3
Length	km	21	11.4
Accelerating gradient	MV/m	31.5	72
Particles per bunch	10^9	20	5.2
Bunches per train	1	1312	352
Pulse length	μs	727	0.244
Pulse repetition rate	Hz	5	50
Beamspot size	nm^2	516×7.7	149×2.0
Average beam power at initial energies	MW	5.3	5.6
Site power (baseline configuration)	MW	111	110

2.1. The International Linear Collider (ILC)

The ILC [2, 3] is a proposed superconducting linear $^{+}e^{-}$ collider, operating as a Higgs factory [4] with a centre-of-mass energy of 250GeV and a luminosity of $1.35{\cdot}10^{34}cm^{-2}s^{-1}$ in the baseline configuration. It is upgradeable in energy up to 1TeV and in luminosity (at 250GeV) by a factor of four in several stages [5]. The overall site length is 20.5km, dominated by the two Main Linacs that comprise (depending on the final gradient) 859 to 939 cryomodules, each housing 8 or 9 superconducting niobium cavities running at 1.3GHz and 2K operating temperature. Rf power is provided by 202 to 220 10MW pulsed klystrons with Marx modulators.

Electrons with 80% polarisation are produced by a laser gun with a strained GaAs/GaAsP photocathode, positrons with 30% polarisation in a rotating conversion target illuminated by a polarised photons from a helical undulator driven by the electron Main Linac beam. A central damping ring complex at 5GeV beam energy provides low (4μm/20nm normalized horizontal/vertical) emittance beams, which are transported to the starting points of the Bunch Compressor / Main Linac section. The final focus provides a $516{\times}7.7nm^2$ beamspot for the experiments, at a total beam power of 5.3MW.

In the baseline configuration, the total electric power consumption is 111MW.

For a linear collider, the luminosity $\mathcal{L}$ can be expressed as

$$\mathcal{L} = \eta \frac{P_{AC}}{E_{\mathrm{CM}}} \cdot \frac{N_e}{4\pi\, \sigma_{\mathrm{x}}^{*}\, \sigma_{\mathrm{y}}^{*}}\, H_{\mathrm{D}}$$

in terms of the Main Linac wall plug power P_{AC}, the Main Linac efficiency η for the transfer of wall plug to beam power, the centre-of-mass energy E_{CM}, the single bunch charge N_e, the beam size $\sigma_{\mathrm{x}}^{*} \times \sigma_{\mathrm{y}}^{*}$ and the enhancement factor H_{D}. The basic choice of the superconducting TESLA technology [10] is based on the goal of maximising the efficiency η. The quality factor Q_0, which is highly dependent on the surface properties (see below), is also affected by fundamental system decisions on rf frequency (1.3GHz) and operating temperature (2K). Operational parameters such as operating gradient, bunch charge and spacing, and pulse length all have been considered in finding a suitable working point within the technological limits.

The trade-offs that need to be considered are between losses in the cavity walls, electrical power for liquid helium cooling, field energy lost after each pulse, size of damping rings. Technological limits for rf pulse lengths, damping ring currents, achievable gradient, cryogenic plant size in terms cooling power and helium mass flow pose various limits on the parameter space.

For example, there is a balance between investment costs for cavities and cryomodules, which are reduced at higher accelerating gradients, and cost for cryogenic plants, which grow with gradient. For the high quality factors of 10^{10} or better targeted at the ILC, the optimum is beyond the gradients that are achievable today [11]

2.2. The Compact Linear Collider (CLIC)

The Compact Linear Collider (CLIC) is a multi-TeV high-luminosity linear $e^{+}e^{-}$ collider under development by the CLIC accelerator collaboration. The CLIC accelerator has been optimised for three energy stages at centre-of-mass energies 380 GeV, 1.5 TeV and 3 TeV [9]. CLIC uses a novel two-beam acceleration technique, with normal-conducting accelerating structures operating in the range of 70-100 MV/m. To reach multi-TeV collision energies in an acceptable site length and at affordable cost, the main linacs use normal conducting X-band accelerating structures; these achieve a high accelerating gradient of 100MV/m. For the first energy stage, a lower gradient of 72MV/m is the optimum to achieve the luminosity goal, which requires a larger beam current than at higher energies. In order to provide the necessary high peak power, the novel drive-beam scheme uses low-frequency high efficiency klystrons to efficiently generate long RF pulses and to store their energy in a long, high-current drive-beam pulse. This beam pulse is used to generate many short, even higher intensity pulses that are distributed alongside the main linac, where they release the stored energy in power extraction and transfer structures in the form of short RF power pulses, transferred via waveguides into the accelerating structures. This concept strongly reduces the cost and power consumption compared with powering the structures directly by klystrons, especially for stages 2 and 3, and is very scalable to higher energies.

The upgrade to higher energies will require lengthening the main linacs. For the RF power the upgrade to 1.5 TeV can be done by increasing the energy and pulse length of the primary drive-beam, while a second drive-beam complex must be added for the upgrade to 3 TeV. An alternative design for the 380 GeV stage has been studied, in which the main linac accelerating structures are directly powered by high efficiency klystrons. The further stages will also in this case be drive-beam based for the reasons mentioned above.

Power and energy efficiency studies have been integrated into the design from the very beginning. The design and parameter choices have been made to supply a certain luminosity at the minimum cost and power. These studies have covered accelerator structures and cavities, but also very importantly high efficiency RF power system with optimal system designs using high efficiency klystrons and modulators. These are also being prototyped.

It is expected that the CLIC - and ILC - power consumptive can be further consolidated and possibly reduced. In particular for stages 2 and 3 of CLIC many technical developments affecting the power have not been included in the current power estimates.

Sustainability studies in general, e.g. power/energy efficiency, using power predominantly in low cost periods as is possible for a linear collider, use of renewable energy sources, and energy/heat recovery where possible, will therefore be a priority for further studies for both LC projects. Such studies were already made with initial parameters for the CLIC Implementation Plan (see chapter 7 in [8]). Other studies include prototyping and use of permanent magnets as described below.

3. SUBSYSTEM AND COMPONENT DESIGN

The overall resource needs of a complete accelerator facility is given by the sum of the resources needed to produce, operate and finally dispose of all its subsystems and components. Optimisation of all these constituents with regard to sustainability is therefore a necessity, starting with those components that dominate resource consumption. Traditionally, this optimisation is performed regarding monetary costs, in particular capital costs for production of components, and operating costs, with an emphasis on electricity costs.

A direct quantification of the ecological footprint, be it greenhouse gas emissions during operation or production, or consumption of problematic materials, is currently performed only sporadically, mostly through translation of electricity consumption into equivalent CO2 emissions. Nonetheless, intense R&D programs are under way with ambitious goals to reduce resource consumption, as illustrated by a few topical examples in the following.

3.1. Superconducting cavities for the ILC

The single biggest consumer of resources in the ILC are the Main Linacs, and within the Main Linac the construction and operation of the superconducting rf cavities. The performance of these cavities has been pushed ever further over the last decades, as illustrated in Fig. 2 [12]. The ILC baseline design assumes an operating gradient of 31.5MV/m, averaged over all installed Main Linac cavities. The immediate R&D goal is to raise this number by 10% to 35MV/m, and to 45MV/m for a potential 1TeV upgrade.

In parallel to the increase in maximum gradient, recent years have seen a lot of progress in improvements of the quality factor Q_0 that describe the losses in the cavity walls through new, improved surface (nitrogen doping and infusion) treatments. The R&D goal is to double the quality factor from 1 to $2 \cdot 10^{10}$. New heat treatments [13] indicate that it may be possible to achieve progress on all fronts: achieve higher gradients at higher quality factors with less use of problematic chemicals due to a reduction of electropolishing processes during production.

In addition, studies are underway and planned to replace bulk niobium with niobium or even Nb3Sn coated copper cavities [14], reducing use of scarce materials and (in the case of Nb3Sn) the prospect to raise the operating temperature from 2K to 4.5K, which would significantly reduce the cooling power needs.

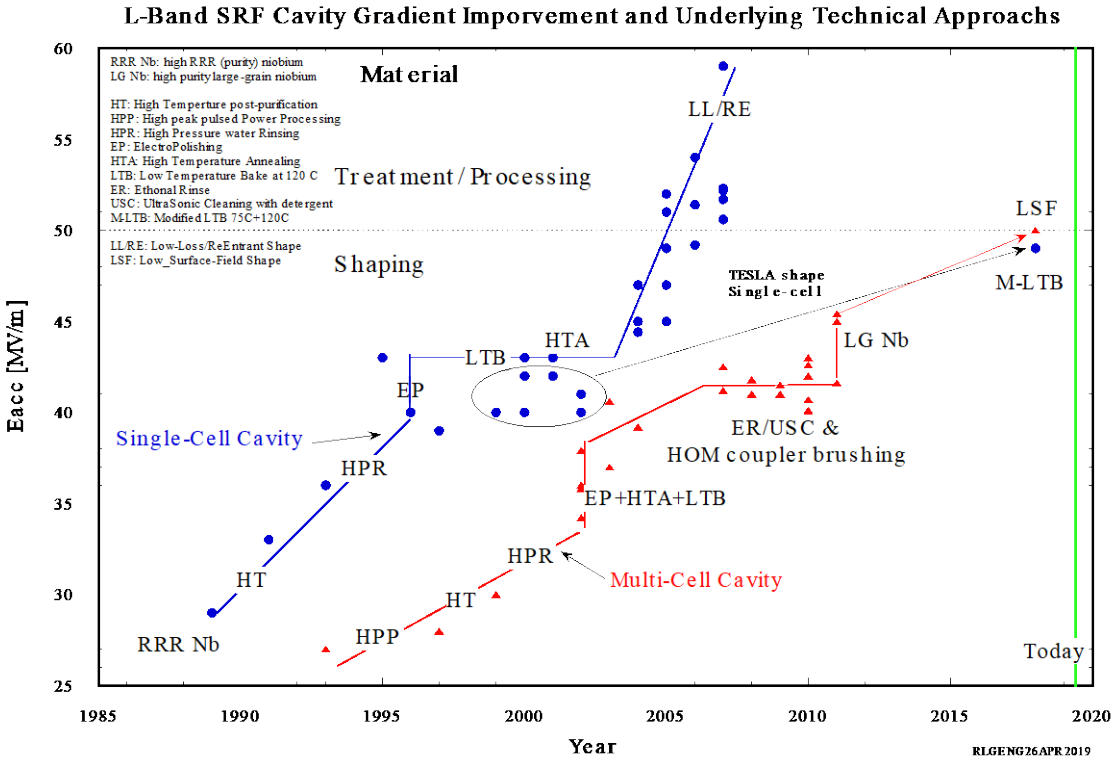

FIG. 2: Evolution of the accelerating gradient of superconducting cavities [24]

3.2. High-efficiency klystrons

The dominant contribution to the linear collider power consumption comes from the acceleration of the beams. The wall-plug to beam power efficiency is of paramount importance. The RF pulses are provided by modulator and klystrons systems. R&D on klystron efficiency have made very significant progress over the last decade, achieving efficiencies significantly above what was considered possible, and even limits, a decade ago. New klystron bunching technologies have been established and evaluated, and much improved computer codes and scaling procedures have been developed and bench marked [15]. A number of high efficiency klystrons has been designed according to these new ideas and/or making use of the new tools. For the linear colliders, efficiencies reaching 80% for the klystrons used for the CLIC drive-beam and ILC main beams are now being considered to be within reach.

3.3. Permanent magnets

Even at 1.5TeV centre-of-mass energy, resistive magnets constitute the second-largest consumer of electric power (after the rf equipment) at CLIC; in particular the drive-beam quadrupoles consume a lot of power. To alleviate this, the Zero-Power Tuneable Optics (ZEPTO) collaboration between CERN and STFC Daresbury Lab has been set up with the goal to provide permanent magnet dipoles and tuneable quadrupoles of the necessary field quality. Several prototype magnets (2 quadrupoles and a dipole) have been manufactured and tested for CLIC, and recently a ZEPTO dipole has been successfully installed in the Diamond Light Source [16].

For the ILC, permanent magnet designs for dipoles and corrector magnets are under consideration in particular for the damping rings [17]. To compensate variations in the magnetic field from temperature changes or ageing, the dipoles have a motor controlled trim rotor. To reduce cost and increase sustainability, the dipoles can be manufactured from ferrite material rather than rare earth based permanent magnets. Solutions for quadrupoles are also under investigation [18].

4. SITE DEVELOPMENT AND OPERATION

4.1. Green ILC program in Tohoku

For the ILC, a comprehensive initiative called the “Green ILC program” has been started in the Tohoku region of Japan where the preferred ILC site is located [19]. This program brings together academia, local government, and the industry in the Tohoku ILC Development Center.

A based on a site power of 120MW, the yearly overall electricity consumption is estimated to be around 700GWh, which corresponds to 320kt CO_2 emissions based on an average CO_2 emission rate of 0.457kg CO_2/kWh as reported by the Tohoku electric power company [20, 21]. The Green ILC program aims to maximise the re-use of heat generated by the accelerator cooling infrastructure, and to directly offset the CO2 emissions by collaboration with the local forestry industry. Extensive use of solar power and heat is also part of the plans.

Furthermore, the Green ILC initiative strives to develop modern forms of living environments for the scientists and workers that will come to Tohoku, with wood as the preferred, sustainable building material.

4.2. Operation of CLIC with electric power from regenerative sources

Given the flexibility on running and power consumption of a linear collider, it is interesting to consider how effectively the accelerator can be powered by renewable energies. First of all, it is likely the overall energy landscape in Europe will shift over the next decades towards renewables, secondly the investment costs of such power sources are decreasing so one can consider moving investments in energy production into the construction costs, hence lowering the operation costs. By installing a portfolio of different renewable generators (different technologies, like wind and photovoltaic (PV), or different types of installations, like photovoltaic modules orientated into different directions) it becomes possible to partly level out the individual fluctuations of single generators in the aggregated generation curve. Such a study was performed for CLIC in 2018 [22], with at that time a pessimistic power consumption of 200 MW, assuming that 1.2×10^7s of operation would be needed annually.

The conclusions were that while it is possible to fully supply the annual electricity demand of the CLIC by installing local wind and PV generators (this could be e.g. achieved by 330 MW-peak PV and 220 MW-peak wind generators, at a cost of slightly more than 10% of the CLIC 380 GeV cost), self-sufficiency during all times can not be reached. However, CLIC could run independently from public electricity supply 54% of the time with the portfolio simulated. About 1/3 of the generated PV and wind energy will be available to export to the public grid even after adjusting the load schedule of CLIC.

It is worth noting, however, that because of the correlation between electricity price and (national) generation from wind and PV, own local generators can generally not step in during times of high energy prize. Large storage systems are still too expensive to shift power accordingly. Besides the direct investment in the generation technology, many aspects of standards, regulations, land-use, landscape-protection etc. would have to be considered. One alternative to own renewable power plants could be the participation in projects of other investors to build large renewable power plants. With a changing energy landscape and cost, reduced power estimates from CLIC (and ILC) and improvements in technology such solutions need to be studied for colliders expected to be operational in 2035-40.

5. SUMMARY, CONCLUSIONS AND OUTLOOK

To summarize, sustainability has become a prioritized goal in the design for future accelerators in high energy physics, in particular the future Higgs factories presently envisaged. Improving and optimising the overall system design, individual subsystems and components, and operational concepts reduces resource consumption during construction and operation, and thus is beneficial to the economic as well as the ecologic footprint. Carbon-neutral accelerator operation is a goal pursued in both projects presented here but requires further work.

Presently, the quantitative evaluation of the resources needed and the environmental impact is focused on electric power consumption and greenhouse gas emissions from electricity generation. A more comprehensive lifecycle impact assessment would entail a broader accounting of GHG emissions, in particular during construction, and cover further factors such as ecotoxicity of raw materials for a more targeted optimisation of sustainability.

REFERENCES

[1] EUROPEAN STRATEGY GROUP, 2020 Update of the European Strategy for Particle Physics, CERB, Geneva 2020, doi:10.17181/ESU2020.

[2] BEHNKE, T., et al., The International Linear Collider Technical Design Report - Volume 1: Executive Summary, arXiv:1306.6327 (2013), DOI:10.48550/arXiv.1306.6327.

[3] ADOLPHSEN, C.et al., The International Linear Collider Technical Design Report - Volume 3.II: Accelerator Baseline Design, arXiv:1306.6328 (2013), DOI:10.48550/arXiv.1306.6328.

[4] EVANS, L. et al., The International Linear Collider Machine Staging Report 2017, arXiv:1711.00568 (2017), DOI:10.48550/arXiv.1711.00568.

[5] ARYSHEV, A. et al. [ILC International Development Team], The International Linear Collider: Report to Snowmass 2021, arXiv:2203.07622 (2022), DOI:10.48550/arXiv.2203.07622.

[6] BURROWS, P.N. et al. (eds.), Updated baseline for a staged Compact Linear Collider. CERN, Geneva, CERN Yellow Reports: Monographs **4** (2016), DOI: 10.5170/CERN-2016-004.

[7] CHARLES, T. K. et al., The Compact Linear Collider (CLIC) – 2018 Summary Report, CERN, Geneva, CERN Yellow Reports Monographs **2** (2018), DOI:10.23731/CYRM-2018-002.

[8] AICHELER, M. et al., The Compact Linear Collider (CLIC) - Project Implementation Plan, CERN, Geneva, CERN Yellow Reports Monographs **4** (2018), DOI:10.23731/CYRM-2018-004.

[9] BRUNNER, O. et al., The CLIC project, arXiv:2203.09186 (2022), DOI:10.48550/arXiv.2203.09186.

[10] TESLA TECHNOLOGY COLLABORATION, https://tesla.desy.de .

[11] ADOLPHSEN, C., Review of Machine Parameter / Cost Relationships, Int. Workshop on Future Linear Colliders, Granada, Spain, Sep 26-30, 2011, https://agenda.linearcollider.org/event/5134/contributions/21462/.

[12] GENG, R. L. et al., Performance of first prototype multi-cell low-surface- eld shape cavity, Proc. SRF2019, Dresden, Germany, 2019, p. 222 (MOP064), DOI:10.18429/JACoW-SRF2019-MOP064.

[13] GRASSELLINO A. et al., Accelerating fields up to 49 MV/m in TESLA-shape superconducting RF niobium cavities via 75°C vacuum bake, arXiv:1806.09824 (2018), DOI: 10.48550/arXiv.1806.09824.

[14] BARZI, E. et al., An Impartial Perspective for Superconducting Nb_3Sn coated Copper RF Cavities for Future Linear Accelerators, arXiv:2203.09718 (2022), DOI: 10.48550/arXiv.2203.09718.

[15] CAI, J., SYRATCHEV, I., Modeling and Technical Design Study of Two-Stage Multibeam Klystron for CLIC, IEEE Trans. Electron. Dev. **67** 8 (2020), 3362-3368, DOI:10.1109/ted.2020.3000191.

[16] BAINBRIDGE, A. et al., Demonstration of `ZEPTO´ Permanent Magnet Technology on Diamond Light Source, Proc. 12th Int. Part. Acc. Conf. (IPAC2021), Campinas, Brazil, 2021, p. 2370. DOI:10.18429/JACoW-IPAC2021-TUPAB365.

[17] IWASHITA Y., TERUNUMA, N., Design study of PM dipole for ILC damping ring, Proc. 9th Int. Part. Acc. Conf. (IPAC'18), Vancouver, BC, Canada, 2018, p. 505. DOI:10.18429/JACoW-IPAC2018-MOPML048.

[18] BROOKS, S., Modified Halbach Magnets for Emerging Accelerator Applications, Proc. 12th Int. Part. Acc. Conf. (IPAC2021), Campinas, Brazil, 2021, p. 1315. DOI:18429/JACoW-IPAC2021-TUXC07.

[19] YOSHIOKA, M. et al., Study on a sustainable energy management system for the ILC, Proc. 17th Ann. Meeting of Part. Acc. Soc. of Japan (PASJ2020), p. 410 https://www.pasj.jp/web_publish/pasj2020/proceedings/PDF/WEPP/WEPP57.pdf.

[20] SAEKI, T., personal communication.

[21] TOHOKU ELECTRIC POWER GROUP, Sustainability Data Book 2021, https://www.tohoku-epco.co.jp/ir/report/integrated_report/pdf/tohoku_sustainability2021en.pdf.

[22] PRASSE, C. et al., Energy load and cost analysis, https://edms.cern.ch/document/2065162/1 (2018).

[23] CERN, Environment report 2017-2018, CERN, Geneva, 2020, DOI:10.25325/CERN-Environment-2020-001.

[24] GENG, R. L., personal communication, 2022.

REGULATORY CONTROL AT THE CONSTRUCTION STAGE OF A RADIOPHARMACEUTICALS PRODUCTION FACILITY WITH CYCLOTRON IN THE CONTEXT OF COVID-19 PANDEMIC

G. E. RABI
Nuclear Regulatory Authority
Buenos Aires, Argentina
Email: grabi@arn.gob.ar

M. R. ESPÓSITO
Nuclear Regulatory Authority
Buenos Aires, Argentina

A. X. MAGGIOLO
Nuclear Regulatory Authority
Buenos Aires, Argentina

Abstract

Inspections and regulatory processes at the construction stage of a radiopharmaceuticals production facility with cyclotron have certain particularities that distinguish them from the processes related to other stages of the life of a facility. Particularly, the construction of a concrete shielding of great thickness, such as a non-self-shielded cyclotron vault, requires a set of specific controls by the regulatory body for the purpose of avoiding construction failures that could ultimately affect the safety conditions during the operational phase.

Due to the pandemic COVID-19 restrictions, the Nuclear Regulatory Authority, through the 'Class I Particle Accelerators Control Department', implemented alternative forms to develop the regulatory tasks associated to a facility denominated 'Cyclotron- Radiopharmacy Laboratory' from Oulton Institute located in Córdoba City, Province of Córdoba, Argentina, during the construction stage that had satisfactory results.

1. INTRODUCTION

The regulatory framework established by the Nuclear Regulatory Authority of Argentina (ARN) determines four stages for the authorization process of a radiopharmaceutical production facility with cyclotron; since it is classified as a Class I facility: construction, commissioning, operation and decommissioning [1]. This scheme of authorization stages is in line with the IAEA recommendations as the state of art for this type of facilities. In such way, in Argentina, the development of the construction stage of a cyclotron - radiopharmacy facility requires an authorization from the regulatory body [2].

This construction stage includes not only the development of civil works, but also the assembly of equipment and components of the facility. The documentation submitted by the applicant to get this authorization has to cover the following topics: facility layout, flow of materials and personnel, shielding design, ventilation system design, radiological impact on workers and the public, etc.[3]

The 'Class I Particle Accelerators Control Sector' of ARN did a detailed analysis of these documents in order to verify that all the radiation safety aspects were properly considered. In March 2020, the ARN granted the authorization of construction to begin the civil work of the facility 'Cyclotron - Radiopharmacy Laboratory' from Oulton Institute located in Córdoba City, Province of Córdoba, Argentina.

Regulatory inspections are a valuable instrument for verifying compliance with the conditions under which the authorization of construction is granted. Furthermore, since March 2020, the Government of Argentina has stablished restrictions to the circulation due to the sanitary emergency that was declared in view of the new coronavirus COVID-19, which affected the development of on-site regulatory tasks.

2. CRITERIA

There are a series of considerations that have to be taken into account in order to verify the conditions stipulated during the design phase, concerning radiation protection of workers, the public and the environment are being followed.

During the construction stage, a large proportion of the regulatory controls are intended to check that some criteria related to the cyclotron vault are followed, such as:

1. A cyclotron vault must be a monolithic structure; this is achieved by a one single cast of concrete or, in case it was not technically possible, by another technical solution that guarantee the shielding capacity of the vault.
2. Formwork and shoring systems must not reduce the shielding capacity; these elements remain inside the structure after the concrete curing decreasing the shielding capacity, so they should be replaced by heavy extern shoring systems.
3. Assembly of ducts ins and outs to the vault must avoid the leakage of neutrons; 90-degree bends over the three cardinal axes are necessary to be placed.
4. Future decommissioning tasks must be foreseen; the adoption of concrete blocks that work as a 'sacrificial' layer that facilitate the future dismantling works of the vault.

The compliance of these criteria has been a challenge for the licensee. Some of these criteria could be applied and others presented some difficulties (that are described below) that made necessary to apply innovative technical solutions.

1. A cyclotron vault must be a monolithic structure,

It was informed to ARN that there was no available concrete supply in Córdoba city to complete one single cast at once. Thus, it was necessary to plan several concrete casts to erect the vault in layers of concrete. A construction through layers of concrete can produce deficiencies in the contact surfaces that could affect the shielding capacity of the vault and the consequent risk of radiation leakages. After a discussion with the facility manager, it was agreed to insert a double wooden frame inside the steel armor, along the perimeter of the vault. A short time after the pour of concrete of the layer is finished, the wooden frame would be retired to produce 'steps' that avoid interface plans between the layers of concrete.

The construction project of the vault that was presented by the facility to ARN is illustrated in figure 1.

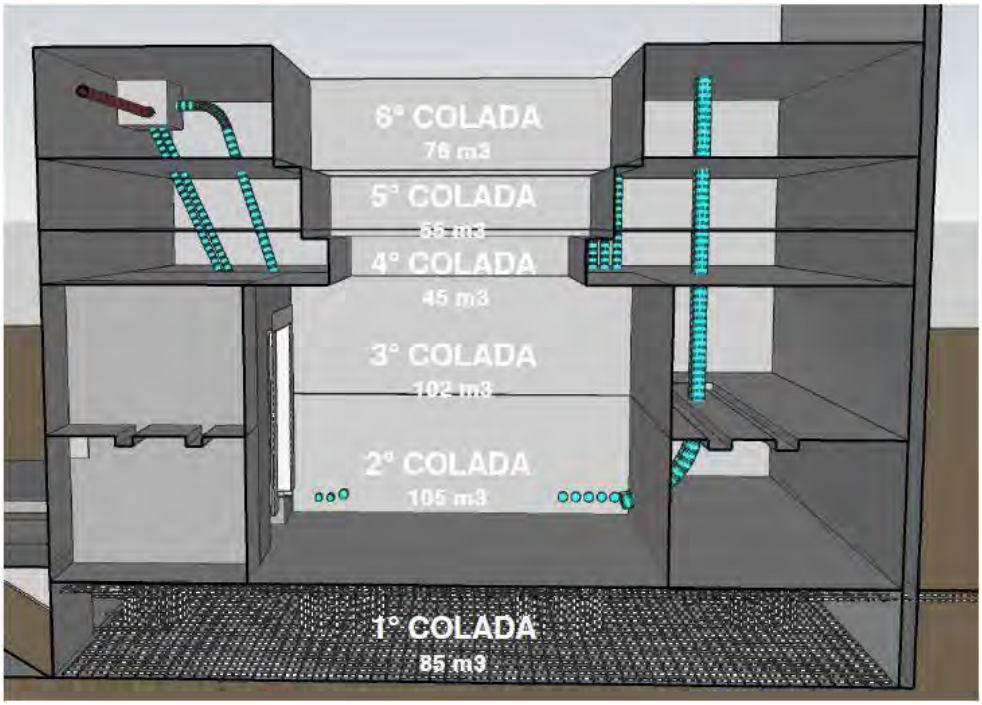

FIG. 1. Vault project with the concrete cast in six layers

The ARN analyzed that plan and suggested to modify the height of the layers n°2 and 3, because the interface surface between those layers matched the proton acceleration plan of the cyclotron and its targets. (*See FIG. 2*)

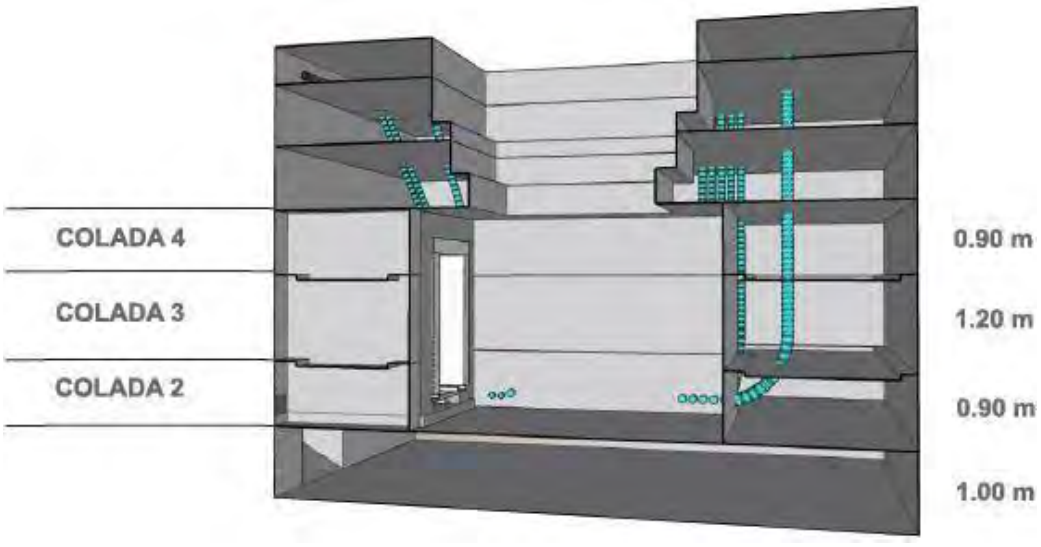

FIG. 2. Vault with the layers' height modified

In addition to this, it was requested to vibrate the concrete with appropriate equipment during the pouring, to prevent the generation of air bags inside the vault shielding.

2. Formwork and shoring systems must not reduce the shielding capacity,

It is common in civil constructions the use of metallic tensors to grew the resistance of the concrete containment during the pouring and simplify the formwork assembly. These tensors remain in the shielding structure and might produce possible radiation leakages due to metal corrosion. For this reason, it is requested to replace the use of tensors for extern shoring systems that have to be able to resist the concrete pressure.

Extern shoring systems were foresaw in this project and these criteria could be successfully complied through the adoption of different kinds of shoring systems. (*See FIG. 3*)

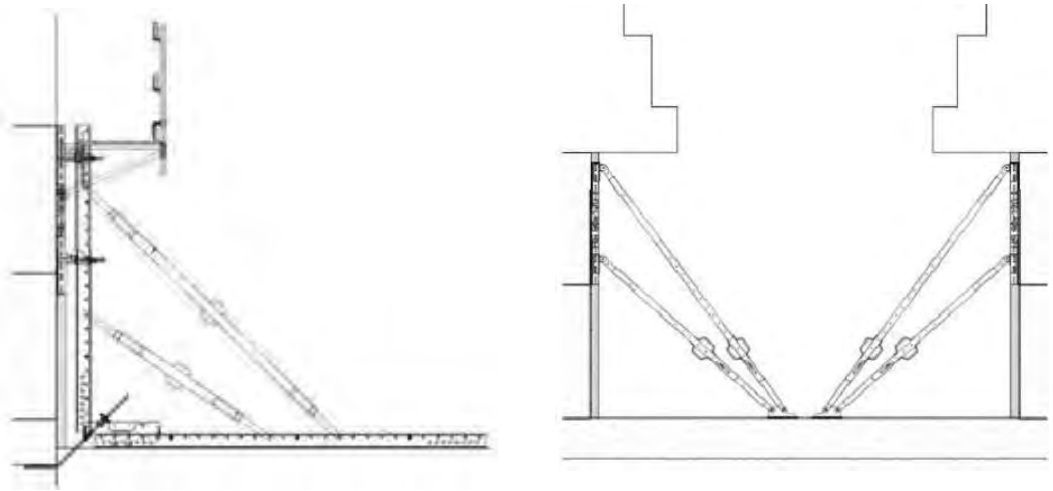

FIG. 3. Shoring systems

3. Assembly of ducts ins and outs to the vault must prevent the leakage of neutrons,

The route of ins and outs ducts to the vault that were presented in the ventilation system project, satisfies the requirements by adopting three 90-degree turns over the cardinal axes preventing neutron leakages. This can be observed in the next figure.

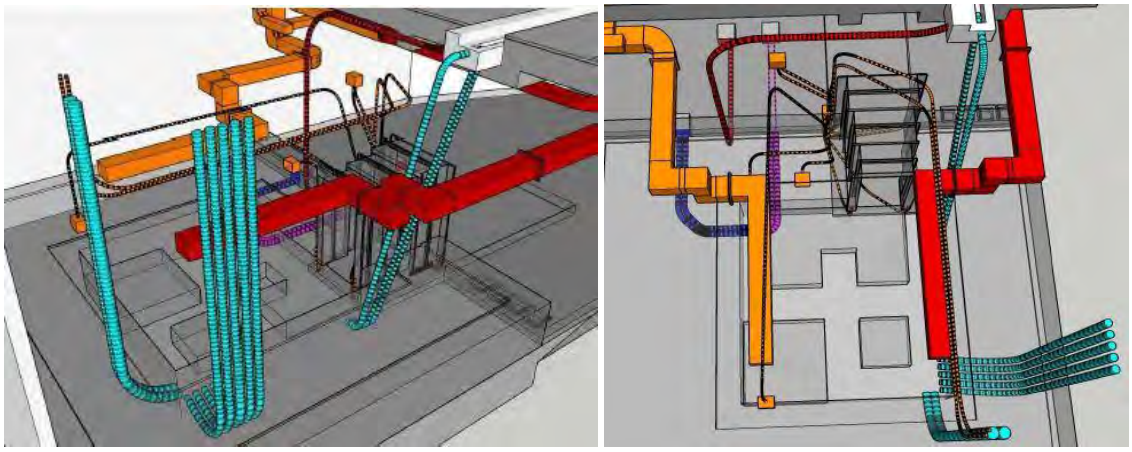

FIG. 4. Project of ins and outs ducts of ventilation system

4. Future decommissioning tasks must be foreseen.

ARN requested the facility to include a sacrificial layer in the vault project. The facility presented a project of concrete blocks with a particular design (*See FIG. 5*). This design of blocks to assemble allows the interior walls of the vault to be covered easily.

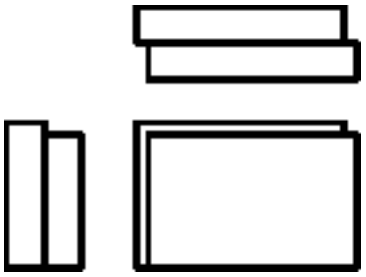

FIG. 5. Concrete blocks project for 'sacrificial' layer

Considering the expected use of local shielding for FDG production targets, the resulting concrete blocks thickness is 10 cm.

3. INSPECTIONS AND REGULATORY CONTROL

The development of inspections during the construction stage and especially prior to the pouring of the concrete, allows the regulatory body to verify whether the criteria described in the previous section have been considered.

The restrictions established due to the COVID-19 pandemic made it difficult to travel to Córdoba city to carry out on-site inspections. Thus, it was required to implement alternative solutions in order to continue with the regulatory control adequately. ARN adapted its regulatory processes incorporating the remote work, and to this extent, the 'Class I Particle Accelerators Sector' followed the execution of the civil works remotely by reviewing photographic reports that the facility sent to the ARN continually.

In this context, photographic records of the civil works were critical, and it was extremely important that workers in charge of taking these photos understood what needed to be depicted in them. For this purpose, a remote meeting between inspectors of ARN and the civil work staff was made. Inspectors of ARN clarified relevant concepts as well as answered questions and the staff could take great pictures of the civil work progress.

The following pictures show the fulfillment of the criteria, according to the approved project.

— A cyclotron vault must be a monolithic structure

FIG. 6. Wooden frame inside the armor previous the concrete cast

FIG. 7. Double wooden frame inside the armor

FIG. 8. The 'step' generated by the wooden frame

FIG. 9. A civil worker vibrating the concrete during the cast

— Formwork and shoring systems must not reduce the shielding capacity,

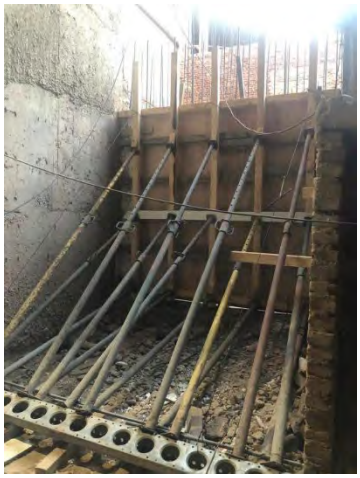

FIG. 10. Shoring system to extern vault wall

FIG. 11. Shoring system to intern vault wall

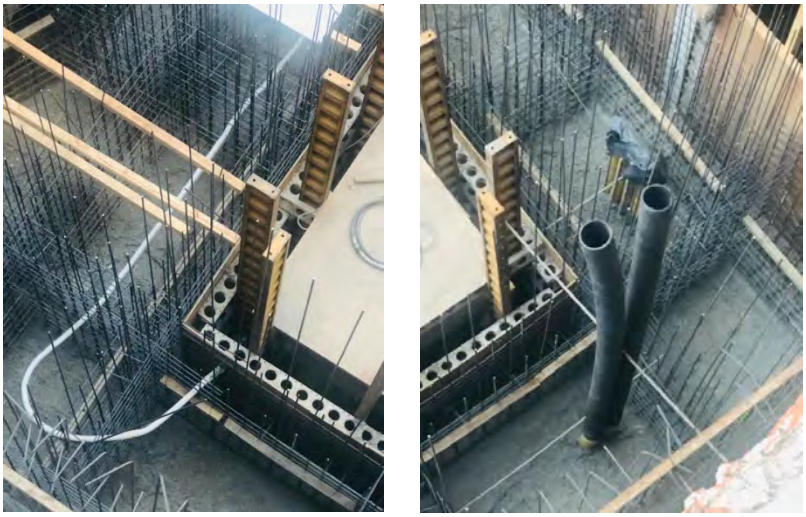

FIG. 12. Absence of intern metallic tensors

— Assembly of ducts ins and outs to the vault must prevent the leakage of neutrons,

FIG. 13. Ins and outs ventilation ducts from the vault

The proper assembly of ventilation ducts was verified by these pictures. In addition to this, the electrical cabling, water, gas and product supply tubing to and from the cyclotron were also properly placed on trenches in the vault floor, connecting to the underside of the cyclotron.

FIG. 14. General services piping

— Future decommissioning tasks must be foreseen.

FIG. 15. Concrete blocks for 'sacrificial' layer

The inner walls of the cyclotron vault were covered with concrete blocks as it was approved in the design phase. These concrete blocks were built on the construction site.

4. CONCLUSIONS

The objectives of the regulatory control during the vault construction were successfully fulfilled. The current criteria in the matter were properly considered and adapted according to the needs and the technical limitations, as it could be observed.

The Covid-19 restrictions forced inspections processes to be adapted and the results obtained by the 'Class I Particle Accelerators Sector' of ARN in the control of construction stage tasks have been very positive until now. The implementation of a remote meeting to exchange knowledge with not only the operators but also the civil work team has been a great decision in order to assure that the verification could be done properly, taking into account that some relevant aspects can be verified only during the concrete cast but not later.

The early participation of the regulatory bodies in the evaluation of the design projects and the fluid communication with the operators could demonstrate that streamlines the progress of the civil work.

Fortunately, a few months after the concrete cast, the restrictions were released and the inspectors of ARN could verify on site that the construction progress is in accordance with the approved project. However, it is valuable to consider that despite the fact that remote controls had satisfactory results, they do not replace on-site verifications; because the remote-control success relies strongly on an effective communication between the licensee and the regulatory body, which could not always be the case.

Currently, the construction authorization is still valid, and this stage continues by the assembly of the radiopharmacy systems and the radiological protection equipment. The cyclotron is already placed and also the hot cells of the radiopharmacy lab. In April of 2022, the external contractors are finishing their construction jobs and the commissioning authorization has been already requested to ARN.

ACKNOWLEDGEMENTS

A special recognition should be given to Oulton Institute authorities and to 'Cyclotron - Radiopharmacy Laboratory' staff who gave permission to show pictures of the work performed in the civil work of the facility.

REFERENCES

[1] Autoridad Regulatoria Nuclear, "Norma AR 10.1.1. - Norma Básica de Seguridad Radiológica - Revisión 4", (2019).

[2] Autoridad Regulatoria Nuclear, "Norma AR 5.1.1. - Exposición ocupacional en aceleradores de partículas Clase I - Revisión 1", (2002).

[3] Autoridad Regulatoria Nuclear, "Norma AR 5.7.1. - Cronograma de la documentación a presentar antes de la operación de un acelerador de partículas - Revisión 1", (2002).

[4] Foro Iberoamericano de Organismos Reguladores Radiológicos y Nucleares (FORO), "Criterios para el licenciamiento y requisitos de inspección en instalaciones con ciclotrones para producción de radioisótopos utilizados en aplicaciones e investigaciones médicas", (2013).

[5] IAEA, TRS Nº471 – "Cyclotron produced radionuclides: Guidelines for setting up a facility", (2009).

[6] IAEA, "Cyclotron Produced Radionuclides: Guidance on Facility Design and Production of [18F]Fluorodeoxyglucose (FDG)", (2012).

HEAVY ION THERAPY MASTERCLASS SCHOOL AND CAPACITY BUILDING FOR FUTURE ION RESEARCH AND THERAPY FACILITIES.

Panagiota FOKA
GSI Helmholtz Centre for Heavy Ion Research Darmstadt, Germany
Email: yiota.foka@cern.ch, p.foka@gsi.de

Aristeidis MAMARAS
Aristotle University of Thessaloniki Thessaloniki, Greece
Email: amamaras@physics.auth.gr

Abstract

The Heavy Ion Therapy MasterClass school took place, online, in May 2021, for first time, attracting over a thousand participants. The unexpected and unprecedented high number of participants, spanning from undergraduate students to practitioners, shows the increasing interest in heavy-ion cancer therapy research and related training. It also demonstrates the enormous potential of the next generation, represented by the young students and early-stage researchers that can then optimally access the heavy-ion therapy centers and become the experts of next generation facilities. The main emphasis of the school was on the use of accelerators for the treatment of cancer tumours, highlighting the role of research centres with prime example the GSI heavy-ion research centre where carbon-ion therapy was pioneered in Europe in the 90s and from where it was implemented in the first European dedicated ion therapy centre. The main feature of the school was its multidisciplinary and interactive approach which stimulated participants, despite its online format. Overview lectures provided the necessary panorama, while focus lectures presented details including medical accelerators and accelerator physics highlighting the importance of the development of novel accelerator technologies. The scientific programme was shaped to target topics in emerging fields, highlighting the role of fundamental research in developing new applications in medicine, particularly cancer diagnostics and treatment. The participants' feedback clearly demonstrated their appreciation, including the inventive format of the school which is described in the paper as means to support capacity building in related fields and in particular in accelerator specializations.

1. INTRODUCTION

The Heavy Ion Therapy Masterclass, HITM, school [1] was organised 17-22 May 2021, "in Sarajevo", but in reality, fully online due to the covid pandemic. It was organised free of charge, within the framework of the HITRIplus [2] project funded by the European Union's H2020 research and innovation programme. It provided a full-week international online masterclass course on heavy-ion cancer therapy research inspired by the format of the Particle Therapy MasterClass, PTMC [3]. Motivated by the received feedback on the PTMC, its format and pedagogical elements were employed for the HITM school. Hence, the school combined lectures with hands-on sessions on treatment planning that were delivered by world's top experts in the field. Leading institutions, research centres, ion therapy facilities, and industry collaboration contributed to its success and conveyed the message that technologies developed for fundamental research find applications for medicine. It was attended by 1050 participants, from all over the world, that ranged from undergraduate students to Masters, PhDs, early stage researchers but also professional lecturers and practitioners; and involved a total of 36 speakers. Participants greatly appreciated the multidisciplinary approach of the school and the presentations from leading experts that started from basics and covered most recent developments and future perspectives in heavy-ion therapy research.

The school run smoothly, it provided enough interactivity, and had a big impact despite the big challenges. Surveys and comments of participants summarise its main elements that distinguished it: its approach, regarding the content, but also its format, was "holistic, multidisciplinary, and original". A "spiral approach" was followed including, from the first day, all topics relevant to heavy-ion therapy, starting with overview presentations and gradually progressing to deeper details, not taking shortcuts. So, beginners and participants from different fields could comfortably follow, advancing every day in all topics, in parallel. Speakers, leading experts in their fields, starting from basic principles, elaborated on topics spanning from accelerator technologies to clinical related subjects. It thus gave the opportunity to have an overview of heavy-ion therapy but also included the last day, state-of-the-art science and cutting-edge technology developments as well as future trends.

Several articles summarised the school including ENLIGHT [4] and CERN Courier [5] while its presentations and recordings are available openly, for anyone interested to follow them, via the HITM school [1] and HITRIplus [2] web pages.

1. HITRIPLUS PROJECT AND SCHOOLS

The HITRIplus [2] is a large consortium of research infrastructures, including CERN [6] and GSI [7], universities, industry, the four existing European heavy-ion therapy centres, and SEEIIST, the South East European Institute for Sustainable Technologies [8]. Its main aims are to support: (a) transnational access, (b) new developments for the future SEEIIST facility and upgrades of the existing ones (c) networking, training and education (capacity building) in related fields in order to sustain the existing and future heavy-ion facilities. Thus, it brings together, the four heavy-ion therapy centres in operation in Europe, including the biophysics programme at the GSI heavy-ion research centre, and opens them in a coordinated way to the medical and research communities. Intensive design work focuses on the design of some novel components of next generation medical accelerators and facilities for cancer tumour therapy research with heavy ions, in collaboration between all partners, based on the expertise of advanced research institutes and of the main European ion therapy centres.

Within the HITRIplus education and training work package, three schools were foreseen, addressing mostly promising early-stage researchers that could then optimally access the European heavy-ion therapy centres. The first one, the Heavy Ion Therapy Masterclass school, started with setting up the basis assuming no prior expertise and putting a strong emphasis to also support capacity building in South East Europe that is lucking expertise in related fields. Hence, the next two schools will explicitly target young researchers that are more advanced in heavy-ion therapy specialised studies. The second HITRIplus school is also planned online, in July 2022, while the third one is envisaged currently in-person or hybrid mode. In order to facilitate sustainability and help create a “cascade effect”, spreading to the max the acquired knowledge, they all foresee “train-the-trainer” sessions. The aim is to train tutors that could then perform back at their home institutes the Particle Therapy MasterClasses [3], that are one-day events addressing high-school students and are described further in the paper and in related conference proceedings [9, 10, 11]. The initial plan was to organise the HITM school in Sarajevo as a further support for ongoing capacity building activities involving the UNSA university [12] which also contributed to the PTMC project. However, due to the covid pandemic it was organized fully online which made possible world-wide participation. The HITM school was the first event of HITRIplus. The interest that attracted, the enthusiastic response of participants and their praising comments, underlying its success, strongly motivated all HITRIplus collaborators to focus on the work ahead.

2. HEAVY ION THERAPY MASTERCLASS SCHOOL

The scientific programme of the Heavy Ion Therapy Masterclass school was shaped to target topics in emerging fields, highlighting the importance of fundamental research and the role of research centres for developing new applications in medicine, particularly the use of accelerators for cancer diagnostics and treatment. Speakers from the heavy-ion therapy centres in Europe contributed highlighting the relevance of fundamental research and its applications for cancer treatment. Participants realised that challenges set by the research projects’ ambitions push high-tech technology which ultimately translates to benefits for society.

The focus of the school was on heavy-ion therapy and its facilities, as presented in the virtual therapy centre of Fig. 1 (curtesy of ENLIGHT) and which was used as a “roadmap” to shape the agenda of the school, starting from the ion sources and all the different elements that bring the beam to the target. It also included hands- on sessions, focusing on treatment planning (Fig. 2), which is the prescription of the therapeutic dose that the treatment accelerator has to deliver. Addressing also the results of the treatment, it included presentations on the radio-biological effectiveness and characteristics of different irradiation modalities. Participants greatly appreciated having the full image: what happens from the beginning to the end. Indeed, one of the main features of the school was its multidisciplinary approach which presented the multidisciplinary facets of heavy-ion therapy and inspirations for interesting career paths in many different fields.

The school was intended for students interested in medical physics and engineering or related subjects which shaped the agenda accordingly including accelerator and magnet technology, gantry design, beam

dynamics, medical imaging, biophysics, radiobiology, dosimetry, treatment planning, clinical aspects of particle therapy, and entrepreneurship aspects of medical research infrastructures. The aim was to attract students that show strong promise and interest to become part of the heavy-ion research community and can then exploit the European heavy-ion therapy research infrastructures. The breakdown of its 1050 participants has shown that participants ranged from undergraduate students to Masters, PhDs, early-stage researchers but also professional lecturers and practitioners. While the participation of about 275 undergraduate students may open them new horizons, the comments of the about 650 Masters, PhDs and young researchers have shown that the HITM school has provided them support and material for their research but also triggered new ideas and collaborations.

FIG. 1. Virtual ion therapy center (courtesy of ENLIGHT).

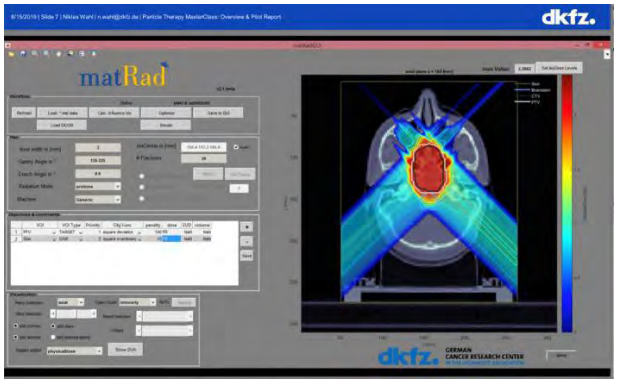

FIG. 2. matRad Treatment Planning toolkit (courtesy of DKFZ).

School format: The format of the HITM school integrated and expanded the basic elements of the masterclasses, as they are performed within the International MasterClasses IMC programme [13], and in particular of the Particle Therapy MasterClass [3]. These masterclasses are one full-day events, that give the opportunity to high-school students to become scientists for a day. The IMC programme runs every year, from mid-February to mid-April, and 2-5 institutes, every day, around the world, invite high-school students to participate, ideally at their premises or online, adapting to the covid pandemic. Thus, the IMC programme attracts every year about 15 000 high-school students from 60 countries involving 255 institutes world-wide. The main aim is to introduce the students to scientific methods by giving them the opportunity to handle real data initially coming from particle-physics experiments at CERN, first from LEP and then LHC. Further expanding its reach, the IMC programme includes currently additional experiments and, most importantly, the new Particle Therapy MasterClass PTMC [3]. The PTMC focuses on applications of accelerators for medicine demonstrating benefits for society from fundamental research that is pushing relevant technologies. Indeed, starting from the first pilot PTMC in 2019 involving GSI, CERN and DKFZ [14], the PTMC in 2021 and 2022 attracted about 1500 high-school students from 20 countries and 37 institutes each year. It was then adapted to address also university students and has expanded its reach to a new generation of scientists.

Therefore, motivated by the received feedback, the format of the newly established full-day Particle Therapy MasterClass, PTMC, and its pedagogical elements, were employed and adapted for the full-week Heavy Ion Therapy MasterClass, HITM, school addressing early stage researchers. The PTMC agenda includes introductory lectures and visits to an experiment or a lab, which is followed by a hands-on session offering the experience to handle real data. Students then prepare a presentation with their results for discussion in a common video- conference among all participants, moderated by an expert. Indeed, as participants commented, an

important aspect that characterised the HITM school was its format which, similarly, included a multitude of pedagogical elements facilitating learning: lectures in the morning; hands-on in the afternoon; students' presentations and discussions of their results with experts; online virtual visits to existing therapy centres guided by their experts; every day started with heavy-ion therapy related videos while participants were connecting; every day ended with social events to provide opportunities for networking and entertainment; the last day was dedicated to "future developments" in the field of heavy-ion therapy research and a "careers fair" in the evening.

Online lectures: Every day the online lectures sessions started with a video, showing an ion therapy procedure in an ion therapy centre to trigger curiosity and interest. Furthermore, it provided an overall visual impression, so that students could relate the specific presentations that followed to the broader image and procedures. The lectures covered a wide range of inter-related topics, supported by videos as much as possible, to keep the interest of students. The first day overview lectures provided the necessary panorama spanning from cancer statistics, benefits of heavy-ion therapy, medical accelerators up to radio-biology related topics. Introductory lectures covered the basics of cancer biology and treatment options, the physics and biology of exposure to ionizing radiation, imaging devices and detectors, as well as accelerators used for cancer diagnosis and treatment. Then, focus lectures presented details, for example, on accelerator physics including ion sources, beam optics, beam delivery systems, controls, as well as exploring linear accelerators for radio-isotope production. These were complemented by contributions on fundamental detector or software developments that are used in medicine for imaging, diagnostics, dosimetry, as they are critical parts of the treatment procedures where, also, the impact of breakthrough developments for physics experiments becomes clear. Experts from the European ion therapy centres contributed with their expertise from the users' point of view.

Highlighting the use of accelerators for society, students were surprised to learn that from about 30 000 accelerators that are in operation world-wide, about 6% is used for research, while 1/3 is used for medicine and the rest for different industrial applications. Adapting technologies and methods developed for fundamental particle physics research, sophisticated medical accelerators can deliver particle beams at a desired depth targeting a tumour, thus becoming an important tool for cancer therapy. Advanced accelerator technologies developed for future projects (such as the proposed future CERN CLIC project) are currently explored for the most advanced therapies (such as FLASH therapy).

The importance of computing and software developments was also highlighted including specialised lectures on accelerators control and machine learning techniques and their possible applications in these fields. Experts of the Cosylab hi-tech company contributed to these targeted lectures and made the connection to industry, a natural continuation providing job opportunities. Such opportunities were further highlighted during the last day careers fair organised in the framework of the social events where the experts of this world-wide leading company organised an open house stand and answered questions of interested participants in the highly specialised field of accelerators controls.

Hands-on: The hands-on sessions on treatment planning were offered every afternoon by DKFZ experts, except for the last day that was dedicated to future developments. First, dedicated lectures introduced the students to necessary concepts such as the concepts of dose calculation, dose optimization and radiotherapy treatment plans. In particular, students could realise here how elemental mathematical concepts (e.g., learned from calculus) are required and applied to solve actual technical problems. The hands-on session itself was based on the matRad open-source treatment planning toolkit (Fig. 2) developed for research and training by DKFZ, the German Cancer Research Centre [15, 16, 17]. MatRad is used to simulate and optimize the therapeutic intensity-modulated dose distribution that the accelerating structures have to deliver to the tumour. While matRad's computations were validated with commercial treatment planning software actually used for therapies, it is not licensed for treatment itself but uses a GPLv3 open-source license. This facilitates matRad's lightweight, flexible, accessible and performant code, useful for research and educational applications. Furthermore, depending on the level of the students, special educational versions can be provided with reduced treatment planning complexity of the GUI.

During the first hands-on session of the HITM school students were introduced to the possibilities of the matRad treatment planning toolkit and were guided through the installation procedure that the DKFZ expert tutors performed online step-by-step based on the instructions document that was attached to the agenda. The tutors also handled any difficulties and problems that the participants experienced during installation.

The next three hands-on sessions were dedicated to using matRad to prepare treatment plans. So, students guided by the DKFZ experts had to prepare their "prescriptions", using photons, protons or carbon ions. During

this stage, but also during the discussion of their treatment plans, students could appreciate the differences of these radiation modalities and use them optimally according to different cases. These cases were based on data, also provided by the DKFZ experts, and included a TG-119 phantom and anonymous computer tomography (CT) scans of head, liver and prostate tumour cases from the CORT dataset [18]. MatRad includes a graphical user interface (GUI) resembling typical commercial systems to present the data in 3D, provides possibilities to rotate interactively and presents slices in 2D projections. The GUI includes graphical tools to visualize the beam directions and volumes to be irradiated. These capabilities were heavily used by the school participants to visualise and optimise their treatment plans. For the dose optimisation, one can use multiple objectives and constraints for dose prescription, e.g., define a minimum and/or maximum dose value to be achieved within a structure or organ [17]. The visual result on the display, based on a colour scale, is very intuitive to comprehend and easy to associate with the resulting histograms of the delivered dose to the target tumour and organs at risk to avoid. Students can select different angles for irradiation to minimize the deposited dose in each trajectory while accumulating the required dose in the target volume. They can witness the different characteristics of protons and carbon ions, that, in contrast to photons, deposit very little energy in the tissues before and practically none after the tumour.

The hands-on sessions were divided into three sections focusing on a certain theme and demonstrating specific properties. The first section was planned with the aim to highlight the difference of photon and charged particle irradiation on the TG-119 phantom, showing, for example, that many beams are required with photons to cover the tumour while the sparing of healthy tissue can be challenging, whereas protons achieve at least similar results with already one or two beams. The second part introduced carbon ions and radio-biological effectiveness on a patient case using the liver and/or head-and-neck case for this exercise. This also introduced versatility to the later videoconference where students presented their results and discussed their findings. The last part critically introduced the "downside" of charged particle therapy, that is, its sensitivity to uncertainties that might change the net range in the patient and distort the planned dose distribution when the patient is, e.g., misaligned.

Hands-on tutors: Participants were really thankful to their tutors, as was witnessed interactively by their enthusiastic comments on the zoom chat but also via the surveys. Indeed, the DKFZ experts managed impressively well the challenging hands-on despite the huge number of participants; one of them was handling questions and problems while the other one was performing the steps of the exercises, based on a write-up that was attached to the agenda. Participants could then repeat and/or complete the exercises based on the recordings that were made available immediately after the end of the session. This was also crucial for the participants at different time zones.

Hands-on results and attendance certificates: Despite the challenges of the school's online mode, the large number of its participants and the different time zones, 180 participants delivered their hands-on results for all days; and 158 were granted a certificate of attendance fulfilling all conditions.

Students' sessions topics: The HITM school gave special attention to students' dedicated sessions. During those sessions, the students were meant to present their hands-on results but also their research activities. Each day the students' session was planned around a certain focus theme. Monday was dedicated to the installation of the matRad treatment planning software. Then, on Tuesday the theme was "from physics to clinics" going from the GSI heavy-ion research centre to the CNAO [19] running heavy-ion therapy centre. Wednesday was dedicated to treatment planning involving experts from CNAO presenting the tools they use for therapy, from the room where they were working on real cases. This was then contrasted to the matRad tools for training and research. On Thursday, the focus was on the International MasterClass programme and the preparation of tutors for the Particle Therapy MasterClasses, practically a "train-the-trainer" session aiming at sustainability. On Friday, the focus was on future facilities, their upgrades, future trends and perspectives; it culminated with the careers fair, during the social events, presenting career opportunities to interested participants and further supporting networking.

Train-the-trainer: One of the afternoons HITM school sessions was dedicated to introducing the IMC programme focusing in particular on the Particle Therapy MasterClasses with the motivation to support sustainability by training the trainer. The aim was to provide the means to the HITM school participants to become tutors, in their turn, performing the PTMC in their home institutes for high-school students; thus, further supporting capacity building in this specific heavy-ion cancer therapy area.

First, the IMC concepts and programmes were presented by the IMC organisers. Then, the results of a Master's student study, from the UNSA university of Sarajevo, demonstrated the pedagogical value of the one-day masterclass events for high-school students. Indeed, specifically designed surveys and analyses of the

accumulated data have clearly shown that students can learn a new topic, even during the one-day masterclass sessions, because of the variety of the employed pedagogical interactive methods and in particular the hands-on experience handling real data and methods.

Next, the necessary concepts and tools for the Particle Therapy MasterClass were introduced highlighting the provided support by the PTMC core team. In order to support the PTMC local organising teams of each participating institute, and prepare their tutors and moderators, weekly dedicated tutorials are offered every year during the IMC seasons but also training sessions at request. The PTMC web pages [3] provide a large variety of material in several languages, including links to the "PTMC in a kit" google drive which contains the necessary material needed to perform the PTMC, including recordings with instructions. In addition, it links to the indico agendas of institutes that performed already the PTMC, including their presentations and other useful material in their local languages. Instructions for installing the matRad specific software are also available via the PTMC web pages, including recordings, explaining the simplified version that was prepared by the DKFZ colleagues for the purposes of the PTMC for high-school students.

Online visits and discussion of results: The HITM lectures were complemented with online visits to heavy-ion research and heavy-ion cancer therapy centres during the afternoon common video-conferencing sessions planned with the aim to discuss the hands-on treatment planning results with their experts. The online visits started with the GSI experimental room where carbon ion therapy was pioneered in Europe, in the 90s. Students were impressed to learn that an experimental room was transformed to a therapy room where some 450 head-and-neck cases were treated with carbon ions and actually see it and listen related details. The virtual visit also included explanations about the pioneering methods of raster scanning [20] and in-room imaging that were then implemented in the hospitals. Indeed, carbon ion treatment of cancer tumours was first implemented in the Heidelberg Ion Therapy centre, HIT [22], based on the GSI successful results showing that 95% of their patients did not present side effects after five years. The GSI experts highlighted that while patients are now treated in dedicated therapy centres, the GSI historic therapy room and its specialised equipment is used for research focusing on the optimisation of treatment of moving organs such as lungs. This virtual visit to a heavy-ion research centre was followed by visits to running heavy-ion therapy centres starting with the CNAO ion therapy centre. The online visit started with a guided tour to its accelerator complex via the dedicated webcam system and included details on its structure and devises given by the CNAO expert technical coordinator who enriched the visit discussing his personal experiences during the design and construction of the accelerating and beam delivery structures. These virtual visits focusing on the technical aspects of the medical accelerators, made it clear to the students that this is the heart of the heavy-ion cancer therapy centres. Then, the focus of the virtual visits was shifted to the significance of the treatment planning. The HITM school participants had the opportunity to see the action in the CNAO respective control room where the CNAO experts presented treatment planning of real cases and their tools. Those were then contrasted to the matRad toolkit tailored for research and education purposes. Indeed, experts from these institutes provided an excellent interactive help, commenting on the students results and answering their questions. These online visits further highlighted the connection between heavy-ion physics and heavy-ion therapy and have clearly demonstrated the relevance of fundamental research and its applications for cancer treatment.

In general, the HITM school highlighted that technology and knowledge transfer "from physics to clinics" resulted in the four carbon-ion therapy centres in Europe. Furthermore, following the PIMMS initiative [21], accelerator experts of the CERN NIMMS group work currently on the design of components for a next generation ion therapy machine adapting hi-tech technologies for medical accelerators. Of particular interest are developments on the so-called gantry, which is the beam delivery system that rotates around the patient to deliver the ions from all needed angles. This was addressed in specialised focus lectures, presenting options for future smaller constructions, by factor about 10 lighter than the existing one in the Heidelberg Ion Therapy HIT [22] centre which weighs 600 tonnes. As an example, Fig. 3 shows the accelerator layout and architect's concepts (courtesy "Kaprinis architects") for a heavy-ion therapy facility which is proposed to be built in South East Europe (SEE). Indeed, the HITM school was followed by several students from SEE countries that they can then become tutors in their turn performing the PTMC in their home institutes thus further supporting capacity building in the area.

Social events: In order to further enhance active interaction and networking between students and lecturers as well as amongst students, a rich programme of social events was included. Several participants had still the

energy to to participate after a long, loaded day in the social events organised every evening and took advantage of the offered networking opportunities. These online social events were based on the specialised SpatialChat [23] platform which offers numerous possibilities to facilitate interactions simulating real-life conditions of groups of participants who, discussing with a wine glass at their hand, would move around from one group to another, from one "room" to another. The creative core team of students, helping with all practical items of the school, fully exploited the SpatialChat characteristics and offered an impressive online environment implementing an interesting programme.

FIG. 3. Architects design of the SEEIIST next ion cancer therapy research facility (courtesy "Kaprinis architects").

A dedicated colourful poster for the evening social events announced the daily programme that included from Monday to Friday: (a) Welcome drinks: giving the opportunity to meet all attendees breaking the ice while getting introduced to the ENLIGHT network by its coordinator. (b) Language café: giving the opportunity to chat about the different cultures of participants, their favourite traditional foods and drinks while reflecting, after a presentation based on statistical data, on the status of cancer-health conditions in their region and possible improvements that they could contribute in the future. (c) Students Q&A: providing the chance to the students to ask questions and seek advice while they were stimulated by the activities discussed by the CERN Knowledge Transfer experts. (d) Tours Games and Disco: providing the environment for entertainment during a "students'-only day" and opportunities for creating friendships and bonds sharing same interests not only at professional life. (e) Career Fair: the highlight of the social events, giving the opportunity to visit different stands organised by several institutes, including CERN, GSI, DKFZ, CNAO, MedAustron, Cosylab. Students had the chance to approach their experts, as in real-life open house events, and get informed of the opportunities offered by each one of these institutes, that spanned from research and medical heavy-ion treatment centres to companies (Fig. 4). In addition to the daily themes, including special drinks, food and entertainment, the social events programme was enriched by the additional touch of the "dress code" every day spanning from smart casual and formal attire to pyjama party. Participants certainly did the most out of it, to the great satisfaction of the organising team seeing their efforts being appreciated. Furthermore, participants suggested to include them during the coffee breaks also, which will be a great improvement for any future online or hybrid events. Indeed, the HITM school social events successfully combined entertainment with networking which is crucial for young students seeking guidance for their future studies and career but also for the specialised institutes to attract the most motivated students that are promising to become members of the heavy-ion therapy community.

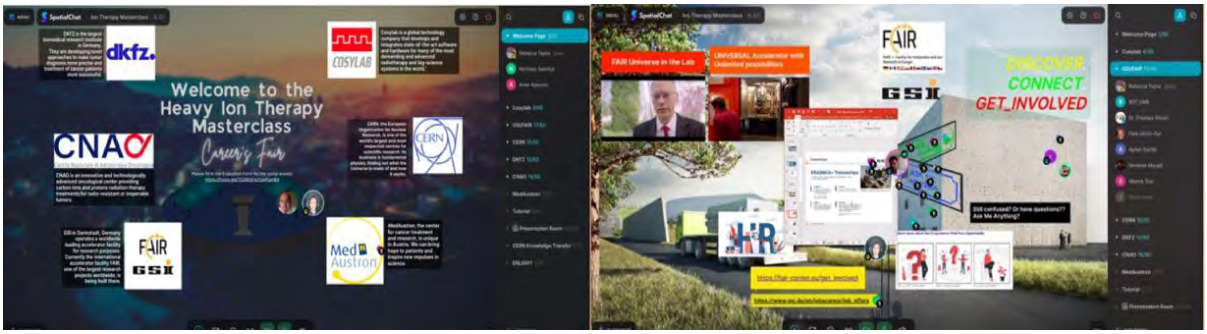

FIG. 4. HITM school social events and career fair in SpatialChat platform.

Networking: The worldwide reach of the HITM school demonstrates the increasing interest in heavy-ion therapy but also the power of networks. Networking is particularly crucial in the multidisciplinary field of heavy-ion cancer treatment to connect experts in different fields that are typically widespread around the globe. In that respect, the role of networking and the role of the ENLIGHT network in particular were detailed during the opening introductory presentation but also during the introductory drinks welcoming participants at the social events at the end of the first day. Furthermore, announcing the school through the ENLIGHT mail lists but also the International MasterClasses, IMC, mail lists, reflected in the worldwide participation to this school. As an example, the maps of Fig. 5 show the participation to the IMC and the HITM school that match almost one-to-one, since the school was announced through their network also.

FIG. 5. World-wide reach of Heavy Ion Therapy Masterclass school (left) similar to the IMC programme reach (right).

Sustainability example: An IMC member from Benha University in Egypt contributed with an interesting initiative by integrating, formally, the whole week HITM school into the curriculum of the university and organised the participation of some 100 university students. Students from different faculties including physics, medical physics, medicine, engineering, agriculture, joined the lectures sessions from a single large auditorium, and the hands-on sessions from dedicated smaller computing lab rooms. Every day, they presented their hands-on results and impressed with the noticeable active participation of female students, a good example of diversity and sharing know-how in general. Noteworthy to mention that the dean not only provided full support, but he highlighted during the opening session the importance of this school that provided their students with the opportunity to participate to specialised courses delivered by leading experts (Fig. 6). Also, noteworthy to mention, the Benha University hosts the PTMC every year with a large participation of high-school students typically attracting over a hundred high-school students every year. Clearly the tutors had a great benefit and support from following the specialised courses of the HITM school.

FIG. 6. Opening session of the HITM school and participation of the Benha university of Egypt integrating the full week course in their curriculum.

Logistics: The platform for the online event was zoom which is convenient and already popular and widely used by several scientific communities. Naturally, the large number of zoom connections posed a challenge which technically was possible to overcome with the CERN expert support. However, it also presented a risk exposing participants to undesired experiences known as “zoom-bombing”. Therefore, the school started with a webinar

style the first morning through which the zoom link was then provided to participants. In addition, a dedicated person from the core organising team was ready to react in case of undesired interventions. This clearly enhanced the possibilities for interactions with participants. To further facilitate interactivity, a shared document was setup where everybody could edit questions that were then answered by the lecturers verbally, while other participants could post further questions on the topic creating a thread. Based on this inventive mode of discussion a total of 450 questions were addressed during the week, as, apparently, the anonymity made participants feel more comfortable to ask questions. In addition, zoom chat and polls were heavily used to keep continuous interaction with participants and react promptly to their needs and requests. Polls, launched unexpectedly, were also used as means for verification that participants indeed followed up the lectures and were useful in the process of granting attendance certificates. Also, to facilitate the process, a dedicated google drive was provided where participants could upload their results from the hands-on sessions in their dedicated folders. This was also a verification, for granting them their "certificate of attendance". In order to remedy the difficulties posed by the different time zones (having participants from Latinoamerica to Australia) the presentations and recordings of the morning lectures were immediately available during the lunch break and of the hands-on sessions in the evening every day. Furthermore, surveys launched every day provided the means to participants to give their opinion and comments.

Statistics: Participants were literally from all over the world, almost equal numbers from European and non-European countries. The school had a good gender balance (Fig. 7) with about 18 female speakers out of a total of 36. In addition, it encouraged students' active participation which resulted in 25 students' presentations. Some of them were arranged in advance in the agenda; however, a good fraction of them was spontaneous, by giving the floor to the students in the students' sessions. The school covered overall 35,5 h, including 18 h of lectures, 7,5 h of hands-on sessions, 5 h of student sessions, and at least 5 h of social events that then run late in the night.

FIG. 7. Diversity and gender balance regarding female tutors and students.

Conclusions: The full-week HITM school addressing university students and the one-day PTMC addressing high-school students make them aware of the different aspects of heavy-ion therapy and of interesting career paths, in emerging fields, where often there is lack of specialised personnel, for example, accelerator physics, medical physics, biophysics etc. They also provide information about upcoming modern techniques for cancer tumour therapy with heavy-ions and new research avenues, where clearly the development of technology and the expertise of research laboratories is crucial. Based on the "train-the-trainer" sustainability model of HITM school, the expectation is that participants of the HITM school will become tutors for the next years PTMCs.

ACKNOWLEDGEMENTS

The Heavy Ion Therapy Masterclass school was organised in the framework of the HITRIplus EU funded project, that received funds from the European Commission's Horizon 2020 Research and Innovation programme under Grant Agreement No 101008548. Therefore, the authors would like to acknowledge the contributions and support of the HITRIplus coordination, the HITRIplus pillar coordinator, and the HITRIplus WP5 education and training coordinator. The authors would also like to acknowledge the contributions of all institutes and presenters as well as of the matRad colleagues that handled the hands-on treatment planning sessions, Niklas Wahl, Hans Peter Wiesser and Joao Seco. Last but not least special thanks go to the core team of organisers and in particular to Damir Skrijelj, Amar Kapic and Rebecca Taylor for their enthusiasm, long hours of work and patience.

REFERENCES

[1] HITM school webpage: https://indico.cern.ch/event/1019104/

[2] HITRIplus project webpage: https://www.hitriplus.eu/

[3] Particle Therapy MasterClass webpage: https://indico.cern.ch/event/840212/

[4] ENLIGHT network webpage: https://enlight.web.cern.ch/

[5] CERN Courier webpage: https://cerncourier.com/

[6] CERN webpage: https://home.cern/

[7] GSI webpage: https://www.gsi.de/start/aktuelles

[8] SEEIIST webpage : https://seeiist.eu

[9] Graczykowski L., Nowakowski P., Foka P., *New developments for ALICE MasterClasses and the new Particle Therapy MasterClass*, in Proceedings of CHEP 2019

[10] Foka P., Particle therapy masterclass, Proceedings of EPS-HEP European Physics Society conference on High Energy Physics, 26-30 July 2021, online, to be published

[11] Foka P., Mamaras A., et al, Particle therapy masterclass, PoS Proceedings of vCONF A Virtual Tribute to Quark Confinement and the Hadron Spectrum Conference, 2-6 August 2021, online, to be published.

[12] UNSA webpage: https://www.unsa.ba

[13] IMC webpage: https://physicsmasterclasses.org/

[14] DKFZ webpage: https://www.dkfz.de/en/index.html

[15] matRad – an open-source dose calculation and treatment planning toolkit, https://github.com/e0404/matRad https://doi.org/10.5281/zenodo.3879615

[16] Cisternas E., Mairani A., Ziegenhein P., Jäkel O., Bangert M. (2015) *matRad - a multi-modality open-source 3D treatment planning toolkit.* In: Jaffray D. (eds) World Congress on Medical Physics and Biomedical Engineering, June 7-12, 2015, Toronto, Canada. IFMBE Proceedings, vol 51. Springer, Cham. https://doi.org/10.1007/978-3-319-19387-8_391

[17] Wieser, H.-P., Cisternas, E., Wahl, N., Ulrich, S., Stadler, A., Mescher, H., Müller, L.-R., Klinge, T., Gabrys, H., Burigo, L., Mairani, A., Ecker, S., Ackermann, B., Ellerbrock, M., Parodi, K., Jäkel, O. and Bangert, M. (2017), *Development of the open-source dose calculation and optimization toolkit matRad.* Med. Phys., 44: 2556-2568. https://doi.org/10.1002/mp.122Mairani A., Ziegenhein P., Jäkel O., Bangert M. (2015) *matRad - a multi-modality open-source 3D treatment planning toolkit.* In: Jaffray D. (eds) World Congress on Medical Physics and Biomedical Engineering, June 7-12, 2015, Toronto, Canada. IFMBE Proceedings, vol 51. Springer, Cham. https://doi.org/10.1007/978-3-319-19387-8_391

[18] D. Craft, M. Bangert, T. Long, D. Papp, J. Unkelbach, *Shared data for intensity modulated radiation therapy (IMRT) optimization research: the CORT dataset*, GigaScience, Volume 3, Issue 1, December 2014, 2047–217X–3–37, https://doi.org/10.1186/2047-217X-3-37

[19] CNAO: https://fondazionecnao.it/en/

[20] Haberer T., et al., Magnetic scanning system for heavy ion therapy NIM A 1993

[21] Bryant, Philip J, *PIMMS: Proton-ion medical machine study,* in CERN Yellow Reports: Monographs, ebook: 10.5170/CERN-2000-006

[22] HIT : https://www.klinikum.uni-heidelberg.de/interdisziplinaere-zentren/heidelberger-ionenstrahl-therapiezentrum-hit/

[23] SpatialChat webpage: https://spatial.chat

THREE DIMENSIONAL NANOWIRE NETWORKS FABRICATED BY ION TRACK NANOTECHNOLOGY AND THEIR APPLICATIONS

M. F. P. WAGNER, K.-O VOSS, C. TRAUTMANN, M. E. TOIMIL-MOLARES
GSI Helmholtzzentrum für Schwerionenforschung
Darmstadt, Germany
Email: F.M.Wagner@gsi.de

Abstract

The existing and future accelerator facilities at GSI and FAIR offer unique opportunities for interdisciplinary research, and in particular, for materials research and nanotechnology. On their way through polymers, swift heavy ions with GeV energy deposit enormous energy densities along their trajectory, causing long nanoscopic damage trails known as ion tracks. Ion-track technology utilizes the small track size (few nm) combined with the extensive track length (up to 100 µm and more) to synthesize and control the geometry of unique high aspect ratio nanostructures such as tailored nanochannels and nanowires. In particular, electrodeposition and ion-track nanotechnology provide an excellent platform for developing unique 3D networks of nanowires with controlled dimension, composition and crystallographic properties. Here, a summary of recent results obtained on the synthesis and characterization of stable 3D architectures of semiconductor and semimetal nanowires, and their implementation in the fields of photoelectrochemistry and thermoelectrics, is presented.

1. INTRODUCTION

The implementation of nanowires for applications such as thermoelectrics, catalysis, plasmonics, or photoelectrochemical water splitting for hydrogen generation requires both, an excellent control on geometry, crystallinity and composition of the individual nanostructures, as well as its successful assembly into 2D and 3D architectures.[1,2,3,4,5,6] Fabrication of 3D nanowire superstructures by e.g. vapour–liquid–solid processes has been reported; however, in most cases the tunability of the relevant parameters is limited.[7,8] Electrodeposition in etched ion-track membranes with interconnected nanochannels, on the other hand, offers high flexibility in the choice of relevant parameters.

Etched ion-track membranes with parallel nanochannels are widely used as templates for the creation of nanowires.[9,10,3,11,12] Their fabrication involves two separate processing steps. First, the template material is irradiated with energetic heavy ions creating so-called ion tracks.[13] High energy heavy-ion beams are provided at large accelerator facilities, such as the universal linear accelerator (UNILAC) of GSI (Darmstadt, Germany). The GSI UNILAC provides heavy ions (up to uranium) of specific energy up to 11.4 MeV/nucleon. Such high energy ion beams have a penetration range in polymers of about 120 µm, enabling the exposure of foils or stacks of polymer foils with thicknesses between ~ 6 and 100 µm.[9] The ion tracks are subsequently selectively dissolved and enlarged into channels by chemical etching. Control over the irradiation and etching conditions enables the production of membranes with channels of predefined geometries, sizes, and aspect ratios, with channel densities varying between a single channel and ~10^{10} cm^{-2}.[9,14,15,16,2] Beyond the etched ion-track templates with parallel channels, the irradiation of polymer foils under several incident angles in consecutive steps, followed by chemical etching resulted in novel etched ion-track membranes with nanochannel arrays tilted at various angles. Electrodeposition in these nanochannel networks, and subsequent removal of the polymer matrix result in highly ordered 3-D nanowire ensembles of various materials such as Pt, Bi, Sb, Cu_2O or ZnO. [2,1,4,17,3,18]

Three dimensional nanowire networks can span over cross-sectional areas of up to several cm^2. The nanowire networks can exhibit surface areas of up to ~250 cm^2 on a 1 cm^2 planar surface. In addition, the junctions between adjacent nanowires render excellent mechanical stability as well as electrical conductivity. The wires mechanically support one another and in case of breakage of individual wires, electrical or thermal transport can still occur via alternative nanowire interconnections. [19,2,1,20,6,21,] With several examples, we will illustrate how 3D nanowire networks combine the advantages and easy handling of macroscopic samples with the size-dependent properties of nanowires.

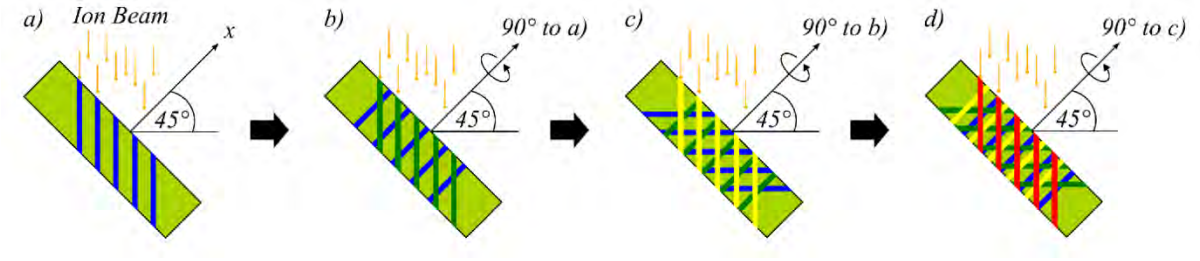

Fig. 1 Irradiation scheme for network templates with intersecting pores. The polymer foils are irradiated sequentially from four different directions (a-d) using swift heavy ions. During each irradiation step the foil is tilted by 45° towards the incoming beam. From M.F.P. Wagner, PhD Thesis, Technische Universität Darmstadt, 2018.[1,4]

2. EXPERIMENTAL

For the preparation of network templates, stacks of up to 4 polycarbonate foils with a thickness of 30 µm (Makrofol N, Bayer AG) are irradiated at an angle of 45° towards the incoming beam, consecutively from four different directions, with an angle of 90° between each direction, with swift heavy ions (typically Au or Bi) with a specific energy of 11.1 MeV/nucleon.[22]

Prior to chemical etching, the irradiated foils are exposed to UV light using a T-30M Vilber Lourmat lamp (30 W, 312 nm). This process is known to decrease the width of the pore size distribution after etching.[23,24,25] Selective chemical etching of the ion tracks performed in 6M NaOH solution at 50 °C, resulted in cylindrical channels.[9,13,24] The nanochannel diameter can be estimated by the radial etching rate (10-12 nm/min).[22] Fig. 2 illustrates various geometries that can be obtained by adjusting geometry and parameters of the etching process. They include channels with asymmetric bullet-like (a) and conical shapes (b), as well as symmetric cylindrical parallel (c) and interconnected (d) arrangements.[14,15,16,3,22] The latter ones are used as templates for the controlled electrodeposition of 3D nanowire networks.

In order to fill the pores by electroplating, first a conductive contact (e.g. ~200 nm thin gold layer) is sputtered on one side of the membrane. This initial layer is further reinforced by electroplating a thicker layer of in most cases gold or copper on top. The conductive layer serves as a working electrode in a three electrode electrochemical cell during the electrodeposition of the material of choice inside the channels. In most cases, the reaction is controlled via the potential (constant or pulsed) in order to avoid the occurrence of side reactions like hydrogen evolution.

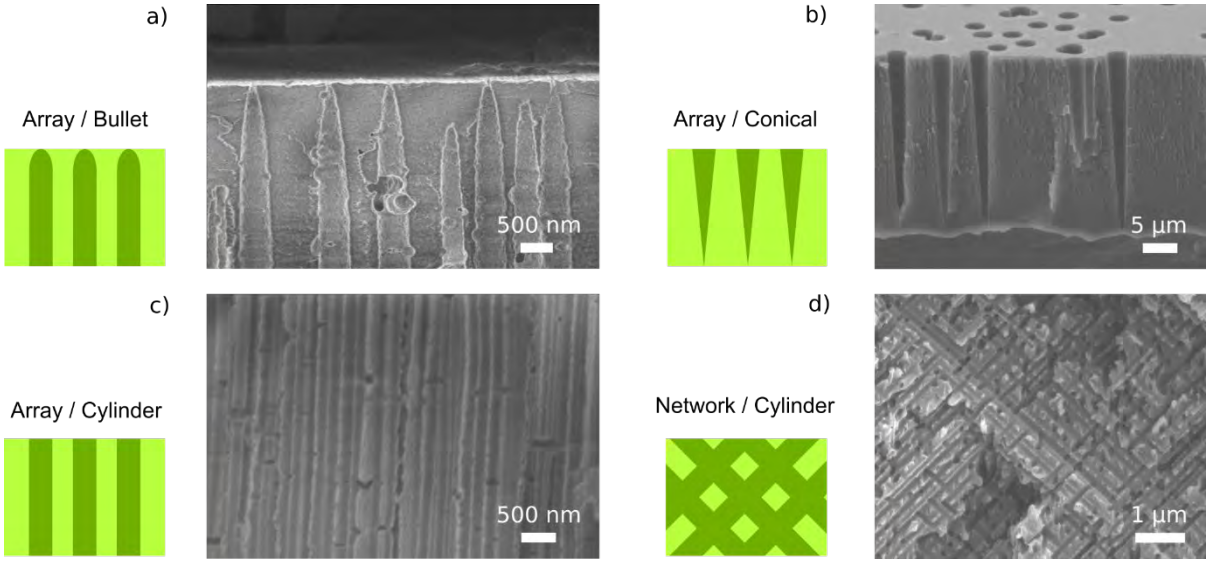

Fig. 2 Schematics and SEM images of possible pore geometries in ion track-etched membranes after the etching process. They include channels with asymmetric bullet-like (a) and conical shapes (b), as well as symmetric cylindrical parallel (c) and interconnected (d) arrangements. Partially adapted from L. Burr, PhD Thesis, Technische Universität Darmstadt, 2017 and L. Movsesyan, PhD Thesis, Technische Universität Darmstadt, 2017.

The electrodeposition process is monitored by recording the current between the working electrode and a counter electrode as a function of time. The electrodeposition parameters and the employed electrolytes determine the chemical composition, crystallinity, and crystallographic orientation of the resulting nanowires. The length of the nanowires can be adjusted by varying the electrodeposition time. Detailed descriptions of the fabrication processes for the presented materials can be found elsewhere. [9,26,3,27,4,1]

The 3D nanowire networks are typically characterized by a variety of methods, such as XRD, SEM and TEM. When direct access to the nanowires is required, the polymer membranes are dissolved in several consecutive baths of dichloromethane.

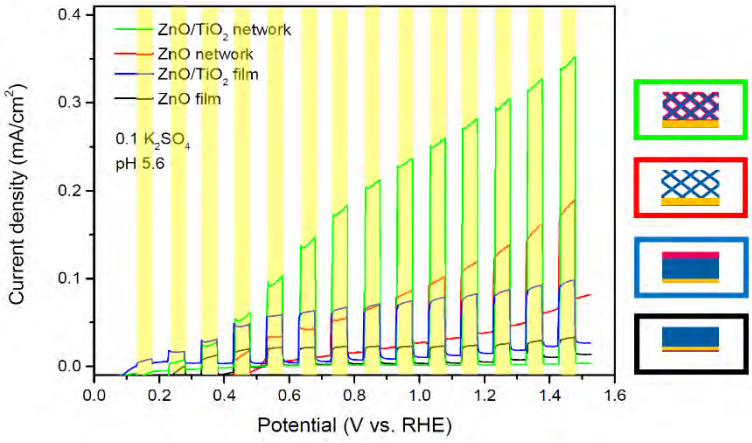

Fig. 3 Measured generated photocurrents for ZnO nanowire networks and ZnO films with and without a TiO2 protection layer during a linear bias voltage sweep. Yellow areas mark when the samples were illuminated, white areas when the samples were in dark. I think one does not right "copy" from… check the standard sentence. From L. Movsesyan et al., © Nanomaterials 8, 693 (2018).

3. RESULTS AND DISCUSSION

Here we show a few representative examples of 3D nanowire networks synthesized by electrodeposition in etched ion-track templates, including their synthesis and characterization.

3.1. ZnO nanowire networks as photoanodes for electrochemical water splitting

The compact design, mechanical stability, and high surface area of semiconducting 3D nanowire-based networks can be advantageous in enhancing the performance of e.g. gas sensors and batteries, as well as facilitating efficient light absorption and charge carrier transport in photoelectrodes.[5,28,29,30,31,32,33,34,35,36,3] The one-dimensional geometry of nanowires is expected to facilitate the transport of charge carriers to the nanowire-electrolyte interface due to short distances in thin nanowires, which in turn should lead to less charge recombination and an increase in photocurrent. Additionally, the large surface to volume ratio generates a large electrode-to-electrolyte interface. [3,33,34,35] The network structure here allows for a mechanically rigid and electrically reliable model system for which the various geometrical parameters can be adjusted independently.[35,3]

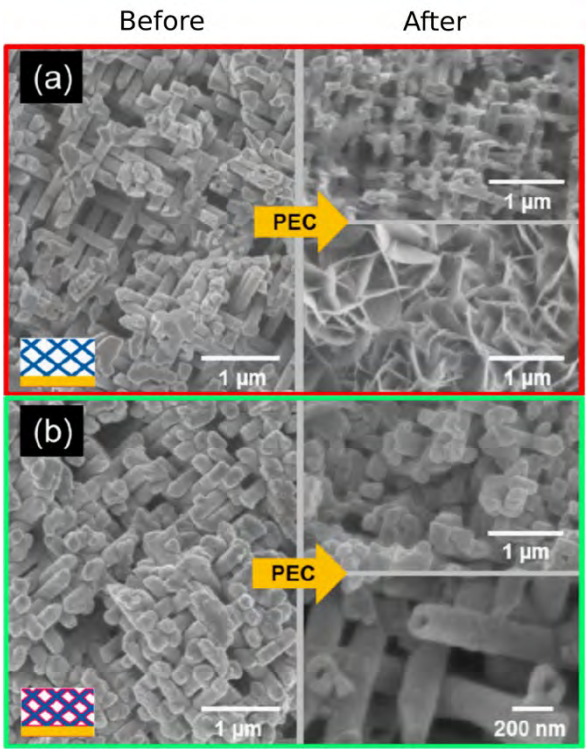

Fig. 4 SEM images of ZnO nanowire networks with and without TiO2 protection layer after photoelectron-chemical experiments. a) After one hour of reaction decay of nanowires and recrystalization of ZnO could be observed. b) After three hours of photocorrosion the network with TiO2 layer shows no or only small effects of photocorrosion. Adapted from L. Movsesyan et al., © Nanomaterials 8, 693 (2018).

To investigate the photoelectrochemical performance of the ZnO networks, the samples were inserted in a photoelectrochemical cell and immersed in 0.1M K_2SO_4 solution with a pH of 5.6. A Ag/AgCl (Sat. KCl) electrode was used as a reference and a Pt-wire as a counter electrode. The sample was then illuminated with an

Arc lamp source with an Xe lamp calibrated at AM 1.5 (1 sun). The illumination generates electron-hole pairs within the material that can be separated by applying a bias voltage. Fig. 3 shows the generated photo-current density as a function of the linearly sweeped bias voltage for ZnO nanowire networks and ZnO thin films, while the light was periodically switched off and on. The networks all had a wire density of ~$5.7 \cdot 10^9$ cm^{-2}, wire diameter of ~150 nm and a height of ~ 30 µm. Here, the potential is reported versus the reversible hydrogen electrode according to $E_{RHE} = E_{ag/AgCl} + 0.059\ pH + E^0_{Ag/AgCl}$. For both cases also samples with a 20 nm thick TiO_2 layer, that was applied by atomic layer deposition is shown. The TiO_2 layer was applied to protect ZnO versus photocorrosion as can be seen in Fig. 4. In general, the networks show a larger photocurrent when compared to the film counterparts. Whereas the films exhibit relatively constant photocurrent densities of 0.02 mA/cm^2 and 0.06 mA/cm2 for at 1.5 V vs. RHE with and without additional TiO_2 respectively, the networks generated 0.1 mA/cm^2 and 0.35 mA/cm^2 that were increasing with increasing bias voltage. The five times increase in generated current of networks was attributed to the geometrical advantages explained above. The higher performance of the TiO_2 coated samples is explained by additional electron-hole pairs generated within the TiO_2 layer and additional contributions to the charge carrier separation by the ZnO-TiO interface, which further helps to reduce the probability of charge carrier recombination.[37,38]

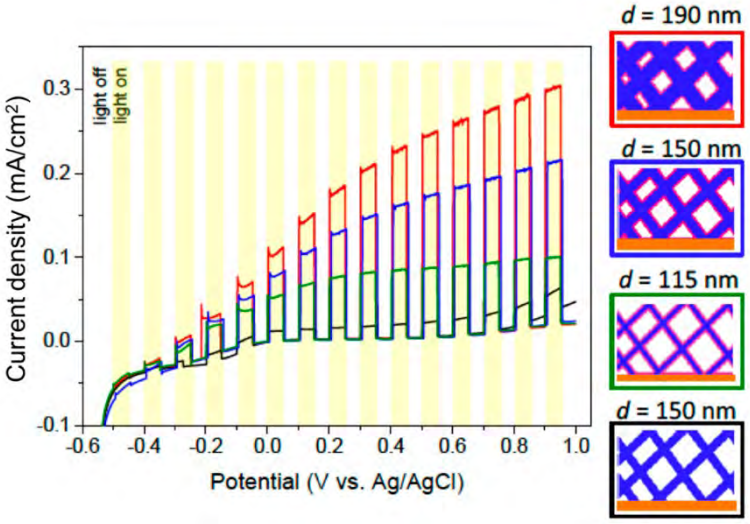

Fig. 5 Measured generated photocurrents for ZnO/TiO2 nanowire networks with different densities during a linear bias voltage sweep. Yellow and white areas mark when the samples were illuminated or in dark, respectively. From L. Movsesyan et al., © Nanomaterials 8, 693 (2018).

Additional experiments were performed on networks covered with 20 nm TiO_2 with a lower nanowire number density of $1.4 \cdot 10^9$ cm^{-2} and various nanowire diameters, shown in *Fig. 5*. Here, the larger the nanowire diameter the denser the network and, correspondingly, the higher the generated photocurrents. This was attributed to a larger amount of photoactive material in the denser networks. Also the variation of the photocurrents in dependence of the applied bias voltage increases with increasing nanowire diameter. In all cases the generated photocurrents of the networks were higher than the corresponding reference value for the thin films. These measurements showed that using nanowire networks as model systems enables a systematic investigation of the geometrical factors influencing the photoelectrochemical water splitting. Similar results were obtained for Cu_2O nanowire-based photocathodes.[17]

3.2. Bi and Sb nanowire networks for thermoelectric applications

The dimensionless thermoelectric figure-of-merit $Z \cdot T = S^2 \cdot \sigma \cdot T / (\lambda_{el} + \lambda_{ph})$ describes the efficiency of the material for thermoelectric applications.[39,40,41] Here, S is the Seebeck coefficient σ is the electrical conductivity and λ_{el}, λ_{ph} are the thermal conductivities by charge carriers and phonons respectively, of a given material. The interdependency of S, σ, and λ_{el} via the charge carrier density hinders the increase of ZT, and commercial thermoelectric materials nowadays exhibit maximal ZT values of ~1.[42,43,40,44] However, for widespread applications of thermoelectric modules a ZT of 3 would be required.[45,46,47]

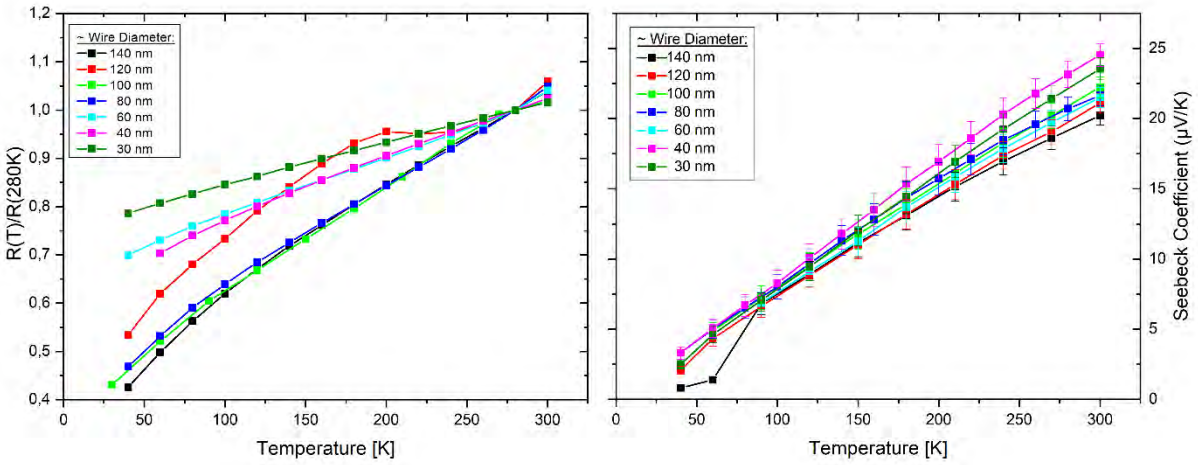

Fig. 6 Relative electrical resistance and Seebeck coefficient of Sb nanowire networks with a nanwire density of $1.4 \cdot 10^9$ i/cm^2 and various wire diametersin dependence of temperature, measured using a custom-build setup introduced elsewhere. Adapted from M.F.P. Wagner, PhD Thesis, Technische Universität Darmstadt, 2018.

The size effects that can occur in nanowires can help to decouple the electrical and thermal transport and thereby open up a route for further improvement of thermoelectric materials.[43,44,48] $Bi_{(1-x)}Sb_x$ bulk has already proven its worth for low temperature thermoelectric applications, and the material system is also ideal to study the influence of size effects on the transport and thermoelectrical properties[40,49,48,50] because the mean free paths of charge carriers and phonons in Bi and Sb at room temperature are in the order of 100 nm, and the Fermi wavelength in the order of 40 nm.[43,51,48,52,53] Size effects are, therefore, exhibited already at relatively large dimensions. Potentially, nanowire arrays exhibiting higher ZT values will yield more efficient thermocouples, of great interest for infrared sensor applications.[54]

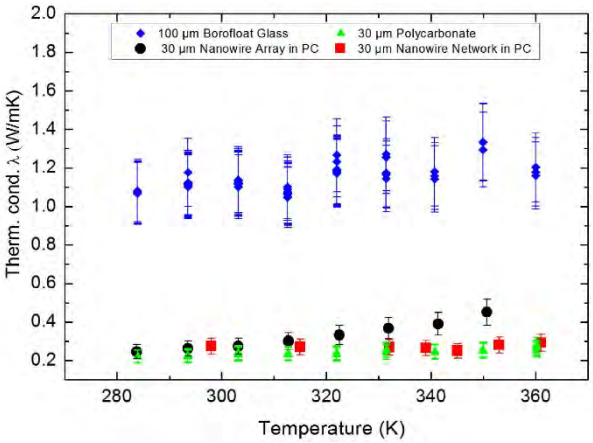

Fig. 7 Measured thermal conductivity of various samples as a function of temperature. The setup and measurement method is introduced elsewhere. From M.F.P. Wagner, PhD Thesis, Technische Universität Darmstadt, 2018.

Crossplane relative electrical resistivity and Seebeck coefficient of Sb nanowire networks as a function of temperature were investigated using a custom-build setup described elsewhere.[55,56,1] Fig. 6 shows the relative electrical resistance and Seebeck coefficient of Sb nanowire networks with ~$1.4 \cdot 10^9$ wires·cm^{-2} and wire diameters ranging between 30 to 140 nm as a function of temperature. The relative electrical resistance exhibits a metallic behaviour in all cases. The electrical resistivity of the nanowire networks with smaller wire diameters is dominated by the scattering of charge carriers with the nanowire surface and on grain boundaries, as theoretically described by Mayadas, Shatzkes, Fuchs, Sondheimer and Dingle, for both thin films and nanowires.[57,58,59,60] Therefore, with decreasing wire diameter, the electrical resistance is less affected by a decrease in temperature and the corresponding increase in mean free path of the charge carriers. The measured Seebeck coefficient for the Sb networks is in the order of 20 – 25 µV/K. Bulk Sb is

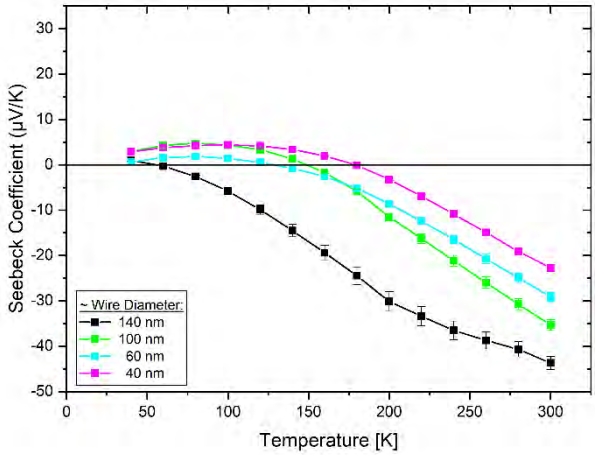

Fig. 8 Seebeck coefficient of Bi nanowire networks with a wire density of $1.4 \cdot 10^9$ i/cm^2 as a function of temperature measured using a custom-build device introduced elsewhere. From M.F.P. Wagner, PhD Thesis, Technische Universität Darmstadt, 2018.

very anisotropic and exhibits a maximal Seebeck coefficient of ~47 μV/K[40] for transport along the binary axis. According to XRD measurements the Sb networks exhibited a {01.2} texture, while also the {10.4} and {11.0} planes could be observed.[22] Due to this the Seebeck coefficient is smaller than ~47 μV/K, but comparable to the Seebeck coefficient of Sb bulk for other crystal orientations. The nanowire networks with smallest diameters exhibit a slightly higher Seebeck coefficient at room temperature, which might be due to small changes in crystallinity for the different wire diameters.[61,62,63] With decreasing temperature, the values monotonously decrease towards zero, as expected.[39,40] Fig. 7 shows the thermal conductivities of the polycarbonate template material as well as Sb nanowire arrays and nanowire networks measured using a method described elsewhere.[4] As comparison, also the well-known thermal conductivity of a Borofloat glass was measured. The thermal conductivity measured for nanowire networks and nanowire arrays (~0.3-0.4 W/mK) is significantly smaller than for bulk Sb (λ = 24 W/mK), which is attributed to enhanced phonon scattering at the nanowire's surfaces.[40,20,21,64] Since the Seebeck coefficient is similar to bulk and thermal conductivity is significantly suppressed, the thermoelectric efficiency ZT is most probably increased for the networks when compared to the bulk material, making nanowire networks promising materials for thermoelectric applications. To demonstrate this, absolute values of the electrical resistance should be measured in the future.

Fig. 8 shows the Seebeck coefficient of Bi nanowire networks with different wire diameters as a function of temperature. The Seebeck coefficients at room temperature are similar to previously reported values for nanowires and are comparable to theoretical values assigned to the bisectrix axis in Bi nanowires.[48,65] The Seebeck coefficient measured at room temperature decreases with decreasing nanowire diameter, due to the limitation of the mean free path of the charge carriers, ans possibly also to the influence of surface states which is more important for higher surface-to-volume ratios.[65,56,66,67] With decreasing temperature, the Seebeck coefficient decreases, exhibiting a change of sign which was not observed in the case of Sb nanowires. The data show that the temperature at which the sign changes occurs depends on the diameter of the nanowires, namely the temperature shifts to higher values with decreasing nanowire diameter. A similar behaviour was theoretically predicted by Murata et al. for Bi nanowires with crystals oriented along the bisectrix axis.[67] According to Murata et al. this sign change can be attributed to a different dependence of hole and electron mobility on nanowire diameter and temperature. In semimetals the Seebeck coefficient S is made up of contributions of holes and electrons according to $S = (S_n\sigma_n + S_p\sigma_p)/(\sigma_n + \sigma_p)$, where $S_{n,p}$ and $\sigma_{n,p}$ are the Seebeck coefficient and electrical conductivity of electrons and holes, respectively.[40] Under the assumption that both charge carrier densities are similar this means that at the transition temperature the mobility of holes becomes larger than the one of electrons.[65] At small dimensions also topological surface states can additionally contribute to transport.[56,66,67] As the properties of topological transport in bismuth and antimony are still under discussion, further transport measurements will unravel new and exciting effects on the transport behavior of tailored Bi and Sb nanostructures.[68]

4. CONCLUSION

Selected examples have been shown to illustrate how three dimensional nanowire networks, with macroscopic sizes (~cm), exhibit size-dependent properties. We predict that such well-defined tailored networks will serve as model systems to elucidate the behavior of porous materials, leading to the improvement of novel devices in several technological fields such as thermoelectrics, photoelectrochemistry, sensing, or catalysis. The combination of ion-track nanotechnology and electroplating yields nanowire networks of a large variety of technological relevant materials, while providing excellent control on their chemical, structural and morphological properties. The large number of well-defined interconnections between adjacent nanowires render the samples a remarkable mechanical stability even without a supporting matrix, as well as an excellent electrical connectivity.

ACKNOWLEDGEMENTS

Activities on the Bi and Sb nanowires are part of the Helmholtz Innovation Pool Project "MadQuanT". The nanowire samples were produced based on UMAT irradiations performed at the beam line X0 at the GSI Helmholtzzentrum für Schwerionenforschung, Darmstadt (Germany) in the frame of FAIR Phase-0.

REFERENCES

[1] Wagner, M. F. P. *et al.* Effects of Size Reduction on the Electrical Transport Properties of 3D Bi Nanowire Networks. *Adv. Electron. Mater.* **7**, 2001069 (2021).

[2] Rauber, M. *et al.* Highly-Ordered Supportless Three-Dimensional Nanowire Networks with Tunable Complexity and Interwire Connectivity for Device Integration. *Nano Lett.* **11**, 2304–2310 (2011).

[3] Movsesyan, L. *et al.* ZnO Nanowire Networks as Photoanode Model Systems for Photoelectrochemical Applications. *Nanomaterials* **8**, 693 (2018).

[4] Wagner, M. F. P., Völklein, F., Reith, H., Trautmann, C. & Toimil-Molares, M. E. Fabrication and thermoelectrical characterization of three-dimensional nanowire networks. *Phys. status solidi* **213**, 610–619 (2016).

[5] Ponzoni, A. *et al.* Ultrasensitive and highly selective gas sensors using three-dimensional tungsten oxide nanowire networks. *Appl. Phys. Lett.* **88**, 203101 (2006).

[6] Huber, T. E. & Graf, M. J. Electronic transport in a three-dimensional network of one-dimensional bismuth quantum wires. *Phys. Rev. B* **60**, 16880–16884 (1999).

[7] Norris, K. J. *et al.* Indium phosphide nanowire network: growth and characterization for thermoelectric conversion. in (eds. Kobayashi, N. P., Talin, A. A. & Islam, M. S.) 84670E (2012). doi:10.1117/12.929861.

[8] Stanley, S. A., Stuttle, C., Caruana, A. J., Cropper, M. D. & Walton, A. S. O. An investigation of the growth of bismuth whiskers and nanowires during physical vapour deposition. *J. Phys. D. Appl. Phys.* **45**, 435304 (2012).

[9] Toimil-Molares, M. E. Characterization and properties of micro- and nanowires of controlled size, composition, and geometry fabricated by electrodeposition and ion-track technology. *Beilstein J. Nanotechnol.* **3**, 860–883 (2012).

[10] Cassinelli, M. Thermoelectric Properties of Bi1-xSbx Nanowires Electrodeposited in Etched Ion-Track Membranes. (Technische Universität Darmstadt, 2016).

[11] Krieg, J. Characterization of individual Bi2Te3 nanowires electrodeposited in etched ion-track membranes for nano-ARPES and electrical transport studies. (TU Darmstadt, 2017).

[12] Müller, S. *et al.* Electrochemical Synthesis of Bi 1– x Sb x Nanowires with Simultaneous Control on Size, Composition, and Surface Roughness. *Cryst. Growth Des.* **12**, 615–621 (2012).

[13] Trautmann, C. Observation and chemical treatment of heavy-ion tracks in polymers. *Nucl. Instruments Methods Phys. Res. Sect. B Beam Interact. with Mater. Atoms* **105**, 81–85 (1995).

[14] Lee, P. L. J. *et al.* Etched ion-track membranes as tailored separators in Li–S batteries. *Nanotechnology* **32**, 365401 (2021).

[15] Ulrich, N. *et al.* Conical Nanotubes Synthesized by Atomic Layer Deposition of Al2O3, TiO2, and SiO2 in Etched Ion-Track Nanochannels. *Nanomaterials* **11**, 1874 (2021).

[16] Laucirica, G. *et al.* Shape matters: Enhanced osmotic energy harvesting in bullet-shaped nanochannels. *Nano Energy* **71**, 104612 (2020).

[17] Yang, F. *et al.* Cu 2 O/TiO 2 Nanowire Assemblies as Photocathodes for Solar Hydrogen Evolution: Influence of Diameter, Length and NumberDensity of Wires. *Zeitschrift für Phys. Chemie* **234**, 1205–1221 (2020).

[18] Caddeo, F. *et al.* Tuning the Size and Shape of NanoMOFs via Templated Electrodeposition and Subsequent Electrochemical Oxidation. *ACS Appl. Mater. Interfaces* **11**, 25378–25387 (2019).

[19] Pennelli, G., Totaro, M., Piotto, M. & Bruschi, P. Seebeck Coefficient of Nanowires Interconnected into Large Area Networks. *Nano Lett.* **13**, 2592–2597 (2013).

[20] Verdier, M., Lacroix, D. & Termentzidis, K. Thermal transport in two- and three-dimensional nanowire networks. *Phys. Rev. B* **98**, 155434 (2018).

[21] Roslyak, O. & Piryatinski, A. Thermoelectric properties of semiconductor nanowire networks. *J. Appl. Phys.* **119**, 125107 (2016).

[22] Wagner, M. F. P. Bi and Sb Nanowire Assemblies for Thermoelectric Applications. (Technische Universität Darmstadt, 2018).

[23] Cornelius, T. W. *et al.* Nanopores in track-etched polymer membranes characterized by small-angle x-ray scattering. *Nanotechnology* **21**, 155702 (2010).

[24] Pépy, G. *et al.* Cylindrical nanochannels in ion-track polycarbonate membranes studied by small-angle X-ray scattering. *J. Appl. Crystallogr.* **40**, s388–s392 (2007).

[25] Ferain, E. & Legras, R. Heavy ion tracks in polycarbonate. Comparison with a heavy ion irradiated model compound (diphenyl carbonate). *Nucl. Instruments Methods Phys. Res. Sect. B Beam Interact. with Mater. Atoms* **82**, 539–548 (1993).

[26] Movsesyan, L., Schubert, I., Yeranyan, L., Trautmann, C. & Eugenia Toimil-Molares, M. Influence of electrodeposition parameters on the structure and morphology of ZnO nanowire arrays and networks synthesized in etched ion-track membranes. *Semicond. Sci. Technol.* **31**, 014006 (2016).
[27] Wagner, M. F. P. Bi and Sb Nanowire Assemblies for Thermoelectric Applications. (2018).
[28] Alenezi, M. R., Henley, S. J., Emerson, N. G. & Silva, S. R. P. From 1D and 2D ZnO nanostructures to 3D hierarchical structures with enhanced gas sensing properties. *Nanoscale* **6**, 235–247 (2014).
[29] Liu, R., Duay, J. & Lee, S. B. Heterogeneous nanostructured electrode materials for electrochemical energy storage. *Chem. Commun.* **47**, 1384–1404 (2011).
[30] Duay, J., Gillette, E., Hu, J. & Lee, S. B. Controlled electrochemical deposition and transformation of hetero-nanoarchitectured electrodes for energy storage. *Phys. Chem. Chem. Phys.* **15**, 7976 (2013).
[31] Wei, D. *et al.* A Nanostructured Electrochromic Supercapacitor. *Nano Lett.* **12**, 1857–1862 (2012).
[32] Hochbaum, A. I. & Yang, P. Semiconductor Nanowires for Energy Conversion. *Chem. Rev.* **110**, 527–546 (2010).
[33] Zhong, M., Ma, Y., Oleynikov, P., Domen, K. & Delaunay, J.-J. A conductive ZnO–ZnGaON nanowire-array-on-a-film photoanode for stable and efficient sunlight water splitting. *Energy Environ. Sci.* **7**, 1693 (2014).
[34] van de Krol, R., Liang, Y. & Schoonman, J. Solar hydrogen production with nanostructured metal oxides. *J. Mater. Chem.* **18**, 2311 (2008).
[35] Shi, J., Hara, Y., Sun, C., Anderson, M. A. & Wang, X. Three-Dimensional High-Density Hierarchical Nanowire Architecture for High-Performance Photoelectrochemical Electrodes. *Nano Lett.* **11**, 3413–3419 (2011).
[36] Wang, Y. *et al.* Fully Solar-Powered Photoelectrochemical Conversion for Simultaneous Energy Storage and Chemical Sensing. *Nano Lett.* **14**, 3668–3673 (2014).
[37] Liu, M., Nam, C.-Y., Black, C. T., Kamcev, J. & Zhang, L. Enhancing Water Splitting Activity and Chemical Stability of Zinc Oxide Nanowire Photoanodes with Ultrathin Titania Shells. *J. Phys. Chem. C* **117**, 13396–13402 (2013).
[38] Hu, S. *et al.* Amorphous TiO 2 coatings stabilize Si, GaAs, and GaP photoanodes for efficient water oxidation. *Science (80-.).* **344**, 1005–1009 (2014).
[39] H. Julian Goldsmid. *Introduction to Thermoelectricity*. (Springer, Berlin, Heidelberg, 2010). doi:10.1007/978-3-642-00716-3.
[40] *Thermoelectrics Handbook. Thermoelectrics Handbook* (CRC Press, 2006).
[41] Vedernikov, M. V. & Iordanishvili, E. K. A.F.Ioffe and origin of modern semiconductor thermoelectric energy conversion. *Int. Conf. Thermoelectr. ICT, Proc.* 37–42 (1998) doi:10.1109/ICT.1998.740313.
[42] Szczech, J. R., Higgins, J. M. & Jin, S. Enhancement of the thermoelectric properties in nanoscale and nanostructured materials. *J. Mater. Chem.* **21**, 4037–4055 (2011).
[43] Heremans, J. P. Low-Dimensional Thermoelectricity. *Acta Phys. Pol. A* **108**, 609–634 (2005).
[44] Cornett, J. E. & Rabin, O. Thermoelectric figure of merit calculations for semiconducting nanowires. *Appl. Phys. Lett.* **98**, 182104 (2011).
[45] Bell, L. E. Cooling, Heating, Generating Power, and Recovering Waste Heat with Thermoelectric Systems. *Science (80-.).* **321**, 1457–1461 (2008).
[46] DiSalvo, F. J. Thermoelectric Cooling and Power Generation. *Science (80-.).* **285**, 703–706 (1999).
[47] Casati, G., Mejía-Monasterio, C. & Prosen, T. Increasing Thermoelectric Efficiency: A Dynamical Systems Approach. *Phys. Rev. Lett.* **101**, 016601 (2008).
[48] Kim, J., Shim, W. & Lee, W. Bismuth nanowire thermoelectrics. *J. Mater. Chem. C* **3**, 11999–12013 (2015).
[49] Lin, Y.-M., Cronin, S. B., Ying, J. Y., Dresselhaus, M. S. & Heremans, J. P. Transport properties of Bi nanowire arrays. *Appl. Phys. Lett.* **76**, 3944–3946 (2000).
[50] Heremans, J. & Thrush, C. M. Thermoelectric power of bismuth nanowires. *Phys. Rev. B* **59**, 12579–12583 (1999).
[51] Cornelius, T. W. & Toimil-Molares, M. E. Finite- and Quantum-Size Effects of Bismuth Nanowires. in *Nanowires* (InTech, 2010). doi:10.5772/39516.
[52] Yang, F. Y. *et al.* Large Magnetoresistance of Electrodeposited Single-Crystal Bismuth Thin Films. *Science (80-.).* **284**, 1335–1337 (1999).
[53] Molares, M. E. T. *et al.* Fabrication and contacting of single Bi nanowires. *Nanotechnology* **15**, S201–S207 (2004).
[54] Lindeberg, M., Yousef, H., Rödjegård, H., Martin, H. & Hjort, K. A PCB-like process for vertically configured thermopiles. *J. Micromechanics Microengineering* **18**, 065021 (2008).
[55] Mueller, S. Morphological, Structural, and Compositional Characterization of Electrodeposited Bi1−xSbx Nanowires. (Ruprecht–Karls–Universit¨at Heidelberg, 2012).

[56] Cassinelli, M. *et al.* Influence of surface states and size effects on the Seebeck coefficient and electrical resistance of Bi 1−x Sb x nanowire arrays. *Nanoscale* **9**, 3169–3179 (2017).
[57] Mayadas, A. F. & Shatzkes, M. Electrical-Resistivity Model for Polycrystalline Films: the Case of Arbitrary Reflection at External Surfaces. *Phys. Rev. B* **1**, 1382–1389 (1970).
[58] Dingle, R. B. The electrical conductivity of thin wires. *Proc. R. Soc. London. Ser. A. Math. Phys. Sci.* **201**, 545–560 (1950).
[59] Fuchs, K. The conductivity of thin metallic films according to the electron theory of metals. *Math. Proc. Cambridge Philos. Soc.* **34**, 100–108 (1938).
[60] Sondheimer, E. H. The mean free path of electrons in metals. *Adv. Phys.* **1**, 1–42 (1952).
[61] Picht, O. *et al.* Tuning the Geometrical and Crystallographic Characteristics of Bi 2 Te 3 Nanowires by Electrodeposition in Ion-Track Membranes. *J. Phys. Chem. C* **116**, 5367–5375 (2012).
[62] Karim, S. *et al.* Synthesis of gold nanowires with controlled crystallographic characteristics. *Appl. Phys. A* **84**, 403–407 (2006).
[63] Liu, J. *et al.* Electrochemical fabrication of single-crystalline and polycrystalline Au nanowires: the influence of deposition parameters. *Nanotechnology* **17**, 1922–1926 (2006).
[64] Hochbaum, A. I. *et al.* Enhanced thermoelectric performance of rough silicon nanowires. *Nature* **451**, 163–167 (2008).
[65] Murata, M., Yamamoto, A., Hasegawa, Y., Komine, T. & Endo, A. Theoretical modeling of electrical resistivity and Seebeck coefficient of bismuth nanowires by considering carrier mean free path limitation. *J. Appl. Phys.* **121**, 014303 (2017).
[66] Shin, H. S. *et al.* The surface-to-volume ratio: a key parameter in the thermoelectric transport of topological insulator Bi 2 Se 3 nanowires †. *Nanoscale* **8**, 13552–13557 (2016).
[67] Gooth, J. *et al.* Thermoelectric performance of classical topological insulator nanowires. *Semicond. Sci. Technol.* **30**, 015015 (2015).
[68] Schindler, F. *et al.* Higher-order topology in bismuth. *Nat. Phys.* **14**, 918–924 (2018).

CHARACTERISTICS OF FINE PARTICULATES ELEMENTAL COMPOSITION OF TWO LARGEST CITIES IN INDONESIA USING ION BEAM ANALYSIS

M. SANTOSO
National Research and Innovation Agency of Indonesia (BRIN)
Bandung, Indonesia
Email: hayat@batan.go.id

D. D. LESTIANI[1], A. ATANACIO[2], D. COHEN[2], M. MANOHAR[2], Z. PASTUOVIC[2], S. KURNIAWATI[1], E. DAMASTUTI[1], D. A. PERMADI[3]
[1]National Research and Innovation Agency of Indonesia (BRIN)
Bandung, Indonesia
[2]ANSTO Centre for Accelerator Science,
Lucas Heights, NSW 2234, Australia
[3]Institut Teknologi Nasional Bandung (ITENAS)
Bandung, Indonesia

Abstract

Urban air pollution is a major problem in Indonesia and has growing recognition especially on the health effect problems resulting from airborne particles exposure. Even some cities have been identified to have high levels of air pollution with an emerging need of source apportionment. Therefore, characterization of the chemical composition of air particulates is a fundamental step for identification of pollutant sources. These chemical compositions are generally at trace levels thus require an accurate and suitable analytical method such as Ion Beam Analysis (IBA) which is fast, effective and sensitive. In this study, a non-destructive IBA method was applied to characterize $PM_{2.5}$ of ambient air samples in the two largest cities in Indonesia, Jakarta and Surabaya, which have different characteristic as urban cities. Several elemental compositions i.e., F, Na, Al, Si, P, S, Cl, K, Ca, Ti, V, Cr, Mn, Fe, Co, Ni, Cu, Zn, As, Br, Rb, Sr, Y, Zr and Pb, were well quantified for both cities. It was found that Surabaya has high concentration of heavy metals such as, Pb, Fe and Zn, while Jakarta has higher level of Cu concentration than other elements. The results can be further utilized to identify their potential sources while at the same time can serve as science-based evidence for particulate matter pollution mitigation program formulation in each city.

1. INTRODUCTION

Fine particulate matter (i.e., $PM_{2.5}$, particles with an aerodynamic diameter equal to or lower than 2.5 μm in ambient air) is known to have a detrimental impact on human health i.e., cardiovascular disease, pulmonary disease, increasing risk of diabetes, Alzheimer and lower cognitive performance [1-3]. Fine particulate matter has been associated to several million deaths annually. In 2019, air pollution was estimated to contribute to nearly 6.7 million deaths worldwide which was dominantly caused is by fine particulate matter [4]. Fine particles are mainly derived from chemical reactions including anthropogenic combustion-related emissions such as vehicular emissions, industrial emissions (e.g., coal), and biomass burning also secondary aerosol which is formed through gas to particle conversion mechanism [5,6]. The assessments of ambient PM concentrations and chemical composition become important to identify the possible sources and their contributions, so the results may support in planning and implementing more effective control policies for PM air pollution [7-9]. Different compositional share of elements to the total PM concentration would likely contribute to different degree of health impacts.

In Indonesia, urban air pollution becomes a major problem and it has growing recognition from the public due to potential detrimental health effects or even premature mortality linked to airborne particles. The country with an estimated population of over 261 million people and becomes the world's 4th most populous country, has experienced increased economic development for the last decades which often led to rapid and unplanned urbanization. Escalation of economic activity associated with increasing intensity in transportation and industrial sectors, lead to the growth of fossil fuel energy use which in turn causing the higher level of air pollution. Several cities in Indonesia have also been identified for their high levels of air pollution, especially in mega and big cities resulting in a public concern on air pollution monitoring in big cities [10]. This problem has been encountered in Jakarta and Surabaya, recognized as the two largest cities in Indonesia in terms of population and administrative areas. As the capital city of Indonesia with total population of nearly 11 million and the largest city in Southeast

Asia, air quality in Jakarta becomes public concern The city has 4 major industrial estates within the city and surrounded by more than 10 industrial estates within radii of 20–30 km from the city center. Most of them consume diesel oil with high sulphur content and low energy efficiency with lack of air pollution control device. The land transportation is characterized with medium to heavy daily traffic jams in all type of roads even though public transport keeps improving. These conditions coupled with local meteorological condition contribute to the deterioration of urban air quality. Our previous study reported that the annual mean of $PM_{2.5}$ in Jakarta from 2010 to 2019 were measured in the range of 15.5 – 31 μg/m^2 and were considered to exceed the Indonesian annual mean national ambient air quality standard (NAAQS) of 15 μg/m^3 [11]. Similar condition has been also encountered in Surabaya which is known as the second largest city in Indonesia. Our previous study showed that the annual mean of $PM_{2.5}$ in Surabaya from 2012 to 2017 were measured in the range of 15 to 20 μg/m^2 which were well above the Indonesian NAAQS [8]. Another study confirmed the contribution of vehicular emission to the high levels of daily concentration of air pollutants [12]. In addition, the city has busiest trading city ports in Asia and it is also surrounded by several industrial estates in its vicinity.

These two cities have been experiencing high levels of fine PM concentrations. Both cities have different intensities in industrial and other anthropogenic activities, thus the characterization of air particulate chemical composition is significantly needed. These chemical compositions are generally at trace levels thus require an accurate and suitable analytical method. Nuclear analytical techniques such as neutron activation analysis (NAA), X-ray fluorescence (XRF) and ion beam analysis (IBA) are highly suitable for characterizing the elemental compositions of PM samples [13-15]. Ion beam analytical technique is particularly suitable for fine particle filter paper analysis since the particle loading on these filters can be considered to be thin targets for MeV ion beams used in their analysis [16]. The IBA techniques offer some advantages such as being considerably fast with only needing a few minutes of analysis, non-destructive, no sample preparation required, able to analyse sub micrograms of samples, and multi-elemental analysis simultaneously [17].

In this study, IBA analysis was applied for the multi-elemental characterization of aerosol fine particles in cities of concerned of Jakarta and Surabaya. The measurement of the PM elemental composition is a key factor in the utilization of the data for the determination of possible sources, whose identification and apportionment are an important step in the air quality management process. Therefore, the objectives of this study were to compare PM elemental compositions in both cities of Jakarta and Surabaya. To the extent possible, detailed information of the measurement results for both cities affected by the difference in the nature of emission sources was provided for formulation of the precise and effective regulations related to the air quality management plan.

2. METHODOLOGY

2.1. Sampling site

Sampling of ambient $PM_{2.5}$ was done for 24-hours using GENT sampler from 2019 – mid 2020 carried in the two target cities. Note that there are differences in the urban setting for both cities, for example the scale of areas and population, type of major industrial activities, as well as the traffic characteristics and the urban sprawl. The sampling was done at the office of Environmental Protection Agency of Jakarta Provincial (Jakarta EPA) located in Central Jakarta as shown in Fig. 1a. This site is in the city center and surrounded by arterial roads with heavy traffic volumes especially during the morning and evening rush hours.

There are two sampling sites in Surabaya: East Surabaya (1) and West Surabaya (2) as seen in Fig. 1b. East-South Surabaya was selected due to the domination of industrial estates while West Surabaya site was selected because it is located close to port, but no metal industries are located surrounding the site.

Sampling was carried out using dichotomous sampler Gent stacked filter unit in each site, once a week, at a flow rate of 15–18 L/min at the two sampling sites. The $PM_{2.5}$ air particulate samples were collected on a 0.4 μm pore size filter for 24-hours using GENT sampler from 2019 – mid 2020. We successfully collected totally 105 samples which consists of: 32 samples from Jakarta, 35 samples from East-South Surabaya and 38 samples from West Surabaya. The samples were delivered back to BATAN laboratory for mass and BC analysis.

2.2. Particulate Matter (PM) and Black Carbon (BC) Analysis

Determination of mass concentration $PM_{2.5}$ was carried out by gravimetric method using Mettler Toledo micro balance. The filters were weighed before and after the sampling period to determine the particulate mass

collected and then divided by the total volume of air that passed through the filter to obtain the particulate mass concentration. Before weighing, the filter must be conditioned in a room with humidity between 45-55% and a temperature of 18-25°C. Fine APM ($PM_{2.5}$) is obtained from the weighing of the sample weights on the fine filter.

Determination of carbon in the filter was based on the process of light reflection. The absorption and reflection of visible light by airborne PM in the filter depends on particle concentration, density, refractive index and size. The black carbon concentrations of the samples were determined by reflectance measurement using a Digital Smoke Stain Reflectometer EEL Model 43D. Measurement of BC in the filter was done based on the light absorption principle to quantify the amount of light that is absorbed by the filter sample using the assumed value of the average coefficient of particle mass absorption of 5.7 m^2/g.

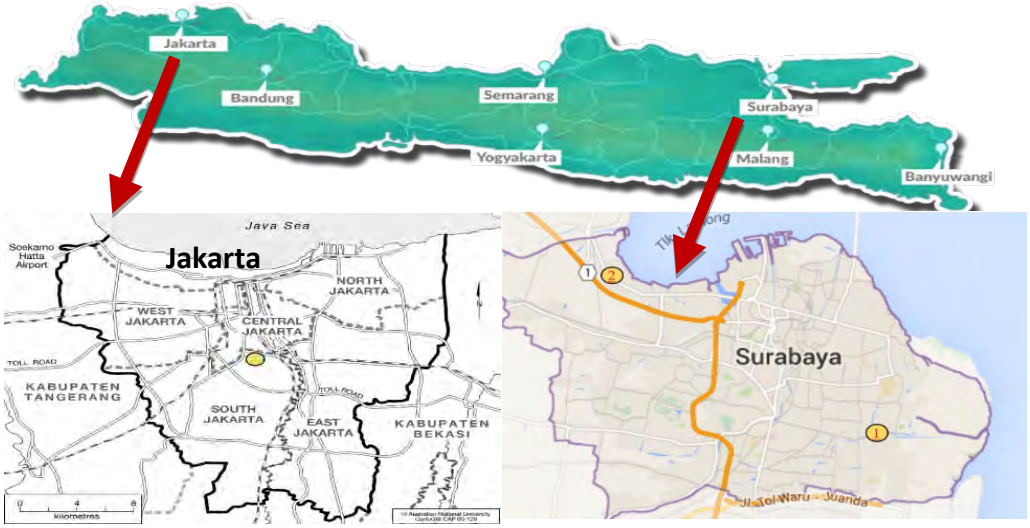

(a) (b)

FIG.1. The sampling locations in Jakarta (a) and Surabaya (b)

2.3. Elemental Analysis

The samples were analysed using a non-destructive IBA techniques including proton induced x-ray emission (PIXE), proton induced gamma-ray emission PIGE), and proton elastic scattering analysis (PESA) at the Australian Nuclear Science and Technology (ANSTO) facility, which has the capability of multi-element analysis with detection limits in the order of ng/cm^2. The IBA technique uses an 8 mm diameter beam of 2-3 MeV protons with 10-15 nA target current. A total of 18 elements were successfully detected such as Na, Al, Si, S, Cl, K, Ca, Ti, V, Cr, Mn, Fe, Ni, Cu, Zn, As, Br, and Pb.

3. RESULTS AND DISCUSSIONS

3.1. PM and BC mass concentration

Comparative analysis was done for the mass concentration (i.e. $PM_{2.5}$ and PM_{10}) and the concentration of black carbon in fine particulate in Jakarta and Surabaya and the results are presented in Table 1. The mean concentrations of $PM_{2.5}$ and PM_{10} in Jakarta were 16.13 and 34.75 $\mu g/m^3$, respectively whereas for Surabaya were 18.52 and 45.18 $\mu g/m^3$, respectively. The results of mean concentrations of $PM_{2.5}$ and PM_{10} in Surabaya were higher than those measured in Jakarta. The 24-hour average $PM_{2.5}$ and PM_{10} mass fraction results for the two cities are shown in Fig. 2. The box represents 25-75% of the distributions of the $PM_{2.5}$ and PM_{10} concentrations while the horizontal bar in the box indicates the median. The points lying outside the range defined by the whiskers (extreme events) are plotted as outlier dots. Second to the previous finding, Fig. 2 showed that the level of average $PM_{2.5}$ and PM_{10} concentrations in Surabaya were also higher than those measured in Jakarta. Note that, PM

concentrations in Surabaya were obtained by averaging the data from 2 sampling sites; East and West Surabaya, which shows the potential contribution of more emission sources to the two sites while only one site was considered for Jakarta. It seemed that contributions of industrial and port emissions to the measured PM were crucial. Especially the shipping emission caused by continuous burning of marine fuel oil (MFO) with sulfur content of more than 10,000 ppm with no control device installed in the tail pipe. Industry also uses heavy diesel oil (HDO) for back-up generator mainly as well as coal.

Strict implementation of Large-Scale Social Restriction (LSSR) policy due to Covid-19 pandemic in the early of 2020 was promulgated and it was reported to significantly reduce the PM concentration especially in Jakarta (Santoso et al., 2021). Jakarta implemented the LSSR policy earlier than Surabaya since March 2020 while the latter implemented the LSSR policy in the end of April 2020. During the implementing months of LSSR, the concentration of $PM_{2.5}$ in Jakarta reduced significantly, reached almost 40% compare to the period months in the previous year [18]. In Surabaya the reduction of $PM_{2.5}$ concentration only 7-15% but has significant decrease in the heavy metal concentration [19]. In addition, Jakarta is very strict in implementing the LSSR because the first Covid case was found in Depok, about 30 km from Jakarta. The implementation of the LSSR in 2020 has affected fuel consumption in Jakarta, including for the industrial sector. Annual fuel consumption for all types of fuel tends to decrease from 2019 to 2020. The reduction rate for diesel consumption reaches 23% which results in a reduction in air pollutant emissions from industrial activities (https://ditppu.menlhk.go.id/simpel/gis/konsumsienergi). LSSR also limits the intensity of mobile transportation, especially on the main roads in the city. The distribution of fuels including gasoline and diesel in 2020 has decreased due to less traffic mobility which is one of the reasons for the low $PM_{2.5}$ in Jakarta. Therefore, it can be concluded that transportation contributed significantly to the measured PM in Jakarta site, while in Surabaya it was mainly contributed by the industrial smelter. Compared to previous study by Santoso et al (2020), the concentrations of $PM_{2.5}$ and PM_{10} measured during the period of 2019-2020 in Jakarta site are lower than those measured in the similar period for the two sites in Surabaya. However, $PM_{2.5}$ values measured for both cities exceeded the Indonesian NAAQS of 15 μg m^{-3} and according to the United States PM_{10} annual standard, both values of PM_{10} from Jakarta and Surabaya are still below the standards of 50 μg m^{-3} [10].

TABLE 1. PM mass and BC concentrations measured in Jakarta and Surabaya

	Surabaya (μg/m^3)[a]		Center Jakarta (μg/m^3)	
	Average	Range	Average	Range
$PM_{2.5}$	18.52 ± 8.09	3.17-33.35	16.13 ± 6.22	5.00-29.29
PM_{10}	45.18 ± 19.92	11.42-92.51	34.75 ± 12.39	10.89-66.74
BC	3.76 ± 1.63	0.53-6.85	3.39 ± 0.75	1.31-5.02

Note: [a] Values were averaged from two sites

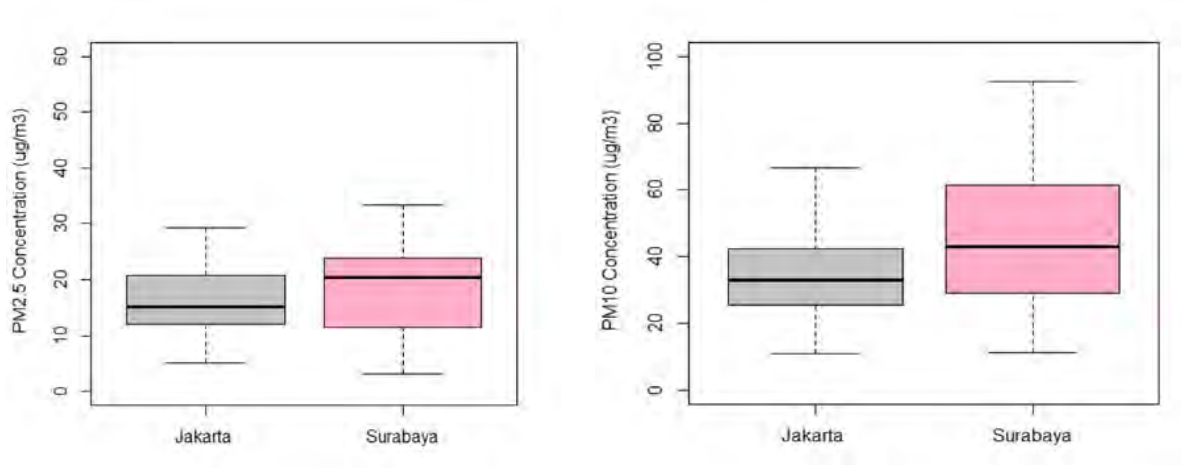

(a) (b)

FIG. 2. Box and whisker plot of $PM_{2.5}$ (a), and PM_{10} (b) concentrations of Jakarta and Surabaya 2019 - mid 2020

The box and whisker plot for the $PM_{2.5}$ Black Carbon (BC) measurements at the Jakarta and Surabaya cities are presented in Fig.3. BC is generally emitted into the atmosphere due to incomplete combustion. In this study, BC measurement was conducted using reflectance method. To avoid inaccuracies in reflectance and absorbance for large particle sizes, the BC measurements were only done for fine APM. Black carbon is a form of impurity from carbon that results from incomplete combustion of fossil fuels or biomass burning. Black carbon (BC) is a major contributor to the fine particulate matter in the atmosphere and responsible for the light absorption by particles [20]. The results of BC concentration are presented in Table 1. The average BC concentrations for Jakarta and Surabaya were 3.39 and 3.76 $\mu g/m^3$, respectively. Similar to the PM concentration, BC concentrations in Surabaya were measured higher than those measured in Jakarta. The first site in Surabaya was close to the industrial areas within 10 km radii with the seasonal reoccurring open burning practice. The second site is close to the port which emits substantial BC emission from the shipping call activity. In addition to the local traffic, the above-mentioned emission sources were potentially contributing to the higher levels of BC measured at the two sites.

The BC concentration of Surabaya site during this study period was the highest compared to other cities in Java Island such as Jakarta, Bandung, Semarang, Tangerang and Yogyakarta obtained from the previous study by Santoso et al. [10]. BC concentration in Jakarta during 2019-2020 tends to increase compared to the 2010-2017 period. Notably, BC concentrations measured at the two cities in this study were far higher compared to the other cities inside and outside Java Island [10]. The BC sources in Jakarta were potentially contributed to motor vehicles as the sampling site in Jakarta is located near one of the busiest arterial roads in the town [21].

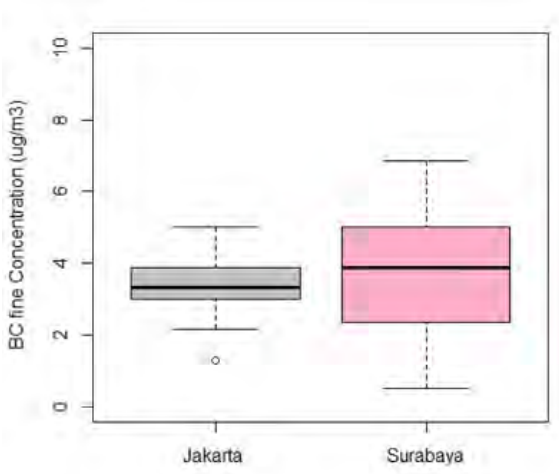

FIG. 3. Box and whisker plot of $PM_{2.5}$ Black Carbon (BC) concentrations of Jakarta and Surabaya 2019 - mid 2020

3.2. $PM_{2.5}$ elemental concentration

Elemental characterization of $PM_{2.5}$ was done using IBA facilities at ANSTO, Australia. IBA techniques of PIXE, PIGE, RBS and PESA were used simultaneously to measure elemental concentrations of more than 20 different elements found in fine particle ($PM_{2.5}$) air pollution, which can be used for characterisation and fingerprint of pollution sources in order to estimate their contributions to the total mass loading. These methods have been demonstrated world-wide for aerosol pollution studies [15,16,22]. These data together with their errors and minimum detectable limits were used in Positive Matrix Factorisation (PMF) analyses to quantitatively determine source fingerprints and their contributions to the total measured fine mass [15,22]. In this study, IBA techniques was applied to fine particulate samples from Surabaya and Jakarta for elemental characterization. The elemental composition of $PM_{2.5}$ of Jakarta and Surabaya are presented in Table 2. The results obtained indicated that the chemical composition of fine particulates of $PM_{2.5}$ in Jakarta was dominated by Sulphur, followed by Aluminium and Silicon as crustal elements which may come from the road dust. The major composition of $PM_{2.5}$ in Surabaya, either form site 1 or site 2, is also Sulphur. The use of fuels containing high concentration of S is one of the main sources of S emissions which may be contributed by industry and shipping. There are several types of diesel fuel or biodiesel that have a sulphur content ranging from 300 to 2500 parts per million (ppm) [23] but

MFO used for shipping certainly has higher range above 10,000 ppm. This is one of the reasons of the high level of S in $PM_{2.5}$ in urban areas of Indonesia. The potassium (K) concentrations in Surabaya were slightly higher than those characterized in Jakarta. Potassium is a key element /finger print of biomass burning. Besides transportation and industry, the higher in K was probably due to open burning activities that are still being carried out in Java including in Surabaya, especially to reduce the volume of household waste or crop residue [24]. Parts of elemental concentrations in $PM_{2.5}$ Surabaya are higher than in Jakarta Al, Si, Zn, Fe, Pb. There are several industrial activities in the vicinity of Surabaya which are located much closer to the 1st sampling site. While in Jakarta, the industrial activities are mainly located more than 15 km away from the sampling site in central Jakarta.

TABLE 2. Elemental concentration of PM2.5 in Surabaya and Jakarta 2019 – mid 2020 using IBA techniques

	Center Jakarta μg/m^3	East Surabaya (1) μg/m^3	West Surabaya (2) μg/m^3
Na	0.30 ± 0.09	0.39 ± 0.14	0.35 ± 0.17
Al	0.67 ± 0.05	0.72 ± 0.10	0.72 ± 0.14
Si	0.92 ± 0.14	1.05 ± 0.22	1.07 ± 0.37
S	1.74 ± 0.67	2.09 ± 0.59	1.64 ± 0.55
Cl	0.23 ± 0.02	0.23 ± 0.03	0.21 ± 0.01
K	0.39 ± 0.12	0.56 ± 0.23	0.47 ± 0.32
Ca	0.20 ± 0.10	0.16 ± 0.07	0.27 ± 0.25
Ti	0.010 ± 0.005	0.016 ± 0.007	0.011 ± 0.008
V	0.00003 ± 0.0002	0.00006 ± 0.0002	0.0004 ± 0.0008
Cr	0.0033 ± 0.0012	0.0046 ± 0.003	0.0031 ± 0.0010
Mn	0.009 ± 0.008	0.019 ± 0.02	0.008 ± 0.005
Fe	0.18 ± 0.07	0.33 ± 0.21	0.22 ± 0.15
Ni	0.0012 ± 0.0006	0.0014 ± 0.001	0.0011 ± 0.0006
Cu	0.017 ± 0.016	0.010 ± 0.005	0.006 ± 0.003
Zn	0.14 ± 0.07	0.61 ± 0.52	0.15 ± 0.19
As	0.0018 ± 0.0015	0.0026 ± 0.003	0.0018 ± 0.0018
Br	0.010 ± 0.010	0.012 ± 0.006	0.006 ± 0.004
Pb	0.044 ± 0.07	0.34 ± 0.38	0.035 ± 0.06

The time series of elemental (S, K, Cu, Mn, Fe, Zn, Pb) concentrations of $PM_{2.5}$ in Jakarta and Surabaya are presented in Fig. 4. It can be seen that S concentrations of Jakarta and Surabaya were in the similar range as well as in between 1st and 2nd sites in Surabaya. This showed strong signal of fuel combustion of diesel fuel from the industry or other activities. Sulphur concentration in Jakarta was measured higher compared to the previous study in 2008-2009 (1.177 μg/m^3) [11]. Notably, sulphur concentrations measured at the two sites were far higher compared to the other cities in Indonesia [10]. Potassium concentrations in Surabaya 1 were higher than those measured in Surabaya 2 and Jakarta which may be sourced from open burning of domestic waste. The concentrations of Fe, Zn, Pb and Mn in Surabaya 1 were higher than those measured in Surabaya 2 and Jakarta due to the close location of the smelter industrial area. As can be seen in Fig. 4, the Surabaya 1 Zn and Pb concentration were peaking at several days during the time period observed. Pb concentrations measured in Surabaya 2 and Jakarta seems to have similar range with the concentrations of Zn, Pb and Mn, except for Fe. Cu concentration measured in Jakarta was 2-3 times higher than Surabaya describing the possibility of the sources from non-ferrous industries. The Cu concentrations of $PM_{2.5}$ in Jakarta were lower than that measured in Iran (up to 167 ng/m^3) or even with the measurement conducted in South Korea (35.7 ng/m^3). However, the levels were measured higher than those measured in Switzerland and Netherland (<10 ng/m^3) [25-27].

Comparison of heavy metal elements Zn, Fe, Mn, and Pb of $PM_{2.5}$ concentration in Jakarta to Surabaya are presented in Fig. 5. The elemental characteristics of Zn Mn, Fe and Pb are known as tracers of steel industry, while Cu and Pb are for the metal industry, and Pb is for acid batteries. The concentrations of Fe, Zn, Pb at Surabaya were significantly higher than those measured in Jakarta. Compared to the steel industry area in the Yangtze River Delta region China, the Fe and Zn concentrations at Surabaya were still lower, except for Pb where the concentration was measured nearly double [28]. The high concentrations of Pb in Surabaya were likely come from Lead Battery smelter in Surabaya's vicinity. Similar results with high level of Mn, Ni, As, Cd, Pb were also found for a scrap iron and steel smelting industry in Nigeria and the results also showed that the source

contribution from metallurgical production reached 6% of the total mass of $PM_{2.5}$ [29]. The IBA techniques were successfully applied to characterize the elemental compositions of $PM_{2.5}$ in Jakarta as well as in Surabaya and showed different characteristics of air quality of each city. The results obtained can then be used to determine the source apportionment in Jakarta and Surabaya to formulate appropriate strategies and policies for PM reduction in each city.

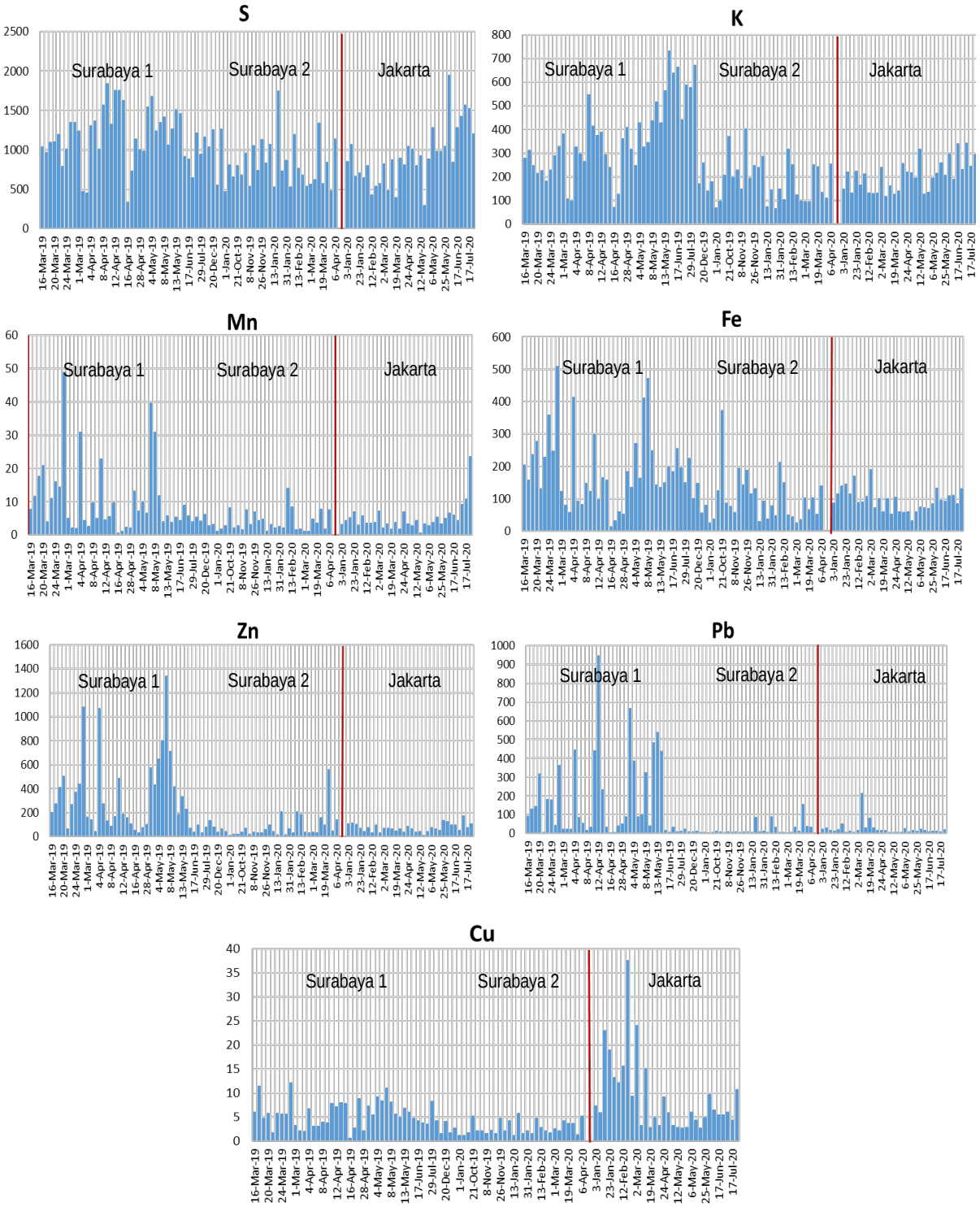

FIG. 4. Time series of S, K, Mn, Fe, Zn, Pb and Cu concentrations of $PM_{2.5}$(in ng/m^3) of Jakarta and Surabaya 2019-mid 2020

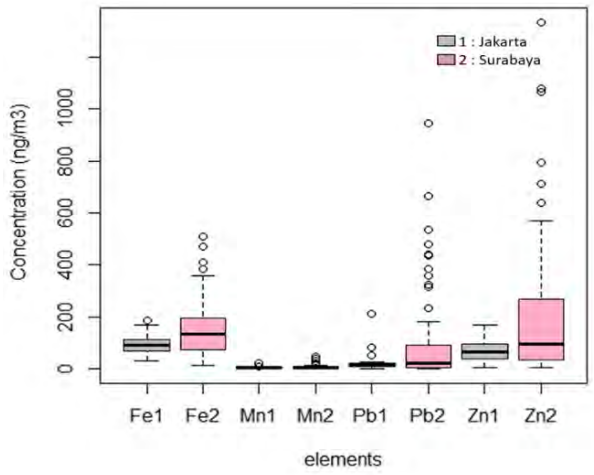

FIG. 5. Box and whisker plot of Fe, Mn, Fe, Pb and Zn concentrations of $PM_{2.5}$ Jakarta and Surabaya 2019 – mid 2020

4. CONCLUSIONS

The results of $PM_{2.5}$ elemental composition in the ambient air using IBA technique analysis was able to provide good and comprehensive results in term of urban PM air pollution characterization. Three sampling locations from Jakarta and Surabaya gave different results according to the characteristics of the area especially the nearby emission sources. The multi-element identification from the IBA analysis was also able to provide an overview of the contribution of emissions from industry to air quality in the surrounding environment. Heavy metal concentrations (Fe, Zn, Mn, Pb) in East Surabaya (1) were higher than those measured in West Surabaya (2) and Jakarta, while higher Cu was found in Jakarta compared to the 2 sites in Surabaya. These results indicated that the concentration of heavy metal in East Surabaya was likely to be correlated with industrial activities in the vicinity. Although the concentration of heavy metals was still below the NAAQS, the problem of its pollution cannot be ignored because it is very harmful to human health even in a low concentration. These results can be used as an early warning to formulate appropriate strategies and policies so that greater losses can be avoided in the two concerned cities.

ACKNOWLEDGEMENTS

The authors gratefully acknowledge support from Lembaga Pengelola Dana Pendidikan (LPDP) under contract number 181/E1/PRN/2020 and IAEA CRP G42008 under Research Contract No. 23527. Thanks are also conveyed to BRIN, ANSTO Australia, DLH East Java, DLH Surabaya, DLH Jakarta, and Institut Teknologi Sepuluh Nopember (ITS). All authors contributed equally to this work.

REFERENCES

[1] RÖNKKÖ, T.J., JALAVA, P.I., HAPPO, M.S., KASURINEN, S., SIPPULA, O., LESKINEN, A., KOPENEN, H., KUUSPALO, K., RUUSUNEN, J., VÄISÄNEN, O., HAO, L., RUUSKANEN, A., ORASCHE, J., FANG, D., ZHANG, L., LEHTINEN, K.E.J., ZHAO, Y., GU, C., WANG, Q., JOKINIEMI, J., KOMPPULA, M., HIRVONEN, M.R., Emissions and atmospheric processes in fluence the chemical composition and toxicological properties of urban air particulate matter in Nanjing, China. Sci. Total Environ. 639 (2018) 1290–1310. https://doi.org/10.1016/j.scitotenv.2018.05.260

[2] LIANG, R., CHEN, R., YIN, P., VAN DONKELAAR, A., MARTIN, R.V., BURNETT, R., COHEN, A.J., BRAUER, M., LIU, C., WANG, W., LEI, J., WANG, L., WANG, L., ZHANG, M., KAN, H., ZHOU, M., Associations of long-term exposure to fine particulate matter and its constituents with cardiovascular mortality: A prospective cohort study in China. Environment International 162 (2022) 107156. https://doi.org/10.1016/j.envint.2022.107156

[3] ARETZ, B., JANSSEN, F., VONK, J.M., HENEKA, M.T., BOEZEN, M.H., DOBLHAMMER, G., Long-term exposure to fine particulate matter, lung function and cognitive performance: A prospective Dutch cohort study on the underlying routes. Environmental Research 201 (2021) 111533. https://doi.org/10.1016/j.envres.2021.111533

[4] HEALTH EFFECTS INSTITUTE. State of Global Air 2020. Special Report. Boston, MA: Health Effects Institute. 2020.

[5] ZHENG, M., XU, K., YUAN, L., CHEN, N., CAO, M.. Fine Particle pH and its Impact on $PM_{2.5}$ Control in a Megacity of Central China. Aerosol Air Qual. Res. 22 (2022) 210394. https://doi.org/10.4209/aaqr.210394

[6] HIEN, T.T., CHI, N.D.T., NGUYEN, N.T., VINH, L.X., TAKENAKA, N. and HUY, D.H. Current Status of Fine Particulate Matter (PM2.5) in Vietnam's Most Populous City, Ho Chi Minh City. Aerosol Air Qual. Res. 19 (2019) 2239-2251. https://doi.org/10.4209/aaqr.2018.12.0471

[7] MANOUSAKAS, M., DIAPOULI, E., PAPAEFTHYMIOU, H., MIGLIORI, A., KARYDAS, A.G., PADILLA ALVAREZ, R., BOGOVAC, M., KAISER, R.B., JAKSIC, M., BOGDANOVIC-RADOVIC, I., ELEFTHERIADIS, K., Source apportionment by PMF on elemental concentrations obtained by PIXE analysis of PM_{10} samples collected at the vicinity of lignite power plants and mines in Megalopolis, Greece. Nucl. Instrum. Methods Phys. Res. B 349 (2015) 114–124.

[8] VILLALOBOS, A.M., AMONOV, M.O., SHAFER, M.M., JAI DEVI, J., GUPTA, T., TRIPATHI, S.N., RANA, K.S., McKENZIE, M., BERGIN, M.H., SCHAUER, J.J., Source apportionment of carbonaceous fine particulate matter ($PM_{2.5}$) in two contrasting cities across the Indo-Gangetic Plain. Atmos. Pollut. Res. 6 (2015) 398–405.

[9] COHEN, D.D., GORTON, D., STELCER, E., HAWAS, O., Accelerator based studies of atmospheric pollution processes. Radiat. Phys. Chem. 71 (2004) 759–767.

[10] SANTOSO, M., LESTIANI D.D., KURNIAWATI, S., DAMASTUTI, E., KUSMARTINI, I., ATMODJO, D.P.D., SARI, D.K., HOPKE, P.K., MUKHTAR, R., MUHTAROM, T., TJAHYADI, A., PARIAN, S., KHOLIK, N., SUTRISNO, D.A., WAHYUDI, D., SITORUS, T.D., DJAMILUS, J., RIADI, A., SUPRIYANTO, J., DAHYAR, N., SONDAKH, S., HOGENDORP, K., WAHYUNI, N., BEJAWAN, I.G. AND SUPRAYADI, L.S. (2020). Assessment of Urban Air Quality in Indonesia. Aerosol Air Qual. Res. 20: 2142–2158. https://doi.org/10.4209/aaqr.2019.09.0451

[11] SANTOSO, M., LESTIANI, D.D., DAMASTUI, E., KURNIAWATI, S., KUSMARTINI, I., ATMODJO, D.P.D., SARI, D.K., MUHTAROM, T., PERMADI, D.D., HOPKE, P.K., Long term characteristics of atmospheric particulate matter and compositions in Jakarta, Indonesia, Atmospheric Pollution Research. **11** 12 (2020) 2215-2225. https://doi.org/10.1016/j.apr.2020.09.006

[12] SYAFEI, A.D., FUJIWARA A., and ZHANG, J., Spatial and temporal factors of air quality in Surabaya city: An analysis based on a multilevel model. Procedia – Sosial and behavioral sciences 138 (2014) 612-622. https://doi.org/10.1016/j.sbspro.2014.07.246

[13] HOPKE, P.K, COHEN, D.D., BEGUM, B.A., BISWAS, S.K., NI, B., PANDIT, G.G., SANTOSO, M., CHUNG, Y.S., DAVY, P., MARKWITZ, A., WAHEED, S., SIDDIQUE, N., SANTOS, F.L., PABROA, P.C.B., SENEVIRATNE, M.C.S., WIMOLWATTANAPUN, W., BUNPRAPOB, S., VUONG, T.B., DUY HIEN, P. and MARKOWICZ, A., Urban air quality in the Asian region. Sci. Total Environ. 404 (2008) 103–112. https://doi.org/10.1016/j.scitotenv.2008.05.039

[14] SANTOSO, M, LESTIANI, D.D., MUKHTAR, R., HAMONANGAN, E., SYAFRUL, H., MARKWITZ, A. and HOPKE, P.K., Preliminary study of the sources of ambient air pollution in Serpong, Indonesia. Atmos. Pollut. Res. 2 (2011) 190–196. https://doi.org/10.5094/APR.2011.024

[15] COHEN, D.D., STELCER, E., ATANACIO, A. and CRAWFORD, J., The application of IBA techniques to air pollution source fingerprinting and source apportionment. Nucl. Instrum. Methods Phys. Res., Sect. B 318 (2014) 113–118. https://doi.org/10.1016/j.nimb.2013.05.093

[16] COHEN, D.D., Applications of simultaneous IBA techniques to aerosol analysisNuclear Instruments and Methods in Physics Research B79 (1993) 385-388.

[17] BEGUM, B.A., BISWAS, S.K., HOPKE, P.K., COHEN, D.D., Multi-element Analysis and Characterization of Atmospheric Particulate Pollution in Dhaka. Aerosol and Air Quality Research. **6** 4 (2006) 334-359.

[18] SANTOSO, M., HOPKE, P.K., PERMADI, D.A., DAMASTUTI, E., LESTIANI, D.D., KURNIAWATI, S., KHOEROTUNNISYA, D., SUKIR, S.K., Multiple Air Quality Monitoring Evidence of the Impacts of Large-scale Social Restrictions during the COVID-19 Pandemic in Jakarta, Indonesia. Aerosol Air Qual. Res. 21 (2021) 200645. https://doi.org/10.4209/aaqr.200645

[19] SANTOSO, M., LESTIANI, D.D., KURNIAWATI, S., DAMASTUTI, E., KUSMARTINI, I., ATMODJO, D.P.D., SARI, D.K., SUTRISNO, Impact of the COVID-19 on Ambient Air Particulate Matter in Surabaya, Indonesia. AIP Conference Proceedings 2381 (2021) 020078. https://doi.org/10.1063/5.0066244

[20] TAHA, G., BOX, G. P., COHEN, D. D., and STELCER, E., Black carbon measurement using laser integrating plate method, Aerosol Sci. Technol. **41** 3 (2007) 266–276.

[21] SANTOSO, M., LESTIANI, D.D., and MARKWITZ, A., Characterization of airborne particulate matter collected at Jakarta roadside of an arterial road. J Radioanal Nucl Chem 297 (2013) 165–169. https://doi.org/10.1007/s10967-012-2350-5

[22] COHEN, D., ATANACIO, A., CRAWFORD, J., and SIEGELE, R., Ion beam techniques for source fingerprinting fine particle air pollution in major Asian-Pacific cities, Nucl. Instruments Methods Phys. Res. Sect. B Beam Interact. with Mater. Atoms, 477 (2020) 122–132.

[23] HARYANTO, B., Climate change and urban air pollution health impacts in Indonesia. In Climate change and air pollution: The impact on human health in developed and developing countries. Akhtar, R. and Palagiano, C. (Eds.), Springer International Publishing, Cham, pp. 215–239 (2018). https://doi.org/10.1007/978-3-319-61346-8_14

[24] PERMADI, D.A., KIM OANH, N.T., Assessment of biomass open burning emissions in Indonesia and potential climate forcing impact, Atmospheric Environment 78 (2013) 250-258. https://doi.org/10.1016/j.atmosenv.2012.10.016

[25] SOLEIMANI, M., AMINI, N., SADEGHIAN, B., WANG, D., FANG, L., Heavy metals and their source identification in particulate matter ($PM_{2.5}$) in Isfahan City, Iran. Journal of Environmental Sciences 72 (2018) 166-175. https://doi.org/10.1016/j.jes.2018.01.002

[26] KIM, K., Present and long-term pollution status of airborne copper in major urban environments, Atmospheric Environment 94 (2014) 1-10. https://doi.org/10.1016/j.atmosenv.2014.04.039

[27] DENIER VAN DER GON, H.A.C., GERLOFS-NIJLAND, M.E., GEHRIG, R., GUSTAFSSON, M., JANSSEN, N., HARRISON, R.M., HULSKOTTE, J., JOHANSSON, C., JOZWICKA, M., KEUKEN, M. Keuken, KRIJGSHELD, K., NTZIACHRISTOS, L., RIEDIKER, M. and CASEE, F.R., The Policy Relevance of Wear Emissions from Road Transport, Now and in the Future—An International Workshop Report and Consensus Statement, Journal of the Air & Waste Management Association, **63** 2 (2013) 136-149. https://doi.org/10.1080/10962247.2012.741055

[28] DAI, Q.L., BI, X.H., WU, J.H., ZHANG, Y.F., WANG, J., XU, H., YAO, L., JIAO, L. and FENG, Y.C., Characterization and Source Identification of Heavy Metals in Ambient PM_{10} and $PM_{2.5}$ in an Integrated Iron and Steel Industry Zone Compared with a Background Site. Aerosol Air Qual. Res. 15 (2015) 875-887. https://doi.org/10.4209/aaqr.2014.09.0226

[29] FAWOLE, O, OWOADE, O., HOPKE, P.K., OLISE, F., LASUN, TUNDE, O., OLANIYI, B., JEGEDE, O., AYOOLA, M., BASHIRU, M., Chemical compositions and source identification of particulate matter ($PM_{2.5}$ and $PM_{2.5–10}$) from a scrap iron and steel smelting industry along the Ife–Ibadan highway, Nigeria. Atmospheric Pollution Research. 6 (2015) 107 - 119. https://doi.org/10.5094/APR.2015.013

RESEARCH ACTIVITIES ON THE CYCLOTRON-BASED RODUCTION OF INNOVATIVE RADIONUCLIDES: THE EXPERIENCE AT THE LEGNARO NATIONAL LABORATORIES OF INFN

G. PUPILLO
Istituto Nazionale di Fisica Nucleare, Laboratori Nazionali di Legnaro (INFN-LNL)
Legnaro (Padova), Italy
Email: gaia.pupillo@lnl.infn.it

A. ANDRIGHETTO
INFN-LNL
Legnaro (Padova), Italy

M. BALLAN
INFN-LNL
Legnaro (Padova), Italy

A. BOSCHI
Department of Chemical, Pharmaceutical and Agricultural Sciences, University of Ferrara and INFN-FE
Ferrara, Italy

S. CISTERNINO
INFN-LNL and Engineering Department, University of Padova
Legnaro (Padova) and Padova, Italy

S. CORRADETTI
INFN-LNL
Legnaro (Padova), Italy

L. DE DOMINICIS
INFN-LNL and Physics and Astronomy Department, University of Padova
Legnaro (Padova) and Padova, Italy

J. ESPOSITO
INFN-LNL
Legnaro (Padova), Italy

E. FIORETTO
INFN-LNL
Legnaro (Padova), Italy

M. MANZOLARO
INFN-LNL
Legnaro (Padova), Italy

P. MARTINI
Department of Environmental and Prevention Sciences, University of Ferrara and INFN-FE
Ferrara, Italy

A. MONETTI
INFN-LNL
Legnaro (Padova), Italy

L. MORSELLI
INFN-LNL and Physics and Earth Science Department, University of Ferrara
Legnaro (Padova) and Ferrara, Italy

L. MOU
INFN-LNL and Physics and Earth Science Department, University of Ferrara
Legnaro (Padova) and Ferrara, Italy

D. SCARPA
INFN-LNL
Legnaro (Padova), Italy

G. SCIACCA
INFN-LNL and Engineering Department, University of Padova
Legnaro (Padova) and Padova, Italy

E. VETTORATO
INFN-LNL
Legnaro (Padova), Italy

Abstract

The cyclotron-based production of radionuclides for medicine is one of the research activities carried out in the framework of the SPES (Selective Production of Exotic Species) project at the Legnaro National Laboratories of the National Institute for Nuclear Physics (INFN-LNL). The heart of SPES is the 70 MeV proton-cyclotron with a dual-beam extraction, installed in 2015 in a new building equipped with ancillary laboratories currently under completion. The project aims at the construction of an advanced ISOL (Isotope Separation On-Line) facility to produce re-accelerated exotic ion beams for nuclear physics studies. The double-beam extraction of the cyclotron also allows to perform multidisciplinary activities, such as radionuclides production for medical applications and neutron-based research. This paper will mainly present the results obtained with the interdisciplinary projects LARAMED (LAboratory of RAdionuclides for MEDicine) and ISOL-pharm. The first one is based on the direct-activation method, and it includes the proton-based production of ^{99m}Tc, ^{67}Cu, $^{52/51}$Mn, ^{47}Sc and recently Tb-isotopes, from the nuclear cross section measurements to the preclinical studies. ISOL-pharm uses the ISOL technique for the development and the production of radioisotopes with high-specific activity, such as ^{111}Ag, going beyond the state-of-art in the field. A consolidated network of collaborations with national and international facilities, including universities and hospitals, characterizes the research activities on radionuclides production at the INFN-LNL.

1. INTRODUCTION

The SPES project at the INFN-LNL has an ambitious scientific program ranging from nuclear physics and astrophysics to interdisciplinary applications [1, 2]. The heart of SPES is the 70 MeV proton-cyclotron [3], capable of providing intense beams (up to 700 μA) also in the dual-extraction configuration. This characteristic will allow to perform not only state-of-the-art experiments with Radioactive Ion Beams (RIBs) [4] but also multidisciplinary research activities, such as radionuclides production for medical applications and neutron-based research. Figure 1 represents the main parts of the SPES project at the INFN-LNL.

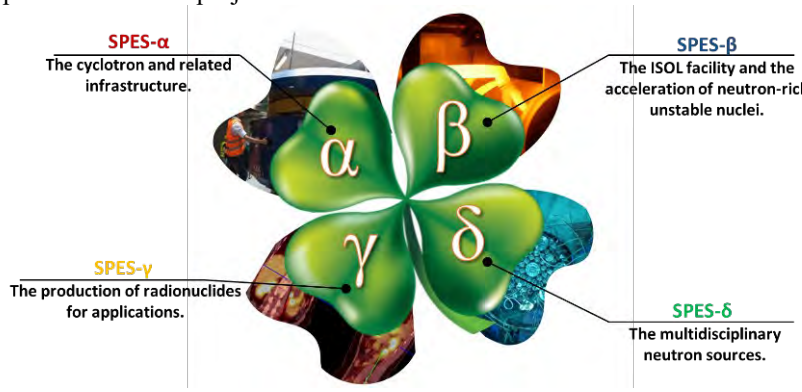

FIG. 1. The SPES-project phases.

Radionuclides are fundamental tools in several applications of nuclear physics, ranging from toxicological to environmental and industrial studies, but play a key role in nuclear medicine, by enabling imaging and treatment in tens of millions of procedures performed worldwide on a yearly basis. Given that the production of medical radionuclides is thus a crucial aspect, and the availability of emerging radionuclides fosters the development of innovative radiopharmaceuticals, the SPES project includes the "The production of radionuclides for applications" as its gamma phase (Figure 1) and the INFN-LNL Research Division contains the "Radioisotope Service for Medicine and Applied Physics" (RMFA) [5, 6]. The activities of the RMFA service include:

— Radionuclide production using direct activation method (LARAMED project) and ISOL technique (ISOLPHARM project), for research in medicine (e.g. new radiopharmaceuticals development) and in applied and interdisciplinary physics (e.g. radiobiology, environmental studies).
— Measurements of proton-induced nuclear cross sections for medical radionuclides production.
— Study, development, and optimization of radiochemical procedures aimed at the separation and purification of radionuclides, development of radiopharmaceuticals.

Since currently the laboratories and infrastructures of the SPES building devoted to these research activities are not yet operative, the SPES-γ research activities rely on a wide network of collaborations, internal and external the LNL, as outlined in the following sections. Figure 2 shows the planimetry of the SPES building at the underground level, where the cyclotron is in the centre and the LARAMED and ISOL-bunkers are indicated on the right and left side of the picture.

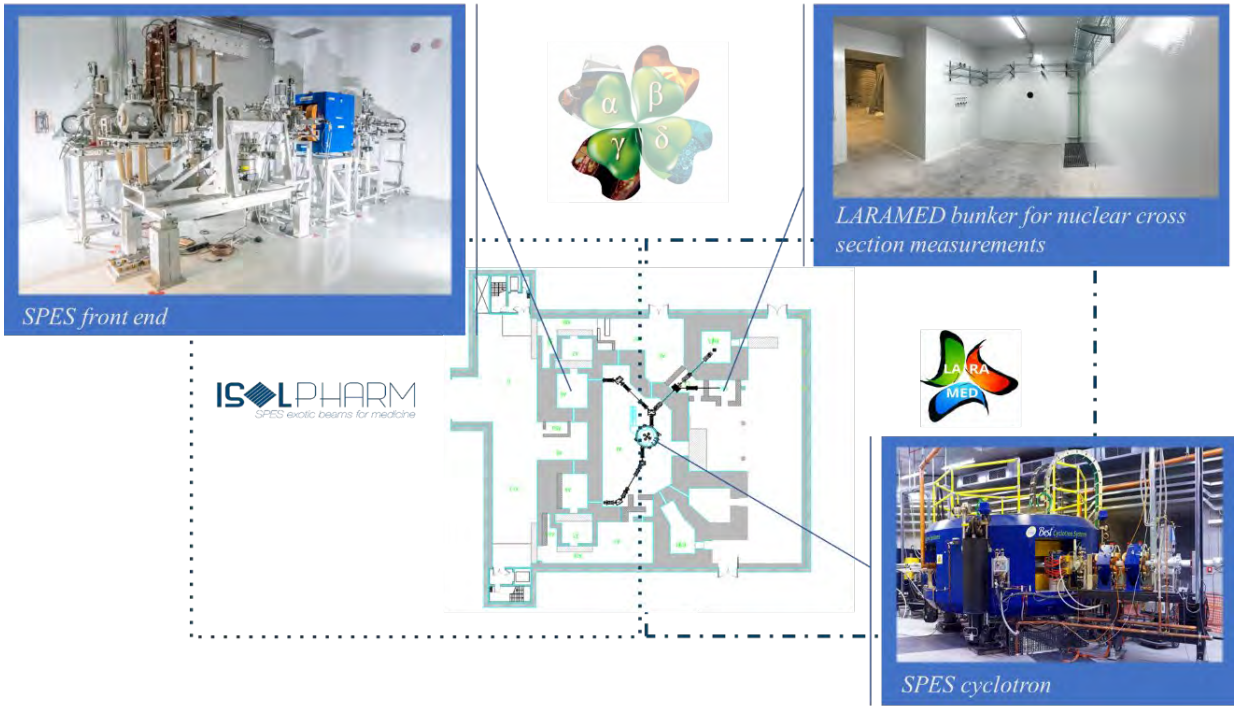

FIG. 2. The SPES building planimetry at the underground level.

Ultimately, the major objective of these research activities is to elect LNL as an internationally recognized hub (in collaboration with other research centres in Europe) aimed at the development of unexplored production methods for novel medical radionuclides, as well as to establish a production facility at LNL for a few relevant medical radionuclides to be distributed to hospitals and clinical departments, to support both preclinical/clinical ongoing research programs and for routine use in patients' treatment. Since only a few examples of this type of high-energy, high-current cyclotrons are currently operating around the world, it becomes plain the potential important role that the INFN-LNL could play in the global scenario, related to the production of unprecedented medical radionuclides. In fact, the LNL are participating as emerging infrastructure also at the European medical isotope programme PRISMAP [7], recently approved by the EU as H2020.

2. LARAMED

The LARAMED project, acronym for LAboratory of RAdioisotopes for MEDicine [8, 9] is funded by the Italian Ministry of University and Research (year 2014 and 2016) at the INFN-LNL. It has been conceived, since the beginning, to meet a double scope. The first one was to develop a more efficient production for well-established radionuclides already playing a key role in nuclear medicine (e.g. ^{99m}Tc) [10-13], while the other was to investigate yet unexplored production routes for novel radionuclides having potential interest in medicine, but still unavailable [14]. The latter may indeed summarize the most interesting aspect of this project, playing a key role in improving approaches in patients' treatment and clinical research purposes. Nonstandard radionuclides production is, indeed, a fundamental step to select new radiopharmaceuticals classes for both diagnostic and therapeutic applications [15].

As shown in Figure 3, the LARAMED research activity is envisaged to cover different topics, ranging from basic nuclear physics (experimental measurements of excitation functions) [16-20], to target technology (design and manufacturing of high-power targets for proton irradiation to produce important medical radionuclides, such as ^{99m}Tc, ^{64}Cu, ^{67}Cu, ^{47}Sc, ^{89}Zr, etc.) [21-25] and radiochemistry (development of highly automated separation/purification techniques and labelling studies of new biological carriers) [26-29]. The synergy between these skills resulted in high-level research on the cyclotron production of conventional and emerging radionuclides. Although LARAMED will be a public research facility, joint ventures with private companies interested in the already available and/or new radionuclides development programs is anyway foreseen.

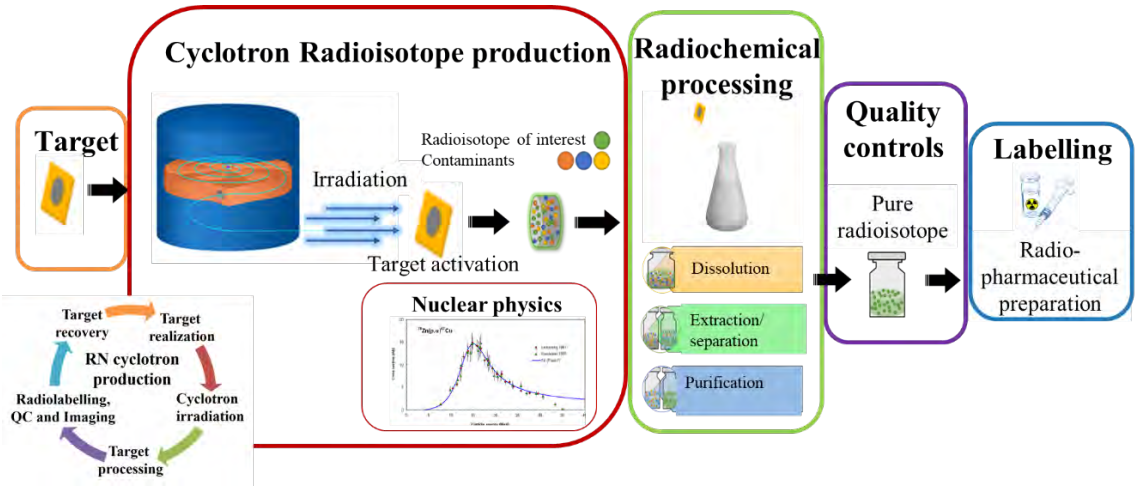

FIG. 3. The medical radionuclide production scheme exploiting the direct activation method.

Regarding the LARAMED facility in the SPES building, it includes:

- The *RILAB Bunkers* (RI#3 and A9c), the first dedicated to irradiation of high power (i.e. up to ~ 10 kW) solid targets and the second dedicated to nuclear cross-sections measurements with low-intensity proton-beams (i.e. up to 100 nA).
- The *RIFAC Bunkers* (RI#1 and RI#2), where two additional beamlines are foreseen to be installed in further years and used to produce massive amounts of radioisotopes, in collaboration with a private partner, to hospitals and clinical departments, for both routine and clinical research purposes.
- The *RILAB Radiochemistry laboratory*, covering all the radiochemical processing aspects and designed to carry out R&D activities on radioisotope production, separation/purification, up to perform all the requested quality control procedures.
- The *RILAB Target-preparation laboratory* where all the new/alternative cold-chemistry technologies devoted to target manufacturing are under development by the LARAMED research group.

In Figure 4 a schematic layout of the building upper floor is shown, along with the area reserved for the future installation of Radiochemistry laboratory for radioisotope/ radiopharmaceutical production dedicated to future RIFAC activities.

FIG. 4. The LARAMED laboratories planimetry at the upper floor of the SPES building.

The LARAMED research activities started 10 years ago with the following projects:

- APOTEMA and TECHN-OSP (INFN-CSN5 funded, 2012-2017), dedicated to the direct ^{99m}Tc production using isotopically enriched ^{100}Mo targets at medical cyclotrons; the results have been also presented in the IAEA CRP focused on "Alternative, non HEU-based, ^{99m}Tc/^{99}Mo supply" (2011-2015).
- COME (INFN-CSN3 funded, 2016), dedicated to the first measurements of the ^{70}Zn(p,x)^{67,64}Cu nuclear reactions above 35 MeV and the ground of the INFN patent on ^{67}Cu multi-layers target [25].
- PASTA (INFN-CSN5 funded, 2017-2018), dedicated to the nuclear cross section measurements for ^{47}Sc production, whose results have been also presented in the IAEA CRP focused on "Radiopharmaceuticals labelled with new emerging radionuclides (^{67}Cu, ^{186}Re, ^{47}Sc)" [15].
- E_PLATE (INFN-CSN5 funded, 2018-2019), dedicated to thin target manufacturing exploiting the High Intensity Vibrational Powder Plating (HIVIPP) technique.
- METRICS (INFN-CSN5 funded, 2018-2021), dedicated to $^{51/52}$Mn accelerator-based production and to the development of innovative radiopharmaceuticals for PET/MRI dual-imaging purposes.
- INTEFF_TOTEM (INFN-CNTT funded, 2021-2022), dedicated to the further development of the INFN patents on targetry for the production on medical radionuclides [24, 25].
- REMIX (INFN-CSN5 funded, 2021-2023), dedicated to the measurements of the ^{49,50}Ti(p,x)^{47}Sc nuclear reactions (exploiting the thin targets developed with the HIVIPP technique) and Tb-radionuclides production (^{149}Tb, ^{152}Tb, ^{155}Tb and ^{161}Tb).

The wide national and international network of collaborations allowed the LARAMED team to enlarge the research topics to nuclear modeling, imaging, dosimetry, etc. [20, 12, 30-32]. The LARAMED network includes the ARRONAX facility (Nantes, France), the Universities of Ferrara, Milano, Padova, Pavia and the Wisconsin University, the CNR in Milano, the LENA laboratory, the Istituto Oncologico Veneto (IOV, Padova, Italy), the Sacro Cuore Don Calabria (Negrar, Verona, Italy) and the Sant'Orsola (Bologna, Italy) hospitals.

3. ISOLPHARM

The general scheme of the ISOLPHARM method [33, 34] is shown in Fig. 5: a production target is hit by protons coming from the SPES cyclotron. Different nuclear reactions activate the generation of several different radioisotopes. Mainly neutron-rich β^- emitters are produced, due to the fact that at SPES and in general in ISOL facilities, uranium carbide is used as a fissile target material. Inside the so-called front-end (shown in Fig. 2), the

target is kept at high temperature (more than 2000 °C) in high vacuum, so that the isotopes can escape from it towards an ion source, where they are ionized (1^+) by means of one of the three available ionization techniques (surface, laser, or plasma). After ionization, the charged radioisotopes are accelerated by means of a 40 kV potential, forming a radioactive ion beam. The following step, mass separation, is crucial for the purposes of ISOLPHARM. This stage allows to have an isobaric beam, removing all isotopic contaminants of the desired element, which are not otherwise chemically removable. These processes represent the scheme of operation of ISOL facilities (top part of Fig. 5) to perform nuclear physics studies by providing radioactive ion beam to experimental users. The new approach introduced by ISOLPHARM is the collection of radioisotopes on a secondary target (ion collection stage). This collector can then be dissolved and chemically purified to eliminate isobaric contaminants. The obtained product can be subsequently used for radiolabeling of specific molecules. These can be delivered to universities or external research centers for preclinical studies (bottom part of Fig. 5).

The key aspects to be underlined for ISOLPHARM are:

— The presence of a strong collaboration between several INFN laboratories and sections and several university departments.
— The production of radionuclides with high specific activity by means of the ISOL technique.
— The INFN patent which proves the innovation and excellence of the project [35].
— The low environmental and social impact, since nuclear reactors are not used for the provision of the radionuclides.

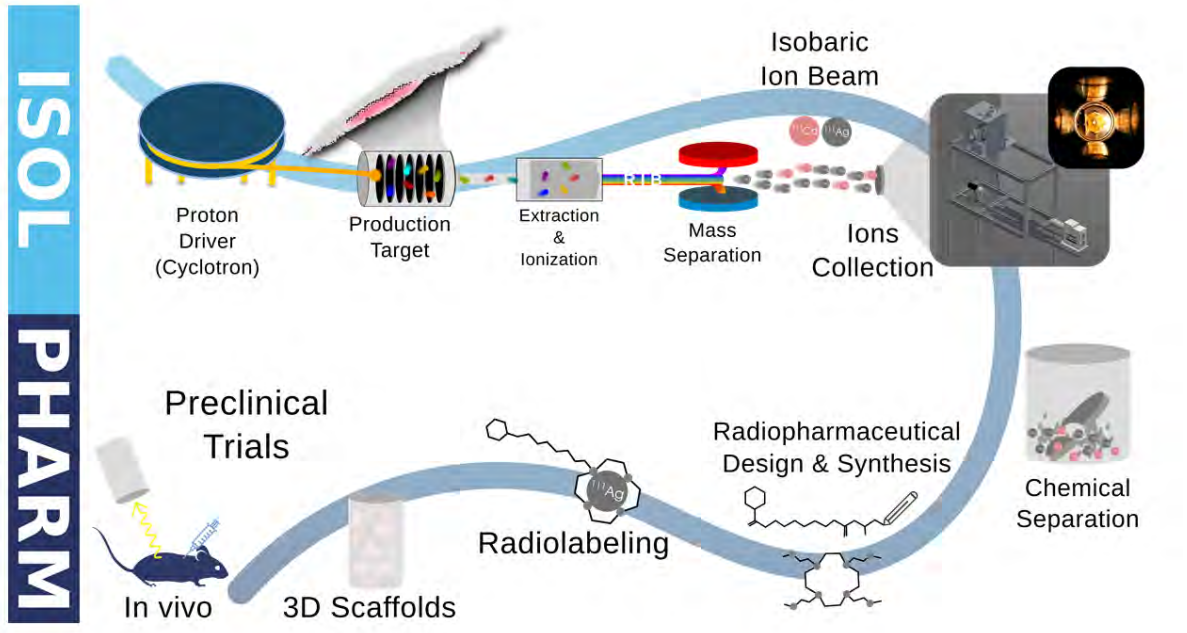

FIG. 5. The ISOLPHARM method.

In the framework of ISOLPHARM, a two-year experiment collaboration project named ISOLPHARM_Ag was financially supported by INFN CSN5 (Commissione Scientifica Nazionale 5) for the years 2018/2019 [36]. Such project aimed at studying and demonstrating as a proof of principle the production and use of the promising ^{111}Ag, an isotope which is produced in huge quantities in the SPES uranium carbide target. Its possible use was investigated both relatively to its ISOL production and to its possible application as a radiopharmaceutical precursor, with both computational and experimental investigations. Computational studies were focused on the development of Monte Carlo codes able to estimate the production and release of ^{111}Ag from the primary target. Such codes were computing intensive, and they were executed with the support of a cloud infrastructure in the CloudVeneto environment. The experimental studies involved: ionization and transport of silver (that will be tested at the SPES Front End using the SPES Plasma Ion Source) [37]; the chemistry studies to develop and

characterize silver complexes [38]; the biological studies on such molecules, to evaluate the interaction of the synthesized complexes with cellular targets [39].

Following the good results obtained in the ISOLPHARM_Ag experiment, a new experiment started in the framework of CSN5, ISOLPHARM_EIRA (2020-2022), in which all the ISOLPHARM collaboration activities are now focused. The ISOLPHARM_EIRA experiment has three main goals, based on the application of the ISOLPHARM method to the production of ^{111}Ag radionuclides as radiopharmaceuticals precursors:

- Physics: production of ^{111}Ag, spectroscopy studies, laser ionization of Ag (Task 1).
- Radiochemistry: synthesis and characterization of chelators, linkers, targeting agents and purification of isotopes (Task 2).
- Biology: biological characterization on cells, scaffold production and 3D cell cultures, in vitro and in vivo studies (Task 3).

The main aim of Task 1 is the production of an appropriate amount of ^{111}Ag to be used in the Task 2 for the radiolabeling of the prepared radiopharmaceutical [40]. ^{111}Ag is produced by means of the traditional technique of neutron capture reaction on enriched ^{110}Pd. The irradiation is performed at the TRIGA Mark II nuclear reactor of the LENA (acronym for "Laboratorio Energia Nucleare Applicata") laboratory of the Pavia University. Several activities are ongoing:

- Production of ^{111}Ag in nuclear reactor, including the design and construction of a semi-automatic device for the extraction and handling of the irradiated samples.
- Spectroscopic studies for the isotopic characterization of the irradiated samples.
- Studies for the laser photoionization of natural Ag.

The final goal of Task 2 is to prepare and characterize the radiopharmaceutical to be used by Task 3, after having achieved the radionuclide produced by Task 1 [41]. Several activities are ongoing:

- Development of purification methods for Ag from Pd and recovery of Pd.
- Development and characterization of chelators for Ag and Cu.
- Synthesis and characterization of fluorescent targeting vectors.

The activities of Task 3 are mainly aimed at the a) preliminary screen and identify via standard fluorescent assays the optimal macromolecules for the b) subsequent more relevant in-vivo test that will be conducted with radiolabeled compounds [42]. Several activities are ongoing:

- Selection of cell lines for in vitro studies.
- In-vitro and in-vivo study of targeting vectors.
- In-vitro studies of targeting vectors with fluorescent targeting agents.
- Design of suitable 3D scaffold for in vitro tissue mimicking.
- In-vitro uptake studies (3D scaffolds) with fluorescent compounds.
- Biodistribution and in vivo imaging.

4. CONCLUSIONS

The SPES-γ will exploit the 70 MeV proton cyclotron to produce radionuclides of medical interest with the direct activation (LARAMED project) and the ISOL technique (ISOLPHARM project). Waiting for the completion of the SPES facility, both projects have a wide national and international network of collaborations to perform multidisciplinary research activities, ranging from nuclear physics to radiochemistry, from material science and targetry to engineering and radiopharmacy. A young team of researchers is involved, and the activities are coordinated by the recent "Radioisotope Service for Medicine and Applied Physics" (RMFA) in the Research Division at the INFN-LNL. The European PRISMAP consortium identifies the INFN-LNL as emerging infrastructure, a unique lab where the potential impact of both production techniques can be studied.

REFERENCES

[1] PRETE, G., The SPES project at the INFN-Laboratori Nazionali di Legnaro, IL NUOVO CIMENTO 38 C (2015) 181, DOI 10.1393/ncc/i2015-15181-3

[2] MARCHI, T. et al., The SPES facility at Legnaro National Laboratories, J. Phys.: Conf. Ser. 1643 (2020) 012036

[3] MAGGIORE, M. et al., SPES: A new cyclotron-based facility for research and applications with high-intensity beams, Modern Physics Letters A VOL. 32, NO. 17 (2017) DOI 10.1142/S0217732317400107

[4] ANDRIGHETTO, A. et al., Spes: An intense source of Neutron-Rich Radioactive Beams at Legnaro, J. Phys.: Conf. Ser. 966 (2018) 012028

[5] INFN-LNL website, Research Division (2022) https://www.lnl.infn.it/en/reasearch-division/

[6] PUPILLO, G. et al., The "Radioisotopi per la Medicina e la Fisica Applicata" Service in the Research Division, LNL Annual Report 2021 (2022) ISSN1828-8561, https://www1.lnl.infn.it/~annrep/index.htm

[7] PRISMAP consortium website (2022) https://www.prismap.eu/

[8] ESPOSITO, J. et al., LARAMED: A Laboratory for Radioisotopes of Medical Interest, Molecules (2019) 24, 20; DOI 10.3390/molecules24010020

[9] PUPILLO, G. et al., The Laramed Project at LNL: ^{67}Cu and ^{47}Sc Production for Theranostic Applications, AIP Conference Proceedings 2295, 020001 (2020) DOI 10.1063/5.0032898

[10] MARTINI, P. et al., In-House Cyclotron Production of High-Purity Tc-99m and Tc-99m Radiopharmaceuticals. Appl Radiat Isotopes (2018) 139, 325–331, DOI 10.1016/j.apradiso.2018.05.033

[11] SKLIAROVA, H. et al., Innovative Target for Production of Technetium-99m by Biomedical Cyclotron, Molecules (2018) 24, 25, DOI 10.3390/molecules24010025

[12] UZUNOV, N. et al., Radioisotopic purity and imaging properties of cyclotron-produced ^{99m}Tc using direct ^{100}Mo(p,2n) reaction, Physics in Medicine and Biology (2018) 63, 185021 DOI 10.1088/ 1361-6560/aadc88

[13] SKLIAROVA, H. et al., Recovery of Molybdenum Precursor Material in the Cyclotron-Based Technetium-99m Production Cycle, Instruments (2019) 3(1), 17 DOI 10.3390/instruments3010017

[14] MOU, L. ^{67}Cu production capabilities: a mini review 2022 Molecules DOI: 10.3390/molecules27051501

[15] JALILIAN, A. R. et al., IAEA Activities on ^{67}Cu, ^{186}Re, ^{47}Sc Theranostic radionuclides and Radiopharmaceuticals in Current Radiopharmaceuticals (2021) DOI 10.2174/1874471013999200928162322

[16] PUPILLO, G. et al., New production cross sections for the theranostic radionuclide ^{67}Cu, Nucl Instrum Meth B (2018) 415, 41-47 DOI 10.1016/j.nimb.2017.10.022

[17] PUPILLO, G. et al., Production of ^{67}Cu by enriched ^{70}Zn targets: first measurements of formation cross sections of ^{67}Cu, ^{64}Cu, ^{67}Ga, ^{66}Ga, ^{69m}Zn and ^{65}Zn in interactions of ^{70}Zn with protons above 45 MeV, Radiochimica Acta (2020) DOI 10.1515/ract-2019-3199

[18] PUPILLO, G. et al., Production of ^{47}Sc with natural vanadium targets: results of the PASTA project (2019) J Radioanal Nucl Ch 297(3) DOI 10.1007/s10967-019-06844-8

[19] PUPILLO, G. et al., Correction to: Production of ^{47}Sc with natural vanadium targets: results of the PASTA project (2021) DOI 10.1007/s10967-021-07791-z

[20] BARBARO, F. et al., New results on proton-induced reactions on Vanadium for ^{47}Sc production and the impact of level densities on theoretical cross sections, PHYSICAL REVIEW C (2021) 104, 044619 DOI: 10.1103/PhysRevC.104.044619

[21] SKLIAROVA, H. et al., Cyclotron Solid Targets Preparation for Medical Radionuclides Production in the Framework of LARAMED Project, J. Phys.: Conf. Ser. (2020) 1548, 012022, DOI 10.1088/1742-6596/1548/1/012022

[22] SKLIAROVA, H. et al., HIVIPP Deposition and Characterization of Isotopically Enriched ^{48}Ti Targets for Nuclear Cross-Section Measurements, Nucl Instrum Meth A (2020) 981, 164371, DOI 10.1016/j.nima.2020.164371

[23] CISTERNINO, S. et al., Target Manufacturing by Spark Plasma Sintering for Efficient ^{89}Zr Production, Nuclear Medicine and Biology (2022) 104–105, 38–46, DOI 10.1016/j.nucmedbio.2021.11.004

[24] PALMIERI, V. et al., Method for Obtaining a Solid Target for Radiopharmaceuticals Production. INFN Patent no. WO/2019/053570 (2019)

[25] MOU, L. et al., A method and a target for the production of ^{67}Cu. INFN Patent no. WO 2019/220224 A1 (2019)

[26] MARTINI, P. et al., A solvent-extraction module for cyclotron production of high-purity technetium-99m, Appl Radiat Isotopes (2016) 118:302-307, DOI 10.1016/j.apradiso.2016.10.002

[27] MARTINI, P. et al., Synthesis and characterization of manganese dithiocarbamate complexes: New evidence of dioxygen activation, Molecules (2021) 26(19) DOI 10.3390/molecules26195954

[28] MARTINI, P. et al., Highly efficient micro-scale liquid-liquid in-flow extraction of ^{99m}Tc from molybdenum, Molecules (2021) 26(18) DOI 10.3390/molecules26185699

[29] SCIACCA, G. et al., A Universal Cassette-Based System for the Dissolution of Solid Targets, Molecules (2021) 26(20), 6255 DOI 10.3390/molecules26206255

[30] DE NARDO, L. et al., Radiation effective dose assessment of [^{51}Mn]- and [^{52}Mn]-chloride, Appl Radiat Isotopes (2019) DOI 10.1016/j.apradiso.2019.108805

[31] DE NARDO, L. et al., Preliminary dosimetric analysis of DOTA-folate radiopharmaceutical radiolabelled with ^{47}Sc produced through ^{nat}V(p,x)^{47}Sc cyclotron irradiation, Physics in Medicine and Biology (2021), DOI 10.1088/1361-6560/abc811

[32] DE NARDO, L. et al., A feasibility study of the Therapeutic Application of a Mixture of $^{64/67}$Cu Radioisotopes produced by cyclotrons with proton irradiation, Medical Physics (2022) DOI 10.1002/mp.15524

[33] BORGNA, F. et al., A preliminary study for the production of high specific activity radionuclides for nuclear medicine obtained with the isotope separation on line technique, Appl Radiat Isotopes 127 (2017) 214-226 DOI 10.1016/j.apradiso.2017.06.022

[34] BORGNA, F. et al., Early Evaluation of Copper Radioisotope Production at ISOLPHARM, Molecules (2018) 23, 2437 DOI 10.3390/molecules23102437

[35] ANDRIGHETTO, A., Method for producing beta emitting radiopharmaceuticals, and beta emitting radiopharmaceuticals thus obtained, INFN Patent No. WO/2015/114424 (2015)

[36] ANDRIGHETTO, A. et al., The ISOLPHARM project: ISOL-based production of radionuclides for medical applications, J Radioanal Nucl Ch (2019) 322:73–77 DOI 10.1007/s10967-019-06698-0

[37] BALLAN, M. et al., Preliminary evaluation of the production of non-carrier added 111Ag as core of a therapeutic radiopharmaceutical in the framework of ISOLPHARM_Ag experiment, Appl Radiat Isotopes 164 (2020) 109258 DOI 10.1016/j.apradiso.2020.109258

[38] TOSATO, M. et al., Highly Stable Silver(I) Complexes with Cyclen-Based Ligands Bearing Sulfide Arms: A Step Toward Silver-111 Labeled Radiopharmaceuticals, Inorg. Chem. 59 (2020) 10907 DOI 10.1021/acs.inorgchem.0c01405

[39] VERONA, M. et al., Preliminary study of a 1,5-benzodiazepine-derivative labelled with indium-111 for CCK-2 receptor targeting, Molecules 26 (2021) 918 DOI 10.3390/molecules26040918

[40] BALLAN, M. et al., Development of implantation substrates for the collection of radionuclides of medical interest produced via ISOL technique at INFN-LNL, Appl Radiat Isotopes (2021) 175 109795 DOI 10.1016/j.apradiso.2021.109795

[41] TOSATO, M. et al., Copper Coordination Chemistry of Sulfur Pendant Cyclen Derivatives: An Attempt to Hinder the Reductive-Induced Demetalation in 64/67Cu Radiopharmaceuticals, Inorg. Chem. 60 (2021) 11530 DOI 10.1021/acs.inorgchem.1c01550

[42] BENFANTE, Viviana et al., A New Preclinical Decision Support System Based on PET Radiomics: A Preliminary Study on the Evaluation of an Innovative64Cu-Labeled Chelator in Mouse Models, J. Imaging 8 (2022) 92 DOI 10.3390/jimaging8040092

IFAST ACCELERATORS FOR SOCIETAL APPLICATIONS

T. R. EDGECOCK
University of Huddersfield
Huddersfield, UK
Email: t.r.edgecock@hud.ac.uk

A. SAGATOVA
Slovak University of Technology
Bratislava, Slovakia

Abstract

IFAST is the latest in a series of EU projects undertaking R&D for particle accelerators and coordinated by CERN. The IFAST Accelerators for Societal Applications task is investigating a range of novel applications of particle accelerators from the medical, environmental and imaging fields, with the aim of identifying those with the most potential. It will then develop a strategy for delivering these applications. In addition, it is studying barriers which are discouraging the uptake of accelerators in industry and elsewhere and attempting to identify ways of overcoming these.

1. INTRODUCTION

The Innovation Fostering in Accelerator Science and Technology (IFAST) EU Horizon 2020 innovation action [1] is the latest in a series of EU funded projects undertaking particle accelerator R&D and coordinated by CERN. The main focus of these projects has been on R&D for accelerators used for research, with the aim of improving performance in many areas. However, starting in Framework Programme 7 with the EuCARD2 project [2], there has been an increasing emphasis on the societal applications in the energy, environmental and medical areas. This is continuing and expanding with IFAST, due to the particular focus on innovation in this programme.

The work package structure of IFAST is shown in Table 1. As required by the EU call, the work is separated into three activities:

(a) Strategies: study groups to define “roadmaps” for specific technologies.
(b) Prototypes: prototyping with industry at higher TRL.
(c) Developments: development, often with industry, at lower TRL.

Each WP usually has at least one of each activity, with the work being done by tasks within the WP.

The relevant WP for the paper is WP12. This has three tasks, as follows:

- Task 12.1: A Strategy for Implementing Novel Societal Applications of Accelerators
- Task 12.2: Design of advanced electron accelerator plant for biohazards treatment
- Task 12.3: Design of Internal RF Ion Source for Cyclotrons

These are a strategy, a development and a prototype, respectively. The paper describes the first of these, Task 12.1. As this is a strategy, the aims of the Task had to meet the appropriate EU requirements. As a result, these are:

- To study some new and important societal applications of accelerators with the aim of developing roadmaps for their innovation:
  - Novel forms of radiotherapy for cancer treatment.
  - Reduction in environmental pollution.
  - New imaging techniques.
  - Improved methods for radioisotope production.
- To develop a strategy to deliver these roadmaps.
- To study the barriers which discourage the use of accelerators in industry.

To achieve these aims, the work of the Task is split into the 6 sub-tasks shown in Table 2.

TABLE 1. THE WORK PACKAGES IN THE IFAST PROJECT

WP number	Description
1	Management, coordination and dissemination
2	Training, communication and outreach for accelerator science and technology
3	Industry engagement
4	Managing innovation, new materials
5	Strategies and milestones for accelerator research and technology
6	Novel particle accelerators concepts and technologies
7	High brightness accelerators for light sources
8	Innovative superconducting magnets
9	Innovative superconducting cavities
10	Advanced accelerator technologies
11	Sustainable concepts and technologies
12	Societal applications
13	Technology infrastructure
14	Ethics requirements

IFAST started on 1st May 2021 and will run for four years. The paper will briefly describe the work done by each sub-task in the first year of activities and the plans for the rest of the project.

TABLE 2. THE SUB-TASKS OF THE PROJECT

Sub-task number	Description	Coordinated by
12.1.1	Management and communication	Rob Edgecock (University of Huddersfield, UK), Andrea Sagatova (Slovak University of Technology, Slovakia)
12.1.2	Novel forms of radiotherapy	Angeles Faus-Golfe (CNRS, France)
12.1.3	Environmental applications of electron beams	Toms Torims (Riga Technical University, Latvia), Andrzej Chmielewski (INCT, Poland)
12.1.4	Accelerator imaging	Graeme Burt (Lancaster University, UK)
12.1.5	Accelerator production of radioisotopes for imaging and therapy	Concepcion Oliver and Diego Obradors (CIEMAT, Spain)
12.1.6	Barriers to accelerator adoption by industry	Andrzej Chmielewski (INCT, Poland) and Andrea Sagatova (Slovak University of Technology, Slovakia)

2. SUB-TASK AIMS AND ACTIVITIES

The main focus of the Task in the first year has been to assess the state of the art in each application area, select those with the most potential and study the main issues facing those applications. This has been done by building on the work of earlier projects in EuCARD2 [2] and ARIES [3], the book “The Applications of Particle Accelerators in Europe” [4] produced by EuCARD2 and discussions with colleagues working on these topics around the world. The following subsections will describe briefly the work done and the conclusions drawn so far.

2.1. Novel forms of radiotherapy

The aims of this sub-task are to study new forms of radiotherapy for cancer treatment that are currently under development, for example FLASH [5] and mini-beams [6], and to investigate novel beams and accelerators able to achieve the optimal requirements for these treatments. FLASH is a technique in which the dose is delivered very quickly. Standard radiotherapy delivers about 2 Gy/min. In FLASH, the dose is delivered very much faster, at least 40 Gy/s, but usually much faster. In trials, this has been shown to be very effective against tumours, while reducing the damage to healthy cells, and hence the side effects of the treatment. With mini-beams, only a part of the tumour is treated, in a grid-like manner. This has also been shown to be effective against the tumour, while sparing healthy cells.

The main issue is that these techniques, in particular ultra-fast FLASH, are difficult to deliver with the current technology used for radiotherapy, linear electron accelerators up to 20 MeV. These tend to be based on rather old technology and although that makes them well-proven and reliable, they cannot easily be adapted to these new therapies. While other projects are developing low energy linear accelerators better able to meet the requirements, the focus of this sub-task is Very High Energy Electron radiotherapy (VHEE), using electron beams of up to about 200 MeV. As well as being able to deliver the dose more accurately in the transverse direction, and hence being better suited to mini-beams, this therapy also has a better dose-depth profile than standard radiotherapy with x-rays or electrons or proton therapy. This has a sharp peak, the position and structure of which depends on the beam energy and the focussing employed [7]. The main problem with VHEE is that this therapy requires higher energy electrons than standard radiotherapy, but the accelerators able to deliver these must still be sufficiently compact and not too expensive. The sub-task is studying ways of doing this, with the aim of developing a strategy for delivering this therapy.

2.2. Environmental applications of electron beams

This sub-task is studying the use of electron beams for removing a wide range of pollutants from air, water and sewage sludge before they enter the environment. The technique works by using electron beams up to 10 MeV to create many radicals in water. These then react with the pollutants. In the case of biological organisms, the radicals damage the DNA or RNA, leading to cell death. With chemicals, they have various reactions usually resulting in the breakup of long molecules [8]. IFAST is studying a number of topics, building on work that started in ARIES and other projects. In particular, it is studying, the removal of contaminants from sewage sludge, from the exhaust gases of marine diesel engines and from the ballast water of ships.

For sewage sludge, it is collaborating with Task 12.2. It is already known that electron beams are very effective against the pathogenic contaminants in sludge [8], with doses of around 10 kGy being able to reduce nearly all possible pathogenic contaminants by at least six orders of magnitude. There are also measurements that suggest if electron beam treatment is used before anaerobic digestion (AD), there are significant increases in biogas production and the sludge is made more digestible, so the same digestor can treatment more sludge [9]. The requirement now is to incorporate an electron beam into a production sewage sludge treatment plant and demonstrate that these results can be achieved in practice. This is what these two Tasks are aiming to do. In addition, this sub-task is also investigating the removal of “modern” contaminants such as microplastics from the sludge and dealing with the issue of AD being a source of anti-microbial resistance (AMR) growth [10].

The use of electron beams has shown much potential for the removal of acid rain causing gases, SO_2 and NO_x, and volatile organic chemicals from the exhaust gases of marine diesel engines [11]. The technique was demonstrated with a real marine diesel engine in ARIES (see Fig 1) and studies are continuing in IFAST. This work includes the development of a toroidal electron accelerator which will surround the exhaust and direct the electron beam inwards through the gas, studies of novel, ultra-thin window materials able to withstand the exhaust gases and the development of a strategy to test the method on an operating ship.

Studies are also being made of the treatment of the ballast water from ships to remove organisms and other pollutants before the water is discharged into the sea. In certain regions, such discharges are not allowed without treating the water.

2.3. Accelerator imaging

This sub-task is exploring innovation in the use of particle beams for imaging, in particular in the security and medical areas. It has made an assessment of which imaging techniques have the most potential and is now examining what the main future requirements are for these. It has selected the following and identified what further studies are required:

- X-ray cargo scanning and non-destructive testing.
    - What are the advances that will shape that market in the next few years?
    - Are there any disruptive technologies?
    - Are there challenges without solutions?
    - Will compact muon sources ever become economic enough to find an application?
- Ion beam analysis for cultural heritage for which new compact radio frequency quadrupole (RFQ) based ion sources have been developed [12].
    - Can these devices be made mobile?
    - What applications is this technology most appropriate for, especially if mobile?
    - Can the technology be improved or made more cost-effective?
- Medical imaging.
    - Proton radiography has a lot of potential but requires 350 MeV protons. How can this be achieved in the most cost-effective manner?
    - Plasma technology offers compact coherent X-ray sources with higher resolution than current X-ray scanners. What is needed to break this technology through to the market?
    - Prompt gamma range verification technology also has much potential in radiotherapy, but how can this be made available in hospitals?

The next step will be to create a strategy for finding answers to the questions raised.

Figure 1: Test of treating the exhaust gases from the diesel engine in a marine tug in Riga harbour using a mobile accelerator from the Fraunhofer FEP Laboratory in Dresden, Germany (courtesy, HERTIS Collaboration)

2.4. Accelerator production of radioisotopes for imaging and therapy.

The sub-task is examining the production of medical imaging, therapeutic and theranostic radioisotopes and assessing improvements that may be required in the near future. It has determined that the following are needed:

- The development of innovative routes of production for therapeutic and diagnostic radionuclides.
- The development of optimized irradiation targets, that are interchangeable to allow use within the whole supply network.
- That there is an urgent need to achieve convergence on the radiation dosimetry and safety aspects of radioisotope use.

- That there is a need to ensure an adequate supply of radioisotopes, with reduction of costs along the whole supply chain.
- The demand for alpha-emitting radionuclides for therapy and theranostics significantly exceeds the supply, so new production routes need to be identified.

The sub-task is now developing a strategy for how these future needs might be met, as well as undertaking a study of how the radioisotope market might evolve in the future.

2.5. Barriers to accelerator adoption by industry.

This sub-task is studying the barriers which are discouraging some companies from benefitting from accelerator technologies. It will also use experience from companies that have successfully introduced them to address these concerns. So far, it has looked at technological, financial and knowledge barriers and identified a number. The accelerators used tend to be based on rather old technology. Although these work well, they can limit the performance that can be achieved. It is possible that technologies developed for research can help, but these must be made reliable and available at reasonable cost before they can be used in machines for industrial and societal applications. Another related concern is an absence of in-house specialized and auxiliary facilities and equipment for accelerator service and maintenance. This can in part be dealt with by the development of remote customer-support technologies. These can be used to monitor the accelerators, identify when servicing is required and aid staff in industry to do maintenance and some repairs. A third barrier identified is the absence of in-house accelerator experts and staff for accelerator operation, service and maintenance. This can be addressed by the introduction of dedicated educational schemes and study programs bringing together accelerator experts, IT engineers and users. Examples of such programs now exist, including the ARIES Massive Online Open Course (MOOC) [13].

The next step for this sub-task is to examine the legislative and security barriers discouraging the adoption of accelerators, before moving onto application specific barriers.

3. CONCLUSIONS

The IFAST Societal Applications Task is studying novel applications of particle accelerators in the medical, environmental and imaging areas. It has been active for one year and in that time has identified applications to focus on and a range of issues that need to be dealt with. The next step will be to develop strategies to overcome these issues and create roadmaps for the delivery of the new applications.

ACKNOWLEDGEMENTS

This project has received funding from the European Union's Horizon 2020 Research and Innovation programme under Grant Agreement Number 101004730.

REFERENCES

[1] https://ifast-project.eu/.
[2] https://eucard2.web.cern.ch/eucard2/.
[3] https://aries.web.cern.ch/.
[4] FAUS-GOLFE, Á. and EDGECOCK, R., Applications of Particle Accelerators in Europe, ISBN 978-83-7814-704- (2017).
[5] ESPLEN, N. et al, Physics and biology of ultrahigh dose-rate (FLASH) radiotherapy: a topical review, Phys. Med. Biol. **65** 23TR03 (2020).
[6] YAN, W., KHAN, M. K., WU, X., SIMONE, C. B., FAN, J., GRESSEN, E., et al, Spatially fractionated radiation therapy: History, present and the future. Clinical and translational radiation oncology, 20, 30-38 (2020).
[7] KOKUREWICZ, K., et al, An experimental study of focused very high energy electron beams for radiotherapy, Communications Physics, 4(1), 1-7 (2021).

[8] SIWEK, M., and EDGECOCK, T., Application of electron beam water radiolysis for sewage sludge treatment—a review, Environmental Science and Pollution Research, 27(34), 42424-42448 (2020).
[9] SHIN, K. and KANG, H., Electron Beam Pretreatment of Sewage Sludge Before Anaerobic Digestion, Appl. Biochem. Biotechnol., vol. 109, pp. 227–239 (2003).
[10] AZIZ, A., SENGAR, A., BASHEER, F., FAROOQI, I. H., and ISA, M. H., Anaerobic digestion in the elimination of antibiotics and antibiotic-resistant genes from the environment – A comprehensive review. Journal of Environmental Chemical Engineering, 10(1), 106423 (2022).
[11] ZWOLINSKA, E., SUN, Y., CHMIELEWSKI, A. G., PAWELEC, A., and BULKA, S., Removal of high concentrations of NOx and SO2 from diesel off-gases using a hybrid electron beam technology, Energy Reports, 6, 952-964 (2020).
[12] MATHOT S., et al, The CERN PIXE-RFQ, a transportable proton accelerator for the machina project, Nuclear Instruments and Methods in Physics Research Section B: Beam Interactions with Materials and Atoms, 459, 153-157 (2019).
[13] http://mooc.particle-accelerators.eu/

TOWARDS COMPACT LASER-DRIVEN ACCELERATORS: EXPLORING THE POTENTIAL OF ADVANCED DOUBLE- LAYER TARGETS

A. MAFFINI
Politecnico di Milano Milano, Italy
Email: alessandro.maffini@polimi.it

F. MIRANI
Politecnico di Milano Milano, Italy

A. FORMENTI
Politecnico di Milano Milano, Italy

D. VAVASSORI
Politecnico di Milano Milano, Italy

D. DELLASEGA
Politecnico di Milano Milano, Italy

V. RUSSO
Politecnico di Milano Milano, Italy

M. ZAVELANI-ROSSI
Politecnico di Milano Milano, Italy

M. PASSONI
Politecnico di Milano Milano, Italy

Abstract

The interest towards compact, cost-effective and versatile accelerators is increasing for many applications of great societal relevance, ranging from nuclear medicine to agriculture, pollution control and cultural heritage analysis and conservation. In this context superintense laser-driven ion acceleration represents a promising alternative to conventional accelerators, addressing some of their limitations.

The great potential of laser-driven ion acceleration has stimulated different research approaches aimed at the enhancement of the acceleration performances, especially in terms of energy and number of accelerated ions. A widely investigated strategy relies on the continuous progress in laser technology, which can ensure an improvement of the relevant laser parameters (pulse energy, intensity, repetiton rate) and hence of the overall acceleration performance. This approach is of primary importance for the advancement of fundamental research and the study of novel laser-plasma interaction regimes; however, since it ultimately relies on the availability of a limited number of top-class, state-of-the-art laser facilities, it cannot find a widespread diffusion in developing countires and will hardly lead to a practical compact and cost-effective alternative to conventional accelerators in the near future. A complementary approach focuses on the optimization of the laser-target coupling, since a more efficient laser absorption results in an enhancement of ion current and energy with reduced requirement on the laser side.

Among the advanced target concepts that have been explored, one appealing option is given by double-layer targets, where a very low-density layer, which acts as the enhanced absorbers, is attached to a micrometric solid foil. In the paper contribution we present some of the most recent results in the field of laser-driven ion acceleration with advanced double-layer targets, with a specific focus on non-destructive material characterization technique.

1. INTRODUCTION

Compact, flexible and versatile ion and neutron are key for many applications scientific and technological applications of great societal relevance. Laser-plasma based ion acceleration are attracting growing interest as a promising solution to circumvent some limitations of conventional accelerators, such as non-tunable energy, high

costs, non-portable size, radioprotection issues. Laser- driven ion acceleration scheme is typically based on the interaction of an ultra-intense ultra-short laser pulse ($I > 10^{18}$ W cm^{-2}) with a target, which rapidly ionizes turning into a plasma. The coupling of the laser with the plasma induces a strong charge separation and, consequently, intense longitudinal electric fields which are responsible for the ion acceleration process [1]. The resulting ion beam can give rise to secondary neutron sources by exploiting a suitable converter material, in the so-called *pitcher-catcher* scheme.

Among the various laser-based ion acceleration mechanisms that have been proposed in the last two decades, the target normal sheath acceleration (TNSA) is one of the most reliable, robust, and understood schemes. In TNSA, laser pulses are focused on micrometric solid target and their energy is partially absorbed by the electrons of the target. Electrons are heated up to relativistic energies and expand towards the back side, generating a very intense longitudinal sheath electric field (few MV μm−1). This field is responsible for the acceleration of the light ions (mostly protons) located on the rear surface of the target. The result is the emission of bunches of light ions (10^{8} up to 10^{12} protons per shot) with a broad energy spectrum (e.g. exponential distribution with an effective temperature in the order of few MeV) and a well-defined cut-off energy, ranging from few MeV up to several tens of MeV.

Thanks to these features, laser-driven ion sources are already of potential practical interest for some applications in the field of Ion Beam Analysis techniques, such as Particle Induced X-ray Emission (PIXE). Nevertheless, in order to make laser-driven acceleration attractive for most challenging applications (e.g., those requiring fast neutron generation), an enhancement in acceleration performance in terms of energy and current of accelerated ions is required.

A widely investigated approach relies on the continuous progress in laser technology along two main directions: multi-petawatt laser systems, characterized high pulse energy (tens to hundreds of J) and low repetition rate (from few shots per minute down to few shots per day) and table-top lasers, with peak powers of tens to hundreds of terawatts (energy from tens of mJ up to few J) and a high repetition rate (from Hz up to kHz regime). A complementary strategy aims at the enhancement of energy and number of accelerated ions by focusing on the on the control and optimization of the laser- target coupling by acting on the target properties [2].

2. DOUBLE-LAYER TARGETS

In this framework, many approaches have been proposed to design, fabricate and test advanced target solutions optimized for specific laser-matter interaction regimes. One of the most interesting possibilities comes from the fact that laser-plasma coupling is governed by the value of the plasma electron density n_e compared with the critical value n_c (i.e., the theoretical density for which the plasma frequency matches the laser optical frequency):

$$n_c = m_e \omega^2 / 4\pi e^2 \qquad \text{(Equation 1)}$$

Where e is the fundamental charge, m_e the electron rest mass and ω is the laser frequency (in Gauss units). If the laser-generated plasma is overdense ($n_e > n_c$), it will reflect most of the laser pulse energy, if it is underdense ($n_e > n_c$) laser will propagate through and the process of electron heating will be inefficient. It has been shown (both theoretically [3] and experimentally [4]) that the laser-plasma coupling is maximum in the near-critical regime ($n_e \sim n_c$), thus allowing for an efficient electron heating that, in turn, results in an enhanced acceleration process.

Exploiting the near-critical interaction regime in TNSA is surely appealing, however it poses a significant challenge from the point of view of material science and technology. Indeed, one can rework Equation 1 to show the typical values of near critical densities as a function of the laser wavelength: the density of nuclei in a fully ionized critical plasma is n_c/Z, and the nuclear mass can be approximated as $A \times m_p$ (being Z the atomic number, A the atomic mass and m_p the proton mass), and hence the mass density of a near-critical material can be expressed in terms of the laser wavelength λ:

$$\rho_c = n_c \frac{A}{Z} m_p = \pi m_p \frac{A}{Z} \frac{1}{R_c} \frac{1}{\lambda^2} \approx \frac{A}{Z} \frac{1.865}{(\lambda[\mu\mathrm{m}])^2} \ \mathrm{mg/cm^3} \qquad \text{(Equation 2)}$$

Where the last equality is obtained by substituting the numerical values of the classical electron radius R_c and the proton mass m_p. Since the typical wavelength of high intensity laser systems is around 0.8–1 μm and the A/Z ratio is around 2 for most elements, the near-critical requirement corresponds to a mass density of few mg cm^{-3} a few times the density of air is standard conditions.

Given that the TNSA process requires a solid target with a flat back surface, very few options are available. One of the most studied involves the design of Double Layer Targets (DLTs) made of a thin solid foil (e.g., a metallic substrate) coated by a near-critical layer. In order to match the critical density value, the near-critical layer should be a very porous material, such as a *nanofoam*. We have extensively studied the production of near-critical layers by means of the Pulsed Laser Deposition (PLD) technique, demonstrating how cluster-assembled carbon nanofoams deposited by PLD represent an ideal material to be used as a near critical layer in DLT configurations [5, 6]. A sketch of a DLT based on PLD carbon nanofoam is shown in Fig. 1.

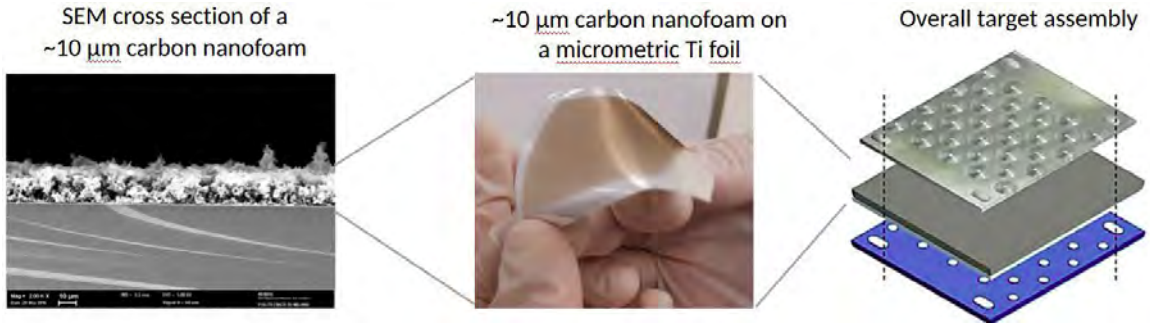

Figure 1: Double-Layer Target based on pulsed laser deposited nanofoam. Left: a Scanning Electron Micrograph of ~10 micron thick near-critical carbon nanofoam. Middle: a photograph of a ~10-micron-thick carbon nanofoam deposited on a micrometric titanium foil. Right: a drawing of the final target assembly (laser propagates downward)

3. CASE STUDY: LASER-DRIVEN MATERIAL CHARACTERIZATION

Among the various techniques belonging to the family of Ion Beam Analysis (IBA), PIXE is particularly suitable to be performed with present-day laser-driven ion sources, given its moderate requirements in terms of ion energies (few MeV/u). Moreover, differently from other IBA techniques, PIXE does not strictly requires a monochromatic source of ions. On the contrary, it can be demostrated that is possible to retrieve the depth profile of elemental concentration using a well- characterized broad-spectrum ion source (the so-called differential PIXE scheme).

We demonstrated the potentials of laser-driven PIXE in an experimental campaign carried out at the Centro de Láseres Pulsados in Salamanca (Spain) using the 200 TW laser VEGA-II [7]. A multi-layered sample made of 2.2 μm thick of chromium deposited onto a millimetric copper substrate has been used as reference sample. In laser-driven acceleration a mixed radiation field (mostly electrons and ions) is present, a feature that is not shared with conventional accelerators. While this could be in principle detrimental for the purpose of IBA, we show that this inherent feature does not represent a limitation. The experiment reported in [7] has been carried out in two different setups, shown in Fig. 2. In the first configuration (Fig.2, left side panels) the irradiation is done with both laser-accelerated electrons and protons. Since the electron contribution to the x-ray generation is dominant, this configuation is dubbed “EDXS” setup, in analogy with the standard Energy Dispersive X-rays Spectroscopy that exploits conventionally accelerated electrons. The proper PIXE setup, in which electrons are removed with a high-field (~0.26 T) magnet placed between the target and the sample. Characterstic x-rays were detected with a charge-coupled device (CCD) that works in single- photon counting mode.

The yield of x-ray generation with electron irradiation is very high, thus allowing for the detection even of trace elements. As shown in Fig. 2 left, bottom peaks of copper and chromium are clearly discernible, thus demonstrating a succesful instance of laser driven EDXS elemental analysis. On the other hand, material analysis in which electron irradiation is present has additional difficulties with respect to pure IBA. In fact, the long electrons range (several mm in solids with MeV energies), the unpredictability of trajectories and the generation of secondaries (δ-rays) capable of inducing ionization are major drawbacks if one is looking for a quantitative

analysis about sample composition. To overcome the aforementioned limitations, we resorted the PIXE setup. The x-rays signal (Fig.2 bottom, left) has been exploited for a quantitative stratigraphic analysis using the procedure described in [8]. Assuming a pure Cr film and Cu substrate, i.e., neglecting the presence of oxygen contamination, we estimate a layer thickness of 1.90 ± 0.39 μm, while including the 7% oxygen contamination of the Cr film we estimate a 2.01 ± 0.39 μm film thickness, a value remarkably close to the actual value of 2.2 μm.

In conclusion we note that, since the number of accelerated protons in this configuration is about 109 to 1010 particles per shot, the resulting current is approximately 1 to 10 nA assuming a 10 Hz repetion rate. These values are compatible with the currents in conventional PIXE analysis for cultural heritage studies.

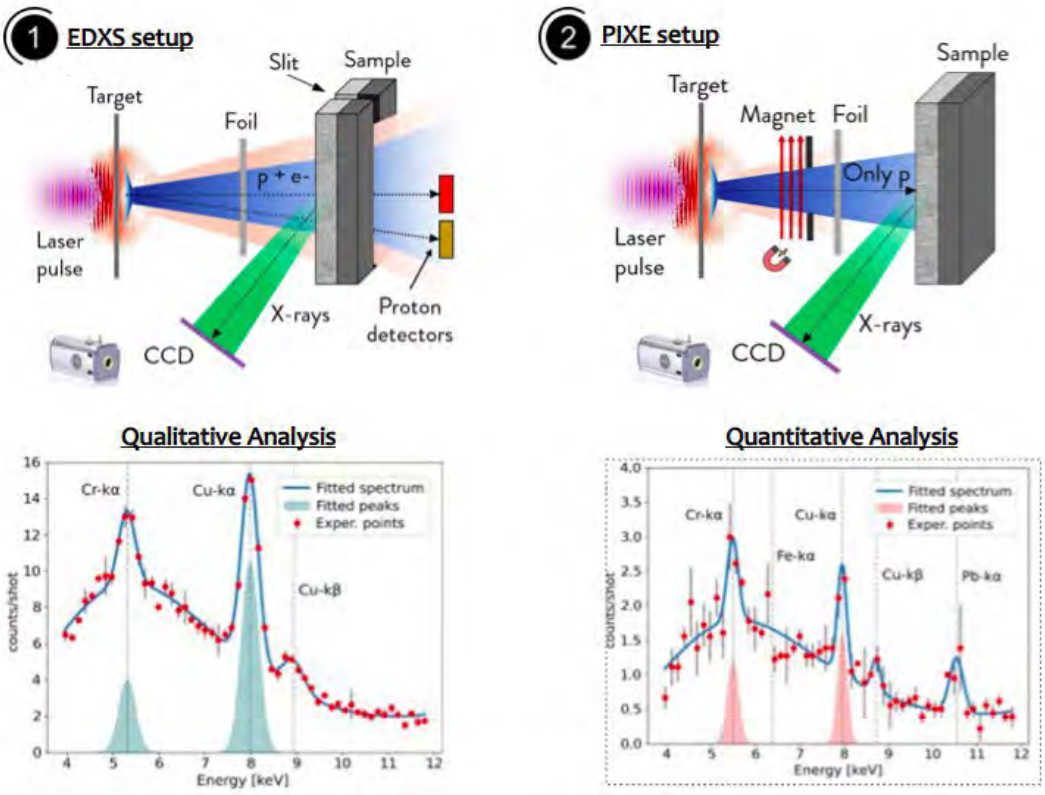

Figure 2: Left, top: EDXS setup, irradiation with both electrons and protons; left, bottom: corresponding characteristic x-ray signal. Right, top: PIXE setup, irradiation with only protons; right, bottom: corresponding x-ray signal, which allows a quantitative characterization of the elemental distribution

ACKNOWLEDGEMENTS

This project has received funding from the European Research Council (ERC) under the European Union's Horizon 2020 research and innovation programme (ENSURE grant agreement No 647554). This work has been carried out within the framework of the EUROfusion Consortium, funded by the European Union via the Euratom Research and Training Programme (Grant Agreement No 101052200 – EUROfusion). Views and opinions expressed are however those of the author(s) only and do not necessarily reflect those of the European Union or the European Commission. Neither the European Union nor the European Commission can be held responsible for them.

REFERENCES

[1] MACCHI A., BORGHESI M, PASSONI, M., Ion acceleration by superintense laser-plasma interaction. Rev. Mod. Phys. 85, 751–793 (2013).

[2] PASSONI M., ET AL., Advanced laser-driven ion sources and their applications in materials and nuclear science. Plasma Phys. Control. Fusion. 62, 14022 (2019).

[3] PAZZAGLIA A., FEDELI L., FROMENTI A., MAFFINI A., PASSONI M., A theoretical model of laser-driven ion acceleration from near-critical double-layer targets. Commun. Phys. 3, 133 (2020)
[4] PRENCIPE I., ET AL., Efficient laser-driven proton and Bremsstrahlung generation from cluster-assembled foam targets, New Journal of Physics, 23 093015 (2021)
[5] MAFFINI A., PAZZAGLIA A., DELLASEGA D., RUSSO V., PASSONI M., Growth dynamics of pulsed laser deposited nanofoams, Physical Review Materials 3, 083404 (2019)
[6] MAFFINI A., ORECCHIA D., PAZZAGLIA A., ZAVELANI-ROSSI M., PASSONI M., Pulsed laser deposition of carbon nanofoam, Applied Surface Science 599, 153859 (2022)
[7] MIRANI F., ET AL., Integrated quantitative PIXE analysis and EDX spectroscopy using a laser-driven particle source, Science Advances 2021; 7 : eabc8660
[8] PASSONI M., FEDELI L., MIRANI F., Superintense Laser-driven ion beam analysis, Scientific Reports 9.1 (2019): 9202

ELECTRON BEAM TECHNOLOGY FOR PRESERVING QUALITY ATTRIBUTES OF MANDARINS FOR ENHANCING EXPORT POTENTIAL

K. A. HOWIE
National Center for Electron Beam Research, Department of Food Science & Technology, Texas A&M University
College Station, Texas, United States of America
Email: khowie1@tamu.edu

S. D. PILLAI
National Center for Electron Beam Research, Department of Food Science & Technology, Texas A&M University
College Station, Texas, United States of America
Email: suresh.pillai@ag.tamu.edu

S. PARSONS
National Center for Electron Beam Research, Department of Food Science & Technology, Texas A&M University
College Station, Texas, United States of America

E. A. BUSTOS-GRIFFIN
NFS Center for Integrated Pest Management, North Carolina State University
Raleigh, North Carolina, United States of America

Abstract

There is a need for countries around the world to increase their exports of agricultural products, as the export of these products adds significantly to the economic development of a country. Agricultural exports such as mandarin oranges and other citrus fruits are of high commercial value and are gaining popularity around the world. However, to deal with strict transboundary phytosanitary requirements, these commodities have to be appropriately treated. Ionizing technologies such as gamma, electron beam (eBeam) and X-ray are suitable technologies. The focus of this study was to determine whether the accelerator technology, namely eBeam technology can be combined with cold temperature storage technology to preserve the quality of mandarins. The science question was pursued was whether cold storage before or after eBeam processing was the most beneficial to preserve mandarin quality. The study was performed with mandarins harvested in two different locations: one in California and the other in Chile. There were three different eBeam dose treatments; 0 Gy (un-treated), 50 Gy, and 150 Gy. The cold temperature + eBeam combination treatments consisted of eBeam treatment at a dose of 50 Gy + 3 or 5 days of storage at 1°C either before or after eBeam treatment. After these combination treatments, the fruit were stored for three weeks; 14 days at 7°C and one week at room temperature. The quality attributes from these combination treatments were evaluated based on standard methods normally utilized for evaluating the quality of fruit in commercial trade, namely Citrus Color Index (CCI), maturity index, weight loss, extractable juice volume, pH, vitamin C, and overall appearance. Overall, the results indicate that the observable differences in these quality parameters were attributable to geographical origin of the mandarins and their stage maturity, rather than the eBeam + cold storage combination treatments. The study highlighted that 150 Gy was detrimental to the fruit quality. These results demonstrate the potential for a new phytosanitary treatment of mandarins which would be 50 Gy , followed by refrigerated storage for 3 days at 1°C. These results suggest that eBeam technology can be technologically compatible with citrus fruits. Economic and technical feasibility analyses to build and operate purpose-built accelerator facilities in citrus growing regions of the world still needed.

1. INTRODUCTION

Oranges (*Citrus sinensis*), mandarins (*Citrus reticulata*), and tangelos (*Citrus tangelo*), are economically important crops worldwide and also have large international markets. However, the trade of citrus fruits is limited due to quarantine restrictions put in place to limit the northward spread of tephritid fruit flies and other exotic species from Mexico [1]. To combat this issue, a generic ionizing radiation dose of 150 Gy has been adopted as an international standard for the treatment of fruit flies in any commodity type [2,3]. At present, there are two

phytosanitary treatments allowed for control fruit flies. The first is to maintain the fruit for 14 days at 1°C, and the second is irradiation at a minimum absorbed dose of 150 Gy. Irradiation treatment has also been adopted by the International Plant Protection Convention (IPPC) as a generic treatment for all fruit flies in any commodity [3]. Both of these treatments affect the quality of the fruit, as exposure to these high ionizing doses damages the oil glands of the citrus peel [4]. This results in brown spotting or pitting on the surface of the fruit, which can impair its quality and adversely affect its market value. Currently, cobalt-60 is the most commonly used ionizing technology in commercial practice. However this legacy phytosanitary treatment method is facing challenges associated with costs, isotope availability, and the transportation of radioactive materials [5,6]. Additionally, the maximum dose the fruits may experience during commercial cobalt-60 operations can be as high as 450 Gy depending on the ionizing radiation field within the irradiation chamber and the configuration of the pallets being exposed to this field [7]. Therefore, other forms of ionizing technologies available for use as phytosanitary treatments are rapidly evolving.

Electron beam and X-ray technologies are now considered to be environmentally and economically sustainable alternatives to cobalt-60 technology. It has been reported that a lower ionizing dose, combined with a shorter and less harsh cold treatment, may be equally effective in preventing fruit fly reproduction when compared to cobalt-60 processing, without damaging the citrus peel oil glands [8,9]. Additionally, the dose rate of eBeam technology is significantly higher than that of cobalt-60 [10]. Therefore, fruit processed using eBeam technology are exposed to the radiation source for shorter periods of time when compared to cobalt-60 processing. This is important from a visual and nutrient quality perspective, as less time spent being subjected to the radiation field is directly correlated with less quality and physicochemical degradation within the fruit [11]. By applying a low radiation dose and reducing the duration of cold storage, the quality of the mandarins as a function of shelf-life will not be affected.

Metabolic and physiological reactions continue to take place and cause unwanted changes in citrus fruits following their harvest, and the rate of these reactions is often influenced by the conditions that the fruits experience during treatment and storage. Citrus fruits are classified as non-climacteric, as their respiration rate does not change once they reach maturity. These fruits are considered to have two independent systems: one involving the exterior of the fruit, or the flavedo because it primarily contains flavonoids, phenolics, carotenoid compounds, and oil glands; and the other involving the interior, or the pulp, that contains pigments, acids and sugars, and bioactive compounds like vitamin C [12]. Since these systems are believed to be independent, they are also believed to have different responses to irradiation treatments. Therefore, the objective of this study was to evaluate these changes as a result of a combination treatment involving low eBeam doses and short cold storage durations. The rationale for this experimental design was to simulate the commercial conditions that citrus fruit experience during transport from the packaging house to the irradiation facility and from the irradiation facility to the retail store.

2. MATERIALS AND METHODS

2.1. Sourcing of Mandarin Oranges and Research Design

This study was conducted on mandarins (*Citrus reticulata*) from two different harvest locations; one in California and the other in Chile. For both studies, the fruits were sourced from a commercial packaging line at Halos – The Wonderful Company in Delano, California. The fruits were shipped via overnight transit to Texas A&M University, with approximately 12 to 15 days elapsing between harvest and arrival. After arrive, the fruits were separated into seven groups (Table 1). Three control groups were selected (0, 50, and 150 Gy) to be compared to four combination treatment groups. There were 50 mandarins per treatment group.

TABLE 1. TREATMENT GROUP DESIGNATIONS

Treatment	Designation
0 Gy Control	0Gy
50 Gy Control	50Gy
150 Gy Control	150Gy
50 Gy + 3 days storage at 1°C	50Gy3D
50 Gy + 5 days storage at 1°C	50Gy5D
3 days storage at 1°C + 50 Gy	3D50Gy
5 days storage at 1°C + 50 Gy	5D50Gy

2.2. Dosimetry and eBeam Treatment

The target eBeam doses were delivered using a 10 MeV, 15 kW linear accelerator. The mandarins were then dose-mapped to determine the dose distribution in the system, the minimum (D_{min}) and maximum (D_{max}) doses, and the Dose Uniformity Ratio (DUR) within the fruits prior to subjecting them to each treatment. The fruits were processed with 11 3/16th high-density polyethylene (HDPE) attenuation sheets, placed above and below the fruit, in order to achieve the minimum and maximum target doses of 50 and 150 Gy, respectively. There were 25 mandarins per tray. The eBeam processing was performed at the National Center for Electron Beam Research at the Texas A&M University, College Station campus. The absorbed eBeam doses within the fruits were measured using L-α-alanine dosimeters (Table 2). Three mandarins were used to measure the absorbed eBeam dose for treatment at 50 and 150 Gy, and dosimeters were inserted into the top, middle, and bottom of each fruit.

TABLE 2. DOSIMETRY DATA

Target Dose (Gy)	Dosimeter Location	Absorbed Dose (Gy)	DUR
50	Top	58.33 ± 24.85	1.76
	Middle	49.00 ± 13.89	
	Bottom	86.33 ± 49.80	
50	Top	50.00 ± 2.65	1.11
	Middle	45.00 ± 1.00	
	Bottom	49.00 ± 2.00	
150	Top	208.33 ± 267.32	1.62
	Middle	218.33 ± 295.89	
	Bottom	135.00 ± 137.71	
150	Top	186.33 ± 61.09	1.16
	Middle	161.33 ± 70.21	
	Bottom	161.00 ± 42.15	

For each control group, 10 fruits were taken for quality assessment at three time points: after treatment, following refrigerated storage (7°C) for 14 days, and following storage at room temperature for one week. For the four treatment groups, the quality was evaluated following the same tine points as the control groups (Figure 1). The quality of the fruits was evaluated through the following physicochemical analyses: juice volume, pH, total soluble solids (TSS), vitamin C, and titratable acidity (TA). The ICM measurements of color and percentage of weight loss were measured in 20 fruits per treatment group, which were monitored throughout storage.

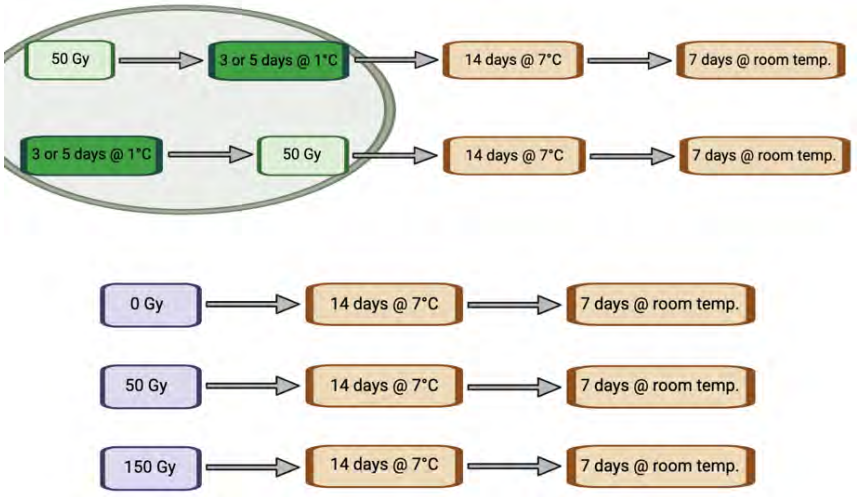

FIG. 1: Image showing the sampling scheme and experimental design of this study.

2.3. Color Determination

The peel color (*L**, *a**, and *b** values) of the 20 mandarins held throughout storage from each treatment group was measured using a calibrated Minolta Colorimeter CR-410 Chroma Meter (Konica Minolta Sensing Americas, Inc., NJ, and USA). A white calibration plate was used to prepare the instrument prior to measurement. Three measurements were taken from each fruit at the equatorial region to obtain an average color reading. These values were then used to determine the CCI of the fruits.

2.4. Determination of Weight Loss

The weight (in grams) of the 20 mandarins held from each treatment group was measured using a digital scale. The results are reported as the average percentage of weight lost by the mandarins.

2.5. Extractable Juice Volume

The mandarins were juiced using a commercially available Hamilton Beach Big Mouth Pro juice extractor and measured using a 100 mL graduated cylinder. A 20 mL aliquot of the juice was used for the pH and TA determination, and the remaining volume was stored under refrigerated conditions in aluminum foil covered, 15 mL polypropylene tubes for approximately one week for the analyses of sugar and vitamin C content.

2.6. Total Soluble Solids (TSS), pH, Titratable Acidity (TA), and Maturity Index

TSS (°Brix) was measured using < 1 mL aliquots of fruit juice and a Rhino Digital Refractometer ATC IP65 (Rhino Technology, Inc., Oakland, CA, USA). The pH of each juice samples was obtained using a MettlerToledo™EasyPlus™Easy Pro Titrator (Mettler-Toledo, LLC, Columbus, OH, USA) and 20 mL of fruit juice. The titrator was calibrated using 1.68 and 4.0 pH buffers prior to measurement. TA (g/100 mL) was determined by titration with 0.1 M NaOH using a MettlerToledo™EasyPlus™Easy Pro Titrator (Mettler-Toledo, LLC, Columbus, OH, USA) and 20 mL of fruit juice. The TSS and TA measurements were used to determine the maturity index of the fruits.

2.7. Vitamin C Content

Vitamin C content (µg/mL) was performed by the Integrated Metabolomics Analysis Core (IMAC) at the Texas A&M University, College Station campus. The vitamin C extraction was done by passing 500 µL of fruit juice through a 0.2 µm nylon filter (Merck Millipore, Burlington, MA) and diluting the filtrate 1:1000 in water. Targeted liquid chromatography (LC-QQQ) analysis was performed on a TSQ Altis mass spectrometer (Thermo Scientific, Waltham, MA) coupled to a binary pump UHPLC (Vanquish, Thermo Scientific), with an injection volume of 10 µL. Chromatographic separation was achieved on a Syneri Fusion 4 µm, 150 mm x 2 mm reverse phase column (Phenomenex, Torrance, CA) maintained at 30°C using a solvent gradient method, with a flow rate of 0.4 mL min^{-1}. Sample acquisition and data analysis was performed using Trace Finder 4.1 (Thermo Scientific).

2.8. Statistical Analysis

For the statistical analysis, JMP Software (Version 14.0, SAS Institute Inc., Cary, NY, USA) was used. One-way analysis of variance (ANOVA) was then utilized to analyze and identify differences between the 7 treatment groups at each time point and within each treatment group across the three time points. A student's t-test was then used to examine statistically significant differences (α=0.05). The results are reported as the mean ± standard deviation.

3. RESULTS

3.1. CCI

The effect of the combination treatment on the CCI of the mandarins is shown in Figure 2. For the California harvested mandarins, all treatment groups experienced decreases in CCI except for the 150Gy and both

of the five-day treatment groups. For the Chile harvested mandarins, all treatment groups experienced decreases in CCI. However, any changes in CCI for both harvest locations were not statistically significant (α=0.01).

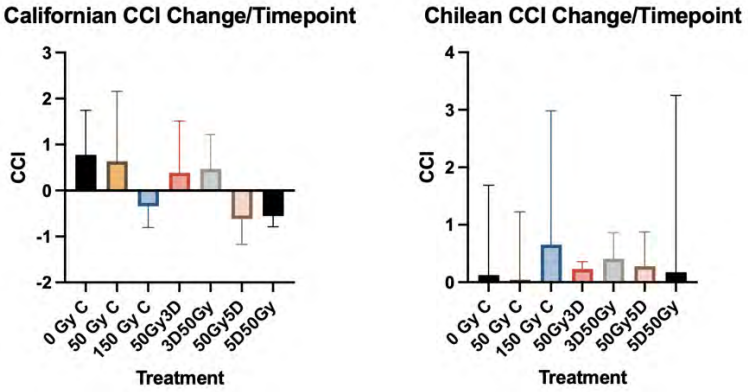

FIG. 2. Graph detailing the average change in CCI value for each of the treatment groups (α=0.01).

3.2. Overall Appearance

The effect of the combination treatments on the overall appearance of the mandarins is shown in Figure 3. For the California harvested mandarins, visual damage such as brown spotting, pitting, and bruising are clearly visible by the third time point in the 150Gy and 50Gy5D samples. Similar brown spotting and dehydration developed in the 0GyC group. Minimal damage is seen in the mandarins that underwent the other three combination treatments. For the Chile harvested mandarins, visual damage and blemishes are clearly visible on the surface of the 150Gy and 5D50Gy samples. It is also shown that already existing brown spots on the fruit peel of the 0GyC, 50GyC, 50Gy5D samples became more pronounced over time. Minimal visual damage can be seen in the mandarins that underwent the combination treatments with a three-day cold storage duration (50Gy3D and 3D50Gy).

FIG. 3. Digital images taken of 20 mandarins held throughout storage.

3.3. Percentage of Weight Loss

The effect of the combination treatments on the percentage of weight loss experienced by the mandarins is shown in Figure 4. For the California harvested mandarins, all treatment groups lost weight during storage except for the 150Gy group. For the Chile harvested mandarins, all of the treatment groups lost weight during storage. However, any changes in the percentage of weight lost by the mandarins in both harvest locations were not statistically significant (α=0.01).

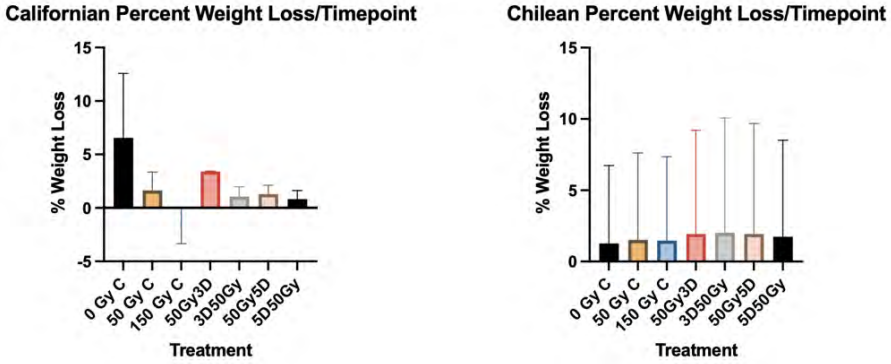

FIG. 4. Graph detailing the average change in percentage of weight loss for each of the treatment groups (α=0.01).

3.4. Extractable Juice Volume

The effect of the combination treatments on the extractable juice volume (mL) of the mandarin fruits is shown in Figure 5. For the California harvested mandarins, losses in extractable juice volume were seen in all of the treatment groups except in the 50GyC, 150GyC, and 5D50Gy samples. For the Chile harvested mandarins, losses in extractable juice volume were seen except in the 50Gy3D and 3D50Gy samples. However, any changes in extractable juice volume for both harvest locations were not statistically significant (α=0.01).

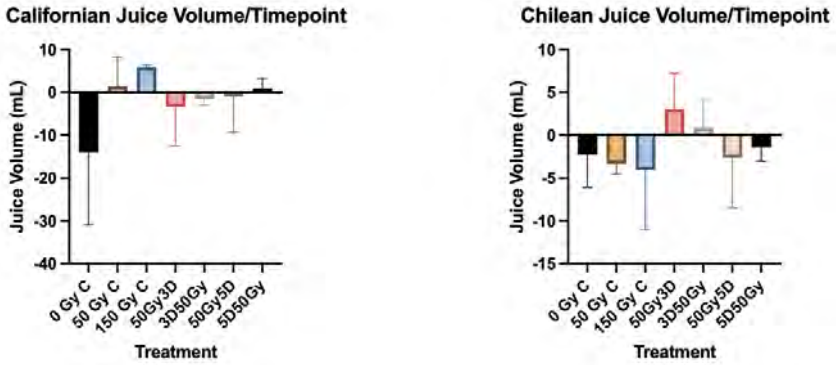

FIG. 5. Graph detailing the average change in juice volume for each of the treatment groups (α=0.01).

3.5. Maturity Index

The effect of the combination treatments on the maturity index (ºBrix/TA) of the mandarin fruits is shown in Figure 6. For the California harvested mandarins, all of the treatments experienced decreases in their maturity index except for the 0Gy and 50Gy5D treatment groups. For the Chile harvested mandarins, all of the treatments experienced decreases in their maturity index during storage except for the 50Gy3D, 3D50Gy, and 5D50Gy treatment groups. However, any changes in the maturity index of the mandarins from both harvest locations were not statistically significant (α=0.01).

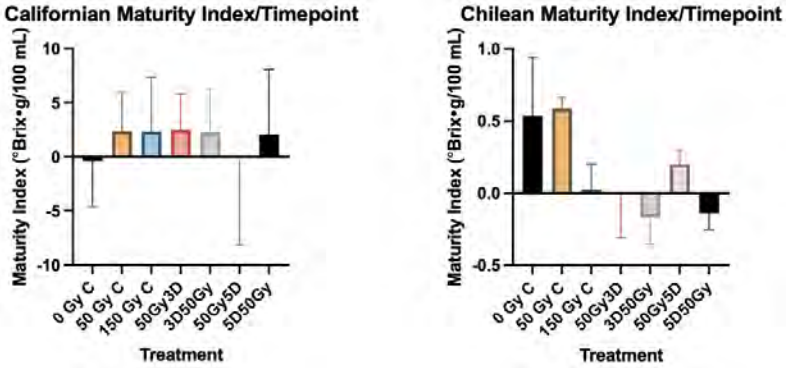

FIG. 6. Graph detailing the average change in maturity index for each of the treatment groups (α=0.01).

3.6. pH

The effect of the combination treatments on the pH of the mandarin fruits is shown in Figure 7. For the California harvested mandarins, all treatment groups experienced increases in pH except for the 0GyC group. For the Chile harvested mandarins, all of the treatment groups experienced increases in pH during storage except for the 50Gy3D, 3D50Gy, and 5D50Gy samples. However, any changes in pH for both harvest locations were not statistically significant (α=0.01).

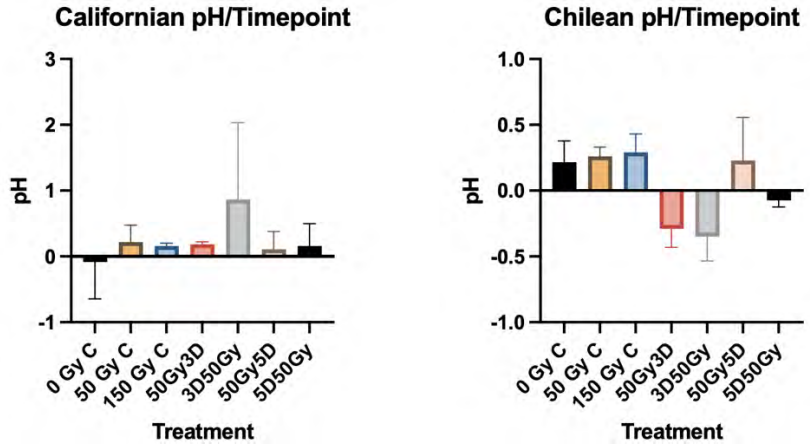

FIG. 7. Graph detailing the average change in pH for each of the treatment groups (α=0.01).

3.7. Vitamin C Content

The effect of the combination treatments on the vitamin C content (μg/mL) of the mandarin fruits is shown in Figure 8. For the California harvested mandarins, all of the treatment groups experienced decreases in vitamin C content except for the 0GyC, 150GyC, and 3D50Gy samples. For the Chile harvested mandarins, all of the treatment groups experienced decreases in vitamin C content. However, any changes in vitamin C content for both harvest locations were not statistically significant (α=0.01).

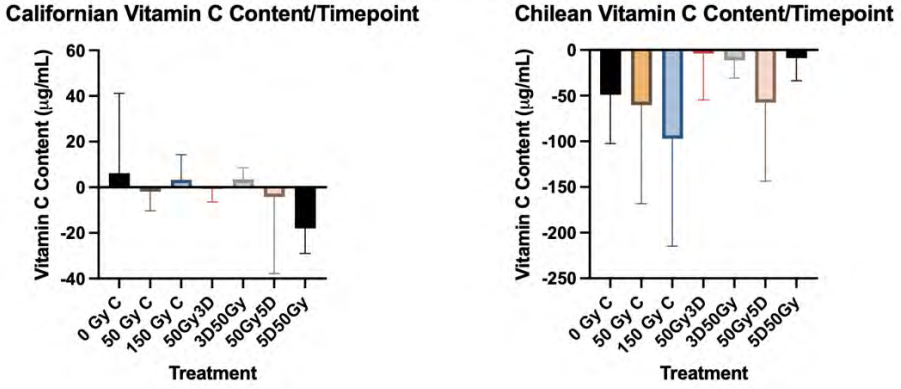

FIG. 8. Graph detailing the average change in vitamin C content for each of the treatment groups (α=0.01).

4. DISCUSSION

The most important attributes for the visual indication of citrus fruit quality are peel color (*L**, *a**, *b**, and CCI values) and overall appearance, and they are also key metrics that influence consumer acceptance [13]. In this study, it was found that the combination treatments had no negative effect on the peel color characteristics in the mandarin fruits. Marked visual damage was seen in the 150GyC mandarins from both harvest locations, which is consistent with previous reports [14,15]. These studies illustrate that this physical damage is understood to be due to the activation of the phenylalanine ammonia-lysate enzyme by irradiation doses, which may enhance the synthesis of phenolic compounds. These compounds are accumulated in the flavedo cell, resulting in cell death

and subsequent peel necrosis and pitting. This deterioration could also be the result of an increase in the transpiration rate of the mandarins in the early stages of storage, which has been reported to induce postharvest senescence of citrus fruits [16,17].

Physiological and mechanical damage as a consequence of storage and treatment conditions has also been reported to impact the amount of weight lost by citrus fruits [18]. Previous studies on mangoes have shown that treatment with ionizing energy may cause similar physiological damage to fruits, possibly due to structural damage to the cells and the breakdown of these cells and their compounds [19]. This damage may contribute to the insignificant amount of weight lost by most of the mandarins during storage, most likely due to water loss. It has been reported that weight loss in tomatoes exposed to ionizing doses in refrigerated storage conditions (10ºC) was significantly less than the weight loss observed in untreated fruits [20]. However, this study concluded that an eBeam treatment consisting of low doses and short cold storage periods are not sufficient in imparting significant effects to the weight of the mandarins.

Citrus fruits are well known sources of ascorbic acid (vitamin C), and it has been reported that this nutrient is particularly sensitive to degradation by ionizing energy and cold storage conditions [21]. Moreover, the degradation products of vitamin C contribute to the formation of brown pigments and subsequent quality losses in citrus juices during storage [22]. However, the results of this study indicate that the combination treatment had no effect on the vitamin C content of the mandarins. It has been reported in a previous study that only doses exceeding 1 kGy significantly reduce the vitamin C content in citrus fruit [23]. Therefore, it can be deduced that vitamin C remained unaffected due to the conditions of the combination treatment, with its low radiation dose and short refrigerated storage period.

The analyses to evaluate the quality of the mandarin pulp following combination treatment included extractable juice volume, TSS, pH, TA, and Maturity Index. Independent of the harvest location, and in spite of the insignificant differences found, there were more changes in extractable juice volume associated with variations of the fruit rather than those associated with irradiation treatment or storage condition. Similar to the weight loss possibly being linked to the transpiration rate in the mandarins, the insignificant decrease in TA in these fruits has also been linked to an increase in transpiration rates [24]. More specifically, organic acids, like citric and malic acid, that normally accumulate in the fruit during development are used in the TCA cycle during ripening which leads to their depletion [25]. Additionally, there were no changes seen in the TSS of the pulp as a result of the combination treatments. This is consistent with other studies which show that, like vitamin C, doses at or below 1 kGy do not alter TSS [25,26].

The criteria for determining the maturity of citrus fruits involves two factors: internal changes to the fruit flesh, or pulp, and external changes in the color of the fruit peel, or flavedo [27]. This study focused on both of these changes to directly measure fruit maturity. Therefore, for the scope of this project, citrus fruits like mandarins are considered to be at peak maturity when their total soluble solids: acidity ratio, or maturity index, has reached a minimal level of palatability and when they showed optimal flavedo colors, which has already been discussed. This study illustrated that the proposed combination treatments did not impact the maturity of the mandarins during storage.

5. CONCLUSION

This study of citrus fruit quality, as a result of the combination treatment consisting of eBeam and cold storage, complements the efficacy studies of the treatment when used for phytosanitary treatment. Therefore, these studies support the adoption of the combination treatment for use in phytosanitary applications. The evaluation of the four different combination treatments in this study on mandarins (*Citrus reticulata*) demonstrated the feasibility of utilizing a phytosanitary treatment involving a 50 Gy eBeam dose and cold storage for 3 days at 1°C. When this treatment is applied to the mature, commercially acceptable fruit, the physiological, chemical, and nutritional qualities are not impacted. Furthermore, this combination treatment allows for the fruit to remain suitable for commercial purposes, without any pitting or discoloration. Ultimately, this study provides strong evidence that the combination treatment can be applied to citrus fruits as an alternative to damaging alternatives. Overall, there is evidence that Chile-harvested mandarins may be more susceptible to physicochemical degradation by eBeam treatment doses as compared to the Californian mandarins. However, whether this difference is due to the time lag differences between the harvests of the mandarins from the two locations or the combination treatment is unknown.

ACKNOWLEDGEMENTS

The authors would like to thank Halos – The Wonderful Company for providing the mandarins for this study. We would also like to thank Mickey Speakmon at the National Center for Electron Beam Research (NCEBR) at Texas A&M University for his efforts in executing the eBeam treatment and dose-mapping, and Cory Klemashevich at the Integrated Metabolomics Analysis Core (IMAC) at Texas A&M University for his work in completing the vitamin C content analysis.

REFERENCES

[1] USDA APHIS | Fruit Flies. (n.d.). Retrieved October 5, 2021, from https://www.aphis.usda.gov/aphis/ourfocus/planthealth/plant-pest-and-disease-programs/pests-and-diseases/fruit-flies/fruit-flies-home

[2] International Standard for Phytosanitary Measures (ISPM) 18. (2003). *Guidelines for the use of irradiation as a phytosanitary measure.* Rome, International Plant Protection Convention (IPPC), Food and Agriculture Organization of the United Nations (FAO).

[3] International Standard for Phytosanitary Measures (ISPM) 28. (2007). *Phytosanitary treatments for regulated pests.* Rome, International Plant Protection Convention (IPPC), Food and Agriculture Organization of the United Nations.

[4] Kader, A. A. (1986). Potential Applications of Ionizing Radiation in Postharvest Handling of Fresh Fruits and Vegetables. *Food Technology, 40*(6), 117 – 121.

[5] Pillai, S. D., & Pillai, E. T. (2021). *Electron beam irradiation technology applications in the food industry.* E. Greenspan, Ed.

[6] Pillai, S. D., & Shayanfar, S. (2015). Introduction to electron beam pasteurization in food processing. *Electron beam pasteurization and complementary food processing technologies* (pp. 3 – 9). Elsevier.

[7] Understanding Gamma Sterilization. (n.d.). Retrieved October 5, 2021, from https://www.biopharminternational.com/view/understanding-gamma-sterilization

[8] Palou, L., Del Rio, M. A., Marcilla, A., Alonso, M., & Jacas Miret, J. A. (2007). Combined postharvest X-ray and cold quarantine treatments against the Mediterranean fruit fly in "Clemenules" mandarins. *Spanish Journal of Agricultural Research, 5*(4), 569.

[9] von Windeguth, D. L., & Gould, W. P. (1990). Gamma Irradiation Followed by Cold Storage as a Quarantine Treatment for Florida Grapefruit Infested with Caribbean Fruit Fly. *The Florida Entomologist, 73*(2), 242.

[10] Miller, R. B. (2006). *Electronic Irradiation of Foods: An Introduction to the Technology (Food Engineering Series)*. Springer.

[11] Hussain, P. R., Suradkar, P., Javaid, S., Akram, H., & Parvez, S. (2016). Influence of postharvest gamma irradiation treatment on the content of bioactive compounds and antioxidant activity of fenugreek (Trigonella foenum-graceum L.) and spinach (Spinacia oleracea L.) leaves. *Innovative Food Science & Emerging Technologies, 33,* 268 – 281.

[12] Kahan, R. S., Monselise, S. P., Riov, J., Koov, J. van, & Chadwick, K. (1968). Comparison of the effect of radiation of various penetrating powers on the damage to citrus fruit peel. *Radiation Botany, 8*(5), 415 – 423.

[13] Liu, C., Zheng, H., Sheng, K., Liu, W., & Zheng, L. (2018). Effects of melatonin treatment on the postharvest quality of strawberry fruit. *Postharvest Biology and Technology, 139,* 47 – 55.

[14] Oufedjikh, H., Mahrouz, M., Amiot, M. J., & Lacroix, M. (2000). Effect of gamma-irradiation on phenolic compounds and phenylalanine ammonia-lyase activity during storage in relation to peel injury from peel of Citrus clementina hort. Ex. tanaka. *Journal of Agricultural and Food Chemistry, 48*(2), 559 – 565.

[15] Pongsri, R., Aimla-or, S., Srilaong, V., Uthairatanakii, A., & Jitareerat, P. (2021). Impact of electron-beam irradiation combined with shellac coating on the suppression of chlorophyll degradation and water loss of lime fruit during storage. *Postharvest Biology and Technology, 172,* 111364.

[16] Yoon, Y., Kim, J., Lee, K., Eun, J., & Park, J. (2020). Effects of electron-beam irradiation on postharvest strawberry quality. *Journal of Food Processing and Preservation, 44*(9).

[17] Strano, M. C., Altieri, G., Admane, N., Genovese, F., & Di Renzo, G. C. (2017). Advance in citrus postharvest management: diseases, cold storage and quality evaluation. In H. Gill & H. Garg (Eds.), *Citrus Pathology.* InTech.

[18] Moreno, M., Castell-Perez, M. E., Gomes, C., Da Silva, P. F., & Moreira, R. G. (2006). Effects of Electron Beam Irradiation on Physical, Textural, and Microstructural Properties of "Tommy Atkins" Mongoes (Mangifera indica L.). *Journal of Food Science, 71*(2), E80 – E86.

[19] Gyimah, L. A., Amoatey, H. M., Boatin, R., Appiah, V., & Odai, B. T. (2020). The impact of gamma irradiation and storage on the physicochemical properties of tomato fruits in Ghana. *Food Quality and Safety, 4*(3), 151 – 157.

[20] Cortés, C., Esteve, M. J., & Frígola, A. (2008). Effect of refrigerated storage on ascorbic acid content of orange juice treated by pulsed electric fields and thermal pasteurization. *European Food Research and Technology, 227*(2), 629 – 635.

[21] Tatum, J. H., Shaw, P. E., & Berry, R. E. (1969). Degradation products from ascorbic acid. *Journal of Agricultural and Food Chemistry, 17*(1), 38 – 40.

[22] Girennavar, B., Javaprakasha, G. K., Mclin, S. E., Maxim, J., Yoo, K. S., & Patil, B. S. (2008). Influence of electron-beam irradiation on bioactive compounds in grapfruits (Citrus paradisi Macf.). *Journal of Agricultural and Food Chemistry, 56*(22), 10941 – 10946.

[23] Moing, A., Renaud, C., Gaudillère, M., Raymond, P., Roudeillac, P., & Denoves-Rothan, B. (2001). Biochemical Changes during Fruit Development of Four Strawberry Cultivars. *Journal of the American Society for Horticultural Science, 126*(4), 394 – 403.

[24] Batista-Silva, W., Nascimento, V. L., Medeiros, D. B., Nunes-Nesi, A., Ribeiro, D. M., Zsögön, A., & Araújo, W. L. (2018). Modifications in organic acid profiles during fruit development and ripening: correlation or causation? *Frontiers in Plant Science, 9,* 1689.

[25] Nam, H.-A., Ramakrishnan, S. R., & Kwon, J.-H. (2019). Effects of electron-beam irradiation on the quality characteristics of mandarin oranges (Citrus unshiu (Swingle) Marcov) during storage. *Food Chemistry, 286,* 338 – 345.

[26] Ramakrishnan, S. R., Jo, Y., Nam, H.-A., Gu, S.-Y., Baek, M.-E., & Kwon, J.-H. (2019). Implications of low-dose e-beam irradiation as a phytosanitary treatment on physicochemical and sensory qualities of grapefruit and lemons during postharvest cold storage. *Scientia Horticulturae, 245,* 1 – 6.

[27] Lado, J., Rodrigo, M. J., & Zacarías, L. (2014). Maturity indicators and citrus fruit quality. *Stewart Postharvest Review, 2*(2), 1 – 6.

LICENSING UNCONVENTIONAL ACCELERATOR PROJECTS: A QUEST FOR THE SAFEST COMPROMISE.

F. SCHMITZ
Bel V
Brussels, Belgium
Email: frederic.schmitz@belv.be

S. VERMOTE
Bel V
Brussels, Belgium

N. NOTERMAN
Bel V
Brussels, Belgium

C. KENNES
Bel V
Brussels, Belgium

Abstract

Recently, exchanges have taken place between operators and the Belgian regulator, FANC (Federal Agency for Nuclear Control) and its technical subsidiary Bel V, concerning unusual applications of accelerators. These new projects presented to the Belgian regulator are not standard and are rather difficult to compare with other installations. They have been designed for various reasons, including an insufficient production capacity for critical radioisotopes used in nuclear medicine for therapy or an alternative production of well-established production routes of radioisotopes used for diagnostic. These special projects represent a regulatory challenge for the regulator to define the appropriate requirements to authorize them making use of the existing legislative corpus.

1. INTRODUCTION

In recent years, technical and administrative exchanges have taken place between operators and the Belgian regulator, FANC[1] (Federal Agency for Nuclear Control) and its technical subsidiary Bel V[2], concerning unusual applications of accelerators[3,4,5]. These projects imply the use of a powerful accelerator as an alternative to classical radioisotopes production routes, or the use of an accelerator as a way to control the amount of the neutrons produced by nuclear fission.

They have been designed for various reasons, including an insufficient production capacity for critical radioisotopes used in medicine for therapy or an alternative production of well-established production routes for radioisotopes used for diagnostic in aging installations.

These special projects represent a regulatory challenge for the regulator to define the appropriate requirements to authorise them making use of the existing legislative corpus. This is particularly relevant for hybrid systems such as accelerator driven systems (ADS) where equipment classified in different categories (according to the regulation) are connected.

2. REGULATORY FRAMEWORK

The Royal Decree of 20 July 2001[6] has established the regulatory framework dealing with the radiation protection of the population, the workers and the environment. The Royal Decree defines four classifications of licensees:

— Class 1 corresponds to facilities where quantities of fissile substances in excess of half a critical mass are used or held. In summary it mainly concerns nuclear power plants, research reactors, fuel factories, waste storage plants and medical radioisotopes facilities handling fissile material;

— Class II corresponds to facilities producing or conditioning radionuclides from irradiated fissile substances, particle accelerators, facilities containing high activity sealed sources, nuclear medicine departments, some types of electronic microscopes, CT scans, X-rays generators with nominal peak voltage higher than 200, … In summary, the type of Class II establishment is very broad, covering very different fields of activity and consequently leading to very different risks for the population, workers and the environment;
— Class III corresponds to facilities that are not covered by Classes I and II, facilities where one or more of the following installations are located: facilities where radioactive substances, including waste, are used or held under conditions that do not give rise to an exemption in accordance with Article 3.1.d. of the Royal Decree of 20 July 2001, installations in which X-ray generating equipment not covered by Article 3.1.b. of the Royal Decree of 20 July 2001 is used;
— Class IV is a class exempt from declaration or authorization. For example: a device that does not create, at any point within 0.1m of its accessible surface and under normal operating conditions, a dose rate greater than 1µSv per hour.

According to the Royal Decree of 20 July 2001, Class III and Class IV are the lowest categories of installations and out of scope of this paper.

3. EVOLUTION OF THE REGULATORY FRAMEWORK

The Belgian Parliament underlined the extreme heterogeneity of Class II installations as defined in the Royal Decree of 20 July 2001 and the lawsuit of an irradiation accident[7,8] speeded up the need to reassess the safety within some installations. Consequently, the Federal Agency for Nuclear Control decided to reform the facility classification by creating a subgroup including the heavy Class II installations, the so called Class IIa facilities[9,10]. The following types of facilities were included in this new classification:

— Facilities producing and conditioning radioisotopes from irradiated fissile substances;
— Particles accelerators used in research or in the frame of radioisotopes production;
— Facilities building accelerators;
— Irradiators used for sterilization purposes.

For all installations falling under classification IIa, additional constraints, having their origin in Class I installations, have been imposed by the regulator:

— A reporting procedure of events and accidents to the regulator must be established and approved by the regulatory body;
— The management of modifications to the installation has to be described in a procedure[11]. The modifications are classified according to their importance in three categories. The smallest ones have to be approved by the internal health physics control, while the most important ones require a modification of the operating license by the regulatory body. For middle modifications, an adaptation of the safety report approved by the regulator is requested;
— The organization of an internal health physics control has to be set-up;
— The drafting of a safety report is mandatory. This safety report is attached to the operating license and must be updated annually or after a modification to the installation. The safety report content has been defined:
  - Chapter I : Introduction;
  - Chapter II : Site characteristics;
  - Chapter III : Description of the installation and the process;
  - Chapter IV : Radiological impact;
  - Chapter V : Safety functions;
  - Chapter VI : Waste management;
  - Chapter VII : Radioprotection;
  - Chapter VIII : Organization;
  - Chapter IX : Technical specification;
  - Chapter X : Dismantling;

- Chapter XI : Internal emergency planning.

— For facilities releasing radioactive gases and/or radioactive liquids, an annual declaration of releases is required;
— New Class IIa operators willing to set up a new facility in Belgium are required to provide a provisional safety report incorporating the latest technical developments as part of the annex of a license application. By this way, the regulatory body ensures that latest improvements in, for example, decommissioning are taken into account by the new operators.

4. FUTURE EVOLUTION OF THE REGULATORY FRAMEWORK

Recently, some new projects presented to the Belgian regulator are not standard and are rather difficult to compare with other "classical" accelerator installations. They have been designed and justified for various reasons, including an insufficient production capacity of critical radioisotopes used in nuclear medicine for therapy or an alternative production of well-established production routes of radioisotopes used for diagnostic, some of them being produced in aging installations. These special projects represent a challenge for the regulator who must find in the existing legislative corpus the best way to license them. This is for instance an issue on hybrid systems like Accelerator Driven Systems (ADS). According to Belgian legislation, the nuclear reactor part must be granted with a Class I license, while the accelerator is supposed to be granted with a Class IIa license. Decoupling the accelerator license from the nuclear reactor one does not make sense from a safety point of view and the regulator will have to take into account, at some points of the process, the interactions resulting from the coupling of these two subsystems.

From a purely technical point of view, the regulator and his technical subsidiary also has to overcome several challenging issues:

— The concepts and designs presented to the regulator are new and essentially based on small-scale research and development (R&D) projects. The scaling up of the results from this research to an industrial level has been done with calculation codes and models sometimes poorly benchmarked. Hence, the validation and verification of these models, sometimes developed internally by the operator, is a challenge for the regulatory body.
— On the other hand, since the project is still in the design phase when the first discussions with the regulator take place, it is not uncommon that as the project evolves, major revisions of the basic design are proposed by the operator, rendering obsolete the safety option selected by the licensee as well as the safety analyses already performed.
— One of the difficulties encountered is also related to the diversity of applications that an accelerator will have to perform. The more scientific objectives the accelerator is designed to achieve, the more complex the machine and its infrastructure become and the more difficult the safety analyses in support of a license application become. It is also assumed that reliability of the operation and the performances of the system are likely to be lower compared to a simpler system.
— The intensive irradiation of targets of unusual design also raised many questions regarding their cooling and the final management of the radioactive waste that will be generated, including in the cooling circuitry. A thorough characterization of the irradiation parameters as well as the introduction of many appropriate interlocks in the machine control system must be evaluated to avoid unacceptable direct damage to the accelerator and possible indirect damage to the environment resulting from failure of the machine and containment barriers.
— Also, many questions are raised about the definition of reference accidents. This is especially the case with ADS, where accidents considered minor or with a certain frequency on an accelerator alone like a flooding of a vacuum chamber can become major once this accelerator is coupled to a reactor.
— A range of external hazards such as earthquakes, aircraft crash accidents, extreme weather conditions are usually not considered in accelerator safety analyses, based on the assumption that stopping the power supply from any cause will stop the beam. However, it would be useful to extend this analysis of external risks to equipment peripheral to the accelerators, such as the cooling circuits, as soon as non-conventional means of cooling are used.

— The acceptance of waste by Ondraf/Niras[12] (the national agency for radioactive waste and enriched fissile materials) and its industrial subsidiary Belgoprocess[13], from these projects may itself be a source of technical problems that must be proactively addressed in the safety analysis of the dossier.
— In terms of dismantling, the legislator wants these unusual accelerator applications to incorporate, wherever possible, the last improvements that have been made and described in the scientific literature in order to facilitate the dismantling:
  - Use of low activation concrete;
  - Reduce the beam loss;
  - Use of fiber glass rebar if it is possible;
  - Remove unnecessary material and peripheral equipment from the bunker;
  - …

There exists a series of guidelines[14] that have been drafted by the regulator and that apply to Class I facilities. These guidelines, for the moment, are not mandatory for class IIa installations. It is therefore regrettable that the monitoring of the installation of an accelerator is, with some exceptions, the sole responsibility of the licensee.

Finally, the external feedback (return of experience = REX) from accelerators similar to the project that has to be licensed is often weak and poorly documented. It may be useful to establish relations with regulators in foreign countries that have already licensed similar facilities.

5. CONCLUSION

Almost 10 years ago, after a reassessment of the safety of accelerator sites following a radiation accident, the legislation was adapted to reinforce the safety of sites holding accelerators. This adaptation was triggered by an awareness of the heterogeneity of accelerators and their applications.

The new projects currently presented to the regulator would again merit a reflection on an adaptation of the legislation taking into account new challenging technical developments.

However, because of the presented administrative and technical issues and the uncertainties that characterize the future of this new projects, the regulator needs to develop a flexible and graded approach to licensing.

This approach implies frequent exchanges and adjustments with the licensee but without compromising the nuclear safety.

REFERENCES

[1] https://fanc.fgov.be
[2] https://www.belv.be
[3] https://www.ire.eu/en/our-activity/ire/smart
[4] https://myrrha.be/
[5] https://www.sckcen.be/en/expertises/technology/accelerators
[6] Royal Decree of 21 July 2001.
[7] https://afcn.fgov.be/fr/situations-durgence/evenements-majeurs-en-belgique/dans-le-secteur-industriel-sterigenics-fleurus
[8] SCHMITZ F., PETERS C., VAN HAESENDONCK M., BEGHIN E., SCHLECHT J., RITACCIO G., *Sterigenics Fleurus safety improvements of the facility,* - IAEA, Technical meeting on enhancing safety and control features of existing radiation processing facilities, Warsaw, 2016,
[9] MINNE E., PETERS C., MOMMAERT C., KENNES C., DEGREEF G., CORTENBOSCH G., SCHMITZ F., VAN HAESENDONCK M., DRYMAEL H., CARLIER P., *Recent evolution in the regulatory framework of the Belgian class II nuclear installations such as irradiators and accelerators,* Eurosafe Forum, Brussels, November 5-6 2012
[10] MINNE, E., CARLIER, P., PETERS, C., MOMMAERT, C., KENNES, C., CORTENBOSCH, G., SCHMITZ, F., VAN HAESENDONCK, M., SCHRAYEN, V., WERTELAERS, A., Belgian class II nuclear facilities such as irradiators and accelerators: Regulatory Body attention points and operating experience feedback, Kerntechniek, Vol.81 n°5, November 2016.

[11] 06/12/21 Règlement technique fixant les critères et modalités de déclaration des modifications dans le cadre de l'article 12 du règlement général
Règlement technique de l'Agence fédérale de Contrôle nucléaire du 6 décembre 2021 fixant les critères et modalités de déclaration des modifications dans le cadre de l'article 12 du règlement général
[12] https://www.niras.be
[13] https://www.belgoprocess.be
[14] 27/05/21 Règlement technique déclinant en termes pratiques l'objectif de sûreté nucléaire conformément à l'article 3/1 de l'AR du 30/11/11 portant prescriptions de sûreté des installations nucléaires. Règlement technique du 27 mai 2021 déclinant en termes pratiques l'objectif de sûreté nucléaire conformément à l'article 3/1 de l'arrêté royal du 30 novembre 2011 portant prescriptions de sûreté des installations nucléaires

ALTERNATING PHASE FOCUSING BEAM DYNAMICS FOR DRIFT TUBE LINACS

S. LAUBER
GSI, HIM, JGU
Darmstadt, Germany
Email: s.lauber@gsi.de

M. BASTEN
HIM, GSI
Darmstadt, Germany

S. YARAMYSHEV
GSI
Darmstadt, Germany

K. AULENBACHER
GSI, HIM, JGU
Darmstadt, Germany

W. BARTH
GSI, HIM, JGU
Darmstadt, Germany

F. D. DZIUBA
JGU
Mainz, Germany

M. DROBA
IAP
Frankfurt, Germany

H. PODLECH
IAP, HFHF
Frankfurt, Germany

M. MISKI-OGLU
HIM, GSI
Darmstadt, Germany

Abstract

In contrast to conventional E-mode resonance accelerators, H-mode DTLs provide for compact linac sections and have been established as highly efficient resonators during the last decades. Thus, H-mode structures are widely applied for heavy-ion acceleration with medium beam energies because of the outstanding capability to provide for high acceleration gradients with relatively low energy consumption. To build upon those advantages, an Alternating Phase Focusing beam dynamics layout has been applied to provide for a resonance accelerator design without internal lenses, which allows for eased commissioning, routine operation, maintenance, and potential future upgrades. The features of such channel are going to be demonstrated on the example of two Interdigital H-mode cavities, separated by an external quadrupole triplet. This setup provides for heavy ion (mass-to-charge $\leq$ 6) acceleration from 300 to 1400 keV/u and is used as injector part of the superconducting continuous wave accelerator HELIAC. Hence, this promising approach generally enables effective and compact routine operation for various applications as super heavy ion research, material science and radiobiological applications as heavy-ion tumor therapy.

1. INTRODUCTION

GSI Helmholtzzentrum für Schwerionenforschung (GSI, Germany) is one of the leading institutions in the research field of superheavy elements. Using heavy ion beams, delivered by the Universal Linear Accelerator (UNILAC) (Barth, et al., 2020), six new heavy elements of the Mendeleyev periodic table have been discovered during the past decades, namely element 107 – 112. Recently, the discovery of new superheavies has become more difficult with increased targeted mass of the new elements, as the probability of successful fusion to obtain new elements decreases. The low fusion probability requires weeks and months longer duration of the experiments (Khuyagbaatar, et al., 2020) with use of the same linac. An increased average beam current will resolve this problem. For this purpose, either the current per bunch or the duty cycle of the delivering machine has to be increased. Since a high peak beam current is impractical to be delivered to the beam targets due to possible damage from heat, a high duty cycle is preferrable. For continuous wave and high duty cycle applications of heavy ion beams, superconducting machines have been proven to be more economic than their normal conducting counterparts (Podlech, 2013).

Currently, the GSI main linac for heavy ion research UNILAC is upgraded (Barth, et al., 2007; Barth, et al., 2022) for beam delivery to the FAIR SIS100 (Spiller, et al., 2020) synchrotron and its various experimental areas, as APPA (Stöhlker, et al., 2015), CBM (Herrmann, 2022), HADES (Lapidus, Gumberidze, Hennino, Rosier, & Ramstein, 2012), NUSTAR (Nilsson, 2015) and PANDA (Schmidt, 2019) among others. The new requirements to the beam are drastically different from the former demands, as the UNILAC will need to deliver high peak-current beam at a low duty cycle. The new objectives of UNILAC operation are different from the beforementioned requirements for superheavy element research. Therefore, a new linear accelerator has been proposed to provide for energy variable, continuous wave heavy ion beam, dedicated to the discovery of new superheavy elements (Minaev, Ratzinger, Podlech, Busch, & Barth, 2009; Schwarz, et al., 2019; Barth, et al., 2017). The Helmholtz Linear Accelerator is going to deliver 1 mA average beam current of different ions from protons to uranium (see TABLE 1). The high average beam current will improve the timeframe for measurement campaigns.

TABLE 1. Helmholtz Linear Accelerator specifications

Quantity	Value	Unit
Frequency	108.408	MHz
Mass-to-charge ratio	1 to 6	
Repetition rate	100	%
Average beam current	1	mA
Beam energy	3.5 to 7.3	MeV/u
Cryomodules	4	
No. SC cavities	12	

The Helmholtz Linear Accelerator was previously planned as superconducting extension (Schwarz, et al., 2019) to the already existing GSI High Charge State Injector (Hochladungsinjektor, HLI) (Klabunde, 1992). Due to new planning directives in conjunction with the upgrade of the UNILAC, it has been decided to provide for a new dedicated injector, employing the HELIAC as an independent accelerator, nevertheless integrated into GSI complex. Thus, a new design of the dedicated HELIAC injector has to be delivered. Following the bunch formation and pre-acceleration in the RFQ, a normal conduction linac section is going to supply beam to the superconducting main linac part. Two normal conduction Interdigital H-mode (IH) cavities will provide for beam acceleration from 300 to 1400 keV/u beam energy (Lauber & others).

It has been decided to adopt IH cavities, as Crossbar H-mode cavities would be too compact for manufacturing, whereas Alvarez-type DTLs lack of energy efficiency. Three approaches for design of the NC injector linac have been previously investigated: designs with one, two, and three separate DTL cavities for heavy ion acceleration from 300 to 1400 keV/u. The layout with two cavities and an intermediate tank is preferred.

A draft with three separately powered IH cavities was dismissed, as the two intertank sections in between the three cavities would have bloated the accelerator length. Furthermore, the operation of three Radio Frequency (RF) amplifiers and many quadrupole lenses could have aggravated operation of such linac due to a high number of control parameters. The operation of one single IH cavity for the design specifications (see TABLE 1) is generally possible. The already existing HLI injector IH cavity employs a single resonator with

embedded quadrupole lenses and is based on the Combined Zero Degree Structure (Kombinierte Null Grad Struktur, KONUS) beam dynamics concept, offering a space-efficient linac (Ratzinger, Hähnel, Tiede, Kaiser, & Almomani, 2019). However, such compact design results in the structure being sensitive to fluctuations of the control parameters during operation and does not feature the desirable beam diagnostics for eased operation.

Another approach to design an efficient single DTL cavity is the application of Alternating Phase Focusing (APF, see SECTION 1.1) beam dynamics. In this concept, internal magnetic lenses for transverse beam focusing are omitted inside the DTL cavity. Instead, positive synchronous phases are used to provide for the required transverse beam focusing. The mandatory longitudinal focusing is achieved with negative synchronous phases, traditionally used in the layout of linacs. In order to achieve beam focusing in all three room directions, positive and negative synchronous phases are used successively in an alternating sequence.

At the Heavy Ion Medical Accelerator facility (HIMAC, Japan), a single-cavity APF-linac is employed (Iwata, et al., Alternating-phase-focused IH-DTL for an injector of heavy-ion medical accelerators, 2006), partially comparable to our design specifications (cf. TABLE 1): a mass to charge ration $A/Z = 3$, an injection energy of 400 keV/u and an output energy of 4 MeV/u of $^{12}C^{4+}$ carbon ions. The HIMAC APF structures length is 3.4 m at a resonance frequency of 200 MHz and a duty cycle of 0.4 %.

The HIMAC APF linac proves the advantages of APF beam dynamics: the linac DTL is uncomplicate for operation, as the only control parameters are the cavity phase and voltage. Therefore, it is highly suited as a medical injector due to rapid recommissioning periods. In general, it has been reported that operation of APF linacs in general can reduce construction and operation costs by about 30 % (Minaev, Ratzinger, & Schlitt, APF or KONUS drift tube structures for medical synchrotron injectors-a comparison, 1999). In comparison to HIMAC, for HELIAC the transported mass-to-charge ratio is twice as high (Lauber & others). Preliminary investigations of a single-cavity APF acceleration system (see SECTION 3.1) for the HELIAC injector indicated high quality beam transport with up to 90% of the design emittance, but no satisfying solution has been found for the 10 % higher design emittance. Also obtaining high beam quality with such high beam emittance requires strict fabrication tolerances.

Thus, for the HELIAC injector it has been decided to adopt a linac design using two APF cavities (see SECTION 3.2), separated by an intertank equipped with a quadrupole triplet for extra transverse beam focusing. The hybrid approach combines the advantages of highly adjustable quadrupole focusing with the low number of control parameters from the APF-concept and reduced construction costs. The intertank also allows the installation of transport and diagnostic equipment, that could not have been installed in a single-cavity machine. In particular, the additional quadrupole triplet is mandatory to cope with varying beam parameters, which could be employed operation of the ECR ion source with very different ion species, as required for material and superheavy ion research.

1.1. Alternating Phase Focusing

The principle of Alternating Phase Focusing has been proposed in 1953 by J. Adlam (Adlam, 1953) and M.Good (Good, 1953) and independently by I. Fainberg in 1956 (Fainberg, 1956). The theoretic background has been developed further in the following years by I. M. Kapchinsky (Kapchinskiy, 1985). But the actual operation of an APF linac has been reported by Y. Iwata et al. (Iwata, et al., Performance of a compact injector for heavy-ion medical accelerators, 2007) in 2007. Apparently, APF was not widely used due to a lack of computer power for design.

APF cavities are highlighted by the absence of magnetic lenses inside the cavity. In order to omit magnetic focusing elements within the cavity, the action of the electric field of the RF gaps is used for beam acceleration and additionally for focusing. But Gauss's law, one of the fundamental Maxwell equations, does not allow simultaneously focusing along all directions in charge free space, $\nabla \vec{E} = 0$. Thus, subsequential longitudinal and transverse electric focusing is necessary to provide for overall beam focusing. Positive and negative synchronous phases (i.e., the RF phase when the accelerated particle beam passes the RF gap) are applied alternatingly to provide for the transversal and longitudinal focusing. Negative phases are routinely applied for acceleration and longitudinal focusing, whereas positive phases for transverse focusing have found wider application during recent decades, although proposed already in 1953 and refined in following years [1-3]. Since then, computational power has increased by several orders as predicted by Moore's Law (Moore, 1965). Recently, it is possible to provide for a design and detailed analysis of the complex beam transport in Alternating Phase Focusing accelerators.

From a beam dynamics point of view, the core task in APF cavity design is selecting the synchronous phases ϕ_i for each gap to obtain the preferred accelerating/focusing properties. The gradual change from negative to positive synchronous phases is realized by altering the $\beta\lambda/2$ resonance acceleration geometry of a cavity. The introduced synchronous phase change $\Delta\phi$ in between two neighboring RF gaps leads to a change of the resonator geometry: the lengths of the tubes inside the DTL cavity are decreased/increased:

$$L_{\text{cell}} = \frac{\beta\lambda}{2} + \beta\lambda\frac{\Delta\phi}{360°} \tag{1}$$

The changed cell length affects the time a particle bunch needs to travel from one RF gap to another. The altered arrival timing of the bunch in the next gap thus leads to a changed synchronous phase.

2. METHODS

In general, the energy gain of a particle with charge q depends on the voltage U_0 in a RF gap, the transit-time factor T_{TTF} and the synchronous phase ϕ (Reiser, 2008).

$$\Delta W = qU_0T_{\text{TTF}}\cos(\phi) \tag{2}$$

Furthermore, the transverse focusing strength $k_{x,y}$ depends on the mass m_0, velocity v, the Lorentz factor γ and the RF wavelength λ (Reiser, 2008)

$$k_{x,y} = -1\frac{\pi qU_0T_{\text{TTF}}}{m_0v^2\gamma^2\lambda}\sin(\phi) \tag{3}$$

The longitudinal focusing strength k_z, is twice as strong (Reiser, 2008):

$$k_z = 2\frac{\pi qU_0T_{\text{TTF}}}{m_0c^2\beta^2\lambda}\sin(\phi) \tag{4}$$

Thus, the focusing properties in all three room-dimensions $u \in \{\text{x}, \text{y}, \text{z}\}$ could be calculated by means of a matrix multiplication of the particle coordinates x in mm and relative velocities x' in mrad with the transport matrix M (Reiser, 2008).

$$M_u\overrightarrow{x_u} = \begin{pmatrix} 1 & 0 \\ k_u/(\beta\gamma)_f & (\beta\gamma)_i/(\beta\gamma)_f \end{pmatrix} \cdot \begin{pmatrix} x_u \\ x'_u \end{pmatrix} \tag{5}$$

For accurate calculation of the beam transport, the volumetric transit-time factor could be used, considering the radial position of the particle r, the aperture radius a, and the gap length g (Reiser, 2008).

$$T_{\text{TTF}}(r) = I_0(Kr)\frac{J_0(2\pi a/\lambda)}{I_0(Ka)}\frac{\sin\left(\pi g/(\beta\lambda)\right)}{\pi g/(\beta\lambda)} \tag{6}$$

The constant K scales reciprocal with the particle velocity $K = 2\pi/(\gamma\beta\lambda)$. The Bessel and modified Bessel functions are denoted as $\text{I}_0(\text{x})$ and $\text{J}_0(\text{x})$.

EQ. (5) is routinely used for efficient calculations of beam dynamics transport because of its vectorized format, by assigning the average phase ϕ_{ref} and a common transit-time factor to all particles. But the mathematical averaging to achieve maximum software performance is not expedient for calculation of the beam dynamics in an APF channel. To cover the features of the overall non-linear beam transport, the tracking must be accurately conducted for each individual particle to account for the coupling of particle phase to transverse focusing. Either, above equations are implemented for tracking of individual particles separately, or already existing modern particle tracking software could be employed.

Nevertheless, the particle tracking from one RF gap to the next could be implemented efficiently by using the drift matrix D and the cell length according to EQ. (1) (Reiser, 2008).

$$D_u\overrightarrow{x_u} = \begin{pmatrix} 1 & L_{\text{cell}}/K_u \\ 0 & 1 \end{pmatrix} \cdot \begin{pmatrix} x_u \\ x'_u \end{pmatrix} \tag{7}$$

The constant K equals to $K_{x,y} = 1$ transversely and to $K_z = \gamma^2$ longitudinally.

The transport through the APF linac is calculated iteratively by updating the particle coordinates $x_{u,i}$ and relative velocities $x'_{u,i}$, as well as the beam energy $E_{\mathrm{kin},i}$ for each gap i directly by applying EQ. (2), (5) and (7).

Also, an input particle distribution must be selected as a starting point of the particle tracking. To analyze the beam dynamics with the lowest number of particles, it is proposed to solely cover the border of the 6D phase space, whilst the inner positions within the hypersphere could be transported with even higher beam quality. To obtain a 6D hypersphere, a multivariate normal distribution must be rescaled according to the 6D Twiss equation (Shor, Feinberg, Halfon, & Berkovits, 2004)

$$\frac{\widehat{\gamma_x}x^2 + 2\widehat{\alpha_x}xx' + \widehat{\beta_x}x'^2}{\widehat{\epsilon_x}} + \frac{\widehat{\gamma_y}y^2 + 2\widehat{\alpha_y}yy' + \widehat{\beta_y}y'^2}{\widehat{\epsilon_y}} + \frac{\widehat{\gamma_z}z^2 + 2\widehat{\alpha_z}zz' + \widehat{\beta_z}z'^2}{\widehat{\epsilon_z}} = 1, \tag{8}$$

using the Twiss parameters $\widehat{\alpha_u}$, $\widehat{\beta_u}$, $\widehat{\gamma_u}$ and $\widehat{\epsilon_u}$. The presented distribution has a total- to RMS-emittance ratio of 6 and therefore corresponds to a Waterbag distribution.

The beam focusing and acceleration within the cavity should be designed to obtain maximum acceleration efficiency with minimum emittance growth. To obtain an appropriate solution, the input Twiss parameters $\widehat{\alpha_u}$, $\widehat{\beta_u}$, $\widehat{\gamma_u}$ and $\widehat{\epsilon_u}$, as well the synchronous phase ϕ_i in each gap must be selected correspondingly. For identification of the optimum variables, many different numeric global and local optimization strategies are available (Virtanen, et al., 2020). A key aspect for optimization of the variables is the adoption of an objective function, translating the designer's requirements to a formal measure. The implemented objective function is detailed in (Lauber & others) and targets minimum emittance growth ξ_u, as well as a high output energy W_{out}.

$$f = \left(\frac{\xi_{x,y} - 1}{t_{x,y}}\right)^2 + \left(\frac{\xi_z - 1}{t_z}\right)^2 + \frac{W_{\mathrm{target}} - W_{\mathrm{out}}}{t_{\mathrm{E}}} \tag{9}$$

The terms of the objective functions are designed to yield a value in between 0 and 1 if the variables are below their corresponding target tolerance t, otherwise the result is a value greater 1. The target energy is intentionally left without exponent to allow for an even higher output energy than targeted, provided that the emittance growth does not increase dramatically.

The variables of the optimization, i.e., the input Twiss parameters $\widehat{\alpha_u}$, $\widehat{\beta_u}$, $\widehat{\gamma_u}$ and $\widehat{\epsilon_u}$, and the synchronous phase ϕ_i in each gap, are constrained. Extreme combinations of Twiss parameters are not desired, as the actual transport systems might not be able to deliver them. The phases in all gaps are at least constrained by the physical length of the drift tubes, as too short cells from rapid changes in the synchronous phase could cause too narrow cell lengths. From an RF point of view, also too long tubes could be impractical due to heat overload. Therefore, in addition to a +90° to -90° boundary of the synchronous phases, multiple constraints must be considered in advance during optimization.

3. RESULTS

In this section, the results of a preliminary single cavity design are discussed (SEC. 3.1), as well as the final design of the HELIAC APF injector linac with two separate cavities (SEC. 3.2). Both designs were obtained using a specifically previously developed optimization framework, wrapping the multi-particle tracking code DYNAMION. In order to put the results in perspective, TABLE 2 outlines the results of the presented and similar APF channels from other authors.

3.1. Single Cavity with Alternating Phase Focusing

A feasibility study was conducted in order to determine, if a single cavity with APF beam dynamics could be realized with the required input emittance. The cavity was optimized for beam transport with a transverse normalized input emittance of 0.8 mm mrad and 64 deg keV/u longitudinally (foreseen by to be delivered by the

preceding RFQ), and a field gradient of 3 MV/m for acceleration from 300 keV/u to 1400 keV/u. The transverse envelopes are limited by the aperture of 10 mm.

The resulting trajectories after optimization are depicted in FIG. 1. No particle loss occurs within the 3.4 m long structure, whereas the 100%-transverse envelope is very close to the aperture and the 90 % envelope size is smaller than half of the aperture along the DTL cavity. The longitudinal 100%-envelope is asymmetric, whereas the 90 % envelope is almost symmetrical. This observation is also reflected by the emittance growth metric. The 90 %-effective emittance growth is about 25 % transversely and only 4 % longitudinally. Those figures of merit are superb, but the total emittance growth and consequently the beam size and potential losses render this result unpreferable for application in a continuous wave linear accelerator, as even few percent particle loss along decades of actual operation could impose degradation of the machine performance.

The model of this single cavity with Alternating Phase Focusing was obtained in about a week of work and does not reflect a final optimum solution, but rather an intermediate one, as it was decided early to design an APF channel using two separate cavities to allow a highly flexible robust routine operation, also necessary to compensate varying beam conditions from operation of the ion source with very different ion species

TABLE 2. Overview on APF linacs worldwide

	HIMAC Medical Synchrotron injector [24]	Compact IH [29]	HELIAC injector - two cavity design [16]	J-PARC Muon Linac [30]	HELIAC injector – one cavity	108MHz Medical Synchrotron injector [19]
Built/Operated	yes	yes	planned	planned	no	no
Year	2007	2000	-	-	-	-
A/Z	3	1	6	0.1	6	3
Input energy (keV/u)	608	40	300	3000	300	300
Output energy (keV/u)	4000	2000	1400	40000	1400	7000
Max gap voltage (kV)	350 [2]	180	260	NA	180	450
Length (m)	3.4374	1.5	4.5 (3)[1]	1.3	3.38	4.3
Frequency (MHz)	200	100	108.4	324	108.4	216.8
Duty factor (%)	0.4	NA	100	0.1 [31]	NA	NA
Number of cells	72	22	56	16	60	78
Aperture (mm)	7	NA (6-8)	9	NA	10	12 and 16
Kilpatrick	1.6	NA	2.5	1.8	NA	NA
Transmission (%)	99.6	80	100	98	100	100
Energy gain (MeV)	10.176	1.96	6.6	3.7	6.6	20.1
Effective gradient (MV/m)	3	1.3	1.5	2.8	2	4.7
Transv. 90% input emit. (norm. mm mrad)	0.68 [18]	NA (1 acceptance)	0.4	NA (0.3 RMS)	0.4	0.32
Transv. emit. growth (%)	0.68 [18]	NA	5	NA (6 RMS)	25	70
Long. 90% input emit. (ns keV/u)	0.68 [18]	NA (0.077 acceptance)	1.64	NA (1.23 RMS)	1.64	0.88
Long. emit. growth (%)	0.68 [18]	NA	3	NA (24 RMS)	4	11

[1] 3 m without the intertank (containing a quadrupole triplet)

3.2. Two Separate Cavities with Alternating Phase Focusing

The second variant to design an APF channel for continuous wave application was realized by employing two separate IH cavities (Cavity-1 & 2) with a quadrupole triplet in between them (Intertank). A detailed report on the design of the channel is published in (Lauber & others). As already mentioned, the triplet is used to compensate beam parameters different from the reference design. Also beam diagnostics as phase probe sensors and beam position monitors will be installed to the channel in the intertank region. The additional beam diagnostics will provide for easy commissioning, as well as routine operation.

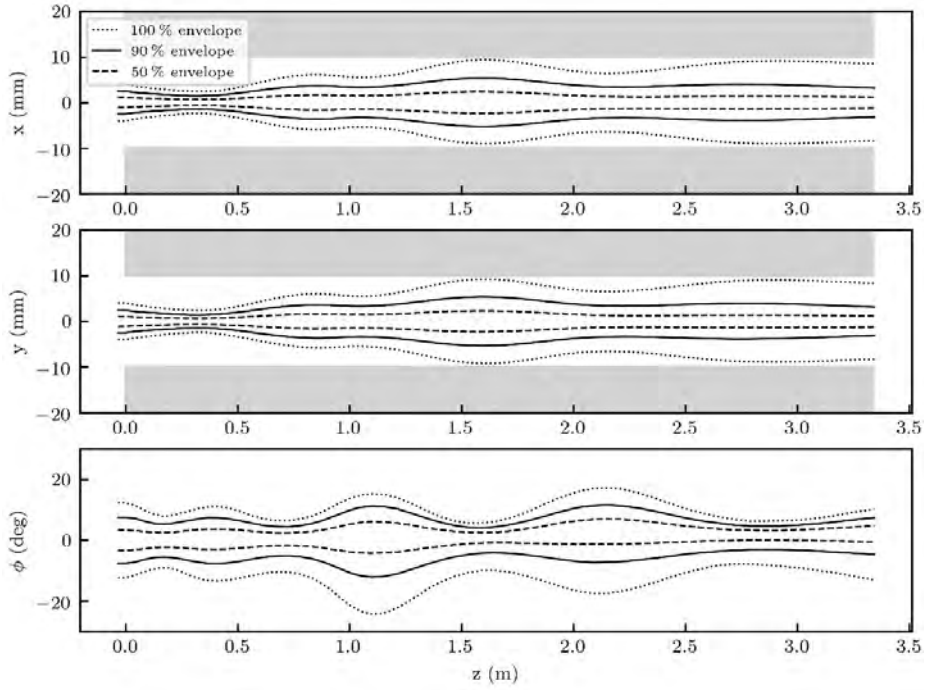

FIG. 1. Beam dynamics draft design of an Alternating Phase Focusing single cavity for acceleration from 300 to 1400 keV/u. An aperture of 10 mm is employed.

The channel was designed employing a field gradient of 3 MV/m and an aperture radius of 9 mm for acceleration of a beam with a transverse normalized emittance of 0.8 mm mrad and 64 deg keV/u longitudinally (the same as for option 1).

For integration into the HELIAC injector, the corresponding beam transport lines have been designed as well and are (additionally to the two designed cavities) depicted in FIG. 2. The Medium Energy Beam Transport system (until 1.9 m), equipped with a quadrupole duplet and a triplet, as well as a rebuncher for longitudinal beam matching to the acceptance of the first cavity. Cavity-1 (1.7 m to 3 m) accelerates the beam to an intermediate energy of 700 keV/u. The quadrupole triplet in the intertank (3 m to 4.5 m) refocuses the transversely divergent beam. A rebuncher is not installed to the intertank, as Cavity-1 provides for dedicated output parameters to match the beam longitudinally to Cavity-2. The beam is accelerated to the final energy of 1400 keV/u along Cavity-2 (4.2 m to 6.1 m). Due to the preceding transverse beam focusing, the synchronous phase pattern in Cavity-2 is oriented rather to beam acceleration than to transverse focusing. The final matching section (> 6.1 m) is equipped with two quadrupole doublets and two rebuncher cavities for full 6D matching of the beam to the acceptance of the superconducting HELIAC. The 90 %-effective emittance growth of the channel is about 5 % transversely and 3 % longitudinally, and thus suited to supply high quality beam to the superconducting HELIAC and subsequent experiments.

4. CONCLUSION

Alternating Phase Focusing cavities are a highly attractive option to extend the length of DTL cavities without employing embedded magnetic lenses within the cavity whilst retaining compactness and effective acceleration. The thereby reduced number of control parameters eases fabrication and facilitates rapid commissioning and stable operation. Two implementations of the APF beam dynamics scheme for $\beta\lambda/2$ drift tube linacs have been elaborated for acceleration of heavy ions from 300 to 1400 keV/u: a single DTL without any magnetic lens, and a channel with two APF cavities separated by an intertank, equipped with an external quadrupole triplet. The first option provides for a 90 %-effective emittance growth of about only 4 % longitudinally, but 25 % transversely. Potential losses due to the total beam size make this option unsuitable for continuous wave operation with 1 mA beam current. This preliminary design could be improved and therefore could be of high interest for applications with a decreased average beam current due to the compactness,

effectiveness and low number of control parameters, i.e., tank phase and voltage. The well-developed second option, with two separate APF cavities and external quadrupole focusing, provides for high beam quality (90 %-emittance growth of about 5 % transversely, 3 % longitudinally) and is adopted as main linac part for the injector of the superconducting Helmholtz Linear Accelerator (HELIAC).

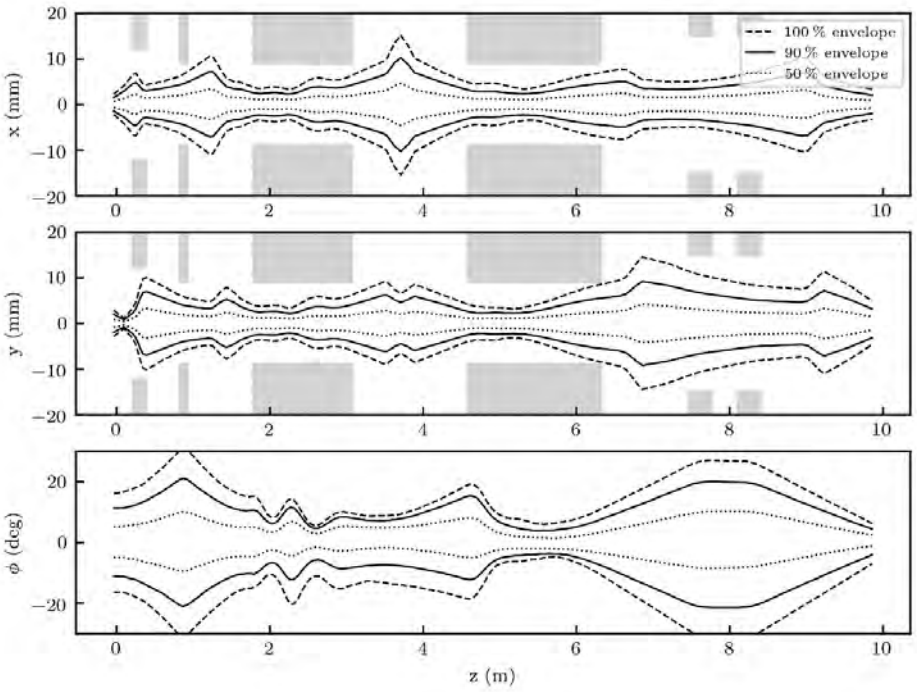

FIG. 2. Design beam envelopes along HELIAC injector linac from RFQ output to SC HELIAC input, employing two APF cavities. The gray blocks indicate the apertures of the quadrupoles, IH cavities and rebunchers.

REFERENCES

[1] W. Barth, R. Hollinger, A. Adonin, M. Miski-Oglu, U. Scheeler et al., "LINAC developments for heavy ion operation at GSI and FAIR," Journal of Instrumentation, vol. 15, p. T12012, 2020.

[2] J. Khuyagbaatar, A. Yakushev, C. E. Düllmann, D. Ackermann, L. L. Andersson and others, "Search for elements 119 and 120," Phys. Rev. C, vol. 102, p. 064602, 2020.

[3] H. Podlech, "Superconducting versus normal conducting cavities," 2013.

[4] W. Barth, W. Bayer, L. Dahl, L. Groening, S. Richter et al., "Upgrade program of the high current heavy ion UNILAC as an injector for FAIR," Nucl. Instrum. Methods Phys. Res. A, vol. 577, p. 211–214, 2007.

[5] W. Barth, G. C. L. Dahl, P. Gerhard, L. Groening, B. Lommel et al., "High current \mathrmU^{40+}-operation in the GSI-UNILAC," 5 2022.

[6] P. Spiller, R. Balss, P. Bartolome, J. Blaurock, U. Blell and others, "The FAIR heavy ion synchrotron SIS100," Journal of Instrumentation, vol. 15, p. T12013–T12013, 2020.

[7] T. Stöhlker, V. Bagnoud, K. Blaum, A. Blazevic, A. Bräuning-Demian et al., "APPA at FAIR: From fundamental to applied research," Nuclear Instruments and Methods in Physics Research Section B: Beam Interactions with Materials and Atoms, vol. 365, 9 2015.

[8] N. Herrmann, "Status and perspectives of the CBM experiment at FAIR," EPJ Web of Conferences, vol. 259, p. 09001, 1 2022.

[9] K. Lapidus, M. Gumberidze, T. Hennino, P. Rosier and B. Ramstein, "The HADES-at-FAIR project," 1 2012.

[10] T. Nilsson, "The NUSTAR project at FAIR," Physica Scripta, vol. T166, p. 014070, 11 2015.

[11] M. Schmidt, "The PANDA Detector at FAIR," Ukrainian Journal of Physics, vol. 64, p. 640, 9 2019.

[12] S. Minaev, U. Ratzinger, H. Podlech, M. Busch and W. Barth, "Superconducting, energy variable heavy ion linac with constant β, multicell cavities of CH-type," Phys. Rev. ST Accel. Beams, vol. 12, p. 120101, 2009.

[13] M. Schwarz, S. Yaramyshev, K. Aulenbacher, W. Barth, M. Basten et al., "Reference beam dynamics layout for the SC CW heavy ion HELIAC at GSI," Nucl. Instrum. Methods Phys. Res. A, p. 163044, 2019.

[14] W. Barth, K. Aulenbacher, M. Basten, F. Dziuba, V. Gettmann et al., "A superconducting CW-linac for heavy ion acceleration at GSIX," EPJ Web Conf., vol. 138, p. 01026, 2017.
[15] J. Klabunde, "The high charge state injector for GSI," in Proc. LINAC'92, 1992.
[16] S. Lauber and others, "An alternating phase focusing injector for heavy ion acceleration".
[17] U. Ratzinger, H. Hähnel, R. Tiede, J. Kaiser and A. Almomani, "Combined zero degree structure beam dynamics and applications," Phys. Rev. Accel. Beams, vol. 22, p. 114801, 2019.
[18] Y. Iwata, S. Yamada, T. Murakami, T. Fujimoto, T. Fujisawa et al., "Alternating-phase-focused IH-DTL for an injector of heavy-ion medical accelerators," Nucl. Instrum. Methods Phys. Res. A, vol. 569, p. 685–696, 2006.
[19] S. Minaev, U. Ratzinger and B. Schlitt, "APF or KONUS drift tube structures for medical synchrotron injectors-a comparison," in Proc. PAC'99, 1999.
[20] J. H. Adlam, "A method of simultaneously focusing and accelerating a beam of Protons," AERE GP/M, 1953.
[21] M. L. Good, "Phase-reversal focusing in linear accelerators," Phys. Rev., vol. 92, p. 538, 1953.
[22] I. B. Fainberg, "Alternating phase focusing," in Proc. Conf. on High Energy Accelerators, CERN, 1956.
[23] M. Kapchinskiy, Theory of linear resonance accelerators, United States: Harwood Academic Pub, 1985.
[24] Y. Iwata, S. Yamada, T. Murakami, T. Fujimoto, T. Fujisawa et al., "Performance of a compact injector for heavy-ion medical accelerators," Nucl. Instrum. Methods Phys. Res. A, vol. 572, p. 1007–1021, 2007.
[25] G. E. Moore, "Cramming more components onto integrated circuits," Electronics, vol. 38, 1965.
[26] M. Reiser, Theory and design of charged particle beams, vol. 2, John Wiley & Sons, Ltd, 2008.
[27] A. Shor, G. Feinberg, S. Halfon and D. Berkovits, "SARAF simulations with 6D waterbag and gaussian distributions," Israel, 2004.
[28] P. Virtanen, R. Gommers, T. E. Oliphant, M. Haberland, T. Reddy et al., "SciPy 1.0: Fundamental algorithms for scientific computing in Python," Nature Methods, vol. 17, p. 261–272, 2020.
[29] T. Hattori, S. Matsui, N. Hayashizaki, H. Tomizawa, T. Yoshida et al., "Compact IH-APF type linac for PIXE and RBS analyses," Nuclear Instruments and Methods in Physics Research Section B: Beam Interactions with Materials and Atoms, vol. 161, pp. 1174-1177, 3 2000.
[30] M. Otani, T. Mibe, M. Yoshida, K. Hasegawa, Y. Kondo et al., "Interdigital H-mode drift-tube linac design with alternative phase focusing for Muon linac," Phys. Rev. Accel. Beams, vol. 19, p. 040101, 2016.
[31] Y. Nakazawa, H. Iinuma, Y. Iwata, Y. Iwashita, M. Otani et al., "Development of inter-digital H-mode drift-tube linac prototype with alternative phase focusing for a Muon linac in the J-PARC Muon G-2/EDM experiment," J. Phys. Conf. Ser., vol. 1350, p. 012054, 2019.

SOCIETAL IMPACT OF THE COMPACT LINEAR COLLIDER STUDY

A. MAGAZINIK
CERN / Tampere University
Geneva, Switzerland / Tampere, Finland
Email: anastasiya.solodko@cern.ch

N. KOKKINIS NTRENIS
University of Applied Science and Arts of Western Switzerland
Geneva, Switzerland

N. CATALAN LASHERAS
CERN
Geneva, Switzerland

S. MAKINEN
University of Turku
Turku, Finland

J. SAUZA BEDOLLA
Lancaster University
Lancaster, The United Kingdom

S. STAPNES
CERN
Geneva, Switzerland

Abstract

In recent years, there is an increasing interest on societal impact of large scientific projects. At strategy meetings for the next particle accelerator for high energy physics, the scientific community recognizes that it is important to demonstrate, not only the academic significance of the project, but also its potential merits in the context of regional, national, and international development; technological and economic impacts for industries; environmental impacts from civil construction and operation; etc. Starting from existing literature on societal impact assessment and its application to Research Infrastructures, the conceptual model framework for CLIC has been built. The research has been mainly centered around publications as knowledge output, human capital impact through the early carrier researchers and technological impact, representing benefits to business. The results take into consideration the very early stage of the international study and demonstrate already beneficial outcomes for society.

1. INTRODUCTION

The past decade has witnessed an increasing interest on the topic of Societal Impact Assessment (SIA). However, there are still challenges when measuring the impact of a given undertaking. Different methodological approaches such as econometric studies, surveys, case studies, do not create a complete and objective picture of the global impact. Assessing basic research outcomes is even more challenging, since it usually requires large government public funds, while societal benefits are often implicit comparing to an applied science project. The societal impact assessment of research infrastructure becomes essential for scientists in demonstrating and highlighting the source of economic value generated for society, besides its absolute technological or scientific significance.

Moreover, the European particle physics community repeatedly raises the question of societal impact during discussions. The community meets to define a strategy for the future developments in fundamental research on physics by evaluating ongoing studies. In an open symposium in Granada in May 2019 [1], the committee highlighted the purely academic significance of an international collider study and its unclear technical and economic ripple effects for the general public. Likewise, the European Strategy update in June 2020 again recommended emphasizing, besides the scientific impact of particle physics, its technological, societal and human capital outcomes [2]. The committee also underlined the importance of partnership with industry and other research institutes as key to sustaining scientific and technological progress, helping drive innovation and bringing about societal benefits. Furthermore, the particle physics attracts young minds and provides them education and training, which are vital for the functionality of RI and of society at large.

Together with the elevated interest in SIA, the community dedicated to assessing societal impact of RI is expanding. Big Science centres, institutes and laboratories around the world are reuniting their knowledge and experience to build a comprehensive assessment model. The work on the assessment framework for LHC [3], already started in 2015. A conceptual model for the evaluation of social benefits had been proposed in the form of a cost-benefit analysis (CBA) [4]. Such study involved several external and internal CERN experts and was supported by the European Commission in its related guide to Cost-Benefit Analysis of Investment Projects issued in 2014 [5]. The developed economic appraisal model was employed afterwards in the appraisal of the

National Hadrontherapy Centre for Cancer Treatment (CNAO) in Italy [6] and for the next generation of LHC, the HL-LHC [7]. Compared to the socio-economic impacts of cancer treatment infrastructure, those of fundamental discoveries are uncertain since they tend to be practically applied much later. While a major part of the societal impacts of CNAO is its direct health benefits to society, the impacts of an accelerator consists mainly of scientific publications, experience gained by the early career researchers, technological spillovers and public outreach. The latest network aiming to fill this gap is RI-PATHS [8], a European project funded by the EU as a consortium of EFIS, CSIL, ESF, ALBA, DESY, CERN, ELIXIR and Fraunhofer ISI. In 2018, the mentioned laboratories joined forces under the RI-PATHS project funded by EU Horizon 2020 to deliver an impact assessment toolkit specifically addressing RIs.

The present work is relevant to a large-scale study on the Compact Linear Collider (CLIC)[1] [9] and to the scientific context within which a research organisation, CERN, operates. CLIC is an international study for a future 50.1 km long machine to collide electrons and positrons head-on up to several teraelectronvolts (TeV) of energy. Building and operating such a large machine with its corresponding infrastructure is extremely costly. In this study, potential effects on different concerned groups such as society, industry and the scientific community are discussed to prove the required investment needs and to show the importance of possible scientific discoveries. Since CLIC is still at the study phase at this point, a SIA can strengthen the decision-making process in the project implementation phase. The assessment is performed before the project construction and operation to find out at what point the study starts producing benefits.

This study identifies the nature and measures of the impacts, considering the project's particularity and novelty. The framework to be constructed herein can be used by policymakers or other stakeholders of large research laboratories to evaluate the relevance and level of achievement of a project. The applied methodology is established based on the previous studies and describes concerned evaluating fields and proposed methods of appraisal.

The paper introduces the methodology and the valuation of human capital formation, technological impact, and knowledge formation. The document also discusses the future study to be done to complete the societal impact assessment of CLIC.

2. METHODOLOGY

The guide to CBA [5] issued by the European commission (EC) presents an economic appraisal tool. After definition of the objectives, technical feasibility, and environmental sustainability, if a project requires financial support (FNPV < 0), an economic analysis has to be performed. The economic net present value (ENPV) for a funded RI (FRI) is calculated as the difference between the discounted total social benefits and the economic costs plus a non-use value term.

$$ENPV_{FRI} = \underbrace{[S + T + H + Str + C]}_{\text{MEASURABLE BENEFITS}} - \underbrace{[K + L_S + L_O + O + E]}_{\text{ECONOMIC COST}} + \overbrace{B_n}^{\text{NON-USE VALUE}}, \quad (1)$$

The terms of this equation are evaluated based on earlier approaches found in literature and are specific to a RI. The detailed description of the measures is discussed in details in the subchapters 2.1 and 2.2 of the present paper. A value of ENPV < 0 indicates that the society is better without the project while ENPV > 0 means the society benefits from the project. Also, according to the EU guide, the ENPV uses accounting prices instead of imperfect market prices, and includes any social and environmental externalities, as in the following equation:

$$NPV = value/(1 + r)^t, \quad (2)$$

where ***r*** is the discount rate, and ***t*** is the time frame of the project.

Fig. 1 shows a finalised methodological CLIC appraisal model. The framework combines EIA [10] with collaboration network assessment, partially emphasising CBA as a well-defined tool that can be used for comparative purposes. The methodology describes all possible evaluating fields and proposed methods for their

[1] Home | CLIC - Compact LInear Collider (no date). Available at: https://clic.cern/ (Accessed: 21 December 2021).

appraisal. The calculation is performed for technological, human capital and knowledge outputs. However, hereinafter, the measurable benefits and costs are discussed for the full SIA model.

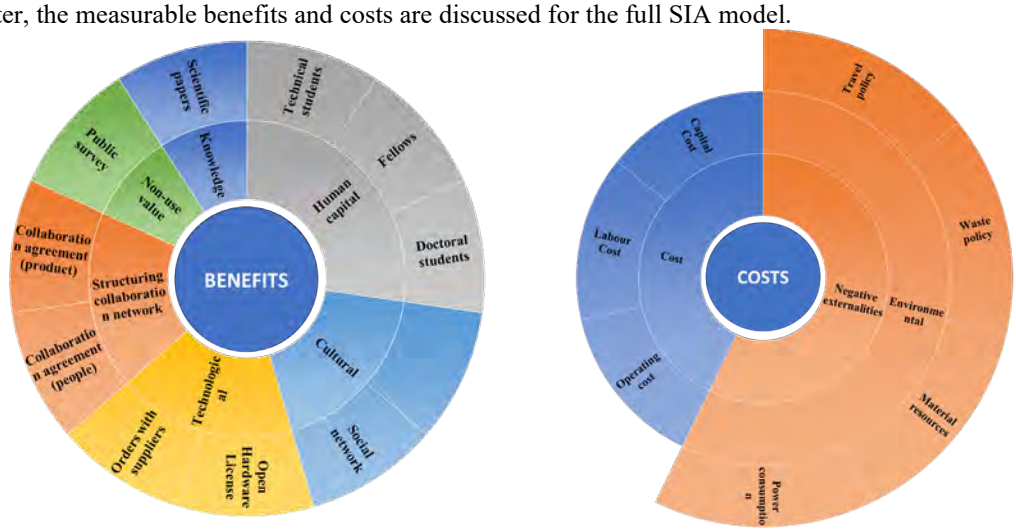

FIG. 1. Benefits and costs for the SIA.

2.1. Measurable benefits

Knowledge outputs (S) are new knowledge created based on produced scientific publications. The aggregate value is determined based on the number of papers and their citations and considering their production time. The indicators are scientific papers, including CLIC notes, publications, and proceedings.

Technological outputs (T) are benefits generated for industrial partners through CERN procurement activities. The value is calculated based on the cumulative value of procurement orders adjudicated to a company, the incremental profits gained through additional sales to third parties and the technology and knowledge acquired "for free" from Open Hardware use. The indicators are procurement orders, suppliers' general information from ORBIS[2] and the Open Hardware Repository[3].

Human capital (H) represents training and educational benefits for early-career researchers (ECRs). The value is calculated based on the salary earned over the entire work career after leaving the project, considering a career length of 35-40 years. The indicators are the number of ECRs, such as technical and doctoral students and fellows.

Cultural output (C) is a factor represented by general cultural activities, such as conferences, events, and visits of the facility, based on the time spent in travelling, travel cost, length of stay, means of transport, areas of origin and number of website visitors, among others. The cultural impact of the CLIC study can be represented and calculated by the following indicators: (1) number of guided tours for students and other visitors of the test facilities such as the showroom, CTF3 [11] and the test module lab [12]; (2) number of public events, such as CERN Open Days [13], focusing on the CLIC representation stands; and (3) social networks. The last one can be evaluated by number of visits to the official CLIC webpage [14], and number of mentions of CLIC in social networks such as Facebook, LinkedIn and Instagram through related posts and tags. The value can be calculated by estimating the travel cost and the time spent in creating a post or a tag. The indicators are activities in social networks, public events and guided tours.

Structuring collaboration (Str) is the value assigned to the formation of scientific collaborative networks. The formation of collaboration network creates benefits at different geographical levels. Universities profit from the common R&D programs in terms of support and scientific inputs from large RIs. Large RIs are good platforms for knowledge dissemination, technology development and concept testing, for which small institutes largely benefit. Moreover, the collaboration network creates additional advantages for industrial partners that have already proven their ability to provide high-quality products or services to other collaboration partners. In the framework of this study, information on different types of collaboration agreements is collected, which forms an

[2] https://www.bvdinfo.com

[3] "Open Hardware Xband components - All Documents." https://espace.cern.ch/project-clic-xband-production/_layouts/15/start.aspx#/Open Hardware Xband components/Forms/AllItems.aspx (accessed Aug. 10, 2021).

overall picture of the universities and institutes involved. CLIC has around 130 collaboration contracts with 180 universities and institutes. The indicators are the number of collaboration agreements and related procurement activities, publications and ECRs related to CLIC. This can be however claimed as a second-tier impact field, and CLIC's correlated share of the impact has to be established.

2.2. Economic costs

The cost estimation is presented in the CLIC project implementation plan (PiP) [15].

Capital cost (K) differs according to the considered stage of the project.

Labour cost (L) defines the cost of the employment need for the construction and operation of the accelerator. The CLIC PiP specifies 11500 FTE-years of explicit labour. Based on the LHC results, 40% scientific and engineering personnel (L_S) and 60% other staff (L_O) are required.

Operating cost (O) represents the ongoing expenses for running a scientific experiment and already built infrastructure.

Negative externalities (E) have been reviewed earlier in the CLIC EIA [16]. Moreover, some estimations of power and energy consumption are reported in the CLIC PiP [15]. The indicators are travel policies, material resources, waste policies and power consumption.

Non-use value (B_n) is a non-use value of a scientific discovery [10], that is, scientific knowledge as a public good, based on the questionnaire for university students as representative future taxpayers, which includes a question about willingness to pay for LHC research activities (a fixed lump sum). A non-use value is created for non-direct users of the scientific discoveries. The impact is mentioned in the CBA for the EIA and SIA. In the case of the LHC [4], the calculation is done based on the results of the survey of non-users, which includes an item on willingness to pay for scientific discoveries. The projection of the mentioned study can be implemented in the CLIC case, since the nature and purpose of those two large infrastructures the LHC project and CLIC study are similar carrying fundamental character. The indicator is the value of willingness to pay provided by non-users via a public survey.

Since the status of CLIC is still that of a study and the infrastructure does not yet exist, its SIA is based on the past. Thus, the cultural impact and non-user impact can be neglected in the initial appraisal step. This study assesses three out of six impact areas: human capital formation, technological impact and knowledge benefits. The earlier studies [17], [18] have mentioned the three categories as the biggest benefits areas. However, structuring collaboration, non-use value and cultural impact are suggested for further appraisal to build a complete picture of the societal impact of CLIC.

Thus, the economic cost for the SIA of the early stage of the CLIC study has only two components: labour and capital cost. The operations cost is related to the operation of the existing infrastructure, of which there is none yet in the case of CLIC. The final comparison between costs and benefits is possible only when all the assessment fields have been measured. Therefore, it is discussed in the framework of further study.

2.3. Technological output

The technological outputs or benefits to firms-suppliers resulting from CERN contracts were already discussed in the earliest study [19] and are presented herein as increased turnover and cost savings:

$$Benefits = Incremental\ Turnover + Cost\ Savings, \quad (3)$$

Moreover, a utility/sales ratio was calculated based on the interviews with related companies [19]. Thus, the corrected utility ratio, equal to 85% of the net utility, is in between 1.4 and 4.2, depending on the various industrial categories. The overall corrected utility/sales ratio reached to 3.0, which is used in the current evaluation of the benefits to business.

$$Utility = Sales \times corrected\ \frac{utility}{sales}\ ratio, \quad (4)$$

Earnings Before Interest, Taxes, Depreciation, and Amortization (EBITDA) is one of the indicators of the financial results of a company and one of the means of comparison of companies' financial effectiveness. Investors use this indicator as an indicator of the expected return of their investment. EBITDA is also used to calculate the profitability ratio – EBITDA margin, which measures how much earnings a firm is generating before interest, taxes, depreciation, and amortisation:

$$EBITDA\ margin = \frac{EBITDA}{total\ revenue}, \quad (5)$$

In other words, the EBITDA margin measures a company's operating profit as a percentage of its revenue and it is used in earlier similar empirical studies [6], [20-22]. EBITDA allows evaluation of the true performance of the company not excluding expenses. The incremental turnover in a company attributed to its relationship with an RI can be computed as follow:

$$Incremental\ turnover = EBITDA \times Utility\ ratio \times sales\ from\ an\ RI, \quad (6)$$

where the sales are equal to the total value of the procurement orders received from CLIC.

The EBITDA margin for CLIC suppliers was extracted from the study's sample via the ORBIS database maintained by the Bureau van Dijk. Based on the survey replies, the final companies' sample comprised 71 firms from 16 countries. The ORBIS database presented information on 69 companies from the sample. Still, some firms' datasheets were not completed, and it was not possible to define the EBITDA margin for 26 companies. Thus, the rest of the sample shows the average EBITDA margin of about 10.4%, with a standard deviation of 7.2%. For benchmarking analysis, the EBITDA margins applied in previous empirical studies are as follows: for LHC, 13.1% [21] and for CNAO, 7% [6].

Moreover, based on the data collected from the survey, the companies indicated an increase in their clients that led to a revenue increase. The companies further showed a wide variation in results, with an average value of 11.1% and a standard deviation of 21.2%. The total volume of external CLIC procurement from 2009 to 2020 associated with selected firms is 28.06 MCHF. The resulting mean value of the corresponding benefits considering the utility ratio is 8.754 MCHF with the standard deviation of 6.06 MCHF (see Table 1).

TABLE 1. TECHNOLOGICAL BENEFITS

Category	Value (MCHF)	Benefits/cost ratio
Incremental turnover		
EBITDA	8.754	0.99
EBITDA (LHC value)	11.03	1.07
Increase in clients (self-estimation from the industrial survey)	9.34	1.01
Cost savings		
Per one download per ten components (see Table 2)	19.1	Incorporated in the above calculation

Another factor of the technological benefit is the cost savings from the use of existing CERN developments and the reduction of the production cost. This part can be presented from several aspects: (1) the use of an existing design to prevent expenses on the research and development work of a company and (2) improvement of product quality and service. For example, the software developed to analyse the LHC experimental data, which was made available for free [21]. The benefit was calculated by multiplying the number of downloads and establishing the price of an equivalent commercial tool.

Open Hardware is one of the knowledge transfer models used at CERN [22] to govern the use, copying, modification and distribution of hardware design documentation, as well as the manufacture and distribution of products [23]. This model has been remarkably successful and is now also being adopted for other types of hardware. This protected dissemination is the only viable option when a private partner needs to take considerable financial and strategic risks in order to adopt and further develop a technology to reach a competitive new market. Opening access to already established concepts helps external collaborators to save resources from developing a product from scratch. Consequently, sticking to the mentioned approach, CLIC's technological benefits are proportional to the avoided cost of the purchase or development of technology from scratch, and the cost of an alternative design or engineering solution for CLIC components. At the end of 2020, after almost two years of use of OHL, 39 users from 18 laboratories and companies were identified as current users of the directory (see Table 2).

Assuming that the research and development time was from 12 to 24 weeks (3 to 6 months); depending on the complexity of the component, including of the RF and the mechanical design, and of the involvement of scientists and engineers; and the average rate of 51 CHF/h and a 40-h work week, the avoided cost is between 24,480 and 48,960 CHF per component. The calculated cost does not include the proof of concept by producing and testing prototypes. Even with this preliminary price the maximum benefits reach 1.9 MCHF (Table 2).

TABLE 2. OPEN HARDWARE X BAND COMPONENTS COST SAVING

Users	Development time	Salary rate	Development price (CHF)	Cost Savings per one download per one component (CHF)	Cost Savings per one download per all presented in OHL component (CHF)
39	12-24 weeks	51 CHF/h	24,480-48,960	954,720-1,909,440	9,547,200-19,094,400

The calculation was done based on the assumption that only a single component was downloaded, while the OHL users are usually interested in the design of multiple components. Currently, the X-band OHL has 10 components under license.

The calculation of the technological outcome combines the calculation of the economic benefits based on the EBITDA with that of the use of the already created conceptual design via the CERN OHL. Thus, the final ratio was calculated as the sum of the two mentioned parts to the total volume of CLIC's external procurement from 2009 to 2020 associated with selected firms. The final ratio demonstrated that the benefit is almost equal to cost, the value is between 0.99 and 1.07. While the previous studies based on the CBA demonstrated the technological outcome as one of the biggest share of overall benefits from the project [6], [21]. The low benefit/cost ratio in the present study is explained by the evaluation at very early phase of the CLIC study, while the construction has not been started. The latter is in line with [21], who discussed a large investment peak during construction involving civil engineering and technical hardware, where suppliers play an essential role. Hence, the most beneficial from companies' perspectives is the construction phase of a RI.

2.4. Human capital output

One of the assessment fields is the human capital formation benefits to ECRs. This is an important output for society, since an RI provides a place for young researchers to work and study and invest in their education by offering them student grants and not less important, a place for first work experience. Thus, ECRs gain important skills and, a kick-off experience with a well-known international organisation, which is worth including in their CV. Moreover, as has already been demonstrated in similar projects, the human capital represents the largest element of the total benefits of the project: for LHC, from 1993 to 2025, around 33% of the total contribution of the main stakeholders [21], and for the next HL-LHC, up to 2038, the benefits raised up to 40% [7]. Both estimations are based on the premium salary expectations, derived from [24]. The latter demonstrated from their analysis of a survey that an extra training in and RI results in valuable skills with 'a price tag' on their learning experience from 5% to 12% compared to what they could expected without their career at CERN.

The beneficiaries of human capital formation in the CLIC study over the period 2009-2019 included three ECR categories: 67 technical students, 106 doctoral students and 63 post-doctoral students or fellows, for a total of 236. The economic benefit can be estimated as an increase in the salary of each person, which depends on several factors combined, such the current employment of a person, the country of work, and the number of years of professional experience. The NPV of the human capital benefit, considering the discount rate of 3%, recommended by the EU's Guide to Cost-Benefit Analysis of Investment Projects [5], is:

$$\sum(Number\ of\ students) \times (Incremental\ salary) \times \binom{discounting\ effect}{over\ 35\ or\ 40\ years} = Human\ capital\ benefit, \quad (7)$$

Human capital benefit is represented by the incremental salary earned over the entire work career after leaving the project and considering the career length, depending on the initial status at CERN: from 35 years for fellows to 40 years for students. The salary premium was calculated based on the data collected from two sources, allowing the benchmarking of the results: (1) $\Delta\ salary_i$ from payscale.com[4], where $\Delta\ salary_i$ is the difference in salaries between skilled and average specialists per profession: engineers, researchers and managers; and (2) percentage premium from the LHC study [17]– of 11.8% (see Table 3). The benefit to cost ratio was between 4.3 and 10 for students and between 0.9 and 1.2 for fellows. The latter is explained by the fact that the funding amount for fellows is higher. Moreover, the salaries are at the Swiss level, which makes them high and difficult to exceed afterwards.

[4] "Payscale - Salary Comparison, Salary Survey, Search Wages." https://www.payscale.com/ (accessed Dec. 18, 2021).

TABLE 3. HUMAN CAPITAL BENEFITS

Category	Value (MCHF)	Benefits/cost ratio
Technical students		
Payscale.com	Over 40 years:142141 CHF Per year: 3554 CHF	6.3
11.8%	Over 40 years: 224621 CHF Per year: 5615 CHF	10
Doctoral students		
Payscale.com	Over 40 years: 223227 CHF Per year: 5580 CHF	4.3
11.8%	Over 40 years: 224621 CHF Per year: 5615 CHF	4.3
Fellows		
Payscale.com	Over 35 years: 165641 CHF Per year: 4441 CHF	0.9
11.8%	Over 35 years: 208805 CHF Per year: 5220 CHF	1.2

2.5. Knowledge output

For the evaluation of the knowledge outputs or benefits of FRIs to scientists the bibliometric techniques applied in several studies [25-28] were used. One of the well-established approaches for evaluating the fundamental science knowledge outputs of large-scale infrastructure was presented in [4] and has been implemented in a health care project (CNAO) [6] and in HL-LHC [7]. The cited studies, compared to other bibliometric studies, went beyond merely evaluating the topics, the number of publications per year and the number of co-authored publications. The studies were aimed at forecasting and monetising the outputs and calculating the ENPV.

There are two important quantities in the calculation of the social value of publications: (1) the marginal cost of an article produced by scientists working in an RI and (2) the total discounted value of the publications. The following important parameters are considered in the calculation [21]: (1) the average annual salary of scientists, (2) the amount of time devoted to research activities, (3) the number of papers produced per year per scientist, (4) the number of citations in L1, (5) the number of references in L1, (6) the amount of time for downloading, reading and understanding the publication and (7) the amount of time needed to decide whether to cite the publication. The last two are assumed to be one hour. According to [21], the social value of scientific outputs is the cost of the publication L0 multiplied by the degree of influence of that piece of knowledge on the scientific community. The latter considers the number of references (n) in each citing paper L1 and is equal to $\sum_{t=0}^{\tau} 1/n_t$.

The calculation of the scientific outputs of CLIC in its early stage reflects the methods used in the aforementioned studies and follows a simplified evaluation path. Publications linked to CLIC were collected from two sources: the CERN Document Service [27] and the Inspire database [28].

The current benefits were estimated based on the number of publications authored by CLIC researchers (L0) and the number of citations by other articles (L1). Moreover, the direct benefits were deemed as the value of the citations of the L1 to L0 papers, as the original cost of producing the publications (Xc) is the cost of the RI. The benefits are considered to be the use of already existing knowledge for future research, which is represented by the citations as well as the references. Assuming that the cost of a citation is

$$X_C = \frac{X}{AV\_REF} \quad , \tag{8}$$

where X is the cost of a single CLIC publication and AV_REF is the average number of references per paper, the benefit is equal to

$$S = Xc \times L1, \tag{9}$$

where S is the knowledge benefit and L1 is the global number of citations of L0. The ratio of the benefits to the costs is computed by the following formula:

$$Ratio = \frac{Benefits}{Costs} = \frac{L1}{AV\_REF}. \quad (10)$$

An earlier research [29] evaluated 41 research journals in different fields. In the physical science field, the number of references was generally between 20 and 50. The authors presented a formula for the references: 14.4+2.2L, depending on the length of the paper (L). Another benchmarking study for CNAO [6] considered the average number of 30 for the references. The sample from the CLIC database indicates an average number of 14.122 references.

Finally, Table 4 shows the parameters for the calculation of the scientific output of CLIC. In the final calculation of the ratio, the cost of the initial publication was considered not important. However, the cost of the paper will depend on the distribution of the authors (fellows, PhD students and senior scientists), since it is directly connected to the time spent for the research and for writing the paper. Moreover, based on the qualifications, the average salary is quite diverse. The calculation based on the abovementioned parameters reached the benefit/cost ratio of 73 to 196.

TABLE 4. LIST OF PARAMETERS FOR THE MONETIZATION OF CLIC ARTICLES

Parameters	
Average annual salary of a researcher (CHF)	Y
Average number of authors per paper	5.9
Yearly productivity	2
Share time for research	60%
Average references per paper [6]	30
Average references per paper [30]	14.4+2.2L=37.8
Average references per paper (the study's sample)	14.122
The cost of the paper	X
Number of cited papers	798
Global number of citations	2768
Average citation	3.48875
Value per citation	X/Av_REF
Benefits	X/Av_REF*2768
Benefits/cost ratio	2768/Av_REF
Results	
Average references per paper [6]	92.3
Average references per paper [30]	73.2
Average references per paper (the study's sample)	196

The results of this study are significant in at least one major respect. They demonstrate the benefits of CLIC to insiders in the science community who had cited CLIC publications in their research. Therefore, the created knowledge is implicated in other research lines. However, the results of this evaluation are not monetised. Further work is required to establish the NPV of the knowledge outcome of CLIC at the development phase of the study. In a future investigation, it may be possible to extend the data from this study by gathering information on the subsequent flows of papers produced by other scientists, including the number of references they contain, and the value of the citations of each paper. Such data will allow for calculation of the value of the publications authored by CLIC researchers and the value of subsequent papers.

3. DISCUSSION

From the current evaluation the highest benefit/cost ratio was seen in the knowledge output components of the CLIC SIA. This can be explained by the focus of this study on the development phase of the CLIC project when intense procurement has not yet started. The intense procurement and employment will take place in the construction and operation phases of the project. Nevertheless, the SIA of CLIC can be completed only by presenting the complete picture and calculating the rest of the impact fields such as the cultural impact, non-use value and network formation, and by eliminating the related costs and the negative externalities presented by the environmental impacts.

The design phase of a RI facilities can be very long and new facilities sometimes developed in the same location as that of previous infrastructures and experiments [21], what is the case for LHC, constructed at the place of the Large Electron-Positron Collider [31]. The costs incurred before the start of the appraisal period, such as costs for feasibility studies undertaken at an earlier date or construction costs already sustained for a previous project, are sunk costs and excluded from the investment costs in an ex-ante project analysis [21]. However, in some cases, a consolidated financial analysis across different funding or management bodies may be helpful. Thus, this study offered the results of the assessment exercise with the real example on the early development phase of the CLIC study to the earlier literature. The benefits were calculated based on the past experience and provided the direct impact from the early phase of the project. Moreover, the developed framework includes a series of suggested crucial measures as assessment of structuring collaborative network as benefit and negative externalities as a cost part of the model.

CBA presented as a reliable empirical methodology for a systematic comparison of positive and negative socio-economic impacts of an investment in RI and there was an increasing consensus that it provided guidance on how to trace the potential of a RI to generate specific societal impacts thanks to the identification of all the expected beneficiaries of the projects. Since a major part of the SIA in this study was built on the pillars of CBA, the chosen approach was assumed to be reliable. However, the casual chains of events from costs/inputs to benefits/output were not among the output of the model, for which additional tools, such as qualitative approaches based on causation theories could be used as a complement [32]. The SIA approach was based on a theory that was well implemented by other scientific laboratories. The theoretical framework supported the results and the expected impacts. The conceptual model allowed for replicability of this study and can be generalised for other RIs.

The validity of this study was assured by capturing most of the effects expected by an RI. The latter was ensured by addressing all expected impacts of RI and ability to measure them. Moreover, the measures used in the study were based on the previous related studies [6-7], [20-22], [24]. However, this study calculated only a part of the possible range of the expected impacts of a RI. Therefore, the validity of this study can be improved by calculating all expected effects presented in the full SIA model.

The SIA of CLIC, this study had several important limitations. The methodology was limited by the strong construction of the theoretical background on Florio's cost-benefit conceptual model. Three appraised fields were distinguished as the most beneficial in Florio's earlier study on LHC, and the same indicators were mostly used in this study. There are some conceptual uncertainties in monetising the benefits from basic science using the econometric approach [33]. The results of the SIA of RIs can be useful for evaluating educational or technology transfer outcomes, but the overall conclusion, if used to assess a project, needs a detailed discussion [33-34]. Moreover, the methodology can introduce a bias to a positive impact and underestimate other possible measures.

Some criticisms of the model can be introduced [35]. Because of its methodology, the spent money always creates benefits. In the most cases, publications get citations, ECRs have a first experience, and companies' EBITDA grows. These are also related to the size of the project, because assessing large projects includes more actors, which means a positive average effect is more probable even if some of the effects are negative. This is true for publications, since not all of them are cited; for companies, since not all of them have a positive yearly balance; and for ECRs, as some of them have their first experience in their home countries, where sometimes, it is quite difficult to beat Swiss salaries. The next steps are to forecast the benefits for the future and to compare such benefits with the costs as was done in the previous topical studies [6], [21].

ACKNOWLEDGEMENTS

We are thankful to our industrial partners who were willing to collaborate and provide the data without which this work would not have been possible. We thank the CERN experts from the Knowledge Transfer and procurement services for sharing with us their know-how and experience.

REFERENCES

[1] European Strategy for Particle Physics Preparatory Group, "Physics Briefing Book," *Contrib. Instrum. Comput.*, vol. 21, 2019.

[2] European Strategy Group for Particle Physics Preparatory, “2020 Update of the European strategy by the European strategy group,” 2020.
[3] L. EVANS and P. BRYANT, “Accelerator and experiments LHC Machine,” 2008.
[4] M. FLORIO and E. SIRTORI, “Social benefits and costs of large scale research infrastructures,” *Technol. Forecast. Soc. Change*, vol. 112, pp. 65–78, Nov. 2016.
[5] D. SARTORI *et al., Guide to Cost-benefit Analysis of Investment Projects: Economic appraisal tool for Cohesion Policy 2014-2020*. December. 2014.
[6] G. BATTISTONI, M. GENCO, M. MARSILIO, C. PANCOTTI, S. ROSSI, and S. VIGNETTI, “Cost-benefit analysis of applied research infrastructure. Evidence from health care ☆ , ☆☆,” *Technol. Forecast. Soc. Chang.*, no. 112, pp. 79–91, 2016.
[7] A. BASTIANIN, “Social Cost Benefit Analysis of HL-LHC CERN HL-LHC and FCC,” no. May, 2018.
[8] A. REID, “Designing a Socio-Economic Impact Framework for Research Infrastructures: Preliminary Lessons from the RI-PATHS Project,” 2021.
[9] M. AICHELER *et al.*, “A Multi-TeV Linear Collider Based on CLIC Technology : CLIC Conceptual Design Report,” CERN-2012-007, 2012.
[10] P.-O. JOHANSSON, “On lessons from energy and environmental cost-benefit analysis,” 2016.
[11] R. RUBER, V. ZIEMANN, T. EKELÖF, A. PALAIA, W. FARABOLINI, and R. CORSINI, “The CTF3 Two-beam Test Stand,” *Nucl. Instruments Methods Phys. Res. Sect. A Accel. Spectrometers, Detect. Assoc. Equip.*, vol. 729, pp. 546–553, Nov. 2013.
[12] F. ROSSI *et al.*, “Study of the Thermo-Mechanical Behavior of the CLIC Two-Beam Modules.” 2013.
[13] “CERN Open Days 2019 | Open Days 2019,” 2019. [Online]. Available: http://opendays.cern/. [Accessed: 19-Dec-2021].
[14] “Home | CLIC - Compact LInear Collider.” [Online]. Available: https://clic.cern/. [Accessed: 07-Dec-2020].
[15] M. AICHELER *et al.*, “CLIC Project Implementation Plan,” *Cern Yellow Reports*, no. CERN-2018-010-M, 2018.
[16] C. S. WAAIJER, “Guidelines and criteria for an environmental impact assessment for a linear collider project,” 2011.
[17] M. FLORIO, S. FORTE, and E. SIRTORI, “Cost-Benefit Analysis of the Large Hadron Collider to 2025 and beyond,” *Technol. Forecast. Soc. Change*, vol. 112, pp. 38–53, 2015.
[18] G. BATTISTONI, M. GENCO, M. MARSILIO, C. PANCOTTI, S. ROSSI, and S. VIGNETTI, “Cost–benefit analysis of applied research infrastructure. Evidence from health care,” 2016.
[19] M. BIANCHI-STREIT *et al.*, “Economic utility resulting from CERN contracts (second study),” 1984.
[20] G. PULIGA, R. MANZINI, and P. BATISTONI, “An Industry and Public Research Organization joint effort for ITER construction: Evaluating the impact,” *Fusion Eng. Des.*, vol. 146, no. October 2018, pp. 187–193, 2018.
[21] M. FLORIO, S. FORTE, C. PANCOTTI, E. SIRTORI, and S. VIGNETTI, “Exploring Cost-Benefit Analysis of Research, Development and Innovation Infrastructures : an Evaluation Framework,” pp. 1–86, 2016.
[22] V. NILSEN and G. ANELLI, “Knowledge transfer at CERN,” *Technol. Forecast. Soc. Change*, vol. 112, pp. 113–120, 2016.
[23] E. CHESTA *et al.*, “Overview of cern technology transfer strategy and accelerator-related activities,” 2013, no. May, p. 3702.
[24] T. CAMPORESI, G. CATALANO, M. FLORIO, and F. GIFFONI, “Experiential learning in high energy physics: A survey of students at the LHC,” *Eur. J. Phys.*, vol. 38, no. 2, p. 025703, Mar. 2017.
[25] R. J. DAVIDSE and A. F. J. VAN RAAN, “Out of particles: Impact of CERN, DESY and SLAC research to fields other than physics,” *Scientometrics*, vol. 40, no. 2, pp. 171–193, 1997.
[26] A. BELZ, “Trends in industry-university relationships,” pp. 1–26, 2016.
[27] “CERN Document Server,” 2020. [Online]. Available: http://cds.cern.ch/. [Accessed: 27-Apr-2020].
[28] “Home - INSPIRE,” 2020. [Online]. Available: https://inspirehep.net/. [Accessed: 27-Apr-2020].
[29] H. A. ABT and E. GARFIELD, “Is the relationship between numbers of references and paper lengths the same for all sciences?,” *J. Am. Soc. Inf. Sci. Technol.*, vol. 53, no. 13, pp. 1106–1112, Nov. 2002.
[30] F. GIFFONI and S. VIGNETTI, “Assessing the socioeconomic impact of research infrastructures: A systematic review of existing approaches and the role of cost-benefit analysis,” *Industria*, vol. 40, no. 1, pp. 75–101, 2019.
[31] S. MYERS, “The LEP Collider, from design to approval and commissioning,” p. 28, 1991.
[32] A. F. GIFFONI *et al.*, “Title : State of play – Literature review,” no. 777563, 2020.
[33] A. J. SALTER and B. R. MARTIN, “The economic benefits of publicly funded basic research: a critical review,” *Res. Policy*, vol. 30, no. 3, pp. 509–532, Mar. 2001.
[34] B. R. MARTIN, “The use of multiple indicators in the assessment of basic research,” vol. 36, no. 3, pp. 343–362, 1996.
[35] H. SCHOPPER, “Some remarks concerning the cost/benefit analysis applied to LHC at CERN,” *Technol. Forecast. Soc. Change*, vol. 112, pp. 54–64, 2016.

MULTI-DISCIPLINARY PHYSICS WITH MEV ION BEAMS AT THE LABORATORI NAZIONALI DI LEGNARO USING THE CN AND AN2000 ACCELERATORS

V. RIGATO
INFN- Laboratori Nazionali di Legnaro
Legnaro (PD) - ITALY
Email: valentino.rigato@lnl.infn.it

Abstract

The paper provides updates and statistics of the activity carried out in the last decades at the Laboratori Nazionali di Legnaro (LNL) of the Istituto Nazionale di Fisica Nucleare (INFN) with the 2.0 MV AN2000 and 6.0 MV CN Van de Graaff accelerators in multi-disciplinary research.

1. INTRODUCTION

Low energy, high brilliance light ions electrostatic accelerators (with ion energies in the approximate range from 0.2 to about 10 MeV) are being extensively used since many years for research in interdisciplinary fields such as material analysis, modification and irradiation in semiconductor, opto-electronic, mechanical and quantum applications and precision medicine, radiation biology and dosimetry studies. Light ion beams (^{1}H, ^{2}H, ^{3}He, ^{4}He) are used in a wide range of intensities from single particle irradiation to tens of eμA, depending on the specific application, with collimated beams of mm size and focussed ion beams with micrometer size.

The rapid developments in materials science in terms of preparation, modification and characterization methodologies for nano-structured materials, new quantum and low dimensional materials, novel sensors and micro- and nano-devices require continuous improvement of the analytical tools (including both accelerators and experimental end-stations) to guarantee the highest spatial resolution, accuracy and sensitivity and an unprecedented capability to control individual ions position at the sub-micrometer scale and the LET distribution. Exploitation of ultraprecise single ion implantation/irradiation is the basis of a next generation of advanced materials and micro/nano-devices. The precise positional control of energetic single ions (keV, MeV or even GeV) at micrometric, nanometric or even atomic scale offers a wide range of emerging applications in fields as diverse as quantum technology, novel detectors, single photon sources and detectors, biomedicine and materials science. This e.g. includes investigating single ion irradiated novel topological materials (2D materials and nano-wires), biological cells or nano-assembling qubits in ultrapure solid-state crystal by deterministic single ion implantation.

Europe has a broad diversity of ion beam centres with manifold research interests and complementary technological features which condition the available ions and the accessible energy ranges. The accelerators at the National Laboratories of Legnaro are recognized as user-oriented research facilities comprising several MeV ion accelerators dedicated to multi-disciplinary research and in particular to Ion beam Analysis and ion irradiation

The MeV ion beam's analytical capabilities, including Rutherford and not-Rutherford Elastic Back-Scattering spectrometry (RBS and EBS), channelling techniques, Nuclear Reaction Analysis (NRA), Elastic Recoil Detection Analysis (ERDA), Particle Induced X-ray Emission (PIXE) and Particle-Induced Gamma Emission (PIGE) offer a wide range of "non-destructive" ion beam methods for high sensitivity and high-resolution materials analysis in many physical, chemical and medical disciplines [1]. A complete view of sample composition can be obtained nowadays by detecting X, gamma and particle simultaneously.

Recent developments in accelerator-based research, such as nuclear microprobe and nanoprobe techniques, and precision targeting with single ion are of growing interest to many research groups working in interdisciplinary fields like quantum materials and sensors, environmental physics, geology, radiation biology, radiation detectors and dosimeters technology, Micro Electrical Mechanical Systems (MEMS) fabrication and biological sensors.

An increasing demand to test the radiation hardness of microcircuits and satellite components subject to ionizing radiation exposure is fostered by the telecommunication industry and space missions' preparation projects.

On the other side, light ions accelerators are successfully used with D, Be and Li-based solid nuclear targets to provide fast neutrons using several MeV protons and deuterons with the $^{7}Li(p,n)^{7}Be$, $^{7}Li(d,n)^{8}Be$, $^{9}Be(p,n)^{9}B$, $^{9}Be(d,n)^{10}B$ reactions as well as energetic protons (~ 15MeV), using the large cross section $^{2}H(^{3}He,p)^{4}He$ nuclear reaction at energies below 1 MeV. Such produced neutrons and protons are being used to study the radiation hardness and single event upset (SEU) in electronic micro-devices and to develop and test new radiation detectors and biological sensors preferably in air.

All these potentialities offered by the MeV electrostatic accelerators are exploited at the LNL confirming the unquestioned laboratory's vocation to be a national resource for Ion Beam Analysis and Ion Beam Modification and irradiation of materials.

The activity carried out with the two Van de Graaff AN2000 and CN accelerators is summarised in the following section.

2. THE VAN DE GRAAFF AN2000 AND CN FACILITIES

The Laboratori Nazionali of Legnaro are an European ion beam research infrastructure with solid programs in nuclear physics and astrophysics with stable and radio-active ion beams, and extensive projects in neutron physics, materials analysis, modification and irradiation with ion beams, and applications in environmental physics, cultural heritage, radiation biology and quantum technologies. The laboratory is equipped with 5 accelerators and a pretty large inventory of interdisciplinary research equipment originally developed in the last six decades. There are five accelerator facilities at LNL: (i) two MeV single-end Van de Graaff accelerators (AN2000 2.2 MV and CN 6.0MV) dedicated to interdisciplinary studies, (ii) one 14.5 MV Tandem accelerator for ions from $^{1}H^{+}$ (~28.2 MeV/A) to $^{197}Au^{16+}$ (~ 1.2 MeV/A), (iii) one linac (ALPI) using rf superconducting cavity accelerator technology for a great variety of ions and energies in the range approximately 7 to 22 MeV/A, (iv) a recently installed 70 MeV, 700μA proton cyclotron.

The AN2000 and CN Van de Graaff accelerators are mainly used in applications of nuclear physics and interdisciplinary studies. All research projects are evaluated and approved by the international Program Advisory Committee of the LNL twice a year. On the average, the user's request exceeds the available beam-time by about 30% for each accelerator.

2.1. AN2000 accelerator

The AN2000 Van de Graaff accelerator, operative in the 1970s, was upgraded in 1990s with the installation of a micro-probe facility capable to focus 2.0 MeV proton beams down to about 1.5 μm spot size in high vacuum. The system is based on the "Oxford" triplet focussing optics and scanning setup. The capabilities of the micro-probe are being exploited mainly for the analysis of semiconductors, detector materials, archaeological samples, geological and nuclear waste related materials and aerosol micro-particles through the micro-PIXE, micro-EBS, and micro-NRA techniques. This facility is also being used for single event experiments consisting of hitting with micrometric precision a given specimen with a predefined number (even one) of projectiles and evaluating on-line the electric charge (IBIC) or light (IBIL) developed from the impact point and/or to study off-line the localized radiation damage and defect generation. Among the systems studied with these techniques it is worth mentioning the continuous effort to study and test new solid-state detectors and to investigate the mechanism of interaction of single particles on microchip devices such as flash memories. In the recent years a system for single ion implantation has been installed for sub-micrometer achromatic precision targeting of devices and materials with the available beams. The system is based on special engineered double micro-collimators and high accuracy nano-positioners for the device under test. It offers the possibility to perform multiple irradiations (at different ions and energies) at fixed position to create individual electro-optical defects and defects arrays in semiconductors. It also allows to irradiate with high position precision low-dimensional quantum materials.

Another application with the micro-probe is Ion Beam Writing (IBW) on synthetic diamond specimens to generate buried graphitic electrically conductive paths with proton and α-particles beams of variable energy, to prepare diamond-based micro-devices and biological micro-sensors.

Besides the micro-probe beam line, there are other three beam lines equipped with scattering chambers for complete Ion Beam Analysis (IBA) including EBS, EBS-Channelling, ERDA, NRA, PIXE and ion-luminescence studies and nuclear cross section measurements with collimated beams.

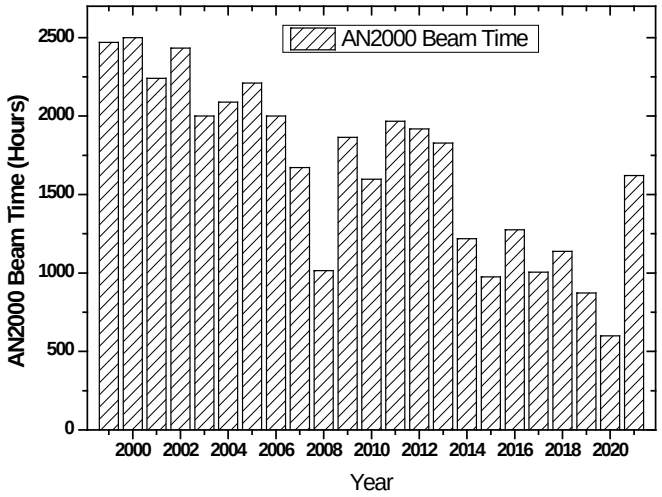

FIG. 1. Yearly beam-time hours delivered on user's targets by the AN2000 accelerator in the past 23 years.

The yearly beam-time on target of the AN2000 in the last two decades is presented in Fig. 1. The research groups accessing the AN2000 facility range from about 15 to 20 per year from Italian and foreign Universities and Research Centres. The decreasing trend of the beam-time provided to user's shown in Fig. 1 is due in great part to the increasing need of servicing and special maintenance of the accelerator and in part to the reduction of personnel for the development of new instrumentation.

Most of the research activity carried out in the AN2000 Laboratory is of analytical nature: PIXE and micro-PIXE analysis, EBS, NRA, ERDA (for stoichiometry analysis and depth profiling of hydrogen and deuterium) are performed routinely with the continuous $^{1}H^{+}$, $^{4}He^{+}$ and $^{3}He^{+}$ beams in the energy range from 200 keV to 2.2 MeV on a great variety of materials and thin films. The subdivision for the last 12 years of the beam-time in the various application fields is shown in Figure 2. As it can be noticed, IBA and micro-probe applications represent a significative amount of the beam time yearly allocation to the users. In recent years the irradiation experiments on satellite components and materials and on new quantum materials are gaining increasing interest. The AN2000 accelerator is also used to perform training of students and young researchers with particular attention to promote Ion Beam Analysis and a quantum-ready workforce.

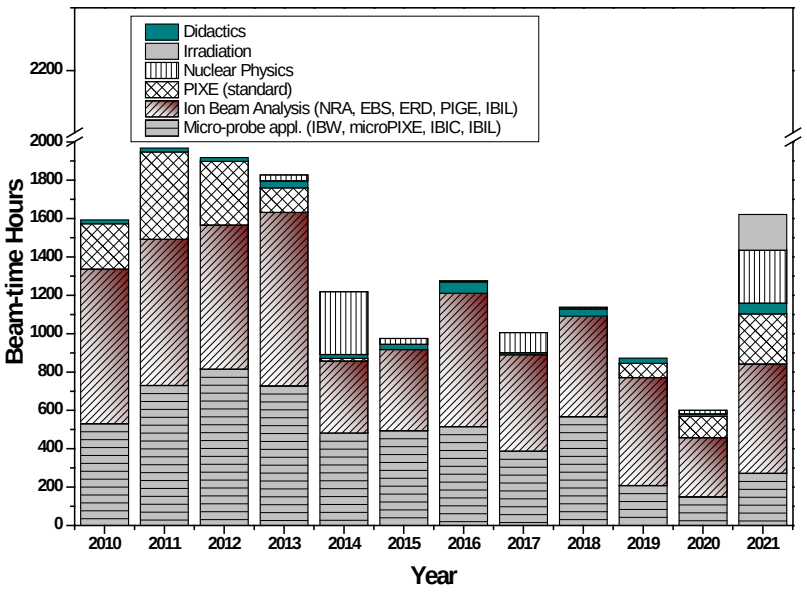

FIG. 2. Yearly beam-time hours delivered on user's targets by the AN2000 accelerator in the past 12 years subdivided in main application fields.

2.2. CN accelerator.

The CN accelerator is operative since 1961. The terminal voltage can be varied from about 1.0 to 6.0 MV allowing for a maximum energy of about 12 MeV for the double charged particles. The ion beams available are $^{1}H^{+}$, $^{1}H_{2}^{+}$, $^{2}H^{+}$, $^{3}He^{+}$, $^{3}He^{++}$, $^{4}He^{+}$, $^{4}He^{++}$, $^{15,14}N^{+}$ either pulsed or continuous. The original pulsing system of the CN provides 3 MHz repetition rate with bunch duration of about 1-2 ns. A new system has been installed, coupled to the original system, to allow for repetition rates at frequency lower than 3MHz by synchronous beam deflection: the supplementary pulsing system is able to suppress a fraction of main beam pulses by deflecting the unwanted ones toward a beam-dumper placed along the beamline. In such way it is possible to get a secondary pulsed beam with variable frequency down to few hundreds' kHz, well suited to carry out neutron TOF experiment in nuclear astrophysics and detector and dosimeters tests.

The shielding of the CN laboratory infrastructure allows the irradiation of Be and Li-based targets with proton and deuteron beams with currents of order of few μA to produce well characterized MeV neutrons beams using three beamlines. Pulsed beams and thin targets permit to produce quasi-monochromatic MeV neutron pulses with ns duration. In addition, a calibrated beam shaping facility for thermal neutrons based on Be target is also available [3-4].

The available beams allow to perform radiation biology studies, dosimeter calibrations and original development of tissue equivalent proportional counters for oncological hadron-therapy and BNCT.

The CN accelerator is complementary to the AN2000 for the analytical purposes: EBS, EBS Channelling, and NRA, PIXE and PIGE are accomplished routinely spanning the entire available energy and particle range using two scattering chambers of which one provides complete simultaneous data acquisition from 6 detectors comprising 1 Si(Li) detector for PIXE, 1 HpGe detector for PIGE and 4 silicon detectors for simultaneous EBS and NRA using in-situ variable stopping foils, to provide maximum flexibility in (d,p), (d,α), (^{3}He,p), (^{3}He,α) NRA. The sample holder is specifically designed for automated analysis of a large number of samples in environmental and materials science studies.

A new facility for large area MeV proton irradiation is also available for irradiating exposed components on satellites in geo-stationary orbits with doses in the range 10^{9} to 10^{16} cm^{-2}.

The research groups accessing the CN facility range from about 15 to 20 per year from Italian and foreign Universities and Research Centres.

The number of beam-time hours per year and the subdivision of the beam-time in the various application fields of the CN in the last 12 years is shown in Fig. 3. As it can be seen, on the average, about 1100 hours are provided to users yearly. Neutron applications, micro- nano- dosimetry, nuclear cross section measurements, IBA and device irradiation represent the most significative fraction of the beam-time yearly allocated to the CN users. The CN accelerator is also used to perform training of students and young researchers in nuclear physics and material science.

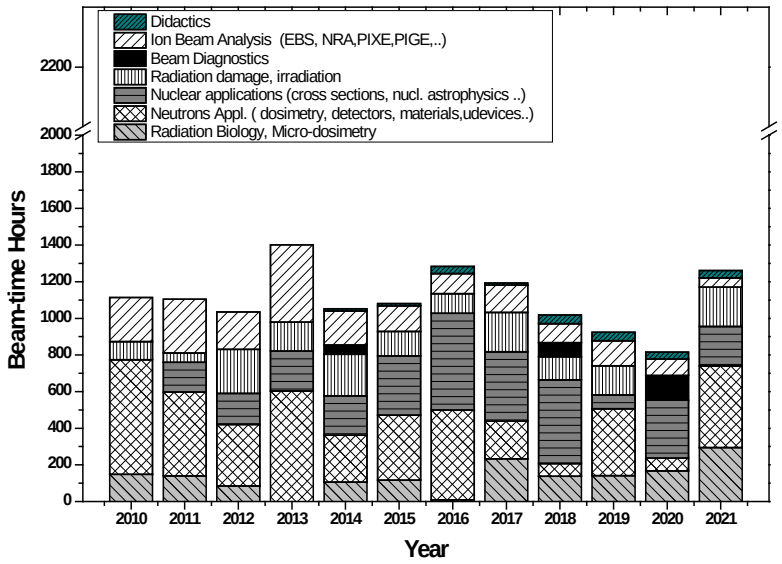

FIG. 3. Yearly beam-time hours delivered on user's targets by the CN accelerator in the past 12 years subdivided in main application fields.

3. CONCLUSIONS AND PERSPECTIVES

The multi-disciplinary and user-oriented nature of LNL is clearly documented by the attraction that the two Van de Graaff MeV accelerators, although quite old, exert on many users involved in academic and applied research in different disciplines of interest not only of INFN but also of a wider multi-disciplinary community. This accounts for an average of about 2500 beam-time hours per year (excluded didactics and servicing) provided by the two accelerators.

Future developments in MeV accelerators at LNL, should take into account the above reported main activities currently carried out by the users willing to do physics with small accelerators at the Legnaro Laboratories and to access the infrastructures in the future to bring innovation and potential return of investment through academic and UE projects and industrial collaborations.

Without entering into the fine details of the daily issues in operating the two accelerators and equipment thereof, which are caused by the considerable age of the two infrastructures (more than 50 years old), we may state that the substantial upgrade of both accelerators and of part the infrastructures and ancillary instrumentation is now mandatory to keep international competitiveness.

The high level of the scientific activity carried out at the AN2000 and CN laboratories is attested by the remarkable number of publications on international journals yearly published by the research teams accessing the two Legnaro infrastructures. Further details might be found in the LNL Annual Report [5], in particular in the “Interdisciplinary physics and instrumentations” section.

ACKNOWLEDGEMENTS

The author wishes to acknowledge the efforts of all the LNL staff daily involved in the operation of the two accelerators for their constant highly professional work.

REFERENCES

[1] JEYNES, C., WEBB, R. P., LOHSTROH, A., Ion Beam Analysis: A Century of Exploiting the Electronic and Nuclear Structure of the Atom for Materials Characterisation; Reviews of Accelerator Science and Technology Vol. 04, No. 01, pp. 41-82 (2011).

[2] Updated information on available ion species and energies may be found in https://www.lnl.infn.it/en/users-info-accelerators

[3] AGOSTEO S. et al., Characterization of the energy distribution of neutrons generated by 5 MeV protons on a thick beryllium target at different emission angles, Applied Radiation and Isotopes, 69 (12), 2011, 1664-1667

[4] CEBALLOS, C. *et al*., Towards the final BSA modelling for the accelerator driven BNCT facility at INFN LNL, Applied Radiation and Isotopes, vol. 69 (12), 2011

[5] The yearly published Annual Reports of the Laboratori di Legnaro may be found in: https://www1.lnl.infn.it/~annrep/index.htm

STUDY OF SILVER NANOPARTICLES UPTAKE BY *Helianthus annuus* CROP IN SALINITY CONDITIONS

C.E.I. dos SANTOS
Physics, Statistics and Mathematic Institute, Federal University of Rio Grande
Santo Antonio da Patrulha, Brazil
Email: carlaiochims@yahoo.com.br

A. KAVČIČ
Biotechnical Faculty, University of Ljubljana
Ljubljana, Slovenia

M. KELEMEN
Low and Medium Energy Departament, Josef Stefan Institute
Ljubljana, Slovenia

P. F. C. JOBIM
Departament of Basic Science/Phisilogy, Federal University of Health Science of Porto Alegre
Porto Alegre, Brazil

P. PELICON
Low and Medium Energy Departament, Josef Stefan Institute
Ljubljana, Slovenia

P. VAVPETIC
Low and Medium Energy Departament, Josef Stefan Institute
Ljubljana, Slovenia

K. VOGEL-MIKUS
Biotechnical Faculty, University of Ljubljana
Ljubljana, Slovenia

Abstract

Engineered nanoparticles (NPs) are used in different industrial products, including cosmetic, pharmaceutics, clothes, electronic and agriculture products. In the past years the use of silver nanoparticles (AgNPs) expanded significantly, especially due to their antibacterial and antifungal properties. Despite the benefits in using AgNPs for different purposes, they enter in the environment can be problematic and have different mechanisms of accumulation, internalization and toxicity in plants. Moreover, plant growth and development is limited by salinity conditions, an abiotic stress parameter, especially in arid, semi-arid and irrigated areas in tropical and sub-tropical places. The germination, seedling and plant growth and, consequently, the productivity of the plants decrease, causing economic and social impacts. In this context, the aim of the present study was to track the uptake of AgNPs by sunflower (*Helianthus annuus*), a metal hyperaccumulator plant. For this, experiments were conducted in soil and hydroponic mediums where plants were treated with salinity and two different concentrations of AgNPs. Four groups were studied: control (without exposure to AgNPs and NaCl), salinity (group exposed to 100 mM of NaCl), AgNPs (group exposed to 5 or 100 $mg.kg^{-1}$ of AgNPs (the lowest concentration was used only in hydroponic experiment) and AgNPs plus salinity (group exposed to 5 or 100 $mg.kg^{-1}$ of AgNPs and 100 mM of NaCl). At the end of the experiments, plants were harvested; roots, shoots and leaves were separated and samples were prepared for elemental analysis, lipid peroxidation and pigment analysis. Results showed the internalization of Ag in the cortex of roots from sunflower crop in hydroponic medium. K content in roots was negatively affected by nanoparticles and salinity treatments. The exposure of sunflower to AgNPs and salinity seems to intensify silver accumulation in leaf and root tissues.

1. INTRODUCTION

Silver (Ag) nanoparticles (NPs) are engineered nanomaterials with widespread application in the industry of everyday products because their antimicrobian and antifungical properties. These metal based nanoparticles received attention in the last years not only due their specific and useful characteristics but also because the risks

that they could cause to the environment, through their uptake by plants and small animals, affecting the food chain and, consequently, the whole ecosystem. Benefits and risks of toxicity for live organisms caused by different types of engineered NPs are not complete understood since they depend on the format, size and composition of the nanomaterials. To know the dynamic of NPs in different mediums like soil, sludge or water, and after they be absorbed by live organisms, detailed studies are required, including the whole cycle of the nanomaterials in the medium and in the respective biological organism which uptake them. Depend on the medium and characteristics of the NPs, they could became dissolved or in agglomerate form and their chemical state could be modified, changing the toxic potential of silver [1]. Since AgNPs have been an important component of a variety of consumer products, it is probable they exist in the environment in consequence of the industrial activity and possible discharge routes. Thus, it is necessary to evaluate their interaction with different live organisms, especially plants because they are producers and, consequently, the base of the food chain [2]. By other side, the use of AgNPs in agriculture increased due the application of nano-encapsulated agrochemicals aiming to optimize the outcomes through soil and culture practices, since AgNPs present antimicrobial and nutritional properties. Moreover, benefits in the use of AgNPs in plant biotechnology have been reported [3]. However, when in high concentrations, AgNPs could accumulated in plant cells, became toxic and inhibit the growth of the plants when applied in high concentrations [3].

Plant growth and development is limited by salinity conditions, an abiotic stress parameter, especially in arid, semi-arid and irrigated areas in tropical and sub-tropical places. In general, the germination, seedling and plant growth and, consequently, the productivity of the plants decrease, causing economic and social impacts [4]. Due the high concentration of sodium (Na) and chlorine (Cl) ions and the inhibition of nutrient uptake from the soil, the plant nutrition is negatively affected. For example, salinity stress disturbs the uptake and accumulation of essential nutrients such as potassium (K) and calcium (Ca) [5]. Thus, field practices have been studied aiming to improve crop development under salinity conditions, such as K application to overcome the effects of salinity in pearl millet [5]. In addition, Hurtado and collaborators [6] reported the benefit in the application of silicon (Si) to sorghum and sunflower crop in salinity environment.

Besides that, the role of nanoparticles in plant development under salinity stress has been studied, especially because the application of nutrients in such nano structures make them better absorbed by the plant cells. The interaction between AgNPs and salinity was evaluated in grass pea germination [7]. The germination speed index was calculated for the different studied treatments, showing a positive result in the application of AgNPs to seed germination when exposed to different salinity levels [7]. Mozafari and collaborators [8] reported the benefits of iron nanoparticles and potassium silicate treatments for grape (Khoshnaw cultivar) exposed to salinity environment.

In the present work, the main aim was to evaluate the uptake of silver nanoparticles by sunflower (*Helianthus annuus*), a metal hyperaccumulator plant [9], exposed to salinity stress, using accelerator's based techniques. Sunflower is an important economic crop, especially in Ukraine, Russian Federation, European Union, Argentine and Turkey, the main worldwide producers [10], used for oil seed and other commodity production, to feed animals and for bioenergy proposes. Moreover, this plant is known to be a metal accumulator, making it an important green option to remove metals from the soil (phytoextraction technology) [11]. Thus, it is essential to understand the AgNPs effect on this plant because i) it could be a source of silver toxicity to other live organisms; ii) it could be used for phytoextraction of silver in contaminated soil; iii) the evaluation of AgNPs role in the plant development under salinity stress is a valuable data for producers from arid, semi-arid and irrigated regions, since it may support new tools and technologies for field practices.

2. MATERIAL AND METHODS

2.1 Samples' experiment design

All experiments regarding the plant crop and sample preparation were conducted at the Department of Biology - Biotechnical Faculty of the University of Ljubljana. Seeds of sunflower (*Helianthus annuus*) were germinated in verniculite at the growth chamber under controlled conditions (photoperiod: 16/8h day/night; cool white fluorescent illumination: 550 μmol m^{-2} s^{-1}; constant temperature: 20 °C; humidity: 50%). When the plants presented two leaves (about 1 cm of length), they were carefully transferred to the crop medium (hydroponic or soil) and kept in the growth chamber during the experiment time. Fig. 1 shows a scheme of the plant crop experiments.

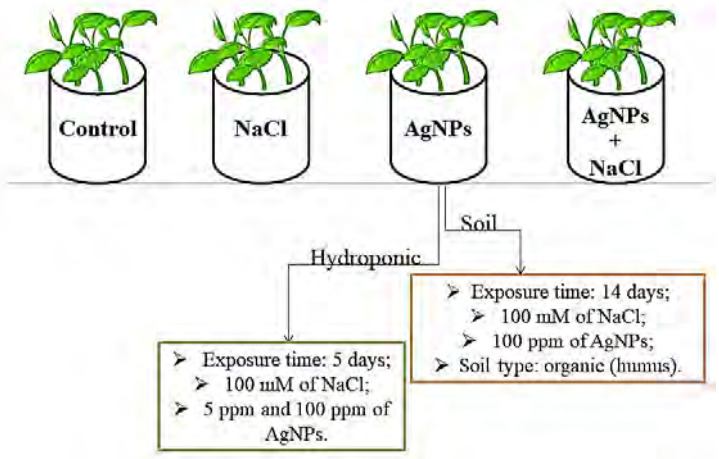

FIG. 1. Scheme of the plant experiments performed in hydroponic and soil crop mediums. In both cases, the plants were kept in the grow chamber under controlled conditions of light, temperature and humidity. The concentrations of AgNPs and salinity as well as the time of exposure is shown.

2.2 Hydroponic experiment

Hydroponic experiments were conducted using both 5 $mg.kg^{-1}$ or 100 $mg.kg^{-1}$ concentrations of AgNPs. For each concentration, four experimental groups were considered: control group, group exposed to 100 mM of salinity solution (NaCl), group exposed to AgNPs (AgNps) and the group exposed to a combination of salinity (100 mM) and AgNPs (NaCl+ AgNPs). For each group, one pot filled with 800 mL of hoagland solution was prepared and four plants were placed in each pot. 100 ml of AgNPs solution (5 or 100 $mg.kg^{-1}$ of AgNPs nanopowder (Sigma Alderich) dissolved in 100 ml of bidestilated water) was added in the pots of groups treated with nanoparticles. Groups treated with salinity received a total solution of 100 mM of NaCl dissolved in bidestilated water, which was applied during three consecutive days to achieve a gradual increase in salinity and therefore reduce the osmotic shock for the plants. Finally, 100 ml of bidestilated water was added to the control group to make equal the volume of solution in all groups. The experiment was repeated twice, totalizing eight plants per group. The exposure time of each repetition was five days.

At the end of the experiment, plants were harvested. Roots, stems and leaves were separated, washed in bidestiled water and properly prepared for elemental micro analysis. Sample preparation for elemental mapping and composition is a crucial step to obtain reliable information about the chemical element's localization in the biological tissues [12, 13]. The procedure followed in this work is described in details by Vogel-Mikus and collaborators [12] and consists in the cryo-fixation of the plant tissue, specimen sectioning at low temperature (about -25 °C) and freeze-drying. The sectioned specimens were 25 µm and 60 µm thicker. After freeze-dried, the integrity of the samples was verified by optical microscopy. Samples were accommodated in specific holders according the analytical technique setup requirements. Additionally, dried and pulverized root material was pressed into pellets for silver chemical speciation analysis.

2.3 Soil experiment

Humus soil (3.5 kg) was contaminated with 100 $mg.kg^{-1}$ of AgNPs nanopowder (Sigma Alderich) dissolved in bidestilated water. The nanoparticle solution was very well mixed with the soil and the mixture was placed inside a black plastic bag to get stabilization for two weeks. After that, sunflower plants were transferred to the appropriate pots filled with the contaminated soil. Again, four plant groups were considered for the experiment: control group, group exposed to 100 mM of salinity solution (NaCl), group exposed to AgNPs (AgNps) and the group exposed to NaCl+ AgNPs. The total solution of salinity was applied during three consecutive days in the plants. Since the experiment took place during two weeks and it was expected plants get bigger than in the hydroponic experiment, four pots per group were prepared, and two plants were accommodated in each pot. In total, eight plants per group were crop. In the end of the period, the plants were carefully harvested and washed with bidestiled water. Roots and leaves were separated and weighted. One fraction of the plant material was

prepared for lipid peroxidation, as an indication of oxidative stress in roots and leaves, following the protocol described by Hodges and collaborators [14]. Lipid peroxidation content was expressed as malonaldehyde (MDA) equivalent production in these plant organs; the other part was freeze-dried during 72 h, approximately. Photosynthetic pigment content was evaluated in dried and pulverized sunflower leaves according Lichtenthaler and Buschmann (2005) [15] methodology. Additionally, elemental analysis was carried out in leaves and roots. For this, samples were prepared in duplicate by pressing the dried and pulverized root and leaves material in pellets. The concentration of Ag was also determined in soil samples. In this case, samples were prepared in triplicate by pressing the soil into pellets.

2.4 Elemental analysis

The uptake of AgNPs by sunflower and the elemental composition of all plant samples were evaluated by X-ray spectroscopies, namely Particle Induced X-ray Emission (PIXE) [16] and X-ray Fluorescence (XRF) [17]. Both techniques provide the elemental composition of the material with good resolution and limit of detection for trace and major elements. Moreover, these methods can be setup for micro analysis, giving a map of the chemical element distribution in the material with resolution about 1 μm or less [18, 19].

In this work, PIXE was carried out by using a focused ion beam combined with a scanning system – in this case known as microPIXE. MicroPIXE measurements were performed at the Low and Medium Energy Departament, of the Josef Stefan Institute (JSI – Ljubljana, SL) [20, 12]. The incident proton beam (3 MeV) on the samples was delivered by a 2 MV Tandetron accelerator. The current was maintained in 150 pA approximately and the time of each scan varied between 3 and 14 h. The emitted X-rays were collected by a silicon drift detector (SDD) and a high-purity germanium (HPGe) detector. Sunflower samples were placed between two thin foils of Pioloform film on the aluminum holder, which was accommodated in a specific metallic support inside the reaction chamber. The pressure inside this chamber was kept about 10^{-6} mbar. PIXE spectra were fitted by GeoPIXE [21] and GUPIXWIN [22] softwares. The incident charge measurements were performed using a chopper.

XRF measurements of plant bulk samples were performed at JSI using a PeduzoT02 system with an americium (Am) excitation source. Elemental concentrations were calculated using AXIL X-ray analysis package [23]. MicroXRF was also carried out to complement results of Ag distribution in root samples. In this case, 25 μm thick root samples were irradiated at the ID-21 XRF beam line of ESRF synchrotron source (Grenoble, FR). The XRF spectra were fitted by PYMCA [24].

Additional analyses of root samples were carried aiming to check the chemical speciation of silver in the plants through X-ray Absorption Near Edge Structure (XANES). The measurements were performed at the P64 beamline of PETRA III (DESY laboratory, Hamburg – Germany) [25]. XANES spectra were fitted by Athena software [26].

2.5 Data analysis

Data of different parameters (lipid peroxidation, pigments, elemental concentration) were taken to perform one way ANOVA followed by Tukey. For each individual experiment every parameter was compared among the treated groups (statistically significant difference: $p<0.05$).

3. RESULTS AND DISCUSSION

3.1 Ag uptake – Hydroponic experiment

Root samples of sunflower exposed to silver nanoparticles (100 $mg.kg^{-1}$) were analyzed by XANES in order to check the chemical state of silver after the interaction with the medium and plant tissues. The analysis of the spectra (data no showed) revealed that the major part of silver was retained as nanoparticles. Some small deviations in the spectra were observed, probably because the introduction of organic ligands, such as sulfur (S) and oxygen (O) due the incorporation of the metal into the plant.

Considering this result, the uptake of AgNPs by sunflower was verified in the plant tissues. Figure 2 shows the localization and concentration of silver in root samples (60 μm thick) of sunflower treated with AgNPs and AgNPs + NaCl, for both concentrations of nanoparticles, obtained by microPIXE. The average concentrations of

Ag in the samples exposed to the higher concentration of AgNPs were (10600 ± 54) mg.kg^{-1} and (2800 ± 50) mg.kg^{-1} in samples of these groups, respectively. Plants treated with 5 mg.kg^{-1} of AgNPs and 5 mg.kg^{-1} + 100 mM of NaCl also uptake silver nanoparticles in the concentrations of (1300 ± 24) mg.kg^{-1} and (358 ± 26) mg.kg^{-1}, respectively. In all elemental maps was observed that Ag is concentrated in the root cortex, with some hot spots in the proximities of the epidermis and less distributed around the xylem. This same pattern of Ag distribution in root samples was also observed using microXRF facility (Figure 3). As expected, silver was not found in roots from control and salinity groups. In root from control group, the fitting of the PIXE spectrum resulted in a concentration value below the minimum detection limit (MDL) (MDL = 117 mg.kg^{-1}). Similar result was found for root samples treated with salinity (MDL = 33 mg.kg^{-1}).

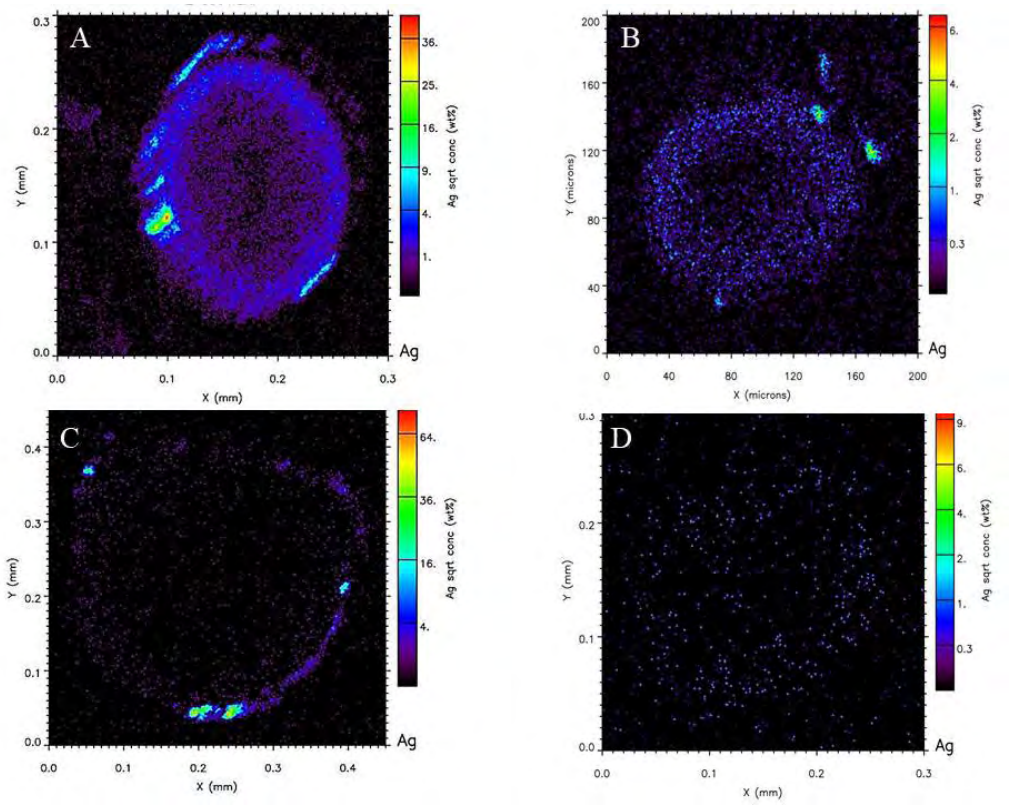

FIG. 2. Silver distribution in root samples of sunflowers exposed to 100 mg.kg^{-1} (A) and 5 mg.kg^{-1} (B) of AgNPs, 100 mg.kg^{-1} AgNPs plus 100 mM of NaCl (C) and 5 mg.kg^{-1} AgNPs plus 100 mM of NaCl (D). The elemental maps were obtained through GeoPIXE fitting of the PIXE spectra..

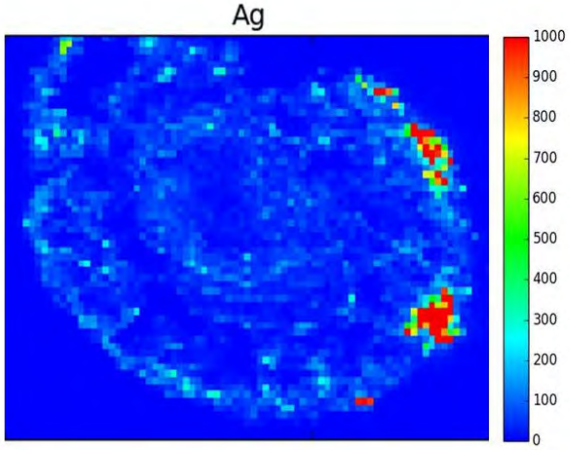

FIG. 3. Silver distribution in root of sunflower exposed to 100 mg.kg^{-1}. The scale bar indicates the silver content qualitatively: less intense Ag signal (blue color) to higher intense Ag signal (red color). Result obtained using microXRF.

Potassium (K) was quantified in root bulk samples by XRF. Figure 4 shows its behavior in function of the treatments. It is notable that the stress caused by salinity and AgNPs have an influence in the absorption of K by the plants and their nutrition. The combination of both treatments increased the concentration of K in the plant tissue in comparison with AgNPs treated group. Positive effect of lower concentrations of AgNPs than 100 mg.kg^{-1} applied to seed germination or plants cultivated in salinity environment was observed for different crops [7, 27]. In the present work, even the lowest concentration of AgNPs (5 mg.kg^{-1}), decreased the potassium absorption by sunflower, corroborating the effect dependence of type and concentration of nanoparticle on the plant development.

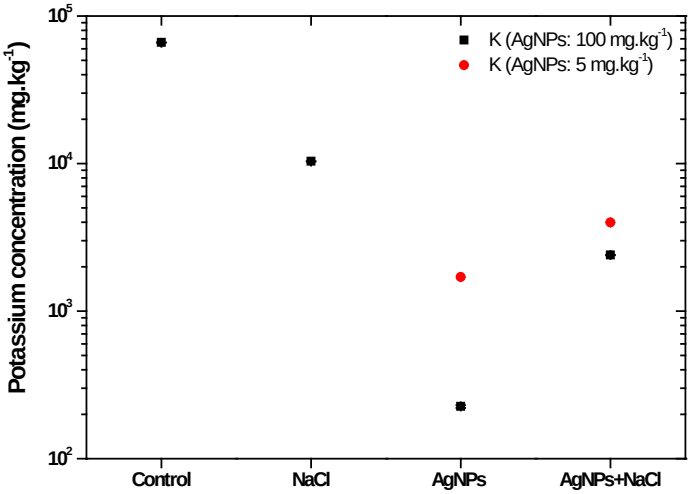

FIG. 4. Potassium concentration in roots of sunflower crop in hydroponic medium. Red circles and black squares correspond to samples from groups treated with 5 mg.kg^{-1} and 100 mg.kg^{-1} of AgNPs, respectively. Uncertain bars are not visible in the plot since they range between 1% to 5% of the concentration value.

In order to study a possible translocation of Ag in the plant tissues, stems and leaves were analyzed by microPIXE. Stems from plants treated 100 mg.kg^{-1} of AgNPs showed a silver concentration of 72 mg.kg^{-1}, which was approximately the MDL value. However, in leaves of the same group was not detected silver above the MDL. Although the low content of Ag in stems, it seems that the stress caused by the treatments with nanoparticles and salinity changed the uptake of nutrients such as calcium (Figure 5). The content of this element decreased in fifty per cent, approximately, in plants treated with AgNPs+NaCl in comparison with the control group.

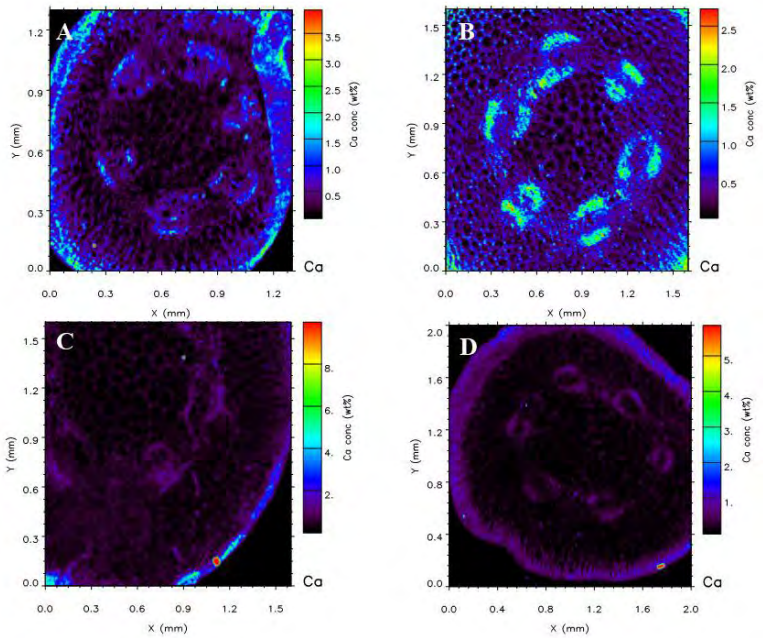

FIG. 5. Calcium distribution in stems from control (A), 100 mM of salinity (NaCl) (B), 100 mg.kg^{-1}of AgNPs (AgNPs) (C) and 100 mg.kg^{-1} AgNPs plus 100 mM of salinity (AgNPs+NaCl) (D) groups. Ca distribution maps were obtained by microPIXE and quantified using GeoPIXE software.

3.2 Ag uptake – Soil experiment

Figure 6 shows the concentration of Ag in soil, root and leaves of sunflower, obtained by XRF. Ag content in samples from Control and Salinity groups was bellow of the LOD. Salinity increased the AgNP uptake in sunflower plants (roots and leaves). Therefore, the concentration of Ag in the soil treated with NaCl+AgNPs is lower than in NaCl-free soil since the AgNPs concentration was the same in the begin of the experiment for both soil groups. (the soil Ag concentrations at the beginning of the experiment were the same).

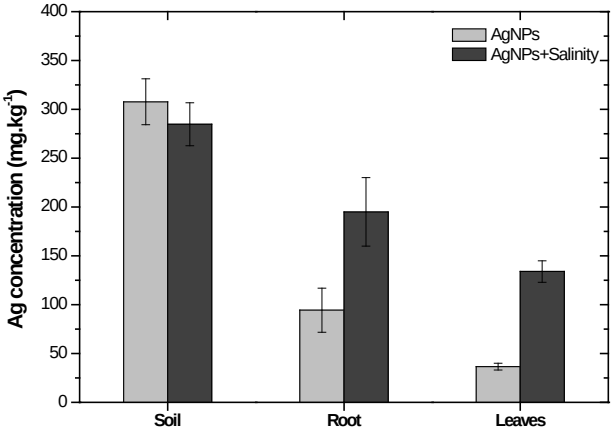

FIG. 6. Ag concentration of soil, roots and leaves of sunflower samples. Data obtained by XRF in triplicate (duplicate for leaves). Uncertain bars correspond to the standard deviation of the mean..

The stress caused in sunflower plants due the esposure to AgNPs and salinity is demonstrated by the results of lipid peroxidation (Figure 7) and pigment analysis (Table 1) The level of chlorophyll A decreased in function of all treatments while chlorophyll B content decreased in the presence of the salinity and with the combination of AgNPs and salinity. However, only salinity did not change carotenoids content in sunflower leaves. In this case, nanoparticles were responsible to decrease carotenoids in the plants and this effect was intensified by the addition of salinity. A decrease in chlorophyll concentration shows a deteriorating effect of the stressors present (either salinity, NP or the combination of both) on the basic plant function, that is photosynthesis. Figure 8 shows how the plants were affected by the treatments. This means that the primary function of the plant is threatened. As already reported, salinity is an important stress parameter to seed germination and plant grown [5]. In the present work, its effect was observed mainly in chlorophyll content. Larue and collaborators [28] reported that AgNPs did not change the content of photosynthetic pigments in lettuce submitted to 1, 10 and 100 µg/g of AgNPs treatment through foliar exposure. These founds corroborate that the interaction of NPs with plants is different for each crop as well as the effect caused by the nanomaterial, which is dependent of the exposure (foliar or radial), crop conditions and nanoparticle characteristics [29].

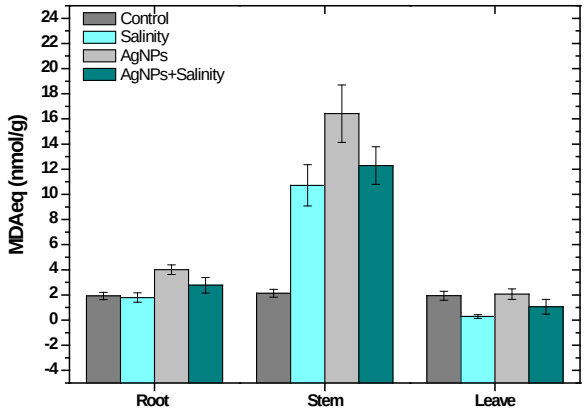

FIG. 7. Lipid peroxidation content in root, stem and leave samples of sunflower crop in soil. Analyses were performed in triplicate. Uncertain bars correspond to the standard deviation of the mean..

TABLE 1. Chlorophyll and carotenoids concentration in leave samples of sunflower crop in soil. Analyses were performed in triplicate. Uncertain bars correspond to the standard deviation of the mean. Different letters in the same colunn mean statistical difference (ANOVA One Way + Tukey: $p<0.05$).

Experimental groups	Chlorophyll A (mg/g)	Chlorophyll B (mg/g)	Carotenoids (mg/g)
Control	5.3556 ± 0.03288^{a}	2.8188 ± 0.10875^{a}	0.9031 ± 0.01256^{a}
Salinity	4.6184 ± 0.18446^{b}	1.8466 ± 0.14983^{b}	0.8411 ± 0.03530^{a}
AgNPs	3.2784 ± 0.395^{c}	$1.4520 \pm 0.08681b,^{c}$	0.6093 ± 0.1964^{b}
AgNPs+Salinity	2.3101 ± 0.09836^{d}	1.1297 ± 0.11816^{c}	0.4210 ± 0.02657^{c}

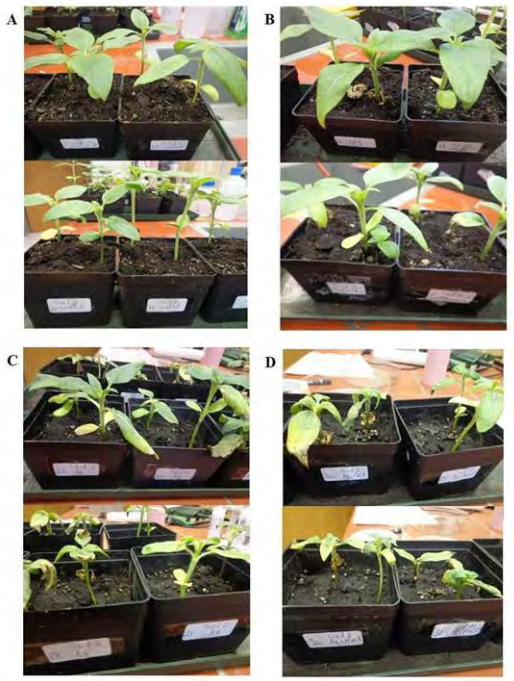

FIG. 8. Sunflower crop in soil at the moment of harvest – 14 days of treatment. A) control group; B) Salinity group; C) AgNPs group and D) AgNPs+Salinity group. The pictures shos the appearance of the plants in the end of the experiment.

4 CONCLUSIONS

It was evaluated the uptake of AgNPs by sunflower crop in soil and hydroponic medium under salinity stress. NPs crossed the root barrier and were relocated in to the upper parts of plants. The exposure to AgNPs and salinity affected the plant growth and development as shown by lipid peroxidation and pigment results. Such effects showed to be dependent on the treatment condition and crop medium. The application of nanoparticles in the agriculture still demanded studies about the uptake and translocation of these nanomaterials by different plant cultures, using different NPs concentration and composition and crop conditions. Results obtained will contribute for the development of a sustainable application of nanomaterials to the agro systems, preserving the environment and ensuring the agri food production safety

ACKNOWLEDGEMENTS

C. E. I. dos Santos thanks CAPES by the pos-doctoral fellowship grant (# POS-DOC 88881.119418/2016-01).

REFERENCES

[1] WANG, J., WANG, W., Salinity influences on the uptake of silver nanoparticles and silver nitrate by marine medaka (*Oryzias melastigma*), Environ. Toxic. Chem. **33** 3 (2014), 632–640.

[2] MONICA, R. C., CREMONINI, R., Nanoparticles and higher plants, Caryologia **62** 2 (2009) 161–165.

[3] SARMAST, M. K., SALEHI, H., Silver nanoparticles: an influential element in plant nanobiotechnology, Mol. Biotec. (2016) DOI 10.1007/s12033-016-9943-0.

[4] ESCHEMBACK,V., BERNERT, M. R., SUCHORONCZEK, A., JADOSKI, S. O., LIMA, A. S., Characteristics of soil salinity in agricultural crops in Brazil, Brazil. J. Appl.Techn. Agric. Sci. **7** 3 (2014) 115–124.

[5] HEIDARI, M., JAMSHIDI, P., Effects of salinity and potassium application on antioxidant enzyme activities and physiological parameters in pearl millet, Agric. Sci. China **10** 2 (2011), 228–237.

[6] HURTADO, A. C., CHICONATO, D. A., PRADO, R. M., JUNIOR, G. S. S., FELISBERTO, G., Silicon attenuates sodium toxicity by improving nutritional efficiency in sorghum and sunflower plants, Plant Phys. Bioch. **142** (2019) 224–233.

[7] HOJJAT, S. S., Effect of interaction between Ag nanoparticles and salinity on germination stages of *Lathyrus sativus* L, Open Access J. Envir. Soil Sci. **2** 2 (2019).

[8] MOZAFARI, A., GHADAKCHI, A., GHADERI, N., Grape response to salinity stress and role of iron nanoparticle and potassium silicate to mitigate salt induced damage under in vitro conditions, Physiol. Mol. Biol. Plants 24 (2018) 25–35.

[9] DHIMAN, S. S., ZHAO, X., LI, J., KIM, D., KALIA, V. C., KIM, I. W., KIM, J. Y., LEE, J. K., Metal accumulation by sunflower (*Helianthus annuus* L.) and the efficacy of its biomass in enzymatic saccharification, PLOS ONE (2017) doi.org/10.1371/journal.pone.0175845.

[10] SHAHBANDEH, M. Production volume of sunflower seed in major producer countries in 2019/2020 (2020), https://www.statista.com/statistics/263928/production-of-sunflower-seed-since-2000-by-major-countries/

[11] STOIKOU, V., ANDRIANOS, V., STASINOS, S., KOSTAKIS, M.G., ATTITI, S., THOMAIDIS, N. S., ZABETAKIS, I., Metal uptake by sunflower (*Helianthus annuus*) irrigated with water polluted with chromium and nickel, Foods **6** 51 (2017), 10.3390/foods6070051.

[12] VOGEL-MIKUS, K., PONGRAC, P., PELICON, P., VAVPETIC, P., POVH, B., BOTHE, H., REGVAR, M., Micro-PIXE analysis for localization and quantification of elements in roots of mycorrhizal metal-tolerant plants, Soil Biol. **18** 227 (2009), 10.1007/978-3-540-95894-9_14.

[13] AUGUSTYNIAK, M., JUCHIMIUK, J., PRZYBYŁOWICZ, W. J., MESJASZ-PRZYBYŁOWICZ, J., BABCZYŃSKA, A., MIGUL, P., Zinc-induced DNA damage and the distribution of metals in the brain of grasshoppers by the comet assay and micro-PIXE, Comp. Bioch. Phys. C **144** V(2006) 242–251.

[14] HODGES, D.M., DELONG, J.M., FORNEY, C.F., PRANGE, R.K., DELONG, J.M., HODGES, D.M., FORNEY, C.F., PRANGE, R.K., Improving the thiobarbituric acid-reactive-substances assay for estimating lipid peroxidation in plant tissues containing anthocyanin and other interfering compounds, Planta **207** (1999) 604–611.

[15] LICHTENTHALER, H.K., BUSCHMANN, C., Chlorophylls and carotenoids: measurement and characterization by UV-VIS spectroscopy. Handb. Food Anal. Chem. **2** 2 (2005)171–178.

[16] JOHANSSON, S. A.E., CAMPBELL, J. L., MALMQVIST, K. G., Particle-Induced X-Ray Emission Spectrometry (PIXE), John Wiley & Sons, New York (1995).

[17] SHACKLEY, M.S., X-Ray Fluorescence Spectrometry (XRF) in Geoarchaeology, LLC (2011).

[18] VOGEL-MIKUS, K., PONGRAC, P., PELICON, P., Micro-PIXE elemental mapping for ionome studies of crop plants, Inter. J. PIXE, **24** 3-4 (2014) 217–233.

[19] COLLINGWOOD, J. F., ADAMS, F., Chemical imaging analysis of the brain with X-ray methods, Spectroc. Acta B **130** (2017) 101–118.

[20] NOVAK, S., DROBNE, D., VALANT, J., PELICON, P., Internalization of consumed TiO_2 nanoparticles by a model invertebrate organism, J. Nanom. (2012) doi:10.1155/2012/658752.

[21] RYAN, C.G., Quantitative trace element imaging using PIXE and the nuclear microprobe, Int. J. Imaging Syst. Technol., Special Issue on Quantitative Image Analysis **11** (2000) 219–230.

[22] CAMPBELL, J. L., BOYD, N. I., GRASSI, N., BONNICK, P., MAXWELL, J. A., Guelph PIXE software package IV, Nucl. Inst. Meth. Phys. Res. B **268** (2010) 3356-3363.

[23] ESPEN, P. V., JANSSENS, K., NOBELS, J., AXIL-PC, software for the analysis of complex x-ray spectra, Chem. Intel. Lab. Syst. **1** (1986) 109-114.

[24] PYMCA. European Synchrotron Radiation Facility (2020), http://pymca.sourceforge.net/

[25] KAVČIČ, A., MIKUŠ, K., DEBELJAK, M., van ELTEREN, J. T., ARČOND, I., KODRED, A., KUMP, P., KARYDAS, A. G., MIGLIORI, A., CZYZYCKI, M., VOGEL-MIKUŠ, K., Localization, ligand environment, bioavailability and toxicity of mercury in *Boletus spp.* and *Scutiger pes-caprae* mushrooms, Ecotox. Envir. Saf. **184** (2019) 109623.

[26] RAVEL, B.; NEWVILLE, M., ATHENA, ARTEMIS, HEPHAESTUS: data analysis for X-ray absorption spectroscopy using IFEFFIT, J. Synch. Rad. **12** (2005) 537–541.

[27] MOHAMED, A. K. S. H., QAYYUM, M. F., ABDEL-HADI, A. M., REHMAN, R. A., ALI, S., RIZWAN, M., Interactive effect of salinity and silver nanoparticles on photosynthetic and biochemical parameters of wheat, Arch. Agron. Soil Sci. (2017), 10.1080/03650340.2017.1300256

[28] LARUE, C., CASTILLO-MICHEL, H., SOBANSKA, S., CÉCILLON, L., BUREAU, S., BARTHÈS, V., OUERDANE, L., CARRIÈRE, M., SARRET, G., Foliar exposure of the crop *Lactuca sativa* to silver nanoparticles: Evidence for internalization and changes in Ag speciation, J. Hazar. Mat. **264** (2014) 98– 106.

[29] PÉREZ-DE-LUQUE, A. Interaction of nanomaterials with plants: what do we need for real applications in agriculture? Front. Environ. Sci. **5** 12, 2017.

HYBRIDISED PRODUCTION OF TECHNETIUM-99M AND TECHNETIUM-101 WITH FLUORINE-18 ON A LOW-ENERGY BIOMEDICAL CYCLOTRON

E. V. JOHNSTONE
Innovative Fuel Solutions, LLC
Las Vegas, Nevada, USA

E. J. MAUSOLF
Innovative Fuel Solutions, LLC
North Las Vegas, Nevada, USA

Natalia MAYORDOMO
Institute of Resource Ecology,
Helmholtz-Zentrum Dresden-Rossendorf
Dresden, Germany
Email: n.mayordomo-herranz@hzdr.de

Abstract

New modes of production and supply of short-lived radioisotopes using accelerators are becoming attractive alternatives to the use of nuclear reactors. In this study, the use of a compact accelerator neutron source (CANS) was implemented to explore the production of ^{99m}Tc and ^{101}Tc. Irradiations were performed with neutrons generated from a 16.5 MeV cyclotron utilising the ^{18}O(p,n)^{18}F reaction during routine ^{18}F[FDG] production in a commercial radiopharmacy. Natural molybdenum targets in metal form were employed for the production of Tc isotopes interest via (n,γ) reactions on ^{98}Mo and ^{100}Mo. The production of ^{99m}Tc and ^{101}Tc under these conditions is considered and discussed.

1. INTRODUCTION

The capability of non-invasive, internal imaging, static or metabolic, of the various anatomical structures, processes, or the disease and detriment of these, has become the desideratum of diagnostics in the medical community. More than tens of millions of positron emission tomography (PET) and single-photon emission computed tomography (SPECT) procedures are administered every year in the United States of America (U.S.) alone. With the ever-growing demand of these procedures, the pursuit of innovative technologies and processes has become an incessant enterprise for establishing techniques and systems that are more work-efficient, cost-effective, and safety-conscious.

Technetium-99m (^{99m}Tc, $t_{1/2}$ = 6.007 h) has been widely used for radiodiagnostic purposes for decades, and it is still one of the most used radioisotopes worldwide constituting approximately 85% of all nuclear medicine procedures conducted. Tc-99m can be produced through various nuclear transmutation methods, but commercially speaking, it is generally derived from molybdenum-99 (^{99}Mo, $t_{1/2}$ = 65.925 h) via ^{235}U targets [1]. However, the current commercial production and distribution of ^{99m}Tc relies on a complex supply-chain that has proven itself prone to disruptions in years past, which was most recently observed during the SARS-CoV-2 pandemic [2]. Ultimately, this leads to delays on diagnoses of patients due to postponed imaging procedures as well as the loss of material and capital.

Compact accelerator neutron sources (CANS) have presented themselves in the last few decades as a potential alternative for the decentralised production and distribution of radioisotopes [3]. In this regard, CANS refer to an array of fundamentally different accelerator sources, such as cyclotrons, radiofrequency quadrupole (RFQ) accelerators, linear accelerators (LINACs) coupled with a photoneutron converter, electrostatic accelerators, laser-driven sources, and neutron generators. With many of these systems neutron fluxes upwards of ~10^{12} n/s are achievable [4]. However, an under-utilised source of neutrons are those originating from (p,n) reactions during routine PET radioisotope production, such as for ^{18}F-based radiopharmaceuticals [5].

For example, over the last few decades routine manufacturing of ^{18}F-fluorodeoxyglucose (FDG), the most frequently implemented PET agent, has greatly evolved. From the bench top synthesis of several doses at a time

to hundreds of doses manufactured in a single production with multiple runs daily, the evolution of ^{18}F[FDG] has become the gold standard for in-house medical radioisotope production. At the present moment, there exists at least one of these facilities with a cyclotron in every single state in the U.S., where states with larger populations, and thus higher demand requirements, may have several. Therefore, the growth in ^{18}F has signified a correlative increase in potential available neutrons that are effectively not being utilised.

The use of complementary neutrons generated in a biomedical cyclotron employing the ^{18}O(p,n)^{18}F reaction has been proposed for radioisotope production [6], although its application for the production of ^{99}Mo / ^{99m}Tc or other Tc isotopes is hardly mentioned in the literature. In one study, ^{99}Mo was implemented as a monitor for neutron flux in a Mo-containing multi-component flux wire measurement, although there was no targeted discussion for its production [7]. In another study, Link and Krohn report using neutrons generated during ^{13}N production, i.e., ^{16}O(p,α)^{13}N, with a 11 MeV Siemens Eclipse at 30 μA over a duration of 0.5 h for producing ^{99}Mo / ^{99m}Tc for teaching purposes. Although only small amounts were generated under these circumstances, the authors propose using (p,n) reactions and longer irradiations for higher output [8]. Considering the information provided in the literature pertaining to neutron production rates and energies, it was of interest to determine whether the simultaneous production ^{99}Mo / ^{99m}Tc and ^{101}Mo / ^{101}Tc with ^{18}F in a biomedical cyclotron was feasible, and if it could be a commercially viable option for production and distribution of these medically relevant radioisotopes.

2. MATERIALS AND METHODOLOGY

Irradiations were performed with complementary neutrons generated on a biomedical cyclotron (Figure 1) during routine ^{18}F production with a ~16.5 MeV proton beam operating between 75 μA and 85 μA. The ^{18}F target material was ^{18}O[H_2O] with a purity of >98.0% ^{18}O. High-yield ^{18}F targets (BTI Targetry) were used [9]. The target bodies are made of Al 6061-T6 with a niobium (Nb) insert and implement a Havar alloy foil (0.04 mm) as a target window. Cooling of the target is performed using water and liquid transfer and pressurisation is used with high-purity helium (He) gas. The ^{18}O[H_2O] target volume is ~3.5 mL.

Several varying geometries including cubes and foils of Mo metal were used for irradiations to determine production of ^{99}Mo. The Mo foil (10 cm x 10 cm x 0.01 cm) with ≥ 99.98% Mo was subdivided into 4-square pieces of dimension (5 cm x 5 cm x 0.01 cm) and approximate masses of ~2.6–3.0 g. Mo target masses and dimensions are presented below in Table 1. Foil samples were positioned underneath the ^{18}F target in position 5 with a piece of Styrofoam moderator placed between the foils and the target. Mo cubes (volume ~1 cm^3, mass ~10.3 g) with 99.95% Mo were used to determine production in thicker targets. Mo cubes were placed in small plastic bags and adhered to either the back of the ^{18}F target directly (Cube 1) or behind the Styrofoam moderator (Cube 2) as shown in Figure 1.

TABLE 1. Characteristics of Mo cube and foil samples used in irradiation experiments.

Mo Sample	Mass (g)	Volume (cm^3)	Surface Area (cm^2)	Moderation
1 - Cube	10.29075	1	1	No
2 - Cube	10.26120	1	1	Yes
1 - Foil	2.94533	~0.25	~25	Yes
2 - Foil	2.59308	~0.25	~25	Yes
3 - Foil	3.03616	~0.25	~25	Yes
4 - Foil	2.52704	~0.25	~25	Yes

Irradiation durations and conditions were logged throughout the course of the workweek. The values generated, such as run time, ^{18}F yield, and beam current, were used to determine relative neutron production rates and relative total neutron output in order to compare with measured values of activity generated in the Mo samples. Scheduled production of ^{18}F in the facility involves at least two and up to three production runs in a typical working

day. The cyclotron is equipped with two ^{18}F targets located in positions 2 and 5 approximately ~28 cm apart at the rear of the targets as shown in Figure 1. For each working day, the two ^{18}F targets were alternated for each corresponding run. Samples were positioned on the back of the ^{18}F target in position 5 with the sample faces oriented perpendicularly to the direction of the incoming proton beam, as well as underneath the ^{18}F target with the sample faces oriented parallel to the beam. Several of the samples underneath the ^{18}F target were also positioned behind two pieces of a Styrofoam moderator to determine the effect of moderation. Although both sample sets were located in the closest proximity to the neutron flux generated on the target in position 5 (Figure 1), it is acknowledged that the samples were also within the bounds of the irradiation field generated by the ^{18}F target in position 2 during operation, albeit at a lower neutron flux and different energy regime.

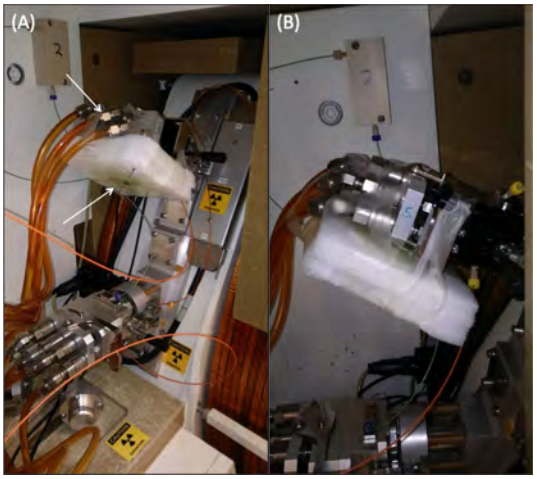

Figure 1. (A) Experimental setup for irradiation of Mo metal samples on a biomedical cyclotron using high yield ^{18}F targets from BTI Targetry. White arrows indicate the position of the samples to be irradiated on the ^{18}F target located in position 5. The top arrow is pointing to the Mo metal block attached directly behind the target, and the bottom arrow is the location of the Mo metal foils behind a Styrofoam moderator. (B) Close-up view of the ^{18}F target and Mo sample configurations from the perpendicular perspective relative to the incoming beam

Radioactivity in the Mo foils was quantitatively determined using a NaI-type gamma spectrometer, taking measurements at various time intervals after end-of-bombardment (EOB). The NaI spectrometer was calibrated with a ^{137}Cs source from North American Scientific with an activity of 2118 Bq at time of use. The detector efficiency was determined to be 10.814% for the ~661 keV peak. It is acknowledged that at lower γ energies (Eγ) that better detector efficiencies are achievable, however, due to time and materials constraints of this study an efficiency plot was not established to determine this. The activities of ^{99}Mo, ^{99m}Tc, and ^{101}Tc were determined using the gamma emissions at 181.1 keV (Iγ = 6.05%), 140.5 keV (Iγ = 89.4%), and 306.8 keV (Iγ = 89.4%). The absolute activity (A) of ^{99}Mo in several samples was calculated as a function of integrated counts under the corresponding peaks (C) and adjusted for background counts (B) at the region of interest (ROI), detector efficiency (ε), decay time after EOB until the measurement (T_d), decay during the measurement time (T_c), and the associated γ-ray emission probability (I_γ) and decay constant (λ) with each distinct isotope using Equation 1 [10]. Furthermore, the reaction rate of ^{99}Mo production in the irradiated samples was also calculated considering the irradiation duration (T_i) with Equation 2 [10].

$$A = \frac{\lambda(C-B)}{\varepsilon I\gamma e^{-\lambda T_d}(1-e^{-\lambda T_c})} \quad \text{Eq. 1}$$

$$R_{Mo-99} = \frac{\lambda(C-B)}{\varepsilon I\gamma(1-e^{-\lambda T_i})e^{-\lambda T_d}(1-e^{-\lambda T_c})} \quad \text{Eq. 2}$$

3. RESULTS AND DISCUSSION

3.1. Complementary Neutron Production on a Low-Energy Cyclotron

At the fundamental level, the endoergic nuclear reaction of an impinging proton on ^{18}O for the production of ^{18}F can be represented by the equation:

$$^{18}O + p \rightarrow {}^{18}F + n \qquad Q = -2.44 \text{ MeV} \quad \text{Eq. 3}$$

The reaction threshold energy is approximately 2.5 MeV with a reaction cross-section maximum of ~550 mb occurring around 5 MeV. Although the ^{18}O transmutation proceeds above and below the maximum cross-section energy, the construction of the target is devised so that the beam terminates within the water target, and it does so with a beam energy as close to the maximum cross-section. For a 16.5 MeV incoming proton beam, slowing of the beam, or beam degradation, is performed within the Havar alloy window and controlled by its relative thickness. According to Equation 3, transmutation of ^{18}O with the addition of a proton is accompanied by the ejection of a neutron from the nucleus. Therefore, for every atom of ^{18}F formed, a neutron is also generated. Thus, the degree of transmutation is dependent upon the number of impinging protons on the target, which can be calculated using Equation 4.

Here, the elemental charge of a proton (q_{proton}) is equal to 1.6 x 10^{-19} Coulombs (C), and 1 microampere (μA) is equivalent to 10^{-6} $C \cdot s^{-1}$. The proton production rate (R_{proton}) for a beam current (I_{beam}) can be calculated as:

$$R_{proton}\left(\frac{proton}{sec}\right) = I_{beam}(\mu A) * 10^{-6}\left(\frac{C}{sec}\right) * \frac{1}{q}\left(\frac{proton}{C}\right) \quad \text{Eq. 4}$$

Under standard operating beam currents, R_p values up to ~1 x 10^{14} protons$\cdot s^{-1}$ are achievable. However, because of scattering events and interactions with the target body, window, and other components, the proton beam is not fully converted into ^{18}F. One indicator of approximating beam conversion efficiency in the target is the saturation activity (SA), which is a function of ^{18}F activity per unit of beam current, i.e., mCi$\cdot \mu A^{-1}$. Using SA of the target and I_{beam} the number of ^{18}F atoms produced per unit time can be determined, and thus the number of neutrons produced ($R_{neutron}$) can be inferred as:

$$R_{neutron}\left(\frac{neutrons}{sec}\right) = I_{beam} * SA\left(\frac{mCi}{\mu A}\right) * 3.7 * 10^{6}\left(\frac{s^{-1}}{mCi}\right) \quad \text{Eq. 5}$$

For determining the thermal neutron flux ($\Phi_{neutron}$, neutrons/cm$^2\cdot$sec) from R_{neutron} as shown in Equation 5, Patterson's formula [10] shown in Equation 6 can be applied, where K (=1.25) is a constant and I is the surface area exposed to the neutron field.

$$\Phi_{neutron}\left(\frac{neutrons}{sec*cm^2}\right) = K\frac{R}{I} \quad \text{Eq. 6}$$

Thus, the higher the saturation activity, the higher the efficiency of beam conversion is and production of neutrons from the target. Likewise, the total activity generated per batch of ^{18}F is equivalent to the total number of neutrons manifested. However, Carroll observed computationally with *ALICE9* that the correlation between neutron production and SA did not trend linearly when proton beam energies exceeded 12 MeV. This was attributed to other energetically accessible $^{18}O(p,x)$ neutron-emitting channels that were not possible under 12 MeV [12]. Likewise, the neutrons resulting only from ^{18}O transmutation do not completely account for the total production within the system. In fact, an array of (p,n) reactions occurs in the irradiation system, such as with nearby parts of the cyclotron or the ^{18}O target including the Havar foil itself that interact with the stray proton beam. Accounting for the entirety of these possible interactions, the reported calculated flux produced from the production of ^{18}F with a proton beam operating at 15 MeV and 75 µA approaches 1.3 x 10^{12} n/s [13].

More accurate determinations of neutron fluxes produced in PET cyclotrons during ^{18}F production have been conducted through experimental flux wire, neutron detection, and dosimetry measurements coupled with multi-system computational modelling, such as Monte Carlo, MCNP, FLUKA, etc. For example, Jeffries *et. al.* have reported the neutron flux generated from a GE PETtrace-800 employing BTI Targetry high yield ^{18}F targets TS-1700 (80 µA) and TS-1650P (72 µA) [14]. Measurements were performed using a variety of activation flux wires with different neutron threshold energies along with comparative modelling via STAYS PNNL, MCNP6, and 3-Group programs. Results determined that the fast neutron flux density adjacent to the target was 1.8 x 10^9 n/cm$^2\cdot$s to 3.0 x 10^9 n/cm$^2\cdot$s with 1 MeV equivalent flux density from 2.4 x 10^9 neutrons/cm$^2\cdot$s to 4.9 x 10^9 n/cm$^2\cdot$s. Castillo analysed modelled data from a compilation of past studies concerning the neutron production on a 16.5 MeV proton beam on an $^{18}O[H_2O]$ target normalised to a beam current of 75 µA [13].

A summary of the data shows that depending on the model employed and physical parameters integrated into the model, the $R_{neutron}$ rate varied from 1.20 x 10^{12} n/s to 1.73 x 10^{12} n/s with neutron fluxes ranging from 2.18 x 10^8 n/cm$^2\cdot$s to 1.45 x 10^8 n/cm$^2\cdot$s. The determined neutron energy distribution spanned a broad energy range

with maxima occurring in the epithermal to fast neutron regime, i.e., 0.01 to 5 MeV, as well as in the thermal region, ≤ 0.025 eV. Bosko [15] also reported on modelled neutron production rates and neutron energy distributions from a GE PETtrace-800. The $R_{neutron}$ was determined for a 16.5 MeV proton beam on a thick $^{18}O[H_2O]$ target to be 3.21 x 10^{11} n/s assuming a 60 μA beam current. The neutron energy distribution ranged from 1 MeV with a relative flux of ~1.1 x 10^{11} n/s and extended to over 10 MeV with gradual drop in flux to ~1.1 x 10^{8} n/s; the majority of the flux focused in the neutron energy range from 1 MeV to 4 MeV. This $R_{neutron}$ value is similar to the one reported by Horitsugi et. al. from the GE Healthcare ALARA reports as 7.13 x 10^{11} n/s at 80 μA during dual port irradiation [16, 17]. Figure 2 shows the correlation between proton beam current and the resulting neutron flux (n/s) for 16.5 and 18.5 MeV cyclotrons from reported values in the literature.

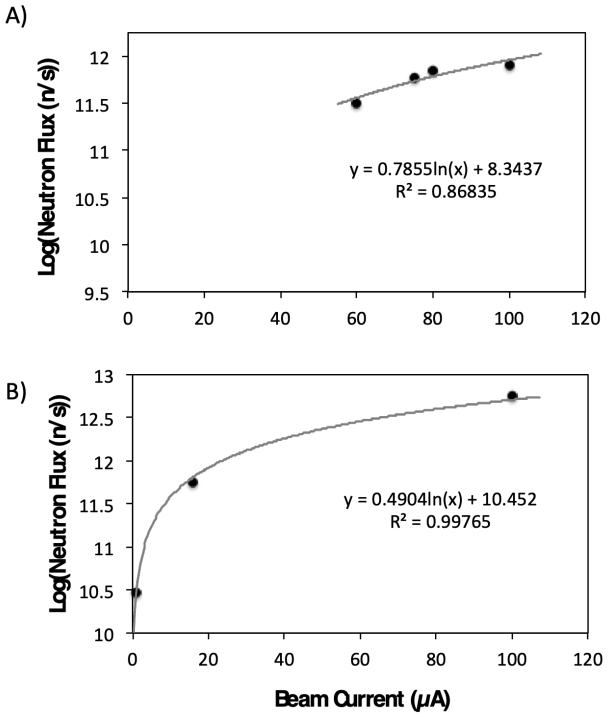

Figure 2. Reported neutron fluxes arising from the $^{18}O(p,n)^{18}F$ transmutation reaction as a function of proton beam current for A) 16.5 MeV and B) 18.5 MeV energy cyclotrons.

Another factor that should be considered is the neutron direction or angular distribution from the target. This is particularly important when considering the placement of a source to be irradiated, where neutron energy distribution and flux can be determined by sample position relative to the neutron source, i.e., $^{18}O[H_2O]$ target. For example, in nuclear reactor scenario, neutrons are emitted isotropically, whereas for accelerators this is not necessarily the case and neutron angular distribution is anisotropic. For accelerators some of the energy from the primary incoming beam will impart some of its energy on the secondary particle emitted, which can lead to scattering as well as backscattering of the secondary particles. Generally, the higher the energy of the incoming proton, the higher the energy of the neutrons produced.

For the transmutation of ^{18}O to ^{18}F with a high-energy proton beam, the majority of the generated neutrons are emitted in the same direction as the incoming proton beam. As mentioned previously, scattering is observed further out from the origin source in the ^{18}O target, where the neutron field becomes more diffuse, although still mostly directionally forward. It is also noted that a lesser, yet significant amount of neutrons are emitted in the opposite direction, or essentially backwards from the target into the incoming proton beam. Specifically, the GE Site Planning Guide states that when compared to the total flux of neutrons in the forward direction, those perpendicular to the incoming particle beam will be 30% less of this value, and those in the backwards direction will be at least 10x lower in magnitude [18].

Irradiations were performed on several Mo metal samples (Table 1) with various physical characteristics, i.e., mass, thickness, surface area, and volume, using the complementary neutrons produced during the production of ^{18}F with a low-energy cyclotron. As previously discussed, the proton-induced transmutation of ^{18}O to ^{18}F results in the liberation of a free neutron, which is directly correlated to the yield of ^{18}F produced in the ^{18}O target. Shown

in Figure 3 is an ^{18}F production curve for a 20-minute irradiation at 75 μA yielding a total of ~1.8 Ci of ^{18}F at EOB. As every atom of ^{18}F generated is equal to at least one neutron, then this would correspond to an average neutron flux of 5.2 x 10^{11} n/s with a total neutron output of 2.3 x 10^{13} in the measured time period. With routine production schedules consisting of 4 to 5 h of operational beam time, the total average neutron output on a system equivalent to the one tested would range between 7.5 x 10^{15} to 9.4 x 10^{15} neutrons in a working day based solely on ^{18}F transmutation, not considering other avenues of neutron production, for example, (*p*,*n*) reactions with the Havar window. In comparison to literature reported values for neutron fluxes in a 16.5 MeV cyclotron, the value inferred from the ^{18}F activity, i.e., 5.2 x 10^{11} n/s, is comparable to the one of Castillo [13], i.e., 6.0 x 10^{11} n/s, at 75 μA, suggesting that the system is likely capable of outputting fluxes upwards of 1 x 10^{12} n/s with all other neutron producing reactions considered.

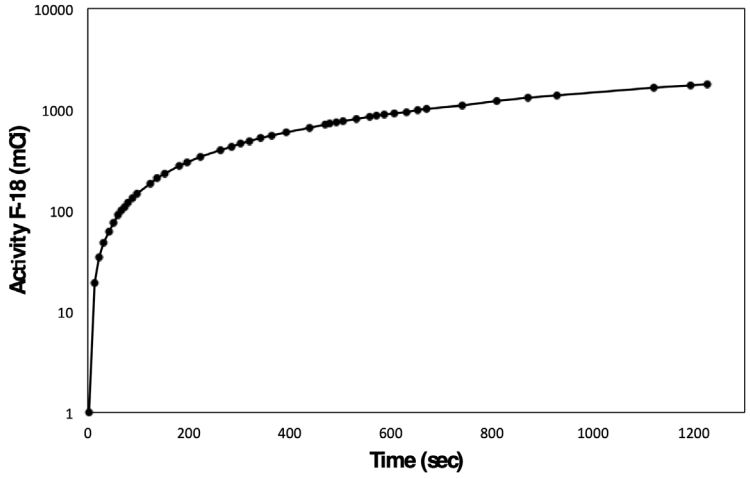

Figure 3. Activity (mCi) of ^{18}F generated as a function of time (s) in an enriched ^{18}O target using the cyclotron and experimental setup described previously with an operating current of 75 μA.

3.2. Hybridised Production of ^{99m}Tc and ^{101}Tc with Complementary Neutrons

Although Mo is characterised by seven naturally occurring isotopes, i.e., ^{92}Mo (14.53%), ^{94}Mo (9.16%), ^{95}Mo (15.84%), ^{96}Mo (16.67%), ^{97}Mo (9.60%), ^{98}Mo (24.39%), ^{100}Mo (9.82%), only ^{98}Mo and ^{100}Mo provide direct routes to the appreciable formation of ^{99}Mo when interacting with neutrons. For ^{98}Mo, the fundamental interaction is via $^{98}Mo(n,\gamma)^{99}Mo$. The neutron capture on ^{98}Mo occurs across a wide range of neutron energies. The thermal neutron capture, i.e., 0.025 eV, on ^{98}Mo has a cross-section ($\sigma_{thermal}$) of approximately 0.137 b. In comparison to the fission-based production of ^{99}Mo with thermalised neutrons, this value is nearly ~270x less for the equivalent irradiation using ^{235}U as the fuel source. Furthermore, neutron capture reactions with thermal neutrons generally yield specific activities of hundreds of mCi/g at most depending upon the neutron flux, the amount of self-shielding effects, and level of enrichment of ^{98}Mo in the target. It is noted that enrichment of ^{98}Mo can increase production yields up to 4x more than natural isotopic samples.

For higher energy neutrons, particularly in the resonance, i.e., 10-300 eV, and intermediate regions, i.e., 300 eV-0.05 MeV, ^{98}Mo exhibits multitudes of enhanced resonance capture maxima. The resulting averaged cross-section of this region ($\sigma_{resonance}$) approaches ~7 b, which is more than 50x than that of $\sigma_{thermal}$ for ^{98}Mo, i.e., 0.130 b. Likewise, it has been established that self-shielding of epithermal neutrons from other Mo isotopes is negligible comparative to interactions with ^{98}Mo [19]. Because of the greater probability of interaction, it has been reported that specific activities up to ~3.4 Ci/g and ~15 Ci/g are achievable for natural and enriched targets, respectively, thus yielding significantly greater outputs in ^{99}Mo [20]. The neutron capture behaviour of ^{98}Mo is quite similar to ^{100}Mo, where $\sigma_{thermal}$ for ^{100}Mo is 0.199 b and $\sigma_{resonance}$ is 3.76 b.

The second accessible pathway for ^{99}Mo production with neutrons via $^{100}Mo(n,2n)^{99}Mo$ only occurs for fast neutrons, (≥ 1 MeV) [21, 22]. The threshold reaction energy is approximately 8 MeV with a cross-section (σ_{fast}) maximum of roughly 1.5 b befalling between 13 and 16 MeV. Relative to $\sigma_{thermal}$ of ^{98}Mo, this value is nearly

11x larger, although for the averaged $\sigma_{resonance}$ of ^{98}Mo, it is about 5x less. However, because of the lower isotopic concentrations of ^{100}Mo in comparison to ^{98}Mo in natural samples, enriched materials can provide up to 10x the production. Due to the higher reaction threshold energy, this pathway is generally associated with production means where the adequate fast neutron fluxes are present [23].

In order to determine the production of ^{99}Mo/^{99m}Tc via neutron activation in an Mo target, several Mo metal samples with varying geometries, i.e., cube versus sheet, were subjected to the neutron field within the cyclotron. Samples were placed in the vicinity of the highest neutron fluxes around the ^{18}F target. Typically samples were arranged prior to ^{18}F production for the given day and either measured at the end of the production day or after several days.

Shown in Figure 4 is the γ-ray spectrum of a Mo cube measured 1.4 h post-EOB following an irradiation of 4.5 h in an un-moderated zone directly behind the ^{18}F target, aligned with the incoming proton beam. The γ-ray spectrum shows the characteristic peaks for ^{99}Mo at 185 keV and 725 keV, ^{99m}Tc at 146 keV, and ^{101}Tc at 311 keV and 531 keV. These are in good agreement with the reported gamma energies for ^{99}Mo at 181.1 keV and 739.5 keV, ^{99m}Tc at 140.5 keV, and ^{101}Tc at 306.8 keV and 531 keV. The presence of ^{99}Mo is most likely attributed to the neutron activation of ^{98}Mo in the target, whereas ^{99m}Tc present is a result of ^{99}Mo decay.

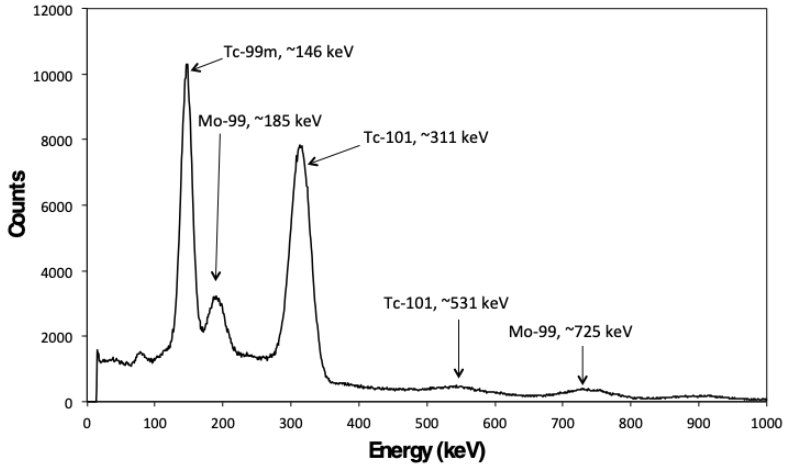

Figure 4. Gamma spectrum of Mo cube after ~1.4 h post EOB showing characteristic peaks for ^{99}Mo, ^{99m}Tc, and ^{101}Tc after being irradiated in a neutron field for ~4.6 h.

The radioisotope ^{101}Tc is also a daughter product, however, from ^{101}Mo, formed via (n,γ) on ^{100}Mo; the absence of any characteristic γ-ray peaks (Eγ = 229.1 keV (2.20%), 257.1 keV (2.77%), 261.1 (20.6%), 359.1. keV (3.31%), 570.1 keV (6.62%)) from ^{101}Mo is due to its shorter half-life ($t_{1/2}$ = 14.16 min.). Unlike ^{101}Mo, which is formed directly during the neutron irradiation, ^{101}Tc being the daughter product still persists and can be seen as one of the more prominent peaks in the spectrum. Likewise, because the irradiation period (~4.6 h) is sufficiently long compared to the half-life of ^{101}Mo to achieve saturation, the concentration of ingrown ^{101}Tc should be equivalent to that of ^{101}Mo at EOB in the Mo target. Therefore, the total amount of ^{101}Tc generated after EOB should be equal to the amount present at EOB plus the amount generated from residual ^{101}Mo decay.

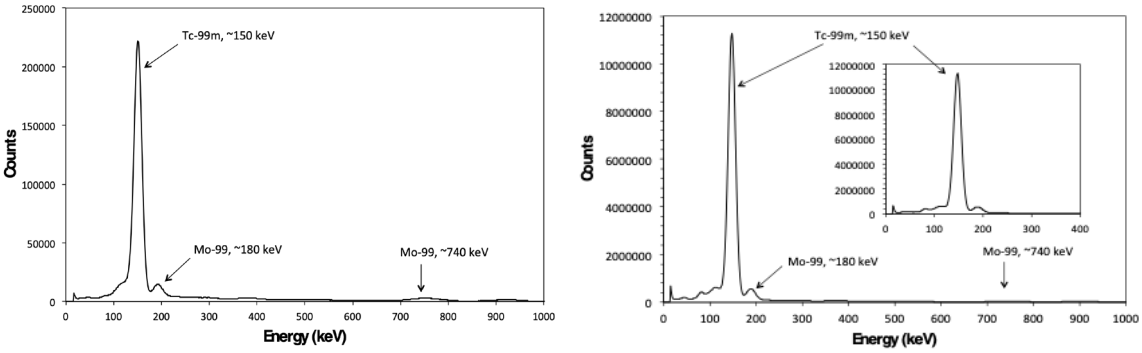

Figure 5. (Left) Gamma spectrum of Mo cube after 26 h post EOB showing characteristic peaks for ^{99}Mo and ^{99m}Tc. (Right) Gamma spectrum (12 h count) of Mo foil acquired 24 h after EOB.

Presented in Figure 5 is the γ-ray measurement of the same Mo cube after 26 h post-EOB. The identified species in the spectrum were ^{99}Mo with peaks at 180 keV and 740 keV, and ^{99m}Tc with a peak at 150 keV. At this point, there was no remaining ^{101}Tc. The peak-to-peak ratio of ^{99m}Tc to ^{99}Mo was determined to be 22.7, which is 6.6x greater than after 1.4 hr post EOB; this time post-EOB correlates to the near-maximum ingrowth of ^{99m}Tc from ^{99}Mo decay.

In Figure 5, the γ-ray spectrum acquired 24 h after EOB of an irradiated Mo foil is presented. The foil was positioned underneath the ^{18}F target and behind several layers of Styrofoam and irradiated within the neutron field for a total duration of 4.6 h. The γ-ray spectrum shows identifiable peaks indicative of ^{99}Mo at 180 keV and 740 keV, and ^{99m}Tc at 150 keV. As expected, no ^{101}Mo and ^{101}Tc were detectable at the time of / during measurement. The γ-ray spectrum here is also comparable with the one shown in Figure 5 for the Mo cube.

The effect of various physical attributes, (i.e., volume, surface area) of the Mo targets and moderation / no moderation of the neutron field utilised in the production of ^{99}Mo / ^{99m}Tc were of particular interest. Three different samples, i.e., two Mo cubes (Cube 1 and Cube 2) and one Mo foil (Foil 1), were compared (Table 3), where all samples were irradiated for similar times (4.3 to 4.6 h) over the course of two production runs, one in which the samples were attached to the ^{18}F used for production (~2.7 h) and a second run during which they were located adjacently to the ^{18}F target being operated (1.6 to 1.9 h); between the two production runs was a pause of approximately 1.5 h, however, for simplicity, ^{99}Mo production only accounted for total irradiation time during operation. The effect of moderation was determined, where Cube 1 was placed in an un-moderated zone behind the ^{18}F target, and Cube 2 was positioned underneath the target behind both a Styrofoam moderator and Foil 1. Final production activities and rates determined using Eq. 1 and Eq. 2, respectively, for ^{99}Mo were normalised for decay after EOB and mass of the targets.

TABLE 2. Comparison of activities and reaction rates of ^{99}Mo in various Mo metal samples after one production day of ^{18}F in a low-energy cyclotron with neutrons generated through the ^{18}O(p,n)^{18}F reaction.

	Cube 1	Cube 2	Foil 1
Mass	10.29075	10.2612	2.94533
Irradiation Time (s)	15540	16500	16500
Time after EOB (s)	98753	37736	39210
Count Time (s)	600	600	600
Total Counts ^{99}Mo	391785	333068	197469
Total ^{18}F Produced (Ci)	19.189	19.649	19.649
^{99}Mo Activity (Bq)	1.28E+05	9.00E+04	5.16E+04
^{99}Mo Activity (Ci)	3.45E-06	2.43E-06	1.40E-06
^{99}Mo Specific Activity (Ci/g)	3.35E-07	2.37E-07	4.74E-07
Spec. Act. ^{99}Mo (Ci/g)/^{18}F (Ci)	1.75E-08	1.21E-08	2.41E-08
Ratio ^{99}Mo (Ci)/^{18}F (Ci)	1.80E-07	1.24E-07	7.10E-08
Reaction Rate of ^{99}Mo (Bq)	2.87E+06	1.91E+06	1.10E+06
Reaction Rate of ^{99}Mo (Ci)	7.77E-05	5.17E-05	3.93E-05
Reaction Rate of ^{99}Mo (Ci/g)	7.55E-06	5.04E-06	1.34E-05

As shown in Table 2, the production and reaction rates of the two Mo cubes are presented. Both cubes exhibited identical volumes and surface areas, however, Cube 1 was subjected to no moderation of the incoming neutron field, whereas the neutron field was relatively moderated prior to interacting with Cube 2. The specific activities of ^{99}Mo normalised to EOB and per gram of sample show that both samples yielded approximately 240 nCi/g to 340 nCi/g of ^{99}Mo produced at EOB after one routine production day of ^{18}F, or ~12 nCi/g•Ci-^{18}F to 18 nCi/g•Ci-^{18}F. The reaction rates of formation of ^{99}Mo in the samples were determined to be 5.0 μCi/g to 7.6 μCi/g, accounting for the irradiation time of each sample. From these values, it is seen that Cube 1 yielded slightly greater values of specific activity and reaction rates in comparison to Cube 2, although not significantly. When taking into consideration that the neutron flux generated perpendicular to the incoming proton beam is 70% of the beam generated in the same direction, the values of Cube 2 when adjusted for this then become 343 nCi/g and 7.1 μCi/g for the specific activity and reaction rate, respectively, and are essentially identical for those of Cube 1. An explanation for this behaviour is as such: although Cube 2 experienced a lower neutron flux than that of Cube 1, the neutron energies due to moderation were more favourable for neutron capture reactions for Cube 2, thus allowing for equivalent production and reaction rates of ^{99}Mo. As discussed previously, neutron capture on ^{98}Mo is greatly favoured within neutron energies of 300 keV to 0.05 MeV, and it quickly diminishes with neutron energies outside of this region. Therefore, if the neutrons coming out of the target have energies greater than 0.05 MeV, which is likely the case, then there will be far less interaction probabilities for capture on ^{98}Mo.

After establishing the approximate yield of ^{99}Mo that could be generated in a single ^{18}F production day, it was of interest to investigate and track production over the course of a several days period. However, it is noted that because ^{18}F production days were not all homogenous, where some days accounted for a single run and others multiple runs, attempting to extract any definitive behaviour of ^{99}Mo/^{99m}Tc production was beyond the limit of the study and only broad trends in the data were to be considered. Figure 6 shows the relative activity of ^{99}Mo produced over the course of several ^{18}F production days. The starting day corresponds to a Friday, after which no irradiations were performed for the following two days over the weekend. Generally, the trend of the curve shows the relative build-in of ^{99}Mo as a function of successive irradiations. Furthermore, this similar trend was also observed when tracking the ingrowth of ^{99m}Tc in the samples, as shown in Figure 6.

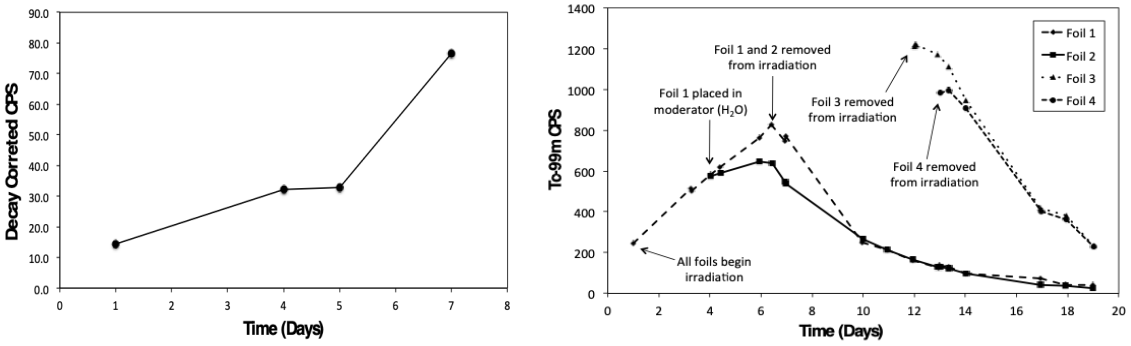

Figure 6. (Left) Production of ^{99}Mo in a Mo foil tracked over several days of irradiation. Days 2 and 3 correspond to a weekend and no irradiations were performed. (Right) Presence of ^{99m}Tc (raw CPS) in Mo foils 1–4 over the duration of the irradiation experiment.

4. CONCLUSION

The purpose of the study was to determine whether it was feasible to co-produce ^{99m}Tc and ^{101}Tc in parallel with ^{18}F using a hybridised system based upon liberated neutrons from the ^{18}O(p,n)^{18}F and other potential associated (p,n) reactions generated with a low-energy biomedical cyclotron. From the data, it was demonstrated that co-production of both isotopes under the tested conditions to be feasible. It is noted that Mo sample design and placement was extremely rudimentary in comparison to what a commercial system would require if much higher quantities of ^{99}Mo / ^{99m}Tc or ^{101}Mo / ^{101}Tc were to be produced, although possibilities for increasing yields, considering target mass, irradiation time, and neutron flux could be applied for scaling. Further experimentation should be performed in order to better understand a system based upon the one proposed here if commercialisation is considered. It is envisioned that if scalable quantities are achievable, then a system like this, in conjunction with the appropriate separation platform for isolating Tc isotopes from irradiated Mo targets, could allow for a more efficient, distributed mode of production of these and other medically relevant radioisotopes [24].

ACKNOWLEDGEMENTS

The authors would like to extend a sincere thanks to Mr. Jim Davis and Shertech Nuclear Laboratories for the use of the cyclotron and facilities. N. Mayordomo acknowledges the funding from the German Federal Ministry of Economic Affairs and Energy (BMWi) for the VESPA II joint project (02E11607B).

REFERENCES

[1] INTERNATIONAL ATOMIC ENERGY AGENCY, Non-HEU Production Technologies for Molybdenum-99 and Technetium-99m, IAEA TECDOC No. NF-T-5.4, IAEA, Vienna (2013).

[2] SADRI, K., DABBAGH, V.R., FORGHANI, M.N., ASADI, M., SADEGUI, R., Lymphoscintigraphy in the Time of COVID-19: Effect of Molybdenum-99 Shortage on Feasibility of Sentinel Node Mapping, Lymphat. Res. Biol. **19** (2021) 134–140.

[3] MAUSOLF, E.J., JOHNSTONE, E.V., MAYORDOMO, N., WILLIAMS, D.L., GUAN, E.Y.Z., GARY, C.K., Fusion-Based Neutron Generator Production of Tc-99m and Tc-101 : A Prospective Avenue to Technetium Theranostics, Pharmaceuticals. **14** (2021) 1–19.

[4] INTERNATIONAL ATOMIC ENERGY AGENCY, Compact accelerator based neutron sources, IAEA TECDOC No. 1981, IAEA, Vienna (2021).

[5] E.V. JOHNSTONE, E.J. MAUSOLF. Hybridized Production of ^{18}F and ^{99m}Tc on a Low-Energy Cyclotron, internal report, IFS, LLC., N. Las Vegas, 2021.

[6] BROCKMAN, J., JEFFERIES, B., ALGIERE, C., NORGARD, P., GAHL, J., "Characterization and utilization of neutron radiation from a PETtrace cyclotron," Conf. AccApp '17, Quebec, 2017.

[7] KONHEISER, J., MÜLLER, S.E., MAGIN, A., NAUMANN, B., FERRARI, A., Source term calculation and validation for ^{18}F-production with a cyclotron for medical applications at HZDR. J. Radiol. Prot. **39** (2019) 906–909.

[8] LINK, J.M., KROHN, K.A., "The use of neutrons from a small cyclotron for making Mo-99 / Tc-99m generators for teaching," Abstracts from 14th Workshop on Targetry and Target Chemistry, Mexico, 41, 2012.

[9] BTI Targetry, LLC., 2020. http://www.btitargetry.com/

[10] KNOLL, G.F., Radiation Detection and Measurement, 4th ed. John Wiley & Sons, Inc., (2010).

[11] PATTERSON, H.W. THOMAS, R.H., DEWERD, L.A., Accelerator Health Physics. Academic Press, New York (1973).

[12] CARROL, L.R., "Estimating the radiation source term for PET isotope targets," Poster Presentation at the 9th Int. Workshop on Targetry and Target Chemistry, Turku, Finland, 23-25 May 2002.

[13] CASTILLO, J.A.B., Flow mapping and estimation of the radiation source term of neutronic fields generated by the GE PETtrace-8 cyclotron. PhD Thesis: Federal University of Minas Gerais, 2017.

[14] JEFFERIES, B.D., ALGIERE, C., GALLAGHER, J.A., NICHOLS, T.H., SO, J.R., LITTLEFIELD, Jr., C.W., QUINN, M., BROCKMAN, J.D., Characterization of the neutron flux during production of ^{18}F at a medical cyclotron and evaluation of the incidental neutron spectrum for neutron damage studies. Appl. Radiat. Isot., **154** (2019) 108892.

[15] BOSKO, A., ZHILCHENKOV, D., REECE, W.D., GE PETtrace cyclotron as a neutron source for boron neutron capture therapy. Appl. Radiat. Isot. **61** (2004) 1057–62.

[16] HORITSUGI, G., FUJIBUCHI, T., YAMAGUCHI, I., ETO, A., IWAMOTO, Y., HASHIMOTO, H., HAMADA, S., OBARA, S., WATANABE, H., HATAZAWA, J. Radiologic assessment of a self-shield with boron-containing water for a compact medical cyclotron. Radiol. Phys. Technol. **5** (2012) 129–137.

[17] GE Healthcare, PETtrace-unshielded machine; summary of source terms, radiation fields and radwaste production. GE Healthcare Report RP001181, 2004.

[18] GE Healthcare, PETtrace 800 series: Site planning guide, class A. Rev. 18, 2017.

[19] BLAAUW, M., RIDIKAS, D., BAYTELESOV, S., BEDREGAL SALAS, P.S., CHAKROVA, Y., EUN-HA, C., DAHALAN, R., FORTUNATO, A.H., JACIMOVIC, R., KLING, A., MUNÕZ, L., MOHAMED, N.M.A., PARKANYI, D., SINGH, T., DONG DUONG, V., Estimation of ^{99}Mo production rates from natural molybdenum in research reactors. J. Radioanal. Nucl. Chem. **311** (2017) 409–418.

[20] RYABCHIKOV, A.I., SKURIDIN, V.S., NESTEROV, E.V., CHIBISOV, E.V., GOLOVKOV, V.M., Obtaining molybdenum-99 in the IRT-T research reactor using resonance neutrons. Nucl Instr. Methods B. **213** (2004) 364–368.

[21] NAGAI, Y., HATSUKAWA, Y., Production of ^{99}Mo for Nuclear Medicine by ^{100}Mo(n,2n)^{99}Mo. J. Phys. Soc. Jpn. **78** (2009) 033201.

[22] CAPOGNI, M., PIETROPAOLO, A., QUINTIERI, L., ANGELONE, M., BOSCHI, A., CAPONE, M., CHERUBINI, N., DE FELICE, P., DODARO, A., DUATTI, A., FAZIO, A., LORETI, S., MARTINI, P., PAGANO, G., PASQUALI, M., PILLON, M., UCCELLI, L., PIZZUTO, A. 14 MeV Neutrons for ^{99}Mo/^{99m}Tc Production: Experiments, Simulations and Perspectives. Molecules. **23(8)** (2018) 1872. https://doi.org/10.3390/molecules23081872

[23] GENTILE, C.A., COHEN, A.B., ASCIONE, G. Production of radionuclide molybdenum-99 in a distributed and in situ fashion. U. S. Patent and Trademark Office, Patent No. 9,318,228. Submitted 26 Apr2011; Published 1 Nov 2012.

[24] MAUSOLF, E.J., JOHNSTONE, E.V. Direct, Continuous Transmutation of Molybdenum (Mo) for the Production and Recovery of Technetium (Tc) and Ruthenium (Ru) Using a Neutron Source. US Patent and Trademark Office. Submitted 2018, under review.

REVIEW OF THE DIFFERENT ACCELERATOR-BASED BNCT FACILITIES WORLWIDE AND AN ASSESSMENT ACCORDING TO THE ALARA CRITERION

M. E. CAPOULAT
National Atomic Energy Commission, CNEA.
Buenos Aires, Argentina
Email: capoulat@tandar.cnea.gov.ar

A. J. KREINER
National Atomic Energy Commission, CNEA.
Buenos Aires, Argentina

Abstract

Presently, there are a number of different facilities for Accelerator-Based Boron Neutron Capture Therapy (AB-BNCT) worldwide. They range from high-energy 30 MeV cyclotrons, medium-energy RFQ-DTL accelerators (8-10 MeV), low-energy electrostatic and RFQ machines (2.3-2.8 MeV), to a very low-energy electrostatic quadrupole accelerator (1.45 MeV). The paper analyses these installations from the point of view of activation. Since these facilities are intended to work in hospital environments one of the guiding criteria should be the ALARA (As Low As Reasonably Achievable) one.

A detailed analysis using MCNP simulations was made to evaluate neutron induced radioactivity produced in the Beam Shaping Assembly. Also, the activation of the target due to the primary beam is evaluated based on evaluated nuclear data bases.

Based on the IAEA RS-G 1.7 Safety Guide, Application of the Concepts of Exclusion, Exemption and Clearance the paper assess the long-term operation sustainability from the point of view of activation.

1. INTRODUCTION

A wide variety of accelerator-based facilities are envisaged worldwide for Accelerator-Based BNCT (AB-BNCT) worldwide. Some of them are already working and even treating patients, and some are under development and construction. They range from high-energy 30 MeV cyclotrons (using the ^{9}Be(p,n) reaction), medium-energy RFQ-DTL accelerators (at 8 and 10 MeV using likewise the ^{9}Be(p,n) reaction), low-energy electrostatic (both Tandem and single-ended), and RFQ machines (working on ^{7}Li(p,n) at about 2.5 MeV), to a very low-energy electrostatic quadrupole ESQ accelerator (working on ^{9}Be(d,n) or ^{13}C(d,n) at 1.45 MeV). Based on the neutron production reaction, target material and beam energy, all AB-BNCT facilities fit to one of the listed in Table 1.

Since these facilities are intended to work in hospital environments one of the guiding criteria should be the ALARA (As Low As Reasonably Achievable) one. Focusing on long-term operation sustainability and on the basis of the ALARA criterion, the production of residual radioactivity should be minimized as much as reasonably possible.

Although the common goal in all AB-BNCT facilities is to produce an, as pure as possible, epithermal neutron beam (in the range of 0.5 eV to 10 keV), production of high-energy neutrons and hence of induced radioactivity varies considerably from one to another. For instance, facilities working with the ^{7}Li(p,n) reaction produce mainly neutrons of less than 1 MeV. Hence, concerning long-term activation, only exothermic and very low-threshold neutron-induced reactions are relevant to assess activation of these facilities. On the other hand, the ones working with 30 MeV protons and the ^{9}Be(p,n) reaction generate neutrons with energies up to 28.1 MeV. In this case there are many more energetically possible neutron-induced reactions that may generate radioactivity on the subsystems of the facility. In an intermediate scenario are the facilities based on 1.45 MeV deuterons (for both ^{9}Be and ^{13}C targets) and those based on 8 MeV protons on ^{9}Be, where maximum neutron energies are, respectively, 5.76, 6.72 and 6.31 MeV. In particular, the deuteron induced reactions have a large proportion of the yield in the less-than-1 MeV energy region (see Table 1) which makes these reactions particularly attractive for BNCT.

The aim of this work is to quantitatively assess the residual radioactivity in a representative group of AB-BNCT facilities, both by the primary (due to the beam) and secondary (due to neutrons) activation.

TABLE 1. AB-BNCT FACILITIES WORLWIDE GROUPED BY NEUTRON PRODUCING REACTION AND BEAM ENERGY

Target-reaction	Beam Energy (MeV)	Beam current goal (mA)	Percentage of yield with energy ≤ 1 MeV at 0º (%)	Institute, Country
^{7}Li(p,n)^{7}Be	2.3-2.8	10-30	100-92 [1]	Helsinki Univ. Hospital, Finland [2] National Cancer Center, Japan [3, 4] Edogawa Hospital, Japan [5] Nagoya University, Japan [6] Shonan Kamakura Hospital, Japan [7] Soreq, Israel [8] Xiamen Humanity Hosp., China [9–11] IHEP, China [12] Budker Inst., Russia [9] CNAO, Italy [9] Birmingham University, UK [13, 14] Granada University, Spain [15]
^{9}Be(p,n)^{9}B	30	1	9 [16]	Kyoto University, Japan [5, 17] Kansai BNCT RC, Japan. [5, 17, 18] Southern Tohoku Hosp., Japan [5, 17, 19]
^{9}Be(p,n)^{9}B	8	10	21 [16]	Tsukuba University, Japan [20, 21] Gachon Univ.-Dawon Medax, Korea [22, 23]
^{9}Be(d,n)^{10}B	1.45	30	66 [24]	CNEA, Argentina [25–28] KIRAMS, Korea*
^{13}C(d,n)^{14}N	1.45	30	70 [29]	CNEA, Argentina [25–27, 30] KIRAMS, Korea*

*Cooperation agreement between CNEA and KIRAMS.

2. PRIMARY ACTIVATION

Primary activation is produced by interaction of the proton or deuteron beam with the different subsystems of the accelerator. This comes from nuclear reactions (p,X) or (d,X), were X stands for any open reaction channel with radioactive products. The radioactive product may be either the ejectile or the heavy product of the reaction. The largest fraction of the beam impinges directly on the target material and hence, this is the most relevant subsystem as far as primary activation is concerned. Table 2 summarizes the radioactive products and nuclear reactions relevant for each projectile and target material.

TABLE 2. NUCLEAR REACTIONS LEADING TO RADIOACTIVE PRODUCTS ON THE DIFFERENT AB-BNCT TARGETS

	Product, $T_{1/2}$	Reaction	Threshold Energy or Q (MeV)
^{7}Li+p	^{7}Be, 53.22 d	^{7}Li(p,n)^{7}Be	E_{thres}=1.88
^{9}Be+p	^{7}Be, 53.22 d	^{9}Be(p,t)^{7}Be	E_{thres}=13.432
		^{9}Be(p,d+n)^{7}Be	E_{thres}=20.4
		^{9}Be(p,p+2n)^{7}Be	E_{thres}=22.9
	tritium, 12.32 y	^{9}Be(p,t)^{7}Be	E_{thres}=13.432
^{9}Be+d	tritium, 12.32 y	^{9}Be(d,t)^{8}Be	Q=4.602
^{13}C+d	tritium, 12.32 y	^{13}C(d,t)^{12}C	Q=1.312
	^{14}C, 5700 y	^{13}C(d,p)^{14}C	Q=5.962

Facilities based on proton beams on lithium targets produce ^{7}Be as the heavy product in the neutron production reaction. This means that radioactive ^{7}Be nuclei are generated at the same rate than neutrons are. For protons on beryllium, there are two well-differentiated scenarios. Facilities working with high-energy 30 MeV protons generate tritium and ^{7}Be. Tritium comes as the ejectile of the (p,t) reaction while ^{7}Be comes as a heavy product. The threshold energy the ^{9}Be(p,t) reaction is 13.432 MeV, and there are no any other open channels producing radioactivity for protons below this energy, hence medium-energy (8-10 MeV) facilities do not produce long-lived radioactivity in the target. For higher proton energies more channels producing ^{7}Be open, being (n,d+n) at 20.4 MeV and (n,p+2n) at 22.9 MeV the most relevant ones [31].

Radioactivity on beryllium and ^{13}C targets is due to tritium produced through the exothermic (d,t) reactions on ^{9}Be and ^{13}C, respectively. On ^{13}C targets some activity of ^{14}C coming from the (d,p) reaction is also expected.

3. SECONDARY ACTIVATION

Secondary activation comes from neutron induced reactions (n,X) on any element exposed to the neutron flux. There are several subsystems that can be activated, such as the Beam Shaping Assembly (BSA), shielding, target assembly, irradiation room walls, the beamline, ancillary equipment, wires, and any other element exposed to neutrons.

Due to the proximity to the neutron source, the most exposed one and hence, potentially highly activated is the BSA. The main role of the BSA is to moderate the neutrons down to the epithermal regime and to efficiently guide them to the element to be irradiated. It also acts as a first shielding for neutrons and gamma rays. The structure, components, size, and materials, depend on the energy distribution of the neutrons produced in the target. A generic design is shown in Fig. 1.

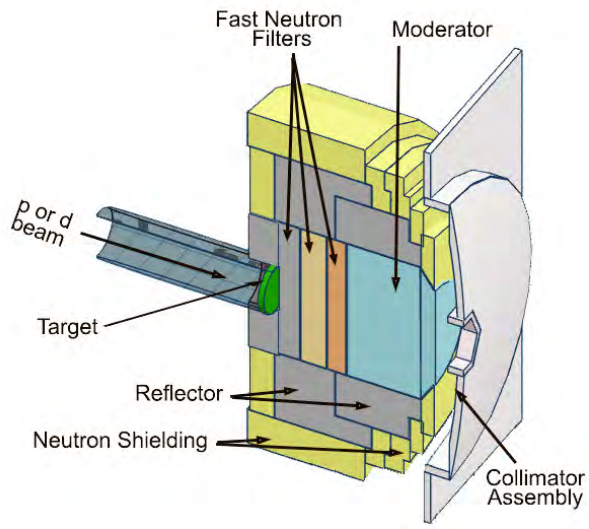

FIG. 1. Schematic view of a typical Beam Shaping Assembly (BSA).

To analyse neutron activation a first approach is to evaluate which of the (n,X) reactions are energetically allowed. Quantitatively, the activity concentration (Bq per gram of material) must be calculated by Monte-Carlo transport of neutrons through the BSA materials. Based on publications of the different AB-BNCT facilities worldwide, a representative group of BSA's was set up and simulated with MNCP 6.1 [32]. Table 3 summarizes their main components.

Each of the BSAs listed in Table 3 were simulated and the accumulated activity concentration after 1 year of operation was calculated. For each radionuclide, the activity concentration was compared to the levels of clearance given for materials in bulk in the IAEA Safety Guide RS-G1.7 [33]. These clearance levels represent the maximum activity concentration tolerable to release radioactive materials from regulatory control. The values are derived for each radionuclide in the IAEA Safety Report Nº44 [34], and correspond to the activity concentration values such that individual effective doses to a critical group (i.e., the public and workers) would be of the order of 10 μSv/a and would have only a very low probability of approaching an individual dose of 1

mSv/a. For materials containing a mixture of radionuclides, the normalized activity concentration (C) must be less than 1:

$$C = \sum_{i=1}^{n} \frac{C_i}{L_i} < 1 \quad (1)$$

where C_i is the concentration (in Bq/g) of the i^{th} radionuclide in the material, L_i is the respective activity concentration for clearance and n is the number of radionuclides present (ref paragraph 4.7 in [33]).

TABLE 3. MAIN COMPONENTS OF THE BEAM SHAPING ASSEMBLIES FOR A REPRESENTATIVE GROUP OF AB-BNCT FACILITIES

	Beam energy, current	Moderator	Fast Neutron Filter	Reflector	References.
^{7}Li+p	2.3 MeV, 30 mA	Fluental, MgF_2 or CaF_2	None	Pb	[35–38]
^{9}Be+p	8.0 MeV, 10 mA	MgF_2	Fe	Pb	[39]
^{9}Be+p	30 MeV, 1 mA	CaF_2	3: Pb+Fe+Al	Pb	[40]
^{9}Be+d	1.45 MeV, 30 mA	2: PTFE+Al	None	Pb	[28, 41]
^{13}C+d	1.45 MeV, 30 mA	2: PTFE +Al	None	Pb	[30, 42]

4. ACTIVITY CALCULATION

Daily operation is usually carried out by alternating hours of continuous irradiation and hours of downtime. During operation, the activity A accumulates as:

$$A(t) = A_0 + \frac{p}{\lambda} \cdot (1 - e^{-\lambda \cdot t}) \quad (2)$$

being t the irradiation time, p the activity production rate, and λ the decay constant of the radioactive residue. A_0 is the initial activity in the element to evaluate. The activity production rate (p, in Bq/h) is the product of the reaction yield (Y, in 1/mA-s), the beam current (in mA) and the decay constant (λ, in 1/h).

During downtime, the activity follows the radioactive decay law:

$$A(t + t') = A(t) \cdot e^{-\lambda \cdot t'} \quad (3)$$

where t' is the length of downtime.

For a given scheme of operation, the accumulated activity in the element lifetime can be calculated by recurrence applying Eqs. 2 and 3 alternatively. For a daily scheme of 8 hours of irradiation followed by 16 hours of downtime, the accumulated activity is:

$$A(N) = \frac{p}{\lambda} \cdot \left(1 - e^{-\lambda \cdot 8\,h}\right) \cdot \frac{1 - \left(e^{-\lambda \cdot 24\,h}\right)^{N}}{1 - e^{-\lambda \cdot 24\,h}} \quad (4)$$

Where N is the target lifetime (in days).

To evaluate primary activation on the target, the activity production rate (p) was calculated from reaction cross-sections $\sigma(E)$ as:

$$p = \lambda \cdot \dot{n} \cdot n_A \int S(E)^{-1} \cdot \sigma(E) \cdot dE \quad (5)$$

Where $\dot{n}$ (in 1/s) is the number of projectiles (protons or deuterons) per second impinging on the target, n_A is the atom density of the target, $S(E)$ is the stopping power. Cross-sections and stopping powers were taken from [31, 43–45]and [46] respectively.

For secondary activation, the group of BSA's listed in Table 3 were simulated with the MNCP 6.1 code [32]. Nuclear reactions leading to radioactive products were considered for each element of the BSA (moderator, fast neutron filters and reflector). All energetically allowed reactions with up to 4 light products were considered.

For a given reaction, the activity production rate p was calculated as

$$p = \lambda \cdot N_A \int \dot{\phi}(E) \cdot \sigma(E) \cdot dE \quad (6)$$

where $\dot{\phi}(E) \cdot dE$ (in 1/cm^2-s) is the neutron flux in the element to evaluate (moderator, fast neutron filters or reflector), $\sigma(E)$ and N_A are, respectively, the cross-section and the number of target atoms for the reaction that generates radioactivity in the element of interest. The integrals in Eq. 6 were calculated as MCNP F4 Tallies with the reaction cross-sections as the tally modifiers (DE and DF cards). Cross-sections were taken from different evaluated databases [43, 47, 48].

5. RESULTS

5.1. Target activation

Table 4 summarizes the radioactivity accumulated for different targets over 1 year of operation with a daily scheme of 8 hours of irradiation a day. The activities reported here are an average of different results based on the indicated reference data.

TABLE 4. RADIOACTITIVY INDUCED FOR DIFFERENT AB-BNCT TARGETS AT THE INDICATED BEAM ENERGY AND CURRENT (IN ORDER OF DECREASING TOTAL ACTIVITY)

	Beam energy, current	Radionuclide: activity	Reference data
^{7}Li+p	2.3 MeV, 30 mA	^{7}Be: 5.7 TBq/y	[43, 49, 50]
^{9}Be+p	30 MeV, 1 mA	^{7}Be: 1.2 TBq/y	[31]
		^{3}H: 51 GBq/y	[31,43]
^{9}Be+d	1.45 MeV, 30 mA	^{3}H: 57 GBq/y	[43,44]
^{13}C+d	1.45 MeV, 30 mA	^{3}H: 9.3 GBq/y	[43,44]
		^{14}C: 28 MBq/y	[43]
^{9}Be+p	8 MeV, 10 mA	Only prompt radiation	[31]

The ^{9}Be+p case for 8 MeV protons is the cleanest target. In this case, all reaction channels leading to radioactivity are energetically forbidden (see Table 2). Only short-lived light radionuclides, such as ^{9}Be(p,n)^{9}B (E_{thres}=2.057 MeV), ^{9}Be(p,d)^{8}Be (Q=570 keV) and ^{9}Be(p,p+n)^{8}Be (E_{thres}=1.850 MeV) are produced. The products are ^{9}B ($T_{1/2}$ = 0.54 keV, decays via proton emission to ^{8}Be) and ^{8}Be which rapidly breaks into two alpha particles with no gamma emission.

The highest activity was obtained for the lithium target. In this case, radioactive ^{7}Be ($T_{1/2}$=53.22 d) is generated through the ^{7}Li(p,n)^{7}Be reaction on the target. A 30-mA proton beam of 2.3 MeV generates 5.7 TBq of ^{7}Be after 1 year of operation of the target. This radionuclide emits gamma rays of 478 keV thus, represents a complication concerning dose to workers given tasks involving handling of the target (i.e., replacement).

In order of importance follows the beryllium target with 30 MeV protons. The activity of ^{7}Be is 1.2 TBq/y, coming from the ^{9}Be (p,t) , ^{9}Be(n,d+n) and ^{9}Be(n,p+2n) reactions (see Table 2). In addition to ^{7}Be, 51 GBq/y of tritium ($T_{1/2}$=12.32 y) are produced through the ^{9}Be(p,t) ^{7}Be reaction. This radionuclide decays emitting very low-energy beta particles (E<18.591 keV) with no gamma rays. These beta particles stop in less-than 1 cm of air, thus radiological risk only arises if inhaled, ingested, or absorbed through the skin.

With deuterons on beryllium and ^{13}C targets only low-energy pure beta emitters are produced. In the beryllium target, 57 GBq/y activity of tritium is generated through the ^{9}Be(d,t) reaction. Concerning the ^{13}C target, tritium and ^{14}C are generated. The activity of tritium (9.3 GBq/y) is considerably lower than in the ^{9}Be target (both with deuterons and 30 MeV protons). The activity of ^{14}C (28 MBq/y) comes from the ^{13}C(d,p) reaction. ^{14}C decay emitting low energy beta particles up to 156 keV (this radiation barely penetrates the outer protective dead layer of the skin) with no gamma rays. Figs. 2 and 3 show the accelerator and a 10 mA beam developed at the Atomic Energy Commission in Buenos Aires, to be used in conjunction with the ^{9}Be(d,n) and ^{13}C(d,n) reactions.

FIG. 2. Single-ended, modular ESQ accelerator. Operates in air for easy maintenance. This machine has 720 kV. The full size one of 1.45 MV is being constructed. Reprinted from Ref. [27]

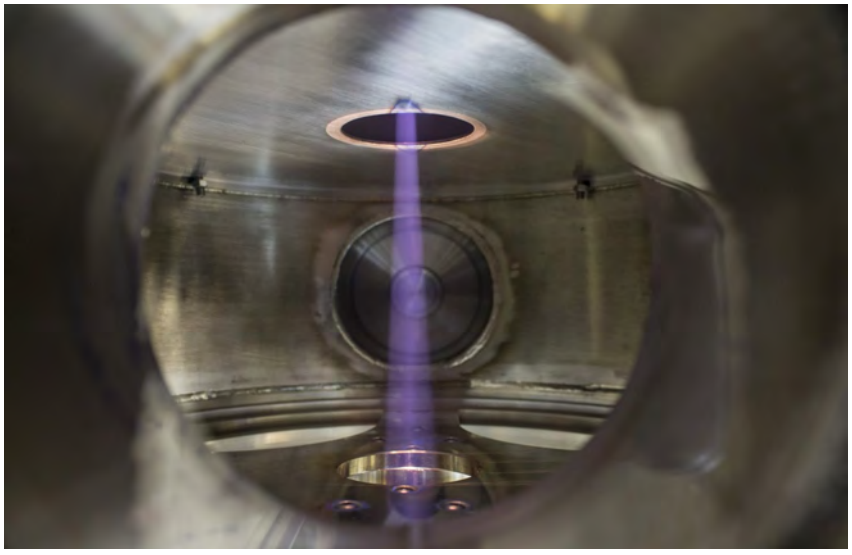

FIG. 3. 10 mA proton beam, as seen through the induced fluorescence in the residual gas in the accelerator column of the ESQ. Reprinted from Ref. [51]

5.2. BSA activation.

From lowest to highest neutron energy, first are the facilities based on the ^{7}Li(p,n) reaction. For protons of 2.3 MeV the maximum neutron energy is 573 keV. Hence, only exothermic and some very low-threshold reactions, are relevant for neutron induced activation in these facilities. These reactions are typically (n,γ) reactions, although for lead and materials containing ^{6}Li there are more reaction channels open (discussed below, §5.2.1).

Following are the facilities based on 1.45 MeV deuterons (both ^{9}Be and ^{13}C targets) and on 8 MeV protons on ^{9}Be. The highest neutron energies are, respectively 5.76, 6.72 and 6.17 MeV. For neutron activation, exothermic and reactions with threshold energies of a few MeV must be considered. For commonly used BSA materials, most (n,p), (n,α) and (n,d) become accessible for neutrons of these energies, although the cross-sections in general are rather low. Finally, facilities based on 30 MeV protons and beryllium targets produce neutrons of up to 28.15 MeV. For some commonly used BSA materials, (n,t) reactions become accessible at about 8-10 MeV. Moreover, above ~10 MeV reaction channels with multiple ejectiles (such as (n,2n), (n,n+p), (n,n+α) etc.) become accessible.

As a general trend, the higher the neutron energy, the higher the number of energetically possible reactions that may generate radioactive products. Activation of each BSA is discussed separately below.

5.2.1. ^{7}Li+p (2.3 MeV)

Moderator materials. Three different moderators were simulated: MgF_2, CaF_2 and Fluental (AlF_3: 69 w-%), metallic aluminium: 30 w-% and LiF:1 w-%).

The MgF_2 moderator does not activate. On natural Mg and F, the only energetically allowed reactions are ^{19}F(n,γ)^{20}F (Q= 6.601 MeV) and ^{26}Mg(n,γ)^{27}Mg (Q=6.443 MeV). The half-lives of ^{20}F and ^{27}Mg are, respectively, $T_{1/2}$=11.07 s and $T_{1/2}$=9.458 m. Due to the short half-lives, these radionuclides will rapidly decay after daily-stop and do not accumulate in the intermediate or long-term. All other energetically allowed reactions produce stable products.

In the CaF_2 moderator, ^{45}Ca ($T_{1/2}$=162.61 d) and ^{47}Ca ($T_{1/2}$=4.536 d) are produced coming from (n,γ) reaction on ^{44}Ca and ^{44}Ca, respectively. Over 1 year operation, the normalized activity concentration is C=101, and the cooling time (i.e., time required to decay below the clearance level) is ~3 y.

The Fluental moderator is the most critical one**.** Long-term radioactivity is due to tritium ($T_{1/2}$ =12.32 y) coming from the exothermic reaction ^{6}Li(n,α)^{3}H (Q=4.783 MeV). The activity concentration of tritium is 14.4 kBq per gram of Fluental and the cooling time is 88 y. Other short-lived radionuclides, such as ^{28}Al ($T_{1/2}$=2.245 m), ^{20}F ($T_{1/2}$=11.07 s), ^{8}Li ($T_{1/2}$=840 ms) are also produced, coming from activation of Al, F and ^{7}Li present in Fluental, with no impact on long-term radioactivity.

Reflector (Pb). There are several exothermic reactions with intermediate-lived radioactive products, as shown in Table 5. For neutrons of less than 573 keV, the reaction cross-sections are, except for ^{208}Pb(n,γ)^{209}Pb, very small. Moreover, simulations showed that the associated activities (of ^{204}Tl, ^{203}Hg, ^{200}Pt and ^{197}Pt) represent less than 0.00001 of the total activity, being all of them well below their clearance levels. The activity of ^{209}Pb ($T_{1/2}$=3.234 d) is the only significant contribution. After 1 year operation, the activity concentration of ^{209}Pb is 705 Bq/g. The IAEA Safety Guide RS-G1.7 does not establish a limit for this radionuclide, so the normalized activity concentration was not calculated. It is worth mentioning that this radionuclide emits beta particles only (no γ) with up to 197.5 keV. Thus, practically all Bremsstrahlung radiation due to the slowing down of beta particles is self-absorbed in the reflector, except a small fraction coming from ^{209}Pb in the outer shell of lead.

5.2.2. ^{9}Be+d and ^{13}C+d, 1.45 MeV

Moderator. The moderator is constituted by slabs of pure aluminum and PTFE. On the PTFE slabs, the long-term activation is due to ^{14}C ($T_{1/2}$=5700 y) only, coming from ^{13}C(n,γ)^{14}C. All other nuclear reactions generate stable or short-lived products ($T_{1/2}$ ~ s). Due to the small isotopic abundance of ^{13}C (1.07%) and to the long-life of the activation product, the activity production rate is expected to be small. In fact, simulations showed that after 1 y operation the accumulated activity of ^{14}C is 0.006 Bq per gram of PTFE, which is far below the clearance level of 1 Bq/g, and it would take about 170 y in operation to exceed this value.

On the aluminum slabs, there is no long-term accumulation of radioactivity. Only ^{28}Al ($T_{1/2}$=2.245 m) and ^{24}Na ($T_{1/2}$=14.997 h) and are produced, coming from (n,γ) and (n,α) reactions on ^{27}Al respectively. The activity of ^{28}Al rapidly decays in a few hours after the end of irradiation, hence does not accumulate. Concerning ^{24}Na, the half-life is comparable to the time in between irradiations, thus, some accumulation is produced. Simulations showed that after 1 year of operation the accumulated activity is 110 Bq per gram of aluminum and takes 4.2 days to decay below 1 Bq/g, the clearance level for ^{24}Na.

Reflector (Pb). As for the Li+p case, the main contribution is ^{209}Pb ($T_{1/2}$=3.234 d) produced through the ^{208}Pb(n,γ)^{209}Pb reaction. The activity after 1 year operation is 290 Bq per gram of lead. In addition to those given in Table 5, some endothermic reactions are accessible (see Table 6), although simulations show that none of the radionuclides exceed their clearance levels, and also, that the total activity is negligible compared to the activity of ^{209}Pb.

TABLE 5. INTERMEDIATE-LIVED RADIOACTIVE PRODUCTS FROM EXOTHERMIC NEUTRON INDUCED REACTIONS ON NATURAL LEAD

Product	$T_{1/2}$	Nuclear Reaction	Q-value	Clearance Level
^{209}Pb	3.234 d	^{208}Pb(n,γ)^{209}Pb	3937.4 keV	-
^{203}Hg	46.594 d	^{206}Pb(n,α)^{203}Hg	7130.1 keV	10 Bq/g
		^{207}Pb(n,n+α)^{203}Hg	392.3 keV	
^{204}Tl	3.783 y	^{204}Pb(n,p)^{204}Tl	18.6 keV	1 Bq/g
^{200}Pt	12.6 h	^{207}Pb(n,2α)^{200}Pt	7369 keV	-
^{197}Pt	19.8915 h	^{204}Pb(n,2α)^{197}Pt	8531 keV	1000 Bq/g

TABLE 6. INTERMEDIATE-LIVED RADIOACTIVE PRODUCTS FROM LOW-THRESHOLD NEUTRON INDUCED REACTIONS ON NATURAL LEAD

Product	$T_{1/2}$	Nuclear Reaction	Threshold Energy	Clearance Level
^{3}H	12.32 y	^{208}Pb(n,t)	6.4 MeV	100 Bq/g
		^{206}Pb(n,t)	6.3 MeV	
		^{204}Pb(n,t)	6.0 MeV	
^{199}Au	3.139 d	^{204}Pb(n,d+α)^{199}Au	3.5 MeV	100 Bq/g
		^{208}Pb(n,n+2α)^{199}Au	5.8 MeV	
^{202}Tl	12.31 d	^{204}Pb(n,t)^{202}Tl	6.0 MeV	10 Bq/g
^{203}Hg	46.594 d	^{204}Pb(n,2p)^{203}Hg	6.4 MeV	10 Bq/g
^{204}Tl	3.783 y	^{206}Pb(n,t) ^{204}Tl	6.3 MeV	1 Bq/g

5.2.3. ^{9}Be +p (8 MeV)

Fast neutron filter. The critical element of this BSA is the iron filter. Table 7 shows the energetically allowed reactions that lead to intermediate and long-lived radioactivity for this material. Also shown are the respective clearance levels. All radioactive products exceed their clearance level after 1 year operation, and the normalized activity concentration after 1 year operation is $C=9.6\times10^{5}$. Almost 98% of the normalized activity is due to ^{54}Mn ($T_{1/2}$=312.2 d), thus the cooling time is mainly determined by this residue. For 1 year of service this time is 18.8 y.

Moderator. A MgF_2 moderator was simulated. In this moderator, ^{24}Na ($T_{1/2}$=14.997 h) is generated due to the ^{24}Mg(n,p)^{24}Na reaction. Simulations showed that the activity concentration of ^{24}Na saturates at ~2 Bq/g after 4 days of operation, thus a longer period of service of the moderator does not lead to more radioactivity. Since the clearance level for ^{24}Na is 1 Bq/g, the cooling time is equal to 1 half-life, independently of the lifetime of the moderator.

TABLE 7. INTERMEDIATE AND LONG-LIVED RADIOACTIVE PRODUCTS FROM EXOTHERMIC AND LOW-THRESHOLD NEUTRON INDUCED REACTIONS ON NATURAL IRON

Product	$T_{1/2}$	Nuclear Reaction	Threshold Energy or Q	Clearance Level
^{54}Mn	312.2 d	^{54}Fe(n,p) ^{54}Mn	Q=85.5 keV	0.1 Bq/g
^{56}Mn	2.5789 h	^{56}Fe(n,p) ^{56}Mn	E_{thresh}=2964.7 keV	10 Bq/g
^{51}Cr	27.7025 d	^{54}Fe(n,α)^{51}Cr	Q=843.3 keV	100 Bq/g
^{59}Fe	44.495 d	^{58}Fe(n,γ)^{59}Fe	Q= 6581 keV	1 Bq/g
^{55}Fe	2.744 y	^{54}Fe(n,γ) ^{55}Fe	Q=9298 keV	1000 Bq/g

Reflector. As for the above mentioned cases (§5.2.1 and 5.2.2) the main contribution is ^{209}Pb ($T_{1/2}$=3.234 d) produced through the ^{208}Pb(n,γ)^{209}Pb reaction. The activity after 1 year operation is 14.3 kBq per gram of lead. The activity concentration of the rest of radionuclides is negligible and do not exceed (when applicable) their clearance levels.

5.2.4. ^{9}Be +p (30 MeV)

Fast neutron filters. There are 3 fast neutron filters in this BSA. Closest to the target is the filter of lead, followed by a second filter (of iron) and a third one of aluminum.

In the lead filter, the most important contribution to the total activity is from ^{203}Pb ($T_{1/2}$=51.92 h), as shown in Table 8. The normalized activity concentration is C=8.7×10^{4}. Concerning long-term activation, ^{204}Tl ($T_{1/2}$=3.783 y) is the most relevant residue to consider, since the cooling time is strongly determined by this isotope. Only for ^{204}Tl, it takes 36.6 y for clearance, and the time required for the whole mixture (C=1) is 37.8 y.

TABLE 8. RADIOACTIVITY INDUCED IN THE LEAD FILTER BY NEUTRONS FROM 30 MEV PROTONS ON A ^{9}BE TARGET, AFTER 1 YEAR OF OPERATION. ONLY RADIONUCLIDES EXCEEDING THE CLEARANCE LEVELS ARE LISTED

Product	$T_{1/2}$	Activity concentration	Clearance Level
^{203}Pb	51.92 h	8.6×10^{5} Bq/g	10 Bq/g
^{203}Hg	46.594 d	2.0×10^{3} Bq/g	10 Bq/g
^{204}Tl	3.783 y	812 Bq/g	1 Bq/g
^{202}Tl	12.31 d	512 Bq/g	10 Bq/g
^{3}H	12.32 y	164 Bq/g	100 Bq/g

In the iron filter, the normalized activity concentration is C=9.2×10^{5}. The most important contribution is from ^{54}Mn ($T_{1/2}$=312.2 d), as shown in Table 9. This radionuclide exceeds the clearance level 8.3×10^{5} times and is the one that most contributes to the high value C. As far as long-term activation is concerned, the dominant contribution is ^{55}Fe ($T_{1/2}$=2.744 y). The cooling time for this radioisotope is 23.1 y, and the cooling time for the whole mixture (C=1) is 26.2 y.

TABLE 9. RADIOACTIVITY INDUCED IN THE IRON FILTER BY NEUTRONS FROM 30 MEV PROTONS ON A ^{9}BE TARGET, AFTER 1 YEAR OF OPERATION. ONLY RADIONUCLIDES EXCEEDING THE CLEARANCE LEVELS ARE LISTED

Product	$T_{1/2}$	Activity concentration	Clearance Level
^{54}Mn	312.2 d	8.3×10^{4} Bq/g	0.1
^{56}Mn	2.5789 h	7.0×10^{5} Bq/g	10
^{59}Fe	44.495 d	1.5×10^{4} Bq/g	1
^{55}Fe	2.744 y	3.4×10^{5} Bq/g	1000
^{52}Mn	5.591 d	3110 Bq/g	1
^{51}Cr	27.7025 d	3470 Bq/g	100
^{3}H	12.32 y	237 Bq/g	100

For the aluminum filter, the normalized activity concentration is C=7.9×10^4, mostly from ^{24}Na ($T_{1/2}$=14.997 h). This radionuclide decays in a relatively short time, thus for the long-term radioactivity only ^{22}Na ($T_{1/2}$=2.6018 y) and ^{3}H ($T_{1/2}$=12.32 y) are relevant. The cooling time for ^{22}Na and ^{3}H are 3.85 y and 5 y, respectively, and cooling time for the mixture (C=1) is 9.45 y.

TABLE 10. RADIOACTIVITY INDUCED IN THE ALUMINIUM FILTER BY NEUTRONS FROM 30 MEV PROTONS ON A ^{9}BE TARGET, AFTER 1 YEAR OF OPERATION

Product	$T_{1/2}$	Activity concentration	Clearance Level
^{24}Na	14.997 h	7.9×10^4 Bq/g	0.1
^{22}Na	2.6018 y	0.28 Bq/g	10
^{3}H	12.32 y	133 Bq/g	100

Moderator. A CaF_2 moderator was simulated. The normalized activity concentration is C=3007 due to ^{45}Ca ($T_{1/2}$=162.61 d), ^{47}Ca ($T_{1/2}$=4.536 d), ^{43}K ($T_{1/2}$=22.3 h) and ^{18}F ($T_{1/2}$=109.77 m). The most relevant one as far as long-term activation is ^{45}Ca. The activity concentration for this radionuclide is 58.4 kBq per gram of CaF_2 after 1 year operation. The time required to decay below the clearance level (100 Bq/g) is ~4 y.

Reflector (Pb). The normalized activity concentration in the reflector is C=1.2×10^3, where the main contribution from ^{203}Pb ($T_{1/2}$=51.92 h) (see Table 11). Also, above the clearance limit are ^{203}Hg ($T_{1/2}$=46.594 d) and ^{204}Tl ($T_{1/2}$=3.783 y), being the latter what determines the cooling time of the reflector (11.6 y).

TABLE 11. RADIOACTIVITY INDUCED IN THE LEAD REFLECTOR BY NEUTRONS FROM 30 MEV PROTONS ON A ^{9}BE TARGET, AFTER 1 YEAR OF OPERATION. ONLY RADIONUCLIDES EXCEEDING THE CLEARANCE LEVELS ARE LISTED

Product	$T_{1/2}$	Activity concentration	Clearance Level
^{203}Pb	51.92 h	1.2×10^4 Bq/g	10 Bq/g
^{203}Hg	46.594 d	112 Bq/g	10 Bq/g
^{204}Tl	3.783 y	8.4 Bq/g	1 Bq/g

6. SUMMARY AND CONCLUSIONS

A wide variety of accelerator-based facilities are envisaged worldwide for BNCT. They can be classified into high (30 MeV), medium (8-10 MeV), low (2.3-2.8 MeV), and very low-bombarding energies (1.45 MeV). Based on publications of the existing facilities, a representative case was assessed for each category from the point of view of activation.

High-energy facilities work with 1 mA of 30 MeV protons on a ^{9}Be target, producing neutrons through the ^{9}Be(p,n) reaction. Neutrons up to 28.15 MeV are generated. At this energy, there are many neutron-induced reactions that lead to the activation of the BSA materials. Simulations showed that after 1 year operation, cooling times of several decades are necessary for clearance, according to the established values in the IAEA Safety Guide. Primary activation of the target (due to the proton beam) will also be high.

For medium-energy facilities, the case of 8 MeV protons on a ^{9}Be target was assessed. This facility produces neutrons also through the ^{9}Be(p,n) reaction, with a beam current of 10 mA. The benefit of working with this energy is the absence of primary activation of the target. All proton induced reactions leading to intermediate or long-term radioactivity are forbidden at bombarding energies below 13.432 MeV. Moreover, the neutron energy is considerably lower than in the high-energy case, thus neutron induced activation is also lower. The only critical element concerning long-term activation is the fast neutron filter (of iron), that requires ~19 y of cooling time after 1 year operation.

For the low-energy group, a facility based on a 30-mA proton beam of 2.3 mA was analyzed. This facility produces neutrons through the ^{7}Li(p,n)^{7}Be. Although the maximum neutron energy is low (573 keV), long-term activation may be produced depending on the choice of the moderator. A Fluental moderator may need, after 1 year of lifetime, 88 y of cooling time due the activity of tritium produced by the activation of ^{6}Li. On the opposite

side, there is no radioactivity if the moderator material is MgF_2. The main drawback for the Li+p is the target activation. Radioactive ^{7}Be produced as the residue of the ^{7}Li(p,n)^{7}Be emits 478 keV gamma rays and may represent a complication for tasks involving handling of the target

For the very low-energy group, 1.45 MeV deuterons on ^{9}Be and ^{13}C targets were evaluated. Both targets produce neutrons through the (d,n) reaction using a deuteron current of 30 mA. The maximum neutron energies are, respectively, 5.76 and 6.72 MeV, but with a large proportion of the yield in the less-than-1 MeV energy region (see Table 1) which makes these reactions particularly attractive for BNCT. These options work with a moderator of pure aluminum and PTFE, with no intermediate or long-term activation. Concerning primary activation (target) only low-energy pure beta emitters are generated.

REFERENCES

[1] ALLEN, D.A., BEYNON, T.D., A design study for an accelerator-based epithermal neutron beam for BNCT, Phys. Med. Biol. **40** 5 (1995) 807–821.

[2] NEUTRON THERAPEUTICS INC, Neutron Therapeutics Installs Europe's First Accelerator-Based Boron Neutron Capture Therapy (BNCT) Platform – On Track for First Cancer Patient Treatment in 2019 (2019), https://www.neutrontherapeutics.com/news/pr-041819/

[3] NAKAMURA, S. et al., Dependence of neutrons generated by ^{7}Li(p,n) reaction on Li thickness under free-air condition in accelerator-based boron neutron capture therapy system employing solid-state Li target, Phys. Medica **58** (2019) 121–130.

[4] NAKAMURA, S. et al., Neutron flux evaluation model provided in the accelerator-based boron neutron capture therapy system employing a solid-state lithium target, Sci. Rep. **11** 1 (2021) 1–13.

[5] KIYANAGI, Y., SAKURAI, Y., KUMADA, H., TANAKA, H., Status of Accelerator-Based BNCT Projects Worldwide, AIP Conference Proceedings, Vol. 2160, American Institute of Physics Inc. (2019) 050012.

[6] WATANABE, K. et al., First experimental verification of the neutron field of Nagoya University Accelerator-driven neutron source for boron neutron capture therapy, Appl. Radiat. Isot. **168** (2021) 109553.

[7] NEUTRON THERAPEUTICS INC, Neutron Therapeutics to Install Its BNCT Cancer Therapy System into Japan's Largest Private Hospital Chain (2019), https://markets.businessinsider.com/news/stocks/neutron-therapeutics-to-install-its-bnct-cancer-therapy-system-into-japan-s-largest-private-hospital-chain-1028357947

[8] HALFON, S. et al., Demonstration of a high-intensity neutron source based on a liquid-lithium target for Accelerator based Boron Neutron Capture Therapy, Appl. Radiat. Isot. **106** (2015) 57–62.

[9] ALEYNIK, V. et al., BINP accelerator based epithermal neutron source, Appl. Radiat. Isot. **69** 12 (2011) 1635–1638.

[10] NEUBORON, BNCT Boron Neutron Capture Therapy New Generation "Radiotherapy & Targeted Therapy" (2022), https://en.neuboron.com/bnct

[11] TAE LIFE SCIENCES, TAE Life Sciences Alphabeam™ System (2020), https://taelifesciences.com/alphabeam-neutron-system/

[12] CHINESE ACADEMY OF SCIENCES, China Builds First Accelerator-Based Facility for Boron Neutron Capture Therapy Experiments (2020), https://english.cas.cn/newsroom/research_news/phys/202008/t20200813_241689.shtml

[13] UNIVERSITY OF BIRMINGHAM, High Flux Accelerator-Driven Neutron Facility (2021), https://www.birmingham.ac.uk/research/activity/nuclear/about-us/facilities/high-flux-neutron-facility.aspx

[14] FREEMAN, T., Boron Neutron Capture Therapy Is Back on the Agenda (2020), https://physicsworld.com/a/boron-neutron-capture-therapy-is-back-on-the-agenda/

[15] PORRAS, I. et al., BNCT research activities at the Granada group and the project NeMeSis: Neutrons for medicine and sciences, towards an accelerator-based facility for new BNCT therapies, medical isotope production and other scientific neutron applications, Appl. Radiat. Isot. **165** (2020) 109247.

[16] INTERNATIONAL ATOMIC ENERGY AGENCY, Advances in Boron Neutron Capture Therapy, In Press.

[17] TANAKA, H. et al., Characteristics comparison between a cyclotron-based neutron source and KUR-HWNIF for boron neutron capture therapy, Nucl. Instrum. Methods Phys. Res. Sect. B Beam Interact. with Mater. Atoms **267** 11 (2009) 1970–1977.

[18] OSAKA MEDICAL COLLEGE KANSAI BNCT MEDICAL CENTER, Kansai BNCT Medical Center, https://www.ompu.ac.jp/kbmc/en.html

[19] SOUTHERN TOHOKU HOSPITAL GROUP, Southern TOHOKU BNCT Research Center (2020), http://www.sthg-jp.com/motion.asp?siteid=100511&menuid=10491&lgid=1

[20] KUMADA, H. et al., Development of beryllium-based neutron target system with three-layer structure for accelerator-based neutron source for boron neutron capture therapy, Appl. Radiat. Isot. **106** (2015) 78–83.

[21] KUMADA, H. et al., Beam Performance of the IBNCT as a Compact Linac-Based BNCT Neutron Source Developed by University of Tsukuba, AIP Conference Proceedings, Vol. 2160, American Institute of Physics Inc. (2019) 050013.

[22] KIM, D.S, "Overview of the A-BNCT System in Korea", presented at Asian Forum for Accelerators and Detectors (AFAD), Daejeon, Korea, 2018.

[23] DAWON MEDAX, A-BNCT | Neutron Beam Generator Based Linear Accelerator (2021), http://dawonmedax.com/en/m31.php

[24] CAPOULAT, M.E. et al., Neutron spectrometry of the ^{9}Be(d (1.45 MeV), n)^{10}B reaction for accelerator-based BNCT, Nucl. Instrum. Methods Phys. Res. Sect. B **445** (2019) 57–62.

[25] KREINER, A.J. et al., A Tandem-electrostatic-quadrupole for accelerator-based BNCT, Nucl. Instrum. Methods Phys. Res. Sect. B **261** 1–2 SPEC. ISS. (2007) 751–754.

[26] CARTELLI, D. et al., Present status of accelerator-based BNCT: Focus on developments in Argentina, Appl. Radiat. Isot. **106** (2015) 18–21.

[27] CARTELLI, D.E. et al., Status of low-energy accelerator-based BNCT worldwide and in Argentina, Appl. Radiat. Isot. **166** (2020) 109315.

[28] CAPOULAT, M.E., MINSKY, D.M., KREINER, A.J., Computational assessment of deep-seated tumor treatment capability of the ^{9}Be(d,n)^{10}B reaction for accelerator-based Boron Neutron Capture Therapy (AB-BNCT), Phys. Medica **30** 2 (2014) 133–146.

[29] COLONNA, N. et al., Measurements of low-energy (d,n) reactions for BNCT, Med. Phys. **26** August (1999) 793–798.

[30] CAPOULAT, M.E., KREINER, A.J., A ^{13}C(d,n)-based epithermal neutron source for Boron Neutron Capture Therapy, Phys. Medica **33** (2017) 106–113.

[31] HERMANNE, A., TARKANYI, F., TAKACS, S., Activation cross sections for production of ^{7}Be by proton and deuteron induced reactions on ^{9}Be: Protons up to 65MeV and deuterons up to 50MeV, Appl. Radiat. Isot. **90** (2014) 203–207.

[32] GOORLEY, T. et al., Initial MCNP6 release overview, Nucl. Technol. **180** 3 (2012) 298–315.

[33] INTERNATIONAL ATOMIC ENERGY AGENCY, Application of the Concepts of Exclusion, Exemption and Clearance, Safety Standard Serires Nº RS-G-1.7, Vienna (2004).

[34] INTERNATIONAL ATOMIC ENERGY AGENCY, Derivation of Activity Concentration Values for Exclusion, Exemption and Clearance, Safety Report Series Nº 44, Vienna (2005).

[35] MINSKY, D.M., KREINER, A.J., VALDA, A.A., AB-BNCT beam shaping assembly based on ^{7}Li(p,n)^{7}Be reaction optimization, Appl. Radiat. Isot. **69** 12 (2011) 1668–1671.

[36] LI, G., JIANG, W., ZHANG, L., CHEN, W., LI, Q., Design of Beam Shaping Assemblies for Accelerator-Based BNCT With Multi-Terminals, Front. Public Heal. **9** (2021) 642561.

[37] URITANI, A. et al., "Design of Beam Shaping Assembly for an Accelerator-Driven BNCT System in Nagoya University", Int. Conf. on Neutron Optics (Proc. Int. Conf. Nara, Japan, 2017), Physical Society of Japan (2018).

[38] TORRES-SÁNCHEZ, P., PORRAS, I., RAMOS-CHERNENKO, N., ARIAS DE SAAVEDRA, F., PRAENA, J., Optimized beam shaping assembly for a 2.1-MeV proton-accelerator-based neutron source for boron neutron capture therapy, Sci. Rep. **11** (2021) 7576.

[39] KUMADA, H. et al., Development of LINAC-Based Neutron Source for Boron Neutron Capture Therapy in University of Tsukuba, Plasma Fusion Res. **13** (2018) 2406006.

[40] TANAKA, H. et al., Experimental verification of beam characteristics for cyclotron-based epithermal neutron source (C-BENS), Appl. Radiat. Isot. **69** 12 (2011) 1642–1645.

[41] BURLON, A.A., ROLDÁN, T. del V, KREINER, A.J., MINSKY, D.M., VALDA, A.A., Nuclear reactions induced by deuterons and their applicability to skin tumor treatment through BNCT, Nucl. Instrum. Methods Phys. Res. Sect. B **266** 22 (2008) 4903–4910.

[42] BURLON, A.A. et al., In-phantom dosimetry for the 13C(d,n)14N reaction as a source for accelerator-based BNCT, Med. Phys. **28** 5 (2001) 796–803.

[43] KONING, A.J. et al., TENDL: Complete Nuclear Data Library for Innovative Nuclear Science and Technology, Nucl. Data Sheets **155** (2019) 1–55.

[44] NAKAYAMA, S., IWAMOTO, O., WATANABE, Y., OGATA, K., JENDL/DEU-2020: deuteron nuclear data library for design studies of accelerator-based neutron sources, J. Nucl. Sci. Technol. **58** 7 (2021) 805–821.

[45] NATIONAL NUCLEAR DATA CENTER, NuDat Database, https://www.nndc.bnl.gov/nudat3/

[46] ZIEGLER, J.F., ZIEGLER, M.D., BIERSACK, J.P., SRIM–The stopping and range of ions in matter (2010), Nucl. Instrum. Methods Phys. Res. Sect. B **268** (2010) 1818–1823.

[47] BROWN, D.A. et al., ENDF/B-VIII.0: The 8th Major Release of the Nuclear Reaction Data Library with CIELO–project Cross Sections, New Standards and Thermal Scattering Data, Nucl. Data Sheets **148** (2018) 1–142.

[48] EUROPEAN ACTIVATION SYSTEM, EAF-2010 Activation Database, https://t2.lanl.gov/nis/data/jeff/EAF2010.html

[49] LEE, C.L., ZHOU, X.L., KUDCHADKER, R.J., HARMON, F., HARKER, Y.D., A Monte Carlo dosimetry-based evaluation of the ^{7}Li(p,n)^{7} Be reaction near threshold for accelerator boron neutron capture therapy, Med. Phys. **27** 1 (2000) 192–202.

[50] JAPAN ATOMIC ENERGY AGENCY, JENDL-4.0/HE Database, https://wwwndc.jaea.go.jp/ftpnd/jendl/jendl40he.html

[51] INTERNATIONAL ATOMIC ENERGY AGENCY, Compact Accelerator Neutron Sources, IAEA-TECDOC-1981, Vienna (2021).

TREATMENT, NOT TERROR: A UNIQUE CANCER TREATMENT PARADIGM FOR DEVELOPING NOVEL LINEAR ACCELERATORS FOR RESOURCE- LIMITED SETTINGS[1,2].

Miles A. POMPER
International Cancer Expert Corps
James Martin Center for Nonproliferation
Washington DC, USA.
milesapomper@hotmail.com

Graeme CAMPBELL BURT
International Cancer Expert Corps
Cockcroft Institute and Lancaster University
Lancaster, UK
g.burt1@lancaster.ac.uk

Suzie L. SHEEY
International Cancer Expert Corps
University of Melbourne, Australia
ANSTO (Australian Nuclear Science and Technology Organisation), Australia
University of Oxford, UK
suzie.sheehy@unimelb.edu.au

Deepa ANGAL-KALININ
STFC Daresbury Laboratory,
Warrington, UK
deepa.angal-kalinin@stfc.ac.uk

Taofeeq ABDALLAH IGE
National Hospital Abuja
University of Abuja
Abuja, Nigeria
igetaofeeq@yahoo.com

C. NORMAN COLEMAN[3]
International Cancer Expert Corps
Washington DC, USA
normcoleman@gmail.com

Eugenia WENDLING
International Cancer Expert Corps
Washington DC, USA
Nina.wendling@iceccancer.org

Manjit DOSANJH
International Cancer Expert Corps
CERN, Geneva, Switzerland
University of Oxford, UK
manjit.dosanjh@cern.ch

Abstract

A transformational approach to two difficult global problems is being pioneered under the concept of "Treatment, not Terror". The first challenge is the potential purposeful (terrorist) or accidental misuse of cobalt-60 radioactive sources intended

[1] **Disclaimer:** This paper is the opinion of the authors and does not represent policy or commentary of their institutions.
[2] **Conflict of interest:** None
[3] Corresponding author

for radiotherapy; the second challenge is the dire need for effective cancer care in low-resource settings globally, including low-middle income countries (LMICs) and geographically isolated populations in high income countries. Radiation therapy is an essential component of cancer care, needed by about 60% of cancer patients. There is the need for a robust linear accelerator (LINAC) that can provide better cancer treatment and avoid the security risks posed by outmoded cobalt-60 radiotherapy machines. Such novel machines could function reliably in challenging environments with harsh climate conditions, unreliable energy sources and potentially long delays for the repair of breakdowns. Also required is a sustainable local workforce with the expertise to operate the LINAC safely and effectively. This paper outlines a novel approach that sees cancer care as part of a healthcare systems solution being developed by the International Cancer Expert Corps (Flex-competence©). This project brings together linear accelerator experts and medical physics and engineering communities, public health and medical experts committed to addressing global health disparities and the nonproliferation community that understand this solution not only improves cancer care and a local economy but also helps build global networks of trusted partners. This substantial global collaborative approach not only uses physics and engineering expertise but also builds on the essential characteristics of physics research for solving large complex problems, building on the synergy that occurs when groups with complementary expertise come together to create and implement unique solutions.

1. INTRODUCTION: THE CONFLUENCE OF PROBLEMS BEING ADDRESSED

In the last decade, experts have recognized that two major socioeconomic challenges could be addressed with the development of a novel linear accelerator (LINAC). With World Health Organization data [1] indicating the rising burden of noncommunicable diseases (NCDs) (predominantly cardiovascular, oncologic, respiratory and metabolic diseases in LMICs) in 2011 the United Nations General Assembly formally recognized NCDs as a global problem. Simultaneously, terrorism concerns and a 2008 National Academy of Sciences study led Congress and the US National Nuclear Security Administration to see the substitution of non-isotopic technology as a means of permanently reducing the threat of radiological terrorism, such as a terrorist "dirty bomb." This view won global endorsement at the 2014 and 2016 Nuclear Security Summit, particularly in a 2016 joint statement in which 22 countries pledged to substitute such technology and replace high-risk radioactive sources, where technologically and economically feasible. Such high-risk sources included cobalt-60 used in radiotherapy machines in many poorer countries [2]. However, a 2015 meeting on non-isotopic alternatives to radiological sources ("alt tech") recognized that cobalt-60 radiotherapy may be the only radiation therapy available for cancer treatment particularly in places with limited infrastructure and relatively poor-security regions, In response, Pomper and Delnoki-Veress promoted an approach termed "Treatment, not Terror" to simultaneously address cancer care and the potential terrorist threat from dangerous radiation sources.[3.4] The International Cancer Expert Corps (ICEC) [5, 6], a global NGO, recognized the need for novel technology for challenging environments [7, 8] and the essential requirement for expertise on-the-ground to manage the patients and sophisticated cancer treatment technology. ICEC has since partnered with LINAC and healthcare systems experts to develop the novel systems solution presented.

2. BUILDING COLLABORATIONS AND DEFINING THE PROBLEM TO BE SOLVED

In the necessary first step, ICEC set out to define, understand and address the challenges faced by the health professionals at the grassroots in LMICs who treat cancer patients with radiotherapy (RT). A number of workshops were held from 2016 – 2020 [6, 7] involving medical and technical experts from CERN, the ICEC and its global membership and, since 2017, the UK Science and Technology Facilities Council (STFC) [9]. ICEC especially involved representatives from LMICs and Official Development Assistance (ODA) countries to understand the challenges and develop effective, innovative solutions, for partners across Africa and in similar resource-limited settings globally.

2.1. Technology challenges

Current RT LINAC technology requires a large number of expert professional staff including radiation oncologists, medical physicists, dosimetrists, service engineers, and radiation therapy technologists to treat patients and to maintain the equipment. In most LMICs there is both a shortage of machines as well as too few engineers to keep the machines working leading to more frequent failures and extended repair timescales.

A landmark study by Atun et al "*Expanding global access to radiotherapy*"[10] spelled out substantial gaps in radiotherapy machines and personnel. It indicated that there was a global shortfall of over 5,000 LINACS

in LMICs [10, 11] and many tens of thousands of personnel including radiation oncologists, medical physicists and radiation technologists [10]. Economic modeling demonstrated that in addition to the approximately one million lives saved each year there is a positive return on investment [10]. Perhaps it is the overwhelming size of the gap that leads to the pessimism toward taking on the global cancer care problem. While there are certainly sincere efforts to improve the situation there has been limited impact on the gap since the 2015 Atun report.[10]

The physicist and global health partnership had a seminal moment during a presentation of ICEC by Drs. Norman Coleman, Manjit Dosanjh, Jacques Bernier and Ugo Amaldi in the *physics section* of the International Conference on Translational Research in Radio-Oncology and Physics for Health in Europe [12]. Amaldi's remarkable offer to help solve the LINAC problem prompted ICEC and collaborators to address this problem as a Grand Challenge and consider innovative models for technology, capacity building and global mentorship.

A call to action was not new, being recognized by global health leaders Paul Farmer, Julio Frenk, Felicia Knaul and others in 2010.[13] But the lack of progress despite calls for action and the Atun models [10] demonstrating RT was good for the economy led to the realization that novel approaches and disruptive changes were necessary to move toward the exponential solution needed to fill the enormous gaps. Simultaneous efforts were undertaken to develop innovative "alternate technology" with a novel linear LINAC [7, 8], the "Flex-competence" healthcare systems approach [14] to bring a collaborative rather than the extant dichotomous approach to infectious diseases and NCDs and alter the skewed funding between the burden of disease versus investment in attacking infectious disease and NCDs [15]. At the American Society of Radiation Oncology in 2020, Coleman emphasized "The Century Challenge" with the need for innovative, global collaborative approaches in that if one well-staffed linear accelerator could be commissioned each week it would take 100 years to meet the existing gap! The "Century Challenge" proposed is how this goal could be accomplished much more rapidly.

2.2. Data

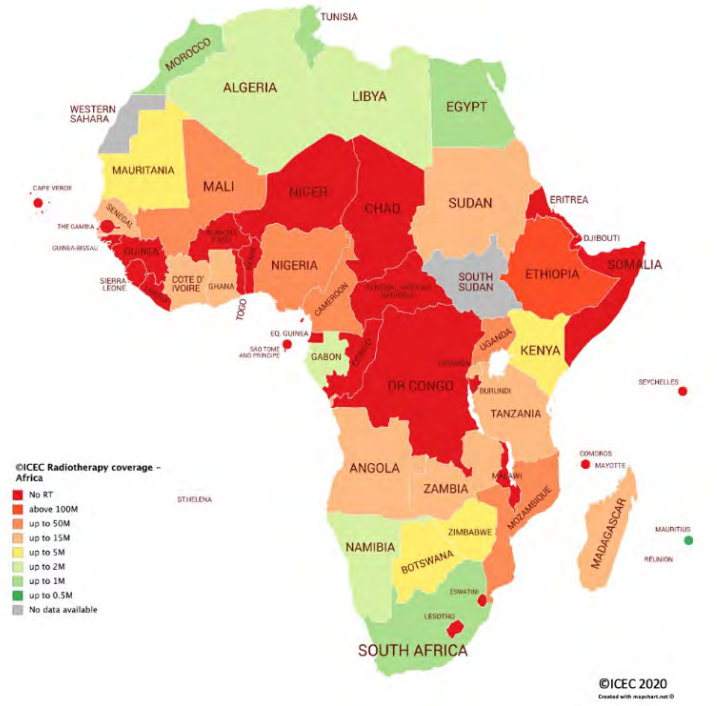

Figure 1: Size of the population per LINAC from Ige et al.[16] *At the time of this survey of all 28 African countries that had LINAC-RT, 27 contries had no LINACS and 12 had only one. Details from the survey and potential solutions are in Linacs to Narrow the Radiotherapy Gap in the CERN Courier [17]. (From [16] with permission.)*

From the series of ICEC workshops, it became clear that while the LINACS used in high- and upper-middle income countries are well suited for their stable infrastructure, technology development was needed to produce a modular, robust machine suited for the challenging environmental conditions and poorer infrastructure in resource-limited locales, while requiring fewer qualified experts to provide reliable treatments.[17] Wroe et al examined log books for dual-energy linacs in LMICS and UMICs in Africa compared to UK (Oxford) as an HIC to evaluate failure rates and duration of the failure in 12 subsystems focusing the analysis on faults that lasted > 1h. For example, air/cooling/generator subsystems systems were problematic in LMICs compared to the HIC.

Vacuum failures caused prolonged problems in LMICs and none in HICs.[18[Detailed data forthcoming from the study by Ige et al (16) demonstrate substantial downtime for linacs in Africa. While the HICs downtime is measured in hours or days, in Africa it is often weeks to months with a machine out of service. That a need for linacs suitable to the challenging environment is apparent to address the ICEC approach of building capacity, capability and credibility so that patients will have treatment outcomes similar to those in well-resourced locales. Moreover, the excellent quality and exciting challenge of building such practices as part of a global effort would encourage people to remain in-country and thereby reduce "brain drain" from LMICs.

3. HEALTHCARE SYSTEM INNOVATION: FLEX-COMPETENCE

3.1. Expertise

ICEC's overarching goal is capacity building through a person-to-person sustainable mentorship model. It builds on the concept of the Peace Corps that ICEC President L. Roth served with in Lesotho in the 1960s. Figure 2 illustrates ICEC's essential mission of mentorship, leading to sustainable on-the-ground programs with the opportunity for global exponential growth.

Fiigure 2: International Cancer Expert Corps implementation of "Treatment not terror". *Capacity building includes innovative enabling technology that will incorporate rapidly changing accomplishments in artificial intelligence (AI) and machine learning (ML) throughout all processes to help enhance the clinician expertise, reduce the need for support personnel and enable the technical personnel to use their time as efficiently as possible for patient-centered cancer care. While RT is an essential component of treatment, the ICEC emphasizes that the entire spectrum of cancer care is necessary including prevention, diagnosis (imaging and pathology), treatment (multi-modality as appropriate), supportive care and long-term follow-up.*
(Figure-original by ICEC)

3.2. Healthcare system: Flex-competence [14]

Well-resourced settings can have a healthcare system responsible for the entire spectrum of disease. Such systems have central referral hospitals with networks of hospitals and clinics within the local communities. The challenges in resource-limited settings reflect not only resource limitations but also how development funders have focused their investments on infectious disease and maternal-child health. These are most worthy of investment, but it is important to balance investment in the NCDs as they have a larger disease burden on the population as reported by Enserink.[15]

Understanding that causes of cancer include both infectious diseases and NCDs makes the dichotomy of investment outdated. Of the NCDs, the spectrum of cancer care includes prevention which addresses the other major NCDs- respiratory, cardiovascular and metabolic. Upon diagnosis cancer requires immediate intervention as do infectious diseases. Furthermore, a number of the major infectious diseases such as tuberculosis and HIV require long-term management akin to that of cancer care.

The Flex-competence approach is illustrated in Figure 3 [14].

4. BUILDING THE TRUSTED GLOBAL NETWORK

4.1. Career paths

The lack of progress in global health is related in part to the lack of value attached professionally to time dedicated to this activity. According to both senior academic leaders and from early career trainees, time spent on global health activities is often perceived negatively as not contributing toward academic advancement and faces difficulty in winning grant support. It also is seen as taking time away from clinical and billable activities. Indeed, time for this is often relegated to weekends and vacations causing personal and family stress. Encouraging counterpoints come from early-career leaders who have made call-to-action,[19] emphasizing the need for global oncologists,[20] and defining a career path.[21] For the field of radiation oncology, Vapiwala and experts with a range of career paths provided an approach to "expanding the denominator" to broaden the appeal of radiation oncology and, in particular, increase the impact from the diverse set of expertise that radiation oncology includes.[22] The recent emphasis on Equity, Inclusion and Diversity by many governments, international agencies, professional organizations, businesses and funding agencies as exemplified by the National Institutes of Health [23] has the potential to enhance and greatly expand careers in global health.

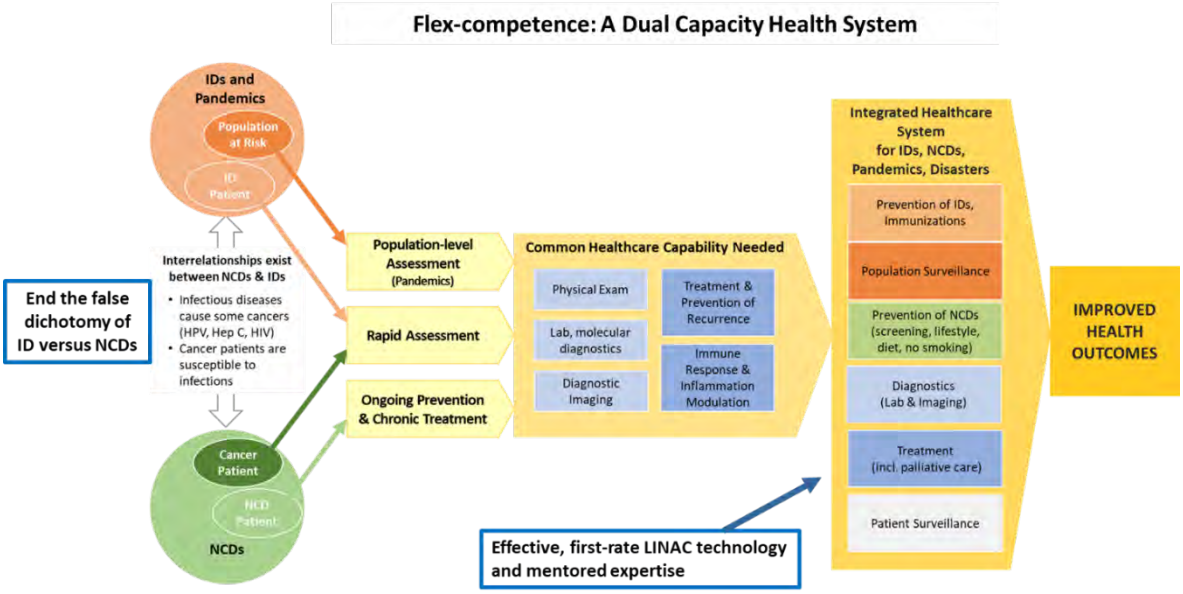

Figure 3: Flex-competence health system approach. *The current approach of dividing investment between infectious diseases and NCDs is not compatible with disease etiology, management approaches and healthcare equity. Bringing cancer care into the system at an early point, as seen in Figure 1, versus much later or almost not at all, is not logical. [Figure from the presentation at the "International Conference on Accelerators for Research and Sustainable Development: From good Practices Towards Socioeconomic Impact (Adapted from [14] with permission.)]*

4.2. Capturing career-long wisdom:

The societal challenge of the increasing proportion of senior professionals who retire with outstanding experience in career-long mentorship led the ICEC to build a model that utilizes senior mentors to mentor both more junior global health mentors and mentees in LMICs. The approach "*Capturing Acquired Wisdom, Enabling Healthful Aging, and Building Multinational Partnerships Through Senior Global Health Mentorship*" is a key part of enabling the exponential growth.[24] Indeed, the practical hands-on approach required by senior mentors who started their careers before the advent of the current enabing technologies can provide highly useful skills to those in LMICs who will likely need them in their more challenging resource-limited environments

5. GLOBAL HEALTH AT AN IAEA LINAC MEETING?!

5.3. Socioeconomic impact

Treating RT as an essential component of effective cancer care will have a broad impact globally. Enabling LINAC technology encompassing a less expensive and more robust machine, the AI/ML assistance in enhancing

machine and enabling medical expertise can help fill the current shortfall of >5,000 LINACs worldwide and the gap of many thousands of skilled personnel needed. The vision of Ugo Amaldi, his colleagues from CERN and partnership with STFC has brought the potential solution to global cancer care to a place where the enormity of the problem looks a lot more solvable. While this remains to be accomplished, the components of the complex systems solutions are falling into place. The recognition of this shortfall is decades old but new paradigms such as "*Treatment, not Terror*" and Flex-competence demonstrate innovative thinking that comes from collaborative ventures.

5.4. African proverb: If you want to go fast, go alone; if you want to go far, go together.

That the key component of ICECs model (Figure 2) began with a discussion with linear accelerator physicists and engineers emphasizes how the team approach of physicists and engineers to address some of the most difficult problems in knowledge and society enable answers unlikely or impossible from individual projects. Both individual and large projects are essential for disruptive thinking and creating paradigm-changing solutions to problems often considered "too hard". Solving the RT gap will also form a foundation for addressing NCDs more generally and infectious diseases including infrastructure for pandemics.[14] Such an innovative healthcare system model has the potential for the necessary exponential growth in cancer care capacity by addressing it as an essential component and not an expensive add-on years later.

Blanchard and colleagues understand the need for big solutions in "*Multisector Collaborations and Global Oncology: The Only Way Forward*."[25] Learning from those who live with the results of healthcare inequality comes the African proverb "If you want to go fast, go alone; if you want to go far, go together." That the cancer care systems needed in LMICs already exists resource-rich settings, perhaps not as efficiently and cost-effective as it might be, indicates that the problem is solvable given the investment. Nelson Mandela perfectly summarized that this global cancer care problem now often considered "too hard" might be viewed: "It always seems impossible, until it is done".

REFERENCES

[1] World Health Statistics. Available at: https://www.who.int/docs/default-source/gho-documents/world-health-statistic-reports/world-health-statistics-2015.pdf (see NCD, Infex disease P 72)

[2] Radioactive sources: applications and alternative technologies. https://www.nap.edu/catalog/26121/radioactive-sources-applications-and-alternative-technologies

[3] Miles Pomper, Ferenc Dalnoki-Veress, and George M. Moore. Treatment, Not Terror: Strategies to Enhance External Beam Cancer Therapy in Developing Countries While Permanently Reducing the Risk of Radiological Terrorism. James Martin Center for Nonproliferation Studies Middlebury Institute of International Studies at Monterey and The Stanley Foundation. Available at: https://stanleycenter.org/publications/report/TreatmentNotTerror212.pdf. Accessed May 6, 2022

[4] Coleman CN, Pomper MA, Chao N, Dalnoki-Veress F, Pistenmaa DA. Treatment, Not Terror: Time for Unique Problem-Solving Partnerships for Cancer Care in Resource-Challenged Environments. J Glob Oncol. 2017 Dec;3(6):687-691. doi: 10.1200/JGO.2016.007591. Epub 2017 Jan 11. PMID: 29244981; PMCID: PMC5735972.;

[5] Coleman CN, Formenti SC, Williams TR, Petereit DG, Soo KC, Wong J, Chao N, Shulman LN, Grover S, Magrath I, Hahn S, Liu FF, DeWeese T, Khleif SN, Steinberg M, Roth L, Pistenmaa DA, Love RR, Mohiuddin M, Vikram B. The international cancer expert corps: a unique approach for sustainable cancer care in low and lower-middle income countries. Front Oncol. 2014 Nov 19;4:333. doi: 10.3389/fonc.2014.00333. PMID: 25478326; PMCID: PMC4237042.

[6] International Cancer Expert Corps. Available at: https://www.iceccancer.org. Accessed May 6, 2022/

[7] Pistenmaa DA, Dosanjh M, Amaldi U, Jaffray D, Zubizarreta E, Holt K, Lievens Y, Pipman Y, Coleman CN; Workshop Participants. Changing the global radiation therapy paradigm. Radiother Oncol. 2018 Sep;128(3):393-399. doi: 10.1016/j.radonc.2018.05.025. Epub 2018 Jun 18. PMID: 29921460.6.

[8] Dosanjh M, Aggarwal A, Pistenmaa D, Amankwaa-Frempong E, Angal-Kalinin D, Boogert S, Brown D, Carlone M, Collier P, Court L, Di Meglio A, Van Dyk J, Grover S, Jaffray DA, Jamieson C, Khader J, Konoplev I, Makwani H, McIntosh P, Militsyn B, Palta J, Sheehy S, Aruah SC, Syratchev I, Zubizarreta E, Coleman CN. Developing Innovative, Robust and Affordable Medical Linear Accelerators for Challenging Environments. Clin Oncol (R Coll Radiol). 2019 Jun;31(6):352-355. doi: 10.1016/j.clon.2019.02.002. Epub 2019 Feb 22. PMID: 30798993..

[9] Science and Technology Facilities Council (STFC). Available at: https://www.ukri.org/councils/stfc/. Accessed May 6, 2022.

[10] Atun R, Jaffray DA, Barton MB, Bray F, Baumann M, Vikram B, Hanna TP, Knaul FM, Lievens Y, Lui TY, Milosevic M, O'Sullivan B, Rodin DL, Rosenblatt E, Van Dyk J, Yap ML, Zubizarreta E, Gospodarowicz M. Expanding global access to radiotherapy. Lancet Oncol. 2015 Sep;16(10):1153-86. doi: 10.1016/S1470-2045(15)00222-3. PMID: 26419354.

[11] Confronting the Global Cancer Crisis: How Nuclear Technologies Can Help https://www.iaea.org/newscenter/statements/confronting-the-global-cancer-crisis-how-nuclear-technologies-can-help. Accessed May 6, 2022.

[12] International Conference on Translational Research in Radio-Oncology and Physics for Health in Europe, in Geneva 2014. Available at: https://indico.cern.ch/event/247527/timetable/?print=1&view=standard. Accessed May 6, 2022.

[13] Farmer P, Frenk J, Knaul FM, Shulman LN, Alleyne G, Armstrong L, Atun R, Blayney D, Chen L, Feachem R, Gospodarowicz M, Gralow J, Gupta S, Langer A, Lob-Levyt J, Neal C, Mbewu A, Mired D, Piot P, Reddy KS, Sachs JD, Sarhan M, Seffrin JR. Expansion of cancer care and control in countries of low and middle income: a call to action. Lancet. 2010 Oct 2;376(9747):1186-93. doi: 10.1016/S0140-6736(10)61152-X. Epub 2010 Aug 13. PMID: 20709386.

[14] Coleman CN, Mansoura MK, Marinissen MJ, Grover S, Dosanjh M, Brereton HD, Roth L, Wendling E, Pistenmaa DA, O'Brien DM. Achieving flexible competence: bridging the investment dichotomy between infectious diseases and cancer. BMJ Glob Health. 2020 Dec;5(12):e003252. doi: 10.1136/bmjgh-2020-003252. PMID: 33303514; PMCID: PMC7733114.

[15] Enserink M. After the windfall. Science. 2014 Sep 12;345(6202):1258-9. doi: 10.1126/science.345.6202.1258. PMID: 25214600.

[16] Ige TA, Jenkins A, Burt G, Angal-Kalinin D, McIntosh P, Coleman CN, Pistenmaa DA, O'Brien D, Dosanjh M. Surveying the Challenges to Improve Linear Accelerator-based Radiation Therapy in Africa: a Unique Collaborative Platform of All 28 African Countries Offering Such Treatment. Clin Oncol (R Coll Radiol). 2021 Dec;33(12):e521-e529. doi: 10.1016/j.clon.2021.05.008. Epub 2021 Jun 9. PMID: 34116903.

[17] Linacs to narrow radiotherapy gap. Available at: https://cerncourier.com/a/linacs-to-narrow-radiotherapy-gap/. Accessed May 6, 2022.

[18] Wroe LM, Ige TA, Asogwa OC, Aruah SC, Grover S, Makufa R, Fitz-Gibbon M, Sheehy SL. Comparative Analysis of Radiotherapy Linear Accelerator Downtime and Failure Modes in the UK, Nigeria and Botswana. Clin Oncol (R Coll Radiol). 2020 Apr;32(4):e111-e118. doi: 10.1016/j.clon.2019.10.010. Epub 2019 Nov 19. PMID: 31757747.

[19] Rodin D, Longo J, Sherertz T, Shah MM, Balagun O, Wendling N, Van Dyk J, Coleman CN, Xu MJ, Grover S. Mobilising Expertise and Resources to Close the Radiotherapy Gap in Cancer Care. Clin Oncol (R Coll Radiol). 2017 Feb;29(2):135-140. doi: 10.1016/j.clon.2016.11.008. Epub 2016 Dec 9. PMID: 27955997

[20] Grover S, Balogun OD, Yamoah K, Groen R, Shah M, Rodin D, Olson AC, Slone JS, Shulman LN, Coleman CN, Hahn SM. Training global oncologists: addressing the global cancer control problem. Front Oncol. 2015 Apr 8;5:80. doi: 10.3389/fonc.2015.00080. Erratum in: Front Oncol. 2015;5:133. PMID: 25905040; PMCID: PMC4389376.

[21] Rodin D, Yap ML, Grover S, Longo JM, Balogun O, Turner S, Eriksen JG, Coleman CN, Giuliani M. Global Health in Radiation Oncology: The Emergence of a New Career Pathway. Semin Radiat Oncol. 2017 Apr;27(2):118-123. doi: 10.1016/j.semradonc.2016.11.003. Epub 2016 Nov 9. PMID: 28325237.

[22] Vapiwala N, Thomas CR Jr, Grover S, Yap ML, Mitin T, Shulman LN, Gospodarowicz MK, Longo J, Petereit DG, Ennis RD, Hayman JA, Rodin D, Buchsbaum JC, Vikram B, Abdel-Wahab M, Epstein AH, Okunieff P, Goldwein J, Kupelian P, Weidhaas JB, Tucker MA, Boice JD Jr, Fuller CD, Thompson RF, Trister AD, Formenti SC, Barcellos-Hoff MH, Jones J, Dharmarajan KV, Zietman AL, Coleman CN. Enhancing Career Paths for Tomorrow's Radiation Oncologists. Int J Radiat Oncol Biol Phys. 2019 Sep 1;105(1):52-63. doi: 10.1016/j.ijrobp.2019.05.025. Epub 2019 May 22. PMID: 31128144; PMCID: PMC7084166.

[23] NIH Office of Equity, Diversity, Inclusion. Available at: https://www.edi.nih.gov/. Accessed May 7, 2022.

[24] Coleman CN, Wong JE, Wendling E, Gospodarowicz M, O'Brien D, Ige TA, Aruah SC, Pistenmaa DA, Amaldi U, Balogun OO, Brereton HD, Formenti S, Schroeder K, Chao N, Grover S, Hahn SM, Metz J, Roth L, Dosanjh M. Capturing Acquired Wisdom, Enabling Healthful Aging, and Building Multinational Partnerships Through Senior Global Health Mentorship. Glob Health Sci Pract. 2020 Dec 23;8(4):626-637. doi: 10.9745/GHSP-D-20-00108. PMID: 33361231; PMCID: PMC7784062.

[25] Blanchard C, Lubuzo B, Asirwa FC, Dlamini X, Msadabwe-Chikuni SC, Mwachiro M, Shyirambere C, Ruhangaza D, Milner DA Jr, Van Loon K, DeBoer R, Mtshali P, Dugan U, Baker E, Shulman LN. Multisector Collaborations and Global Oncology: The Only Way Forward. JCO Glob Oncol. 2021 Jan;7:153-161. doi: 10.1200/GO.20.00492. PMID: 33493021; PMCID: PMC8081550.

ACCELERATOR-BASED NEUTRON SOURCE FOR BORON NEUTRON CAPTURE THERAPY AND OTHER APPLICATIONS

S. YU. TASKAEV
Budker Institute of Nuclear Physics
Novosibirsk, Russia
Email: taskaev@inp.nsk.su

Abstract

An accelerator-based neutron source has been proposed and created at the Budker Institute of Nuclear Physics in Novosibirsk, Russia. The source comprises an original design tandem accelerator, solid lithium target, and a neutron beam shaping assembly. The neutron source is capable to produce the high neutron flux in various energy ranges, from thermal to fast, for boron neutron capture therapy, as well as for other applications. The paper describes the facility, its features and the results obtained with its use.

1. INTRODUCTION

The main objective for the accelerator based BNCT system is to design a compact neutron source that best satisfies the BNCT requirements [1], namely, a source of beam of epithermal neutrons with minimized fraction of fast and thermal neutrons. In order to form the narrowest neutron spectrum within the epithermal energy range, it was proposed to use the ^{7}Li(p,n)^{7}Be reaction with a high-current low-energy proton beam for BNCT [2]. Experimental implementation of the proposal required two decades of research, culminating in the creation of a compact reliable neutron source demanded by BNCT and other applications. In the paper, we give a description of the constituent parts of the neutron source, its features and the results obtained with its use.

2. EXPERIMENTAL FACILITY

The layout of the facility is shown in Fig. 1. The neutron source comprises an original design tandem accelerator, solid lithium target, a neutron beam shaping assembly, and is placed in two bunkers as shown in Fig. 1. Each bunker is 10.8 m × 9.1 m and 10 m height, the wall thickness of the bunker is from 1.2 m to 1.3 m, the wall thickness between the bunkers is 1.47 m. The facility has the ability to place a lithium target in 5 positions; in Fig. 1 they are marked as positions A, B, C, D, E.

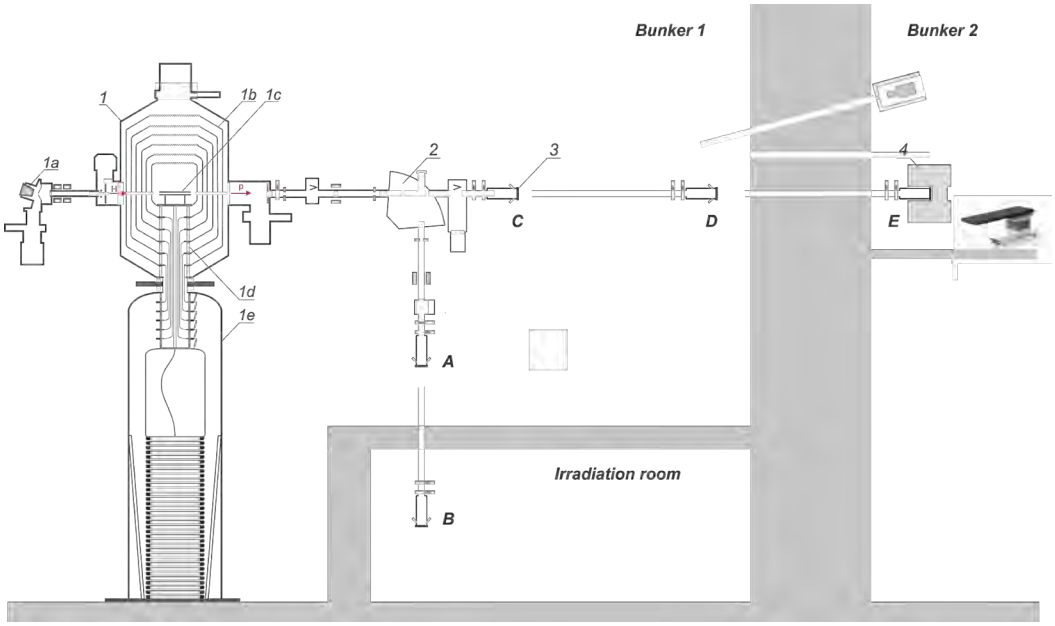

FIG. 1. Layout of the experimental facility: 1 – vacuum insulated tandem accelerator (1a – negative ion source, 1b - intermediate and high-voltage electrodes, 1c – gas stripper, 1d – feedthrough insulator, 1e – high voltage power supply), 2 – bending magnet, 3 – lithium target, 4 – beam shaping assembly. A, B, C, D, E –lithium target placement positions.

In order to generate a high-current low-energy proton beam, a DC tandem accelerator is used. The term "tandem" means that the applied DC accelerating voltage is used twice. Negative hydrogen ions are injected to the input of the tandem accelerator, accelerated by a positive potential applied to the central electrode, then stripped to the positive ions, and accelerated again by the same potential. A key advantage of the tandem acceleration concept is to reduce the necessary accelerating voltage by half, which tremendously simplifies electrostatic insulation and consequently reduces the size and cost of the accelerator.

The BINP tandem accelerator, which was named as Vacuum Insulated Tandem Accelerator (VITA), has a specific design that does not involve accelerating tubes, unlike conventional tandem accelerators. Instead of those, the nested intermediate electrodes (*1b*) fixed at a feedthrough insulator (*1d*) is used, as shown in Fig. 1. The advantage of such an arrangement is moving ceramic parts of the feedthrough insulator far enough from the ion beam, thus increasing the high-voltage strength of the accelerating gaps given high ion beam current. A consequence of this design was also a fast rate of ion acceleration – up to 25 keV/cm.

The proton beam energy can be varied within a range of 0.6 MeV – 2.3 MeV keeping a high-energy stability 0.1 %. The beam current can also be varied in a wide range (from 0.1 mA to 10 mA) with high current stability (0.4 %) [3]. The tandem accelerator is also capable of generating a deuteron beam with similar characteristics [4].

In the design of the neutron target, the following factors were considered:

1) The lithium layer must be thick enough to slow down protons in it only to the neutron generation threshold of 1.882 MeV. This can decrease the accompanying 0.478 MeV γ-ray flux and the temperature on the lithium surface.
2) The lithium layer must consist of pure lithium to maximize the neutron yield. The neutron yield from the lithium hydride, oxide, and fluoride is 1.43, 2, and 3.3 times lower than that from pure lithium, respectively.
3) The lithium layer must remain solid to prevent backstreaming of the lithium vapor and ^{7}Be in the beam duct.
4) The substrate must be intensively cooled to maintain the lithium layer in the solid state during its heating by the powerful proton beam.
5) The substrate on which the lithium layer is deposited must be thin. This enables optimization of the moderator and placing the moderator close to the neutron generation surface.
6) The substrate must be resistant to radiation damage.
7) The target plate must be easily removable at the end of the target life.
8) All materials of the target assembly should have minimal activation by neutrons.

Lithium target 10 cm in diameter has three layers: a thin layer of pure lithium to generate neutrons in ^{7}Li(p,n)^{7}Be reactions; a thin layer of material totally resistant to radiation blistering [5]; and a thin copper substrate for efficient heat removal. Thermal evaporating of lithium in a vacuum on copper substrate is carried out on a specially designed stand. The practical application of our proposed non-destructive in situ method for measuring the thickness of lithium [6] made it possible to optimize the deposition of a layer of lithium uniform in thickness. This target provides a stable neutron yield for a long time (at least the treatment time for 340 patients, as was measured) with an acceptably low level of contamination of the beam transport path by the inevitably formed radioactive isotope beryllium-7 [7].

A Beam Shaping Assembly (BSA) is applied to convert neutron flux into a beam of epithermal neutrons with characteristics suitable for clinical applications. We use two BSA. The first BSA consists of a magnesium fluoride moderator, a composite reflector (graphite in the front hemisphere and lead in the back), an absorber, and a filter [8]. Second BSA is a plexiglas moderator 72 mm thick.

3. FACULTY APPLICATIONS

In Boron Neutron Capture Therapy, the total absorbed dose is the sum of four dose components with different RBE: boron dose; high-LET dose from the ^{14}N(n,p)^{14}C reaction ("nitrogen" dose); fast neutron dose; γ-ray dose. We developed a new approach for measuring boron dose, nitrogen dose and fast neutron dose. A small-sized neutron detector (1 mm × 1 mm in diameter) with two cast polystyrene scintillators one of which is enriched in boron has been developed and is being used for dosimetry of boron dose and γ-ray dose [9]. For

measuring nitrogen dose and fast neutron dose we proposed a new approach: the cell lines are irradiated by γ-radiation and mixed radiation (neutron and γ-radiation) for the same time measuring γ-ray dose. After that by comparing the doses of γ-radiation causing the same effect, for example, survival, determine the doses due to high-LET particles dose [10]. We have developed a boron delivery drug loaded with gold, which allows *in situ* absorbed dose evaluation in BNCT [11].

As a result of studies carried out at the facility, it has been established that the neutron irradiation of U251 and T98G human glioma cells, pre-incubated in the medium with boron, leads to a significant suppression of their vitality [12]. Irradiation of immunodeficient mice with grafted human glioblastoma with pre-injection of ^{10}B-enriched drugs results in their reduce or suspend or their complete recovery [13]. The experience gained allows us to successfully treat pets with spontaneous tumors [14].

Since BNCT is a binary technique, another important aspect is the boron delivery drug. A large number of new drugs have been tested at the facility [11, 13, 15-19], and more are expected.

The developed neutron source became a prototype of the commercial neutron beam system for hospital-based BNCT. This neutron source is installed at the new BNCT Center at Xiamen Humanity Hospital in Xiamen, P.R. China. The next two such sources are made for National Oncological Hadron Therapy Center (CNAO) in Pavia (Italy), and for National Medical Research Center of Oncology in Moscow (Russia).

Using the accelerator blistering of metal surface under proton implantation [20] and its effect on the neutron yield [7] have been studied in detail. The ^{7}Li(p,p'γ)^{7}Li reaction cross section [21], the ^{7}Li(p,α)α reaction cross section [22], the 478 keV photon yield from a thick lithium target [21], and the neutron yield from lithium target in ^{7}Li(p,n)^{7}Be reaction[23] have been measured.

The source was used to measure the content of hazardous impurities in boron carbide samples developed for thermonuclear fusion reactor ITER [24, 25].

The source was used for radiation tests of perspective materials by fast neutrons [4] with a fluency of 10^{14} to 10^{15} neutrons/cm^2. These prospective materials were: i) fibers of the laser calorimeter calibration system of the CMS electromagnetic detector developed for the High-Luminosity Large Hadron Collider in CERN, ii) photomultipliers and DC-DC converters for ATLAS detector in CERN, iii) diamond neutron detector and boron carbide ceramics for ITER, iv) neodymium magnets for high power linac of the Kurchatov Institute. Users were given the opportunity to measure the parameters of the studied samples in real time and see the parameters of the facility.

4. CONCLUSION

A compact neutron source has been proposed and created at the Budker Institute of Nuclear Physics in Novosibirsk, Russia. The source comprises an original design tandem accelerator, solid lithium target, and a neutron beam shaping assembly. The neutron source produces the high neutron flux for boron neutron capture therapy, as well as for other applications. The neutron source has been used and is planned to be used for a variety of different scientific studies including clinical trials.

ACKNOWLEDGEMENTS

This research was funded by Russian Science Foundation, grant number 19-72-30005.

REFERENCES

[1] Sauerwein, W.A.G., Wittig, A., Moss, R., Nakagawa, Y. (Eds.), Neutron Capture Therapy: Principles and Applications; Springer: Heidelberg, New York, Dordrecht, London, 2012.

[2] Bayanov, B., Belov, V., Bender, E., *et al*., Accelerator based neutron source for the neutron-capture and fast neutron therapy at hospital, Nuclear Instr. and Methods in Physics Research A 413/2-3 (1998) 397–426.

[3] Taskaev, S., Berendeev, E., Bikchurina, M., *et al*., Neutron Source Based on Vacuum Insulated Tandem Accelerator and Lithium Target. Biology 10 (2021) 350.

[4] Kasatov, D., Koshkarev, A., Makarov, A., Ostreinov, G., Taskaev, S., Shchudlo, I., Fast-neutron source based on a vacuum-insulated tandem accelerator and a lithium target. Instruments and Experimental Techniques 63 (2020) 611–615.

[5] Taskaev, S., Makarov, A., Sokolova, E., Systems, devices, and methods for deformation reduction and resistance in metallic bodies, United States Patent no. US 2022/0030696 A1, Jan. 27, 2022.

[6] Kasatov, D., Kolesnikov, Ia., Koshkarev, A., Makarov, A., Sokolova, E., Shchudlo, I., Taskaev, S., Method for in situ measuring the thickness of a lithium layer, JINST 15 (2020) P10006.

[7] Bykov, T., Goloshevskii, N., Gromilov, S., *et al*., *In situ* study of the blistering effect of copper with a thin lithium layer on the neutron yield in the ^{7}Li(p,n)^{7}Be reaction, Nuclear Inst. and Methods in Physics Research B 481 (2020) 62–81.

[8] Zaidi, L., Belgaid, M., Taskaev, S., Khelifi, R., Beam shaping assembly design of ^{7}Li(p,n)^{7}Be neutron source for boron neutron capture therapy of deep-seated tumor. Appl. Radiat. Isot. 139 (2028) 316–324.

[9] Bykov, T., Kasatov, D., Koshkarev, A., *et al*., Evaluation of depth-dose profiles in a water phantom at the BNCT facility at BINP, JINST 16 (2021) P10016.

[10] Dymova, M., Dmitrieva, M., Kuligina, E., *et al*., Method of measuring high-LET particles dose, Radiation Research 196 (2021) 192-196.

[11] Zaboronok, A., Taskaev, S., Volkova, O., *et al*., Gold Nanoparticles Permit *In Situ* Absorbed Dose Evaluation in Boron Neutron Capture Therapy for Malignant Tumors, Pharmaceutics 13 (2021) 1490.

[12] Sato, E., Zaboronok, A., Yamamoto, T., *et al*., Radiobiological response of U251MG, CHO-K1 and V79 cell lines to accelerator-based boron neutron capture therapy, J. Radiat. Res. 59 (2018) 101-107.

[13] Zavjalov, E., Zaboronok, A., Kanygin, V., *et al*., Accelerator-based boron neutron capture therapy for malignant glioma: a pilot neutron irradiation study using boron phenylalanine, sodium borocaptate and liposomal borocaptate with a heterotopic U87 glioblastoma model in SCID mice, Intern. J. Radiat. Biol. 96 (2020) 868-878.

[14] Kanygin, V., Kichigin, A., Zaboronok, A., *et al*., *In vivo* Accelerator-based Boron Neutron Capture Therapy for Spontaneous Tumors in Large Animals: Case Series, Biology 11 (2022) 138.

[15] Uspenskii, S., Khaptakhanova, P., Zaboronok, A., *et al.,* Elemental Boron Nanoparticles: Production by Ultrasonication in Aqueous Medium and Application in Boron Neutron Capture Therapy, Doklady Chemistry 491 (2020) 45–48.

[16] Vorobyeva, M., Dymova, M., Novopashina, D., *et al.*, Tumor Cell-Specific 2'-Fluoro RNA Aptamer Conjugated with Closo-Dodecaborate as a Potential Agent for Boron Neutron Capture Therapy, International Journal of Molecular Sciences 22 (2021) 7326.

[17] Popova, T., Dymova, M., Koroleva, L., *et al*., Homocystamide conjugates of human serum albumin as a platform to prepare bimodal multidrug delivery systems for boron-neutron capture therapy, Molecules 26 (2021) 6537.

[18] Zaboronok, A., Khaptakhanova, P., Uspenskii, S., *et al*., Polymer-Stabilized Elemental Boron Nanoparticles for Boron Neutron Capture Therapy: Initial Irradiation Experiments, Pharmaceutics 14 (2022) 761.

[19] Aiyyzhy, K., Barmina, E., Zavestovskaya, I., *et al*., Laser ablation of Fe_2B target enriched in ^{10}B content for boron neutron capture therapy, Laser Physics Letters 19 (2022) 066002.

[20] Badrutdinov, A., Bykov, T., Gromilov, S., *et al*., *In situ* observations of blistering of a metal irradiated with 2-MeV protons, Metals 7 (2017) 558.

[21] Taskaev, S., Bykov, T., Kasatov, D., *et al*., Measurement of the ^{7}Li(p,p'γ)^{7}Li reaction cross-section and 478 keV photon yield from a thick lithium target at proton energies from 0.65 MeV to 2.225 MeV, Nuclear Instr. and Methods in Physics Research B 502 (2021) 85-94.

[22] Taskaev, S., Bikchurina, M., Bykov, T., et al., Cross-section measurement for the ^{7}Li(p,α)^{4}He reaction at proton energies 0.6 - 2 MeV, Nuclear Instr. and Methods in Physics Research B (2022) (under review).

[23] Bikchurina, M., Bykov, T., Kasatov, D., *et al*., The measurement of the neutron yield of the ^{7}Li(p,n)^{7}Be reaction in lithium targets, Biology 10 (2021) 824.

[24] Shoshin, A., Burdakov, A., Ivantsivskiy, M., *et al.*, Test results of boron carbide ceramics for ITER port protection, Fusion Engineering and Design 168 (2021) 112426.

[25] Shoshin, A., Burdakov, A., Ivantsivskiy, M., *et al.,* Integration of ITER diagnostic ports at the Budker Institute, Fusion Engineering and Design 178 (2022) 113114.

ION BEAM USAGE IN ENVIRONMENTAL CHARACTERIZATION

L. POPA-SIMIL
LAVM llc
Los Alamos, USA
Email: lps@lavmllc.com

Abstract

There are many circumstances we were interested in getting more knowledge on environmental atomic and molecular composition, as monitoring pollution, identifying pollution sources, looking for air, water and soil on surface and underground composition. Accelerator based techniques offer a large palette of measurement capabilities, with high sensibility and accuracy, requiring small samples but they are expensive and time consuming, and need to be organized in such a manner to get a holistic characterization of an array of interest in a single sampling, or repetitive for trend identification. First 1980s sets of measurements were using gamma-spectroscopy associated to geodesic studies for singular events forensics. Samples from environment were taken and measured for elemental and molecular composition using, PIXE, PIGE, CPAA and NAA. Atmospheric pollution, and atmospheric corrosion, became important, and we have used TLA method to characterize the material corrosion in air, and simultaneously measure the acidity in air using special filtration unit in parallel, and taking precipitation samples.

During 1990s we were interested in tracking pollution, and we used the protocols developed by Nagoya Technical Univ., Prof. Susumu Amemyia, which was based on mobile air samplers with 0.4μ and 8μ pores, tuned for industrial pollution, and the IMPROVE protocol, developed with Prof. Thomas Cahill at UC Davis, CA participation, using 2.5 μ and 10 μ filters, simulating better human bucko-pharyngeal cavity, augmented with nearby soil, vegetation and water samples.

Using the lessons learned, in order to get competitive, fast and useful data, there is the need to consolidate the accelerators in clusters application ready, with some process automation, able to process many samples a day under quality assurance standards. Another direction is to develop mobile equipment for on-site measurements that will deliver the primary data collected during the sampling time, covering all aspects of the studied area.

1. INTRODUCTION

Accelerator based techniques especially IBA (Ion Beam Analysis) offers elemental elements high performance measurements, with capability to go deep into details, but environmental measurements address more aspects than simply knowing momentary elemental composition of some samples.

1.1. Environment measurements expertise evolution

Starting in 1980 in Romania, I have started measuring environment as related to singular events, to industrial pollution and general environment research using nuclear technologies. By 1980s we started measuring environmental radioactivity for forensic purposes, but we encountered many complications due to heterogeneous nature of radioisotope distributions and space radioactivity. Chernobyl accident found us so unprepared to reliably characterize the impact in air, on ground and water. Post-accident we developed a combination of measurements, aiming to identify the contamination not only with radioactive material, but with chemicals made of stable elements also. The interest was to correlate various contaminants in air bound to various size aerosols, and we started developing our multi-stage stacked filter unit, that was applied successfully to water, lubricant and wine filtration. Have been developed tangential filtering units to filter large volumes. Atmospheric pollution was another niche where the high sensitive IBA (Ion Beam Analysis) methods were prone to success. Here appeared the need for measuring bio-samples and organic substances with high saturated vapour pressure which are evaporating in vacuum and under beam's energy deposition as heat, led us to the development of methods with beam extracted in air, or controlled atmosphere, generically called bio-PIXE.

During 1990s we were interested in tracking pollution, and we used the protocols developed by Nagoya Technical Univ., Prof. Susumu Amemyia, which was based on mobile air samplers with 0.4μ and 8μ pores, tuned for industrial pollution [1], and the IMPROVE protocol, developed with Prof. Thomas Cahill at UC Davis, CA participation, using 10 μ and 2.5 μ filters, simulating better human bucko-pharyngeal cavity [2], augmented with nearby soil, vegetation and water samplers. Starting from mid 1980s we have added remote sensing capabilities using "Landsat" thermal and multi-spectral vision for characterizing short range transportation, where the data

were correlated with elemental analyses of samples from the area in order to produce signature patterns for image automatic identification. Measurements across US, Europe and Romania were made, mainly measured by PIXE and XRF, while stoichiometry was used to identify substances by educated guess.

After year 2000, at Los Alamos, NM soil and vegetables samples were taken to scale the impact in the area of the so called “nuclear legacy”, on local environment and looked to more evolved AMS methods using RGAs in order to better identify the molecular compositions and develop accelerator based forensic installation, using both the analytical and radiolysis capabilities, in an effort to extract maximum information from the measurements, sometimes needed to be performed in real-time.

These experiments drive us to the conclusion that for best accurate and complete results one has to use a plurality of methods applied quasi-simultaneously on the same sample.

In most of the cases was difficult to say which was the real contribution of a singular event on the composition of elements and molecules in an area, and most often we used in volume sampling to obtain the densities of each component, and from those variation to estimate the single event’s contribution. In this case accelerators have to cooperate doing simultaneously elemental analysis and atomic mass spectroscopy, to identify all molecular species, and to corroborate these results with CPAA, NAA and RBS for solid samples. Radioactivity is also an important feature and makes a more complex image. In some cases, using radiolysis and sequential measurements allows obtaining more complete information about volatile substances, which may be detected with Residual gases analysers on line with the beam, is sample temperature is also considered by using IR imager.

It has been detected an affinity between some substances and elements to associate with certain particulates and aerosols, as in the case of wine clearing by ultrafiltration, where wen removing a class of particulates was changing the wine scent and aromas, and a study in depth was required to better understand these manifestations. For example vinegar molecules were blended on 0.3 PM particulates, but after removing the 0.1 PM particles wine becomes diluted vodka with no taste.

Using the lessons learned, in order to get competitive, fast and useful data, there is the need to consolidate the accelerators in clusters application ready, with some process automation, able to process many samples a day under quality assurance standards. Another direction is to develop mobile equipment for on-site measurements that will deliver the primary data collected during the sampling time, covering all aspects of the studied area. That will represent virtual centres of excellence, assuring accelerators an important role in environmental and micro-particle knowledge progress.

1.2. Holistic view on environment investigation

The assembly of living & non-living organisms and even the space around that community is termed as an ecosystem. There is a specific area for different types of ecosystems, and all the organisms & the environment, where we understand the surroundings or conditions in which a living entity, as a person, animal, or plant lives or operates, interact with each other in that particular area. We distinguish air, aquatic and terrestrial and combinations of them may form an ecosystem.

In order to know if an ecosystem is safe, one needs to know a lot of details about it starting from living beings down to atomic and molecular composition, to which one adds the main events and modifications that may affect it. The changes in this composition it is called pollution when introduction of harmful materials into the environment takes place. Pollutants can be natural, such as volcanic ash, or may be the result of a human activity, such as trash or runoff produced by factories, and usually they damage the quality of air, water, and land [1].

2. ENVIRONMENT MEASUREMENTS

The environment measurements evolved gradually, driven by threat agents, as preparedness initiative in order to develop necessary knowledge and infrastructure for the task. As general characteristic of our expertise, we allocated a lot of time and effort developing measurement and interpretation methods and devices, but after implementing and using them we learned that it was not enough; we analysed the failures and the results took lessons learned and applied corrections and improvements. The hardest level to achieve was to make the resultant knowledge really useful, and applying it to drive to profit for the involved society.

2.1. Radioactivity measurement

During 1980s the close observation of singular effects was done by taking specific actions to identify a possible pollution resulted from that, and in most of the cases that was reduced to terrain measurements in order to identify any changes that possibly occurred in that area due to a reported event. The most common measurements were those of gamma radiation, X, alpha, beta, γ, plus EM, gravitation and weather.

The equipment used as FIG 1 shows was a Canberra 30 multichannel analyser over a 4-chanel Tektronix oscilloscope having nearby some nuclear electronics in NIM rack and some other standard, receiving signal from two NaI spectrometric gages inserted in a lead shield; in conclusion laboratory grade inadequate used in open environment with some adaptations and precautions. Underneath there are two portable GM radiation detectors. On the right side in FIG. 2 there are two images of the radiation measurement system deployed in terrain using an SUV. The result was a spectrum or numbers on a pre-calibrated SCA gates indicating the radiation rate for various energies specific to various isotopes we intended to identify.

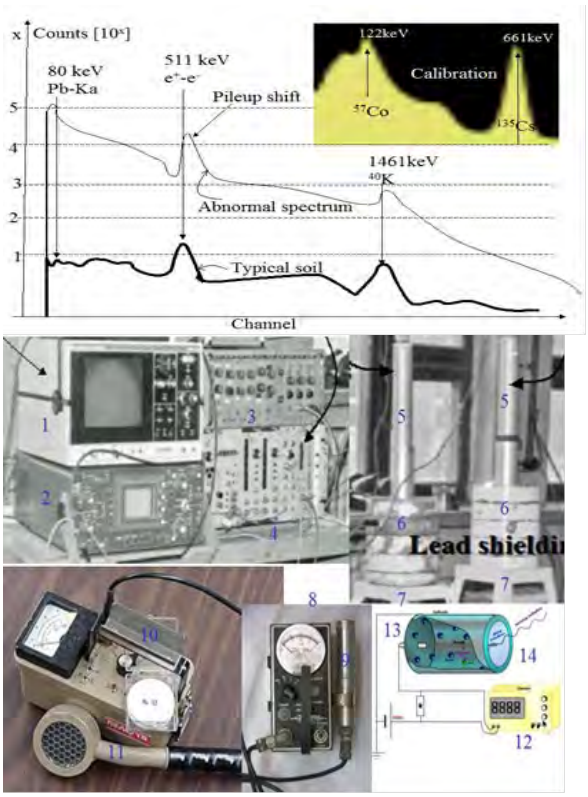

FIG. 1: 1980s radiation measurement devices and soil NaI gamma spectrum

FIG. 2: Mobile NaI gamma spectrometry of ground

The problem was that almost all the time we were missing the initial (before the presumed incident) radiation measurement and had to compare lateral measurements and use reasoning to say that the anomalous measurements are due or not to the previously reported incident. The problem was that a good background measurement that took about 10 min. and the equipment power consumption was high, at about 500+W, difficult to provide from car batteries therefore the measurement sessions were short, of about 2-3h, followed by a recharging break. We learned that connecting 2,3 gages at the same equipment does not increase too much the total required power. Soil samples were taken for analysis at soil specialized laboratory with low gamma background and analytic chemistry capabilities. In most of the cases was difficult to assign the findings to the related event, and measurement results had mainly an anecdotic value, being stored in a database. We also learned about the need of using two spectrometric gages one pointed towards ground and another towards atmosphere to measure and compensate for cosmic background, which may vary during the acquisition time, and may be influenced by atmospheric conditions too.

2.2. Atmospheric corrosion on solid samples measurement

In 1980 air corrosion was a rare, exotic subject, most of the educated people trend to ignore that, and to minimize the effects of pollution too, My mentor Eng. Livovschi P. had a collection of samples metal foils was exposed on a wall in Campulung, AG., Romania and from time to time, about every quarter, I.A.Aro Metrology division, where using a high accuracy calliper, made by the Tessa Co. in Switzerland, with accuracy better than 0.1 micron, was measuring the dimension of the samples. In 1983 we tried to improve this experiment providing radioactive labelling to few samples (3 samples, a brass (RL_ Brass), copper (RL_Cu) and steel (RL_Fe) (RL stands for Radioactive Labelled)) [3] and measure in parallel with the rest, not to perturb too much his experiment, which also contained Chromium (Cr), Aluminium (Al), tin (Zn), lead (Pb), as shown in FIG. 3

After radioactive labelling, the parts were measured by me using a spectrometric gauge, and by Metrology Department with Tessatronic micro-meter and the results were similar inside a margin of error of 15%, and are presented in Fig. 2 in the bottom-right side chart.

These measurements were made for about 10 years, from 1982 to 1992, in Campulung Muscel town, shown in Fig. 2 in aerial view, and between 1984-1986 radioactive samples have been used, both in Campulung and Bucharest due to radiation decay time. In that time, Campulung had a chemical plant producing synthetic fibres, a cement plant and a car factory. Pollution was mainly due to cogeneration and exhausts from these plants. Bucharest had a more complicated pollution picture, with lots of cars and plants.

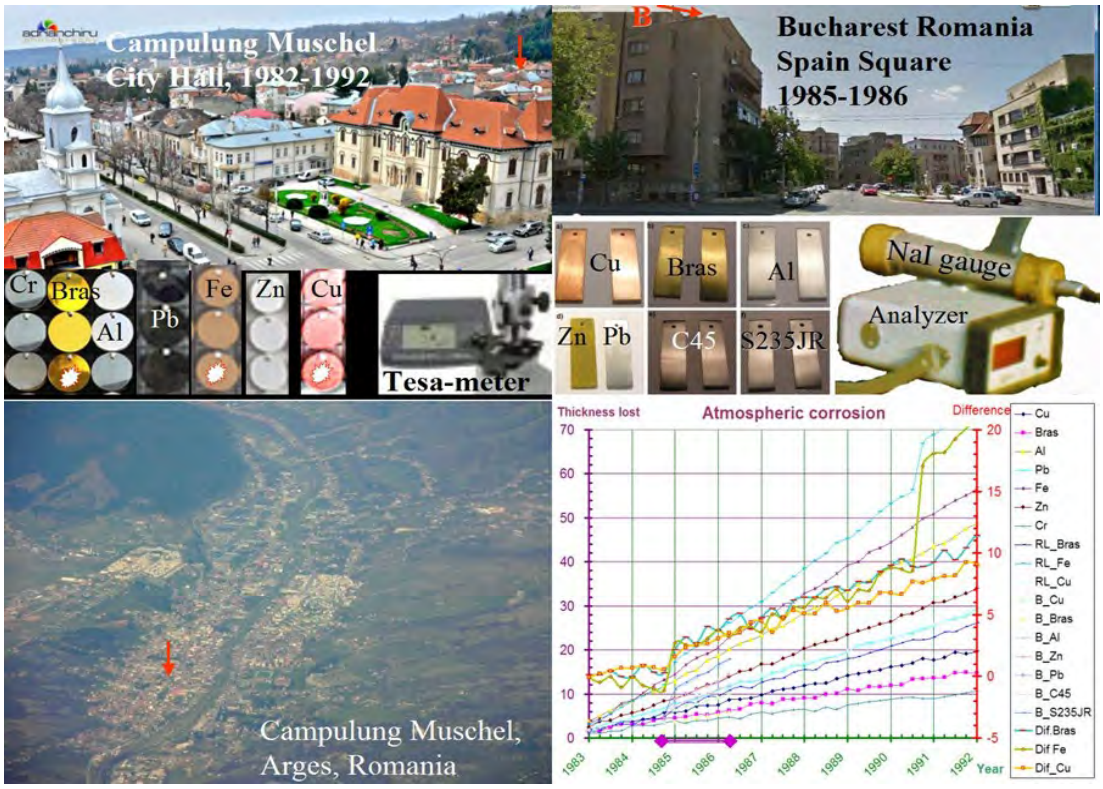

FIG. 3: Atmospheric corrosion locations and results for various materials

By 1988 it was observed that radioactive labelling modifies the properties of the structure and is prone to indicate corrosion by 30-70% faster than usual. In fact on his samples I have applied 1 micro-Amp.*Hour, in a volume of 50 microns and 1 cm^2. The concentration of H atoms was about 25 $*10^{15}$ atoms in about 5 * 10^{20} Fe atoms, result a concentration of 50 ppm of Hydrogen. The concentration of radioactive atoms was about 5 ppb, that is a relatively small trace, but what matters most is the number of dislocations induced into the target lattice and the thermal annealing proceed induced by irradiation, warming up the surface by few hundred Celsius degrees, because a power of about 15 W was applied into 5 mm^3 of material, driving to a power density of about 3 kW/cc, that is at the limit of material resistance, in spite we have used air jet cooling.

That was a very important learning; I had further applied in labelling as a precaution, and studied the effect on material under irradiation, being introduced in the labelling procedure as a quality assurance measure.

2.3. Aerosol particulate measurement by PIXE

At later time, starting from 1994, due to two international collaborations and a new attitude towards environment developed mainly after 1990, we have started measuring the pollution in various places in Romania and abroad. Cooperation was made with Nagoya University, Prof. Susumu Amemyia who developed an industrial pollution mobile aerosol tracking system, based on a staked filter unit using Millipore foil filters of 0.4 microns and 8 microns [4]. A second cooperation was done with U.C. Davis CA. Prof. Thomas Cahill who developed the "IMPROVE" (Interagency Monitoring of Protected Visual Environments) air quality protocol.

Prof. Cahill developed a stacked filtering unit that simulates the buccal- pharyngeal cavity retention, having a front filter of 2.5 microns and a 10 microns second filter.

We were thinking of unifying their two methods, because might have a better significance, as for example:-

particles bigger than 10 μm are due to local transportation, having a Stokes falling speed in mm/s maintaining in atmosphere for less than 1 day, but in windy conditions are airborne;

- particles with 2.5 μm< PM < 10 μm are retained in the nose filtering system and pharynges, are mainly airborne, and we lose the entire content of smaller particles.
- particles with 0.4 μm < PM < 2.5 μm are retained in the lungs, clogging there and some over time being dissolved or expelled, and with Susumu's filter we lose all smaller particles.
- particles smaller than 0.4 microns are passing through lung's walls into blood, influencing metabolism and mode, and here is one of the dangers nano-particles are presenting for users and manufacturers, and special protection measures have to be taken. We were interested in smaller particles and suggested the introduction of supplementary filter, but technologic difficulties made us postpone the idea;
- particles 0.4 μm < PM < 2.5 μm are also due to long range atmospheric transportation, and have a complex range, density, shape, chemical affinity correlation. We encounter these in upper atmosphere during Chernobyl pollution in May 1986, we observed that were mainly connected with water aerosols, mainly behaving like fog, but we were unprepared to perform coherent measurements [5].

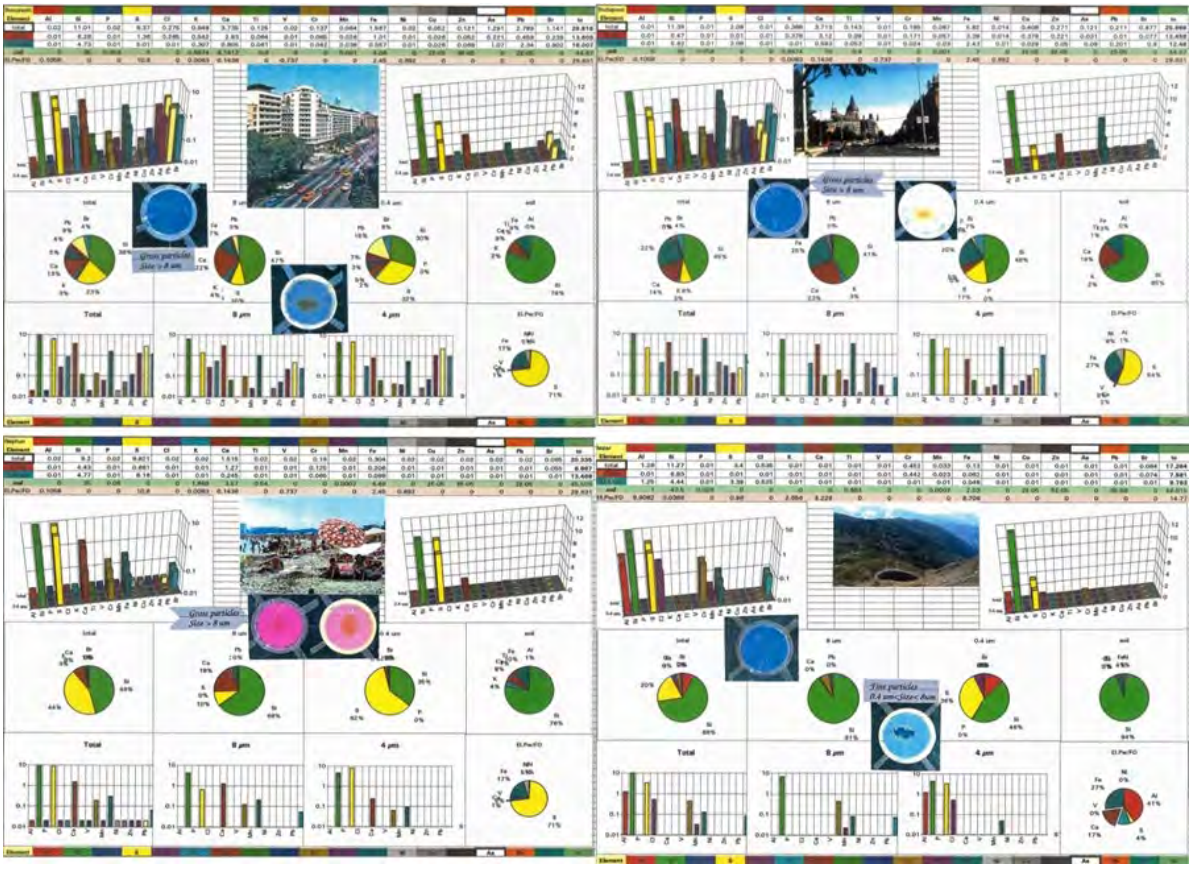

FIG. 4: Measurement of elemental pollution in various places (Bucharest, Budapest, Neptun, Balea Lake)

In spite we had available our membrane filter production at NIPNE-VDG Tandem, of Dr. Isabella Valcov, filters of 0.4 μm that we might like to use, but due to lack of resources in this complex system stacked filter unit, that to end up with a liquid or gel filter total collector, we never made the next development step.

We have used Amemyia's VDG system and measured pollution in various places, and the results are shown in FIG. 4, with the intent to correlate with corrosion information. This did not work out so well, because the bulk of atmospheric information was missing, and measurements remained just some numbers.

In FIG. 4 top-left is shown the results of pollution measurements in Bucharest Romania, on ½ mile N from University square, near Romanian Athenaeum, in the top-right is a measurement in Centre of Budapest, than in bottom left is a measurement on the Black Sea west beach in Neptune resort, and near Balea Lake, in Fagaras mountains at an altitude of 2300 m (about 7300 ft). In each image there are given a table of PIXE measurements, in the top, showing on columns header the detected elements and on lines, the separation between filters where 8 μm is meaning, all the particles with PM (Particle Magnitude) > 8 μm, and a residual amount of smaller particles (unknown for us); 0.4 μm means all the particles with 0.4 μm < PM < 8 μm and a residual amount of smaller particles also remained unknown for us. In the dark squares on blue disk is the filter picture as it was taken out from the sampler, and after being measured in the 4 MeV proton beam, that produced a dark burnup spot due beam power deposition heating and lack of cooling. Tom Cahill used to prevent this used a tiny He/Ar gas flow on the back of the filter, but we did only after observing this effect.

The problem was, the accuracy of the measurement, because due to heat up the vapour pressure of various solid particles present on filter, equals the vacuum pressure and evaporation/sublimation process occurs, and the concentration of that particle is reducing during the measurement [6].

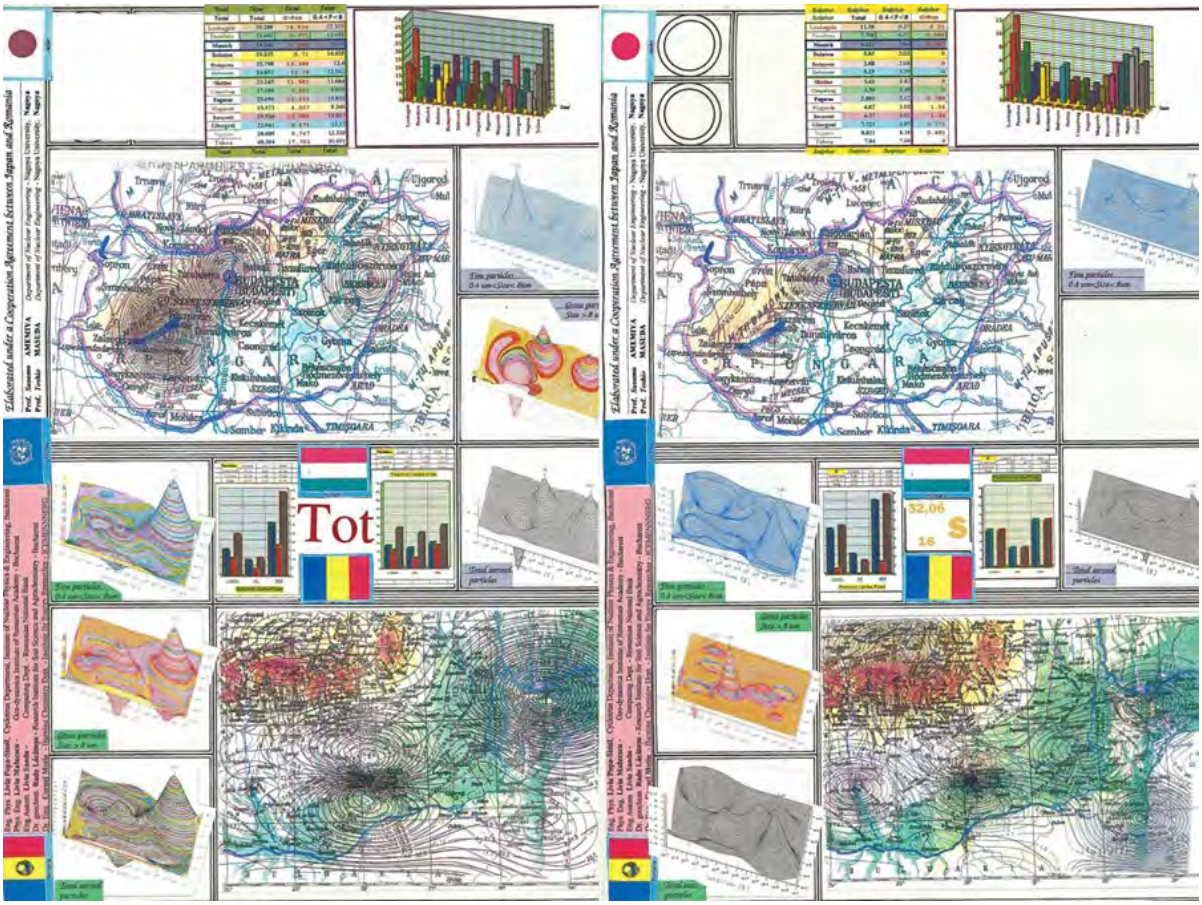

FIG. 5: Maps of pollution and elemental distributions in SE Romania and Hungary

We did two thinks to compensate for this effect:

- we took out the proton beam in air, and consider the X ray attenuation
- we made sequential acquisitions, dividing in 4 or 8 a regular acquisition duration.
- A better solution might have been to use a double stage RGA-300 and monitor the sample vapours from the vacuum application down to target evaporation under beam.

Next year in 1995 we performed another set of measurements with the intent to see the variation for a larger area on each element, and a sample of data is presented in Fig. 4.

In Fig. 4 are given the maps of Romania and the NW neighbour Hungary, as we have taken in cooperation with Susumu Amemyia, in summer of 1995, for the total particulates, on the left side and Sulphur on the right side, as samples, because we have another 19 elements measured, that may make this content too bulky, and is not related to the corrosion subject discussed here.

The images are divided in half, the upper side is about contain 2 maps, one of Hungary, in top and one of Romania underneath, and over each are overlapped the iso-levels of density of concentration in air (mg/m^3) for the 3 particle magnitude categories (Total, Coarse, Fine) and nearby there are given 3D views of the distributions, a list with places and measured concentrations for analysed element and charts showing the magnitudes. By 1997 we have extended the area of study in Europe tracing the pollution along Bucharest to Lisboan, [7] road, and improving the maps over Romania. In this case we tried taking mud and dusting samples in the road vicinity, in order to subtract the weight of short-range transportation, but the discrepancies become even higher[8]. Later we tried to use remote sensing data, and satellite imagery to correlate the spectral signature with field composition, in order to distinguish after applying weather behaviour previous air reaching a sampling point what came from local transport and what is in air from long range transportation, and that helped us using the mobile sampling with a network step of less than 100 km to localize pollution sources with less than 10 km accuracy. Some luck was also needed. In this process we have extended the use of ion beam accelerator, not only for performing PIXE and PIGE for elemental identification, but also applying RBS mm beam over various magnitude filters to better understand the elemental composition and associations inside aerosolized particulates, as in Chernobyl case where ^{131}I and ^{135}Cs associated in water droplets carried by wind and giving pollutant rains.

3. DISCUSSIONS

Based on these measurements, we succeeded to map in some approximation the distribution of each element, using stoichiometry we estimated the amounts of chemical combinations present in air.

In the measurements, we measured only solid particulates with very low vapour pressure, which did not evaporate in vacuum and under beam heating.

We had used remote sensing for local transportation validation, as well the soil and all available pollution data.

We had localized the pollution sources with an accuracy of few miles, using a grid of 100 miles step weather data and some luck.

We have failed to make any correlation between the corrosion wear rate previously measured and the airborne solid particulates, elemental concentrations we have measured and I have understood, why, and developed corrective measures

3.1. New equipment development

The corrosion measurement may be used as a comparative tool for the degree of air chemical cleanness between locations, but it is difficult to calibrate and correlate with weather events. The corrosion speed depends on many factors that makes any correlation attempt very difficult, but is a good reference if one has enough time and long term measurement reproducibility, in order to get the work done.

3.1.1. Aerosol particulate measurement

Based on lessons learned from previous experiments we simply understand that the accelerator based measurements have to be accompanied by collateral data measured with additional instrumentation, in order to corroborate all information available, and develop the right knowledge.

The system presented in FIG. 6 was designed for environmental anti-terrorism applications and top-left is shown a pattern of polymer/explosive radiolysis, in main detectable gases using X ray exposure., that may be considered to be introduced as an RGA in the PIXE irradiation chamber to measure the gases released during elemental analysis due to beam power deposition and associated radiation damage[9]. On the sample filters also aerosols and chemical fractions with high vapour pressure are on that trend to evaporate during vacuum

application, therefore we proposed a more complicated PIXE analysis and using a dual stage RGA and vacuum with moderate heat from laser and IR spectrometer for molecular identification of volatiles, and then a vacuum stage, using PIXE and RGA for elemental composition identification, finally completed by a neutron activation analysis, for light species, designed as a sequential or parallel test.

That will come at a cost of $20-$50 per sample. Improve the aerosol sampler with an ultrasonic concentrator with FX and Particle magnitude measurement capability as seen in top-right picture, and a snifter, as in bottom-left picture, as a multi-gas analyser, to build the device sketched in bottom left side of Fig. 6, able to take samples that are locally stored by the robotic arm, for weekly or monthly delivery, but also transmit real time data for basic air quality monitoring, as an integrated device for safety and security system network [10].

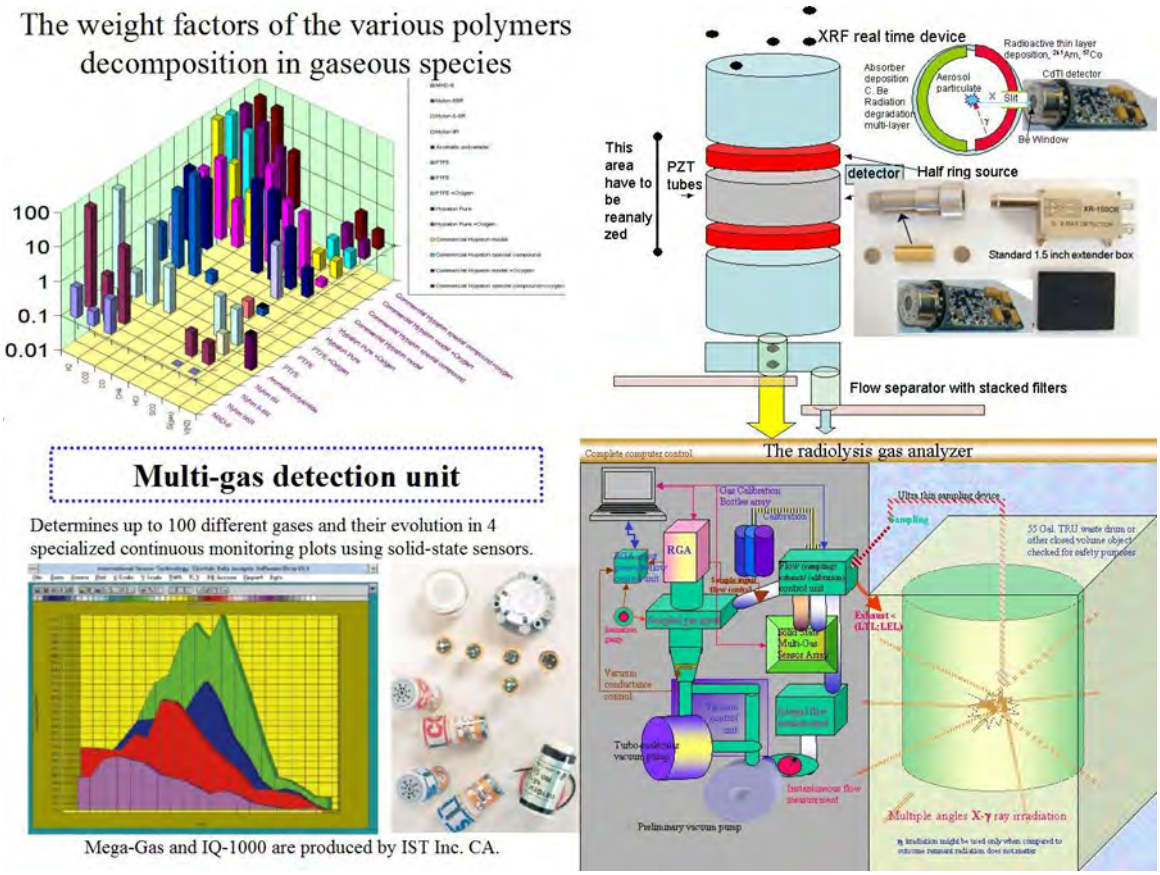

FIG. 6 – New enhancements possible to bring to aerosol sampler

A long-term device has to be similar with Improve system developed by Prof. Tom Cahill, with automatic sample filters loading that include more filtration stages as 20; 10; 5; 2.5; 1; 0.8; 0.5 and 0.2 microns, that to operate together with a particle magnitude meter. In parallel it will need a separate unit for organic fractions and bio-organisms. Before exposing the samples to vacuum, a high resolution image and initial weight might be important. The vacuum application and later the ion beam for PIGE and PIXE have to be done assisted by a RGA in order to analyse the volatiles elemental and molecular composition. It is useful to add in parallel with particulate accumulation an industrial gas analyser and a weather station connected and accumulating data that will be assigned to each sample. Water composition may be similarly analysed, by a filtration unit first and then taking a liquid sample for AMS, that may operate on spot using quadruple separators or laboratory grade accelerator based for high sensitivity trace analysis.

3.1.2. Mobile network for fast environment voxel diagnosis

A main problem we encounter and was difficult to solve was the usefulness of acquired knowledge, meaning by this that we need that knowledge level that to empower us to apply corrections to that environment voxel that to be profitable for all participants and stakeholders, and by this to recover the costs. In order to do this

we need to upgrade the system with a set of airborne measurement devices, and to add all the kind of collateral samples we may take from soil, underground water and water bodies, in a synchronous manner, correlate with local weather as seen in Fig. 7. In this case the procedure becomes as complex as a military operation and costly too, requiring a lot of logistics. The amount of test equipment grows and the number of samples that have to be analysed grows too. Depending on variability the observation time will be fixed.

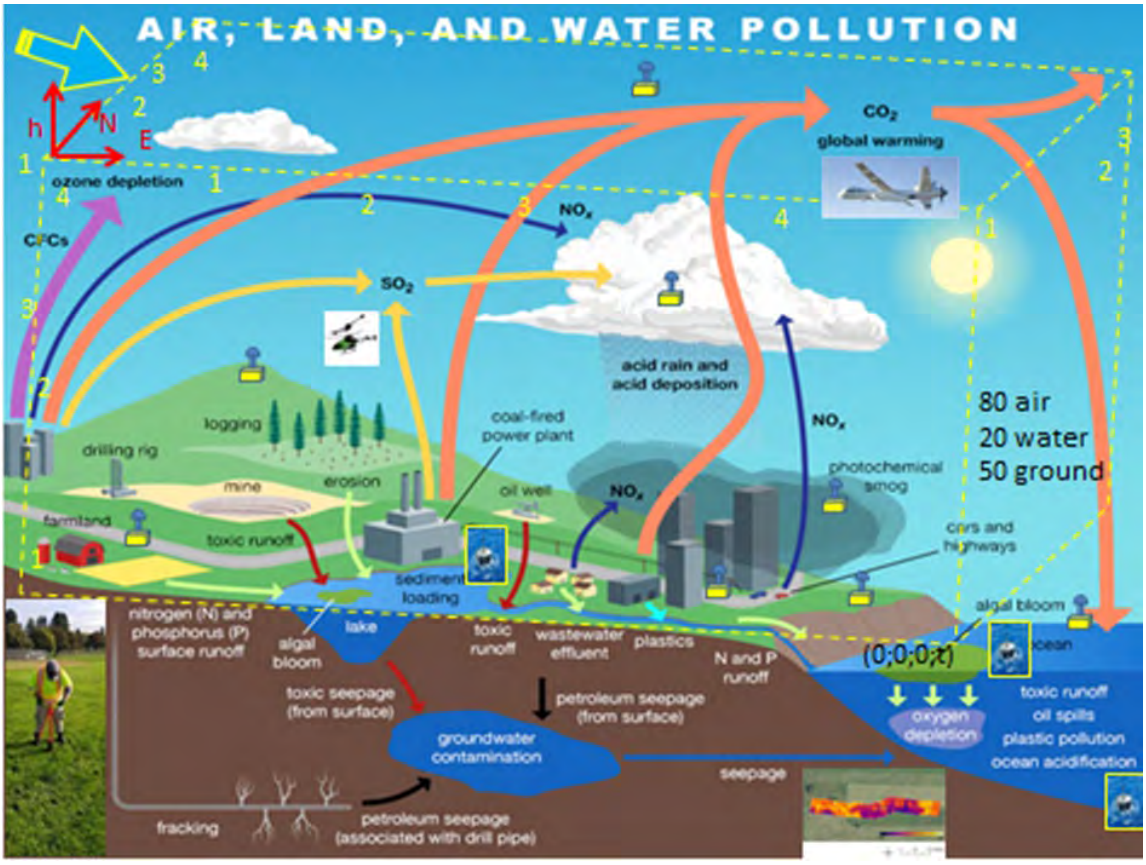

FIG. 6 – Complexity of establishing an effective measurement network

Fig 6 presents an ad-hock network of measurement that is aiming to perform synchronous measurements, and it turns obvious that about 20 helicopters with RF control are needed in addition to other equipment.

3.2. Accelerator usage and suggested improvements

The main task to be performed is elemental analysis, but the measurements have to be monitored by using an RGA with dual stage in order to identify the evaporating particle composition too, together with radiolysis products. In order to study the micro-structure, and isotopes dimensional distribution one may use micro-RBS beam. PIGE may be selectively applied for identifying those elements with prompt γ emission.

Other measurement methods have to be added, with improved equipment that to be able to see also the variability in sample content and create a model for the studied voxel, that to allow the identification of the sensitive points and determine the right corrective actions.

4. CONCLUSIONS

The development of these advanced measurement system must be optimized based on assessment of value of knowledge vs. the capabilities to use the knowledge, improve and get a reasonable ROI (return of investment), except the measurements for the sake of science.

The use of accelerators brings high sensitivity data, contributing to superior understanding.

The cost of a single measurement may be as high as $100k per single shot in an Ev, if the required equipment is already developed and available, that may drive the cost up to $10M or more being recommended

as such device to be developed at government level, requiring a specialized team up to 100 people, with various specializations and a significant accelerator time of minimum 1 week (95% operation time) for a single Ev shot, where Ev will have Dx dimensions usually smaller than a 10 miles cube.

Development of advanced measurement protocols under Quality Assurance norms, and advanced data acquisition, storage, processing and visualization, even using AI processing is a must to be able to lossless handle this huge amount of data.

One needs to understand that the winners are not those who know but those who can, and that is recommended to proactively use knowledge acquired to favourably change the things to improve and steward/protect the Environment, having a reasonable ROI.

ACKNOWLEDGEMENTS

Special gratitude to Prof. Susumu Amemyia from Nagoya Univ. and Prof. Emeritus Thomas Cahill from UC Davis, CA for their precious advices, teachings and collaboration and to my colleagues Dr. Petru Racolta, Eng.Chem. Dana Voiculescu, Dr. Claudiu Muntele, Acad.Dr. Eugen Ivanov and to NIPNE-HH cyclotron team, and Nagoya Univ. and Croker accelerator teams

REFERENCES

[1] Susumu Amemiya, Toshio Masuda, Liviu Popa-Simil . “PIXE analysis of atmospheric particulate matter collected at various places”, International Conference ISRP-6. Rabat, Maroc (1995).

[2] Thomas Cahill, “The PLXE global aerosol collaboration”, (Liviu Popa-Simil included), “Spatial and seasonal distribution of sulphate aerosols on global scale”, - VII International Conference on PIXE and its Analytical Applications, Padua, Italy 26-30, P 5.23-24, (1995).

[3] Popa-Simil L., “A reliable method in material loss investigation – PIXE”, The 6th International Conference on PIXE and its Analytical Applications, Waseda, Tokyo, Japan, July 20-24, (1992).

[4] Racolta P.M.,.Popa-Simil L., Alexandreanu B., Mateescu L., “Thin layer activation-based evaluation of tribological behaviour of light ion-implanted metallic samples”, Nuclear Instruments and Methods in Physics Research Section B: Beam Interactions with Materials and Atoms Volumes 127–128, Pages 949-953, 2 May (1997).

[5] Susumu Amemiya, Toshio Masuda, Liviu PopaSimi-“Pixe analysis of atmospheric particulate matter collected at various places “, Applied Radiation and Isotopes, (1995)

[6] Amemiya, Susumu & Masuda, Toshio & Popa-Simil, Liviu & Mateescu, Liviu, “Comparative analysis of aerosols elemental distribution in some Romanian regions”, Nuclear Instruments & Methods in Physics Research Section B-beam Interactions with Materials and Atoms -NUCL INSTRUM METH PHYS RES B. 109. 450-458, (1996).

[7] Innegraeve, O, Blanchet, X, Muntele, C I, Muntele, I C, Zimmerman, R L, Popa-Simil, L, Voiculescu, D, Racolta, P M, and Ila, D., “PIXE pollution studies across Europe”. Nuclear Instruments and Methods in Physics Research. Section B, Beam Interactions with Materials and Atoms, United States., (2002).

[8] Susumu Amemiya, Toshio Masuda, Liviu Popa-Simil, Claudiu Muntele, Dana Voiculescu and Petru Mihai Racolta, “Environmental Studies In Some Romanian Regions”, International Journal of PIXE, Vol. 09, No. 1&2, pp. 29-33 (1999)

[9] Popa-Simil L., “A Bio-PIXE micro-elemental mapping analyses approach” July 16-18,1992, Sendai,Japan International Symposium on Bio-PIXE (1992)

[10] Popa-Simil L., “Forensics environment characterization mobile device”, LANL communications, (2004).

STATUS REPORT OF THE N_TOF FACILITY AFTER THE 2ND CERN LONG SHUTDOWN PERIOD

N. PATRONIS for the n_TOF collaboration
European Organization for Nuclear Research (CERN)
Geneva, Switzerland
and
Department of Physics, University of Ioannina
Ioannina, Greece
Email: npatronis@uoi.gr

Abstract

During the second long shutdown period of CERN, several upgrade activities took place at the n_TOF facility. The most important ones where the replacement of the lead spallation target with a next generation liquid nitrogen cooled lead target and the establishment of a new experimental area at a very short distance from the target. In this contribution, the core commissioning actions are described along with very preliminary results. Furthermore, some indicative current and future measurements are briefly reported.

1. INTRODUCTION

The neutron time-of-flight (n_TOF) facility is based on the idea of Carlo Rubbia [1] of establishing a high intensity neutron source at CERN by taking the advantage of the on-site accelerator complex. The facility became operational in 2001. The motivation for the construction of this neutron time-of-flight facility was the deduction of high accuracy nuclear data for energy applications [2] and nuclear astrophysics studies [3].

In particular, a main activity at the n_TOF facility is to obtain nuclear data relevant for the development of innovative systems for energy production and nuclear waste transmutation, through accelerator-driven systems (ADS) and Generation IV fast neutron reactors [4]. High accuracy, high precision and high-resolution cross section data are needed, in a wide energy range, for a variety of major and minor actinides [5], as well as for coolant, spallation and structural materials [6]. Considering also that all the chemical elements of the cosmos, heavier than iron, are mainly produced through neutron capture reactions the second major branch of scientific research within n_TOF is oriented to the study of neutron induced reactions of astrophysical interest [3].

Since its first year of operation and up to the year 2018, the n_TOF facility went through different phases of operation as defined by significant upgrades/milestones. During the 2nd long shutdown period of CERN (LS2), several upgrade actions of the n_TOF facility were realized. Within this contribution, the upgrade activities of the facility will be briefly described along with the performed commissioning activities.

2. THE N_TOF FACILITY

The neutron production at n_TOF is based on spallation reactions induced by 20 GeV proton pulses delivered from the CERN Proton Synchrotron (PS) with a nominal intensity of 7 - 8 × 10^{12} protons/pulse. The maximum repetition rate of the delivered proton pulses is 0.8 Hz while the time width of each pulse is 7 ns (rms) allowing for excellent energy resolution, even in the GeV neutron energy region.

Fig. 1 shows a layout of the facility with the two established experimental areas: Experimental Area 1 (EAR-1), located at the end of a horizontal 185 m long flight path, was commissioned in 2001 and is used for measurements requiring very high neutron energy resolution. The recently commissioned (2014) vertical Experimental Area 2 (EAR-2) is located at a much shorter distance of 19 m, providing high neutron flux for measurements on small and/or radioactive samples. In both experimental areas, charged particles are removed by the corresponding “sweeping magnets” while the beam aperture is defined through two collimators and other additional shielding elements. In this way, well defined and well-shaped neutron beams result along with low background conditions. The main characteristics of the two experimental areas of the n_TOF facility are summarized in Table 1.

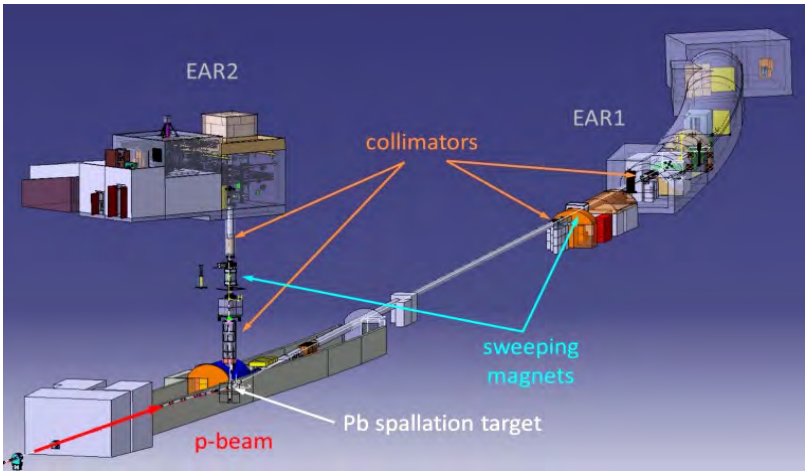

FIG. 1. The layout of the n_TOF facility at CERN. The proton beam, the lead spallation target and the main components of each beam line are presented

TABLE 1. MAIN CHARACTERISTICS OF THE EXPERIMENTAL AREAS OF THE n_TOF FACILITY

	EAR 1	EAR 2
Energy range	10 meV – 1 GeV	10 meV - 100 MeV
Energy resolution	10^{-4} – 10^{-2}	10^{-3} – 10^{-2}
The two options of neutron beam collimator ∅ (cm)	1.8/8.0	3.0/6.7
Neutrons/pulse for each neutron beam collimation option	5.5×10^5 / 1.2×10^7	2.2×10^7 / 2.0×10^8

3. UPGRADE ACTIONS DURING LS2

During the CERN 2nd Long Shutdown period (LS2) within the years 2019-2020 several upgrade activities were realized at the n_TOF facility leading to a successful transition into its 4th phase of operation.

The most important upgrade (action) was the replacement of the lead spallation target that served the facility for more than ten years with a new target. The new spallation target is a sliced, liquid nitrogen cooled lead target. More details on the new lead spallation target can be found in [7].

The second major development during the LS2 period was the establishment of a new experimental area located at about 3m distance on the side of the lead spallation target aiming mostly to neutron activation studies. This new experimental area, named as NEAR station [8], offers a much higher neutron flux than EAR1 and EAR2. The enhanced neutron flux is instrumental when limitations on the sample mass are imposed, as for instance when radioactive samples are considered. In the activation area of the NEAR Station, nuclear astrophysics measurements are foreseen after appropriate filtering of the neutron beam towards quasi Maxwellian shaped energy distributions that correspond to different stellar temperatures. The proof-of-principle of beam energy filtering using B4C filters is one of the approved and running experiments of the n_TOF 2022 campaign [9]. Besides the NEAR activation area, the irradiation NEAR sub-area is also operational, with material irradiation hardness studies taking place already in 2022. In this sub-are the samples are placed in specially designed air-tight holders and the handling of the samples is performed by a robot.

Besides the aforementioned major upgrade actions, several additional significant developments of the n_TOF facility took place during LS2. For instance, the collimator system of EAR1 was replaced with a new one that allows much faster exchange between different beam apertures. Furthermore, the EAR1 beam line sweeping electromagnet was replaced by a permanent magnet allowing stable operation and zero energy consumption.

Moreover, in addition to upgrades improving the neutron beam characteristics, the n_TOF teams took advantage of the LS2 period to develop, characterize and to deliver innovative detection setups (e.g. [10, 11]) that provide the ability to perform a new series of measurements and to investigate previously unexplored physics cases.

4. COMMISSIONING ACTIVITIES AFTER LS2

Given the important upgrades during LS2, the neutron beams of both TOF experimental areas (EAR1 & EAR2) of the n_TOF facility were commissioned thoroughly. For this purpose, different detection setups were utilized. Concerning the flux determination, ^{235}U(n,f), ^{10}B(n,a) and ^{6}Li(n,α) where used as reference reactions by applying different setups as given in Table 2 and depicted in Fig.2 and Fig. 3. Besides the neutron beam flux, the beam spatial profile was determined by means of the position sensitive PPAC detectors and by 3x3 mm Timepix detectors [12]. The neutron energy resolution was studied by measuring well known neutron resonances of different neutron capture reactions using liquid scintillation C_6D_6 γ-ray detectors. The detection setups and the corresponding reference reactions that were used are summarized in Table 2.

The analysis of the commissioning data is ongoing. Preliminary results show that in EAR1 the neutron flux is not very different with respect to the previous phase, while for EAR2 a significant increase in the neutron flux is expected along with much smoother neutron energy distribution and improved neutron energy resolution.

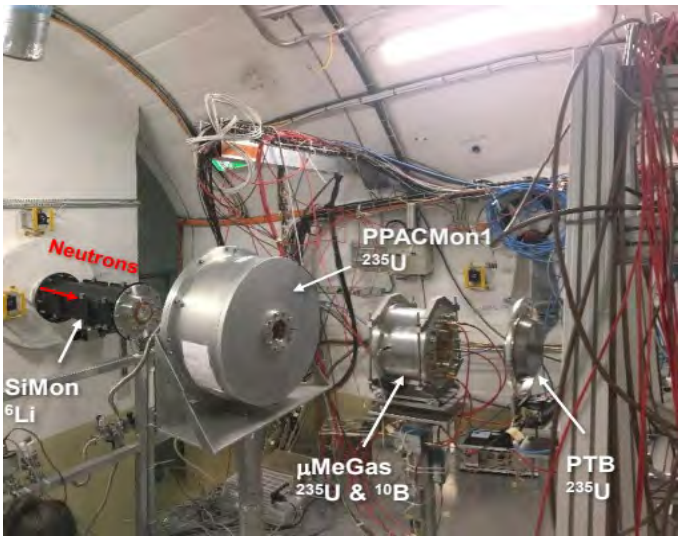

FIG 2. The EAR1 flux measurement setup. The four detection setups along with the adopted reference sample can be seen.

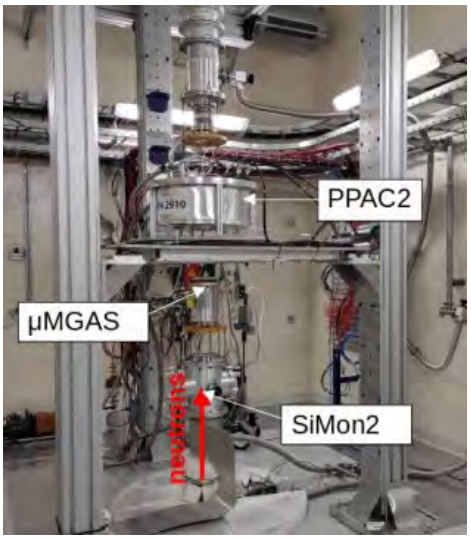

FIG 3. The EAR2 flux measurement setup. The three detection setups can be seen.

TABLE 2. ADOPTED EXPERIMENTAL SETUPS & METHODS FOR THE n_TOF PHASE 4 COMMISSIONING

Detector	EAR 1	EAR 2
Micromegas/flux	^{235}U(n,f), ^{10}B(n,α)	^{235}U(n,f), ^{10}B(n,α)
PPAC/flux& beam profile	^{235}U(n,f)	^{235}U(n,f)
Silicon Monitor/flux	^{6}Li(n,α)	^{6}Li(n,α)
PTB fission chamber [17]/flux	^{235}U(n,f)	---
C_6D_6/resolution function	^{197}Au(n,γ), ^{nat}Ir(n,γ), ^{nat}Fe(n,γ), ^{nat}Si(n,γ)	^{197}Au(n,γ), ^{nat}U(n,γ), ^{nat}Ir(n,γ), ^{nat}Fe(n,γ), ^{77}Se(n,γ)
TimePix	PE for n,p conversion	PE for n,p conversion

5. CONCLUSIONS AND OUTLOOK

During the 2nd Long Shutdown period of CERN, significant upgrade actions of the n_TOF facility were successfully accomplished, with the most important ones being the replacement of the lead spallation target with a new one and the establishment of the NEAR station. These significant changes define the starting point of the 4th Phase of operation of the n_TOF facility. Thanks to the development of innovative detection setups [10,11], the experimental investigation of previously unexplored physics cases becomes feasible (e.g., ^{79}Se(n,γ)[13]). In current and future experimental campaigns, an ambitious physics program is being realised, including nuclear astrophysics studies, fission reaction measurements (e.g. ^{243}Am(n,f) [14]), detector development and proof-of-principle studies (e.g. [15], [16]).

REFERENCES

[1] C. RUBBIA et al., CERN-LHC-98-002-EET, CERN, Geneva, 1998.
[2] M. SALVATORES, J. Nucl. Sci. Tech. Suppl. 2 (2002) 4-12.
[3] N. COLONNA et al., Eur. Phys. J. Web of Conf. 165 (2017) 01014.
[4] G. ALIBERTI et al., Ann. Nucl. Energy 22 (2006) 700-733.
[5] N. COLONNA et al., Eur. Phys. J. A 56 (2020) 48.
[6] F. GUNSING et al., Eur. Phys. J. Plus 131 (2016) 371.
[7] R. ESPOSITO et al., Phys. Rev. Acc. And Beams 24 (2021) 093001.
[8] M. FERRARI et al., arxiv.org, arXiv:2202.12809v2 (2022), arXiv:2202.12809v2
[9] M. E. STAMATI et al., CERN-INTC-2022-008 ; INTC-P-623 (2022), https://cds.cern.ch/record/2798978
[10] V. BABIANO et al., Eur. Phys. J. A 57 (2021) 197.
[11] C. DOMINGO-PARDO, Nucl. Instr. And Methods in Phys. Res. A 825 (2016), 78
[12] X. LlOPART et al., Nucl. Instr. And Methods in Phys. Res. A 581 (2007), 485
[13] V. BABIANO et al., CERN-INTC-2020-065 ; INTC-P-580 (2020), https://cds.cern.ch/record/2731962
[14] N. PATRONIS et al., CERN-INTC-2020-048 ; INTC-P-566 (2020), https://cds.cern.ch/record/2730930
[15] M. BARBAGALLO et al., CERN-INTC-2021-025 ; INTC-I-230 (2021), https://cds.cern.ch/record/2765698
[16] L. COSENTINO et al., CERN-INTC-2022-019 ; INTC-P-629 (2022), https://cds.cern.ch/record/2809189
[17] D.B. GAYTHER, Metrologia 27 (1990), 221

THE NEUTRON FACILITY AT NCSR 'DEMOKRITOS' AND NEUTRON ACTIVATION RESEARCH ACTIVITIES OF NTUA

R. VLASTOU
National Technical University of Athens
Athens, Greece
Email: vlastou@central.ntua.gr

Abstract

At the 5.5 MV Tandem T11/25 Accelerator Laboratory of NCSR "Demokritos" quasi-monoenergetic neutron beams can be produced in the energy ranges ~ 15-21 MeV by means of the $^{3}H(d,n)^{4}He$ reaction, ~ 4-11 MeV via the $^{2}H(d,n)^{3}He$ reaction, ~ 2.0-5.3 MeV using the $^{3}H(p,n)^{3}He$ reaction and ~120-650 keV via the $^{7}Li(p,n)^{7}Be$ reaction. The maximum flux has been determined to be of the order of 10^{5}-10^{6} n/cm^{2}s, implementing reference reactions, while the flux variation of the neutron beam is monitored using a BF3 detector and a BC501A scintillator. The neutron beams have been characterized using the multiple foil activation technique as well as extensive simulations and have been used for cross section measurements of neutron induced reactions implementing again the activation technique.

1. INTRODUCTION

Studies of neutron induced reactions are of considerable interest, not only for their importance to fundamental research in Nuclear Physics and Astrophysics, but also for practical applications in medicine, nuclear technology, dosimetry and industry. The main technological applications are related to the design of innovative Generation-IV reactors and Accelerator Driven Systems (ADS) for the future production of clean and safe nuclear energy as well as for the transmutation of nuclear waste. All these tasks require improved nuclear data and cross sections of high precision for neutron induced reactions on various isotopes. It is thus of major importance that the performance of the neutron sources is well understood and that the experimental conditions are well characterized.

In view of the above remarks and in absence of time-of-flight capabilities, the neutron facility at the Athens 5.5MV tandem accelerator of NCSR "Demokritos" has been characterised by means of Monte Carlo simulations using mainly the code MCNP and the multiple foil activation technique. The high energy neutron beams produced via the $^{2}H(d,n)^{3}He$ and $^{3}H(d,n)^{4}He$ reactions, have been extensively used for threshold reaction cross section measurements on various isotopes with the activation technique, while the low energy neutron beams from the $^{3}H(p,n)^{3}He$ reaction have been used for in-beam fission cross section measurements on actinides with Micromegas detectors.

The details of the description and the characteristics of the neutron production facility will be presented in this paper along with an overview of the neutron activation campaign.

2. THE NEUTRON FACILITY

The neutron facility at the tandem accelerator of NCSR "Demokritos" can deliver quasi-monoenergetic neutron beams at different energies through the following four reactions:

- ~ 120 – 650 keV via the $^{7}Li(p,n)^{7}Be$ reaction
- ~ 2 – 5.3 MeV via the $^{3}H(p,n)^{3}He$ reaction
- ~ 4.0 – 11.4 MeV via the $^{2}H(d,n)^{3}He$ reaction
- ~ 16 – 20 MeV via the $^{3}H(d,n)^{4}He$ reaction

The target assemblies for all these reactions are air cooled during the proton or deuteron beam irradiations. Two collimators of 5- and 6-mm diameter are used and the beam current is measured both at the collimators and the target and is kept at ~ 700nA - 1μA. The tandem accelerator is currently under major upgrade through the national research infrastructure grant CALIBRA/EYIE and the beam current is expected to be considerably increased in the near future. The flux variation of the neutron beam is monitored by a BF3 detector placed at a distance of 2-3 m from the neutron producing target. The spectra of the BF3 monitor are stored at regular time

intervals (~100sec) in a separate ADC during the irradiation process, while the absolute flux of the beam is obtained with respect to the cross section of reference reactions (^{27}Al(n,α), ^{197}Au(n,2n) and ^{93}Nb(n,2n)) and varies from 10^5-10^6n/cm^{2}s. The beam current on the target is also recorded in another ADC during the same time intervals, in order to test the reliability of the BF3 counter during long irradiation periods. In addition, a BC501A scintillator detector is used for the investigation of the neutron beam energy distribution.

A neutron source is considered mono-energetic when the energy spectrum consists of a single line with an energy width which is much less than the energy itself. Such mono-energetic neutrons can be produced by two-body reactions; however, a real source will not only produce these primary neutrons, but also "parasitic" ones, which vary in energy from the thermal region up to a few MeVs. Parasitic neutrons mainly stem from a) deuteron break up reactions, such as ^{3}H(d,pn)^{3}H, ^{2}H(d,n)^{3}He, which start to contribute significantly above 3.2MeV deuteron energy b) from reactions of the d and p beam with the target material, as for example Mo, Ti and Cu and reactions with C, due to the carbon built up in the target and the beam line and even with O due to oxidization processes c) moreover, the deuteron beam that is implanted in the target yields background neutrons from the ^{2}H(d,n)^{4}He reaction. In the case of gas targets the contribution from these background neutrons can relatively easily be determined via gas-in/gas-out measurements, for solid targets however, the task to perform a blank measurement using a non-tritium containing dummy target is a somewhat more demanding task d) finally, another contribution to the parasitic neutrons is coming from scattering of neutrons from the walls, ceiling and objects in the experimental room and the experimental set up, leading to a low energy tail in the neutron spectrum.

The study of neutron energy spectra generated by all the four above mentioned reactions, is carried out with detailed Monte Carlo simulations using the MCNP5 code [1]. The description of the neutron source imported in MCNP5 is generated by the NeuSDesc (Neutron Source Description) code [2]. The program takes into consideration the energy loss, energy spread and angular straggling of the protons or deuterons in the target assembly through the program SRIM 2008 and calculates average neutron energies, fluences and resolutions. The details of the neutron beams produced via these four reactions along with results from different techniques used for the neutron beam characterisation, will be presented below.

2.1. The ^{7}Li(p,n)^{7}Be reaction

For the neutron production via the ^{7}Li(p,n)^{7}Be reaction, a ^{7}LiF target on Al backing is used along with proton beams in the energy range 1.9 – 2.4 MeV to produce purely mono-energetic neutrons at zero degrees between 120 keV and 650 keV, respectively. At proton energies above 2.4 MeV, neutron emission to the 1st excited state in ^{7}Be at 429 keV is possible and produces a second group of mono-energetic neutrons. The BC501A scintillator detector was used to investigate the neutron energy spectra from this reaction. By rejecting the gamma pulses, the recoil energy spectra in the liquid scintillator can be reconstucted, as shown in Fig.1 in the case of the ^{7}Li(p,n)^{7}Be reaction at proton beam energies set at 2.3 and 2.7 MeV, respectively. At 2.3 MeV, the recoil spectrum corresponds to purely mono-energetic neutrons of 0.57 MeV, as indicated by the arrow, while at 2.7 MeV, apart from the main production of neutrons at 0.997 MeV, a second bump appears in the spectrum corresponding to the 0.502 MeV neutrons arising from the first excited state of ^{7}Be.

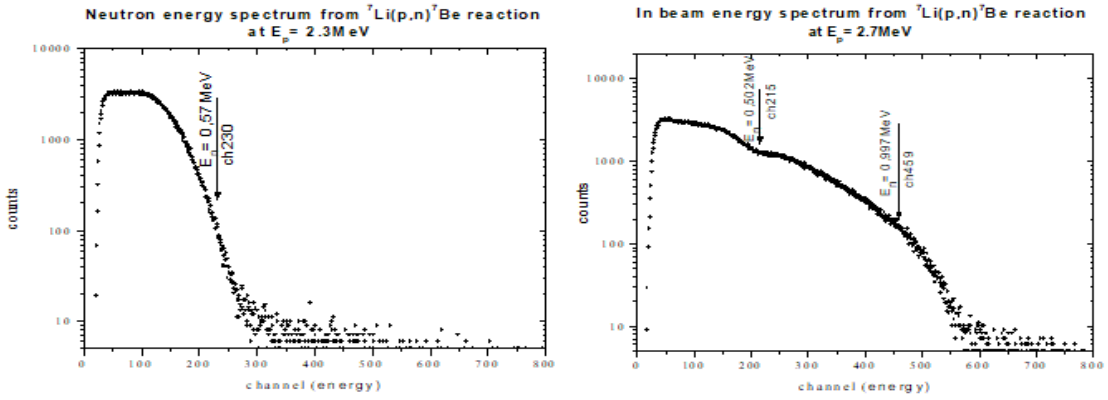

FIG. 1. Recoil energy spectra in the BC501A liquid scintillator, using the neutron beam from the ^{7}Li(p,n) reaction at 2.3 and 2.7 MeV.

The spectra shown in Fig. 1 were used for the energy calibration of the BC501A scintillator detector in the low energy region.

2.2. The $^{3}H(p,n)^{3}He$ reaction

For the neutron production via the $^{3}H(p,n)^{3}He$ reaction, a Ti-tritiated target is used, consisting of a 2.1 mg/cm^2 Ti-T layer on a 1mm thick Cu backing for good heat conduction. Two 5μm Mo foils were placed in front of the target in order to degrade the beam energy. Proton beams in the energy range 3.4 – 6.5 MeV have been used to produce neutrons between 2 and 5.3 MeV. Purely mono-energetic neutrons are generated in the range ~ 2-3 MeV, while at higher energies (p,n) reactions on Mo, Ti, Cu, C and ^{2}H implanted in the TiT target from previous irradiations, become important and can lead to distinct peaks in the neutron spectra [3]. Extensive MCNP5 simulations coupled with NeuSDesc results, have been performed, as described in [3]. In an attempt to investigate the parasitic neutrons in more detail and include all the interactions of the proton beam with the experimental setup used to generate neutrons, biased Monte Carlo simulations have been performed implementing the GEANT4 code [4]. Preliminary results for the 2.5 MeV neutrons are presented in Fig.2.

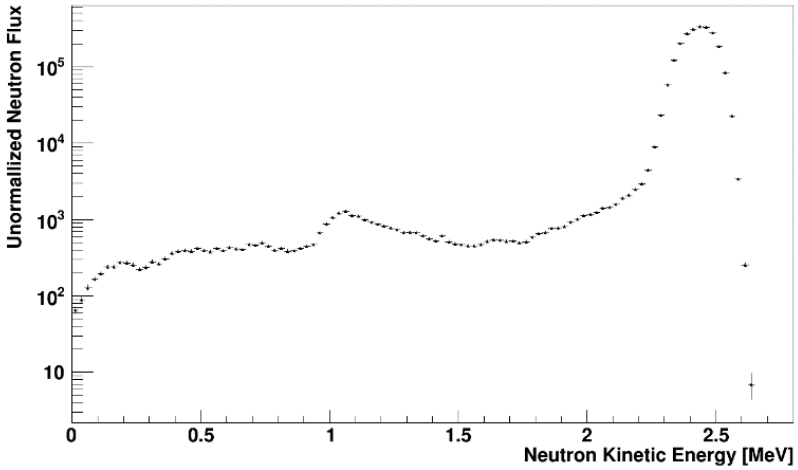

FIG. 2. Simulated neutron flux for the $^{3}H(p,n)$ reaction at 2.5MeV implementing the GEANT code[5].

2.3. The $^{2}H(d,n)^{3}He$ reaction

For the neutron production via the $^{2}H(d,n)^{3}He$ reaction, a 3.7 cm long and 1 cm diameter deuterium gas cell pressurized to ~1 atm is used, with a 5μm Mo entrance foil and a 1mm Pt foil for the beam stop. The neutrons lie in the energy range ~ 4-11.2 MeV, at the corresponding deuteron beam energies 0.8-8.2 MeV. The energy spectrum and the characteristics of the beam have been studied by means of the multiple foil activation technique in combination with the SULSA code [6] as well as with the liquid scintillator BC501A and deconvolution of its recoil energy spectra using the DIFBAS code [7]. The results from this investigation are described in detail in [8] and are shown in Fig. 3. These results are in consistency with the neutron energy spectra deduced with the code SULSA, within the limitations of the multiple foil activation technique.

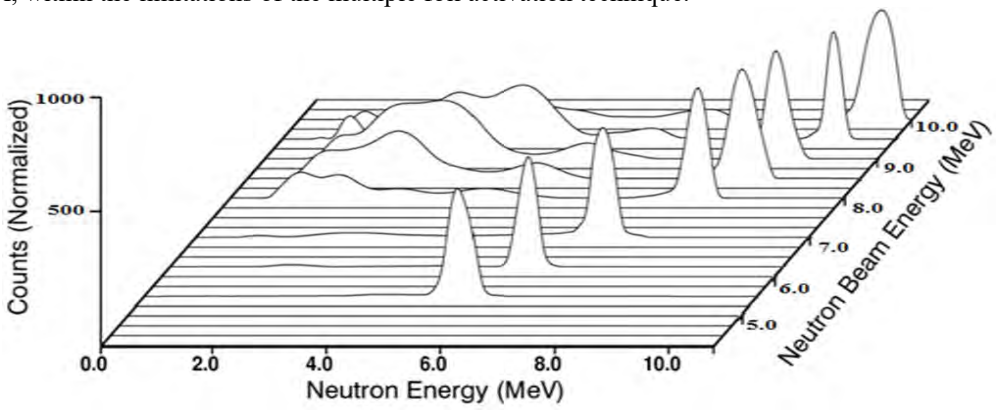

FIG.3. The energy distribution of the neutron flux from the $^{2}H(d,n)$ reaction deduced via the DIFBAS code.

In addition, MCNP5 simulations have been performed in order to study the neutron flux energy distribution around 0° with respect to the beam line axis.

2.4. The $^{3}H(d,n)^{4}He$ reaction

For the neutron production via the $^{3}H(d,n)^{4}He$ reaction, the same Ti-tritiated target used in the case of the $^{3}H(p,n)^{3}He$ reaction, is implemented. The produced neutrons lie in the region 15.3-20.9 MeV at the corresponding deuteron beam energies 2.0-4.3 MeV. The study of neutron energy spectra generated by deuterons on the Ti-tritiated target was carried out utilizing the NeuSDesc (Neutron Source Description) output file for Monte Carlo simulations using the MCNP5 code. Furthermore, several foils were irradiated at different energies, most of them corresponding to reference reactions, in order to extract experimentally the neutron beam fluence. By taking into account the detailed geometry of the experimental setup for each irradiation, the neutron fluence in the successive foils was simulated and the results were compared with the experimental ones. As an example, the results at (17.9 ± 0.3) MeV for the irradiation of Al-Au-Ir-Al-Er-Al-Au sequence of foils in the target assembly, are presented in Fig. 4. The experimental and simulated neutron fluence in the successive foils seem to be in very good agreement, indicating that the simulations are successful and can thus be trusted for the estimation of the neutron fluence.

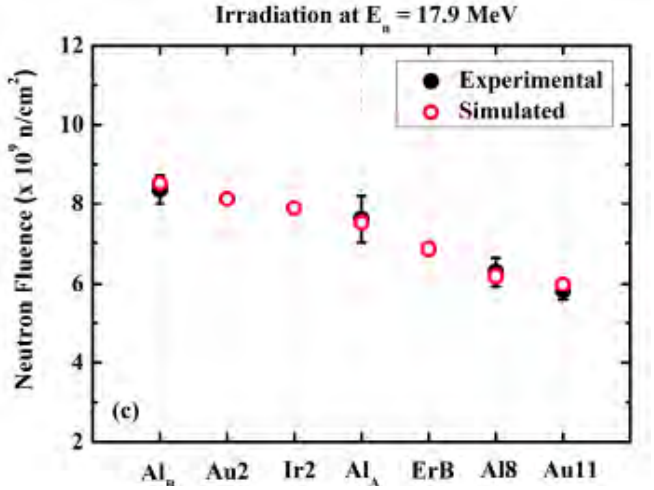

FIG. 4. Experimental neutron fluences in the reference foils along with the simulated ones, obtained by means of the MCNP5 code, for the irradiations at 17.9MeV.

The simulated neutron fluence energy spectrum at 17.9 MeV is shown in Fig. 5.

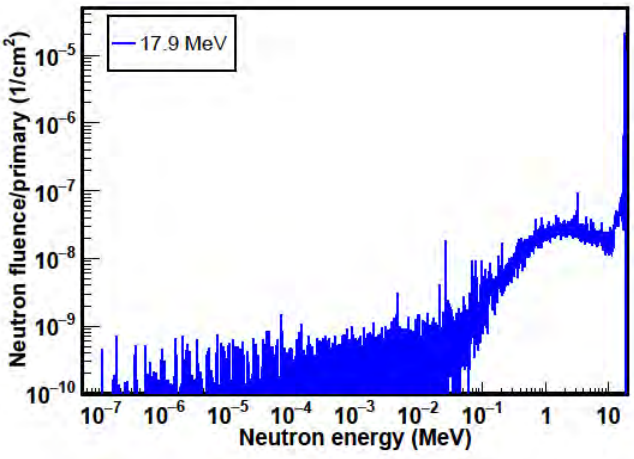

FIG. 5. Simulated neutron fluence from MCNP5 at 17.9MeV.

The long tail of parasitic neutrons is illustrated in Fig. 5, which is about three orders of magnitude lower than the main beam. However, these neutrons may cause significant problems in cross section measurements of

reactions which are sensitive to low energy neutrons, such as fission reactions. Thus, in facilities where the neutron ToF technique is not applied, only reactions with a high energy threshold can be safely measured with mono-energetic neutrons, since the low energy parasitic neutrons cannot affect the cross-section measurements, provided that the reference reaction used for the determination of the absolute neutron flux also has a threshold in the same energy region.

3. ACTIVATION CROSS SECTION MEASUREMENTS

3.1. Experimental procedure

The neutron beam at NCSR "Demokritos" has been extensively used over the past 15 years by the NTUA (National Technical University of Athens) group, for the measurement of (n,2n) and occasionally (n,3n), (n,p), (n,α) reaction cross sections on several isotopes of Am, Hf, Ir, Ge and Au, with the activation technique [9-20]. For all these measurements neutron beams were used in the energy region from ~7-11 MeV produced via the $^{2}H(d,n)^{3}He$ reaction as well as from ~15-21 MeV derived via the $^{3}H(d,n)^{4}He$ reaction. High purity foils were used for these measurements and were stacked between two Al reference foils for the irradiation. Apart from the $^{27}Al(n,\alpha)$ reference reaction other reactions such as $^{197}Au(n,2n)$ and $^{93}Nb(n,2n)$ have been also used to accurately determine the neutron flux. After the end of the irradiation the induced γ-ray activity of the samples and the reference targets were measured off- line by HPGe detectors. The activity measurements of all samples were normally carried out at a distance of ~10 cm from the detector window, thus there was no need for significant pile-up or true coincidence summing effect corrections. At the same distance, a ^{152}Eu point source was placed in order to determine the absolute efficiency of each detector. Additionally, the experimental set up was always simulated with the use of the MCNP code, for the estimation of the neutron flux, the self-absorption of the γ-rays in the sample, the effect of parasitic neutrons which accompany the beam etc.

3.2 Theoretical calculations

All the above-mentioned reactions are relevant to practical applications for nuclear technology, high energy neutron dosimetry, detector physics, medical applications etc., but they are also important for the investigation of model parameters in statistical model calculations. Thus, the study of the measured reactions is usually accompanied by theoretical cross section calculations in the framework of the Hauser-Feshbach theory, using the latest versions of the EMPIRE [21] and TALYS [22] codes. The calculations are carried out in a wide energy range for the measured data of each reaction as well as for the data reported in literature.

From all the measured neutron induced reaction cross sections on isotopes of Am, Hf, Ir, Ge and Au, the reactions on Au and Ir will be mentioned in more detail, since the (n,2n) reactions on ^{191}Ir and ^{197}Au lead to the population of both ground and isomeric states of the residual nuclei. The theoretical study of these reactions, due to the existence of high spin isomeric states, is a powerful tool for obtaining information on the structure of the involved nuclei and thus constitutes an open field of study. The simultaneous reproduction of the isomeric and ground state cross sections along with other channels where data are available in literature, sets a significant constraint, rendering theoretical calculations quite sensitive to the choice of specific nuclear model parameters.

In the case of the $^{197}Au(n,2n)^{196}Au^{g+m1+m2}$ and $^{197}Au(n,2n)^{196}Au^{m2}$ reactions, cross sections were measured in the energy range 9.0-10.5 MeV [13] and 15.3-20.9 MeV [18]. This data, along with all other data available in literature, as well as data for the (n,3n), (n,elastic), (n,α), (n,p) and (n,total) competing reactions, were simultaneously reproduced in a satisfactory way by both EMPIRE and TALYS calculations [18]. The high angular momenta treatment in the EGSM level density model in the EMPIRE code, helped to reproduce the experimental values of the isomeric cross sections as it affects more efficiently the spin distribution of level densities above the critical excitation energy. In TALYS, a small increase of the spin cut-off parameter via the "Rspincut" keyword, was sufficient to successfully reproduce the cross section of the isomeric state along with all other competing channels.

In the case of the $^{191}Ir(n,2n)^{190}Ir^{g+m1}$ and $^{191}Ir(n,2n)^{190}Ir^{m2}$ reactions, cross sections were measured in the energy range 10-11.3 MeV [12] and 15.3-20.9 MeV [19]. This data, along with all other data from literature, as well as data for the (n,3n), (n,p) and (n,total) competing reactions and data for the other isotope $^{193}Ir(n,2n)$, $^{193}Ir(n,\alpha)$, ^{193}Ir (n,p) and ^{193}Ir (n,total) were reproduced in a satisfactory way by the EMPIRE and TALYS

calculations [19]. It is interesting to note that these calculations were performed with a similar combination of model parameters that had also been successfully used in the case of the neighbouring ^{197}Au nucleus. This constitutes an encouraging confirmation of how accurately the theoretical models can reproduce the experimental results in this mass region. These similarities in the theoretical parametrization are not that surprising since both Au and Ir nuclei belong to the transitional region from well deformed to spherical nuclei near the shell closure Z = 82 (Os–Pb region), where high spin intruder configurations result in high spin isomeric states unable to communicate with neighboring states. It would be quite interesting to continue this investigation for the next nucleus Tl in this mass region. Indeed, measurements are planned to be carried out in the near future for the ^{203}Th(n,2n) reaction at the neutron facility of NCSR "Demokritos".

4. SUMMARY

Neutron beams are produced at the tandem accelerator of NCSR "Demokritos" in Athens at energies varying in the range from about 120keV to 21MeV by means of the following proton and deuteron induced reactions: ^{7}Li(p,n)^{7}Be, ^{3}H(p,n)^{3}He, ^{2}H(d,n)^{3}He and ^{3}H(d,n)^{4}He. A comprehensive understanding of the energy dependence of the produced neutron beam flux is of major importance for the reliability of neutron induced reaction cross section measurements. Thus, for all these four reactions several techniques have been used for this investigation, such as the unfolding method applied to the multiple foil activation results and the deconvolution of recoil energy spectra taken via the BC501A liquid scintillator detector at various neutron energies. Furthermore, extensive Monte Carlo simulations by means of the MCNP5 and GEANT4 codes have been performed to study the neutron energy spectra in conjunction with other experimental techniques like gas-in gas-out tests, irradiations with and without a Cd foil in front of reference foils etc. The neutron beams have been used for the measurements of (n,2n) and occasionally (n,3n), (n,p), (n,α) reaction cross sections on isotopes of Am, Hf, Ir, Ge and Au, with the activation method. The investigation of these reaction cross sections is followed by theoretical calculations implementing the codes EMPIRE and TALYS. The tandem accelerator at NCSR "Demokritos" is currently under renovation and in the near future these techniques will be applied again for the investigation of the upgraded neutron beams, while the neutron activation measurements will continue to be an important research project of the Nuclear Physics group at the National Technical University of Athens.

ACKNOWLEDGEMENTS

Numerous members of the Nuclear Physics community in Greece have contributed to this work: the staff members M. Kokkoris, M. Diakaki, N. Patronis, A. Tsinganis, S. Harissopulos, A. Lagoyannis, M. Axiotis, P. Demetriou, M. Serris and mainly the PhD students V. Michalopoulou, A. Kalamara, A. Stamatopoulos, S. Chasapoglou, Z. Eleme, E. Georgali as well as many undergraduate and postgraduate students. They are all gratefully acknowledged.

Acknowledgements are also due to the project CALIBRA/EYIE (MIS 5002799), which is implemented under the Action "Reinforcement of the Research and Innovation Infrastructures", funded by the Operational Program "Competitiveness, Entrepreneurship and Innovation" (NSRF 2014-2020) and co-financed by Greece and the European Union (European Regional Development Fund).

REFERENCES

[1] J. ARMSTRONG et al., ed. C.J. Werner, MCNP Users Manual – Code Version 6.2, (LA-UR-17-29981, 2017)
[2] E. BIRGERSSON and G. LOEVESTAM, ''NeuSDesc-Neutron Source Description Software Manual,'' 2009. JRC Scientific and Technical Reports..and Technical Reports
[3] V. MICHALOPOULOU et al., Eur. Phys. J. A (2021) 57:277
[4] J. ALLISON et al., Nucl. Instr. Meth. in Phys. Res. A835(2016)186.
[5] K. KAPPERONI, MSc thesis, National Technical University of Athens, 2022.
[6] S. SUDAR, A solution for the neutron spectrum unfolding problem without using an input spectrum, INDC (HUN)-0261, IAEA, Vienna, 1989.
[7] M. TICHY, PTB Laboratory Report PTB-7.2-1993-1, Braunschweig,1993

[8] R. VLASTOU et al. Nucl. Instr. Meth. B269 (2011)3266
[9] G. PERDIKAKIS et al., Phys. Rev. C 73(2006)067601
[10] M. SERRIS et al., Nucl. Instr. Meth. Phys. Res. B261(2007)941
[11] S. GALANOPOULOS et al., Nucl. Instr. Meth. Phys. Res. B261(2007)969
[12] N. PATRONIS et al., Phys.Rev.C 75(2007)034607
[13] A. TSINGANIS et al., Phys.Rev.C 83 (2010)024609
[14] M. SERRIS et al., Phys. Rev. C 86(2012)034602
[15] A. KALAMARA et al., Nucl. Data Sheets 119 (2014)
[16] R. VLASTOU at al., Physics Procedia 66(2015)425
[17] A. KALAMARA et al., Phys.Rev.C 93(2016)014610
[18] A. KALAMARA et al., Phys.Rev.C 97(2018)034615
[19] A. KALAMARA, et al., Phys. Rev. C 98, 034607 (2018)
[20] R. VLASTOU et al., EPJ Web of Conferences 239, 01028 (2020)
[21] M. HERMAN et al., ‘‘Empire: Nuclear Reaction Model Code System for Data Evaluation,’’ Nuclear Data Sheets, vol. 108, no. 12, pp. 2655 – 2715, 2007. Special Issue on Evaluations of Neutron Cross Sections.
[22] A. KONING, S. HILAIRE and S. GORIELY, ‘‘TALYS-1.8,’’ tech. rep., 2015.

METALLACARBORANES FOR PROTON THERAPY USING RESEARCH ACCELERATORS: A PILOT STUDY

Teresa PINHEIRO
IBB, Instituto de Bioengenharia e Biociências, Departamento de Engenharia e Ciências Nucleares, Instituto Superior Técnico, Universidade de Lisboa
Lisboa, Portugal
Email: teresa.pinheiro@tecnico.ulisboa.pt

Luis C. ALVES
Centro de Ciências e Tecnologias Nucleares, Departamento de Engenharia e Ciências Nucleares, Instituto Superior Técnico, Universidade de Lisboa, Lisboa, Portugal

Victoria CORREGIDOR
Centro de Ciências e Tecnologias Nucleares, Departamento de Engenharia e Ciências Nucleares, Instituto Superior Técnico, Universidade de Lisboa
Lisboa, Portugal

Francesc TEIXIDOR
Institut de Ciència de Materials de Barcelona (ICMAB-CSIC), Campus UAB, 08193 Bellaterra Barcelona, Spain.

Clara VIÑAS
Institut de Ciència de Materials de Barcelona (ICMAB-CSIC), Campus UAB, 08193 Bellaterra Barcelona, Spain.

Fernanda MARQUES
Centro de Ciências e Tecnologias Nucleares, Departamento de Engenharia e Ciências Nucleares, Instituto Superior Técnico, Universidade de Lisboa
Lisboa, Portugal

Abstract

The feasibility of using an external beam microprobe facility to explore the biological effects generated by proton irradiation in cultured cells is demonstrated. An in-air irradiation set-up was developed that allows energy tuning and enables estimating the flux and dose deposition in cells. A pilot study on the effect new of metallacarborane molecules as radiosensitizer towards human glioblastoma cells was carried out. This served as a proof of concept for the enhancement effect of proton irradiation induced by the presence of boron in the compounds, which undergoes fusion via the $^{11}B(p,\alpha)\alpha\alpha$ reaction. Details of the experimental set-up and physical parameters measured are presented. Also, preliminary results of cell's irradiation and uncertainties are discussed anticipating the advances that have been achieved by our group in this field.

1. INTRODUCTION

The use of energetic proton beams offers advantages in cancer treatment including tumour confinement and higher LET (linear energy transfer). Recently, new drugs with greater selectivity for tumour cells that enable increasing the RBE (relative biological effectiveness) for protons have been investigated. These new drugs are constituted by carborane boron clusters, containing 10 atoms of boron each, coordinated by a central metal ion [1]. The theoretical background of the use of metallacarboranes as radiosensitizers is the presence of boron, which may increase the effect of protons on cell death due to the $^{11}B(p,\alpha)\alpha\alpha$ nuclear fusion reaction [2]. This reaction shows a major resonance near $E_p = 0.675$ MeV with isotropic distribution and a high cross section of the order of 1 barn. The reaction consists of a two-step sequential decay yielding three α-particles. The de-excitation of ^{12}C, the first intermediate reaction product, yields one α-particle with energy near 4 MeV and ^{8}Be, which in turns splits in two α-particles of 2.74 MeV each [3-5].

Due to these characteristics, the reaction has become very attractive in the context of medical applications of proton therapy as emitted α-particles range in water is of the order of a cell dimension. In this context, energetic

beams generated by research accelerators can be useful to demonstrate the potential of metallacarboranes as radiosensitizers for proton therapy. This is very important for proton therapy modality, as there is an urgent need to improve the efficacy of protons in cancer treatment. Thus, enhancing local dose inside tumours upon exposure to radiation, increasing RBE for protons, and reducing the effective radiation dose are factors that ultimately converge to improve the efficacy of treatment [1,6]. This can be achieved through a synergistic cell-killing effect of metallacarboranes when combined with radiation.

2. STUDY DESIGN

By using research accelerators to generate energetic protons and by extracting the proton beam to air, live cells can be irradiated under controlled conditions, and their dose-dependent viability subsequently assessed. Therefore, a pilot study was planned to demonstrate the enhancement effect of proton-boron reaction in cell-killing. To assess the biological effects, a tumour cell model (human glioblastoma, U87 cells) exposed to new metallacarborane compounds (Fe-carborane, FeC, and an iodinated analog, I_2FeC) was used. The cellular viability as a function of deposited dose will be used as the endpoint for the effect of proton irradiation. Details of the experimental setup, geometry of irradiation, energy tuning of the proton beam, physical parameters measured and calculated as well as cell irradiation protocol will be comprehensively described in the sections below.

3. EXPERIMENTAL SETUP

Experiments were done at ambient pressure using the external beam facility of the nuclear microprobe (Oxford Microbeams Ltd., UK) installed at the 2.5 MV single ended Van de Graaff accelerator of the IST (Instituto Superior Técnico, Universidade de Lisboa, Portugal) [7,8]. The technical details of the nuclear microprobe and external beam facility were previously described [8-10].

In Fig. 1 the schematic of the nuclear microprobe and experimental setup used in this study can be depicted. The beam is extracted from the vacuum chamber to air through an exit nozzle. In the particular set-up used in this study, a nozzle with 2.9 mm internal diameter was used to extract the beam through a 6.3 µm thick Mylar window and scanned over an area of interest. The 96-well plate (where the cells are incubated) was positioned perpendicular to the beam path on a x-y-z table. The distance of the sample (cell monolayer at the bottom of the wells) from the exit window was of 13.4 mm. In this pathway besides the 6.3 µm thick Mylar window of the exit nozzle, a 12.6 µm thick Mylar window covering the 96-well plate was used, separating the air path, which is fractionated in two sections, i.e., 2mm from the exit nozzle to the Mylar cover of the plate and 11.4 mm to the bottom of the well.

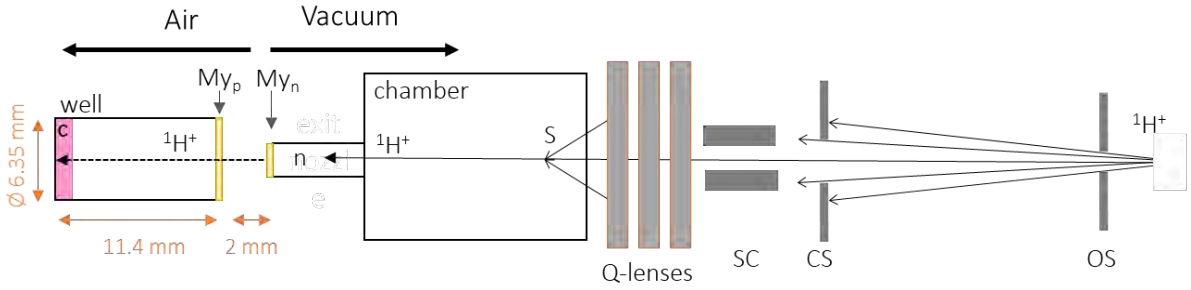

FIG. 1. The IST nuclear microprobe schematic (not on scale) including the external beam setup used for cell irradiation. The microprobe configuration consists of object slits (OS) for beam current control, collimation slits (CS) for beam divergence control, the magnetic quadrupole triplet (Q-lenses) [7] for beam focusing on the focus plane (S) inside the irradiation chamber (vacuum) where the sample is positioned. The scanning coils (SC) are located before the lenses. The vacuum chamber configuration accommodates several detectors [7,8] and enables the adaptation, at the rear, of a cylindrical cap having at its end a nozzle (n) supporting a vacuum tight extraction window (My_n). The schematic of the setup for cell irradiation in air represents one unit well of a typical 96-well plate for cell culture. In the used experimental configuration, the extracted $^1H^+$ beam encountered the cell monolayer (c) after traversing the air path and a Mylar foil (My_p) which covers the cell culture plate. The external set-up includes a x-y-z table for sample positioning, enables detectors for sample characterization (e.g., PIXE) and accommodates a minicamera that helps on sample visualization and alignment [9,10].

3.1. Calculation of the energy loss

The 2.0 MeV proton energy was tuned to ensure that the resonance energy near E_p = 0.675 MeV of the $^{11}B(p,\alpha)\alpha\alpha$ nuclear fusion reaction was reached at the sample cell layer. Both air and Mylar foils served as attenuators for the proton beam. The calculations were carried out using SRIM opensource software [11]. The sequence of attenuators consisted of: 1) Mylar foil of 6.3 µm thickness for extraction the proton beam from vacuum to air; 2) 2 mm air path; 3) Mylar foil of 12.6 µm thickness covering the 96-well plate where cells were incubated; 4) 11.4 mm air path. The beam encountered the cell layer with an entrance energy of 1.27 MeV. The energy loss in the cell layer was also simulated with SRIM, considering liquid water as a medium equivalent to a cell. The transmitted energy in 30 µm and 40 µm water (estimated cell layer thickness; see section 4) and corresponding LET is displayed in Table 1.

TABLE 1. SRIM simulations [11] of transmitted energy in the cell layer for an entrance energy of 1.27 MeV protons (simulation nº of particles =1000; values are x±SD) and the corresponding value of LET.

Cell Layer thickness (µm)	Transmitted energy (keV)	LET (keV/µm)
30	477±28	26.43
40	15±2	31.38

3.2. Beam focusing and scan size estimation

A proton beam of 2.0 MeV was focused (triplet of quadrupole lenses, Oxford Microbeams Ltd. [7]) in vacuum [7] to dimensions of ~3×4 µm^2. When the beam is extracted to air the spatial resolution degrades compared to analysis performed in vacuum, mainly due to beam divergence. For routine conditions (with beam currents of ~100 pA) typical spatial resolution of ~70×70 µm^2 can be achieved [8,10]. The beam resolution quality can be verified using a microscopy copper grid positioned at a convenient distance from the exit nozzle that allows the accommodation of a PIXE detector. Thus, scanning the beam over the sample an image of the grid can be obtained (Fig. 2-A). Most importantly, the grid imaging is an adequate methodology to define the scan dimension and to ensure that the irradiated area is the same for all the samples analysed in the same run. This can be done by setting a mask using the OMDAQ2007 acquisition software features (Fig. 2-B).

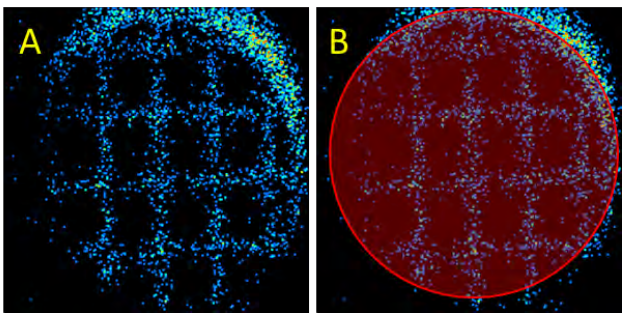

FIG. 2. Image of 50-mesh microscopy copper grid (A) recorded in air at the external microprobe setup and the same image with a mask over-imposed (red circle) delimiting the defined irradiation area (B). Grid specifications: 3.05mm external diameter; pitch 500 µm; hole 450 µm; bar 50 µm).

Although the diameter of the exit nozzle (2.9 mm) sets the limit of the maximum scanning area at the exit, beam divergence across the air path cannot be disregarded. As can be depicted in Fig. 2, the maximum dimensions of the scan at a position of the grid ~3 mm distant from the exit nozzle is larger than the whole area of the microscopy grid (3.05 cm diameter). Thus, to obtain more reliable dimensions of the scan at the position of irradiation on the x-y-z table, a commercial material was used, that emits a bright fluorescence (visible wavelengths) following proton irradiation (Fig. 3). The average size of the irradiated area over 3 runs was 0.134±0.006 cm^2, which represents an uncertainty < 5%. The illuminated area of the target provided the best possible estimation of the irradiation area which is required for further calculation of proton flux and dose.

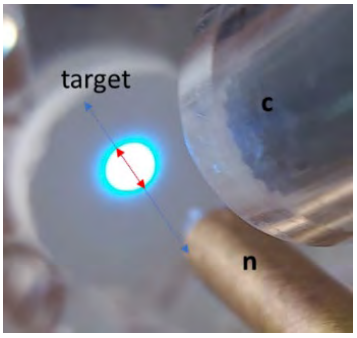

FIG. 3. Photograph of the standard material (target) during proton irradiation showing the bright fluorescence spot that corresponds to the scanned area. The red and blue arrows represent the diameters of the scan (unknown) and the target (known), respectively; n – tip of the nozzle (beam extraction system); c – mini-camera.

In the context of cell irradiation, other relevant parameter to consider is the homogeneous distribution of particles impinging over the sample surface in the defined area. As far as beam stability can be monitored (see section 3.3) the even distribution of protons during irradiation is guaranteed by setting the speed of the scanning (time spent by the beam at each beam position or pixel) at a convenient level (e.g., 10 μs). Therefore, the time required to perform a 256×256 pixels scan is ~ 0.65 s.

3.3. Charge measurement to estimate the flux of protons impinging on the cell layer

In this preliminary study the flux of protons was controlled on real time by monitoring the count rate measured by the acquisition system (OMDAQ2007). During cell irradiation the count rate was kept below 200 Hz, which corresponded to ~1.5-2.5×10^7 protons/s. To estimate the flux of protons impinging on the cell monolayer, the EBS (elastic backscattered spectrometry) spectra of a gold reference material was periodically analyzed to obtain a normalization factor, Q_f [12], to the live charge (Q_{live}), recorded in the acquisition system (OMDAQ2007). The spectra of the gold standard were collected in the vacuum chamber.

The flux can be estimated as in eq. 1:

$$Flux(nº\ of\ protons.cm^2.s^{-1}) = \frac{Q_{live} \times Q_f}{irradiation\ area} \qquad \text{Eq. 1.}$$

As reference, a spherical cell of 30 μm diameter irradiated with a flux of 2×10^8 protons.cm^{-2}.s^{-1} receives ca. 1600 protons/s.

To obtain the flux of protons arriving at the cell layers of each irradiated well, an average value of the charge measurements carried out during the entire irradiation run for each assay (before starting the irradiation of the wells, 3-wells intercalary measurements and after irradiation) was considered. Uncertainties in flux calculation were in a range of 20% to 40%, mainly due to fluctuations in beam current and consequently on charge measurements.

4. IRRADIATION OF CELL CULTURES

Glioblastoma U87 cells were grown in 96-well cell plates in an adequate number to form a monolayer. Two Fe carborane compounds, FeC and an iodinated analogue I_2FeC, were used in this study [1]. Cells were incubated for 24h with FeC and I_2FeC. Non-treated cells served as controls. The concentrations of the compounds were selected according to the cytotoxic activity study previously performed. The medium concentrations of FeC and I_2FeC used in this pilot study were 50 μM and 10 μM, respectively, which correspond to concentrations below the IC_{50} value.

After the incubation period the culture medium was replaced with fresh medium before irradiation to ensure that only viable cells remain attached to the bottom of the well and that the FeC and I_2FeC compounds taken up by the cells would be responsible for the observed effects. For each assay two sets of controls (non-treated cells) and cells treated with FeC and I_2FeC compounds were prepared, one was irradiated and another was non-irradiated. Twelve wells (one column of the 96-well plate) were considered in each assay for each condition tested, treated and controls, non-irradiated and irradiated (Fig. 5).

Just before proton irradiation, the excess culture medium was removed, ensuring that just the cell monolayer remains adherent at the bottom of the well with culture medium filling interstitial spaces between cells.

The U87 cell's dimensions are in the range of 20-30 µm. This way, a water equivalent depth of approximately 30-40 µm can be assumed for the cell layer and cells remain with minimal life supporting conditions until the end of the experiment.

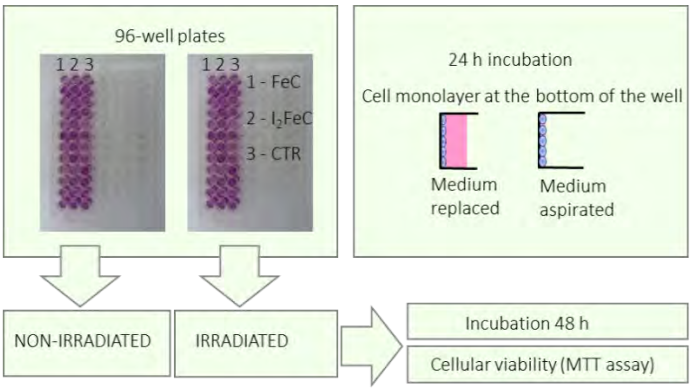

FIG. 5. Schematic of the proton irradiation assay.

The U87 cells were irradiated for 10 s at ambient pressure with a 1.27 MeV proton beam at the entrance of the cell layer, as described above, to ensure that boron resonance of 675 keV was reached within the cell layer. The effective dimensions of the scanned area over the cell layer was ~33% of the total area of the well. The estimated average dose delivered in each well was of 0.98 kGy/s to 1.17 kGy/s, whether considering a 30 or 40 cell layer thickness. In average it can be assumed that a dose of 1 kGy/s was delivered in each well.

The cellular viability as a function of deposited dose was used as the endpoint for the effect of proton irradiation. To this end, after U87 cell's irradiation, fresh medium was added, and cellular viability assessed after 48 h of incubation [13]. A decrease of the cellular viability after proton irradiation was observed for U87 cells. In controls, proton irradiation caused a decrease of approximately 20% relative to non-irradiated cells, whereas in FeC and I_2FeC treated cells a significant decrease of ca. 50% was observed (Fig. 6).

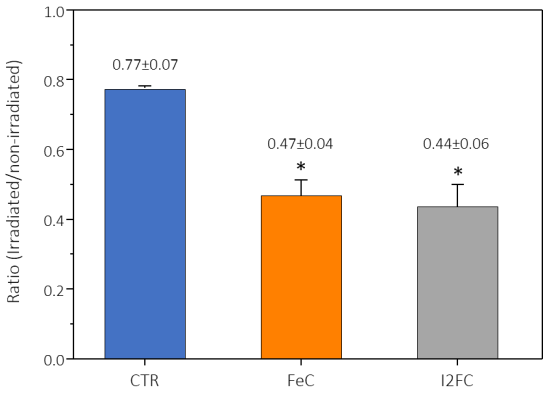

FIG. 6. Viability of U87 cells after proton irradiation, measured with a colorimetric method, the MTT assay. Ratios between irradiated and non-irradiated cells for controls and for those cells treated with FeC and I_2FeC compounds are plotted. Significant differences to non-irradiated cells (*) are indicated in the graph ($p<0.05$).

Noteworthy, only 33% of the cells in each well were irradiated and the viability assay reflects all the cells in the nonolayer (in each well). Nevertheless, a pronounced decrease in the viability of FeC and I_2FeC treated cells after proton irradiation was observed. The effect cannot be attributed to cytotoxicity of Fe carborane compounds against U87 cells. A screening of cytotoxic activity conducted before irradiation showed that for the concentrations used in this study only a small decrease in viability (5-15%) was observed in treated cells when compared to controls. All together the results suggest that a strong cell-killing effect is caused by the presence of Fe carborane compounds in cells following proton irradiation. Recent studies reported on the usefulness of other boron cluster's carriers as radiosensitizers for proton therapy using breast cancer [14] and prostate cancer [15] cell lines.

5. FINAL REMARKS

The magnitude of the decline in the viability of cells incubated with the boron compounds FeC and its iodinated analogue I_2FeC, was well above the direct effects caused by proton irradiation alone in non-treated cells.

The viability decrease observed in our study may derive from α-particles generated in the nuclear fusion reaction as these particles may have direct consequences in the irradiated cells where they are generated and possibly in those contiguous to the irradiated area. The estimated range of these α-particles in water is of the order of 16-25 μm, which is in the range of U87 cell dimensions.

A major limitation of this work refers to the uncertainties in charge determination and therefore on the estimation of dose. Improvements in the experimental setup are ongoing to collect charge during irradiation period of each well. In addition, a validation step with a Monte Carlo (MC) model will be performed to compare several MC and experimental parameters, such as divergence of the beam, energy spectrum, the variation of the Bragg peak depending on the point of reaction and the variation of the maximum dose.

Finally, this pilot study provided evidences for the proof of concept that Fe carboranes, FeC and I_2FeC compounds magnify cell-killing after proton irradiation, acting as radiosensitizers and that the mechanism may be associated with the presence of boron and the nuclear fusion reaction with protons.

ACKNOWLEDGEMENTS

This work was supported by Fundação para a Ciência e Tecnologia (projects UID/Multi/04349/2019, PTDC/MEDQUI/29649/2017, UIDB/04565/2020, UIDP/04565/2020 - iBB/IST and LA/P/0140/2020 - Associate Laboratory Institute for Health and Bioeconomy - i4HB) and from the Spanish Ministerio de Economía y Competitividad (PID2019-106832RB-I00), the Generalitat de Catalunya (2017SGR1720).

REFERENCES

[1] García-Mendiola, T., Bayon-Pizarro, V,. Zaulet, A., Fuentes, I., Pariente, F., Teixidor, F., Viñas, C. Lorenzo, E., Metallacarboranes as tunable redox potential electrochemical indicators for screening of gene mutation. Chem. Sci., 2016, 7, 5786-5797.

[2] Yoon, D.-K., Jung, J.-Y., Suha, T.S., Application of proton boron fusion reaction to radiation therapy: A Monte Carlo simulation study. Appl. Phys Lett 105 (2014) 223507.

[3] Moreau D.C., Potentiality of the proton-boron fuel for controlled thermonuclear fusion. Nucl. Fusion, 17 (1977) 13-20

[4] Spraker, M.C., Ahmed, M.W., Blackston, M.A., Brown, N., France III, R. H., Henshaw, S. S., Perdue, B. A., Prior, R. M., Seo, P.-N., Stave, S, Weller, H.R., The $^{11}B(p,\alpha)^{8}Be \rightarrow \alpha + \alpha$ and the $^{11}B(\alpha,\alpha)^{11}B$ reactions at energies below 5.4 MeV. J. Fusion Energ., 31 (2012) 357–367.

[5] Ruggiero, A.G., Nuclear Fusion of Protons with Boron. Contribution to Conference on Prospects for Heavy Ion Inertial Fusion, Aghia Pelaghia, Crete, Greece, September 26 – October 1 (1992). https://inis.iaea.org/collection/NCLCollectionStore/_Public/24/028/24028563.pdf (accessed 9-6-2022).

[6] Cirrone, G.A.P., Manti, L., Margarone, D., Petringa, G., Giuffrida, L., Minopoli, A., Picciotto, A., Russo, G., Cammarata, F., Pisciotta, P., Perozziello, F.M., Romano, F., Marchese, V., Milluzzo, G., Scuderi, V., Cuttone, G., Korn, G., First experimental proof of Proton Boron Capture Therapy (PBCT) to enhance protontherapy effectiveness. Sci. Rep., 8 (2018) 1141.

[7] http://www.microbeams.co.uk/ (accessed 9-6-2022).

[8] Alves, L.C., Breese, M.B.H., Alves, E., Paúl, A., da Silva, M.R., da Silva M.F., Soares, J.C., Micron-scale analysis of SiC/SiCf composites using the new Lisbon nuclear microprobe. Nucl. Instrum. Meth. B, 161-163 (2000) 334-338.

[9] Corregidor, V., Alves, L.C., Vilarigues, M., Silva, R.C., The external ion beam facility in Portugal for studying culture heritage. e-Conservation Magazine, 22 (2011) 41-52.

[10] Corregidor, V., Oliveira, A.R., Rodrigues, P.A., Alves, L.C., Paintings on copper by the Flemish artist Frans Francken II: PIXE characterization by external beam. Nucl. Instrum. Meth. B, 348 (2015) 291-295.

[11] http://www.srim.org (accessed 9-6-2022).

[12] Grime, G.W., The "Q factor" method: quantitative microPIXE analysis using RBS normalisation. Nucl. Instrum. Meth. B, 109/110 (1996) 170-174.

[13] Marques, A., Belchior, A., Silva, F., Marques, F., Campello, M.P.C., Pinheiro, T., Santos, P., Santos, L., Matos, A.P.A., Paulo, A., Dose Rate Effects on the Selective Radiosensitization of Prostate Cells by GRPR-Targeted Gold Nanoparticles. Int. J. Mol. Sci. 2022, 23, 5279.

[14] Murphy, N., McCarthy, E., Dwyer, R., Farràs, P., Boron clusters as breast cancer therapeutics. J. Inorg. Biochem., 218 (2021) 111412.

[15] Bláha, P., Feoli, C., Agosteo, S., Calvaruso, M., Cammarata, F.P., Catalano, R., Ciocca, M., Cirrone, G.A.P., Conte, V., Cuttone, G., Facoetti, A., Forte, G.I., Giuffrida, L., Magro, G., Margarone, D., Minafra, L., Petringa, G., Pucci, G., Ricciardi, V., Rosa, E., Russo, G., Manti, L., The Proton-Boron Reaction Increases the Radiobiological Effectiveness of Clinical Low- and High-Energy Proton Beams: Novel Experimental Evidence and Perspectives. Front. Oncol., 11 (2021) 682647.

COMPATIBILIZATION OF WASTE TIRE RUBBER/POLY(ETHYLENE-CO-VINYL ACETATE) BLENDS USING LIQUID RUBBER AND ELECTRON BEAM IRRADIATION.

Rubber Recycling

S. RAMARAD
Heriot-Watt University Malaysia
Engineering and Physical Sciences School,
Putrajaya, Malaysia.
Email: R.Suganti@hw.ac.uk

C. T. RATNAM
Malaysia Nuclear Agency
Bangi, Malaysia.

Abstract

Accumulation of rubber waste is a pressing global issue. Tires are complex bulky rubber composite which has received global recycling attention. At the end of life, tires are collected, shredded, segregated, ground and down-sized into rubber recyclates, more commonly known as waste tire rubber. These waste tire rubber, having undergone a lifetime on the road and downsizing processes, has poor properties and is not favored in high-end applications. Many researchers have attempted to blend waste tire rubber with plastic to produce thermoplastic elastomer. However, one of the most prominent drawbacks of these thermoplastic elastomers was the poor interfacial adhesion which results in poor mechanical properties. In this study, the above mentioned problem was addressed by blending 50 wt% of reclaimed waste tire rubber (WTR) with 50 wt% of poly(ethylene-co-vinyl acetate) (EVA) which was compatibilized using liquid styrene-butadiene rubber (LR). Compatibilized blends were prepared using an internal mixer. The blends were later subjected to electron beam irradiation with doses ranging from 50 to 200 kGy. While compatibilization on its own did not distinctly enhance the properties of the blends, the irradiation remarkably enhances mechanical and dynamic mechanical properties of the blend by at least 2 folds compared to un-irradiated blends.

1. INTRODUCTION

The world is consuming finite resources, and producing vast quantities of products as well as waste, leading to unsustainable patterns of consumption and production. It is essential to move away from the traditional linear "make, use and dispose" economy, to a circular model. A circular economy is defined as an economic system aimed at minimising waste and making the most of resources [1]. This regenerative approach is in contrast to the traditional linear economy [2]. In order to achieve this, intense planning of the entire lifecycle of a manufactured product, which involves the production, utilisation and retirement phases, is essential [3]. The rubber industry is one of the many industries facing the problem in establishing circular economy due to lack in successful recycling motives [4].

Tires are the major consumer of raw rubber and has a short lifetime. At the end of tire life, an estimated 67% of material is recyclable and reusable [5]. Tire making industries has been investing many different approaches to achieve circular economy. However, recycling tire rubber has been a difficult process due to the complex structure and mixture of materials [6]. Tires need to be shredded, segregated and granulated before it can be converted into ground tire rubber (GTR). This can be processed further with the use of chemicals to obtained reclaimed tire rubber (RTR) [7].

Having undergone a life on road, post life processing and chemical treatments; GTR and RTR has very poor properties and are not fit to be converted to other useful products as it is. Hence, many has tried incorporating GTR and RTR into thermoplastics such as PP and PE to formulate a new thermoplastic elastomer [8]. However, one of the major setback was the poor properties resulting from the lack of interfacial adhesion [9].

Alternative methods such as irradiation on tire rubber based thermoplastic elastomers blends has been heavily reported [10]. The results are varied from positive to negative enhancements in many different properties. Exposure to irradiation such as gamma ray and electron beam can induce crosslink and chain-scission within the polymer matric. The dominance of either process will influence the resulting properties of the blends.

In this study, attempt was made to compatibilize RTR and ethylene vinyl acetate (EVA) blend using liquid rubber and electron beam irradiation. The aim was to enhance the interfacial adhesion and thereby enhancing the mechanical and dynamic properties.

2. METHODOLOGY

In this section, the materials and methods used to conduct the work is presented.

2.1. Materials

Poly(ethylene-co-vinyl acetate) (Grade EVA N8045), EVA, having 18% vinyl acetate content with melt flow index value of 2.3 g/10 min and a density of 0.947 g/cm^3 was purchased from the TPI POLENA Public Limited Company, Thailand. Reclaimed tire rubber (RECLAIM Rubberplas C), RTR, from waste, heavy duty tires used in this study was supplied by Rubplast Sdn. Bhd., Malaysia. General properties of the RTR are 48% rubber hydrocarbon, 5% ash content, 15% acetone extract, 25% carbon black fillers and density of 1.3 g/cm^3. The styrene butadiene based liquid rubber (LR) supplied by Kuraray Co. Ltd. Japan had a density of 0.95 g/cm^3; molecular weight of 8500 and glass transition temperature of -14 °C.

2.2. Compounding and compression molding

EVA, RTR and LR were melt blended in an internal mixer (Brabender Plasticoder PL2000-6 equipped with co-rotating blades and a mixing head with a volumetric capacity of 69 cm^3). The rotor speed was set at 50 rpm while blending temperature was set at 120 °C.

EVA was fed into the internal mixer chamber and allowed to melt for two minutes, followed by the addition of RTR and LR. EVA, RTR and LR were allowed to mix for 8 minutes before collecting the blends from the internal mixer. LR loading was set at 1, 3, 5 and 10% based on rubber weight. The control blend (without compatibilizer) was set at 50 wt% RTR and 50 wt% EVA and designated as 50RTR. The compatibilized blends were designated as 1LR, 3LR, 5LR and 10LR with the number corresponding to the loading of LR.

2.3. Compounding and compression molding

The compounded materials collected from internal mixer were placed in a mould for compression molding in between the platens of an automated hydraulic heated press (LP-S-50 Scientific Hot and Cold Press). The platens were pre-heated to 130 °C. The molding cycles involve 3 minutes of preheating without pressure to melt the materials; followed by 20 seconds of pressure cycling between 0 to 10 MPa to distribute the melted material in the cavity and dislodge any air bubbles; and 3 minutes of holding pressure at 10 MPa.

Following the holding time, cooling procedure was imposed by carefully removing the mould from the heated press to the adjacent cooling press equipped with water circulating channels pumped with chilled (20 °C) water. Cooling procedure was done for 2 minutes under 10 MPa holding pressure to eliminate non-uniform cooling and warping of the slabs. The cooling rate of the mould was estimated to be between 40 to 50 °C/min. The slabs are then carefully removed from the mould cavity and excess/flash on the slabs was trimmed with a sharp knife.

2.4. Electron beam irradiation

The molded slabs were irradiated using 3 MeV electron beam accelerator (model NHV-EPS-3000) at doses 50, 100, 150 and 200 kGy. The acceleration energy, beam current and dose rate were 2 MeV, 5 mA, and 50 kGy per pass, respectively.

2.5. Gel content analysis

The gel content of the samples was determined according to ASTM D2765. Approximately 3 mg weighed samples were placed in a stainless-steel wire of 120 mesh size. Three replicates were prepared for each sample. The samples placed in wire mesh were then extracted in boiling Toluene using a Soxhlet apparatus for 24 hours

to dissolve the soluble content. Samples were then collected and dried in an oven at 70 °C until a constant weight is obtained. Gel content was calculated as per Equation 1 below.

$$\text{Gel content (\%)} = (w_1/w_0) \times 100 \quad \text{Equation 1}$$

where, w_0 and w_1 are the dried weight of the sample before and after extraction, respectively.

2.6. Tensile testing

Tensile test specimens were punched out using Wallace die cutter from compression molded slabs. The specimens had a gauge length of 25 mm, width of 6 mm and thickness of 1 mm. Tensile properties measurements were performed at ambient temperature according to ASTM D412 using a computerized tensile tester (Toyoseiki, Japan) with a load cell of 10kN. The crosshead speed was set at 50mm/min for all samples. Data for tensile strength, modulus at 100% elongation and elongation at break were recorded. At least 7 specimens were used for each set of blend and average results were taken as the resultant value. Standard deviation of the results was less than 10%.

2.7. Dynamic mechanical analysis

DMA was performed in dual cantilever mode using a dynamic mechanical analyzer (TA Instrument TA01 DMA 2980). The temperature interval was - 80 to 100 °C with a heating rate of 5 °C/min, using a frequency of 1 Hz. The samples were cut out to the dimension of 60 x 12 x 3 mm from compression molded slabs. The sample dimensions were kept as similar as possible in order to obtain an accurate comparison. Variation of storage modulus, loss modulus and tan δ values with temperature were recorded. E' and E'' are defined as storage and loss modulus respectively. Peak of tan δ is taken as the glass transition temperature (Tg) of the sample.

3. RESULTS & DISCUSSION

Liquid rubber such as liquid natural rubber has been successfully used as a compatibilizer in thermoplastic elastomer blends [11, 12]. Also, studies utilizing ground tire rubber (GTR) in thermoplastic elastomer observed the encapsulation of GTR by the rubber component and good mechanical properties [13-16]. In this study, low molecular weight liquid styrene butadiene rubber (LR) was used, to improve the adhesion between RTR and EVA. Figure 1 shows the schematic representation of RTR/EVA blend compatibilization by LR. RTR phase is encapsulated by LR, efficiently decreasing the interfacial tension. This improves the dispersion of RTR in EVA matrix. Similar observation was also reported in GTR/LDPE blends compatibilized by elastomers [17]. Furthermore, the free chains of LR can co-mingle with both free devulcanized chains of RTR and EVA matrix, improving the interfacial adhesion. Upon irradiation, both EVA and RTR can be adhered together through formation of crosslinks between these co-mingling chains [18, 19].

Figure 2 below shows the gel content of the blends under the influence of LR loading and irradiation dosage. Generally, the gel content is an estimation of yield of irradiation induced crosslinking. 50RTR shows 23.8% of the gel content prior to irradiation (0kGy), affirming the presence of readily existing crosslinks within its matrix. This gel content is the contribution of existing crosslinked structure within the reclaimed tire rubber. LR compatibilized blends showed slightly higher gel content before irradiation (0 kGy) compared to the control, 50RTR blend. All the blends recorded a proportional increase in gel content with respect to irradiation dose starting from 100 kGy onwards. This indicates that 50RTR blends require a minimum of 100 kGy irradiation dose for net effective crosslinking process to take place. LR compatibilized blends, though had slightly higher gel content before irradiation, resulted in comparable gel content yield to control blend from 100 up to 200 kGy irradiation dose. This clearly shows, LR acted as a physical compatibilizer and did not participate in the chemical crosslinking process of the blends.

Figure 3 shows the influence of LR loading and irradiation dosage on tensile strength and elongation at break of the blends. At 0 kGy, LR compatibilized blends recorded lower tensile strength values compared to control blend. The lower values are attributed to the presence of LR which is a low molecular weight substance. A small decrease in tensile strength was also noticed with increasing LR loadings. Similar observation was also reported on liquid natural rubber compatibilized NR/LLDPE blends and NR/HDPE blends [11, 20]. Dispersion of LR into EVA chains might indeed decrease the crystallinity of the EVA phase resulting in the decreasing trend

of tensile strength with increasing LR loading. Irradiation enhanced the tensile strength of the blends by about 10 to 15% compared to non-irradiated blends. The higher the LR loading the lower the enhancement in tensile strength following irradiation despite gel content analysis indicating similar level of crosslinking happening in all compatibilized blends. This is due to increased amount of low molecular weight LR renders the blend softer leading to premature rupture of the samples.

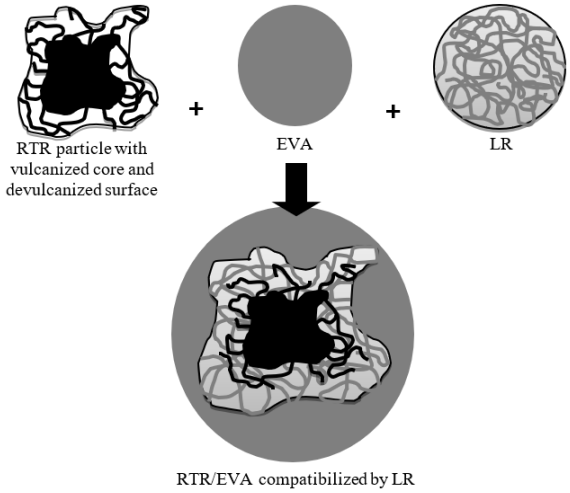

FIG. 1. Representation of physical compatibilization by LR on EVA/RTR blends

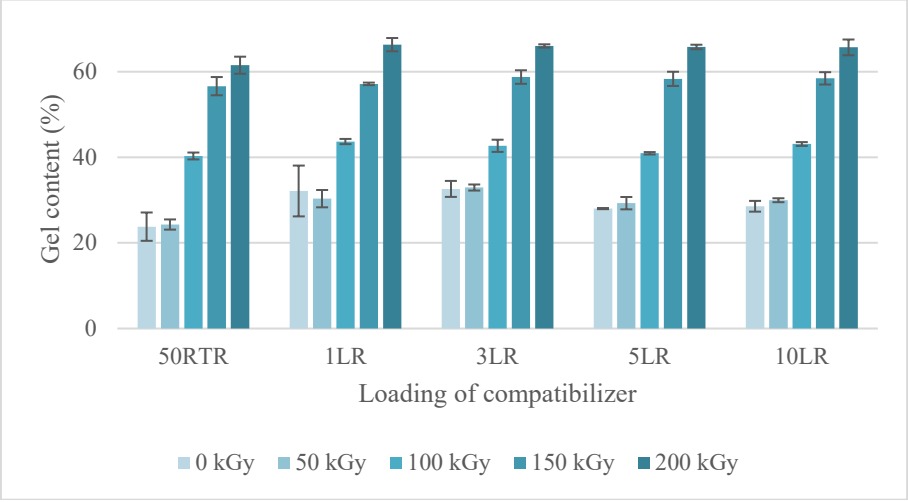

FIG. 2. Influence of LR loading and irradiation on gel content of 50RTR blends.

Figure 3b shows increasing LR loading does not influence the elongation at break of non-irradiated blend. LR is a low molecular weight rubber, which presents itself in the interphase area of RTR/EVA blend, reducing the interfacial tension and improving RTR dispersion, thereby allowing the matrix to elongate a little further before rupture [21]. However, LR also effectively enhances the interfacial adhesion and thereby limits the feasibility of the EVA matrix to elongate. Increasing the irradiation dose, decreases the elongation at break of LR compatibilized blends. Formation of crosslinks induced by irradiation increases the stiffness of the blends resulting in a decrease of elongation at break.

Figures 4 illustrates the storage modulus, loss modulus and tan delta profiles of 50RTR and LR compatibilized blends, before and after 200 kGy irradiation. All the blends, before and after irradiation clearly displayed glass, transition and rubbery characteristics in the storage modulus curve (Figure 4a). Storage modulus was highest in the glassy region and rapidly decreases from transition region and displayed a plateau rubbery curve. Before irradiation, LR compatibilized blend showed decrease in the storage modulus within glass and transition region compared to 50RTR blend.

3LR blend which showed reduction in storage modulus before irradiation (due to plasticizing effect of LR), improved tremendously upon irradiation as the elasticity of the blend increases with efficient crosslink formation in LR. Previous studies have shown an increase in interphase thickness in the presence of compatibilizer [21]. Compatibilizer with higher molecular weight tends to form thicker interphase compared to the fully stretched length of the compatibilizer chain. These findings enhance the fact that presence of an effective compatibilizer restricts the mobility of the matrix chains. Thus, effective compatibilization renders a composite stiffer recording higher storage modulus.

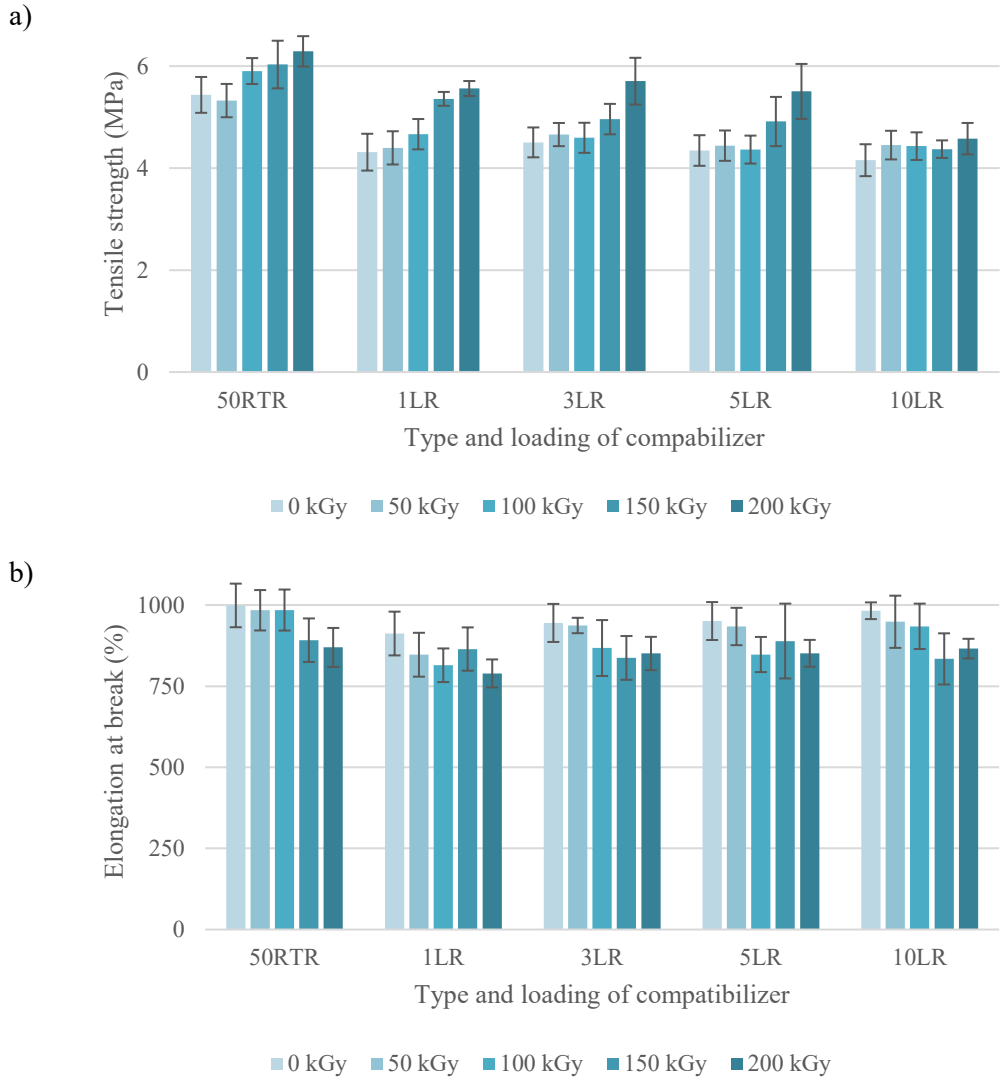

FIG. 3. Influence of LR loading and irradiation on a) tensile strength and b) elongation at break of 50RTR blends.

3LR blend which showed reduction in storage modulus before irradiation (due to plasticizing effect of LR), improved tremendously upon irradiation as the elasticity of the blend increases with efficient crosslink formation in LR. Previous studies have shown an increase in interphase thickness in the presence of compatibilizer [21]. Compatibilizer with higher molecular weight tends to form thicker interphase compared to the fully stretched length of the compatibilizer chain. These findings enhance the fact that presence of an effective compatibilizer restricts the mobility of the matrix chains. Thus, effective compatibilization renders a composite stiffer recording higher storage modulus.

Figure 4b shows the loss modulus curve which peaks at the transition temperature range. 3LR compatibilized blends recorded a peak temperature of -16.8 °C, a slight decrease by 3 °C, compared to 50RTR. However, no distinct change was observed in the loss modulus peak height. This is again due to physical compatibilizing nature of LR. The slight reduction in loss modulus peak temperature in 3LR compatibilized blend might possibly be due to the contribution of lower Tg values of LR. Interestingly, 3LR compatibilized blend, upon

irradiation, showed shifting of loss modulus peak temperature and height to -18.2 °C (decreased by 1.4 °C) and 374.5 MPa (increased by 140.5 MPa), respectively, compared to non-irradiated counterpart.

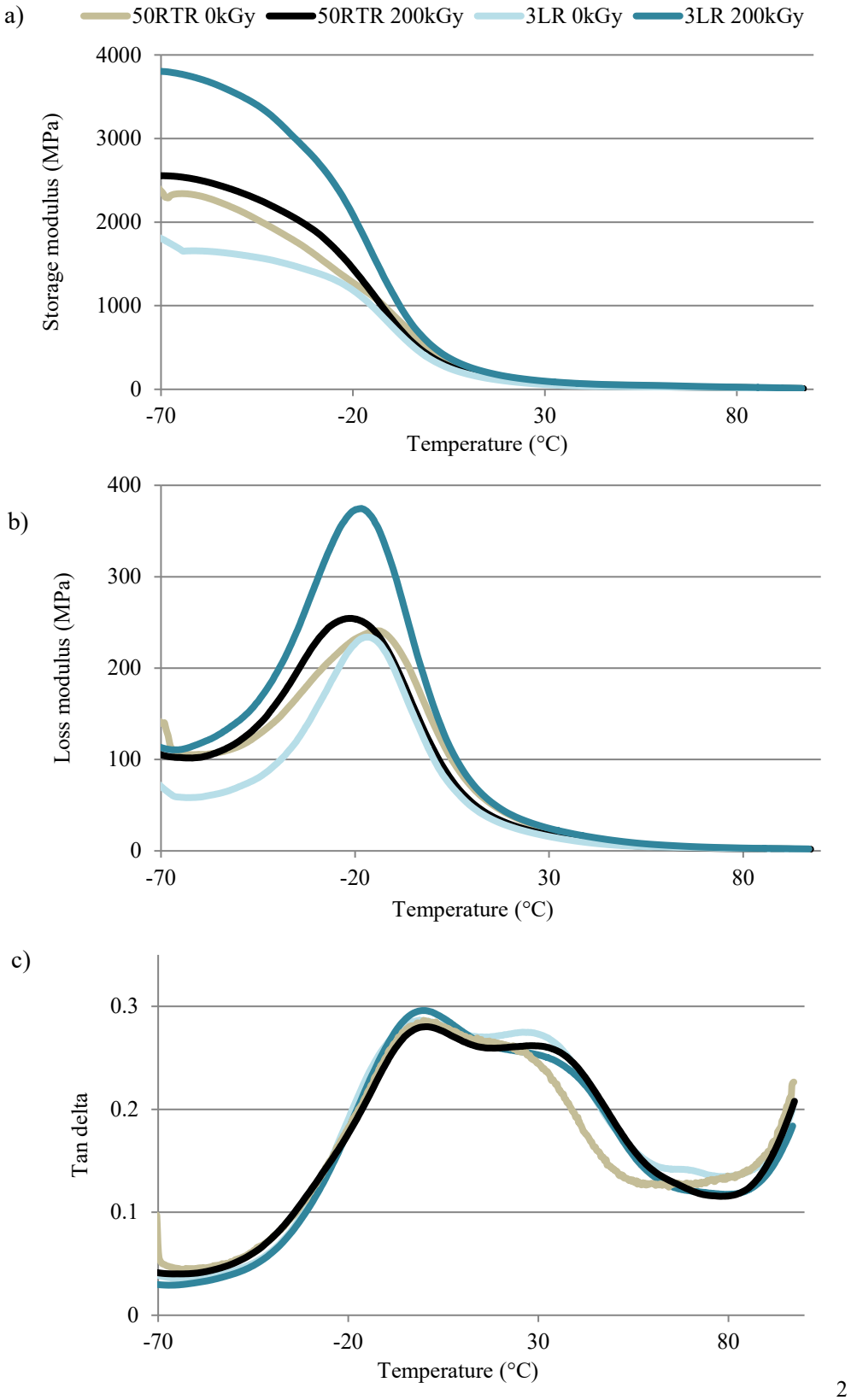

2

FIG. 4. Influence of LR compatibilization and irradiation on a) storage modulus and b) loss modulus and c) tan delta of 50RTR blends.

Apparently, irradiation induced crosslinking of LR in LR compatibilized blends increases the portion of viscous component in the blend, resulting in increased energy loss in the blend. As compared to irradiated 50RTR, irradiated 3LR blend displayed enhanced loss modulus up to rubbery region (50 °C). This clearly indicates LR have effectively compatibilized the blends and enhanced the dynamic mechanical properties upon irradiation.

Figure 4b shows the loss modulus curve which peaks at the transition temperature range. 3LR compatibilized blends recorded a peak temperature of -16.8 °C, a slight decrease by 3 °C, compared to 50RTR. However, no distinct change was observed in the loss modulus peak height. This is again due to physical compatibilizing nature of LR. The slight reduction in loss modulus peak temperature in 3LR compatibilized blend might possibly be due to the contribution of lower Tg values of LR. Interestingly, 3LR compatibilized blend, upon irradiation, showed shifting of loss modulus peak temperature and height to -18.2 °C (decreased by 1.4 °C) and 374.5 MPa (increased by 140.5 MPa), respectively, compared to non-irradiated counterpart. Apparently, irradiation induced crosslinking of LR in LR compatibilized blends increases the portion of viscous component in the blend, resulting in increased energy loss in the blend. As compared to irradiated 50RTR, irradiated 3LR blend displayed enhanced loss modulus up to rubbery region (50 °C). This clearly indicates LR have effectively compatibilized the blends and enhanced the dynamic mechanical properties upon irradiation.

Tan delta property (Figure 4c) was the least affected by compatibilization and irradiation of 50RTR blend as the peak temperature and height remained around 0 °C and 0.3, respectively. Similar observation was also reported for NBR/EVA blends [22] and PP/NR blends [23]. The breadth of tan delta curve, before irradiation, increased with compatibilization. Compatibilization leads to improved dispersion of RTR in EVA matrix, resulting in increased heterogeneity of the blends. In contrary to 50RTR blend, no increased broadening was observed in the compatibilized blends upon irradiation, suggesting no changes in heterogeneity or presence of side chains in irradiated blends. In a two-phase system, where two polymers are far from being completely miscible, no compatibilizer is likely to change it into one phase system. However, LR compatibilizer acts only as interfacial agents by effectively improving RTR dispersion in EVA, preventing coalescence of RTR particles and reducing interfacial tension [21, 24].

4. CONCLUSION

The study reported on influence of LR compatibilization and electron beam irradiation on enhancing the properties of RTR/EVA blend. Gel content analysis indicated formation of net crosslinking upon irradiation. While tensile strength and elongation barely improved in the presence of LR, irradiation did clearly enhance the said properties. The most prominent enhancement was noted in dynamic mechanical properties of both LR compatibilized and irradiated blends. Hence, LR and irradiation can be used as a mean to enhance the property of 50RTR blend.

ACKNOWLEDGEMENTS

Author would like to acknowledge Nuclear Malaysia and University of Nottingham Malaysia Campus for the financial support during the experimentation.

REFERENCES

[1] Hartley, K., R. van Santen, and J. Kirchherr, *Policies for transitioning towards a circular economy: Expectations from the European Union (EU).* Resources, Conservation and Recycling, 2020. **155**: p. 104634.

[2] Morseletto, P., *Targets for a circular economy.* Resources, Conservation and Recycling, 2020. **153**: p. 104553.

[3] Sherwood, J., *The significance of biomass in a circular economy.* Bioresource Technology, 2020. **300**: p. 122755.

[4] Rada, E.C. and L. Cioca, *Optimizing the Methodology of Characterization of Municipal Solid Waste in EU Under a Circular Economy Perspective.* Energy Procedia, 2017. **119**: p. 72-85.

[5] Ramarad, S., et al., *Waste tire rubber in polymer blends: A review on the evolution, properties and future.* Progress in Materials Science, 2015. **72**: p. 100-140.

[6] Ramarad, S., et al., *Improving the properties of reclaimed waste tire rubber by blending with poly(ethylene-co-vinyl acetate) and electron beam irradiation.* Journal of Applied Polymer Science, 2015. **132**(11).

[7] Barbosa, R. and J.D. Ambrósio, *Devulcanization of natural rubber compounds by extrusion using thermoplastics and characterization of revulcanized compounds.* Journal of Polymer Research, 2019. **26**(7): p. 160.

[8] Sripornsawat, B., S. Saiwari, and C. Nakason, *Thermoplastic vulcanizates based on waste truck tire rubber and copolyester blends reinforced with carbon black.* Waste Management, 2018. **79**: p. 638-646.

[9] Song, P., S. Li, and S. Wang, *Interfacial interaction between degraded ground tire rubber and polyethylene.* Polymer Degradation and Stability, 2017. **143**: p. 85-94.

[10] Ramarad, S., et al., *Improved crystallinity and dynamic mechanical properties of reclaimed waste tire rubber/EVA blends under the influence of electron beam irradiation.* Radiation Physics and Chemistry, 2017. **130**: p. 362-370.

[11] Dahlan, H.M., M.D. Khairul Zaman, and A. Ibrahim, *The morphology and thermal properties of liquid natural rubber (LNR)-compatibilized 60/40 NR/LLDPE blends.* Polymer Testing, 2002. **21**(8): p. 905-911.

[12] Shashidhara, G.M. and K.G. Pradeepa, *Preparation and characterization of polyamide 6/liquid natural rubber blends.* Journal of Applied Polymer Science, 2014. **131**(2).

[13] Naskar, A.K., A.K. Bhowmick, and S.K. De, *Thermoplastic elastomeric composition based on ground rubber tire.* Polymer Engineering & Science, 2001. **41**(6): p. 1087-1098.

[14] Cañavate, J., et al., *Formulations for thermoplastic vulcanizates based on high density polyethylene, ethylene-propylene-diene monomer, and ground tyre rubber.* Journal of Composite Materials, 2011. **45**(11): p. 1189-1200.

[15] Abou Zeid, M.M., et al., *Effect of gamma irradiation on ethylene propylene diene terpolymer rubber composites.* Nuclear Instruments and Methods in Physics Research Section B: Beam Interactions with Materials and Atoms, 2008. **266**(1): p. 111-116.

[16] Li, Y., Y. Zhang, and Y.X. Zhang, *Structure and mechanical properties of SRP/HDPE/POE (EPR or EPDM) composites.* Polymer Testing, 2003. **22**(8): p. 859-865.

[17] Formela, K., J. Korol, and M.R. Saeb, *Interfacially modified LDPE/GTR composites with non-polar elastomers: From microstructure to macro-behavior.* Polymer Testing, 2015. **42**: p. 89-98.

[18] Dahlan, H.M., M.D.K. Zaman, and A. Ibrahim, *Liquid natural rubber (LNR) as a compatibiliser in NR/LLDPE blends—II: the effects of electron-beam (EB) irradiation.* Radiation Physics and Chemistry, 2002. **64**(5): p. 429-436.

[19] Noriman, N.Z., et al., *The Effect of Electron Beam (EB) Irradiation in Presence of TMPTA on Cure Characteristics and Mechanical Properties of Styrene Butadiene Rubber/Recycled Acrylonitrile-Butadiene Rubber (SBR/NBRr) Blends.* Polymer-Plastics Technology and Engineering, 2010. **49**(3): p. 228-236.

[20] Nakason, C., A. Worlee, and S. Salaeh, *Effect of vulcanization systems on properties and recyclability of dynamically cured epoxidized natural rubber/polypropylene blends.* Polymer Testing, 2008. **27**(7): p. 858-869.

[21] Moly, K.A., et al., *Correlation between the morphology and dynamic mechanical properties of ethylene vinyl acetate/linear low-density polyethylene blends: Effects of the blend ratio and compatibilization.* Journal of Applied Polymer Science, 2006. **100**(6): p. 4526-4538.

[22] Jansen, P., F.G. Garcia, and B.G. Soares, *Effect of mercapto-modified ethylene–vinyl acetate on the curing parameters and mechanical and dynamic mechanical properties of vulcanized nitrile rubber/ethylene–vinyl acetate blends.* Journal of Applied Polymer Science, 2003. **90**(9): p. 2391-2399.

[23] George, S., et al., *Dynamic mechanical properties of isotactic polypropylene/nitrile rubber blends: Effects of blend ratio, reactive compatibilization, and dynamic vulcanization.* Journal of Polymer Science Part B: Polymer Physics, 1997. **35**(14): p. 2309-2327.

[24] John, B., et al., *Dynamic mechanical behavior of high-density polyethylene/ethylene vinyl acetate copolymer blends: The effects of the blend ratio, reactive compatibilization, and dynamic vulcanization.* Journal of Applied Polymer Science, 2003. **87**(13): p. 2083-2099.

ELECTRON BEAM PROCESSING TO IMPROVE BIODEGRADABLE POLYMERS AND FOR INDUSTRIAL WASTEWATER TREATMENT AND RECYCLING

W. A. P. CALVO
Nuclear and Energy Research Institute (IPEN-CNEN)
Sao Paulo/SP, Brazil
Email: wapcalvo@ipen.br

P. M. MUNHOZ[1], S. L. SOMESSARI[1], C. L. DUARTE[1], S. I. BORRELY[1], F. E. SPRENGER[1], A. FEHER[1], [1]F. F. LAINETTI[1], R. R. GASPAR[1], F. C. NASCIMENTO[1], L. G. A. SILVA[1], J. HARADA[1], A. BRAGA[2], M. RODRIGUES[2], M. H. O. SAMPA[1]
[1]Nuclear and Energy Research Institute (IPEN-CNEN)
[2]Truckvan Industry
Sao Paulo/SP, Brazil

Abstract

The aim of the two studies was to apply the electron beam radiation technology for controlling plastic pollution and environmental protection. (1) Mobile irradiation unit - The treatment of wastewater and industrial effluents by electron beam irradiation is a promising technique. The design and construction of a mobile unit by the Nuclear and Energy Research Institute, containing an electron beam accelerator of 0.7 MeV and 20 kW is innovative to demonstrate the effects and positive results of this technology. The mobile unit has as one of its main advantages the possibility of treating effluents in the place where the source is located, eliminating costs and bureaucratic problems associated with the transportation of waste, besides publicizing the technology in several places in the country. To implement the project, IPEN-CNEN has been consolidating partnerships with national and international companies. The resources for the development of the unit have been supplied by the Brazilian Innovation Agency (FINEP Process N. 01.18.0073.00 - Implementation of mobile facilities to make the technology generated available to the productive sector and society) and International Atomic Energy Agency, financing the "IAEA TC Project BRA1035 - Mobile electron beam accelerator to treat and recycle industrial effluents". The Institute has associated with a specialized company (Truckvan Industry) in an innovation project for the unit design and development. (2) PBAT/PLA polymeric blend Ecovio® - The mechanical properties of the biodegradable polymer were evaluated. Products, such as injected packaging, films for tube production, plastic bags, packaging for cosmetics and food packaging, among others made with this biodegradable polymeric blend need to be resistant to cross sectional demands, impact and thermal stability and should have an average lifetime of 1 to 5 years. Then, it is recommended to use the PBAT/PLA polymeric blend Ecovio® irradiated by electron beam with adsorbed dose of 65 kGy.

1. INTRODUCTION

In the world, there is a growing increase in the demand for water for human consumption, as well as the prioritization of the use of available water resources for public supply. The United Nations World Water Development Report 2017 estimates global freshwater withdrawals at 3,928 km³ per year. An estimated 44% (1,716 km³ per year) of this water is consumed, mainly by agriculture through evaporation in irrigated cropland. The remaining 56% (2,212 km³ per year) is released into the environment as wastewater in the form of municipal and industrial effluent and agricultural drainage water. Globally, it is likely that over 80% of wastewater is released to the environment without adequate treatment.

On the other hand, almost 79% of the total plastics produced worldwide were discarded directly into the environment. Therefore, 6.5 billion tons of plastics may have caused negative environmental impacts, denigrating the image of the plastics, as well as damaging the environment and global sustainability. To solve this problem, one of the ways is the use of biodegradable polymers, which are used for making consumer goods and when discarded are degraded faster than products made with non-biodegradable polymers, thus contributing to global sustainability.

1.1. Industrial wastewater treatment and recycling

In developing countries, such as Brazil, about 90% of wastewater is dumped untreated into rivers, lakes or oceans. Therefore, it is necessary to adopt strategies that aim to maximize the use of water resources and minimize the negative impacts related to the generation of effluents by the industries. The necessity to preserve the environment as well as the demand for sustainable development has generated various actions by non-governmental groups and changes in legislation in many countries. As a consequence, restrictions have been imposed regarding the release of effluents into the environment. Currently, several technologies are used in the treatment of industrial effluents for recovery and reuse of these waters [1-2].

The irradiation system with an electron accelerator allows treating different types of effluents. Depending on the effluent, the amount of ionizing radiation energy required for treatment may vary, as well as the amount of treated effluent per day [3]. In this context, the Radiation Technology Center at IPEN-CNEN decided to develop and build a mobile electron beam irradiation facility for the treatment of industrial effluents in the place where the source is located, without the transportation of wastes [4]. The type of treated effluent, the treatment cost per m^3/day and other information regarding the cost of maintenance and operation of the mobile irradiation facility were obtained from the Business Plan of the Mobile Facility [5-6].

1.2. Biodegradable polymers

Almost 79% of the total plastics produced worldwide were discarded directly into the environment. Therefore, 6.5 billion tons of plastics may have caused negative environmental impacts, denigrating the image of the plastics, as well as damaging the environment and global sustainability. To solve this problem, one of the ways is the use of biodegradable polymers, which are used for making consumer goods and when discarded are degraded faster than products made with non-biodegradable polymers, thus contributing to global sustainability.

Biopolymer classification in relation to the environment can be observed in Fig. 1. In the horizontal axis the polymer is evaluated in relation to its biodegradability and in the vertical axis the raw materials of this polymer are evaluated based on whether they are renewably sourced [7].

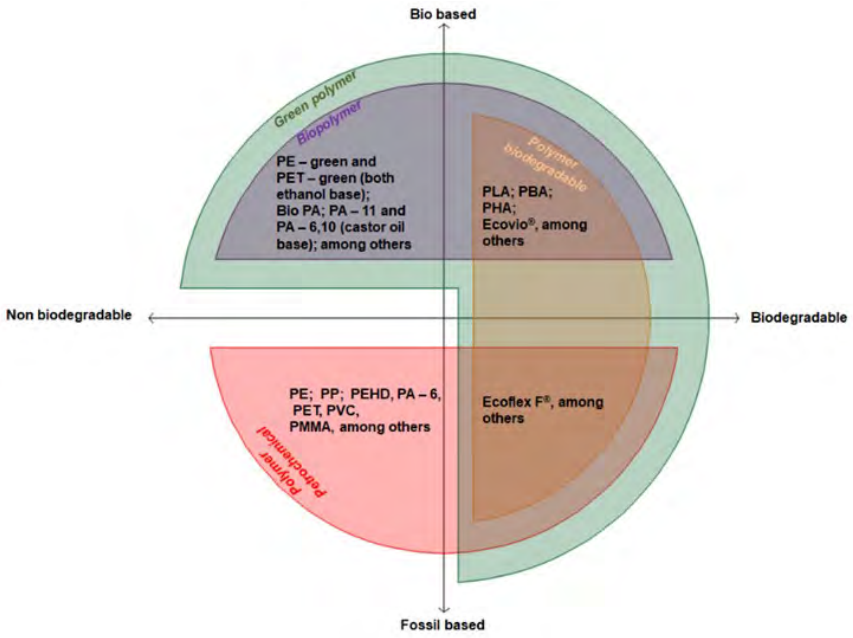

FIG.1: Classification of polymers based on environmental criteria.

In Fig. 1, the first, second and fourth quadrants represent the green polymers. The first and second quadrants represent the biopolymers and the biodegradable polymers are represented by the first and fourth quadrants. Finally, the third and fourth quadrants represent the petrochemical polymers. The designation as a green polymer is used to differentiate all polymers from the petrochemical polymers. When a polymer is classified

as biodegradable, it should automatically be classified as a green polymer. It may also be a biopolymer if this biodegradable polymer was produced from a renewable source. Therefore, the PBAT/PLA polymeric blend polymers can be classified as both biodegradable biopolymers and green polymers.

In the 21st Century there is a concern about the development of biodegradable polymers, with the launch of PLA [Poly (lactic acid)] in 2003, Ecovio® in 2006 and Ecoflex®, produced from renewable sources in 2010, among others. Attention is also being paid to biodegradable polymers in several searches [8].

For PBAT and PLA, theirs world productions were 300,000 and 334,000 tons in 2019, respectively, which represent approximately 25% and 28% of the world's production of the biodegradable polymers in that year. Increases in production were due the increased market competitiveness of both biodegradable polymers in relation to other polymers [9]. However, prior researches have indicated that electron beam irradiation may affect the mechanical properties of the polymeric blend PBAT/PLA. Afterward, a systematic evaluation of these effects is warranted.

2. MATERIAL AND METHODS

2.1. Mobile irradiation unit

A 3D model study of the control room and laboratory space was done to facilitate understanding the internal distribution of the laboratory analysis equipment (Gas Chromatography Mass Spectrometry, Total Organic Carbon and UV-Visible Spectroscopy). The irradiation system with industrial electron accelerator (700 keV, 28 mA, 20 kW, scan horn 640 mm) allows treating different types of effluents. Depending on the effluent, the amount of ionizing radiation energy required for treatment may vary, as well as the amount of treated effluent per day. For the construction of the mobile unit, the estimated cost is about US$ 1.5 million. In the Fig. 2 is shown the architectural design of the mobile electron beam irradiation facility developed by IPEN-CNEN in partnership with Truckvan Industry.

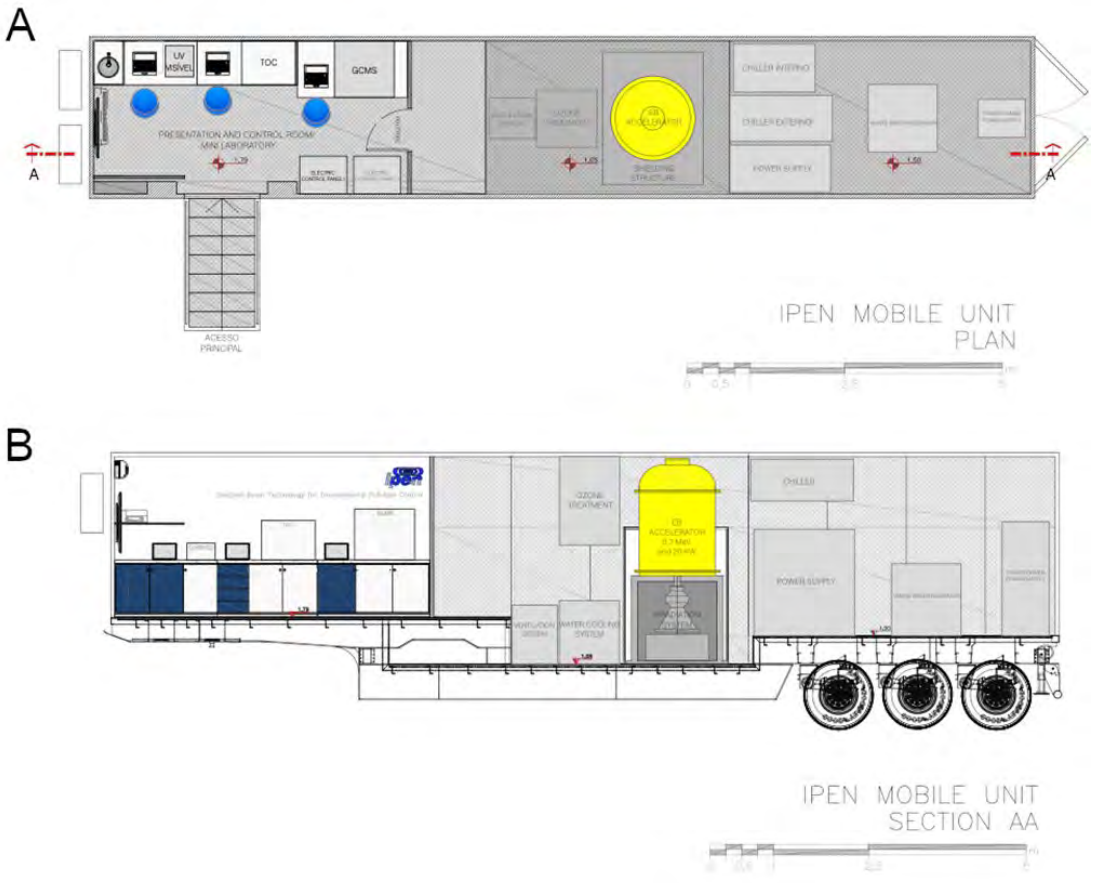

FIG.2: Architectural drawings of the IPEN-CNEN's mobile facility Plan(A) and section AA(B).

In the Fig. 2, the cart is divided into three separate parts: (a) Control room and laboratory for analyses, technical and scientific dissemination of the technology; (b) Industrial electron beam accelerator, hydraulic units, ventilation system, cooler and bunker with irradiation device; (c) Transformer and power source supply.

2.2. PBAT/PLA polymeric blend Ecovio®

The polymeric blend Ecovio® was the material used in this research. It is composed by 80% of renewable compounds, since the PLA and PBAT are made with 100% and at least 64% of renewable resources, respectively. The PBAT/PLA polymeric blend is completely made from biodegradable products, and can be classified as a biopolymer, green polymer and biodegradable polymer, also has a translucent semi-crystalline structure and good thermal stability up to 230ºC.

The PBAT/PLA samples were injected using the Hatian PL 1600 injection molding machine and irradiated by electron beam, as shown in Fig. 3. This process was performed using an electron beam accelerator type Dynamitron®, model DC1500/25/4, manufactured by Radiation Dynamics Inc. (RDI), energy of 1.5 MeV, electric beam current of 25 mA, a scan of 1200 mm and power of 37.5 kW. The irradiation parameters were energy 1.437 MeV, beam width of 1000 mm, electric beam current of 3.26 mA, dose rate of 13.35 kGy.s-1 and dose per tray pass was 5 kGy. PBAT/PLA samples were irradiated at the absorbed doses of 5, 10, 15, 25, 50, 65 and 80 kGy.

FIG.3: PBAT/PLA irradiated samples by electron beam.

Both irradiated and non-irradiated samples were characterized by Izod pendulum impact resistance, tensile strength at rupture, shore D hardness, thermogravimetric analysis (TG) and differential scanning calorimetry (DSC) tests.

3. RESULTS AND DISCUSSION

3.1. Treatment capacity and costs by type of effluent

The type of treated effluent, the treatment cost per m^3/day and other information regarding the cost of maintenance and operation of the mobile irradiation facility are presented in Table 1. All data were obtained from the Business Plan of the Mobile Facility.

This study achievement was based mainly on bibliographic research, mobile unit structures analysis, visits to Truckvan Industry (responsible for chassis and shelter construction of the mobile irradiation facility) and exchange information between the company managers and operators involved in the project. Furthermore, alternative materials and equipment were searched, and designers consulted to project the laboratory installation. In the project, the priority was to ensure adequate and safe working conditions for operators [10].

To attend the installation necessities, several distribution trials and volumetric studies were done to optimize the area distribution. At this point was crucial to know all the equipment that would be used for the facility operation, to search mainly for approximate dimensions and weights, and then start the structural design.

Regarding the mobile laboratory, several layout options have been developed to better meet the needs of each device and its users. The layout has been discussed with the objective of facilitating the maintenance of the equipment (CG-MS, UV-Vis and TOC); operators well-being and ergonomics; space optimization and also to make compatible the need for the presence of equipment and space for operators.

The structural part of the truck is already built and ready to receive all the equipment that needs to be installed in mobile facility, as shown in Fig. 4.

TABLE 1. Quantities of energy, treatment capacity and costs by type of effluent treated in the Mobile Facility.

Effluent	Dose (kGy)	Amount (m^3/day)	Power (kW)	Capital cost (Million US$)	*Variable cost **(Variable and fixed costs) (US$)	Cost/m^3 of effluent treated (US$)
Removal of geosmine (GEO) and methilisoborneol (MIB) from drinking water	1	1,000	20	1.5	0.20 (0.38)	0.60 (1.14)
Removal of industrial textile dyeing from wastewater	2	500	20	1.5	0.20 (0.38)	1.20 (2.28)
Elimination of coliforms from raw sewage, secondary and chlorinated effluents	3	340	20	1.5	0.20 (0.38)	1.77 (3.36)
Removal of organic compounds from petroleum production water	20	50	20	1.5	0.20 (0.38)	12.0 (22.8)
Removal of PCB from transformers oils	50	20	20	1.5	0.20 (0.38)	30.1 (57.1)

* Variable cost only (maintenance, electricity and labor); and
** Both variable and fixed costs (depreciation, bank interest and management).

FIG.4: Mobile electron beam irradiation unit for the treatment of industrial effluents in Brazil.

3.2. Results of mechanical and thermal analyses

It is shown in Fig. 5 the general results of the mechanical and thermal analyses of the PBAT/PLA polymeric blend Ecovio® irradiated by electron beam with absorbed doses of 5, 10, 15, 25, 50, 65 and 80 kGy carried out.

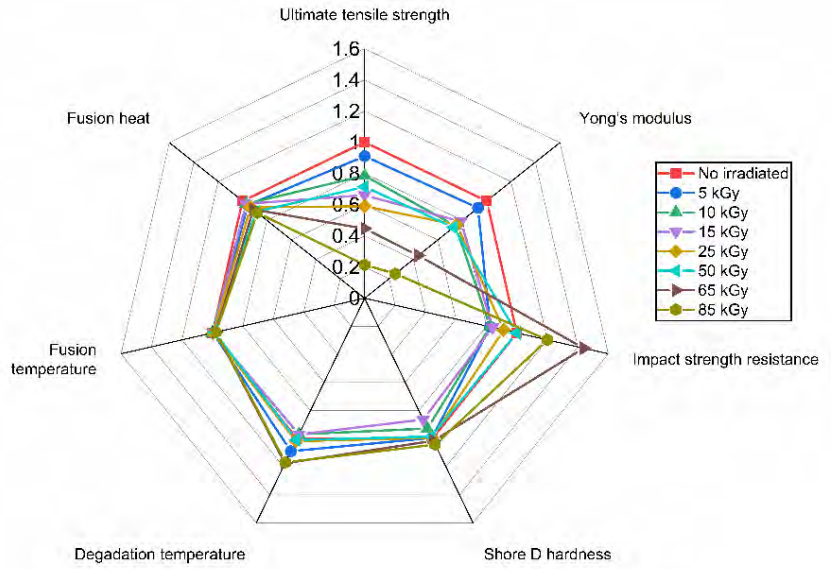

FIG.5: Results of mechanical and thermal analyzes of the PBAT/PLA polymeric blend as a function of the absorption dose.

The results showed an increase of 44% in relation to Izod impact resistance and an increase of 17.4% in thermal stability at a dose of 65 kGy. In this dose was not a substantial change in shore D hardness. However, the module of elasticity decreased 56% and tensile strength at rupture decreased 55% at the same radiation dose. In an absorbed dose of 80 kGy was observed a reduction of the 2.4% in melting temperature and 12.1% in fusion rate. In relation to elongation, significant alterations caused by electron beam irradiation were not observed.

4. CONCLUSION

The design and construction of a mobile unit containing an electron beam accelerator (700 keV and 20 kW) is innovative to demonstrate the effects and positive results of this technology to treat wastewater and industrial effluents for reuse, with particular focus on wastewaters having organic pollutants (reactive dyes and pharmaceutical residues). The Nuclear Energy Research Institute has consolidated partnerships with national and international companies, aiming at the development of a mobile beam irradiation unit which would provide assistance in the treatment of industrial effluents, disseminating this technology in several areas of Brazil. Moreover, this study also designed an internal layout of the mobile unit, focusing on the constructive characteristics, on the materials used in the construction and on the specified equipment that will be installed for industrial effluents treatment and samples analysis.

Radiation technology has been used to control environmental pollution. In this circumstance, electron beam irradiation with an industrial accelerator (1.5 MeV, 25 mA and 37.5 kW) increases at 17.4% in thermal stability and at 44% in Forthe Izod impact resistance of PBAT/PLA polymeric blend Ecovio® with an absorbed dose of 65 kGy. Then, PBAT/PLA irradiated by electron beam is biodegradable and can be used to produce injected products, bags, packaging for food and cosmetics.

ACKNOWLEDGEMENTS

The authors would like to thank the International Atomic Energy Agency (IAEA), Brazilian Innovation Agency (FINEP), National Council for Scientific and Technological Development (CNPq) and IPEN-CNEN for the research and financial support.

REFERENCES

[1] INTERNATIONAL ATOMIC ENERGY AGENCY. “Office of Public Information and Communication. Scientific Forum 2015: Radiation Technology Helps China’s Industries Make Water Cleaner” (2015). Available in:<https://www.iaea.org/newscenter/news/scientific-forum-2015-radiation-technology-helps-china%E2%80%99s-industries-make-water-cleaner>. Access: 19 Jun. 2022.

[2] INTERNATIONAL ATOMIC ENERGY AGENCY. “Radiation Treatment of Wastewater for Reuse with Particular Focus on Wastewaters Containing Organic Pollutants”. IAEA-TECDOC-1855.Viena, Austria (2018). Available in: <https://www-pub.iaea.org/MTCD/Publications/PDF/TE-1855web.pdf> Access: 19 Jun. 2022.

[3] ZIMEK, Z.; ROMAN, K.; DLUGON, S.; GLUSZEWSKI, W.; SUDLITZ, M. “Research Laboratory and Feasibility Study for Industrial Wastewater Effluents Treatment by Radiation”. IAEA-TECDOC-1855 (2018).

[4] SAMPA, M.H.O.; RELA, P.R.; DUARTE, C.L. “Industrial Wastewater Treatment in Brazil Using Electron Beam Accelerator”. Editors: William J. Cooper, Kevin E. O'Shea and Randolph D. Curry, in Environmental Applications of Ionizing Radiation, v.33, p.521-530, John Wiley & Sounds, Inc. (1998).

[5] HAN, B.; KIM, S.; KIM, J. “Electron Beam Technology in Korean Industries”. Journal of the Korean Physical Society, v.59, n.2, p.542-545 (2011).

[6] HAN, B.; KIM, J.; KANG, W.; CHOI, J. S.; JEONG, K.Y. “Development of mobile electron beam plant for environmental applications”. Radiation Physics and Chemistry, v.124, p.174-178 (2015).

[7] MUNHOZ, P.M.; SILVA, L.G.A.; HARADA, J.; NASCIMENTO, F.C.; CALVO, W.A.P. “Poly (butylene adipate co-terephthalate)/poly (lactic acid) (PBAT/PLA) blend characterization processed by electron beam” (2020).

[8] KODAMA, Y. “Degradability: Enzymatic and in Simulated Compost Soil of PLA/PCL Blend and on Their Composite with Coconut Fiber”. Biodegradation of Hazardous and Special Products p.105 (2013).

[9] PEI, L.; SCHMIDT, M.; WEI, W. “Conversion of biomass into bioplastics and their potential environmental impacts. Biotechnology of Biopolymers”, p.57-74 (2011).

[10] INTERNATIONAL ATOMIC ENERGY AGENCY. “Specific Safety Guide No.SSG-8 Radiation Safety of Gamma, Electron and X Ray Irradiation Facilities” (2010). Available in: <https://www-pub.iaea.org/MTCD/publications/PDF/Pub1454_web.pdf >. Access: 19 Jun. 2022.

AN OVERVIEW OF THE SOUTH AFRICAN ISOTOPE FACILITY (SAIF) PROJECT

I. L. STRYDOM
iThemba LABS
Cape Town, South Africa

F. AZAIEZ
iThemba LABS
Cape Town, South Africa
Email: f.azaiez@ilabs.nrf.ac.za

Abstract

The South African Isotope Facility (SAIF) is a project to establish a new facility based on the production and usage of unstable isotopes for nuclear science and nuclear medicine. Phase-1 of SAIF is a new radioisotope production facility currently under construction at iThemba LABS in Cape Town and scheduled for completion in 2022. A commercial 70 MeV proton cyclotron from IBA with a number of beam lines equipped with isotope production stations, are being installed in retrofitted concrete vaults. The facility will be supported by new infrastructure and services which are being constructed. The completion of SAIF will greatly increase the radioisotope production capability of iThemba LABS, and enable the existing Separated Sector Cyclotron to be dedicated to produce stable ion beams and to post-accelerate unstable isotopes from phase-2 of SAIF for nuclear physics and nuclear astrophysics research activities. An overview of the SAIF project (Phase 1) from the inception phase through to the construction phase is provided here, discussing all related workstreams and progress made to date. A more detailed discussion of some specific systems is given, including the design of the isotope production stations, target handling system, and a new radioactive waste management facility.

1. INTRODUCTION

iThemba LABS is a national facility of the National Research Foundation (NRF) in South Africa, an entity of the Department of Science and Innovation. The mandate of iThemba LABS is to operate a number of cyclotrons for purposes of conducting research in subatomic physics, producing medical radioisotopes and performing patient treatment using proton and neutron beam therapeutic protocols.

The available beam time of the facility was historically divided more-or-less equally between the above-mentioned operational mandates since its commissioning in the early 1980's. However, in recent years the ageing facility for patient treatment was no longer compatible with modern neutron/proton treatment protocols and the patient treatment service was subsequently discontinued a few years ago. Since then, the allocation of available beam time gradually became more weighted towards medical radioisotope production due to growing demand for radioisotope products from the public and private health sectors. Today, iThemba LABS is a key producer and supplier of medical radioisotopes which are distributed throughout South Africa and globally into ~60 countries. As a result of this demand growth for radioisotopes, more than 50% of beam time is currently utilised for radioisotope production.

The demand for increased beam time for subatomic physics research at iThemba LABS as well as the necessity to continue to serve the health sector both locally and globally are the main driving factors for phase 1 of the South African Isotope Facility (SAIF) project which was conceived several years ago and which started officially in 2019 when the first budget for the SAIF project was approved. The SAIF project involves the installation of a new 70 MeV cyclotron into the decommissioned patient therapy vaults at iThemba LABS and which will be dedicated to radioisotope production. This will in turn release the existing Separated Sector Cyclotron complex to be fully dedicated to the subatomic and nuclear physics research programmes of the international scientific user base of iThemba LABS.

2. EXISTING ACCELERATOR FACILITIES AT ITHEMBA LABS

A number of existing accelerator facilities are currently in operation at iThemba LABS. The main facility is located at Faure near Cape Town, South Africa where the following accelerators are installed:

— 200 MeV Separated Sector Cyclotron (SSC)
— 8 MeV Solid Pole injector Cyclotron (SPC1) with internal PIG ion source for proton beams
— 8 MeV Solid Pole injector Cyclotron (SPC2) with a number of external ion sources for both light and heavy ion production
— A number of experimental beam lines dedicated to neutron production, gamma ray arrays (ALBA and Aphrodite facilities) and radiation biophysics
— K600 magnetic spectrometer for light ions
— 11 MeV self-shielded cyclotron for F-18 production
— Hotlab and cleanroom complex for chemical extraction and production of radiochemical and radiopharmaceutical products under cGMP conditions
— 3MV Tandetron accelerator and beam lines for materials research using Ion Beam Analysis (IBA) and microprobe analysis.

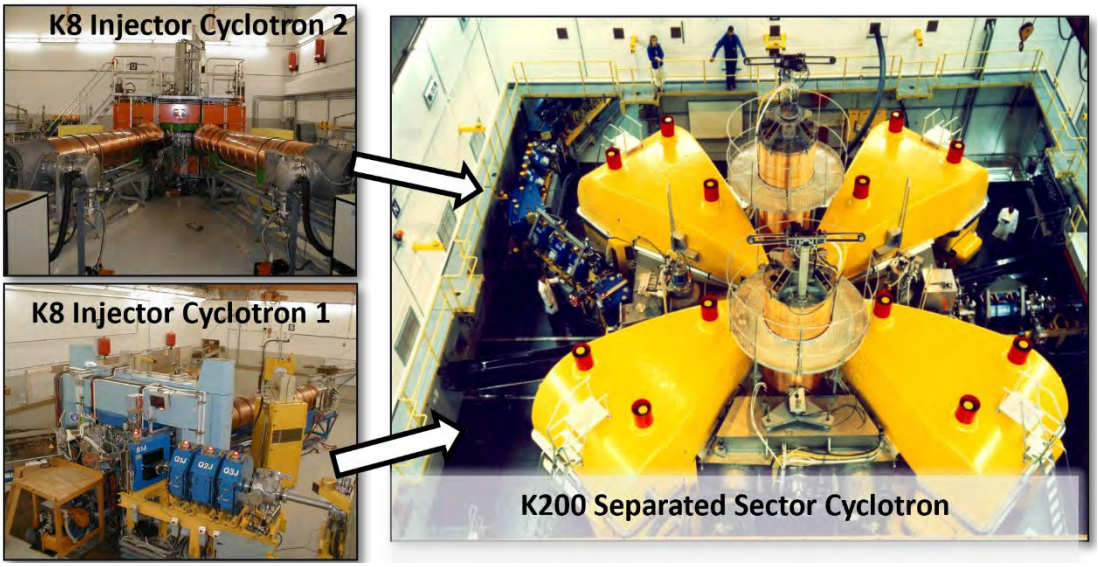

FIG. 1: Photograph of the 200 MeV Separated Sector Cyclotron (SSC) and SPC1/SPC2 injector cyclotrons in Cape Town.

Additionally, a 6MV tandem accelerator is in operation in Johannesburg, South Africa. This facility is dedicated to materials research using IBA, microprobe analysis as well as Accelerator Mass Spectrometry (AMS).

FIG. 2: Photograph of the Tandem AMS facility in Johannesburg.

3. MOTIVATION FOR SOUTH AFRICAN ISOTOPE FACILITY (SAIF) PROJECT

The oversubscription of beam time on the existing SSC complex and the increasing interest for research with unstable isotopes led to the concept of establishing the South African Isotope Facility (SAIF) which involves in its first phase the procurement and installation of a new 70 MeV cyclotron, four beam transport lines and target stations to be dedicated to radioisotope production. Once fully commissioned, this will release approximately 50% of SSC beam time currently allocated for radioisotope production to be used for subatomic and nuclear physics research programmes of the international scientific user base of iThemba LABS.

The SAIF facility was conceptualised to be housed in the three vaults of the decommissioned patient treatment facility, where the cyclotron would be installed in the centre vault with beam transport lines leading into two adjoining target vaults on either side which will house the four target stations.

The re-purposing of the existing vaults previously used for the patient therapy programme would realise significant cost savings for the SAIF project, but also introduced some spatial constraints for the installation of equipment and radiation shielding requirements which had to be met. The general layout of the SAIF facility is shown in *FIG. 3* below.

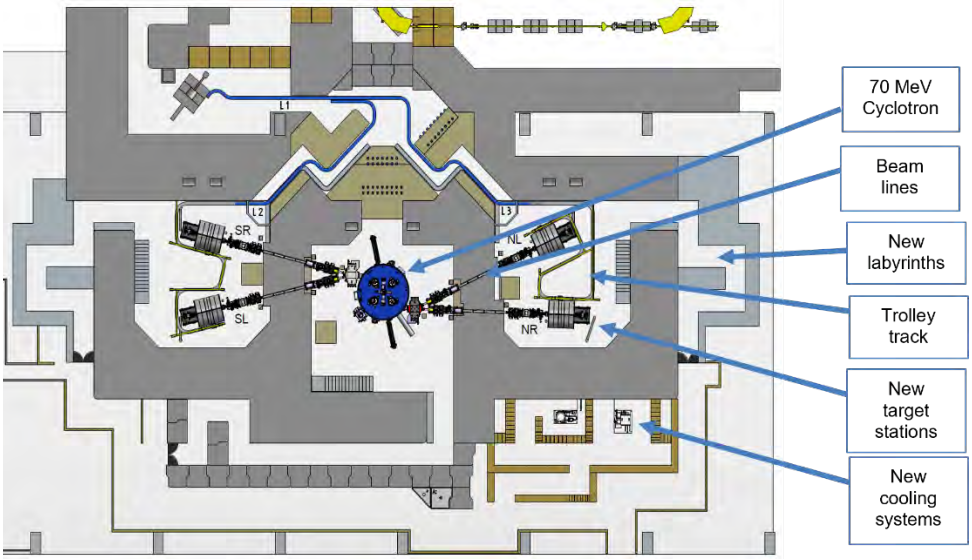

FIG. 3. General layout of the SAIF facility in the three existing vaults.

The first budget allocation for the SAIF project was approved in 2018 when the project formally launched. The execution of the project was planned within five major workstreams:

- 70 MeV cyclotron and beamline procurement
- Additional beamline equipment development and manufacturing
- New target stations manufacturing
- New building construction for utility services and radioactive waste disposal
- Regulatory licensing

4. CURRENT STATUS OF THE SOUTH AFRICAN ISOTOPE FACILITY (SAIF) PROJECT

The SAIF project is currently in the construction phase with equipment procurement taking place in parallel. The status of the various workstreams is further described in detail below.

4.1. Procurement of 70 MeV cyclotron

Following a competitive bidding process, IBA Radiopharma Solutions in Belgium was appointed to manufacture and supply a commercially available Cyclone 70P cyclotron with four beam transport lines for the SAIF facility. The C70 cyclotron can supply variable energy proton beams with energy from 30 – 70 MeV and

up to 750 uA beam intensity. It has the capability to extract two beams simultaneously from two extraction ports with up to 375 uA intensity each.

A multicusp ion source can provide 10 mA of H- current for injection into the cyclotron. The cyclotron is equipped with a 1.6 T four-sector magnet, a directly coupled RF system with 2 dees operating in the 4th harmonic mode. The four beam transport lines are fully equipped with beam diagnostics, Faraday cups and neutron shutters to isolate the cyclotron vault from the two target vaults.

The C70 cyclotron successfully passed factory acceptance testing in Belgium in July 2021 and was delivered to South Africa in December 2021. It was finally installed in the centre vault in April 2022. Due to space constraints imposed by the use of existing concrete vaults for the new facility, special logistical arrangements had to be made to install the heavy cyclotron parts inside the vaults. The vault walls extend 10m above ground level inside an existing building. In addition, the capacity of the overhead crane inside the building was insufficient to lift the heavy cyclotron parts, being the two magnet yokes weighing ~ 60 ton each.

A special temporary gantry therefore had to be constructed on the vault walls to lift the two magnet yokes over the 7 m high wall and to install them in the designated position inside the vault, as shown in *FIG. 4* below.

FIG. 4: Rigging of the magnet yokes into the centre vault.

FIG. 5: The C70 cyclotron installed in its final position

4.2. Additional beam line equipment development and manufacturing

In addition to the beam transport line equipment supplied by IBA Radiopharma Solutions, iThemba LABS is also implementing a beam sweeper/steerer facility designed to sweep the proton beam in a circular pattern over the target surface. This is required to assist with dissipation of up to 26 kW of heat from the target capsule with diameter of 54 mm.

The beam sweeping is achieved by constructing a sweeper magnet with two H-type dipole magnets operating with 90 degrees phase difference which is placed directly in front of the target system at the end of the beam transport lines.

The sweeper magnet makes use of a ceramic beam pipe inside the magnet in order to minimise the generation of Eddy currents and subsequent power losses and heat generation.

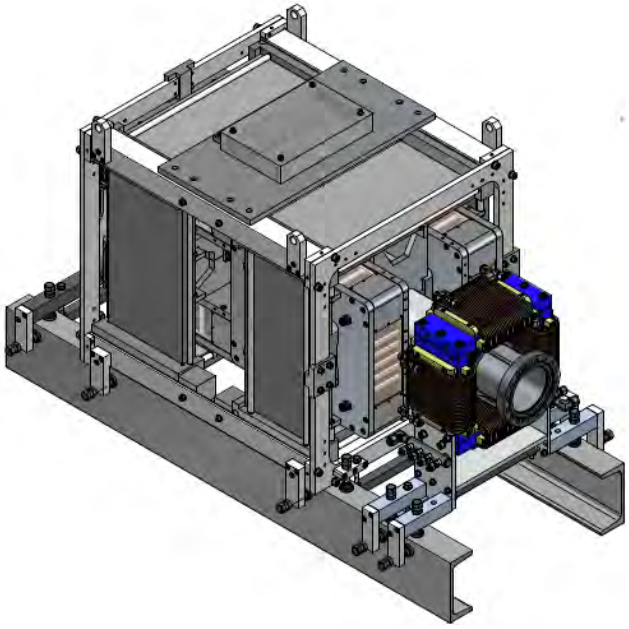

FIG. 6: The beam sweeper magnet.

4.3. New target station manufacturing

The target system is based on an in-house development[1] of a target station design that has been in use in the existing radioisotope facility for some 25 years. The target station provides for placement of the target capsule in front of the beam using a pneumatically controlled robot arm, retrieval of the target holder at the completion of bombardment and placement of the target holder on a trolley system to transfer the target from the target station to the radiochemical process facility some 120m distant from the target vaults.

The target station furthermore provides local radiation shielding inside the target vault by using a combination of shielding elements manufactured from steel, lead and borated wax. The target station is designed with a motorised mechanism to open and close the shielding elements to allow for placement and retrieval of the target holder with the robotic arm.

The target station provides pressurised water cooling to the target capsule through a pusher arm mechanism as well as helium cooling to a vacuum window which separates the beam line vacuum from atmosphere in front of the target capsule.

A prototype target station without the heavy shielding elements was manufactured and installed to assist with development of the electronic control systems of the mechanical systems and target transport system, as well as to qualify the designs of the cooling systems and target transporter.

4.4. New building construction for utility services and waste disposal

Construction works are currently underway on various infrastructure modifications and additions required for the SAIF project. These include the following:

— Construction of new plant rooms for a main water-cooling system and electrical distribution (including rotary UPS systems);
— Structural modifications to the existing vaults to accommodate the new C70 cyclotron and beam transport lines, as well as to provide new entry labyrinths for radiation shielding;
— Construction of new facilities to house the various electronics, power supplies, cooling systems and control room for the C70 cyclotron;
— Construction of a new building to house the radioactive waste processing and storage facility;
— Manufacturing of the new target cooling systems;
— Installation of new ventilation systems required to maintain the specified air changes and air pressure cascades of the cyclotron and target vaults;
— Installation of the supervisory control systems for vault clearance and safety interlocking.

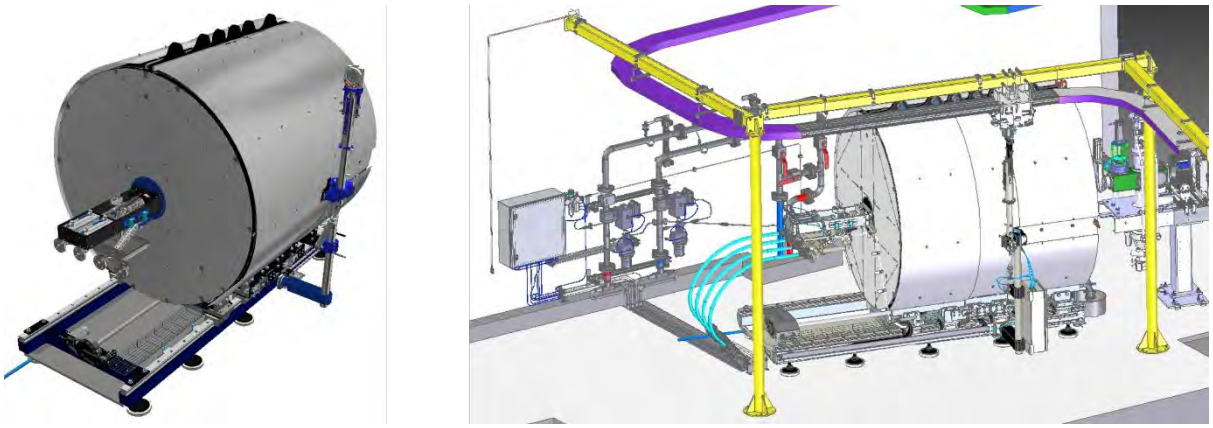

FIG. 7: 3D models of the SAIF target station showing the pneumatically controlled pusher arm and robot arm mechanisms.

FIG. 8: The prototype target station being commissioned.

The structural modifications to the cyclotron and target vaults were informed by the radiation shielding requirements as dictated by the facility licencing conditions. The radiation levels inside and outside the vault areas were simulated by using the FLUKA simulation software under worst-case conditions for dose conversion factors (FLUKA option EWT74) based on data sets from ICRP74.

FIG. 9: *Bird's eye view of the new mechanical and electrical plant rooms under construction*

4.5. Regulatory licensing

An important aspect of the SAIF project is to obtain the necessary regulatory licenses for the new facility. In this respect, a license to import the cyclotron and beam transport line equipment was granted by the regulatory authority (Department of Health) on 8 Oct 2019. This follow a process of basic design with safety assessment, submission of plans and designs as well as decommissioning strategies and construction reports.

Subsequently, a license to install the cyclotron and beam transport line equipment was granted on 18 Nov 2020.

Application for a license to operate the C70 cyclotron will be launched when the facility is ready for cold commissioning, when further safety case documentation will be submitted for approval.

5. SUMMARY

Construction and equipment installation on the South African Isotope Facility (SAIF) project are in progress. An overview of the status of the SAIF facility is provided, where progress with the installation of a new 70 MeV cyclotron and beam transport lines, manufacturing of the target stations and additional beam line equipment, and construction of buildings for utility services is reported.

Completion of the project is scheduled for the end of 2022 when first beam will be extracted from the cyclotron. Final site acceptance testing of the C70 cyclotron is planned for February 2023 after which production of radioisotopes can commence.

ACKNOWLEDGEMENTS

The following institutions are acknowledged: a) National Research Foundation (South Africa) and b) IBA Radiopharma Solutions (Belgium)

REFERENCES

[1] STEYN, G.F. et al, Development of New Target Stations for the South African Isotope Facility, Instruments **2** 29 (2018).

ACCELERATOR MASS SPECTROMETRY: AN ANALYTICAL TOOL WITH APPLICATIONS FOR A SUSTAINABLE SOCIETY*S*

William E. KIESER
Department of Physics and A. E. Lalonde AMS Laboratory
University of Ottawa
Ottawa, Canada
Email: Liam.Kieser@uOttawa.ca

Abstract

Accelerator Mass Spectrometry (AMS) adds the techniques of charged particle acceleration to the basic principles of Isotope Ratio Mass Spectrometry (IRMS) to provide extremely low detection capability (below 1 femtogram) of rare isotopes in in samples of natural materials as small as 1 mg. Depending on the element selected and the configuration of the equipment, sensitivities can reach one part in 10^{15}. The advantages of this small sample size and high sensitivity include the economic benefit of collecting, shipping and preparing much smaller samples, and also the ability to analyse specific chemical compounds within the sample, so that the pathway taken by that compound through complex systems can be more precisely traced or, in the case of radioactive isotopes, more precise chronological information can be provided. The paper begins with a basic overview of AMS technology, with an emphasis on how the use of higher energy contributes to this enhanced sensitivity, then provides several examples or new AMS technologies which reduce the energy and space requirements for such systems, and follows with several examples of applications which contribute to the investigation of sustainability in other areas of environmental concern.

1. INTRODUCTION

1.1. Requirements leading to the development of AMS

The use of accelerators to increase the sensitivity of mass spectrometry has had a long history, dating back to 1939 when Alvarez and Cornog used the recently developed Berkeley cyclotron to identify the existence of ^{3}He in a sample of ^{4}He at a ratio of $^{3}He/^{4}He \approx 1 \times 1x10^{-6}$ [1]. However, such measurements remained isolated experiments until the development of tandem electrostatic accelerators [2] and the negative ion sources needed to provide anions from solid, rather than only gas samples [3]. During this time, the technique for measuring the age of organic samples developed by Libby [4] using the counting of β particles from the decay of ^{14}C in the sample was gaining widespread use in the fields of Earth and environmental science as well a in Archaeometry as the half-life of ^{14}C (5730 a) permitted good chronological measurements for late Quaternary geological evens and for the development of human societies. By the mid 1970s, the demand for precise and rapid ^{14}C dating was exceeding the capacity of the decay-counting method, even with improvements of newer technology, such as liquid scintillation counting. Mass spectrometry at this time was still hindered by the overwhelming presence of the isobar ^{14}N with very nearly the same mass ($\Delta M/M = 3.06 \times 10^{-4}$). This barrier was overcome in 1977 by Purser et al [5], who showed that the negative ion of ^{14}N (needed for injection into tandem electrostatic accelerators) is unstable whereas that of ^{14}C was relatively robust. This was followed quickly by several papers demonstrating the use of tandem electrostatic accelerators, equipped with Middleton type caesium sputter ion sources [3], to provide ^{14}C measurements with acceptable accuracy [6,7]. The two key technical requirements: ion energy provided by the tandem accelerator and high ion currents from the sputter source were now in place

1.2. Expansion to applications beyond ^{14}C

Following this initial discovery, the number of isotopes which could be easily analysed expanded rapidly: ^{10}Be [8[, ^{36}Cl [9] and ^{129}I [10]. Within another decade, these included the actinides [11] and, for example, a less abundant isotope ^{236}U. In the over 40 years of the availability or AMS analyses, many applications in Earth, environmental, planetary, biomedical and cultural sciences have been developed. Of particular interest to sustainability are the contributions made to climate change research using ^{14}C and more recently ^{26}Al, ^{36}Cl and ^{10}Be, to provide details about previous climate change events and to monitor the specific events associated with current changes, such as permafrost thawing, sources of atmospheric methane, or carbon cycling in the oceans.

For the energy sector, atmospheric measurements of ^{14}C are used to assess the efficacy of bio-remediation programs for fossil fuel spills and the actinides and fission fragments are analysed to monitor the production, use and disposal of nuclear fuel. Cultural applications include collaborations with indigenous communities to provide chronologies for events chronicled in oral histories, some of which include their adaptation to earlier environmental changes.

1.3. AMS and Sustainability

There are currently approximately 160 AMS systems in operation throughout the world, ranging in acceleration voltage from 200 kV to 15 MV, a number which has doubled in the past 10 years. However, as the space and cost of such equipment scales with the terminal voltage, manufacturers and many of their clients are opting for smaller systems. Those which operate at the lowest of these voltages are specifically designed for one element (typically carbon isotopes), which permits the use of permanent, instead of electro-magnets – a significant saving in operating costs. In addition, there are a number of multi-element machines coming on line which operate at 300 kV. In both cases, these systems can be equipped with integrated sample preparation equipment, such as elemental analysers, carbonate analysis systems or even IRMS systems for abundant stable isotope analyses of the same sample – a further economy in labour and time.

2. TECHNIQUES WHICH ENABLE AMS SENSITIVITY

2.1 Challenges and Solutions

The requirement to measure isotope ratios at very low concentrations (typically 1 part in $10^{12} – 10^{15}$) sets AMS apart from IRMS in several ways:

— An increased presence of isobars (atoms or molecules of a different element which have a mass so close to the mass of the rara isotope of interest that they are not resolvable by conventional mass analysis techniques, such as magnet-electric analyzer combinations or radio-frequency quadrupoles (RFQs)) The initial solution provided by AMS, as described in section 1.1, is the use of negative ions. However, this solution provides only a few, albeit important solutions – 14C (14N), 26Al (26Mg) and 129I (129Xe). For molecular isobars, the accelerator provides the energy necessary to break up the molecules in the accelerator terminal electron stripping canal (see Figure 1). For other atomic isobars, the accelerator provides the energy required to use energy loss methods such as energy degrader foils or gas-filled magnets. These combined with a gas ionization detector can, with sufficient energy, resolve most isobar issues.

— The low concentration of the rare isotope of interest, as well as the increasingly smaller samples that require analysis require an ion source which can efficiently generate high currents. For example, whereas an IRMS instrument can provide precise results with a nano-ampere beam of analyte ions, an AMS source requires 10s to 100s of micro-amperes to provide rare isotope analyses with sufficient precision to achieve statistical precisions of between 1% and 1‰. These are typically sources which sputter solid samples with a high current of Cs” ions, but some systems are now using electron cyclotron resonance (ECR) sources and charge changing where necessary.

2.2 Basic Parts of an AMS system

As most AMS systems still use tandem electrostatic accelerators, the technique will be illustrated using such systems. Some smaller systems use only a single high voltage acceleration gap as indicated in ref [13], but many of the principles are common to both approaches. The main parts of a tandem accelerator-based system are summarized in Pig 1.

The low energy spectrometer section, which includes the ion source, an electric analyser to select a precise ion energy (if needed) and an injection magnet which selects the ions of a specific momentum. Together these two elements define the mass selected for injection. Most systems include a method for rapid switching between the rare and abundant isotopes, usually by accelerating or decelerating either the rare and/or abundant ions before and after the magnet, thus adjust the ion momentum appropriately.

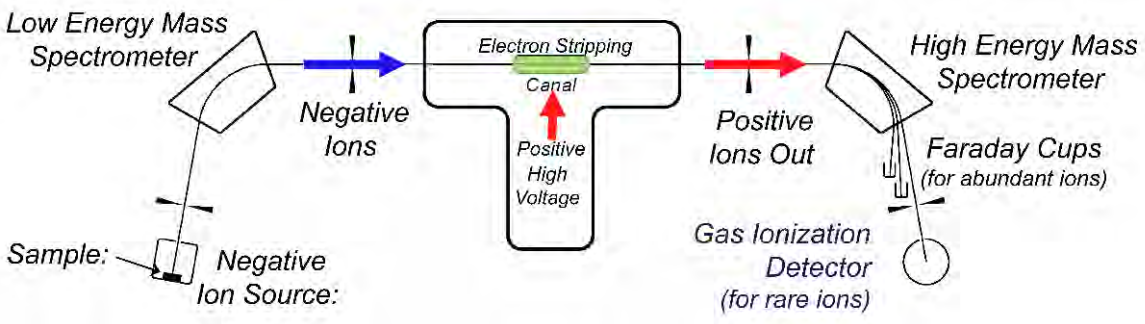

Figure 1: Basic parts of an AMS system using a tandem electrostatic accelerator

The accelerator section includes the high voltage power supply, graded vacuum tubes to conduct the ions to and from the high voltage terminal and an electron stripping device in the terminal. This can be either a foil or a windowless gas cell, with a pump to recirculate the stripping gas. This removes electrons from the incoming beam and provides positive ions for further acceleration. With sufficient foil thickness or gas pressure and appropriate ion velocity, molecular ions can be disintegrated into their constituent atoms and the charge state of the positive ions can be optimized to facilitate further analysis.

The high energy spectrometer section includes the magnets and electric analysers required for the analysis of the positive rare ion beam as well as Faraday cups, usually following the first magnet, to measure the current of the abundant beam(s) and a gas ionization or silicon detector to count the positive rare ions. The gas ionization detector provides extremely low noise, single atom counting as well as energy loss information, which can be useful in further isobar discrimination. A particular implementation of these sections is shown in Fig 2, a schematic of the AMS system at the Lalonde AMS Lab in Ottawa.

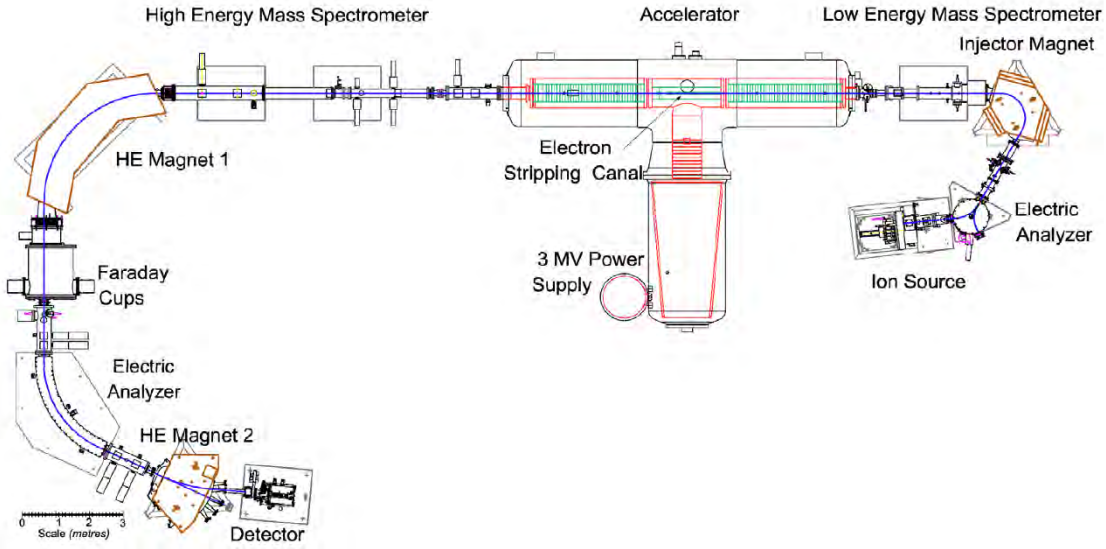

Figure 2: The AMS system at the Lalonde AMS Lab, University of Ottawa. Due to building constraints, the ion beam direction is from right to left.

3. SUSTAINABILITY IN AMS TECHNOLOGY

3.1 Smaller AMS Systems.

Accelerator manufacturers, in some cases for over a decade, have been building smaller AMS systems, which require significantly less space (a capital cost reduction) as well as less electrical power for their operation. These can be broadly divided into two types:

— Low energy tandem accelerators, using high voltage terminal voltages of between 200 and 300 kV [14, 15]. Due to the shorter distance to the accelerator terminal, such instruments often provide better transmission efficiency through the accelerator than their larger counterparts
— Single stage AMS systems in which either the high energy (more usual) or the low energy spectrometer section is placed on a high voltage platform [13, 16]. These systems, with only one short accelerator tube also exhibit enhanced transmission efficiency.

3.2 Single Element AMS systems.

In larger systems, magnets typically consume the most power (more than the accelerator) Systems built for specific isotope analysis (e.g., ^{14}C), can use permanent magnets with a small coil for minor adjustments. In addition to conserving electrical power, such magnets eliminate the need for water cooling of the coils, necessary for a conventional electromagnet.

An example of a single element system for ^{14}C (MICADAS^{TM} Ionplus AG) recently installed at the Lalonde AMS Lab, is shown in Fig 3 and the high energy permanent magnet in Fig 4 below.

Figure 3: Single Element ^{14}C System installed at Lalonde AMS

Figure 4: High Energy Permanent Magnet with upper yoke lifted during assembly. Note the small size of the trim coil compared with the space available for a water-cooled full power coil.

4. EXAMPLES OF APPLICATIONS PROMOTING SUSTAINABILITY IN OTHER FIELDS

4.1 Carbon in the Arctic Environment

It is now well established that the Arctic (and the Antarctic) regions are experiencing the effects of almost a doubling of the current increase in global average temperatures. In terms of carbon storage or emission, this represents a “two-edged sword”, as although the reduced ice cover in the ocean regions permits an increase in biological carbon sequestration in the water column and the sediments, this could easily be overwhelmed by the thawing of permafrost regions with a release of methane as well as carbon dioxide.

AMS carbon isotope analysis has played an important role in the testing of models predicting sea-level rise and glacial isostatic adjustment [17] as the timing of the changes since the last glacial maximum (~203 ka B.P.) matches well the half-life of ^{14}C. On-going studies of carbon in the water column [18] and sediments [19] already providing information about the region’s response to previous climate changes.

The small sample AMS capability will increase the use of Compound Specific Radiocarbon Analysis (CSRA). The original intention of this approach was to reduce the possibility of heterogeneous sources of 14C in samples. While recent work [20] have shown that this is not necessarily the case the technique can be improved by reducing the size of the samples. The increased efficiency of the new smaller AMS systems is expected to contribute to further developments of this technique.

4.2 Bio-remediation of hydrocarbon spills

The process of using naturally occurring bacteria to remediate sites where hydrocarbon fluids have been spilled or leaked into the ground is monitored by analysing the carbon isotope ratio of the CO_2 released with other soil gases. If the CO2 is modern or nearly so, the bacteria are not processing the hydrocarbons, but more recently formed deposits, such as forest fire debris. To analyse a soil gas sample directly requires a large gas volume, an expensive and cumbersome collection, handling and shipping process, as well as further processing by the AMS lab.

In an alternative method [21], by passing the soil gas through aa filter bed of $Ba(OH)_2$, the CO_2 reacts with the $Ba(OH)_2$ and produces $BaCO_3$. Filter cartridges can simply be loaded with $Ba(OH)_2$ in a local lab and are use by commercial operators to test remediation sites. Exposed filter cartridges are economically returned to the AMS lab and can be analysed using an automated Carbonate Handling System connected directly to the AMS ion source.

5. SUMMARY

For almost 45 years, AMS has provided highly sensitive isotope analyses for Earth, environmental, archaeometric, bio-medical and materials sciences. New AMS systems and techniques are being developed which require less energy, space and sample preparation time. Applications continue to be developed which are making an impact on research that is important for the sustainability of our society.

ACKNOWLEDGEMENTS

Funding for the equipment and operation of the A. E. Lalonde AMS Laboratory has been provided by the Canada Foundation for Innovation and the Ontario Research Fund. Development work has been assisted by the Natural Sciences and Engineering Research Council of Canada.

The author is grateful for support from and discussions with, the team of scientists and skilled technicians at the A. E. Lalonde AMS Lab.

REFERENCES

[1] L. W. Alvarez & R. Cornog (1939) ^{3}He in helium, Phys. Rev. 50, p.378

[2] L. W. Alvarez LW. (1951). Energy doubling in dc accelerators. Rev Sci Instr 22 p.705–706.

[3] R. Middleton 1977. On producing negative ion beams of magnesium and calcium in a caesium sputter source. Nucl Instr Meth 141:373–375.

[4] W. R. Libby, E. C. Anderson & J. R. Arnold, 1949, Age Determination by Radiocarbon Content: World-Wide Assay of Natural Radiocarbon, Science, 109(2827) p. 227

[5] K. H. Purser et al, (1977) An Attempt to Detct Stable N- ions from a sputter ion source and some implications of the results for the design of tandems for ultra-sensitive carbon analysis, Rev Phys Appl 12, p.1487

[6] D. E. Nelson, R. G. Korteling, W. R. Stott (1977) Carbon-14: Direct Detection at Natural Concentrations, Science 1988(4316) p.507-508

[7] C. L. Bennet et al, (1977) Radiocarbon Dating Using Electrostatic Accelerators Negative Ions Provide the Key, Science 198(4316) p.508-510

[8] Kilius, L. r. et al (1980) Measurement of ^{10}Be/9Be Ratios Using An Electrostatic Tandem Accelerator, Nucl. Instr. & Methods 171 p.5-360

[9] Elmore D. et al (1979) Analysis of ^{36}CI in environmental water samples using an electrostatic accelerator, Nature 277 p.22

[10] Elmore D. et al (1980) Determination of ^{129}1 using tandem accelerator mass spectrometry, Nature 286 p.138.

[11] X-L Zhao et al (1994) Radium, actinides, and their molecular negative ions from a cesium sputter ion source, Nucl.. Instr. & Methods B 92 p.258-264

[12] X-L Zhao et al (1994) The first detection of naturally-occurring ^{236}U with accelerator mass spectrometry, Nucl. Instr. & Methods B 92 p.249-253

[13] S.P.H.T.Freeman (2010) Improved SSAMS Performance, Nucl Instr. & Methods B 268 p.715-717
[14] K. Fenclov´a et al (2021) Initial tests of ^{26}Al fluoride target matrix on MILEA AMS system, Nucl. Instr. & Methods B 503 p.45-52
[15] G. Scognamiglio et al (2021) Low-energy 14C and multi-element HVE AMS systems, Nucl. Instr & Methods B 492 p.29-33
[16] T. J. Ognibene et al, (2019) Trials and tribulations in the first three years in operation of the SSAMS for biomedical ^{14}C-AMS at LLNL, Nucl. Instr. & Methods B, 438, p.166-171
[17] R. Peltier (2004) Global Glacial Isostacy and the Surface of the Ice Age Earth: The ICE-5G (VM2) Model and GRACE Annu. Rev. Earth Planet. Sci. 32 p.111–49
[18] S. R. Beaupré., B. D. Walker & E. R.M. Druffel (2020) The two-component model coincidence: Evaluating the validity of marine dissolved organic radiocarbon as a stableconservative tracer at Station M. Deep Sea Res Part Ii Top Stud. Oceanogr, 173 p. 104737
[19] A. de Vernal, et al (2020) Natural variability of the Arctic Ocean Sea ice during the present interglacial. Proc. of the National Academy of Sciences U S A. 117(420 p.26069–26075
[20] G Mollenhauer and J Rethemeyer 2009 Compound-specific radiocarbon analysis Analytical challenges and applications, IOP Conf. Ser.: Earth Environ. Sci. 012006
[21] Lindsay Shaw, M.Sc. Thesis, University of Ottawa.

HOW SUPPORT FOR MACHINE-BASED SOURCES OF RADIATION CONTRIBUTES TO SUSTAINABLE DEVELOPMENT

Sarah NORRIS
Office of Radiological Security (ORS) - Department of Energy/National Nuclear Security Administration (DOE/NNSA)
Washington, DC, USA
Email: Sarah.Norris@nnsa.doe.gov

Matthew KESKULA
Argonne National Laboratory
Washington, DC, USA

Abstract

As stated by the International Atomic Energy Agency (IAEA), radiation-generating technologies can be used in support of 9 of the 17 United Nations Sustainable Development Goals (UN SDGs). The U.S. Department of Energy/National Nuclear Security Administration's (DOE/NNSA) Office of Radiological Security (ORS), with the mission to prevent radioactive materials from being used in malicious acts, is working to improve options for and adoption of advanced machine-based sources of radiation. In addition to supporting radiological security, these activities directly support the broader development goals of the IAEA. This paper will focus on how the following three areas of ORS work contribute to both security and sustainable development: cancer therapy with medical Linear Accelerators (LINACs), X-ray blood irradiation, and electron beam (e-beam) technologies for reuse of resources and wastes.

Machine-based sources of radiation often provide key advantages over traditional, radioactive source-based means of generating radiation. For instance, X-ray blood irradiators allow consistent, and typically higher throughput across the lifespan of the device. E-beam technology can also play a significant role in providing clean water for growing urban populations around the world. While these technologies having operational, business, and security benefits, ORS recognizes that these technologies present challenges in terms of needing reliable power supply, trained/educated staff, and accessible service providers. This paper will highlight these challenges and ORS's perspectives on how the international community can work to address them. Time is of the essence, and advanced machine-based, radiation-generating technologies are essential to confronting the challenges associated with ensuring sustainable development.

1. INTRODUCTION

According to the International Atomic Energy Agency (IAEA), radiation-generating technologies can be used to support 9 out of the 17 United Nations Sustainable Development Goals (UN SDGs), as they have the ability to affect human health, food growth and safety, and environmental remediation, among sectors [1]. These radiation-generating technologies can include devices that rely on radioisotopes to generate radiation and machine-based radiation generators. While radioactive materials have social benefit across a variety of applications, these benefits must be considered alongside the concern of radioactive materials being misused, and the negative societal and economic impacts such an incident, accidental or intentional, could bring.

The U.S. Department of Energy/National Nuclear Security Administration's (DOE/NNSA) Office of Radiological Security (ORS) works to prevent the use of radioactive materials in acts of radiological terrorism and encourage the development and use of non-radioisotope-based technologies where possible. ORS supports the development and implementation of advanced machine-based ionizing radiation technologies, including electron beam (e-beam) and X-ray, in a variety of application spaces, including cancer care, the blood supply, food security, and environmental remediation. In many cases, these technologies provide equivalent (or superior) results to their radioisotopic counterparts. However, challenges remain to consistent implementation, including the need for reliable electricity supply, trained/educated staff, and consistently accessible service providers. Finding solutions to these challenges across a variety of application spaces can allow the meeting of joint goals of an improved radiological security environment and widespread access to beneficial radiation technologies, with benefits for humans and the planet writ large.

2. THE USE OF RADIATION TECHNOLOGIES FOR SUSTAINABLE DEVELOPMENT GOALS

In 2015, the UN adopted 17 aspirational SDG goals, meant to serve as a "universal call to action to end poverty, protect the planet, and ensure that by 2030 all people enjoy peace and prosperity" [2]. These goals cover a wide range of social, environmental, and human security challenges and are meant to be implemented in a sustainable manner for long-term benefit.

The use of ionizing radiation technologies, both gamma and machine-based, is a key step in countries aiming to achieve the SDGs by the 2030 deadline. These technologies, many in service for decades, are used commonly throughout the world and provide benefits to human health, food security, and environmental remediation efforts. The use of gamma radiation was often the first foray into using radiation technologies in these applications, and many gamma devices remain in use today; however, many technologies that rely on machine-generated radiation have been developed and have gained more widespread acceptance in recent years. The figure below highlights some intersections between ionizing radiation technologies and the SDGs.

UN Sustainable Development Goal (SDG)	SDG Description	Applications of Interest
Zero hunger	End hunger, achieve food security and improved nutrition and promote sustainable agriculture	• Phytosanitary treatment & food irradiation • Sterile Insect Technique (SIT) • Plant mutation breeding • Seed irradiation
Good health and well-being	Ensure healthy lives and promote well-being for all at all ages	• Radiotherapy • Blood irradiation • Medical research • Medical product sterilization
Clean water and sanitation	Ensure availability and sustainable management of water and sanitation for all	• Wastewater treatment
Industry, innovation, & infrastructure	Build resilient infrastructure, promote inclusive and sustainable industrialization, and foster innovation	• Non-Destructive Testing
Life below water	Conserve and sustainably use the oceans, sea and marine resources for sustainable development	• Plastics/polymer reuse and recycling
Partnerships for the goals	Strengthen the means of implementation and revitalize the global partnership for sustainable development	• Contributions to the IAEA that facilitate the use of machine-based ionizing radiation technologies

FIG. 1- Synergies between radiation technologies and UN SDGs

Machine-based radiation generators have low security risks, whereas certain radioisotopes pose an inherent security risk, as they can be used by malicious actors as the basis for a radiological weapon. If these radioisotopes fall outside of regulatory control, or if proper end-of-life management is not factored into the lifecycle operation of a radioisotopic device, they are vulnerable to neglect and eventually misuse, which can cause substantial psychological and economic damage, even if accidental. In 1987, the city of Goiania, Brazil suffered significant economic, physical, and psychological disruption as a result of an accidental misuse and spreading of radioactive material from an abandoned device that had fallen outside of regulatory control. Machine-based radiation generators, conversely, do not generate radiation if the system components are not complete, operational, and powered on, minimizing the risk for a radiological weapon or an accidental misuse.

3. NNSA OFFICE OF RADIOLOGICAL SECURITY

ORS works to enhance U.S. and global security by preventing high-activity radioactive sources (primarily Cobalt-60, Cesium-137, Iridium-192, and Americium-241) from being used malicious acts, like acts of terrorism. ORS achieves this through its Protect, Remove, and Reduce programs. The Reduce program works to achieve permanent risk reduction both domestically and internationally by encouraging the development and use of non-radioisotopic alternative technologies. This program focuses on four strategic approaches to achieve these goals, including encouraging policy that that facilitates or incentivizes the development and implementation of non-radioisotopic technologies (primarily machine-based sources of ionizing radiation); supporting research and development efforts related to the use of existing and new non-radioisotopic technologies; providing tools and forums that facilitate information exchange among users, industry, academia, and government personnel; facilitating the implementation of machine-based technologies, which includes the provision of logistics and cost incentives for replacing some radioisotopic sources with technically viable and operationally sustainable alternatives. These efforts have resulted in the replacement of over 280 radioactive source-based devices worldwide, primarily Cesium-137-based (Cs-137), as of June 2022, alongside increased awareness of the ionizing

radiation technology options, benefits of using of non-radioisotopic technologies, policy and regulatory enablers, and research meant to fill technical and policy gaps in the implementation of machine-based technologies.

As machine-based sources of ionizing radiation, which utilize electricity to generate radiation, are often viable replacements for radioisotopes, ORS is keenly interested in the continued development of these advanced radiation generators. These accelerator technologies are used in a variety of application spaces, some of which are highlighted below.

Machine-Based Radiation Generating Devices	Application Examples
• Self-shielded X-ray Irradiators	• Research Irradiation • Blood Irradiation • Sterile Insect Technique (SIT) • Seed irradiation • Plant Mutation Breeding
• Medical Linear Accelerators (LINACs)	• Radiotherapy
• Industrial Electron Beam and X-ray	• Medical Device Sterilization • Phytosanitary Treatment & Food Irradiation • Plastics and Material Modification • Wastewater Treatment
• Mobile X-ray	• Non-Destructive Testing

FIG. 2- Prominent Machine-Based Radiation Generating Devices and their Applications

4. ORS ENGAGEMENT ON MACHINE BASED RADIATION TECHNOLOGIES AND SDG'S

4.1. External Beam Radiotherapy

External beam radiotherapy is one of the primary tools for treating cancers. As cancer rates increase worldwide, the need for capable, accessible, and robust radiotherapy services will continue to grow. Cobalt-60 (Co-60) traditionally was used for external beam radiotherapy and continues to be used in some parts of the world. However, medical linear accelerators (LINACs) have substantially overtaken Co-60 as the most common means of delivering radiotherapy machines in the world and are now considered the standard for radiotherapy treatment.

Medical LINACs hold key advantages over Co-60 machines, and many of these advantages help to minimize the gap in overall patient treatment needed for the global cancer burden. Given the lack of source decay in a LINAC (Co-60's half-life is 5.26 years), treatment times can be consistent throughout the lifespan of the device. This, coupled with LINACs' improved patient treatment times (given the nature of their beam generation), allows for superior patient throughput without negatively impacting quality of care for patients. As LINACs are the standard treatment for radiotherapy and have been for some time, significant research and development efforts exist to optimize these systems, leading to improved access to advanced technical machinery, treatment options, and improved beam accuracy through advanced techniques, which minimizes the harm to healthy tissue for patients. New developments in LINAC technology aim to improve system resilience and function in challenging environments, while at the same time decreasing costs and improving treatment affordability. Lastly, medical LINACs do not require radioactive material security systems or costly and complicated radioactive waste management.

ORS Support for LINAC Use in External Beam Radiotherapy

ORS support for the adoption of medical LINACs continues to grow internationally. While ORS support is rooted in its security mission, this work is making a small contribution to the realization of the third SDG – "Good Health and Well Being." However, given the large capital investment inherent in procuring radiotherapy devices, ORS does not directly purchase medical LINACs. ORS does engage with the IAEA's Programme for Action for Cancer Therapy (PACT) and various regional Divisions within Technical Cooperation (TC) to provide funding, on a cost-sharing basis, for projects supporting procurement of LINACs in Member States. For example, ORS provided $4.5 million USD in 2021 in support of the procurement of four LINACs. ORS also pledged an in-kind contribution for maintenance and repair, to include spare parts, for the medical LINAC at IAEA Dosimetry

Laboratory in Seibersdorf, which was opened in 2019 to support Member States with dosimetry calibration and training, among other things. On a bilateral basis, ORS works with international partners to remove disused Co-60 radiotherapy devices that are being replaced with machine-based technologies. These sources are then placed in safe and secure long-term storage or disposal. ORS also has helped with infrastructure modifications for facilities looking to transition away from radioisotopes. One prominent example of this involves ORS support for bunker modifications needed to install a medical LINAC, as many Co-60 bunkers do not have adequate shielding to accommodate some of the modern medical LINAC systems. However, this issue has become less of a concern in recent years with the development of new LINAC systems that can be placed in existing bunkers. Reliable electricity is important for continued patient treatment and integrity of LINAC components, and another example of ORS-supported infrastructure modifications that facilitate machine-based technologies includes installation of uninterrupted power supply (UPS) systems to improve a facility's electrical resiliency. ORS also works with other offices in DOE/NNSA to support research and development aimed at developing medical LINACs that meet operational challenges present in markets with inconsistent power, are more affordable, use resilient components, and do not require complicated servicing.

4.2. Blood and Research Irradiation

In many countries, blood is irradiated before transfusion to ensure patient safety, a component of ensuring human health. Irradiation inactivates the donated blood's lymphocytes, eliminating the risk of transfusion-associated graft-vs-host disease (TAGVHD), a rare but typically fatal condition associated with transfusions. Traditionally, blood irradiation has been achieved with self-shielded Cs-137 irradiators containing Category 1 levels of radioactive material. Self-shielded irradiators refer to devices in which the shielding required for machine operation is integrated into the design of the device, leaving the irradiation chamber inaccessible during operation. Recently, X-ray blood irradiators have become more reliable and efficient, and have grown in recognition and use both domestically and internationally as viable replacements.

Research irradiators are used in a variety of studies involving cells, tissue or small laboratory animals as well as nonbiological material. Traditionally, these devices also rely on Category 1 levels of Cs-137 or Co-60, depending on the machine specifics. The use of X-ray machines, however, has continued to grow for many of these sub-applications as well.

X-rays offer several prominent advantages over radioactive-source-based options. X-ray sources do not decay over time, meaning that radiation times and throughput remain consistent through the lifecycle of the device, whether research or blood-oriented. X-ray devices also permit a broader range of energies to be used to conduct research areas across a range of subjects. Blood throughputs can also be higher with X-ray, allowing for improved facility efficiency. X-rays require less physical security than radioactive sources, which simplifies operation and workflow. Finally, the lack of radioisotopic sources means that no radioactive waste management needs to occur at the end of life of an X-ray system.

ORS Support for X-ray Use in Blood and Research Irradiation

ORS support for the use of X-ray devices as self-shielded irradiators for blood and research irradiation is its most advanced and recognizable effort related to encouraging radiological risk reduction. Considering the advantages of using X-ray listed above, ORS support in this area also contributes to the realization of the third SDG – "Good Health and Well Being." In the United States, the Cesium Irradiator Replacement Program (CIRP) has led to the removal of over 245 radioactive source-based self-shielded irradiators (both blood and research) from hospitals, research facilities, and blood banks to safe and secure disposition. More importantly for sustainable development, ORS has replaced over 35 radioactive-source based irradiators internationally with X-ray systems since the program began in 2016. Financial support was provided for the safe and secure radioactive source removal and the X-ray purchase price, installation, and maintenance for one year. Finally, ORS has worked with other DOE/NNSA offices to support research and development efforts for new, more effective, more economical, or more robust X-ray systems that can handle challenging infrastructure environments and meet market demands. For example, ORS and its agency partners are supporting industry in the development of a series of flat-panel X-ray sources that would reduce the size and complexity of x-ray irradiators and improve reliability, dose uniformity, and dose targeting.

4.3. Irradiation for Environmental and Agricultural Problems

Growing populations, climate variability and extremes, and conflict challenge global food security. Foodstuffs can be treated with radiation to inactivate pathogens, which can improve the products' shelf life and food safety by minimizing the risk of foodborne illness; they also can undergo "phytosanitary" treatments, where radiation is used to inactivate pests that may be present in shipments of foodstuffs that could prove harmful to crops elsewhere. Given the positive impacts irradiation has in reducing product loss, enabling trade, and food safety (all related to the SDG of "Zero Hunger"), the irradiation of food and phytosanitary treatments will become increasingly important. Food can also be treated in several ways with radiation. Co-60 remains the predominant method of irradiating foodstuffs, though the use of electron beam and X-ray technology is increasing worldwide.

Though the technical requirements for food irradiation and phytosanitary irradiation differ, accelerator-based systems provide several distinct advantages over radioisotopic options. Accelerators can deposit dose at higher rates than Co-60, on the order of seconds (for electron beam) or minutes (for X-ray) instead of possible hours (for gamma). This provides different advantages between these modalities; for electron beam, the rapid dose deposition can allow for very high throughputs, although one must consider packaging or the use of two beams to achieve desired penetration depth. For X-ray, pallets similar to those treated in Co-60 panoramic irradiators can be treated in less time. In either case, improved throughputs can lead to improved economics if processing systems are optimized. Accelerator-based alternatives also provide a solution to supply chain challenges with Co-60, which in the best of circumstances requires years to manufacture in nuclear reactors. As economic and political pressures challenge the supply of Co-60, reliance on it for sterilization can prove logistically challenging. Additionally, not relying on a radioisotope eliminates the need for regularly transporting and handling hazardous material to re-source a sterilization facility.

Radiation technologies also can be used to treat a range of wastes to allow for reuse, including industrial and medical wastewaters, industrial sludges, and plastics. As wastewater disposal, water availability, and plastics waste become increasing concerns under a growing population and a changing climate, irradiation treatment will be an increasingly important resource in achieving the SDG of "Clean Water and Sanitation," among others. These treatments can have positive impacts on the environment and human access to resources. Radiation can be used at lower doses to treat pathogens in wastewaters, which can help in providing clean sources of water. At higher doses, radiation can be used to treat chemical sludges and plastics to improve recycling characteristics or create other products of value from the components of the sludges. Some pilot facilities have utilized electron beam facilities for wastewater treatments, both in the United States and internationally; notably, a pilot facility for treating dyes in wastewater recently opened in China. Co-60 can be used to treat certain types of sludges.

As in food irradiation, accelerator technologies allow for more facility design flexibility and are capable of depositing doses at a higher rate than radioisotopes. This is particularly of value in reuse applications, given the customization and high throughputs needed to ensure profitability. Additionally, accelerators facilitate independence from global radioisotope supply challenges, which is particularly significant in applications where hundreds of thousands of curies of activity may be needed from radioactive sources.

ORS Support for Use of E-Beam and X-ray for Environmental and Agricultural Irradiation

Given its short existence and early focus on self-shielded irradiators, ORS's Reduce program is only beginning to support the development and adoption of accelerators for larger commercial uses. Primarily, ORS supports subject matter experts and researchers in conducting comparison studies and sharing information and best practices with interested potential users. In this regard, ORS's partnership with and support for technology installation at Texas A&M University's National Center for Electron Beam Research (NCEBR), which is an IAEA Collaborating Center, is crucial. NCEBR works with U.S. and international partners to conduct testing on a variety of medical, food, and other products with accelerator and gamma technologies at a variety of energy levels and doses. By expanding the accelerator energy and power options at NCEBR, they will be able to offer additional and more diverse product testing and validation services, including to international partners. ORS also supports NCEBR in conducting of comparison, feasibility, and cost/benefit studies to support the international transition to accelerator-based systems.

Regarding irradiation for water and plastics reuse, ORS is supporting research and bilateral technical exchanges related to the use of accelerator technologies. Additionally, ORS is supporting the IAEA's NUclear

TEChnology for Controlling Plastic Pollution (NUTEC), which will facilitate the growth of Member State expertise on and capabilities for using accelerator technologies for plastic upcycling and downcycling [5].

5. CHALLENGES

Although the use of machine-based ionizing radiation technologies presents many valuable operational and security benefits, ORS recognises that several significant challenges continue to hinder adoption of these technologies, and particularly in low- and middle-income countries. For example, accelerator technologies, particularly high-power sterilization systems and medical LINACs, can have higher initial procurement costs than their radioactive source-based options. In addition, these technologies require adequate and reliable electricity supply for continuous operation, and inconsistent power can lead to machine damage in some cases. Trained staff also are required for effective operation and maintenance, requiring an educational pathway to develop the necessary skills. Finally, as machine-based ionizing radiation technologies are typically more complex than radioactive source-based options, access to viable service providers and spare parts is crucial to keep systems in operation.

Global input from government, users, and industry is needed to meet these challenges. First, awareness raising of technology options is important. One way that ORS supports awareness raising is by connecting prospective users with experienced users or researchers who can share information and experience about using the machine-based technologies (it is important to note ORS's vendor-agnostic approach in these engagements). Another example of awareness raising is the annual Ad Hoc Working Group on Alternatives to High-Activity Radioactive Sources, which is co-chaired by France, Germany, and the United States and aims to facilitate an international exchange of experience and perspectives on machine-based technology adoption, use, and development. This meeting is open to governments, technology users, non-governmental organizations, and sometimes industry. Whatever the venue may be, new and diverse perspectives always are needed. As awareness of the value of machine-based ionizing radiation technologies increases, ensuring that these forums continue and grow is essential.

For technical challenges, the need to develop resilient, affordable, and easy-to-use technologies that can operate effectively in resource-constrained environments is important. Industry must understand and respond to market and user demands, but governments can also help catalyse innovative technology development. Another important aspect in the sustainability of machine-based technologies is having affordable, local service providers and accessibility to spare parts. ORS encourages governments and users to talk to vendors about how to ensure service and spare parts are quickly accessible in the case of downtime, and to reach out to the international community when support is needed.

Lastly, in order to address resource limitations preventing the adoption of machine-based technologies, there is an opportunity for the security and research communities to engage more with government and international organizations and banks focused on sustainable development. The lack of reliable electricity and water, or the absence of relevant education and training programs, cannot be addressed overnight; however, bridges can be built with the sustainable development community to discuss the relevance of ionizing radiation technologies to Sustainable Development Goals, and specifically *how* to make machine-based ionizing radiation technologies a sustainable option.

6. CONCLUSION

Machine-based ionizing radiation technologies can provide results that are meaningful to the UN's Sustainable Development Goals, including those that address healthcare, food security, and clean water. These results are delivered without the additional security risks and costs that come with the use of radioactive sources. While real challenges exist to implementing sustainable accelerator systems, including meeting power requirements and guaranteeing spare part accessibility, momentum to meet these challenges continues to expand. Further engagement and projects aimed at encouraging the adoption of accelerator technologies will have positive impacts for security, human health, and the planet.

ACKNOWLEDGEMENTS

This material is based upon work supported by the U.S. Department of Energy, National Nuclear Security Administration-Office of Defense Nuclear Nonproliferation's Global Material Security, under contract DE-AC02-06CH11357.

REFERENCES

[1] International Atomic Energy Agency. "Sustainable Development Goals". International Atomic Energy Agency. (2021), https://www.iaea.org/about/overview/sustainable-development-goals

[2] United Nations. "The SDGs In Action". UNDP. (2021), https://www.undp.org/sustainable-development-goals

[3] International Irradiation Association. "A Comparison of Gamma, E-Beam, X-ray, and Ethylene Oxide Technologies for the Industrial Sterilization of Medical Devices and Healthcare Products". IIA, 2017.

[4] International Irradiation Association. "A Comparison of Gamma, E-Beam, X-ray, and Ethylene Oxide Technologies for the Industrial Sterilization of Medical Devices and Healthcare Products". IIA, 2017.

[5] International Atomic Energy Agency. "NUclear TEChnology for Controlling Plastic Pollution". International Atomic Energy Agency, 2021.

FULL PAPERS

from poster presentations

ION BEAMS AND ACCELERATORS FOR BIOLOGY-ORIENTATED APPLICATIONS AND RESEARCH – CMU PRACTICES

L.D. YU[1,2]
Email: yuld@thep-center.org

B. PHANCHAISRI[1,2,3], J. TECHARANG[1,2,3], U. TIPPAWAN[1], T. BOONYAWAN[4], T. VILAITHONG[2]

[1] Plasma and Beam Physics Research Facility, Department of Physics and Materials Science, Faculty of Science, Chiang Mai University, Chiang Mai 50200, Thailand
[2] Thailand Center of Excellence in Physics, Commission on Higher Education, 328 Si Ayutthaya Road, Bangkok 10400, Thailand
[3] Science and Technology Research Institute, Chiang Mai University, Chiang Mai 50200, Thailand
[4] PET/CT & Cyclotron Center, Center for Medical Excellence, Chiang Mai University, Chiang Mai 50200, Thailand

Abstract

Applications and researcr of ion beams and accelerators for the biology-orientated issues have been rigorously developed at Chiang Mai University (CMU), Thailand, the national ion beam and accelerator research center, for two decades. The work is highly multiple, touching equipment development, genetic engineering, materials science, analytical technology, cell and molecular biology, biomedicine, and life science. CMU has more than ten various types of ion accelerators and implanters with ion energy in the range of < keV – 20 MeV for the work in this direction. Relevant applications involved ion-beam-assisted gene/DNA transfer in bacterial, plant and mammalian cells, ion beam induced mutations in rice, horticultural plants, vegetables and bacteria, ion-bombardment altered cell adhesion on material surfaces, ion beam analysis of biological samples, ion beam lithography of biological microfluidic devices/patterns, and cyclotron-production of radiopharmaceuticals for diagnostic services. Research concerned covered physical mechanisms of ion-beam-assisted gene/DNA transfer into cells and ion-beam-induced mutations of cells, low-energy ion bombardment effect on DNA strand breaks including both experimental ultra-low energy ion bombardment of naked DNA and computer program simulations of ultra-low energy ion impact on DNA, single-ion irradiation of cells for hyper low dose effect on cancer cell death, and cyclotron manufacture of radiopharmaceuticals for multi-purpose diagnostics.

1. INTRODUCTION

Ion beam is a branch of physics. The objects or targets of ion beams can be every type of materials in principle, and hence certainly biological living matter and materials served for biology and medicine are included. Here, word ‘biology’ has a very broad range of contents, including not only pure biology (including plants, animals, and microorganisms, from body to cell to DNA) but also agriculture (including horticulture and food), medicine, life and health, and materials and devices for biology uses. Table 1 depicts the scope of ion beam biology. Being the unique ion beam center in Thailand, Chiang Mai University (CMU) has rigorously developed ion beam technology with the particular focus on biological applications. Based on the technical capabilities of our ion beam facilities which are low-energy (mostly, < 200 keV) ion implanters, our research has been following the low-energy-ion-beam train of thoughts. In comparison with high-energy ion beams which can normally only do mutation induction, the low-energy ion beams served as a special ion beam biotechnology tool [1] provide us with advantageous opportunities by the capabilities of performing multi-topics investigations, including not only mutation induction, but also ion-beam-assisted gene/DNA transfer, fundamental studies on ion-DNA interaction, as well as ion beam modification of biomaterials for medicine uses. In addition, CMU has a 1.7-MV accelerator applied for ion beam analysis of biosamples and ion beam lithography of micro-biodevices and a 20-MeV cyclotron working on pharmaceutical manufacture for medical diagnosis and therapy.

2. FACILITIES

The ion-beam/accelerator facilities at CMU for biology-oriented applications and research include 150-kV mass-analyzed (CMU1) [2], non-mass-analyzed horizontal (CMU2) [3] and vertical compact ion implanters [4],

TABLE 1. ION BEAM BIOLOGY SCOPE FRAME. *: CMU work implemented. ^: CMU work in plan.

Overall umbrella	Secondary category	Tertiary category	Objects/contents	Objectives
Ion Beam Biology	Ion beam genetics	Ion beam assisted gene transfer	Bacteria*	For genetic modification
			Plants*	For genetic modification
			Mammals*	Study stem cell therapy
		Ion beam mutation induction	Food crops*	Rice, wheat, corn, etc. for yield and quality improvements
			Horticultural plants & vegetables*	Flowers and various vegetable species for quality improvements
			Other economic crops and environmental plants^	Rubber, cotton, etc. for yield and quality improvements; water weeds to control the growth, etc.
			Bacteria*	For gene identification
			Insects^	Mosquito sterilization
	Ion beam life science	Ion beam biomedicine	Ion beam therapy	Cancers
			Isotopes for diagnosis and treatment*	Cyclotron ion beam production of the isotopes
			Ion beam modification of biomaterials*	Enhancement of cell attachment
				Improve mechanical and chemical properties of artificial components for lifetime extension
			Ion beam formation of nanoparticles & patterns	For drug or stem cell delivery
				For neuro cell patterning to study brain neurology
			Ion beam lithography of biomedicine micro-devices*	Fabrications of microfluidic devices, and lab-on-chips, etc.
			Low-energy ion/plasma skin treatment*	For skin beauty and wound recovery
			Ion beam sterilization of hospital items^	Contaminated clothes and bed sheets, and disposals
		Ion beam health safety	Ion beam irradiation health effects^	Study accelerator safety and nuclear accident dangers
		Space travel irradiation risk assessment	Simulation of cosmic particle irradiation onto astronauts	Study the effect at high energy but low dose
		Ion-cell interaction fundamentals	Ion irradiation of cells^	Study cell response to irradiation
			Single ion irradiation of cells^	Study bystander effect, hyper low dose effect on cell death
		Ion-DNA interaction fundamentals	Low-energy ion bombardment of DNA*	Study DNA strand breaks, e.g. single strand break (SSB) and double strand break (DSB) and mutation patterns
			Computer simulation*	
	Ion beam biology analysis	Tissue or cells elemental determination	Concentrations*	Normal beam
			Mapping/imaging*	Microbeam
		Environmental monitoring analysis	Plant and animal cell element analysis^	For monitoring environmental changes
		Biological archaeology analysis	Analysis of archeological biological items*	Determine ages and study ancient climate, geological and environmental changes
		Analysis for food science & technology	Food quality and food container/package materials analyses^	For food safety monitoring
	Ion beam treatments	Ion beam/plasma food sterilization	Slowing decay of foods and liquids^	Benefit food industry
		Ion beam nano-structuring of materials	Ion beam induction of nanostructure for candidate material agents	Fabrication of loss control fertilizers which are normal fertilizers mixed with the agents*

respectively, 220-kV Varian ion implanter, 30-kV bioengineering-specialized vertical ion implanter (CMU3) [5], 25-kV plasma immersion ion implanter (PIII) [6], 10-kV neutralized ion beam implanter [7], low-energy single ion implanter, low-energy Mark II broad-beam high-output ion source-based ion implanter, 1.7-MV Tandetron tandem accelerator, and 20-MeV (H^-) cyclotron. Except the Varian ion implanter, the Tandetron accelerator and the cyclotron which are commercial machines, most of the facilities have been in-house developed. CMU1 has been applied to ion beam assisted DNA transfer and ion beam induced mutation, CMU2 and the compact ion implanter have been the main work horse for ion beam induction of mutations, the Varian implanter applied to ion beam modification of bio-membranes for cell adhesion modification, CMU3 applied to ion beam assisted gene transfection in mammalian cells and studies of low-energy ion bombardment effect on naked DNA and physical mechanisms involved in gene transfer and mutation inductions as well as the single ion implantation, PIII applied to low-energy ion bombardment effect on DNA, the ion beam neutralizer applied in studying ion charge effect on ion-beam-assisted DNA transfer through cell envelope materials, the Mark-II source-based ion implanter for high-output and broad beam application to mutation induction, the Tandetron accelerator with its beamline [8] applied in ion beam analysis of biological samples as well as microbeam application in lithography of biological micro-apparatus, and the cyclotron applied in production of pharmaceuticals for medical diagnosis.

3. APPLICATIONS AND RESEARCH

3.1. Ion-beam-assisted gene/DNA transfer

Ion-beam-assisted gene transfer was implemented, as the first application of ion beam biology at CMU, in the plant, bacterium, yeast and animal cells. These four types of cells have different cell envelope structures, as shown in Table 2, and the cell envelope is critical for ion beam assisted gene transfer. For different types of cells, ion beam conditions were adjusted to adapt the different cell envelopes, particularly in terms of the thickness, to make the gene transfer available. The general protocol of ion-beam-assisted DNA transfer includes steps of (1) specimen preparation, (2) specimen exposure to vacuum, (3) ion beam bombardment, (4) post-bombardment treatment, (5) transferring or transfection, and (6) observation and confirmation or analysis of the character expression of the transferred gene. Table 2 summarizes our experiments on ion-beam-assisted gene/DNA transfer or transfection in various types of cells. We also carried out studies on mechanisms involved in the process. We found that only when the cell envelope was appropriately tailored or modified by the ion beam to such a degree that the envelope permeability was enhanced but not severely damaged so that the cell could still be alive, DNA transfer could be successful. The cell envelope material is represented by cellulose, $C_6H_{10}O_5$. Manmade cellulose membranes were used to mimic the plant cell envelope for investigate the ion-beam induced materials modification. We found formations of bubbles, cracks, micro-craters and chain-scission on/in the membranes. These modified structures were speculated to play roles in enhancing the membrane permeability, which was then confirmed by measured increase in the diffusion coefficient of plasmid DNA through the membrane.

3.2. Ion beam induction of mutation

There is not a commonly applicable protocol of ion beam induction of mutation, while the protocol depends on the biological target, including the target type, plant or bacterium or yeast or even animal, and the target part, seed or tissue or cell. Nevertheless, in principle, the steps may include

- Preparation of the samples and specimens of seeds or tissues or cells
- Ion beam bombardment of the specimens
- Culture and growing of the bombarded material
- Observation and screening of the favorable variations
- Development of the selected variation to M2 and M3 generation to obtain mutants
- Stabilization of the mutants up to many generations
- Genetic analysis of the stabilized mutants
- Registration of the mutant lines to the government for official approval
- Distribution of the registered and approved mutant seeds to the production society for commercialization.

TABLE 2. CELL ENVELOPE STRUCTURES AND ROUGH THICKNESSES OF PLANT, BACTERIUM, YEAST AND ANIMAL CELLS[#] (not in scale).

Cell types	Plant	Animal	Bacteria	Yeast
Schematic of the cell	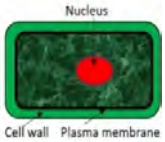	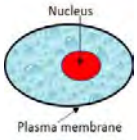	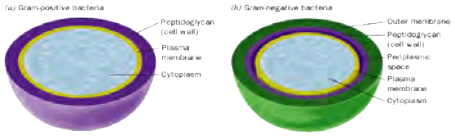	
Cell envelope thickness	0.1 – 10 µm	10 nm	(a) Gram-positive: 20 – 80 nm, (b) Gram-negative: 20 nm (bacterial cell as prokaryote has no nucleus)	10 – 100 nm
Cell example	*Curcuma* embryo	HEp-2 human laryngeal epitheloid cancer cell	*Escherichia coli* (*E. coli*) strain DH5α	*Saccharomyces cerevisiae* strain W303C
Ion beam	Ar^+, N^+; 15-30 keV; $5 \times 10^{14} – 3 \times 10^{16}$ ions/cm^2	N^+; 7-28 keV; $10^{15} – 10^{16}$ ions/cm^2	Ar^+, N^+; 26 keV; 0.5, 1, 2, and 4×10^{15} ions/cm^2	N^+; 50- and 60-keV; $1 – 100 \times 10^{15}$ ions/cm^2
Exogen-ous molecule	Neutral Red (NR) vital dye	Plasmid pEGFPN2	DNA plasmids: pGEM2, pGEM-T easy, pGFP, pUC18, p35s and pBI221	pYGFP and pYlip plasmids
Key results [ref]	NR molecule penetration depends on beam condition and cell type [9,10]	Only 14 keV, 3×10^{15} ions/cm^2 achieved transfection [11]	At fixed ion energy, the successful gene transfer, indicated by gene color expression and antibiotic survival, assisted by ion beam bombardment depends on the ion species, fluence, and the DNA size [12,13]	50-keV with 5, 10 and 20×10^{15} ions/cm^2 achieved successful gene transfer [14]

[#]The information can be easily found from many textbooks and websites.

As rice is the staple of Thailand, induction of rice mutation breeding has naturally become the first choice of the ion beam mutation research. Table 3 summarizes the experiments that have been carried out at CMU in this aspect. In all of the experiments, special technical cares were generally taken. Prior to the ion beam treatment, to break the rice dormancy, the rough seeds were first incubated at 49°C for 5 days. The incubated seeds were manually dehusked to expose the embryos and individually placed in holes of special rice seed sample holders in such a way that the embryos were faced to the ion beam incident direction. From our experiments, the mutation induction frequency was found around orders of 0.1-1‰. Up to now we have had 15 Thai Jasmine rice mutants induced by ion beams, namely, HyKOS3, HyKOS3-1, HyKOS16, HyKOS21, HyKOS22, FRK-1, MSY-1-2, MSY-1-3, MSY-4, OSSY-22, OSSY-23, MRD6-11 MRD6-12, OSSY-8 and OSSY-25 already registered and approved following the Plant Variety Act, B.E. 2518 and the Plant Variety Protection Act, B.E. 2542, Department of Agriculture, Royal Thai Government, Thailand.

We have also worked on other plants and organisms including flowers, vegetables and bacteria for mutation induction. On flowers, some information regarding the experiments is summarized in Table 4. Mutations at the DNA level was also confirmed [26]. On vegetables, mutation induction in the purple yard long bean (*Vigna unguiculata* ssp. *sesquipedalis*) cv. Nan1 was conducted using 80-keV N-ion beam to a fluence of 3×10^{17} ion/cm^2 to implant the bean seeds [28]. After planting to M3, mutants showed dark purple pods, earlier flowering, higher yield with more pod numbers per plant, longer pods, and higher pod weight [28]. On bacteria, cells of *Bacillus licheniformis*, which was shown to suppress conidia germination of the fungus and reduce symptoms caused by the disease *in planta*, were bombarded by N-ion beam at energy of 28–50 keV to a fluence range of $1–10 \times 10^{15}$ ions/cm^2. After this treatment, one mutant was found which had lost its antagonistic property. Molecular biology analysis identified the gene involved in the property expression [29]. The gene was transferred into yeast cells which were then conveniently applied in protection of the flowers from fungal infection [30,31].

Why low-energy ion beam bombardment of seeds can induce mutation has been always curious, as the seed coat is thicker than the ion range. We thoroughly studied the mechanisms and found the possibilities. We can now depict the entire process of low-energy heavy ion irradiation of crop seeds for mutation induction, as schematically shown in Fig. 1.

3.3. Low and ultra-low energy ion bombardment of DNA

The ion energy which is originally low loses in the traveling paths through the materials of the cell envelope and substance inside the cell to a further low level and finally the ion energy deposition onto DNA to change DNA for mutation induction dominantly occurs around the Bragg peak and hence the ion energy becomes very low at this stage. To understand what happens at this final stage of ion implantation to DNA, studies on very low energy ion bombardment effects on DNA changes are necessary. We carried out investigations on the calculation of the low-energy ion range in DNA [32], ion bombardment using ions at low energy, around keV (Table 5), and ultra-low energy, down to 10 eV (Table 6), using various ion species and looking for ion beam condition thresholds of inducing double strand breaks (DSBs), and computer simulations.

TABLE 3. A SUMMARY OF THE EXPERIMENTS ON LOW-ENERGY ION-BEAM-INDUCED RICE MUTATIONS.

Rice	Ion beam	Phenotypic variation	Genetic variation
Thai purple rice (*Oryza sativa* indica strain Purple); 400 seeds/fluence. [15]	60-kV accelerated mixed N-ions; Fluences: 1, 4, and 8 × 10^{16} ions/cm^2; Facility: CMU2	2 mutants obtained from 1 × 10^{16} ions/cm^2: green pigment appearing in the leaf blade and stem sheath	Additional DNA fragment encoding partial sequence of protein belonging to members of P450 protein family
Thai jasmine rice (Oryza sativa L. cv. KDML 105); 800 seeds/fluence. [16]	Mixed N-ions at 60–125 keV; Fluences: 1×10^{16}–5×10^{17} ions/cm^2; Facility: CMU2	Mutants obtained: PKOS1 (60 kV, 2×10^{17} ions/cm^2): photoperiod insensitive and short in stature. TKOS4 (80 kV, 8×10^{16} ions/cm^2): photoperiod insensitive, tall, and early-flowering. BKOS6 (60 kV, 2×10^{16} ions/cm^2): photoperiod insensitive, short, early maturing HyKOS1: photoperiod-insensitive, short, and late-flowering [17].	Additional fragments, BKPK10450 and BKPH15400, detected by PCR reaction in BKOS6, belonging to members of anthocyanin and cytochrome P450, respectively. Expressions of transcripts of genes in the semidwarf and spindly mutants correlated with genes *OsSPY* and *14-3-3*, respectively [18].
Thai jasmine rice (Oryza sativa L. cv. KDML 105); 4,800 seeds. [19]	Mixed N-ions accelerated by 60 kV; Fluence: 4×10^{16} ions/cm^2; Facility: CMU2	Mutant: BKOS: strikingly short, photoperiod-insensitive, deep purple color in multiple tissues	Anthocyanin synthase enzyme expressed (but not in wild type) [19]; the highest total phenol content and improved antioxidant activities [20]
Primary ion-beam-induced mutant BKOS6 of Thai jasmine rice (Oryza sativa L. cv. KDML 105); 6,000 seeds. [21]	Mixed N-ions accelerated by 60 or 80 kV; Fluence: 1, 2×10^{16} ions/cm^2; Facility: CMU2	Mutant HyKOS21: photoperiod insensitivity, semi-dwarfness, high yield potential, the highest seed storability among 7 tested varieties with a seed germination percentage nearly two times as that of the original KDML 105	The lipid peroxidation level of the mutant seeds the lowest; lacked expression of lipoxygenase isoenzyme *lox1* and *lox2* and expressed only *lox3* in seeds
Thai jasmine rice (Oryza sativa L. cv. KDML 105); 22,800 seeds. 6,000 BKOS6 seeds. [22,23]	Mixed N-ions accelerated by 60, 80, 100 kV; Fluence: 1, 2, 4, 8×10^{16} ions/cm^2; Facility: CMU2	23 mutants from KDML 105 and 6 mutants from BKOS6 (for details in phenotypes, refer to [22])	Polymorphisms distinguished from that of KDML105; four additional fragments in mutant profiles encoding proteins involved in the high yield characteristics [23]
		HyKOS22 (bred up to M8 generation, obtained under the beam condition of 60 kV and 2×10^{16} ions/cm^2): drought tolerance + high yield, in contrast to original KDML 105 and drought tolerant check variety, CT9993 [24]	Genetic changes confirmed by established microsatellite DNA markers, suggesting both insertions and deletions induced by ion bombardment [24]
Sangyod Phatthalung (SYP) rice variety (*Oryza sativa* L. cv. Sangyod Phatthalung); 7,000 seeds. [25]	Mixed N-ions accelerated by 50 kV; Fluence: 4×10^{16} ions/cm^2; Facility: non-mass-analyzing vertical compact ion implanter	7 mutants: photoperiod insensitive, shorter, higher number of panicles, better water absorption index and pasting properties, resulted in an increased rice vermicelli production yield	Point mutations and deletion present in the examined locus; genetic changes were polymorphic, leading to possible additional genetic changes and differences among the mutants

In order to obtain ultra-low-energy ion beam, we designed and constructed a deceleration lens [48]. The results experimentally confirmed that ion irradiation of naked DNA at energy as low as the order of 10 eV could definitely induce DNA strand breaks in terms of SSBs and DSBs, depending on ion energy, fluence, ion mass and inertia, generally speaking, the higher the energy and fluence, the heavier the mass and the more active the ion, the easier the induction, with correlated thresholds discovered [41]. Computer simulations were also performed to touch the molecular levels. Monte Carlo methods [43], molecular dynamics [44,45] and Geant4-DNA software [46] were applied, respectively. An important result obtained is that ion irradiation effect on DNA changes is not random but preferential.

TABLE 4. A SUMMARY OF INFORMATION ON FLOWER EXPERIMENTS.

Flower species (Ref.)	Samples	Ion beam condition	Variations/Mutations
Dendranthema morifolium (Chrysanthemum), the variety Reagan Dark [26]	Receptacles, 10 pieces/fluence 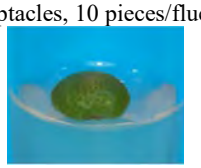 diameter: several mm	60-keV N-ions, fluences of 1, 2, 4, 6 and 8×10^{16} ions/cm^2 (150-kV mass-analyzed heavy ion implanter)	14 plants with steak on petal; 1 plant with color change (under 4×10^{16} ions/cm^2): 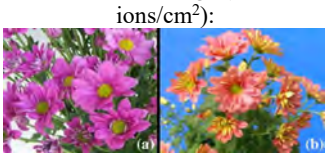 (a) Control. (b) Mutant
Rosa hybrids [26]	Internode sections well wound by parafilm 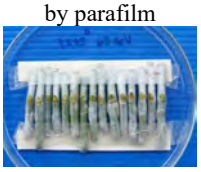	60, 80 and 100-keV N-ions, fluences of 1, 5 and 10×10^{16} ions/cm^2 (150-kV mass-analyzed heavy ion implanter)	3 plants with flowers having more petals (under 80 and 100 keV, 1×10^{16} ions/cm^2) 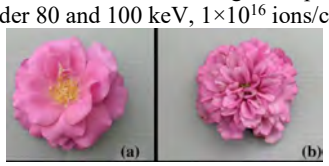 (a) Control. (b) Mutant
Petunia, the variety Dream Midnight Blue [26]	F_1 hybrid seeds  Seed size: ≤ 0.5 mm	60-keV N-ions, fluences of 1, 2, 4, 6, 8 and 10×10^{16} ions/cm^2 (150-kV mass-analyzed heavy ion implanter)	On average 10% plants malformed  (a) Control. (b) Mutant (under 1×10^{16} ions/cm^2)
Clitoria ternatea L., Butterfly pea [27]	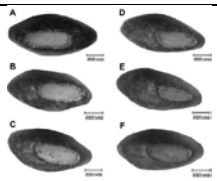 Seed size: 0.1 mm (scale bar: 20 μm) A: control, B – F: 1, 2, 4, 8, and 12×10^{16} ions/cm^2, respectively	50-keV N-ions, fluences of 1, 2, 4, 8, and 12×10^{16} ions/cm^2 (220-kV Varian ion implanter)	In M1, 1/150 mutated in dwarf character (at 12×10^{16} ions/cm^2), and in M2 and M3 (photo below), mutants drastically reduced the climbing habit with smaller leaves and flowers. 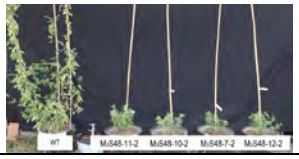

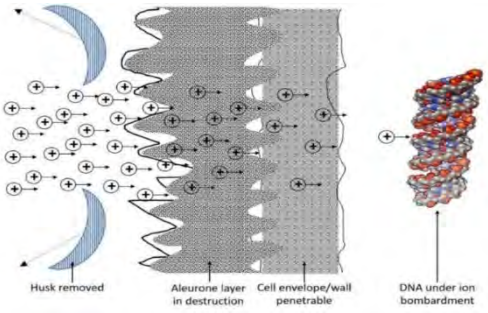

Fig. 1. Schematic (the cross section of a plant cell, including, from left to right, outside of the cell, the cell envelope and the nuclear DNA, not in scale) of the process and probability of low-energy heavy ion beam irradiation induction of mutation. ⊕→ represents an ion with its incident direction. The number of ions and the ion energy are decreasing from left to right, and down to DNA, both become ultra-small and low, due to the ion loss in the interaction with the materials in the path and the energy loss.

3.4. Ion bombardment modification of biomaterial surface for human cell attachment

One of the biological properties on the material surface is human cell attachment which is sometimes required such as in cases of artificial components but sometimes avoided such as in cases of wound dressings. Ion bombardment treatment of the biomaterial surface has been developed as an effective method for the biomaterials modification. In our experiment [47,48], the ion bombardment was operated using the PIII machine with nitrogen or argon as the working gas. The biomaterial was artificially fabricated chitosan membranes, $C_6H_{11}O_4N$. The cell lines were human skin (or dermal) fibroblasts F1544 and amelanotic melanoma cell line C32, skin cancer cells. The results showed that Ar-PIII had an enhancement effect on the cell attachment while N-PIII had an inhibition effect. The cell filopodia more liked to extend and spread on the Ar-treated surface while the filopodia had footknobs to anchor their development on the N-treated surface.

TABLE 5. A SUMMARY OF EXPERIMENTS ON LOW-ENERGY ION BOMBARDMENT OF NAKED DNA (unless *-marked that is pUC19 which is similar to pUC18 but the MCS region is reversed, all are pGFP).

Particle species	Energy (keV)	Fluence (ions/cm^2)	Facility	Main results	Ref.
(Vacuum only)	0	0	PIII chamber	Low pressures only induced SSBs but no DSBs, mainly depending on the pressure change rate but not the pressure itself; low pressures had no effect on mutation induction in DNA-transferred *E. coli*	[33]
N and Ar ions	2.5 and 5, respectively	3, 6, 9 × 10^{13}	CMU3	SSBs and DSBs increased with increasing of the fluence; lighter and active N-ions more effective than heavier and inert Ar-ions in inducing DNA changes; mutation induced in the changed DNA transferred *E. coli*	[34]
N and Ar ions	0, 1.25, 2.5 keV (bias: 0 and -2.5 kV)	0, 10^{11}, 10^{12}, 10^{13}	PIII	SSBs increased with increasing of the fluence, while no DSBs observed; in the DNA transferred *E. coli*, mutation induction only observed for biased (1.25 and 2.5 keV) PIII bombarded DNA but not for un-biased PIII bombarded DNA; DNA sequences differed in some fragments between original and bombarded DNAs	[35]
N and Ar ions and neutrals	2.5 keV	10^{11}, 10^{12}, 10^{13}	Ion beam neutralizer	Charged and neutralized ion beams produced similar amounts of DNA changes in SSBs and DSBs, but ion bombardment had more probability to induce mutation in the DNA transferred *E. coli*; heavier Ar-ions induced the bacterial mutation more than lighter N-ions did, increased with increasing of the fluence	[36]
N ions	Negative bias: 2.5, 3.5, 5, 7, 9 kV	0.5, 1, 2, 4, 6 × 10^{15}	PIII	The bombarded DNA- and *lacZ*-gene-fragment-transferred *E. coli* mutation was induced with the frequency linearly proportional to the ion energy and fluence; ion bombardment induced damage to the *lacZ* gene was identified as the dominant mutation source; the DNA mutation types were dominated by the base substitution and cytosine had the highest radiation-sensitivity	[37]*

3.5. Ion beam lithography for microfluidic biochips

Two economic MeV-ion microbeam techniques, programmable L-shape blade micro-aperture collimated microbeam and tapered capillary microbeam, have been developed for application in microfluidic biomedical device fabrications [49]. In the L-shape blade micro-aperture system [50], the combination of the movements of the pair of the blades in X- and Y-directions realizes a micro-aperture which controls the microbeam in a μm-rectangular/square shape with a size down to 1 μm in minimum. The materials irradiated included positive or negative tone poly(methyl methacrylate) (PMMA), poly(dimethylsiloxane) (PDMS) and amorphous silica (SiO_2). Some examples of applications in MeV-microbeam lithography of microfluidic devices using the L-shaped micro-aperture have been reported [50,51,52]. In the tapered glass microcapillary system [49,53,54], the tapered glass capillary tube is mounted on a holder plate whose position is adjustable by using a pair of micro-linear translation stages for alignment. In MeV-proton lithography, normally the capillary microbeam had a relatively higher beam current or intensity due to a focusing effect, while the aperture microbeam had a more homogeneous distribution of the beam intensity in the beam spot.

TABLE 6. A SUMMARY OF EXPERIMENTS ON ULTRA-LOW ENERGY ION BOMBARDMENT OF NAKED DNA, pGFP, APPLYING THE DECELERATION LENS.

Ion species	Ion energy (eV)	Fluence (ions/cm^2)	Main results	Ref.
N_2^+	64, thus 32 for final N^+	10^{15}	DSBs induced	[38]
Ar^+	242, 304, 407, 510	10^{15}	SSBs induced only, but no DSBs observed	[39]
Ar^+	50, 100, 300, 750, 1000	1, 2, 4 × 10^{15}	SSBs and DSBs induced. The induction of the DNA form changes was ion energy and fluence dependent: the ion energy and fluence thresholds for DNA change from the supercoiled and relaxed forms to the linear form were 750 eV for 2×10^{15} ions/cm^2, or 1 keV for 1×10^{15} ions/cm^2, respectively	[40]
He^+ N^+	100, 300, 1,000, 1,500; 26, 52, 100, 400, 600, 2,000	1, 2, 4 × 10^{15}	The ion energy and fluence thresholds, in terms of the areal energy density, to induce DNA DSBs were found to be 300 eV/Å^2 and 100-150 eV/Å^2 for He- and Ar-ion (from the result obtained from the study shown in the row above) bombardments, respectively, and lower for active N-ions	[41]
C^+	50, 100, 300	1, 2, 4 × 10^{15}	DSBs induced, depending on the ion energy and fluence. The threshold of C-ion beam conditions for DSB occurrence was found to be a minimum energy of 50 eV with fluence 4×10^{15} ions/cm^2, or a minimum fluence of 1×10^{15} ions/cm^2 with ion energy 100 eV or higher	[42]

3.6. Ion beam analysis of biological living materials

We mainly applied particle induced X-ray emission (PIXE) to analyze various biological samples. We used macro beam for measurements of the elemental concentrations of rice grains including ion-beam-induced mutants, human blood, medicinal plant tissues including roots, stems and leaves, and human cardiac muscle, etc. [55], while using capillary microbeam for elemental concentration mapping of plant leaves, particularly focusing on the crossing area between the veins and laminas [56]. Cooperated with Kyoto University, Japan, we also carried out secondary ion mass spectrometry (SIMS) analysis of bio-macromolecules (see next part).

3.7. SIMS (Secondary Ion Mass Spectrometry)

Preliminary work on conceptual designing and construction of SIMS systems was carried out for analysis of biomolecules at CMU. There were two versions of the ion mass separation of the spectrometer proposed based on the time-of-flight (ToF) technique [57] and the quadrupole mass analyzer [58]. In SIMS analysis of biomolecules, we cooperated with Kyoto University utilizing their home-developed combined gas-cluster ion beam (GCIB) + quadrupole-ToF (Q-ToF) tandem mass spectrometer (MS/MS) SIMS system, or GCIB-Q-ToF (MS/MS) SIMS [59]. In the experiment, GCIB bombarded large biomolecules and MS/MS SIMS analyzed produced molecular fragments [60]. The biomolecules were DSPC (1,2-distearoyl-sn-glycero-3-phosphocholine, C44H88NO8P, monoisotopic molecular weight 789.6 Da), angiotensin II (C50H71N13O12, monoisotopic molecular weight 1045.5 Da) and leucine enkephalin. The secondary ion products from these biomolecules under Ar-cluster ion beam (Ar_{2000}^+) bombardment at energy of 10 keV were investigated. The protonated molecular ions $[M+H]^+$ at high masses and fragment species were observed. The secondary ion yield (SIY) tendencies of the dissociated DSPC, angiotensin II, and leucine enkephalin ions as a function of the collision energy were studied.

3.8. Cyclotron for medicine

The objective of the PET/CT & Cyclotron Center, CMU (PCCCMU) is to provide high standard healthcare technology to patients in Thailand's northernmost regions, and to deliver improved diagnoses and therapeutic treatments for cancer and other chronic diseases like cardiac and dementia. In addition to capacity building, we have established a new 200-m^2 PET radiopharmaceutical laboratory, complete with a 20-MeV cyclotron, five hot cells for PET radiopharmaceutical synthesis, a solid target for Cu-64, I-123 and I-124. The cyclotron contributes in two main directions to radiopharmaceuticals for diagnostic services and research. Table 7 lists the isotopic radionuclides and radiopharmaceuticals produced at PCCCMU with their relevant properties and applications [61].

3.9. Single ion irradiation of cells

In cooperation with the Surrey Ion Beam Centre (SIBC), we used the SIBC nanobeam line to carry out single ion irradiation of cells [62]. Chinese hamster V79 cell line was used as a human cancer cell substitute. The ion was 3.8-MeV proton and both single ion and broad beam irradiations were adopted for comparison. After irradiation and cell incubation, the number of surviving colonies as a function of the number of the irradiating ions was measured for the cell survival fraction curve. A lower survival for the single ion beam irradiation than that of the broad beam case was observed, implying the hypersensitivity for the cell to respond to ultra-low dose and bystander effect, which was lacked in the broad beam irradiation.

TABLE 7. ISOTOPIC RADIONUCLIDES AND THEIR RADIOPHARMACEUTICALS PRODUCED AT PCCCMU AND RELEVANT PROPERTIES AND BIOMEDICAL APPLICATIONS. β^+: positron emission. EC: electron capture.

Isotopic radio-nuclide	Target material	Nuclear reaction	Ion energy (MeV)	Half-life	Decay mode (% proportion)	Radio-Pharmaceu-tical	Examples of biomedical applications
^{18}F	O-18 enriched water (^{18}O-H_2O)	$^{18}O(p,n)^{18}F$	3-16	110 min	β^+(97), EC(3)	^{18}F-FDG	Glucose metabolism
						^{18}F-PSMA-1007	Prostate cancer
						^{18}F-NaF	Bone scintigraphy
^{13}N	H_2O+5mM ethanol	$^{16}O(p,\alpha)^{13}N$	7-16	9.97 min	β^+(100)	^{13}N-Ammonia	Myocardial perfusion imaging (MPI)
^{11}C	N_2 + 0.5%O_2	$^{14}N(p,\alpha)^{11}C$	3-13	20.4 min	β^+(100)	^{11}C-Methionine	Amino acids metabolism
						^{11}C-Choline	Biosynthesis of phospholipid
						^{11}C-Acetate	Cell oxidative metabolism, prostate and liver tumors
^{15}O	N_2	$^{14}N(d,n)^{15}O$	0-8	122 sec	β^+(100)	^{15}O-Water	Myocardial perfusion imaging (MPI)
^{124}I	$^{124}TeO_2$ + 5%Al_2O_3	$^{124}Te(p,n)^{124}I$	9-14	4.18 days	β^+(22), EC(78)	^{124}I-NaI	Thyroid diagnostics

4. SUMMARY

Ion beams and accelerators at CMU have been vigorously applied in biology-oriented fields, covering genetics, biomaterials, biomedicine devices, biological analysis, and medicine, etc. Our experiments and research have demonstrated significant potentials of ion beams and accelerators in service of something more related to human lives and thus socioeconomics.

ACKNOWLEDGEMENTS

We wish to thank sincerely all of researchers of CMU as well as international collaborators involved in the work for their various contributions. Besides many funding agencies, the research have been particularly supported by IAEA through a number of projects.

REFERENCES

[1] Yu, Z.L. (Chinese original), Yu, L.D., Vilaithong, T. and Brown, I. (Eng. translators), Introduction to Ion Beam Biotechnology, Springer, New York, 2006.

[2] Suwannakachorn, D., Boonyawan, D., Green, J.P., Aumkaew, S., Thongleurm, C., Vichaisirimongkol, P., Vilaithong, T., Nucl. Instr. Meth. B **89** (1994) 354-356.

[3] Davydov, S., Yu, L.D., Yotsombat, B., Intarasiri, S., Thongleurm, C., A-no, V., Vilaithong, T., Rhodes, M.W., Surf. Coat. Technol. **131** (2000) 558-562.

[4] Singkarat, S., Wijaikhum, A., Suwannakachorn, D., Tippawan, U., Intarasiri, S., Bootkul, D., Phanchaisri, B., Techarung, J., Rhodes, M.W., Suwankosum, R., Rattanarin, S., Yu, L.D., Nucl. Instr. Meth. B **365** (2015) 414-418.
[5] Yu, L.D. Sangyuenyongpipat, S., Sriprom, C., Thongleurm, C., Suwanksum, R., Tondee, N., Prakrajang, K., Vilaithong, T., Brown, I.G., Wiedemann, H., Nucl. Instr. Meth. B **257** (2007) 790-795.
[6] Boonyawan, D., Suanpoot, P., Vilaithong, T., Surf. Coat. Technol. **112** (1999) 314-317.
[7] Medhisuwakul, M., Boonyawan, D. and Vilaithong, T., Rev. Sci. Instr. **75** (2004) 1684-1686.
[8] Tippawan, U., Kamwanna, T., Yu, L.D., Intarasiri, S., Puttaraksa, N., Unai, S., Singkarat, S., Electrotechnica & Electronica (E+E) **51** 5-6 (2016) 334-343.
[9] Vilaithong, T., Yu, L.D., Alisi, C., Phanchaisri, B., Apavatjrut, P., Anuntalabhochai, S., Surf. Coat. Technol. **128-129** (2000) 133-138.
[10] Apavatjrut, P., Alisi, C., Phanchaisri, B., Yu, L.D., Anuntalabhochai, S. and Vilaithong, T., ScienceAsia **29** (2003) 99-107.
[11] Wongkham, W., Sririwichitchai, R., Inthanon, K., Puangwanna, T., Nambuddee, M., Thongkumkoon, P., Prakrajang, K., Yu, L.D., Vacuum **90** (2013) 89-96.
[12] Anuntalabhochai, S., Chandej, R., Phanchaisri, B., Yu, L.D., Vilaithong, T., Brown, I.G., Appl. Phys. Lett. **78** (2001) 2393-2395.
[13] Phanchaisri, B., Yu, L.D., Anuntalabhochai, S., Chandej, R., Apavatjrut, P., Vilaithong, T., Brown, I.G., Surf. Coat. Technol. **158-159** (2002) 624-629.
[14] Anuntalabhochai, S., Chandej, R., Sanguansermsri, M., Ladpala, S., Cutler, R.W., Vilaithong, T., Surf. Coat. Technol. **203** (2009) 2521-2524.
[15] Anuntalabhochai, S., Chandej, R., Phanchaisri, B., Yu, L.D., Promthep, S., Jamjod, S. and Vilaithong, T., Proceedings of the Ninth Asia Pacific Physics Conference (9th APPC), Hanoi, Vietnam, October 25-31, 2004, Session 10: Applied Physics, 10-24C.
[16] Phanchaisri, B., Chundet, R., Yu, L.D., Vilaithong, T., Jamjod, S., Anuntalabhochai, S., Surf. Coat. Technol. **201** (2007) 8024-8028.
[17] Boonrueng, N., Anuntalabhochai, S., Jampeetong, A., Rice Science **20** 3 (2013) 213-219.
[18] Phanchaisri, B., Samsang, N., Yu, L.D., Singkarat, S., Anuntalabhochai, S., Mutation Research/Fundamental and Molecular Mechanisms of Mutagenesis **734** (2012) 56-61.
[19] Chundet, R., Cutler, R.W., Anuntalabhochai, S., Int. Res. J. of Plant Sci. **3** 6 (2012) 120-126.
[20] Semsang, N., Kawaree, R., Cutler, R.W., Chundet, R., Yu, L.D. and Anuntalabhochai, S., Nat. Prod. Res. **26** 12 (2012) 1145-1151.
[21] Semsang, N., Techarang, J., Yu, L.D., Phanchaisri, B., Nucl. Instr. Meth. B **425** (2018) 32-37.
[22] Techarang, J., Yu, L.D., Phanchaisri, B., Proceedings of the 22nd International Conference on Ion Implantation Technology, 2018, IEEE, eds.: V. Haublein and H. Ryssel, 372-376.
[23] Phanchaisri, B., Techarang, J., Semsang, N. and Yu, L.D., J. of Phys.: Conf. Series **1380** (2019) 012072.
[24] Khitka, B., Phanchaisri, B., Sutipatanasomboon, A., Nuangmek, W., Yu, L.D. and Techarang, J., Nucl. Instr. Meth. B **492** (2021) 34-42.
[25] Techarang, J., Sutipatanasomboon, A., Yu, L.D., Tippawan, U., Phanchaisri, B., Nucl. Instr. Meth. B **459** (2019) 43-49.
[26] Krasaechai, A., Yu, L.D., Sirisawad, T., Phornsawatchai, T., Bundithya, W., Taya, U., Anuntalabhochai, S., Vilaithong, T., Surf. Coat. Technol. **203** (2009) 2525-2530.
[27] Thumdeea, S., Chareonlertthanakit, N., Chuaoen, P. and Tiyayon, C., Acta Hortic. **1282** (2020) 413-420. ISHS 2020, XXX IHC – Proc. II Int. Symp. on Plant Breeding in Horticulture, Eds.: N. Sari et al. DOI 10.17660/ActaHortic.2020.1282.62.
[28] Hlungkaew, T., Phanacharoensawad, R. and Yu, L.D., Mutation Induction in Purple Yard Long Bean (*Vigna unguiculata* ssp. *sesquipedalis*) cv. Nan1 by Low Energy Ion Beam (in Thai with an English abstract), Proceedings of the 53rd Kasetsart University Annual Conference, 3-6 February 2015, Faculty of Agriculture, Kasetsart University, Bangkok, Thailand, 446-453.
[29] Mahadtanapuk, S., Yu, L.D., Cutler, R., Vilaithong, T., Anuntalabhochai, S., Surf. Coat. Technol. **201** (2007) 8029-8033.
[30] Mahadtanapuk, S., Sanguansermsri, M., Yu, L.D., Vilaithong, T., Anuntalabhochai, S., Surf. Coat. Technol. **203** (2009) 2546-2549.

[31] Mahadtanapuk, S., Teraarusiri, W., Nanakorn, W., Yu, L.D., Thongkumkoon, P., Anuntalabhochai, S., Nucl. Instr. Meth. B **326** (2014) 209-213.
[32] Yu, L.D., Kamwanna, T., Brown, I.G., Phys. Med. Biol. **54** (2009) 5009-5022.
[33] Sarapirom, S., Thongkumkoon, P., Anuntalabhochai, S., Yu, L.D., Vacuum **86** (2011) 374-379.
[34] Norarat, R., Semsang, N., Anuntalabhochai, S., Yu, L.D., Nucl. Instr. Meth. B **267** (2009) 1650-1653.
[35] Sarapirom, S., Sangwijit, K., Anuntalabhochai, S., Yu, L.D., Surf. Coat. Technol. **204** (2010) 2960-2965.
[36] Sarapirom, S., Thongkumkoon, P., Prakrajang, K., Anuntalabhochai, S., Yu, L.D., Nucl. Instr. Meth. B **272** (2012) 377-381.
[37] Jaichuen, C., Chundet, R., Yu, L.D., Thongkumkoon, P., Anuntalabhochai, S., Surf. Coat. Technol. **229** (2013) 180-185.
[38] Thopan, P., Prakrajang, K., Thongkumkoon, P., Suwannakachorn, D., Yu, L.D., Nucl. Instr. Meth. B **307** (2013) 618-623.
[39] Thopan, P., Thongkumkoon, P., Prakrajang, K., Suwannakachorn, D., Yu, L.D., Ultra-low-energy (<10 eV/u) ion beam bombardment effect on naked DNA, Nucl. Instr. Meth. B **326** (2014) 200-203.
[40] Thopan, P., Yu, L.D., Tippawan, U., Critical low-energy Ar-ion beam conditions to induce direct DNA double strand break, Surf. Coat. Technol. **306** (2016) 313-318.
[41] Thopan, P., Yu, L.D., Brown, I.G. and Tippawan, U., Radiation Research **188** 4 (2017) 426-432.
[42] Thopan, P., Yu, L.D., Tippawan, U., Modification effect of low-energy (~10 eV/amu) C-ion beams on naked DNA, Nucl. Instr. Meth. B **451** (2019) 14-17.
[43] Ngaojampa, C., Nimmanpipug, P., Yu, L.D., Anuntalabhochai, S., Lee, V.S., J. of Molecular Graphics and Modelling **28** (2010) 533-539.
[44] Ngaojampa, C., Nimmanpipug, P., Yu, L.D., Anuntalabhochai, S., Lee, V.S., Nucl. Instr. Meth. B **269** (2011)504.
[45] Lee, V.S., Ngaojampa, C., Nimmanpipug, P., Yu, L.D., Surf. Coat. Technol. **306** (2016) 222-228.
[46] Nimmanpipug, P., Lee, V.S., Kruanopparatana, P., Yu, L.D., Nucl. Instr. Meth. B **475** (2020) 77-83.
[47] Saranwong, N., Inthanon, K., Wongkham, W., Wanichapichat, P., Suwannakachorn, D. and Yu, L.D., Nucl. Instr. Meth. B **272** (2012) 386-390.
[48] Inthanon, K., Saranwong, N., Wongkham, W., Wanichapichart, P., Prakrajang, K., Suwannakachorn, D., Yu, L.D., Surf. Coat. Technol. **229** 25 (2013) 112-119.
[49] Singkarat, S., Puttaraksa, N., Unai, S., Yu, L.D., Singkarat, K., Pussadee, N., Whitlow, H.J. and Tippawan, U., Nucl. Instru. Meth. B **404** (2017) 58-64.
[50] Puttaraksa, N., Unai, S., Rhodes, M.W., Singkarat, K., Whitlow, H.J., Singkarat, S., Nucl. Instr. Meth. B **272** (2012) 149-152.
[51] Gorelick, S., Sajavaara, T., Laitinen, M., Puttaraksa, N., Whitlow, H.J., MRS Proc. **1020** (2007), 1020-GG03-04.
[52] Puttaraksa, N., Napari, M., Merilainen, L., Whitlow, H., Sajavaara, T., and Gilbert, L., Nucl. Instr. Meth. B 306 (2013) 302-306.
[53] Unai, S., Focusing and Flux/Fluence Optimization of 2 MeV Proton Microbeam for Ion Beam Lithography Applications, Ph.D. Thesis, Chiang Mai University, 2013.
[54] Wongke, S., Yu, L.D., Tippawan, U., MeV-proton capillary microbeam PIXE mapping study of solution diffusion in paper, Proceedings of the IBA-PIXE-SIMS international conference, 11-15 Oct. 2021, virtual, IOP: Conference Series, 2022, in press.
[55] Wongke, S., Natyanun, S., Yu, L.D., Chaiwai, C., and Tippawan, U., Chiang Mai J. Sci. **48** 1 (2021) 252-262.
[56] Wongke, S., Yu, L.D., Natyanun, S., Unai, S., Sarapirom, S., Pussadee, N., Tippawan, U., Surf. Coat. Technol **399** (2020) 126126.
[57] Wattanavatee, K., Development of a time-of-flight secondary ion mass spectrometer, M.Sc. Thesis, 2003, Chiang Mai University, http://cmuir.cmu.ac.th/handle/6653943832/33685.
[58] Keawmui, Y., Development of a secondary ion mass spectrometer prototype using quadrupole mass spectrometry, M.Sc. Thesis, 2005, Chiang Mai University, http://cmuir.cmu.ac.th/handle/6653943832/33980.
[59] Thopan, P., Seki, T., Yu, L.D., Tippawan, U., Matsuo, J., Nucl. Instr. Meth. B **450** (2019) 139-143.
[60] Thopan, P., Seki, T., Yu, L.D., Tippawan, U., Matsuo, J., Nucl. Instr. Meth. B **448** (2019) 11-18.
[61] Boonyawan, T., Wimolwattanasarn, K., Phumruamjai, J., Kalyanamitra, K., Ekmahachai, M. and Phongsri, J., Chiang Mai Med. J. **60** 1 (2021) 125-134.
[62] Prakrajang, K., Jeynes, J.C.G., Merchant, M.J., Kirkby, K., Kirkby, N., Thopan, P., Yu, L.D., Nucl. Instr. Meth. B **307** (2013) 586–591.

POSSIBILITY OF USING SLUDGE FROM DRINKING WATER TREATMENT PLANT AS FERTILIZER IN AGRICULTURE AFTER E-BEAM TREATMENT: EFFECTS OF AGING

Ivica T. VUJCIC
Vinca Institute of Nuclear Sciences, National Institute of the Republic of Serbia – University of Belgrade
Laboratory for Radiation Chemistry and Physics
Belgrade, Serbia
Email: ivica@vinca.rs

Nikola R. MIRKOVIC
MDMG Invest-Chem
Belgrade, Serbia

Slobodan B. MASIC
Vinca Institute of Nuclear Sciences, National Institute of the Republic of Serbia – University of Belgrade
Laboratory for Radiation Chemistry and Physics
Belgrade, Serbia

Abstract

Using accelerators in treating waste sludge from a drinking water treatment plant is a well-known technique. Ionizing radiation is an effective method for neutralizing microorganisms from waste sludge. Sludge treated in this way can be used as fertilizer in agriculture. Treated sludge can increase the humus content of the soil, the physical condition of soils, can enrich the soil with micronutrients such as phosphorus, potassium, sulfur, calcium, magnesium, and micronutrients. However, if it is not used as a fertilizer immediately, but after a storage period, the content of microorganisms and mold in the sludge can increase, sludge can change its physicochemical characteristics, or the ratio of total nutrients. The research aimed to determine whether sludge treated with gamma radiation can be used as fertilizer, after a storage period of 15 months.

1. INTRODUCTION

Drinking water is water that is used in drink or food preparation; and potable water is water that is safe to be used as drinking water. The amount of drinking water required to maintain good health varies, and depends on physical activity level, age, health-related issues, and environmental conditions. With the increase in the world population and the decrease of natural drinking water stocks, there is a growing demand for drinking water treatment plants worldwide. Using accelerators is an effective method for neutralizing microorganisms from waste sludge [29, 30, 31]. Sludge treated in this way can be used as fertilizer in agriculture [32, 33]. Sludge can increase the humus content of the soil [34,35], the physical condition of soils [36], can enrich the soil with micronutrients such as phosphorus, potassium, sulfur, calcium, magnesium, and micronutrients [37].

However, if it is not used immediately as a fertilizer, but after a storage period, the content of microorganisms and mold content in the sludge can increase. In the paper, the total number of microorganisms and molds in the sludge were performed. The samples were examined immediately after e-beam treatment and after 15 months of storage in a dark and dry place. It was shown that the content of microorganisms did not increase after the storage period. The study showed that the samples' aging does not affect the change in physicochemical characteristics. Finally, the results shows that the heavy metal content stays into permeative values. All these values meet the Council Directive No. 86/278/EEC requirements for the use of sludge as fertilizer in agriculture

2. MATERIALS AND METHODS

2.1. Sample collection

After the flocculation process in the drinking water plant, the waste sludge samples were collected from the bottom of a precipitator. They are packed in plastic zip bags (Figure 1) and irradiated with varying irradiation doses.

FIG. 1 Waste sludge samples irradiated with e-beam

2.2. E-beam irradiation

Electron irradiation was performed at the University Centre of Electron Accelerators in Trencín, Slovakia, using a pulsed scanning beam (3.5 μs pulse duration with 120 Hz beam repetition rate) of 5 MeV electrons vertically emitted from linear accelerator UELR 5-1S. Samples were irradiated with different irradiation doses: 1 kGy, 3 kGy, 5 kGy, 10 kGy, 25 kGy. The average dose rate was 135 kG·h-1. The B3 radiochromic films/spectrophotometer dosimetric system [41] was used to control absorbed irradiation doses.

2.3. Aging

After irradiation, physicochemical characteristics, microbiological analysis, determination of heavy metals and total nutrient in sludge were performed. The same batch of sludge was stored in a dark place at 15°C for aging before subsequent analysis. The storage time length was 15 months.

2.4. Microbiological analysis

The total number of microorganisms and molds in non-irradiated samples and samples irradiated with different gamma and electronic radiation doses was determined in an accredited microbiological laboratory, following the Ph. Eur. 7.0 (2.6.12. – Microbiological examination of non-sterile products (total viable aerobic count), and 2.6.13. – Microbiological examination of non-sterile products (total viable aerobic count)). Samples were analyzed immediately after irradiation, as well after 15 months.

2.5. Determination of the heavy metal concentration in sludge

To determine the concentration of heavy metals (Cd, Co, Pb, Ni, Cr, and Cu) in sludge samples, they were dissolved in HF, HClO4, and HCl acids. After the dissolution, Ni, Cr, and Cu content were determined using AAS (Perkin Elmer PinAAcle 900T). For the quantitative analyses of As, Hg, and Se, the waste sludge samples were dissolved in HNO3, HClO4, H2SO4, and HCl acids. After the dissolution, the content was determined using Mercury Hydride System AAS (Perkin Elmer PinAAcle 900T).

3. RESULTS AND DISCUSSION

3.1. Physicochemical characteristics

Physicochemical characteristics of waste sludge treated with 25 kGy, immediately after treatment and after aging for 15 months are shown in Table 1.

TABLE 1. PHYSICOCHEMICAL CHARACTERISTICS OF SLUDGE SAMPLES COLLECTED FROM A DRINKING WATER TREATMENT PLANT

Parameter	Treated with e-beam, measured immediately after treatment	Treated with e-beam, measured after 15 months	Permitted values for sludge to be used as a soil improver
pH	5.98	5.32	4-7
electrical conductivity	1486	1488	<3000
cation exchange capacity	108	107	>25
volatile solids	46	29	-

From Table 1 one can see a slight decrease in the pH value after 15 months of storage, because of the CO_2 production and oxidation of ammonia [47]. In any case, the values obtained are still above the minimum allowable value given in the Law on Plant Nutrients and Land Breeders. The conductivity and Cation exchange capacity of the treated sludge hardly changes as a function of time. The values of solid solvents decrease over time due to the natural drying of the sludge.

3.2. Determination of total number of microorganisms and molds in sludge

Determination of total number of microorganisms and molds in sludge were performed immediately after e-beam irradiation and after 15 months to assess the impact of aging. The results are shown in Table 2.

TABLE 2. TOTAL NUMBER OF MICROORGANISMS AND MOLD ANALYSED IMMEDIATELY AFTER IRRADIATION, AS WELL AS AFTER 15 MONTHS OF STORAGE

Dose, kGy	0	1	3	5	10	25
Total number of microorganisms (cfu·ml^{-1}), June 2019	24500	12500	1700	80	0	0
Total number of microorganisms (cfu·ml^{-1}), September 2020	5200	1000	500	0	0	0
Molds (cfu·ml^{-1}), June 2019	95	22	18	0	0	0
Molds (cfu·ml^{-1}), September 2020	80	15	7	0	0	0

From Table 2, one can see that the total number of microorganisms decreases significantly even with small doses of radiation. These results are expected and found in the literature [29, 30, 31, 48]. A dose of 5 kGy is sufficient to reduce the total number of microorganisms to the level allowed for sludge to be used as fertilizer in agriculture. A dose of 10 kGy is adequate for the destruction of all microorganisms in the sludge.

The second row shows the total number of microorganisms of the same samples after aging for 15 months in closed bags. The total number of microorganisms decreases concerning the samples analysed immediately after irradiation. It is explained by the lack of oxygen in the bags. As a result, microorganisms cannot grow [49].

Also, aging does not affect the increase in mold content in all samples. A dose of 5 kGy is enough to neutralize all the mold from the samples.

3.3. Determination of heavy metals in sludge

According to the EU Directives, the maximum quantity of heavy metals in sludge that could be used as a fertilizer is defined [52, 53]. Table 3 shows the limit values of heavy metal concentrations in sludge for agricultural use (mg / kg dry matter) and the content of heavy metals before and after e-beam irradiation with a dose of 10

kGy. This dose was chosen because 10 kGy was sufficient to eliminate all microorganisms from the dried treated waste sludge. Values are shown for sludge tested immediately after ionizing radiation treatment and after 15 months of storage.

TABLE 3. THE CONTENT OF HEAVY METALS BEFORE AND AFTER IRRADIATION WITH A DOSE OF 10 kGy

Heavy metal	Limit values, mg/kg dry matter	Irradiated with a dose of 10 kGy e-beam irradiation, measured after treatment mg/kg dry matter	Irradiated with a dose of 10 kGy e-beam irradiation, measured after 15 mounts mg/kg dry matter
Cadmium	20 to 40	19	19
Copper	1000 to 1750	388	390
Nickel	300 to 400	54.8	55.0
Lead	750 to 1200	123	120
Zinc	2500 to 4000	170	170
Mercury	16 to 25	8.20	8.19
Chromium	100	38.5	39.1
Arsenic	29	9.70	9.70
Selenium	0.7	0.0682	0.0672

Table 3 shows that the content of heavy metals in the waste sludge obtained from the drinking water treatment plant is significantly lower than the limit values [48]. The heavy metals content was determined immediately after the treatment with ionizing radiation and after 15 months of storage. It is known from the literature that ionizing radiation can reduce some heavy metal ions, but the total heavy metal content remains the same [54, 55]. It can be concluded that this sludge is under the Directives for use in agriculture, as far as the content of heavy metals is concerned, so the irradiated waste sludge is favourable for further application as a fertilizer in agriculture.

3.4. Determination of the total nutrient in sludge

The essential nutrients (N, P, K) in the treated sludge were examined. The test was performed immediately after irradiation with a dose of 10 kGy and 15 months after irradiation. The results are shown in Table 4.

TABLE 4. THE CONTENT OF TOTAL NUTRIENT IN SLUDGE IMMEDIATELY AFTER IRRADIATION WITH A DOSE OF 10 KGY AND 15 MONTHS AFTER IRRADIATION

Nutrient	Irradiated with a dose of 10 kGy e-beam irradiation, measured after treatment %	Irradiated with a dose of 10 kGy e-beam irradiation, measured after 15 mounts %
Nitrogen	1.9	2.0
Phosphorous	1.9	1.8
Potassium	0.19	0.18

Table 4 shows that the primary nutrients' values do not change when the sludge is stored in the described manner, in closed bags in a dark and dry place. A dark and dry place protects fertilizer products from exposure to UV rays and reduces freezing risk. With UV exposure, some fertilizer granules can heat, which decomposes the nitrates contained within.

4. CONCLUSION

The use of high-energy ionizing radiation is a successful method for the deactivation of microorganisms from waste sludge. Sludge treated in this way can be used as fertilizer in agriculture. In the paper, the influence

of aging on the microbiological properties of sludge treated with e-beam was investigated. It was found that after 15 months of storage, no microorganisms develop in the treated sludge if it is stored packed in plastic bags in a dark and dry place. In that case, the total number of microorganisms even decreases. The aging of sludge samples under these conditions does not affect the increase of mold content either. Also, it has been shown that aging does not affect physicochemical characteristics, changes in total nutrients, and concentration of heavy metal under these storage conditions. It can be concluded that waste sludge from drinking water treatment plants, treated with ionizing irradiation, has excellent potential to be used as fertilizer in agriculture.

ACKNOWLEDGEMENTS

The research was funded by the Ministry of Education, Science and Technological Development of the Republic of Serbia and the IAEA (CRP Project No: F23034 - Radiation Technologies for Treatment of Emerging Organic Pollutants).

REFERENCES

[1] GETOFF, N. (1996). Radiation-induced degradation of water pollutants—state of the art. Radiation Physics and Chemistry, 47(4), 581–593. doi:10.1016/0969-806x(95)00059-7

[2] RAWAT, K. P., SHARMA, A., RAO, S. M. (1998). Microbiological and physicochemical analysis of radiation disinfected municipal sewage. Water Research, 32(3), 737–740. doi:10.1016/s0043-1354(97)00220-0

[3] CHMIELEWSKI A. G., SUDLITZ, M. (2019). 'Zero energy' electron beam technology for sludge hygienization. Nukleonika 64, 55-63

[4] RATHOD, P. H., PATEL, J. C., SHAH, M. R., JHALA, A. J. (2009). Recycling gamma irradiated sewage sludge as fertilizer: A case study using onion (Alium cepa). Applied Soil Ecology, 41(2), 223–233. doi:10.1016/j.apsoil.2008.11.001

[5] YIN, Y., WANG, J. (2015). Biohydrogen production using waste activated sludge disintegrated by gamma irradiation. Applied Energy, 155, 434–439. doi:10.1016/j.apenergy.2015.05.105

[6] MTSHALI, J., TIRUNEH, A., FADIRAN, A. (2014). Characterization of Sewage Sludge Generated from Wastewater Treatment Plants in Swaziland in Relation to Agricultural Uses, Resources and Environment, 4(4), 190-199. doi: 10.5923/j.re.20140404.02

[7] PAKHNENKOA, E.P., ERMAKOVA, A.V., AND UBUGUNOVB, L.L. (2009). Influence of sewage sludge from sludge beds of Ulan-Ude on the soil properties and the yield and quality of potatoes. Moscow University Soil Science Bulletin 64(4), 175–181

[8] KHALEEL, R., K. REDDY, K.R. AND OVERCASH, M.R. (1981). Changes in soil physical properties due to organic waste applications: A Review. Journal of Environmental Quality, 10, 133-41.

[9] ZAMAN M, CAMERON K.C., DI, H.J. AND INUBUSHI, K. (2002). Changes in mineral N, microbial biomass and enzyme activities in different soil depths after surface applications of dairy shed effluent and chemical fertilizer. Nutr Cycl Agroecosyst, 63, 275–290.

[10] SOARES, C. (2006). Radiochromic film dosimetry. Elsevier B.V. doi: 10.1016/j.radmeas.2007.01.007

[11] LUKLEMA, L. (1969). Factors affecting pH change in alkaline wastewater treatment—I. Water Research, 3(12), 913–930. doi:10.1016/0043-1354(69)90075-x

[12] RANKOVIĆ, B., SAGATOVA, A., VUJČIĆ, I., MAŠIĆ, S., VELJOVIĆ, Đ., PAVIĆEVIĆ, V., & KAMBEROVIĆ, Ž. (2020). Utilization of gamma and e-beam irradiation in the treatment of waste sludge from a drinking water treatment plant. Radiation Physics and Chemistry, 109174. doi:10.1016/j.radphyschem.2020.109174

SHIELDING CONSIDERATIONS OF A BUNKER TO BE TAKEN INTO ACCOUNT BY THE REGULATORY BODY FOR AUTHORIZATION PURPOSES: *Case study of radiotherapy center in Mali.*

A. COULIBALY
Department of Malian Radiation Protection Agency (AMARAP)
Bamako, Mali
Email: coulibalyadama274@yahoo.fr

A. M. DICKO, T. SAMAKE, N. KONE
Department of Malian Radiation Protection Agency (AMARAP)
Bamako, Mali

Abstract

For radiation safety purposes, the barriers thicknesses must be designed to attenuate the primary beam and scatter radiations. The purpose of this work was to check the provided thicknesses by experts about bunker of the only radiotherapy center in Mali according to NCRP 151 recommendations. The obtained results proved that the thicknesses of primary barriers vary between 200 and 224 cm of concrete with a mean value equal to 216 cm and the secondary barriers vary between 84 and 138 cm of concrete with a mean value equal to 103 cm. Considering the different parameters and results such as provided thicknesses of the bunker by experts, conventional treatment techniques (workload), shielding design goals, use and occupancy factors; the regulatory body concluded this bunker will protect efficiently workers and public around its vicinity against ionizing radiations.

1. INTRODUCTION

Structural shielding design in a bunker of accelerator's installations aims to limit radiation exposures to members of the public and employees to an acceptable level, i.e., to reduce the effective dose coming from accelerator to a point outside the bunker as low as reasonably achievable. Shielding design is particularly concerned with attenuation of primary beam and secondary radiations in the form of head leakage of accelerator, patient and wall scatter. Thus, finding the optimum barrier thickness is an essential requirement for the safety of facilities [1-2]. Recommendations and technical information for the shielding design and evaluation for the accelerator facilities, using megavoltage x-ray and gamma-ray, are fully described in Report No. 151 of the National Council on Radiation Protection and Measurements (NCRP) [3] of the USA. This book is one of the most suitable documents to estimate shielding requirements in medical installations using linear accelerators.

The decree No 2014-0931/P-RM (of December 31st, 2014) fixing the rules of protection against ionizing radiations, safety and security of ionizing radiations sources [4], treats in general all aspects related to radiation protection in Mali especially: requirements to be fulfilled by facilities in order to be authorized, safety and security of workers exposed to ionizing radiations, protection of population and environment against harmful effects of ionizing radiations, etc.

For building any bunker able to host an accelerator for medical or research activities, the owner of facility in collaboration with a qualify expert, medical physicist and an architect must establish some detailed plans of facility with the different thicknesses of the bunker (in concrete or lead of primary and secondary barriers) and other areas close to this bunker. Those plans will define also the rooms, control boot, emergency buttons, offices of staff and the conduits (cables for ventilation or cooling, AC, calibration, cooling, etc.). It is in that same concept AMARAP studied the provided plan of radiotherapy center located inside the hospital of MALI in Moribabougou-Bamako for authorization purposes. This is the only radiotherapy center around the country. The objectives of this work were to:

- re-calculate the primary and secondary barrier thicknesses of the bunker of the only radiotherapy center in MALI according to the NCRP Report n°151 methods for authorization purposes;
- compare these calculated results to the provided results;
- understand protection systems implemented by the facility for radiological safety and security of workers and the population in vicinity.

[1] *General Director of Malian Radiation Protection Agency (AMARAP)*

The shielding of the main door of the bunker was not included in this paper because it was provided with the LINAC by the manufacturer.

2. MATERIALS AND METHODS

The calculation methods to evaluate barriers thicknesses were carried out for a treatment room with a LINAC Elekta Compact, with maximum nominal energy of 6 MV. The LINAC isocenter located at 1 m from the radiation source and it was assumed a symmetric distribution of gantry treatment angles. NCRP methods are based on the tenth-value layer (TVL) concept. It was used, in this study, the TVL for ordinary concrete. The used workload in this work was weekly workload (W). In terms of use factor (U), occupancy factor (T) and shielding design goals (P), for workers and public members, it was used NCRP 151 approach (referred to the plans of the facility and NCRP values).

2.1. Information from Architectural Plan (Building Plan)

2.1.1. Description of the radiation treatment room (Bunker)

The radiation treatment room has a rectangular ground plot (7.65 x 4.90 m^2) with a maze-access and an altitude of 3.0 m (up to the suspended ceiling). The distance from ceiling to the ground is 3.1 m. Sliding motorized and shielded door is fixed to the main entrance of the radiation treatment room, Control room and other compartments are close to the bunker. See figure 1 for more details.

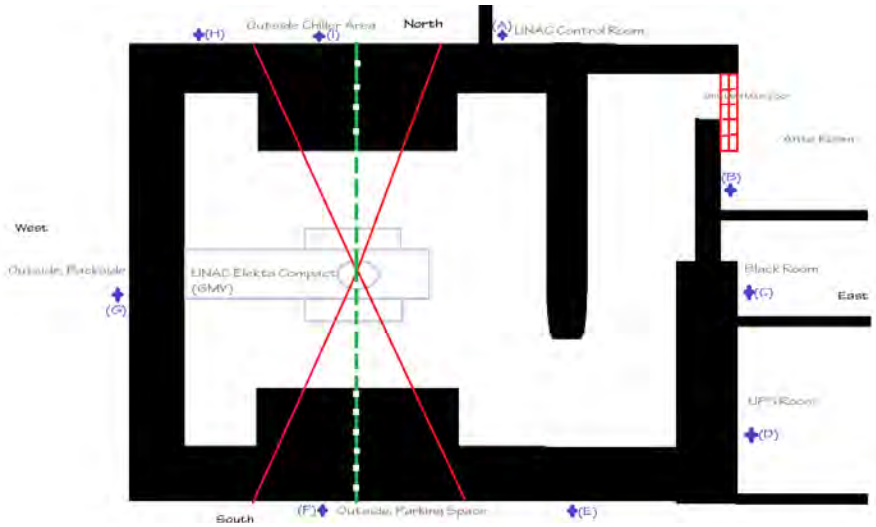

FIG. 1: Plan with measurement points plotted and designation of different compartments beside the radiation treatment room. Green line is the normal to the isocenter of the LINAC and red lines are the directions of primary beam.

2.1.2. Methods of Shielding calculations used by AMARAP (NCRP 151 methods)

Basic considerations: For any practice related to the use of ionizing radiation, the main objective for the shielding in terms of radiation protection is to reduce $I_{(out)}$ to the authorized values for public or workers (see figure 2).

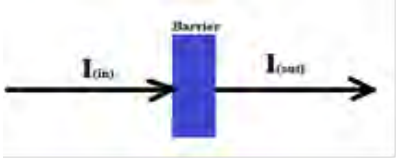

FIG. 2

$$B_{(x)} = \frac{I_{(out)}}{I_{(in)}} \qquad \text{Equation (2.1)}$$

B(x) is the barrier transmission factor to determine in order to know the thickness of specified barrier and I is the intensity of the radiation. For accelerator bunker, there are two (02) barriers called primary and secondary barriers.

TABLE 1. PARAMETERS BY ZONE[#)]

Position	Zone	P Shielding design Goal ($Sv.week^{-1}$)	Distance from LINAC Isocenter to the interest point (m)	Angle to the normal (°C)	Occupancy factor (T)	Use Factor (U)
A	Controlled	1.210^{-4}	3,3	30	1	1
B	Controlled	1.210^{-4}	3,8	60		
C	Controlled	1.210^{-4}	4	90		
D	Controlled	1.210^{-4}	4,2	135		
E	Uncontrolled	2.10^{-5}	3,7	135		
F	Uncontrolled	2.10^{-5}	3,3	0		
G	Uncontrolled	2.10^{-5}	3	90		
H	Uncontrolled	2.10^{-5}	3,2	315		
I	Uncontrolled	2.10^{-5}	3,1	0		
Ceiling	Uncontrolled	2.10^{-5}	3,4	60		

[#)] Under the radiation treatment room (Bunker) is the basement of the building. Hence, there are no accessible areas below this room.

2.1.3. Calculation of B(x) and thickness for primary barriers

The primary barrier is expected to adequately attenuate the dose equivalent beyond the barrier that results from secondary products of the photon beam. For an adequate barrier the ratio of the dose equivalent transmitted through the barrier to the shielding design goal (P) needs to be less than or equal to one. Hence the transmission factor of the primary barrier (B_{pri}) that will reduce the radiation field to an acceptable level is given by Equation (2.2).

$$\mathbf{B_{(pri)}} = \frac{\boldsymbol{Pd_{pri}^2}}{\boldsymbol{WUT}} \qquad \text{Equation (2.2)}$$

P is the shielding design goal (expressed as dose equivalent) beyond the barrier and is usually given for a weekly time frame (Sv.week–1), dpri is the distance from the x-ray target to the point protected(meters), W is the workload or photon absorbed dose delivered at 1 m from the x-ray target per week (Gy.week–1), U is the use factor or fraction of the workload that the primary beam is directed at the barrier in question, T is the occupancy factor for the protected location or fraction of the workweek that a person is present beyond the barrier. This location is usually assumed to be 0.3 m beyond the barrier in question (tabulated values)

The thickness of the barrier can then be determined using tenth-value layers (TVL) based on the energy of the accelerator and type of shielding material. In this case, the required number (n) of TVLs is given by Equation (2.3) and the barrier thickness (tbarrier) is given by Equation (2.4).

$$n = -\log(B_{pri}) \qquad \text{Equation (2.3)}$$

$$t_{(barrier)} = TVL_1 + (n-1)TVL_e \qquad \text{Equation (2.4)}$$

where, TVL_1 and TVL_e are called tenth-value layer first and equilibrium respectively, these values are tabulated, (see appendix B, table B.2 of NCRP report N°151).

2.1.4. Calculation of B(x) and thickness for secondary barriers

Secondary barriers need to be designed to adequately protect individuals beyond the accelerator room from leakage radiation, scattered radiation from the patient, scattered radiation from the walls, and secondary radiations (including photo neutrons and neutron capture gamma rays) produced in the accelerator head or in scattering throughout the room.

Leakage radiation from the head of accelerator and scattered radiation from patient and walls of bunker can differ, the secondary-barrier requirements for each are typically computed separately and compared in order to arrive at the final recommended thickness.

The barrier transmission for scattered radiation by the patient (B_{ps}) is given by Equation (2.5).

$$B_{ps} = \frac{P}{a\,W\,T} d_{sca}^2 d_{sec}^2 \frac{400}{F} \qquad \text{Equation (2.5)}$$

where, d_{sca} and d_{sec} are the distance from the x-ray target to the patient or scattering surface and the distance from the scattering object to the point protected respectively (meters), a is a scatter fraction or fraction of the primary-beam absorbed dose that scatters from the patient at a particular angle (see table B.4 of NCRP 151), F is a field area at mid-depth of the patient at 1 m (40 x 40 cm^2).The value 400 assumes the scatter fractions are normalized to those measured for a 20 cm × 20 cm field size, P, W and T are defined in equation (2.2). The barrier thickness of scattered radiations (patient and walls) is given by Equation (2.6),

$$t_{(barrier)} = n \times TVL_s \qquad \text{Equation (2.6)}$$

and the TVL_s for the patient-scattered radiation values are given by NCRP report 151 (table B.5a of Appendix B).

The barrier thickness of scattered radiations (patient and walls) is given by equation (2.6) and the barrier transmission for leakage radiation by the head of accelerator (BL) is given by equation (2.7).

$t_{(barrier)} = n \times TVL_s$ Eq. (2.6)

$$B_L = \frac{1000\,P\,d_L^2}{W\,T} \qquad \text{Eq. (2.7)}$$

The amount of leakage radiation coming from the head of accelerator is assumed to be 0,1% of the workload (useful beam), d_L is the distance from head to the point of interest beyond the secondary barrier (meter). The barrier thickness of leakage from the head of LINAC (6 MV) is given by equation (2.8).

$$t_{(barrier)} = TVL_1 + (n-1)TVL_e \qquad \text{Equation (2.8)}$$

If the thickness of the required barrier is about the same for each secondary component: 1 HVL is added to the larger of the two barrier thicknesses. If the two thicknesses differ by a TVL or more, the larger barrier thickness is used.

3. RESULTS AND DISCUSSIONS

In Mali, the regulatory shielding design goals (dose equivalent) for public and workers from practices due to the ionizing radiation are respectively 1 $mSv.year^{-1}$ (which is 2.10^{-5} $Sv.week^{-1}$) and 20 $mSv.year^{-1}$ (this dose is optimized to 6 $mSv.year^{-1}$ which is 1.210^{-4} $Sv.week^{-1}$) [3]. All the rooms or other location areas beside the bunker were considered to be fully occupied (occupancy factor is equal to 1) and the use factor of 1 was assumed for all adjacent areas.

According to the international requirements for calculation of radiation protection shielding, a workload of 1000 $Gy.week^{-1}$ was assumed. The measurements are performed with the maximum field size of the collimator of 40 x 40 cm^2 at isocenter. The thickness of different barriers was expressed in centimeter of concrete.

TABLE 2. PRIMARY BARRIERS RESULTS

Location	Type of Zone	P ($Sv.week^{-1}$)	d_{pri} (m)	W ($Sv.week^{-1}$)	T	U	$B_{(pri)}$	n	TVL_1 (cm)	TVL_e (cm)	$t_{barrier}$ (cm)
F	Uncontrolled	2.00E-05	3.3	1000	1	1	2.2E-07	6.7	37	33	224
I	Controlled	1.20E-04	3.1	1000	1	1	1.2E-06	5.9	37	33	200
Ceiling	Uncontrolled	2.00E-05	3.4	1000	1	1	2.3E-07	6.6	37	33	223

TABLE 3. RESULTS FROM SCATTERED RADIATIONS FROM PATIENT AND WALLS

Location	Type of Zone	P Sv.week^{-1}	W Sv.week^{-1}	T	a (angle θ)	d_{sca} (m)	d_{sec} (m)	F	$B_{(pri)}$	N	TVL_s (cm)	$t_{barrier}$ (cm)
A	Controlled	1.20E-04	1000	1	2.77E-03	1	3.3	1600	1.18E-04	3.93	26	102.14
B	Controlled	1.20E-04	1000	1	8.24E-04	1	3.8	1600	5.26E-04	3.28	21	68.86
C	Controlled	1.20E-04	1000	1	4.26E-04	1	4	1600	1.13E-03	2.95	17	50.12
D	Uncontrolled	2.00E-05	1000	1	3.00E-04	1	4.1	1600	2.80E-04	3.55	15	53.29
E	Uncontrolled	2.00E-05	1000	1	3.00E-04	1	3.7	1600	2.28E-04	3.64	15	54.63
G	Uncontrolled	2.00E-05	1000	1	4.26E-04	1	3	1600	1.06E-04	3.98	17	67.60
H	Controlled	1.20E-04	1000	1	3.00E-04	1	3.2	1600	1.02E-03	2.99	15	44.85
Ceiling	Uncontrolled	2.00E-05	1000	1	8.24E-04	1	3.8	1600	8.76E-05	4.06	34	137.95

TABLE 4. RESULTS FROM LEAKAGE RADIATION FROM THE HEAD OF LINAC

Location	Type of Zone	P (Sv.week^{-1})	W (Sv.week^{-1})	T	d_L (m)	$B_{(pri)}$	n	TVL_1 (cm)	TVL_e (cm)	$t_{barrier}$ (cm)
A	Controlled	1.20E-04	1000	1	3.3	1.31E-03	2.9	34	29	88.63
B	Controlled	1.20E-04	1000	1	3.8	1.73E-03	2.8	34	29	85.08
C	Controlled	1.20E-04	1000	1	4	1.92E-03	2.7	34	29	83.78
D	Uncontrolled	2.00E-05	1000	1	4.1	3.36E-04	3.5	34	29	105.73
E	Uncontrolled	2.00E-05	1000	1	3.7	2.74E-04	3.6	34	29	108.31
G	Uncontrolled	2.00E-05	1000	1	3	1.80E-04	3.7	34	29	113.6
H	Controlled	1.20E-04	1000	1	3.2	1.23E-03	2.9	34	29	89.41
Ceiling	Uncontrolled	2.00E-05	1000	1	3.8	2.89E-04	3.5	34	29	107.64

TABLE 5. COMBINED RESULTS FROM SCATTERED AND LEAKAGE RADIATIONS

Location	t_{scat}	t_{Leak}	t_{Leak}- t_{scatt}	> TVL_e(29cm)	t_{new} (cm)
A	102.14	88.63	13.51	No	110.87
B	68.86	85.08	16.22	No	93.81
C	50.12	83.78	33.66	Yes	83.78
D	53.29	105.78	52.49	Yes	85.46
E	54.63	108.73	54.1	Yes	108.73
G	67.6	113.6	46	Yes	113.6
H	44.85	89.41	44.56	Yes	89.41
Ceiling	137.95	107.64	30.31	Yes	137.95

TABLE 5. COMBINED RESULTS FROM SCATTERED AND LEAKAGE RADIATIONS

Location	t_{scat}	t_{Leak}	t_{Leak}- t_{scatt}	> TVL_e(29cm)	t_{new} (cm)
A	102.14	88.63	13.51	No	110.87
B	68.86	85.08	16.22	No	93.81
C	50.12	83.78	33.66	Yes	83.78
D	53.29	105.78	52.49	Yes	85.46
E	54.63	108.73	54.1	Yes	108.73
G	67.6	113.6	46	Yes	113.6
H	44.85	89.41	44.56	Yes	89.41
Ceiling	137.95	107.64	30.31	Yes	137.95

TABLE 6. COMPARISON BETWEEN THE OBTAINED SHIELDING RESULTS BY AMARAP AND PROVIDED RESULTS BY ARCHITECT AND QUALIFIED EXPERTS

Thicknesses of Barrier in Concrete (cm)			
Location	AMARAP Results	Provided Results from experts of "Hôpital du Mali"[4]	Obervations
Primary Barriers			
F	224	235	Good thickness
I	200	235	
Ceiling	223	235	
Secondary Barriers			
A	110,87	141	Good thickness
B	93,81	60	Thickness should be completed by the shielding maze and door of bunker
C	83,78	60	
D	85,46	117	Good thickness
E	108,73	141	
G	113,6	140	
H	89,41	141	
Ceiling	137,95	141	

The thicknesses of primary barriers were calculated, and the results were expressed in table 2, the minimum and maximum values were respectively 200 to 224 cm of concrete with a mean value equal to 216 cm of concrete. The thicknesses of secondary barriers were calculated by combining the thicknesses from scattered radiations and leakage (see table 5); the minimum and maximum values were respectively 84 to 138 cm of concrete with a mean value around 103 cm of concrete.

Table 6 is the comparison between the calculated thicknesses by AMARAP and the provided values by experts. This comparison revealed that, the provided thicknesses (primary and secondary) of bunker by experts were acceptable except areas B (Ante room) and C (Black room). For these two (02) areas, the provided values (60 cm of concrete for both) were below the calculated values (around 94 cm of concrete for area B and 84 cm of concrete for area C). In the design plan, there is a maze before the barrier of areas B and C (see fig.1). In order to

complete the missing thickness of these areas, the thickness of the maze must be around 34 cm of concrete. The main door (principal entrance) must be shielded in lead with a thickness equivalent to 94 cm of concrete.

4. CONCLUSIONS AND RECCOMMENDATIONS

The thicknesses of primary and secondary barriers for LINAC 6 MV Elekta-Compact bunker were calculated using NCRP report 151 by regulatory body (AMARAP) in order to check the provided thicknesses for authorization purposes. The results showed that, the calculated thicknesses of different locations were bigger than the ones provided except location B and C. But in the building plan, there is maze, and the thickness of this maze must around 40 cm of concrete. Before the beginning of the operation, some regulatory controls or inspections were carried out and they reported that the bunker protects efficiently workers and public around its vicinity against ionizing radiations.

The Direction of AMARAP listed the recommendations below to the responsible radiotherapy center of "Hôpital du MALI":

- inform in advance the direction of AMARAP of any modifications about shielding of bunker,
- inform in advance the direction of AMARAP about the acquisition of new LINAC whose the energy is high than 6 MV,
- inform in advance the direction of AMARAP for using others treatment techniques such as IMRT (Intensity Modulated radiation Therapy), TBI (Total Body Irradiation), etc. in order to recalculate the workload. These techniques provide more equivalent dose to the patient,
- make sure that all the conducts (cables for cooling, calibrations and others) carried out on the secondary barriers,
- do not touch to the integrity (shielding) of the primary barriers.

ACKNOWLEDGEMENTS

We thank the direction of AMARAP through its General Director Dr. Nagantié KONE, the direction of "Hôpital du MALI" especially the responsible of radiotherapy center and any person who worked for the realization of this project. We can't end this work without thank our other colleagues especially the staff DCST.

REFERENCES

[1] M. J. Rodrigues, M.E.Poli; Shielding Evaluation for a Radiotherapy Bunker by NCRP 151 and Portuguese Regulation on Radiation Safety.

[2] V. C. Berdasco, Radiotherapy bunker design as a function of technique used: 3D-CRT, IMRT, TBI and SRS. Economic impact evaluation, october 2018.

[3] National Council on Radiation Protection and Measurements, Structural Shielding Design and Evaluation for Megavoltage X- and Gamma-Ray Radiotherapy Facilities, NCRP Report No.151, December 2005).

[4] Decret N°2014-0931/P-RM, Fixant les Règles Relatives à la Protection contre les Rayonnements Ionisants à la Sûreté et la Sécurité des Sources de Rayonnements Ionisants au Mali, du 31 Decembre 2014.

THE RIANBOW ION-SOLID INTERACTION POTENTIAL

S. PETROVIĆ
VINČA Institute of Nuclear Sciences - National Institute of the Republic of Serbia,\
University of Belgrade, Belgrade, Serbia
Email: petrovs@vin.bg.ac.rs

N. STARČEVIĆ
VINČA Institute of Nuclear Sciences - National Institute of the Republic of Serbia,
University of Belgrade, Belgrade, Serbia

M. ĆOSIĆ
VINČA Institute of Nuclear Sciences - National Institute of the Republic of Serbia,
University of Belgrade, Belgrade, Serbia

Abstract

In the article it is reported on the rainbow morphological method to construct an accurate interaction potential, in the case of transmission of 6 MeV protons through <110> Si crystal. The thickness of the crystal was 50 nm. The obtained proton-silicon interaction was named the rainbow interaction potential. It represents extension of the work on the rainbow interaction potential for 27 <100> and <111> cubic crystals: vanadium, chromium, iron, niobium, molybdenum, barium, europium, tantalum, tungsten (BCC crystallographic structure), aluminium, calcium, nickel, copper, strontium, rhodium, palladium, silver, cerium, ytterbium, iridium, platinum, gold, lead and thorium (FCC crystallographic structure), silicon, germanium and tin (diamond type crystallographic structure). Construction of the rainbow interaction potential was based on the fact that it was possible to merge the ZBL interaction potential, for small impact parameters, and the Moliere interaction potential, for large impact parameters, by changing only one fitting parameter in the Moliere interaction potential. Results of the work show that in the case under consideration the same procedure is possible. Moreover, the value of the fitting parameter is close to the values of the same parameter for the <100> and <111> cubic crystals.

1. INTRODUCTION

Recent rapid development of the nanoscience and the nanotechnology imposes new challenges with respect to the basic assumptions considering ion-solid collisions: the energy loss averaging over the impact parameters, the equilibrium charge state distribution and the use of a universal ion-atom interaction potential. The problem of the ion-atom interaction potential will be considered here [1].

The most frequently used ion-atom interaction potential in solids is the ZBL interaction potential [2]. It is based on the so-called universal screening function $a_{ZBL} = (\frac{9\pi^3}{128})^{1/3}(Z_1^p + Z_2^p)^{-1}a_0$, a_0 is the Bohr radius:

$$V_{ZBL} = \frac{Z_1 Z_2 e^2}{R}\sum_{i=1}^{4}\alpha_i \exp\left(-\frac{\beta_i R}{a_{ZBL}}\right), \quad (1)$$

where Z_1 and Z_2 are the atomic numbers of ion and atom, respectively, e is the elementary charge, R is the distance between ion and atom, α_i = (0.1818, 0.5099, 0.2802, 0.02817), β_i= (3.2, 0.9423, 0.4028, 0.2016) and p = 0.23 are the fitting parameters.

Assuming Thomas-Fermi model of atom and its analytical approximation proposed by Moliere [3] one can construct the interatomic potential with the Thomas-Fermi screening radius $a_{TF} = (\frac{9\pi^3}{128})^{1/3}Z_2^{-1/3}a_0$:

$$V_M = \frac{Z_1 Z_2 e^2}{R}\sum_{i=1}^{3}\gamma_i \exp\left(-\frac{\delta_i R}{a_{TF}}\right), \quad (2)$$

where γ_i = (0.10, 0.55, 0.35) and δ_i = (6, 1.2, 0.3) are the fitting parameters. Since the Thomas-Fermi screening radius does not depend on the projectile, which in most cases is not physically feasible, one can introduce the Firsov screening radius $a_F = (\frac{9\pi^3}{128})^{1/3}(Z_1^{1/2} + Z_2^{1/2})^{-2/3}a_0$ [4] getting the same expression (2) by changing δ_i to $\delta_i' = \frac{a_F}{a_{TF}}\delta_i$. In this way, it is possible to use expression $V_M = \frac{Z_1 Z_2 e^2}{R}\sum_{i=1}^{3}\gamma_i \exp\left(-\frac{\delta_i' R}{a_F}\right)$, instead of (2). As a result one can include explicitly the influence of the projectile in the screening function.

2. THEORY

In the transmission channeling process one can always define the mapping from the impact parameter plane, which coincides with the entrance plane of a crystal, to the transmission angle plane: $\theta_x = \theta_x(x_0, y_0)$ and $\theta_y = \theta_y(x_0, y_0)$, where x_0 and y_0 are coordinates of the impact parameter of an ion, and θ_x and θ_y are coordinates of its transmission angle. Theory of the crystal rainbow has been developed taking into account that the ion differential transmission cross section for small exit angles of transmitted ions reads [5]:

$$\sigma_{diff}(b) = \frac{1}{|J_\theta(b)|}, \tag{2}$$

where $J_\theta(b) = \partial_{x_0}\theta_x\partial_{y_0}\theta_y - \partial_{y_0}\theta_x\partial_{x_0}\theta_y$ is the Jacobian of the mapping (1). Therefore, the equation: $J_\theta(x_0, y_0) = 0$, defines the rainbow lines in the impact parameter plane. By mappings the rainbow lines in the impact parameter plane one obtains the rainbow lines in the transmission angle plane. It can be shown that all pronounced maxima in the corresponding angular distribution of transmitted ions are determined by the rainbow lines in the transmission angle plane [5-7].

Recently, it has been shown that the rainbow lines can be used to obtain the rainbow interaction potential, which can accurately explain the experimental angular distributions for 0.7-2 MeV protons transmitted through 55 nm thick <100> Si crystal [7]. The used method for the construction of the rainbow potential is based on the following assumptions (i) the ZBL potential is accurate for small impact parameters, (ii) the Moliere potential is accurate for large impact parameters [8], and (iii) the rainbow lines in the scattering angle plane generated by the rainbow potential should match, at the same time, the rainbow lines generated by the ZBL potential, corresponding to small impact parameters, and the rainbow lines generated by the Moliere potential, for the large impact parameters. This method can be named the rainbow morphological method. The remarkable result is that it is possible to obtain the rainbow interaction potential by changing only one parameter in the Moliere potential, δ_2' [7]. This work has been theoretically extended to the case of 27 <100> and <111> cubic crystals: vanadium, chromium, iron, niobium, molybdenum, barium, europium, tantalum, tungsten (BCC crystallographic structure), aluminium, calcium, nickel, copper, strontium, rhodium, palladium, silver, cerium, ytterbium, iridium, platinum, gold, lead and thorium (FCC crystallographic structure), silicon, germanium and tin (diamond type crystallographic structure) [9, 10]. The analysis has shown that for all the <100> cubic crystals, the new parameter δ_2', which is designated by δ_{2r}', is equal to 1.828, while for the <111> cubic crystals, δ_{2r}' = 1.475.

In the work presented here, the method for obtaining the rainbow interaction potential is applied in the case of 6 MeV protons transmitted through 50 nm thick <110> Si crystal.

3. RESULTS

Fig. 1 shows the rainbow lines in the impact parameter plane for <110> Si crystal channel generated in the fitting procedure by the ZBL interaction potential – black line, the Moliere interaction potential – blue line, and the rainbow interaction potential – red line. The channel is a rhomb with symmetric pars of atomic string located around apexes of the rhomb.

Fig. 2 presents the rainbow lines in the angular transmission plane corresponding to the rainbows presented in Fig. 1. It is clear that in the central part of angular transmission plane (larger impact parameters) the rainbow line generated by the rainbow potential is very close to the rainbow line generated by the Moliere potential. In the fitting procedure the corresponding points along the line θ_y = 0 coincide. At the same time, the rainbow line generated by the rainbow potential is very close to the rainbow line generated by the ZBL potential for outer rainbow lines, corresponding to larger angles (smaller impact parameters). Also, in the fitting procedure, the corresponding points along the line θ_y = 0 coincide. Main result is that the fitting procedure requires changing only one parameter in the Moliere interaction potential, as in the cases of <100> and <111> cubic crystals mentioned above, so as δ_{2r}' = 1.388.

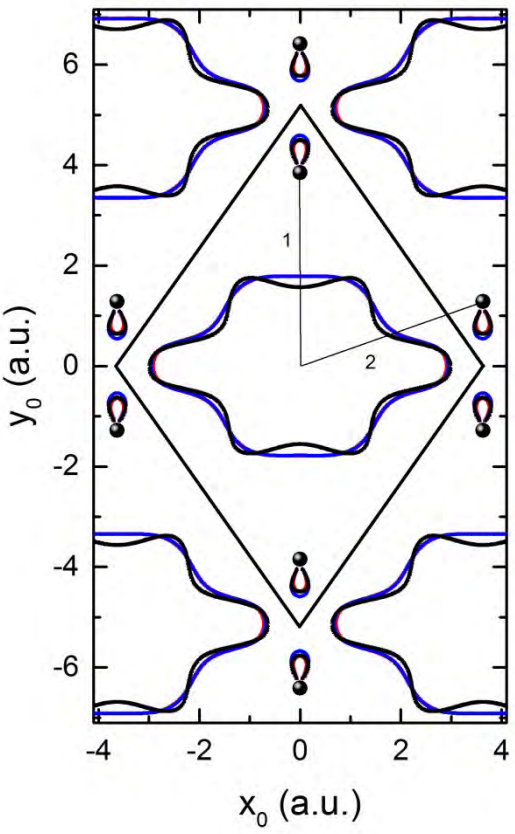

FIG. 1. The rainbow lines in the impact parameter plane generated by the ZBL – black lines, the Moliere – blue lines, and the rainbow interaction potential – red lines. Spheres represent the atomic strings.

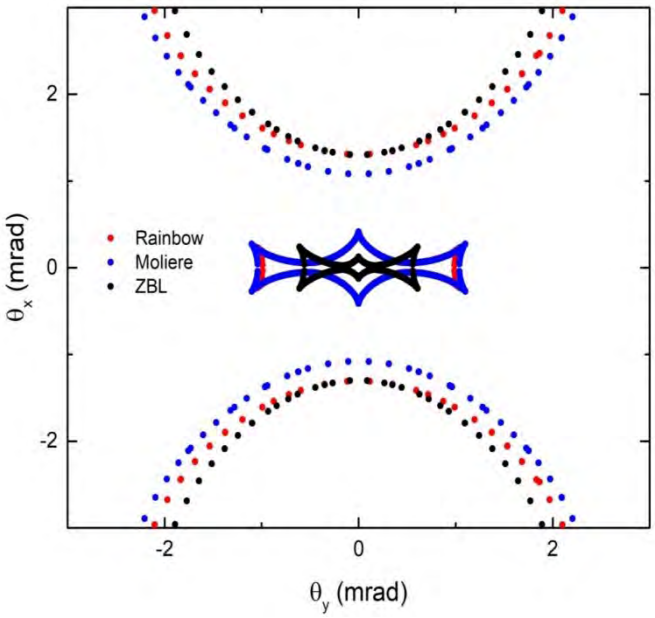

FIG. 2. The rainbow lines in the scattering angle plane generated by the ZBL – black lines, the Moliere – blue lines, and the rainbow interaction potential – red lines.

The comparison between the obtained ZBL, Moliere and rainbow interaction potentials along directions 1 and 2, presented in Fig.1., are shown in Figs. 3 and 4, respectively. In both figures it is clear than the rainbow interaction potential very well approximates the ZBL potential for the small impact parameters while, at the same time, very well approximates the Moliere potential for the large impact parameters. In this way merging of the ZBL and Moliere interaction potentials applying the rainbow morphological method has been achieved.

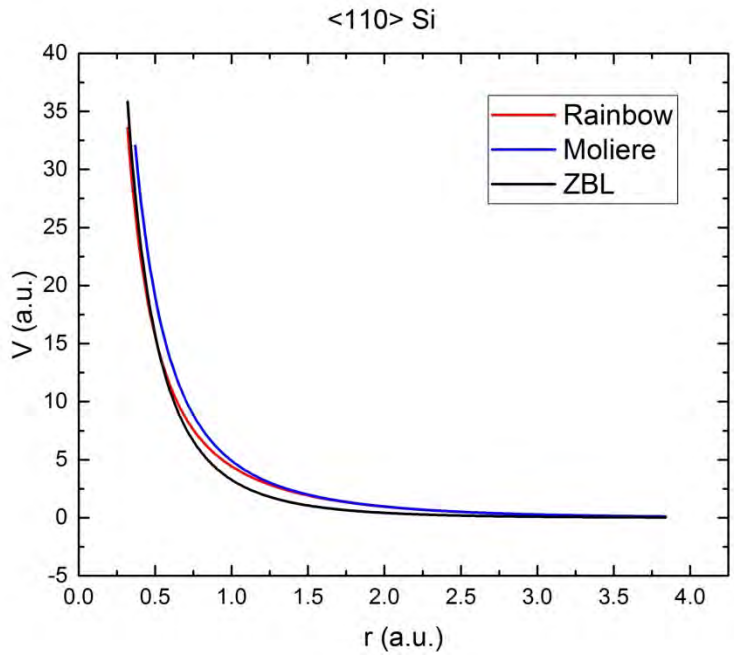

FIG. 3. The rainbow interaction potential – red line, the Moliere interaction potential – blue line, and the ZBL interaction potential – black line, along the direction 1 in Fig.1.

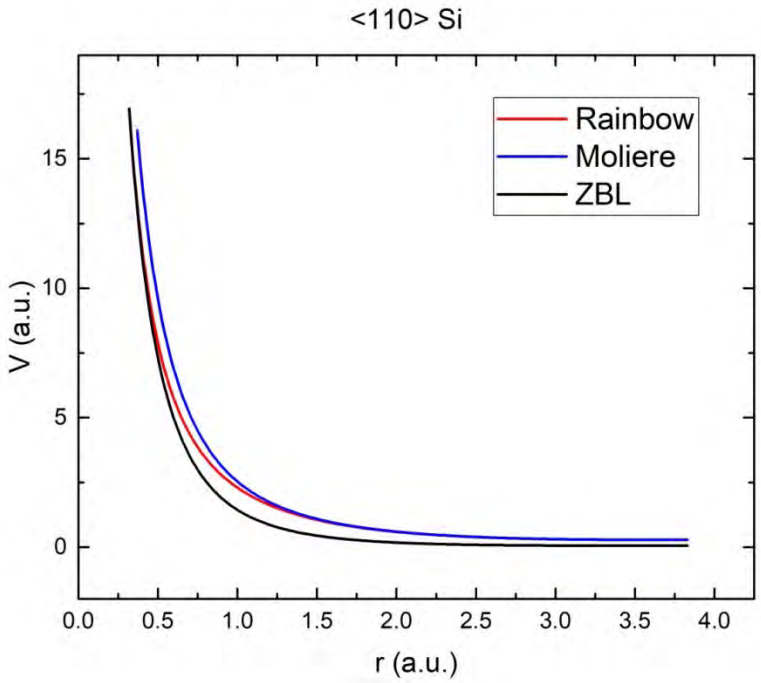

FIG. 4. The rainbow interaction potential – red line, the Moliere interaction potential – blue line, and the ZBL interaction potential – black line, along the direction 2 in Fig.1

4. CONCLUSIONS

The rainbow interaction potential $V_R = \frac{Z_1 Z_2 e^2}{R} \sum_{i=1}^{3} \gamma_i \exp\left(-\frac{\delta'_{ir} R}{a_F}\right)$, with the parameters $\delta'_{ir} = \left(\frac{a_F}{a_{TF}}\ \delta_1, 1.388, \frac{a_F}{a_{TF}}\ \delta_3\right)$, $\delta_1 = 6.0$ and $\delta_3 = 0.3$, has been obtained for the <110> Si crystal applying the rainbow morphological method. It merges the ZBL and the Moliere potential for the whole range of the impact parameters. It should be noted that value of the parameter δ'_{2r} is close to the values of the parameters δ'_{2r} for the <100> and <111> cubic crystals.

ACKNOWLEDGEMENTS

The authors acknowledge the support by the Ministry of Education, Science and Technological Development of Serbia.

REFERENCES

[1] NASTASI, M., MAYER, J. W., HIRVONEN, J. K., Ion-Solid Interaction: Fundamentals and applications, Cambridge University Press, Cambridge (1996).

[2] ZIRGLER, J. F., BIERSACK J. P., LITTMARK U., The Stopping and Range of Ions in Solids, Pergamon Press, New York (1985).

[3] MOLIERE, G., Theorie der Streuung schneller geladener Teilchen I: Einzelstreuung am abgeschirmten Coulomb-Feld, Z. Naturforsch. A **2** (1947) 133 (in German).

[4] FIRSOV, O. B., Calculation of the interaction potential of atoms, JETP **6** (1958) 534.

[5] PETROVIĆ, S., MILETIĆ, L., NEŠKOVIĆ, N., Theory of rainbows in thin crystals: the explanation of ion channeling applied to Ne10+ ions transmitted through a <100> Si thin crystal, Phys. Rev. B **61** (2000) 184.

[6] MOTAPOTHULA, M., PETROVIĆ, S., NEŠKOVIĆ, N., DANG, Z. Y., BREESE M. B. H., RANA M. A., OSMAN A., Origin of ringlike angular distributions observed in rainbow channeling in ultrathin crystals, Phys. Rev. B **86** (2012) 205426.

[7] PETROVIĆ, S., NEŠKOVIĆ, ĆOSIĆ M., MOTAPOTHULA, M., BREESE M. B. H., Proton-silicon interaction potential extracted from high-resolution measurements of crystal rainbows, Nucl. Instr. Meth. Phys. Res. B **360** (2015) 23.

[8] KRAUSE, H. F., BARRETT, J. H., DATZ, S., DITTNER, P. F., JONES, N. L., GOMEZ del CAMPO, J., VANE, C. R., *Angular distribution of ions axially channeled in a very thin crystal: Experimental and theoretical results*, Phys. Rev. A **49** (1994) 283.

[9] PETROVIĆ, S., STARČEVIĆ, N., ĆOSIĆ M., Universal axial (001) rainbow channeling interaction potential, Nucl. Instr. Meth. Phys. Res. B **447** (2019) 79.

[10] STARČEVIĆ, N., PETROVIĆ, S., Crystal rainbow channeling potential for 〈1 0 0〉 and 〈1 1 1〉 cubic crystallographic crystals, Nucl. Instr. Meth. Phys. Res. B **499** (2021) 39.

CURRENT DEVELOPMENT STATUS OF THE LINAC-BASED BNCT DEVICE OF THE IBNCT TSUKUBA PROJECT

H. KUMADA
University of Tsukuba
Tsukuba, Ibaraki, Japan
Email: kumada@pmrc.tsukuba.ac.jp

Abstract

In recent years, boron neutron capture therapy (BNCT) has attracted attention as a treatment for various cancers. As BNCT requires high-intensity neutrons for treatment, clinical studies worldwide have been conducted using research reactors. Recent progress in accelerator technologies has made it possible to perform BNCT using accelerator-based neutron sources instead of reactors. Hence, many institutes and manufacturers worldwide are developing compact accelerator-based neutron source devices for BNCT. In this context, the Ibaraki-Boron Neutron Capture Therapy (iBNCT) project is developing the "iBNCT001," a demonstration linear accelerator-based neutron source for BNCT. The iBNCT001 generates a neutron beam via a reaction between 8 MeV protons and a beryllium target. Currently, the linear accelerator (linac) of the iBNCT001 can operate with an average proton current of 2.1 mA. Experiments using a water phantom were performed to confirm the characteristics of the neutron beam. The measurement results proved that a maximum thermal neutron flux in the phantom of approximately 1.40×10^9 (n/cm^2/s) for a normal beam aperture 150 mm in diameter. The neutron intensity was sufficient to complete irradiation within 30 min for BNCT. Extended collimators protruding 100 mm from the wall were developed in addition to normal beam apertures. The extended collimators avoided interference between the patient's body and the wall during irradiation of head and neck cancers. The measurement results for the extended collimator proved that irradiation with the extended collimator can be completed within 1 h when for a neutron beam with an average proton current of 2.0 mA.

1. INTRODUCTION

In recent years, boron neutron capture therapy (BNCT) has attracted attention as a radiation therapy for intractable and recurrent cancer [1]. BNCT is currently categorized as radiation therapy because a neutron beam is irradiated from a beam irradiation device to the affected region of a patient. However, unlike conventional external radiation therapy, BNCT is considered a next-generation radiation therapy because it involves a reaction with a drug that accumulates in cancer cells. In BNCT, a drug that can selectively accumulate in cancer cells is administered to the patient before neutron irradiation. This drug contains concentrated (>99.9%) boron-10. Irradiation of the tumor region where the boron-containing drug is accumulated with a neutron beam causes the release of alpha-particles and lithium-7 in each tumor cell due to a reaction between low-energy neutrons and boron-10. The range for both released particles in the cells is <10 μm, which is approximately the same size as human cells. Furthermore, the two particles are high linear energy transfer (LET) particles. Thus, the particles selectively destroy tumor cells while avoiding critical damage to healthy tissues around the tumor, even in tumor cells infiltrating healthy tissues. Fig.1 shows a schematic of the BNCT principle.

However, this therapy requires a high-intensity neutron source. Clinical studies since the 1990s using epithermal neutron beams required an epithermal neutron flux of $5x10^8$ (n/cm^2/s) or more at the beam aperture. The requirements for the neutron beam in BNCT were introduced in the International Atomic Energy Agency Current Status of Neutron Capture Therapy (IAEA TECDOC-1223) [2]. Therefore, BNCT has been performed worldwide using research reactors. Clinical studies of BNCT for the treatment of malignant brain tumors, head-and-neck cancer, malignant melanoma, etc. have been reported in 1,000 cases or more worldwide, with excellent results. However, until recently, BNCT has not been established and spread widely as an effective cancer treatment method due to the requirement for a nuclear reactor. It is difficult to build new reactors; moreover, in Japan, it is impossible to build a research reactor for installation in a hospital. In recent years, BNCT using an accelerator-based neutron source has attracted attention to address this limitation. Progress in technologies for both accelerator and neutron generation has made it possible to generate the neutrons required for BNCT treatment with a small accelerator. The availability of a small accelerator-based BNCT device in hospitals will allow patients to receive treatment. Furthermore, it is expected that BNCT can advance from clinical studies to insurance and advanced medical care. Therefore, many institutes and manufacturers worldwide are developing compact accelerator-based neutron source devices for BNCT. Among the first manufacturers is Sumitomo Heavy Industry Ltd., which produces "NueCure", a cyclotron-based BNCT treatment device [3]. The device was approved in Japan in 2020

and has been installed in two hospitals, with treatment using this device for head-and-neck cancer provided as insurance medical care in Japan since June 2020.

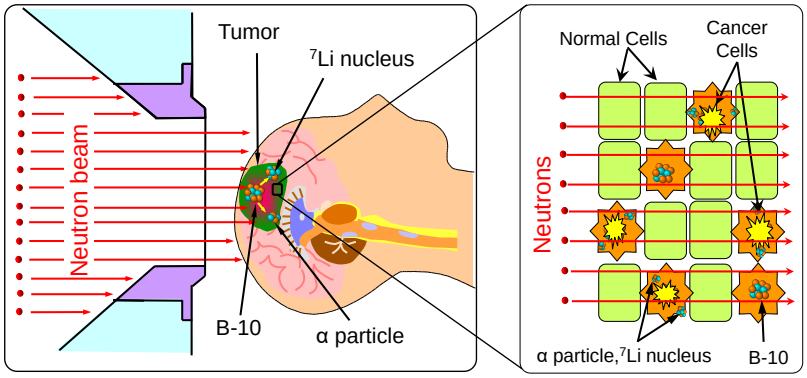

FIG.1. Principle of boron neutron capture therapy.

In this context, the "iBNCT," a project team aimed at developing an accelerator based BNCT device, was launched in 2011 [4]. The iBNCT project team, an industry-academia-government collaboration, includes the University of Tsukuba, the high-energy accelerator research organization, Japan Atomic Energy Agency, Ibaraki Prefecture, and several manufacturers related to the accelerator. This project is working to develop a a demonstration of an accelerator based BNCT device, iBNCT001, and has already successfully generated a neutron beam with sufficient intensity for treatment. We are currently preparing to conduct clinical studies using the iBNCT001 for future regulatory approval applications for this device. As part of this activity, we are performing experiments to measure the neutron beam characteristics of the device. In this project, new beam collimators that are effective for treatment were also developed and the characteristics of the collimators were measured.

The outlines of the device and the characteristics of the neutron beam obtained from the measurements are introduced.

2. MATERIALS AND METHODS

2.1. Accelerator-based neutron source of the iBNCT001

In the design stage of iBNCT001, the iBNCT team's accelerator-based BNCT device, we decided to adopt beryllium as the target material [5]. We next discussed the energy of the proton beam incident on the beryllium. To easily operate and maintain the device in a hospital, we believed that the radio-activation of the device by neutrons during treatment should be reduced as much as possible. However, high neutron intensity is also required. If the proton energy is too low, it is not possible to obtain the neutron intensity required for treatment. Based on various analyses, the proton beam energy was set to 8 MeV. The neutron energy emitted from the beryllium target by the reaction with 8 MeV protons is ≤6.1 MeV, which is relatively low. Therefore, the potential radio-activation of most of the materials forming the device will be suppressed. Treatment completion in <1 hour required the generation of epithermal neutrons with a flux of ≥5 × 10^{8} (n/cm^{2}/s) at the beam aperture. To obtain this neutron intensity, protons of a few milliamperes have to irradiate to the beryllium. Hence, at the design stage, we set an average proton current of ≥5 mA in the accelerator. Finally, we chose a linear accelerator (linac) to produce the required proton beam. The linac of the iBNCT001 consists of a radio-frequency quadrupole (RFQ) and a drift tube linac (DTL). The first RFQ accelerates the proton from the ion source to 3 MeV, while the second DTL increases further the proton speed to 8 MeV. Fig. 1(a) shows the RFQ and DTL of the iBNCT001 installed in the accelerator room, while Fig. 1(b) shows the irradiation room of iBNCT001. The patient couch was set near a normal beam aperture of 120 mm. Table 1 lists the main specifications of the proposed device for the year 2022.

The energy of neutrons emitted from beryllium targets is higher than that of epithermal neutrons applied for treatment. Therefore, a beam-shaping assembly (BSA) that can adjust the energy of neutrons is placed between the beryllium target and the patient. The BSA of the iBNCT001 consists of a moderator, collimator, and shielding. The moderator cuts high-energy neutrons that are unnecessary for treatment and reduces their energy to the epithermal region. The collimator focuses the neutrons used for treatment on the beam aperture. Finally, the neutrons are released from the beam aperture toward the patient.

The beam aperture, which is attached to the edge of the collimator, can be changed depending on the tumor location and size. Several types of beam apertures have been developed, all of which are circular. The shapes of the beam apertures include "normal beam aperture," and "extended collimator." The position of the neutron release surface of the normal beam aperture is the same as that of the surrounding wall. Normal beam apertures with diameters of 120 and 150 mm have been prepared. However, in extended collimators, the neutron-release surface of the beam aperture protrudes 100 mm from the surrounding wall to create a space between the patient's body and the wall. The extended collimator is useful for irradiation, especially in patients with head and neck cancer, because it can suppress interference between the patient's shoulder and the wall. Extended collimators with diameters of 10, 120, and 150 mm have been produced.

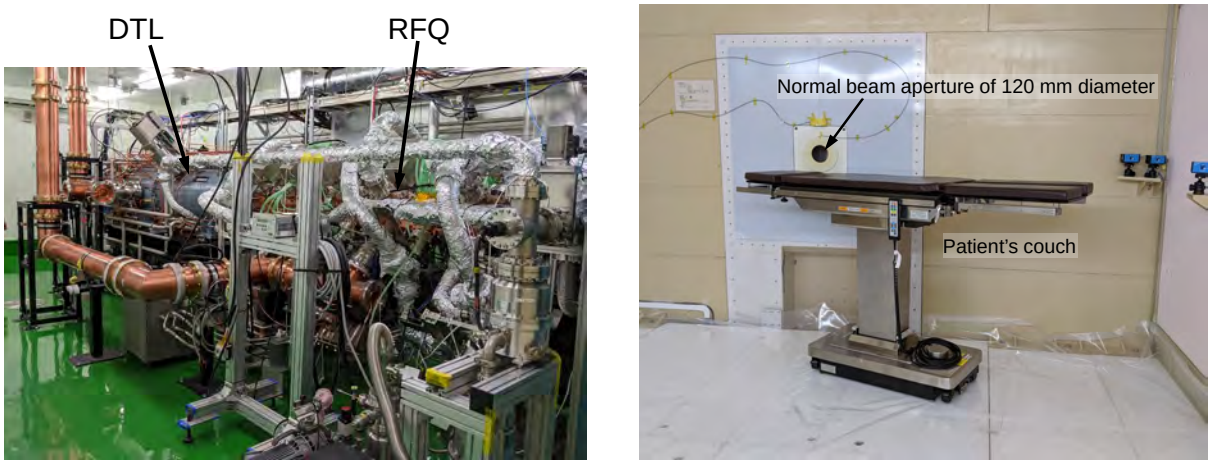

(a) Linac of iBNCT001 installed in an accelerator room (b) Irradiation room of the iBNCT001

FIG.2. Linac of the iBNCT001 installed in the accelerator (a) and irradiation (b) rooms.

TABLE 1. Main specifications of the iBNCT001

Items	Values
Accelerator type	RFQ and DLT type linac
Proton energy	8 MeV
Proton pulse width	1 ms
RF frequency	324 MHz
Average proton current	>5.0 mA
Target material	Beryllium
Diameter of the beam aperture	Normal beam aperture: 120 mm, 150 mm
	Extended collimator: 100 mm, 120 mm, 150 mm

2.2. Neutron beam performance of the iBNCT001

The production of the accelerator and BSA and the assembly of the iBNCT001 were completed in 2016. The neutron beam was successfully generated in the same year. However, at that time, the average current was as small as approximately 0.1 mA, which was not sufficient for treatment. Subsequently, the accelerator was improved and upgraded to incrementally increase the average proton current, with an average linac current of 1.4 mA by 2018 [6]. Furthermore, in 2019, the average current was 2.1 mA, with a stable and continuous neutron beam. In future BNCT treatment, we plan to perform irradiation by generating a neutron beam under operating conditions with an average current of 2.1 mA. We conducted various physical characterization measurements to confirm whether the neutron beam generated under this operating condition was applicable to treatment. First, the characteristics of the neutron beam emitted from the beam aperture were measured under free-in-air conditions. The neutron spectrum of the beam was measured using a Bonner sphere spectrometer [7]. The measurement results demonstrated that the device could generate epithermal neutrons as designed. The flux of the epithermal neutron was approximately 7.0×10^8 (n/cm^2/s) under the operating condition of an average current of 2.1 mA. This intensity was higher than that recommended by IAEA-TEC DOC-1223 and is sufficient for BNCT treatment. Table 2 shows several neutron beam characteristics based on the measurement results and Monte Carlo analysis.

TABLE 2. Beam characteristics of the iBNCT001 in free-in-air conditions

Items	Values
Linac operating conditions:	
Repetition cycle	75 Hz
Proton average current	2.1 mA
Beam Aperture	Normal beam aperture, 120 mm diameter
Neutron characteristics:	
Epithermal neutron flux	7.0×10^{8} (n/cm^2/s)
Gamma-ray dose rate in the epithermal beam	0.04 (Gy/h)
Ratio of thermal neutron per epithermal neutron	0.01
Fast neutron component per epithermal neutron	3.8×10^{-13} (Gycm^2/n)
Gamma-ray component per epithermal neutron	2.8×10^{-14} (Gycm^2/n)

2.3. Water phantom experiments

To confirm the effects and influence of the iBNCT001 neutron beam when used to irradiate a living body, the physical characteristic measurements were first made during irradiation of a water phantom before conducting biological experiments in cells and mice. Fig. 3(a) shows a schematic of the experiments using the normal beam aperture, with a rectangular water phantom set to the irradiation position behind the beam port. Fig.3(b) shows a photograph of the phantom experiment to measure the distribution of the thermal neutron flux in the phantom with an extended collimator.

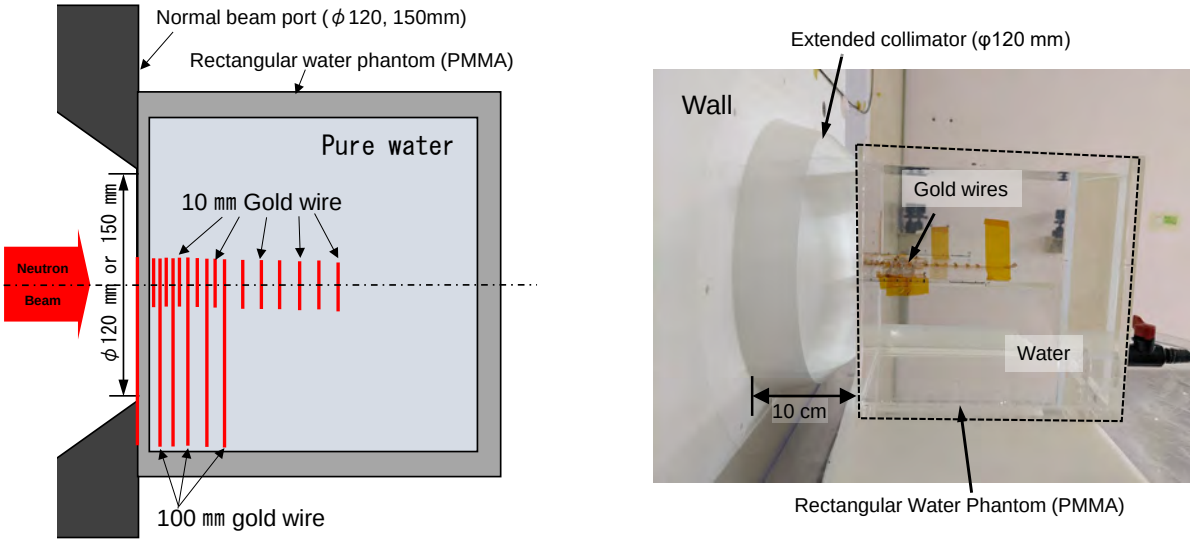

(a) Schema of the phantom experiment

(b) Phantom experiment with the extended collimator

FIG.3. Schema of the water phantom experiment (a) and a photograph of a phantom experiment with an extended collimator 120 mm diameter.

The experiments utilized a 20 × 20 x 20 cm rectangular water phantom that simulated a human head as clinical studies for malignant brain tumors and head-and-neck cancers are planned. The phantom was made of polymethyl methacrylate (PMMA), with wall thicknesses of 10 mm except for the front side (beam side), which was 3 mm. The inside of the phantom can be filled with pure water, and detectors for neutrons and photons can be placed inside the phantom. Multiple thin gold (Au-197) wires 0.25 mm in diameter were set inside the phantom for the measurement of the distribution of the thermal neutron flux. The water phantom was then set at the irradiation position behind the diameter of the beam aperture.

The experiment used normal beam apertures with diameters of 120 and 150 mm. The neutron distribution for an extended collimator 120 mm in diameter was also measured. After neutron irradiation of the phantom, the radioactivity of each gold wire was measured using a Ge detector, and the fluxes were determined using the activation foil method [8].

3. RESULTS AND DISCUSSION

Fig.4(a) shows the three distributions of the thermal neutron flux on the beam axis for the normal beam aperture with diameters of 120 mm, 150 mm, and an extended collimator with a diameter of 120 mm. Fig. 4(b) shows the profiles for each relative distribution, in which the flux values at each depth were divided by the maximum value for each beam aperture.

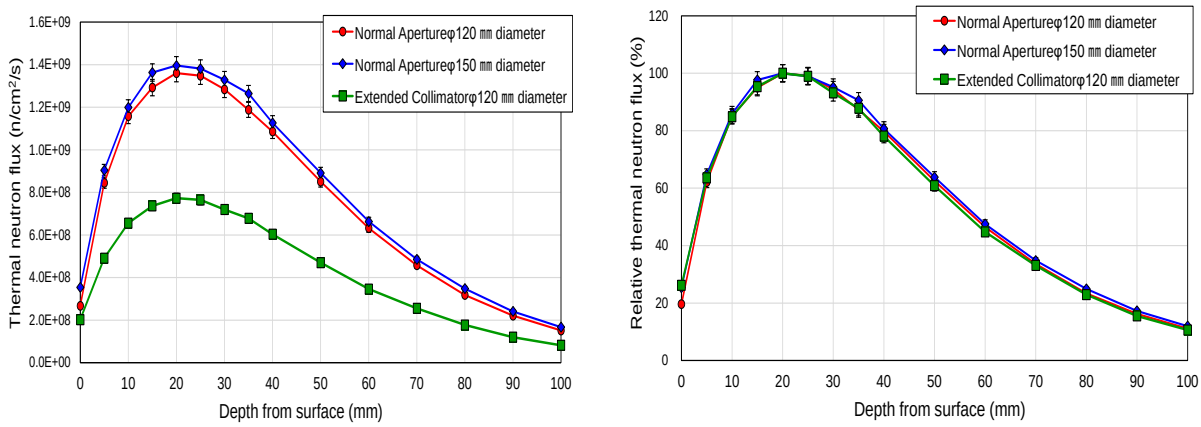

(a) Distributions of thermal neutron flux in average current of 2.0 mA (b) Relative distribution profiles of thermal neutron

FIG. 4. Distributions of thermal neutron flux on the beam axis for each beam aperture

The maximum thermal fluxes for both normal beam apertures were 1.36 and 1.40 $\times 10^9$ (n/cm^2/s), respectively. The position of the peak was the same for all apertures; namely, 20 mm from the phantom surface on the beam axis. In the distributions for the deep direction, for the normal beam apertures, the intensity of the φ150 mm beam was only a few percent higher than that for the φ150 mm beam. However, the shape of the distribution in the deep direction was almost the same. The irradiation times were also approximately the same. Therefore, each beam aperture could be used in the same manner. For typical cases of malignant brain tumors and head and neck cancer, irradiation is expected to be completed in approximately 30 min. An appropriate beam aperture can be chosen depending on the tumor size.

The maximum thermal flux of the extended collimator was approximately 0.8×10^9 (n/cm^2/s). The intensity of the extended collimator was approximately 40% lower than that of the normal beam aperture because it protruded 10 cm from the wall. The irradiation time using the extended collimator in typical treatment cases was approximately 55 min or less. The distribution profile in the deep direction for the extended collimator was almost the same as that for the normal beam apertures. These results demonstrate that the extended collimator can be used for actual treatment as irradiation can be completed within 1 h.

4. CONCLUSIONS

The iBNCT project developed the iBNCT001, a demonstration device providing a LINAC-based neutron source that can be used for BNCT. The average current of the LINAC is currently 2.1 mA and neutrons are generated by irradiating the beryllium target with accelerated protons. The device successfully generated an epithermal neutron beam with sufficient intensity for treatment. To conduct clinical studies in the near future, the physical characteristics of the neutron beam of the iBNCT001 were assessed and several neutron irradiation experiments were performed. The neutron irradiation experiments were performed using a water phantom simulating a human head. The experimental results, in combination with the normal beam apertures, demonstrated that high-intensity thermal neutrons can be generated in the human body. Using normal beam apertures, irradiation was completed in half an hour. The application of an extended collimator created a space between the patient and the wall around the beam aperture; thus, the patient can receive irradiation while maintaining a comfortable posture, thus potentially improving irradiation accuracy. Based on the physical measurement findings, non-clinical studies are currently being performed using mouse irradiation to confirm the biological characteristics of the beam. We plan to conduct clinical studies with actual patients as soon as possible after these physical measurements and biological experiments.

REFERENCES

[1] SWEET, W.H.. Early history of the development of boron neutron capture therapy of tumors, J. Neuro-Oncol. **33** (1997), 19–26.

[2] International Atomic Energy Agency, IAEA-TECDOC-1223, International Atomic Energy Agency, 2001

[3] TANAKA, H., SAKURAI, Y., SUZUKI, M., MASUNAGA, S., KINASHI, Y., KASHINO, G., LIU, Y., MATSUMOTO, T., YAJIMA, S., TSUTSUI, H., and ONO K., Characteristics comparison between a cyclotron-based neutron source and KUR-HWNIF for boron neutron capture therapy. Nucl. Instrum. Methods Phys. Res. B **267**, (2009), 1970–1977.

[4] KUMADA, H., MATSUMURA, A., SAKURAI, H., SAKAE, T., YOSHIOKA, M., KOBAYASHI, H., MATSUMOTO, H., KIYANAGI, Y., SHIBATA, T., and NAKASHIMA, H., Project for the development of the linac based NCT facility in University of Tsukuba, Appl. Radiat. Isot. **88** (2014), 211–215.

[5] KUMADA, H., KURIHARA, T., YOSHIOKA, M., KOBAYASHI, H., MATSUMOTO, H., SUGANO, T., SAKURAI, H., SAKAE, T., and MATSUMURA, A., Development of beryllium-based neutron target system with three-layer structure for accelerator-based neutron source for boron neutron capture therapy, Appl. Radiat. Isot. **106** (2015), 78–83.

[6] KUMADA, H., TAKADA, K, TANAKA, S., TANAKA, S., MATSUMOTO, Y., NAITO, F., KURIHARA, T., SUGIMURA, T., SATO, M., MATSUMURA, A., SAKURAI, H., and SAKAE, T., Evaluation of the characteristics of the neutron beam of a linac-based neutron source for boron neutron capture therapy, Appl. Radiat. Isot. **165** (2020), 109246.

[7] MASUDA, A., MATSUMOTO, TAKADA, K., ONISHI, T., KOTAKI, K., SUGIMOTO, H., KUMADA, H., HARANO, H., and SAKAE, T., Neutron spectral fluence measurements using a Bonner sphere spectrometer in the development of the iBNCT accelerator-based neutron source, Appl. Radiat. Isot. **127** (2017), 47–51.

[8] TANAKA, H., SAKURAI, Y., SUZUKI, M., MASUNAGA, S., MITSUMOTO, T., FUJITA, K., KASHINO, G., KINASHI, Y., LIU, Y.., TAKADA, M., ONO, K., and MARUHASHI, A., Experimental verification of beam characteristics for cyclotron-based epithermal neutron source (C-BENS). Appl. Radiat. Isot. **69** (2011), 1642–1645

VENTILATION AIR SYSTEM ISSUE AT THE UNIVERSITY OF COSTA RICA'S CYCLOTRON FACILITY

E. MORA-RAMIREZ
Atomic, Nuclear and Molecular Science Research Center, University of Costa Rica
San Jose, Costa Rica
Email: erick.mora@ucr.ac.cr

E. CORRALES-CORRALES
Atomic, Nuclear and Molecular Science Research Center, University of Costa Rica
San Jose, Costa Rica
Email: ernesto.corrales@ucr.ac.cr

Abstract

A ventilation issue was detected during the acceptance tests of the first Cyclotron installed in CICANUM research center, at the Universidad de Costa Rica. The incident occurred when gaseous ^{18}F leaked thought a damaged vial cap, but because the hot cell internal bag was not connected during that test, the radioactive gas was sent to the outlet pipe and eventually dumped to the atmosphere, but then detected inside the building by the fixed radiation environmental sensors. To avoid this kind of events happening again, an analysis of the installed HVAC system was performed. Air parcel trajectory models and *in situ* data and instrumentation were used to test the hypothesis raised out the assessment. This work concludes the incident was caused by a recirculation of released radioactive gases, caused by an inconvenient geometric configuration of its HVAC's inlet and outlet. The problem was partially fixed rotating the exhaust pipe 100° and extending its length by 20 meters from its original position. Intermediate components were also implemented to delay possible emergent discharges of radioactive gases.

1. INTRODUCTION

First Cyclotron in Costa Rica was installed in 2020 at the Center for Research in Atomic, Nuclear and Molecular Sciences (CICANUM) at the Universidad de Costa Rica, San Jose. During the first acceptance tests of the Cyclotron, components and systems should be verified before producing any isotope. Considering the tender process, the first isotope to be tested was the ^{18}F, which it will be used for ^{18}F-FDG production. One of the first acceptance tests is to verify that ^{18}F arrives to the hot cells, so that enriched water was sent from the operator's room cabinet to the cyclotron's target and then, from there, to the stated hot cell. This initial test was performed correctly.

Next step was to prepare the hot cell to produce ^{18}F-FDG, in this case the irradiation of enriched water occurred and then it was sent to the hot cell but when this isotope arrived at the activity vial, and a gas leakage on the vial cap arose and eventually that gas was dumped through the building ventilation exhaust pipe, which is located two floors above the production floor, where the test were taking place. The ventilation exhaust pipe has an environmental detector which is used to estimate the number of counts per minute release to the atmosphere. This detector showed an increase of activity from the background level.

Few seconds after the release of radioactive gas to the exhaust pipe, the environmental detectors into the production floor, outside the hot cells, were showing an increase of the background activity as the radioactive gas was released. Due to the small amount of activity prepared for the acceptance test, the amount of gas isotope released to the ventilation exhaust pipe was also small but enough to be detected by those environmental detectors in the facility.

Because our country does not have any regulation regarding releasing radioactive gas to the atmosphere, CICANUM staff considered that an increase of background gas activity released to the atmosphere may represent an incident. From our point of view the presence of radioactive gas into the production floor denotes a radiation incident that needs to be corrected, due to the amount of activity used in the test. If the produced activity was higher, then the amount of leakage could be higher as well.

To correct this issue, a building gas flow analysis occurred, considering local air parcel trajectories. CICANUM staff concludes that there was a recirculation of the dumped gas from the hot cells that should be fixed by changing the configuration of exhaust pipe of the HVAC (heating, ventilation and air conditioning) system of the building.

The goal of this work was to develop a proposal for the practical geometric change of that exhaust, to avoid recirculation events of potentially radioactive gaseous waste through the building ventilation system, which could trigger radiation incidents into the production floor.

2. GENERAL METHODOLOGY

12.1. Analysis of the HVAC system installed

Before starting any test in the installation, CICANUM staff were really concern about the initial arrangement of the HVAC system installed. In principle, the company in charge of this system performed several tests to verify that there was not any possible recirculation on air/gas from the outlet into the inlet pipe.

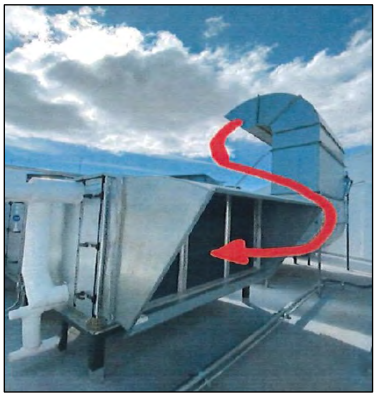

FIG. 1. Initial inlet and outlet pipe HVAC system arrangement installed in the building and possible radioactive gas trajectory entering production main floor.

For the analysis of the geometric configuration of the inlet and outlet of the installed HVAC system in the building, illustrations of *FIG. 2* were prepared to summarize the discussion of hypothetical ways in which the recirculation of radioactive material would take place.

FIG. 2. Wind direction incidence over the inlet/outlet of the HVAC system that generates recirculation. Direct recirculation (left), indirect recirculation (right).

In the left-side image, the direct recirculation is given when the external air is flowing in a particular direction and tends to mix with the exhausted gases of the outlet pipe so the air flow from the outlet of the HVAC system to its inlet, therefore, cooling those gases and sending them to the production floor again.

In the right-side image, indirect recirculation way is showed, where the external air mix with the outlet but moving as a group and colliding against a building wall and losing its energy. In this case external air mix changes its direction to stay close or redirecting itself to the inlet pipe of the HVAC system. Then, eventually the external air mix could be incorporated into the production floor of the building.

12.2. Local air parcel trajectories

The analysis of the geometric configuration of the inlet and outlet of the HVAC system were faced with a geographic air trajectory study, using Hybrid Single Particle Lagrangian Integrated Trajectory Model (HYSPLIT) by the NOAA Air resources laboratory [1].

HYSPLIT model is a complete system for computing simple air parcel trajectories, as well as complex transport, dispersion, chemical transformation, and deposition simulations. According to its webpage, it is one of the most extensively used atmospheric transport and dispersion models in the atmospheric sciences community.

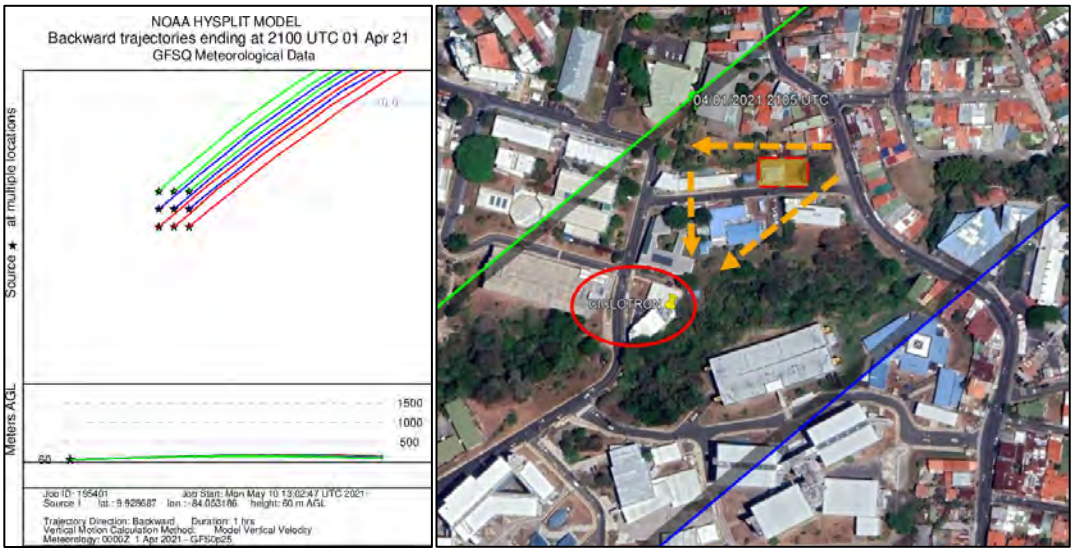

FIG. 3. HYSPLIT model for wind trajectory in backward approximation. From the building coordinates during the recirculation incident [1] (left). HYSPLIT kml file data over a terrain view using Google Earth [2], the Ciclotrón building is inside the red ellipse (right).

The HYSPLIT model generates simple maps and provides .kml files, used to display geographic data in an Earth browser such as Google Earth, as show in the images of *FIG. 3*

For our specific configuration, the outcome (external air mix) essentially follows a parcel trajectory of air backward, considering the HVAC system localization and a specific range of time set in hours. This range of time could be modified according to different needs, and it varies from hours to several days.

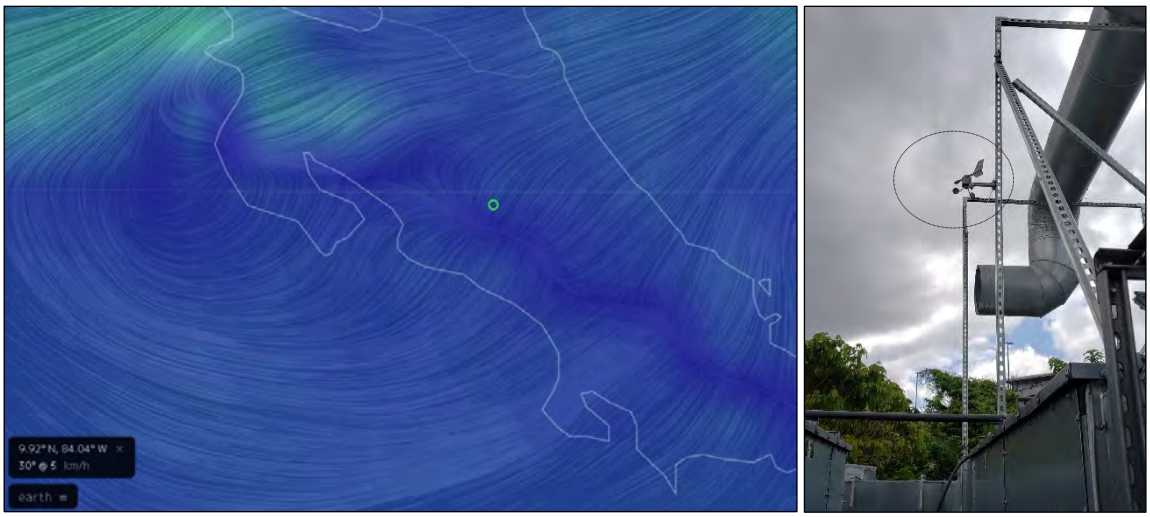

FIG. 4. Wind direction incidence over the building based the Earth Wind Map, using data of the GFS, NCEP and US National Weather Service [4],. The small green circle in the map is showing the ciclotron's building location (left). The anemometer to verify wind direction predictions was placed between the outlet and inlet of the HVAC system (right).

In *FIG. 3*, image at the right, orange arrows represent common wind trajectory directions (vectors) in the area where the building is placed. In same figure, CICANUM gas laboratory (GasLab) is enclosed in a red rectangle. GasLab provides data to define the vectors shown, to understand the most common movement of external air mix in the area. The orange arrows agreed the HYSPLIT wind trajectory generated by archive for the day of the incident.

This associated laboratory launch meteorological balloons in regular bases, collecting local wind behaviour data as part of its research project which has several years in place at CICANUM, as shown in several of their publications [3].

To validate wind direction proposed by the HYSPLIT results, an anemometer was placed between the main HVAC's inlet and its outlet of the building for several weeks, to assess the wind direction at that point and sustain the wind direction arguments based on the outcome of the modelers, *FIG. 4*.

13. PROPOSED AND IMPLEMENTED CHANGES

13.3. HVAC exhaust pipe modification

Bearing in mind factors as intervention time, costs and some technical considerations, some configurations were discussed with engineers of the company in charge of the modification. The selected proposal for the exhaust pipe change consisted in a horizontal rotation of the pipe to direct its outlet downwind and extended its length, supported over the roof of the building, to avoid recirculation due to changes in wind direction. The proposed modification can be seen in *FIG. 5*.

FIG. 5. Inlet (blue triangle) and exhaust pipe (orange-red rectangle) representations for change proposal with an over-position representation of the modelled wind direction, at the day and time where the recirculation incident took place.

As a result, next changes were implemented: one horizontal rotation of nearly 100° at the elbow of the exhaust pipe, and an extension of 20 meters in the length of the exhaust pipe, which is now resting over the roof of the building, as shows *FIG. 6*.

13.4. Intermediate component to delay dumped gases

The synthesis hot cell has an internal bag to prevent gas leakage from the hot cell while synthesis process is performed. If the internal bag fails, a Geiger Müller detector within the hot cell closes a set of pneumatic valves to hold any gas leakage. If the pneumatic valves fail, an intermediate component delays the travel of dumped gases towards the exhaust pipe before releasing it into the atmosphere. The intermediate component consists of 500 meters of tubing at the end of an array of valves to evacuate the resulting gases of the synthesis if the two previous methods fail.

The *FIG. 7* shows the delay line prototype schematic, designed to be placed at the maintenance room in the back of the 6 hot cells installed at the production floor of the facility. Part of the prototype, the manifold with the 500 meters of TPE-U tubing, has been built and installed to the ^{18}F hot cell, but the pumping system for the bag into the hot cell chamber will be implemented on the second half of 2022.

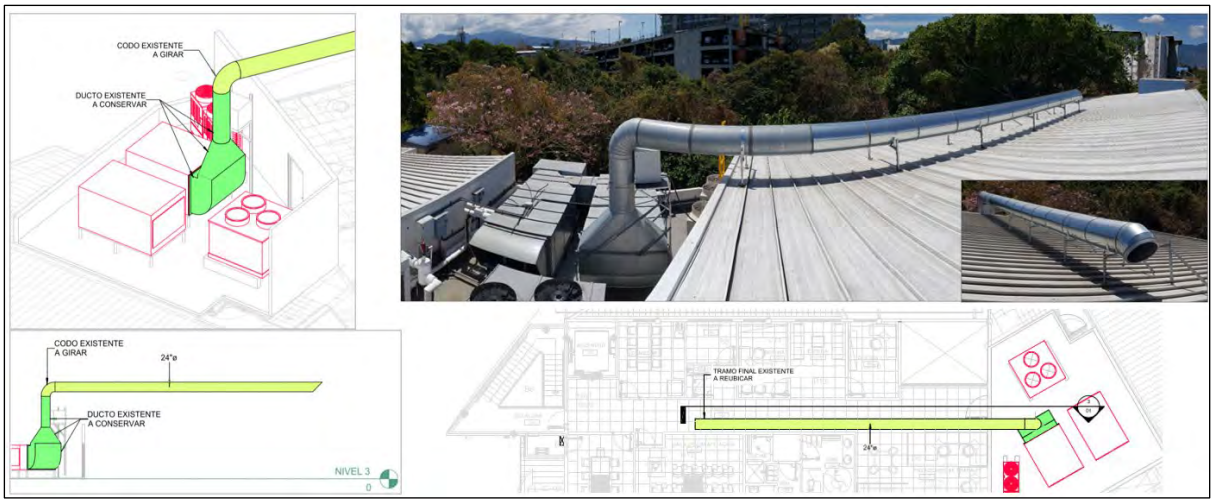

FIG. 6. The physical changes applied over the exhaust pipe of the HVAC system of the building.

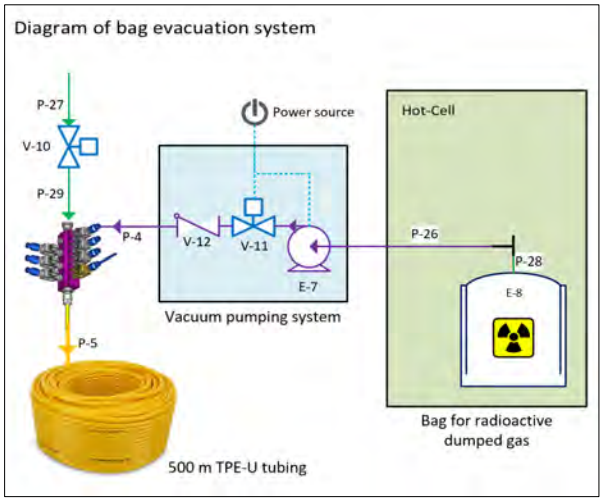

FIG. 7. Delay line prototype schematic, for the hot cells.

14. CONCLUSIONS

The incident analysis gave us the opportunity to understand where the problem was and work on it. This analysis of this issue showed that the activity vial had a tiny gap within its cap, the gap was eliminated using a rubber o-ring, in this way there is not gas leakage at all.

HVAC system configuration requires a meticulous analysis for these types of installations to prevent recirculation of radioactive gases that can affect workers or processes in such facilities. Our solution considered wind speed and direction using HYSPLIT model. Incident analysis gave a solution to prevent this type of events within our hot cells. Along with that study, hot cell intermediate components are in place to contain its dumped gases enough time to reduce its activity before being released to the main exhaust pipe.

The modifications have proved to work properly. We have replicated the initial issue and there was not radiation gas detected by the environmental system, even when the intermediate component is not attached to the hot cells output.

ACKNOWLEDGEMENTS

The authors gratefully acknowledge: Universidad de Costa Rica/CICANUM and the International Atomic Energy Agency for the financial support for the IAEA CN-301, ID 041. Authors also gratefully thanks to ELVATRON S.A., Navarro y Aviles, OEPI (UCR) and all CICANUM Staff for helping in the incident analysis.

REFERENCES

[1] The National Oceanic and Atmospheric Administration (NOAA), "HYSPLIT – Air Resources Laboratory." https://www.arl.noaa.gov/hysplit/

[2] Google LLC, "Google Earth." https://earth.google.com/

[3] J. A. Diaz, H. B. Selkirk, G. A. Morris, N. A. Krotkov, D. C. Pieri, and E. Corrales, "In-Situ Detection of SO2 Plumes in Costa Rica from Turrialba Volcano using Balloon-borne Sondes," *Am. Geophys. Union*, Dec. 2012.

[4] "Earth, a global map of wind, weather, and ocean conditions." https://earth.nullschool.net/

DEVELOPMENT AND APPLICATION OF INDICATORS FOR THE ASSESSMENT OF RADIATION SAFETY SYSTEMS IN RADIOPHARMACEUTICALS PRODUCTION FACILITIES WITH CYCLOTRON

A. X. MAGGIOLO
Nuclear Regulatory Authority
Buenos Aires, Argentina
Email: amaggiolo@arn.gob.ar

M. R. ESPÓSITO
Nuclear Regulatory Authority
Buenos Aires, Argentina

G. E. RABI
Nuclear Regulatory Authority
Buenos Aires, Argentina

Abstract

The 'Class I Particle Accelerators Control Sector' of the Nuclear Regulatory Authority developed a tool that helps perform safety assessments of radiopharmaceuticals production facilities with cyclotrons. This tool was designed for the evaluation of safety systems implementation at the facilities and for monitoring the application of radiation safety standards in facilities that are currently operating. The paper presents indicators regarding safety systems considering the guidelines described in the document 'Criterios para el licenciamiento y requisitos de inspección en instalaciones con ciclotrones para producción de radioisótopos utilizados en aplicaciones e investigaciones médicas' (2013) from Foro Iberoamericano de Organismos Reguladores Radiológicos y Nucleares [1]. These indicators are intended to measure the level of adequacy of each facility compared to what is recommended in the referenced document. The indicators were collected and presented in an organized way using spreadsheets and graphics which makes easier its display and allows its interpretation depending on different criteria such as the type of safety system or type of facility. Finally, the follow up of these indicators was done from 2018 to 2021 and a tendency to improvement was detected as a consequence of the update of procedures and also due to the implementation of new safety systems. Moreover, through this tool, the Nuclear Regulatory Authority could monitor indirectly the success of the regulatory functions in the increase of the level of intrinsic safety at cyclotron facilities.

1. INTRODUCTION

Radiopharmaceuticals production facilities with cyclotron have to implement radiation safety systems in order to control and mitigate not only external exposure risks due to gamma and neutron fields generated during the cyclotron operation and the radioisotope production, but also internal exposure and surface contamination that may occur while working with unsealed sources.

Safety systems have to be prioritized in the features planned in the design of the facility and can be complemented with operational procedures with the purpose of ensuring the protection of workers, the public and the environment.

The design of these systems depend on different factors such as the equipment, for example, whether the cyclotron is self-shielded or not; the production processes that are carried out; the radioisotopes produced; etc. In addition, normal operational situations as well as incidents and accidents need to be considered during the design of this type of facilities.

The 'Class I Particle Accelerators Control Sector' of the Nuclear Regulatory Authority is the sector in charge of the regulatory control of radiopharmaceuticals production facilities with cyclotrons. The sector detected the need of a tool that helped perform safety assessments, particularly for the evaluation of safety systems implementation and the application of radiation safety standards at the facilities under regulatory control.

For its development, the document 'Criterios para el licenciamiento y requisitos de inspección en instalaciones con ciclotrones para producción de radioisótopos utilizados en aplicaciones e investigaciones médicas' (2013) [1] from Foro Iberoamericano de Organismos Reguladores Radiológicos y Nucleares was taken

as the primal reference, considering the guidelines presented there for interlocks, alarms, manual safety systems, plans and records. This document was chosen because it was considered the most representative of the state of the art concerning radiation safety in this type of facilities when the tool was developed.

In the paper, the conditions at cyclotron facilities that are in operation stage from Argentina are analysed. There are currently five facilities in operation stage, two of which have self-shielded cyclotrons, and the main radiopharmaceutical produced in the country is FDG.

The result of the analysis is presented using indicators that were developed by the 'Class I Particle Accelerators Control Sector'. The indicators are intended to measure the level of adequacy of each facility compared to what is recommended in the referenced document. They are collected and presented in an organized way using a spreadsheet and graphics which makes easier its display and allows its interpretation depending on different criteria such as the type of safety system or type of facility.

2. METHODS

The indicators were developed following the guidelines in [1]. For the purpose of the paper, they were divided in three categories: plans, safety systems (which includes interlocks, manual systems and alarms), and records. Each category consists of a list of requirements that are expected to be fulfilled by the cyclotrons facilities.

- Plans.
  - Site and location;
  - Facility layout, rooms function and distribution;
  - Location of cyclotron, hot cells and transfer lines;
  - Communication between rooms;
  - Flow of personnel and materials;
  - Room classification;
  - Identification and location of safety equipment and monitors;
  - Air flow and differential pressure in hot cells and rooms;
  - Constructive plans, indicating materials, shielding width, ventilation, electrical and other ducts, and filters.
- Interlocks.
  - Last person buttons (for non-self-shielded cyclotrons);
  - Single key system;
  - Vault door interlock associated with the cyclotron operation; for self- shielded cyclotrons irradiation only possible when the self-shielding is closed.
  - Vault door interlock due to high dose rate and/or monitor failure;
  - Hot cells doors interlock due to high dose rate and/or monitor failure;
  - Interlock due to differential pressure loss in cyclotron vault and hot cells;
  - Radioactive material transfer between cyclotron and hot cells only allowed when the pressure level in the hot cell is adequate and the door is closed;
  - Irradiation conditioned to the liquid level in liquid self-shielded cyclotrons;
  - Self-shielding movements not allowed during radioactive material transfer is completed;
  - Leak tightness test of the target, transfer lines and synthesis modules for gas production before.
- Manual systems.
  - Emergency buttons;
  - Manual system for opening the vault door internally.
- Audible and visual alarms.
  - Cyclotron operational status;
  - High dose rate in area monitors;
  - Transfer of radioactive material between the cyclotron and hot cells;
  - Failures in ventilation systems (differential pressure loss);
  - Area monitors failure;
  - Opening of vault door, hot cell's doors or opening of self-shielding;
  - Level of discharges in chimney;
  - Increase in activity concentration in different rooms;

- Reduction of the liquid level of self-shielding;
- Temperature change in the cyclotron vault (for liquid self-shielded cyclotrons).

— Records.
- Staff and visitors access to the facility
- Discharges and estimation of public doses
- Occupational exposure (staff doses)
- Optimization program
- Radiological surveillance – monitoring
- Operational and production
- Radiological events and/or accidents reports
- Maintenance
- Radioactive waste
- Training
- Safety systems testing
- Calibration sources inventory and its calibration certificates
- List of radiological equipment
- Calibration certificates of radiological equipment
- Inspections and audits reports
- Packages, shipping and sales

Once these categories were established, it was necessary to perform a safety assessment in order to determine the level of adequacy for each category. The safety assessment was done mainly by reviewing the documentation and procedures of the facilities, such as: the safety report, operational procedures, maintenance procedures, monitoring reports, emergency preparedness and response plan, etc. The process of reviewing these documents is aimed also to verify the compliance to the requirements established in the regulation applicable to this type of facilities ([2], [3] and [4]). Other relevant information could also be obtained by other means, for example, during regulatory inspections.

By doing this assessment, it could be determined whether a requirement was fully, partially or not fulfilled. With the aim of having a numerical representation, it was arbitrarily assigned a value of '2' for those requirements that were fully met; for those that were partially met, a value of '1'; and for those that were not met, a value of '0'.

Afterwards, the percentage of adequacy was calculated considering the total points obtained. For this calculation, it was also taken into account the type of facility, as there are requirements that apply only in certain cases. For example, some interlocks may not be needed if the cyclotron is self-shielded whereas others are only applicable in those cases. Moreover, some safety systems are related to liquid self-shielded cyclotrons.

The results of the assessments were collected using a spreadsheet in which the indicators were calculated. A sample of the spreadsheet is shown in Fig. 1. For the purpose of the paper, the facilities were named *A*, *B*, *C*, *D* and *E*.

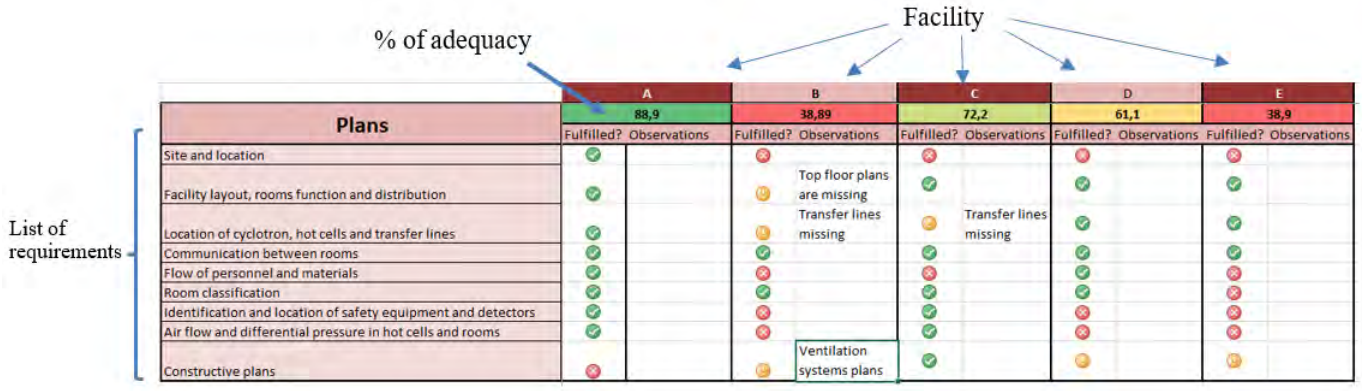

FIG. 1. Sample table with the result of safety assessments.

For each facility there are two columns: in the first one it is selected if the requirement is fully (green), partially (orange) or not fulfilled (red); in the second one, any other observation or comment can be added. The second column does not necessarily have to be completed, it is just to add further comments or additional information that could be useful.

The spreadsheet has also the option to save the indicator values in a different table with the date. This option has the purpose of recording the indicators over time so that it can be analysed the development of each facility.

3. RESULTS

The indicators were measured from 2018 to 2021, taking into consideration the list of requirements presented in section 2.

The following charts show the evolution of the indicators from 2018 to 2021 for facilities A to E. In Fig. 2 it can be observed the percentage of adequacy throughout the years regarding the plans listed in the previous section. It can be seen that, in general, all the facilities improved the information presented in their plans. It should be noted that *Facility E* was the one that had the biggest improvement, especially between 2020 and 2021, due to the update of their plans in the context of the process of authorization of an expansion of the facility.

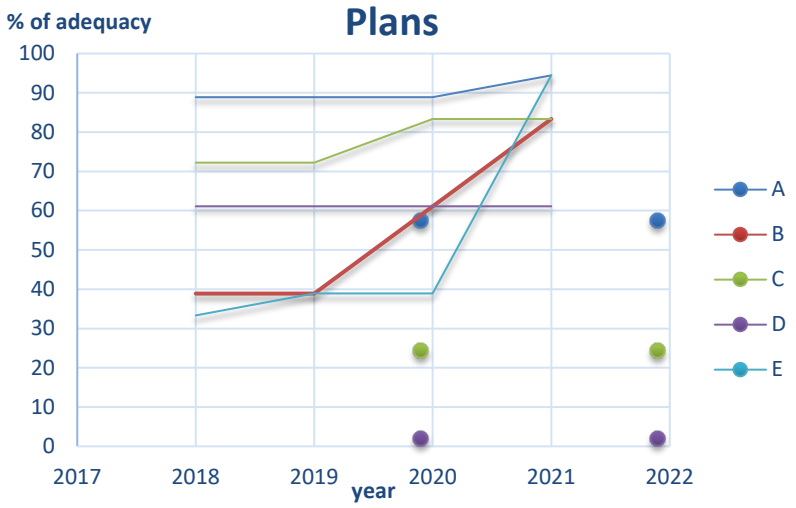

FIG. 2. Percentage of adequacy of plans for facilities A to E, from 2018 to 2021.

In Fig.3 it is showed the percentage of adequacy of safety systems (including interlocks, alarms and manual systems) over time. There are some points in which the percentage drops because, for example, a safety system was out of service due to failure of a radiation monitor. However, the general tendency is positive and whenever a problem with a safety system was detected, it was repaired or compensated in order to maintain or improve the level of safety.

Furthermore, it is observed that *Facility B* improved significantly its safety systems. One major improvement was the addition of a last person button, which is an extremely relevant interlock in a non-self-shielded cyclotron to assure that the vault is empty before irradiation and prevent accidents.

Figure 4 shows the evolution of the percentage of adequacy of records over time. It can be observed that in 2021 the level of adequacy is over 80% for all the facilities.

The results of the last assessment are shown in Fig.5. It can be observed that the general conditions are within an acceptable level of adequacy. Regarding safety systems, *Facility D* is the one with the least fulfilment with nearly 50% of adequacy because it does not have modern equipment in the radiopharmacy laboratory. However, the facility is in process of updating the laboratory and relevant improvements are expected in the upcoming year.

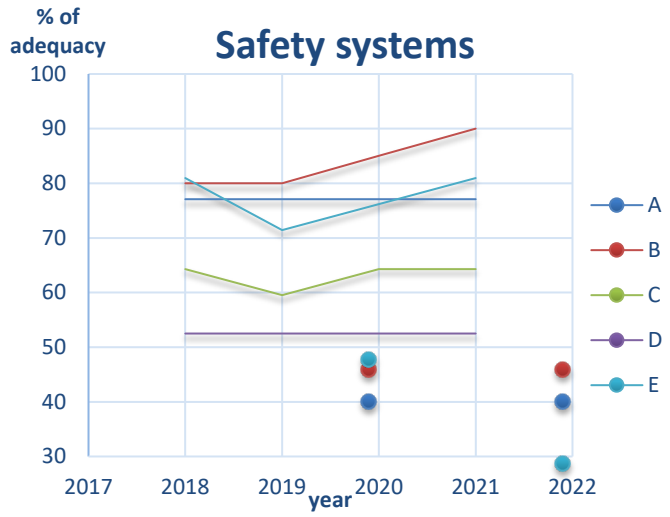

FIG. 3. Percentage of adequacy of safety systems for facilities A to E, from 2018 to 2021

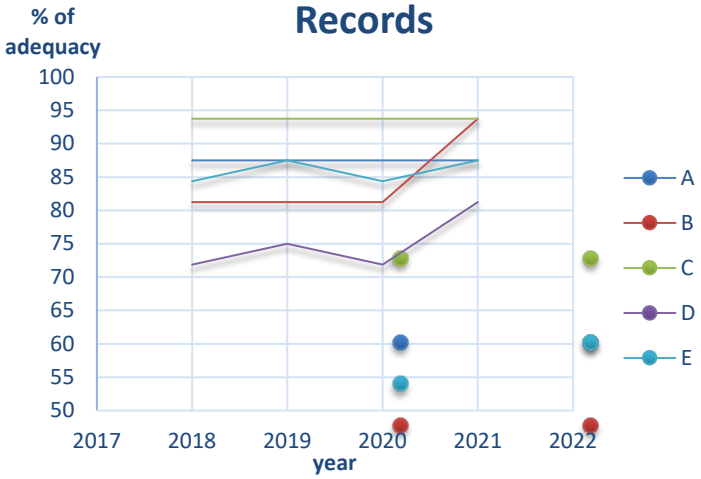

FIG. 4. Percentage of adequacy of records for facilities A to E, from 2018 to 2021.

When the implementation of a safety system is not available or it is not feasible, procedures have to be implemented with the objective of replacing temporarily the lack of the safety system. In this case, the requirement is classified as "partially met" for the indicator calculation, which corresponds to a value of "1".

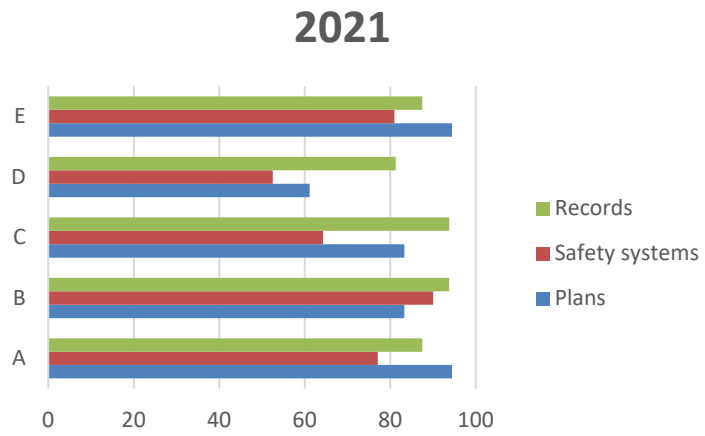

FIG. 5. Results in the 2021 for facilities A to E

4. CONCLUSIONS

Through the development and implementation of the tool presented in the paper, it was possible to not only measure but also to follow up over time the general safety conditions in radiopharmaceuticals production facilities with cyclotron.

In the first place, the indicators developed by the 'Class I Particle Accelerators Control Sector' proved to be useful, as it is a systematic way to measure the results of the safety assessments done by the regulatory body. It also allowed to record and to follow the evolution of the indicators throughout the years in a simplified way, because the spreadsheet is easy to update.

Furthermore, the indicators helped to detect which aspects had to be improved in the different facilities. In this regard, it could be observed that the general tendency was towards improvement in all three of the categories (plans, safety systems and records). Nonetheless, if a significant drop in the percentage of compliance happens to be detected, the regulatory body needs to take further actions to determine the causes and to assure the re-establishment of the previous safety conditions. In this way, the regulatory body can monitor indirectly the regulatory functions in the increase of the level of intrinsic safety at cyclotron facilities.

For the above mentioned reasons, performing safety assessments with the aid of this kind of tool is really valuable for the regulatory body, but it also has to assure that all the safety systems and records are implemented. Thus, this task has to be complemented with regulatory inspections in which it can be verified that safety systems are operating correctly and records are being completed. Additionally, the process of developing this instrument is really fruitful for safety inspectors because it leads them to study deeply the characteristics and safety aspects of the facilities under regulatory control.

It has to be noted that the results presented in the paper are limited to the facilities that are currently in operational stage in Argentina, but the same analysis can be applied to other stages of the life of a facility, such as construction, commissioning and decommissioning. In these cases, the list of requirements should be extended considering the particularities of each stage. It could also be developed an equivalent tool for other type of facilities.

Overall, it is important to highlight that the enforcement of new standards in facilities that are already constructed and have been operating for several years is not an easy task for the regulatory body. However, it is one of the main goals of the regulator to ensure that the safety conditions always tend to be better and stay aligned as much as possible with the state of the art for this type of facilities. Then, counting with a tool as the one presented in the paper is remarkably helpful to review the evolution of the safety conditions and to pursue said objective.

REFERENCES

[1] FORO IBEROAMERICANO DE ORGANISMOS REGULADORES RADIOLÓGICOS Y NUCLEARES, Criterios para el licenciamiento y requisitos de inspección en instalaciones con ciclotrones para producción de radioisótopos utilizados en aplicaciones e investigaciones médicas, (2013).

[2] AUTORIDAD REGULATORIA NUCLEAR, Norma AR 10.1.1. - Norma Básica de Seguridad Radiológica - Revisión 4, Argentina (2019).

[3] AUTORIDAD REGULATORIA NUCLEAR, Norma AR 5.1.1. - Exposición ocupacional en aceleradores de partículas Clase I - Revisión 1, Argentina (2002).

[4] AUTORIDAD REGULATORIA NUCLEAR, Norma AR 5.7.1. - Cronograma de la documentación a presentar antes de la operación de un acelerador de partículas - Revisión 1, Argentina (2002).

[5] INTERNATIONAL ATOMIC ENERGY AGENCY, Cyclotron produced radionuclides: Guidelines for setting up a facility, Technical Report Series No 471, Vienna (2009)

REGULATORY FRAMEWORK ADOPTED BY THE NUCLEAR REGULATORY AUTHORITY OF ARGENTINA FOR THE LICENSING OF THE ARGENTINE CENTER OF PROTON THERAPY AND PROGRESS ACHIEVED

G. E. RABI
Nuclear Regulatory Authority
Buenos Aires, Argentina
Email: grabi@arn.gob.ar

L. D. MARTIRI
Nuclear Regulatory Authority
Buenos Aires, Argentina

Abstract

The Argentine public health system is currently carrying out the project of the Argentine Proton Therapy Center (CeArP), being the first in the region to incorporate high-energy proton beams for cancer treatment. This center is designed to have two treatment rooms and a Research and Development laboratory, provided with a 230MeV proton beam generated by a cyclotron. This project represents a challenge for the regulatory body, the Nuclear Regulatory Authority of Argentina (ARN), as it does not have a specific regulatory framework or staff with prior experience in this technology. The paper summarizes the activities conducted by the ARN during the CeArP licensing process, describes the regulatory approach adopted and the implemented steps to strengthen its capacities. Finally, the milestones achieved so far, the lessons learned and future plans are presented in the paper, as well as the challenges caused by COVID-19 pandemic that led to adapting de regulatory process with remote collaborative work to analyze the documentation.

1. INTRODUCTION

In 2016, the National Commission of Atomic Energy (CNEA) notified to the Nuclear Regulatory Authority of Argentina (ARN) the plan to carry out the project of the Argentine Proton Therapy Center (CeArP). The original project included a treatment room and a Research and Development laboratory, provided with a 230MeV proton beam generated by a cyclotron. Despite pauses in the project that delayed construction, progress continued and modifications were implemented, adding one more treatment room to the original design. The placement has been defined in Buenos Aires City, in a strategic zone, next to the Oncology Institute “Dr. Angel H. Roffo” and the “Nuclear Medicine Center Foundation (FCDN)”.

This center would be the first in Latin-America with this type of technology, representing a challenge not only for the entity in charge to operate the facility, but also on the regulatory side. During this time ARN had to work improving their technical capabilities to deal with this new technology properly. Furthermore, the regulatory framework of ARN had to be adapted to carry out the regulatory processes in a proper way.

Finally, in February 2021, the Responsible Entity presented the documentation formalizing the beginning of the licensing process of the facility.

2. REGULATORY APPROACH

The ARN is facing this regulatory endeavour working on different strategies. Since the beginning of the project, the development of technical capabilities of the personnel has been a priority. Furthermore, adapting the regulatory framework and different organizational aspects in order to facilitate the licensing processes to a new technology has been a great challenge.

2.1. Training

Since ARN was notified of the Argentine Proton Therapy Center (CeArP) project in 2016, efforts are being made by the regulatory body to further develop the technical capabilities of its human resources, through the participation of members of the evaluation group in technical meetings, workshops, specializations studies, collaboration projects with other regulatory bodies and internal training sessions related to proton therapy, among others.

2.1.1. Participation in technical meetings, workshops

ARN has encouraged the participation of the personnel in technical meetings and workshops; events as a technical meeting in the University of Philadelphia that took place in 2016 with the vendor of the center, or the 1st Argentine Workshop of Proton Therapy in 2019.

2.1.2. Specialization Studies

Most of the members of the evaluation group have completed the IAEA funded Specialization Course in Radiological Protection and Safety of Radiation Sources. Moreover, one member chose the licensing of a proton therapy center as the final project for the Specialization.

Additionally, another member embarked on master's studies through a Fulbright scholarship in the United States, at the University of Florida, which houses an active proton therapy center. He was able to take different courses on various topics relevant to the licensing of the center and participate in the Penn Radiation Oncology, "Fifth Annual course in Proton Therapy", in November 2018.

2.1.3. Internal training sessions

A comprehensive reading of IAEA-TECDOC 1891 was performed; the document was distributed among the personnel for its reading and study after its publication in January 2020. A session was organized to discuss the most relevant topics of the document.

2.1.4. Collaboration projects with other regulatory bodies

There is a collaboration project signed in 2021 between ARN and CNEN (the regulatory body of Brazil), where it was included the cooperation in 'Proton therapy and authorization processes in high energy cyclotrons'. Thus, exchange activities were programmed including remote virtual meetings and technical visits in Argentinian and Brazilian facilities. The authorization processes for facilities' personnel were also included in the agenda, which is in progress.

2.2. Regulatory framework

The Nuclear Regulatory Authority of Argentina (ARN) is the responsible of establish, develop and implement a regulatory regime for all nuclear activities carried out in Argentina. The national law Act 24.804, which came into force on April 25, 1997, gives to the ARN the power of dictate the country standards. The regulatory framework of the nuclear activity is sustained by 64 regulatory standards and 10 regulatory guides. It classifies the facilities as Class I, Class II and Class III considering the following criteria [1]:

- radiation sources in the facility or practice,
- environmental radiological impact,
- radiological consequences of potential exposures,
- the ocupational doses and,
- technological complexity.

From the Argentine regulatory framework, does not emerge a direct classification for a proton therapy facility. This classification is not trivial, since all the medical applications with accelerators are classified as Class II facilities and cyclotrons are generally considered Class I. But in this case, the facility was considered as one single element.

ARN has strengthened its regulatory framework for authorization and processes oversight, to ensure that national and international standards are met. For this purpose, ARN has defined some general guidelines related with the authorization processes of the facility and the regulatory task assignments.

2.2.1. Authorization process

The Argentine Proton Therapy Center (CeArP) was categorized as a Class I facility. This classification was defined using a graded approach, considering not only the radiological risk of its operation, but also the consequences of an incidental/accidental event and its technological complexity [3]. The authorization process is being implemented in four stages, with construction, commissioning, operation and decommissioning authorizations, as established by the ARN standards for Class I facilities and the recommendation of IAEA.

2.2.2. ARN Strategic plan

The authorization process of the Proton Therapy Center has been included as a priority in the ARN strategic plan for 2021-2025. In this manner, ARN reaffirms its commitment to radiation safety with the corresponding allocation of resources [5].

2.2.3. Creation of the Project

To carry out these regulatory endeavours, a multidisciplinary working group was formed by the ARN, with strategic personnel with background in regulatory affairs in an attempt to leverage prior experience. The creation of the 'Licensing Project of the Argentine Center of Proton Therapy' gives a formal structure, but taking into account that their members belong to different working areas of the ARN with their own responsibilities.

The 'Project' has its following objectives:

- Manage the licensing of the facility, until the eventual granting of the Operating License,
- Plan regulatory activities related to licensing,
- Generate the necessary communications with the Responsible Entity,
- Manage documentation related to licensing,
- Coordinate the necessary evaluations and give intervention to suitable personnel of the "Class I Particle Accelerators" sector and the "Radiotherapy and Brachytherapy" department, in addition to submitting requests for external evaluations to management, when necessary,
- Prepare the relevant reports

The 'Project' depends on the 'Radiation Safety, Safeguards and Security' Department of ARN and it is essentially formed by two sectors: "Class I Particle Accelerators Control" and "Radiotherapy and Brachytherapy". Two members of other ARN sectors with experience in safety assessments have been summoned to the working group, and to this day, it is composed of six members.

3. RESULTS

After several years of work, results are starting to be seen in each of the lines of action in which the ARN has advanced.

3.1. Training

The training activities carried out to date have given satisfactory results, being able to strengthen the capacities of the staff introducing themselves in the particularities of the proton therapy. In addition, the trainings have allowed the personnel of the two main sectors participant to be able to get involved in the regulatory aspects that derive from the other and thus increase the technical capacities of the group.

There are some other activities planned to be carried out soon, as the technical visits of experts and the development of knowledge exchange activities with other regulatory bodies with experience on authorization and inspection process of this technology.

3.2. Authorization processes

3.2.1. Facility

In February 2021, the Responsible Entity submitted to the ARN the Preliminary Safety Report required for granting the construction authorization, which has been evaluated by the working group of the 'Licensing Project of the Argentine Center of Proton Therapy'. Due to the COVID-19 restrictions, the regulatory processes needed to be adapted; in this way, the safety assessment of this documentation was realized remotely.

Virtual technical meetings were realized for this purpose, where technical discussion enriched the group work. Other ARN sectors have contributed to the evaluation working in specific topics. Technical reports with the safety assessment conclusions were made and circulated among the group.

At the moment, the experience of virtual work in safety assessment has been very positive for this working group. The work has been smooth and efficient, and it is expected to continue in this way with the evaluation of the remainder documentation that it is expected to come.

3.2.2. Staff

Facility personnel will be authorized through a mixed licensing scheme, combining the staff licensing process applicable to Class I facilities with the one for obtaining individual permits that applies to Class II facilities [6] [7]. This licensing scheme has been developed by applying a graded approach to existing ARN standards for staff licensing during the evaluation of the proposed organizational structure of the Proton Therapy Center. Emphasis will be placed on ensuring adequate education and training for all positions in the organization chart, as well as the application of an Integrated Safety Management System that includes a program for the promotion of a strong safety culture, according to ARN standards, in particular **AR 10.6.1** "Management System for Safety" and GSR Part 3 [8].

4. CONCLUSION

The efforts made by the ARN since the notification of the construction plan to assume the licensing of a new technology, such as proton therapy, are showing promising results.

On one hand, special efforts have been made to support and promote staff training. The ARN understood from the beginning that the training process must be continuous and once started, the skills of the personnel must be maintained and improved. From 2016 to date, several training activities have been completed with satisfactory results. It is planned to continue in this direction in the years to come.

On the other hand, it has been necessary to strengthen the regulatory framework in order to carry out the licensing process in accordance with national and international standards. For this reason, work is being done on the application of a graded approach both to the licensing of the facility itself and in the personnel licensing process, with visible progress.

To meet the aforementioned objectives, the development of an 'ad hoc' working group, with complementary backgrounds, can be considered an adequate decision. Proof of this is the work carried out, within the context of the restrictions due to the pandemic, delivering concrete results such the complete evaluation of the first version of the Preliminary Safety Report.

Finally, the ARN's commitment to safety and good practices has been demonstrated, which are not only expressed in documents such as the strategic plan, but also in regulatory actions and we hope to continue on this path.

REFERENCES

[1] Autoridad Regulatoria Nuclear, "Norma AR 10.1.1. - Norma Básica de Seguridad Radiológica - Revisión 4", (2019).
[2] Autoridad Regulatoria Nuclear, "Norma AR 0.0.1. - Licenciamiento de instalaciones Clase I - Revisión 2", (2002).
[3] Autoridad Regulatoria Nuclear, "Norma AR 5.1.1. - Exposición ocupacional en aceleradores de partículas Clase I - Revisión 1", (2002).
[4] Autoridad Regulatoria Nuclear, "Norma AR 5.7.1. - Cronograma de la documentación a presentar antes de la operación de un acelerador de partículas - Revisión 1", (2002).
[5] Autoridad Regulatoria Nuclear, "Plan Estratégico Institucional 2021-2025", (2021)
[6] Autoridad Regulatoria Nuclear, "Norma AR 0.11.1. - Licenciamiento de personal de instalaciones Clase I - Revisión 3", (2002).
[7] Autoridad Regulatoria Nuclear, "Norma AR 8.11.3. - Permisos individuales para especialistas y técnicos en física de la radioterapia - Revisión 0", (2006).
[8] Autoridad Regulatoria Nuclear, "Norma AR 10.6.1. - Sistema de gestión para la seguridad en las instalaciones y prácticas - Revisión 0", (2020).
[9] IAEA, TECDOC-1891 – "Regulatory Control of the Safety of Ion Radiotherapy Facilities", (2020) AAPM task group 224: Comprehensive proton therapy machine quality assurance, (2019)
[10] PTCOG Safety Group Report On Aspects of Safety in Particle Therapy – Version 2, (2016)
[11] Autoridad Regulatoria Nuclear, "Norma AR 8.2.2. - Operación de aceleradores lineales de uso médico - Revisión 1", (2002).

MULTIPURPOSE ELECTRON BEAM FACILITY IN SLOVAKIA FOR RESEARCH AND INDUSTRIAL APPLICATIONS

A. SAGATOVA
Slovak University of Technology in Bratislava, Faculty of Electrical Engineering and Information Technologies, Institute of Nuclear and Physical Engineering
Bratislava, Slovakia
Email: andrea.sagatova@stuba.sk

M. FULOP
ABRS s.r.o.
Samorin, Slovakia

M. PAVLOVIC
Slovak University of Technology in Bratislava, Faculty of Electrical Engineering and Information Technologies, Institute of Nuclear and Physical Engineering
Bratislava, Slovakia

S. KOTOROVA
Slovak University of Technology in Bratislava, Faculty of Electrical Engineering and Information Technologies, Institute of Nuclear and Physical Engineering
Bratislava, Slovakia

Abstract

The paper reports on basic parameters, operational experience and application potential of the electron-beam irradiation facility at the University Centre of Electron Accelerators of the Slovak Medical University. The centre is based on a 5 MeV 1 kW linear electron accelerator UELR-5-1S equipped with a beam-scanning system and a conveyor line. Although it could be used also for routine radiation processing in an industrial-like mode, its main purpose was focused to research. The research possibilities are presented in terms of deliverable types of radiation (electron beam or bremsstrahlung), available doses and dose-rates, ranges of electron beam in different materials and other relevant parameters. They are also demonstrated by examples of some research activities and most significant scientific achievements.

1. INTRODUCTION

Radiation processing belongs nowadays to modern and widely used tools for modification of material properties in a well-controlled way. It can be applied to variety of materials ranging from polymers (cross-linking) [1], elastomers (vulcanization), medical products (sterilization), food, chemical pollutants of environment (disintegration) and many others [2, 3]. These applications have reached an industrial-scale level and dedicated electron machines are commercially available as integral built-in parts of production lines.

Radiation processing had not been well-developed technology in Slovakia before 2011. It included one cyclotron for positron radioisotope production [4] and two electron beam (EB) accelerators as parts of production lines for sterilization and tyre crosslinking, those in private companies of foreign ownership. Accelerator utilization for research purposes was minimal. Situation changed during last decade. Since 2011 more ion accelerators have been installed, 3MV Pelletron tandem accelerator for material research and dating at Comenius University in Bratislava [5], 6 MV tandem accelerator and 500 kV ion implanter of Slovak University of Technology for material research in Trnava as well as 2 MV tandem accelerator of Slovak Academy of Sciences in Piestany.

Research possibilities were widened also by a new electron accelerator of Slovak Medical University placed in Trencin, designed for research and also industrial purposes. This multipurpose facility started its operation in 2012 with one main goal to introduce the radiation treatment technology into practise in Slovakia.

Physics research represents another application domain of electron accelerators. Here, radiation processing can be used for two main purposes: (1) as a technological tool for intentional and custom-tailored control of material properties of interest, and (2) as a tool for studying radiation damage, radiation hardness, aging, degradation and other radiation-induced effects in different materials, material structures, or even complex systems like integrated circuits, radiation detectors and electronic devices. The research possibilities are

determined by deliverable types of radiation, achievable doses, dose-rates, ranges of electron beam in the material of interest etc. These parameters depend mainly on the beam characteristics and technical limits of the beam-delivery system. In the paper, we describe and discuss the above parameters for the UELR-5-1S linear electron accelerator at the University Centre of Electron Accelerators of the Slovak Medical University located in Trencin, Slovakia. Discussion is completed by demonstrative examples of some research activities and significant scientific results that have been achieved at this laboratory so far.

2. MULTIPURPOSE ELECTRON BEAM FACILITY IN TRENCIN

2.1. Irradiation facility

The facility is equipped with a 5 MeV electron LINAC (Fig. 1) and it has been focused on research purposes and on introduction of radiation processing in the country, when starting its operation in 2012. Research possibilities are influenced by accelerator parameters and in this case adjustable energy, scanning width, beam repetition rate as well as conveyor velocity and its distance from accelerator exit window lead to wide range of available dose-rates applied. The ranges of the most relevant accelerator parameters are listed in Table 1. The nominal electron energy of 5 MeV can be modified in the range from 3.6 up to 6.2 MeV. The beam repetition-rate together with the beam scanning width and the distance of irradiated object from the accelerator exit window tune the achievable dose-rate during irradiation. Practically, during irradiation with 5 MeV electrons on conveyor, the dose-rate can vary from 10 to 5600 kGy/h.

The accelerator can use a water cooled tungsten target of 3 mm thickness, so two types of radiation are available (electron beam and bremsstrahlung), which spreads its fields of application and research possibilities. Due to low efficiency of conversion, the dose rates for X-ray treatment are in different but also wide range from 26 up to 1400 Gy/h.

FIG. 1. Photograph of the accelerator (left) and view into irradiating room (right).

TABLE 1. PARAMETERS OF THE LINEAR ELECTRON ACCELERATOR UELR-5-1S

Parameter	Ranges
Maximal beam power	1 kW
Beam energy	3.6 – 6.2 MeV
Beam scanning width	40, 45, 50 cm
Beam scanning frequency	0.25 – 5 Hz
Beam repetition-rate	5 – 240 Hz
Beam initial diameter	11 mm
Maximal distance from exit window	170 cm

2.2. Dosimetry

A routine dosimetric system used at the facility is based on B3 radiochromic films (1 cm in diameter and 18 μm thick films of pararosaniline dye dissolved in polyvinyl butyral). Ionizing radiation activates the B3 dye centres which in turn cause the B3 film to undergo a predictable colour change from clear to deepening shades of pink magenta. The radio chemical yield of the dye results in a colour change that is evaluated by a Spectrophotometer Genesys20. The routine dosimetric system can be used in the range of doses of 1 – 100 kGy. The B3 dosimetric system is calibrated by RISO polystyrene calorimeters, traceable to national standards. For dosimetry of lower doses, in the range of Gy, the FARMER ionization chamber is used at the facility.

2.3. Software simulation tools

The dose absorbed in an object irradiated by high-energy electrons depends on parameters of irradiating particle (its energy, fluence) and on the parameters of irradiated object (its density, elemental composition, dimensions and arrangement in the electron beam). Moreover, the absorbed dose varies with the depth of irradiated material. The facility is equipped with the software for the simulation of electron-beam, X-ray and gamma-ray radiation processing, the RT-Office, designed especially for calculation of absorbed dose in objects irradiated with scanned electron beam. The code has several modes, which are dedicated to particular type of irradiated objects: thin multilayer flat packages (ModePEB), products on industrial radiation-technological lines (ModeRTL) and multilayer circular objects like wires, cables and pipes (ModeCEB) by pulsed electron beam of energy from 0.1 up to 25 MeV. The code contains also the programme for objects irradiated by X-ray beams (ModeXR) in an industrial radiation facility based on electron accelerator with X-ray converter in the energy range from 1 to 50 MeV.

This way, the dose depth profile for chosen object is simulated, which is then verified by experimental irradiation of prepared phantom, finally followed by irradiation of the object. The examples of dose depth profiles of chosen materials irradiated by 5 MeV electrons with 10 Hz beam repetition rate are depicted in Fig. 2. It can be seen, that the dose firstly increases with the depth of material and after reaching the maximum value, the decrease to zero (practical range) can be observed. The practical range of electrons in particular material depends strongly on the material density (Table 2.) and its elemental composition.

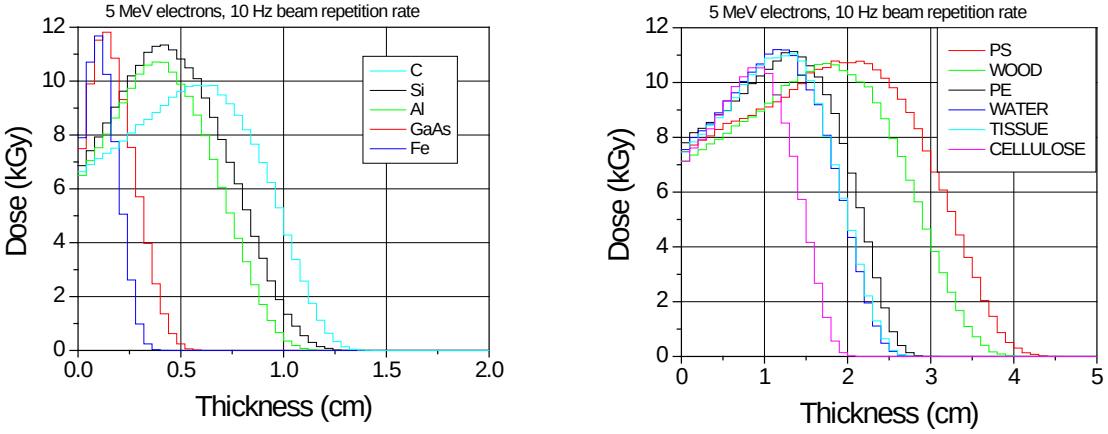

FIG. 2. Dose depth profiles of 5 MeV electrons in materials from elements (left) and from suitable compounds for radiation treatment (right).

The dose depth profile and particularly the practical electron range in material is strongly dependant on the electron kinetic energy, as it can be seen in Fig. 3. Here, the dose depth profiles of high-energy electrons in silicon are depicted for three different energies of electrons: the minimal energy (3.6 MeV), the nominal energy (5 MeV) and for the maximum energy (6.2 MeV) obtainable by the accelerator. The maximum dose absorbed by the object can be very well controlled by the period of irradiation or conveyor velocity. Preserving the period of irradiation, the maximum dose will be managed by the electron beam repetition rate, which influences the dose rate. In Fig. 4, the dose depth profiles of 5 MeV electrons in polyethylene (PE) are shown. As the repetition rate of the beam increases, the maximum dose grows as well.

TABLE 2. DENSITY OF MATERIALS PREPARED FOR IRRADIATION

Material	Density (g/cm^3)	Material	Density (g/cm^3)
Fe	7.87	Water	1
GaAs	5.32	Soft tissue	1
Al	2.70	PE	0.93
Si	2.33	Birch wood	0.71
C	2.26	PS	0.64
Cellulose	1.40	Old wood	0.50

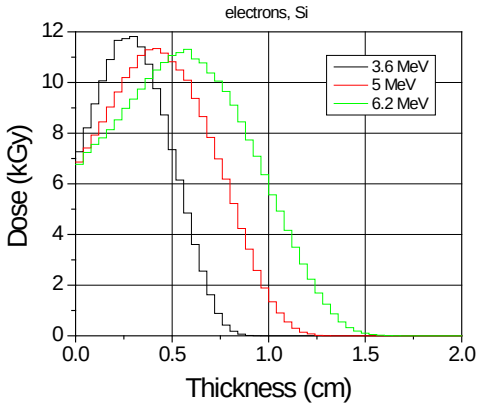

FIG. 3. Dose depth profiles of electrons of various energies in silicon

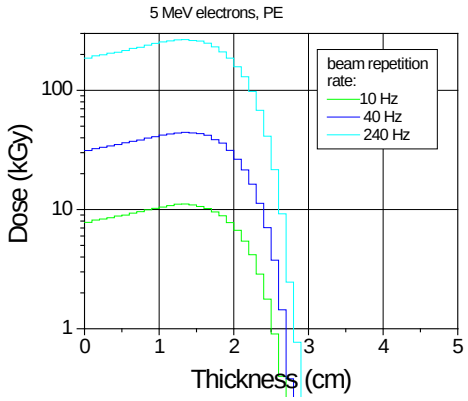

FIG. 4. Dose depth profiles of 5 MeV electrons of various beam repetition rate in polyethylene

It is obvious, that the dose depth distribution of electrons varies from material to material and for practical reasons the prompt calculation of treatable material thickness would be very useful, especially in the research field, where objects are specific and diverse. Based on the experience from preparations of irradiations, the simple function for ideal material thickness treatable by 5 MeV electrons connected to its density was prepared. In relevant density range of materials the simulations of dose depth profiles were calculated using ModeRTL. The ideal material thickness was set as a thickness of material, where the dose of electrons reaches the same value like on its surface for one-side irradiation. In the case of double-side irradiation, the ideal material thickness was determined as the thickness, when the dose in the middle of the material is equal to dose on both surfaces, see Fig. 5. The obtained values of ideal thickness were depicted with respect to material densities. Simple semi-empirical functions were obtained fitting the obtained points (Fig. 6) for one-side irradiation: $t_o\ [cm] = 1.87/d$ and for double side irradiation: $t_d\ [cm] = 4.31/d$, where d is the density of the material in [g/cm^3].

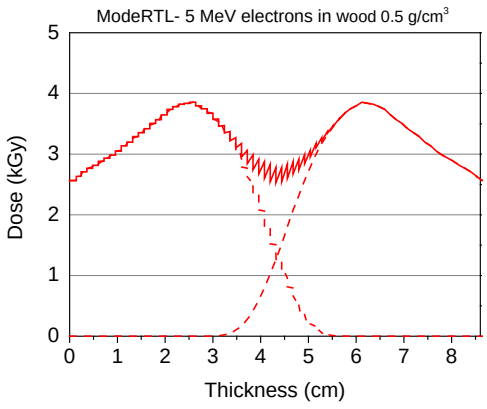

FIG. 5. Dose depth distribution of 5 MeV electrons in wood during double-side irradiation.

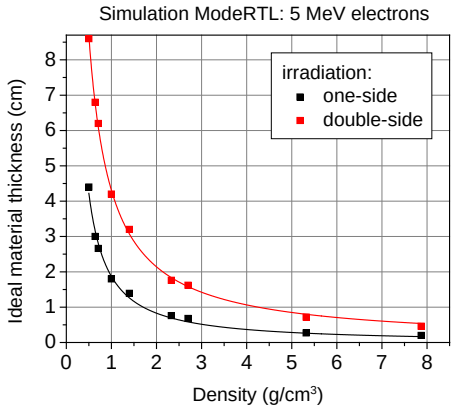

FIG 6. Graphical demonstration of ideal material thickness for treatment by 5 MeV electrons with respect to its density.

3. PRACTICAL ACHIEVEMENTS

During a decade since the multipurpose electron beam facility in Trencin has started its operation, wide range of research experiments was realized with many promising socioeconomic impacts. The research activities have been in the field of radiation aging, medicine, environment and cultural heritage.

3.1. Radiation aging

Estimating the lifetime of devices in radiation harsh environment like accelerator facilities, nuclear power plants or space can be performed by radiation hardness tests at accelerators. A long term study of semiconductor detectors of ionizing radiation based on GaAs (Fig. 7) was realized at the facility. For 5 years the detectors were irradiated by 5 MeV electrons systematically increasing the cumulative dose from 1 to 2000 kGy and testing their spectrometric properties [6]. Another example of radiation hardness tests conducted at the facility was irradiation of semiconductor devices (Fig. 8) for the power supply source for the first Slovak satellite, the skCUBE [7], which launched in June 2017. The devices were tested by doses of X-rays up to 1.3 kGy representing the dose accumulated in devices during approximately 3 years at planned orbit of the satellite in 400 km distance from the Earth surface.

FIG. 7. Photograph of GaAs detectors of ionizing radiation prepared for irradiation.

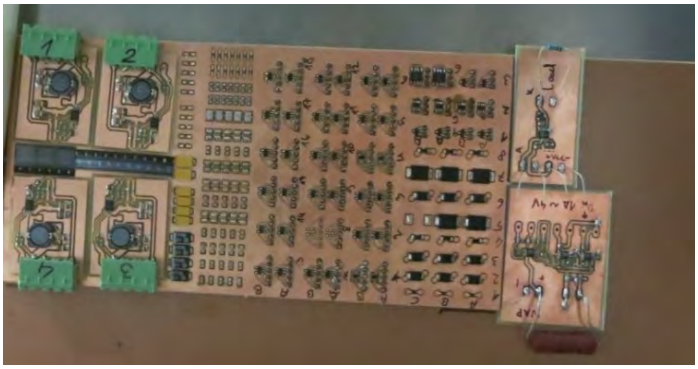

FIG. 8. Photograph of semiconductor devices prepared for irradiation.

3.2. Human health

The facility utilized the high dose rate during irradiation to decontaminate the transplants placed on dry ice like corneas (Fig. 9) dedicated for transplantation or animal skin (Fig. 10) utilized for protection of burned tissue until the new skin is grown. Interesting results were achieved during research, where the facility simulated radiotherapy for molecular hydrogen research in biomedicine [8]. Here the doses of X-rays in the range from 10 to 20 Gy were delivered.

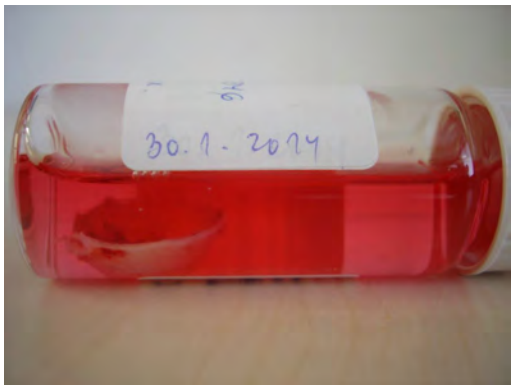

FIG. 9. Photograph of cornea in ethylene-oxide solution prepared for irradiation.

FIG. 10. Photograph of animal skin on dry ice prepared for irradiation.

3.3. Environment

Polychlorinated biphenyls (PCBs) are chemically and thermally stable hydrophobic compounds which were widely used in industry until their toxicity was revealed. Unfortunately they were released also into the environment, like in Eastern Slovakia. Their concentration in the sediments of the canal Strážsky kanál exceeds allowed limits more than ten times for years. The facility has studied the possibility of their radiation degradation. Various co-solvents and doses were combined to achieve the most effective radiolythic dechlorination of PCBs in canal sediments [9, 10]. The facility participated also at comparison of electron beam vs. gamma ray irradiation of sludge from drinking-water-treatment plant with the aim to decontaminate the sludge from microorganisms. The doses of 5 MeV electrons used were in the range from 1 to 25 kGy [11].

3.4. Cultural heritage

The facility participated at the preservation of late gothic wooden altar (1516) from St. George Church in Spišská Sobota in Poprad, Slovakia. Altar parts were heavily attacted by woodworms. Radiation treatment of altar wings (Fig. 11) (4.5 cm thick) by electron dose 1.8-1.4 kGy, wooden sculptures by X-ray dose 3-0.4 kGy was realized in September 2018 [12]. The altar was then restorated at the Monuments Board of the SR at Levoča ateliers. Successful installation of renovated altar followed in August 2019.

FIG. 11. Photograph of altar wing prepared for irradiation.

4. CONCLUSIONS

The operational experience and wide application potential of the electron-beam irradiation facility at the University Centre of Electron Accelerators of the Slovak Medical University is reviewed. This facility is used for scientific research and the knowledge gained from this research is used in the field of applied science, e.g. radiation hardness of detectors of ionizing radiation, electronics for space applications and accelerator and nuclear power plant components. The research is also focused on the use of electron beam irradiation equipment in medicine, environment, cultural heritage and education. In medicine we collaborated on research of radiation treatment of skin, corneas and in the research aimed on radiotherapy. Our research is aimed also to the serious environmental problematics in Slovakia, the contamination of soil and ground water by PCB (PolyChlorinated Biphenyls), were we use the accelerator to decontaminate environment. We collaborated with Serbian colleagues in research on radiation treatment of waste sludge from drinking-water-treatment plant. Big impact might also have our successful story of preservation of a late-gothic wooden altar with help of radiation, which will open the gates for utilization the radiation technologies in the field of cultural heritage in Slovakia. On the theoretical side, the simulations of dose depth profiles calculated using ModeRTL can be used to select the appropriate sample thickness for efficient treatment.

ACKNOWLEDGEMENTS

This work was supported by the International Atomic Energy Agency TC project RER1021 “Enhancing the Use of Radiation Technologies in Industry and Environment” and CRP F23034 under Research Contract No. 24270 as well as by the European Union’s Horizon 2020 Research and Innovation programme under GA No 101004730.

REFERENCES

[1] M. Ueno et al., *Journal of power sources,* **196**, Issue 10 (2011) 4756.
[2] R.L. Clough, *Nucl. Instr. Meth. in Phys. Res. B,* **185**, Issues 1-4 (2001) 8.
[3] EXECUTIVE SUMMARY, IAEA Technical Meeting on Deployment of Clean (Green) Radiation Technology for Environmental Remediation, IAEA Headquarters, Vienna, Austria, June 16-20, 2014
[4] https://www.biont.sk/
[5] https://fmph.uniba.sk/en/microsites/kjfb/department-of-nuclear-physics-and-biophysics/veda-a-vyskum/vedecke-skupiny/centa/tandem-accelerator-of-ions/
[6] SAGATOVA, A., ZATKO, B., NECAS, V., FULOP, M. Radiation hardness limits in gamma spectrometry of semi-insulating GaAs detectors irradiated by 5 MeV electrons, JINST **15** (2020) C01024.
[7] SAGATOVA, A., MAGYAR, M., FULOP, M., NECAS, V., RAFAJ, M. Radiation hardness of commercial semiconductor devices for first Slovak CUBESAT, *Proceedings of the 21th International Workshop on Applied Physics of Condensed Matter (APCOM, 2015),* FEI STU, Bratislava (2015), 380-383. ISBN 978-80-227-4373-0
[8] KURA, B., KALOCAYOVA, B., SZEIFFOVA BACOVA, B., FULOP, M., SAGATOVA, A., SYKORA, M., ANDELOVA, K., ABUAWAD, Z., SLEZAK, J. The effect of selected drugs on the mitigation of myocardial injury caused by gamma radiation. *Canadian Journal of Physiology and Pharmacology* ***99*** *1* (2021) 80-88. doi: 10.1139/cjpp-2020-0323.
[9] DARÁŽOVÁ, Ľ., ŠAGÁTOVÁ, A., NEČAS, V., FÜLÖP, M., HAN, B. Radiation degradation of PCBs in sediments: comparison between two methods, Acta Polytechnica CTU Proceedings 4: 19-21, (2016) DOI: 10.14311/AP.2016.4.0019
[10] FÜLÖP, M., PAJDLHAUSER, D., ŠIPLÁK, D., ŠAGÁTOVÁ, A., HYBLER, P. Accelerator technology for environmentally friendly PCB degradation, *The industrial and environmental applications of electron beams*, Institute of Nuclear Chemistry and technology, Warszawa, (2015) 103-108. ISBN 978-83933935-7-2
[11] RANKOVIC, B., ŠAGÁTOVÁ, A., VUJCIC, I., MASIC, S., VELJOVIC, D., PAVICEVIC, V., KAMBEROVIC, Z. Utilization of gamma and e-beam irradiation in the treatment of waste sludge from a drinking water treatment plant, Radiation Physics and Chemistry **177** (2020) 109174
[12] ŠAGÁTOVÁ, A., FULOP, M., PAVLOVIČ, M., SEDLAČKOVÁ, K., NEČAS, V.: Electron Beam Accelerator with Conversion to X-rays: Optimal Radiation Type According to Application, Radiation Physics and Chemistry **172** (2020) 108789, DOI https://doi.org/10.1016/j.radphyschem.2020.108789

RADIATION ISODOSE MEASUREMENTS INSIDE INTERACTION CHAMBER DURING THE COMMISSIONING EXPERIMENTS OF THE CETAL FACILITY- GAS TARGET CASE.

E. STANCU,
National Institute for Laser, Plasma and Radiation Physics (INFLPR)
Magurele, Romania
Email: elena.stancu@inflpr.ro

C. DIPLASU, G. GIUBEGA, M. SERBANESCU, A. MARCU, R. UNGUREANU, G. COJOCARU, M. ZAMFIRESCU
National Institute for Laser, Plasma and Radiation Physics (INFLPR)
Magurele, Romania

Abstract

The high-power laser facilities has demonstrated their ability to accelerate ion beams to considerable energies. The CETAL facility owns a 1 PW laser. High power laser beam interaction with a gas target under Laser Wakefield Acceleration results in a high energy electron beam. Due to exceeding norms limits, the CETAL facility proceeded the full commissioning phase considering radiation protection requirements. In the paper we present the measured values of isodose inside the interaction chamber for different experimental periods. The measurements were performed using gafchromic EBT3 films. The films were positioned around the interaction point. All measured values were normalized for 30 cm distance. The measured values show that the measured values are high enough and have to be considered for radiation protection purposes.

1. INTRODUCTION

PW class laser installations are able to generate ionising radiation upon interaction with the target. Nowadays there are more than 50 high power laser systems in use or in development throughout the world [1]. The laser wake field acceleration by the interaction of the high-power laser beam and gas target trap and accelerate high energy electrons towards relativistic velocities. A part of them is able to accelerate particle beams in relativistic regime and generate high energy electron, proton or ion beams by specific mechanisms. For example, electrons can be accelerated when the intensities of the laser pulses are higher than IL ~ 10^{18} W / cm^2, because the energy gain of an electron at a distance of the order of an atomic diameter exceeds the binding energy of the electrons in the outer energy shells of the atom, and therefore ionisation occurs, mainly by the field effect. Subsequently, longitudinal plasma waves develop in the wake of the laser pulse, which accelerates the electrons to high energies (hundreds of MeV) over short distances (less than 1 millimetre).

Two of these high-power lasers are developed in Romania: first developed is from INFLPR, CETAL, and second one ELI-NP [2]. CETAL-PW laboratory in INFLPR is hosting a Ti:Sa PW class laser system (800 nm, 25 fs, 25 J, 0.1Hz) with a pulse power of up to 1 PW.

INFLPR during the commission of the CETAL-PW laser demonstrated the ability to accelerate electron beams to considerable high energies.

2. HIGH POWER LASER BEAM – GAS TARGET INTERACTION AT CETAL FACILITY

One of the types of experiments performed during the commissioning activities was ultra-intense laser interaction with gas target aiming to accelerate high energy electrons. For these experiments the laser wake field acceleration (LWFA) mechanism was considered [3].

At CETAL-PW, accelerated electron beams with maximum energies up to ~500 MeV were obtained by laser wake field acceleration (LWFA) in supersonic gas jet targets using a classical experimental setup, as it is shown in Fig. 1. Ultra-short laser pulses of 35 fs with energies up to 5 J before compression were focused with an off-axis f/27 parabolic mirror in a focal spot of 35 μm in diameter so that the energy on the target level effectively used for the acceleration process was up to 1.2 J.

The gas target is a supersonic jet produced with a gas valve properly synchronised with the laser pulse. In order to enhance the LWFA process, instead of pure He, a mixture of He 99% with N_2 ~ 1% was used to produce a supersonic jet with a 3 mm diameter 10° Laval profile nozzle, with a density in the range 10^{18} - 10^{19} cm^{-3}.

The electron energy distribution was measured with a magnetic dipole electron spectrometer. The high-intensity magnetic field (0.86 T) inside the spectrometer, was created using permanent magnets with a length of 80 mm and a gap of 10 mm. In order to precisely define the electron entrance point in the magnetic field, a lead brick with 2 mm central pierce was used as a collimator.

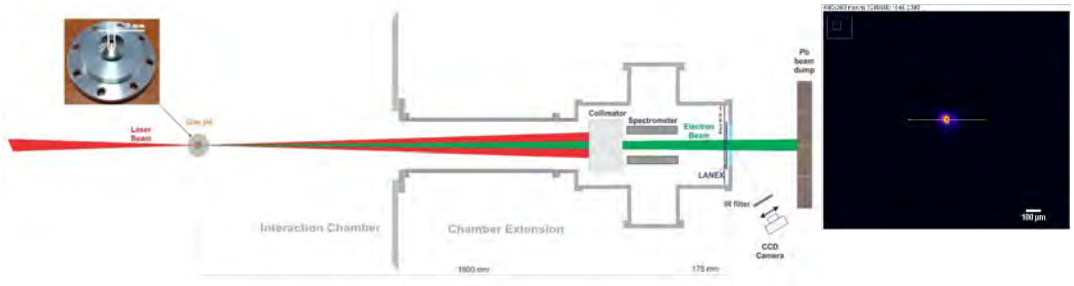

(a) (b)

FIG. 1. Sketch of the experimental set-up for laser-plasma electron acceleration (a) and the focus image (b).

Depending on the laser-plasma conditions (parameters), electron beams with different types of spectral characteristics were obtained. Examples of electron spectra, measured with the high-resolution magnetic spectrometer are presented in Fig. 2.

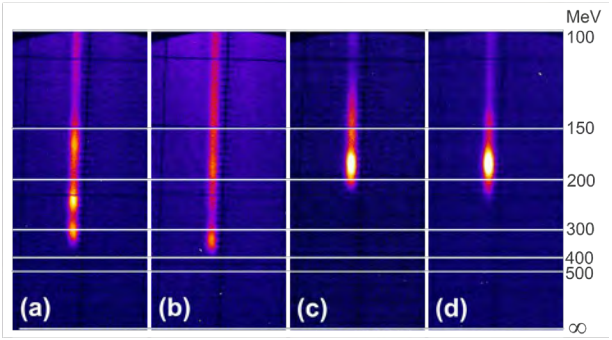

FIG. 2 Electron spectra as raw data from the LANEX screen;
τ_L=35 fs, w_0=17 µm
a) E_{LonF}=1.26 J, ne = 3.2 x 10^{18} cm^{-3} ;
b) E_{LonF}=1.16 J, ne = 3.2 x 10^{18} cm^{-3}

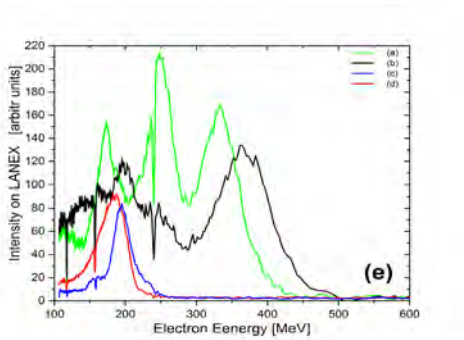

Electron relative spectra, as profile curves

c) E_{LonF}=1.06 J, ne = 4.4 x 10^{18} cm^{-3} ;
d) E_{LonF}=1.06 J, ne= 5.2 x 10^{18} cm^{-3}

3. ISODOSE MEASUREMENTS INSIDE INTERACTION CHAMBER

INFLPR demonstrated the ability to accelerate electron beams to considerable high energies in interaction of the ultra-intense laser pulses with gas targets, during the commission of the CETAL-PW laser system. For these experiments the laser wake field acceleration (LWFA) mechanism was considered [3].

Isodose measurements inside the interaction chamber represent the dose measurements around the focus. During the interaction of the laser beam and target the high electromagnetic field is presented. The interaction takes place in an interaction chamber in vacuum. During the experiments the exposure doses have been measured around the interaction point. The experimental isodose measured inside the interaction chamber are performed in the presence of a high electromagnetic field in vacuum. Due to these experimental characteristics of the experimental set-up, the dosimetry systems which can be used are limited. For this reason, passive dosimeters, like gafchromic films, were chosen.

For each experiment inside the interaction chamber, the radiation isodose measurements were performed using EBT3 gafchromic films. It is used to protect the sensitive layer of the EBT3 gafchromic film from exposure to ultraviolet radiation. The EBT3 films respond in a wide dose range: 0.01 – 40 Gy. The response of the EBT3 film is independent of the radiation incident angle and has energy independent dose response. The EBT3 films are used in dosimetry measurements of the photon, electron and proton beams. EBT3 films turn black by themselves.

Optical density of the exposed films is measured using a special dedicated transmission scanner type EPSON Expression 11000XL scanner. Gafchromic films are scanned using a high resolution of 4800 dpi in transmission mode. Calibration curve of the response of the EBT3 gafchromic film was performed in an electron beam delivered by a medical linear accelerator [4].

The interaction takes place in an interaction chamber in vacuum. The laser pulses generated by the CETAL-PW laser system focused on a gaseous target can produce accelerated electron beams. To achieve this, a valve was used to properly synchronise the gas jet with the laser beam. He + N_2 gas targets were used in these experiments. For each experiment inside the interaction chamber the radiation isodose measurements were performed using EBT3 gafchromic films. The distribution of the detectors used for isodose measurements inside the interaction chamber is presented in Fig. 3.

(a) (b)

FIG. 3. Position of EBT3 detectors (a) inside the interaction chamber (b) for radiation isodose measurements.

During the experiments, the gafchromic films were screened at optical radiation with Al foil. Due to the experimental conditions, which involve vacuuming and unwinding the interaction chamber, it is not possible to perform isodose measurements for each laser pulse. The detectors were read after the accumulation of a noticeable degree of blackening due to exposure to ionising radiation following the laser-target interaction.

The radiation isodose measurements were normalised at a distance of 30 cm from the target. Table 1 shows the measured values of radiation dose for specific measurement period. The results are normed at a distance of 30cm from the target. The high energy accelerated electrons on forward the laser beam were measured outside the interaction chamber. Radiation doses measured in high energy electron beam axes are not presented in this paper.

TABLE 1. MEASURED VALUES FOR RADIATION ISODOSE MEASUREMENTS, Gy, INSIDE THE INTERACTION CHAMBER FOR DIFFERENT EXPERIMENT PERIOD

Measurement point	27.08-17.10.2019	28.10.2019	29.10-10.12.2019	11.02-19.04.2021	19.04-03.06.2021	03.06-02.09.2021
1 (340°)	12	13,4	5,1	0,18	0,20	0,07
2 (51°)	5,7	4,5	8,9	1,30	3,66	0,13
3 (78°)	2,4	1,7	2,5	0,75	14,52	0,38
4 (102°)	1,3	1,3	2,3	0,89	1,20	0,42
5 (135°)	7,2	4,4	1,5	0,78	5,79	0,16
6 (226°)	13,8	13,9	3,1	0,31	0,29	0,10

The isodose measurements diagrams according to the Table 1 data are presented in Fig 4. Due to the experimental conditions, which involve vacuuming and unwinding the interaction chamber, the isodose measurements cannot be made in real time (for each laser shot).

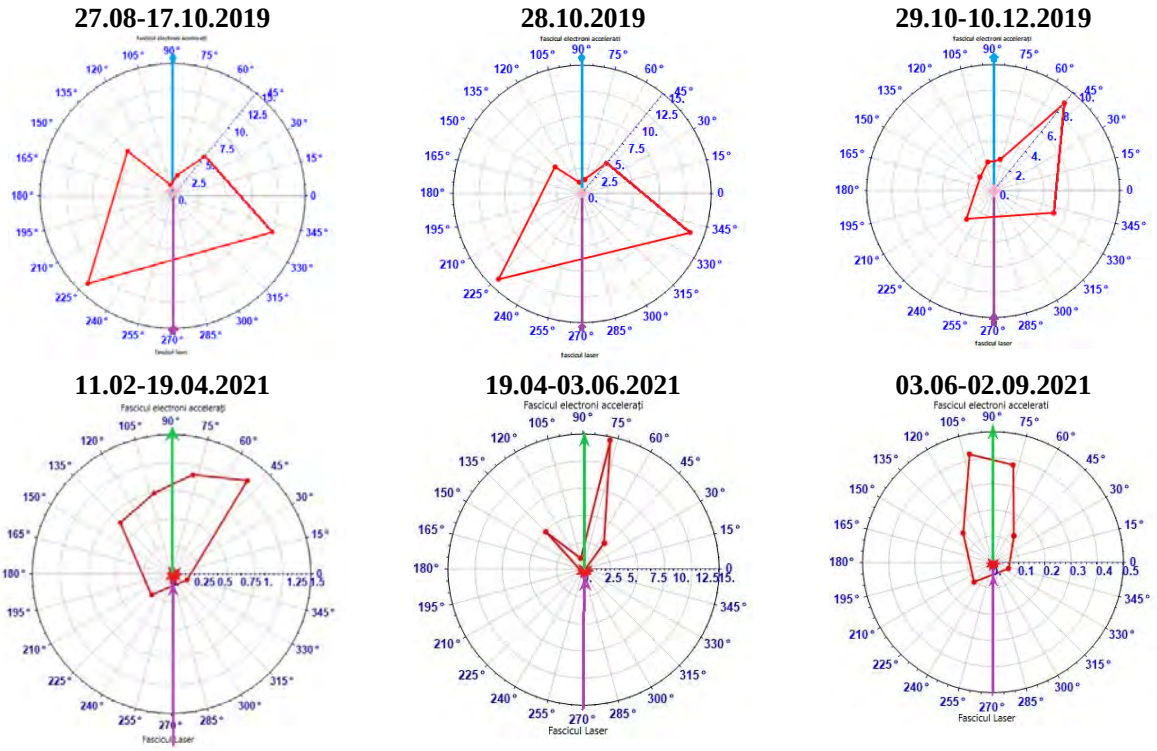

FIG. 4. Radiation isodose measurements during high power laser target interaction.

Isodose distribution of the radiation dose measurements inside interaction chambers shows the dose level exceeds the exemption levels for radiation protection purposes. The isodose distribution depends on the high-power laser target interaction parameters. Isodose distribution also shows that a part of the dose is backward. This suggests the necessity of the experimental geometry consideration for all parts inside the interaction chamber.

4. CONCLUSIONS

In this paper there are presented measured values for radiation isodoses obtained during the high-power laser gas target interaction.

Experimental data of radiation isodoses, obtained at CETAL-PW during high-power laser-gas target interaction, are presented. Isodose measurements shows a high level of exposure inside interaction chamber. The Gy level was achieved. Also, the isodose shows a backward exposure due to laser-target interaction. The isodose shapes suggests the necessity to consider full geometry setup inside interaction chamber to avoid scattering radiation.

The measured values suggest that they need to be considered for the evaluation of experimental data and for radiation protection purposes.

ACKNOWLEDGEMENTS

This work was supported by the Romanian Ministry of Education and Research, under Romanian National Nucleu Program LAPLAS VI - contract no. 16N/2019.

We thank the IAEA for supporting us to participate at the International Conference on Accelerators for Research and Sustainable Development: from good practices towards socio-economic impact (CN-301), Vienna, Austria; 23-27 May 2022.

REFERENCES

[1] ICUIL website: https://www.icuil.org/pdf/icuil-world-map-2020.pdf, Accessed on 21.09.2021.

[2] http://cetal.inflpr.ro/newsite/pw_facility

[3] DIPLASU, C., GIUBEGA, G., UNGUREANU, R., COJOCARU, G., SERBANESCU, M., MARCU, A., STANCU, E., ACHIM, A., ZAMFIRESCU, M., "Commissioning experiment on laser-plasma electron acceleration in supersonic gas jet at CETAL-PW laser facility", Rom. Rep. Phys. 73, 401 (2021).

[4] GROZA, A.; CHIROSCA, A.; STANCU, E.; BUTOI, B.; SERBANESCU, M.; DREGHICI, D.B.; GANCIU, M. Assessment of Angular Spectral Distributions of Laser Accelerated Particles for Simulation of Radiation Dose Map in Target Normal Sheath Acceleration Regime of High Power Laser-Thin Solid Target Interaction—Comparison with Experiments. Appl. Sci. 2020, 10, 4390.

DEGRADATION OF AMINO ACIDS BY MeV NITROGEN IONS

C.A.P. DA COSTA†[1]
Physics Departament, Pontifical Catholic University of Rio de Janeiro (PUC-Rio)
Rio de Janeiro, Brazil
Email: cintia-apc@hotmail.com

E. F. DA SILVEIRA
Physics Departament, Pontifical Catholic University of Rio de Janeiro (PUC-Rio)
Rio de Janeiro, Brazil

Abstract

The occurrence of amino acids in meteorites and comets raises questions about how they have been formed in cosmic environments, as well as how long they can survive in outer space; radioresistance is essential information to predict half-lives and make advances on the origins of life studies. Furthermore, amino acid radiolysis is of Medical Physics interest. The main objective of the current work is to analyze, via infrared spectrometry, how destruction cross section of pure valine exposed to energetic ion radiation depends on projectile's energy and charge. Apparent destruction cross sections (σ_d^{ap}) and sputtering yields (Y_0) for this amino acid irradiated by MeV N^{q+} ions were measured. Degradation of the amino acid valine by nitrogen beams under different conditions such as several charge states (N^{q+}, q = 1, 2 and 3) and energies (1.5 and 6.0 MeV) is analyzed. From experimental data of this and previous measurements it is concluded that: i) an approximately linear dependence between the apparent destruction cross section and the electronic stopping power (S_e) is proposed for MeV projectiles, and for samples at room temperature; and ii) σ_d^{ap} results concerning multi-charged nitrogen ion beams are discussed. As astrophysical application, cosmic ray half-lives for valine are estimated to be about 10 million years in the interstellar medium; concerning hadronterapy, the question is whether to decrease the initial projectile charge state may be useful.

1. INTRODUCTION

Degradation of organic materials exposed to ionizing radiation has an enormous relevance in areas such as Medical Physics (Radiotherapy, production and application of radioisotopes), Radiological Security of nuclear plants and large accelerator laboratories, manned missions in the Solar System, and Astrochemistry (evolution of molecular species in the Universe). Although main lines concerning the interaction of energetic electrons, ions and photons with organic matter are under research since long time, specific information is still necessary.

The focus of this work is in one of these specific systems: MeV ion beams impinging on prebiotic molecules. The scenario can be constrained as well, represented by the following question: what is the degradation rate of some common amino acids exposed to Solar Wind or to Galactic Cosmic Rays?

Indeed, the main amino acids (vital for living beings) and some other complex organic molecules (COMs) have been found in meteorites such as Murray, Murchison, Nogoya and Mokoia [1–3]. In particular, glycine (Gly) has been detected indirectly by the Stardust probe in dust traces of the comet 81P/Wild 2 [4], and directly, in considerable large quantities, in jets of the comet 67P/Churyumov-Gerasimenko by the Rosetta mission [5]. The detection of valine (Val) molecules has not been confirmed yet, but since these materials are present in meteorites, they might exist elsewhere in the outer space too. Moreover, if larger molecules such as PAHs (Polycyclic Aromatic Hydrocarbons) exist throughout diverse astronomical environments [6], the detection of amino acids in the interstellar medium is expected.

In space, those materials are exposed to several kinds of radiation. From an abiotic origin of life point of view, relevant questions appear, such as: does space radiation have a role in the synthesis of COMs? Is cosmic organic matter responsible for the existence of life as we know? Considering astronomical low temperature and pressure conditions, the "Chemistry of life" would not be able to occur spontaneously in these environments: some kind of catalyzer should be necessary. The specific places where those materials occur are also very important. For instance, molecules within asteroids or comets are shielded from short-range radiation, being available then to be delivered in hospitable zones where more complex organic chemistry may happen until the

---

†*Present Address: Research Center for Ions, Materials And Photonic (CIMAP - GANIL), CAEN – FRANCE*

development of life. Nevertheless, for this same example, such molecules could be exposed to radionuclide decay inside the considered celestial bodies [7–9]. Furthermore, the low albedo (dark gray) of these astrophysical specimens is probably related to the graphitization / carbonization of carbon-content material existing on their surfaces: ionizing radiation turns the condensed original material (e.g., CH_4, $HCONH_2$, CO_2) into carbon enriched compounds as polymeric C_nH_2 chains or tholins [10, 11]. It is significant, then, to explore how amino acids are affected by energetic ions, similar to those constituents of cosmic radiation, in order to estimate their radioresistance, and respective half-lives in astronomical environments.

In hadrontherapy, it is well known that the beam energy is crucial for irradiations: the highest stopping power must occur in the tumor region [12]. Because this region is generally deep, the ion beam is in the so called equilibrium charge state and does not depend on the external beam charge state. However, the point here is that molecular destruction rate of the patient's skin is significantly reduced if the initial charge state of the ion beam is decreased. The relevant question becomes how deep MeV heavy ion beams take to reach their equilibrium charge. The measurement of valine (as a typical biological material) destruction cross section as a function of the nitrogen beam charge state is a contribution in this direction. The employed nitrogen beam energy were about 1 MeV (two orders of magnitude lower than beams used in hadronterapy), and the valine samples thickness were around 40 nm.

The goals of the present work are:

— Determine cross sections of valine irradiated by nitrogen MeV ions;
— Confirm whether valine cross section depends linearly on the beam stopping power, and discuss the projectile charge effects on degradation;
— Study the projectile-material interaction, and the physical processes behind experimental results;
— Estimate relevant parameters, such as degradation rates, that might be useful for other research areas.

Sections 2 and 3 describe the experimental techniques and results of the current research, respectively. In Section 4 results are discussed, as well as possible applications. The main conclusions are presented in Section 5.

2. EXPERIMENTAL SETUP

Valine dissociation by nitrogen MeV ions was monitored at the PUC-Rio Van de Graaff Laboratory. Ion beams of 1.5 MeV N^+, N^{2+}, N^{3+} and 6.0 MeV N^{2+} were produced by a Van de Graaff accelerator and bombarded, perpendicularly, the targets at room temperature. Distinct charged projectiles were obtained by accelerating N^+ projectiles, selecting the desired kinetic energy by a 90º analysing magnet, introducing the beam in a gas stripper to create N^{q+} ions and filtering a given projectile charge state by 15º magnet. The pressure in the stripper was varied in order to maximize the beam intensity for that charge state.

The residual gas pressure in the vacuum chamber was around 10^{-7} mbar; for a detailed description, see Pilling et al. (2013) [13] and da Costa et al. (2021) [14]. Evolution of sample destruction was monitored by a JASCO FTIR-4100 infrared spectrometer. The Fourier Transform Infrared spectroscopy (FTIR) spectra were acquired over the 3500–700 cm^{-1} range, in transmission mode; spectral resolution of 2.0 cm^{-1} and averaging 70 scans.

Thin films, ~ 25 – 65 nm, of valine (Sigma Aldrich, 99% purity) were deposited in vacuum onto ZnSe substrates. Valine density was taken as 1.32 g cm^{-3} [15].

3. RESULTS

3.1. Beam charge state (N^{q+})

Five L-valine samples, ~ 25 nm thick, were bombarded by 1.5 MeV N^+, N^+, N^{2+}, N^{3+} and 6.0 MeV N^{2+}. Different charge states were obtained by a selector magnet, as described in section 2. For each beam the evolutions of the IR bands 3190-2430, 1602-1579 (1507), and 1337-1320 (1330) cm^{-1} were followed and their respective normalized integrated absorbance is displayed on Figures 1 (a) – (c) and 2; lines are fittings and the obtained destruction cross sections are presented in the same color code.

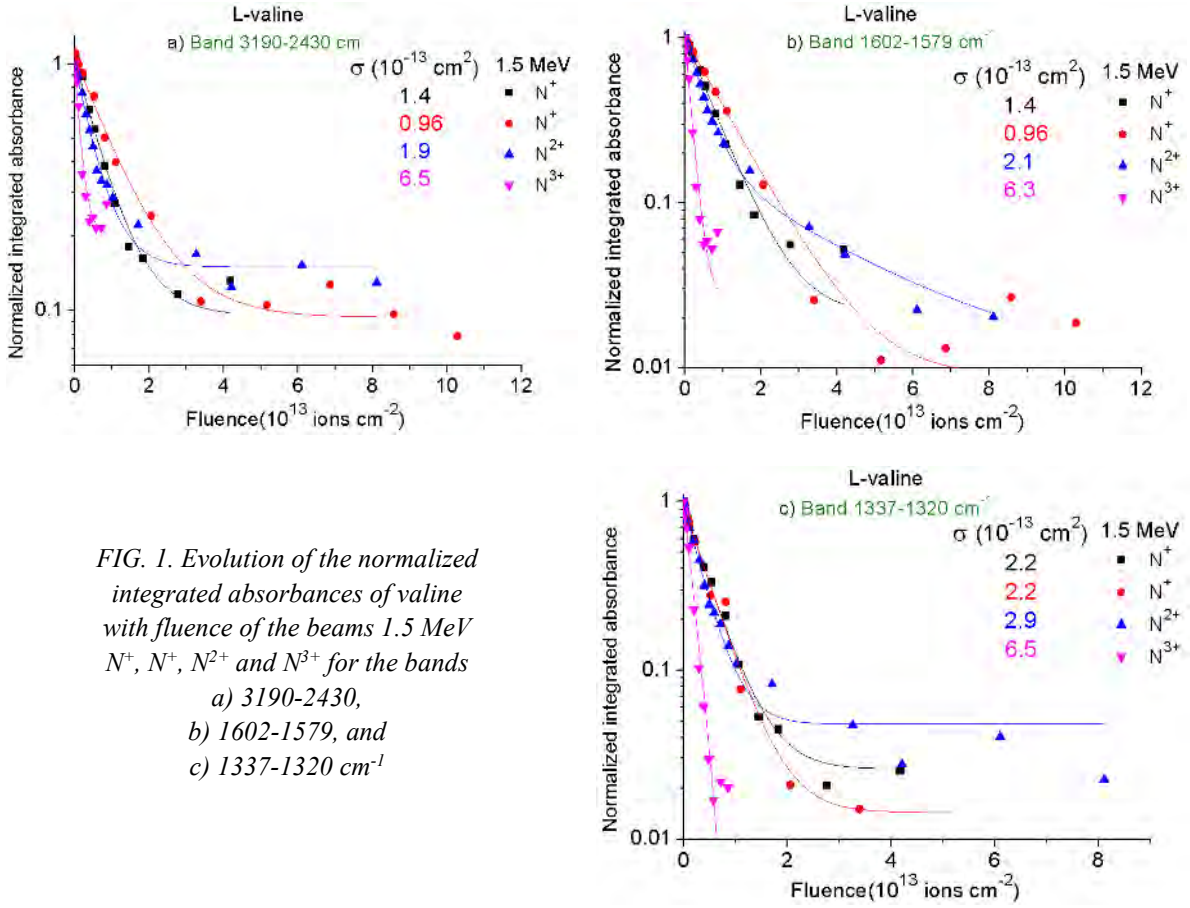

FIG. 1. Evolution of the normalized integrated absorbances of valine with fluence of the beams 1.5 MeV N^+, N^+, N^{2+} and N^{3+} for the bands a) 3190-2430, b) 1602-1579, and c) 1337-1320 cm^{-1}

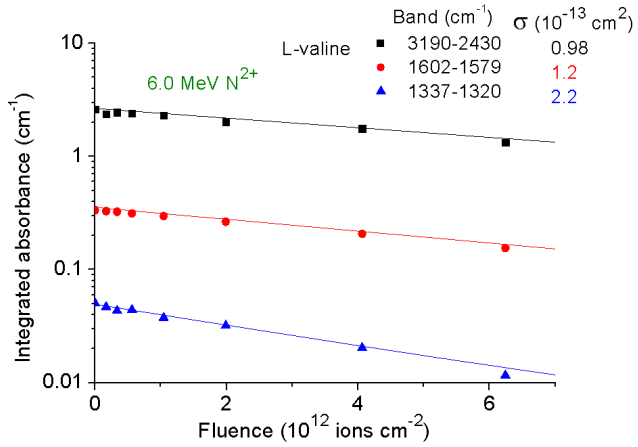

FIG. 2. Evolution of the normalized integrated absorbances of valine with fluence of the beam 6.0 MeV N^{2+} for the bands 3190-2430, 1602-1579, and 1337-1320 cm^{-1}.

Table 1 summarizes the fitting parameters. The strong decrease of the integrated absorbance of the 1337-1320 band may be attributed to sputtering.

3.2. Dependence on Sample thickness

Three L-valine samples with thicknesses 27.5, 44.2 and 64.9 nm were irradiated by ions of 1.5 MeV N^+. In figures 3 (a) – (c), the evolutions of these three samples in function of beam fluence is presented for the 3190-2430, 1602-1579 and 1337-1320 cm^{-1} bands. Table 2 summarizes the fitting parameters.

TABLE 1. Parameters obtained from the fitting of the integrated absorbances decay with the function $S(F) = S_0 \exp(-\sigma F) + S_\infty$. Data from valine irradiated by 1.5 and 6.0 MeV multi-charged nitrogen beams.

Sample	Beam	Band (cm^{-1})	S_0 (cm^{-1})	σ (10^{-16} cm^2)	S_∞ (cm^{-1})
L-Val	1.5 MeV N^+	3190-2430	0.95	1400	0.096
		1602-1579	0.99	1400	0.01
		1337-1320	0.91	2200	0.026
	1.5 MeV N^+	3190-2430	0.97	960	0.094
		1602-1579	0.99	960	0.01
		1337-1320	0.94	2200	0.014
	1.5 MeV N^{2+}	3190-2430	0.85	1900	0.15
		1602-1579	0.83	2100	0.17
		1337-1320	0.92	2900	0.048
	1.5 MeV N^{3+}	3190-2430	0.82	6500	0.20
		1602-1579	0.96	6300	0.03
		1337-1320	0.99	6500	-
	6.0 MeV N^{2+}	3190-2430	2.65	980	-
		1602-1579	0.35	1200	-
		1337-1320	0.048	2200	-

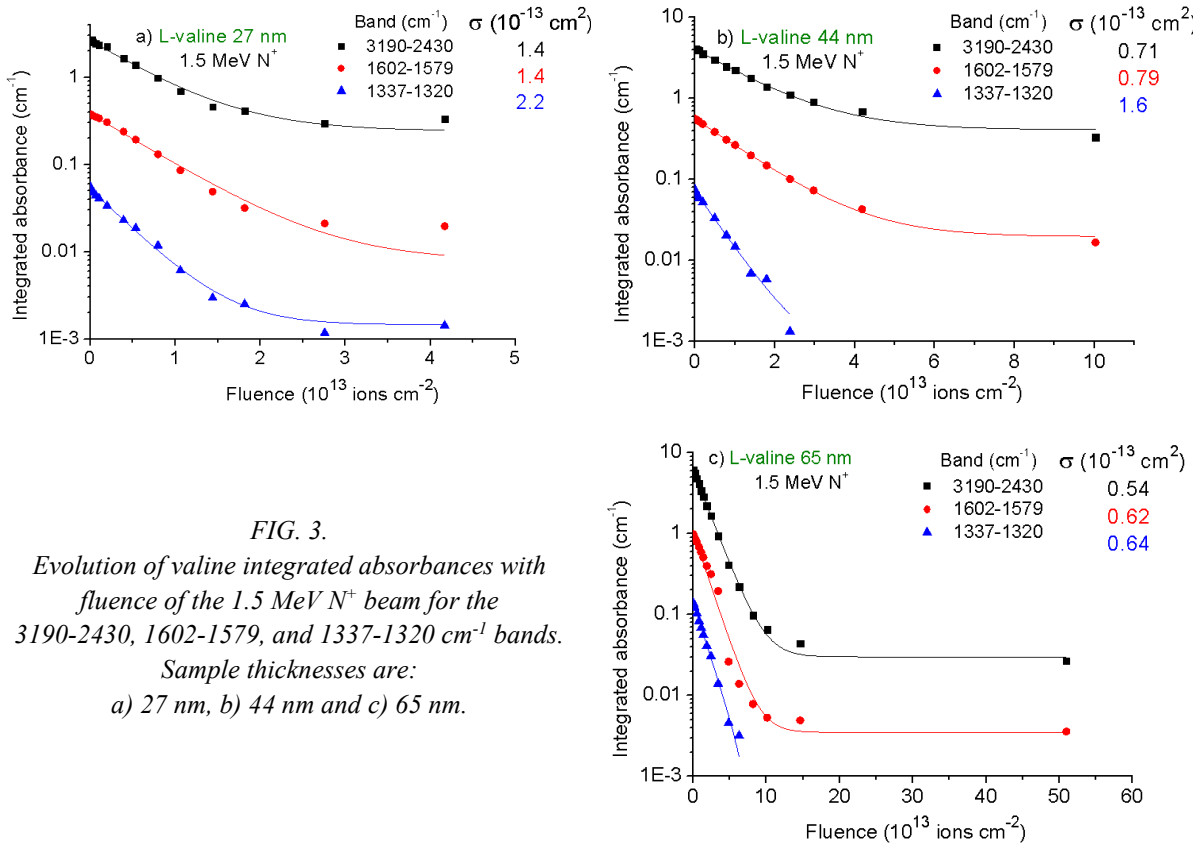

FIG. 3.
Evolution of valine integrated absorbances with fluence of the 1.5 MeV N^+ beam for the 3190-2430, 1602-1579, and 1337-1320 cm^{-1} bands. Sample thicknesses are: a) 27 nm, b) 44 nm and c) 65 nm.

4. DISCUSSION

4.1. Multi-charged beams

Sputtering and radiolysis are sensitive to projectile charge; yields of both processes are expected to be proportional to $S_e^n \sim (q^2)^n$. For icy samples, n = 2 have been reported for sputtering (e.g. Seperuelo-Duarte et al.

(2010) [16]) and n = 1 to 1.5 for radiolysis. Experiments with multi-charged beams were carried out to verify the sensitivity of amino acid's damage to the projectile charge. The measurements involved experimental challenges such as production, selection, transport and monitoring of multi-charged beams. The high sensitivity of stopping powers on projectile charge state indicates that further experiments are necessary to be compared with the current results.

1.5 MeV N^+ ions were produced by the Van de Graaff accelerator and selected by the 90º analyzing magnet. The residual gas inside the 4.9 m long canalization between this magnet and the switching one was raised to around 10^{-4} mbar for enhancing ion beam charge exchange. At 1.5 MeV energy, projectiles have v = 4.5 x 10^3 km/s, and the equilibrium charge state distribution is N^{3+} (48%), N^{2+} (27%), N^{4+} (19%), N^{1+} (4%) and N^{5+} (2%) [17]. The average equilibrium charge state is, therefore, q_{eq} = 2.9; CasP (Convolution approximation for swift Particles) prediction is 2.1 [18].

After, crossing a 10^{-6} mbar residual gas, the N^+, N^{2+} and N^{3+} charge state beams were selected by an adequate magnetic field at the switching magnet and transported via a ~5 m canalization up to the UHV section (at <10^{-7} mbar), see Pilling et al. (2013) [13]. Fluence was calculated assuming that no charge exchange has occurred between the switching magnet and the Faraday cup inside the FTIR chamber.

Valine samples, ~ 25 nm thick, were irradiated by 1.5 MeV N^{q+} with charge states q = 1, 2 and 3. Samples must be thin enough, not only to be traversed by the beam, but also for allowing it (ideally) to exit without reaching the equilibrium charge. On the other hand, 15-20 nm is typically the thinnest initial thickness range compatible to the infrared spectrometer sensibility, considering that the decrease of absorbances with beam fluence should be strong enough for permitting the σ_d^{ap} measurement.

For each experiment, the average σ_d^{ap} was calculated from three bands analyzed in Fig. 1 – see Table 3. Clearly, the higher the projectile charge, the greater the apparent destruction cross section measured.

TABLE 2. Parameters obtained from the fitting of the integrated absorbances decay with the function $S(F) = S_0 \exp(-\sigma F) + S_\infty$. Data from valine with distinct thicknesses irradiated by 1.5 MeV N^+.

Thickness (nm)	Band (cm^{-1})	S_0 (cm^{-1})	σ (10^{-16} cm^2)	S_∞ (cm^{-1})
27	3190-2430	2.40	1400	0.24
	1602-1579	0.37	1400	0.008
	1337-1320	0.051	2200	0.0014
44	3190-2430	3.66	710	0.41
	1602-1579	0.54	790	0.020
	1337-1320	0.071	1600	0.001
65	3190-2430	6.07	540	0.03
	1602-1579	1.02	620	0.0035
	1337-1320	0.14	640	-

TABLE 3. Apparent destruction cross sections of 1.5 MeV N^{q+} on valine samples.

Charge state	σ_d^{ap} (10^{-13} cm^2)			
	Analyzed band (cm^{-1})			Average
	3190-2430	1602-1579	1337-1320	
1+	1.4	1.4	2.2	1.7 ± 0.5
1+	0.96	0.96	2.2	1.4 ± 0.8
2+	1.9	2.1	2.9	2.3 ± 0.6
3+	6.5	6.3	6.5	6.4 ± 0.1

Under the perspective of a radiolysis analysis, Figure 4 (a) shows the average σ_d^{ap} dependence on q^2. Then, as $\sigma^{3+}/\sigma^+ = 4.1$ and $\sigma^{2+} / \sigma^+ = 1.5$, the average beam charge state ratios inside the samples are ~ 2.0 and 1.2 (instead of 3 and 2) for N^{3+}/N^+ and N^{2+}/N^+, respectively. By combining Eq. (1) with Joy-Luo-Bethe-Bloch's formula [19, 20], the average cross section for a projectile with charge z and velocity v can be estimated as

$$\sigma_d^{ap}(q,v) = a\, S_e(q,v) = a\, S_e^{e^-}(v)\, q^2 = \sigma_d^{ap}(e^-,v)\, q^2, \qquad (1)$$

where $S_e^{e^-}(v)$ and σ_d^{ap} (e^-,v) are the stopping power and the destruction cross section for electron projectiles with the same velocity v, respectively. For a dominant radiolysis damage, a proportionality is expected in a graph σ_d^{ap} (q,v) versus q^2, in which σ_d^{ap} (e^-,v) is the angular coefficient, if no charge exchange occurs inside the sample. 1.5 MeV N ions and 59 eV electrons have the same velocity: v = 4.5 x 10^3 km/s. For valine, a = 1.0 x 10^{-20} cm^3 keV^{-1}; 59 eV electrons have $S_e^{e^-}$ ~ 8 eV Å $^{-1}$ = 8 x 10^5 keV cm^{-1}; the Joy-Luo formula with k = 0.6 provides σ_d^{ap} (e^-,v) = 0.8 x 10^{-14} cm^2. This result is to be compared with the angular coefficient of experimental data (dotted line in Fig. 4), which is roughly 6 x 10^{-14} cm^2 (per square charge state). CasP results, imposing no charge exchange inside the sample, agree with the cross section ~ 1 x 10^{-14} cm^2 for q = 1; on the other hand, it predicts an angular coefficient of 0.4 x10^{-14} cm^2, twice lower than Joy-Luo result, but much lower than the experimental value. A discussion on equilibrium charge state follows.

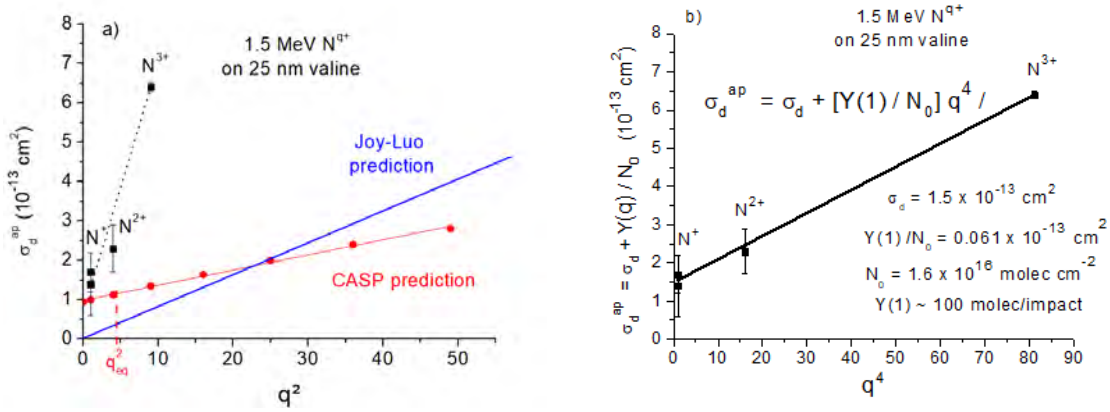

FIG. 4. σ_d^{ap} dependence on initial beam charge state; 1.5 MeV N^{q+} beam impinging on valine 25 nm thick: q = 1, 1, 2 and 3. a) Linear fitting of data (dotted line) has a slope = 6 x 10^{-14} cm^2 per square charge state. The Bethe-Bloch's function prediction is valid if no charge exchange occurs. When a neutral 1.5 MeV N projectile enters in a solid target, it looses one or more electrons; therefore, in average, collisions in the bulk occur with $q \neq 0$ and σ_d^{ap} cannot be zero. In contrast, CasP predicts this stopping power (and σ_d^{ap}) correctly [18]. b) Assuming only sputtering ($\sigma_d^{ap} \sim q^4$).

Inside a solid, a projectile with initial charge state q captures and loses electrons until its charge state reaches an average equilibrium value, q_{eq} [21-23]. Equation (2) is the expression for this equilibrium charge according to Bohr's adiabatic criterion, where the projectile electrons with orbital velocities smaller than the projectile translation velocity are removed during the collision cascade with target atoms [24]; Z_p being the projectile atomic number, v its velocity and v_B the Bohr's velocity.

$$q_{eq} = Z_p \left[1 - exp\left(\frac{-125\, v}{137\, v_B Z_p^{2/3}}\right)\right] \qquad (2)$$

Figure 5 presents the predicted equilibrium charge, acording to Eq. (2), in function of nitrogen projectile velocities. A nitrogen projectile with 1.5 MeV of kinetic energy has the velocity v = 0.45 cm ns^{-1} and a predicted equilibrium charge of q_{eq} ~ 2.8. Other q_{eq} expressions from more refined models, as those of Montenegro et al. (1982) [25], Heckman et al. (1963) [26] and Grande and Schiwietz (1998) [18] give similar results within 10% error [22]; for simplicity, Eq. (2) is the approach taken.

The projectile charge evolves asymptotically inside the material from q (the incident projectile charge) to reach q_{eq} (the final projectile mean charge). Between q and q_{eq} the charge has a transient or average value that is a function of the covered distance by the projectile, $q_{av}(s)$. Bohr has proposed that the projectile charge state inside a material should be written as Eq. (3) [27]:

$$q_{av}(s) = q_{eq} + (q - q_{eq}) exp\left(-\frac{s}{\lambda_q}\right) \qquad (3)$$

with s being the projectile's covered distance along the track, and λ_q the characteristic relaxation length of the solid. Based on Eq. (3), Fig. 6 presents $q_{av}(s)$ for 1.5 MeV N^{q+} ion beams with initial charge states q = 1 and q = 3 impinging on a solid of icy water. Both beams reach the equilibrium charge around s = 4 nm inside the sample. Although the λ_q value for valine is not known, the rougthly linear relationship between σ_d^{ap} and q^2 in Fig. 4 suggests that λ_q is is much higher than 4 nm and comparable to the sample thickness.

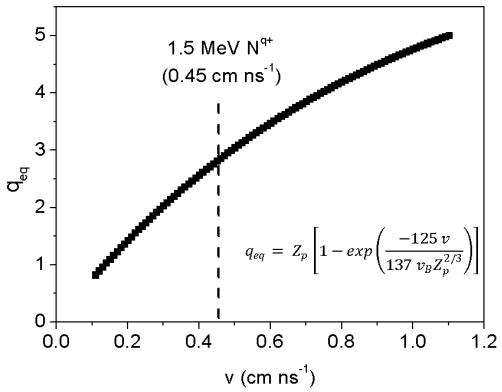

FIG. 5. Equilibrium charge state in function of nitrogen ions velocities. The vertical dash line indicates the velocity of the beam used in this data set.

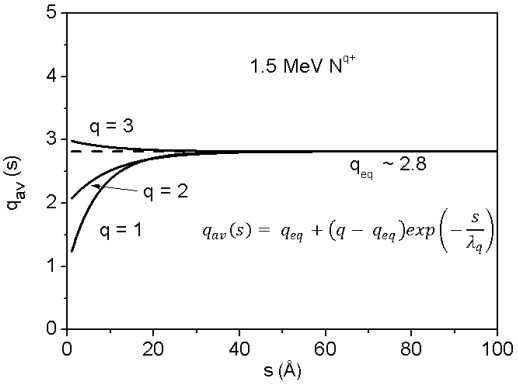

FIG. 6. Average charge state curves in function of the distances reached inside a solid of icy water (λ_q ~ 10 Å) by 1.5 MeV N^{q+} ion beams with initial charges 1 and 3 [22]. For valine, λ_q is not known, but the order of magnitude is expected to be the same.

The disagreement by one order of magnitude presented in Figure 4 (a) reflects that either an experimental difficulty occurs (e.g., the actual beam charge state impinging on the sample is not well known), or sputtering is relevant. In the latter direction, Figure 4 (b) shows the average σ_d^{ap} dependence on q^4. Considering $Y(q) = Y(1)\, q^4$, the surprisingly good linear fitting $\sigma_d^{ap}(q) = \sigma_d^{ap}(0) + (Y(1)/N_0)\, q^4$ provides $\sigma_d^{ap}(0) = 1.5 \times 10^{-13}$ cm^2 and $Y(1)/N_0 = 0.061 \times 10^{-13}$ cm^2. Since the sample thickness $z_{sp} = 25$ nm corresponds to $N_0 = 1.6 \times 10^{16}$ molec cm^{-2}, one gets $Y(1) \sim 100$ molec per impact.

4.2. Sputtering measurement from distinct thick targets

Fig. 3 displays data of valine samples with distinct thicknesses bombarded by 1.5 MeV N^+. Figures 7 (a) – (c) present the normalized column densities for three samples as a function of F/N_0. The green dashed curves are fittings of the average behavior of the considered bands.

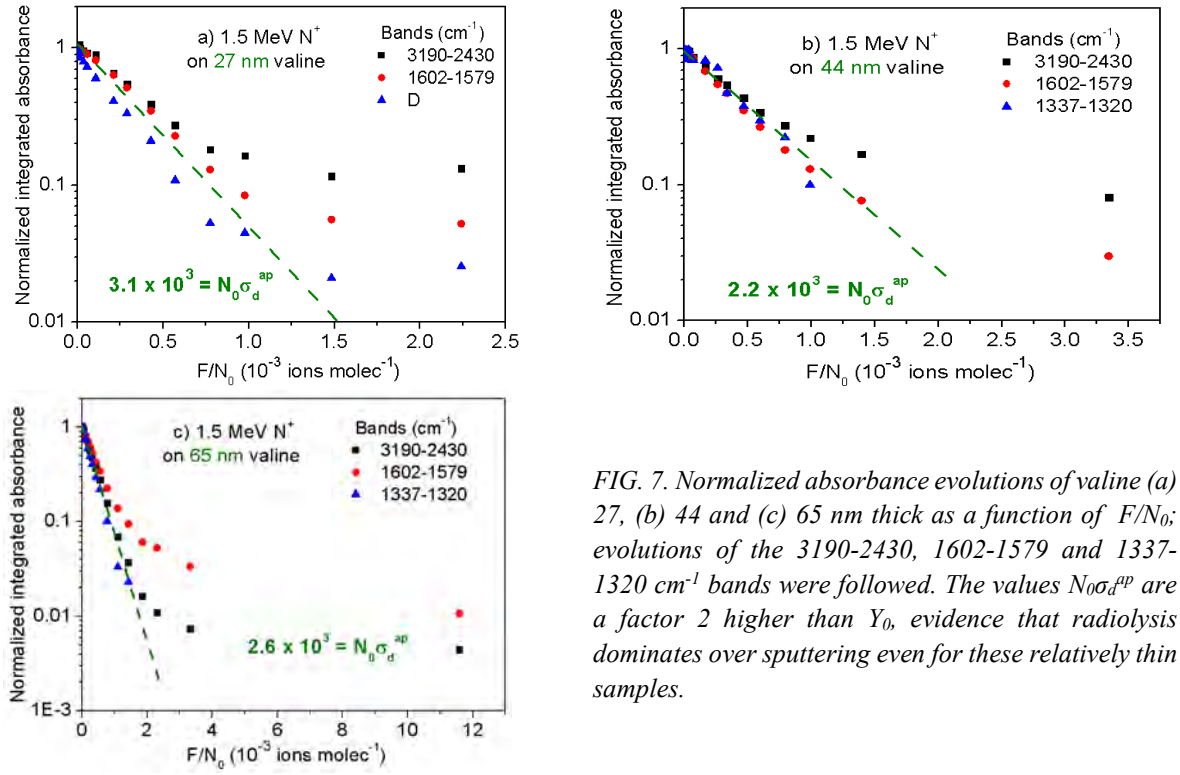

FIG. 7. Normalized absorbance evolutions of valine (a) 27, (b) 44 and (c) 65 nm thick as a function of F/N_0; evolutions of the 3190-2430, 1602-1579 and 1337-1320 cm^{-1} bands were followed. The values $N_0\sigma_d^{ap}$ are a factor 2 higher than Y_0, evidence that radiolysis dominates over sputtering even for these relatively thin samples.

Another analysis of the same fact is exhibited in Fig. 8. The dispersion of the analyzed bands on each measurement is not negligible, see Table 4. Since $\sigma_d^{ap} = \sigma_d + Y_0/N_0$, the average σ_d^{ap} is plotted as a function of the inverse of the corresponding initial column density, in an attempt to measure individually σ_d and Y_0. From Fig. 8, Y_0 is approximately 1300 ± 700 molecules per impact, and $\sigma_d = (7.0 \pm 3) \times 10^{-14}$ cm^2. For thin and thick films, the sputtering yield is 2 to 20 times lower than the rate $N_0\sigma_d^{ap}$. The finding that $Y_0 \sim 10^3$ molecules per impact is to be compared with the sputtering yield for ices, which are two orders of magnitude higher (e.g., Mejía et al. (2020) [28]).

TABLE 4. Apparent destruction cross sections of 27, 44 and 65 nm valine samples.

Thickness (nm)	N_0 (10^{16} cm^{-2})	σ_d^{ap} (10^{-14} cm^2)				$N_0\,\sigma_d^{ap}$
		Analyzed band (cm^{-1})			Average	
		3190-2430	1602-1579	1337-1320		
25	1.6	9.6	9.6	22	14 ± 8	2240
27.5	1.8	14	14	22	17 ± 5	3060
44	3.0	7.1	7.9	-	10 ± 6	2250
65	4.4	5.4	6.2	6.4	6.0 ± 0.6	2640
230	15	7.2	-	7.6	11* ± 4	16x10^3

*Average performed with the σ_d of the bands presented in the table and those of the 1279-1261, 957-937, 782-763, and 726-705 cm^{-1} bands [29].

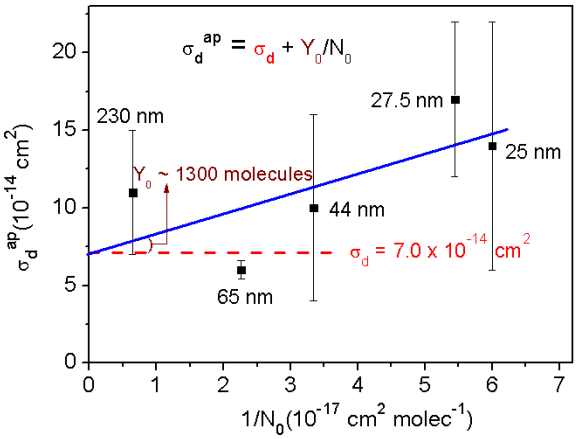

FIG. 8. Average apparent destruction cross section of valine irradiated by 1.5 MeV N^+ in function of the inverse initial column density. $Y_0 \sim 1300 \pm 700$ molecules/projectile and $\sigma_d = (7.0 \pm 3) \times 10^{-14}$ cm^2 are the estimated sputtering yield and destruction cross section, respectively.

5. CONCLUSIONS

Nitrogen MeV ions under distinct conditions (different beam energies and charges) were employed to irradiate valine. FTIR spectroscopy analysis provides the following conclusions:

- Changing projectile species has no effect on the sample chemical modification, with exception of their destruction absolute cross sections that depend on the deposited dose;
- Radiolysis and sputtering are the phenomena responsible for the amino acids degradation - with the main reactions being decarboxylation and deamination [30-32]. Column densities decrease exponentially as a function of beam fluence. FTIR technique is not able to discriminate the effects of the two processes, so that only the sum of them, $\sigma_d^{ap} = \sigma_d + Y_0/N_0$, is determined;
- For MeV ion beams, it turns out that σ_d^{ap} data is compatible with the suggestion that it is proportional to the electronic stopping power and, consequently, to the absorbed dose. Indeed, this relationship holds for glycine and phenylalanine and for similar organic materials such as adenine (e.g., [30, 33]). However $\sigma_d^{ap} = aS_e^n$, with n = 1.0, is not valid for condensed gases, where values lay in-between $1.3 \leq n \leq 1.5$ [34-36];

— For five valine samples with different thicknesses, the sputtering yield, Y_0, for the beam 1.5 MeV N^+ is estimated to be around 1300 ± 700 molecules per impact, while the absolute destruction cross section, σ_d, is predicted to be (7.0 ± 3) x 10^{-14} cm^2 (see Fig. 8);
— Preliminary results with multi-charged beams show that experimental data do not agree qualitatively with σ_d^{ap} predictions based on Joy-Luo or CasP calculations. The finding that $\sigma_d^{ap} \sim q^4$ indicates that for charge states $q > 2$ sputtering damaging effects dominate over the radiolysis ones and yields $Y_0 \sim 100$ precursors per impact for 1.5 MeV N^+ beam. This yield is one order of magnitude lower than the one estimated from varying sample thicknesses;
— If the incident projectile charge is different from the equilibrium charge, multi-charged beam analysis predicts that radiolysis damage rate varies in the bulk along the characteristic relaxation length λ_q. This values, for MeV N^{q+} beams, are in the nanometer range, a distance too short for hadronterapy aplications. Increasing the beam energy into the 100 MeV – 1 GeV range will enlarge λ_q by orders of magnitude, but, unfortunately, it is still too short to compensate the difficulties and costs that a high energy and low charge beam brings.

ACKNOWLEDGEMENTS

This study was financed in part by the Coordenação de Aperfeiçoamento de Pessoal de Nível Superior - Brasil (CAPES) – Finance Code 001. We acknowledge the Brazilian agencies FAPERJ (E-26/201.769/2017, E-26/202.843/2018 and E-26/200.413/2020) and CNPq (PDS n° 118349/2017-1) for partial financial support.

REFERENCES

[1] Cronin, J. R. and Moore, C. B. (1971). Amino Acid Analyses of the Murchison, Murray, and Allende Carbonaceous Chondrites. Science 172 1327–9.
[2] Wolman, Y., Haverland, W. J. and Miller, S. L. (1972). Nonprotein Amino Acids from Spark Discharges and Their Comparison with the Murchison Meteorite Amino Acids. Proceedings of the National Academy of Sciences 69 809–11.
[3] Cronin, J. R. and Moore, C. B. (1976). Amino acids of the Nogoya and Mokoia carbonaceous chondrites. Geochimica et Cosmochimica Acta 40 853–7.
[4] Elsila, J. E., Glavin, D. P. and Dworkin, J. P. (2009). Cometary glycine detected in samples returned by Stardust. Meteoritics & Planetary Science 44 1323–30.
[5] Altwegg, K., Balsiger, H., Bar-Nun, A., Berthelier, J.-J., Bieler, A., Bochsler, P., Briois, C., Calmonte, U., Combi, M. R., Cottin, H., De Keyser, J., Dhooghe, F., Fiethe, B., Fuselier, S. A., Gasc, S., Gombosi, T. I., Hansen, K. C., Haessig, M., Jäckel, A., Kopp, E., Korth, A., Le Roy, L., Mall, U., Marty, B., Mousis, O., Owen, T., Rème, H., Rubin, M., Sémon, T., Tzou, C.-Y., Hunter Waite, J. and Wurz, P. (2016). Prebiotic chemicals—amino acid and phosphorus—in the coma of comet 67P/Churyumov-Gerasimenko. Sci. Adv. 2 e1600285.
[6] Cruz-Diaz, G. A., Erickson, S. E., Silveira, E. F. da, Ricca, A., de Barros, A. L. F., da Costa, C. A. P., Pereira, R. C. and Mattioda, A. L. (2019). PAH Products and Processing by Different Energy Sources. ApJ 882 44.
[7] Iglesias-Groth, S., Cataldo, F., Ursini, O. and Manchado, A. (2010). Amino acids in comets and meteorites: stability under gamma radiation and preservation of the enantiomeric excess: Amino acids in comets and meteorites. Monthly Notices of the Royal Astronomical Society no-no.
[8] Cataldo, F., Angelini, G., Iglesias-Groth, S. and Manchado, A. (2011). Solid state radiolysis of amino acids in an astrochemical perspective. Radiation Physics and Chemistry 80 57–65.
[9] Cataldo, F., Ragni, P., Iglesias-Groth, S. and Manchado, A. (2011). A detailed analysis of the properties of radiolyzed proteinaceous amino acids. J Radioanal Nucl Chem 287 903–11.
[10] Sagan, C. and Khare, B. N. (1979). Tholins: organic chemistry of interstellar grains and gas. Nature 277 102–7.
[11] Strazzulla, G. (1997). Ion irradiation: Its relevance to the evolution of complex organics in the outer solar system. Advances in Space Research 19 1077–84.
[12] Degiovanni A., Amaldi, U. (2015). History of hadron therapy accelerators. Physica Medica, 31 322–332.
[13] Pilling, S., Mendes, L. A. V., Bordalo, V., Guaman, C. F. M., Ponciano, C. R. and da Silveira, E. F. (2013). The Influence of Crystallinity Degree on the Glycine Decomposition Induced by 1 MeV Proton Bombardment in Space Analog Conditions. Astrobiology 13 79–91.

[14] da Costa, C. A. P., Souza-Corrêa, J. A. and da Silveira, E. F. (2021). Infrared analysis of Glycine dissociation by MeV ions and keV electrons. Monthly Notices of the Royal Astronomical Society 502 2105–19.
[15] ANON. (1989). The Merck Index. Merck & Co. Inc.: Rahway, NJ.
[16] Seperuelo Duarte, E., Domaracka, A., Boduch, P., Rothard, H. and Dartois, E. (2010). Laboratory simulation of heavy-ion cosmic-ray interaction with condensed CO.
[17] Wittkower, A. B. (1973). Equilibrium-Charge-State Distributions Of Energetic Ions (Z ~ 2) In Gaseous And Solid Media. 5 54.
[18] Grande, P. L. and Schiwietz, G. (1998). Impact-parameter dependence of the electronic energy loss of fast ions. Phys. Rev. A 58 3796–801.
[19] Bethe, H. A., Ashkin, J. and et al. (1953). Experimental nuclear physic.
[20] Joy, D. C. and Luo, S. (1989). An empirical stopping power relationship for low-energy electrons. Scanning 11 176–80.
[21] Betz, H.-D. (1972). Charge state and charge-changing cross sections of fast heavy ions penetrating through gaseous and solid media.
[22] Toapanta, P. D. I. (2006). Extensão Do Modelo De Traço Nuclear Para Descrever A Dessorção Iônica: Aplicação Aos Agregados De Água. PUC-Rio, Rio de Janeiro.
[23] Niggas, A., Creutzburg, S., Schwestka, J., Wöckinger, B., Gupta, T., Grande, P. L., Eder, D., Marques, J. P., Bayer, B. C., Aumayr, F., Bennett, R. and Wilhelm, R. A. (2021). Peeling graphite layer by layer reveals the charge exchange dynamics of ions inside a solid. Commun Phys 4 180.
[24] Nastasi, M., Michael, N., Mayer, J., Hirvonen, J. K. and James, M. (1996). Ion-solid interactions: fundamentals and applications. Cambridge University Press.
[25] Montenegro, E. C., Cruz, S. A. and Vargas-Aburto, C. (1982). A universal equation for the electronic stopping of ions in solids. Physics Letters A 92 195–202.
[26] Heckman, H. H., Hubbard, E. L. and Simon, W. G. (1963). Electronic Charge Distributions for Heavy Ions at High Velocities. Phys. Rev. 129 1240–9.
[27] Bohr, N. Velocity-Range Relation for Fission Fragments. 6.
[28] Mejía, C., de Barros, A. L. F., Rothard, H., Boduch, P. and da Silveira, E. F. (2020). Radiolysis of Ices by Cosmic-Rays: CH 4 and H 2 O Ices Mixtures Irradiated by 40 MeV 58 Ni 11+ Ions. ApJ 894 132.
[29] da Costa, C. A. P., Muniz, G. S. V., Boduch, P., Rothard, H. and Silveira, E. F. da. (2020). Valine Radiolysis by H+, He+, N+, and S15+ MeV Ions. IJMS 21 1893.
[30] Gerakines, P. A., Hudson, R. L., Moore, M. H. and Bell, J.-L. (2012). In situ measurements of the radiation stability of amino acids at 15–140 K. Icarus 220 647–59.
[31] Meshitsuka, G., Shindo, K., Minegishi, A., Suguro, H. and Shinozaki, Y. (1964). Radiolysis of Solid Glycine. BCSJ 37 928–30.
[32] Gerakines, P. A. and Hudson, R. L. (2013). Glycine's radiolytic destruction in ices: first in situ laboratory measurements for Mars. Astrobiology 647–55.
[33] Vignoli Muniz, G. S., Mejía, C. F., Martinez, R., Auge, B., Rothard, H., Domaracka, A. and Boduch, P. (2017). Radioresistance of Adenine to Cosmic Rays. Astrobiology 17 298–308.
[34] de Barros, A. L. F., Bordalo, V., Seperuelo Duarte, E., F da Silveira, E., Domaracka, A., Rothard, H. and Boduch, P. (2011). Cosmic ray impact on astrophysical ices: laboratory studies on heavy ion irradiation of methane. A&A 531 A160.
[35] Andrade, D. P. P., de Barros, A. L. F., Pilling, S., Domaracka, A., Rothard, H., Boduch, P. and da Silveira, E. F. (2013). Chemical reactions induced in frozen formic acid by heavy ion cosmic rays. Monthly Notices of the Royal Astronomical Society 430 787–96.
[36] Mejía, C. F., de Barros, A. L. F., Bordalo, V., da Silveira, E. F., Boduch, P., Domaracka, A. and Rothard, H. (2013). Cosmic ray–ice interaction studied by radiolysis of 15 K methane ice with MeV O, Fe and Zn ions. Monthly Notices of the Royal Astronomical Society 433 2368–79.

DEVELOPMENTAL WORK ON ECONOMIC PRODUCTION OF HIGH AND LOW SPECIFIC ACTIVITY ^{64}CU – SUITABLE FOR PRECLINICAL STUDIES USING ACCELERATOR NEUTRONS

A. GOPALAKRISHNA
Board of Radiation and Isotope Technology,
Mumbai , India
Email: garjun68@yahoo.co.uk

Amit KUMAR
Board of Radiation and Isotope Technology,
Mumbai , India

P. MALETHA, KAMALDEEP, S. V. SURYANARAYANA, H. NAIK, B. K. NAYAK, S. P. KULKARNI
Bhabha Atomic Research Centre,
Mumbai , India

P. MUKHERJEE
Board of Radiation and Isotope Technology,
Mumbai , India

Abstract

^{64}Cu is a theranostic radioisotope which is generating interest in the field of PET imaging and planning of therapy. Several radiochemical and pre-clinical studies need to be carried out to establish suitability and stability of new ^{64}Cu radiopharmaceuticals. However, obtaining ^{64}Cu is an expensive process as it is typically available via proton irradiation of enriched ^{64}Ni in a medical cyclotron. The paper investigates an economical method of obtaining ^{64}Cu with activity levels suitable for research scale production / radiochemical experiments utilizing accelerator neutrons. Natural foils of Cu and Zn were irradiated in the neutron field produced during the irradiation of ^{18}O, in the routine production of ^{18}F via the ^{18}O(p,n)^{18}F route in a medical cyclotron. Evaluation of yields of ^{64}Cu and radionuclidic impurities were determined by the quantification of the photo-peaks by off-line gamma -ray spectrometry. No carrier added ^{64}Cu was separated from the irradiated zinc by solvent extraction with high radionuclidic purity and separation yields of > 90%. The average yields of low specific activity and high specific activity ^{64}Cu at the end of bombardment was 455 and 861 Bq/g*microampere*h respectively.

1. INTRODUCTION

^{64}Cu has generated interest in the field of PET imaging and planning of therapy [1], as it decays by three different routes, namely, electron capture, β− and β+ decay. Its half-life of 12.8 h also makes it suitable for versatile applications.

The utility of reactor produced low specific activity (LSA) ^{64}Cu produced via ^{63}Cu(n,γ)^{64}Cu reaction and its use in the form of [^{64}Cu]$CuCl_2$ as a radiopharmaceutical for PET imaging of prostate cancer and glioblastoma patients have been demonstrated [2]. However the utilization of ^{64}Cu is mostly limited to studies, sourcing no carrier added high specific activity (HSA) ^{64}Cu, produced via the ^{64}Ni(p, n)^{64}Cu route in a medical cyclotron [3] . ^{64}Ni has a natural abundance of < 1 %. An enriched ^{64}Ni target is required to produce ^{64}Cu, increasing the cost of the radiochemical and pre-clinical studies that need to be carried out to establish suitability and stability of new ^{64}Cu radiopharmaceuticals.

Radiochemical studies and uptake studies performed on mice use activity of the order of only a few hundred microcuries [4, 5] This study investigates the potential of an economical method for research scale production of ^{64}Cu utilizing accelerator neutrons produced in the routine irradiation of ^{18}O in a medical cyclotron.

2. MATERIALS AND METHODS

2.1 Neutron Source and Irradiation parameters

The study was carried out in the medical cyclotron facility of PETtrace-800 cyclotron at the Radiation Medicine Centre, Mumbai, India. The cyclotron accelerates protons and deuterons to fixed energies of 16.5 MeV and 8.4 MeV respectively. The six target assemblies of liquid and gaseous targets (Fig 1), enables production of ^{13}N, ^{15}O, ^{11}C and ^{18}F. However, to meet current demands of nuclear medicine centres, the cyclotron is used for regular production of only the ^{18}F isotope in 12 - 15 irradiations per week. The ^{18}F routine production is carried out via the $^{18}O(p,n)^{18}F$ route in the liquid target irradiation system. ^{18}F produced is converted to [^{18}F] radiopharmaceuticals - [^{18}F] FDG, [^{18}F] FET, [^{18}F] FLT and [^{18}F] NaF, as per the requirement. The Table 1 illustrates the features of the cyclotron and target irradiation system. Natural foils of Cu, and Zn, were irradiated in the neutron field. The proton beam current was set at 55 microamperes.

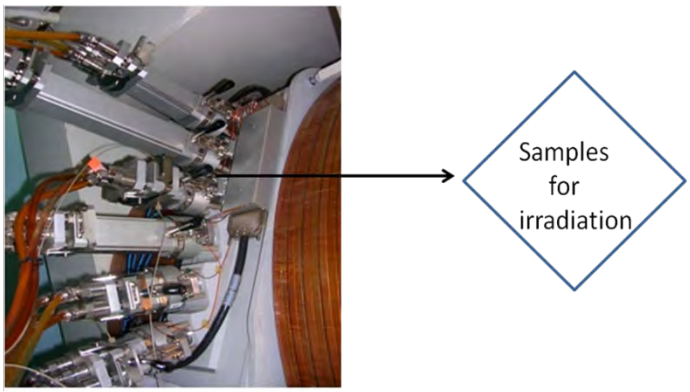

FIG. 1: Target irradiation systems in the Medical Cyclotron facility and experimental setup for irradiation

TABLE 1: Features of the Cyclotron and target irradiation system

Cyclotron	PETtrace 800
Proton energy	16.5 MeV (Fixed)
Beam Current (H^-)	1 – 75 μA (Variable)
Liquid target irradiation system	Target- $H_2{}^{18}O$ water ^{18}O enrichment - 98% Volume - 2.4 mL Cavity- Ag

2.1. Evaluation of the yield of ^{64}Cu and radionuclidic impurities

Radioactivity levels of ^{64}Cu and other radioisotopes co-produced were determined by the quantification of photo-peaks by off-line gamma-ray spectrometry [6]. The γ-ray counting of radionuclides was performed using a pre-calibrated HPGe detector coupled to a PC based 4K channel analyzer. The energy and efficiency calibration of the detector system was carried out using a standard ^{152}Eu source. Radioactivity levels of ^{64}Cu and of the radionuclidic impurities ^{65}Zn, ^{69m}Zn were determined by the quantification of the photo-peak counts of the 1345.8 keV, 1115.5 keV, 438.6 keV γ-lines respectively. Co-produced ^{67}Cu was quantified by the 184.6 keV γ-line. Spectroscopy software, Interwinner 7 was used for the analysis.

2.2. Separation of ^{64}Cu from irradiated zinc

The irradiated zinc was dissolved in concentrated hydrochloric acid and evaporated to dryness. No carrier added ^{64}Cu was separated from the irradiated zinc via solvent extraction [6-8]. Solvent extraction with dithizone (diphenylthiocarbazone) dissolved in CCl_4, a water immiscible medium was carried out. The Fig 2 shows the

schematic of the radiochemical separation process. The separation yields were determined by measuring the ^{64}Cu activity before and after the separation.

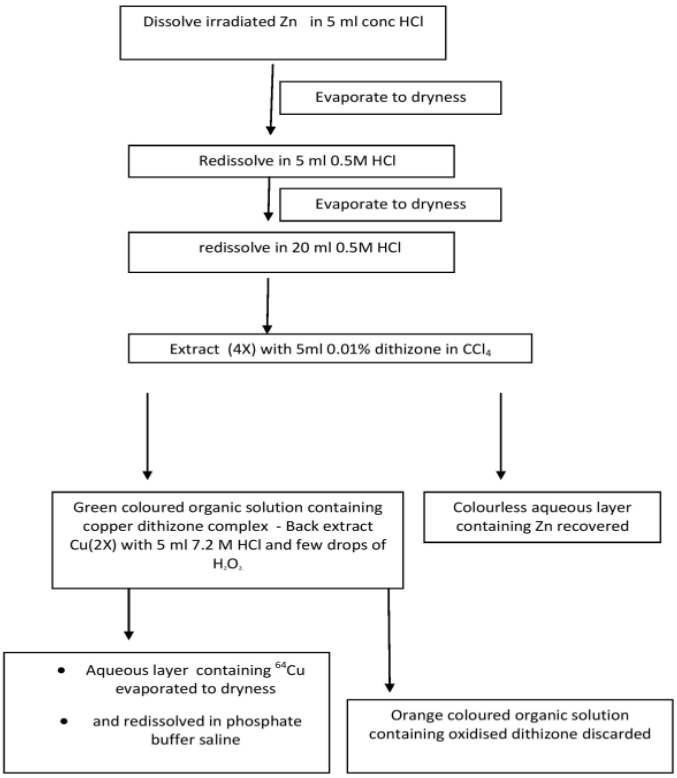

FIG. 2: Schematic of the radiochemical separation process

3. RESULTS AND DISCUSSION

3.3. Neutron Source

Neutron generators, cyclotrons and electron linear accelerators that could be used as a Compact Accelerator Based Neutron Source (CANS) are available as 'commercial off the shelf' varieties [9,10]. The accelerator neutrons produced via the $^{18}O(p,n)^{18}F$ route range from thermal to fast [11]. The unfolded neutron spectrum is shown in Fig 3 [11]. The neutron flux is anisotropic to the incoming proton beam.

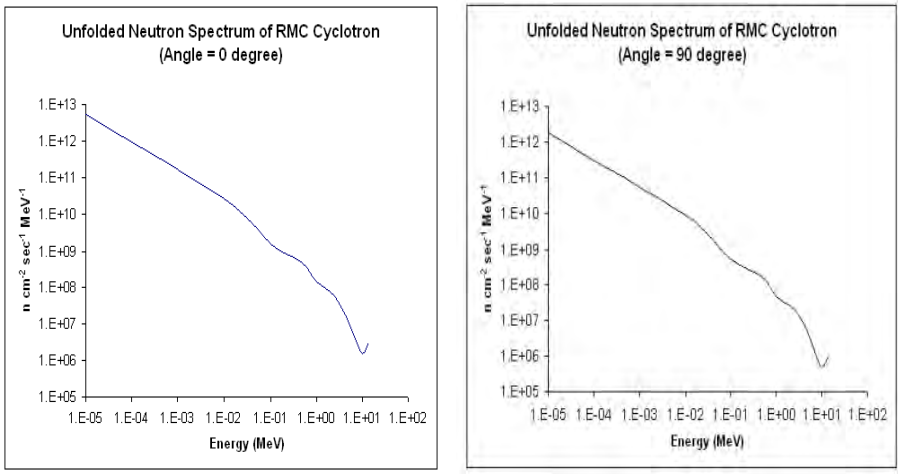

FIG. 3: Unfolded neutron spectrum [11]

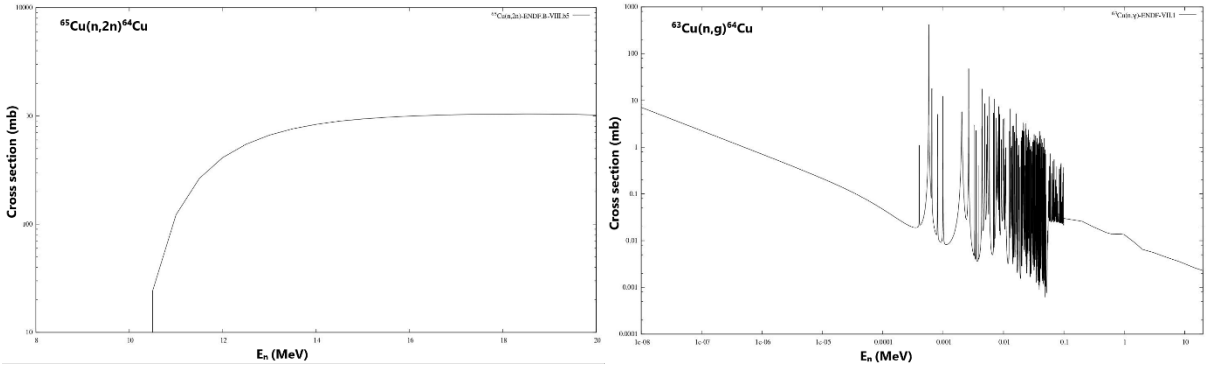

FIG 4: Excitation function of ^{65}Cu(n,2n)^{64}Cu and ^{63}Cu(n,g)^{64}Cu

3.4. LSA ^{64}Cu

Correlating the neutron spectrum (Fig 3) and the excitation functions of ^{64}Cu produced via ^{65}Cu(n,2n)^{64}Cu and ^{63}Cu(n,g)^{64}Cu (Fig 4), it can be inferred that LSA ^{64}Cu is formed via a dual route ^{65}Cu(n,2n)^{64}Cu + ^{63}Cu(n,g)^{64}Cu in the irradiated natural Cu foil. The Table 2 shows that the average cumulative activity of LSA ^{64}Cu produced is 455 ± 26 Bq/g*microampere*h at the end of bombardment (EOB).

TABLE 2: YIELDS OF LOW SPECIFIC ACTIVITY ^{64}Cu AT EOB

Irradiation time (h)	Target and weight (g)	^{64}Cu (Bq/ g*microampere*h)
1.1	Cu (0.02)	431
1.2	Cu (0.022)	483
1.1	Cu (0.02)	452

3.5. HSA ^{64}Cu

The radionuclides ^{64}Cu, ^{67}Cu, ^{65}Zn and ^{69m}Zn co-produced via the various (n,x) routes [6] were identified via gamma spectrometry of the irradiated Zn foil. As seen from Table 3, the average yields of high specific activity ^{64}Cu is 861 ± 15 Bq/g*microampere*h at EOB. The level of co-produced ^{67}Cu was 3 orders less than the ^{64}Cu produced at EOB. The ^{64}Cu and ^{67}Cu coproduced are inseparable and the ratio of ^{67}Cu/^{64}Cu post EOB increases due to the differences in their half-lives (Fig 5). The radioisotopes ^{64}Cu and ^{67}Cu are a theranostic pair and ^{64}Cu can be used as a tracer to study the uptake of ^{67}Cu, as the biological behaviour of these isotopes *in vivo* is expected to be equivalent.

TABLE 3: YIELDS OF HIGH SPECIFIC ACTIVITY ^{64}Cu AT EOB

Irradiation time (h)	Target and weight (g)	^{64}Cu (Bq/ g*microampere*h)
1.1	Zn (0.026)	879
1.2	Zn (2.1)	851
1.1	Zn (2.1)	855

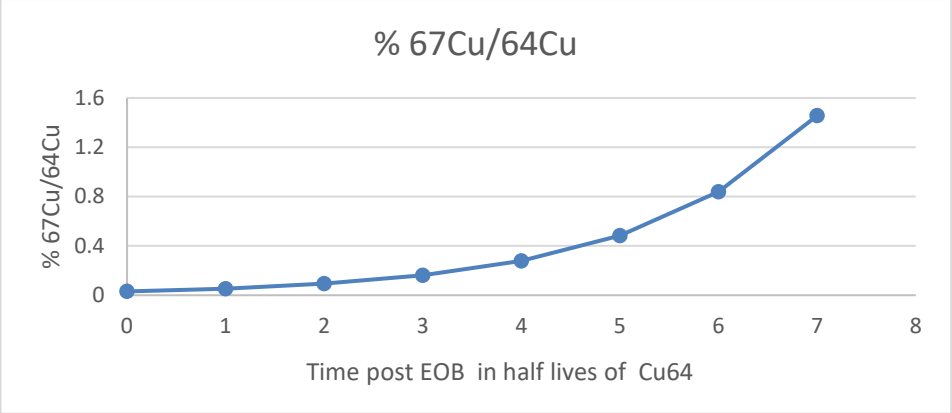

FIG 5: % ^{67}Cu/^{64}Cu post EOB

3.6. Separation of ^{64,67}Cu from irradiated Zn

The solvent extraction method is based on the selective extraction of Cu dithizonate into an organic solvent from a dilute acidic solution of the Zn target and back extraction of Cu into the aqueous phase. Dithizone is selective for Cu in the pH range 2–5, and for Zn in the pH range 6.5–9.5. The Fig 6 shows that the radionuclide impurities ^{65}Zn and ^{69m}Zn are not detected in the separated ^{64}Cu, indicating achievement of high radionuclidic purity. Shielding out the thermal neutrons will help in reducing the levels of coproduced ^{65}Zn, enabling easier handling of the irradiated Zn targets. High separation yields of > 90%, with high radionuclidic purity and good reproducibility was achieved.

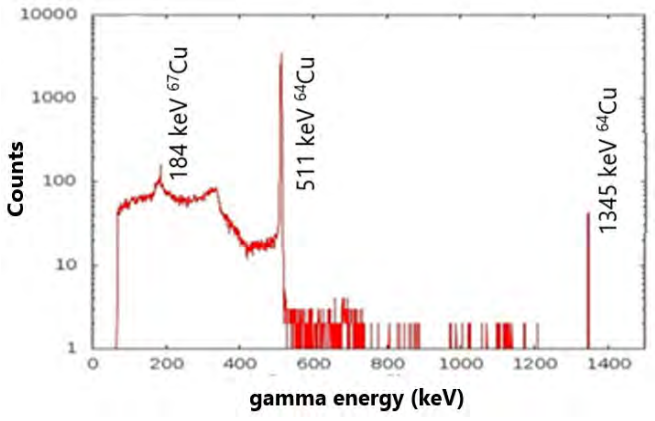

FIG 6: Gamma spectrometry of separated ^{64,67}Cu from the irradiated Zn foil

4. CONCLUSION

In this paper, we demonstrate an economical method of obtaining low and high specific activity ^{64}Cu via accelerator neutron bombardment of natural Cu and Zn. LSA ^{64}Cu is produced via a dual route ^{65}Cu(n,2n)^{64}Cu + ^{63}Cu(n,g)^{64}Cu in the irradiated natural Cu foil. Separation yields of > 90% of HSA ^{64}Cu inseparable from ^{67}Cu was obtained from the irradiated natural Zn foil. The potential use of a cocktail of mixed isotopes of the same element with different decays and energies may improve the therapeutic effect and is an interesting consideration to explore.

The growth and spread of medical cyclotrons is taking place across the globe, providing potential avenues for research scale production of ^{64}Cu via the accelerator neutrons. Utilization of these secondary neutrons requires no extra capital investment and holds promise for research scale production of other medically useful radioisotopes via various (n,x) reactions [12], without interrupting the regular production and supply of ^{18}F-radiopharmaceuticals.

ACKNOWLEDGEMENTS

The authors thank Dr Chanda Arjun, Board of Radiation and Isotope Technology and the colleagues at Radiation Medicine Centre for their technical support.

REFERENCES

[1] Zhou Y, Li J, Xu X, Zhao M, Zhang B, Deng S, Wu Y. 64Cu-based radiopharmaceuticals in molecular imaging. Technology in cancer research & treatment 18 (2019) 1-10

[2] Chakravarty R, Shetty P, Nair K.V, Rajeswari A, Jagadeesan K.C, Sarma H.D, Rangarajan V, Krishnatry R, Chakraborty S. Reactor produced [64Cu]CuCl2 as a PET radiopharmaceutical for cancer imaging: from radiochemistry laboratory to nuclear medicine clinic. Ann Nucl Med 34, 12 (2020) 899–910.

[3] McCarthy D.W, Shefer R.E, Klinkowstein R.E, Bass L.A, Margeneau W.H, Cutler C.S, Anderson C.J, Welch M.J. Efficient production of high specific activity 64Cu using a biomedical cyclotron. Nucl med and biol. 24(1) (1997) 35-43.

[4] Johnsen A.M, Heidrich B.J, Durrant C.B, Bascom A.J, Ünlü K. Reactor production of 64Cu and 67Cu using enriched zinc target material. Journal of Radioanalytical and Nuclear Chemistry 305(1) (2015) 61-71.

[5] Gopalakrishna A, Chakraborty S, Chakraborty A. Low specific activity 64 Cu ions-bio-marker for melanoma. In Proceedings of the fourth international conference on application of radiotracers and energetic beams in sciences (2018).

[6] Gopalakrishna, A., Suryanarayana, S.V., Naik, H., Dixit, T.S., Nayak, B.K., Kumar, A., Maletha, P., Thakur, K., Deshpande, A., Krishnan, R. and Banerjee, S.,. Production, separation and supply prospects of ^{67}Cu with the development of fast neutron sources and photonuclear technology. *Radiochimica Acta*, *106*(7) (2018) 549-557.

[7] Dasgupta, A. K., Mausner, L. F., Srivastava, S. C.: A new separation procedure for 67Cu from proton irradiated Zn. Appl. Radiat.Isot. 42, (1991) 371-376

[8] Smith N.A, Bowers D.L, Ehst D.A. The production, separation, and use of 67Cu for radioimmunotherapy: a review. Appl. Radiat.Isot. 70(10) (2012) 2377-83.

[9] Compact Accelerator Based Neutron Sources, IAEA-TECDOC-1981, IAEA, Vienna (2021)

[10] Mausolf E.J, Johnstone E.V, Mayordomo N, Williams D.L, Guan E.Y, Gary C.K. Fusion-Based Neutron Generator Production of Tc-99m and Tc-101: A Prospective Avenue to Technetium Theranostics. Pharmaceuticals 14(9) 875. (2021) 1-19

[11] Sathian, V., Phadnis, U.V., Sharma, D.N., Deepa, S., & Soni, P.S. Neutron spectrum measurement in a medical Cyclotron. IRPA 12: 12 International congress of the International Radiation Protection Association (IRPA): Strengthening radiation protection worldwide, Argentina: SAR. (2008).

[12] Engle J.W, Birnbaum E.R, Fassbender M.E, John K.D, Nortier F.M. Parasitic isotope production with cyclotron beam generated neutrons. In Proceedings of the 20th international conference on cyclotrons and their applications, Vancouver (2013) 16-20

UTILIZATION OF 30 MEV DAE MEDICAL CYCLOTRON FOR PRODUCTION OF MEDICALLY USEFUL RADIOISOTOPES AND CORRESPONDING RADIOPHARMACEUTICALS

Sankha CHATTOPADHYAY
Regional Centre, BRIT, VECC, MCF, Chakgaria
Kolkata, 700094 India
Email: sankha@vecc.gov.in

Pradip MUKHERJEE
Board of Radiation & Isotope Technology, Vashi Complex, Sector 20
Vashi, Navi Mumbai-400703, India

Abstract

Cyclotrons are extensively used to produce radioisotopes for diagnostic and therapeutic use for cancer care. In India, the IBA Cyclone-30, 30MeV, 350μA proton cyclotron has been commissioned and made operational in September, 2018 for the production of radioisotopes/radiopharmaceuticals for medical application. The cyclotron has five beamlines, out of which three beamlines are dedicated for the production of radioisotopes for medical use. This cyclotron has the potential to produce SPECT (Single-Photon Emission Computed Tomography) Isotopes (^{67}Ga, ^{111}In, ^{123}I, ^{201}Tl etc.), PET (Positron Emission Tomography) isotopes (F-18, Ge-68/Ga-68 generator for in situ production of Ga-68, Ga-68, Cu-64, Zr-89, I-124 etc.) and therapeutic isotope like Pd-103. Herein, the production of ^{18}F-FDG, ^{68}Ga-PSMA-11 and ^{201}TlCl radiopharmaceuticals using Cyclone-30 has been reported. The specification of the radiopharmaceuticals complies with norms of the regulatory bodies in India. Presently, India is importing long lived SPECT Isotopes. The high cost of imported isotopes makes the treatment expensive. Indigenous production is going to be a boon to make the treatment cost more affordable.

1. INTRODUCTION

Currently, ^{18}F-FDG is the most successful PET radiopharmaceutical so far. The advancement in synthesis and quality control of ^{18}F-FDG, together with its approval by the US FDA and the availability of reimbursement, are probably the main reasons for the flourish of clinical PET. The labelled ^{18}F-FDG compound has a relatively short shelf life, which is dominated by the physical decay of ^{18}F with a half-life of 109.8 minutes, or slightly less than 2 hours. Still, this half-life is sufficiently long to allow shipping the compound to remote PET scanning facilities, in contrast to other medical radioisotopes like ^{11}C. In PET imaging, ^{18}F-FDG can be used for the assessment of glucose metabolism in the heart, lungs [1], and the brain. It is also used for imaging tumors in oncology, where a static ^{18}F-FDG PET scan is performed and the tumor ^{18}F-FDG uptake is analyzed in terms of Standardized Uptake Value (SUV). ^{18}F-FDG is taken up by cells, phosphorylated by hexokinase (whose mitochondrial form is greatly elevated in rapidly growing malignant tumours), [2] and retained by tissues with high metabolic activity, such as most types of malignant tumours. As a result, FDG-PET can be used for diagnosis, staging, and monitoring treatment of cancers, particularly in Hodgkin's disease, non-Hodgkin lymphoma, colorectal cancer, breast cancer, melanoma, and lung cancer. It has also been approved for use in diagnosing Alzheimer's disease.

The SPECT isotope ^{201}Tl ($t_{1/2}$ = 73.06 hours) in the form of ^{201}TlCl is a diagnostic myocardial flow tracer to detect coronary artery disease and to assess myocardial viability, with an accuracy comparable to that of positron emission tomography. Other medical applications of the same include possible assessment of physiology, as a renal medullary imaging agent, and for tumor detection [3]. ^{201}TlCl has higher myocardial extraction fraction (85%) compared to ^{99m}Tc-MIBI (65%) and ^{99m}Tc-Tetrofosmin (60%). The lower myocardial extraction fraction of ^{99m}Tc-MIBI and ^{99m}Tc-Tetrofosmin results in underestimation of blood flow at high flow compared to ^{201}TlCl [4]. Clearance half-life is faster in case of ^{201}TlCl compared to ^{99m}Tc-MIBI and ^{99m}Tc-Tetrofosmin [5]. ^{201}Tl decays to stable Mercury-201 (^{201}Hg) nuclide via electron capture with the emission of mercury K-X-rays of 69 - 83 keV (90%) along with γ-rays of 135 keV and 167 keV in total abundance of 10%. ^{201}Tl is produced in Cyclone-30 using solid target via ^{203}Tl(p,3n)^{201}Pb → ^{201}Tl nuclear reaction utilizing a proton (energy: 28MeV) beam current of 50μA for up to 6-8h. The potential radionuclidic impurities in Thallium-201 produced with during the above nuclear reaction are Thallium-200 (^{200}Tl, t1/2 = 26 h), Thallium-202 (^{202}Tl, t1/2 = 12.2 d) and Lead-203 (^{203}Pb,

t1/2 = 52 h). However, the percentage for formation of ^{200}Tl, ^{202}Tl and ^{203}Pb can be controlled by optimizing the incident proton energy (28MeV) on the target during irradiation and giving an optimum decay time of 32 h for ^{201}Pb to ^{201}Tl [6]. The allowed limits for ^{200}Tl, ^{202}Tl and ^{203}Pb were 0.6%, 1.2% and 0.2% expressed as a percentage of ^{201}Tl injection activity at calibration date and time [7]. There are many approaches that address the wet separation of ^{201}Pb from ^{203}Tl and ^{201}Tl from ^{201}Pb from a dissolved solid target, typically ending with ^{201}TlCl as the product. Such approaches include ion exchange resin chromatography and solvent/solvent extraction [8]. Ion exchange column chromatography and solvent extraction methods have been employed by us for radiochemical separation and purification of ^{201}Tl from dissolved solid target. We herein report a semi-automated production of curie level, pharmaceutical grade ^{201}TlCl using IBA Chemistry module.

Gallium-68 (^{68}Ga, $t_{1/2}$ = 67.8 min) possesses great potential in nuclear medicine [9,10] being extensively used in labelling of biomolecules like somatostatin and PSMA inhibitor analogues [11,12,13,14]. ^{68}Ga decays to stable Zinc-68 (^{68}Zn) nuclide via electron capture (11%) and positron decay (89%) and is generally produced via ^{68}Ge/^{68}Ga generators [15,9]. An alternative method to produce ^{68}Ga is by cyclotron using high enriched ^{68}Zn via the ^{68}Zn(p,n)^{68}Ga reaction [16,17,18]. There are many approaches that address the wet separation of 68Ga and ^{68}Zn from a dissolved solid target, typically ending with [^{68}Ga]$GaCl_3$ as the product. Such approaches include solid phase extraction, solvent extraction, and precipitation [19,20]. Ion Exchange column chromatography and solvent extraction methods have been employed by us for radiochemical separation and purification of ^{68}Ga from dissolved solid target. Due to the increasing demand for various ^{68}Ga based radiopharmaceuticals production and applications entering clinical trials worldwide, there is a need to produce large quantity of ^{68}Ga. Hence, $^{68}GaCl_3$ is produced on medium energy cyclotron via the ^{68}Zn(p,n)^{68}Ga reaction which is useful for production of large quantity of ^{68}Ga. The starting material is a solid target in the form of a target plate, since solid target will always have a higher concentration of zinc, which leads to significantly higher yields. Furthermore, the ^{68}Ga must be separated from the bulk parent ^{68}Zn isotope and purified to remove any unwanted metal contaminants. The end product obtained is $^{68}GaCl_3$, which is similar to the eluate obtained from the ^{68}Ge/^{68}Ga generator, is then used as a solution for radiolabelling to prepare ^{68}Ga-based diagnostic radiopharmaceuticals like ^{68}Ga-PSMA-11, ^{68}Ga-DOTA-TATE. Currently, [^{68}Ga]Ga-PSMA-11 (Glu-NH-CO-Lys-(Ahx)-[[^{68}Ga]Ga-HBED-CC] (HBED CC: N,N'-Bis(2-hydroxy-5-(ethylene-be-tacarboxy)benzyl)ethylenediamine N,N'-diacetic acid) is among the most widely used agents for prostate cancer PET/CT imaging. Prostate cancer is one of the leading causes of morbidity and death in men in the western world, and the second most common cancer in men worldwide [21]. We herein report a semi-automated production of curie level, pharmaceutical grade [^{68}Ga]$GaCl_3$ radiochemical and [^{68}Ga]Ga-PSMA-11 radiopharmaceutical using IBA Chemistry module.

2. PRODUCTION OF DIFFERENT RADIOISOTOPES AND RADIOPHARMACEUTICALS

2.1. ^{18}F-FDG Radiopharmaceutical using IBA-SYNTHERA Module

2.1.1. Production of ^{18}F from O-18-Water and Synthesis of ^{18}F-FDG

[^{18}F]fluoride ion/[^{18}O]water was transferred from target to chemistry module following which the synthesis of ^{18}F-FDG (Fig. 1) was carried out using automated, closed loop and computer-controlled IBA synthera module (Fig. 2) inside Comecer make Hotcells (75 mm Pb thickness wall). ABX, Germany reagents and ancillary kits along with IFP (Integrated Fluidic Processor) are utilized in the IBA Synthera module for the synthesis and purification of ^{18}F-FDG (Fig. 3). The F-18 is produced in the cyclotron by irradiation of $H_2{}^{18}O$ (97% enriched) [^{18}O(p,n)^{18}F] using 18 MeV proton beam (35-45 μA current) for 30 min to 2 hours (Fig. 4 and Fig. 5). The dispensing of the product is carried out using TIMOTHEO-LT dispensing module inside Comecer dispensing Hotcell having ISO Class A environment. The final ^{18}F-FDG product obtained from IBA Synthera synthesis module is collected in 30 ml sterile glass vial (supplied by ABX Germany) containing 0.68 ml of 14.6% sodium chloride (inactive ingredient) to make the final solution isotonic, in the dispensing hotcells. The production yield of ^{18}F-FDG varied from 65-70 % (without decay correction). A 0.5 ml of sample from each FDG batch was taken in a sterile vial for Q. C. analysis. The physico-chemical and bio quality control tests were performed as per USP specifications with satisfactory results.

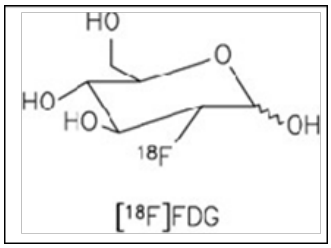

FIG. 1. Structure of ^{18}F-FDG

FIG. 2. IBA-SYNTHERA Module

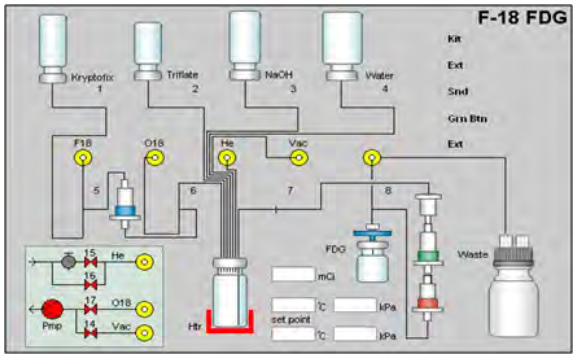

FIG. 3. ^{18}F-FDG Synthesis Flow Diagram

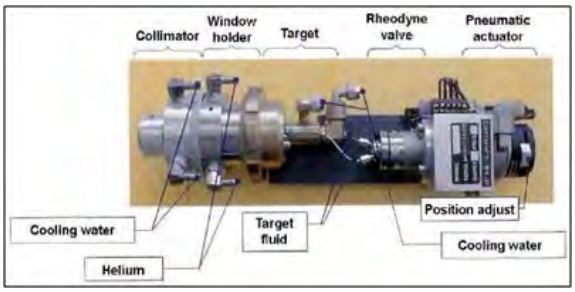

FIG. 4. F-18 water target

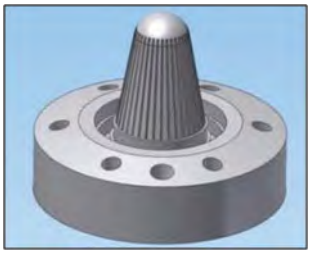

FIG. 5. Conical shaped Niobium cavity for O-18 water

2.1.2. Quality Control Results

- The physicochemical quality control tests of ^{18}F-FDG were performed by its checking appearance, pH, radiochemical purity by either method A (HPLC) or method B (TLC). The HPLC system is more expensive and elaborate than the TLC system, radionuclides purity by HPGe method.
- The radioactivity assay i.e. yields determination and half-life estimation were performed in dose calibrator.
- The presence of bacterial endotoxin in the ^{18}F-FDG were assayed by Charles River's Endosafe PTS (Portable Endotoxin Testing System).
- The sterility testing for every individual batch of ^{18}F-FDG has been inoculated on both fluid thioglycolate medium (FTM) and soybean casein digest medium (SCDM) within 30 hours of production at 37°C and 25°C respectively.
- The residual solvent in ^{18}F-FDG i.e., ethanol and acetonitrile were estimated in Gas chromatography (GC).
- The radiochemical purity of the ^{18}F-FDG has been found to be 100% by using TLC method (Fig. 6).
- The radionuclidic purity was greater than 99.9% (determined by HPGe) (Fig. 7).
- The presence of Kryptofix in the final product was found to be less than 22 µg/ml.
- The residual solvent ethanol and ACN in ^{18}F-FDG were within the specified value (GC method) (Fig. 8).
- HPLC study is required to know any radiochemical impurities like $^{18}F^-$, ^{18}F-FDM and ^{18}F-ClDG are present or not (Fig. 9 and Fig. 10).
- The Bacterial endotoxin in ^{18}F-FDG was found <10 EU/ml determined by PTS method.
- Each batch was evaluated for sterility test and each batch passes the sterility test.
- PET-CT scan of ^{18}F-FDG was carried out in North City Centre, Kolkata (Fig. 11).
- Results are shown in Table 1.

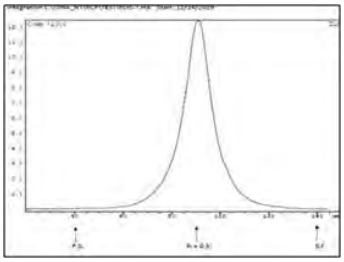

FIG. 6. TLC spectra of ^{18}F-FDG

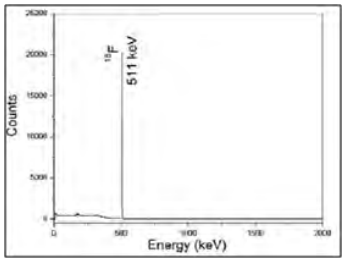

FIG. 7. HPGe spectra of ^{18}F

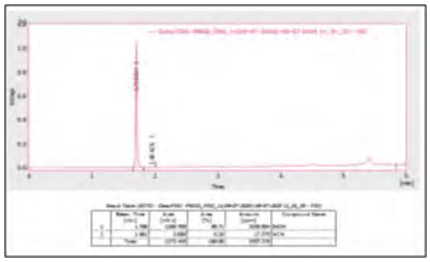

FIG. 8. GC spectra of ^{18}F-FDG

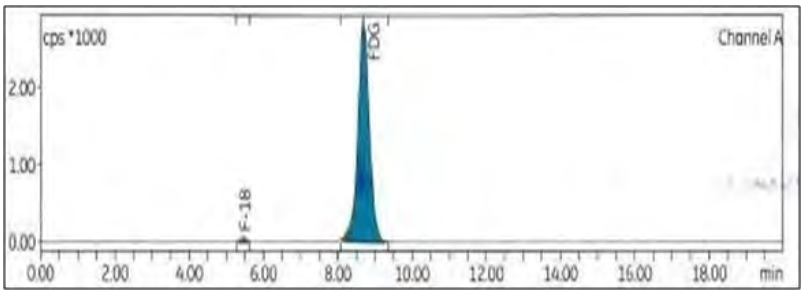

FIG. 9. HPLC spectra of ^{18}F-FDG

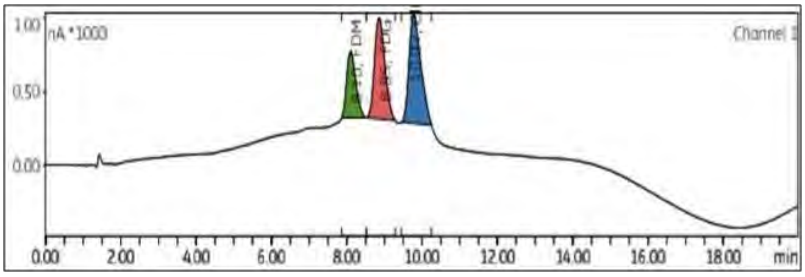

FIG. 10. HPLC spectra of cold samples of FDM, FDG & ClDG

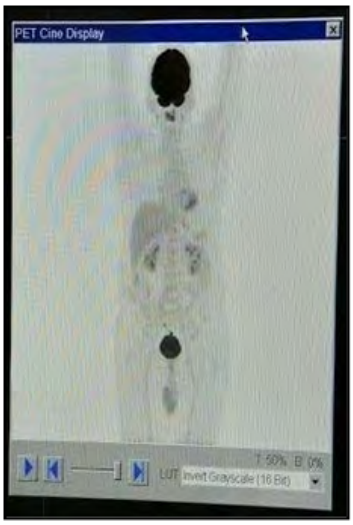

FIG. 11. PET-CT scan of 18F-FDG carried out in North City Centre, Kolkata

TABLE 1. PHYSICOCHEMICAL AND BIOLOGICAL QUALITY CONTROL TESTS OF ^{18}F-FDG

Batch no.	Appearance	pH	Half life (min)	RC Purity (%)	RN Purity (%)	Kryptofix (<22 µg/ml)	Acetonitrile (ppm)	Ethanol (ppm)	BET test (<10 EU/ml)	Sterility test
1	Clear solution	6.5	109.1	100	99.9	Passed	17.88	1705.96	Passed	Passed
2	Clear solution	6.0	110.76	100	99.9	Passed	14.04	1756.94	Passed	Passed
3	Clear solution	6.0	109.9	100	99.9	Passed	18.21	1641.40	Passed	Passed
4	Clear solution	6.5	108.9	100	99.9	Passed	<5	1344.48	Passed	Passed
5	Clear solution	6.0	109.5	100	99.9	Passed	14.60	1481.30	Passed	Passed
6	Clear solution	6.5	109.8	100	99.9	Passed	15.59	1506.85	Passed	Passed

2.2. Radioactive Thallium-201 in the form of ^{201}TlCl suitable for diagnostic uses in patients

2.2.1. Irradiation of the target

^{201}Tl has been produced on medium energy cyclotron, Cyclone-30, via the ^{203}Tl(p,3n)^{201}Pb → ^{201}Tl nuclear reaction. The starting material is a solid target in the form of a target plate electrodeposited with enriched Thallium-203 (Fig. 12 and Fig. 13), which leads to significantly higher yields. Further the ^{201}Tl must be separated from the bulk parent ^{203}Tl and ^{201}Pb isotope and purified to remove any unwanted metal contaminants. The end product has been supplied as a ready-to-use sterile, pyrogen free, isotonic aqueous solution of radioactive Thallium-201 (^{201}Tl) in the form of thallous chloride solution for intravenous administration. Irradiations of the

electrodeposited (~ 74 - 75 µm) ^{203}Tl targets were carried out with the 28MeV proton beam energy and 50µA beam current for up to 6-8h (n=6) at 6° angle. During the irradiation the target assembly (Fig. 14 and Fig. 15) was water cooled with a flow rate of 9 liter/min. Beam current/charge deposited on the target was monitored with a current integrator.

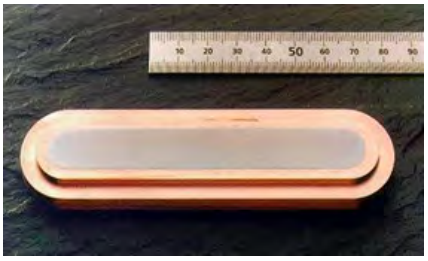

FIG. 12. ^{203}Tl Target

FIG.13. Electrodeposition vessel

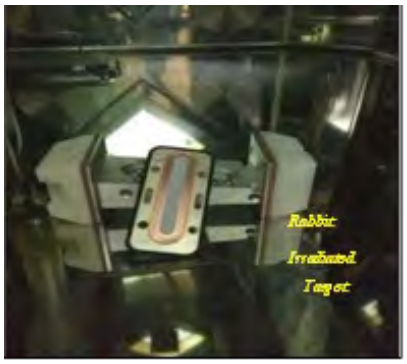

FIG. 14. Irradiated target system received in the receiving Hotcell.

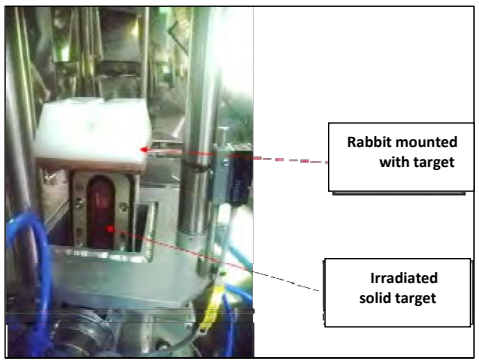

FIG. 15. Irradiated enriched Tl-203 Target with Rabbit System in Receiving Hotcell.

2.2.2. Dissolution of the irradiated thallium target and separation of ^{201}Tl from ^{201}Pb

The original script for the Tl-201 chemistry-1 and chemistry-2 was supplied for production of [Tl-201]TlCl and thus required modifications while working on our system (Fig. 16 and Fig. 17).

Chemistry-I: The irradiated target was dissolved in 25 ml of 0.7 N HNO_3 (containing 100 mg $Pb(NO_3)_2$). 201Pb was precipitated as $^{201}PbSO_4$ by using 10 ml of 3.6 N H_2SO_4. The first dissolution of $^{201}PbSO_4$ was carried out with 10 ml of 0.1 M Na_2EDTA (pH ~ 9.0), while second dissolution was carried out with 10 ml of 0.1 M Na_2EDTA (pH ~ 5.4). $^{203}Tl^{3+}$ was reduced to $^{203}Tl^{+}$ by bubbling SO_2 gas. Ion Exchange Chromatography using Dowex 50W-X8 resin (100-200 mesh, H^+ form) was employed to remove co-precipitated $^{203}Tl^{+}$. Cation exchange chromatography was employed to adsorb $^{203}Tl^{+}$ in the column while the ^{201}PbEDTA complex was collected in column eluate. $^{201}PbEDTA^{2-}$ complex was stored for 32 h for decay of $^{201}Pb^{2+}$ either to $^{201}Tl^{3+}$ or $^{201}Tl^{+}$.

Chemistry-II: Post 32 h decay, $^{201}Pb^{2+}$ (in the form of ^{201}PbEDTA mother solution) was converted to either $^{201}Tl^{3+}$ or $^{201}Tl^{+}$. The reduction of $^{201}Tl^{3+}$ to $^{201}Tl^{+}$ was carried out by bubbling SO_2 gas through the mother PbEDTA solution until a pH~3 is attained. Post reduction, the pH of reduced $^{201}Tl^{+}$ in mother PbEDTA solution was adjusted to ~ 5.4 by using 1 N NaOH. The mother PbEDTA solution containing $^{201}Tl^{+}$ was passed through Dowex 50W-X8 resin (100-200 mesh, H^+ form) chromatographic column. $^{201}Tl^{+}$ was adsorbed in the column while PbEDTA was collected as eluate in waste flask. The adsorbed $^{201}Tl^{+}$ was eluted from cation exchange chromatographic column using 15 ml of 6 N HCl. Further $^{201}Tl^{+}$ was oxidized to $^{201}Tl^{3+}$ using ozone. Solvent extraction of $^{201}Tl^{3+}$ from aqueous phase (HCl) to organic phase (DIPE) was carried out utilizing 20 ml DIPE (DIPE saturated with 6 N HCl). Reduction of $^{201}Tl^{3+}$ to $^{201}Tl^{+}$ was carried out by SO_2 gas in aqueous phase (0.005N HCl). Post reduction, $^{201}Tl^{+}$ was back extracted into 20 ml of 0.005N HCl. After successful removal of DIPE from aqueous phase, finally 201TlCl ($^{201}Tl^{+}$ form, in 0.005N HCl) was collected. pH of ^{201}TlCl was adjusted to 6 - 7 using 1N NaOH and was diluted with 0.9% NaCl. ^{201}TlCl (in 0.9% NaCl) was filtered with sterile pyrogen free 0.20 µm PES membrane syringe filter. ^{201}TlCl ($^{201}Tl^{+}$ form) solution obtained was assayed for radioactive concentration and suitable activity was dispensed into sterile pyrogen free glass vials for supply.

The entire operation was carried out in aseptic environment using ultrapure grade chemicals and sterile and pyrogen-free glassware to ensure the purity (radionuclide, radiochemical and chemical), sterility and apyrogenicity of the product. The physicochemical quality control and BET assay was completed prior to supply of the product. Sterility was initiated within the same day of production. Following the revised configurations and the designed steps, the script was accordingly modified. The whole process of chemical separation and purification has been carried out in GMP certified hot cell and semi-automated radiochemistry module under aseptic environment for efficient, rapid and easy handling.

FIG. 16. Thallium Chemistry hotcell with Tl-chemistry module

FIG. 17. Thallium Chemistry External Panel: computer-based controller system

2.2.3. Quality Control Results

- The radiochemical purity of ^{201}TlCl was 100% (PC method) (Fig. 18).
- The metal content of ^{201}TlCl (Fe, Cu and Tl) were within the specified values.
- The Bacterial Endotoxin in ^{201}TlCl was < 6 EU/ml (PTS method).
- The residual solvent DIPE in 201TlCl was within the specified value (GC method) (Fig. 19).
- The radionuclidic purity of 201Tl was > 99% (determined by HPGe) (Fig. 20).
- Each batch were evaluated for sterility test and each batch passed the sterility test.
- PECT-CT scan of ^{201}TlCl was carried out in NH Rabindranath Tagore, International Institute of Cardiac Sciences, Kolkata (Fig. 21).
- Results are shown in Table 2.

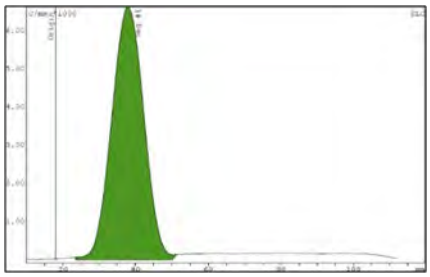

FIG. 18. PC spectra of ^{201}TlCl

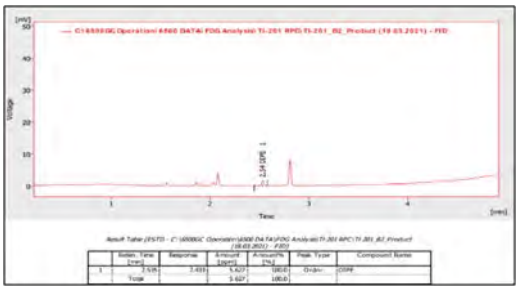

FIG. 19. GC spectra of ^{201}TlCl

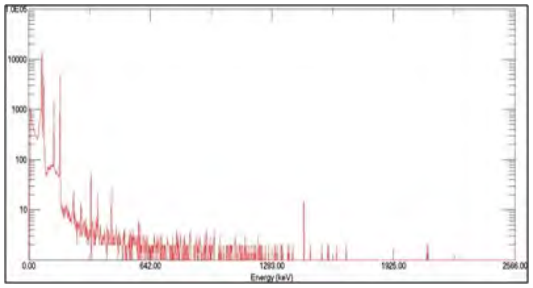

FIG. 20. HPGe spectra of ^{201}TlCl

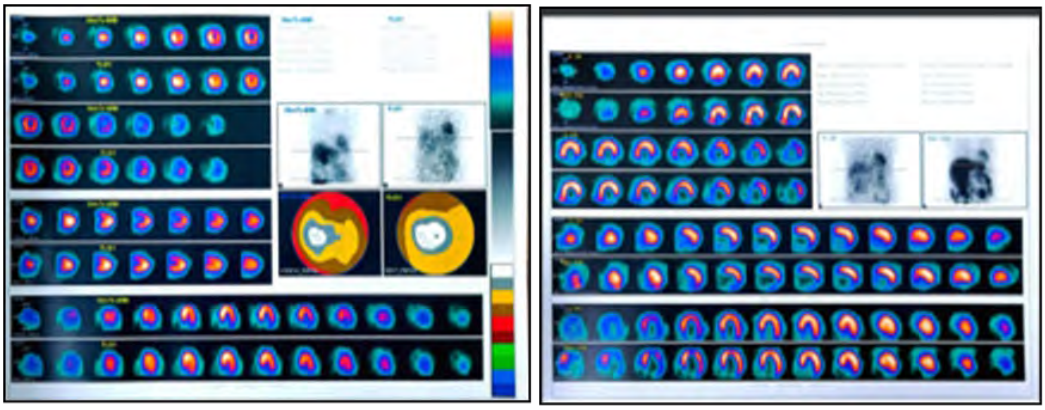

FIG. 21. Two cardiac studies (Rest-Stress on 18/12/2021 for ischemia evaluation and rest only for viability assessment on 20/12/2021) using GE Discovery 670DR SPECT-CT scanner in patients for suspected coronary artery disease evaluation: A comparison between ^{201}TlCl vs ^{99m}Tc-MIBI performed on same patients.

TABLE 2. PHYSICOCHEMICAL AND BIOLOGICAL QUALITY CONTROL TESTS OF ^{201}TlCl

Batch no.	Appearance	pH	Half life (hrs)	RC Purity (%)	RN Purity (%)	Fe (Fe^{2+}) µg/ml)	Cu (Cu^{2+}) µg/ml)	Tl (Tl^{+}) µg/ml)	BET test (<6 EU/ml)	Sterility test
1	Clear solution	5.0	73.68	100	99.79	< 3	BDL	< 2	Passed	Passed
2	Clear solution	6.0	73.20	100	99.98	< 3	BDL	< 2	Passed	Passed
3	Clear solution	5.0	73.08	100	99.88	< 3	BDL	< 2	Passed	Passed
4	Clear solution	6.5	73.57	100	99.85	< 3	BDL	< 2	Passed	Passed
5	Clear solution	5.0	73.08	100	99.80	< 3	BDL	< 2	Passed	Passed
6	Clear solution	5.5	73.18	100	99.82	< 3	BDL	< 2	Passed	Passed

2.3. Indigenous module for $^{68}GaCl_3$ radiochemical and ^{68}Ga-PSMA-11 radiopharmaceutical synthesis

2.3.1. Irradiation of the target

Irradiations of the electrodeposited (~ 94.5 – 95.5 µm) ^{68}Zn targets (Fig. 22) were carried out with the 15MeV proton beam of up to 60µA for 25 minutes (n=6) at 6° angle. During the irradiation the target assembly was water cooled with a flow rate of 9 liter/min. Beam current/charge deposited on the target was monitored with a current integrator.

2.3.2. Dissolution of the irradiated gallium target and separation of ^{68}Ga from ^{68}Zn

The original script for the Ga-67 chemistry was supplied by VUB for production of Ga-67 radiochemical and thus required modifications while working on our system. Beam energy was accordingly adjusted to obtain Ga-68 in curie quantity.

FIG. 22. Electroplated Zinc-68 targets

FIG. 23. Module for $^{68}GaCl_3$ and ^{68}Ga-PSMA-11 synthesis

2.3.3. Production of $^{68}GaCl_3$ radiochemical

Irradiated target was placed in the dissolution unit of automated radiochemistry module (Fig. 23) using master-slave manipulator. It was then dissolved using 20 ml of 10 N HCl (containing 100 µL H_2O_2). The enriched ^{68}Zn and carrier free Ga rapidly dissolved in this medium. Upon complete dissolution of the target material, about ~ 10 mg of Cu from Cu backings was co-dissolved. Dowex 50W-X8 resin (100-200 mesh, H^+ form) was packed in column (dimension of column: 1.33 cm2 internal cross section area x 6 cm height). The column was preconditioned with 40 ml of 9 N HCl at a flow-rate of 2.0 ml / min. Separation of ^{68}Ga from Cu and ^{68}Zn was carried out by cation exchange chromatography using preconditioned Dowex 50W-X8 resin column (100 - 200 mesh, H^+ form). Stripping solution was applied to the chromatographic column at a flow-rate of 1.7 ml / min. The ^{68}Ga is adsorbed quantitatively, while the Cu and ^{68}Zn pass into the storage flask (68Zn recovery storage flask). Interstitial Zn and Cu was removed from the column with 25 ml of 9 N HCl. ^{68}Ga was eluted with 20 ml of 3.75 N HCl from the column and the eluate is collected in extractor present inside radiochemistry module. Concentration of HCl was adjusted prior to extraction of ^{68}Ga in DIPE for optimum extraction. 7 N HCl is the optimum concentration of HCl for ^{68}Ga extraction from HCl into DIPE. In extractor (containing ^{68}Ga eluate), 20 ml of 10 N HCl was added so as the concentration of HCl increases from 3.75 N to 7 N. Solvent extraction of ^{68}Ga from HCl to DIPE takes place by introducing 15 ml DIPE (DIPE saturated with 7N HCl) to extractor. Both the layers {aqueous (HCl) and organic(DIPE)} were mixed by bubbling N_2 gas through the aqueous layer. Post separation of both the phases, the HCl layer was transferred to waste-flask inside the radiochemistry module.

2.3.4. Preparation of $^{68}GaCl_3$ radiochemical

Back extraction was performed with DIPE in extractor after addition of 10 - 20 ml of 0.005N HCl. Finally, 0.005 N HCl layers was collected in the $^{68}GaCl_3$ flask inside radiochemistry module, whereas DIPE phase was transferred to the waste flask inside the radiochemistry module. Traces of DIPE was removed from ^{68}GaCl3 solution present in the flask and homogenization of the content was carried out by bubbling N_2 through the solution for 5 minutes at 90°C.

2.3.5. Synthesis of ^{68}Ga-PSMA-11 radiopharmaceutical

Radiolabelling was performed by adding buffer + peptide (PSMA-11, 100 µg) mixture (3 ml) to the reaction vial and heating for 10 mins at 95°C. 3 ml water for injection was added to the reaction vial. The mixture was passed through C-18 column and the waste was collected in the waste vial. 3 ml water for injection was again added to wash the C-18 column; collected in the waste vial. ^{68}Ga-PSMA-11 was eluted from the C-18 column using 3 ml 50% (v/v) EtOH and collected in the product vial containing 5 ml 0.9% saline. Column was washed with 2 ml water for injection and collected in the product vial.

2.3.6. Dispensing of ^{68}Ga-PSMA-11 radiopharmaceutical

The resultant ^{68}Ga-PSMA-11 radiopharmaceutical solution was filtered using sterile pyrogen free 0.20 µm PES membrane syringe filter. Small aliquots (0.5 ml) of clinical grade ^{68}Ga-PSMA-11 solution was dispensed into sterile, pyrogen-free glass vials using the automatic dispensing system as per customer requirement. The glass vials were sealed with 25 KGy γ irradiated, sterile, pyrogen-free bromobutyl rubber closures and crimped with aluminum caps (pre swabbed with 70% ethanol). The sealed glass vials were transferred to a cylindrical lead container (LP-30), surrounded by thermocol and placed inside an outer container made up of HDPE (TPPL-1) and sealed before being dispatched to hospitals.

The entire operation was carried out in an aseptic environment using ultrapure grade chemicals and sterile and pyrogen-free glassware to ensure the purity (radionuclide, radiochemical and chemical), sterility and apyrogenicity of the product. Physico-chemical and biological quality control of [^{68}Ga]Ga-PSMA-11 were optimized and carried out and they are in accordance with USP monograph, International Pharmacopeia and Indian Pharmacopeia. The clinical results from PET-CT Cardiac studies performed at Netaji Subhas Chandra Bose Cancer Hospital, AMRI Hospitals (Dhakuria), Command Hospital (Eastern Command, Alipore Road), Kolkata add support to the use of our ^{68}Ga-PSMA-11 as a pharmaceutical grade diagnostic radiopharmaceutical.

2.3.7. Quality Control Results

- The radiochemical purity of $^{68}GaCl_3$ was ≥ 99.9% (TLC & HPLC method) (Fig. 24 and Fig. 25).
- The residual solvent DIPE in $^{68}GaCl_3$ was within the specified value (GC method) (Fig. 26).
- The radionuclidic purity of ^{68}Ga was > 98% (determined by HPGe) (Fig. 27).
- The radiochemical purity of ^{68}Ga-PSMA-11 was ≥ 95% (TLC, PC & HPLC method) (Fig. 28, Fig. 29 and Fig. 30).
- The metal content of $^{68}GaCl_3$ (Fe, Cu and Zn) were within the specified values.
- The Bacterial endotoxin in $^{68}GaCl_3$ and ^{68}Ga-PSMA-11 was < 5 EU/mL (PTS method).
- Each batch were evaluated for sterility test and each batch passed the sterility test.
- A typical PET-CT scan of ^{68}Ga-PSMA-11 of a patient diagnosed with prostate carcinoma is given below (Fig. 31).
- Results are shown in Table 3.

TABLE 3. PHYSICOCHEMICAL AND BIOLOGICAL QUALITY CONTROL TESTS OF $^{68}GaCl_3$

Batch no.	Appearance	pH	Half life (min)	RC Purity (%)	RN Purity ^{68}Ga (^{67}Ga) (%)	Fe µg/ml	Cu µg/ml	Zn µg/ml	BET test (<3 EU/ml)	Sterility test
1	Clear solution	< 2	69	100	99.95 (0.05)	< 3	BDL	BDL	Passed	Passed
2	Clear solution	< 2	69	100	99.89 (0.11)	< 3	BDL	BDL	Passed	Passed
3	Clear solution	< 2	69	100	99.85 (0.15)	< 3	BDL	BDL	Passed	Passed
4	Clear solution	< 2	69	100	99.97 (0.03)	< 3	BDL	BDL	Passed	Passed
5	Clear solution	< 2	69	100	99.81 (0.19)	< 3	BDL	BDL	Passed	Passed
6	Clear solution	< 2	69	100	99.83 (0.17)	< 3	BDL	BDL	Passed	Passed

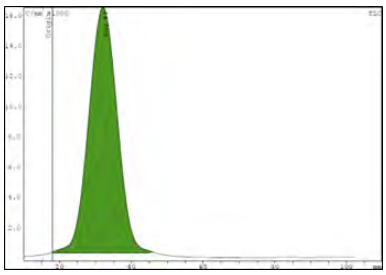

FIG. 24. TLC spectra of $^{68}GaCl_3$

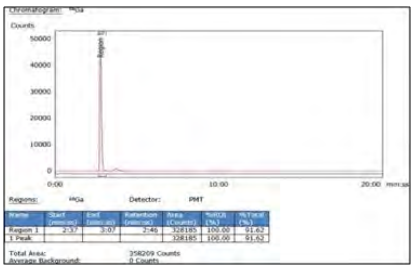

FIG.25. HPLC spectra of $^{68}GaCl_3$

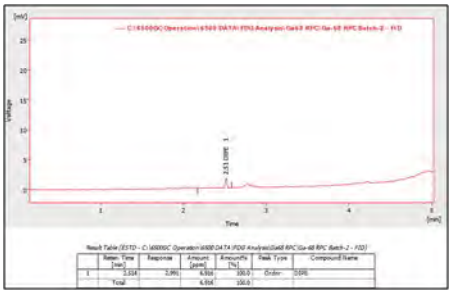

FIG. 26. GC spectra of $^{68}GaCl_3$

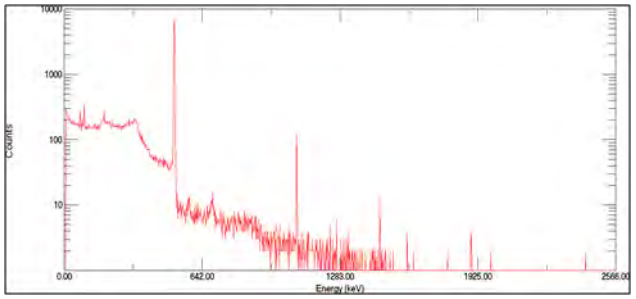

FIG. 27. HPGe spectra of $^{68}GaCl_3$

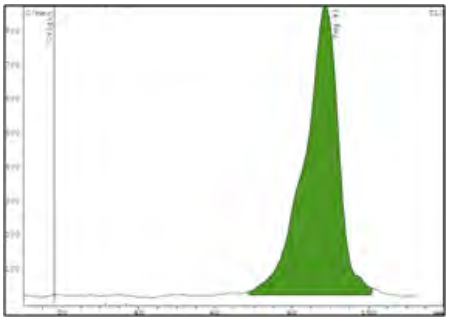

FIG. 28. TLC spectra of [^{68}Ga]Ga-PSMA-11

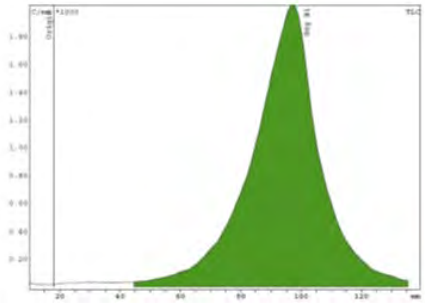

FIG. 29. PC spectra of [68Ga]Ga-PSMA-11

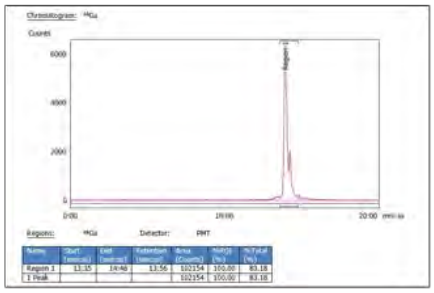

FIG. 30. HPLC spectra of [68Ga]Ga-PSMA-11

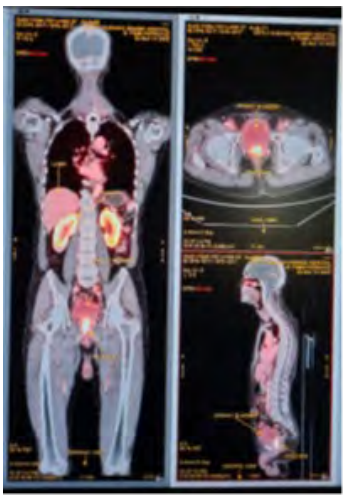

FIG. 31. PET-CT image of [68Ga]Ga-PSMA-11

ACKNOWLEDGEMENTS

The authors acknowledge Director VECC, Dr. Sumit Som for his support and Nuclear Medicine Centres in Kolkata for participation in clinical studies. The authors also acknowledge Ms. Shayantani Ash, Dr. Sujata Saha Das, Ms. Luna Barua, Mr. D. G. Mahesh, Mr. Samarjit Singha, Ms. Madhusmita, Mr. Umesh Kumar and Md. Nayer Alam for their contribution to this work.

REFERENCES

[1] MEYER, G.J., MATZKE, K.H., HAMACHER, K., FUCHTNER, F., STEINBACH, J., NOTOHAMIPRODJO, G., ZIJLSTRA, S., The stability of 2-[F]fluoro-deoxy-D-glucose towards epimerisation under alkaline conditions. Applied Radiation and Isotopes, Volume 51, Issue 1 (July 1999) 37-41.

[2] RIJIN, CJSV., HERSCHEID, JCM., VISSER. GWM., HOEKSTRA. A., On the stereoselectivity of the reaction of [18F]acetylhypofluoride with glucals. International Journal of Applied Radiation and Isotope. (1984) 36:111– 115.

[3] LEBOWITZ, E., GREENE, M. W., FAIRCHILD, R., BRADLEY-MOORE, P. R., ATKINS, H. L., ANSARI, A. N., RICHARDS, P., BELGRAVE, E., Thallium-201 for medical use. I. Journal of Nuclear Medicine. (1975) 16(2),151-155.

[4] SCHWAIGER, M., MELIN, J., Cardiological applications of nuclear medicine. THE LANCET (1999) 354, 661-666.

[5] MIKOLAJCZAK, R., GARNUSZEK, P., Radiopharmaceuticals in cardiology. Nuclear Medicine Review. 15(1), (2012) 39–45.

[6] QAIM, S. M., WEINREICH. R., OLLIG. H., 1979. Production of ^{201}T1 and ^{203}Pb via proton induced nuclear reactions on natural thallium. International Journal of Applied Radiation and Isotope. (1979) 30(2), 85-95.

[7] USP Monographs: Thallous Chloride Tl-201 Injection. 2008. USP29-NF24. Page 2108.

[8] Cyclotron Produced Radionuclides: Physical Characteristics and Production Methods. IAEA-TRS-468. IAEA, Vienna, (2009).

[9] VELIKYAN, I., ^{68}Ga-based radiopharmaceuticals: production and application relationship. Molecules 20 (2015) 12913–12943.

[10] [10] RAHBAR, K., et al, German multicenter study investigating ^{177}Lu-PSMA-617 radioligand therapy in advanced prostate cancer patients. Journal of Nuclear Medicine 58 (2017) 85–90

[11] AMOR-COARASA, A., SCHOENDORF, M., MECKEL, M., VALLABHAJOSULA, S., BABICH, J.W., Comprehensive quality control of the ITG ^{68}Ge/^{68}Ga generator and synthesis of ^{68}Ga-DOTATOC and ^{68}Ga-PSMA-HBED-CC for clinical imaging. J. Nucl. Med. 57, (2012) 1402–1405.

[12] BANERJEE, S.R., POMPER, M.G., Clinical applications of gallium-68. Applied Radiation and Isotopes 76, (2013) 2–13.

[13] OBERG, K., Gallium-68 somatostatin receptor PET/CT: is it time to replace ^{111}Indium DTPA octreotide for patients with neuroendocrine tumors? Endocrine 42, (2012) 3–4.

[14] SCHWENCK, J., REMPP, H., REISCHL, G., KRUCK, S., STENZL, A., NIKOLAOU, K., PFANNENBERG, C., LA FOUGERE, C., Comparison of ^{68}Ga-labelled PSMA-11 and ^{11}C-choline in the detection of prostate cancer metastases by PET/CT. Eur. J. Nucl. Med. Mol. Imaging 44, (2017) 92–101.

[15] TIROSH, A., KEBEBEW, E., The utility of ^{68}Ga-DOTATATE positron-emission tomography/computed tomography in the diagnosis, management, follow-up and prognosis of neuroendocrine tumors. Future Oncol. 14, (2018) 111–122.

[16] ALVES, F., ALVES, V.H., NEVES, A.C.B., DO CARMO, S.J.C., NACTERGAL, B., HELLAS, V., KRAL, E., Gonçalves-Gameiro, C., Abrunhosa, A.J., 2017. Cyclotron production of Ga-68 for human use from liquid targets: from theory to practice. AIP Conf. Proc. 1845, 020001 https://doi.org/10.1063/1.4983532

[17] BLASER, J.P., BOEHM, F., MARMIER, P., PEASLEE, D.C., Fonctions d'excitation de la reaction (p, n). (I). Helv. Phys. Acta 24, (1951) 3–38

[18] HOWE, H.A., (p, n) cross sections of copper and zinc. Physical. Review. (1958) 109, 6–8.

[19] SZELECSENYI, F., BOOTHE, T.E., TAKACS, S., TARKANYI, F., TAVANO, E., 1998. Evaluated cross section and thick target yield data bases of Zn + p processes for practical applications. Applied Radiation and Isotope 49, (1998) 1005–1032.

[20] International Atomic Energy Agency. Gallium-68 Cyclotron Production. IAEA-TECDOC-1863. IAEA, Vienna, (2019).

[21] SADEGHI, M., KAKAVAND, T., RAJABIFAR, S., MOKHTARI, L., RAHIMI-NEZHAD, A., Cyclotron production of ^{68}Ga via proton-induced reaction on ^{68}Zn target, Nukleonika 54 (2009) 25.

[22] BOIS, F., NOIROT, C., DIETEMANN, S., MAINTA, I. C., ZILLI, T., GARIBOTTO, V., WALTER, M. A., [^{68}Ga]Ga-PSMA-11 in prostate cancer : a comprehensive review. Am J Nucl Med Mol Imaging 10(6), (2020) 349-374.

REVIEW OF 20 YEARS OF INDUSTRIAL APPLICATIONS OF ION BEAM AND RADIATION TECHNIQUES

L. POPA-SIMIL
LAVM llc
Los Alamos, USA
Email: lps@lavmllc.com

Abstract

The present work summarizes the applicative researches performed during 1978s and 2006s in Romania using Ion beam based technologies, radiation based technologies and many other measurement techniques to characterize various technological objects as engines, gear boxes, pumps, tools and materials with emphasis on material loss vs. performances. Tribology studies were performed together with material studies, and assembly performances using a large variety of measurement methods and devices. In order to improve speed and accuracy of tribology thin and Ultra-Thin Layer Activation (U-TLA) method have been used producing a radioactive layer on a selected surface of a technological part, measured for quality assurance with auto-radiography and spectroscopy. The part was mounted in the installation and its radioactivity decrease faster than the natural decay was considered to be due to material loss by wear, corrosion or abrasion.

Measuring in real time all operational parameters opens possibility of determining inter-correlations among them, and improves quality of information obtain by testing. During this 20+ y period several hundred experiments have been performed and testing procedure have been gradually developed following quality assurance principles, being transformed into a turn-key procedure, with clear steps, stages, control means and methods, integrating other nuclear and non-nuclear technologies. Methods as XRF, PIXE, RBS, UTLA, NAA, Gama Spectrometry, were integrated with optical, acoustical, mechanical and electrical methods using automated data acquisition, computer processing and results interpretation, benchmarking the computer simulation and using lessons learned for further improvements, following a spiral of evolution. The results were outstanding, assuring industrial customer with the capability to shorten the time from design to market, cheaper and more accurate than with usual methods which were integrated in the measurement process, together with quality assurance tests, increasing the market competitiveness. This activity ended after 2000 due to drastic decay in demand during EU integration.

1. INTRODUCTION

The beginning of tribology one may be considered by year 1900BC during Djehutihotep reign, is known best for the famous decoration inside his tomb that represents the transport of a colossal statue of him that was nearly 6.8 metres (22.3 ft) high, 58 t being transported by 172 workers using ropes and a slide, in an effort that is facilitated by pouring water in front of the slide.

1.1. Brief history

By 1943Ferris, is patenting a method to measure material loss using radioactive tracers [1], and since late 1960's neutron activation was used, in spite of its disadvantage of making the labelled parts highly radioactive.

Starting from 1960s, with Cyclotrons started to be used in these tribology applications [2], because of the opportunity to create a thin layer of radioactive material, labelling surfaces of interest for tribology, only and drastically reducing overall part's radioactivity, and implicitly gaining several orders of magnitude in sensitivity and easiness of operation. Renowned nuclear laboratories as KFK [3] and Harwell [4] pioneered the field

By 1977 NIPNE-HH Cyclotron was directed to develop economic contracts to accelerate industrial development by knowledge transfer in joint studies. Staring by 1978 under the leadership of Dr. Ivanov and Plostinaru, Phys. Petru Racolta started a new group aiming to TLA development and pursuing applications in economy. For the beginning the Accelerator Applications group started with the development and homologation of the nuclear method and meanwhile performing incipient studies of wear to industrial research institutes [5-7], as seen in FIG. 1,2. By 1981 he was granted a research stage at KFK Cyclotron, where Dr. Herman Schweickert introduced him to their approach in labelling and tribology related measurement that stimulated his imagination and inspired him in the future work, having KFK as a model. The work environment in Romania was different, from Germany, and he had to improvise and bridge many gaps to get practical results. The early studies started with feasibility tests on rotation of piston rings inside a ICE (Internal Combustion Engine) and lubricant characterization [8] and by 1987 Dr. Racolta sustained his PhD. Dissertation work [9].

The NIPNE-Cyclotron Application group developed, and by 1984, I was admitted in, developing engine related applications [10-12]. These researches have been developed in cooperation with specialists from Machines Building Industry and R&D units as Polytechnic Institute, Universities, Engine and hydraulic equipment research groups.

1.2. TLA/UTLA project evolution

The research development was random, based on the research contracts and interest of various industrial partners, but was coherent into setting in place all needed pieces of knowledge and procedures as finally to obtain a "turn-key", service performed following Quality assurance norms.

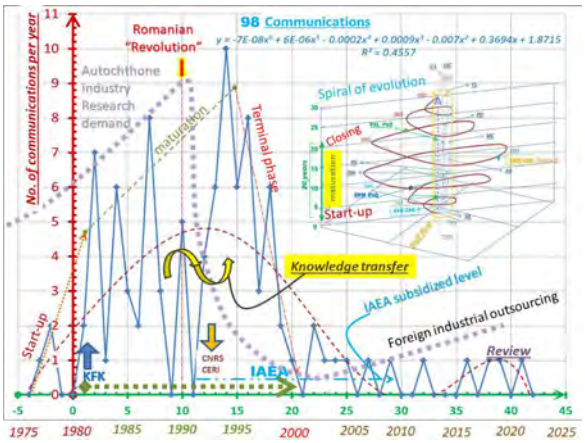

FIG. 1 Life-cycle of the TLA project

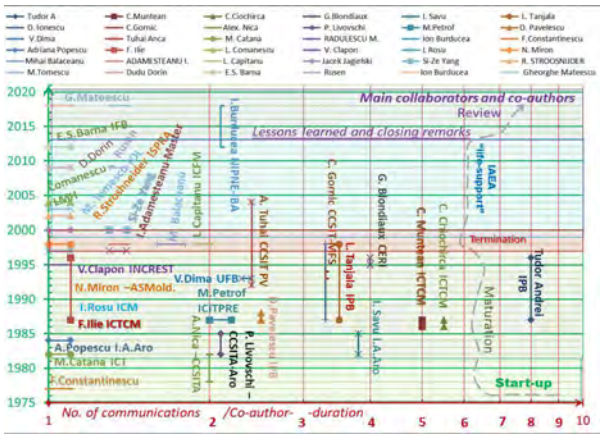

FIG. 2 Main collaborators and project phases map

During 1980s, maturation phase was reached, the method was diversified and applied to a wide range of materials and applications, research team was stable and reached up to 6 researchers at Cyclotron accelerator only, working in interdisciplinary teams with industrial partners, involving technicians also[13,14]. During mid 1980s complementary ion based Analysis (IBA) methods as XRF, PIXE, CPAA and RBS were added complementary [15, 16]. The interest for micro and nano particles analysis in filtration systems and other fluid environments was, addressed in almost every experiment [17], and many communications was made, having many industrial research collaborations as seen in FIG. 1,2. UTLA technique was gradually developed up to mid-1990's [18] as recoil was used for sub-micron surface labelling and for isotope production self-separation in heterogeneous structures. IAEA supported our research efforts with research grants for wear of industrial parts, and characterization of material surface hardening by ionic implantation. BY 1993, we boosted CNRS-CERI activities in the field, during a reciprocal know-how exchange stage.

1.2.1. Charged particles Thin Layer Activation dimming and final stages

Starting from 1990 the Romanian industry started its decay, on the premises of industrial equipment scrap & salvage in a wild capitalism as preliminary stage for European Integration mainly as a consumption market as it is today. The decay in the industry was reflected in decay in the demand for new research that continued up to 2000 aggravated by the "brain drain", where most of the researchers left to do "programmatic work" in western laboratories. In spite the method reached the "turn-key", stage with a high level of quality assurance, the industrial research demand plummeted.

After Romania's integration in the European Union, the TLA method was applied to some fundamental researches in bio-medical devices, nano-tribology and calibrations of the method [19], mainly under "life-support" funds from IAEA, as seen in FIG.1. In the new context of global economy, based on very few manufacturers of originally, local researched products, the demand for such measurements drastically decreased, the domain becoming dormant where this domain qualified by government as an expensive service for private sector was not funded from research budgets, that has driven to an end of these activities and an opportunity for closing remarks and lessons learned.

2. TYPES OF APPLICATIONS

The "QA turn-key" test protocol presented before have been developed and used for each type of industrial or military application, being diversified and developed based on the previous work lessons learned. There are many applications developed over the time that were improved continuously following an evolution curve, and drawing near to complex application of quality standards.[13,14]

2.1. Thermal engines

Various ICE (Diesel and Otto) were studied with respect to improving the running-in, where was possible to bring cost avoiding to company, FIG. 3,4 and lubricant oil wear measurement and classification [10].

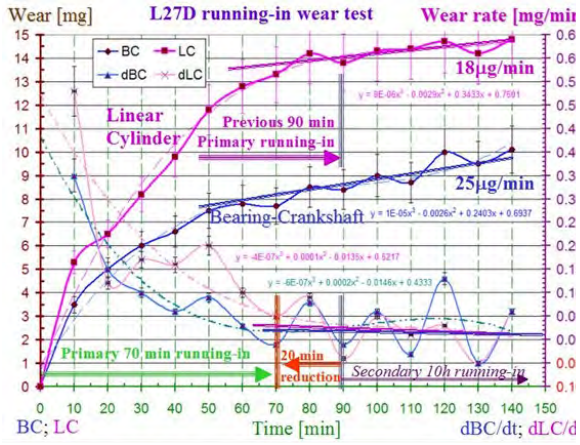

FIG. 3. The Crankshaft bearing and Cylinder liner wear measurement

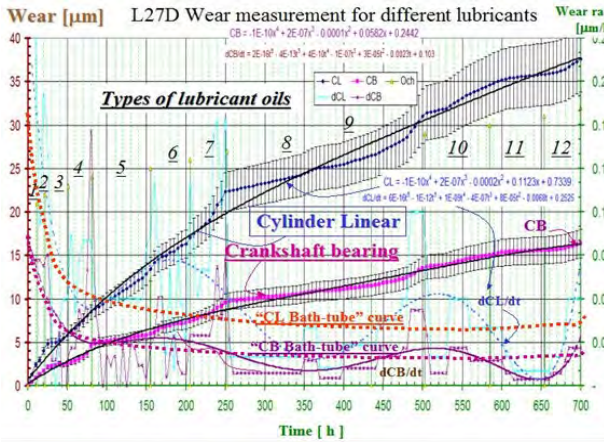

FIG.4 The wear of crankshaft bearing and cylinder liner as a function of running time

Engine operating life study and wear rate dependence on various operating parameters as revolution speed, torque, temperature in water and lubricant, lubricant consumption by burning in engine as function of torque and revolution speed [13,14].

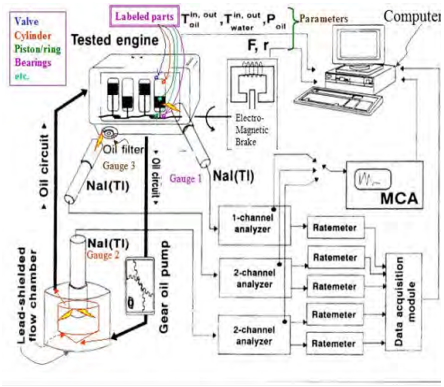

FIG. 5 Schematic block diagram of wear measurement by TLA

FIG. 6 The engine test bench – radiation detection setups, electronic control equipment and data acquisition

Various materials and surface treatments used for engine betterment as surface hardening by thermos-chemical treatments as annealing, nitration, boron implant etc., were tested over the time together with a large range of lubricants brands. Equipment evolution runs parallel with test programs developments, allowing us to reach high performances. General measurement scheme is seen in FIG.5, and a complex structure using 26 SCAs, 1 MCA and was measuring wear on 4 parts simultaneously measured in a 4' shielding low background detection system, with combined paper and data recording is shown in FIG.6, where the engine is placed on a test bench left outside the picture. Using the developed equipment in various applications basically we determined the charts briefly presented in FIG.7 where one may see the evolution of wear in the first 90 min. from start of a new engine measured with about 30 s response time, and ng/cm2 sensitivity. Then, in FIG.8 are presented the results for the

entire engine life measurements, (1-2 years 24/7), where all parameters are plotted as function of time and engine's dynamic parameters as (RPM, Torque, temperatures, pressures, flows, etc.). Various lubricant characterization and optimization are made, materials and surface's treatments optimization, is performed.

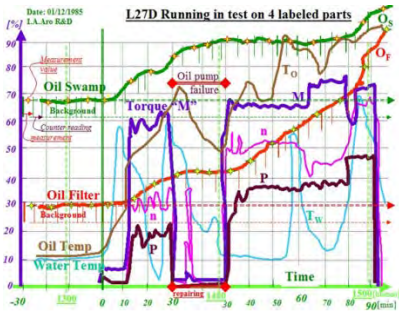

Fig. 7 real time running-in measurement the first 1.5h

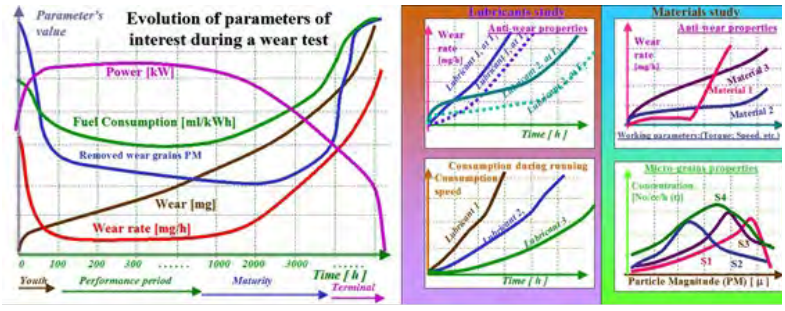

Fig. 8 Engine life-time wear measurements, lubricant and material surface characterization, wear particle magnitude

Using complementary methods as stack filtrations we obtained wear particle's dimensional distributions [14] resulted in various engine circumstances, and further by mili-PIXE and RBS we analysed elemental concentrations and combinations giving the right importance to corpuscular aspects, and related phenomena.

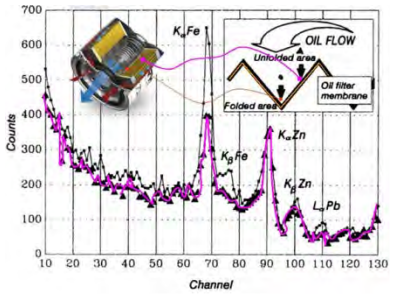

FIG.9 PIXE on an oil filter deposition

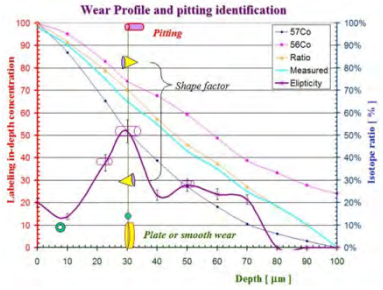

FIG. 10 – Pitting detection by double 13MeV d labeling

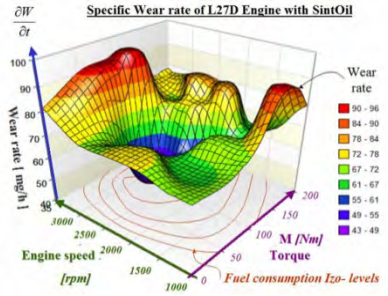

FIG.11 L27 Engine wear rate as function of Torque & RPM

FIG.9 shows that inside the oil filter the wear particle deposition is larger in the fold due to paper structure and lubricant flow modifications. In FIG.11 is presented a wear rate dependence on engine's RPM and torque, with engine regulated fluids pressure, temperature and flows. To detect the wear type in a surface 13MeV deuteron labelling is used, where by measuring the ratio between the 122keV and 847 keV gamma lines is possible to have a clue of the wear particle shapes and position during dislocation shown in FIG.10 [13].

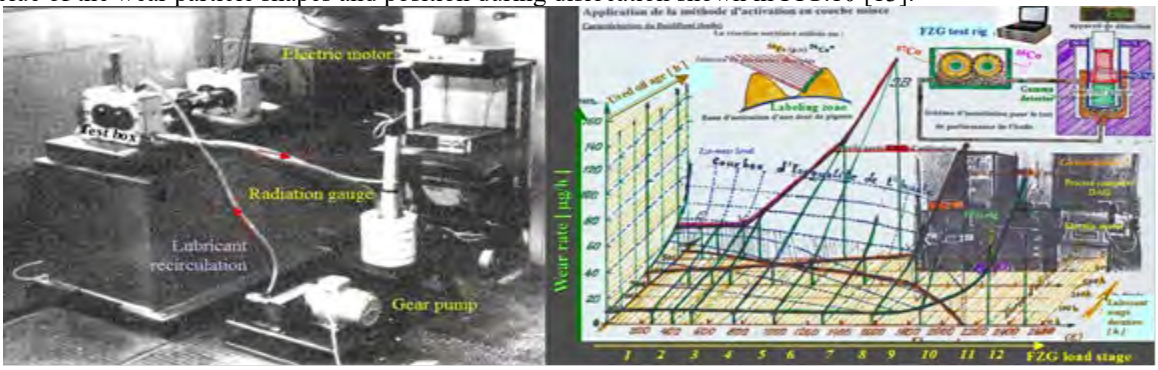

FIG.13 – Transmission lubricant scuffing pressure measurements.

2.2. Gears and mechanical transmissions were studied in various devices

Study of gear's tooth wear as a function of lubricant's scuffing properties, FIG.13 shows a FZG testbed modified for TLA and the results obtained in about 2 weeks to characterize the variation of the scuffing pressure at lubricant film breakdown with aging at a constant average temperature (red horizontal curve).

a. Worm gears' materials and operating regimes

b. Differential transmissions wear as function of torque and revolution speed,
c. Study of effect of geometric aberrations on differential wear at microbuses
d. Ferguson wet transmission wear made by XRF and TLA

2.3. c) Study of ball bearings and seals used in engines as:

a. Ball bearing fabrication dispersion induced wear
b. Rubber wear of flywheel seal

Gear measurements represented a large activity, studying the tribology aspects that included:

2.4. Study of lubricants for various applications as:

a. Lubricants used in gears using TLA enhanced FZG test rig for scuffing load tests
b. Lubricants used in engines as mineral and synthetic oils, additives, by measuring the wear of various engine parts, and
c. Lubricants consumption inside the thermal engine using tritium labelling

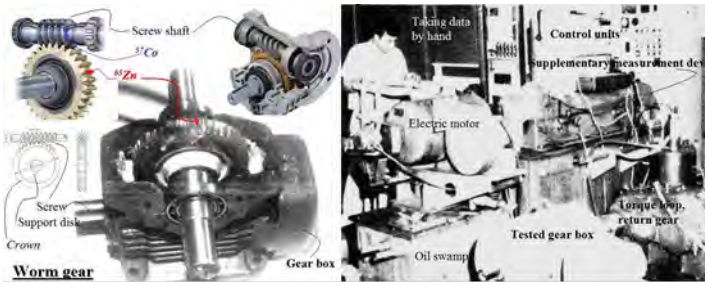

FIG.14 –Differential Worm gear details and measurement testbed

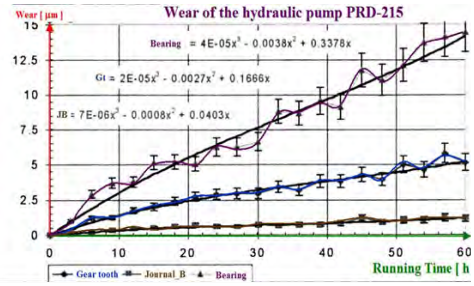

FIG.15 PRD hydraulic transmission pump wear rate

In FIG. 14 a worm-gear testbed is presented, and in FIG. 15 is given the wear of a hydraulic pump used in tanks hydraulic transmission on tooth front and back side and on the bearing.

2.5. Fundamental Material study on tribologic machines simultaneous with machine improvement by implementing computer control and TLA method as:

a. Timken machine was used to study
   i. Surface enhancement by thermo-chemical annealing
   ii. Wear Mechanism To Friction Contact Of Thermoplastic / Steel Couple
   iii. Metallic Surface's Wear Mechanism
b. Falex machine, used to study wear as well material transfer between parts in friction contact
c. Pin on disc
d. Four Ball Machine

In FIG. 16 there are given the results obtained measuring the material loss by 4 new methods not usually employed, because traditionally the wear is measuring by weighting the sample disc before and after the wear process. The upper left side is by differential autoradiography, underneath is by profile-meter, by TLA and by height of wheel lever. The most complete was the TLA which when desired the shapes of grains could be also known. The other 4 methods where added as supplementary controls in the novel computer controlled machine which had been built. The TLA chart shows the variation of wear with contact pressure too.

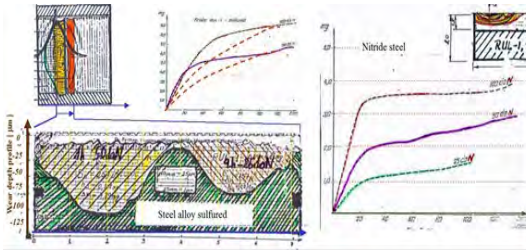

FIG.16 – Timken measurements

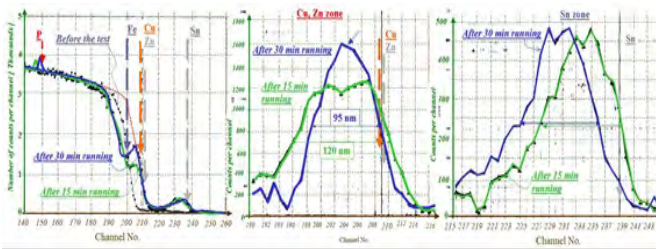

Fig. 17. Falex material transfer RBS measurements

An interesting fact that was shown in FIG. 17, is material transfer by wear. Measured by radioactivity as well by RBS, for a Falex machine using a bronze alloy the peaks of phosphorus (P), Iron (Fe), copper, zinc (Cu, Zn), and tin (Sn) that may be interpreted against Abbott roughness profiles. This result was much more than the researches expected, who were very happy with the measurement speed and accuracy only.

e. Technologic material loss in Fluid environments was studied for Diesel injection systems as Rotary pumps using nitride parts as cam, roles pistons, injectors pin and seat as function of flow and pressure as shown in FIG.18, running on a testbed shown in FIG. 19, testing gas and liquid nitriding material hardening.

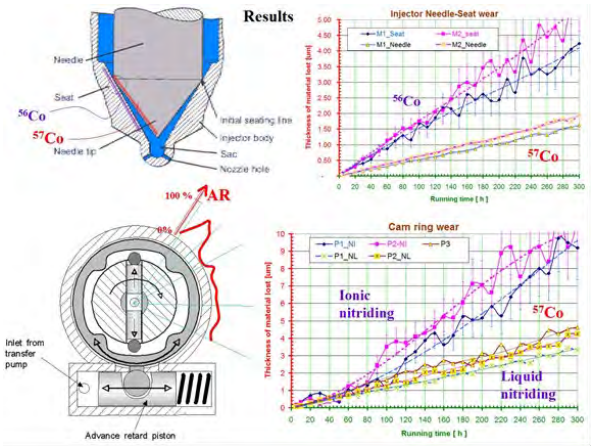

FIG.18 Diesel injector and rotary cam wear

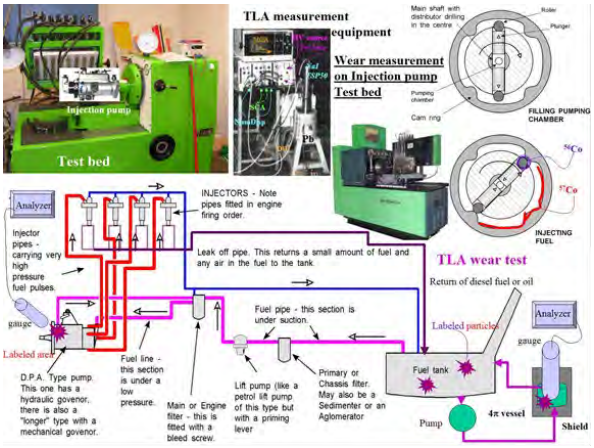

FIG. 19 TLA diesel injector testbed

f. Hydraulic equipment was studied as:

i. Water jet abrasion corrosion of steel and other materials for underwater applications

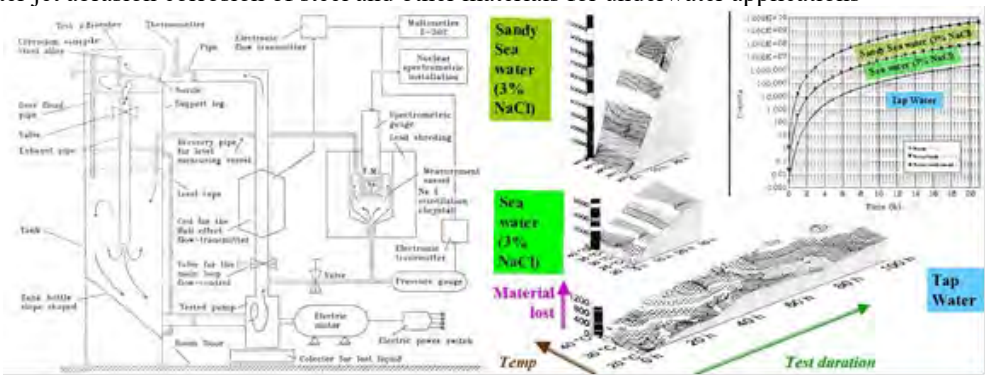

FIG.20 – Sand and salt loaded water jet corrosion abrasion testbed with measurement results on the right for water, salty water and sand loaded, salty water.

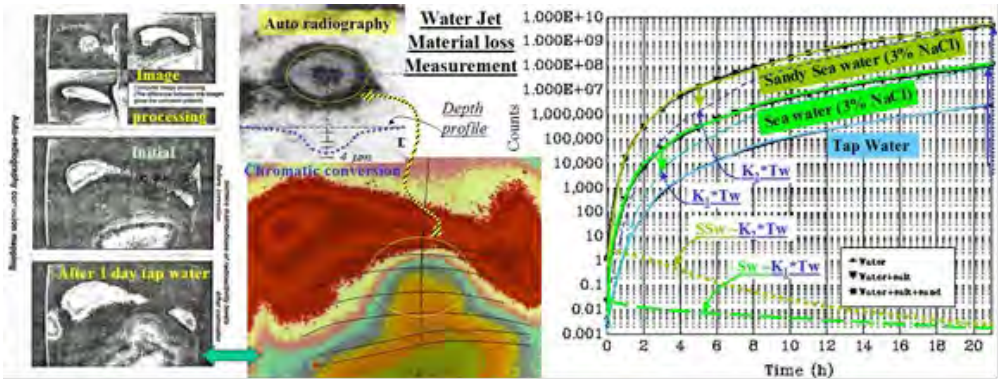

FIG.21. The use of auto-radiography method to profile wear density vs. TLA and profile measurement results for a steel blade in a water jet.

FIG.20 shows the water jet testbed that measures corrosion, abrasion in jet as function of liquid's temperature as shown in 3D charts on the right. In FIG. 21 there are presented the results using differential auto-radiography, for izo-level wear spot profiling vs. profile-meter. A 10 m/s, ϕ5mm water jet was applied 10 h on a steal plate leaving a corrosion-abrasion crater that was measured at the end, while during test remnant radioactivity measurements were performed continuously [13, 14].

ii. Cavitation enhanced corrosion in propellers and reversible pump-turbine devices

iii. Various hydro-transport pumps

A more complex testbed was made to optimize to wear and abrasion the internal profile of hydraulic equipment as centrifugal pumps and turbines running at smaller scale 1:5 or 1;10, and as function of the wear density results to modify profile as to obtain an optimum material loss density in order to preserve hydraulic parameters the entire operation life. FIG. 22 shows on the right a technician adjusting flow in the measurement testbed loop. The centrifugal pump's blades and disks were labelled with different radioisotopes ^{56}Co, ^{57}Co.

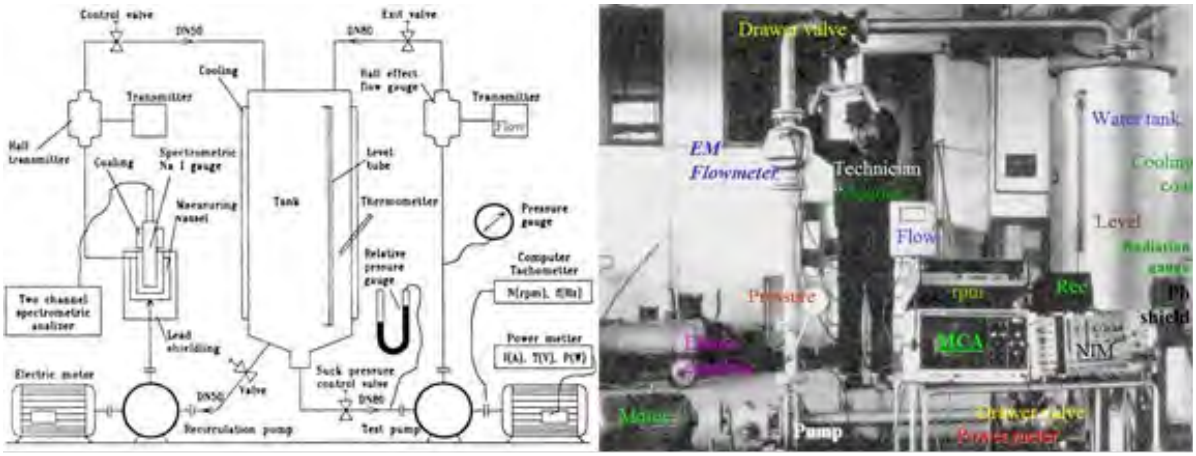

FIG.22 – The hydro-transport and reversible turbines TLA compatible testbed

FiG. 23,24 shows disk autoradiography in the middle chart the evolution of material loss along hydraulic tube.

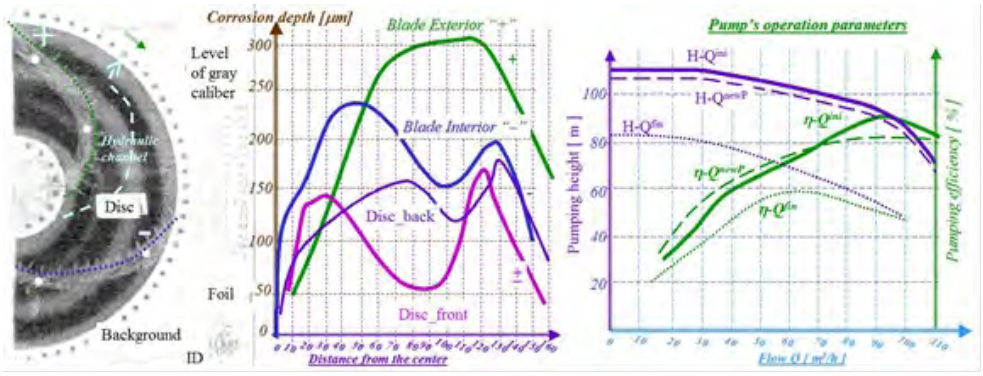

Fig.23 – TLA measurement results, along the profile along hydraulic channel by differential γ-spectroscopy and by remnant and concentration method correlated with pump's hydraulic parameters

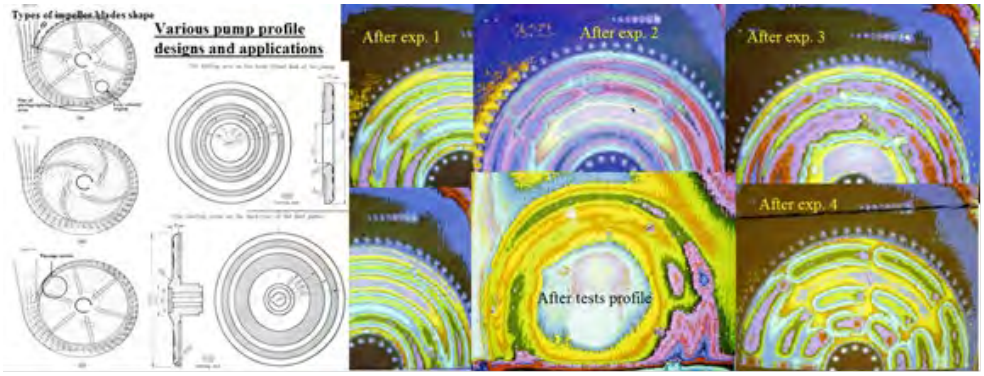

Fig. 24 – the use of differential auto-radiographic method to map the material loss surface density on disks in order to see its variation along hydraulic channel

A sample of the results is presented in Figs. 23,24 in order to show how the profile of hydraulic channel and material wall thickness was optimized in the process.

g. Behaviour of material in hot gases and plasma equipment as:

i. Gas inert generator and Gas turbines and nozzles material qualification

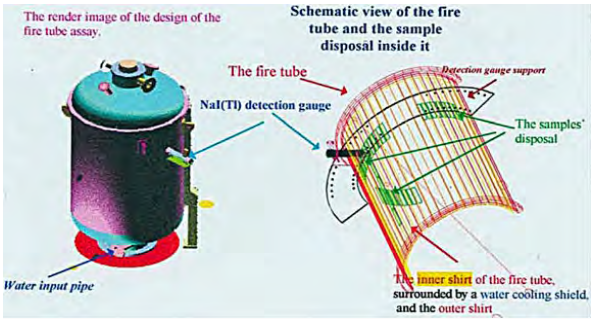

FIG.25 – Inert gas material testbed design

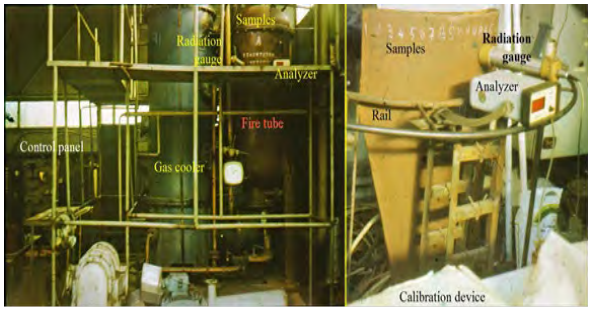

FIG. 26 Experimental testbed and calibration

The research had the purpose to produce advanced inert gas generators of maritime applications, and to test materials resilience in fire for gas turbines construction, as seen in FIG. 26, 27. The test bed was a complex structure as seen in FIG. 25, 26 that had the capability to test more than 20 samples simultaneously, based on advanced radiation interference and background calculations and cancelation. Research extended on 3 y.

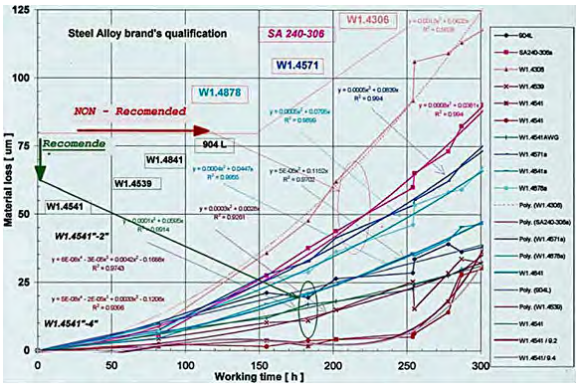

FIG.26 Material selection for fire resilience

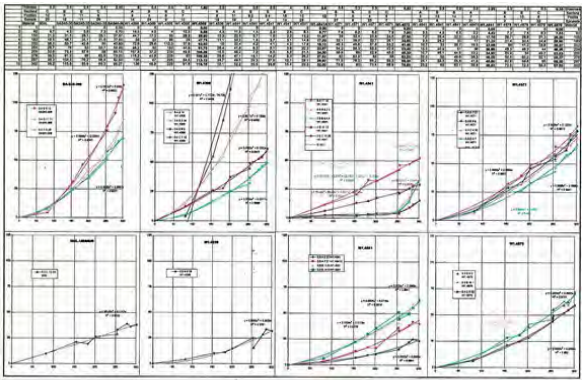

FIG. 27 – Comparative test results

h. Air exposed metals' corrosion, as depending on air pollution

i. Maritime oil extraction rig corrosion inside sea-to-sea floor

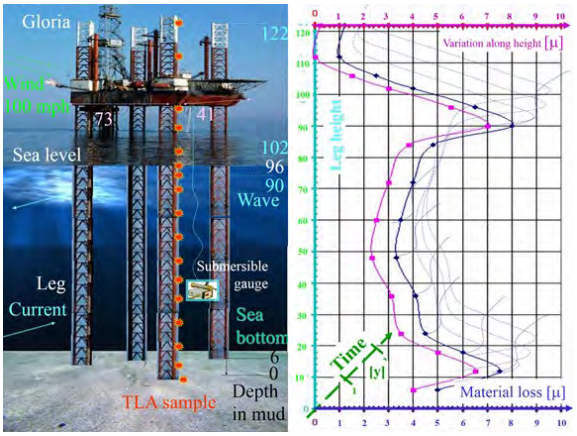

FIG.28 – Gloria leg corrosion test

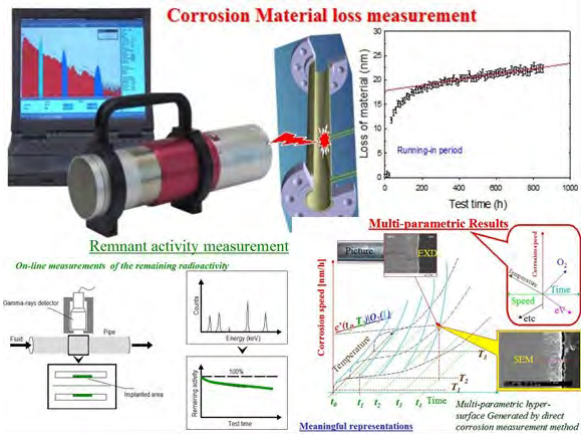

FIG. 29 – LBE corrosion measurement

FIG. 28 showed the setup of various steel samples placed with belts on the oil-rig in order to estimate the corrosion speed in the sea waters, while FIG. 29 shows the possible designed performances a TLA/UTLA setup may reach studying the corrosion speed in LBE (Lead Bismuth Eutectic) used at FBR (Fast Breeder Reactor) cooling. Other applications include liquid metal corrosion for fast breeder nuclear reactors.

Methodological aspects of UTLA technique were considered together with labelling process material's properties modifications, starting from the very beginning at measurement method homologation, and were improved all the time, based on the lessons learned after each experiment.

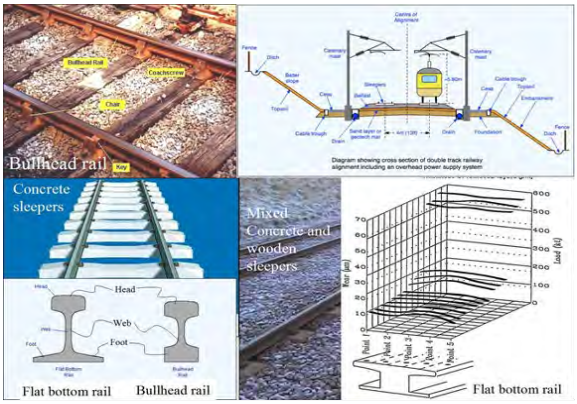

FIG. 30 - Rail top surface wear

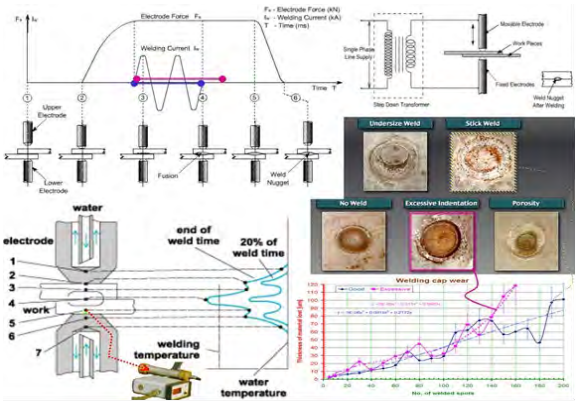

FIG. 31 – Resistive spot Welding cups wear

Military equipment gun barrels, tank engines were also analysed with interesting results, helping improve production quality. Wear in electric parts had a special attention as, spark plugs' material loss, breaker plots flash erosion, contactors rail trolley, resistive welding caps, etc.

Rail way wear measurement was performed as function of load and traffic FIG.30 shows the rail top surface wear as function of position and traffic load. And FIG. 31 shows the material loss in Cu-Be spot-welding inserts measured using a GM detector.

i. Tools material loss was an interesting application for lathe insert made of TiC synthetic materials.

Synthetic Basalt wear measurements in slides applications and study of influence of various machining process on material's surface composition

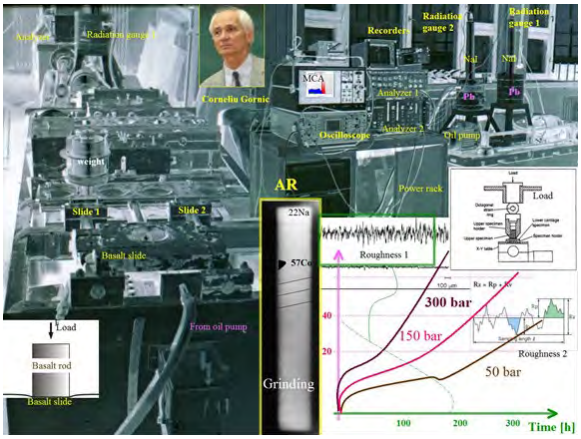

FIG. 32 – Basalt slide wear test

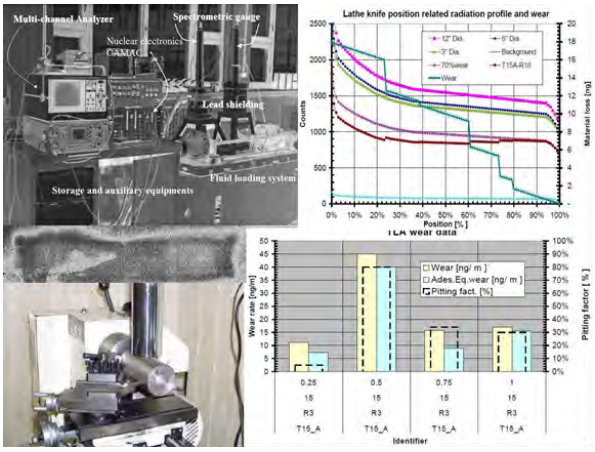

FIG. 33 – Lathe ceramic insert wear test

In FIG. 32 is presented the basalt slide wear test equipment and results as function of time and applied pressure, and in FIG. 33 one may see the measurements of the material loss in a lathe ceramic insert, made of TiC as function of time, position, removed material thickness for various ceramics compositions.

In fine mechanisms wear study by TLA was applied on cassette recorder head wear, dot/needle printer, sewing machines, and vacuum pumps tests. Technologic material loss in MEMS and NEMS was a subject for future developments. These applications were performed on regular basis and some of them as demonstration tests aiming to obtain contracts for continuous research.

3. CONCLUSIONS

The work on TLA started by 1977 and ended after 2010, was led by Dr. P. Racolta who has >80 communications, Dr. L.Popa-Simil with >55 communications and obtained the PhD on this domain, coordinated by Dr. E. Ivanov with >25 communications, and was based on more than 200 industrial research cooperation. The work has benefited from IAEA support, for developing and passing difficult moments, but its existence was dependent on the vigor of local industrial research, whose disappearance drove these works to an end. The main lesson learned

is that the high-tech, no matter its performances it is developed in the areas where there is both the culture and the need for using it, that makes the balance between demand and supply. For the period of applications the knowledge gain leaped forward the customers, creating a competitive edge, in an non-uniform development, with many drawbacks that finally pounded the activity, and showed that narrow, cutting edge knowledge is not enough to sustain and maintain a prosperous development of an activity, and all is submissive to general rules of competition in open markets. With IAEA's support at critical moments the TLA activity had a 20 years of prosperous evolution ending with the knowledge of a quality assured turn-key test and research procedure.

ACKNOWLEDGEMENTS

I am grateful to all of those with whom I have had the pleasure to work during this and other related projects. Each of the team members have provided me extensive personal and professional guidance and taught me a great deal about both scientific research and life in general. I would especially like to thank Dr. Petru Mihai Racolta, the team leader as my colleague and mentor and Acad. Dorel Bali my PhD supervisor, as he has taught me more than I could ever give him credit for here. He has shown me, by his example, what a good scientist and person should be. We are grateful for funding to AIEA and other sponsors of the research. Distinguished gratitude to our friend and mentor Dr. Herman Schveickert, from KFK Cyclotron, for his advices and life model, to Dr. Thierry Sauvage from CNRS-CERI, and to all our collaborators who supported the research and co-authored various papers over the time.

REFERENCES

[1] Ferris S.W., "Wear test method and composition", US. Pat. 2,315,845 Apr. 6, 1943.
[2] Kollmann, K., D. Stegemann: Use of radioactive isotopes for Research tasks in mechanical engineering, Kerntechnik 4, H.2 (1962) p. 41.
[3] Essig, G.: Physical-technical basics for wear measurements the thin film difference process, nuclear research center Karlsruhe, report KfK 2517 (1978).
[4] Conlon, T.W.: Thin Layer Activation by Accelerated Ions – Application to Measurement of Industrial Wear, Wear 29, H.1 (1974) pp. 69-80
[5] Nica A., Racolta P.M., "The application of a novel method using radioactivity to evaluate the wear of piston engines", Tribotehnica 78, p.763, Bucharest 1978.
[6] Racolta P.M., Nicuti E.,Ivanov E.A., "Method and measurement equipment using radioactive isotopes to control wear in closed lubricant circuits", Tribotehnica 82, p.381, Bucharest 1982
[7] Nica A., Racolta P.M., "Method and equipment for machine parts wear measurement using residual radioactivity differential method", Tribotehnica 82, p.227, Bucharest 1982
[8] Racolta P.M., Stan-Sion C., "Technologies of measurement using radioisotopes for automotive industry researches", Tribotehnica 84, p.423, Bucharest 1984.
[9] Racolta P.M., "Tribology applications of radio-isotopes embedded in metallic structures", Ph.D. Thesis, Institute for Atomic Physics, Bucharest, Ro., 1987
[10] Popa-Simil L., Savu I., "Wear studies on engine parts by radioactive tracers methods", Proceedings of 'The 5th Conference on "Research Activity in the Factory's Laboratory for Production, I.A.Aro Clmpulung-AG, Romania, Dec. 6-8,1983
[11] Popa-Simil L., Savu I., Livovschi P., Sfaraila V., "The study of engines' wear by thin layer activation method", Magazine of Machines Building, Nr.6, pg.333-340, Jun. 1985.
[12] Racolta P., Popa-Simil L., Ivanov E.A., "Method of study of the influences of the irradiation damages on metallic structures", Proceedings of Progress in Physics Meeting, Bucharest, July, 1987.
[13] POPA-SIMIL L., Real-Time, High-Performance Technologic Material Loss Measurement, Apple Books, (2016).
[14] POPA-SIMIL L., Measuring Corrosion Abrasion in Various Solid-Fluid Systems Using Nuclear Methods, Tribology, Prototyping (Accelerator industrial applications) Kindle Edition (2019)
[15] Constantin F., Constantinescu B., Dima S., Plostinaru D., Popa-Simil L., "Methods and Installations of elemental analyses of impurities using X-Ray Nuclear Techniques for determining the composition and percentage of the wear and corrosion products in oils, fuels and cooling waters", 'Studies and Researches on Physics Magazine 42/3, pg.311-319, Bucharest 1990.

[16] Racolta P.M., Popa-Simil L., Alexandreanu B., “Combined Use of PLXE and TLA for Material Loss Investigation”, 7th International Conference on PIXE and its Analitica1 Applications, Padua, Italy, May 26-30. 1995.
[17] Popa-Simil L., Racolta P.M., Vilcov I., Georgescu E., “Applications of the filtering membranes and the radioactive tracers method for the study of some tribologycal aspects”, “Tribology" Magazine. Bucharest, Aug. 1987.
[18] Muntele C.I., Popa Simil L.,. Racolta P.M., Voiculescu D., “The recoil implantation technique developed at the U-120 cyclotron in Bucharest”, AIP Conference Proceedings 475 (1), 558 (1999)
[19] Blondiaux, G., Dragulescu, E., Racolta P.M., Craciun L., Serban A., Stroosnijder, R., “Development of Calibration Methods For Tla And Utla”. Europeean Commission Center of Excelence, 2002

PROGRESS IN ELECTRON BEAM INDUCED GRAFTING FOR DEVELOPMENT OF ION CONDUCTING MEMBRANES FOR POLYMER ELECTROLYTE FUEL CELLS IN MALAYSIA.

Mohamed Mahmoud NASEF[a,b]

[a]Malaysia Japan International Institute of Technology, Universiti Teknologi Malaysia
Kuala Lumpur, Malaysia, and

[b]Center of Hydrogen Energy, Universiti Teknologi Malaysia
Kuala Lumpur, Malaysia

Email: mahmoudeithar@cheme.utm.my

Abstract

This article briefly reviews the progress taking place in the development of ion conducting membranes (ICMs) using radiation induced graft copolymerization (RIGC) initiated by electron beam (EB) in Malaysia. Three types of ICMs for direct method fuel cell (DMFC) and high temperature proton exchange membrane fuel cell (HT-PEMFC) and alkaline electrolyte membrane fuel cell (AEMFC) were prepared. The ICM for DMFC was prepared by RIGC of 4-vinylpyridine (4-VP) onto EB irradiated *Syn*-polypropylene (*s*-PP) nanofibrous sheet followed by immobilization of phosphotungstenic acid ($H_3PW_{12}O_{40}$, PTA) and subsequent casting of 2 thin layers of Nafion solutions leading to 3-layer (3L) composite membrane with high conductivity and less water dependency beside having superior methanol barrier properties compared to Nafion 115 at both low and high methanol concentrations. The ICM for HT-PEMFC was prepared by grafting a binary mixture of 4-VP/1-vinylimidazole (1-VIm) onto EB-irradiated poly(ethylene-*co*-tetrafluoroethylene) (ETFE) followed by doping with phosphoric acid (PA). The incorporation of two basic monomers was highly effective in enhancing PA doping level, proton conductivity and overall performance of the membrane in fuel cell operated at 120°C. The ICM for AEMFC was prepared by incorporating imidazolium head groups to EB irradiated nanofibrous *s*-PP grafted with vinylbenzyl chloride (VBC), crosslinked by 1,8-octanediamine and functionalized with -OH group. The membranes displayed not only high ion exchange capacity (1.9 mmol/g) but also high ionic conductivity (130 mS/cm at 80°C) and reasonable alkaline stability. The membrane showed a high-power density reaching 440 mW/cm^2 at a current density of 910 mA/cm^2 when combined with electrodes using diamine crosslinked quaternised polysulfone binder at 80°C making it a promising candidate for application in AEMFC. It can be concluded that EB is highly effective in facilitating the development of ICMs precursors for various polymer electrolyte fuel cells.

1. INTRODUCTION

There is a strong demand for migration from the reliance on fossil fuels to renewable energy. This is to reduce greenhouse gas emissions to mitigate climate change and global warming. Electrochemical Energy systems such as fuel cells (FCs) are promising sustainable energy candidates suitable for supporting the shift to renewable energy [1]. FC, which is a system converting the free energy of fuel at the anode (e.g., H_2) into electricity in presence of an oxidant at the cathode (e.g., O_2) without combustion and releasing water as waste, uses ion conducting membrane (ICM) to transfer ions between electrodes and prevent bulk mixing reactants. The ions that can be transferred between electrodes are H^+ in both high temperature-proton exchange membrane fuel cell (HT-PEMFC) and direct methanol fuel cell (DMFC). The former is known as H_2/O_2 FC and is operated at a temperature range of 100-200^{o}C to enhance the performance (increase tolerance to CO gas, speed up electrode kinetics and increase fuel use efficiency) and reduce the complexity of the system, whereas the latter uses liquid fuel such as methanol giving it simplicity and suitability for portal uses. On the other hand, OH^- is transferred in ICM (anion exchange membrane in this case) from cathode to anode in the alkaline electrolyte membrane fuel cell (AEMFC), which has the advantage of using less-precious metals to make the electrodes. Commercial ICMs for FCs are challenged by a few issues including high cost, high methanol crossover (in DMFC) [2] and loss of fuel barrier properties in HT-PEMFC in addition to low ion exchange capacity and conductivity in AEMFC [3]. This situation raised the demand for development of alternative ICMs with enhanced properties and cheaper costs.

Radiation-induced graft copolymerization (RIGC) is a highly effective method for development of ICMs with the advantage of being more environmentally friendly compared to chemical grafting providing efficient means to control the degree of grafting (DG) and the level of the covalently bonded ionic moiety imparted to the

polymer substrate present in a film form and thus allow facile preparation of defect free membranes with desired properties [4]. The ICM preparation starts with irradiation from high energy sources such as γ-rays or EB triggering the formation of radicals that provides sites for reaction with desired monomers under controlled conditions allowing incorporation of desired functional groups. Interestingly, the use of EB provides significant advantages including not only speedy processing, controlled penetration depth and ease of operation but also it is radiation hazardless and more suitable for industrial application [5]. This made EB more appealing for irradiation of various polymer films to initiate grafting for the preparation of ICMs for FC applications in our work.

2. RADIATION GRAFTED ICM FOR DMFC

The membrane preparation was carried out by RIGC of 4-VP onto EB-irradiated electrospun *s*-PP with a dose of 20 kGy and a monomer concentration of 50 vol% in THF, temperature of 60°C and reaction time of 6 h. The obtained poly(4-VP) grafted nanofibrous s-PP sheets were loaded with PWA and subsequently coated with 2 layers of Nafion solution leading to 3-L composite membrane. The physicochemical properties of the obtained ICM are summarized in Table 1. Both 3-L membranes with PWA loading of 51 and 45% showed superior proton conductivity and selectivity in addition to having better methanol barrier properties and less-water dependency.

TABLE 1. Properties of 3-L composite membranes for DMFC [6]

Membrane	PWA loading (%)	Thickness	Water uptake (%) at 30°C	Proton conductivity (mS /cm)	CH_3OH permeability × 10^8 (cm^2/s)	Selectivity $\times 10^8$ ($mS.s/cm^3$)
3-L1	51	95	5.2	58.6	3.60	16.3
3-L2	46	95	5.0	40.0	3.00	13.2
Nafion 115	N/A	127	13.1	23.2	104	0.50

The performance in DEMFC depicted in Fig. 1 showed that both 3-L membranes demonstrated a higher open circuit voltage (OCV) of 6.3% and power density of 49.6% compared to Nafion 115 membrane when 2M methanol was used as a fuel at 60°C. Higher performance was also obtained with 5 M methanol fuel [6]. Such higher performance could be attributed to the lower methanol crossover and higher membrane selectivity coupled with high proton conductivity.

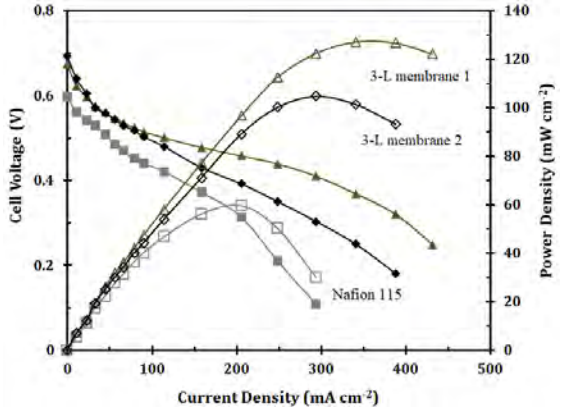

FIG. 1: Polarization curves of DMFC single cell with two 3-L membranes and Nafion 115 membrane. Operating conditions of anode are: 2 M methanol, 4 mL/min and 60°C.

3. RADIATION GRAFTED ICM FOR HT-PEMFC

Phosphoric acid (PA) doped membranes based on polybenzimidazole (PBI) have low proton conductivity and acid leaching problems. ICMs based on alkaline film grafted with 4-VP or 1-VIm monomer were proposed to enhance PA doping levels, yet their performance was unsatisfactory. Thus, grafting a mixture of 4-VP and 1-VIm onto ETFE film is likely to yield more alkaline intermediate films allowing more PA doping that led to higher conductivity than counterparts grafted with either single monomer. The membrane was prepared by RIGC mixture of 4-VP and 1-VIm (60/40, v:v) in 40 vol% deionized water at 60°C onto EB irradiated ETFE films followed by treatment with 85% PA and the plausible structure of the obtained membrane is illustrated in Fig. 2.

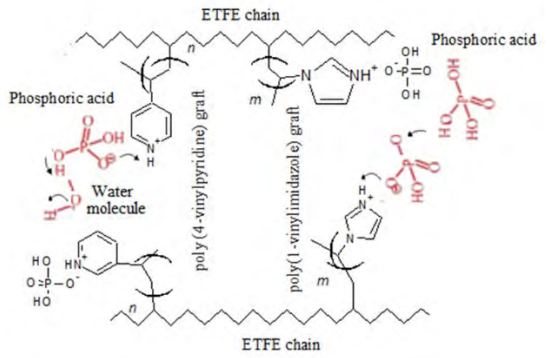

FIG. 2. Preparation of PA doped membranes based on EB irradiated ETFE film grafting with 4-VP/1-VIm.

The obtained ICM has homogenous graft distribution as depicted in Fig. 3. More importantly, the membrane showed a higher PA doping level and a less water dependency than the counterparts obtained by RIGC of 4-VP or 1-VIm alone. The membrane also showed a proton conductivity higher than PA doped PBI membrane at 120 °C. This was accompanied by a power density of 278 mw/cm^2 using partially humified gases of 20% RH when tested in FC compared to 226 mw/cm^2 at dry conditions under the same operating conditions as indicated by polarization curves shown in Fig. 4.

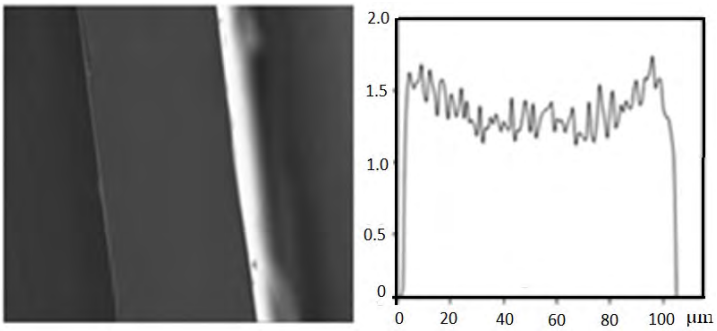

FIG. 3: Cross-sectional SEM image of acid doped ICM with phosphorus profiling across it.

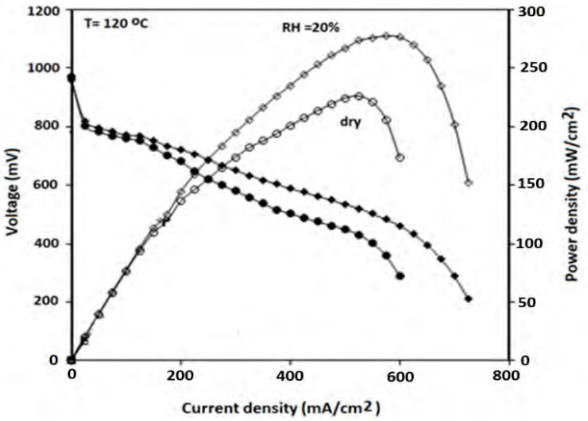

FIG. 4. Polarization curves of HT-PEMFC single cell with PA doped membranes tested under dry and 20% RH. The cell operated at 120 °C with H_2 and O_2 follow rates of 600 and 300 ml/min, respectively.

4. RADIATION GRAFTED ICM FOR AEMFC

Commercial ICMs for AEMFC are mainly challenged by low IEC and -OH conductivity. Radiation grafted membranes offer alternatives with improved properties. An imidazolium (Im) OH conductive containing ICM was prepared by RIGC of VBC onto EB irradiated nanofibrous s-PP sheet at 5 kGy/pass to a total dose of 35 kGy in an emulsion medium composed of a mixture of 5 wt% of VBC and 0.5 wt% of Tween-20 in DI water that was homogenized for 1 h at room temperature and flushed with N_2 gas for 30 min. The reaction vessel was water placed in a water bath at 50 °C for 10 h. The grafted samples were removed and cleaned then crosslinked with 1,8-octanediamine (ODA) and subsequently functionalized with Im groups as illustrated in Fig. 6 [7].

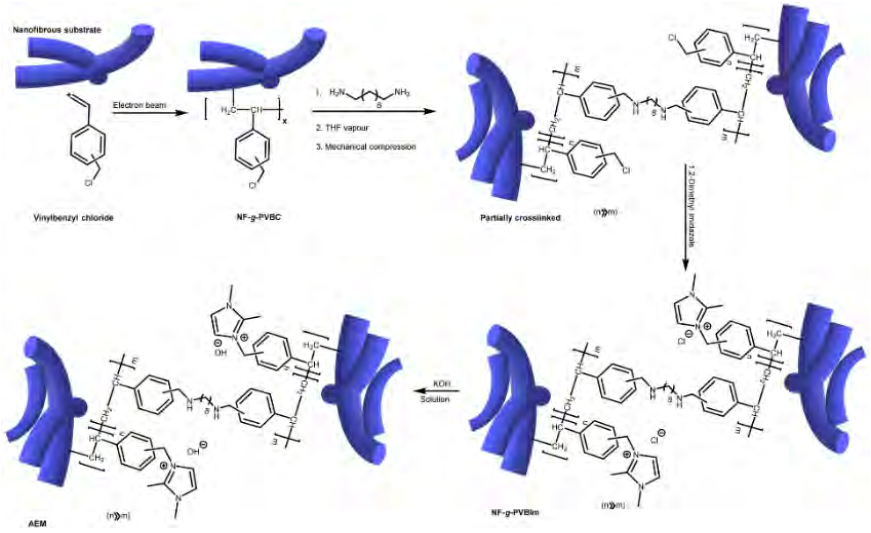

FIG. 5: Preparation of Im-containing membranes based on EB irradiated ETFE film grafting with VBC crosslinking with ODA and alkalisation with KOH [7].

The obtained membrane has a high IEC of 1.9 mmol/g and displayed OH conductivity of 130 mS/cm at 80 °C. The fuel cell performance shown Fig. 7 demonstrated a power density of 440 mA/cm^2 when tested under H_2 and O_2 flow rates of 200 ml/min, RH of 90% and 80 °C.

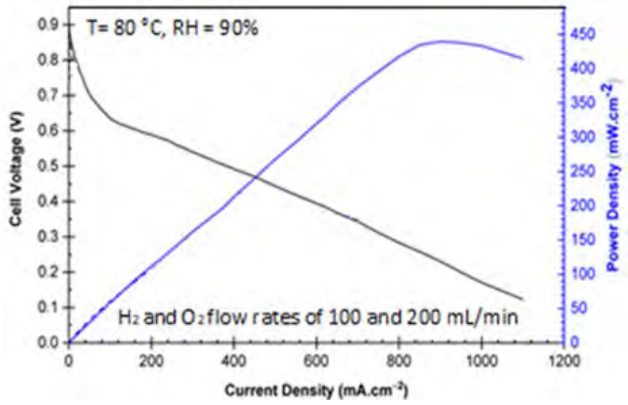

FIG. 6: Polarization curves of AEMFC with of Im-containing membrane [7].

5. CONCLUSIONS

EB was successfully used to initiate the preparation of 3 types of IEMs by RIGC of various monomers onto selected substrates. The adopted RIGC method led to ICMs with improved electrochemical properties and improved performances in fuel cells. The level of properties improvement depends on the amount of grafted moiety when functionalized.

ACKNOWLEDGEMENTS

The contributions of my co-workers E. Abozari, A. Ahmad, P. Sithambaranathan to the performed work is highly acknowledged. The Malaysian Nuclear Agency is thanked for the irradiation of samples and collaboration through T. M. Ting. MOHE and UTM are also thanked for the funds. The sponsorship to attend this event by IAEA is highly appreciated.

REFERENCES

[1] WALKOWIAK-KULIKOWSKA, J., WOLSKA, J., KORONIAK, H., Polymers application in proton exchange membranes for fuel cells, Physical Sciences Reviews, 2 (8), 2017, 20170018.

[2] HOSSEINPOUR, M. SAHOO, M., PEREZ-PAGE, M., BAYLIS, S.R., PATEL, F., HOLMES, S.M., Improving the performance of direct methanol fuel cells by implementing multilayer membranes blended with cellulose nanocrystals, Int. J. Hydrogen Energy, 44 (57) 2019, 30409.
[3] DAS, G., CHOI, J.-H., NGUYEN, P.K.T., KIM, D.-J., YOON, Y.S., Anion Exchange Membranes for Fuel Cell Application: A Review. Polymers 14, 2022, 1197.
[4] GUBLER, L., Polymer design strategies for radiation-grafted fuel cell membranes, Advanced Energy Materials, 2014, 4, 1300827.
[5] NASEF, M.M., GUPTA, B., SHAMELI, K., VERMA, C, ALI, R.R., TING, T.M. Engineered Bioactive polymeric surfaces by radiation induced graft copolymerization: strategies and applications. Polymers (Basel), 13(18), 2021, 3102.
[6] ABOUZARI-LOTF, E., NASEF, M. M., GHASSEMI, H., ZAKERI, M., AHMAD, A., ABDOLLAHI, Y., Improved methanol barrier property of Nafion hybrid membrane by incorporating nanofibrous interlayer self-immobilized with high level of phosphotungstic acid. ACS Applied Materials & Interfaces, 7 (31), 2015, 17008.
[7] ABOUZARI LOTF, E. JACOB, M.V., GHASSEMI, H., ZAKERI, M., NASEF, M.M., ABDOLAHI, Y., ABBASI, A., AHMAD, A., Highly conductive anion exchange membranes based on polymer networks containing imidazolium functionalised side chains, Scientific reports, 11, 2021, 3764.

ACCELERATORS USE TO ENGINEER NANO-MATERIALS FOR ENERGY

L. POPA-SIMIL
LAVM llc
Los Alamos, USA
Email: lps@lavmllc.com

Abstract

Starting from 1980 we looked for improvements in nuclear materials and the related energy devices with emphasis on materials. The novel nuclear materials for fission were developed in 5 families; each of them is intended to bring in harmony the structure with a nuclear agent active inside that material as:

- Micro-hetero structures, generally called “cer-Liq-Mesh” that self-separates the fission products from the nuclear fuel and minimizes their fuel damage, allowing breed &burn to near perfect burning; the fission products behave like medium mass accelerated ions, where the use of accelerators will help test the novel material structure and optimize it.
- Nano-hetero structures generically called “CIci”, that form a super-capacitor, charged by nuclear energy and directly discharged as electricity; This structure has broad use for almost all moving nuclear particles except neutrons and gamma, and for each type of particle, the use of a similar accelerated one bring a valuable contribution to material selection and optimization as well to the entire structure test and characterization.
- Nano-clustered structure that enhances self-separation of transmutation products; where the initial idea was generated by UTLA method development, where the recoil energy is used for implantation, but because this energy inside neutron zones is small, nano-cluster enhanced selective diffusion properties are also used. Using low energy accelerators/implanters we may test various nano-clustered structures.
- Fractal immiscible materials with radiation damage self-repairing capabilities eliminating the need for re-cladding in near perfect burning structures. The dimensions of these structures may be optimized using ion-beams simulating the radiation damage inside nuclear reactors.
- Nano-structures with active NEMS used as fast control of nuclear reactivity by guiding neutrons in desired directions or ultralight shielding for mobile reactors. The guiding is similar to radiation channeling being possible to use ion-beams to test the NEMS operation.

1. INTRODUCTION

Civil nuclear power is in free fall due to the production cost competition with methane gas and renewables, safety and security issues and other drawbacks specific to the technology. It is not yet extinct but the guild is talking about its renaissance, ignoring that it is not about fictitious Phoenix bird, but a very real thing and its rejuvenation may be achieved only by solving its problems. The actual nuclear technology is 70 years old; it is mature, and any little progress becomes harder to achieve, therefore the nuclear power has to reinvent itself, and this is not hopeless. We know for about 2500 years, when first nano-material ‘Damascus steel”, has been unconsciously invented and used to make “Damascus swords” with exceptional properties, that materials determine the ultimate properties of the objects made from, and in this modern endeavour in nuclear materials accelerators plays a tremendous role, in inventing and perfecting novel micro-nano-hetero structures from idea to application, and they already did. Starting from 1980s we developed novel ideas for the betterment of nuclear power applications, which followed a spiral of evolution, as Fig. 1 shows, up to present when achieved TRL=3 (Technology Readiness Level), and prototypes should be built. The basic concept being the development were transferred from accelerator practice, and helped the development of 6 families of materials, each used to solve a nuclear reactor problem. The actual nuclear energy has lower CO2 emission, but because it is in its infancy, it is based on homogeneous “hot-rod” technology, it is complex, expensive and raises security and proliferation issues, has the potential for large scale accidents, and generates difficulties in dealing with waste fuel dispositioning.

The novel developed families of engineered nano-materials eliminate almost all the drawbacks of the actual nuclear power, rendering it among the most efficient and environmental friendly energy source. Developing and optimizing these novel energy materials require intensive accelerator use in fundamental knowledge development and structural optimization experiments. The use of these advanced materials in future nuclear energy related application will render a high efficiency, minimal nuclear waste, and optimal nuclear fuel cycle, isotope, fission and fusion “batteries”, delivering the needed planetary clean energy at will for the next 10,000 years, and even more.

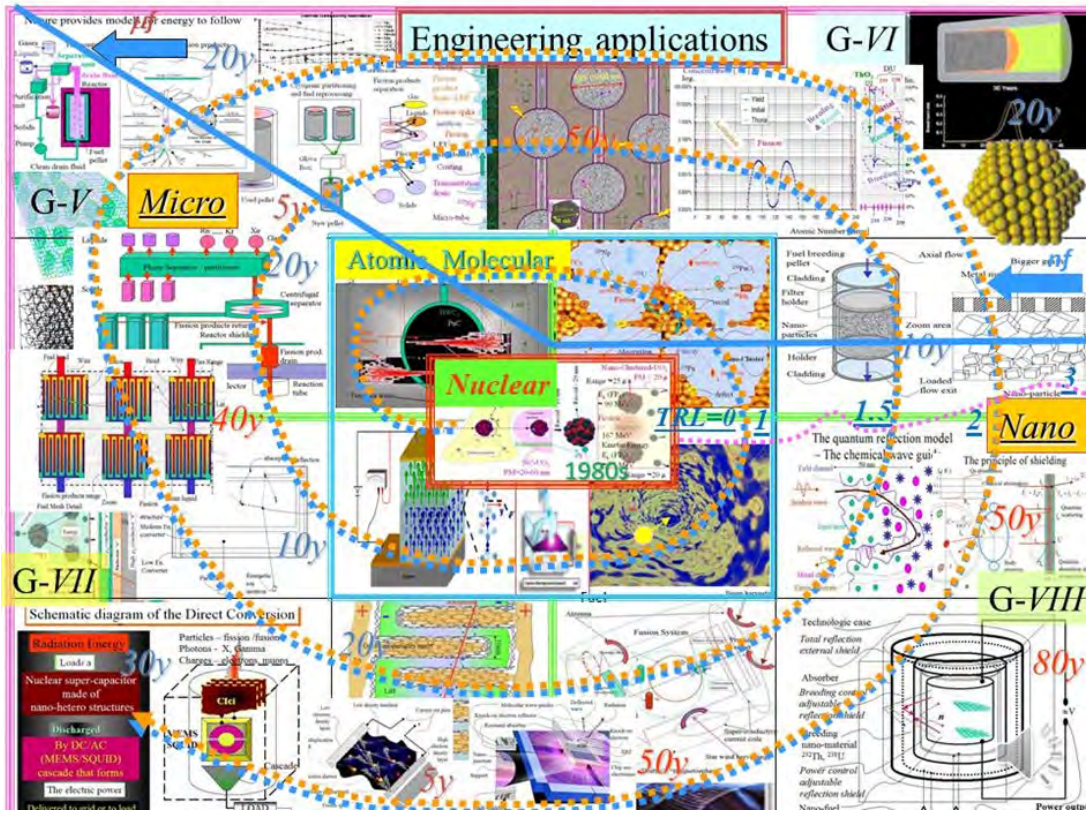

FIG. 1 Engineered, nano-nuclear materials knowledge evolution from concept to application

During the entire research period showed in Fig. 1 with a spiral of evolution accelerators had a primordial role in conceiving, developing the concepts and further providing means to build and optimize the structure, from the early stage of understanding the nuclear reaction kinematics to the interaction of fission products with matter inside the active reactor core.

1.1. Fission Products as Accelerated Particles

During fission of ^{235}U triggered by absorption of a thermal neutron, fission releases over time about 203 MeV, from which 167 MeV as kinetic energy of the fission products, shared according conservation rules.

As seen on isotopic map, in Fig. 2, it shows that after absorbing a neutron, the compound ^{236}U is breaking into two symmetrical products relative to median mass (^{118}Pd, marked by the pink line), having n in excess as one may see the reddish ellipses, with elements marked after the probability of occurrence. Instantly, due to very high instability of the primordial fission products, few neutrons during the first fs (femyo-second) after fission, split-off taking away about 8 MeV in kinetic energy, cooling down the fission product and forming what is called prompt neutron. After this, FPs follow sequences of betta decays, resulted from excess n disintegration, see the red arrows, crawling towards stability region, marked by black dots, forming isotopes stability region, in the mapped data offered by Brookhaven natl. Lab. nndc.bnl website [1]. On the bottom-right is a chart, showing probability of occurrence distribution as function of atomic mass number “A” that is a 2D integral of the 3D isotope occurrence probability performed at some moment in time usually being placed between orange double line and stable isotope location. On the right is presented the case of decay of a FP pair, starting with ^{89}Kr and ^{144}Ba, elements belonging to group 8 and respectively to group 2 of Mendeleev table, which after the chain of beta decays end up in stable elements ^{89}Y, group 3B and ^{144}Nd, a 4th Lanthanide, changing their chemical properties, atomic structure due to beta decay. Some time, in about 0.3% of the cases, the neutron does not promptly evaporate from the fission product but a little bit later, creating the delayed neutrons, so useful for nuclear reactor controllability [1,2]. It is known that the shape of fission products depends on the type of actinide and neutron energy and possible on some local quantum states.

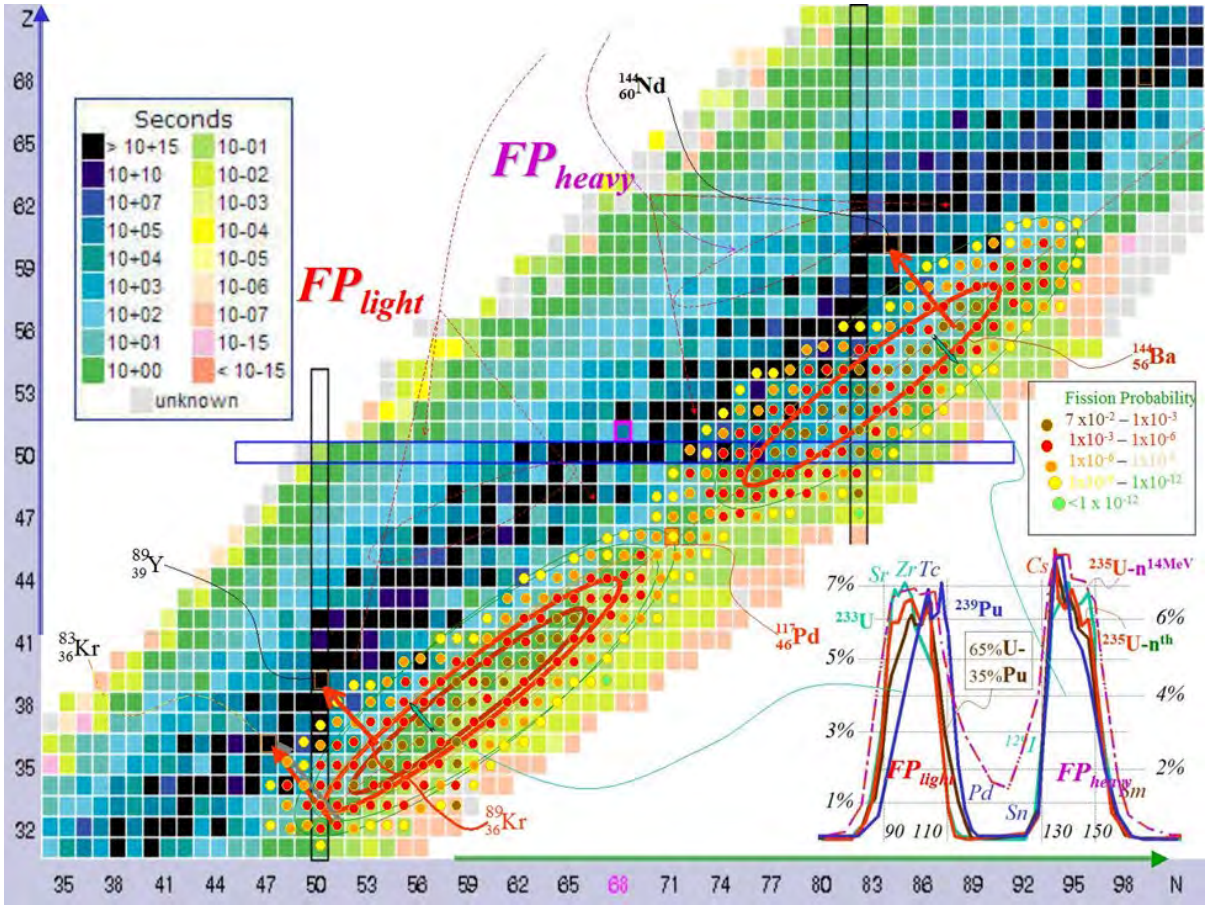

FIG. 2: Details on Fission Products production process

1.2. Fission products effects in nuclear fuel

As one may see in Fig. 2 FP represent a very complex problem for nuclear reactor welfare, being the main cause of fuel's premature damage, power limitations and LOCA accident consequences, ending up in nuclear accidents as shown in Fig. 1 many ending in meltdown and FP release.

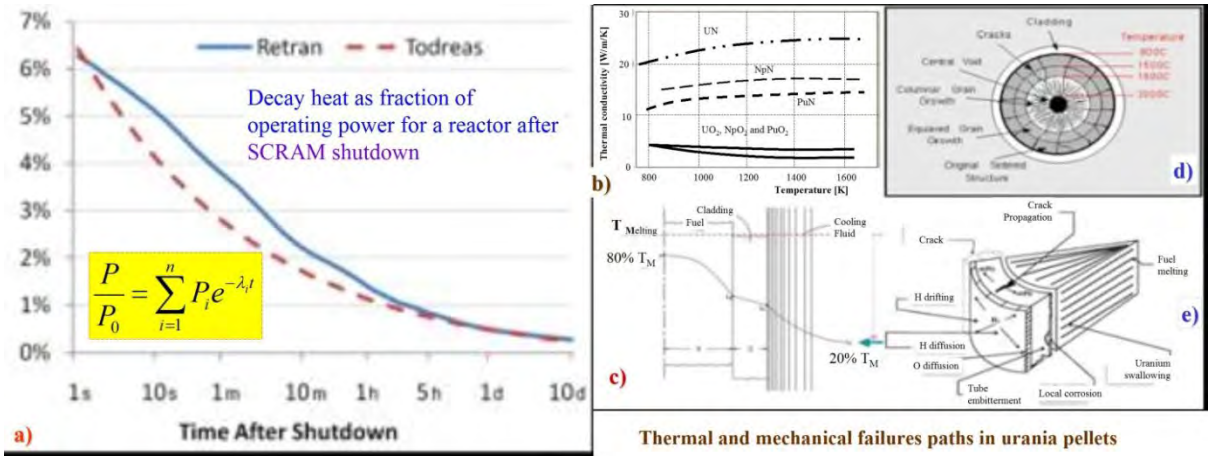

FIG. 3: Actual fuel induced issues for thermal nuclear reactor safety a) –Decay heat after SCRUM; b) Thermal conductivity of nuclear fuels; c) temperature radial distribution in fuel cell; d) nuclear fuel failing mechanisms; e) pellet slice falling issues

As previously shown, FPs take away about 8 MeV per fission in beta decay, makes nuclear reactor require intensive cooling after shut down, as Fig. 6a shows. This is associated with about another 8 MeV for the antineutrino release, which is basically lost, from energy point of view, but may become useful in the future

neutrino strategic communication and detection. Low thermal conductivity Fig.6b,c and elasticity of ceramic fuel, corroborated with specific power deposition pattern, makes nuclear fuel crack at every power cycle, creating paths for FPs to reach cladding and escape in the cooling agent, is briefly shown in Fig. 6d,e

In order to solve this problem is needed to better understand this nuclear fuel damage in its smallest detail and here the accelerator knowledge provided a boost [2].

1.3. Accelerator knowledge use in FPs' behavior understanding

The analogy between FP and medium mass accelerated charged particles is outstanding. Immediately after leaving the "close neighborhood" of the fissioned nucleus, that is of few lattice constants in radius, usually smaller than 1 nm, FP s behave like accelerated ion beams, hitting a material surface that is made of the fuel constituents, and Bethe-Bloch formula may be successfully used, in its modern form of SRIM MC code. This characterizes the interaction between charged particles and matter, respectively FPs and fuel, because much less than 1% of FPs have the opportunity to directly interact with fuel's cladding. Using SRIM it was possible to simulate and understand various aspects of the stopping of the FPs in the fuel and cladding, as shown in FIG. 4 and to develop new material structures able to avoid structural damage, and even more to be able to self-separate the fission products from the fuel. The novel design of micro-hetero structure exhibits exceptional other collateral properties that have driven towards a novel nuclear fuel structure generically called "cer-liq-mesh".

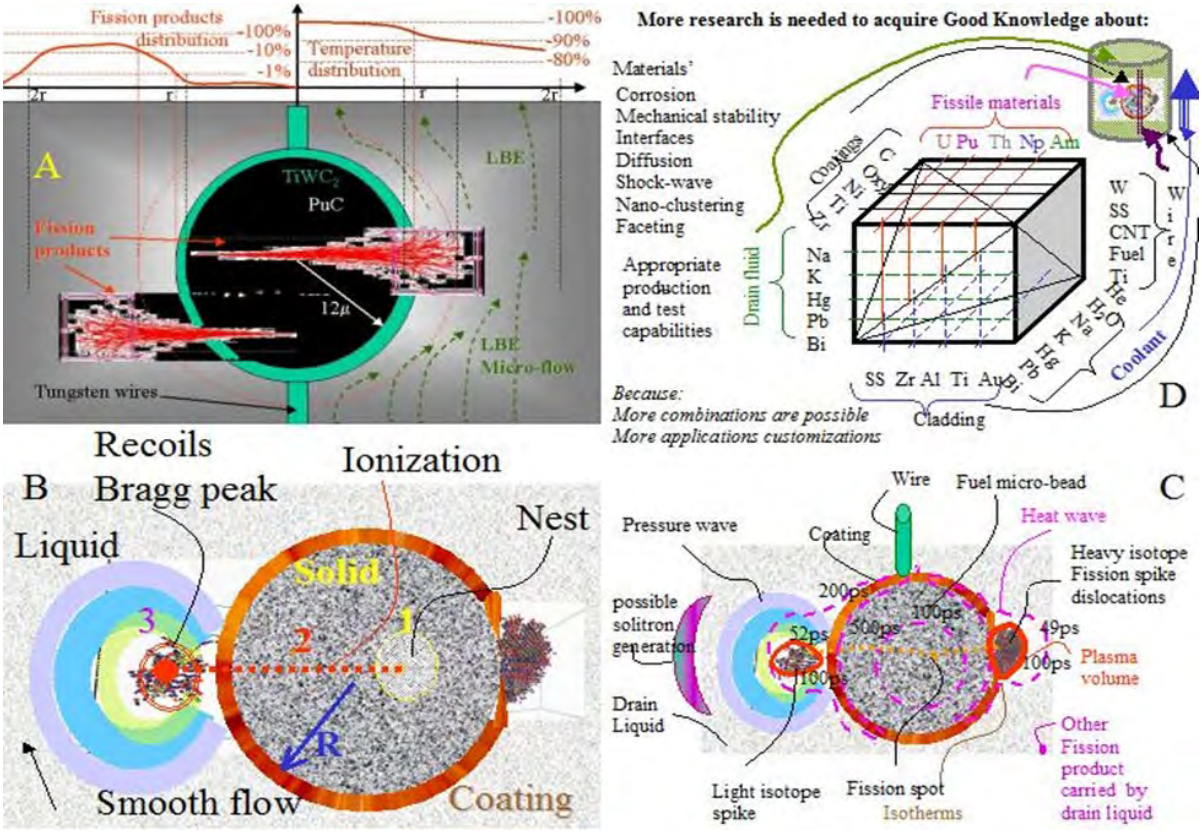

FIG. 4: Heterogeneity by design applied in "cer-liq-mesh" fuel structure; A –Fission kinematics in novel micro-bead structure; B - Processes in micro-hetero fuel bead; C - MD details on fission products effects; D - Material diversity to fabricate a fuel pellet.

Fig. 4 D shows that there are several combinations that may be used and work well to create a fuel pellet with identical properties of the actual fuel, that to offer the advantages of micro-hetero-fuel without major changes in the nuclear reactor structure. The critical feature is at the boundary between the fuel bead and drain liquid, when Bragg peak is in coating that has to recover in izo-morphism, protecting bead, is simulated using accelerators.

2. TYPES OF ENGINEERED NANO-NUCLEAR STRUCTURES

2.1. Micro-hetero structures, generally called “cer-Liq-Mesh”

FIG. 4A shows the new design of metallic uranium 10 microns in diameter bead supported on a tungsten micro-wire immersed in a liquid metal. Inside the bead there are presented the trajectories of FPs stopping in that area. Stopping range is longer than bead’s dimensions therefore FPs are stopping inside the liquid metal. FIG. 4B shows the main zones of the fission process, where “1” is the near-by zone, “2” is the ionization stopping range, and “3” is the recoil nuclei end of range, also known as Bragg peak. FIG. 4C shows the results of a molecular dynamics (MD) simulation, showing that the FPs’ stopping process takes about 50 ps, there are about 100, 000 dpa for each FP. Because most of dpa take place in liquid metal, a cavitation-like explosion-implosion takes place and no remnant dislocation survives, only FP is immersed and bound to liquid, which is a great progress compared to solid structure where more than 10,000 dpa are left over each fission act. In FIG. 4A was given a constructive example, but FIG. 4D shows the real complexity of the problem, where various aspects and properties have to be mitigated.

The new fuel material produced using accelerator knowledge allows the construction of nuclear reactors with exceptional properties, where power density may be increased by a factor of 4, construction may be simplified, the fuel self-separates the FPs that are easy to extract without using the actual chemistry, but simple thermo-mechanical procedures. Due to this easy FP extraction, separation and partitioning followed by fuel usage, fuel cycle is drastically modified.

More, accelerators may be use to effectively measure the parameters of the new fuel, its reactivity and capability to self-separate FPs based on fission reaction’s kinematics.

2.2. Nuclear Energy conversion in Electricity

During this analysis on heating mechanisms in nuclear fuel using SRIM and e-Casino MC codes showed that is possible to engineer a meta-material that resembles a heterogeneous super-capacitor, that loads from the kinetic energy of the nuclear particle crossing it and discharges as electricity as shown in FIG. 5e.

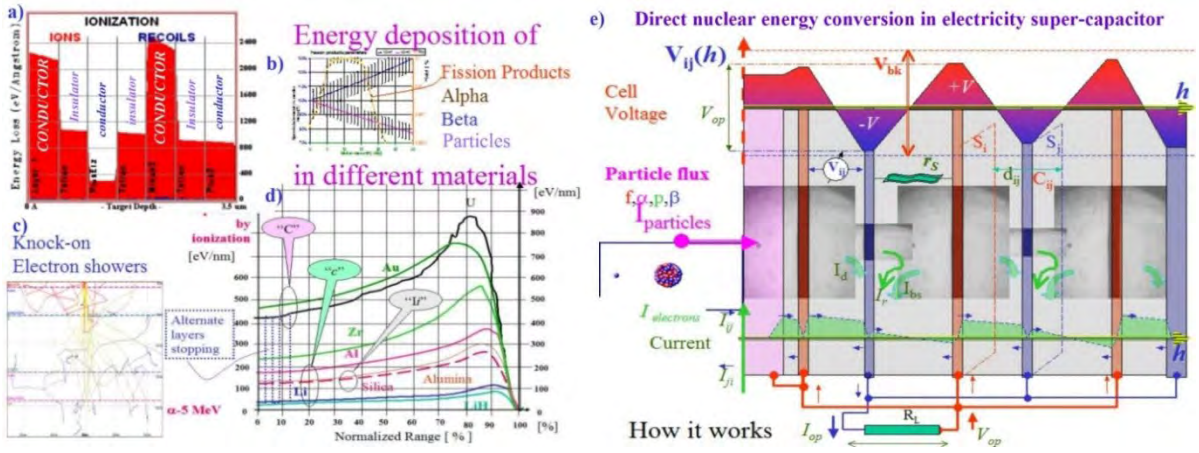

FIG. 5 Development of meta-materials for direct nuclear energy conversion in electricity a) SRIM Ionization simulation; b) FPs as accelerated ions; c) Primary knock-on electron trajectories; d) Ionization stopping power deposition in various materials; e) principle of direct nuclear energy conversion [3].

FIG. 5a shows the case of an alpha battery meta-material, comprising of alternating layers, few nm thick, of high electron density conductors “C”, separated by insulators “I” and “i” and low density electron conductors “c”, repeated to cover the entire moving particles’ stopping range. The idea is that during charged particle stopping process, the “C” layers will emit a large shower of knock-on electrons than the “c” layers as the chart in top-left of Fig. 8a shows, in a SRIM simulation, that led to the meta-material capacitor like construction shown in FIG. 5e. Knock-on electrons interact with other electrons forming showers and are tunnelling through the insulator layer and stop in the next conductive layer, polarizing the layers, as the e-Casino electron path simulation in FIG. 5c shows. There are many materials that exhibit these properties, as the plot in FIG. 5d for few materials of interest

showing ionization versus the relative stopping range. In the FIG. 5b there are shown main particles of interest, which exhibit stopping ranges in mm or less range, in order to harvest their energy. The chart shows the fission product energy distribution as function of abatement from the central mass, and shows that the lighter FP usually has higher energy and speed than its heavier partner.

This type of meta-materials may handle impressive power density in the range of kW/mm3, bout 1000 times higher than the actual nuclear fuel, based on heat flow power transport, based on phonons and electrons, because it may be interpreted as being dominant electron-based cooling. The amount of energy that was not removed by electric conduction has to be removed by heat flow, and that is a limiting factor in the acceptable power density. A single layer alpha battery made of this meta-material using ^{238}Pu will look like a paper sheet being about 50 micron thick.

The research and development of this material intensively uses particle accelerators for material parameters optimization, energy conversion efficiency measurement, and construction, and the structure itself was discovered during a failed accelerator experiment by 1980s which aimed to measure beam's temperatures.

2.3. Nuclear Transmutation Products Extraction and Fuel Cycle

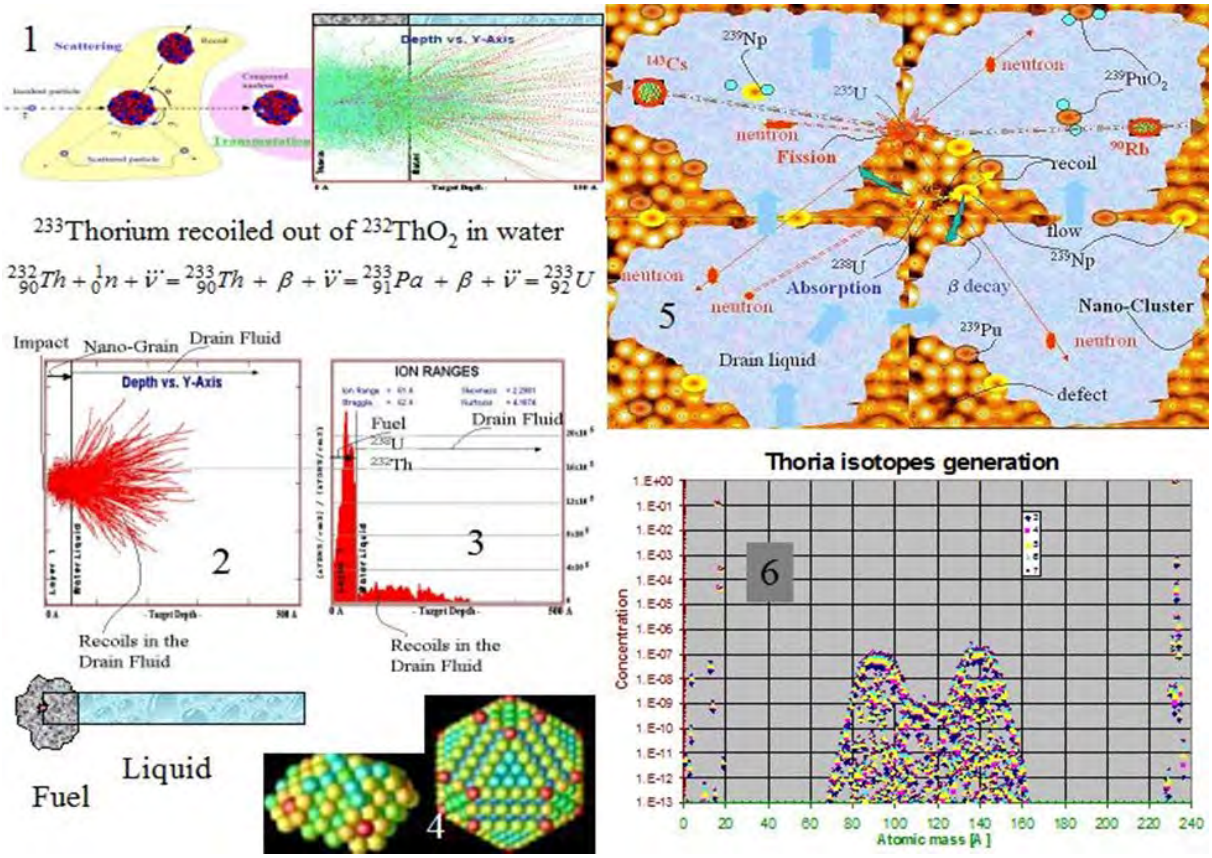

FIG. 6: Mechanisms of separation in nano-beaded hetero materials: 1 – Nuclear reaction schematics; 2 – Recoils paths by SRIM; 3 – Ion ranges; 4 – Nano-cluster with impurities on interface; 5 – processes in a hetero nano-clustered structure; 6 – Th breeding inventory.

FIG. 6-1, is the first part of the process in FIG. 2, where after a neutron absorption, a compound nucleus is formed, that recoils a little bit from its initial position in the lattice, shown in SRIM simulation nearby, where 5 nm thin foil of thoria covered by water have been considered, in order to mimic a nano-cluster. The chart "2" show trajectories of recoils in the structure shown under it, formed of a 10 nm diameter, nano-bead immersed in water while the chart "3", shows the distribution of recoiled particle density along the radius. In picture"4" it is shown a nano-cluster structure with some impurity atoms, in red, on surface. Picture "5" shows a section through a thoria hetero-structure, showing trajectories of main particles resulted in that reaction. Chart "6" shows isotopic production calculated with ORIGEN code for thorium fuel [4]. From the radioactivity point of view, in a 1 cm^3

sealed fuel pellet it may reach hundreds of Sv/h, having a thermal power of less than 10W, while after 1 month it decays by 3 om (orders of magnitude) being easy to reprocess in a specialize glovebox.

In accelerator technology recoil implantation is a well-known radioactive labelling process that works together with nano cluster mechanisms to produce direct separation of TPs. And in this case it may be used to simulate the behaviour of nano-cluster fluid interfaces as function of radioactivity, temperature, etc.

2.4. Nuclear Reactor Control using guiding nano-structures

The actual nuclear reactor control is based on electro-mechanical systems, that are slow and mainly uses delayed neutrons to control the process that makes reactor manoeuvrability low.

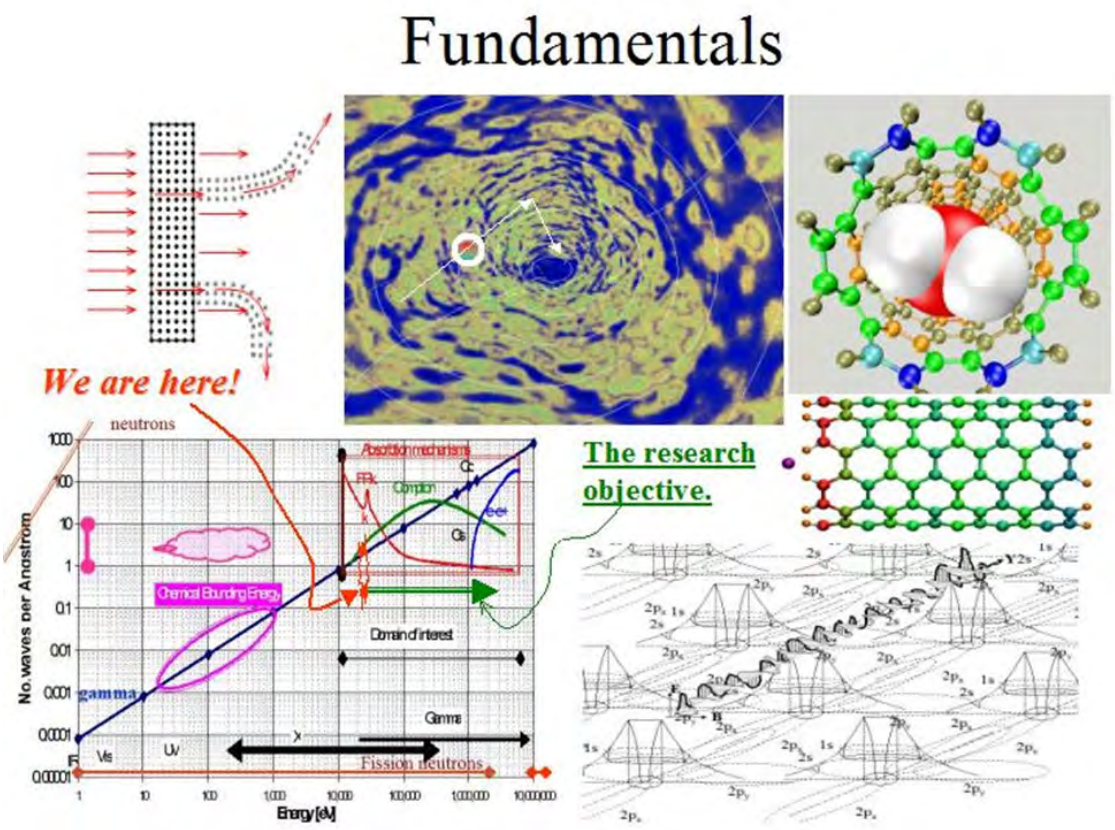

FIG. 7 – Principles of neutron guiding or channelling in nano-structures

It is anticipated that using channelling process, discovered using accelerators by 1970s, where neutrons to be trapped and guided in nano-structures with capability to switch their trajectory using electronic controlled NEMS devices, to produce more efficient nuclear reactor control systems able to use prompt neutrons, making the reaction time by 1,000 times faster [5].

Inside a nuclear reactor this control blanket made of guiding nano-structures may turn out coming neutrons into core to increase reactivity or direct them into an absorbent material for radioisotope production. FIG. 10 shows a layer of the blanket in upper-left side, and underneath a chart showing the number of wavelength per angstrom, showing overlapped the energy domain for nuclear applications. In top centre is an ideographic view of the magnetic fields a neutron may encounter traveling inside a nano-tube. On the right side is shown a water molecule traveling inside a CNT, obtained by MD simulation. On the bottom-right is depicted a neutron associated wavelet traveling inside an atomic structure, and bouncing on electron orbitals magnetic moments. Accelerators are further used to test this material, during construction, generating neutrons and gamma rays and using IBA technologies. The channelling properties of nanostructures are well known for charged particles, what it remains to do is to engineer such nanostructures able to trap neutrons inside with larger angle than the actual grazing angle and to attach the trajectory switch on it controlled by electric field, generically calling it a NEMS. This feature will make the guiding material suitable for being used for reactor criticality control, and applications in modulating radiation, criticality and even reactor's neutrino emission.

2.5. Nuclear Reactor Structural Materials Degradation and Safety

Cladding material is seldom exposed to FP induced damage, but it is exposed to neutron and gamma rat damage that renders it unsafe after a burnup of less than 100MWDay/kg, that is not compatible with near perfect burning requirements and recladding is needed.

A novel composite material made of immiscible fractions may be used instead.

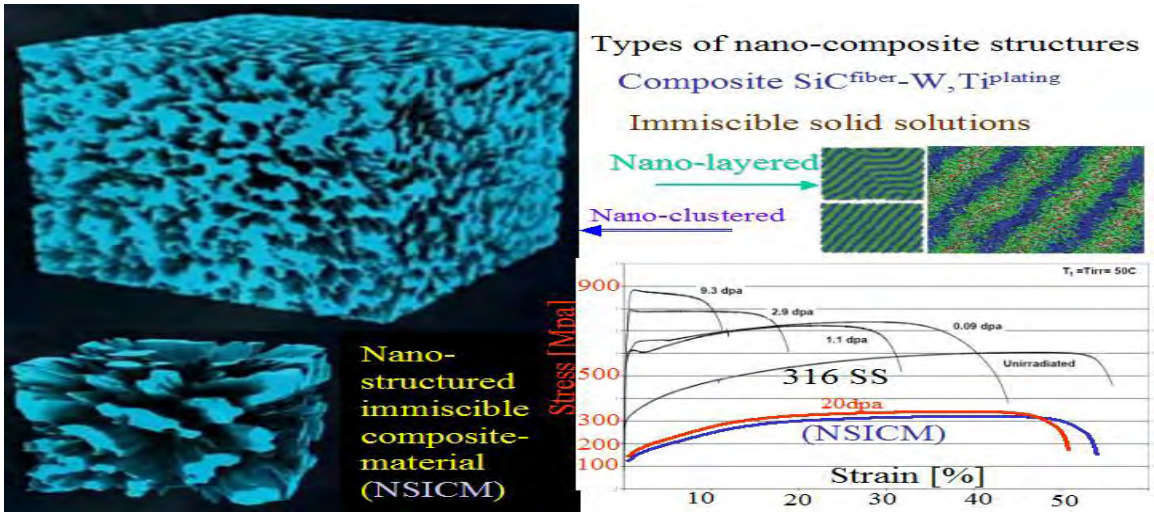

FIG. 8 Novel multi-phase material structure and anticipated properties

This new material "NSICM" shown in FIG. 8 may not have the performances of stainless steel but will assure the same performances over a large radiation dose, which will allow fabrication of a thicker cladding to offer same mechanical properties.

3. THE USE OF ACCELERATORS IN DEVELOPING NANO-HETERO-NUCLEAR MATERIALS

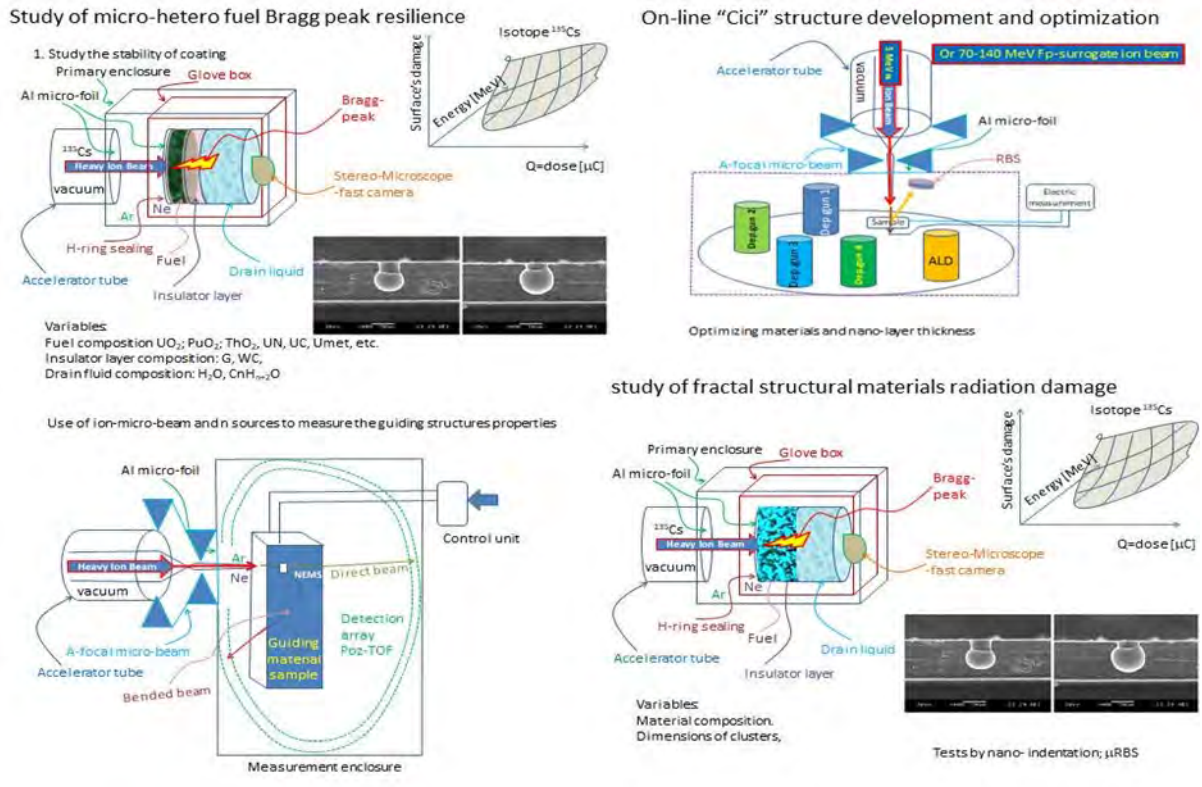

FIG. 9 – accelerator use to develop micro-nano engineered nuclear hetero-structures

As one may see, accelerators are indispensable tools in the development of novel micro-nano nuclear materials, able to speed up the R&D process by an order of magnitude. It will start with micro-hetero structures as FIG. 9 shows in upper left side, implanting surrogates of fission products to generate Bragg peak in the interfaces. The use of a 5 MeV beam or 60 MeV to 150 MeV FPs surrogate to optimize the layers of a direct nuclear energy conversion structure may be done by measuring the beam current before and after entering the structure, and using RBS to profile the thickness and interpenetration of different nano-layers. In lower-left side is shown how a micro-beam may be used to characterize a nano-guiding structure used for nuclear reactor control, switching the neutron direction from leaving the active zone, to returning into ha being switched by means a NEMS device acting on each track. Similar measurement but this time using accelerator to simulate and measure radiation damage into fractal materials is presented on lower-right side. The big advantage using accelerators instead direct exposure in nuclear reactor, resides in its analytical capabilities, possibility of using various size of beams, from micron to cm size, various incidence angles, particle beams and energies distinctly covering the entire palette of functional circumstances the future products may encounter in normal running.

Active quantum environments is a frontier domain in nuclear physics, that may be explored using accelerators in various modes, from producing the environment to triggering the quantum exchange and to visualize different aspects of collective quantum interactions helping us to understand the relationship between material quantum assemblies and quantum fields, in the attempt to master the processes and control them to our advantage [6].

4. CONCLUSIONS

Novel nano-micro engineered materials developed using knowledge gained in accelerator applications will provide the necessary support for the development of new generations of nuclear reactors and advanced nuclear applications.

Accelerators will be further used during the research, production and test of the novel nano-nuclear materials, and may be integrated in nuclear power structures, because they allow small scale simulations with full access for observations of the effects obtained inside a nuclear reactor core critical structure with little and difficult access for real time observations on the tested structure.

ACKNOWLEDGEMENTS

I am grateful to all of those with whom I have had the pleasure to work during this and other related projects. Each of the team members have provided me extensive personal and professional guidance and taught me a great deal about both scientific research and life in general. I would especially like to thank Prof. Ionel Purica, Acad. Ioan-Iovitz Popescu, Dr. Geavidt Musa, Dr. Michael Nastasi the team leader as my coordinator and mentor, he has taught me more than I could ever give him credit for here. They have shown me, by example, what a good scientist and person should be. Deep gratitude to our friends, Dr. Gordon Jarvinen and Dr. David Poston, from LANL, for advices and life model, and to all our collaborators who supported the research and co-authored various papers over time.

REFERENCES

[1] BNL, NNDC “Interactive Chart of Nuclides” - NNDC https://www.nndc.bnl.gov/nudat3/, (2022)
[2] POPA-SIMIL L.,“Applied Nano-technologies Improves Nuclear Power Safety and Performances” (Nano-technologies in Nuclear Power, Book 1), Kindle Edition (2012).
[3] POPA-SIMIL L., “Strategic space applications of nano-engineered nuclear-materials”, Apple Books, (2015).
[4] POPA-SIMIL, L., Nuclear Power Renaissance Based on Engineered Micro-Nano-Nuclear Materials. Energy and Power Engineering, 13, 65-74, (2021).
[5] POPA-SIMIL L., Nano-structured nuclear radiation shielding. US20110001065, (2011)
[6] POPA-SIMIL L., The Fusion Battery, A Novel Type of Nuclear Battery and Potential Outcomes and Applications (Nuclear Power - Fusion Book 1), Kindle Edition (2012)

MOBILE FACILITY FOR GAMMA-ACTIVATION ANALYSIS OF GOLD ORES

V. V. GOSTILO
Baltic Scientific Instruments, Ltd.
Riga, Latvia
Email: office@bsi.lv

A. D. SOKOLOV
Baltic Scientific Instruments, Ltd.
Riga, Latvia
Email: office@bsi.lv

M. I. DEMSKY
CORAD
St-Petersburg, Russian Federation
Email: mdemsky@mail.ru

Abstract

Results of the development and research of characteristics of a new gamma-activation analysis (GAA) facility, created for quantitative analysis of gold-bearing ores in real conditions of a gold-mining enterprise, are presented. Linear electron accelerator УЭЛР-8-10А (P ≤ 10 kW, E=7-9 MeV), maximally adapted to the tasks of GAA, was used for irradiation. Gamma-radiation was registered by a two-channel precision gamma spectrometer based on hemispherical HPGe detectors with a diameter of 110 mm.

The values of gold detection limit (3σ), measured from the spectra of certified reference samples with an ultra-low background level, were 0.025-0.028 ppm with single irradiation. In this case, the root-mean-square measurement error for a gold concentration of 1 ppm did not exceed 8%, and 4% for a concentration of 10 ppm. The GAA facility provides the analysis of coarse-ground samples (1-3 mm) with a capacity of at least 65 samples per hour.

1. INTRODUCTION

Gamma activation analysis (GAA) is a unique method for analyzing samples at all stages of the search, exploration and production of gold, as well as other precious (noble) metals and related elements [1-6]. The essence of the method consists in irradiating large-mass ore samples with high-energy gamma quanta, generated by a linear electron accelerator (LINAC), and recording the induced activity of excited gold nuclei (isomers) using a gamma spectrometer. The advantages of this method were discussed in detail in [1-6].

These benefits were first realized in three GAA industrial laboratories, commissioned at the Muruntau mine, Uzbekistan in 1977, in Magadan, Russia in 1979 and in Batagay, Russia in 1986 [3]. Currently, only one of the three commissioned laboratories is operating – at the Muruntau mine, Uzbekistan. After modernization of the main systems, the gold detection limit (DL) in this laboratory is 0.04 ppm (3σ) with a measurement error of less than 10% for gold concentrations of 1.08 ppm [7-11]. At the same time, the laboratory demonstrates remarkable productivity – at least 120 measurements per hour. In 2020, about 1 700 000 samples were measured on two measurement lines with two LINACs.

In recent years, due to the intensification of work on the exploration and development of deposits of gold and rare earth elements on all continents, there has been an increase in the interest of both mining enterprises and development companies in the precise and prompt determination of the concentrations of these elements. The Australian company Chrysos Corporation, in partnership with the Chinese company Nuctech, has recently created its first commercial prototype of a facility using GAA technology for gold [6,12,13]. As a result, a gold detection limit of 0.03 ppm (3σ) is declared with a measurement error of 7-8% for a gold concentration of 0.3 ppm and 4.0% for a gold concentration of 1.0 ppm. It should be noted that the analytical productivity of the equipment is 72 samples per hour.

This work is devoted to the results of the development and study of the characteristics of "Au-Isomer", a new industrial GAA facility created for PAVLIK Gold Ore Company, Russia [14]. The entire complex of the

"Au-Isomer" GAA facility being put into operation, is designed as a mobile one; its design allows disassembling the GAA facility and transporting it to another mine in four 40-foot containers. When developing and studying the characteristics of the GAA facility itself, the design, principle of operation and characteristics of which are presented in this work, the main efforts of the developers were aimed at providing high productivity of gold analysis and at the same time ensuring its high sensitivity and accuracy.

2. FACILITY DESIGN

The facility has dimensions of 7.1 x 4.5 m and a height of 4.1 m together with a crane, designed for assembly and disassembly of the radiation shield (Fig. 1). Outside the facility, in separate rooms, a power supply unit for the accelerator is located, and a chiller for cooling the target of the LINAC.

FIG. 1. "Au-Isomer" gamma-activation analysis facility.

The installation works in a fully automatic mode; the algorithm of its operation is presented below (Fig. 2). Containers with ore samples 1, installed on the receiving conveyor 2 of the GAA facility's Sample Transportation System, are fed through conveyor 3 to channel 4, along which the containers are rolled to the target 5 of the LINAC. During irradiation, containers are rotated by drive 6 to ensure uniform distribution of the dose in the container volume.

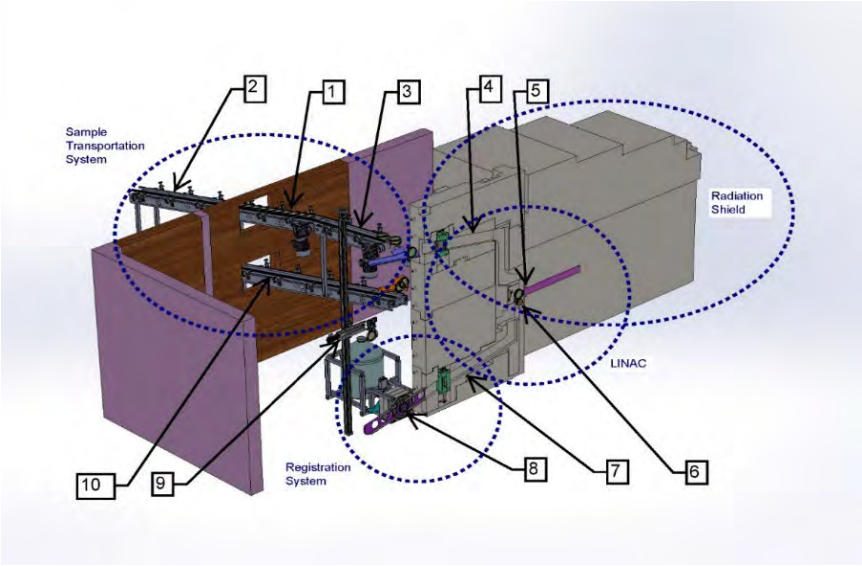

FIG. 2. The GAA facility sketch drawing.

Channels 4 and 7, like the LINAC, are surrounded by Radiation Shield. After irradiation, the containers are rolled down channel 7 to precision spectrometers 8 of the Registration System to measure the induced activity. After measurement, the containers are lifted by a lifting mechanism 9 of the Sample Transportation System for unloading onto a containers' return conveyor 10 or loading into channel 4 for re-irradiation. The decision to re-irradiate is carried out by a computer program at a low signal level in the energy range of radiation of the gold isomer. The containers measured for the second time will alternate in channels 4 and 7 with the containers measured for the first time, and the barcode system of the containers at the entrance to channel 4 will inform the computer control system of which container went to irradiation.

At present, time specifications for the developed GAA facility's operating procedure are as follows: moving the container to the barcode reader area – 10 sec, to the irradiation area after reading the barcode – 2 sec; irradiation – 10 sec; moving the container to the detectors of the registration system after irradiation – 2 sec; measurement – 15 sec; making a decision on re-irradiation – 0.5 sec, unloading – 12 sec. Thus, the total time of one analysis is about 52 seconds, which provides an analysis throughput of at least 60-65 analyzes per hour. It is planned in the near future to reduce the time of samples feed to the reader, starting from the second sample to 3 seconds, and the time of unloading – to 9 seconds. Thus, the total time of one analysis will be about 47 seconds, which will provide an analysis throughput of at least 75 analyzes per hour. This is less than in Muruntau (120 s/h), but comparable to Chrysos (72 s/h) [12].

2.1. Linear Electron Accelerator (LINAC)

In the developed facility, a LINAC УЭЛР-8-10А [15,16] of the Corad company was used, which was maximally adapted to the tasks of GAA (Fig. 3). The accelerator generates an electron beam with a power of up to 10 kW and electron energy adjustable in the range of 7-9 MeV. The ability to adjust the electron energy and maintain it at a stable level provides ample opportunity for optimizing sample irradiation conditions to suppress lines of interfering elements that may overlap with gold lines in the GAA spectrum. In turn, this allows increasing the accuracy of determining the gold in the sample and reducing the limit of its detection.

Circuits for stabilizing the amplitude of the beam current pulse, the coolant temperature and the level of microwave power supplied to the input of the accelerating section ensure the stability of the bremsstrahlung intensity and electron energy in the accelerator within 2%. As a microwave power amplifier in a LINAC, the klystrons КИУ-268 (Torium, Russia), VKS-8262F (CPI, U.S.A.) or TH2173F (Thales Electron Devices, France) can be used. The high-voltage power supply of the klystron and the electron source is provided by two highly efficient semiconductor modulators. The accelerator is powered from a three-phase network 380/220 V, 50 Hz, the maximum power consumption of the accelerator is 80 kW.

FIG. 3. LINAC in the "maintenance position", outside of the radiation shield.

2.2. Radiation shield

In the developed GAA facility, the LINAC and the system for moving containers with samples are placed in an iron collapsible radiation shield in order to prevent the radiation from affecting personnel and the background level when registering induced activity. The radiation shield provides a level of background radiation at any point around its enclosure of no more than 1 μSv/h. This level of radiation background formally allows the installation of "Au-Isomer" in ordinary industrial premises without the allocation of a sanitary protection zone and a restricted area.

The radiation shield consists of iron blocks; their weight does not exceed 2.4 tons. The total weight of the radiation shield is 118 tons. All assembly work is carried out using a conventional overhead track crane with a lifting capacity of up to 3.5 tons, which is a part of the facility. Dismantling front protection blocks provides access to the sample container transportation system. Disassembling the blocks at the rear of the shield provides the ability to roll the accelerator out of the shield for maintenance and repair. This procedure takes no more than 20 minutes. The mobility of the complex is contingent on the possibility of disassembling the radiation shield and transporting it to another facility (mine), if necessary, in four trucks.

2.3. Radiation registration system

The GAA facility registration system determines practically all of its metrological characteristics. It is a two-channel precision gamma spectrometer based on hemispherical HPGe detectors with a diameter of 110 mm in each channel (Fig. 4) [17]. Detectors of such a large diameter were developed by us specifically for the tasks of detecting gold in ore samples. Unique values of the energy resolution ((702-726) eV at 122 keV and (1337-1375) eV at 662 keV) with a high relative detection efficiency of gamma radiation (80%), allow for high sensitivity and accuracy of the gold concentration analysis. The detectors are cooled with liquid nitrogen. Processing and amplification of signals from detectors are carried out by a Boson multichannel analyzer equipped with analytical software that records, calculates and analyzes the spectra of all samples [18]. The registration system contains only a passive shield of HPGe detectors and does not contain active shielding.

FIG. 4. BSI production of large diameter HPGe detectors for gold analysis.

2.4. Container transportation system

The container transportation system for this project is developed on the basis of standard industrial automation components; the overall control of the system is fully automatic, carried out using the industrial Unitronic controller with a touch-screen display. The container transportation system performs the functions of containers' alternate reception, their transfer to the irradiation zone, then to the measurement zone, return to the irradiation zone or moving them to the storage location. During the container movement, the transportation system reads all information about the analyzed sample from the barcodes.

3. SAMPLE PREPARATION

Preparation of sample material for analysis is the most important technological procedure of any analytical method; it is what the accuracy of the analysis is largely dependent on [1-3,6]. The developed method of sample preparation for GAA of gold does not contradict the basic requirements of the analytical work quality management system for quantitative methods of analysis [19]. The responsibility for the quality of sampling and the representativeness of the initial geological sample lies with the acquirer of the analysis. Taking into account the vast experience in the practical implementation of the GAA method for gold (Muruntau and Batagay laboratories), the following optimal sample analysis scheme has been worked out. For analysis, the GAA laboratory is given an analytical sample weighing 1 kg with <3.0 mm fragmentation size. The GAA receives a sub-sample weighing 0.5 kg (approximately ½ part of the analytical sample). Depending on the bulk density, this is a complete standard container for GAA. It has been experimentally established that the bulk density of a finely ground material with a particle size <0.10 mm can vary over a wide range, while the mass of a sample of a standard GAA container is in the range from 250 to 400 grams.

Prepared samples are packed in containers made of radiation-resistant plastic, securing at least 100 irradiation cycles. The diameter of the container was chosen equal to the diameter of the largest presently possible HPGe detector – 110 mm, and the thickness – 45 mm, which provides a sample weight of 500 ± 50 g (depending on the bulk density) and, therefore, good representativeness of the results (Fig. 5).

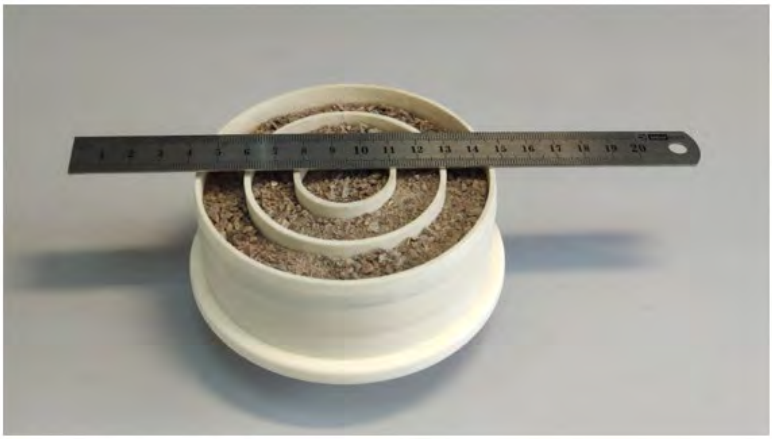

FIG. 5. BSI production of large diameter HPGe detectors for gold analysis.

After carrying out all the sample preparation operations, the necessary identification data of the packed samples (number, weight, date of measurements, etc.) are entered into the computer, which is followed by labelling of the containers with barcodes. The containers, ready for measurements, are moved from the sample preparation room of the GAA Laboratory to the sample loading and unloading room and are placed on the conveyor of the container transportation system, which delivers the samples to the irradiation zone.

4. THE GAA FACILITY'S CHARACTERISTICS RESEARCH AND DISCUSSION

4.1 Calibration

The metrological characteristics of the newly developed GAA facility for gold have been investigated and confirmed during acceptance tests, during which more than 2000 analyzes were carried out. Calibration of the facility before the start of measurements was carried out using reference samples provided by the PAVLIK company, manufactured and certified by VIMS and MST [20,21]. Samples with a content of 1.27 ÷ 24.3 ppm were irradiated once for 10 seconds and, after cooling for 2 seconds, were delivered to the registration area. The spectrum was acquired during 15 seconds. To ensure the precision of the calibration in the range of low gold concentrations, samples of 0.160 and 0.400 ppm were irradiated and tested 4 times, after which the average value of the gold concentration was calculated.

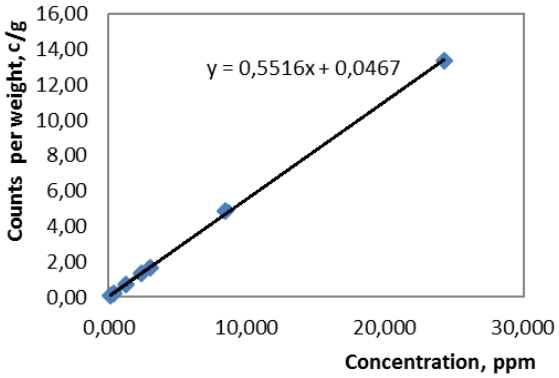

FIG. 6. Dependence of the gold peak of complete absorption area at 279 keV on the gold content in reference samples.

Figure 6 shows a plot of the dependence (based on the results of calibration) of the 279 keV gold peak area of the total absorption, reduced to one gram of the analyzed sample, on the concentration of gold in the reference sample (regression dependence). Subsequently, in the course of measurements, the stability of the calibration of the facility was monitored automatically by feeding a high gold content (24.3 g/t) reference sample for analysis every 3 hours of operation of the facility. To ensure the precision of calibration in the range of low gold concentrations, samples of 0.160 and 0.400 ppm were irradiated and tested 4 times, upon which the average value of gold concentration was calculated.

TABLE 1. PARAMETERS OF REFERENCE SAMPLES AND TESTING RESULTS

Sample №	Reference sample	Au content	Irradiation number	2021.08.31					Average value, ppm	SD, ppм	RMSD, %
				12:10	13:29	14:40	15:57	16:56			
1	OREAS 682	0,074	4	0,087	0,094	0,031	0,105	0,090	0,081	0,030	40,74
2	VIMS211GO	0,160	4	0,303	0,165	0,209	0,109	0,221	0,201	0,085	53,40
3	MST SG147f	0,310	3	0,315	0,316	0,322	0,316	0,361	0,326	0,027	8,60
4	VIMS212GO	0,400	3	0,446	0,359	0,332	0,426	0,400	0,393	0,048	11,92
5	MST Gq157d	0,850	1	0,823	0,916	0,819	0,945	0,888	0,878	0,064	7,56
6	VIMS213GO	1,270	1	1,392	1,245	1,319	1,466	1,479	1,380	0,158	12,45
7	VIMS214GO	2,380	1	2,533	2,463	2,420	2,591	2,420	2,485	0,140	5,87
8	MST 173e	3,000	1	2,987	3,193	3,069	3,162	2,989	3,080	0,131	4,36
10	MST G172f	8,400	1	8,841	8,922	8,275	8,701	8,940	8,736	0,465	5,54
11	VIMS215GO	8,440	1	8,974	8,759	9,590	9,223	8,932	9,096	0,801	9,49
13	MST SGq156i	11,200	1	9,129	8,864	9,003	8,953	9,238	9,037	2,422	21,63
14	VIMS216GO	11,500	1	12,635	12,213	12,706	12,271	12,376	12,440	1,074	9,34
15	VIMS217GO	24,800	1	25,623	25,619	25,507	26,278	25,352	25,676	1,041	4,20
16	VIMS185GO(S)	34,500	1	34,652	34,050	34,235	33,859	34,664	34,292	0,428	1,24

To check the calibration accuracy, multiple analysis of reference samples within a wide range of gold concentrations (0.074 - 34.5 ppm), was performed. The results of the measurements are shown in Table 1. All measurements were carried out 5 times, the values of standard deviation (SD) and root-mean-square deviations (RMSD) of concentration were calculated from the results of the measurements.

4.2 Study of the gold detection limit (DL)

To determine the DL of the developed GAA facility, we used ultra-low background samples manufactured and certified by the MST and Rosdragmet firms [21,22]. Ultra-low background samples were made of purified natural quartz sand with the addition of gold: MST SG147f with a gold content of 0.312 ppm, MST Gq157d –

0.85 ppm, sample 27006101 – 1.908 ppm. All spectra were recorded after single irradiation for 10 s and a spectrum acquisition time of 15 s. For example, the spectrum of the MST Gq157d sample is shown in Fig. 7. To the left of the gold peak, a Hafnium peak is seen in the spectrum of MST Gq157d. The MST SG147f 's spectra contain trace concentrations of Barium and Yttrium, and the spectrum of the 27006101 sample contains Selenium Se-77m (not shown). However, these trace amounts of impurities do not affect the background characteristics of the samples when determining DL for gold.

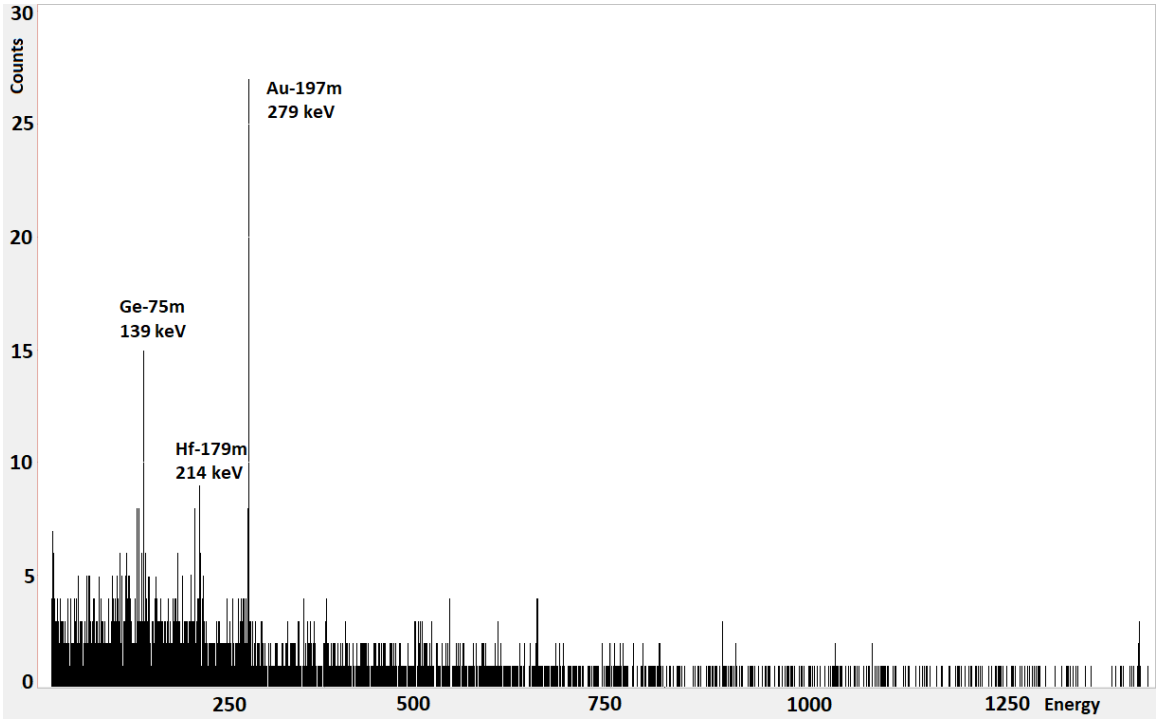

FIG. 7. Spectrum of MST Gq157d sample (single irradiation – 10 sec; spectrum set – 15 sec).

The gold detection limit DL was determined in accordance with the international standard [23]:

$$DL[ppm] = \frac{C * 3 * \sqrt{Nf * \Delta Au/\Delta f}}{\mathrm{NAu}}$$

where, C is the concentration of gold in the sample [ppm], NAu is the number of impulses in the peak of gold, Nf is the number of background pulses in the selected zone, ΔAu is the width of the gold peak in the channels, Δf is the width of the selected background zone in the channels.

According to calculations, the DL values determined from the spectra of certified ultra-low background samples MST SG147f, MST Gq157d, and 27006101 with single irradiation for 10 s and a spectrum acquisition time of 15 s were 0.028, 0.025, and 0.027 ppm (3σ), respectively. The achieved DL level exceeds the DL levels in previous works on the GAA of gold-bearing ores [7-11, 13].

4.3 Accuracy of measurements

An equally important characteristic of GAA is the measurement accuracy [24], which would provide gold concentration values. We conducted a study of statistical errors in the analysis of samples with gold content in the concentration range from 0.312 to 24.3 ppm. Each sample was tested six times with single irradiation. The results obtained were used to determine the average value of gold concentration and a relative standard deviation (SD) from the passport value of the concentration. The test results are graphically presented in Figure 8, and in tabular form, those are given in Table 2. The data show that for the gold concentration of about 1 ppm the root-mean-square deviation does not exceed 8%, and for a concentration of 10 ppm – 4%.

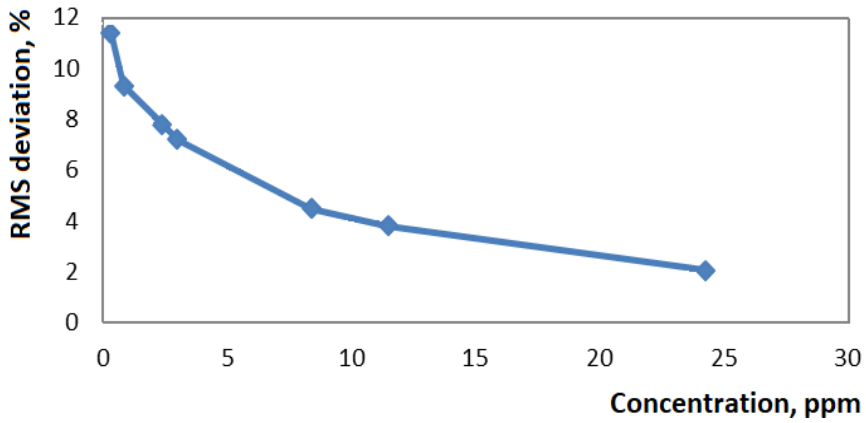

FIG. 8.
Graph of the relative standard deviation dependence on the measured concentration of gold for different concentrations

TABLE 2. STATISTICAL ERRORS IN THE ANALYSIS OF REFERENCE SAMPLES WITH GOLD CONTENT IN THE CONCENTRATION RANGE FROM 0.312 TO 24.3 PPM

Reference sample	Gold concent., ppm	DL, 3σ, ppм	Average concent. value, ppм	SD, ppм	RMSD, %
MST SG147f	0.312	0,034	0.331	0.036	11.390
MST Gq157d	0.850	0,031	0.885	0.079	9.320
VIMS214GO	2.380	0,078	2.334	0.186	7.800
MST G173e	3.000	0,090	2.908	0.216	7.190
MST G172f	8.400	0,085	8.658	0.376	4.480
VIMS216GO	11.500	0,078	11.731	0.439	3,810
MST209	24.300	0,030	24.312	0.501	2.060

4.4 Stability of the results of gold concentration determination

To study the stability of the results of determining the gold concentration in our experiments, we used samples MST209 with a gold concentration of 24.3 ppm, VIMS212GO with a gold concentration of 0.4 ppm and MST SGBlank10 with a gold concentration of less than 0.005 ppm. The measurements were carried out for 6 consecutive days, 5 measurements per day at different times, with constant calibration coefficients and irradiation modes. Thus, MST 209 and MST SGBlank10 samples were tested 30 times with single irradiation. The VIMS212GO sample was analyzed six times. Based on the test results, the mean concentration value and deviation from the mean value were calculated for each sample. The deviation of the measured concentration from the reference for the sample of 0.4 ppm was less than 6.5% and less than 1.0% for the sample of 24.3 ppm. Studies have shown high stability of the results.

In addition, the results of measuring the gold concentration in a sample that does not contain gold were also analyzed for stability. The sample used was MST SGBlank10 with a gold concentration of less than 0.005 ppm. Each measured concentration value for the MST SGBlank10 sample is the average of five measurements with single irradiation of the sample. The test results are shown in Figure 9. Studies have shown that the deviation of the concentration measured in each cycle from the reference does not exceed 0.011 ppm.

4.5 Precision and repeatability of results

Testing of the GAA facility for precision and repeatability [24] of measurement results was carried out on "wild card" samples provided by PAVLIK. In the first stage, the concentration of gold in 30 samples was measured with single irradiation. Based on the measurement results, 17 samples were taken, the gold content of which evenly covers the range of gold concentrations from 0.1 to 20 ppm. The collected samples were tested twice consecutively on the first day and then again on the second day. The measurements were carried out with single irradiation and unchanged settings in the measuring system.

The measurement precision [24] was determined from the obtained values of the concentration of two adjacent measurements on the first and second days. The deviation of each measurement from the average in the concentration range of 0.1-1.0 ppm was 3.78%. The deviation of each measurement from the average in the concentration range of 2.0 ÷ 20.0 ppm was 0.96%.

The repeatability of measurements [24] was determined from the obtained values of the concentration of two successive measurements on the first and second days. The deviation of each measurement from the average in the concentration range of 0.1-1.0 ppm was 1.68%. The deviation of each measurement from the average in the concentration range of 2.0 ÷ 20.0 ppm was 1.4%.

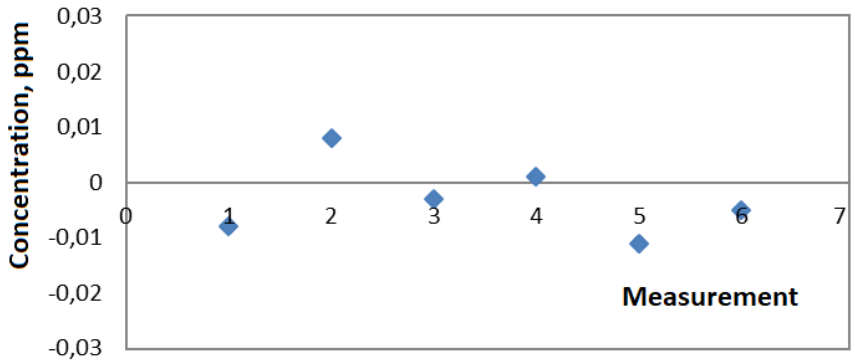

FIG. 9.
Graph of the relative standard deviation dependence on the measured concentration of gold for different concentrations.

4.6 Investigation of real ores

The spectra of the real samples of gold-containing ore with the presence of various associated elements were studied. Our test results, obtained with real ore samples, have confirmed the effectivity of the analysis for the following elements: Au, Ag, As, Ba, Br, Cd, Er, Ge, Hf, Hg, In, Ir, Lu, Pb, Pt, Rh, Se, Sn, Th, U, Y, and W. The concentrations of all these elements can be accurately measured by developing appropriate measurement techniques. In the process of spectra measurements, it was noted that the main input to the background pedestal where the peaks of gold, silver, hafnium and other associated elements are situated, is specified by the products of the photofission of uranium and thorium. The content of uranium in ore samples provided to us was estimated as ~ 40-50 g/t, thorium ~ 100 g/t, barium ~300 g/t, and yttrium ~ 200 g/t.

4.7 Metrological Certification

The Au-Isomer GAA facility has been certified by the State Test and Measurement Instrument Certification Center of the D.I. Mendeleev All-Russian Institute for Metrology (VNIIM), as per the state GOST R 8.568-2017 standard, and recognized as suitable for use in testing samples of rocks, ores and products of their processing for gold content by the method of gamma activation analysis using a UELR-8-10A linear electron accelerator (certificate № 209/06-2021 of 15.10.2021).

A measuring technique "Determination of gold in rocks, ores and products of their analysis by the method of gamma activation using a UELR-8-10A linear electron accelerator" for the facility has passed the metrological certification, as well (certificate No 2121/209 - (RA.RURU10494) -2021, dated 17.12.2021).

5. CONCLUSION

In the course of characteristics studies, more than 2000 analyzes were carried out on the developed "Au-Isomer" GAA facility. The facility demonstrated excellent DL values – (0.025-0.028) ppm with single irradiation for 10 sec and a spectrum acquisition time of 15 sec. In this case, the root-mean-square measurement error for a gold concentration of 1 ppm did not exceed 8%, and for a concentration of 10 ppm – 4%. The "Au-Isomer" provides an analysis capacity of at least 65 samples per hour with the possibility of further increasing the productivity up to 75 samples per hour.

REFERENCES

[1] Hoffman, E.L., Clark, J.R., Yeager, J.R., Gold analysis-fire assaying and alternative methods, Expl. and Mining Geol., Vol. 7, No 1&2 (1998) 155–160.

[2] Morse, J.G., Nuclear Methods in Mineral Exploration and Production, Elsevier (1977).

[3] Bourmistenko, Yu.N., Photonuclear Analysis of Materials Composition, M.: Energoatomizdat (1986).

[4] Bourmistenko, Yu.N., Ivanov, I.N., Sviridova, V.V., Feoktistov, Yu.N., Computer-selected optimization of activation analysis methods, J. Radioanal. Chem., v. 40 (1977) 147–153.

[5] Sammut, D., Gamma activation analysis. A new gold standard? Chem. in Austral. (February 2016) 18–21.

[6] Tickner, J., Ganly, B., Lovric, B., O'Dwyer, J., Improving the sensitivity and accuracy of gamma activation analysis for the rapid determination of gold in mineral ores. Appl. radiat. and isotop.: incl. data, instrument. and methods for use in agricult., indust. and med. (2017) 122:28–36.

[7] Navoi Mining and Metallurgical Company, https://www.ngmk.uz/en/

[8] Sokolov A.D., Burmistenko, Y.N., Gostilo, V.V., Titov, V.L. Industrial gamma-activation assay system for gold ore analysis, Miner. Engineer., vol.117 (January 2018) 179–181.

[9] Sokolov, A.D., Demsky, M.I., Gostilo, V.V., Hasikova, E.I., Titov, V.L., “Gold ore analysis using industrial gamma-activation assay system”, ALTA (Australia, Perth, 2017), www.altamet.com.au/conferences/alta-2017 (2017), 146–153.

[10] Sokolov, A., Gostilo, V., Demsky, M., Hasikova, E., “Optimization of an industrial gamma-activation assay system for the analysis of gold and rare earth metal ores”, ALTA (Australia, Perth, 2018), Gold-PM Proceedings ISBN: 978-0-9946425-4-7 (2018).

[11] Sokolov, A., Gostilo, V., Demsky, M., Hasikova, E., Performance optimization of an industrial gamma activation assay system for analysing gold and rare metal ores, The J. of the South. Afr. Instit. of Min. and Metallur. (SAIMM), v. 119, (May 2019) 509–513.

[12] Chrysos Photon Assay, https://chrysos.com.au/

[13] Taylor, A., Technological trends in the field of gold ore processing and gold recovery, Gold min. (Zolotodobicha), No. 8 (249), (2019).

[14] Pavlik Gold Ore Company, https://www.pavlik-gold.ru

[15] Demsky, M.I., Pesterev, A.G., Gostilo, V.V., Efremova, N.V., Device for gamma activation analysis, Patent for utility model, No. 203146 (01/25/2021).

[16] Basyl, D.S., Bondarenko, T.V., Gusarova, M.A. et al., “New 10 MeV high power linac for industrial application”, IPAC (Korea, Busan, 2016), Proceedings of IPAC 2016, TUPOW023, 1794–1796.

[17] Nurgalejev, R., Pohuliai, S., Sokolov, A., Gostilo, V., Vanpaemel, J., Spectrometric performance of a HPGe semi-planar detector with large diameter, NIM-A, v. 985 (2021).

[18] Baltic Scientific Instruments, Multi Channel Analyzer BOSON, http://bsi.lv/en/products/electronics/multi-channel-analyzer-boson/

[19] Russian state standard OST 41-08-272-04 “Analytical quality management. Methods for geological quality control of analytical work”, https://www.rts-tender.ru/poisk/gost/r-iso-5725-4-2002

[20] All-Russian Scientific-Research Institute of Mineral Resources named after N.M.Fedorovsky, www.vims-geo.ru

[21] Scientific and Technical Center "Mineral Standards", http://minstandart.com

[22] RosDragMet Ltd., https://rosdragmet63.ru

[23] International Standard ISO 11929-1:2019, Determination of the characteristic limits (decision threshold, detection limit and limits of the coverage interval) for measurements of ionizing radiation - Fundamentals and application- Part 1: Elementary applications, https://www.iso.org/standard/69579.html [accessed on 06.10.2021]

[24] The International ISO Standard 5725-1-2002, Accuracy (trueness and precision) of measurement methods and results, Moscow, Standartinform (2009), https://docs.cntd.ru/document/1200029975

[25] The D.I. Mendeleev All-Russian Institute for Metrology (VNIIM), https://www.vniim.org/info.html

NEUTRON-INDUCED FISSION STUDIES AT NCSR "DEMOKRITOS" BY THE NTUA

V. MICHALOPOULOU
National Technical University of Athens
Zografou, Athens, Greece
Email: veatriki.michalopoulou@cern.ch

M. DIAKAKI, R. VLASTOU, M. KOKKORIS, A. STAMATOPOULOS,
S. CHASAPOGLOU, G. GKATIS, A. TSANTIRI, A. TSINGANIS
National Technical University of Athens
Zografou, Athens, Greece

A. KALAMARA
National Technical University of Athens
Zografou, Athens, Greece
National Centre of Scientific Research "Demokritos"
Agia Paraskevi/Athens, Greece

N. PATRONIS, Z. ELEME
University of Ioannina
Ioannina, Greece

M. AXIOTIS, A. LAGOYANNIS
Tandem Accelerator Laboratory, Institute of Nuclear and Particle Physics
National Centre of Scientific Research "Demokritos"
Aghia Paraskevi, Athens, Greece

Abstract

The neutron beam facility of the 5.5 MV Tandem T11/25 Accelerator Laboratory of the NCSR "Demokritos" has been extensively used over the past 10 years for fission cross section measurements on various actinides (^{237}Np, ^{234}U, ^{236}U, ^{232}Th), at and above the fission threshold. All these isotopes are very important for the design of advanced nuclear systems for a more clean and safe future energy production, as well as for the dissemination of nuclear waste. The neutron beam is produced via the ^{7}Li(p, n), the ^{3}H(p,n), the ^{2}H(d,n) and the ^{3}H(p,n) reactions, depending on the energy range of interest. The neutron flux (of typically 10^{5}-10^{6} n/cm^{2}/s) is calculated by means of the reference ^{235}U(n,f) and ^{238}U(n,f) cross sections. Special attention is given to the study of the neutron beam (monochromaticity, propagation of neutron beam among the targets etc.), due to the lack of effective threshold for the fission cross section, via detailed Monte Carlo simulations and experimental checks. The detection system consists of a stack of ionization gas cells based on the Micromegas Microbulk technology for the detection of the fission fragments. The final experimental points, which are made publicly available at the scientific community via the EXFOR database, have low uncertainties of the order of 5%. An overview of the experimental campaign, the description of the setup and the analysis as well as the future perspectives will be presented and discussed.

1. INTRODUCTION

Accurate data on neutron-induced reactions are required for the study and development of new generation nuclear systems and alternative fuel cycles, with the scope of making the production of energy through nuclear power economical, proliferation resistant, safer and sustainable. In addition, the study of fission cross-sections on actinides acts as a baseline for the advance and development of the theoretical nuclear models of fission, with the scope to understand the fission process and study the fission characteristics.

In this framework, over the past 10 years, an extensive study of neutron-induced fission cross-sections at and above the fission threshold of various actinides has been carried out at the neutron beam facility of the National Centre for Scientific Research "Demokritos" by the Nuclear Physics Group of the National Technical University of Athens. The measurements were carried out with quasi-monoenergetic neutron beams produced via charged particle reactions on solid and gas targets, while the detection of the fission fragments was achieved with the use of Micromegas detectors. Special attention was given to the estimation of the parasitic neutrons present in the

experimental area, through experimental techniques, as well as Monte Carlo simulations of the neutron beam and experimental setup. The experimental data of the measurements are published and available in the Experimental Nuclear Reaction Data library (EXFOR) [1]. An overview of the above-mentioned measurements and analysis techniques is presented in the paper.

2. EXPERIMENTAL SETUP

The experiments were performed at the 5.5 MV Van de Graaf Tandem Accelerator of the National Centre for Scientific Research "Demokritos" over the past ten years. The production of the neutron beams was achieved via the ^{7}Li(p,n), ^{3}H(p,n), ^{2}H(d,n) and ^{3}H(d,n) reactions, depending on the energy range of interest in each particular measurement, achieving this way cross-section points from the fission threshold up to 18 MeV. The ^{235}U(n.f) and ^{238}U(n,f) cross-sections were used as reference, in order to estimate the neutron fluence incident in the targets. However, it is important to note that the ^{235}U is affected by low energy parasitic neutrons present in the experimental area, thus it was used as reference only in the cases where the contribution of these parasitic neutrons was considered to be negligible.

The targets used in the experiments (^{232}Th, ^{234}U, ^{236}U, ^{237}Np) were characterized by alpha spectroscopy, implementing silicon surface barriers detectors. More specifically, the setup was calibrated by a ^{241}Am alpha source prior to the target measurements [2]. Then, when necessary, additional FLUKA simulations [3] were performed in order to deconvolute the alpha peak of interest from the contaminants present in the target [4], as seen in Fig. 1. In some cases, additional Rutherford Backscattering measurements were performed in order to estimate the homogeneity of the targets [5].

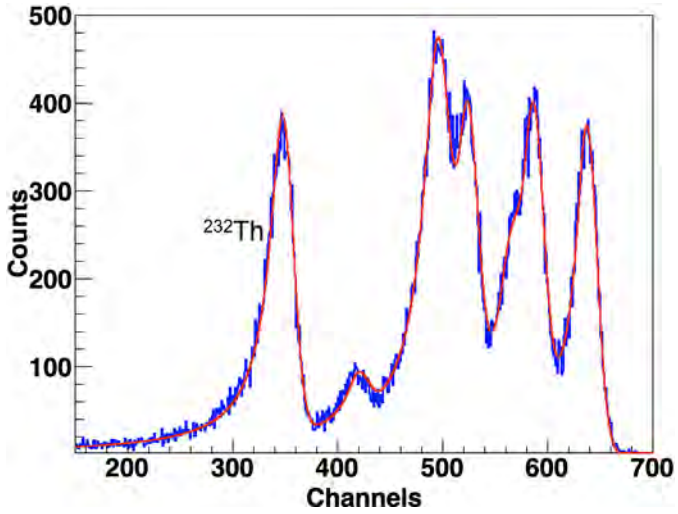

FIG. 1: Experimental alpha spectroscopy spectrum (blue line) along with the FLUKA simulations (red line), where the first peak is the ^{232}Th alpha peak and the rest of the peaks originate from the daughter nuclei.

For the detection of the fission fragments a setup based on the Micromegas gas detectors was used [6, 7]. Each target, acting as the drift electrode, was coupled to a Micromegas detector. From each fission event, one of the created fission fragments enters the detector gas and it is detected, through the energy it deposits in the detector gas. The efficiency of the detector is ~1, while the covered solid angle ~2π. The signal created is collected, after multiplied by avalanches in the mesh region, by a fast preamplifier and it is then fed to conventional electronic modules (amplifier, MCA).

3. DATA ANALYSIS

The neutron-induced fission cross-section at each neutron energy was estimated via the following expression

$$\sigma(E) = \frac{C_{tar}(E)}{C_{ref}(E)} \cdot \frac{\Phi_{ref}(E)}{\Phi_{tar}(E)} \cdot \frac{N_{ref}}{N_{tar}} \cdot \sigma_{ref}(E) \cdot \frac{f_{tar}(E)}{f_{ref}(E)}$$

where C are the counts estimated from the amplitude spectra, Φ is the fluence incident in the target, N is the areal density of the target, σ_{ref} is the cross-section of the reference target and f are various correction factors applied

to the estimated counts that include the dead time correction, correction for the amplitude cut introduced in the analysis to avoid counting alpha counts as fission fragments, correction for the difference in the fluence between the measuring target and the reference target mainly due to the different position with respect to the neutron beam and correction for the parasitic neutrons present in the experimental area, while the subscripts "*tar*" and "*ref*" refer to the measured and reference target respectively.

More specifically, the counts at each neutron energy and each target are estimated from the integration of the spectrum, after applying a suitable amplitude cut to reject the α-particles from the natural radioactivity of the actinide targets present in the low amplitudes of the spectrum. Then, in order to account for the lost fission fragment signals under the α peak, Monte Carlo simulations were performed with the FLUKA code, along with the GEF code [8] to provide the information regarding the energy and mass of the fission fragments of each target, in order to estimate the energy deposition of the fission fragments in the detector gas. The simulated energy deposition spectrum was then calibrated and convoluted with an appropriate function in order to reproduce the experimental one. Thus, the lost fission fragments could be estimated with high accuracy. The experimental and simulated spectra are shown in Fig. 2, where a very good agreement between the two is observed.

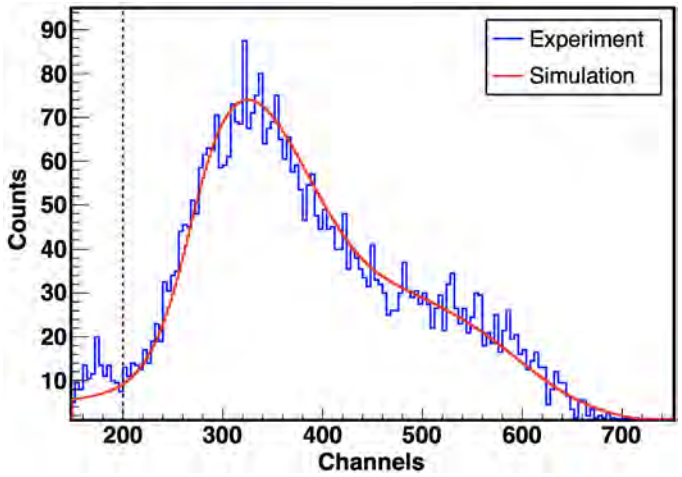

FIG. 2: Experimental fission spectrum (blue line) along with the simulated one (red line) after calibration and convolution with appropriate function. The black dashed line represents the amplitude cut introduced in the analysis.

Additional Monte Carlo simulations were performed with the MCNP code [9], along with the NeuSDesc code [10] for the description of the neutron source, in order to estimate the neutron fluence incident at each target. This is mainly a geometrical correction, originating from the different distances of the targets with respect to the neutron source. Additionally, from these simulations an estimation and correction for low energy parasitic neutrons can be made, by convoluting the flux incident at each target with the reference cross-section of the target [2, 11]. In addition, for the ^{2}H(d,n) reaction the deuteron break-up in the deuterium gas is also taken into account by the simulations. In Fig. 3 the neutron fluence estimated at 10 MeV for the ^{2}H(d,n) neutron producing reaction is presented, where the break-up peak is also present in the spectrum.

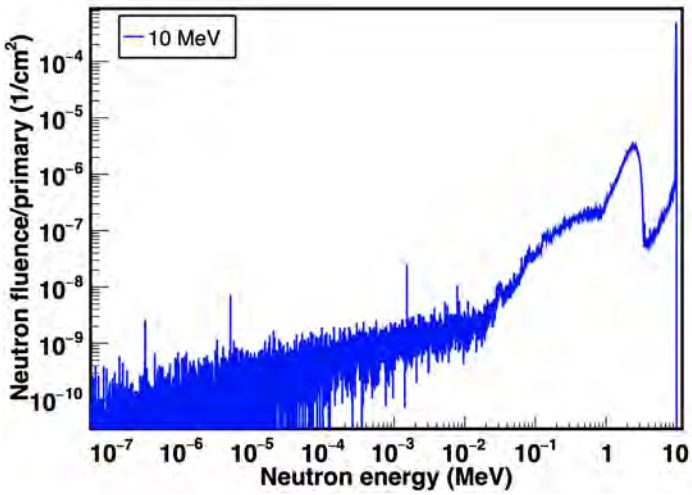

FIG. 3: Simulated neutron fluence for 10 MeV neutrons produced via the ^{2}H(d,n) reaction. The neutron break-up peak is apparent in the spectrum.

In parallel, a thorough study regarding the higher energy parasitic neutrons present in the experimental area has been conducted [3]. These parasitic neutrons originate from interactions of the particle beam with materials in the beam line (^{12}C, ^{16}O, etc.) and the target containers, as well as materials present on the target itself. In order to ensure accurate cross-section results, the similarity in the shape of the cross-section between the reference target and the measuring target, in the regions where these high energy parasitic neutrons are created, is important in order to minimize the effect of these parasitic neutrons. For each reaction measured, an analysis of the effect of the parasitic neutrons is made, depending on the neutron producing reaction and, on the reference, and measuring target. Additional experimental techniques are implemented, as the gasin/gasout method for the ^{2}H(d,n) reaction, where measurements are taken for the same neutron energy with and without the deuterium gas, in order to estimate the contribution of the deuterons impinging in the beam line and the materials of the gas cell [2, 5, 6], while the same technique was used for the ^{3}H solid target [3] as well.

4. RESULTS

Cross-section results have been obtained for the neutron-induced fission of

- ^{237}Np in the energy range 4.5-5.3 MeV measured with the ^{2}H(d,n) reaction [5].
- ^{234}U in the energy range 400-700 keV, 5.5-10.5 MeV and 14.8-17.8 MeV measured with the ^{7}Li(p,n) ^{2}H(d,n) and ^{3}H(d,n) reactions respectively [2, 12].
- ^{236}U in the energy range 4.5-10 MeV measured with the ^{2}H(d,n) [11].
- ^{232}Th in the energy range 2-18 MeV measured with the ^{3}H(p,n), ^{2}H(d,n) and ^{3}H(d,n) reactions [3].

The cross-section data points are available in the EXFOR database [1], while some the latest results concerning the cross-section measurements of ^{232}Th and ^{236}U are presented in Fig. 4 and Fig. 5 respectively.

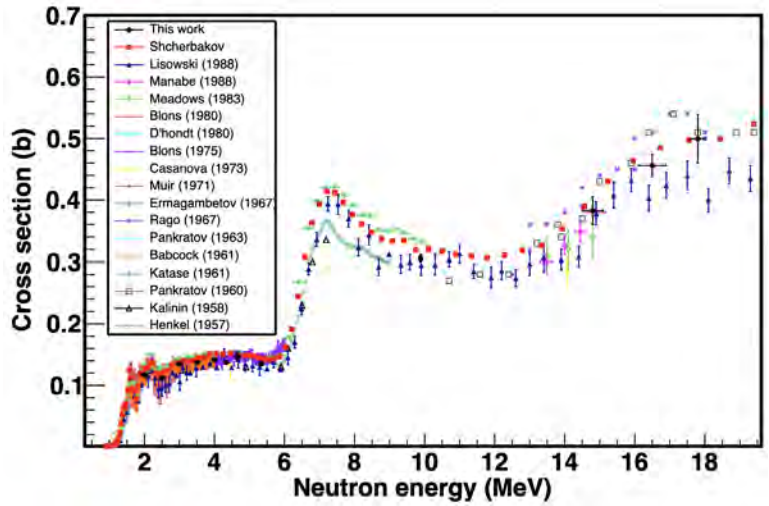

FIG. 4: Cross-section results for the ^{232}Th(n,f) reaction (black points) in the energy range 2-18 MeV, along with the available datasets available in EXFOR.

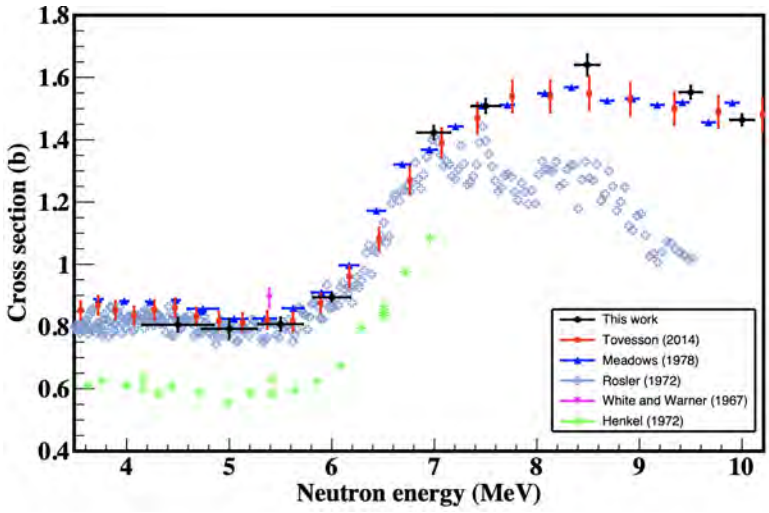

FIG. 5: Cross-section results for the ^{236}U(n,f) reaction (black points) in the energy range 4.5-10 MeV, along with the available datasets available in EXFOR.

5. CONCLUSIONS AND FUTURE PERPSPECTIVES

During the last 10 years the Nuclear Physics Group of NTUA has conducted a series of neutron-induced fission cross-section measurements on actinides at the neutron beam facility of the National Centre of Scientific Research "Demokritos". These measurements are compared in the relevant publications with the other existing experimental data and evaluated libraries and are generally found to be in good agreement with certain datasets. The measurements aim to produce data, which can assist in the study and design of advanced nuclear systems and alternative fuel cycles, as well as in the study of the fission process and fission characteristics.

An analysis procedure, which is thorough and detailed, has been developed in order to extract accurate cross-section results, with special attention given to the study of parasitic neutrons based on experimental and simulated techniques. As a next step, Monte Carlo simulations are being performed with the GEANT4 code [13], in order to have an estimation of the interaction of the charged particle beam, with the beamline and target materials, along with the simulation of the neutron beam.

Finally, measurements on the highly radioactive ^{233}U are scheduled to be performed in the neutron beam facility of "Demokritos", which will yield interesting new data to complement the existing results.

ACKNOWLEDGEMENTS

We acknowledge the support of this work by the project CALIBRA/EYIE (MIS 5002799), which is implemented under the Action "Reinforcement of the Research and Innovation Infrastructures", funded by the Operational Program "Competitiveness, Entrepreneurship and Innovation" (NSRF 20142020) and co-financed by Greece and the European Union (European Regional Development Fund).

This research is implemented through IKY scholarships program and co-financed by the European Union (European Social Fund —ESF) and Greek national funds through the action entitled "Reinforcement of Postdoctoral Researchers -2nd call (MIS 5033021)", in the framework of the Operational Programme "Human Resources Development Program, Education and Lifelong Learning" of the National Strategic Reference Framework.

REFERENCES

[1] ZERKIN, V.V., PRITYCHENKO, B., The experimental nuclear reaction data (EXFOR): Extended computer database and Web retrieval system, Nucl. Instrum. Methods A 888 (2018) 31.

[2] STAMATOPOULOS, A. et al., Measurement of the ^{234}U(n, f) cross-section with quasi-monoenergetic beams in the keV and MeV range using a Micromegas detector assembly, Eur. Phys. J. A 54 (2018) 7.

[3] MICHALOPOULOU, V. et al., Measurement of the ^{232}Th(n,f) cross section with quasi-monoenergetic neutron beams in the energy range 2-18 MeV, Eur. Phys. J. A 57 (2021) 277.

[4] BOHLEN, T.T. et al., The FLUKA Code: Developments and Challenges for High Energy and Medical Applications, Nucl. Data Sheets 120 (2014) 211.

[5] DIAKAKI, M. et al., Determination of the ^{237}Np(n,f) reaction cross section for E_n = 4.5-5.3 MeV, using a MicroMegas detector assembly, Eur. Phys. J. A 49 (2013) 62.

[6] GIOMATARIS, Y., Development and prospects of the new gaseous detector "Micromegas", Nucl. Instrum. Methods, A 419 239 (1998).

[7] ANDRIAMONJE, S. et al., A New 2D-micromegas Detector for Neutron Beam Diagnostic at n_TOF, J. Korean Phys. Soc. 59 (2011) 1597.

[8] SCHMIDT, K.-H., JURADO, B., AMOUROUX, C., SCHMITT, C., General Description of Fission Observables: GEF Model Code, Nucl. Data Sheets 131, (2016) 107.

[9] ARMSTRONG, J. et al., ed. C.J. Werner, MCNP User's Manual - Code Version 6.2, (LA-UR-17-29981, 2017)

[10] BIRGERSSON, E., LOEVESTAM, G. NeuSDesc neutron source description software manual, Technical Report, EUR 23794 EN (European Commission, 2009).

[11] DIAKAKI, M. et al., Measurement of the ^{236}U(n,f) cross section at fast neutron energies with Micromegas Detectors, EPJ Web Conf. 239, (2020) 05001.

[12] KALAMARA, A., et al., Measurement of the ^{234}U(n,f) cross section in the energy range between 14.8 and 17.8 MeV using Micromegas detectors, EPJ Web Conf. 239, (2020) 05005.

[13] ALLISON, J., et al., Recent developments in Geant4, Nucl. Instr. and Meth. A835, (2016) 186-225.

EFFECTS OF STERILIZATION IRRADIATION ON PROPERTIES OF COMMERCIALLY AVAILABLE PET MATERIALS USED IN THE PRODUCTION OF VACUUM TUBES FOR BLOOD SAMPLING

V. A. SHARAPOVA
UrFU named after the first President of Russia B. N. Yeltsin
Ekaterinburg/ Russian Federation
Email: v.a.sharapova@urfu.ru

I. S. KAMANTSEV
Institute of Mechanical Engineering, Ural Branch of the Russian Academy of Sciences
Ekaterinburg/ Russian Federation

V. P. SHVEYKIN
Institute of Mechanical Engineering, Ural Branch of the Russian Academy of Sciences
Ekaterinburg/ Russian Federation

V. Y. IVANOV
UrFU named after the first President of Russia B. N. Yeltsin
Ekaterinburg/ Russian Federation

O. N. RYABUKHIN
UrFU named after the first President of Russia B. N. Yeltsin
Ekaterinburg/ Russian Federation

Abstract

The effect of irradiation with accelerated electrons (energy 8.5 MeV, dose 5 kGy) on the physical properties of medical products made of polyethylene terephthalate (PET) was studied by methods of assessing the visible light transmission. The identified post-radiation changes from irradiation with electrons of 5 kGy confirm some changes in PET products during the radiation sterilization procedure.

1. INTRODUCTION

The introduction of radiation technologies into the production or post-processing of products made of polymers and plastics makes it relevant to study the processes occurring in such materials under the influence of radiation [1]. Polyethylene terephthalate (PET) is the most widely consumed in the polyester fiber segment. PET packaging is currently actively replacing such traditional types of pharmaceutical, medical and laboratory packaging as glass and cardboard. However, due to their heat sensitivity, PET medical products require so-called “cold” sterilization methods. To date, there are methods of sparing "cold" sterilization of medical devices with low-temperature atmospheric plasma [2], which allows achieving the necessary bactericidal effect while maintaining the necessary physical and chemical properties of medical devices. At the same time, an industrial method for sterilizing medical devices, which makes it possible to sterilize objects directly in a sealed package, is the treatment with accelerated electrons with energies below the threshold for the occurrence of nuclear reactions (usually up to 10 MeV). The method allows you to process large volumes of products in a short time without opening the factory packaging. The state standart ISO 11137-1-2011, which regulates the radiation sterilization procedure in the Russian Federation, defines a sterilization dose range of 15–25 kGy. The choice of dose from the normalized range is primarily carried out from the conditions of ensuring the established requirements for sterility. On the other hand, the radiation sterilization procedure should not significantly impair the consumer properties of products [3]. In this regard, the search for sensitive methods for assessing the post-radiation changes in the physicochemical properties of PET medical products seems to be relevant.

The material for the study was samples of medical PET tubes for blood sampling produced by Zdravmedtech-E JSC. Samples were irradiated with accelerated electrons at the Innovation and Implementation Center for Radiation Sterilization of the Ural Federal University (UrFU). The irradiation dose was 5 kGy at an

electron energy of 8.5 MeV. At the same time, the paper did not set the task of establishing the lower threshold of the sterilization dose, but the main purpose of the work was to assess the sensitivity of the method to determining the initial stages of changes in the physicochemical properties of irradiated materials [4].

It is known [5] that exposure to ionizing radiation leads to a change in the physicochemical properties of materials. Also, according to the study [6], for this material, an electron irradiation dose of 1 MGy leads to a drop in ultimate strength by 15–30%. Due to the fact that their vibrational and optical spectra also depend on the chemical composition and structure of substances, it was decided to analyze the change in the transmission of visible light through test tubes [7].

2. RESULTS AND DISCUSSION

Two series of tests were carried out to evaluate the change in the optical properties of PET tubes. In the first series, the task was to analyze the change in the refractive index. For this purpose, an optical system was assembled, shown in Fig. 1.

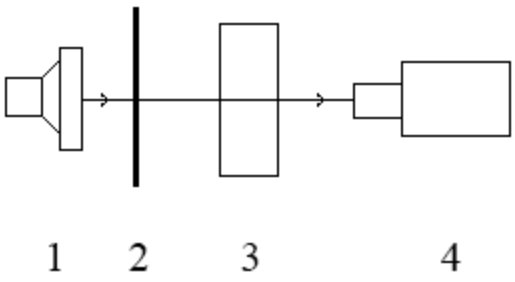

FIG. 1. Optical installation for the analysis of samples on a transmission. The presented installation includes an illuminator (1), a matte diffuser (2), an object (3), a video camera (4).

The illuminator is a powerful source of uniform radiation - an LED assembly with a luminous flux of 880 lm. As a matte diffuser, a substrate made of a randomly reinforced composite material with cellulose filler was used, on which a scale grid was previously applied. The samples were placed in a horizontal plane between a matte diffuser and a video camera on a special mount. The mount ensured the identity of the position of the irradiated and non-irradiated samples during the shooting process. Registration of a uniform light flux, as well as the light flux passing through the irradiated and non-irradiated samples, was performed on the camera in turn. A black-and-white camera Videoscan-415 was used as a video camera with the possibility of programmatically changing the exposure time. Within each series of tests, the exposure time was selected so that the radiation brightness in the controlled area was in the range of average values.

During the experiments, several series of surveys were made. Based on the obtained images, the change in the intensity of the light flux passing through the samples was analyzed, and a comparison table was compiled between the samples that were irradiated and the samples without irradiation. The camcorder generates 8-bit black and white images with a range of gray shades, expressed in signal levels from 0 to 255.

Since real products were used as the object under study, it is possible that during the manufacturing process their walls may have some differences in thickness, even within the same batch, so there was a need to apply a technique for analyzing the size of the zone and the contribution of defects to the study pattern. Measurements of the signal levels characterizing the brightness of an object were carried out by averaging the values around the selected point for areas of 2x2, 3x3, 4x4 and 5x5 pixels in order to select the optimal size of the area.

Initially, about 15 measurements were made for each sample at various random points. This was done in order to collect a large amount of data and take into account possible errors and inaccuracies associated with the geometric dimensions of various samples, as well as wall thickness parameters. The calculation of the values was carried out in several stages:

1. The values of the signal intensities around each point for each area were entered into a separate array.
2. The arithmetic mean value of the signal level for each array was found.
3. The results were then compared between samples, after irradiation and without irradiation, and all samples were compared with the original image of the frosted diffuser.

For example, the data obtained from two points for different objects (Fig. 2).

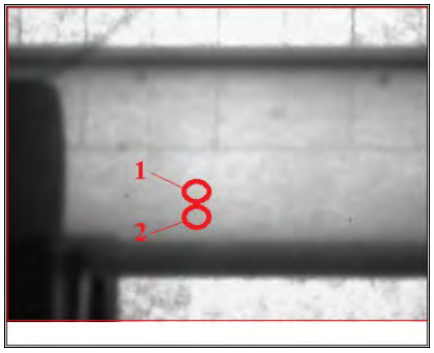

FIG. 2. Location of signal levels characterizing the center of the measurement area, 1 – with coordinates (332;342), 2 – with coordinates (332;382).

Formula for calculating intensity distribution:

$$I = \frac{(I_{pure.} - I_{irrad.})}{I_{pure.}} * 100\%,$$

where, I_{pure} is the arithmetic mean of the intensities at each point for the selected area in the unirradiated sample, and $I_{irrad.}$ is the same value for the sample after irradiation, taken for a region of the same size and at the same point. The value is given as a percentage, and its positive value indicates that for a pure sample, the signal levels are on average higher than for an irradiated one.

Similarly, the difference in intensity between the original image and all samples was calculated. The data are presented in Table 1.

TABLE 1. AVERAGE INTENSITY OF THE ORIGINAL IMAGE AND LIGHT TRANSMISSION

Sample	332;342				332;382			
	2x2	3x3	4x4	5x5	2x2	3x3	4x4	5x5
9 ml irradiated	23.54%	23.10%	23.47%	23.44%	29.42%	29.77%	30.35%	30.31%
9 ml pure	22.02%	22.15%	21.95%	21.82%	27.58%	27.77%	28.34%	28.53%
5 ml irradiated	10.40%	10.66%	11.18%	11.14%	14.20%	14.97%	16.24%	16.79%
5 ml pure	4.55%	3.97%	3.91%	3.98%	11.54%	11.61%	12.13%	11.98%
2 ml irradiated	13.64%	14.03%	14.16%	14.27%	19.51%	19.83%	20.40%	21.07%
2 ml pure	12.42%	12.28%	11.94%	11.93%	17.88%	17.74%	17.96%	17.91%

On average, a relative change in intensity of 3-4% to non-irradiated samples was observed. The change in intensity indicates that the object began to transmit less light after irradiation, which probably indicates a deterioration in its optical properties, i.e. about a proportional increase in the refractive index. With an increase in the field of analysis, the spread of values increases by 0.5-2%. From the point of view of geometry, the most accurate values seem to be for samples with a volume of 9 ml. Their lateral surface is the largest of those presented, and, probably, therefore, the effect of geometry with an increase in the size of the controlled area was less, and the discrepancies in the values for different areas do not exceed 0.5%. The same cannot be said about samples of smaller size, in which, in addition to the processes described above, associated with a decrease in the transparency of the sample under the action of irradiation, the geometry of the sample also has a significant effect. The spread of values for such samples is about 2%.

According to classical ideas about glasses and other optically transparent objects, as the refractive index increases, the reflection coefficient also increases in them [8], in order to test our previous theory, it is enough to establish that the reflection coefficient also increases. In this case, if we place the light source away from the chamber, as shown in Fig. 3, and record the light reflected from the walls of the tube, then its intensity for the irradiated samples should be higher.

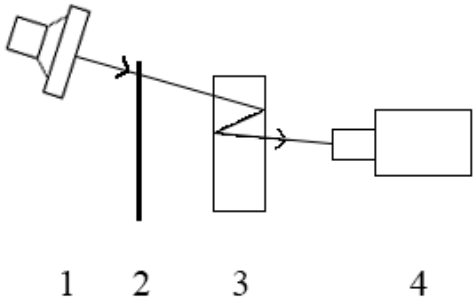

FIG. 3. Optical system for reflectance analysis and an example sample image. The numbering of the objects of the optical system corresponds to Fig. 1

For this series of tests, many points in various segments of the image were taken into account, and the most characteristic ones were selected from them. Figure 4 shows the location of points for one of the samples. The points were chosen at some distance from the light source and from the edges of the sample in order to exclude the influence of the geometry and position of the samples. The results of a series of tests fully confirmed the hypothesis put forward and showed an increase in the intensity of the reflected flux by 7–10% for various points in the region of the sample. The data is presented in Figure 5.

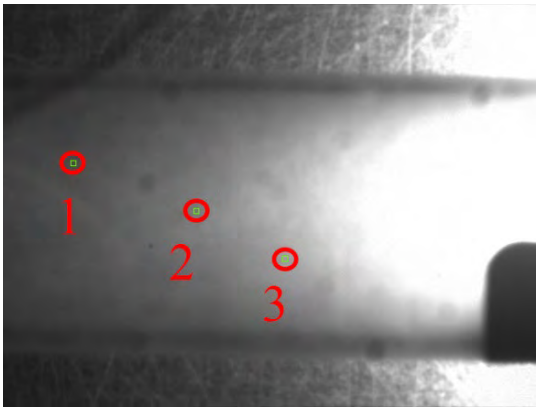

FIG. 4. Image of the sample with the designation of the studied areas for points: 1- (100; 230), 2- (280; 300), 3- (410; 370).

From the graphs in Figure 5 it can be seen that the intensity of the reflected light flux is greater where the object was irradiated, which in turn may indicate an increase in the reflection coefficient and, as a result, an increase in the refractive index. This kind of approach can also be used for optical control of products in a stream production, in the case when it is not possible to unambiguously determine the location of the sample on the conveyor belt and its exact position relative to the camera and light source. Thanks to this kind of research and more statistical measurements, this task can be accomplished.

It should be noted that when testing samples in transmission, a series of tests showed the closest possible results for different samples, only if the points were selected in the area where the signal intensity was in the range of 180-240 shades of gray. Thus, the most reliable results can be obtained for brighter regions. At the same time, when testing for the analysis of the reflection coefficient, the opposite picture was observed and the average range was chosen from 50 to 100 shades of gray, i.e. darker areas were selected for study. This is generally obvious, since when determining the refractive index, the object by its presence leads to a decrease in the final brightness of the emitter, and when determining the reflection coefficient, it is required that the background image be as dark as possible. This is necessary to enhance the contrast between the background radiation level and the signal level reflected from the sample walls.

Thus, because of the experiments, it was found that in the presented samples after irradiation, there is a completely distinguishable deterioration in the optical properties, according to a preliminary estimate, by 5-6%, more details about the nature of the change in the physical properties of the material can be learned with an increase in the dose of irradiation.

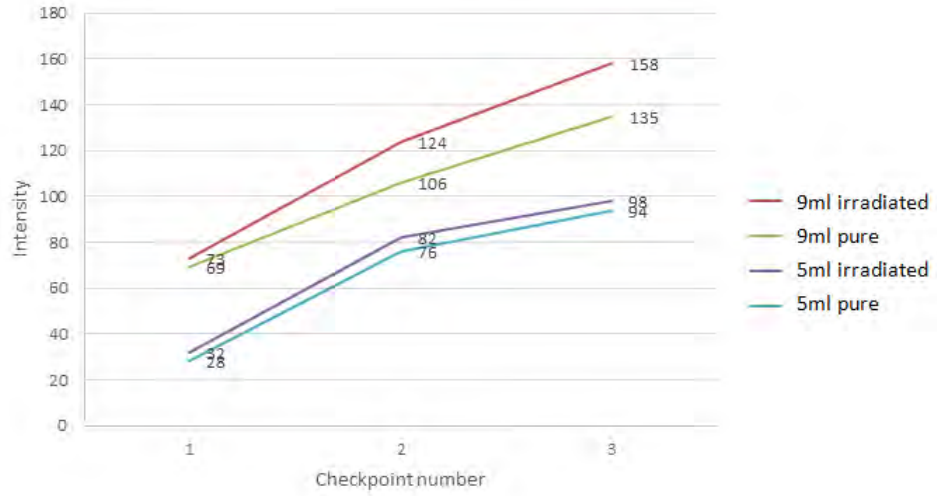

FIG. 5. Graph of the distribution of the radiation intensity of the light flux for points: 1 (100;230), 2 (280;300), 3 (410;370).

3. CONCLUSION

It has been established that exposure to irradiation of 5 kGy affects the transmission of visible light. According to the results of earlier IR spectroscopy, this effect is associated with a decrease in the number of C–H bonds [9]. The decrease in C-H bonds, apparently, is associated with the process of dehydrogenation of the test tube material, which in turn changes the optical properties of the object under study - leads to an increase in the refractive index and a proportional increase in the reflection coefficient.

ACKNOWLEDGEMENTS

The work was supported by the IAEA (IAEA) under contract CRP F23035.
Conflict of Interest: The authors declare that they have no conflict of interest.

REFERENCES

[1] Controlling of Degradation Effects in Radiation Processing of Polymers, IAEA-TECDOC-1617, IAEA, Vienna (2009).

[2] Filippova, E.K., Karpov, D.A., Gradoboev, A.V., Sokhoreva VV, Pichugin, V.F. “Influence of low-temperature plasma and γ radiation on the surface properties of PET track membranes”, Inorganic Materials: Applied Research **5** (2016) 664–672.

[3] Kornev, I.I., Sterilization of medical products in medical institutions, ANMI, Moscow (2000).

[4] GOST R 53696-2009. Non-destructive control. Optical Methods: Terms and Definitions, Moscow, 2010.

[5] Stankevich, V.M., Pleskachevsky, Yu.M., Smirnov, V.V., “Ionizing Radiation Effect on Physico-Mechanical Characteristics of Thermoplastic Polymer Materials”, 4-th International Conference «Interaction of Radiation with Solids», October 3-5, 2001, Minsk, Belarus (2001)

[6] Klinshpont, E.R., Milinchuk, V.K., Tupikov, V.I., “Radiation resistance of polymer materials”, Atomic Energy 76 **5** (1994) 422–426.

[7] Prasad, Sh.G., De, A., De, U., “Structural and Optical Investigations of Radiation Damage in Transparent PET Polymer Films”, International Journal of Spectroscopy, **1** 7 (2011) 1–4. DOI:10.1155/2011/810936

[8] Handbook of engineering materials, Volume 4. Gosgortekhizdat, Leningrad (1960).

[9] Sharapova, V.A., Kamantsev, I.S., Shveikin, V.P., Ivanov, V.Yu., Ryabukhin, O.V., “Investigation of the influence of accelerated electron irradiation on the physical properties of polyethylene terephthalate”, Letters to the journal of technical physics, **5** 48 (2022) 30–33 DOI: 10.21883/PJTF.2022.05.52153.19068

MODELLING OF THE RADIATION AND SHIELDING OF THE SOUTH AFRICAN ISOTOPE FACILITY USING FLUKA

A. H. BARNARD
iThemba LABS
Cape Town, South Africa
Email: hbarnard@tlabs.ac.za

P. BEUKES, J. I. BROODRYK, G. F. STEYN, I. L. STRYDOM
iThemba LABS
Cape Town, South Africa

Abstract

The South African Isotope Facility (SAIF) is a radioisotope production facility currently under construction at iThemba LABS in Cape Town. A commercial 70 MeV proton cyclotron from IBA with a number of beam lines equipped with isotope production stations are being installed in retrofitted concrete vaults. The completion of SAIF will greatly increase the radioisotope production capability of iThemba LABS and enable the existing Separated Sector Cyclotron to be dedicated to nuclear research activities. As part of the design process of the SAIF facility, radiation and shielding calculations were performed using FLUKA to assess the expected dose levels for radiation safety purposes. An overview of the simulations is provided, discussing the FLUKA setup and initial validation simulations performed to gain confidence in the results. A more detailed discussion of some specific systems is given, specifically: A multi-layered iron-wax-lead neutron shield of the isotope production stations; a louvre type shield for use in pre-existing air ducting labyrinths; access labyrinths used by a robotic target transport system; and radiation leakage through gaps between the concrete roof beams in the vaults. As part of an experimental validation campaign an experiment to assess the leakage rate between the roof beams was performed in an existing vault and this is compared to the FLUKA predictions.

1. INTRODUCTION

The South African Isotope Facility (SAIF) is a new radioisotope production facility under construction at iThemba LABS in Cape Town, where it will replace an existing isotope production system based on the 34-year-old K=200 Separated Sector Cyclotron (SSC) [1]. The SAIF project, shown in Fig. 1, is being constructed in retrofitted concrete vaults and consists of a central vault containing a 70 MeV proton cyclotron from IBA as well as two production vaults located on opposite sides of the cyclotron vault. Each production vault is connected to the cyclotron vault with two beam lines, enabling four target stations to be served by the dual-port cyclotron. The completion of SAIF will greatly increase the radioisotope production capability of iThemba LABS, and enable the existing Separated Sector Cyclotron to be dedicated to nuclear research activities. As part of the design process of the SAIF facility, radiation and shielding calculations were performed using FLUKA to assess the expected dose levels for radiation safety purposes.

2. FLUKA SETUP

For these simulations the default PRECISIO card was used. This results in longer simulations, but produces the best results. This setting activates low energy neutron transport (LOW-NEUT card), and a particle transport threshold of 100 keV is applied for all species, except neutrons, which are transported down to thermal energies (PART-THR card). The physics cards consisted of COALESCE to activate coalescence and EVAPORAT to activate the new evaporation model with heavy fragmentation.

Substantial use was made of BIASING to speed up calculations through the thick shielding. Alternatively, a two-step method was used, where the phase space of radiation reaching a subregion was recorded in a first simulation and then a second simulation was run that sourced its primary particles by sampling from the previously recorded phase space. The recording was made using a USRBDX card and USERWEIG to run the fluscw.f function each time a particle crossed into the recording region (preferably a BLCKHOLE). The fluscw.f function writes the particle details to a recording file. A second simulation then selects primary particles by sampling randomly from the recording file. This is done using a modified version of the source.f function. The recorded

particles can also be used to construct a more continuous phase space, for example by Gaussian fitting. Selecting primary particles from a continuous phase space gives smoother results.

Scoring was performed using USRBIN and AUXSCORE was used to select the EWT74 option which used worst case fluence to dose equivalent conversion coefficients.

3. SHIELDING OF THE SAIF VAULTS

The main sources of radiation include the cyclotron due to a conservatively assumed 5% beam loss (37.5 uA) on the cyclotron walls, beam striking Faraday cups in the cyclotron vault (50 uA), Faraday cups in the production vaults (5 uA) and the target bombardment stations (375 uA). In all these cases the maximum proton energy of 70 MeV is used. The main shielding is provided by three concrete vaults shown in Fig. 1, with nominally 3 m thick walls, and removable concrete roof beams that can be stacked in 0.75 m high layers, shown in Fig. 2. The cyclotron vault roof will be 2.25 m thick, while the production vaults have 1.5 m thick roofs. Additionally, the isotope production stations are provided with a multi-layered local shielding system, reducing the dose and activation of material in the production vaults by a factor of around 1000.

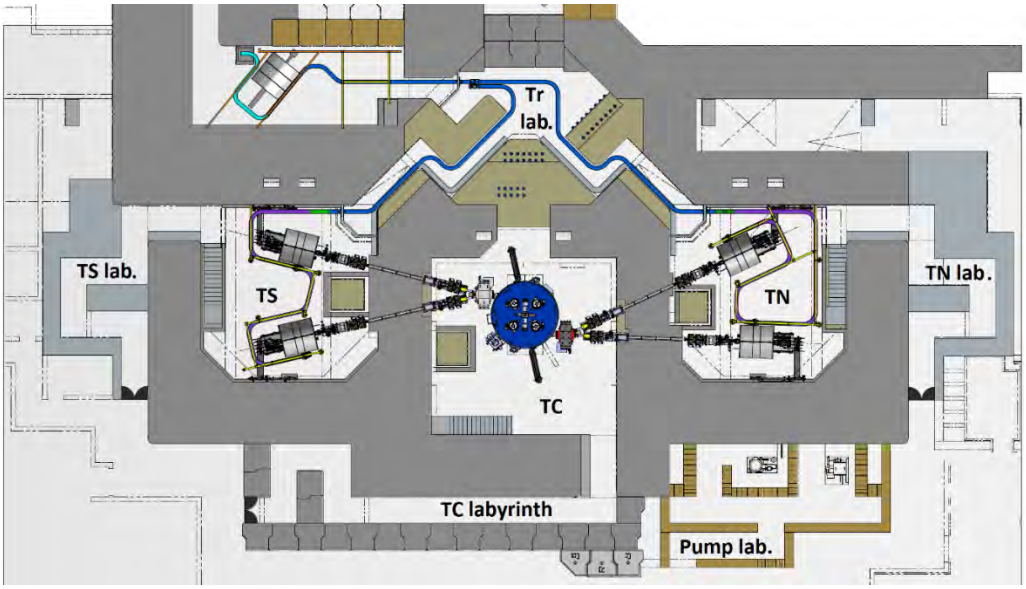

FIG. 1: Layout of SAIF facility, showing the central cyclotron vault (TC) and two production vaults (TN and TS) containing the four isotope production stations. The access labyrinths to the vaults (TS lab, TC lab, TN lab) and the robotic trolley labyrinth (Tr lab) are shown as well as the pump room and its labyrinth (Pump lab).

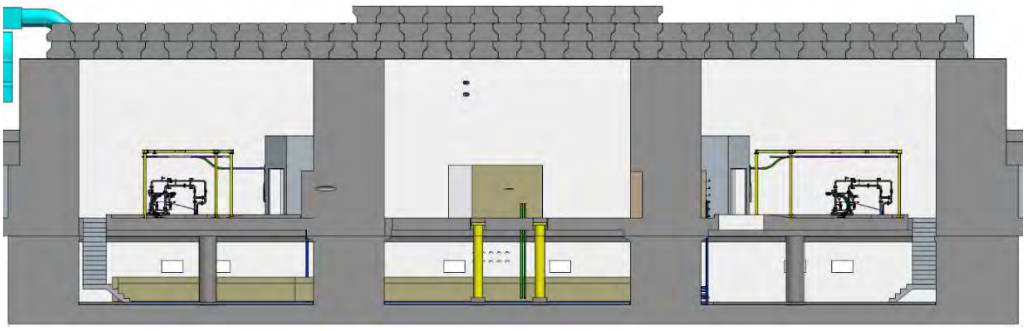

FIG. 2. Vertical section of the SAIF vaults showing the roof thicknesses as well as the vaults and the basements.

The concrete vaults are existing structures previously used for particle therapy. New concrete access labyrinths have been constructed, both for people and for a robotic target transporter. Modifications to the existing air ducting labyrinths cast into the walls have been necessary to improve the shielding.

4. INITIAL VALIDATION OF THE FLUKA SIMULATIONS

To check if the FLUKA simulations of the concrete vaults were producing reasonable results, a few initial simulations were performed and the results compared to measurements and published results.

4.1. Source term and attenuation length of neutrons in concrete

A Fluka model was made of a 70 MeV proton beam striking a thick copper target, with the resulting neutron radiation passing through a concrete wall. The neutron dose equivalent in the forward direction was measured at various depths in the wall, and the result was a near exponential decrease, corresponding to an attenuation length of 44 g/cm^2. This corresponded well to published attenuation lengths for various elements present in concrete, ranging from 39-43 g/cm^2 [2]. The source term in the forward direction (the dose equivalent produced per proton striking the copper target) was simulated to be 0.75 x 10^{-16} Sv/proton which is about 55% of the published value. This shows the FLUKA simulations to be accurate to within a factor of about two.

4.2. Neutron dose rate of a proton beam striking a Faraday cup

A physical experiment was performed using the SSC at iThemba LABS where a 10 uA 66 MeV proton beam was stopped on a number of copper Faraday cups [3]. The dose rate was then measured on the outside of concrete slabs with thicknesses ranging from 1.5 m to 2 m. This setup was modelled in FLUKA, and a comparison between the measured and simulated results is given below in Table 1. In these cases, FLUKA is accurate to within less than a factor of two.

TABLE 1. EXPERIMENTAL AND FLUKA DOSE RATES FOR DIRECT CONCRETE PENETRATION

Location	Concrete Thickness (cm)	FLUKA dose rate (uSv/h)	Experimental dose rate (uSv/h)	Difference (%)
FC-11X	150	260	210	24
FC-4I	150	260	190	36
FC-7I	200	7	6	17

5. MULTI-LAYERED NEUTRON SHIELD IN THE ISOTOPE PRODUCTION STATION

The radiation emitted by the 375 uA 70 MeV proton beam striking the isotope production target is attenuated by a movable local shield, referred to as the isotope production station (IPS), that almost encloses the target. The IPS is made up of three layers: 50 cm iron, 20 cm borated paraffin wax, and finally 4 cm lead [4]. The iron slows down fast neutrons, the wax thermalizes the neutrons and most of the neutrons are then absorbed by boron, resulting in a soft gamma, while a small fraction of the neutrons is absorbed by hydrogen, resulting in a hard gamma. These gammas are attenuated by the final lead layer. Previous studies have optimised the thickness of the layers to reduce the overall dose, but considered simplified geometries [5]. The practical construction of the IPS introduced several potential weaknesses in the shielding, and these had to be modelled carefully to obtain a suitable design.

5.3. Gaps between movable sections

The IPS consists of three sections, a front, middle and rear section, and they can slide along rails to open the station in order to insert or extract a target, or for other maintenance. This can result in gaps between the sections, through which radiation can escape, especially since the large shape of the IPS means that manufacturing errors of around 5 mm can be expected. The solution, determined using FLUKA modelling, is to step the mating surfaces where the sections meet to create a mini labyrinth, as shown in Fig. 3.

5.4. Access for helium supply pipes

The beam pipe entering the IPS is terminated by a set of two helium cooled vacuum windows located inside the shielding. A supply and return pipe provide the helium gas, and a suitable route for these pipes is required.

The access route must not deteriorate the shielding, but it must also be as simple as possible, since the vacuum window assembly will need replacing from time to time. The solution is to use straight pipes, running perpendicular to the beam, but offset 13 cm sideways and 5 cm backwards from the target, as shown in Fig. 3. The pipes also point downwards, directing escaped radiation into the floor.

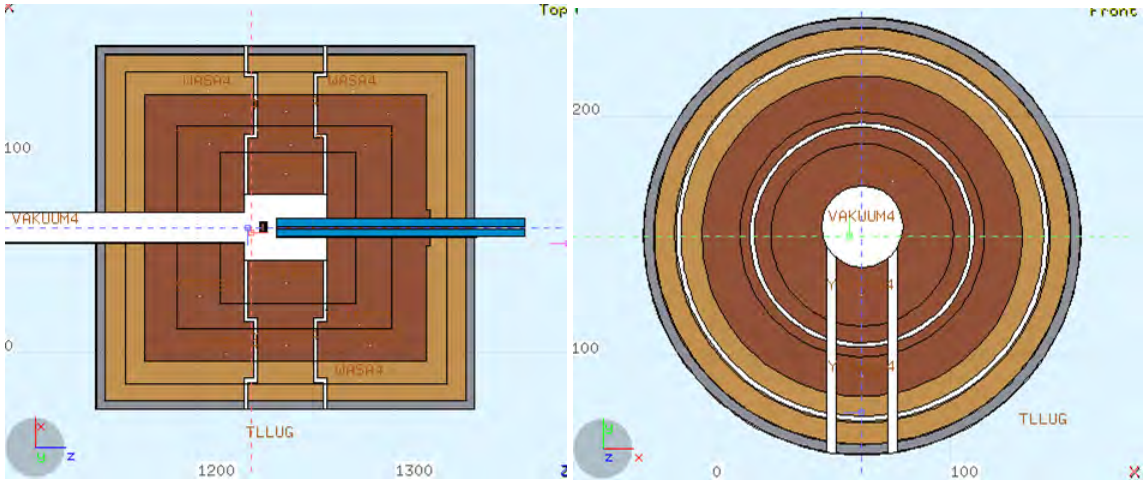

FIG. 3. – Cross sections of the IPS. Left: the three shielding sections (front, middle and rear) with their stepped mating pattern produces small labyrinths (white lines). Right: helium access pipes entering the IPS in a straight line but offset from the target and pointing downwards.

5.5. Access for helium supply pipes

The beam pipe entering the IPS is terminated by a set of two helium cooled vacuum windows located inside the shielding. A supply and return pipe provide the helium gas, and a suitable route for these pipes is required. The access route must not deteriorate the shielding, but it must also be as simple as possible, since the vacuum window assembly will need replacing from time to time. The solution is to use straight pipes, running perpendicular to the beam, but offset 13 cm sideways and 5 cm backwards from the target, as shown in Fig. 3. The pipes also point downwards, directing escaped radiation into the floor.

5.6. Water cooling pipes

The water cooling to the target is provided by an inlet and outlet pipe, positioned concentrically around each other, and pointing in the forward direction away from the target, as shown in Fig. 4. From a shielding point of view this is not ideal, since a lot of fast neutrons will be ejected down the water-cooling pipes, and the water will not provide as good shielding as iron. On the other hand, the water-only section is long and narrow, providing a small solid angle as seen from the target, and the water will scatter some neutrons into the surrounding iron. The leakage was modelled and found not to be significant. Overall, the main source of radiation leaving the IPS remains the neutrons emitted backwards from the target down the beam pipe as shown in Fig. 5.

6. LOUVRE TYPE SHIELD FOR USE IN PRE-EXISTING AIR DUCTING LABYRINTHS

The existing concrete vaults contain cast-in air ducting labyrinths. Simulations showed that these labyrinths were inadequate for stopping neutrons. Different possibilities were considered, ranging from adding more concrete to extend the labyrinths, to lining the inside walls of the vaults with an iron-plastic cladding to limit the neutrons entering the ducting. In the end it was decided to install a louvre type shield inside the air ducting where the existing ducting exits the vaults. The louvres are made of mild steel, and are shown in Fig. 6, while their effect on the radiation travelling down the air ducting is more-or-less equivalent to 50 cm of concrete, as shown in Fig. 7.

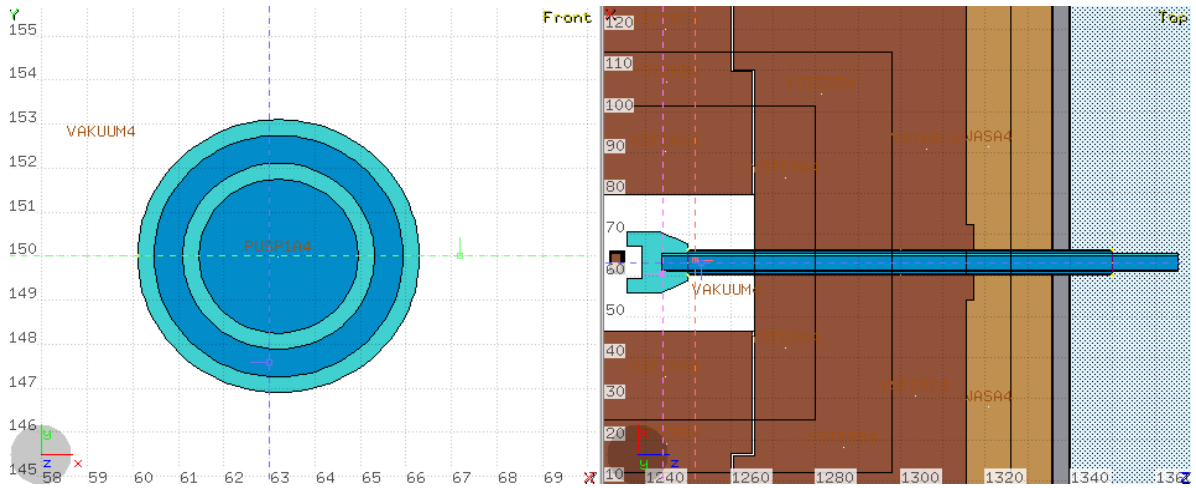

FIG. 4: Concentric water pipes leave the IPS in the forward direction, potentially weakening the shielding. The outer light-blue colour is stainless steel, and the inner dark-blue colour is water. In the right hand picture the forward direction is to the right.

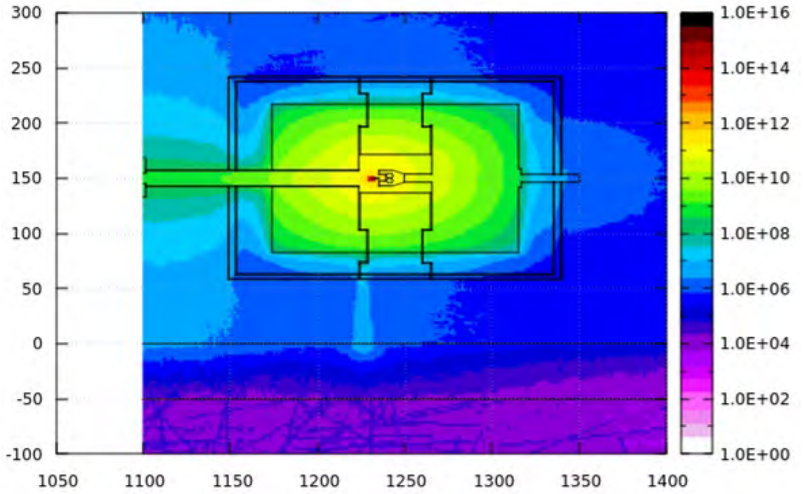

FIG. 5: Dose rate (uSv/h) due to a 375 uA 70 MeV proton beam on the target in the IPS. There is no discernible leakage through the mating labyrinth. The dose rate in the forward direction (to the right) is similar to the dose rate vertically upwards, indicating that the leakage through the water pipes is not significant. The leakage through the Helium access pipes is noticeable but is directed straight downward into the concrete floor.

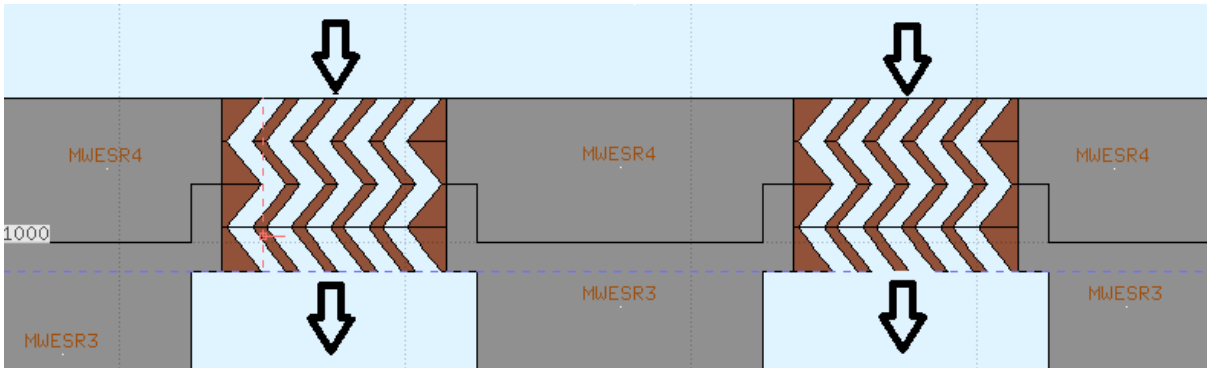

FIG. 6: The louvres (brown) are installed in existing ducting to allow for easy air passage (shown by arrows) while shielding against slow neutrons.

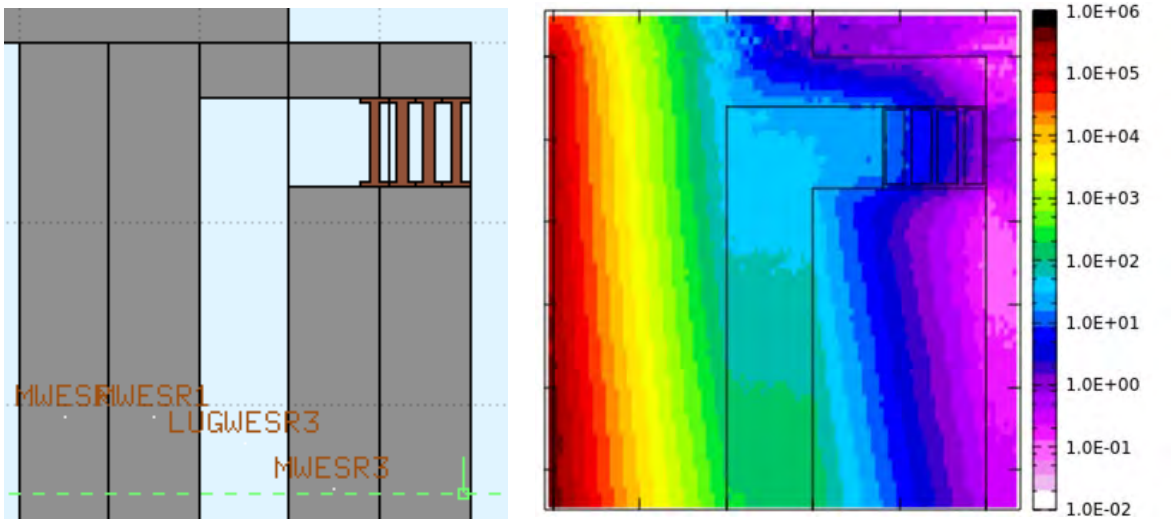

FIG. 7. – Left: This shows a cross section of the air ducting labyrinth inside a concrete wall, with the louvre shielding installed (top right of image). Right: Dose rate (uSv/h) due to 5 uA 70 MeV protons on a Faraday cup in the TS vault. The louvre provides shielding reduces the dose rate by a factor of 20.

7. ACCESS LABYRINTHS USED BY ROBOTIC TARGET TRANSPORT SYSTEM

The IPS is served by a robotic trolley that transports activated targets between the production vaults and hot cells located in a different part of the SAIF facility. The section of the route where the trolley enters and leaves the production vault is referred to as the trolley labyrinth. The trolley labyrinth also serves as a passageway for access between the different vaults, when people are transporting activated components and do not wish to leave the red-classified radiation area. The trolley labyrinth should therefore prevent radiation from travelling between any of the three areas that it is simultaneously serving. Fig 8. Shows the calculated radiation travelling through the trolley labyrinth during normal operation of one of the production vaults, while Fig 9. shows the gamma radiation from a fully irradiated target as it is being transported along the trolley labyrinth.

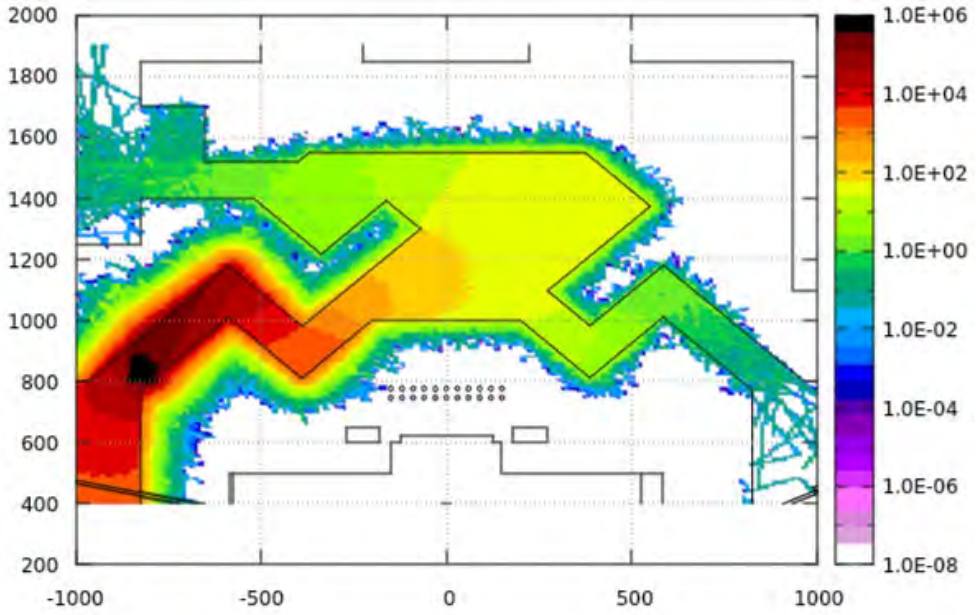

FIG. 8: Total dose equivalent (uSv/h) from 5 uA 70 MeV protons on a Faraday cup in the TS vault. This is a two-step simulation with the secondary source located at the trolley labyrinth entrance. The dose in the adjacent rooms is less than 1 uSv/h.

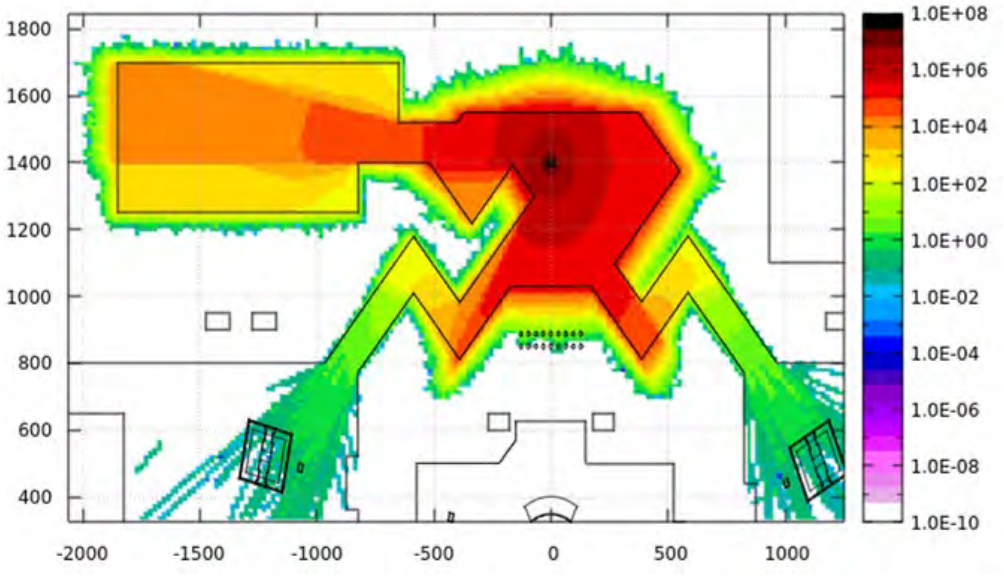

FIG. 9: Total dose equivalent (uSv/h) from 160 Ci of 22Na. This simulates the maximum dose expected when transporting a fully irradiated target through the trolley labyrinth.

8. RADIATION LEAKAGE THROUGH GAPS BETWEEN CONCRETE ROOF BEAMS

The roofs of the vaults consist of stacked interlocking concrete beams. While the beams provide adequate vertical shielding, some radiation can escape through small gaps between the beams where they don't interlock perfectly. A physical experiment was performed at the SSC vault at iThemba Labs, where a 10uA 66MeV beam was stopped on a copper Faraday cup, and the leakage along an inter-beam gap was measured. This was found to be 75 uSv/h, which is significant. A long round sandbag was then inserted into the gap to various depths, and the dose rate was recorded outside the gap. For a 1 m bag the dose rate was reduced to 6 uSv/h, which is a 10-fold reduction, and provides an easy solution to this shielding problem.

This situation was also modelled in FLUKA, which was challenging since only a very small fraction of the neutrons in the vault escaped along the inter-beam gaps. The FLUKA simulation therefore made use of the two-step phase-space sampling to focus only on the region of interest, and this was further augmented with importance biasing in the gap and surrounding material. In agreement with the experimental observations it was found that the only significant escape of radiation was between the bottom layer of roof beams and the walls on which they rest. The results of these simulations and a comparison with the experimental values are shown in Table 2 while a plot of the radiation escaping down the gap is shown in Fig. 10.

TABLE 2. EXPERIMENTAL AND FLUKA DOSE RATES FOR LEAKAGE ALONG BEAM GAPS

Length of sand bag in inter-beam hole (cm)	FLUKA dose rate (uSv/h)	Experimental dose rate (uSv/h)	Difference (%)
0	35	75	53
50	13	24	45
100	3	6	50

9. CONCLUSION

FLUKA has proven to be an extremely useful design tool during the SAIF project. Initial validation tests provided confidence that the program is being used correctly and producing reliable results. From these tests it was clear that the FLUKA results correspond to actual measurements within a factor of 2 to 3. FLUKA simulations have assisted in the design of numerous shielding components that would have been extremely difficult to evaluate in a different manner.

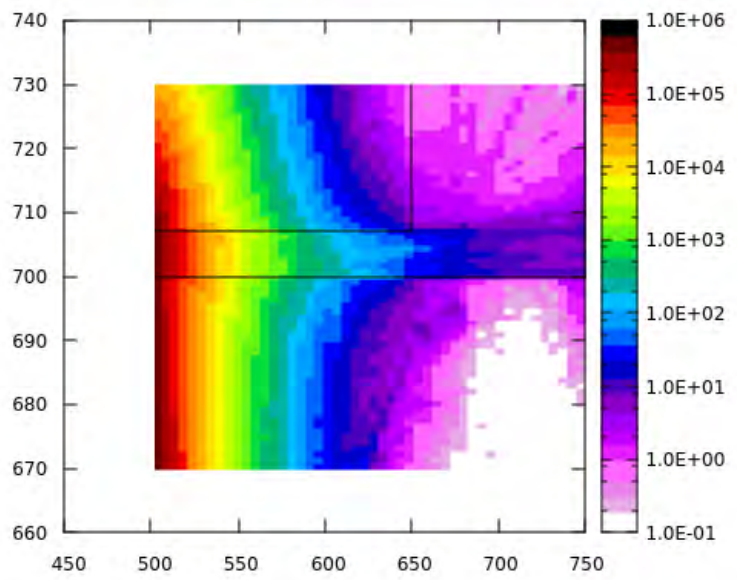

FIG. 10. – Total dose equivalent (uSv/h) of the radiation escaping through the gaps between the roof beams, produced by 37.5 uA (5% beam loss) 70 MeV protons striking the cyclotron vacuum chamber wall.

REFERENCES

[1] Conradie, J.L., et al., "The South African Isotope Facility", in Proc. 9th Int. Particle Accelerator Conf. (IPAC'18), Vancouver (2018) doi:10.18429/JACoW-IPAC2018-TUZGBF4

[2] Chen, C.C., et al., Calculations of neutron shielding data for 10–100 MeV proton accelerators, Radiation Protection Dosimetry, Volume 116, Issue 1-4, 20 December 2005, Pages 245–251, https://doi.org/10.1093/rpd/nci193

[3] Botha, A.H., iThemba LABS, unpublished data

[4] Steyn, G.F., et al., Development of new target stations for the South African Isotope Facility, Instruments 2.4 (2018): 29.

[5] Vermeulen, C. Production of Radionuclides with Medium Energy Protons with the Emphasis on Targetry, PhD dissertation, Stellenbosch University (2014)

AMAZON CERAMICS AND THEIR COLOR PALETTE – THE USE OF ION BEAM ANALYSIS TO DETERMINE THE PIGMENTS

S. C. LIMA, E. G NEVES, R. ALMEIDA*
University of São Paulo, Museum of Archeology and Ethnology,
São Paulo, Brazil
*ARQUEOTROP São Paulo
São Paulo, Brazil

M. A. RIZZUTTO, P. H. O. V. CAMPOS, C. L. RODRIGEUS, T. F. SILVA,
University of São Paulo, Physics Institute São Paulo/São Paulo, Brazil
Email: rizzutto@if.usp.br

Abstract

Despite the knowledge and discussion of archaeological polychrome ceramics in the Amazon for more than half a century, their material characterization still needs further studies and analysis. The description of these ceramics continues to be guided, in most cases, exclusively by the aesthetic aspect (macroscopic) and not by their technological and material characteristics (microscopic). In other words, despite the wide geographical distribution and variability of ceramic style, descriptions of polychrome ceramics are often restricted to observing the presence or absence of engobes and paints with colors mainly determined as white, red, and black. This work aimed to characterize the pigments and their use in ceramic decoration to collaborate with heritage conservation and archaeology in identifying specific technological choices. And investigate the variability of materials present that are so characteristic of Amazonian ceramics and their polychromies. Therefore, archaeometry analyses: binocular magnifying glass, Particle Induced X-ray Emission (PIXE) and Scanning Electron Macroscopic (SEM) were used to characterize a set of polychrome fragments from five archaeological sites in the Central and Northern Amazon region associated with the Polychrome Tradition of the Amazon – Tauary [1,2], Conjunto Villas [1,3], Vila Nova II [4], São João [5] and Hatahara [6,7,8] (spanning a broad spectrum from 100 BC. to 1300 A.D). The proposed analysis with ion beams comes from the better capability to separate the pictorial layers and thus better study the decoration technology of this set of ancient ceramic fragments. Measurements were performed with proton beams in the particle accelerator of the Institute of Physics of the University of São Paulo. Elements such as P, K, Ca, Ti, Fe and Mn were identified in different pigments, and their correlations will be discussed.

1. INTRODUCTION

Ceramics with polychrome decoration are commonly associated with the Amazon Polychrome Tradition and refers to a set of great technological diversity of elements that are dispersed over more than 6400km of distance, in more than 300 scientific sites and a chronology that spans over 1000 years [4,8,9,10]). The presence of black and/or red paint on the white engobe and fluted are techniques highlighted as recognisable elements of polychrome ceramic, despite its known regional variability [1].

When polychromies are discussed, every time refer to the presence of a pictorial layer, of some coating that covers the object. Whichever coating is used, a great deal of technical knowledge is required to handle behaviour differences between the clay body and coat which might lead to shrinkage, melting, etc., during the drying and firing of the artefact. The pictorial layers of the polychrome`s ceramics are white or red material (engobe), in direct contact with the ceramic body and completely covering it. And a layer of white and/or red and/or brown paint forming motifs with well-defined borders on the previous layer or directly on the ceramic paste, partially covering it.

Although we find studies that talk about the use of hematite for red colouring [11], such studies rarely address the variation of shades. The red paint can be made from rich iron clays or enriched with iron oxide. Several factors might influence the chromatic variation that the red engobe or painted motifs can present after firing, from orange to brownish and black. This variation can occur due to differences in composition and the firing atmosphere and temperature or the relationship with the thickness of the applied engobe layer. About the white pigment, usually applied as a thick coating layer, recurrent in Amazonian ceramics. Generally, the term 'tabatinga' is used generically to describe white clays or engobes with varying compaction, gloss and colour after fire treatment.

The description of the colour appears to be not enough to understand the complexity of materials and techniques involved in the polychrome surface finish of Amazonian ceramics. The dark brown painted motifs, often described as black, reveal the inaccuracy of such descriptions, which do not benefit from observing other physical features such as thickness, granulometry, or the transparency, for instance. And they also proved not to be sufficient for discussion of possible degradation and conservation processes [12] that can affect differently varied raw materials and techniques used in the manufacturing of ceramics

2. SAMPLE SET AND ANALYSIS PROCEDURE

Due to the immensity of polychrome ceramic sets and the scope of debates on archaeological cultural traditions in the Amazon, the sample set selected for this research is still restricted to feed broad discussions and does not have this intention. However, through a set of archaeometry analyses, we sought to see, on a new scale, the pictorial layer of ceramics associated with the Polychrome Tradition, searching for possible indicators of technological differences which could help in future studies of archaeological ceramics.

The archaeometry study was carried out with a set of 53 shards of polychrome ceramics from five archaeological sites – Tauary and Conjunto Vilas, located on Lake Tefé and São João on Lake Caiambé, all located in the middle of Solimões River; Vila Nova II, on the Negro River; and Hatahara, on the confluence of Negro and Solimões River, state of Amazonas, Brazil, shown in figure 1. The choice of the sample set was made in collaboration and with the support of researchers from the Laboratory of Archaeology of the Tropics - ARQUEOTROP, from the Museum of Archeology and Ethnology of USP to characterize the diverse colors of polychromies, as can see in figure 2.

FIG.1. Location of the archaeological sites in Amazonas State, Brazil.

The analysis of these fragments was firstly performed with macroscopic scale observation with a binocular magnifying glass, then with Particle Induced X-ray Emission (PIXE) and Scanning Electron Macroscopic (SEM)). The visible view used a binocular glass and a digital microscope Dino-Lite. The chemical element identifications in the paste and paint layers were performed using the external beam setup at LAMFI (Laboratory of Material Analysis by Ionic Beams) of the University of São Paulo, Physics Institute. The PIXE-LAMFI setup comprises

[13] two XR-100CR Si-PIN Amptek X-Ray Detectors [14] with 12.5μm thick beryllium window and a 4.4mm2 active area, 500μm depletion depth and 145eV resolution at the Mn − Kα line.

The PIXE technique with an external proton beam setup was chosen due to the non-destructive characteristic, penetration depth, measurements without any sample preparation, greater flexibility in positioning the fragment in relation to the detectors and the beam, and the possibility of using millimeter beams, and the reduction of thermal effects. The 2.4 MeV proton energy has an approximately 30-40 um depth profile. This low penetration is valuable for pigment analysis, allowing a better understanding of the materials that overlap forming the pictorial layer, that is, to see the ceramic stratigraphy. About 6 to 7 points were performed in different regions of the fragments, with areas of the paste, outer face (pigments and shadows) and inner face.

Scanning Electron Macroscopic (SEM) images were obtained in the Laboratório de Filmes Finos of the University of São Paulo, Physics Institute, using a system Jeol model 6460LV. The goal was to investigate the composition variability and thickness of pictorial layers and determine the formation of the engobe fusion with the ceramic mass during firing.

Engobe melting means that this fluid clay layer transforms during firing into a well-agglomerated and resistant coating, with a decrease in porosity that results in increased compaction and surface gloss. The sintering

of the engobe might occurs as a function of the granulometry (thin and homogeneity) and/or the composition and/or high temperatures maintained for a sufficient period during firing.

FIG. 2. Ceramics fragments from different cultures with color and shade variations

3. RESULTS AND DISCUSSIONS

The analysis of SEM and PIXE allows a better understanding of the adhesion of the engobe to the ceramics body and enables the identification of the element present in the colours and the mixture of them to produce the shadows.

3.1. Scanning Electron Microscopic

As an example of the visible image, figure 3 shows a binocular magnifying glass and SEM images. The ceramics Vila Nova II (VN111.11) presents brown and white polychrome thin layers of approximately 100□m thickness. Ceramics Vilas (CV991) also white and brown polychrome presents ~50-80μm.

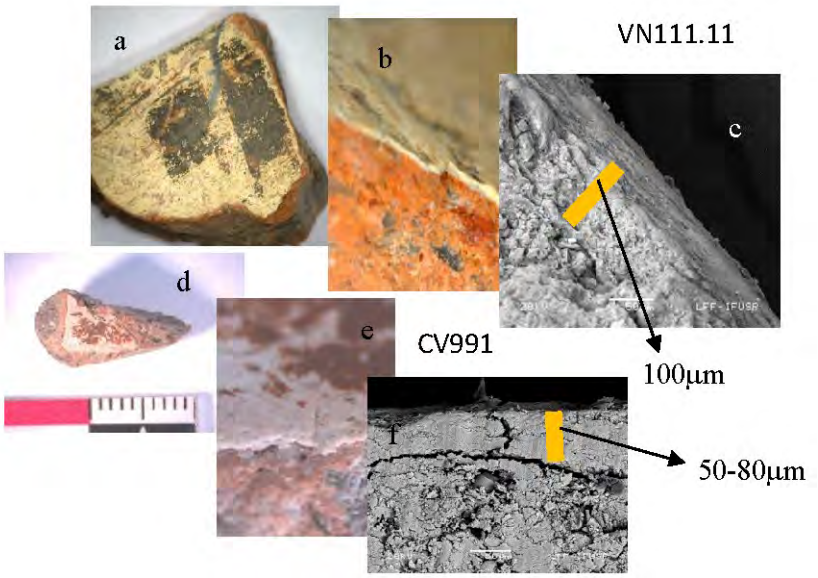

FIG. 3. Superior: Vila Nova II ceramic fragment (VN111.11) image with (a) visible, (b) binocular magnifying glass and (c) SEM with 20kV. Inferior, image with: (d) visible, (e) binocular magnifying glass, (f) SEM with 20kV.

3.2. White Pigments

It is common to observe that the polychromic ceramics of different cultures from Amazonia present a significant variability of texture and sintering of the pictorial layer, especially regarding the white engobe layer. Sometimes it is observed partial melting of the engobe, or semi-vitrification, with a resistant (sintered) final layer on the outer surface, but with a powdery texture in the layer just below, at its interface with the ceramic mass. Identifying this characteristic can be decisive for defining the adequate cleaning processes for the material since removing the external layer can expose the underlying layer of the engobe, which can solubilize it with water.

By characterizing major elements carried out by PIXE, it was possible to identify and differentiate the white engobe present in the fragments from the five archaeological sites. We observed a variation in thickness, compaction, and gloss related to the variability in the chemical composition of these engobes.

At the Vila Nova II archaeological site, we observed white engobes with clays rich in potassium and titanium, with varying proportions between these elements (figure 4 – VN111.11).

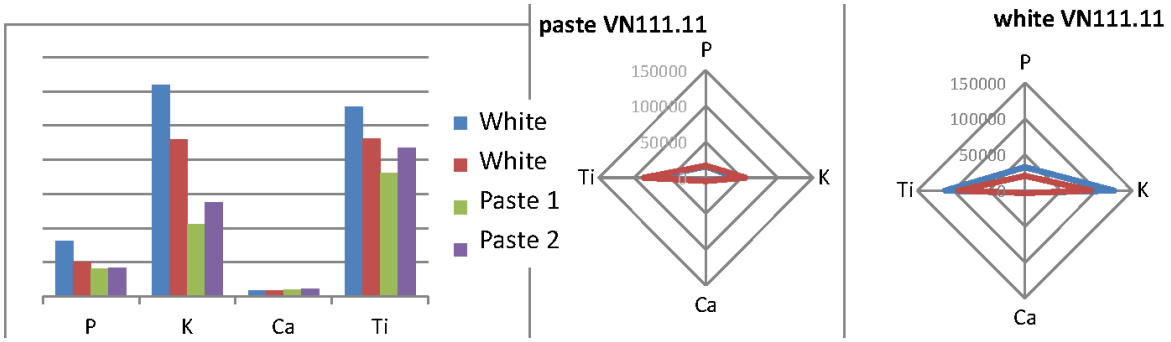

FIG. 4. Bar and star graphics showing the relative variation of the normalized integrated area of each element present in the PIXE spectra of each fragment from Vila Nova II

At the Conjunto Vilas archaeological site, we observed a clear difference between the white engobe of the fragments from the most superficial levels of the site stratigraphy (for example, the fragment CV991), rich in potassium and calcium, and titanium (figure 5) in the deeper levels, also with an inverse proportion relationship between calcium and phosphorus related with the ceramic paste. This same difference between white engobes of fragments from superficial and deep levels of the archaeological context was also observed in the fragments from the São João site.

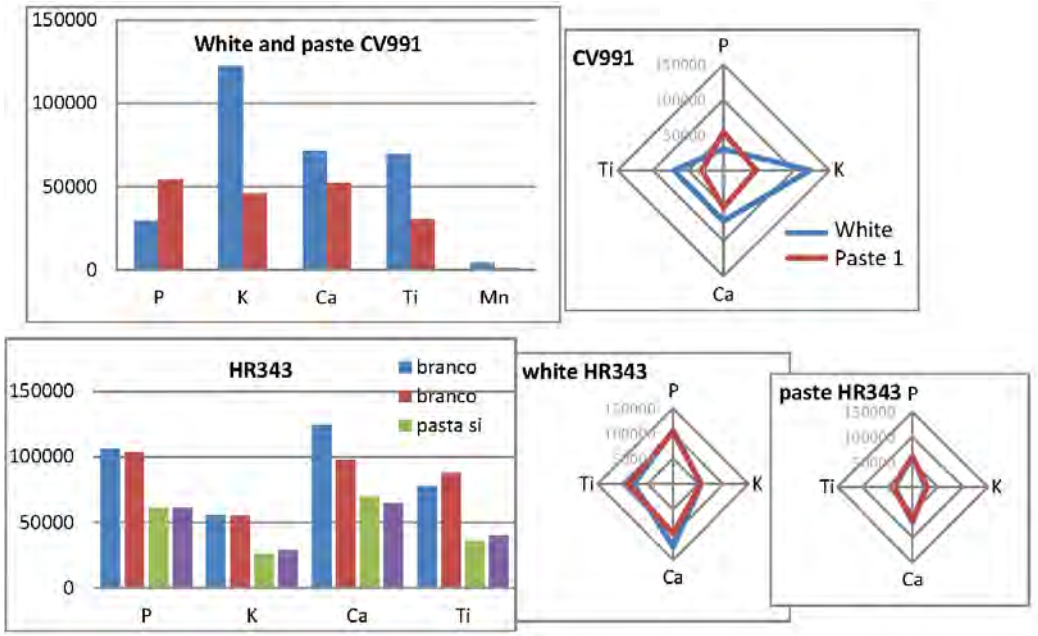

FIG. 5. Bar and star graphics showing the relative variation of the normalized integrated area of each element present in the PIXE spectra of each fragment. Upper: Conjunto Vilas (CV991). Lower: Hatahara (HR343)

The high calcium/phosphorus ratio in Hatahara samples is evident in the composition of the engobe (figure 5), and different from the composition of the paste (measurements were performed on the surface and ceramic core, which led to the exclusion of the hypothesis of contamination from the archaeological context, since the proportionality between these elements is only repeated in the measurements of the white engobe). Suggest the possibility of using hydroxyapatite in the composition of white engobe. From a physical-chemical point of view, this technological choice would make sense as hydroxyapatite acts as a strong fluxing material, considerably lowering the melting temperature of this engobe, which would then result in a more cohesive and less porous layer without changing other features.

3.3. Red, brown and black pigments

The red engobe can be made from rich clays and/or enriched with iron oxide and clayey ocher. Several factors influence the chromatic variation that the red engobe can present after firing, from orange to brownish and black. This variation can occur due to differences in composition but also due to the firing temperature, the relationship with the thickness of the applied layer, as well as the low presence of oxygen (in a reducing or partially reducing atmosphere), which can cause the transformation of the red to dark brown or black due to the transformation of ferric oxide (hematite) into ferrous-ferric oxide (magnetite) [15,16].

The analyses of the brown and red pigments of the same fragments analysed before are present in figure 6 below.

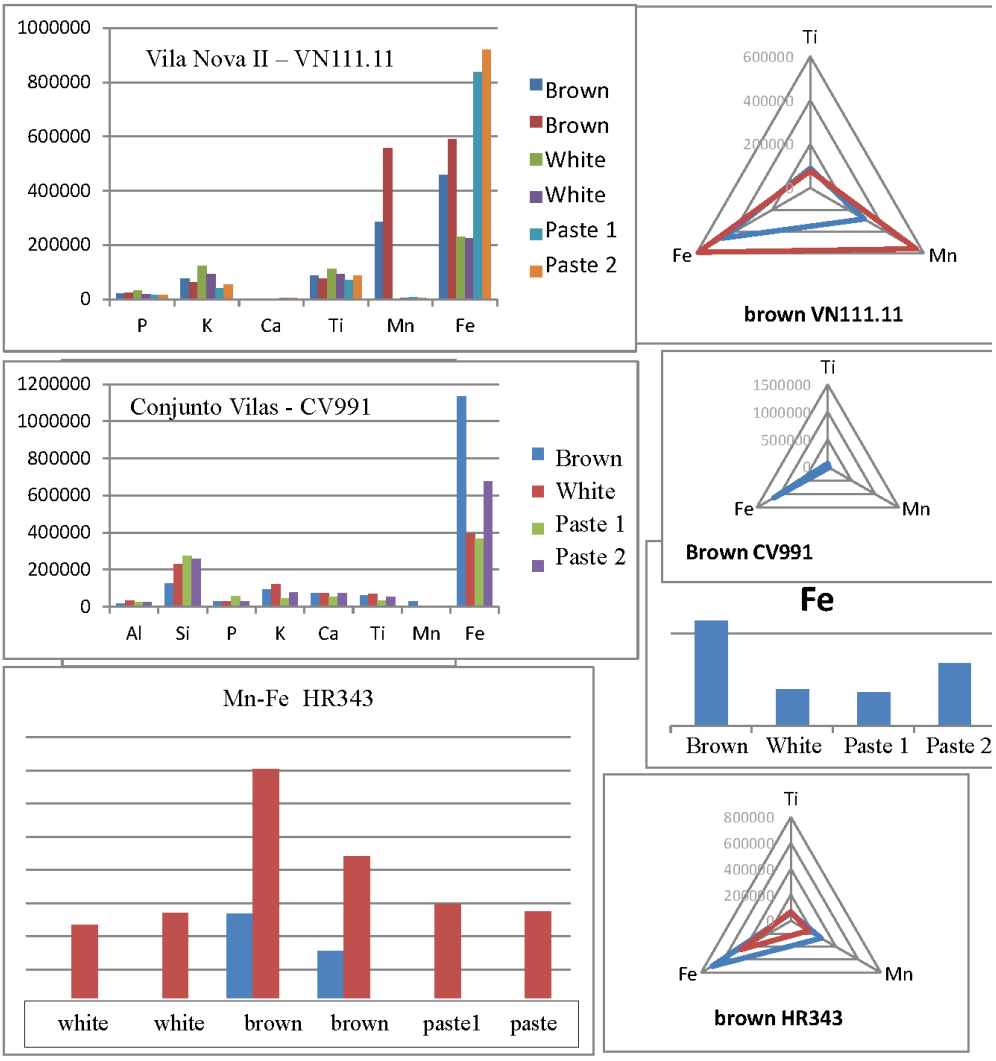

FIG. 6. Bar and star graphics show the relative variation of the normalized integrated area of each element present in the PIXE spectra of each fragment. Upper: Conjunto Vila NOVA II (VN111.11). Medium Vilas (CV991). Lower: Hatahara (HR343).

4. CONCLUSIONS

The different white measures by PIXE allow determine the relationship between some elements and allow to make some groups based on significant associations between the major elements, such as white composed with Ca + P, white with K and less quantity of Ti, Ca, P, white with the equality of Ti and K and finally white pigment with Ti > K. Nevertheless, it will be necessary to expand the set of fragments with the presence of white engobe analyzed to be able to infer more precisely about these relationships. It is essential to point out that due to the penetration and precision characteristics of the archaeometry analysis used (PIXE) and the thickness of these engobes, the results of the measurements carried out in the white engobe, and the ceramic paste are visibly different, that is, the paste does not have the same correlation proportionality between the same elements.

The same characteristics allow differentiating the brown pigment mainly into two groups, composed majoritarian of Fe, and another with a significant value of Mn. This difference in the chemical composition was correlated to macroscopic physical differences in compaction (fusion), gloss, and appearance of the paint layer. The brown layer with enrichment of iron present cast and good coverage, the layer with Mn is commonly grainier and more fragile.

ACKNOWLEDGEMENTS

This work was partially supported by Fundação de Amparo à Pesquisa do Estado de São Paulo (FAPESP) and Conselho Nacional de Desenvolvimento Científico e Tecnológico (CNPq), Brazilian research funding agencies. This work is a part of the projects: FAPESP No. 2014/01968-1 and No. 2018/12191-9 and INCT-FNA Proc. CNPq No. 464898/2014-5.

REFERENCES

[1] BELLETTI, J. S., "*A Arqueologia do Lago Tefé e a Expansão Polícroma"*. Dissertação de Mestrado em Arqueologia do Museu de Arqueologia e Etnologia da Universidade de São Paulo, 2015. doi: 10.11606/D.71.2015.tde-13102015-153201.

[2] OLIVEIRA, E., "*Potes que encantam: estilo e agência da cerâmica polícroma da Amazônia Central"*. Dissertação de Mestrado em Arqueologia, Museu de Arqueologia e Etnologia, Universidade de São Paulo, 2016. doi: 10.11606/D.71.2016.tde-21072016-152452.

[3] OLIVEIRA, L.S.S., ABREU, C.M., FERREIRA, F., LOPES, R., ALMEIDA, F., TAMANAHA, E., BELLETTI, J.S.,

[4] MACHADO, R., RIZZUTTO, M., SOUZA, D. "Archeometric study of pottery shards from Conjunto Vilas and São João, Amazon". *Radiation Physics and Chemistry, vol 167*. (2020) 10.8303.doi: 10.1016/j.radphyschem.2019.04.053.

[5] NEVES, E. G., "Sob os tempos do equinócio: oito mil anos de história na Amazônia central (6.500 ac – 1.500 dc)". Tese apresentada para Concurso de Título de Livre-Docente, Museu de Arqueologia e Etnologia, Universidade de São Paulo, São Paulo, 2012.

[6] LOPES, R.C.D.A. "A tradição policroma da Amazonia no contexto do Médio Rio Solimões (AM)". Dissertação de Mestrado em Arqueologia. Universidade Federal de Sergipe. 2018.

[7] MACHADO, J. "Montículos artificiais na Amazônia Central: Um estudo de caso do sítio Hatahara". Dissertação de Mestrado. Museu de Arqueologia e Etnologia, Universidade de São Paulo, São Paulo. 2005

[8] LIMA, H. P. "História das caretas: A Tradição Borda Incisa na Amazônia Central". Tese de Doutorado em Arqueologia. Museu de Arqueologia e Etnologia, Universidade de São Paulo, São Paulo. 2008. doi:10.11606/T.71.2008.tde- 22092008-125315

[9] TAMANAHA, E. K. "Ocupação Polícroma no Baixo e Médio rio Solimões, Estado do Amazonas". Dissertação de Mestrado em Arqueologia do Museu de Arqueologia e Etnologia da USP, 2012. doi: 10.11606/D.71.2012.tde-05062012-104830

[10] TAMANAHA, Eduardo K. & NEVES, Eduardo Góes. "800 anos de ocupação da Tradição Polícroma da Amazônia: um panorama histórico no Baixo Rio Solimões". Anuário Antropológico/2013, Brasília, UnB, 2014, 39 (2): 45-67.

[11] BELLETTI, J.S. "A Tradição Policroma da Amazonia", in BARRETO, C.; LIMA, H.P. & BETANCOURT, C. J. (eds) Cerâmicas arqueológicas da Amazônia: rumo a uma nova síntese. Belém, IPHAN: Ministério da Cultura, 2016.

[12] LEAL, R. S., “Estudo Arqueométrico de Cerâmicas Arqueológicas Marajoara”, Dissertação de Mestrado, Universidade Federal do Piauí, Teresina, 2005.
[13] LIMA, S. L., “Conservação Arqueológica: uma reflexão a partir de estudos de caso no Brasil”, Projeto FAPESP 2014/01968-1, 2014, Universidade de São Paulo
[14] Silva T, Rodrigues C, Added N, Rizzutto M, Tabacniks M, Mangiarotti A, Curado J, Aguirre F, Aguero N, Allegro
[15] P. et al. “Elemental mapping of large samples by external ion beam analysis with sub-millimeter resolution and its applications”, Nuclear Instruments and Methods in Physics Research Section B: Beam Interactions with Materials and Atoms 422, (2018) 68–77 doi:10.1016/j.nimb.2018.03.006
[16] XR-100CR SI-PIN X-ray detector. https://www.amptek.com/internal-products/ , Acess april, 2022.
[17] DI CAPRIO, N.C. “Ceramica in Archeologia 2: antiche tecniche di lavorazione e moderni metodi di indagine”. Roma: L’Erma di Bretschneider, 2007.
[18] SHEPARD, A. “Ceramics for the archaeologist”. Washington: Carnegie Institution of Washington. 1985.

International Conference on

Accelerators for Research and Sustainable Development:

From Good Practices Towards Socioeconomic Impact

23–27 May 2022

IAEA Headquarters, Vienna, Austria

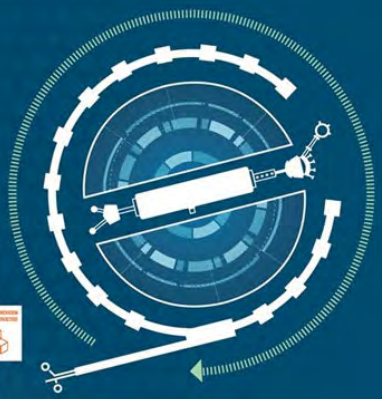

IAEA
International Atomic Energy Agency
Atoms for Peace and Development

CN-301
#Accelerators2022
www.iaea.org/events/accconf22

Particle accelerators

are tools for scientific discoveries and socioeconomic development

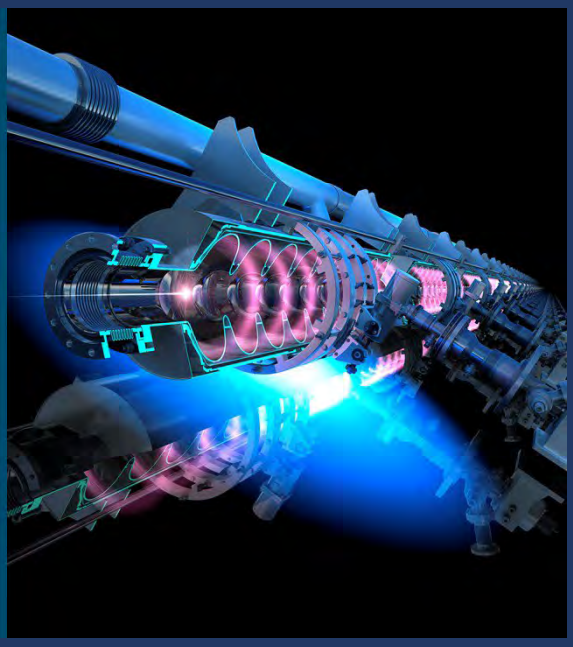

Cyclotrons

produce life-saving radioisotopes for cancer diagnosis and treatment

Tandem accelerators

monitor environmental pollution, support cultural heritage science and materials research

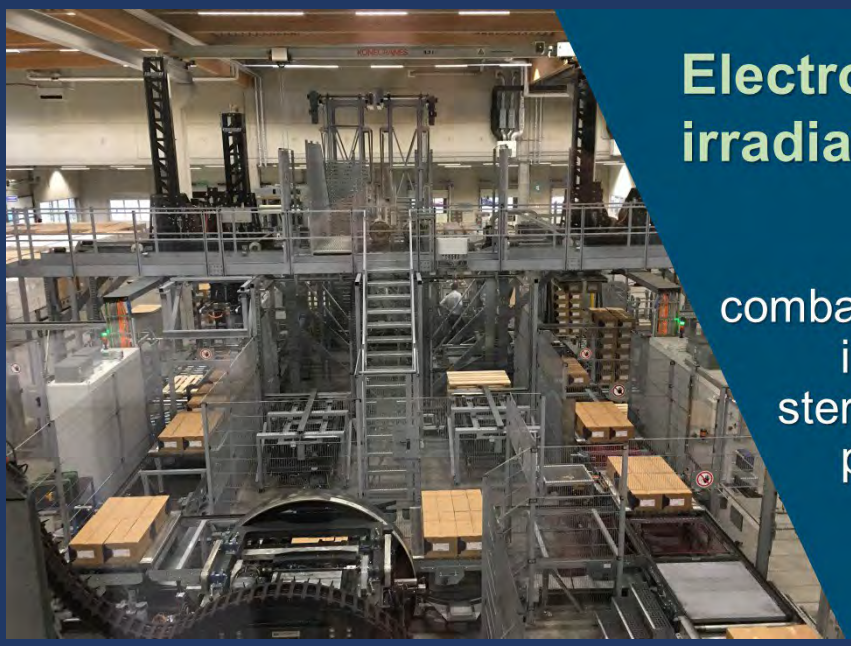

Electron-beam irradiators

combat food-borne illnesses and sterilize medical products and devices

Synchrotron light sources

reveal the structure of proteins and viruses and optimize vaccines and new drugs